Atmos
Program

unclas

ICSU

International Council of Scientific Unions

SCOSTEP

Scientific Committee on Solar-Terrestrial Physics
J. G. Roederer, President
W. I. Axford, Vice President
C. H. Liu, Scientific Secretary

MAP ORGANIZATION

MIDDLE ATMOSPHERE PROGRAM STEERING COMMITTEE
S. A. Bowhill, SCOSTEP, Chairman
K. Labitzke, COSPAR, Vice Chairman
C. H. Liu, SCOSTEP, Secretary

H. S. Ahluwalia, IUPAP
R. D. Bojkov, WMO
A. D. Danilov, COSPAR
J. C. Gille, COSPAR
I. Hirota, IUGG/IAMAP
A. H. Manson, SCOSTEP

T. Nagata, SCAR
R. G. Roper, IUGG/IAMAP
P. C. Simon, IAU
J. Taubenheim, IUGG/IAGA
T. E. VanZandt, URSI
R. A. Vincent, URSI

MAP STANDING COMMITTEES

Data Management -- G. Hartmann and I. Hirota, Co-Chairmen
Publications -- Belva Edwards, Chairman

MAP STUDY GROUPS

MSG-5 Ions and Aerosols, F. Arnold and M. P. McCormick, Co-Chairmen
MSG-8 Atmospheric Chemistry, G. Witt, Chairman
MSG-9 Measurement of Middle Atmosphere Parameters by Long Duration
        Balloon Flights, J. E. Blamont, Chairman

MAP PROJECTS

	Coordinator		Coordinator
AMA:	T. Hirasawa	MAC-SINE:	E. V. Thrane
ATMAP:	J. M. Forbes	MAE:	R. A. Goldberg
DYNAMICS:	K. Labitzke	MASH:	A. O'Neill
GLOBMET:	R. G. Roper	NIEO:	S. Kato
GLOBUS:	J. P. Pommereau	OZMAP:	D. F. Heath
GOSSA:	M. P. McCormick	SSIM:	P. C. Simon
GRATMAP:	D. C. Fritts	SUPER CAMP:	E. Kopp
MAC-EPSILON:	E. V. Thrane	WINE	U. von Zahn

MAP REGIONAL CONSULTATIVE GROUP

Europe: M. L. Chanin, Chairman

MIDDLE

ATMOSPHERE

PROGRAM

HANDBOOK
FOR MAP

Volume 28

Extended Abstracts
Fourth Workshop on Technical and
Scientific Aspects of MST Radar
Kyoto, November 28 - December 2, 1988

Edited by
C. H. Liu
Belva Edwards

August 1989

CONTENTS

TECHNIQUES FOR STUDYING GRAVITY WAVES AND TURBULENCE

INTERCOMPARISON AND CALIBRATION OF WIND AND WAVE MEASUREMENTS AT VARIOUS FREQUENCIES

PROGRESS IN EXISTING AND PLANNED MST AND ST RADARS

HARDWARE DESIGN FOR MST, ST RADARS AND BOUNDARY LAYER/LOWER TROPOSPHERE PROFILERS

SIGNAL PROCESSING

DATA MANAGEMENT

THE EFFECTS OF SAMPLING STRATEGY ON ESTIMATES
OF THE MEAN VERTICAL VELOCITY

G. D. Nastrom
St. Cloud State University, St. Cloud, MN 56301

K. S. Gage and W. L. Ecklund
Aeronomy Laboratory, NOAA, Boulder, CO 80303

1. INTRODUCTION

The purpose of this paper is to examine the effects of various temporal sampling strategies on estimates of the time-mean vertical velocity from MST radar measurements. Because the spectrum of atmospheric vertical velocity covers a complete range of frequencies, some variance will be missed whenever the temporal sampling is not continuous. This unresolved, or missed, variance contributes to the uncertainty of mean values based on the available observations along with other effects such as aliasing of the observed frequency spectrum. In recent years there have been several studies which have used time-means of the vertical velocity. For example, Nastrom, et al.(1985), compared time-means of vertical velocity from MST radar measurements with large-scale values based on radiosonde data, and Larsen, et al.(1988), compared them with ECMWF model forecasts of vertical velocity. Balsley, et al. (1988) used time mean vertical velocities to study tropical motions. Strauch, et al. (1987), found that it is important to include the effects of large vertical motion in the measurements of the horizontal wind components from obliquely directed radar beams. For these and other purposes it is important to use the sampling strategy which will yield the mean value with the smallest possible uncertainty under given experimental constraints, and to estimate the magnitude of the uncertainty once a sampling strategy is selected. This paper will explore these issues.

Data used for this study are vertical velocities from the Flatland VHF radar. The radar operating parameters and examples of the data are given by Green, et al. (1988). Briefly, during the period of record used here, March through May, 1987, the radar was operated with one beam which was pointed vertically. Doppler spectra were averaged for about 2.5 minutes and then recorded on tape along with their moments. The available data are thus quasi-continuous in time as only a few seconds gap was missed each data processing and recording cycle. In practice, some

observations are missing due to insufficient signal-to-noise ratio of the doppler spectrum, or other problems such as contamination by aircraft. Also, there are occasional short gaps due to equipment malfunction. For the analyses of frequency spectra and the autocorrelation function given here a segment of data was not used at a given height if a gap longer than 10 minutes was found.

2. STATISTICAL FEATURES

The fluctuation of vertical velocity at Flatland is primarily due to short period gravity waves. This can be seen in the frequency spectrum (Figure 1) which shows that most of the energy falls between about 10 and 30 minutes period. The coordinates in Figure 1 are area preserving, i.e., the variance in a given frequency band is proportional to the area under the curve. From comparisons with a model of a spectrum of gravity waves subjected to doppler shifting by horizontal winds, Van Zandt, et al. (1989), conclude that the observed spectrum at Flatland is due mostly to gravity waves. This is in contrast to the spectra of vertical velocity at locations in or near mountains where the vertical velocity spectra show the effects of standing lee wave activity as reviewed by Ecklund, et al. (1986).

Because a large portion of the variance at Flatland is due to relatively high frequency variations we should expect that a relatively high sampling rate will be required to avoid large uncertainties in mean values computed from the observations. In Figure 1 we note that the peak variance is found at about 12 minutes period, and in order to avoid serious sampling problems we might expect that observations should be taken more often than about half this period. i.e., every 6 minutes or so. A more rigorous estimate of the time between independent observations can be obtained from analyses of the autocorrelation function as discussed next.

Figure 2 shows the autocorrelation function, R(t), at Flatland at 5 km for lags less than about 15 minutes and, for comparison, the R(t) functions at Poker Flat, Alaska, from Nastrom and Gage (1983). R(t) can be used to estimate the effective time between independent observations (T) using the relation (Leith, 1973)

$$T = 2 \int_0^\infty R(t) \, dt$$

(1)

where t is the lag; an important application of T is in computing statistical significance levels (Mitchell, et al.,
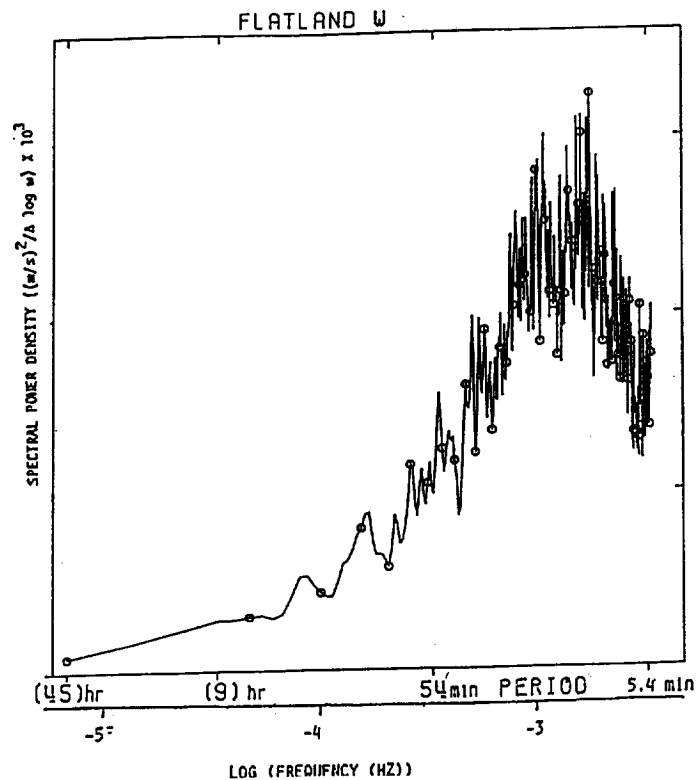
Figure 1. Average of 34 spectra of vertical velocity over 48-hour data periods at Flatland during March through September 1987, in area preserving coordinates.
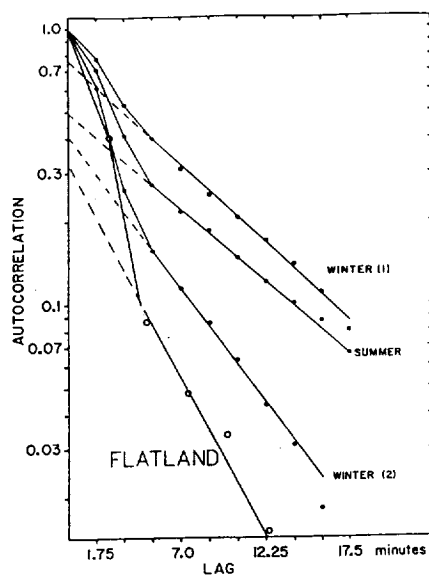
Figure 2. Autocorrelation function of vertical velocity at Flatland and at Poker Flat. See text.

1966). Nastrom and Gage (1983) found that at Poker Flat T ranged from about 15 minutes for the curves labeled "winter 1" and "summer", which represent active periods, to about 9 minutes for the curve labeled "winter 2", which represents quiet periods. There were not enough cases to prepare a summer curve for quiet periods, and only the curve for active times is shown. The curve labeled "Flatland" was prepared by averaging the autocorrelation functions from each six-hour period. The data were linearly interpolated to 153-second intervals and residuals from a linear trend line fit by least squares were used to compute R(t). Note that the average curve at Flatland decreases more rapidly than all curves from Poker Flat, suggesting that the vertical velocity at Flatland has a relatively short "memory". The semi-logarithmic plots in Figure 2 show that an appropriate analytic model after about lag 5-minutes is R(t) = c exp(-vt). At shorter lags the observed curves fall above this model, suggesting that the observed autocorrelation function is a mixed first-order moving average, first-order autoregressive process as discussed in more detail by Nastrom and Gage (1983). Using eq. 1 we estimate that T at Flatland is 5.1 minutes, which is less than for all the curves at Poker Flat. Also, we note that this estimate of 5.1 minutes is near the 6 minutes inferred above from Figure 1. This result does not mean that observations should be taken only each 5.1 minutes, but rather that, on the average, independent information is gained only at this rate. In fact, considerable uncertainty of the mean is found when only every-other observation is used (i.e., with data spaced about 5.1 minutes), as discussed next.

3. EFFECTS OF SAMPLING STRATEGY

The analysis approach we will use will be to form averages over one- ,two-, three-, and six-hour periods using the complete set of observations. These averages will be used as the standards for comparison. Next, the data set will be degraded to simulate various sampling strategies and the mean values thus obtained will be compared with the "true" mean values based on complete data. This procedure will give estimates of the uncertainty of measurement due to temporal sampling strategy. There are, of course, other sources of uncertainty, such as system limitations and the effects of spatial averaging, which must be considered in practice and which are beyond the scope of this study.

Four schemes were used to illustrate the effects of a strategy which uses incomplete sampling. Three of them use one-half of the data but in varying sized segments: the first uses alternate observations, the second uses data for every-other 10 minutes, and the third uses data for every-other 30 minutes. Each of these could simulate a strategy applied in a field experiment where, for example, the radar

was used to gather vertical data half of the time and oblique data half of the time. The fourth strategy uses data for the first 12 minutes of each hour, similar to the observation cycle of the data used by Larsen, et al. (1988). The results from these strategies will be labeled "alt obs", "0-10 min", "0-30 min", and "12 min" in Figures 3 and 4 and in Table 1.

RMS differences between mean values based on these four sampling strategies and the "true" mean computed from all available data are given in Figure 3 as functions of averaging period. Two patterns are evident in Figure 3: first, the RMS differences decrease with increasing averaging time. This decrease is consistent with the notion that the degraded observation cycles are sufficient to resolve long-period variations reflected in the left-hand tail of the spectrum in Figure 1, and that the variance due to longer periods thus contributes to the uncertainty of the mean only for shorter averaging periods.

The second pattern seen in Figure 3 is that larger gaps between data samples lead to larger uncertainty of the estimates of the mean. This effect reflects the increased spectral leakage caused by longer gaps as pointed out by Baer and Tribbia (1976). They found that there is reduced spectral fidelity for all frequencies higher than the frequency corresponding to the longest gap in a data sequence. The reduced spectral fidelity in the present context leads to greater uncertainty of the estimate of the mean value.

Finally, we note that the uncertainty of the estimate of the mean is relatively very large when only 12 minutes of data per hour are used. For a one-hour averaging period the RMS difference from the true mean is nearly 9 cm s^{-1} for this strategy, which is over half as large as the standard deviation of all data (about 14 cm s^{-1}).

Other statistical quantities can be used to illustrate the patterns seen in Figure 3. For example, Figure 4 shows the mean deviation, defined as the average absolute value of the difference between the true mean and that from the various sampling strategies, in a format similar to Figure 3. The patterns are consistent with those in Figure 3, although the numerical values of this measure of uncertainty are about two-thirds as large as the RMS values.

Another measure of the capability of one estimate of the mean to track the true mean is the linear correlation coefficient, r. Table 1 gives the values of r over N pairs of means with the true mean for the same averaging times and sampling strategies used in Figures 3 and 4. The percentage of variance in one variable explained by another is given by 100 r^2. Applying the results in Table 1 shows that for all
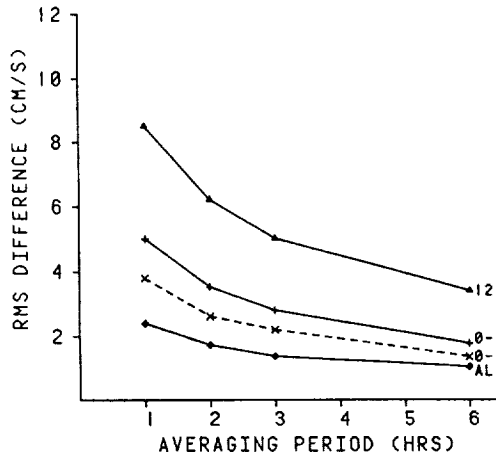
Figure 3. RMS difference of mean vertical velocity as a function of averaging time for various sampling strategies from the mean based on complete data.
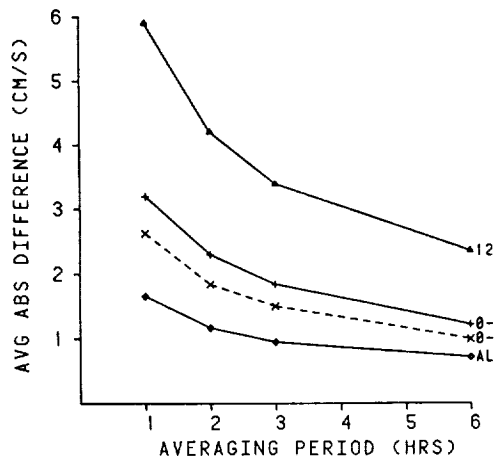
Figure 4. As in Figure 3, except for the mean deviation, i.e., the average absolute value of the differences in the means.

Table 1. Correlation of mean values from different sampling strategies with the "true" mean value.

AVERAGING PERIOD	1 hr	2 hrs	3 hrs	6 hrs
N	1951	652	652	308
ALT OBS	0.94	0.95	0.96	0.97
0-10 MIN	0.87	0.90	0.91	0.94
0-30 MIN	0.82	0.86	0.88	0.90
12 MIN	0.62	0.68	0.73	0.80

averaging periods the strategy of using alternate 2.5-minute data intervals accounts for 90 percent or more of the variance of the true mean in all cases here, while using every-other 10-minute period accounts for over 80 percent of the variance for averaging periods of 2 hours or more. At the extreme, using only the first 12 minutes of each hour the estimates of the means account for less than 50 percent of the variance of the true mean except for the 6-hour averaging period. These results show that the uncertainty of estimates of the mean vertical velocity is minimized when the average length of gaps in the data is minimized.

4. CONCLUSIONS.

Analysis of vertical velocities measured by the Flatland MST radar during the spring of 1987 has led to the following conclusions:

1. The autocorrelation function of vertical velocity resembles that expected for a mixed first-order moving-average, first-order autoregressive process.

2. The average time between independent observations in the data from Flatland used here is about 5 minutes.

3. The uncertainty of the mean value of vertical velocity decreases as the averaging period used to compute the mean increases.

4. The uncertainty of the mean value of vertical velocity increases as the length of gaps in the data increases. Because of this effect, every effort should be made to minimize gaps in samples of vertical velocity in future field programs.

These results are concerned only with temporal sampling, and in practice other effects such as instrument errors may require attention. In particular, they are based on data from a single station, and neglect any sampling uncertainties which might arise from spatial variability. It remains as a future experiment to compare averages from nearby stations as functions of averaging time, sampling strategy, and other variables to study such effects.

5. REFERENCES.

Baer, F., and J. J. Tribbia, 1976: Spectral fidelity of gappy data. Tellus, 28, 215-227.

Balsley, B. B., W. L. Ecklund, D. A. Carter, A. C. Riddle and K. S. Gage, 1988: Average vertical motions in the tropical atmosphere observed by a radar wind profiler on Pohnpei (7°N Latitude, 157° Longitude). J. Atmos. Sci., 45, 396-405.

Ecklund, W. L., K. S. Gage, G. D. Nastrom, and B. B. Balsley, 1986: A preliminary climatology of the spectrum of vertical velocity observed by clear-air doppler radar. J. Clim. Appl. Meteor., 25, 885-892.

Green, J. L., K. S. Gage, T. E. Van Zandt, W. L. Clark, J. M. Warnock, and G. D. Nastrom, 1988: Observations of vertical velocity over Illinois by the Flatland radar. Geophys. Res. Lett., 15,269-272.

Larsen, M. F., J. Rottger, and T. S. Dennis, 1988: A comparison of operational analysis and VHF wind profiler vertical velocities. Mon. Wea. Rev., 48-59.

Leith, C., 1973: The standard error of time-average estimates of climatic means. J. Appl. Meteor., 12, 1066-1069.

Mitchell, J. M., Jr., et al., 1966: Climatic Change. WMO Technical Note No. 79, Secretariat fo the WMO, Geneva, 79 pp.

Nastrom, G. D., and K. S. Gage, 1983: A brief climatology of vertical air motions from MST radar data at Poker Flat, Alaska. Preprints, 21st Conf. on Radar Meteorology, Edmonton, 135-140, Am. Meteor. Soc., Boston.

Nastrom, G. D., W. L. Ecklund, and K. S. Gage, 1985: Direct measurement of large-scale vertical velocities using clear-air doppler radars. Mon. Wea. Rev., 113, 708-718.

Strauch, R. G., B. L. Weber, A. S. Frisch, C. G. Little, D. A. Merritt, K. P. Moran, and D. C. Welsh, 1987: The precision and relative accuracy of profiler wind measurements. J. Atmos. Ocean. Tech., 4, 563-571.

Van Zandt, T. E., G. D. Nastrom, J. L. Green and K. S. Gage, 1989: Frequency spectra of vertical velocity from Flatland VHF radar data. J. Atmos. Sci., in preparation.

A METHOD FOR SINGLE-RADAR VORTICITY MEASUREMENTS?

M. F. LARSEN
Department of Physics and Astronomy
Clemson University
Clemson, SC 29631

INTRODUCTION

A common mode of operation for conventional meteorological precipitation radars has been the VAD (Variable Azimuth Display) method in which the antenna is kept at a constant zenith angle but scanned in azimuth. The measurements then provide the line-of-sight velocity as a function of azimuth for the particular elevation used in the scan. BROWNING AND WEXLER (1968) and WILSON AND MILLER (1972) have discussed the various flow-field parameters that can be derived from the measurements in some detail. For example, the best fit of the first harmonic to the line-of-sight velocity variation over 360° gives the direction and magnitude of the mean wind over the sampled area. The average of the line-of-sight velocities, i. e., the zeroth harmonic, indicates either a vertical velocity or a divergence in the horizontal flow. The wind field deformation can also be calculated from the measured parameters by using the best fit harmonic parameters. In theory, higher harmonics can be used to derive information about the second and higher order derivates of the flow over the sampled area, but the information has never been used in practice, to my knowledge.

Although the VAD technique provides a wealth of data, there are two disadvantages to the method. The first is that there is an ambiguity between the divergence and vertical velocity contribution to the measurements. The second is that the method does not provide any measurement of the vorticity, which is another fundamental flow-field parameter.

RADAR NETWORK VORTICITY MEASUREMENTS

The reason for the lack of information about the vorticity in a VAD measurement can be understood by considering the method for calculating the divergence and vorticity from wind measurements over a network consisting of balloons, radars, or other instruments that provide vector winds at a series of locations. We can use Stokes' Theorem to write

$$\int \vec{\nabla} \times \vec{V} \cdot d\vec{S} = \oint \vec{V} \cdot d\vec{l} \tag{1}$$

where $\vec{V}$ is the horizontal velocity and the integration for the line integral on the right is perimeter of the area used in the integral on the left. The vorticity on the left-hand-side of the equation can be brought outside the integral if the value is constant over the area. Then

$$\hat{\mathbf{k}} \cdot (\vec{\nabla} \times \vec{V}) = \frac{1}{A} \oint \vec{V} \cdot \vec{dl} \qquad (2)$$

where A is the total area and $\hat{\mathbf{k}}$ is a unit vector pointing vertically upward. If the vorticity is not constant, the calculated value becomes the average value over the area enclosed within the line integral.

A similar expression can be used to calculate the divergence of the horizontal wind, namely

$$\vec{\nabla} \cdot \vec{V} = \frac{1}{A} \oint \hat{\mathbf{k}} \cdot (\vec{V} \times \vec{dl}) \qquad (3)$$

where $\hat{\mathbf{k}}$ is a unit vector in the positive vertical direction. At least three vector wind measurements in a triangular array are needed to calculate the vorticity and divergence. The former quantity is then proportional to the line integral of the velocities around the triangle, and the latter quantity is proportional to the integral of the velocity component perpendicular to the line segments that define the triangle. The method can easily be extrapolated to include more than three stations.

If we consider a single radar instead of a network, equation (3) shows that the VAD measurement provides a measure of the divergence because the velocity component measured by the radar is always perpendicular to the direction in which it is scanning so that $\vec{V} \times \vec{dl}$ is obtained. Equation (2) requires the velocity component perpendicular to the beam direction, a quantity not provided by the VAD technique.

SPACED ANTENNA VORTICITY MEASUREMENTS

The discussion so far has focused on the VAD technique which usually involves measurements at a large number of azimuths with a mechanically-steered antenna. However, the Doppler method used in most MST radar or wind profiler measurements is in essence a simplified VAD. The number of independent beam directions then determines the number of flow field parameters that can be derived from the measurements. MST radars often utilize a vertical beam which gives the vertical velocity directly from the Doppler shift, and thus eliminates the vertical velocity/divergence ambiguity which is characteristic of precipitation radar VAD measurements. When the scattering is from precipitation, a vertical beam is not useful in resolving the ambiguity since the vertical velocity is the fall velocity of the precipitation and is not related to the divergence in the horizontal flow field. At least three off-vertical beams pointed along different azimuths are needed to measure the divergence in the horizontal flow, although often pairs of north/south and east/west beams are chosen in practice.

The Doppler method used for MST radar wind profiling cannot be used to obtain information about

the vorticity since it is a simplified form of the VAD method, and the latter technique provides no information about the rotation in the flow. Besides the considerations in the previous section, we can reach the same conclusion by considering a five-beam system directly. One beam is vertical and serves to eliminate the vertical velocity contamination in the off-vertical beams. The other beams are at the same off-vertical angle and pointed along the east, west, north, and south directions. The vertical component of the vorticity is given by

$$\hat{k}\cdot(\vec{\nabla}x\vec{V}) = \frac{\partial v}{\partial x} - \frac{\partial u}{\partial y} \tag{4}$$

where u and v are the eastward and northward velocity components, respectively. The coordinate system is such that x is positive toward east and y is positive toward north. The eastward and westward beams give information about the variation in the u velocity component but only along the x direction. The northward and southward beams give information about the variation of the v component but only along the y direction. Rotating the coordinate system in the horizontal plane obviously does not change the situation.

The spaced antenna technique has been described in detail by Larsen and Röttger (1989) and references therein. The method uses the cross-correlation of the signal in at least three spaced receivers deployed in a triangular array to determine the horizontal velocity of the diffraction pattern in the medium overhead. The diffraction pattern is created by the turbulent variations in the refractive index. Therefore, to the extent that the Taylor hypothesis holds, and the turbulence moves with the mean wind, the measurement gives the horizontal wind velocity. The Taylor hypothesis is also assumed to hold in the Doppler method measurements. The advantage of the spaced antenna method for vorticity measurements is that the velocity components obtained are perpendicular to the beam direction, and, therefore, would appear to be useful in the expression given in equation (2).

A triangular array is most common in spaced antenna measurements. First, consider three receiving antennas aligned so that one is at the origin of the coordinate system and the other two are spaced along the x and y axes. The diffraction pattern velocities measured along the x and y axes are then related to the flow velocity by the expressions (e. g., BRIGGS, 1984)

$$V_x = \frac{V}{\sin\phi} \tag{5a}$$

$$V_y = \frac{V}{\cos\phi} \tag{5b}$$

where V is the magnitude of the flow velocity and ϕ is the direction of the flow measured from north. The trace velocities are derived from the lag at which the cross-correlation in the signal in two of the antennas maximizes. The relevant expressions are

$$V_x = \frac{d_x}{\tau_x} \tag{6a}$$

$$V_y = \frac{d_y}{\tau_y} \tag{6b}$$

where d_x and d_y are the separation of the antennas in the x and y directions and τ_x and τ_y are the respective lags.

If $d_x = d_y = d$, which we will assume for the remainder, we have the following relationships,

$$\tan\phi = \frac{\tau_x}{\tau_y} \tag{7a}$$

$$\sin\phi = \frac{\tau_x}{\left(\tau_x^2 + \tau_y^2\right)^{1/2}} \tag{7b}$$

$$\cos\phi = \frac{\tau_y}{\left(\tau_x^2 + \tau_y^2\right)^{1/2}} \tag{7c}$$

The velocity components are then given by

$$v_x = V \cdot \sin\phi = d \frac{\tau_x}{\tau_x^2 + \tau_y^2} \tag{8a}$$

$$v_y = V \cdot \cos\phi = d \frac{\tau_y}{\tau_x^2 + \tau_y^2} \tag{8b}$$

The remaining analysis could be carried out by considering the three-antenna system, but a four-antenna system of the type shown schematically in Figure 1 will be used instead to simplify the
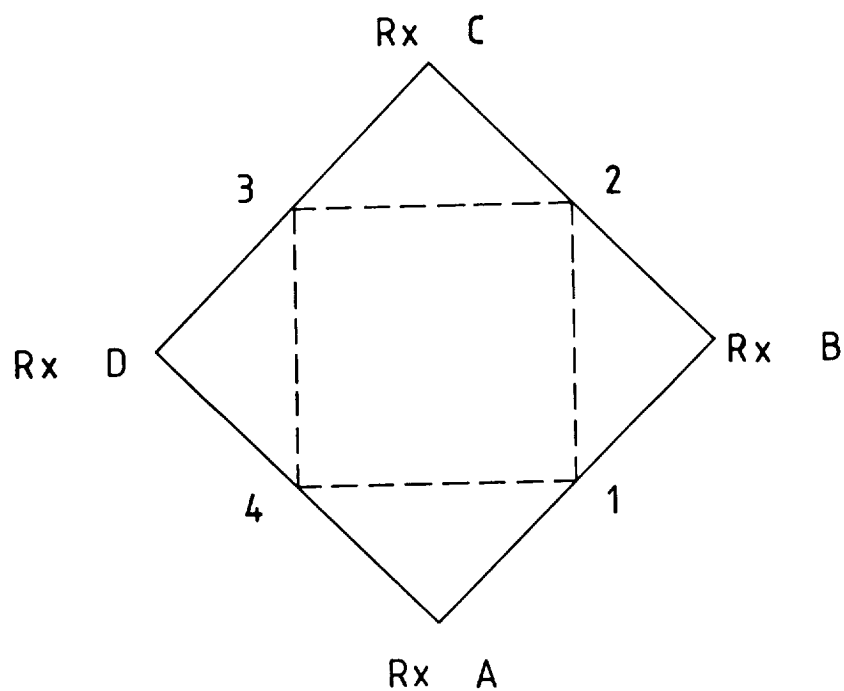
Figure 1. Schematic showing spaced antenna system with four receiving antennas labeled A, B, C, and D. The dashed lines join the points midway between two adjacent receiving antennas. The path of integration for the vorticity and divergence calculation is along the square outlined by the dashed lines.

expressions. The corresponding expressions for three spaced antennas will be of the same form but with different multiplicative factors.

Each combination of three receiving antennas (ABC, BCD, CDA, and DAB) yields the horizontal vector velocity representative of a point somewhere along the lines that connect the midpoints between the antennas, shown by the dashed lines in Figure 1. If the x axis is aligned parallel to the D-A direction and the y axis is aligned parallel to the D-C direction, the velocity component parallel to the dashed line segment 4-1, for example, will be given by

$$V_{diag} = v_x \cdot \cos 45^\circ + v_y \cdot \cos 45^\circ$$

$$= d \left(\frac{\tau_x + \tau_y}{\tau_x{}^2 + \tau_y{}^2} \right) \frac{\sqrt{2}}{2} \tag{9}$$

Then for one side of the embedded square defined by the dashed lines, the contribution is

$$\int \vec{V} \cdot \vec{dl} = \frac{\sqrt{2}}{2} d \cdot d \left(\frac{\tau_x + \tau_y}{\tau_x{}^2 + \tau_y{}^2} \right) \frac{\sqrt{2}}{2} = \frac{1}{2} d^2 \left(\frac{\tau_x + \tau_y}{\tau_x{}^2 + \tau_y{}^2} \right) \tag{10}$$

Sum the contributions from the four sides and divide by the area of the embedded square to get

$$\hat{k} \cdot (\vec{\nabla} \times \vec{V}) = \sum_{i=1}^{n} \left(\frac{\tau_i + \tau_{i+1}}{\tau_i{}^2 + \tau_{i+1}{}^2} \right) \tag{11}$$

where τ_1, for example, is the lag from Antenna A to Antenna B. The lags are taken to be positive in the counterclockwise sense from A to B, B to C, C to D, and D to A.

The spaced antenna vorticity measurements can be understood more directly by considering a flow directed from left to right in Figure 1. Rotation in the flow implies that the velocities in the upper half of the figure must be faster or slower than the velocities in the lower half. Antennas BCD will then

provide a velocity measurement that is different from the DAB measurement, and the difference between the two measurements is related to the vorticity in the flow.

The expression for the divergence involves the component of the velocity perpendicular to each of the four sides and leads, by similar arguments, to the expression

$$\vec{\nabla} \cdot \vec{V} = \sum_{i=1}^{n} \left(\frac{\tau_i - \tau_{i+1}}{\tau_i^2 + \tau_{i+1}^2} \right) \tag{12}$$

The entire derivation has used the so-called apparent velocities which are valid if the refractivity pattern does not fade significantly during the time required for the pattern to move from one antenna to the next. VINCENT et al. (1987) have shown that the difference between true and apparent velocities becomes significant in the upper troposphere and above. The vorticity measurement is the same in principle if the appropriate corrections are made for the pattern fading, although the expressions become more complicated.

CONCLUSION

The technique outlined here appears to have potential for single-radar vorticity measurements. Vorticity and divergence measurements with a network of radars is acceptable in many cases when the scale sizes of interest are larger than or comparable to the spacing of the radars in the network, but for studies of the dynamics of small-scale phenomena, such as the mixing in tropopause folds or the turbulent dissipation associated with the breakdown of small-scale waves, a technique that uses a single radar is needed. While the method is straightforward in principle, it remains to be seen if the measurement will be meaningful in practice when the measurement errors are taken into account.

There has been considerable debate in recent years about the differences and similarities between the spaced antenna and Doppler methods for wind profiling. Several studies have shown that the spaced antenna method provides wind information of quality comparable to the Doppler method. Arguments about the anticipated advantages of spaced antenna systems have been presented, but, while the arguments seem reasonable, no detailed studies have been carried out to show that the advantages are real. The vorticity measurement capability appears to constitute a clear difference between the spaced antenna and Doppler methods, since the latter technique does not provide information about the flow rotation.

REFERENCES

Briggs, B. H., The analysis of spaced sensor records by correlation techniques, Handbook for MAP, 13, R. A. Vincent (ed.), 166-186, 1984.

Browning, K. A., and R. Wexler, A determination of kinematic properties of a wind field using Doppler radar, J. Appl. Meteor., 7, 105-113, 1968.

Larsen, M. F., and J. Röttger, The spaced antenna technique for radar wind profiling, J. Atmos. Ocean. Tech., in press, 1989.

Vincent, R. A., P. T. May, W. K. Hocking, W. G. Elford, B. H. Candy, and B. H. Briggs, First results with the Adelaide VHF radar: Spaced antenna studies of tropospheric winds, J. Atmos. Terr. Phys., 49, 353-366, 1987.

Wilson, D. A., and L. J. Miller, Atmospheric motion by Doppler radar, Chapter 13 in Remote Sensing of the Troposphere, V. E. Derr (ed.), Wave Propagation Lab, NOAA/ERL, Boulder, Colorado, 1972.

APPLICATION OF MST DATA TO NUMERICAL WEATHER PREDICTION

Meta E. Sienkiewicz and Tzvi Gal-Chen

University of Oklahoma
Norman, Oklahoma,   73019

1.   INTRODUCTION

Numerical weather prediction (NWP) is concerned with weather prediction through numerical integration of the hydrodynamic and thermodynamic equations that govern atmospheric motions. One concern in NWP is the specification of the initial conditions. The NWP models currently in use rely primarily on rawinsonde data taken on a large scale network twice daily to provide the initial conditions for the forecasts. Additional data such as that provided by a network of wind Profilers adds detail to the initial conditions and can improve the quality of the forecasts. The details provided by the wind measurements may be retained better by the models if a temperature field is also specified.

Our research concerns deriving temperature fields from measurements of wind profiles and their changes with time. The method involves taking equations much like what are used in the numerical models, the horizontal equations of motion, and forming a Poisson equation to be solved at each horizontal level desired to get a a temperature field. We are also investigating the improvement to the temperature fields which can be obtained by adding measurements from ground-based and satellite based microwave radiometers. The retrieval method derives a weighted combination of wind-derived temperatures and microwave radiances through use of the radiative transfer equation.

2.   THEORY

The theoretical basis for this retrieval method is presented in more detail in GAL-CHEN (1988). What follows is a brief overview of the basic ideas behind the method.

In this method, an estimate of the three-dimensional field of temperature is sought using two sources of data: (1) vertical profiles of wind and their changes with time as measured by a wind Profiler network, and (2) microwave radiance measurements from satellites and/or a network of ground-based radiometers. To accomplish the retrieval we need to provide additional information on the relationship between the measured quantities and the desired field, temperature.

First, consider the relationship between radiance and the vertical profile of temperature. Radiometers can be thought of as measuring a weighted average of the temperature profile in the vertical. The measurement made by a radiometer is determined by the radiative transfer equation, which may be written in a simplified form for a ground based radiometer as

$$I(v) = \int_{P_s}^{0} K(v,p)\ T(p)\ dp + T_{BACK}\ e^{-\tau(v)} \tag{1}$$

where $I(v)$ is the radiance measured by the radiometer in the frequency channel v. $K(v, p)$ is a weighting function determined by the rate of change with height (or pressure) of transmission of radiation at frequency v. $T_{BACK}(v)\ e^{-\tau(v)}$ is the background radiation from space reaching the Earth's surface. The form for a satellite radiometer is similar to (1) but includes a term expressing radiation from the Earth's surface.

Inversion of the measurement of $I(v)$ to get $T(p)$ is an ill-posed problem; it is possible to find many different temperature profiles which generate the same distribution of brightness temperatures at specified frequencies. Thus, it is

necessary to add additional information to perform the temperature retrieval. Inversion methods for radiance measurements include "physical" retrieval where a first guess profile is modified to produce the measured radiances; and "statistical" retrieval, using the covariances between measurements in different frequency channels and temperatures measured at given pressure levels to derive fitted coefficients relating measured radiances and temperature profiles. More detailed discussions of temperature retrieval from radiometer measurements may be found in many places (e.g. WESTWATER AND STRAND,1972, RODGERS, 1976, and others).

The second relationship to consider is that of the measurements of wind (and its change with time) and the temperature field. This relationship is described by the horizontal equations of motion and the hydrostatic equation. The horizontal equations of motion in (x, y, p) coordinates are

$$Du / Dt = - \partial \phi / \partial x + F_1 + fv \tag{2}$$

$$Dv / Dt = - \partial \phi / \partial y + F_2 - fu \tag{3}$$

where u and v are the horizontal components of wind in the x- and y- directions, respectively, $f (= 2\omega \sin \varphi)$ is the Coriolis parameter, and F_1, F_2 represent the x- and y- components of the turbulent forces. With knowledge of the three-dimensional wind field and its change with time (and, additionally, some form of frictional parameterization) we can calculate all the terms in the equations except the horizontal gradients of geopotential, ϕ. Solving for these terms, we can rearrange (2) and (3) and write:

$$\partial \phi / \partial x = F \tag{4}$$

$$\partial \phi / \partial y = G \tag{5}$$

GAL-CHEN (1978) and HANE AND SCOTT (1978) have proposed a least square solution of (4) and (5), by solving the variational problem:

$$\int \int (\partial \phi / \partial x - F)^2 + (\partial \phi / \partial y - G)^2 = Min. \tag{6}$$

The solution of this variational problem is a Poisson equation for ϕ:

$$\nabla^2_H \phi = \partial F / \partial x + \partial G / \partial y \tag{7}$$

Here ∇^2_H is the horizontal Laplacian. When (7) is expanded the form of this divergence equation is

$$- \nabla^2_H \phi = \frac{\partial D}{\partial t} + u\frac{\partial D}{\partial x} + v\frac{\partial D}{\partial y} + D^2 + \omega\frac{\partial D}{\partial p} + \frac{\partial \omega}{\partial x}\frac{\partial u}{\partial p} + \frac{\partial \omega}{\partial y}\frac{\partial v}{\partial p}$$

$$- 2 J(u,v) - f \zeta - \left(\frac{\partial F_1}{\partial x} + \frac{\partial F_2}{\partial y}\right) \tag{8}$$

(where D is the divergence of the horizontal wind, $D = \partial u/\partial x + \partial v/\partial y$)

The boundary conditions for the above problem may be either Dirichlet conditions (specifying ϕ on the boundary) or Neumann conditions (specifying the derivative of ϕ normal to the boundary). With Neumann boundary conditions that the solution for ϕ is found only to within a constant, so additional information, such as the mean value of height at a level or a height value at a grid point must be supplied. The horizontal gradients of ϕ are uniquely determined, however.

Once ϕ is determined on more than on level one may obtain mean layer virtual temperature T_v by the hydrostatic relation:

$$\partial \phi / \partial (\ln p) = - R T_v \tag{9}$$

Use of the full divergence equation (8) to retrieve geopotential may not be practical as accurate evaluation of the terms involving ω could be difficult to accomplish. GAL-CHEN(1988) presents a scale analysis of the momentum equations applied in a frontal zone where the flow possesses two length scales, deriving a form of the divergence equation where the contributions of ω are dropped. To get

this form of the divergence equation from the variational problem (7) one drops the terms involving ω from the calculation of F and G.

Given the measurements of wind profiles and radiances, and the relationships of these to the three dimensional temperature field we can then define some optimal combination of the two kinds of data to obtain the temperature field. The formulation which incorporates the observed radiances into the retrieval procedure is discussed in GAL-CHEN(1988), a brief recapitulation is presented below. To achieve consistency with the previous sections this discussion deals only with the microwave region.

The basic idea is to modify $\nabla_H T^f$, which is the estimate of the horizontal (virtual) temperature gradient obtained from the horizontal divergence equation, to another (hopefully better) form $\nabla_H T$ such that the radiative transfer equation (1) is better satisfied. It is also desired that $\nabla_H T$ remains as close as possible to the unmodified form $\nabla_H T^f$. This defines the following variational problem:

Find a function T such that

$$\int_S \int_{P_s}^0 \beta_0 \, [\nabla_H (T - T^f) \,]^2 \, dp \, dS +$$
$$\sum_V \beta_V \int_S \, [\nabla_H \, (\int_{P_s}^0 K(V,p,p_s) \, T(p) \, dp - I_V) \,]^2 dS = Min. \qquad (10)$$

where S is a symbol for a horizontal area. (Here I_V incorporates the transmission term in (1) and is adjusted to represent a weighted virtual temperature.) The reason for dealing with gradients of radiance instead of dealing with the quantity itself is that due to calibration errors and other unknown biases an absolute measurement of radiance is less accurate than a relative one (MENZEL et al., 1981). The solution of the variational problem shows that the T field must satisfy

$$\nabla_H \cdot \beta_0 \nabla_H T + \sum_V \beta_V \, K(V,p) \, \nabla_H^2 \int_P K(V,p') \, T(p') \, dp'$$
$$= \nabla_H \cdot \beta_0 \, \nabla_H \, T^f + \sum_V \beta_V \, K(V,p) \, \nabla_H^2 \, I(V) \qquad (11)$$

The parameters β_0, β_V; $V = 1,2,...,N$ (N — the number of channels) are "properly" selected weights, chosen based on our relative confidence in the various sources of information. For instance, β_0 and the β_V's can be chosen to be inversely proportional to the squares of the standard deviations of the errors associated with each term of the l.h.s. of (10) above. We take $\beta_0 = \beta_0(x,y,p)$ to take into account the fact that in the boundary layer dynamical retrievals using the divergence equation are suspect and should therefore be assigned a low weight (MODICA AND WARNER, 1987).

After some manipulations GAL-CHEN (1988) shows that the minimization problem (10),(11) can be reduced to that of solving at each horizontal level a Poisson equation with Neumann or Dirichlet type boundary conditions.

3.   EXPERIMENTAL RESULTS

To verify our retrieval algorithm we are using the Observing System Experiment methodology discussed e.g. by RAMAMURTHY AND CARR (1987). Wind and temperature soundings from extensive field experiments are available, and can be used along with an assumed form of the radiative transfer equation to simulate observations from a network of Profilers. This approach is in contrast to the Observing System Simulation Experiment (OSSE) approach, where the "observations" used are produced by a numerical model, and the dynamics are constrained to follow the equations used in the numerical model. In the OSE approach, no particular constraints are applied to the wind measurements.

The data we are using are from the AVE/VAS Ground Truth Field Experiment (HILL AND TURNER, 1983). Radiosonde data were taken at 24 National Weather Service

stations at 3-hourly intervals on 4 separate days in the spring of 1982. These data represent a variety of weather conditions, unlike some other experiments conducted to measure specific kinds of weather. The 3-hourly observation interval gives better resolution of changes in atmospheric conditions with time than the normal 12-hourly synoptic observations. Results presented here were derived using data from AVE/VAS II (6-7 March 1982).

Measurements from microwave radiometers were simulated by integrating the measured temperature profiles in the vertical with weighting functions similar to those illustrated in WESTWATER et al. (1985). Brightness temperatures (proportional to radiance, but with units of temperature) from four ground-based microwave channels and two satellite microwave channels were generated. The wind data used to represent Profiler winds were from the sounding data interpolated to 25-mb levels, as were the temperature and height data used for the verification fields.

To produce the wind-derived height and temperature fields, the u- and v-components of the wind (slightly smoothed in the vertical) at constant pressure levels between 825 mb and 100 mb were interpolated to a 1° latitude-longitude grid using the BARNES (1973) successive correction interpolation scheme. These data were used to calculate the F and G terms (eqns (2)-(5), but omitting terms involving vertical advection) by second-order centered finite differences. The gradients of the F and G terms were used to calculate the forcing function of the Poisson equation for ϕ. This Poisson equation with Neumann boundary conditions was solved by successive over-relaxation. The difference of ϕ between pressure levels was calculated and divided by R to yield mean layer virtual temperature over a 50-mb layer, which is used in the combined retrieval as the first guess temperature T^f.

Fig. 1 shows the RMS differences between retrieved height fields and those analyzed from the radiosonde data. The different curves show the effect of using different approximations to the divergence equation. The geostrophic approximation (in which only the Coriolis force was retained) showed the worst results above 500 mb. The balance equation approximation which neglects tendencies and the approximation which included the time derivative term performed generally the same.

The results of one test calculation of a simplified form of equation (11) are presented. The simplifications include (a) calculation of I_v from gridded virtual temperatures (without added random error), (b) input of "true" temperatures analyzed from the radiosonde data for levels below 800 mb and adjustment of temperature only from 800-125 mb instead of starting the integration at the Earth's surface (to avoid problems related to terrain variation across the network), and (c) use of a simple form of the parameters β_0, β_v; $v = 1,2,...,N$ which did not include any variation in the vertical. The weights used were: $\beta_0 = 0.2$, $\beta_v(52.85) = 0.2$, $\beta_v(53.85) = 0.125$, $\beta_v(55.45) = 0.05$, $\beta_v(58.80) = 0.025$, $\beta_v(53.74) = 0.2$, and $\beta_v(54.96) = 0.2$.

Fig. 2 shows the RMS differences between retrieved and analyzed virtual temperatures for the retrieval from wind information and for the combined retrieval. The curve marked with crosses shows the error associated with calculating temperature from 50-mb layer thicknesses compared to virtual temperature measured at a given pressure level, and so represents a kind of minimum interpolation error. The combined retrieval gave improved error statistics at nearly all levels although these were very small above 700 mb (where the ground based measurements had little effect). The dashed extension of the wind retrieval curve below 800 mb shows results from wind retrievals in terrain following (x,y,σ) coordinates. These clearly show the poorness of the retrieval in the boundary layer near the Earth when only wind information is used. Obviously the wind observations will need to be supplemented with other observations (such as may become available with the RASS system). We are currently working on the combined retrieval method in (x,y,σ) coordinates, and expect to see similar improvements to the retrieved temperatures in the lower layers near the Earth.

Fig. 3 shows a comparison between the observed 700 mb temperatures and those retrieved from the wind data and using the combined retrieval. The analysis from the combined retrieval is slightly closer to the observed temperatures. The change
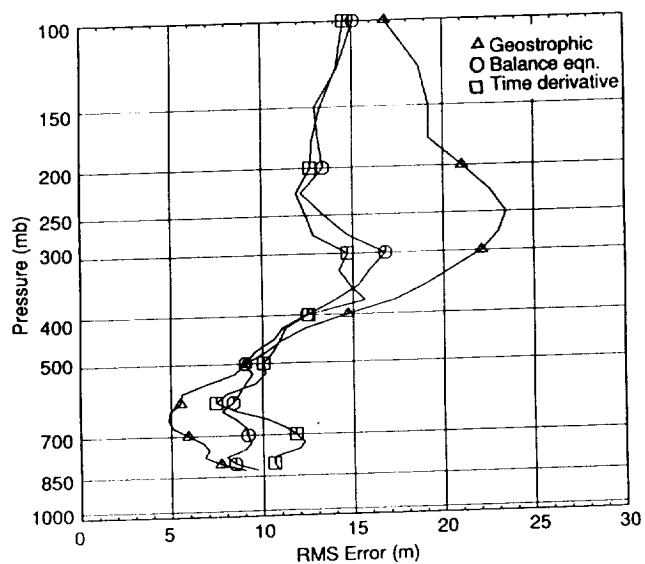
Fig. 1 RMS errors associated with retrievals of height from wind data. Curves represent different approximations to the full dynamical equations.
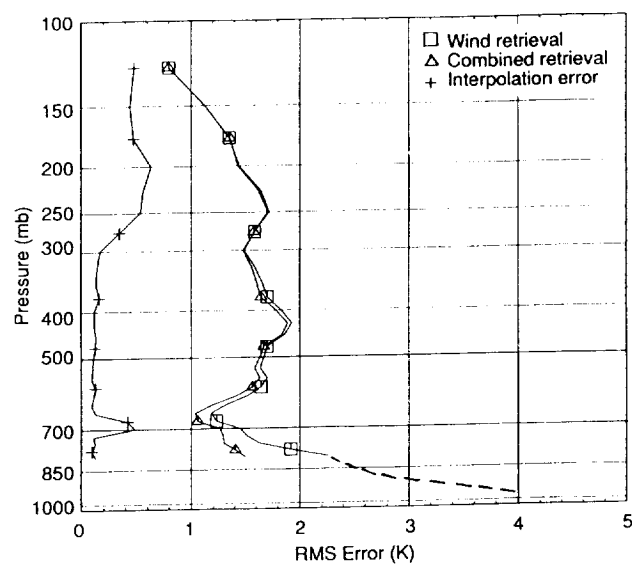
Fig. 2 RMS errors associated with combined retrievals (wind and radiances are used as sources of information). (+) represents interpolation error of calculating temperature from 50- mb thicknesses.
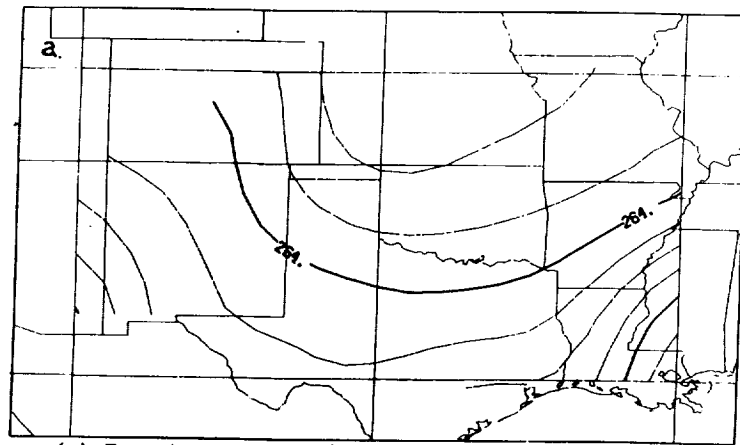
(a) True temperature field measured by radiosonde.
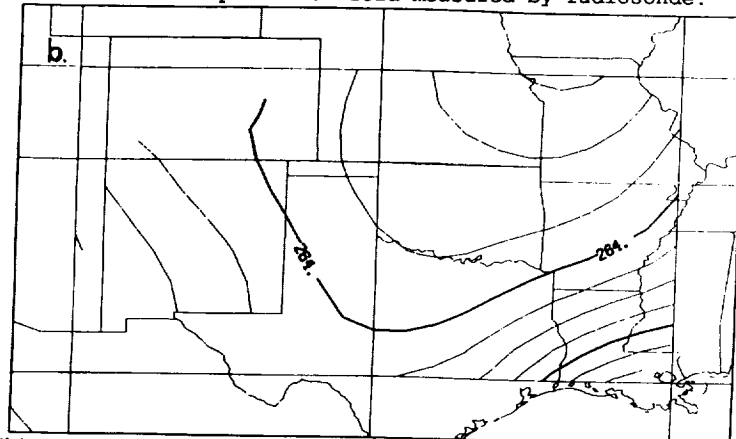
(b) Temperature field retrieved using wind information only.
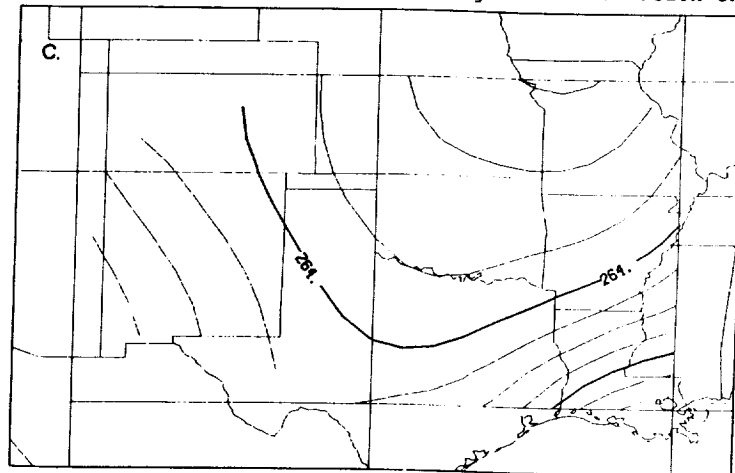
(c) Temperature field retrieved using wind and radiance information.

Fig 3. 700 mb virtual temperature fields for 0000 UTC, 7 March 1982.

is consistent with the 0.2 K improvement in RMS error at 700 mb shown in Fig. 2. The amount of improvement of the temperature analysis depends on the difference of the measured radiance from the radiances that would be produced by the first guess temperature field retrieved from winds alone. In this case, the "true" and "first guess" radiances were very close so only limited improvement was possible.

5. SUMMARY

Using wind information, the horizontal equations of motion, and the hydrostatic relation, it is possible to retrieve temperature fields that have RMS errors ≤ 2 K in the mid- to upper troposphere but with greater error near the Earth's surface. A retrieval method has been developed which combines the temperature retrieved from wind data with radiances measured from ground and satellite based microwave radiometers. This method has been shown to reduce the analysis error by more than 0.5 K in the lower troposphere for the test case examined. The retrieval method may also be adapted to use different (e.g. terrain following) coordinate systems and to include other sources of data if desired.

6. REFERENCES

Gal-Chen, T., A method for the initialization of the anelastic equations: Implications for matching models with observations. *Mon. Wea. Rev.*, **106**, 587-596, 1978.

_____, A theory for the retrievals of virtual temperature from the remote measurements of horizontal winds and thermal radiation. *Mon. Wea. Rev.*, **116**, 1302-1319, 1988.

Hane, C. E., and B. Scott, Temperature and pressure perturbations with convective clouds derived from detailed air motion information: Preliminary testing. *Mon. Wea. Rev.*, **106**, 654-661, 1978.

Hill, C. K., and R. E. Turner, NASA's AVE/VAS program. *Bull. Amer. Meteor. Soc.*, **64**, 796-797, 1983.

Menzel, W. P., W. Smith, and L. Herman, Visible infrared spin-scan radiometer atmospheric sounder radiometric calibration: an inflight evaluation from intercomparisons with HIRS and radiosonde measurements. *Applied Optics*, **20**, 3641-3644, 1981.

Modica, G. M., and T. T. Warner, The error associated with use of various forms of the divergence equation to diagnose geopotential and temperature. *Mon. Wea. Rev.*, **115**, 455-462, 1987.

Ramamurthy, M.K., and F. H. Carr, Four dimensional data assimilation in the monsoon region. Part I: Experiments with wind data. *Mon. Wea. Rev.*, **115**, 1678-1706, 1987.

Rodgers, C. D., Retrieval of atmospheric temperature and composition from remote measurements of thermal radiation. *Rev. Geophys. Space Phys.*, **14**, 609-624, 1976.

Westwater, E. R., and O. N. Strand, Inversion Techniques. In, *Remote Sensing of the Troposphere*. V. E. Derr, Ed. , National Oceanic and Atmospheric Administration. USA, Superintendent of Documents, USA Government Printing Office, Washington, D.C., Ch. 16, 16-1 - 16-13, 1972.

_____, W. Zhenhui, N. C. Grody and L.M. McMillin, Remote sensing of temperature profiles from the satellite-based microwave sounding unit and the ground-based profiler. *J. Atmos. Ocean Technol.*, **2**, 97-109, 1985.

PRE-STORM OBSERVATIONS OF A SQUALL LINE PASSAGE
WITH A VHF DOPPLER RADAR WIND PROFILER

J. G. YOE[1], M. F. LARSEN[1], and E. J. ZIPSER[2]

[1] Department of Physics and Astronomy
Clemson University
Clemson, SC 29631-1911

[2] NCAR
Box 3000
Boulder, CO 80303

ABSTRACT

On June 10-11, 1985, a squall line passed the McPherson, Kansas, VHF wind profiler during the O-K PRE-STORM experiment. The mature squall line had an intense convective leading edge and a broad trailing stratiform precipitation region. The Doppler power spectra for the period exhibited double peaks corresponding to both turbulent scattering and precipitation scattering during the periods of heavy rain. A nonlinear least-squares fitting of the spectra was applied in order to estimate the mean radial velocity separately for the two types of scatterers. From the clear air velocities obtained in this way, we have identified the various features of the vertical and horizontal flow associated with the squall line passage. We have also compared the flow observations made by a pair of scanning 5-cm Doppler radars with the VHF data. The data set shows some of the problems that will be faced in using and analyzing profiler data obtained during precipitation events.

INTRODUCTION

During the past decade the use of the Doppler wind profiling technique has steadily gained acceptance in the meteorological community to the point that procedures have been developed for operational analysis of the data (see, e. g., RÖTTGER AND LARSEN, 1989, for a review). Often only the first moment of the spectrum, after DC subtraction, is used as an estimate of the line-of-sight velocity, and vertical profiles of the horizontal wind velocity are obtained by means of a consensus averaging technique. For each range gate, velocity estimates are produced every five or six minutes, and the hourly average radial velocity is estimated from the largest group of values which lie within a prescribed tolerance of one another for the averaging period. STRAUCH et al. (1987) carried out fairly extensive tests of the procedures by using the redundancy in data from a five-beam 405-MHz profiler to make independent hourly estimates of the horizontal wind components for a month in clear air. They calculated the standard error expected for a three-beam profiler in such an environment to be 1.3 m s^{-1} if the vertical air motion is taken into account. A number of studies have been carried out in which

clear air wind profiles obtained with Doppler radars have been compared to those obtained by nearby radiosondes, and although such comparisons are by no means exhaustive they generally claim reasonable agreement between the two methods (see RÖTTGER AND LARSEN, 1989, for summaries of a number of the studies).

The presence of precipitation gives rise to several problems in using Doppler radar to measure the wind field. At UHF, the received signal is generally dominated by scatter from precipitation (LARSEN AND RÖTTGER, 1987). As a result the measured radial velocity will be the projection of the preciptation fall speed on the line of sight. At VHF, the contributions from turbulent scattering will dominate for light rainfall rates, but the precipitation scattering will be of comparable magnitude and must be identified and separated in order to obtain profiles of clear air motion when the rainfall rates are heavier. Processing algorithms which perform reasonably well when applied to data acquired during clear conditions are of questionable value in analyzing data obtained in a precipitating environment, particulary when systems evolve rapidly. Consensus averaging techniques intended to improve the hourly estimates of the winds may form erroneous averages when the winds change significantly from profile to profile. If precipitation or clear air motion evolves or fluctuates during the averaging period, as in a convective storm, it may be impossible to form a consensus for that period (AUGUSTINE AND ZIPSER, 1987), or a consensus average may not be representative of the period as a whole. A second problem is that a first moment estimate of the line-of-sight velocity will be misleading when double peaked spectra are measured since the velocity estimate will fall between the turbulent scattering and precipitation scattering peaks. These problems need to be assessed if Doppler radar wind profilers are to provide useful information during precipitation events. Since the most interesting mesoscale dynamics occur in connection with precipitating systems, the problems are at the heart of the use of wind profilers as part of an operational mesoscale observing system.

Relatively few studies have dealt with the use of Doppler radar to observe precipitation. FUKAO et al. (1985) observed light stratiform rain with the Japanese VHF MU radar and deduced the wind field by identifying the turbulence contribution of the received signal. Their comparison of the horizontal motion of clear air to that of precipitation showed excellent agreement. LARSEN AND RÖTTGER (1987) examined the doubled-peaked spectra associated with a thunderstorm observed with the SOUSY VHF radar located in West Germany. They suggested the possibility of using a combination of VHF and UHF radars for cloud physics research. For example, knowledge of vertical air motion obtained from the VHF system would allow the calculation of corrected terminal velocities of precipitation and parameterization of drop-size distributions observed with the UHF radar. Indeed, WAKASUGI et al. (1986, 1987) calculated such distributions from VHF signals alone by application of a nonlinear least-squares fitting of spectra obtained in stratiform rain with the MU radar. FORBES AND CARROLL

(1987) made some limited determinations of air and precipitation vertical velocities from UHF spectra obtained during a thunderstorm. WUERTZ et al. (1988) repeated the experiment of Strauch et al. during the summer of 1986 in Colorado, using periods when precipitation was present in the radar beam. They found the measurement error in hourly profiles of the horizontal wind to be 2-4 m s^{-1} during periods of precipitation. They were able to use consensus averaging without modification if the precipitation was spatially and temporally homogeneous, but found that for time-varying precipitation the off-zenith radial velocities had to be corrected for precipitation fall speed before consensus averaging. A few pioneering works (SMULL AND HOUZE, 1985, 1987a,b; SRIVASTAVA et al., 1986; KESSINGER et al., 1987) have utilized a variety of Doppler radar systems to study the kinematic features associated with squall lines.

In this paper we present observations made with a VHF Doppler wind profiler of the wind field associated with the passage of a mid-latitude squall line. An alternative method of estimating the wind vector has been used and is described herein. The observed flow is compared to that measured by a pair of 5-cm scanning Doppler radars operated in the vicinity of the wind profiler.

THE 10-11 JUNE 1985 SQUALL LINE AND THE McPHERSON PROFILER

The OK-PRESTORM experiment was conducted in May and June, 1985 and has been described in detail by CUNNING (1986). As part of the measurement campaign, a VHF Doppler wind profiler was installed and operated at McPherson, Kansas, by NCAR. The McPherson profiler was operated at a frequency of 49.25 Mhz in a three beam configuration. A pulse width of 1 μs gave a height resolution of 150 m starting at 2.1 km AGL. The operating parameters of the McPherson radar are summarized in Table 1. A complete sampling over all three beam orientations required just over 40 s. The time series of the received quadrature signals was recorded on magnetic tape, allowing for the subsequent calculation the Doppler power spectra.

Two NCAR 5-cm Doppler radars, CP-3 and CP-4, were also deployed as part of the OK-PRESTORM program at the locations shown in Fig. 1. During most of the 10-11 June event these systems were operated in a three-dimensional conical scanning mode, in which the line of sight Doppler velocity was measured as a function of range and azimuthal angle for a number of elevation angles. This procedure allowed extended VAD (EVAD) analysis (SRIVASTAVA et al., 1985; RUTLEDGE et al., 1988) of the data to be made in the stratiform region. The EVAD technique calls for the horizontal wind components to be calculated for a series of heights around the perimeter of a cylinder centered about the radar. From this the vertical profile of the horizontal wind at the center of the cylinder and the

Table 1. Operating Parameters for the VHF Wind Profiler at McPherson, KS

Frequency	49.25 Mhz
Number of beams	3
Orientation of oblique beams	8 degrees off zenith
Peak power	125 kW
Average power	5 kW
Antenna aperture	49 m by 49 m
Height resolution	150 m
Number of gates sampled	133
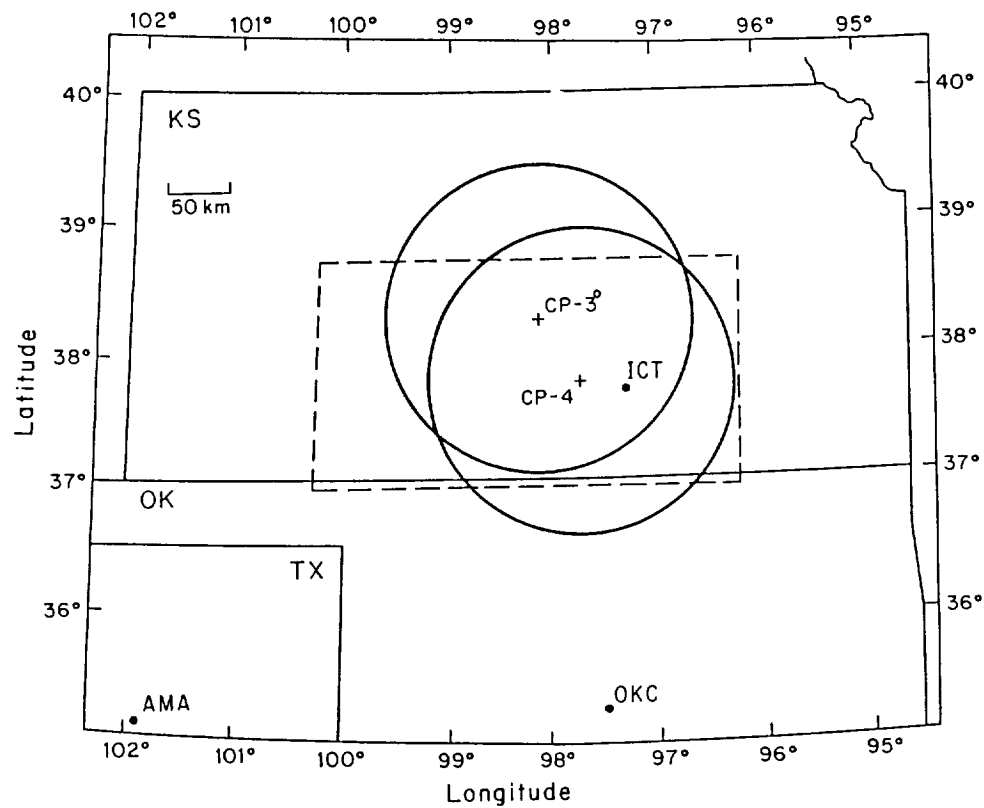
Figure 1. Map showing the locations of the NCAR CP-3 and CP-4 (+) radars and the McPherson VHF profiler (o) during the O-K PRE-STORM campaign. The large circles indicate areal coverage of CP-3 and CP-4. (from RUTLEDGE et al., 1988).

divergence within the circular boundary are obtained. Integration of the divergence yields the profile of vertical air motion. The McPherson site lay well within the scanning range of both the NCAR radars. For one hour shortly after the passage of the convective line, CP-4 was operated at vertical incidence.

By approximately 2000 GMT on 10 June a squall line had developed over southwest Kansas. The system intensified as it propagated eastward and southeastward. Composite digitized reflectivity data from three National Weather Service weather radars located at Wichita, Kansas; Oklahoma City, Oklahoma; and Amarillo, Texas, is shown in Fig. 2 for 0151 GMT on 11 June, with darker regions denoting higher reflectivities. The leading convective edge of the squall line is evident as a narrow band of high reflectivity stretching over 700 km and oriented roughly from northeast to southwest. A broad region of trailing stratiform precipitation is evident behind the line of high reflectivity. The squall line had reached or surpassed maturity at this time, and the leading edge had passed the McPherson profiler and the CP-3 and CP-4 radars. The operation of the McPherson profiler was suspended from 0130 GMT until 0230 GMT on June 11 during the most intense portion of the storm.

ANALYSIS OF THE DATA

The complex time series data recorded before and after the squall line passage were converted to Doppler power spectra by means of a complex fast Fourier transform (FFT). Spectra from the zenith-pointing beam were incoherently averaged over 10 minutes and the noise level determined by use of the method originally suggested by HILDEBRAND AND SEKHON (1974). The reflectivity at vertical incidence is shown in Fig. 3a and 3b. The signal strengths in clear air conditions always decrease by ~2 dB/km with height. Therefore, the reflectivity contours generally show enhancements below 6 km for the particular contouring levels chosen in this case. Enhanced reflectivities stretch higher to 12 or 13 km before 2100 GMT on June 10 indicating the presence of a local thunderstorm near McPherson. The enhancements above 6 km after 0100 GMT show the convective edge of the squall line. There is also a barely perceptible band of higher reflectivities near 14 km, corresponding to the height of the tropopause.

In Fig. 3b, the specular echoes from the tropopause are more clearly evident at heights between 14.5 and 14.0 km, with the altitude descending as time progresses. The reflectivities below 12 km tapered off gradually as the squall line passed the radar until more typical clear air values were reached around 0500 GMT. Strong increases in the noise level are evident near 0300, 0410, and 0500 GMT. These echoes are most likely associated with lightning echoes. The lightning data presented by RUTLEDGE AND McGORMAN (1988) show lightning to be present near the radar at these times.

Domain: 700 X 700 km   Radar: Composit
Contours <dBz>= 15,30,40,45,50,55   Tilt (max)= .5; (min)= .7

Satellite File: /Pre_Storm/Sat/f851620200.sat

Latitude: 34.000 Longitude: -104.000
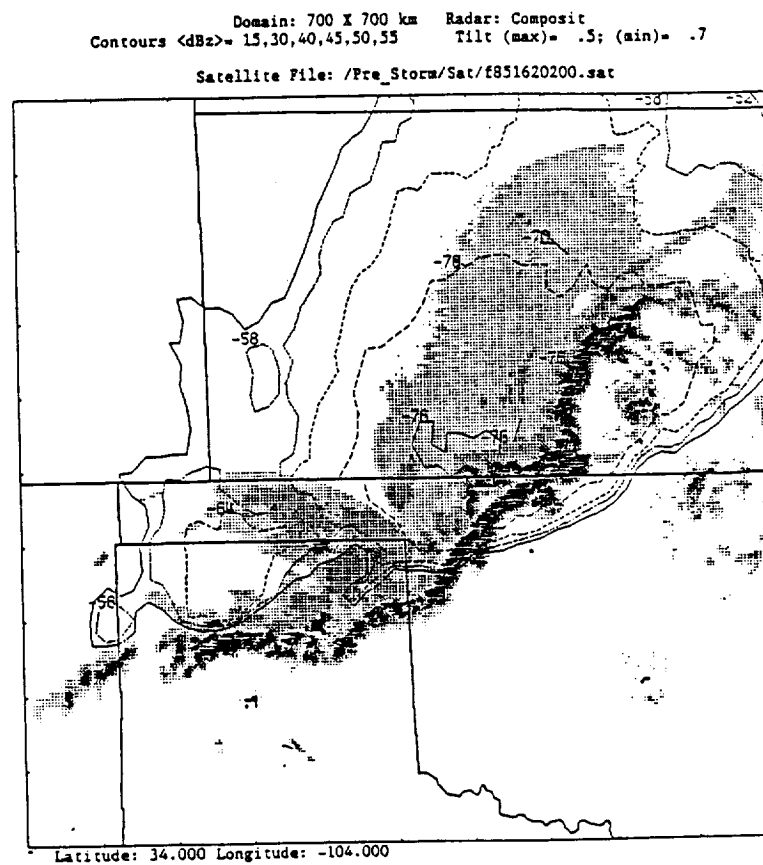
Figure 2. Composite reflectivity measured with NWS weather radars at Wichita, KS, Oklahoma City, OK, and Amarillo, TX. Data from 0151 GMT 11 June. Darker shading indicates higher reflectivity. (by SIKDAR and ZIPSER, private communication, 1987)

REFLECTIVITY (3dB cont. int.)

a

22.   23.   24.

10 JUNE   11 JUNE

REFLECTIVITY (3 dB cont. int.)

b   3.   4.   5.   6.

11 JUNE
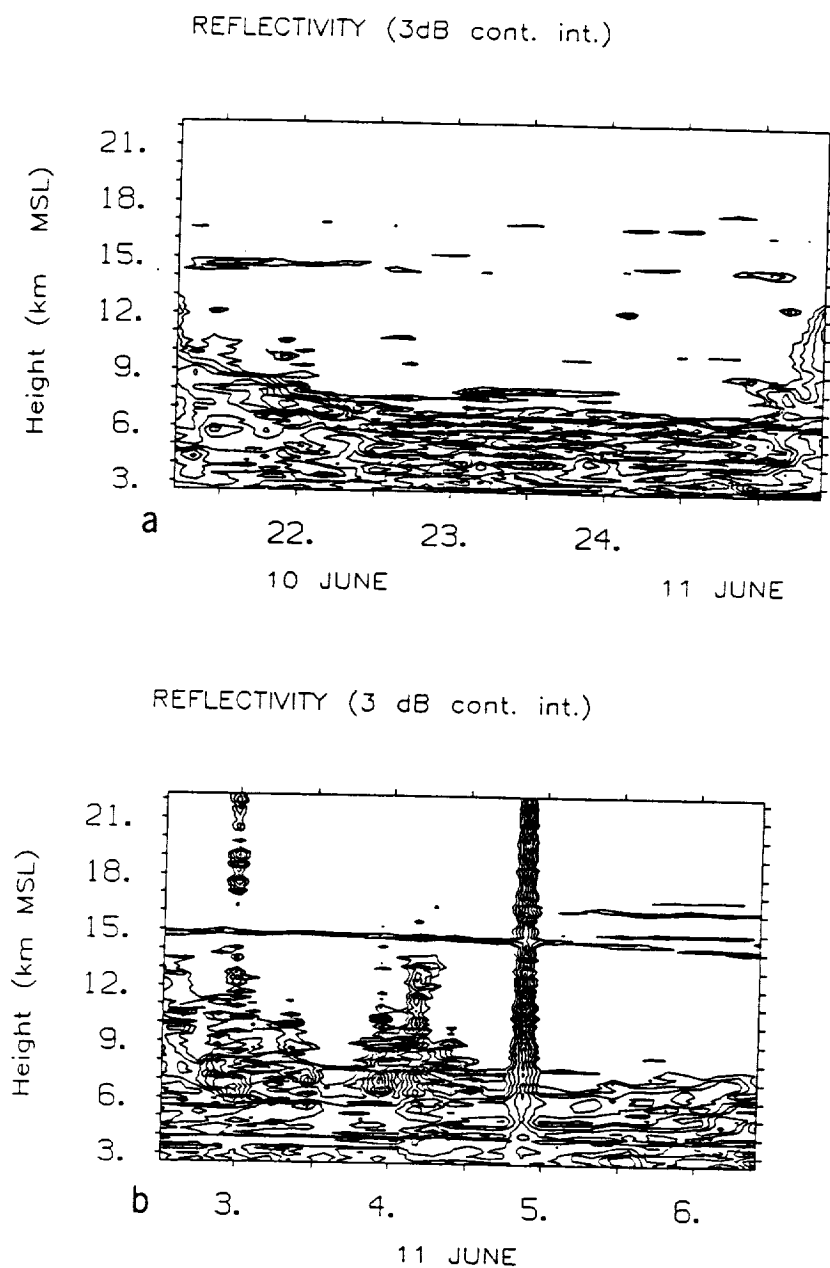
Figure 3.   a. Reflectivity at vertical incidence measured with the VHF wind
profiler at McPherson, KS for the pre-squall period. Contour intervals at 3 dB starting from peak
value. b. Same as (a.) for the post-squall period.

In clear air conditions, spectra averaged over as much as 5 min can be meaningful when the flow conditions are changing slowly. During the squall line passage, the best possible time resolution was needed in order to describe the flows associated with the squall line and to account for the contribution of precipitation in some of the lower altitude spectra during periods of heavy rain. Therefore, no initial incoherent averaging of the spectra was applied, giving a time resolution of 40 s. A nonlinear least-squares fitting was used to estimate the mean radial velocity of the turbulent and precipitation scatterers within each sampling volume. Some of the spectra contained a single peak due to turbulent scattering while others contained a secondary peak caused by scattering from precipitaion particles. Each spectrum was normalized to its peak and a single Gaussian was fitted to the data. If the residual exceeded a critical value, a second Gaussian was incorporated in the fit to the spectrum. The double-Gaussian was retained only if it yielded a smaller residual. However, if neither attempt provided a suitably close approximation of the signal, the data point was flagged so that a velocity value for the gate and time could be interpolated from neighboring values. For the double-peaked spectra, the peak corresponding to the greater velocity toward the radar was assumed to be the precipitation signal and the remaining peak was taken to be the air velocity component. The contribution of the vertical air motion to the radial velocities measured along the off-zenith beams was subtracted in order to provide the most accurate estimate of the horizontal wind.

RESULTS

The horizontal flow relative to the squall line measured at McPherson during the early hours of 11 June is shown in the upper panel of Fig. 4. Note that time increases to the left in the figure so that the time/height cross-section can be viewed as a spatial cross-section of the storm at a single time. A downward-sloping rear inflow jet is evident at midlevel altitudes between 3 and 5-6 km, as well as a strong front to rear flow aloft. The features are in general agreement with the cross-section observed with the scanning CP-4 radar at 0414 GMT except that the boundary between the low-level rear inflow and upper level outflow shows a greater slope in the CP-4 data and reaches a higher altitude. The velocity magnitudes are similar in both sets of observations. Although the agreement is encouraging, discrepancies are to be expected since the McPherson profiler provided height measurements at a single location over a period of 3-4 hr while the CP-4 data was obtained from a single scan near the midpoint in the profiler observations.

In Fig. 5, a comparison of a single 7 minute averaged profile of the relative horizontal flow at McPherson at 0410 GMT, plotted as a solid line, and the relative flow measured with CP-4 at 0345 GMT and CP-3 at 0334 GMT, denoted respectively by + and 0, is shown. The time of the profiler data was selected to account for the lag due to the spatial seperation of the radars. There is good

VREL (m/s)   MCPHERSON
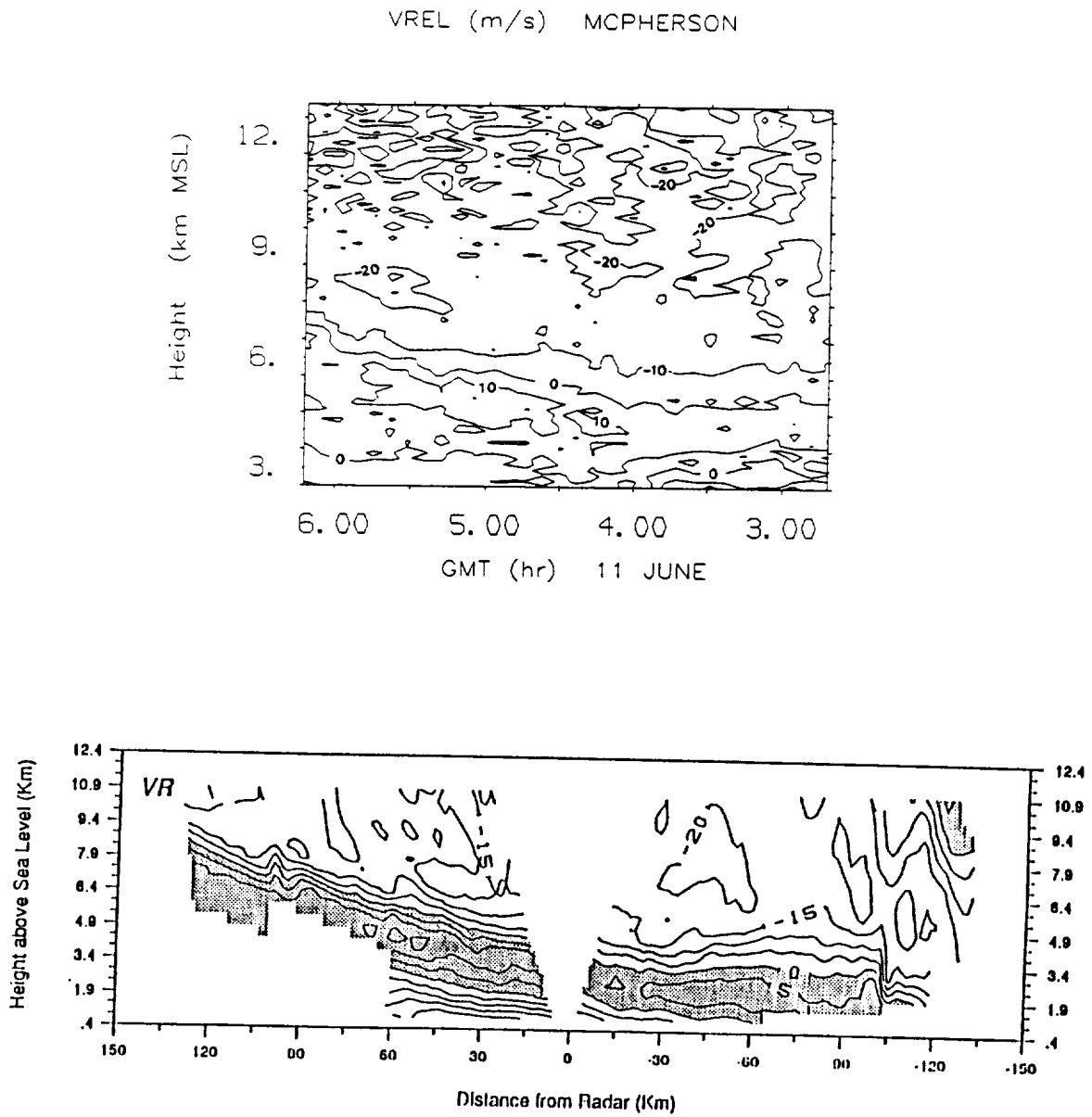
Figure 4. System-relative horizontal flow (VREL) in m s^{-1}. Positive values indicate flow from left to right. Data acquired with the VHF profiler is displayed in upper panel; RHI data from CP-4 (from RUTLEDGE et al., 1988) in lower panel.

0410 GMT 11 JUNE MCPHERSON
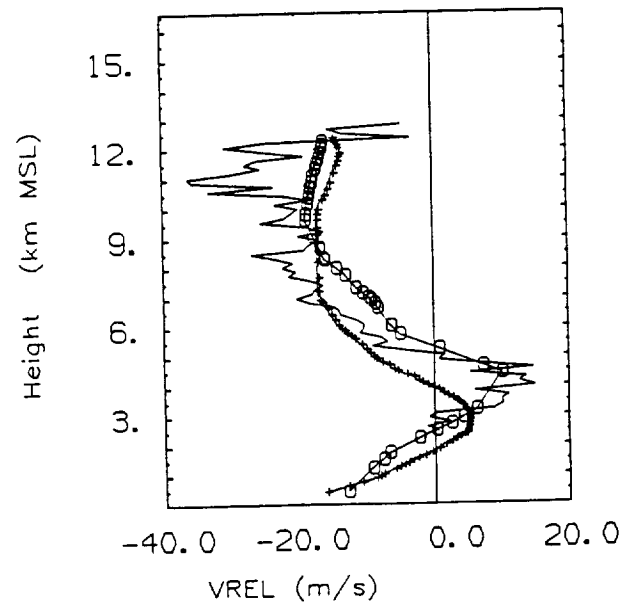
Figure 5. Single profiles of relative horizontal flow (Vrel) in m s^{-1} with CP-4 (+), CP-3 (0), and VHF profiler (-). Sign convention as in fig. 4. CP-3 and CP-4 data by RUTLEDGE et al. (1988) using EVAD analysis.

w (m/s)   MCPHERSON

GMT (hr)   11 JUNE

11-JUN-85   w

Time (minutes after 0233 Z)
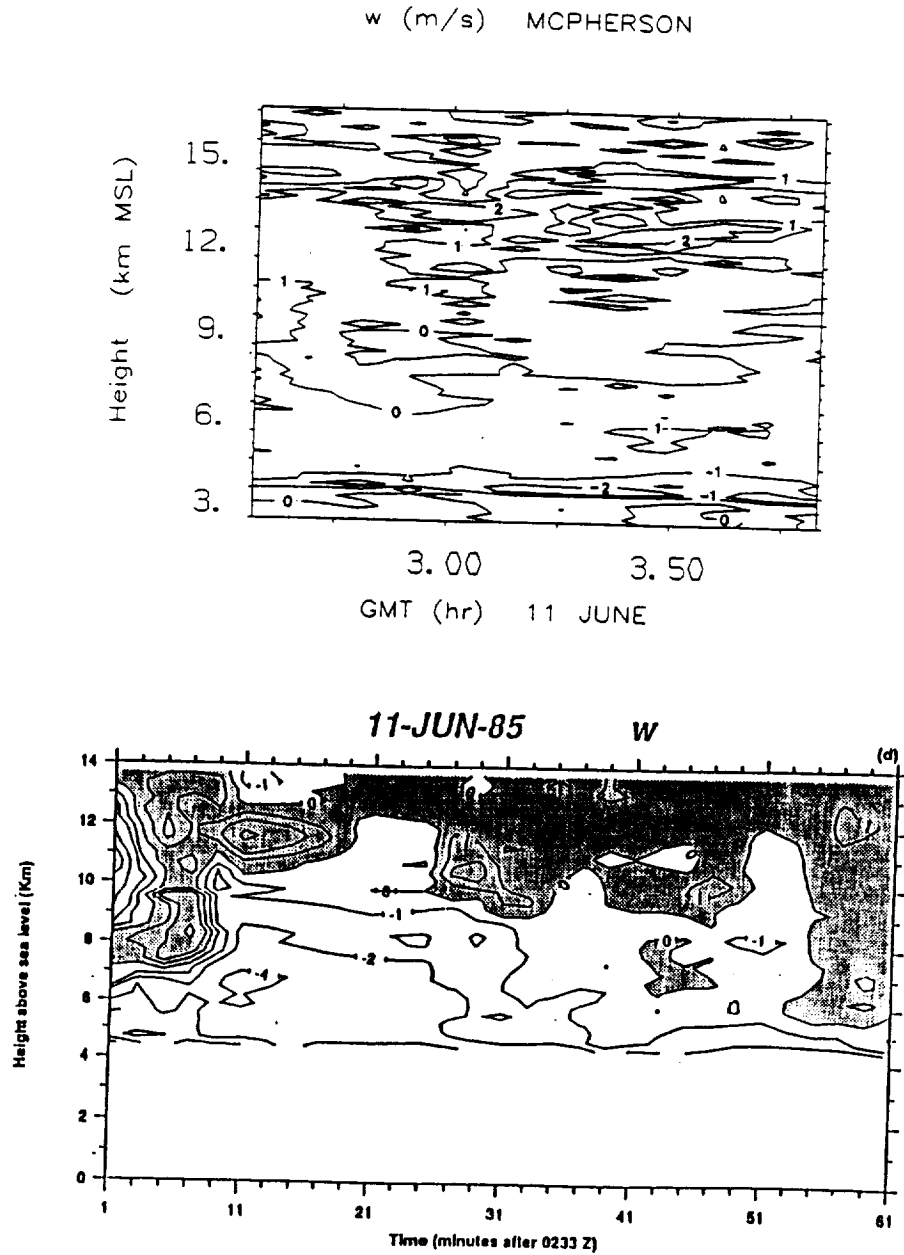
Figure 6. Vertical velocity (w) in m s⁻¹. Positive values indicate upward flow. Data from the profiler is displayed in the upper panel; data from CP-4 (RUTLEDGE, private communication, 1988) operating at vertical incidence is shown below.

0410 GMT 11 JUNE   MCPHERSON
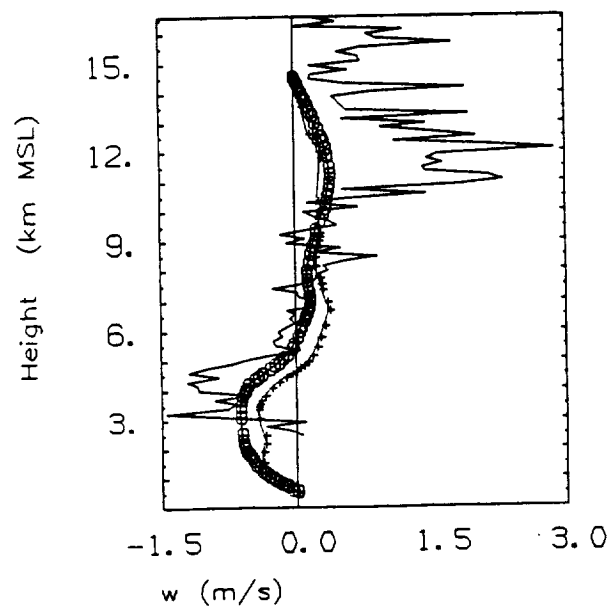
Figure 7. Single profiles of vertical velocity (w) in m s^{-1} with CP-4 (+), CP-3 (0), and VHF profiler (-). Sign convention as in fig. 6. CP-3 and CP-4 data by RUTLEDGE et al. (1988) using EVAD analysis.

agreement between the three curves but particularly between the profiler and the CP-4 data. The profiler, however, shows larger negative velocities between 10 and 12 km than either of the other two radars.

The vertical air motion measured in the stratiform precipitation region by the profiler is shown in the upper panel in Fig. 6, and the corresponding measurements obtained by the CP-4 radar operated at vertical incidence are shown in the lower panel. The CP-4 values represent an attempt to estimate vertical air velocity w by deriving particle fallspeed V_p from the observed reflectivity and adding to it the measured Doppler velocity W. Only data above the melting layer are included for CP-4. A strong updraft is evident during the first 10 min after 0233 GMT in the CP-4 data, but there is only a slight indication of a similar feature in the profiler vertical velocity data. However, the vertical velocities are predominantly positive above 10 km in both data sets. The magnitudes are comparable in both measurements after 0243 GMT but stronger in the CP-4 data between 0233 and 0243 GMT. The strong updrafts may have been highly localized in this case so that they were only evident above the CP-4 radar.

Fig. 7 shows a comparison of vertical velocity profiles measured with the profiler at McPherson at 0410 GMT, and CP-3 and CP-4 at 0334 and 0345 GMT, respectively. There is good agreement between the measurements below 10 km. All three profiles indicate downdrafts below 5-6 km and updrafts at the higher altitudes. Above 10 km, the profiler shows an abrupt increase in the magnitude of the updrafts which is not corroborated by the other two measurements.

The discrepancy at the upper heights is apparently due to a loss of signal-to-noise ratio in the profiler measurements. In a small height range near 14.5 km, the reflectivities increase due to the aspect sensitive echoes associated with the tropopause. Near the tropopause, smaller vertical velocities were produced with values in better agreement with the meteorological radar measurements. Averaging over longer time intervals will improve the detectability of the signal in the upper range gates, but increasing the averaging will only be sensible if the velocity values remain nearly constant over a longer period. The latter condition is generally fulfilled in clear air conditions but not during active periods such as the squall-line passage. The height coverage afforded by a particular radar is dependent on the transmitter power and antenna area. The particular combination used in the McPherson system produced good signal-to-noise ratios for 40-s spectra up to ~10 km altitude.

CONCLUSIONS

The vertical velocity measurement capability of the radar wind profiler technique shows a great deal of potential for studies of mesoscale dynamics. However, verification of the radar measurements has been a problem since there is no other technique with comparable accuracy for direct vertical velocity

measurements. Several studies have compared the profiler measurements to vertical velocities calculated from standard radiosonde data. Such comparisons have increased our confidence in the measurements, but discrepancies can generally be explained away by considering the differences in the sampling schemes associated with the two data sets. The EVAD method used with conventional meteorological radars only works during precipitation events such as the squall line passage studied here. Nonetheless, there is an opportunity for comparison with the VHF profiler data when the turbulent and precipitation scatter components in the spectra are carefully separated as we have done. The profiles measured with the two types of instrumentation are in good agreement over a broad height range, although the profiler measurements led to apparently erroneous values at heights in the upper troposphere. The agreement between the two measurement techniques indicates the great potential of the profilers for studies of active mesoscale systems, such as squall lines.

REFERENCES

Augustine, J. A., and E. J. Zipser, The Use of Wind Profilers in a Mesoscale Experiment, *Bull. Amer. Meteor. Soc.*, *68*, 4-17, 1987.

Cunning, J. B., The Oklahoma-Kansas Preliminary Regional Experiment for STORM Central, *Bull. Amer. Meteor. Soc.*, *67*, 1478-1486, 1986.

Forbes, G. S., and L. A. Carroll, Wind Profiler Studies of Severe Thunderstorms, *Earth and Mineral Sciences*, *57*, 7-9, 1987.

Fukao, S., K. Waksugi, T. Sato, S. Morimoto, T. Tsuda, I. Hirota, and S. Kato, Direct measurement of air and precipitation particle motion by a very high frequency Doppler radar, *Nature*, *316*, 712-714, 1985.

Hildebrand, P. H., and R. S. Sekhon, Objective Determination of the Noise Level in Doppler Spectra, *J. Appl. Meteor.*, *13*, 808-811, 1974.

Kessinger, C. J., P. S. Ray, and C. E. Hane, The 19 May 1977 Oklahoma squall line Part I: A multiple Doppler analysis of convective and stratiform structure, *J. Atmos. Sci.*, *44*, 2840-2864, 1987

Larsen, M. F., and J. Röttger, Observations of Thunderstorm Reflectivities and Doppler Velocities Measured at VHF and UHF, *J. Atmos. Ocean. Tech.*, *4*, 151-159, 1987.

Röttger, J., and M. F. Larsen, UHF/VHF Radar Techniques for Atmospheric Research and Wind Profiler Applications, *Radar in Meteorology*, 1989.

Rutledge, S. A., R. A. Houze, M. I. Biggerstaff, and T. Matejka, The Oklahoma-Kansas Mesoscale Convective System of 10-11 June 1985 : Precipitation Structure and Single-Doppler Radar Analysis, *Mon. Wea. Rev.*, *116*, 1409-1430, 1988.

Rutledge, S. A., and McGorman, D. R., Cloud-to-Ground Lightning Activity in the 10-11 June 1985 Mesoscale Convective System Observed during the Oklahoma-Kansas PRE-STORM Project, *Mon. Wea. Rev.*, *116*, 1393-1408, 1988.

Smull, B. F., and R. A. Houze, Jr., A Midlatitude Squall Line with a Trailing Region of Stratiform Rain: Radar and Satellite Observations, *Mon. Wea. Rev.*, *113*, 117-133, 1985.

Smull, B. F., and Houze, R. A., Jr., Dual-Doppler Analysis of a Midlatitude Squall Line a Trailing Region of Stratiform Rain, *J. Atmos. Sci.*, *44*, 2128-2148, 1987a.

Smull, B. F., and Houze, R. A., Jr., Rear Inflow in Squall Lines with Trailing Stratiform Precipitation, *Mon. Wea. Rev.*, *115*, 2869-2889, 1987b.

Srivastava, R. C., T. J. Matejka, and T. J. Lorello, Doppler Radar Study of the Trailing Anvil Region Associated with a Squall Line, *J. Atmos. Sci.*, *43*, 356-377, 1988.

Strauch, R. G., B. L. Weber, A. S. Frisch, C. G. Little, D. A. Merritt, K. P. Moran, and D. C. Welsh, The Precision and Accuracy of Wind Profiler Measurements, *J. Atmos. Ocean. Tech.*, *4*, 563-571, 1987.

Wakasugi, K., A. Mizutani, M. Matsuo, S. Fukao, S. Kato, A Direct Method for Deriving Drop-Size Distribution and Vertical Air Velocities from VHF Doppler Radar Spectra, *J. Atmos. Ocean. Tech.*, *3*, 623-629, 1986.

Wakasugi, K., A. Mizutani, M. Matsuo, S. Fukao, S. Kato, Further Discussion on Deriving Drop-Size Distribution and Vertical Air Velocity Directly from VHF Doppler Radar Spectra, *J. Atmos. Ocean. Tech.*, *4*, 170-179, 1987.

Wuertz, D. B., B. L. Weber, R. G. Strauch, A. S. Frisch, C. G. Little, D. A. Merritt, K. P. Moran, and D. C. Welsh, Effects of Precipitation on UHF Wind Profiler Measurements, *J. Atmos. Ocean. Tech.*, *5*. 450-465, 1988.

FLATLAND RADAR MEASUREMENTS OF TROPOPAUSE HEIGHTS AND COMPARISON OF SPECULAR ECHO STRENGTH WITH MODEL ESTIMATES

J.M. Warnock, K.S. Gage, and J.L. Green

Aeronomy Laboratory
National Oceanic and Atmospheric Administration
Boulder, CO 80303

1. INTRODUCTION

Specular echoes are observed routinely by clear-air Doppler radars operating at lower VHF. They are detected from heights where the static stability is strong and are detected only when the antenna is pointed near the vertical direction (e.g., GAGE AND GREEN, 1978; RÖTTGER AND LIU, 1978; GAGE et al., 1981; LARSEN AND RÖTTGER, 1982; TSUDA et al, 1986; HOCKING et al, 1986). Considerable progress has been made during the past decade both in modeling these echoes (e.g., GAGE, et al, 1981; HOCKING AND RÖTTGER, 1983, DOVIAK AND ZRNIC, 1984; GAGE et al, 1985), and in developing an objective tropopause-detection method using the relation between atmospheric stability and the strength of the specular echoes (GAGE AND GREEN, 1982; GAGE et al., 1986; SWEEZY AND WESTWATER, 1986). Until recently, however, most clear-air VHF Doppler radars were located in or near mountainous terrain, so that all of the above studies were made in regions where orographic effects are important. Therefore, in May, 1988 an experimental campaign was conducted at the Flatland VHF clear-air Doppler radar site, which is located in very flat terrain far removed from mountainous regions, to study specular echoes in this region of simple topography.

2. DESCRIPTION OF EXPERIMENT

The Flatland radar (GREEN et al., 1988) is located about 8 km west of the Champaign-Urbana, Illinois, airport [40.05° N, 88.38° W, 212 m above mean sea level (MSL)]. This clear-air Doppler radar operates at a frequency of 49.8 MHz (6.02 m wavelength). During this experiment the antenna was pointed in the vertical direction, the peak and average transmitted power were about 10 kw and 150 watts, respectively, and the pulse length and matching range resolution were 750 m. The antenna has an area of about 2500 m squared, and the efficiency factor, α, for the radar system was 0.5. Useful data was obtained in two height regions: from 5 km to about 7 or 8 km, and from the tropopause to about 15 km.

In this study we compare the strength of the vertically-looking radar echoes with the modified Fresnel scatter model given by GAGE et al. (1985). From this model, the normalized signal power S_v (watts) is given by

$$S_v = 10^{17} \frac{\alpha^2 \ P_T \ A_e^2}{16 \ \lambda^2 \ 10^3} \left(\frac{\Delta r}{10^3}\right) \ [\bar{M} \ F_1(\lambda)]^2 \qquad (1)$$

where $\bar{M}$ is the mean gradient of generalized potential radio refractive index (OTTERSTEN, 1969), and $F_1(\lambda)$ is taken to be $0.08 \ m^{-1/2}$. $\bar{M}$ was calculated from the CLASS balloon-soundings data. CLASS is a high-resolution research-quality upper-air balloon-sounding system developed by NCAR (LAURITSEN et al., 1986). The data used in this study were ten-second smoothed data. The usual ascent rate was about 3 m/s or slower, which gave a height resolution of about 30 m/s or better. The balloon launch site was located about 40 m east of the Flatland radar antenna.

3. PRELIMINARY RESULTS

Comparison of radar S_v profiles with model estimates

An example of the radar S_v height profiles and corresponding balloon temperature and model estimate profiles are shown in the figure. Height profiles of radar S_v are shown in panel (A). The log S_v scale is relative, and the magnitude of the radar data is determined by comparing it with a model profile (described below). In this preliminary study, standard methods were used to scale the Doppler spectra. Panel (A) summarizes the radar measurements for an hour. The median profile of all the profiles taken during an hour is given by the solid line. The extreme values for the hour are given by the short dashed line, and the upper and lower quartiles are the dashed-dotted lines.
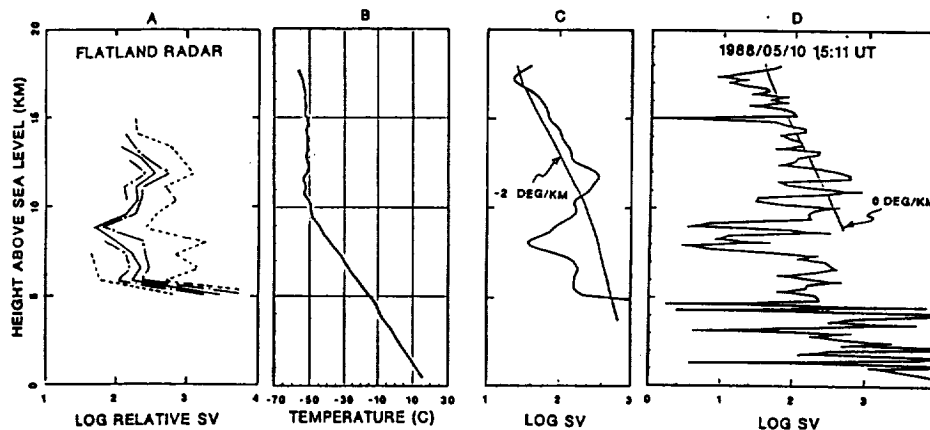
Figure. Height profiles of Flatland radar measurements, temperature, and model estimates for 15-16 hours UT on 10 May 1988.

(A) Profile of radar S_v (=SV on the Figure). The solid line is the median of the measurements for the hour, the dotted lines are the extreme values, and the dash-dot lines are the upper and lower quartiles, respectively.

(B) Temperature profile from CLASS sounding. The balloon was launched at 1011 UT on 10 May 1988.

(C) Smoothed model estimate and test -2°/km profiles. Both profiles are derived from the CLASS balloon sounding data.

(D) Model estimate and test 0°/km profiles. Both profiles are derived from the CLASS balloon sounding data.

Panel (D) shows the model profile calculated from equation (1) using the CLASS upper air data to compute $\bar{M}$ using all the high-resolution data. Note the very large fluctuations in S_v. To compare the model S_v profile with the radar S_v profile, the high-resolution model was smoothed with a Gaussian filter, which roughly approximates the radar range gate height function. Panel (C) shows this smoothed model profile. In this example the shape of the smoothed model and radar profile agree well.

Tropopause height determination

Panel (B) shows the temperature profile. In this example the temperature tropopause is poorly defined. We find that an objective two-step procedure using both the smoothed and high-resolution model profile leads to a more accurate model tropopause height determination than simply using either profile alone. This procedure is easily demonstrated by using panels (C) and (D) of the Figure. The first step [shown in panel (C)] is to find the intersection of the smooth profile with a -2°/km temperature gradient test profile. This is similar to the usual procedure except that the model profile is smoothed. The tropopause test begins at the 500 mb level (about 5.6 km) and proceeds upwards. We look for an intersection between the two curves such that the model is less than the test curve below the intersection and greater than the test curve above the intersection. Furthermore, the model must remain larger than the test curve for two km above the intersection. This first step gives a lower estimate to the model tropopause height.

The second step of this model tropopause-detection procedure is to find the intersection of the high-resolution model profile with a 0°/km temperature gradient test curve as shown in panel (D). This step begins at the height of the tropopause estimated in step one and proceeds upwards until an intersection between the two curves is found with the same sense as in step one. The height of this intersection is the model tropopause height. The 0°/km test curve gives accurate results for this data set, but a different test temperature gradient value may be better at other locations or seasons. Because the first test is applied to the smoothed profile, this two-step procedure is very robust. In this example, the temperature, model, and radar tropopause heights are 10.82, 10.81, and 11.09 km, respectively.

4. CONCLUSIONS

The shape of height profiles of specular echo strength measured in the tropopause and lower stratosphere by the Flatland radar agree well with the modified Fresnel scatter model (GAGE et al., 1985) computed from upper-air balloon data. The radar tropopause height can be determined accurately even with a radar system operating with low transmitted power.

5. ACKNOWLEDGEMENT

6. REFERENCES

Doviak, R.J., and D.S. Zrnic (1984), Reflection and scatter formula for anisotropically turbulent air, Radio Sci., 19, 325-336.

Gage, K.S., B.B. Balsley, and J.L. Green (1981), Fresnel scattering model for the specular echoes observed by VHF radar, Radio Sci., 16, 1447-1453.

Gage, K.S., W.L. Ecklund, and B.B. Balsley (1985), A modified Fresnel scattering model for the parameterization of Fresnel returns, Radio Sci., 20, 1493-1501.

Gage, K.S., W.L. Ecklund, A.C. Riddle, and B.B. Balsley (1986), Objective tropopause height determination using low-resolution VHF radar observations, J. Tech., 3, 248-254.

Gage, K.S., and J.L. Green (1978), Evidence for specular reflection from monostatic VHF radar observations of the stratosphere, Radio Sci., 13, 991-1001.

Gage, K.S. and J.L. Green (1982), An objective technique for the determination of tropopause height from VHF radar observations, J. Appl. Meteorol., 21, 1150-1154.

Green, J.L., K.S. Gage, T.E. VanZandt, W.L. Clark, J.M. Warnock, and G.D. Nastrom (1988), Observations of vertical velocity over Illinois by the Flatland radar, Geophys. Res. Lett., 15, 269-272.

Hocking, W.K., and J. Röttger (1983), Pulse-length dependence of radar signal strengths for Fresnel backscatter, Radio Sci., 18, 1312-1324.

Hocking, W.K., R. Rüster, and P. Czechowsky (1986), Absolute reflectivities and aspect sensitivities of VHF radio wave scatterers measured with the SOUSY radar, J. Atmos. Terr. Phys., 48, 131-144.

Larsen, M.F., and J. Röttger (1983), Comparison of tropopause height and frontal boundary locations based on radar and radiosonde data, Geophys. Res. Lett., 10, 325-328.

Lauritsen, D., Z. Malekmadani, C. Morel, and R. McBeth (1987), The cross-chain Loran atmospheric sounding system, Preprint volume, Sixth Symp. on Meteorol. Observ. and Instrum., Jan. 12-16, New Orleans, LA, 340-343.

Ottersten, H. (1969), Mean vertical gradient of potential refractive index in turbulent mixing and radar detection of CAT, Radio Sci., 4, 1247-1249.

Röttger, J., and C.H. Liu (1978), Partial reflection and scattering of VHF radar signals from the clear atmosphere, Geophys. Res. Lett., 5, 357-360.

Sweezy, W.B., and E.R. Westwater (1986), A comparison of methods for determining tropopause height from VHF radar observations, J. Tech., 3, 324-332.

Tsuda, T., T. Sato, K. Hirose, S.Fukao, and S. Kato (1986), MU radar observations of the aspect sensitivity of backscattered VHF echo power in the tropopause and lower stratosphere, Radio Sci., 21, 971-980.

CLEAR AIR RADAR OBSERVATIONS OF THE GREAT OCTOBER STORM OF 1987

M. CROCHET[1], E. BAZILE[1], F. CUQ[1][2], F.M. RALPH[2]
S.V. VENKATESWARAN[2]

(1) L.S.E.E.T., Université de Toulon, UA 705 CNRS, 639 Bd des Armaris, 83100 TOULON, FRANCE

(2) Department of Atmospheric Sciences UCLA, LOS ANGELES, CAL, USA

Radar Provence was measuring the three dimensional wind velocities and the reflectivity above its location at Lannion, Brittany (48° 45'N, 3° 26'W) beginning from several days prior to the great october storm of 1987. The wind measurements were obtained for most of the troposphere and lower stratosphere with a time resolution of 4 minutes and a height resolution of 600 meters. Time-height cross-sections of suitably averaged horizontal and vertical wind velocities are presented in this paper for a 48 hour period terminated by the power supply failure at 22 UT october 15 coinciding with the most intense phase of the storm. In addition, thermal advection patterns derived from the vertical shears of the horizontal wind and evolution of tropopause altitude derived from the enhancement of reflectivity due to large stability (BAZILE,1988) are also shown. It is found that the velocity patterns and the thermal advection pattern give a mutually consistent picture of the evolution of the storm and of the frontal surfaces, as viewed from the radar station (CROCHET et al.,1989).

REFERENCE

BAZILE E. (1988) - "La mesure de l'advection thermique. Une application du radar ST ?" : rapport de stage Météo.

CROCHET M., F. CUQ, F.M. RALPH and S.V. VENKATESWARAN (1989) - "Clear air radar observations of the great october storm of 1987" - Submitted to Dynamics of Oceans and Atmospheres.

A TRANS-PACIFIC NETWORK OF WIND-PROFILING DOPPLER RADARS FOR TROPICAL ATMOSPHERIC RESEARCH

K. S. Gage, B. B. Balsley, and W. L. Ecklund,

Aeronomy Laboratory
National Oceanic and Atmospheric Administration
Boulder, Colorado, 80303

R. F. Woodman

Instituto Geofisico del Peru
Lima, 100 Peru 00612

S. K. Avery

Cooperative Institute for Research in the Environmental Sciences
University of Colorado
Boulder, Colorado   80309

1.   INTRODUCTION

The past decade has seen a rapid increase in the use of wind-profiling Doppler radars in atmospheric research (GAGE, 1989). With a few notable exceptions most atmospheric research using wind profilers has been carried out with individual radars. With the current wide-spread acceptance of clear-air radar wind-profiling technology, field programs are increasingly taking advantage of the continuous wind observations available from wind profilers. At the same time several companies have become active in developing and marketing wind profilers. With the deployment of the 30 station network of wind profilers in the central United States, it appears evident that we are on the threshold of a new era in which wind profilers will become an integral part of the next generation weather observing system.

While much of the wind profiler research community has been focused on mid-latitude atmospheric research, the Aeronomy Laboratory's Tropical Dynamics and Climate Program has focused its attention on the use of wind profilers in the tropics to study the scale interactions that take place between tropical convection and large-scale atmospheric circulation systems. Because the wind profilers observe vertical as well as horizontal motions, the relationship between atmospheric vertical motions and convective systems in the tropics can now be examined directly. In addition, the wind observations from the new wind profilers augment the existing base of conventional observations available in the tropics. For example, wind observations from Christmas Island are routinely transmitted via GOES satellite and input into the Global Telecommunications System (GTS) for world-wide dissemination. These observations are already being used routinely by the National Meteorological Center (NMC) and the European Centre for Medium Range Weather Forecasts (ECMWF) in their analysis and forecast products (GAGE et al., 1988).

This paper is broadly concerned with the application of wind profiling technology to tropical atmospheric research. Specifically, we will present some preliminary results of wind profiler studies of tropical convection and discuss the construction of a trans-Pacific wind profiler network as it relates to studies of equatorial waves and large-scale atmospheric circulation systems associated with El Niño-Southern Oscillation (ENSO) phenomena.

2. CONVENTIONAL WIND OBSERVATIONS IN THE TROPICS

The tropics are poorly observed compared to the populated land masses in the temperate latitudes. Over the vast oceans the only wind observations that are available above the surface come from two major sources. Where clouds are present, cloud drift winds are determined routinely from satellite imagery. Typically, these winds are limited to two height ranges: the 850-900 mb region and the 200-300 mb region. The accuracy of this method was found by HUBERT AND THOMASELL (1979) to be no better than ± 5 ms^{-1}. At the 250 mb level additional wind information is available from commercial aircraft. While their precision is excellent (± 1 ms^{-1}), their height distribution and geographical coverage is very limited.

Routine wind soundings are available only from a sparse network of rawinsonde stations. Figure 1 shows the locations of rawinsonde stations in the tropical Pacific. The map shows the locations of stations that are included in the NCAR archive of upper-air data (R. JENNE, private communication). The solid triangles refer to stations with a record of data longer than twenty years. Stations marked by the open triangles have records shorter than twenty years. Most of these stations have ceased operation in the last decade or so. Even some of the stations with longer records are no longer in operation or do not have complete records. Examples of these are Momote (2°S, 147°E), Raboul (4°S, 152°E) and Lima (12°S, 77°W). The trend over the last two decades has been in the direction of a decreasing data base for rawinsonde stations over the tropical Pacific.
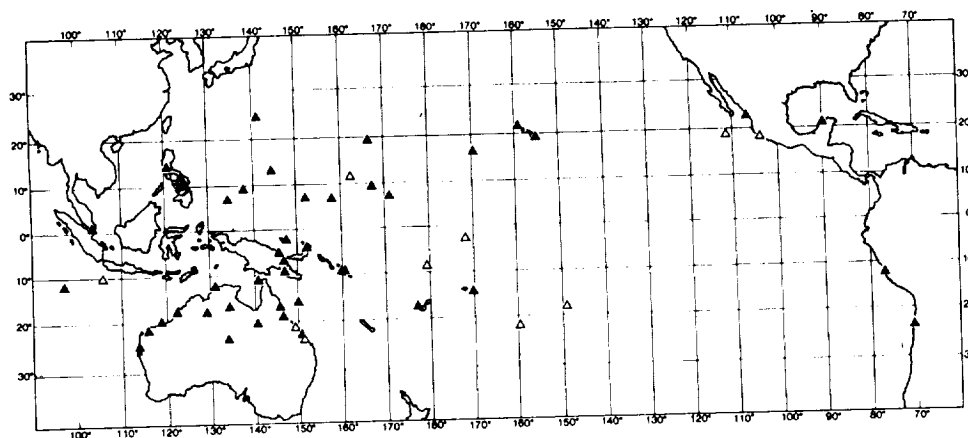
Figure 1. The distribution of tropical rawinsonde stations for which significant data is included in the NCAR archives.

Excluding the Australian stations, most of the stations in Figure 1 are located on islands in the western Pacific. Even amongst the relatively dense station network that is located in the western Pacific, relatively few stations are located within five degrees of the equator. In fact, in Figure 1, Singapore (1°N, 104°E) is the only station located within 5 degrees of the equator that is currently in operation and has a long record of archived data. For many purposes the equatorial Pacific sector is greatly undersampled.

3. WIND PROFILER RELATED RESEARCH IN THE TROPICAL PACIFIC

Several wind-profiling Doppler radars have been operated in the tropics and sub-tropics. These include the Jicamarca radar (12°S, 77°W) located near Lima, Peru, the Arecibo radar (18°N, 67°W) located in Puerto Rico and the Chung-Li radar (25°N, 121°E) located in Taiwan. These radars operate primarily on a campaign basis and except for Chung-Li are engaged mostly in middle and upper atmosphere research.

The Aeronomy Laboratory has been involved with the use of wind profilers in the tropics since 1984 when the Pohnpei wind profiler was installed. The Pohnpei profiler has been used to measure continuously vertical velocities over Pohnpei. These vertical motions have been related to convective storms and rainfall by BALSLEY et al. (1988) and the influence of topography at Pohnpei on the observed vertical motions has been considered by BALSLEY AND CARTER (1989). The Christmas Island radar was constructed by the Aeronomy Laboratory in 1985 and became operational in April 1986. The Christmas Island wind profiler has three fixed beams and routinely measures horizontal and vertical velocities. Wind observations from the Christmas Island profiler are routinely transmitted via satellite and input onto the GTS. GAGE et al. (1988) have recently examined the Christmas Island wind observations in comparison to analyzed wind fields produced operationally by the NMC and ECMWF. They found that the inclusion of the Christmas Island wind observations led to considerable improvement in the analyzed winds at least in the vicinity of Christmas Island.

The ability of wind-profiling Doppler radars to measure directly vertical motions provides a useful technique for observing tropical convective systems. Figure 2 shows the signature of a deep convective system as it passed over the Pohnpei radar on 20 November 1984. Strong updrafts as shown here probably represent the first direct measurement of the convective "hot towers" discussed by RIEHL AND MALKUS (1958). These convective storms are invariably associated with heavy rain as recorded at the surface.
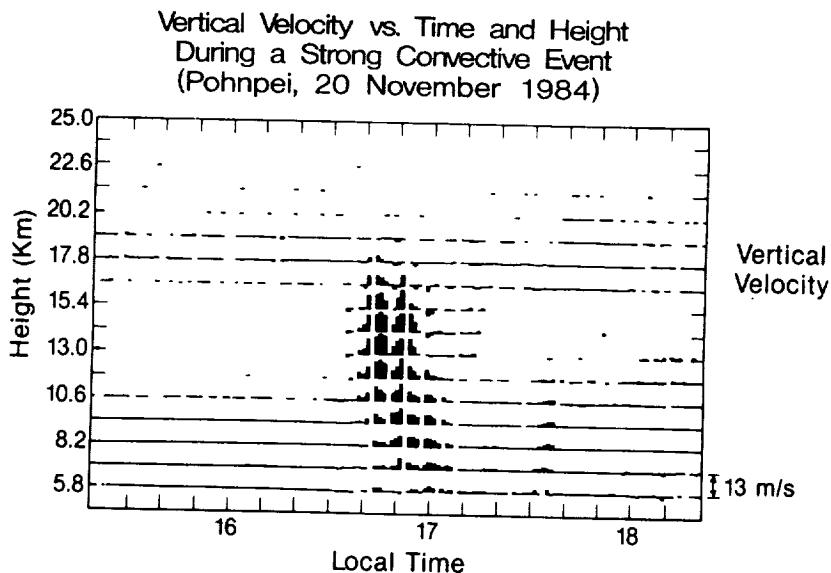
Figure 2. Signature of convective "hot tower" as seen by the Pohnpei wind profiler.

Average vertical motions seen by the Pohnpei wind profiler during its first two years of operation have been stratified by rainfall rate from surface measurements to reveal how the vertical motion field is affected by the presence or absence of convection. The results of this study published by BALSLEY et al. (1988) are shown in Figures 3-5. Figure 3 shows the results obtained when the heaviest rainfall periods are averaged. The most intense vertical motions of magnitude 100-200 cm s^{-1} are observed in the height range of 8-14 km. Also shown on Figure 3 is the vertical velocity profile deduced by GAMACHE AND HOUZE (1982) for the eastern Atlantic during GATE. The direct measurements are seen to yield peak velocities to considerably higher altitudes than for Gamache and Houze's result. Indirect measurements of average vertical motions in convective systems over the western Pacific have been determined by REED AND RECKER (1971) and these also show a similar disparity with the GATE results. The vertical profile of condensation heating is related to the vertical motion profile. As pointed out by HARTMANN et al. (1984), the vertical distribution of diabatic heating in the tropics is important for the parameterization of global climate models.

Mean Vertical Wind Profiles in Predominantly Convective Rain Regions
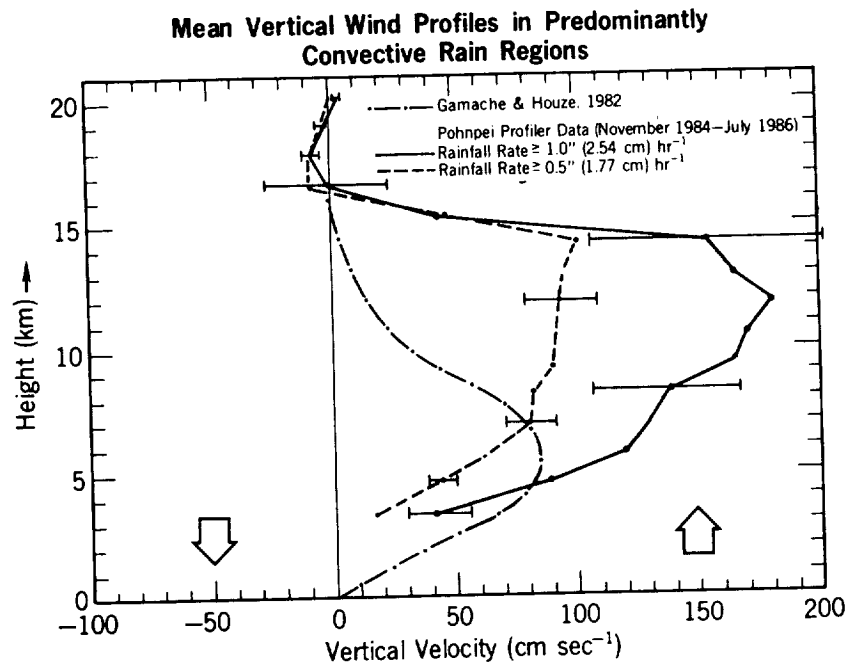
Figure 3. Average vertical wind profiles from the Pohnpei profiler for rainfall rates corresponding as closely as possible to convective conditions. (After BALSLEY et al. 1988).

Much of the rain that falls in the tropics is now thought to be associated with mesoscale convective systems. Rainfall in the tropical convective systems is comprised of heavy showers of limited duration and lighter, more persistent rainfall. The persistent rainfall is called stratiform rain and is inherent to the mesoscale convective system. Figure 4 shows average vertical motions in predominantly stratiform rainfall regions as deduced from the direct

vertical velocity measurements using the Pohnpei wind profiler. The observed
profile at Pohnpei is very consistent with the profile determined for GATE by
GAMACHE AND HOUZE (1985). The downward velocity at the lowest heights is
commonly associated with stratiform rain in mesoscale convective systems.

**Mean Vertical Wind Profiles in
Predominantly Stratiform Rain Regions**
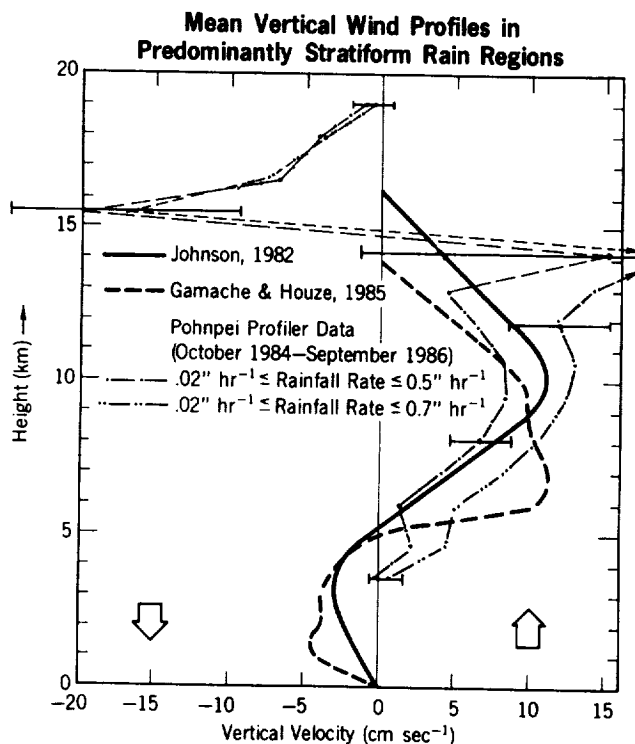
Figure 4. Average vertical wind profiles from the Pohnpei
profiler between October 1984 and September 1986 for
rainfall rates corresponding as closely as possible
to stratiform conditions. (After BALSLEY et al. 1988).

For predominantly clear conditions at Pohnpei, average vertical motion is
observed to be downward at all heights as shown in Figure 5. The magnitude of
the mean descending motion is what is required to balance the radiative cooling
to space. In magnitude and shape the Pohnpei measurements agree well with
indirect determinations by REED AND RECKER (1971) and McBRIDE AND GRAY (1980).

The Christmas Island wind profiler has provided routine measurements of
horizontal and vertical velocities since late March 1986. A sample day plot of
wind vectors for Christmas Island is shown in Figure 6. Wind observations from
Christmas Island are routinely used by NMC and ECMWF in their operational
analysis and forecast products. GAGE et al. (1988) compared the Christmas
Island observations with the analyses of both centers. A sample comparison for
zonal winds at 500 mb is shown in Figure 7. Statistics of the standard devia-
tion and bias of the observed winds relative to the analyses is shown in
Figures 8 and 9, respectively. Improvement is considerable in both standard
deviation and bias after the introduction of the winds into the analyses. The
Christmas Island winds were first used in the NMC analyses in mid-January 1987
and in the ECMWF analyses in April 1987.

**Mean Vertical Wind Profiles for
Predominantly Clear Conditions**

McBride & Gray (1980)
Reed and Recker (1971)
Pohnpei (Profiler Data
(December 1984—
June 1985)

Height (km)

Vertical Wind Velocity (cm/s)
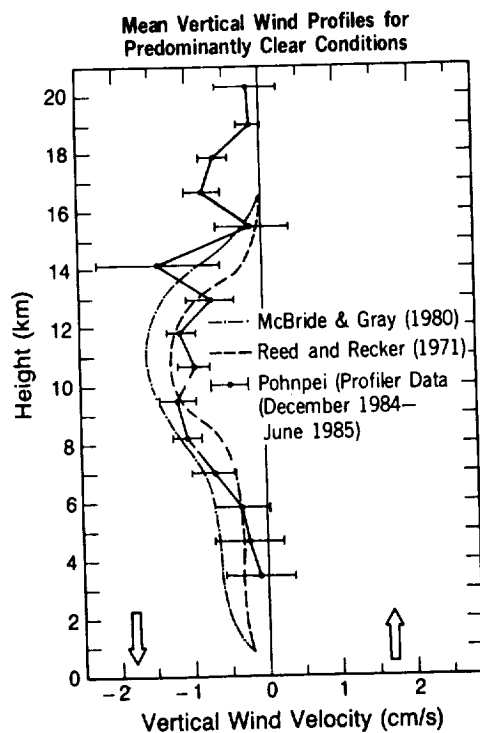
Figure 5.   Average vertical wind profile determined by the
Pohnpei wind profiler for 250 hourly periods between
December 1984 and June 1985, when the sky cover was
≤ 30% as determined by the Pohnpei weather station.
(After BALSLEY et al. 1988).

CHRISTMAS ISLAND PROFILER
(HORIZONTAL WIND VECTORS)

N
W E
S

Height (km)

22 MARCH 1986   60.0 Minute Averages

25 m/s
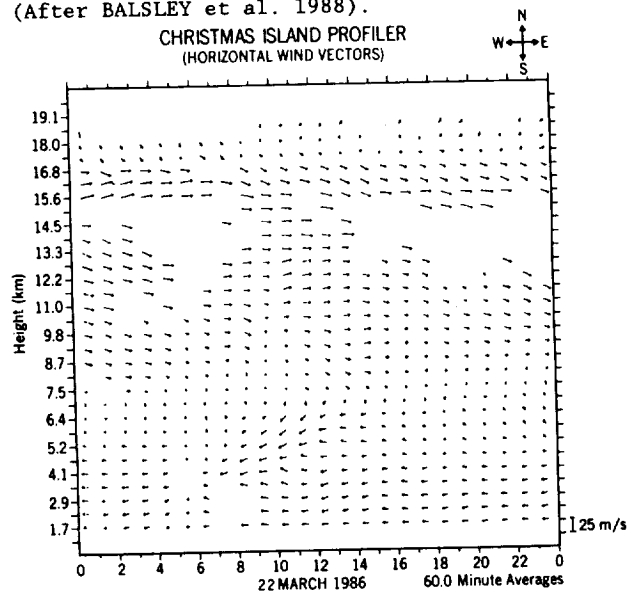
Figure 6.   Time-Height vector plot of Christmas Island winds
observed on 22 March 1986.
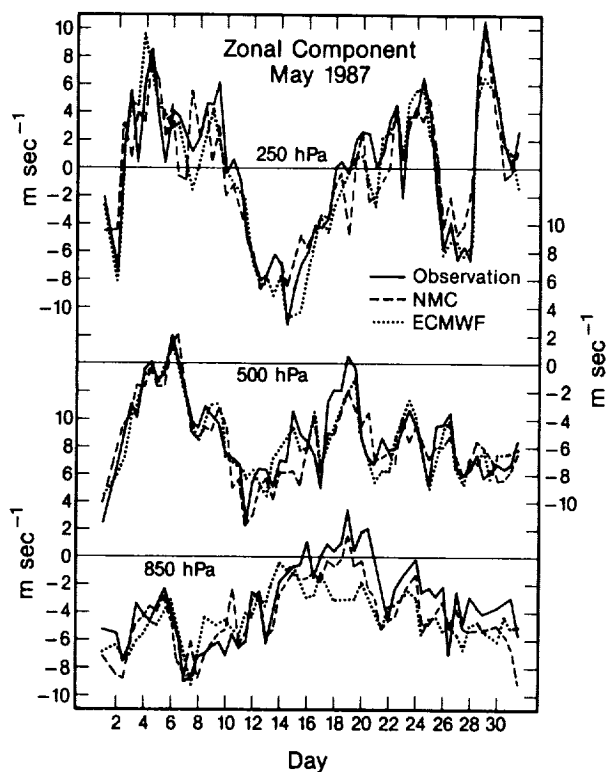
Figure 7. Multi-Height time series of zonal winds observed at Christmas Island for the month of May 1987. Interpolated NMC and ECMWF analyses are shown for comparison. (After GAGE et al. 1988).
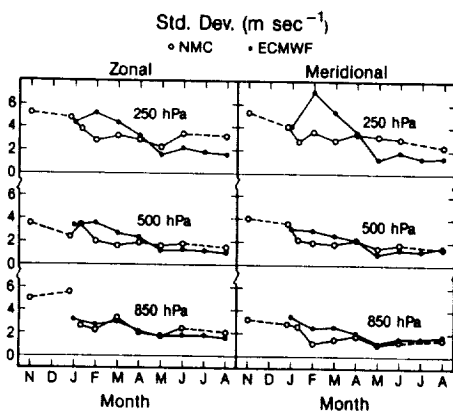
Figure 8. Time series of monthly standard deviation of Christmas Island winds compared to NMC and ECMWF analyses. (After GAGE et al. 1988)
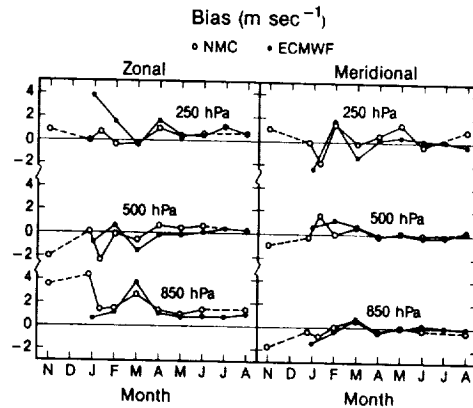
Figure 9. Time series of monthly bias of Christmas Island winds compared to NMC and ECMWF analyses. (After GAGE et al. 1988).

4. A TRANS-PACIFIC NETWORK OF WIND PROFILERS

The atmosphere across the tropical Pacific is far from uniform. Sea surface temperatures are typically much warmer in the western Pacific than they are in the central and eastern Pacific. Convection tends to be concentrated over the warm water which normally resides in the western Pacific. As shown in Figure 10, large-scale ascent typically occurs centered over the western Pacific and Indonesian maritime continent. The zonal circulation across the Pacific basin is referred to as the Walker Circulation. This zonal circulation is most pronounced during the anti El-Niño phase of the Southern Oscillation which represents the quasi-periodic interannual variation of the Walker circulation (RASMUSSON AND WALLACE, 1983).

EAST-WEST (WALKER) CIRCULATION ALONG EQUATOR

High
tropospheric
isobaric
surface

Low
tropospheric
isobaric
surface

INDIAN   PACIFIC   ATLANTIC

0°   90°E   180°   90°W   0°
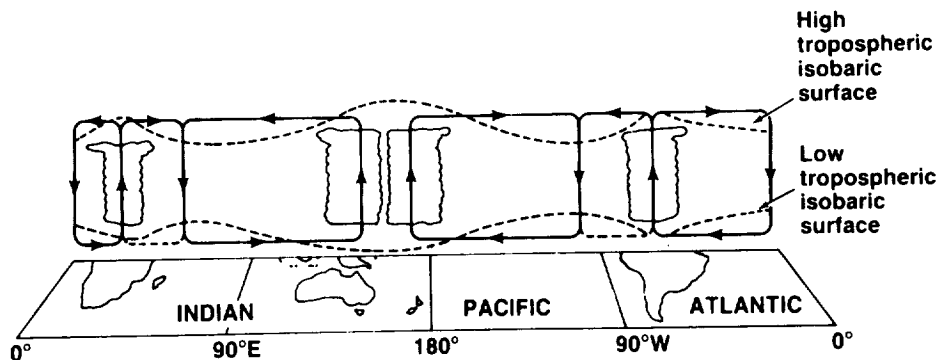
From P.J. Webster's Article in
Large-Scale Dynamical Processes In the Atmosphere
Hoskins and Pearce, Eds.,1983

Figure 10. Walker circulation along the equator. (After WEBSTER, 1983)

The intra-seasonal, seasonal, and interannual variations in tropical sea surface temperature, tropical convection and atmospheric circulation systems is a subject of much contemporary research. Variations in the longitudinal distribution of tropical convection are evident in patterns of outgoing long-wave radiation measured by satellite (LAU AND CHAN, 1985). Systematic patterns of low-level convergence and upper-level divergence are clearly associated with the regions of most intense convection (WEICKMANN, 1983). The influence of the non-uniform distribution of tropical convection across the Pacific basin is evident in the longitudinal variation of tropopause properties as discussed by GAGE et al. (1987). Recent diagnostic studies by REID et al. (1989) show that the influence of the ENSO signal can be seen at least into the lower stratosphere. It is thought that the influence of the varying tropical heating patterns create global teleconnections that influence weather around the globe (HOREL AND WALLACE, 1981).

Clearly, an understanding of the coupled ocean atmosphere dynamics that governs the ENSO phenomena is of prime importance in making further progress in climate forecasting. The Tropical Ocean Global Atmosphere (TOGA) Program is an international program designed to develop an understanding of the coupled ocean atmosphere system over the tropics. An important part of the TOGA effort is an intensive ten-year monitoring program to observe the tropical oceans and atmosphere.

Evidence is accumulating that the western Pacific region plays a key role in the initiation of ENSO events (LUKAS, 1988). Since the processes that give rise to the El Niño are so poorly understood, a coordinated effort is needed in the western Pacific to develop the requisite understanding to make further progress (LUKAS AND WEBSTER, 1988). The TOGA Coupled Ocean Atmosphere Response Experiment (COARE) is planned for the early 1990s.

Figure 11 shows the Pacific Ocean basin and the location of the proposed network of wind profilers. Profilers are already located at Pohnpei and Christmas Island. At the eastern end of the network a wind profiler is under construction at Piura, Peru. At the western end we plan to construct a wind profiler at Biak, Indonesia, in cooperation with the Indonesian National Institute of Aeronautics and Aerospace (LAPAN). When the planned International Equatorial Observatory (IEO) is taken into account, a truly international network of at least five wind profilers will eventually span the equatorial Pacific.

TRANS-PACIFIC PROFILER NETWORK
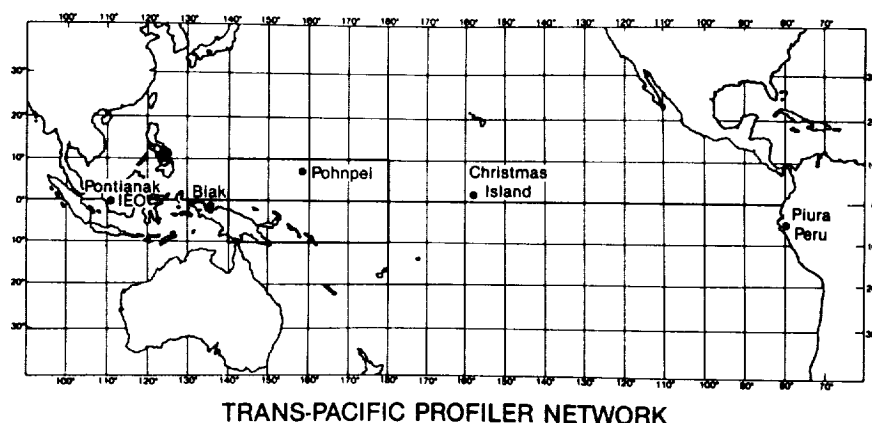
Figure 11. Planned trans-Pacific network of tropical wind profilers.

Wind observations from the proposed network should greatly aid the TOGA observational effort and provide a valuable new source of observations to explore a variety of dynamical phenomena in the tropics. The western stations should be well placed to be of use to the TOGA COARE experiment. The proximity of the network stations to the equator and the lack of other near-equatorial stations will provide a new source of observations for the study of equatorial waves.

The vanishing of the Coriolis force along the equator gives rise to a spectrum of equatorially trapped wave modes in the atmosphere and ocean (GILL, 1982). The oceanic Kelvin waves play an important role in the dynamics of the El Niño. The atmospheric equatorial waves that are known to play an important role in atmospheric dynamics include the large-scale eastward propagating Kelvin waves and the westward propagating mixed Rossby-gravity waves. Both types of waves reside primarily in the tropical lower stratosphere.

Also in the lower stratosphere, but on a much longer time scale, the QBO is one of the more pronounced quasi-periodic wind oscillations in the atmosphere. The QBO is dynamically linked to the upward propagating equatorial waves that deposit their momentum in the lower stratosphere (HOLTON AND LINDZEN, 1972). Using the method of VINCENT AND REID (1983) it should be possible to use a sensitive wind-profiling Doppler radar to observe the momentum deposition in the lower stratosphere.

In addition to the Kelvin and mixed Rossby-gravity waves, significant tropospheric wind oscillations on the intraseasonal time scales have also been identified. The 40-60 day oscillations identified by MADDEN AND JULIAN (1971) are clearly related to a large-scale modulation of tropical convection (WEICKMANN, 1983; LAU AND CHAN, 1985) and are accompanied by systematic patterns of convergence and divergence in the tropical tropospheric wind fields.

Observations from the trans-Pacific network of tropical wind profilers when analyzed in conjunction with other types of data should help improve our understanding of the interactions that take place between tropical convection, equatorial waves and large-scale tropical circulation systems. These scale interactions together with the air-sea interactions that are the subject of TOGA research need to be understood before further progress can be made on seasonal climate predictions.

5. CONCLUDING REMARKS

Consideration of the current base of wind observations that are used in contemporary operational global analyses and forecasts shows major deficiencies over the tropics. Furthermore, owing to the diversity of tropical circulation systems ranging from the scale of convection to the scale of the Walker and Hadley circulations, there is a need to better understand the scale interactions that take place in the tropical atmosphere. At the same time it is important to press forward on research aimed at a better understanding of the coupled dynamics of the atmosphere and ocean.

A network of wind profilers spanning the tropical Pacific can contribute substantially to further progress in understanding the dynamics of the tropical atmosphere. Additionally, observations from the wind profilers could be used to overcome deficiencies in the global observation system. Furthermore, long continuous records of wind observations from these stations should prove invaluable in monitoring interannual variations in large-scale atmospheric circulation systems.

The wind profilers described here generally do not observe below about two kilometers. Because of the importance of the tropical boundary layer and the relative lack of observations that are currently available, an intensive effort should be made to complement the large wind profilers with smaller lower tropospheric wind profilers. A lower tropospheric profiler that meets this need has recently been developed (ECKLUND et al. 1988). This lower tropospheric wind profiler can be deployed in networks at a fraction of the cost of larger wind profilers, suggesting that eventually nested grids of large and small profilers may be desirable. We are also working together with colleagues at NCAR to develop an Integrated Sounding System (ISS) that would combine surface observations with upper-level balloon soundings of wind and temperature and continuous wind observations using the lower tropospheric wind profiler. This development should satisfy the need for a sounding system capable of monitoring temperature and wind fields.

6. ACKNOWLEDGEMENTS

54

7. REFERENCES

Balsley, B. B., W. L. Ecklund, D. A. Carter, A. C. Riddle, and K. S. Gage (1988). Average vertical motions in the tropical atmosphere observed by a radar wind profiler on Pohnpei (7°N latitude, 157°E longitude), J. Atmos. Sci., 45, 396-405.

Balsley, B. B. and D. A. Carter (1989), Mountain waves in the tropical Pacific atmosphere: a comparison of vertical wind fluctuations over Pohnpei and Christmas Island using VHF wind profilers, submitted to J. Atmos. Sci.

Ecklund, W. L., D. A. Carter and B. B. Balsley (1989), A UHF wind profiler for the boundary layer: brief description and initial results, J. Tech., 5, 432-441.

Gage, K. S. and G. C. Reid (1987), Longitudinal variations in tropical tropopause properties in relation to tropical convection and El Niño-Southern Oscillation events, J.G.R., 92, 14,197-14,203.

Gage, K. S., J. R. McAfee, W. G. Collins, D. Söderman, H. Böttger, A. Radford, and B. B. Balsley (1988), A comparison of winds observed at Christmas Island using a wind-profiling Doppler radar with NMC and ECMWF analyses, Bull. Amer. Meteorol. Soc., 69, 1041-1046.

Gage, K. S. (1989), "The structure and dynamics of the free atmosphere as observed by VHF/UHF radar", Chapter 28a in Radar in Meteorology, D. Atlas, ed., A.M.S., Boston, in press.

Gamache, J. F. and R. A. Houze, Jr. (1982), Mesoscale air motions associated with a tropical squall line, Monthly Weather Rev., 110, 118-135.

Gamache, J. F. and R. A. Houze, Jr. (1985), Further analysis of the composite wind and thermodynamic structure of the 12 September GATE squall line, Monthly Weather Rev., 113, 1241-1259.

Gill, A. E. (1982), Atmosphere-Ocean Dynamics, Academic Press, New York.

Hartmann, D. L., H. H. Hendon, and R. A. Houze, Jr. (1984), Some implications of the mesoscale circulations in tropical cloud clusters for large-scale dynamics and climate, J. Atmos. Sci., 41, 113-121.

Holton J. R. and R. S. Lindzen (1972), An updated theory for the quasi-biennial oscillation of the tropical stratosphere, J. Atmos. Sci., 29, 1076-1080.

Horel, J. D. and J. M. Wallace (1981), Planetary-scale atmospheric phenomena associated with the Southern Oscillation, Monthly Weather Rev., 109, 813-819.

Hubert, L. F. and A. Thomasell, Jr. (1979), Error characteristics of satellite-derived winds, NOAA/NESS Tech. Rept. 79, 35 pp.

Johnson, R. H. (1982), Vertical motion in near-equatorial winter monsoon convection, J. Meteorol. Soc. Japan, 60, 682-689.

Lau, K.-M. and P. H. Chan (1985), Aspects of the 40-50 day oscillation during the northern winter as inferred from outgoing longwave radiation, Monthly Weather Rev., 113, 1889-1909.

Lukas, R. and P. Webster (1988), Proceedings of the U.S. TOGA Western Pacific Workshop, USTOGA8, U.S. TOGA Program Office, NOAA.

Lukas, R. (1988), On the role of the western Pacific air-sea interaction in the El Niño/Southern Oscillation phenomenon, in Proceedings of the U.S. TOGA Western Pacific Workshop, USTOGA8, R. Lukas and P. Webster, eds., U.S. TOGA Program Office, NOAA.

Madden, R. D. and P. Julian, (1971), Detection of a 40-50 day oscillation in the zonal wind in the tropical Pacific, J. Atmos. Sci., 28, 702-708.

McBride, J. L. and W. M. Gray (1988), Mass divergence in tropical weather systems: paper II. Large-scale controls on convection, Quart. J. Roy. Meteorol. Soc., 106, 517-538.

Rasmusson, E. M. and J. M. Wallace (1983), Meteorological aspects of the El Niño/Southern Oscillation, Science, 222, 1195-1201.

Reed, R. J. and E. E. Recker (1971), Structure and properties of synoptic-scale wave disturbances in the equatorial western Pacific, J. Atmos. Sci., 28, 1117-1133.

Reid, G. C., K. S. Gage and J. R. McAfee, (1989), The thermal response of the tropical atmosphere to variations in equatorial Pacific sea-surface temperature, submitted to J.G.R.

Riehl, H. and J. S. Malkus (1958), On the heat balance in the equatorial trough zone, Geophysica, 6, 503-548.

Vincent, R. A. and I. M. Reid, (1983) , HF Doppler measurements of mesospheric gravity wave momentum fluxes, J. Atmos. Sci., 40, 1321-1333.

Webster, P. J., (1983) "Large-scale structure of the tropical atmosphere", in Large-Scale Dynamical Processes in the Atmosphere, B. J. Hoskins and R. P. Pearce, eds., Academic Press, pp. 235-275.

Weickmann, K. M. (1983), Intraseasonal circulation and outgoing longwave radiation modes during the northern hemisphere winter, Monthly Weather Rev., 111, 1838-1858.

Dynamics of the Equatorial Middle Atmosphere (Overview)

Susumu Kato

Radio Atmospheric Science Center,
Kyoto University, Uji, Kyoto 611, JAPAN

Equatorial dynamics is unique because the Coriolis force vanishes at the equator tending to make atmospheric waves non-evanescent for all periods. With increasing latitudes, increasingly shorter period waves tend to be evanescent reaching the minimum threshold as 12 hrs at the pole. In the case of tides positive modes are mainly enhanced there in the equatorial region.

As to the excitation of these waves, the equatorial region is very active thermally and dynamically. The atmosphere-ocean interaction is also very intense. In spite of the importance of the region, we have been fairly ignorant of real situations of the region because of poor atmospheric observation network along the equator. Note that no MST radar station exists there. Considering the present circumstance the recent observation with ST radars by NOAA people as discussed at this workshop must be very significant. Specifically, very long vertical wavelength of diurnal tides observed at Ponape (Avery *et al.*) seems peculiar and inconsistent with numerical simulations as discussed by Aso at the Workshop. However, such observation must be considered seriously in future. One of most interesting and important dynamical phenomena would be the presence of the QBO which is now believed to be caused by the interaction of the background zonal flow and equatorial waves as Kelvin Waves and Rossby Gravity Waves. Precise observational studies with MST radars would be a very exciting problem. Note that recently the QBO is found to be very extended both horizontally and vertically, presenting an important index of the middle atmosphere general circulation.

A COMPARISON OF NUMERICAL MODELLINGS OF TIDES WITH OBSERVATIONS IN THE LOW LATITUDE MIDDLE ATMOSPHERE

T.Aso

Department of Electrical Engineering
Kyoto University, Kyoto 606
Japan

Introduction

Recent developments in atmospheric radars have indicated the possibility of illuminating the behavior of tides throughout the whole regions of the middle atmosphere. The ATMAP program during the MAP, coordinated by FORBES(1985), has greatly contributed to critical delineation of tidal structures by virtue of the global cooperation between modellers and observationalists. Comparisons of horizontal structures, however, reveal the scarcity of data at equatorial latitudes which, as indicated by KATO(1986), constitute a major route of solar energy to the atmosphere. Here we will compare some numerical modellings of steady atmospheric tides with sparse or intermittent observations at lower latitudes which have so far been obtained by ground-based radar and meteorological rocket launchings.

Numerical modellings

Numerical modellings are based on the inviscid model in which background mean zonal wind and associated latitudinal temperature profile are taken into account (ASO & KATO, 1984). Also referred to are the calculations by the classical theory, the EGM (Equivalent Gravity Modes) formalism (LINDZEN, 1970) and the comprehensive viscid model (FORBES, 1982a,b; ASO et al., 1987) at equinoxes. Only recently the inviscid model is applied to calculate short vertical wavelength diurnal tide which requires smaller grid size to maintain numerical accuracies. (FORBES & HAGAN ,1988; also cf. VIAL, 1986) Also, we have modified our code by expanding the latitudinal structures in terms of the orthogonal functions rather than discretizing.

Some of the results

Fig. 1 shows a comparison of the calculations of the altitude profiles of northerly (left) and westerly wind component of the semidiurnal tides at $15°N$ for the inviscid model assuming the solstitial background wind. Numerical schemes are by the finite difference method (dashed-dot curves),and the function expansion method (solid curves) where the associated Legendre functions of degrees up to 16 are considered. It is seen that two schemes for the inviscid calculations give consistent results. Also shown are the one calculated by the classical theory (dot curves), and the inviscid one based on the modified forcing function (broken curves) in which thermal drive due to radiative heating of water vapor falls off more rapidly. It is seen that the two forcings produce no drastic change to the altitude structure of the semidiurnal tide, but the background wind does contribute to some alterations from the classical theory. A comparison with a GCM calculation of 12 layer model up to 1 mb level (TOKIOKA and YAGAI, 1987) also gives reasonable agreement for the migrating semidiurnal component at December solstice.
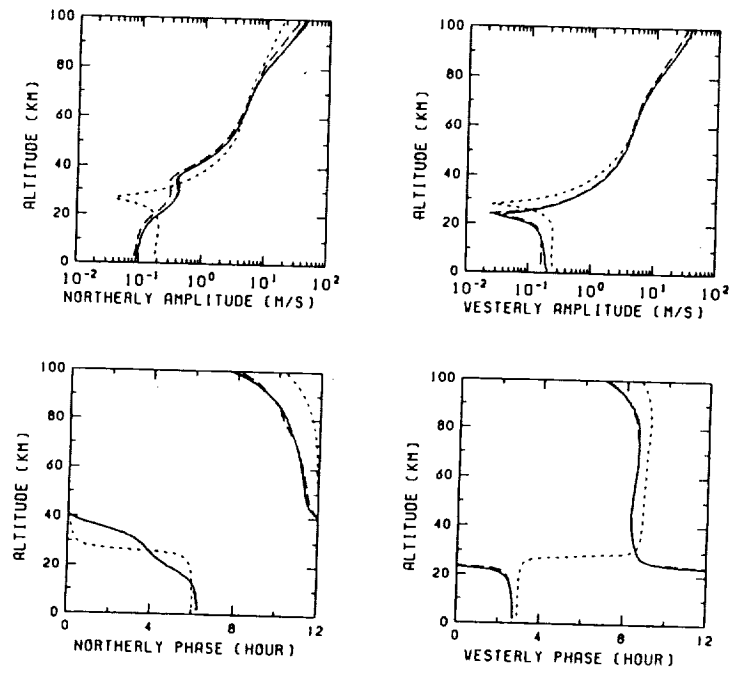
Fig.1 Inviscid model calculations of the northerly(left) and
westerly wind component of the semidiurnal tide for various
models.   See text for details.

Fig. 2 shows a comparison with the Jicamarca radar observations of the semidiurnal northerly and westerly wind component in October to December in the lower stratosphere (FUKAO et al, 1981a, 1981b). Calculations are inviscid model for December solstice (solid and dashed-dot curves as in Fig. 1), modified forcing (dot curves), classical theory (dashed-double-dot curves) and the one by LINDZEN and HONG(1974) (broken curves). It is seen that the observed amplitude is larger than the numerical modellings. The phase profiles in the October and December runs remain comparatively constant, consistent with the migrating tidal theory, but the phase reversal associated with node at around 30 km is not clearly detected. While, November run (squares) shows rapid phase change corresponding to short vertical wavelength of about 10 km. This suggests, as is mentioned by the author, the existence of irregular component as the non-migrating tide or the contamination by other wave modes, which may sometimes jeopardize quantitative interpretation of these snap-shot observations within the framework of migrating tidal theory.

For the mesospheric region, comparisons are made in Fig. 3 for the Jicamarca observations by our run in 1981 (MAEKAWA et al, 1986) and by COUNTRYMAN and DOLAS (1982). The calculations are the inviscid and classical modellings as in Fig. 2, together with the viscid one by FORBES (1982b) (open circle). The amplitude of the zonal wind component of the semidiurnal tide agrees with modellings. The observed phase values are almost consistent with each other below 80 km; inferred vertical wavelength is slightly short compared with theoretical predictions though the phase value is in proximity to observations at lower altitudes.

For the diurnal tide, inviscid model calculation by the function expansion method still loses some accuracy due to its small-scale vertical structures compared with the semidiurnal component. Tentatively, we compare the observations at Jicamarca in October to December (FUKAO et al, 1981b, MAEKAWA et al, 1986) with December solstice calculations in Fig. 4. In the figure, solid curves refer to the inviscid model with maximum degree of 40 for the orthogonal function, and dashed-dot curves to the classical calculation. It is noted that the observations are roughly compatible with theory with some irregular excursions in phase. Early winter observations of the zonal wind component in May (shown by + in the same plot for comparison) show rather large amplitude and short vertical wavelength of about 10 km, which is consistent with the predominance of non-migrating tides, and is not reproducible by the migrating mode calculation.

Rocket observations at tropical region summarized by GROVES (1980) are compared with the numerical calculations. Most of the data are on a short-term basis. It is seen that the basic structures of amplitude and phase roughly correspond to calculations, but the irregular features such as is not compatible with geographic conjugacy across the equator, are at times superposed upon it. Averaged structures of the rocket observations of the diurnal northerly wind component at Ascension Island as given by REED et al (1969) is compared in Fig. 5 with various modellings between 30 and 60 km region at equinoctial low latitudes. The calculations include the viscid calculations for the equinoctial mean wind regimes (solid curves) (ASO et al., 1987), EGM formalism invoking (1,1)+(1,3)+(1,-2) modes (dashed-double-dot curves), the classical calculation (broken curves) and FORBES's calculation (FORBES, 1982a) (solid triangle). Though the observed phase becomes erratic at around 40 km where amplitude reaches minimum, reasonable agreement is evident for both amplitude and phase profiles on an averaged sense.

ALTITUDE (KM)

NORTHERLY AMPLITUDE (M/S)

ALTITUDE (KM)

VESTERLY AMPLITUDE (M/S)

ALTITUDE (KM)

NORTHERLY PHASE (HOUR)

ALTITUDE (KM)

VESTERLY PHASE (HOUR)

OBSERVATION- JICAMARCA

—○— 3 — 4 OCT 1977
—●— 6 — 8 DEC 1977
--□-- 14 - 16 NOV 1977
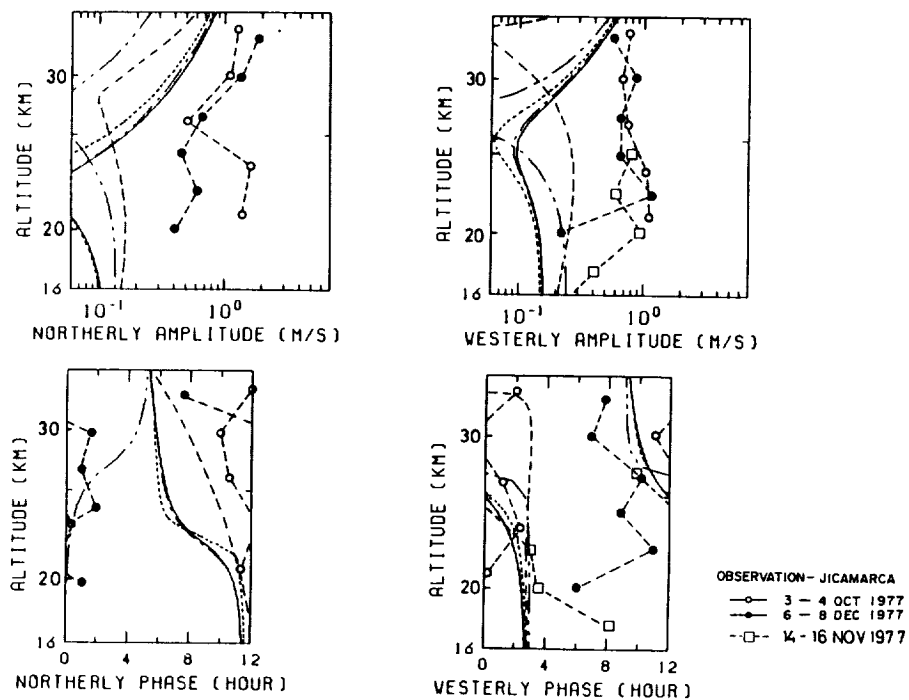
Fig.2 A comparison of the semidiurnal tide for the Jicamarca
lower stratospheric observations by FUKAO et al. (1981a,b)
with numerical modellings. See text for details.

Amplitude (ms⁻¹)

Hour of maximum eastward

JICAMARCA

19 - 21 NOV 1981

FITTING

—●— DC + 12 HR

—●— DC + 24/12 HRS

--□-- DC + 5/2 DAYS
+ 24/12 HRS
NIGHT TIME DATA SET 2200

COUNTRYMAN AND DOLAS 1982

···+··· DEC 20-22 1976

···X··· OCT 3-6 1977

FORBES 1982

○
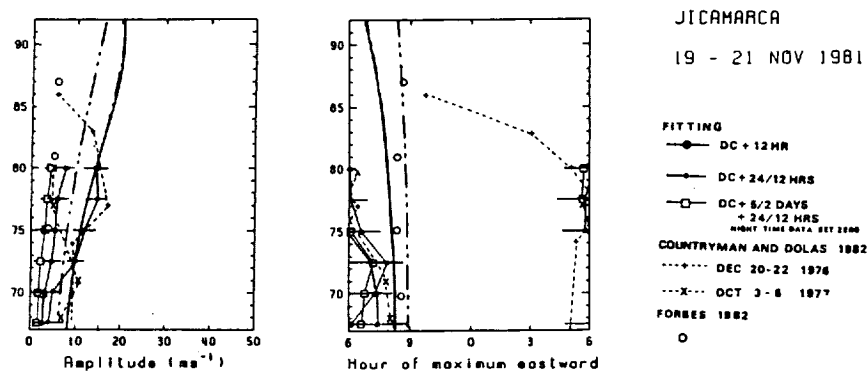
Fig.3 A comparison of the semidiurnal tide for the Jicamarca
mesospheric observations by MAEKAWA et al. (1986) and
COUNTRYMAN and DOLAS (1982) with numerical modellings. See
text for details.
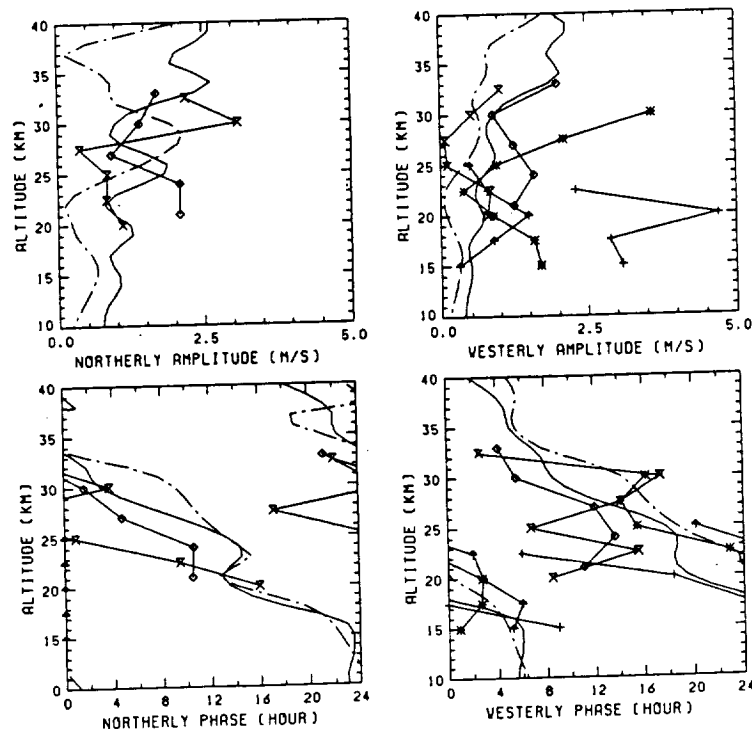
Fig.4 A comparison of the diurnal tide for the Jicamarca lower
stratospheric observations by FUKAO et al. (1981a,b) and
MAEKAWA et al.(1986) with numerical modellings. See text
for details.
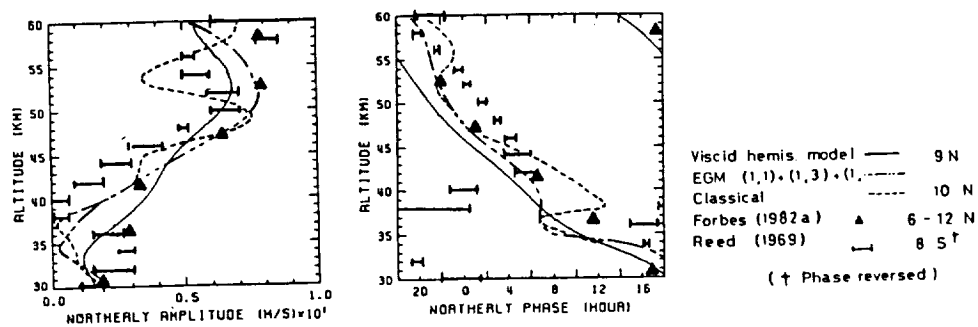
Fig.5 A comparison of the diurnal northerly wind component for
the averaged structures of the rocket observations at
Ascension Island by REED et al (1969) with various numerical
modellings at equinoxes.

Recently TSUDA and KATO (1988) calculated the diurnal non-migrating tide generated solely by assuming localized heat source due to land sea differences. Their results suggest amplitude of 2 to 3 m/sec near 20 km and vertical wavelength as short as 2 to 5 km. Rocket data at tropical latitudes averaged over several days , by and large, indicate slightly more moderate phase progression and also energy flow from above, thus the modelling based on the combination of steady migrating tide and the non-migrating tide as carried out by Forbes and Groves (1987) will properly delineate tidal observations especially at equatorial lower altitudes.

Conclusions

Brief comparison of low latitude tidal observations at lower altitudes with numerical modelling of tides reveals that the steady tidal theory basically or on an averaged sense agrees with observations, and considerations on the irregularity due to non-migrating tide and other non-tidal components might resolve some of the discrepancy and variabilities.

At higher altitudes, tides are more properly delineated by existing tidal theory, and further sophistication with respect to forcings, mean wind, dissipation and interaction processes warrants more adequate delineation of tidal variability.

References

Aso, T. and S. Kato (1984), Linearized steady calculations of semidiurnal tides in the middle atmosphere, Dyn. Middle Atmosphere, 173-180.

Aso, T., S. Ito, and S. Kato (1987), Background wind effect on the diurnal tide in the middle atmosphere, J. Geomag. Geoelectr., 39, 297-305.

Countryman, I. D. , and P. M. Dolas (1982), Observations on tides in the equatorial mesosphere, J. Geophys. Res., 87(C2), 1336-1342.

Forbes, J. M. (1982a), Atmospheric tides 1. Model description and results for the solar diurnal component, J. Geophys. Res., 87(A7), 5222-5240.

Forbes, J. M. (1982b), Atmospheric tides 2. The solar and lunar semidiurnal components, J. Geophys. Res., 87(A7), 5241-5252.

Forbes, J. M. (1985), Atmospheric tides middle atmosphere (ATMAP): Report of the November/December 1981, and May 1982, observational campaigns, Handbook for MAP, 17, 36-43; also Atmospheric tides below 80 km, 16, 157-163.

Forbes, J. M. and G. V. Groves (1987), Diurnal propagating tides in the low-latitude middle atmosphere, J. Atmos. Terr. Phys., 49(2), 153-164.

Forbes, J. M. and M. E. Hagan (1988), Diurnal propagating tide in the presence of mean winds and dissipation: a numerical investigation, Planet. Space Sci., 36(6), 579-590.

Fukao, S., Y. Maekawa, and S. Kato (1981a), A semidiurnal wind oscillation with short vertical wavelength observed in the tropical lower stratosphere, J. Geomag. Geoelectr., 33, 421-427.

Fukao, S., K. Aoki, K. Wakasugi, T.Tsuda, S. Kato , and D. A. Fleisch (1981b), Some further results on the lower stratospheric winds and waves over Jicamarca, J. Atmos. Terr. Phys., 43(7), 649-661.

Groves, G. V. (1980), Seasonal and diurnal variations of middle atmosphere winds, Phil. Trans. R. Soc. Lond., A296, 19-40.

Kato, S. (1986), EMA (Equatorial middle atmosphere), Handbook for MAP, 23, 73.

Lindzen, R.S. (1970), Internal gravity waves in atmospheres with realistic

dissipation and temperature part I. Mathematical development and propagation of waves into the thermosphere, Geophys. Fluid Dyn., 1, 303–355.

Lindzen, R. S., and S. -S. Hong (1974), Effects of mean winds and horizontal temperature gradients on solar and lunar semidiurnal tides in the atmosphere, J. Atmos. Sci., 31, 1421–1446.

Maekawa, Y., T. Aso, J. Rottger, P. Czechowsky, R. Ruster, G. Schmidt, I. Hirota, R. F. Woodman, and S. Kato (1986), A cooperative synchronous observation of winds and tides in the tropical lower stratosphere and mesosphere using VHF radars at Jicamarca and Aecibo, J. Geomag. Geoelectr., 38, 81–97.

Reed, R. J., M. J. Oard, and M. Sieminski (1969), A comparison of observed and theoretical diurnal tidal motions between 30 and 60 kilometers, Mon. Wea. Rev., 97(6), 456–459.

Tokioka, T. and I. Yagai (1987), Atmospheric tides appearing in a global atmospheric general circulation model, J. Meteor. Soc. Japan, 65,423–438.

Tsuda, T. and S. Kato (1988), Diurnal non-migrating tides excited by a differential heating due to land-sea distribution, Submitted to J. Meteor. Soc. Japan.

Vial, F. (1986), Numerical simulations of atmospheric tides for solstice conditions, J. Geophys. Res., 91(A8), 8955–8969.

OBSERVATIONS OF EQUATORIAL MESOSPHERIC MEAN WINDS AND TIDES

S.K. Avery, R.L. Obert, and J.P. Avery

University of Colorado, Boulder, CO, USA

A meteor echo and detection system has been designed for use on many VHF radars. This system operates in parallel with the normal operation of ST/MST radars except for the lengthening of the interpulse period to avoid range aliasing in the 80-100 km height range. The prototype system is described in WANG (1988) and has been modified to incorporate a more robust detection algorithm using discrete Fourier transforms. The system has been field tested on the ST radar at Platteville, Colorado and performance tested on the Poker Flat, Alaska MST radar. We have packaged the system for use in remote areas and have installed it on the NOAA ST radar located at Christmas Island (2° N, 158° W). In this presentation I will describe the mean winds and tides during August and September 1988 that were observed using this system.

The average meteor echo rate on the east antenna beam as a function of height for August-September is shown in Figure 1 (top). The height profile is typical of what we expect from a VHF radar. The echo rates are small compared with a regular meteor radar system because of the narrow antenna beamwidth used with ST radars. An anomalous echo was observed during August 8-11. As seen in Figure 1 (bottom) this echo occurred between 92-96 km and is either an echo from the electrojet, or from clear-air turbulence, or possibly from space debris. The average diurnal echo rate on the east antenna beam for this same period is shown in Figure 2 (top). Peak echo rates occur during the morning hours. The day/night ratio is approximately 3:1. The anomalous echoes occurred between 1600-1900 local time (Figure 2, bottom).

The monthly mean winds for August and September are shown in Figure 3. In general the winds are westward with peak magnitudes of 12 ms^{-1}. The wind crosses over to an eastward direction at approximately 96 km. The meridional profile generally shows southward winds at lower heights with northward above 96 km. The weekly averages (not shown) indicate significant long period wave activity.

The diurnal tide height profile for August is shown in Figure 4. Average amplitudes are 20-40 ms^{-1} which are considerablylarger than what models suggest. Long vertical wavelength modes are apparent in the meridonal component. The zonal component shows evidence of a mixture of higher order modes.

The semidiurnal tide is weaker than the diurnal tide (Figure 5.) Amplitudes are approximately 10 ms^{-1}. During August there was a peak in the amplitude of 30 ms^{-1} confined to a fairly narrow (3 km) layer at a height of 91 km. The observed phase indicates a propagating wave with a vertical wavelength of 48 km. The dashed lines in this figure represent the results from a new model which simulates *monthly* semidiurnal tidal structure VIAL & FORBES, (1988).

The model amplitudes are weaker than what is observed. There is excellent agreement in the meridional component between the model and observations. The model zonal component shows an evanescent mode structure whereas the observed structure represents a propagating mode.

The Christmas Island MEDAC system is providing us with the first long-term measurements of equatorial mesospheric winds. We plan to do a thorough analysis of the long period temporal variability of the winds. We will also be comparing our results with those obtained with a 2.6 MHZ radar which will be installed by R. Vincent in the near future.

REFERENCES

Wang, S.T., D. Tetenbaum, B.B. Balsley, R.L. Obert, S.K. Avery, and J.P. Avery, A meteor echo detection and collection system for use on VHF radars, *Radio Science, 23,* 46-54, 1988.

Vial, F. and J. Forbes, Private communication, 1988.

CHRISTMAS ISLAND (1988)
DAYS 221-274
ZONAL ECHOES/HOUR VS. HEIGHT

CHRISTMAS ISLAND (1988)
DAYS 221-274
ZONAL ECHOES/HOUR VS. TIME OF DAY

CHRISTMAS ISLAND (1988)
DAYS 221-224
ZONAL ECHOES/HOUR VS. HEIGHT

CHRISTMAS ISLAND (1988)
DAYS 221-224
ZONAL ECHOES/HOUR VS. TIME OF DAY
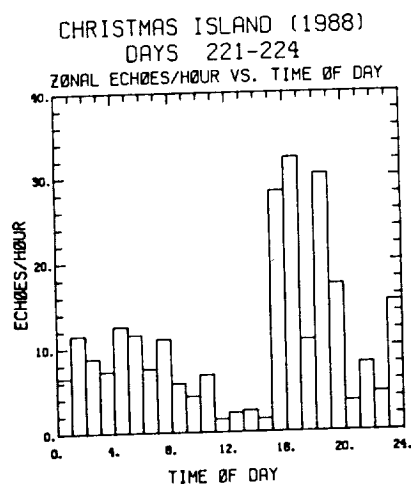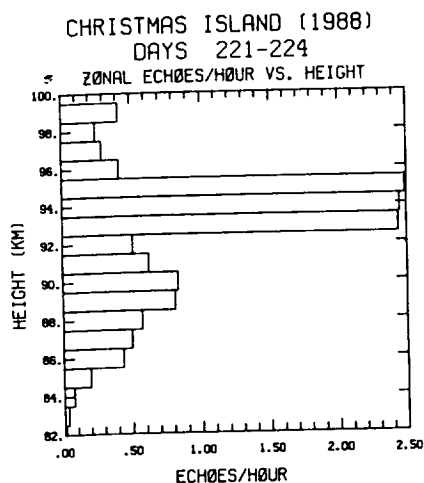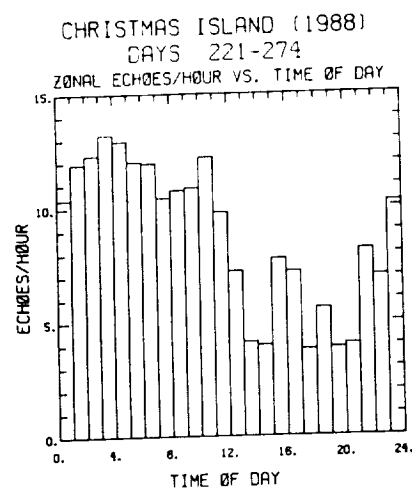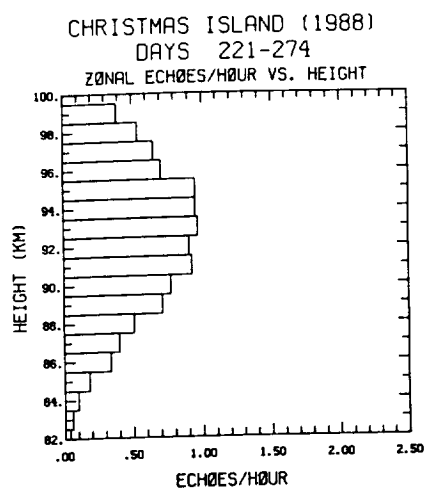
Figure 1. (top) Average meteor echo rate as a function of height for August-September. (bottom) Echo rate profile during period when anomalous echoes were observed, August 8-11, 1988.

Figure 2. (top) Average diurnal echo rate for August-September, 1988. (bottom) Diurnal echo rate during period of anomalous echoes.

CHRISTMAS ISLAND (1988)
MEANS
DAYS 221-244

CHRISTMAS ISLAND (1988)
24 HOUR TIDE AMP.
DAYS 221-244

CHRISTMAS ISLAND (1988)
MEANS
DAYS 245-274

CHRISTMAS ISLAND (1988)
24 HOUR TIDE PHASE
DAYS 221-244
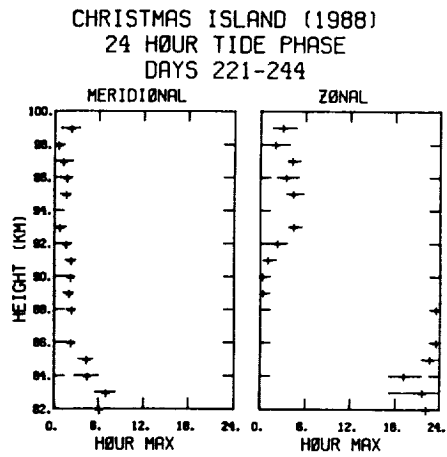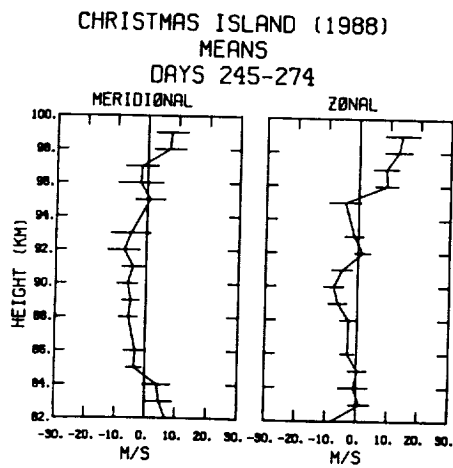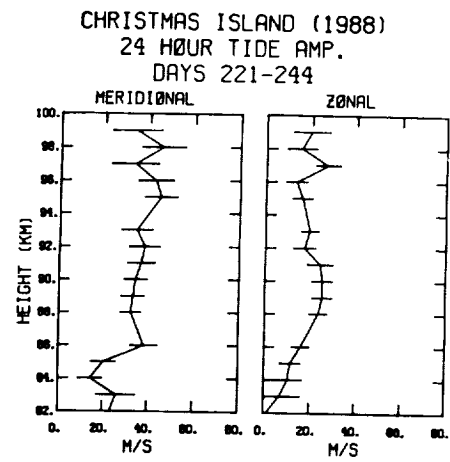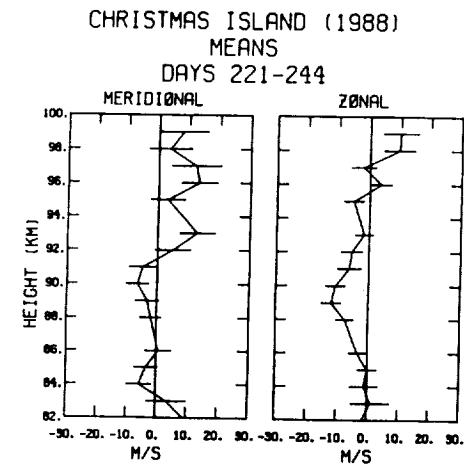
Figure 3. Mean winds for the months of August (top) and September (bottom). Positive values correspond to eastward and northward winds.

Figure 4. Diurnal tide height profile (amplitude and phase) for August.
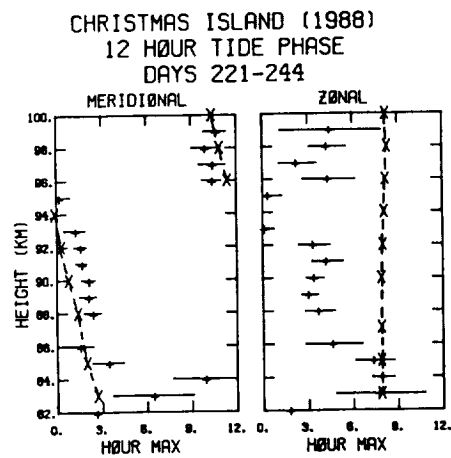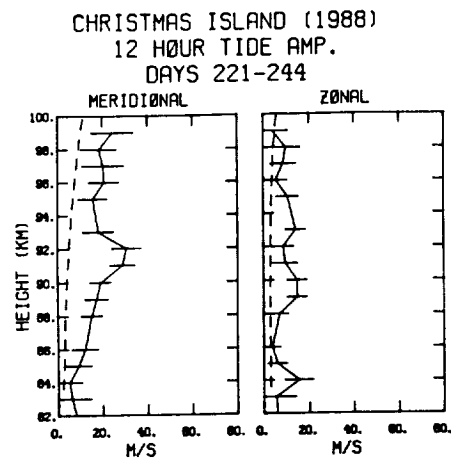
Figure 5. Semidiurnal tide height profile (amplitude and phase) for August.

THE INTERPRETATION OF MST RADAR ECHOES:
THE PRESENT KNOWLEDGE OF THE SCATTERING/REFLECTION AND THE
IRREGULARITY GENERATION MECHANISMS
(Keynote Paper Session 3)

Jürgen Röttger[*]
EISCAT Scientific Association
P.O.Box 812
S-981 28 Kiruna, Sweden
(* on leave from Max-Planck-Institut für Aeronomie)

INTRODUCTION

There is no unified opinion noticeable yet which mechanism may be the most relevant to cause the echoes of MST radars from the mesosphere, stratosphere and the troposphere. We only could distinguish so far between the major process of scattering/reflection from refractive index irregularities due to temperature, humidity and electron density fluctuations on the one side and the other two processes, namely scatter from hydro-meteors in the troposphere as well as incoherent scatter from free electrons in the mesosphere, which cause the observed radar echoes. The major echoing process can be described by several mechanisms as is delineated in the following Table 1.

Table 1

MODELS FOR

SCATTER/REFLECTION MECHANISMS

OF MST RADAR SIGNALS

(conceptual synopsis)

Mechanism	Angular Spectrum	Coherence Time	Reflectivity Structure
BRAGG SCATTER (a) isotropic (b) anisotropic	constant wide	short short	random turbulence (a) isotropic (b) anisotropic
FRESNEL SCATTER (a) stratified (b) spread	narrow wide	intermediate intermediate	multiple laminae in stable environment (a) horizontally stratified (b) range, angle spread
FRESNEL (partial) REFLECTION (a) specular (b) diffuse	narrow very narrow	long very long	one dominating lamina in stable environment (a) very smooth (b) corrugated (rough)

In order to explain the relevant MST radar observations, two different basic echoing mechanisms are required, namely scattering and reflection. These, however, have to be adapted into quite diverse deviations from these two idealistic cases. For monostatic radars, backscatter and reflection arises from the component of the spatial spectrum of the variation of the refractive index n, whose spatial scale along the axis of the radar beam is half the radar wavelength, i.e. a few meters for low VHF and less than a meter at UHF. This process has been called Bragg or turbulence scatter if a radar volume is homogeneously filled with randomly distributed and fluctuating irregularities; whereas it is called (partial) reflection if an inhomogeneity in form of stable discontinuities or steps of the refractive index exists. The latter case most likely occurs at longer radar wavelengths. We know that these two idealized cases rarely occur but have to be replaced by more realistic models.

Since it is well documented from the aspect sensitivity and persistency of radar echoes that partial reflections from steep vertical gradients of the refractive index (discontinuities) are observed by vertically beaming radars operating around 50 MHz, we have to extend the radar equation for this condition. When applying this combined radar equation, essential assumptions for a meaningful interpretation have to be fulfilled which frequently are found not to be realistic. For the applicability for the scattered part of the signal, the scattering volume has to be homogeneously filled with irregularities; otherwise a filling factor has to be introduced. The scattering process has to be isotropic; otherwise the scattered power would depend on the look angle of the antenna. One also has to consider that the amplitude reflection coefficient cannot be uniquely determined, since it strongly depends on the shape of the refractive index profile within a distance of less than one radar wavelength (namely the spatial Fourier transform of the profile, evaluated at half the radar wavelength). It is also frequently observed that there is more than one partially reflecting discontinuity in the radar volume, and then the reflection coefficient is an even more uncertain parameter.

BRAGG SCATTER, FRESNEL SCATTER, AND FRESNEL REFLECTION

It is not readily possible to discriminate between the different basic processes of scattering and partial reflection without investigating particular features of the radar echoes, such as their aspect sensitivity, temporal and spatial coherency and their spectral shape. In general it has become accustomed in the MST radar community to apply a nomenclature which is basing on the principal schematics of the different refractive index formations shown in Fig. 1. There exist many papers dealing with the theory as well as experimental methods to investigate the scattering and reflection mechanisms and we will only delineate the basic characteristics (see list of references at the end of this paper for details). We have to note here that the applicability of these mechanisms to explain echoes from the atmosphere depend on the wavelength of the used radars. The reason is that the refractive index variations, which cause the echoes, have no unified characteristics at the different spatial scales corresponding to the radar wavelengths and Fresnel zones.

The principle scattering mechanism is frequently called **Bragg scatter** and the term turbulence scatter is also used, or more recently also the term "Pekeris scatter" (Gossard, personal communication 1988). The Bragg scatter can be isotropic, i.e. without causing a radar aspect sensitivity, if the turbulent irregularities of refractive index are homogeneously random and statistically similar in all directions. Bragg scatter can be anisotropic, causing an aspect sensitivity if the statistical properties of the irregularities, namely their correlation distances, are dependent on direction. Although the angular (spatial) dependence of the radar echoes, i.e. the aspect sensitivity, for these two
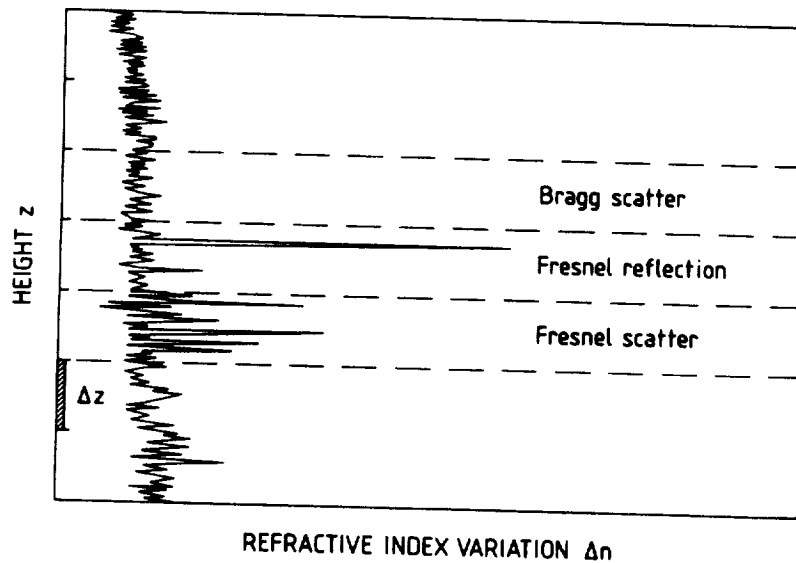
Fig. 1. Schematic depiction of the spatial variations δn of the refractive
index n in the vertical direction z (from Röttger and Larsen, 1989). Depending
on the structure of n within the range gate δz, the different processes of
Bragg scatter, Fresnel scatter and Fresnel reflection can occur. The abscissa
n could also resemble the horizontal direction x, namely indicating schemati-
cally the relative horizontal extent of surfaces of constant refractive index
variations (or their horizontal correlation distance) for the different pro-
cesses. Note that Bragg scatter occurs at every range where the variation of n
is similar to that in the indicated range δz. Thermal electron density fluctu-
ations, which cause incoherent (Thomson) scatter from the mesosphere, are much
weaker than the indicated variations of n, whereas the scatter cross sections
of precipitation is usually larger than the indicated changes of n.

processes - isotropic and anisotropic Bragg scatter - is different, the temporal
variations of the radar echoes should be similar because of the randomly fluctu-
ating irregularities. The Doppler spectrum should approximately reveal a Gaus-
sian shape.

Fresnel scatter occurs if, instead of a random ensemble of irregularities,
just a few refractive index discontinuities in vertical direction exist in the
range gate. These discontinuities are still randomly distributed in the verti-
cal, but have a large correlation distance in the horizontal direction. The
radar echo characteristics resemble a distinct aspect sensitivity, but because
the discontinuities are statistically independent, the temporal echo character-
istics should be similar to those of Bragg scatter. Because of the statistical
distribution of the discontinuities, the average power profile should fairly
smoothly vary with altitude.

Fresnel reflection is observed if a single, dominating discontinuity of the refractive index exists in vertical direction, which has a large horizontal extent, similar to the ensemble of discontinuities for the case of Fresnel scattering. A very distinct aspect sensitivity should be observed. High resolution vertical power profiles or height-time intensity plots should reveal outstanding spikes, or thin and persistent structures, respectively. Also the temporal characteristics should indicate long coherence times. This kind of process is also called "partial reflection", because only a very small fraction of the incident power is reflected. Fresnel reflection is also called "specular reflection" by some authors if the horizontal surface of the discontinuity is assumed to be very smooth, and it is called "diffuse reflection" if the discontinuity is assumed to be corrugated or somewhat rough. The case of anisotropic scatter has been considered, too, and appears to offer another realistic possibility to explain the scattering mechanism.

Fresnel scatter and reflection occur more likely on longer radar wavelengths, i.e. in the low VHF band. The terms Fresnel scatter and Fresnel reflection have been introduced due to the condition that the horizontal correlation distance of the discontinuities is in the order of the Fresnel zone $(z \cdot \Lambda)^{1/2}$. For correlation distances smaller than a fraction of the Fresnel zone, Bragg scatter has to be considered. The Fresnel zones of radars in the UHF and VHF band are usually smaller than the region in the troposphere and stratosphere, which is illuminated by the radar beam. Thus, the beam width limiting effect has not to be considered. It is perceived that the definition of Fresnel scatter and Fresnel reflection depends on the range gate width, i.e., it is more likely to observe Fresnel scatter with coarse height resolution, and to observe Fresnel reflection with good height resolution. The discontinuities must be in the order of a radar wavelength, or less in vertical direction, but widely extended in horizontal direction, which, because of diffusion reasons, is more likely to happen at larger vertical scales. The nomenclature of thin "sheets" or "laminae" to describe the 50 MHz observations was taken from oceanography where a similar fine structure is observed. The reason for the coexistence of refractive index turbulence and discrete discontinuities (sheets) could be for instance due to the gradients developing at boundaries of turbulence layers, or some other yet unproved mechanisms. Simulations and computations, compared with distribution functions of radar echoes on 50 MHz, demonstrate that signals do occur from certain altitudes which are consistent with the model of reflection from a single, diffuse sheet, causing focussing and defocussing.

Although a fine structure of radar echo power is also observed on 430 MHz on 440 MHz and on 2380 MHz, it is not obvious that the fine structure observed on 50 MHz with vertical beam, is of similar origin or nature. It is likely that radars in the UHF band will detect Bragg scatter only, whereas radars in the VHF band will usually detect a combination of the different processes, particularly when using a vertical beam. There are apparently weak Gaussian-shaped background spectra observed on which narrow spikes are superimposed. The Gaussian parts of the spectra are supposed to be partly due to Bragg scatter from a background of turbulence, and partly due to scatter from off-vertical irregularities carried by the wind (beam width broadening). The superimposed spikes in discrete frequency bins are either due to Fresnel scatter, or more likely due to Fresnel or diffuse reflection from a rough surface, i.e. several discrete regions of high reflection coefficient which move with different velocities. It is noted that the spectra of 50 MHz radars are not particularly governed by the spikes if the antenna is pointed far enough off-zenith (> 10°-15°), such that the (isotropic) Bragg scatter component dominates. It is also noted from spectra, as well as from the aspect sensitivity, that Fresnel scatter and particularly Fresnel reflection yield generally a larger echo power than Bragg scatter from turbulence.

CONSEQUENCES OF THE SCATTERING/REFLECTION PROCESSES

With near vertical beam of 50 MHz radars the observed echoes are usually a combination of the summarized scattering/reflection processes, although one mechanism may dominate at any given time, and the relative contributions of humidity and temperature also vary. These effects have consequences for (a) the interpretation of the MST radar echoes, (b) the analysis methods and data acquisition procedures, as well as (c) the technical design of the radar hardware, and (d) the choice of operating methods. The essential considerations, particularly holding for radars operating on VHF, are summarized here:

(1) The deduction of the turbulence refractive index structure constant C_n^2 from signal power or velocity fluctuations is difficult. The determination of the reflection coefficient is possible, in principle, but it does not allow the shape of the reflecting laminae to be deduced. It is not yet conceivable how to make a clear distinction between the contributions of humidity and temperature variations to the scattering/reflection process in the lower and middle troposphere. The estimate of velocity fluctuations, i.e. the turbulence energy dissipation rate ϵ from C_n^2, is not accurately possible. The discrimination between Fresnel reflection, Fresnel scatter, anisotropic and isotropic Bragg scatter is not unambiguous. These processes can even be regarded as interrelated.

(2) Non-volume filling scatter and reflection from several laminae have an influence on the accuracy of velocity determinations. The often simultaneously occurring scattered and reflected signal components need to be separated and treated by different analysis procedures. The effective beam angle is changed due to anisotropic scatter and reflection.

(3) If off-vertical beams are used, antenna sidelobes close to the zenith direction have to be sufficiently suppressed to reduce unwanted signals of reflected components. Otherwise signal power and velocity estimates will be inaccurate.

(4) It is noted that, in addition to the evident aspect sensitivity and a larger persistency, the echoes due to Fresnel scatter and Fresnel reflection are frequently much stronger than the echoes due to Bragg scatter. This enhances the radar sensitivity and allows 50 MHz radars to detect echoes from larger altitudes with vertical beam than with off-vertical beam.

(5) The so-called Doppler method is more convenient and applicable for measuring wind profiles when scattering processes are dominant (i.e. at large off-vertical beams at VHF, or at UHF generally). The spaced antenna method, using vertical beams, may be more efficient for measuring wind profiles when Fresnel scatter or reflection processes are dominant, i.e. at VHF. The Doppler method has been applied most frequently, but the spaced antenna method has further advantages, as will be explained in the following chapter.

On-going work on the subjects summarized under items 1-4 will likely shed more light on the processes, resolve remaining ambiguities and lead to a generalized procedure for deducing atmospheric parameters with an optimum accuracy and reliability. The difference of these mechanisms could be resolved by some measurement techniques which allow to partly discriminate between these mechanisms.

THE USE OF NEW TECHNIQUES

MST radars are usually operated in the Doppler mode, where several antenna beam directions are used to deduce the three-dimensional wind velocities from the Doppler spectrum. Occasionally also the so-called spaced antenna mode is applied to deduce the wind velocity from the cross correlation analysis of sig-
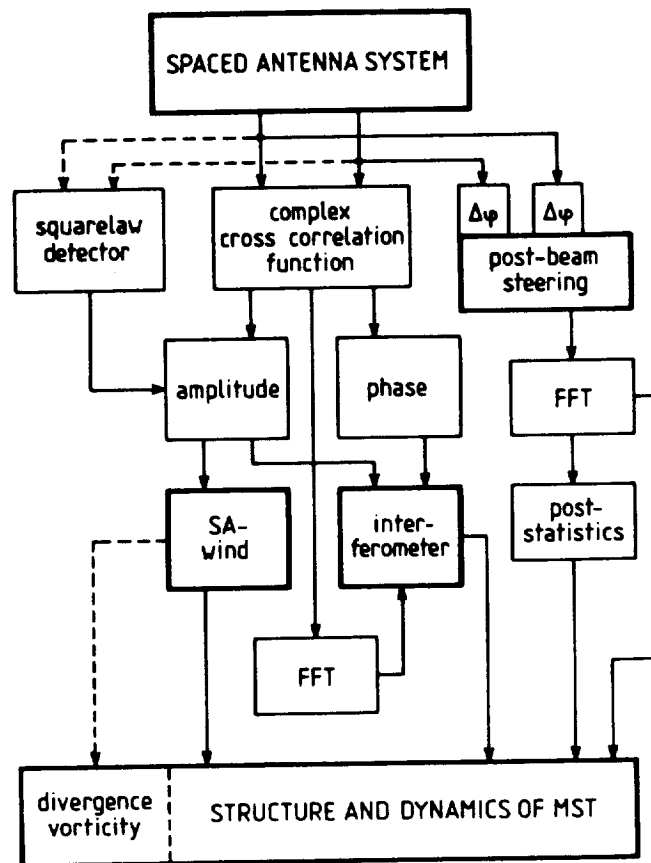
Fig. 2. The scheme of measurement and analysis techniques
of the spaced antenna configuration of an MST radar.

nals received at separate antennas. Both these methods of course allow the
measurement of some additional parameters, such as the signal power, the cohe-
rence time, the angular dependence or the spatial coherence as well as the
amplitude distribution functions. These are useful parameters to study the
scattering/reflection mechanism. Neither the Doppler nor the spaced antenna
method need the measurement of the spatial distribution of the signal phases on
the ground. In this paper we will point out some advantages of amplitude and
phase measurements with a spaced antenna set-up and prove the applicability of
this radar interferometer method to deduce additional signal parameters, which
the conventional Doppler and spaced antenna methods cannot supply.

In accordance to the term frequency domain interferometry, the method using several antennas is called the spatial domain interferometry or simply spatial interferometry. The frequency domain interferometry allows to improve the resolution in the radial (i.e, range) direction, whereas the spatial domain interferometry improves the resolution in the direction perpendicular to the beam direction (i.e., mostly horizontal). The latter method allows for instance to measure the angular spectrum (i.e., the aspect sensitivity), the incidence angle, the corrected vertical and horizontal velocity as well as to determine horizontal phase velocities of atmospheric gravity waves and to track turbulence blobs. Post-beam-steering and the cross spectra analysis can be applied to study waves and turbulence in the stratosphere and the mesosphere, respectively. The original method of cross spectrum and coherence analysis was developed to study scattering from E-region irregularities with the 50-MHz Jicamarca VHF radar. This method was also applied to measure incidence angles with the Chung-Li VHF radar and to investigate polar mesosphere summer echoes with the 224-MHz EISCAT VHF radar. We envisage essentially more details of the scattering/reflection mechanism by the application of the spatial and frequency domain interferometry.

In Fig. 2 we have summarized the different methods which can be applied with MST radar in the spaced antenna mode to measure atmospheric parameters. This is particularly emphasised since it is often thought that the spaced antenna method is barely the "spaced antenna drift" technique to measure the drift speed of refractive index irregularities and deduce the horizontal wind. This technique is only a minor part of the total, indicated by the branch including the square-law detector in Fig. 2. All further applications make use of the phase information, such as the interferometer, the post-beam-steering and the post-statistics method used with the SOUSY and the Jicamarca VHF radar, respectively.

POSSIBLE MECHANISMS TO GENERATE CERTAIN TYPES OF RADAR ECHOES

Some processes which could be generation mechanisms for the observed radar echo structures should now briefly be discussed. These mostly are related to atmosphere dynamic processes such as those outlined in Table 2, which shows the interrelation of atmospheric waves and turbulence as seen by MST radar.

Long-period waves undergo non-linear steepening or tilting when their phase velocity C approaches the wind velocity U. Through the approach of superadiabatic lapse rate and velocity shear, Kelvin-Helmholtz instability (KHI) is activated and quasi two-dimensional turbulence is generated. Turbulence scatter or Fresnel reflection from the boundaries of the turbulence layers can occur. Also steep temperature inversions (stable sheets or laminae) could be caused by the steepened waves, which can be seen by Fresnel reflection.

Short-period waves, propagating upwards from lower atmospheric sources or generated in-situ by KHI or by two-dimensional turbulence arising from long-period waves, undulate these layers of turbulence or the laminae of temperature inversions. Besides of transferring energy to long-period wave modes by wave-wave interaction these short-period waves can grow in amplitude by KHI (local generation) or due to energy conservation of upward propagating waves. Non-linear tilting, steepening and/or parametric instability can occur. The development of tilting can be observed by Fresnel reflection due to the concurrent distortion of isotherms during KHI.

Non-linear tilting of short period waves can cause overturning and breaking through the Rayleigh-Taylor instability (RTI). Since this happens at certain phases of the wave, localized regions of small-scale turbulence occur. These are seen by VHF radars as blobs or bursts, which are propagating with the phase speed of the wave. Blobs can spread into wider spatial scales by multiple repe-

Table 2

Interrelation of Waves and Turbulence as Seen by Radar (from Röttger, 1987)

long-period waves

$C \to U$

nonlinear steepening

of

velocity shear,
lapse rate
(unstable)

temperature inversions
(stable)

KHI

quasi-2-D
turbulence

turbulence scatter

or

Fresnel reflection
from
boundary of
turbulence layer

in situ

Fresnel reflection
(MST radar)
due to
persistent
sheets or laminae

short-period waves

wave–wave
interaction

undulate

layers of turbulence

sheets

growth of wave amplitude by KHI (local generation) or
from energy conservation of upward-propagating waves

nonlinear steepening,
parametric instability

nonlinear
wave tilting

distortion of
isotherms during
KHI

RTI
overturning,
breaking

Fresnel reflection
and
scattering

Secondary KHI

RTI etc.

turbulence blobs

decay into
turbulence layers

strong
turbulence
blobs

scattering

Fresnel scatter

generation of
temperature gradients,
dissolve into multiple sheets

tition of KHI/RTI and cause thick layers of strong turbulence. Through the turbulence layers corrugated temperature gradients are generated and the layers can dissolve into multiple sheets or laminae which can be regarded as remnants of active turbulence. Again waves, generated elsewhere, can undulate these turbulence layers and the laminae. We, thus, close the dynamical circle to explain the simultaneous observations of often independent, individual small- and meso-scale gravity waves and turbulence.

The described interrelation of a variety of dynamical phenomena in the atmosphere can explain the earlier recognized characteristics of VHF radar echoes, namely blobs, sheets and layers. They are consistent with accepted theories and observations of gravity waves and instabilities and they also support the notion of a coexistence of gravity waves and turbulence in the middle atmosphere.

CONCLUSION

The interpretation of radar returns from the clear air has been and still is in a long-lasting dispute. Is this just resulting from a semantic misunderstanding or preference of approaches to study the phenomenon or does it result from different physical phenomena? There are certainly different meteorological and aeronomical phenomena, which cause the different signal characteristics. In any case we can discriminate between the two extreme models of the echoing process itself: Scatter by random, non-deterministic fluctuations of the refractive index in space and time, which can be isotropic and anisotropic. These fluctuations result from neutral air turbulence of convective or dynamic origin. The anisotropic approach, however, is already at the limit of becoming deterministic in two coordinates. Reflection is from a refractive index discontinuity between horizontally stratified air masses of different refractive index, resulting from horizontal flow pattern, radiation, evaporation or electron density structures in the mesosphere. There are also clear indications for the coexistence of the two major mechanisms, namely the thin and almost horizontally stratified laminae of refractive index, which appear to be corrugated by background turbulence, the pronounced aspect sensitivity and long persistency which transits into isotropy and random fluctuations at larger aspect angles and the non-Gaussian shape of the Doppler spectra and signal components.

The transition between the classical turbulence scatter and reflection mechanisms and the scatter from hydrometeors needs to be considered also and will be discussed elsewhere as will the transition of turbulence scatter to incoherent scatter (Thomson scatter from the ionosphere). The former has for instance been done at the MU radar where the drop-size distribution was derived. The latter has been investigated at the EISCAT radars as polar mesosphere summer echoes (PMSE), which are neither generated by incoherent scatter nor turbulence scatter.

There had been some interesting recent developments and approaches for improving our understanding of the radar returns and the atmospheric structure, these are: The measurement of the frequency dependence of the MST radar echoes, the analysis of the signal statistics, modelling of the structures and the resulting radar returns, interferometer applications in space and frequency, vorticity and divergence measurements for instance. Further understanding will be gained by the combination of radar measurements with other methods, such as in-situ measurements with balloons, rockets and aircrafts. Also the extension of radar systems by radio-acoustic-sounding systems (RASS), LIDAR and SCIDAR (Scintillation measurements) is turning out to be very useful.

More details on the mentioned observations, mechanisms, interpretations and techniques can be found in the following list of references.

REFERENCES:

Adams, G.W., D.P. Edwards and J.W. Brosnahan (1985), The imaging Doppler inter-ferometer: Data analysis, Radio Sci., 20, 1481-1492.

Adams, G.W., J.W. Brosnahan, D.C. Walden and S.F. Nerney (1986), Mesospheric observations using a 2.66-MHz radar as an imaging Doppler interferometer: de-scription and first results, J. Geophys. Res., 91, 1671-1683.

Balsley, B.B., W.L. Ecklund, D.A. Carter, A.C. Riddle and K.S. Gage (1988), Average vertical motions in the tropical atmosphere observed by a radar wind profiler on Pohnpei (7°N latitude, 157°E longitude), J. Atmos. Sci., 45, 396-405.

Barat, J. (1982), Some characteristics of clear-air turbulence in the middle stratosphere, J. Atmos. Sci., 39, 2553-2564.

Briggs, B.H. (1980), Radar observations of atmospheric winds and turbulence: a comparison of techniques, J. Atmos. Terr. Phys., 42, 823-833.

Czechowsky, P., G. Schmidt and H. Kopka (1983), Medium frequency radar observa-tions in the middle atmosphere, J. Atmos. Terr. Phys., 45, 729-732.

Czechowsky, P., I.M. Reid and R. Rüster (1988), VHF radar measurements of the aspect sensitivity of the summer polar mesopause echoes over Andenes (69°N, 16°E), Norway, Geophys. Res. Lett., 15, 1259-1262.

Dalaudier, F., M. Crochet and C. Sidi (1989), Direct comparison between in situ and radar measurements of temperature fluctuation spectra: a puzzling result, (to appear in Radio Sci.).

Dewan, E.M. (1985), On the nature of atmospheric waves and turbulence, Radio Sci., 20, 1301-1307.

Doviak, R.J. and D.S. Zrnic (1984), Reflection and scatter formula of anisotro-pically turbulent air, Radio Sci., 19, 325-336.

Ecklund, W.L., D.A. Carter and B.B. Balsley (1988), A UHF wind profiler for the boundary layer: brief description and initial results, J. Atmos. Ocean. Tech-nol., 5, 432-441.

Farley, D.T., H.M. Ierkic and B.G. Fejer (1981), Radar interferometry: a new technique for studying plasma turbulence in the ionosphere, J. Geophys. Res., 86, 1467-1472.

Fritts, D.C. and P.K. Rastogi (1985), Convective and dynamical instabilities due to gravity wave motions in the lower and middle atmosphere: theory and observa-tions, Radio Sci., 20, 1247-1277.

Fukao, S., Y. Maekawa, T. Sato and S. Kato (1985), Fine structure in mesospheric wind fluctuations observed by the Arecibo UHF Doppler radar, J. Geophys. Res., 90, 7547-7556.

Fukao, S., K. Wakasugi, T. Sato, S. Morimoto, T. Tsuda, I. Hirota, I. Kimura and S. Kato (1985), Direct measurement of air and precipitation particle motion by VHF Doppler radar, Nature, 316, 712.

Fukao, S., T. Sato, T. Tsuda, M. Yamamoto and S. Kato (1986), High resolution turbulence observations in the middle and lower atmosphere by the MU radar with fast beam steerability: preliminary results, J. Atmos. Terr. Phys., 48, 1269-1278.

Fukao, S., T. Sato, T. Tsuda, S. Kato, M. Inaba and I. Kimura (1988), VHF Doppler radar determination of the momentum flux in the upper troposphere and lower stratosphere: comparison between the three- and four-beam methods, J. Atmos. Ocean. Technol., 5, 57-69.

Gage, K.S. (1989), The structure and dynamics of the free atmosphere as observed by VHF/UHF radar, in: Radar in Meteorology (D. Atlas, ed.) (to be publ. by Amer. Meteor. Soc., Boston, MA).

Gage, K.S. and J.L. Green (1979), Tropopause detection by partial specular reflection using VHF radar, Science, 203, 1238-1240.

Gage, K.S. and B.B. Balsley (1980), On the scattering and reflection mechanisms contributing to clear air radar echoes from the troposphere, stratosphere and mesosphere, Radio Sci., 15, 243-257.

Gage, K.S., D.A. Carter and W.L. Ecklund (1981), The effect of gravity waves on specular echoes observed by the Poker Flat MST radar, Geophys. Res. Lett., 8, 599-602.

Gossard, E.E. (1989), Radar research on the atmospheric boundary layer, in: Radar in Meteorology (D. Atlas, ed.) (to be publ. by Amer. Meteor. Soc., Boston, MA).

Gossard, E.E. and N. Sengupta (1988), Measuring gradients of meteorological properties in elevated layers with a surface-based Doppler radar, Radio Sci., 23, 625-639.

Gossard, E.E., R.B. Chadwick, W.D. Neff and K.P. Moran (1982), The use of-ground-based Doppler radars to measure gradients, fluxes and structure parameters in elevated layers, J. Appl. Meteor., 21, 211-226.

Gossard, E.E., J.E. Gaynor, R.J. Zamora and W.D. Neff (1985), Finestructure of elevated stable layers observed by sounder and in situ tower sensors, J. Atmos. Sci., 42, 2156-2169.

Green, J.L. and K.S. Gage (1985), A reeximination of the range resolution dependence of backscattered power observed by VHF radars at vertical incidence, Radio Sci., 20, 1001-1005.

Green, J.L. and J. Vernin (1984), Simultaneous remote sensing of atmospheric turbulence by radar optical means: a comparison, ESA SP-215 (Proc. of IGARSS'84 Symposium, Strasbourg 27-30 August 1984), 467-472 (publ. by ESA Scientific & Technical Publications Branch).

Hocking, W.K. (1983), On the extraction of atmospheric turbulence parameters from radar backscatter Doppler spectra - I. Theory, J. Atmos. Terr. Phys., 45, 89-102.

Hocking, W.K. (1985), Measurement of turbulent energy dissipation rates in the middle atmosphere by radar techniques: a review, Radio Sci., 20, 1403-1422.

Hocking, W.K. (1986), Observation and measurement of turbulence in the middle atmosphere with a VHF radar, J. Atmos. Terr. Phys., 48, 655-670.

Hocking, W.K. (1987a), Turbulence in the region 80-120 km, Adv. Space Res., 7, (10)171-(10)181.

Hocking, W.K. (1987b), Radar studies of small scale structure in the upper middle atmosphere and lower ionosphere, Adv. Space Res., 7, (10)327-(10)338.

Hocking, W.K. (1987), Reduction of the effects of non-stationarity in studies of amplitude statistics of radio wave backscatter, J. Atmos. Terr. Phys., 49, 1119-1131.

Hocking, W.K. (1988), Two years of continuous measurements of turbulence parameters in the upper mesosphere and lower thermosphere made with a 2-MHz radar, J. Geophys. Res., 93, 2475-2491.

Hocking, W.K. and J. Röttger (1983), Pulse length dependence of radar signal strengths for Fresnel backscatter, Radio Sci., 18, 1312-1324.

Hocking, W.K. and R.A. Vincent (1982), Comparative observations of D region HF partial reflections at 2 and 6 MHz, J. Geophys. Res., 87, 7615-7624.

Hocking, W.K., R. Rüster and P. Czechowsky (1986), Absolute reflectivities and aspect sensitivities of VHF radio wave scatterers measured with the SOUSY radar, J. Atmos. Terr. Phys., 48, 131-144.

Kelley, M.C., D.T. Farley and J. Röttger (1987), The effect of cluster ions on anomalous VHF backscatter from the summer polar mesosphere, Geophys. Res. Lett., 14, 1031-1034.

Kudeki, E. (1988), Radar interferometer observations of mesospheric echoing layers at Jicamarca, J. Geophys. Res., 93, 5413-5421.

Kudeki, E. and G.R. Stitt (1987), Frequency domain interferometry: a high resolution radar technique for studies of atmospheric turbulence, Geophys. Res. Lett., 14, 198-201.

Kudeki, E., B.G. Fejer, D.T. Farley and H.M. Ierkic (1981), Interferometer studies of equatorial F region irregularities and drifts, Geophys. Res. Lett., 8, 377-380.

Kuo, F.S., C.C. Chen, S.I. Liu, J. Röttger and C.H. Liu (1987), Systematic behavior of signal statistics of MST radar echoes from clear air and their interpretation, Radio Sci., 22, 1043-1052.

Kuo, F.-S. and S.-I. Liu (1988), Radar echo signal statistics, Manuscript.

Lhermitte, R.M. (1969), Note on the observation of small-scale atmospheric turbulence by Doppler radar techniques, Radio Sci., 4, 1241-1246.

Liu, C.H. (1987), Verification of scattering/reflection mechanisms for clear air radar echoes, Manuscript (comments to Gage review AMS 1987/88).

Maekawa, Y., S. Fukao, T. Sato, S. Kato and R.F. Woodman (1984), Internal inertial-gravity waves in the tropical lower stratosphere observed by the Arecibo radar, J. Atmos. Sci., 41, 2359-2367.

Manson, A.H. and C.E. Meek (1987), Small-scale features in the middle atmosphere wind field at Saskatoon, Canada (52°N, 107°W): an analysis of MF radar data with rocket comparisons, J. Atmos. Sci., 44, 3661-3672.

May, P.T. (1988), Statistical errors in the determination of wind velocities by the spaced antenna technique, J. Atmos. Terr. Phys., 50, 21-32.

May, P.T., R.G. Strauch and K.P. Moran (1988), The altitude coverage of temperature measurements using RASS with wind profiler radars, Geophys. Res. Lett., 15, 1381-1384.

Meek, C.E. and A.H. Manson (1987), Medium frequency interferometry at Saskatoon, Canada, Physica Scripta, 35, 917-921.

Meek, C.E. and A.H. Manson (1988), Vertically propagating features in MF radar signal strength, Paper presented at Fourth Workshop on Technical and Scientific Aspects of MST Radar, Kyoto, Japan, 29 Nov.-2 Dec. 1988.

Muraoka, Y., T. Sugiyama, K. Kawahira, T. Sato, T. Tsuda, S. Fukao and S. Kato (1988), Cause of a monochromatic inertia-gravity wave breaking observed by the MU radar, Geophys. Res. Lett., 15, 1349-1352.

Muraoka, Y., T. Sugiyama, K. Kawahira, T. Sato, T. Tsuda, S. Fukao and S. Kato (1988), Formation of mesospheric VHF echoing layers due to a gravity wave motion, J. Atmos. Terr. Phys., 50, 819-829.

Nastrom, G.D., W.L. Ecklund, K.S. Gage and R.G. Strauch (1985), The diurnal variation of backscattered power from VHF Doppler radar measurements in Colorado and Alaska, Radio Sci., 20, 1509-1517.

Nastrom, G.D., K.S. Gage and W.L. Ecklund (1986), Variability of turbulence, 4-20 km, in Colorado and Alaska from MST radar observations, J. Geophys. Res., 91, 6722-6734.

Olesen, J.K. and K.E. Jacobsen (1987), On atmospheric jet-streams with CAT (Clear Air Turbulence) as a possible source of HF radar echoes and abnormal electric fields, Report IR 205, Division of Geophysics, Danish Meteorological Institute, Copenhagen, Danmark.

Rastogi, P.K. and O. Holt (1981), On detecting reflections in presence of scattering from amplitude statistics with application to D region partial reflections, Radio Sci., 16, 1431-1443.

Rastogi, P.K., J.D. Mathews, W.-P. Ying and J. Röttger (1988), Simultaneous VHF and UHF radar observations of the mesosphere at Arecibo during a solar flare: a check on the gradient-mixing hypothesis, Radio Sci., 23, 97-105.

Reid, I.M. (1988), MF Doppler and spaced antenna radar measurements of upper middle atmosphere winds, J. Atmos. Terr. Phys., 50, 117-134.

Reid, I.M., R. Rüster and G. Schmidt (1987), VHF radar observations of cat's-eye-like structures at mesospheric heights, Nature, 327, 43-45.

Röttger, J. (1980a), Structure and dynamics of the stratosphere and mesosphere revealed by VHF radar investigations, J. Pure Appl. Geophys., 118, 494-527.

Röttger, J. (1980b), Reflection and scattering of VHF radar signals from atmospheric refractivity structures, Radio Sci., 15, 259-276.

Röttger, J. (1981), Investigations of lower and middle atmosphere dynamics with spaced antenna drifts radars, J. Atmos. Terr. Phys., 43, 277-292.

Röttger, J. (1987), VHF radar measurements of small-scale and meso-scale dynamical processes in the middle atmosphere, Phil. Trans. R. Soc. Lond. A, 323, 611-628.

Röttger, J. (1989), The instrumental principles of coherent and incoherent scatter radars and the configuration of radar system hardware, Handbook for MAP (to be publ.).

Röttger, J. and H.M. Ierkic (1985), Postset beam steering and interferometer applications of VHF radars to study winds, waves, and turbulence in the lower and middle atmosphere, Radio Sci., 20, 1461-1480.

Röttger, J. and M.F. Larsen (1989), UHF/VHF radar techniques for atmospheric research and wind profiler applications, in: Radar in Meteorology (D. Atlas, ed.) (to be publ. by Amer. Meteor. Soc., Boston, MA).

Röttger, J., M.T. Rietveld, C. La Hoz, T. Hall, M.C. Kelley and W. Swartz (1989), Polar mesosphere summer echoes observed with the EISCAT 933-MHz radar and the CUPRI 46.9-MHz radar, Handbook for MAP, this issue.

Royrvik, O. (1983), VHF radar signals scattered from the equatorial mesosphere, Radio Sci., 18, 1325-1335.

Royrvik, O. (1985a), Relationship between scattered power and correlation time in VHF radar signals, Radio Sci., 20, 212-220.

Royrvik, O. (1985b), Radar comparison of 2.66 MHz and 40.92 MHz signals scattered from the mesosphere, Radio Sci., 20, 1423.

Royrvik, O. and K.L. Miller (1981), Nonthermal scattering of radio waves near 150 km above Jicamarca, Peru, J. Geophys. Res., 86, 180-188.

Royrvik, O., K.P. Gibbs and S.A. Bowhill (1982), VHF power scattered from the mesosphere at mid-latitudes, J. Geophys. Res., 87, 2501-2508.

Sato, T. and R.F. Woodman (1982), Fine altitude resolution observations of stratospheric turbulent layers by the Arecibo 430 MHz radar, J. Atmos. Sci., 39, 2546-2552.

Sato, T., T. Tsuda, S. Kato, S. Morimoto, S. Fukao and I. Kimura (1985), High-resolution MST observations of turbulence by using the MU radar, Radio Sci., 20, 1452-1460.

Sheen, D.R., C.H. Liu and J. Röttger (1985), A study of signal statistics of VHF radar echoes from clear air, J. Atmos. Terr. Phys., 47, 675-684.

Strauch, R.G., B.L. Weber, A.S. Frisch, C.G. Little, D.A. Merritt, K.P. Moran and D.C. Welsh (1987), The precision and relative accuracy of profiler wind measurements, J. Atmos. Ocean. Technol., 4, 563-571.

Thomas, L., R.J. Winder and R. Rüster (1986), The characteristics of VHF radar echoes from the tropopause region near a jet stream, J. Atmos. Terr. Phys., 48, 261-265.

Thrane, E.V., O. Andreassen, T. Blix, B. Grandal, A. Brekke, C.R. Philbrick, F.J. Schmidlin, H.U. Widdel, U. von Zahn and F.J. Lübken (1985), Neutral air turbulence in the upper atmosphere observed during the Energy Budget Campaign, J. Atmos. Terr. Phys., 47, 243-264.

Tsuda, T., T. Sato, K. Hirose, S. Fukao and S. Kato (1986), MU radar observations of the aspect sensitivity of backscattered VHF echo power in the troposphere and lower stratosphere, Radio Sci., 21, 971-980.

Tsuda, T., P.T. May, T. Sato, S. Kato and S. Fukao (1988), Simultaneous observations of reflection echoes and refractive index gradient in the troposphere and lower stratosphere, Radio Sci., 23, 655-665.

Ulwick, J.C., K.D. Baker, M.C. Kelley, B.B. Balsley and W.L. Ecklund (1988), Comparison of simultaneous MST radar and electron density probe measurements during STATE, J. Geophys. Res., 93, 6989-7000.

VanZandt, T.E. and D.C. Fritts (1989), A theory of enhanced saturation of the gravity wave spectrum due to increases in atmospheric stability, Pure Appl. Geophys. (in press).

Vincent, R.A. and J. Röttger (1980), Spaced antenna VHF radar observations of tropospheric velocities and irregularities, Radio Sci., 15, 319-335.

Vincent, R.A., P.T. May, W.K. Hocking, W.G. Elford, B.H. Candy and B.H. Briggs (1987), First results with the Adelaide VHF radar: spaced antenna studies of tropospheric winds, J. Atmos. Terr. Phys., 49, 353-366.

Wakasugi, K., A. Mizutani, M. Matsuo, S. Fukao and S. Kato (1986), A direct method of deriving drop-size distribution and vertical air velocities from VHF Doppler radar spectra, J. Atmos. Oceanic Techn., 3, 623-629.

Warnock, J.M. and T.E. VanZandt (1985), A statistical model to estimate the refractivity turbulence structure constant C_n^2 in the free atmosphere, NOAA Technical Memorandum ERL AL-10, Aeronomy Laboratory, NOAA, Boulder, CO/U.S.A.

Waterman, A.T., T.-Z. Hu, P. Czechowsky and J. Röttger (1985), Measurement of anisotropic permittivity structure of upper troposphere with clear-air radar, Radio Sci., 20, 1580-1592.

Watkins, B.J., C.R. Philbrick and B.B. Balsley (1988), Turbulence energy dissipation rates and inner scale sizes from rocket and radar data, J. Geophys. Res., 93, 7009-7014.

Woodman, R.F. (1980a), High-altitude resolution stratosperic measurements with the Arecibo 2380 MHz radar, Radio Sci., 15, 423-430.

Woodman, R.F. (1980b), High-altitude resolution stratospheric measurements with the Arecibo 430 MHz radar, Radio Sci., 15, 417-422.

Woodman, R.F. and Y.-H. Chu (1989), Aspect sensitivity measurements of VHF backscatter made with the Chung-Li radar, Handbook for MAP, this issue.

Wuertz, D.B., B.L. Weber, R.G. Strauch, A.S. Frisch, C.G. Little, D.A. Merritt, K.P. Moran and D.C. Welsh (1988), Effects of precipitation on UHF wind profiler measurements, J. Atmos. Ocean. Technol., 5, 450-465.

ASPECT SENSITIVITY OF MESOPAUSE SUMMER ECHOES AT VHF

Iain M. Reid and Peter Czechowsky

Max–Planck–Institut für Aeronomie, Katlenburg–Lindau, FRG.

The mobile SOUSY VHF (53.5 MHz) Radar, located near Andenes (69°N, 16°E) on the Norwegian Island of Andøya, has been used to measure the aspect sensitivity of the very strong radar returns obtained from near the summer polar mesopause. This so-called Polar Mesopause Summer Echo (PMSE) exhibits substantial aspect sensitivity, with angular polar diagrams of the backscatter of 2–10° half–power half–width for a two day average. Because the half–power thickness of the echo is less than 1 km, and the associated radar returns very strong, the grating lobes of the antenna polar diagram can be utilized as additional beams, and the power returned at angles of 35 and 38° off–zenith obtained. After correction for the antenna polar diagram, the powers measured in the grating lobes are about 20 dB less than those returned from the zenith. These measurements provide a estimate of the ratio of the specular to the turbulent contributions to the backscatter. A similar echo occurs at mesopause heights in summer at higher mid–latitudes (52°N). It too exhibits substantial aspect sensitivity, with a half–power half–width of about 6°. A more complete description of these results is given in CZECHOWSKY et al. (1988), REID et al. (1988) and CZECHOWSKY and REID (1989).

REFERENCES

Czechowsky, P. and I. M. Reid and R. Rüster, VHF radar measurements of the aspect sensitivity of the summer polar mesopause echoes over Andenes (69°N, 16°E), Norway, *Geophys. Res. Lett.*, in press, 1988.

Czechowsky, P. and I. M. Reid, VHF radar observations of mesospheric structures at different latitudes, to be submitted to *Radio Sci.*, 1989.

Hocking, W. K., R. Rüster and P. Czechowsky, Absolute reflectivities and aspect sensitivities of VHF radio wave scatters measured with the SOUSY radar, *J. Atmos. Terr. Phys.*, 48, 131, 1986.

Reid, I. M., P. Czechowsky, R. Rüster and G. Schmidt, First VHF radar measurements of mesopause summer echoes at mid–latitudes, *Geophys. Res. Lett.*, in press, 1988.
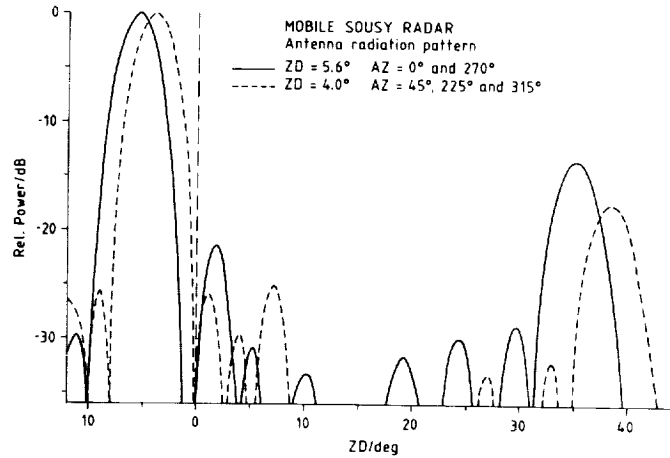
Fig. 1 Antenna radiation pattern of the mobile SOUSY VHF Radar located at Andenes in northern Norway. The solid line represents the polar diagram for an off-zenith angle of 5.6° at planes parallel ($AZ = 0°$) and perpendicular ($AZ = 270°$) to the dipole direction. The dashed line shows the diagram for an off-zenith angle of 4° in directions of $AZ = 45°, 225°$ and 315° to the dipole direction. [After CZECHOWSKY et al., 1988]
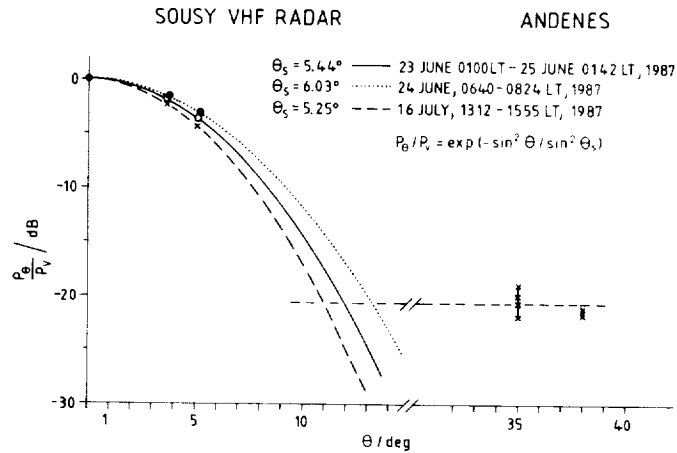
Fig. 2 Backscattered power measured with the main beam at off-zenith directions of 4° and 5.6° and with the grating lobes at 35° and 40° (see Figure 1) relative to that received in the vertical beam. The three curves represent the returned power as a function of the off-zenith angle θ given by: $P_\theta/P_V = exp(-sin^2\theta/sin^2\theta_S)$ where θ_S is the half width of the angular polar diagram of the backscatter. The measurements obtained with the grating lobes of the antenna in Andenes provide an estimate of the ratio of the specular to the turbulent contributions of the backscatter [after CZECHOWSKY et al., 1988].

SOUSY VHF RADAR   16-20 JUNE 1987   ANDENES
77.8 - 91.6 km

--x-- AZ=0°, θ_s=7.7°;
—●— AZ=270°, θ_s=6.8°;

$\dfrac{P_{\theta}}{P_{ver}}$ / dB

θ / deg

Fig. 4 Relative power based on measurements using the same antenna configuration as described in Figure 2, but for an average of 5 days [CZECHOWSKY and REID, in preparation, 1989].

SOUSY VHF RADAR   24 JUNE 1987   0640-0824 LT   ANDENES

P_v/dB

$\dfrac{P_{obl}}{P_v}$ / dB

θ_S/deg

σ_v/ms^{-1}

z / km

— ZD=5.6°
-- ZD=4.0°

● ZD=5.6°
× ZD=4.0°

Fig. 3 (a) Mean power (P_V) measured in the vertical beam for a period of 144 min, (b) ratio of the power observed in the off-zenith directions of 4° and 5.6°, (c) half-width (θ_S) of the angular polar diagram of the backscatter and (d) mean spectral width (σ_V) for the vertical beam, uncorrected (solid line) and corrected (dotted line) for beam broadening. The spectral half-width due to beam broadening was calculated using [see e.g. HOCKING et al., 1986]: $f_{1/2} = arcsin[(sin^{-2}\theta_S/ln2 + sin^{-2}\theta_B)^{1/2}]2v/\lambda$. where λ is the radar wavelength (5.6 m), v the horizontal velocity and θ_B is the actual half-power half beam width of the antenna radiation pattern [after CZECHOWSKY et al., 1988].

Fig. 5 Mean power profiles for 5 days measured at Andenes with the vertical and the off-zenith beam directions. The "layer" detected at 104 km altitude is the image of the main layer detected in the grating lobe at an off-zenith of 35° [CZECHOWSKY and REID, in preparation, 1989].
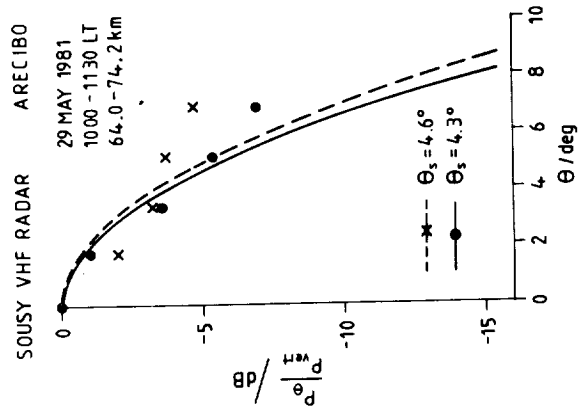
Fig. 7 Relative power measured in Arecibo (Puerto Rico) at different off-zenith angles relative to that received in the vertical beam. The curves and θ_S are calculated according to the equation given in the caption of Figure 2 [CZECHOWSKY and REID, in preparation, 1989].
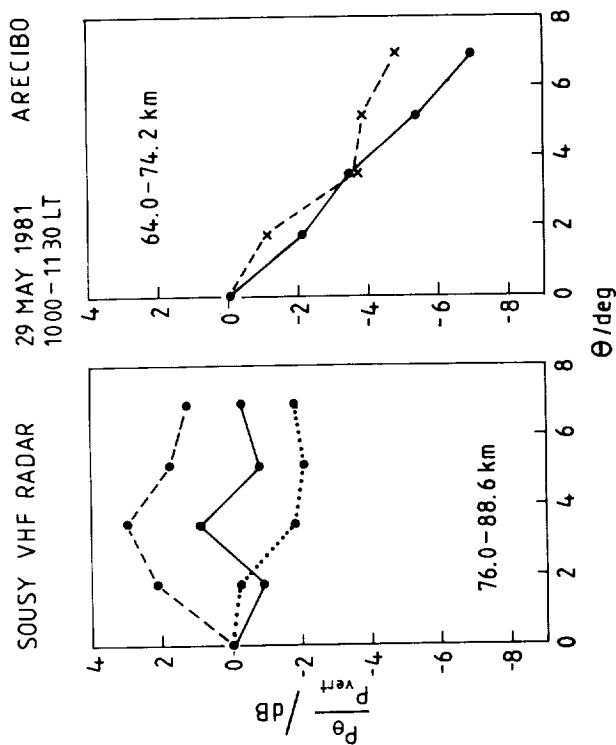
Fig. 6 Backscattered power measured in Arecibo (Puerto Rico) at different off-zenith angles for two altitude ranges. Above 75 km the scatter process is isotropic, whereas below 75 km partial reflection dominates. [CZECHOWSKY and REID, in preparation, 1989]

SOUSY VHF RADAR   7 JULY 1988   HARZ

$\dfrac{P_\theta}{P_{vert}}$ /dB

1126 - 1216 LT

84.6 - 86.1 km

θ_s = 6.27°

θ/deg
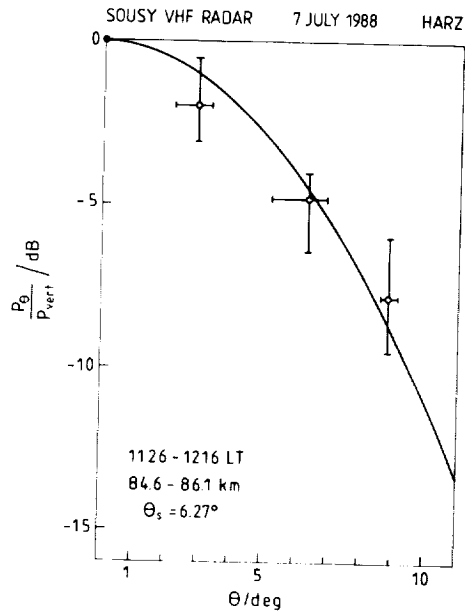
Fig. 8 Echo powers measured with the stationary SOUSY VHF Radar in the Harz mountains (FRG), relative to that received from the vertical direction, plotted as a function of off-zenith angle. The half width of the angular distribution of the backscatter was calculated according to the formular given in Figure 2 [after REID et al., 1988].

USING VERTICALLY POINTING BROAD BEAM TO MEASURE ATMOSPHERIC ASPECT SENSITIVITY OF VHF RADAR ECHOES

Y. H. Chu[1], R. F. Woodman[2], C. H. Liu[3], J. K.Chao[1], and J. Röttger[4]

[1]Department of Atmospheric Physics, National Central University, Chung-Li, Taiwan, ROC
[2]Instituto Geofisico del Peru, Apartado 3747, Lima 100, Peru
[3]Dept. of Electrical and Computer Engineering,University of Illinois, Urbana, IL 61801
[4]EISCAT Scientific Association, Box 705, Kiruna, Sweden

ABSTRACT

Conventionally, atmospheric aspect sensitivity of VHF radar echoes is measured using a narrow beam radar in order to avoid the complications due to broad beam effects. However, in this study, a new technique using beam broadening effects has been developed. It used the relatively broad antenna beam (half power beam width is 7.4 deg) of the vertically pointing antenna of the new Chung-Li VHF radar. The aspect sensitivity measurement using this method is straightforward and free from the convolution effects introduced by the finite width of the antenna beam pattern. The observed value at heights from 2 to 8 km is about 0.5 dB/deg to 1 dB/deg which agrees very well with other measurements.

INTRODUCTION

Since WOODMAN and GUILLEN (1974) successfully measured the stratospheric and mesospheric wind field and turbulence with the Jicamarca VHF radar by using the modern MST radar technique, the fields of VHF radar probing the lower and middle atmosphere have been established. It is well known that, using powerful VHF radars, many important atmospheric parameters and dynamic phenomena, such as 3-dimensional wind fields, tropopause height, atmospheric refractive index structure constant (C_n^2), turbulent energy dissipation rate, atmospheric stability, gravity wave characteristics, turbulent structure, etc., can be measured or observed (GAGE and GREEN, 1978, 1979; RÖTTGER, 1980; VANZANDT et al., 1978; HOCKING, 1983a,b, 1985, 1987).

There are many kinds of echo mechanisms proposed by different scientific workers to explain the properties of MST radar returns. The so-called "isotropic turbulent scattering" proposed by BOOKER and GORDON (1950) explained the results of troposcattering; GAGE and BALSLEY (1980) and DOVIAK and ZRNIC (1984) took "anisotropic turbulent scattering" for illustrating the phenomenon of atmospheric aspect sensitivity (GAGE and GREEN, 1978; RÖTTGER et al., 1981; TSUDA et al., 1986). The concept of "Fresnel scattering" was introduced by GAGE et al. (1981) to account for the echoes from volume filling of specular layers observed by VHF radar. "Fresnel reflection" (or partial reflection) is also an important echo mechanism of MST radar and has been confirmed by many experimenters (RÖTTGER and LIU, 1978; RÖTTGER, 1980) and the echo mechanism of "diffuse reflection" has been discussed by RÖTTGER (1980).

Atmospheric aspect sensitivity (or angular spectrum) has been measured with MST radars for many years (RÖTTGER and VINCENT, 1978; VINCENT and RÖTTGER, 1980; RÖTTGER et al., 1981; WATERMAN et al., 1985; SATO et al., 1985; TSUDA et al., 1986; HOCKING et al., 1986). The width of the angular spectrum is closely related to atmospheric stability: the more stable the atmosphere, the more narrow the angular spectral width, and vice versa. The physical mechanisms that cause the angular dependence of VHF radar echo power are not yet fully understood. However, there are two possible echo mechanisms responsible for the aspect sensitivity which have been discussed extensively by many scientific workers. One is diffusive reflection from the corrugated refractive index surface (RATCLIFFE, 1956; RÖTTGER, 1980), and the other is anisotropic turbulent scattering (DOVIAK and ZRNIC, 1984; WATERMAN et al., 1985; WOODMAN and CHU, 1988).

The existence of aspect sensitivity will influence the accuracy of the atmospheric parameters evaluated from the Doppler spectrum of vertical or close to zenith pointing radar returns, such as horizontal wind velocity, turbulent rms velocity, etc. (RÖTTGER, 1980; TSUDA et al., 1986; HOCKING et al., 1986; HOCKING, 1987). Therefore, it is very important to measure accurately the correct aspect sensitivity before making an evaluation of atmospheric parameters from a VHF radar Doppler spectrum. The current method of aspect sensitivity measurement used at most MST radars around the world is the so-called beam swinging method, that is, tilting the radar beam continuously toward different zenith angles, the aspect sensitivity will then be obtained after evaluating the echo power for each pointing direction. The aspect sensitivity measured with this method is different from the actual one, because of the convolution effect with the antenna beam pattern. In this paper, a new method of aspect sensitivity measurement by using the beam broadening effect from the Doppler spectrum of vertically pointing radar beams, developed at the Chung-Li VHF radar in Taiwan, ROC, (WOODMAN and CHU, 1988), will be introduced and the results of measurements are also presented and discussed.

CHARACTERISTICS OF THE CHUNG-LI VHF RADAR

The Chung-Li VHF radar is located on the campus of the National Central University in Taiwan, ROC, (25°N, 121°E). The operation of this radar began on June 1,1985. It consists of three identical and independent modules, the antenna area and peak transmitted power of each module are 1600 m^2 and 60 kW, respectively. The antenna module is composed of 64 (8x8) Yagi antennas arranged in a square of sides 40 m. The antenna configuration is shown in Figure 1. The radar frequency is 52.2 MHz (radar wavelength is 5.77m), and the pulse width can be set as 1, 2, 4, 8, and 16 μs arbitrarily. The maximum duty cycle is 2%. The phase code is a complementary code with 2, 4, 8, or 16 elements. The direction of the radar beam for each antenna module or for full antenna aperture can be pointed independently from zenith toward northeast, southeast, southwest, northwest with fixed zenith angle 17° and the beams can also be pointed vertically. The azimuth angle for the off-vertically pointing beams are shown in Figure 1. The half power beam width (HPBW) for each module and full aperture is 7.4° and 5°, respectively. The maximum probing range is about 1 to 25 km. However, occasionally, the echoes of mesospheric irregularities can be observed (CHU et al., 1988a). The characteristics are summarized in Table 1.

THE METHOD OF ASPECT SENSITIVITY MEASUREMENT WITH VERTICALLY POINTING RADAR BEAMS

The Doppler spectral width is an extremely important VHF radar echo parameter. Much atmospheric information, such as turbulent rms velocity and energy dissipation rates, can be evaluated from this radar parameter. However, there are quite a few physical mechanisms which can contaminate the width of the Doppler spectrum. For example, the beam broadening effect, wind shear effect, and gravity wave oscillation effect will broaden the Doppler spectral width (ATLAS et al., 1964; GAGE and BALSLEY, 1978; BRIGGS, 1980; HOCKING, 1983a,b, 1985, 1986), whereas the Doppler spectral width will also be narrowed by the aspect sensitivity for vertical or close to vertical pointing radar beams (RÖTTGER, 1981; WOODMAN and CHU, 1988). Therefore, because of the broadening and the narrowing effects coexisting in the observed Doppler spectrum, the estimation of true atmospheric information from spectral width will be impossible if the contaminating factors are not thoroughly removed from the spectrum.

For a sufficiently broad antenna beam, if the echoing mechanism is isotropic turbulent scattering, the observed echo power at a specified Doppler frequency, f, will then be the integration result of the echo power scattered from the refractive index fluctuations which are located linearly within the radar volume with the corresponding angular positions and arranged perpendicularly to the horizontal wind direction. From Figure 2 it is easy to show that the signals returned from the irregularities located on the line AB will have the same Doppler frequency, f, and the mathematical relation between f and zenith angle Θ measured along the horizontal wind direction will be

$$f = -2 U \Theta / \lambda \qquad (1)$$

AB = 45 m
AC = 45 m
BC = 40 m
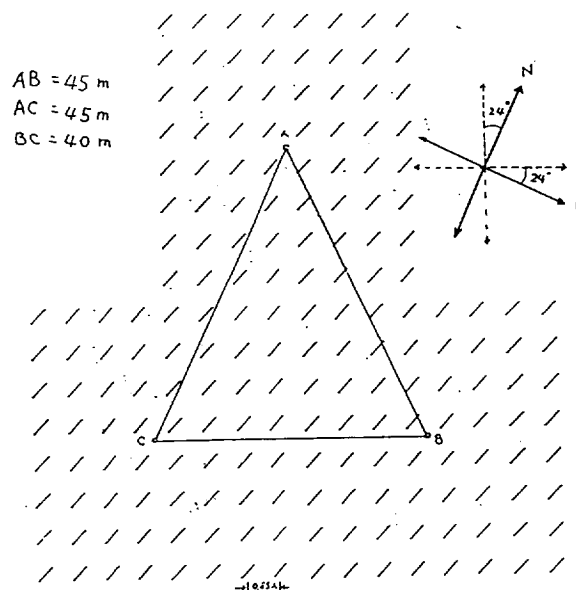
Figure 1. The configuration of the Chung-Li VHF radar antenna. The arrows with dashed tails are the pointing directions of the radar beam and the arrows with solid tails are the geographic direction.

Table 1. The Characteristics of the Chung-Li VHF radar.

Location	Chung-Li, Taiwan (25°N, 121°E)
Frequency	52.2 MHz
Wavelength	5.77 m
Peak transmitter power (for each module)	60 kW
Pulse width	1 - 16 μs
Maximum duty cycle	2%
Antenna	
Type	3 square arrays of Yagi (8x8)
HPBW	7°
Steerability	Vertical and North, East, South, West with 17° zenith angle
Total geometrical area	3x1600 m^2

where U is the horizontal wind speed, λ is the radar wavelength. The Doppler spectrum thus obtained is called the beam broadening Doppler spectrum or nonturbulent Doppler spectrum (HOCKING, 1983a). However, if there is aspect sensitivity in existence, the shape of the observed Doppler spectrum for a vertically pointing broad antenna beam will be determined from the multiplication effect between the beam broadening Doppler spectrum and the aspect sensitivity if the wind shear, turbulent fluctuation and gravity wave oscillation effects are all neglected, as shown in Figure 3. The dashed curve in Figure 3 represents the aspect sensitivity, A(f), the dotted curve is the beam broadening Doppler spectrum, B(f), responsible for a given horizontal wind speed and the antenna beam pattern, and the solid curve represents the observed Doppler spectrum, S(f). Therefore, the mathematical relationship between S(f), B(f), and A(f) can be described as follows:

$$S(f) = A(f) \cdot B(f) \tag{2}$$

The beam broadening spectrum can be easily estimated if the Gaussian assumption of the antenna beam pattern is made and the horizontal wind speed is known. The width of this spectrum will be (HOCKING, 1985; CHU, 1986):

$$\sigma = U\, \Theta_{0.5}/(2\sqrt{2 \ln 2}) \tag{3}$$

where σ is the beam broadening spectral width, $\Theta_{0.5}$ is the HPBW. Therefore, the aspect sensitivity, $A(\Theta)$, will be evaluated by the following equation:

$$\text{LoG } A\,(\Theta) = \text{Log } S(f) - \text{Log } B(f) \tag{4}$$

where the relationship between f and Θ is shown in equation (1). The aspect sensitivity measured in this way results from the narrowing effect on the beam broadening Doppler spectrum of the vertically pointing radar beam. The beam broadening effect contributed to the observed Doppler spectrum will be remarkable if the antenna beam width is broad enough. This fact can be proven from the exercise taken as follows: for the Chung-Li VHF radar the HPBW is 7.4°, if the horizontal wind speed is assumed to be 10 m/s, the beam broadening Doppler spectral width will be 0.56 m/s calculated from equation (3), while the spectral width contributed from turbulent fluctuations and gravity wave oscillations is less than 0.3 and 0.1 m/s during quiet conditions, respectively (SATO and WOODMAN, 1982; CARTER et al., 1984). Therefore, because the beam broadening effect is much larger than the turbulent and gravity wave effect contributed to the observed Doppler spectral width, it is practicable for a broad antenna beam to measure the aspect sensitivity in terms of beam broadening Doppler spectrum for a vertically pointing radar beam. In the following section an experiment of aspect sensitivity measurement, made by the Chung-Li VHF radar, and the observed results are presented and discussed.

EXPERIMENT AND RESULTS

The data used here were observed at the Chung-Li VHF radar on April 23, 1986, 0723 - 0809 LT. The three antenna beams were tilted toward northeast, northwest, and zenith directions, respectively. The pulse width was selected as 2 μs (300 meters range resolution), interpulse period (IPP) was 500 μs and coherent integration time was 0.25 s. The altitude of observation started at 1.8 km and 40 range gates were set. The FFT of 64 points was performed and 170 resulting raw spectra were averaged incoherently for the radar returns of each channel and each range gate. The normalized averaged Doppler spectra are shown in Figure 4, plotted with the solid curve. From the two oblique Doppler spectra, the mean horizontal wind velocity can be estimated by use of the moment method for each range gate if the signal-to-noise ratio is high enough. The profile of the horizontal mean speed measured is shown in Figure 5, plotted with the solid curve. The dashed curve in Figure 5 is the rawinsonde wind observed at the Pan-Chiao station apart from the Chung-Li VHF radar about 25 km northeast. Once the horizontal wind speed is evaluated, the beam broadening spectrum will be determined exactly according to equation (3) if the antenna beam pattern is assumed to be Gaussian shaped. The normalized beam broadening spectra are shown in Figure 4, plotted with the dotted curve. The beam broadening spectra are not evaluated above
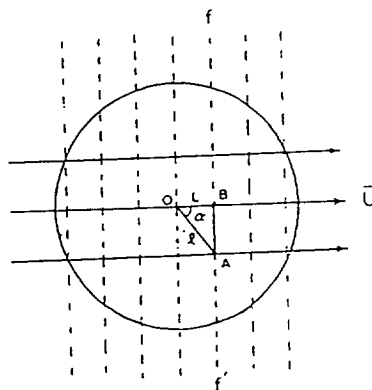
Figure 2. The solid circle represents the radar volume of vertical pointing at specified altitude z, U is the horizontal mean wind velocity, O is the zenith point, L is the distance between O and point B, which L = δz, δ is the zenith angle of point B. The Doppler frequency shifts at points B and A arising from the drifting effect are identical if U is constant.
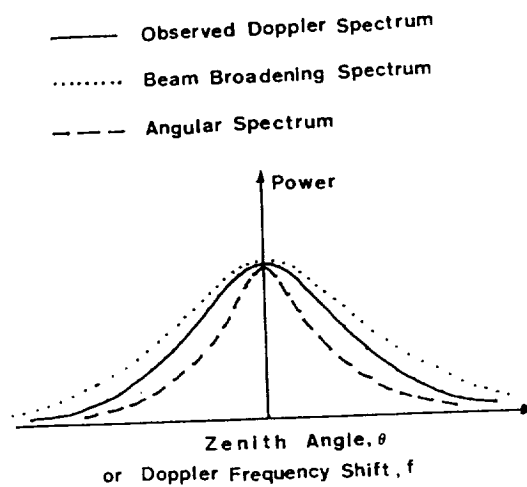
Figure 3. The schematic relationship between observed Doppler spectrum (solid curve), beam broadening spectrum (dotted curve) and angular spectrum (dashed curve), where the relationship between Doppler frequency shift, f, and zenith angle, Θ, is shown in equation (1).

ORIGINAL PAGE IS
OF POOR QUALITY
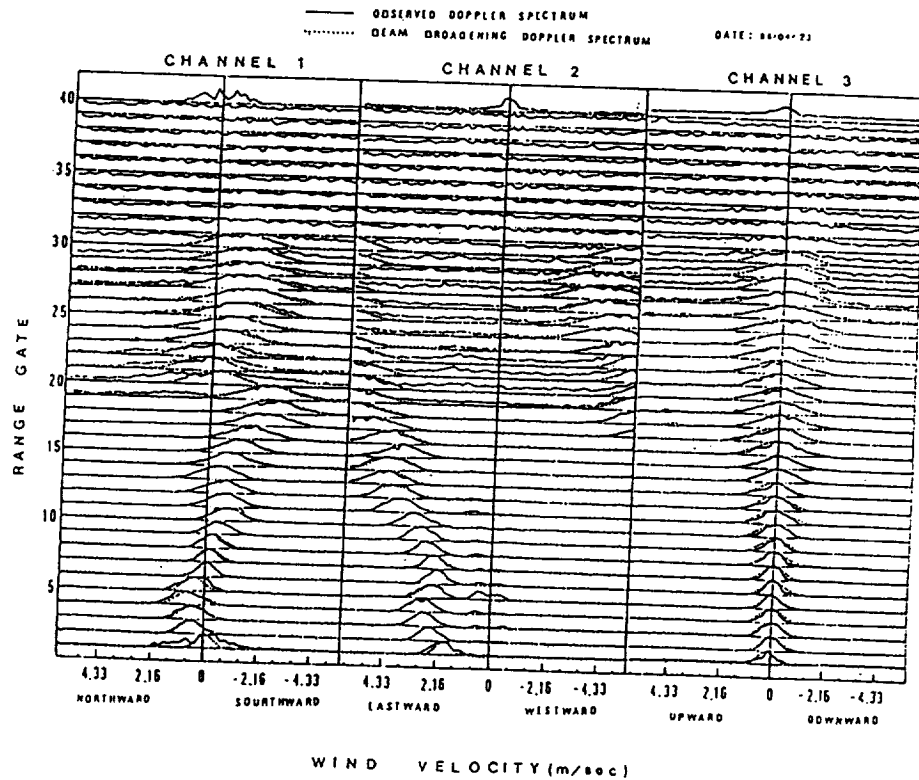
Figure 4. Comparison between normalized observed Doppler spectras (solid curve) and theoretical beam broadened Doppler spectra (dotted curve).
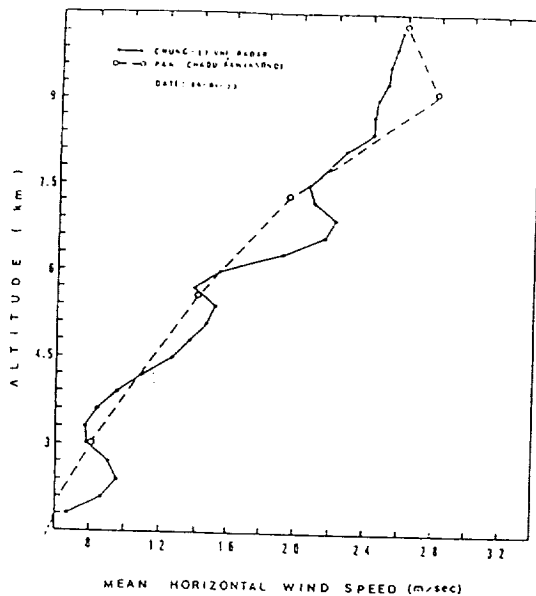
Figure 5. The comparison between radar-observed mean horizontal wind speed and rawinsonde wind speed.

range gate 30 because the signal-to-noise ratio is too low to calculate the accurate mean horizontal wind velocity. Comparing the observed and theoretical beam broadening Doppler spectra, it is obvious that the former are systematically narrower than the latter for vertical Doppler spectra, whereas, for oblique Doppler spectra, the former are broader than or equal to the latter. These phenomena can be seen more clearly from Figure 6 in which the abscissa is the beam broadening spectral width and the ordinate is the observed Doppler spectral width. It is noticed that some points distributed in panel (a) and panel (b) of Figure 6 (for oblique Doppler spectra) are deviated much from the line with slope 1. It is because the signal-to-noise ratio at these altitudes is not high enough so that the true Doppler spectral widths cannot be evaluated accurately from the observed Doppler spectra. However, the data quality for vertical Doppler spectra is quite good, as referred to Figure 4. Therefore, the aspect sensitivity can be estimated from the observed vertical Doppler spectra and the theoretical beam broadening spectra according to the previous illustration in equation (4). The measured aspect sensitivities at a specified altitude are shown in Figure 7 with the open circles. It is evident from Figure 7 that, in general, the echo powers decrease at the rate of 0.3 to 1 dB/deg, and the levelling of the aspect sensitivity can also be observed at a certain altitude. Specifically, there is no angular dependence of echo power at altitude 5.7 km. These features can be reconfirmed from Figure 8, in which the profiles of echo power for the three antenna beams and the generalized potential refractive index gradient, M, are presented. The aspect sensitivities at the altitude marked with the arrows in Figure 8 have been shown in Figure 7. The definition of M is (TATARSKII, 1961; VANZANDT et al., 1978)

$$M = -77.6 \times 10^{-6} \frac{P}{T} (\frac{\partial \ln\Theta}{\partial z}) [1 + \frac{15500 \, q}{T} (1 - \frac{1}{2} \frac{\partial \ln \, q/\partial z}{\partial \ln\Theta/\partial z})] \tag{5}$$

where P is the atmospheric pressure (mb), T is the temperature (K), q is the specific humidity and Θ is the potential temperature (°K). It is obvious that atmospheric stability is related to the value of M^2, the higher the stability, the larger the value of M^2. From Figure 8 it is clear that the profiles of echo power and M^2 are matched very well. This characteristic has been confirmed by many scientific workers (GAGE et al., 1981; TATARSKII, 1961; GAGE and BALSLEY, 1980). The correctness of the aspect sensitivity measured with the Chung-Li VHF radar by using the vertical Doppler spectrum and beam broadening effect can be further proven if the echo power of the oblique beam and vertical beam are compared. The echo power of the radar beam toward northwest is not available for comparison in this study because of the contamination by the intense cosmic noise from the Cygnus A radio star (PAN, 1987). After examining the echo power profiles of the vertical and oblique (toward northeast) radar beams in Figure 8, it is apparent that there are large aspect sensitivities existing in the atmosphere below 5.1 km and above 7.2 km with the echo power difference of 10 to 15 dB and 5 to 10 dB, respectively. However, there are little power differences (less than 2 dB) around the altitude 5.7 km. The aspect sensitivities measured at the specified altitude from the echo power profile of vertical and oblique beams are also plotted in Figure 7 with the crosses. Noting that the zenith angle of the oblique radar beam is 17°, it implies that the echo power of the oblique beam observed can be expected as the result of isotropic turbulent scattering, that is, no angular dependence. Therefore, the echo power of the oblique beam will be located at the levelling of the aspect sensitivity. From Figure 7 it is evident that the aspect sensitivity measured from these two independent methods are consistent. It is concluded that the method of aspect sensitivity measurement in terms of observed vertical Doppler spectrum and beam broadening effect developed at Chung-Li is practicable and correct.

DISCUSSION AND CONCLUSION

There are many assumptions in the method of aspect sensitivity measurement introduced in this study, such as the Gaussian antenna beam pattern, neglection of the wind shear, turbulent fluctuation and gravity wave oscillation broadening effect in the observed vertical Doppler spectrum. In general, the assumption of the Gaussian antenna pattern can be accepted if the angular range concerned in a broad antenna beam is limited within the range ± HPBW/2 measured from the main beam axis, that is, ± 4° for the Chung-Li radar. On the other hand, the wind shear effect will be very small and can be neglected if the antenna beam is pointed vertically and the range resolution is fine enough. The gravity wave effect can also be neglected if the time period for the averaged Doppler spectral estimation is shorter than 5 minutes (HOCKING, 1986) or the

CHUNG-LI VHF RADAR
86/04/23
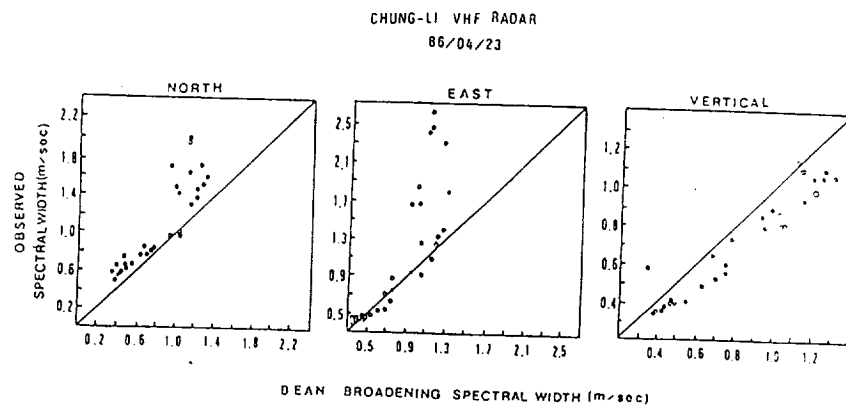
Figure 6. The scatter diagram of observed spectral width and beam broadening spectral width.
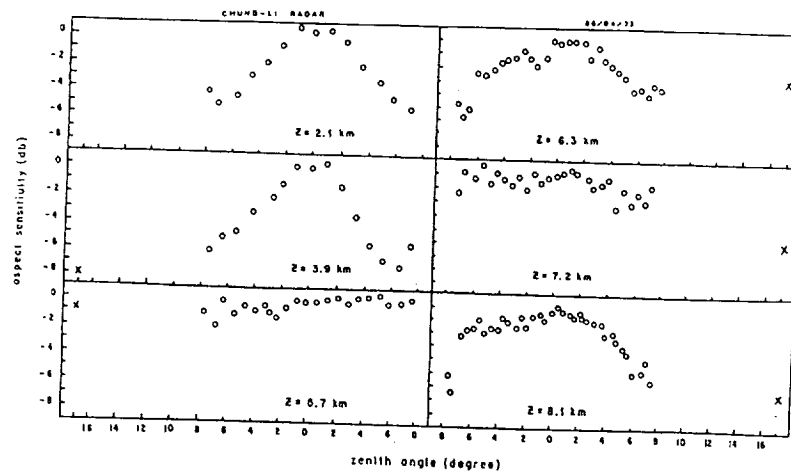
Figure 7. The aspect sensitivity measured with the Chung-Li VHF radar. The open circle curve represents the measurement results from the observed Doppler spectrum for vertically pointing beams and the cross is the echo power difference between vertical and oblique beams.
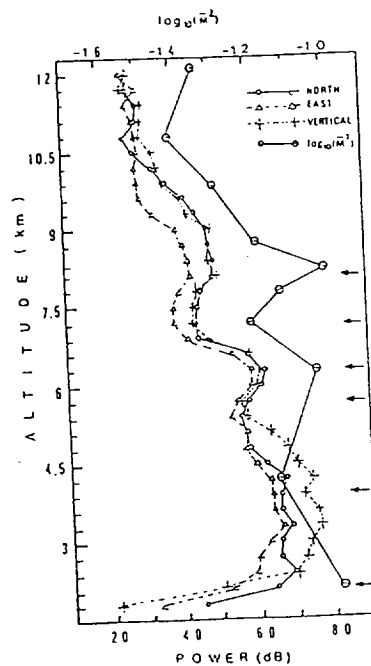
Figure 8. The profiles of echo power for beams toward north, east, and vertically pointing and M^2 calculated from meteorological data observed at the Pan Chaio rawinsonde station.

atmospheric condition is very quiet (CARTER et al., 1984). As for the turbulent broadening effect, the degree of its contribution to the vertical Doppler spectral width can be estimated from the comparison between the width of the observed oblique Doppler spectrum and the beam broadening spectrum. If the former is larger than the latter, it implies that the turbulent broadening effect will be very important and cannot be neglected. Under this situation, although the detailed structure of the aspect sensitivity cannot be evaluated from the observed vertical Doppler spectrum, the characteristic width of aspect sensitivity will be calculated from the information of beam broadening spectral width, vertical and oblique observed Doppler spectral width (CHU, 1988). However, if the observed oblique Doppler spectral width is equal or approximate to the vertical one, it implies that the turbulent fluctuation will be so weak that the turbulent effect can be neglected. From Figure 4 it is clear that the observed oblique spectral widths are approximate to the beam broadening spectral width, that is, the turbulent effect can be neglected during this observation. The gravity wave effect can be neglected also because there are no gravity waves existing in this observation after examining the time series of radial wind fluctuation. Therefore, because of no contamination from wind shear, turbulent and gravity wave effect, the result of aspect sensitivity measurement shown in Figure 7 is the true one.

In general, the disadvantages of the traditional beam swinging method for aspect sensitivity measurements are (1) the spatial fine structure of aspect sensitivity cannot be measured because of the convolution effect with the antenna beam pattern; (2) the temporal resolution of aspect sensitivity cannot be high enough because of the time consumed for the radar beam swing; (3) the actual angular distribution of echo power cannot be measured because the zenith angle from which the most echo power is returned is not the angle the radar beam pointed. Of course, these disadvantages can be eliminated if the pencil-like narrow radar beam is used for observation. Because of no beam swinging and convolution of the antenna beam pattern, the disadvantages mentioned above will not exist in the measurement results of aspect sensitivity introduced in this study. Therefore, the quality of aspect sensitivity measured from the broad radar beam pointed vertically is better than the beam swinging method.

From the previous discussion, it is concluded that for a VHF radar with which the aspect sensitivity cannot be measured by using the beam swinging method, the measurement methods in terms of beam broadening effect on the vertically pointing radar beam will be applied if the antenna beam is broad enough and the horizontal wind speed can be evaluated precisely.

REFERENCES

Atlas, D., Advances in radar meteorology, in *Advances in Geophysics, 10*, 318-479, Academic Press, New York, 1964.

Booker, H. G., and W. E. Gordon, A theory of radio scattering in the troposphere, *Proc. IRE, 39*, 401-412, 1950.

Briggs, B. H., Radar observations of atmospheric winds and turbulences: a comparison of techniques, *J. Atmos. Terr. Phys, 42*, 823-833, 1980.

Carter, D. A., B. B. Balsley, W. L. Ecklund, M. Crochet, A. C. Riddle, and R. Garello, Tropospheric gravity waves observed by the closely spaced ST radar, *Handbook for MAP, 14*, 219-228, 1984.

Chu, Y. H., The study of beam broadening effect of Doppler spectral width on Chung-Li VHF radar, Tech. Rep. (in Chinese), 1986.

Chu, Y. H., The study of MST radar echoing mechanism, Ph.D. Thesis (in Chinese), National Central University, 1988.

Chu, Y. H., J. K. Chao, and C. H. Liu, Mesospheric observations using the Chung-Li VHF radar, this volume, 1988a.

Doviak, R. J., and D. S. Zrnic, *Doppler Radar and Weather Observation*, Academic Press, 1984.

Gage, K. S., and J. L. Green, Evidence for specular reflection from monostatic VHF radar observations of the stratosphere, *Radio Sci., 13*, 991-1001, 1978.

Gage, K. S., and J.L. Green, Tropopause detection by partial specular reflection using VHF radar, *Science, 203*, 1238, 1979.

Gage, K. S., and B. B. Balsley, On the scattering and reflection mechanism contributing to clear air radar echoes from the troposphere, stratosphere and mesosphere, *Radio Sci., 15*, 243-257, 1980.

Gage, K. S., B. B. Balsley, and J. L. Green, Fresnel scattering model for the specular echoes observed by VHF radar, *Radio Sci., 16*, 1447-1453, 1981.

Hocking, W. K., On the extraction of atmospheric turbulence parameters from radar backscatter Doppler spectra - 1. Theory, *J. Atmos. Terr. Phys, 45*, 89-102, 1983a.

Hocking, W. I., Mesospheric turbulence intensities measured with a VHF radar at 35 S - II, *J. Atmos. Terr Phys., 45*, 103-113, 1983b.

Hocking, W. K., Measurement of turbulent energy dissipation rate in the middle atmosphere by radar technique: A review, *Radio Sci., 20*, 1405-1422, 1985.

Hocking, W. K., R. Ruster, and P. Czechowsky, Absolute reflectivities and aspect sensitivities of VHF radar wave scatterers measured with the SOUSY radar, *J. Atmos. Terr. Phys., 48*, 131-144, 1986.

Hocking, W.K., Reduction of the effects of non-stationarity in studies of amplitude statistics of radio wave backscatter, *J. Atmos. Terr. Phys., 49*, 1119-1131, 1987.

Pan, T. J., The radiation pattern of Chung-Li VHF radar antenna, M.S. Thesis (in Chinese) National Central University, 1987.

Ratcliffe, J. A., Some aspects of diffraction theory and their application to the ionosphere, *Rep. Prog. Phys., 19*, 188-267, 1956.

Röttger, J., Reflection and scattering of VHF radar signals from atmospheric reflection structure, *Radio Sci., 15*, 259-276, 1980.

Röttger, J., and C. H. Liu, Partial reflection and scattering of VHF signals from the clear atmosphere, *Geophys. Res. Lett, 5*, 357-360, 1978.

Röttger, J., and R. A. Vincent, VHF radar studies of tropospheric velocities and irregularities using spaced antenna techniques, *Geophys. Res. Lett., 5*, 917-920, 1978.

Röttger, J., P. Czechowsky, and G. Schmidt, First low-power VHF radar observations of tropospheric, stratospheric and mesospheric winds and turbulence at the Arecibo observatory, *J. Atmos. Terr. Phys., 43*, 789-800, 1981.

Sato, T., and R. F. Woodman, Fine altitude resolution observations of the stratospheric turbulent layers by the Arecibo 430 MHz radar, *J. Atmos. Sci., 39*, 2546-2552, 1982.

Tatarskii, V. I., *Wave Propagation in a Turbulent Medium*, McGraw-Hill, New York, 1961.

Tsuda, T., T. Sato, K. Hirose, S. Fukao, and S. Kato, MU radar observations of the aspect sensitivity of backscattered VHF echo power in the troposphere and lower stratosphere, *Radio Sci., 21*, 971-980, 1986.

VanZandt, T. E., J. L. Green, K. S. Gage, and W. L. Clark, Vertical profiles of reflectivity turbulence structure constant: comparison of observation by the Sunset radar with a new theoretical model, *Radio Sci., 13*, 819-829, 1978.

Vincent, R. A., and J. Röttger, Spaced antenna VHF radar observations of tropospheric velocities and irregularities, *Radio Sci., 15*, 319-335, 1980.

Waterman, A. T., T. Z. Hu, P. Czechowsky, and J. Röttger, Measurement of anisotropic permittivity structure of upper troposphere with clear-air radar, *Radio Sci., 20*, 1580-1592, 1985.

Woodman, R. F., and Y. H. Chu, Aspect sensitivity measurements of VHF backscatter made with the Chung-Li radar: Plausible mechanism, submitted to *Radio Sci.*, 1988.

Woodman, R. F., and W. E. Guillen, Radar observations of winds and turbulence in the stratosphere and mesosphere, *J. Atmos. Sci., 31*, 495-505, 1974.

ASPECT SENSITIVITY MEASUREMENTS OF VHF BACKSCATTER MADE WITH THE CHUNG-LI RADAR: PLAUSIBLE MECHANISMS[1]

R. F. Woodman

Jicamarca Radio Observatory
Instituto Geofisico del Peru
Lima, Peru

Y.-H. Chu

National Central University
Chung-Li, Taiwan, ROC

A new technique, using beam broadening effects, has been developed to measure the aspect sensitivity of atmospheric clear-air VHF-radar echoes. It uses the relativity broad antenna beam of the vertical pointing antenna of the new Chung-Li ST-radar (25°N, 120°E). The aspect sensitivity measurement using this method is straightforward and free from convolution effects introduced by the finite width of the antenna beam pattern. The observed results agree very well with other measurements.

The authors propose a turbulent layer model to explain the aspect sensitivity of the echoes. In this model, anisotropic turbulence is confined to a very thin (few meters) region at the boundary of a turbulent layer. This region is responsible for the aspect sensitivity of the echoes obtained from the vertical direction. The isotropic echoes obtained from the oblique beam arise from the isotropic turbulence embedded in the center of the layer, with 30 to 300 meters in vertical extent. We show in an Appendix that the magnitude of the partial reflection coefficient is much more sensitive to the shape, length scale and smoothness, than to the slope of the refractive index profile. Therefore, the functional shape of the refractive index profile is very important for estimating the reflection coefficient. Large errors can be made when assuming, for simplicity, nonphysical profiles. For partial reflecting mechanisms to be important, step-like discontinuities, confined within length scales of the order of meter, would be required.

A Relation between Specular Reflection Echoes and Refractive Index Gradient in the Troposphere and Lower Stratosphere

T. Tsuda[1], P. T. May[2], T. Sato[3],
S. Kato[1] and S. Fukao[1]

(1) *Radio Atmospheric Science Center, Kyoto University*
(2) *CIRES, University of Colorado*
(3) *Department of Electrical Engineering, Kyoto University*

1 INTRODUCTION

MST radars operated at VHF and UHF utilize a physical principle that radiowaves in these frequency bands are scattered and/or reflected by fluctuations in the radio refractive index of the atmosphere. It is fairly widely accepted that for VHF radar observations isotropic turbulent scattering is dominant in the oblique directions, and reflection from stratified layers becomes dominant in the vertical direction [*Gage and Green*, 1978; *Röttger and Liu*, 1978; *Hocking and Röttger*, 1983; *Tsuda et al.*, 1986].

This study is concerned with a relation between reflection echoes observed from the vertical direction in the troposphere and lower stratosphere with the MU radar and refractive index gradient simultaneously measured by a radiosonde launched from the MU radar site.

2 REFRACTIVE INDEX GRADIENT

The vertical gradient of potential refractive index M in the dry atmosphere, i.e. neglecting humidity, is defined as:

$$M = -77.6 \times 10^{-6} \frac{p}{T} \frac{N^2}{g} \tag{1}$$

where p, T and N are the atmospheric pressure, temperature and Brunt-Väisälä (buoyancy) frequency, respectively [*e.g., Gage et al.*, 1985]. Note that since p/T is proportional to air density, M is proportional to N^2 and air density. Therefore, M generally decreases with the scale height of air density (approximately 7 km) in the stratosphere where the background value of N^2 is roughly constant. Relative fluctuations of air density are of an order of T'/T_0, where T' and T_0 are the fluctuating and background components of

temperature profile. Since $T'/T_0 < 1/100$, the fine vertical structure of M is mainly determined by the N^2 profile.

The received echo power for the Fresnel reflection is expressed as follows:

$$P_v = \frac{P_t \lambda^2 G^2}{16\pi^2 r^2} \rho^2 \tag{2}$$

where P_t, λ, r, G and ρ are the transmitted power, radar wavelength, range, antenna gain and reflection coefficient, respectively. The reflection coefficient is assumed to be proportional to M^2 and the intensity of fluctuations with a vertical scale of half of the radio wavelength $E(2k)$ [*VanZandt and Vincent*, 1982: *Gage et al.*, 1985], i.e.

$$\rho^2 = CM^2 E(2k) \tag{3}$$

where C is a constant which is determined by the radar wavelength and the height resolution of the radar sampling volume.

On the other hand, for isotropic turbulent scattering the radar reflectivity η has a relation expressed as

$$\eta = \epsilon \frac{M^2}{N^2} \tag{4}$$

where ϵ is the eddy dissipation rate within a turbulent layer [*Gage et al.*, 1980].

Considering (1) η becomes proportional to $N^2 \epsilon$ in the dry atmosphere, while ρ^2 for Fresnel reflection/scattering becomes proportional to $N^4 E(2k)$. Therefore, these two scattering/reflection mechanisms are characterized by proportionality to either N^2 or N^4 as well as the turbulence parameters.

For convenience we now define a normalized signal-to-noise ratio (SNR) in the vertical direction S_v after compensating for the range-squared effect as follows:

$$S_v = \frac{P_v}{P_N} \left(\frac{R}{10}\right)^2 \tag{5}$$

where, P_N and R are the noise power and the range in km, respectively. The reflection coefficient described in equation (3) becomes proportional to S_v.

3   DESCRIPTION OF THE EXPERIMENT

The vertical echo power has been oversampled every 75 m at altitudes between 5.4–21 km with a height resolution of 150 m and a time resolution of about 74 s by the MU radar (35°N, 136°E) in September 1986.

During the radar observations a radiosonde was launched from the MU radar site, which can sample temperature, pressure and humidity every one second (5 m resolution). We have averaged these profiles over 30 m in order to reduce the quantization error and to

obtain equally spaced points from the irregularly spaced original data points, and further smoothed by using a running mean window over five adjacent points, which gives the temperature profile with the height resolution of 150 m similar to that for the MU radar observations.

Although the tropopause was located at around 15 km, the vertical temperature gradient at 10–15 km altitudes is relatively gradual, and therefore, this altitude region seems to be fairly stable than in the region below 10 km.

4 RESULTS AND DISCUSSION

Fig. 1 (a) shows M^2 (dashed line) and P_v (solid line) profiles measured between 10 and 20 km, where M^2 is determined by using vertical spacings of 150 m for the calculation of temperature gradients, and P_v is averaged for 43 min. Peak values of M^2 range from $10^{-17} - 10^{-18}$, and a typical vertical spacing of these peaks is 1–2 km in this height range.

The S_v profile shows peaks with similar vertical spacings as those in the M^2 profile below about 15 km, and slightly smaller spacings above 15 km. The ratio of S_v between the peaks and valleys is about 20 and 10 dB below and above 15 km, respectively, which is also consistent with the range of variation of M^2.

Overall agreement between the M^2 and P_v profiles below 14 km is excellent except for differences in intensity at a valley about 11.8 km altitude, and a discrepancy of the altitude of a valley near 13 km.

At altitudes of 14–15 km, which correspond to the region just below the tropopause, S_v is attenuated relative to M^2 by 5–10 dB more than other altitude regions. In the height range from 15 to 18 km, S_v and M^2 generally show similar height structures, although the M^2 profile is smoother. Above 18 km, S_v tends to decrease more rapidly than M^2.

The ratio between S_v and M^2 plotted in Fig. 1 (b) shows a variation ranging from –15 to 15 dB from the mean value. However, the large excursion from the mean mostly occurs at valleys of S_v, where estimation of echo power is less reliable than that at peaks. The spacial variation of M^2 might also be the cause of the excursion, because the horizontal distance between the MU radar and the radiosonde could become as large as several tens kilometers at these altitudes. A full circle in Fig. 1 (b) corresponds to a determination at a peak of S_v whose location is indicated by a short horizontal bar in Fig. 1 (a). The mean value of the ratio at the peaks is 189.5 dB with a standard deviation of 2.4 dB indicated as straight vertical lines in Fig. 1 (b).

A linear regression or a cross correlation analysis between $\log M^2$ and $\log S_v$ gives a quantitative idea about the relation between these two profiles. Since the measurement accuracy of M^2 does not seem to be affected by the intensity of M^2 itself, and on the other hand, the determination of S_v becomes worse when the SNR is small, we have assumed $\log M^2$ as the independent variable, and $\log S_v$ the dependent variable in the
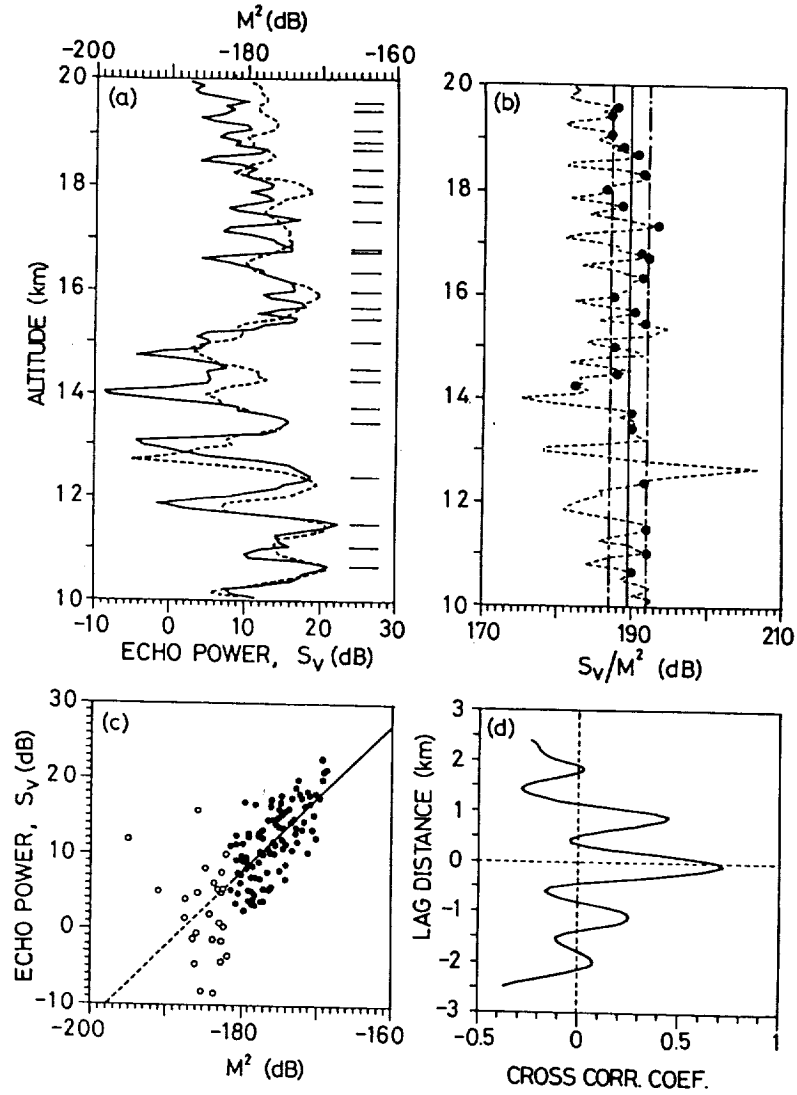
Figure 1: Comparison analyses between M^2 and S_v: (a) simultaneous plot, where solid and broken lines correspond to S_v and M^2, respectively, (b) ratio, (c) a linear regression curve, and (d) cross correlation coefficient.

linear regression analysis plotted in Fig. 1 (c). The slope of the linearly fitted curve is 0.98 with a standard deviation of 0.1 for the range of M^2 larger than -183 dB. The cross correlation value between M^2 and S_v for the entire range of variables is about 0.7 as shown in Fig. 1 (d).

In summary, the measured M^2 profile agrees well with the S_v down to the radar height resolution of 150 m, indicating that the height structure of the vertical echo power with a resolution of 150 m is mainly determined by M^2, thus by $(N^2)^2$. This implies that in equation (3) M^2 varies much more than the factor $E(2k)$. Unfortunately, we can not determine the origin of the refractive index fluctuations with a scale of 3 m (half of the radar wavelength) from our observations. However, the linear relation between S_v and M^2 suggests that the energy density of 3 m scale fluctuations $E(2k)$ seems to be distributed rather uniformly with height, although $E(2k)$ is certainly another important factor to determine the intensity of the reflection coefficient.

This study also suggests that intense peaks in the vertical echo power profiles, which normally have vertical spacings ranging from several hundred meters to a few kilometers, represent the local enhancement of Brunt-Väisälä frequency probably induced by gravity wave activities through their modification of the temperature field.

References

Gage, K., S., J. L. Green, and T. E. VanZandt, Use of Doppler radar for the measurement of atmospheric turbulence parameters from the intensity of clear-air echoes, *Radio Sci.*, *15*, 407-416, 1980.

Gage, K. S., and J. L. Green, Evidence for specular reflection from monostatic VHF radar observations of the stratosphere, *Radio Sci.*, *13*, 991-1001, 1978.

Gage, K. S., W. L. Ecklund, and B. B. Balsley, A modified Fresnel scattering model for parameterization of Fresnel returns, *Radio Sci.*, *20*, 1493-1501, 1985.

Hocking, W. K., and J. Röttger, Pulse length dependence of radar signal strengths for Fresnel backscatter, *Radio Sci.*, *18*, 1312-1324, 1983.

Röttger, J., and C. H. Liu, Partial reflection and scattering of VHF radar signals from the clear atmosphere, *Geophys. Res. Lett.*, *5*, 357-360, 1978.

Tsuda, T., T. Sato, K. Hirose, S. Fukao, and S. Kato, MU radar observations of the aspect sensitivity of backscattered VHF echo power in the troposphere and lower stratosphere, *Radio Sci.*, *21*, 971-980, 1986.

VanZandt, T. E., and R. A. Vincent, Is VHF Fresnel reflectivity due to low-frequency buoyancy waves? *Handbook for MAP*, *9*, 78-80, 1983.

ON THE PARTIAL REFLECTION FORMULA[1]

R. F. Woodman

Jicamarca Radio Observatory
Instituto Geofisico del Peru
Lima, Peru

Y.-H. Chu

National Central University
Chung-Li, Taiwan, ROC

The following formula is often quoted in the literature to evaluate the reflectivity of a refractive index profile, $n(z)$:

$$R = \int_{-L/2}^{L/2} \frac{1}{n} \frac{dn}{dz} \exp(-jk_s z) \, dz \; .$$

Also, it is commonly assumed for simplicity a constant slope profile, under the impression that it is the slope what determines the reflectivity. Under this conditions, or whenever an integrand, or its derivatives deviate from zero at the limits of integration at $\pm L/2$, the limits introduce a discontinuity which can largely overestimate the reflectivity. The difference between R^2 (power received) of a constant slope profile, evaluated in this form, and a error–function profile with a characteristic slope of ten meters, is 2000 decibel. It is shown that the continuity and smoothness of the profile is more important than the characteristic slope. An error function profile needs a characteristic length as small as a meter or less , and a difference of a fraction of a degree in temperature, to produce the reflectivities observed.

FINE-STRUCTURE OF DOPPLER SPECTRA
OF POLAR MESOSPHERE SUMMER ECHOES (PMSE)
OBSERVED WITH THE EISCAT 224-MHZ RADAR

J. Röttger*, C. La Hoz
EISCAT Scientific Association
P.O. Box 812, S-981 28 Kiruna, Sweden
(* on leave from Max-Planck-Institut für Aeronomie)

ABSTRACT:

Polar Mesosphere Summer Echoes Echoes detected on 224 MHZ are described with particular emphasis on spectral features detected with high time and frequency resolution. It is supposed that the particular fine-structure of these echoes results from very localized and strong scattering regions or even partially reflecting structures of the refractive index being o a sporadic or spread nature.

INTRODUCTION

The multi-national campaign MAC/SINE (Middle Atmosphere Cooperation/ Summer In Northern Europe) to study the middle atmosphere was carried out in summer 1987 in northern Scandinavia. The particular purpose of this campaign was to investigate with rockets and ground-based methods the large-scale dynamics and structure of the middle atmosphere as well as gravity waves and turbulence. The EISCAT VHF radar was involved in the operations and almost 70 hours of observation time were provided by Germany, Norway, Sweden and the EISCAT Scientific Association. It turned out that the EISCAT VHF radar contributed substantially to this campaign, particularly enforced by the exciting detection of the new category of lower ionospheric echoes on 224 MHz: The polar mesosphere summer echoes, PMSE. The first observations of these echoes were described by HOPPE et al. (1988) and RÖTTGER et al. (1988). Similar echoes were earlier observed with 50-MHz radars in polar regions by ECKLUND and BALSLEY (1981) and CZECHOWSKY and RÜSTER (1985). We discuss in this paper some typical features of the polar mesosphere summer echoes observed on 224 MHz, in particular their Doppler spectra and the variability of the echo power.

EXPERIMENTAL SET-UP AND FIRST HIGH-RESOLUTION OBSERVATIONS

The interesting outcome of the EISCAT observations during the MAC/SINE campaign was the occurrence of the polar mesosphere summer echoes (PMSE), which were observed with the EISCAT VHF Radar from altitudes between 80 and 90 km. The standard GEN-11 program (13-baud Barker code with 1.05 km baud length, e.g., TURUNEN, 1986), which was originally designed for incoherent scatter observations, was applied in the beginning of the campaign. The EISCAT VHF system was run with two klystrons at a total power of 2 MW and 8% duty cycle making use of the full VHF antenna, which was pointed to the zenith. In Fig. 1 three real-time graphic copies are displayed, which show the first observations of these strong echoes (courtesy of C. Hall and U.P. Hoppe).

It was argued that these echoes, which were first described in the paper by HOPPE et al. (1988), cannot be explained by the usual incoherent-scatter echoes from the D-region (e.g., MATHEWS, 1984). Coherent mesospheric echoes should also not be detectable at 224 MHz because electron density irregularities, resulting from neutral turbulence, should not be present at the radar Bragg wavelength of

EISCAT VHF Radar   SP-SI-GEN-11-V
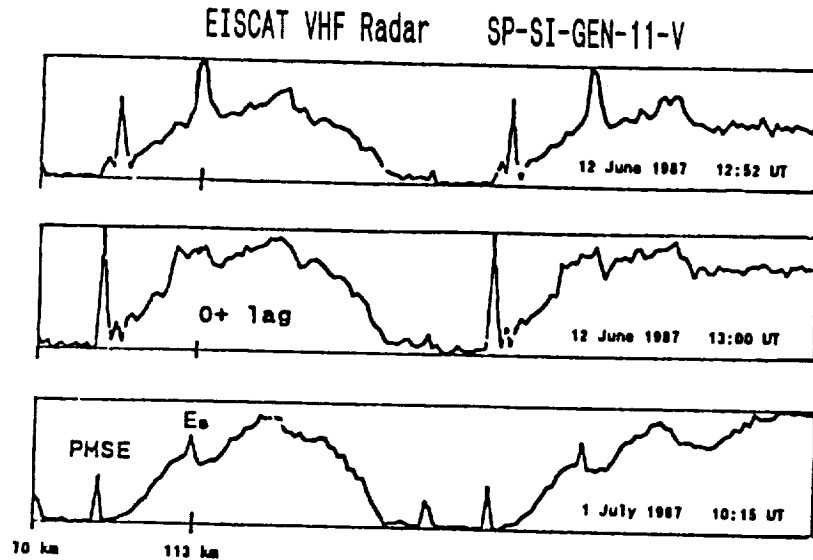
Fig. 1   First real-time graphic display of polar mesosphere summer echoes from altitudes between 80 km and 90 km (courtesy of C. Hall and U.P. Hoppe).

67 cm (half the wavelength of the 224 MHz radar). Following conventional theories of turbulence scattering applied to the standard mesosphere-stratosphere-troposphere MST-radars, such echoes should not even occur on th usual MST radar frequencies of 50 MHz (e.g., HOCKING, 1985). Explanations of possible scattering and generation mechanisms are outlined in a paper by RÖTTGER and LA HOZ (1989).

Since there were indications of very narrow spectral features which could not be resolved with the originally applied radar program, a new high resolution program was designed basing on the early pulse schemes used for mesosphere studies. This program (SP-EI-MESO-V) allows a spectral resolution of 0.42 Hz in contrast to the 10.7 Hz resolution of the other applied program GEN-11. It also uses a 13-baud Barker code with 1.05 km altitude resolution and covers the altitudes from 78.5 km to 90.0 km. The pulse-to-pulse modulation scheme was applied to adapt for the long coherence times of these echoes and to resolve their corresponding narrow spectral width. Since coherent integration was not implemented at that time, a very long interpulse period of 18.7 ms had to be used to achieve a long enough data interval (2.4 s) with 128 data points in order to obtain the necessary resolution of 0.42 Hz. From these complex data the autocorrelation functions (ACF) were computed on-line, and two ACFs were accumulated and dumped every 5 seconds. The VHF transmitter was operated at the same peak power of about 2 MW as during the GEN-11 operations. Due to the long interpulse period, however, only a low duty cycle of 0.48% resulted, yielding an average power of 96 kW. The full antenna of 40m x 120m aperture was used with a vertical beam· With 65% antenna aperture efficiency, the peak power-aperture product was 6 x 10^9 Wm^2. Operation with this particular program was carried out over 22 hours on 5 days in the first half of July 1987.

Because the PMSE were unusually strong we cannot exclude that occasionally some receiver non-linearity did occur. With the applied analysis scheme the effect is that the maximum power would be underestimated and some sidebands could be generated which would cause a fraction of the echo power to be spilled into higher Doppler frequencies. The effect on the Doppler spectrum width should not be noticeable in the present analysis procedure.

In the companion paper by RÖTTGER et al. (1989) some characteristics of gravity waves occurring in connection with the polar mesosphere summer echoes (PMSE) observed with this radar program are described. In this paper we will concentrate on some peculiar features of high-time and high-frequency resolution spectra, since it was quite frequently noted that the spectra are very narrow, sometimes bi- or multi-modal and frequently quite changeable in time and height.

FINE-STRUCTURE OF DOPPLER SPECTRA

The individual spectrograms shown in several figures of RÖTTGER et al. (1989) prove the variable spectral width. We noticed that the width can take values differing by almost an order of magnitude. Relating the spectrum width tentatively to turbulent fluctuations of the scattering structures we find variations from very weak r.m.s. fluctuating velocities of less than 1 ms^{-1} up to quite severe fluctuations of about 10 ms^{-1}. Some extreme examples of spectra are shown in Figure 2. Note that in all our analyses we have subtracted the noise, and the displays, thus, show only the signal amplitude or the power. The PMSE spectra in Fig. 2 are centered in each case on the frequency bin with the maximum amplitude A_m. The value $A_m = 10$ corresponds to about 15 dB signal-to-noise ratio. We will deduce the absolute signal power in a later chapter when we estimate the radar reflectivity of the 224-MHz PMSE. We already noticed from the signal peak at 85 km in Fig. 1 that the PMSE is much stronger than the incoherent scatter background in the D-region.

EISCAT VHF RADAR (224 MHz)
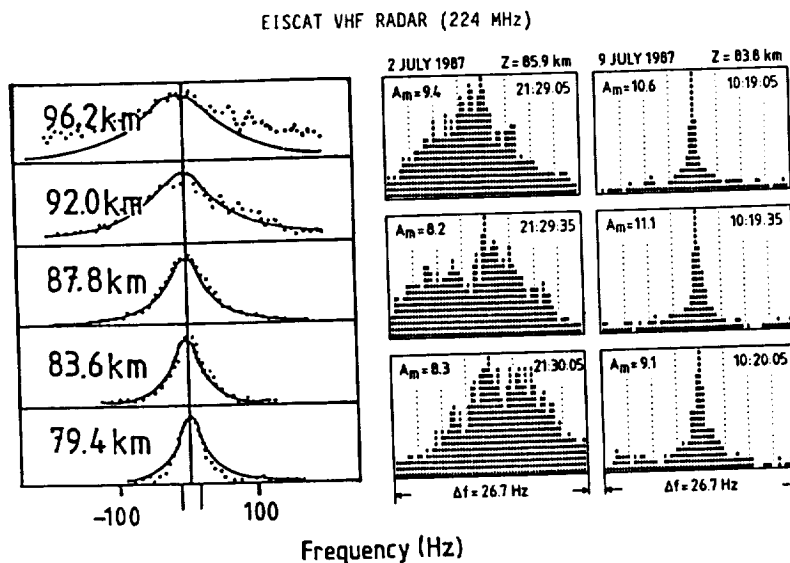
Fig. 2 Spectra of incoherent scatter signals (left-hand panel, after HALL et al., 1987) and of coherent-scatter polar mesosphere summer echoes measured with the EISCAT 224-MHz radar in Tromsö, Norway. The center panel shows the widest spectra and the right-hand panel the narrowest spectra, which were found so far in PMSE analyses.

EISCAT VHF Radar   9 July 1987   09:41:10 - 09:41:40 UT   z = 84.85 km
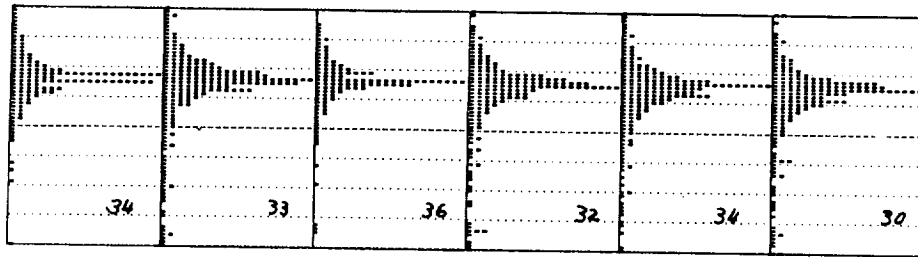
Fig. 3   Time series of self-normalised Doppler spectra with time reso-
lution of 5 seconds. The number in the boxes gives the signal plus
noise amplitude in dB, which was used to normalise the spectra. The
spectra show the normalised linear amplitudes.

The widest spectral width observed during PMSE conditions, namely 10-15 Hz, is
much narrower than the width of 50-100 Hz of an incoherent scatter echo from 80-
90 km altitude. This is proved by the spectra shown on the left-hand side of
Fig. 2. Whereas the incoherent scatter spectra are of Lorentzian or Gaussian
shape, the PMSE spectra consist of an ensemble of several narrow-band spectra (2
July 1987) or even a single high-amplitude spike superimposed on a weaker and
wider spectral background (9 July 1987). These observations are consistent with
the hypothesis that fairly small and localized refractive index structures
coexist within a volume of 1 km in vertical and about 2 km in horizontal extent
(given by the beam width), which move with different differential velocity. This
also means that the structures causing the PMSE unlikely fill the scattering
volume homogeneously. The spiky structure of the spectra can be regarded to be
due to some kind of amplitude modulation which results from quickly growing and
decaying scattering structures. This is an indication that the scattering pro-
cess is intermittent and not stationary (e.g., HOCKING, 1987). Under usual
conditions the latter situation should not occur for incoherent scatter or for
pure turbulence scatter.

In Fig. 3 we show a series of spectra deduced from single data dumps with the
best achievable time resolution of 5 seconds. We clearly notice the separated
peaks. Note also that the spectral amplitudes are displayed and not the spectral
power in order not to suppress the wider and weak wings of the spectra. We
regard the occurrence of the spikes on the spectra not to represent the normal
statistical fluctuations rather than to be of some deterministic nature. This
assumption can be supported by the displays of self-normalized dynamic spectra,
which are shown in Figures 4a and 4b. These displays allow to trace single spec-
tral spikes as function of time and frequency. At 84.85 km we for instance
notice over some 30 seconds at the beginning of the display that a single very
narrow spike dominated the spectrum, which later splitted up into two or a few
spikes. One kilometer higher in the next range gate, the spectrum was split from
the beginning into two or more peaks of about equal amplitude. In this range
gate some kind of braided structure characterised the spectrum. This means that
there were two distinct reflectors or very narrow scattering layers which moved
radially with slightly different velocity. The velocity difference must have
been changing gently within several ten seconds, resulting in a small variation
of the Doppler frequency of the spectral spikes which even could join into one
narrow spike. This then results in some kind of braided structure of the Doppler
spectrum. The total amplitude of the signal in the corresponding range gate is
shown in the upper panel of the Figures 4a and 4b. We notice that there is no
obvious relation of the quite variable signal amplitude with the described fine-
scale features of the spectra. Thus, the scattering/reflection cross section did
not at all depend on these velocity variations.
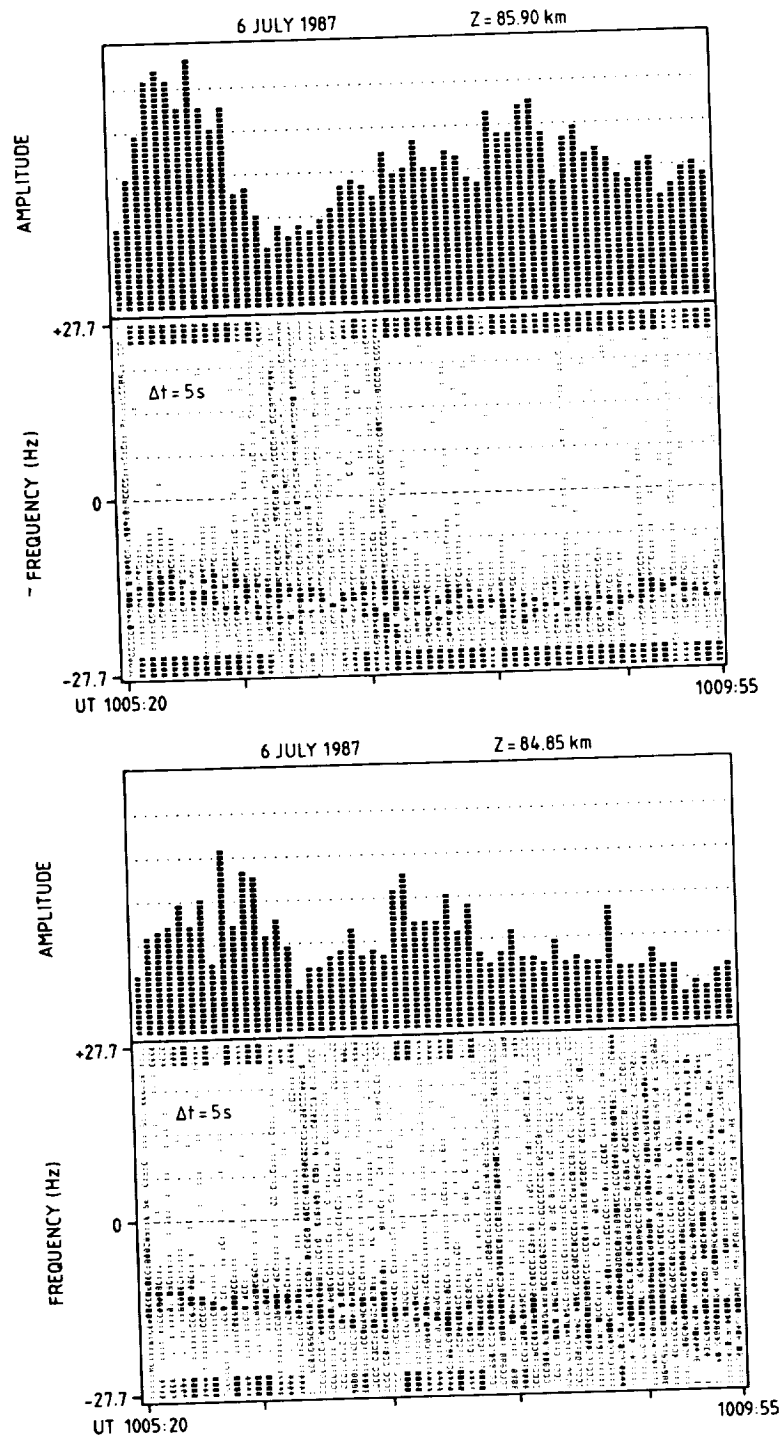
Fig. 4   High-time resolution Doppler spectrograms and the corresponding
signal amplitudes for two adjacent range gates.

In Fig. 5 we show a more recent example of dynamic spectra which were obtained with a different radar experiment. In the right-hand panels we again notice the splitting of spectral peaks into a braided structure (although at larger time scales) as well as a separation and a sudden jump in Doppler frequency. In the spectra of the left-hand panels some kind of micro-jumps do occur. We have explained the possible cause of these particular features in the companion paper (RÖTTGER et al., 1989).

The assumption that the refractive index structures, which cause the PMSE, are fairly narrow is supported by the spectra displayed in Fig. 6. These are series of spectra from 3 adjacent range gates and we definitely notice very narrow spectra in the centre range gate. Whereas these spectra are fairly persistent at the beginning, a sudden jump occurs towards the end of the display. The lower range gate shows almost no signal, whereas fairly wide and fluctuating spectra occur in the upper range gate.

The observed short-term fine-structure would be smeared out when spectra are averaged over 1 minute or so, which is frequently done in several analyses. The quasi-braided structure will also not show up in low-spectral-resolution experiments, such as those with the incoherent scatter program GEN-11. It is also assumed to be smeared out with wide-beam radars, with a beam width larger than 1-2 degree.

EISCAT VHF Radar   (PMSE88)   1 July 1988
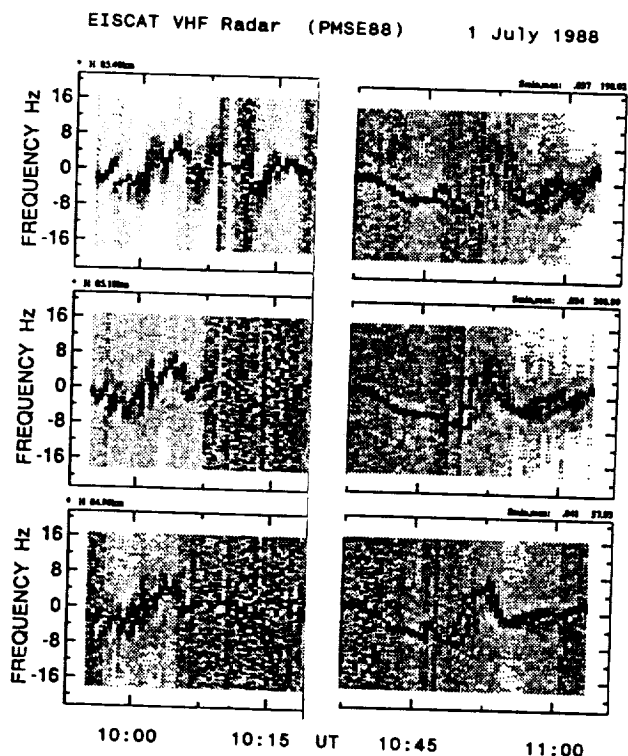
Fig. 5   Self-normalised spectrograms of PMSE around 84 km and 85 km observed with 300 m altitude resolution applying complementary coding (see details in La Hoz et al., 1989).
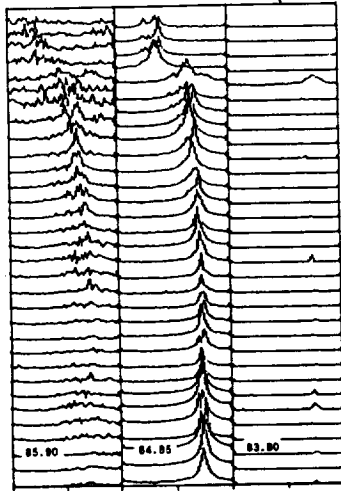
Fig. 6 Amplitude of Doppler spectra
of 3 altitude gates at 83.80, 84.85
and 85.90 km measured with 10 s
time resolution on 6 July 1987
between 10:18 and 10:23 UT. The
noise level is subtracted from the
displays. It is noticeable that the
spectra exhibit completely differ-
ent characteristics in the altitude
gates separated by only 1.05 km.

We must assume that the quasi-braided structure in the spectra is determini-
stic and not due to random scatterers. The extremely narrow spectral spikes are
consistent with a fairly stable and only weakly turbulent reflectivity struc-
ture. The possible explanation that the narrow spectra together with the sub-
stantially large echo amplitude are caused by Fresnel reflection from a thin
spreaded lamina of reflectivity structure could sound acceptable. Some simpli-
fied model can be proposed which assumes that the short-term (time scales of
seconds) quasi-periodic behaviour of Doppler spectral lines could be due to
focussing/defocussing or interference of ray paths originating from Fresnel
reflection from different locations of the refractive index surface which is
undulated by a wave disturbance. A relation of particular features of VHF radar
echoes, like power bursts and cat's eye structures in the reflectivity profiles,
to wave disturbances or instabilities was suggested by KLOSTERMEYER and RÜSTER
(1984) and REID et al. (1987). CZECHOWSKY et al. (1988) have also found an
aspect sensitivity, which they assumed to be consistent with a reflection mecha-
nism. In the paper by RÖTTGER and LA HOZ (1989) possible mechanisms will be
described, which could cause the steep gradients of reflectivity, namely the
electron density variations, and which will be needed to explain the described
spectral features.

CONCLUSION

We have discussed in this paper some fine structures of PMSE, which we could
envisage to result from very localized and strong scattering regions or even
partially reflecting structures of the refractive index in the polar summer
mesosphere. These structures, which do not fill a volume of some 1 km vertical
and horizontal extent, are most likely corrugated or split into substructures
and, thus, cause the evident intermittency of the PMSE. In analogy with iono-
spheric irregularities in the E- or F-region we may term the particular D-re-
gion/mesospheric irregularities, which cause the polar mesosphere summer echoes,
to be of a sporadic or spread nature. RÖTTGER and LA HOZ (1989) will discuss
some possible geophysical mechanisms which could generate these structures.

114

REFERENCES

Czechowsky, P. and R. Rüster (1985), Power spectra of mesospheric velocities in polar regions, Handbook for MAP, 18 (S. Kato, ed.), 207-211 (publ. by SCOSTEP Secretariat, Dept. Elec. Engin., Univ. of Illinois, Urbana, IL).

Czechowsky, P., I.M. Reid and R. Rüster (1988), VHF radar measurements of the aspect sensitivity of the summer polar mesopause echoes over Andenes (69°N, 16°E), Norway, Geophys. Res. Lett., 15, 1259-1262.

Hall, C., U.-P. Hoppe, P.J.S. Williams and G.O.L. Jones (1987), Mesospheric measurements using the EISCAT VHF system: first results and their interpretation, Geophys. Res. Lett., 14, 1187-1190.

Hocking, W.K. (1985), Measurement of turbulent energy dissipation rates in the middle atmosphere by radar techniques: a review, Radio Sci., 20, 1403-1422.

Hocking, W.K. (1987), Reduction of the effects of non-stationarity in studies of amplitude statistics of radio wave backscatter, J. Atmos. Terr. Phys., 49, 1119-1131.

Hoppe, U.-P., C. Hall and J. Röttger (1988), First observations of summer polar mesospheric backscatter with a 224 MHz radar, Geophys. Res. Lett., 15, 28-31.

Kelley, M.C., D.T. Farley and J. Röttger (1987), The effect of cluster ions on anomalous VHF backscatter from the summer polar mesosphere, Geophys. Res. Lett., 14, 1031-1034.

Klostermeyer, J. and R. Rüster (1984), VHF radar observation of wave instability and turbulence in the mesosphere, Adv. Space Res., 4, 79-82.

La Hoz, C., J. Röttger and S.J. Franke (1989), Dynamic spectra of polar mesosphere summer echoes, Handbook for MAP (this issue).

Mathews, J.D. (1984), The incoherent scatter radar as a tool for studying the ionospheric D-region, J. Atmos. Terr. Phys., 46, 975-986.

Reid, I.M., R. Rüster and G. Schmidt (1987), VHF radar observations of cat's-eye-like structures at mesospheric heights, Nature, 327, 43-45.

Röttger, J., C. La Hoz, M.C. Kelley, U.-P. Hoppe and C. Hall (1988), The structure and dynamics of polar mesosphere summer echoes observed with the EISCAT 224 MHz radar, Geophys. Res. Lett., 15, 1353-1356.

Röttger, J. and C. La Hoz (1989), The fine-structure od Doppler spectra and signal power characteristics of polar mesosphere summer echoes observed with the EISCAT 224-MHz radar, to be submitted to Jour. Atmos. Terr. Phys.

Röttger, J., C. La Hoz, S.J. Franke and C.H. Liu (1989), Gravity wave steepening and tilting detected in high-resolution Doppler spectra of polar mesosphere summer echoes (PMSE) observed with the EISCAT 224-MHz radar, Handbook for MAP (this issue).

Turunen, T. (1986), GEN-SYSTEM - a new experimental philosophy for EISCAT radars, J. Atmos. Terr. Phys., 48, 777-785.

CHARACTERISTICS OF VHF RADAR ECHO POWER IN THE TAIWAN AREA

Y. H. Chu[1], T. S. Hsu[1], C. H. Liu[2], J. K. Chao[1], and J. Röttger[3]

[1]Department of Atmospheric Physics, National Central University, Chung-Li, Taiwan, ROC
[2]Department of Electrical and Computer Engineering, University of Illinois, Urbana, IL 61801
[3]EISCAT Scientific Association, Box 705, Kiruna, Sweden

In this report the gradients of the generalized potential refractive index (denoted by M) over the Taiwan area are analyzed. The definition of M is (OTTERSEN, 1969):

$$M = -77.6 \times 10^{-6} \frac{P}{T} (\frac{\partial \ln \Theta}{\partial z}) [1 + \frac{15500\, q}{T} (1 - \frac{1}{2} \frac{\partial \ln q / \partial z}{\partial \ln \Theta / \partial z})] \qquad (1)$$

$$\underbrace{\qquad\qquad\qquad}_{\text{dry term}} \quad \underbrace{\qquad\qquad\qquad}_{\text{wet term}}$$

where P is the atmospheric pressure (mb), T is the temperature (°K), q is the specific humidity, Θ is the potential temperature (°K) and z is the altitude. The terms in the brackets are called the dry term and wet term, respectively, depending on the humidity contribution. It is found that over the Taiwan area, in general, below 8 km the contribution of water vapor to M is larger than the dry air by about 1 or 2 orders of magnitude, and above 8 km the humidity contribution to M vanishes as shown in the example of Figure 1, in which the solid, dotted and dashed curves represent the profiles of log (M^2), wet term, and dry term, respectively.

From the echoing theory of MST radar (GAGE et al., 1985; GAGE and BALSLEY, 1980), it is obvious that no matter what the echo mechanism is, the echo powers are always proportional to the values of M^2, that is

for reflection: $Pr = e^2 \cdot Pt \cdot Ae^2 \cdot \Delta r \cdot M^2 \cdot F^2(2k,z) / (16 \cdot z^2 \cdot \lambda^2)$ (2)

for scattering: $Pr = e^2 \cdot 0.69 \cdot \lambda^{1/3} \cdot Pt \cdot Ae \cdot \Delta r \cdot M^2 \cdot Lo^{4/3} / (64 \cdot z^2)$ (3)

where e is the efficiency of the antenna and transmission line, Pr is the received echo power, Pt is the transmitted power, Ae is the effective antenna area, λ is the wavelength, Δr is the range resolution, M is the gradient of the generalized potential refractive index, Lo is the outer scale of the turbulent spectrum, F(2k,z) is related to the spectrum of vertical displacement, and z is the altitude. Therefore, from equations (2) and (3), it is apparent that the linear relationship between Pr and M^2 can be expected if the logarithmic operations are taken for both sides of (2) and (3). Figure 2 is the scatter diagrams of log(Pr·z^2) and log(M^2) for different months, where the range correction to echo powers have been made to avoid the altitude bias. From Figure 2 it is clear that the linear correlation coefficient of log(Pr·z^2) and log(M^2) for every month is always between 0.5 to 0.6 and also the values of the correlation coefficient do not show the significant monthly variations. Although the correlation between the echo power and M^2 is quite good, as shown in Figure 1, however because the magnitude of M is dominated by the humidity contribution below 8 km over the Taiwan area, one must be very careful in using VHF radar echo power data to deduce the atmospheric temperature profile as suggested by GAGE and GREEN (1982).

It seems from Figure 2 that the correlation between the echo power and M^2 is independent of the weather condition. However, according to the following analysis, we found that it is not true. Figure 3 is the path of typhoon Wayne when it passed through the Taiwan area from August 20 to September 5, 1986, and Figure 4 shows the scatter diagrams of log(Pr·z^2) and log(M^2) for the days during the typhoon invasion. Note that the correlation between the echo power and M^2
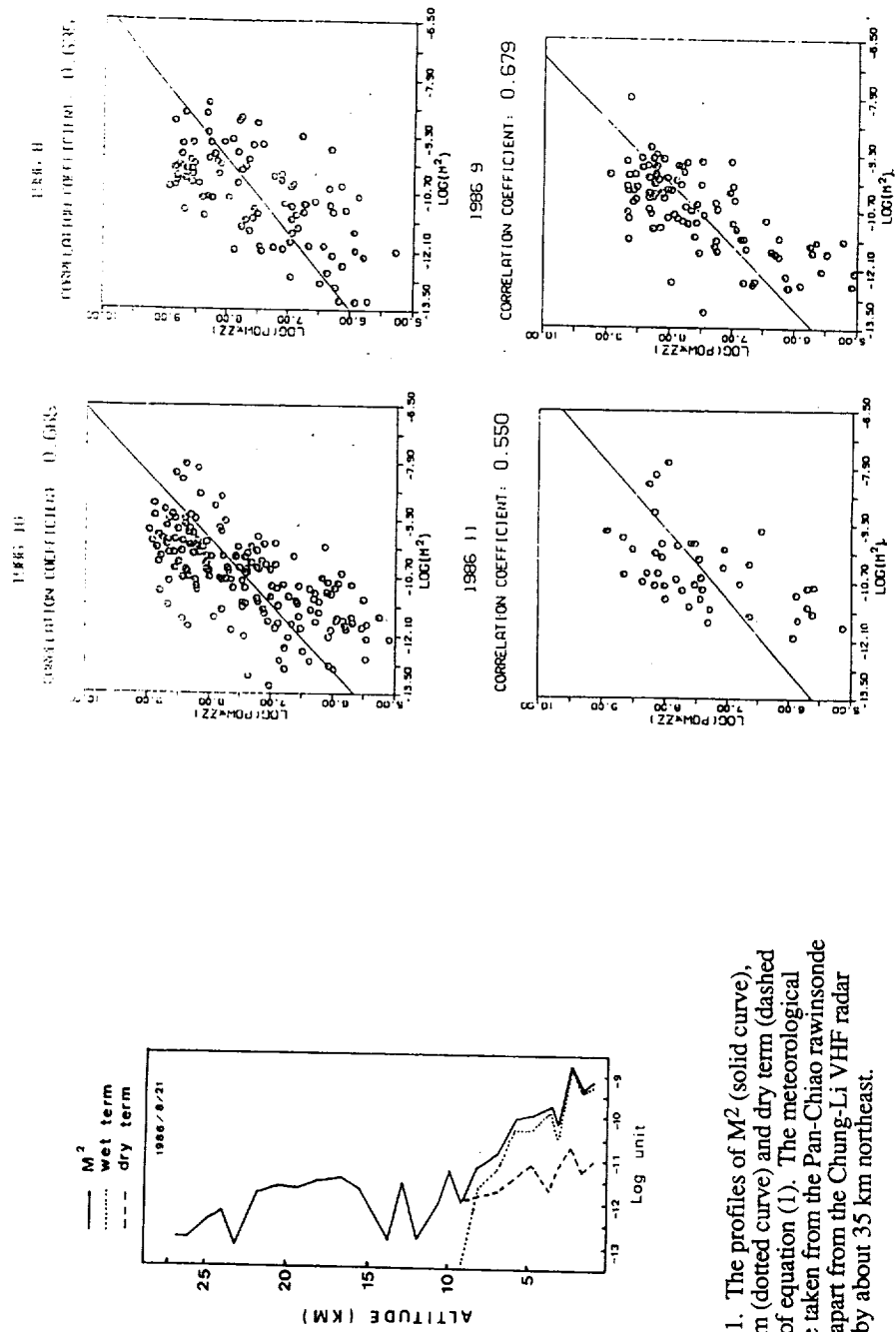
Figure 2. The scatter diagrams of echo power and M^2 for different months' data.

Figure 1. The profiles of M^2 (solid curve), wet term (dotted curve) and dry term (dashed curve) of equation (1). The meteorological data are taken from the Pan-Chiao rawinsonde station apart from the Chung-Li VHF radar station by about 35 km northeast.
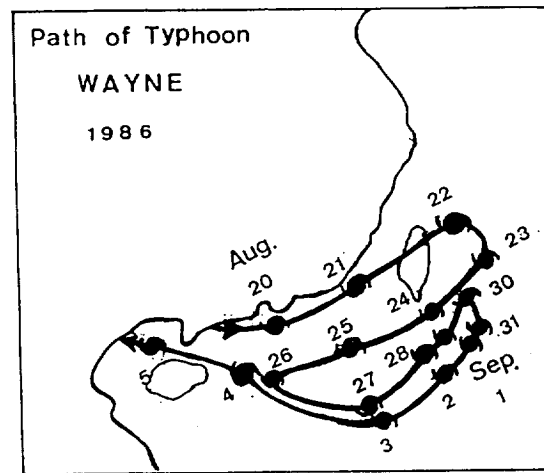
Figure 3. The path of typhoon Wayne passing through Taiwan island in the period August 20 to September 5, 1986.
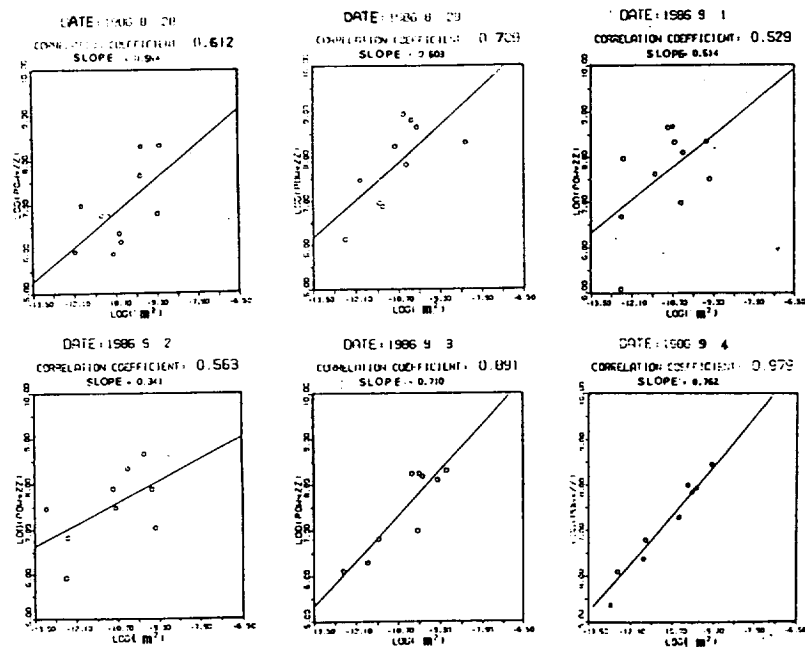
Figure 4. The scatter diagrams of echo power and M^2 for the dates during the typhoon Wayne period.

are pretty good and the slopes of the regression lines are between 0.3 to 0.7. Whereas Figure 5 shows the correlation between the echo power and M^2 in a weather condition of high pressure system coverage over the Taiwan area. In this case the correlation coefficients are still high; however, the slopes of the regression lines are different from the case of typhoon Wayne, the values of the former are between 1.0 to 1.8. Therefore, it can be concluded that different weather conditions correspond to different slopes of the regression lines of echo power and M^2. As a matter of fact, this result can be inferred theoretically from equations (2) and (3). For the echo mechanism of the layer reflection, (2) can be rewritten as

$$\log(Pr \cdot z^2) \ (dB) = a \log(M^2) + R \tag{4}$$

where a is the slope of this line and is equal to 1, and the value of R is dependent on the radar parameters only. However, for the echo mechanism of the turbulent scattering, the result is different. According to the theoretical work by WEINSTOCK (1978), Lo is proportional to the potential temperature gradient, that is

$$Lo^{4/3} = c(d\ln\Theta/dz)^{-1} \tag{5}$$

where c is the proportional constant. Substituting (5) and (1) into (3), and the assumption of dry atmosphere is made, (3) can be rewritten as

$$\log(Pr \cdot z^2) = b \log(M^2) + S \tag{6}$$

where the value of b will be 0.5 and the magnitude of S is dependent on the radar parameters only. From the above discussion it is obvious that for highly disturbed conditions, for example during the typhoon period, the echo mechanism will be dominated by turbulent scattering and the slope of the regression line between the echo power and M^2 will be approximated to 0.5. However, for a highly stable environment, for example during the period of high pressure system coverage, the echo mechanism of the layer reflection cannot be neglected and the slope of that will be close to 1. This conclusion has been confirmed by the observations shown in Figures 4 and 5.

The echo power profile variations of the Chung-Li VHF radar during the period of typhoon Ellen are also studied. Figure 6 is the trajectory of this typhoon passing by the Taiwan area in the time from October 11 to 19, 1986, and Figure 7 is the echo power profiles corresponding to the dates before and after typhoon Ellen passed by. The upper and middle panels of Figure 7 are the echo power profiles measured with obliquely pointing antenna beams (17° zenith angle) toward east and north, respectively, and the lowest panel is the profiles observed by vertically pointing antenna beams. It is apparent that no matter what the pointing direction of the antenna beam is, when typhoon Ellen was close to Taiwan island during the period from October 14 to 18, the maximum detectable altitude where the Chung-Li VHF radar can reach will be raised up gradually with time, as shown in Figure 7, marked with dashed line. However, as typhoon Ellen goes away, the maximum detectable altitude will be lowered again.

In summary, the echo powers measured with the Chung-Li VHF radar are studied. The correlation between the echo power and the gradient of the generalized potential refractive index for one month's data is high, and correlation coefficients seem to have no monthly variation. After very carefully examining the relation between weather conditions and the slopes of the regression line of the echo power and M^2, it is found that different weather conditions are responsible for the different slopes of the regression line of the echo power and M^2. In fact, this result can also be predicted theoretically from the analysis of the radar equation. The echo power profiles during the typhoon period are also analyzed. The results show that the maximum height where the Chung-Li VHF radar can reach will be higher than if there were no typhoon nearby.
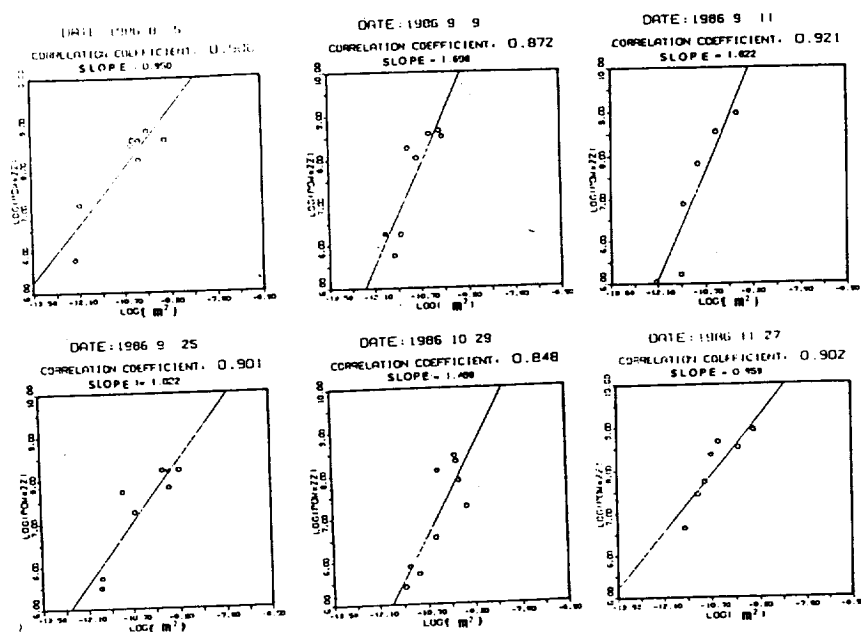
Figure 5. The scatter diagrams of echo power and M^2 for the weather condition of high pressure system coverage over the Taiwan area.
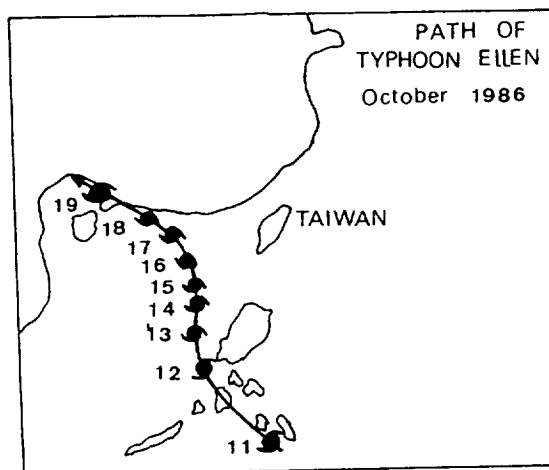
Figure 6. The path of typhoon Ellen nearby Taiwan island in the period October 11 to 19, 1986.
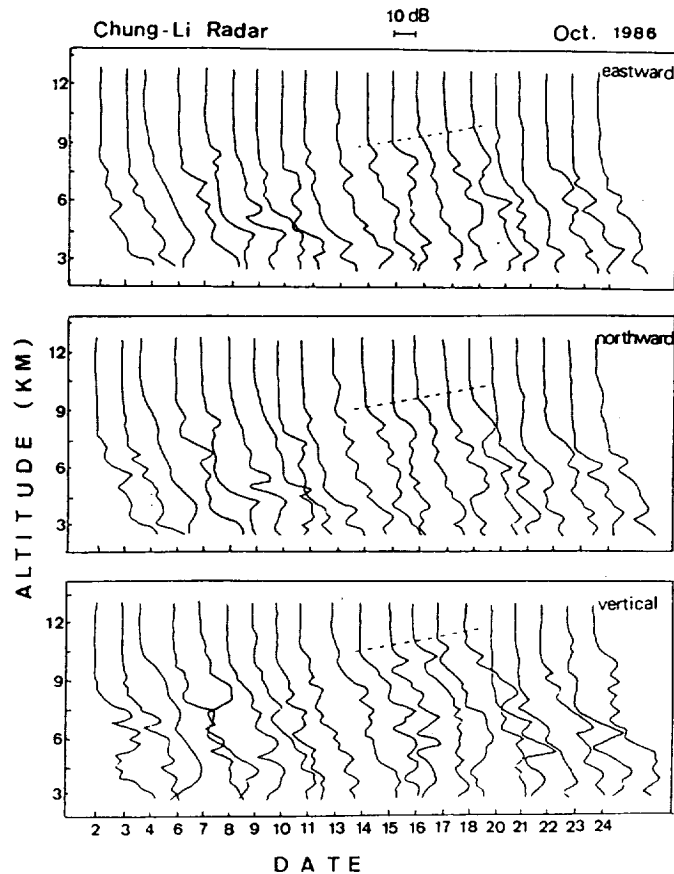
Figure 7. The time series of echo power profiles measured with the Chung-Li VHF radar in October 1986. The upper and middle panels represent the echo power profiles observed by obliquely pointing antenna beams with 17° zenith angle toward east and north, respectively, and the lowest panel is the echo power profiles measured with vertically pointing beam. The period marked by the dashed line is the time of typhoon Ellen nearby Taiwan island as shown in Figure 6.

REFERENCES

Gage, K. S., and B. B. Balsley, On the scattering and reflection mechanisms contributing to clear air radar echoes from the troposphere, stratosphere, and mesosphere, *Radio Sci., 15*, 243-257, 1980.

Gage, K. S., and J. L. Green, A technique for determining the temperature profile from VHF radar observations, *J. Appl. Meteorol., 21*, 1146-1149, 1982.

Gage, K. S., W. L. Ecklund, and B. B. Balsley, A modified Fresnel scattering model for the parameterization of Fresnel returns, *Radio Sci., 20*, 1493-1501, 1985.

Ottersten, H., Radar backscattering from the turbulent clear atmosphere, *Radio Sci., 12*, 1251-1255, 1969.

Weinstock, J., Vertical turbulent diffusion in a stably stratified fluid, *J. Atmos. Sci., 35*, 1022-1027, 1978.

THE THEORETICAL STUDY OF THE STATISTICAL CHARACTERISTICS OF THE RADAR ECHOES FROM A VHF RADAR

Y. H. Chu and J. K. Chao

Department of Atmospheric Physics
National Central University
Chung-Li, Taiwan 32054, ROC

C. H. Liu

Department of Electrical and Computer Engineering
University of Illinois
Urbana, IL 61801

ABSTRACT

It is assumed that VHF radar echoes consist of contributions from both isotropic turbulences and anisotropic irregularities. Let the inphase and quadrature components of the radar echo satisfy the central limit theorem, and their phases are randomly distributed symmetrically with respect to zero. If the phase and the amplitude of the radar echo are independent and uncorrelated to each other, then the probability density function of the amplitude of the radar echo is derived using a theory of random variables. After some complicated calculations, the Rayleigh distribution, the Rice distribution and the Hoyte distribution can be obtained as a special limit in each case of the derived probability density function. It is further shown that the theoretical value of the Nakagami M parameter of the radar echo can be derived as well. The magnitude of M depends on the average value of the radar echo from the anisotropic irregularities μ, and its standard deviation σ. If $\sigma^2 = (\sqrt{2}-1)\mu^2$ then M = 1; if $\sigma^2 > (\sqrt{2}-1)\mu^2$, then m < 1; and if $\sigma^2 < (\sqrt{2}-1)\mu^2$, then M > 1. Therefore, one has to be very careful when the Nakagami M parameter is used to distinguish echo mechanisms.

INTRODUCTION

From the observation of aspect sensitivity, it is realized that the targets of the VHF radar existing in the atmosphere consist of isotropic turbulences and anisotropic refractive index irregularities. The characteristics of the former are straightforward; however, the latter are very complicated and need more investigation. There are many modeled echo mechanisms proposed to explain the relation between structures of VHF radar targets and the properties of VHF radar echo signals. For example, isotropic turbulent scattering (BOOKER and GORDON, 1950); anisotropic turbulent scattering (GAGE and BALSLEY, 1980; DOVIAK and Zrnic, 1984); Fresnel reflection (RÖTTGER and LIU, 1978); diffuse reflection (RÖTTGER, 1980) and Fresnel scattering (GAGE et al., 1981). Different echo mechanisms correspond to the targets which cause the different returns of VHF radar. Therefore, according to some criteria, it is possible to distinguish the echo mechanisms from the analysis of the VHF radar echo signals. Statistical methods have been used frequently to distinguish the VHF radar echo mechanism by many scientific workers (RÖTTGER, 1980; SHEEN et al., 1985; HOCKING, 1987; KUO et al., 1987). Conventionally, the criteria of the statistical method are such that if the probability density function (pdf) of the echo amplitude is Rayleigh, or the Nakagami M parameter is equal to 1, the echo mechanism will be isotropic turbulent scattering; if the pdf of the amplitude is Rice, or the M parameter is greater than 1, the echo mechanism can be considered as the combination of partial reflection and isotropic turbulent scattering; if the pdf of amplitude is Hoyte, or the value of the M parameter is less than 1, the echo mechanism will be diffuse reflection or anisotropic turbulent scattering.

In this paper, we shall point out that the conventional criteria of statistical method in echo mechanism discrimination are not so accurate, and the relation between pdf and the Nakagami M parameter of VHF radar echo signals are also not straightforward. Under some assumptions, the generalized pdf and theoretical Nakagami M parameter of amplitude for VHF radar echo signals

have been derived. It is shown that the special cases of the generalized pfd derived in this paper and the values of the Nakagami M parameter depend on both the mean value and the variance of the returns from anisotropic irregularities.

DERIVATION OF AMPLITUDE PROBABILITY DISTRIBUTION

From the measurement of aspect sensitivity with VHF radar it is reasonable to assume that the echoes of VHF radar are composed of the signals from isotropic turbulent scattering and returns from anisotropic irregularities. If the echoing processes of VHF radar are considered as stochastic processes, the echo signal will then be treated as the random variable. Therefore, the observed echo signal can be represented as the combination of two random variables, one is responsible for the process of isotropic scattering and the other corresponds to the echoing process of anisotropic irregularities, that is,

$$E_{obs} = E_{iso} + E_{aniso} \tag{1}$$

where E means random variable. Let the numerical value of random variable E_{obs} be r, hence

$$r = A \exp(i\Theta) = x + iy = \sum_j a_j \exp(i\varphi_j) \tag{2}$$

where A and Θ are the amplitude and the phase of r, x and y are the inphase and quadrature components of the observed echo signal, respectively; a_j and φ_j are the amplitude and phase of the echo signal yielded from jth target in the radar volume, respectively. Assume that (a) the statistical properties of x and y satisfy the central limit theorem, that is, the pdf of x and y can be described by Gaussian distribution and be represented as

$$P(x) = N(m_x, S^2x) \tag{3}$$

$$P(y) = N(m_y, S^2y) \tag{4}$$

where m_x and m_y are the mean value of x and y, S_x^2 and S_y^2 are the variance of x and y, respectively; (b) φ_j are randomly distributed but symmetrically with respect to zero; (c) a_j and φ_j are independent and uncorrelated to each other (d) the pdf of random variable of isotropic scattering is Rayleigh distribution with variance $2S_2^2$, (e) the mean and variance of random variable E_{aniso} are $\bar{m}$ and S_a^2, respectively. After tedious and complicated calculation, the pdf of the echo signal amplitude A is

$$P(A) = T \cdot U \cdot V \tag{5}$$

where

$$T = A/(S\sqrt{S^2 + S_a^2}) \tag{6}$$

$$U = \exp(-A^2/(2 \cdot S^2) - \bar{m}^2/(2 \cdot S_a^2)) \tag{7}$$

$$V = \sum_{n=0}^{\infty} \frac{1}{n} \left(\frac{\bar{m}^2 S^4 - A^2 \cdot S_a^4}{2 \cdot S^2 S_a^2 (S^2 + S_a^2)} \right)^n P_{2n} \left(\frac{\bar{m} S^2}{\sqrt{\bar{m}^2 S^4 - A^2 \cdot S_a^4}} \right) \tag{8}$$

$$S_x^2 = S^2 + S_a^2 \tag{9}$$

$$S_y = S \tag{10}$$

$$m_x = \bar{m} \tag{11}$$

and $P_{2n}(\cdot)$ is the Legendre function of the first kind.

From equation (5) to equation (8) some discussion can be made as follows:

(a) For the condition of $\bar{m} = 0$ but $S_a \neq 0$, because

$$P_{2n}(o) = (-1)^n(1 \cdot 3 \cdot 5 ... (2n-1))/(2^n \cdot n!) \qquad (12)$$

and

$$\exp(x) \, I_0(x) = \sum_{n=0}^{\infty} (x^n \cdot 1 \cdot 3 \cdot 5 ... (2n-1))/(n!)^2 \qquad (13)$$

where $I_0(x)$ is the modified Bessel function of the zero order, in this case, the pdf of amplitude will become

$$P(A) = T' \cdot U' \cdot V' \qquad (14)$$

where

$$T' = A/\left(S\sqrt{S^2 + S_a^2}\right) \qquad (15)$$

$$U' = \exp(-A^2/(2 \cdot S^2) + A^2 S_a^2/(4 \cdot S^4 + 4S^2 \cdot S_a^2)) \qquad (16)$$

$$V' = I_0(A^2 S_a^2/(4 \cdot S^4 + 4S^2 \cdot S_a^2)) \qquad (17)$$

The pdf as shown in equations (14) to (17) is the so-called Hoyte distribution, or M distribution.

(b) For the conditions of $\bar{m} = 0$ and $S_a = 0$, in this case from (14) to (17), it is easy to show that the pdf of amplitude will be

$$P(A) = A/S^2 \exp(-A^2/(2 \cdot S^2)) \qquad (18)$$

This is the exact Rayleigh distribution.

(c) For the conditions of $\bar{m} \neq 0$ but $S_a = 0$, after tedious and complicated calculation the pdf of the amplitude will be obtained as

$$P(A) = A/S^2 \exp(-(A^2 + \bar{m}^2)(2 \cdot S^2))I_0(A \cdot \bar{m}/S^2) \qquad (19)$$

This is the Rice distribution. The curves of pdf described in (4) to (7) are plotted in Figures 1 and 2 for different $\bar{m}$, S and S_a values.

DERIVATION OF THEORETICAL NAKAGAMI M PARAMETER

The definition of the Nakagami M parameter is

$$M = <A^2>^2/(<A^4> - <A^2>^2) \qquad (20)$$

where $<\cdot>$ means ensemble average. According to the same assumptions as mentioned in the last section, it is easy to evaluate $<A^2>$ and $<A^4>$ as follows:

$$<A^2> = 2 \cdot S^2 + S_a^2 + \bar{m}^2 \qquad (21)$$

$$<A^4> = 8 \cdot S^4 + \bar{m}^4 + 6 \cdot S_a^2 \bar{m}^2 + 3 \cdot S_a^4 + 8 \cdot S^2 S_a^2 + 8 \cdot S^2 \bar{m}^2 \qquad (22)$$

Substituting (21) and (22) into (20), and after arrangement, we have

$$M = 1 - 1/(1 + Q) \qquad (23)$$
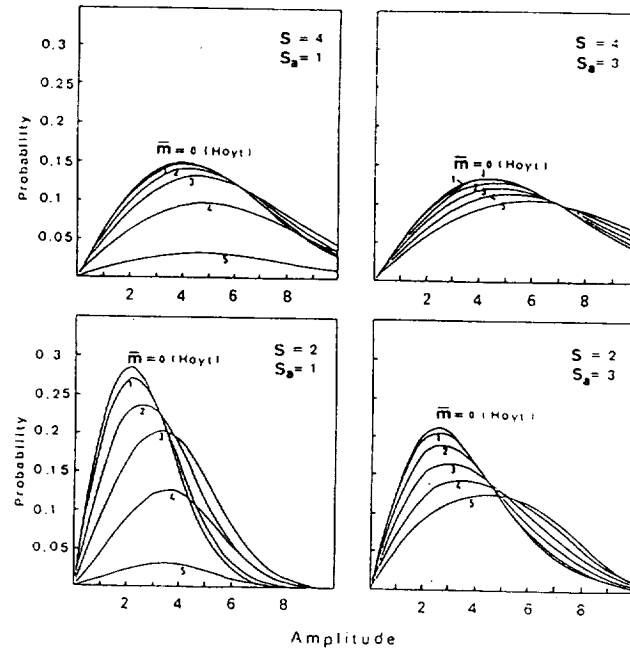
Figure 1. The curves of generalized probability density function for different values of S (variance of isotropic scattering signals), S_a (variance of returns of anisotropic irregularities) and $\bar{m}$ (mean value of returns of anisotropic irregularities).
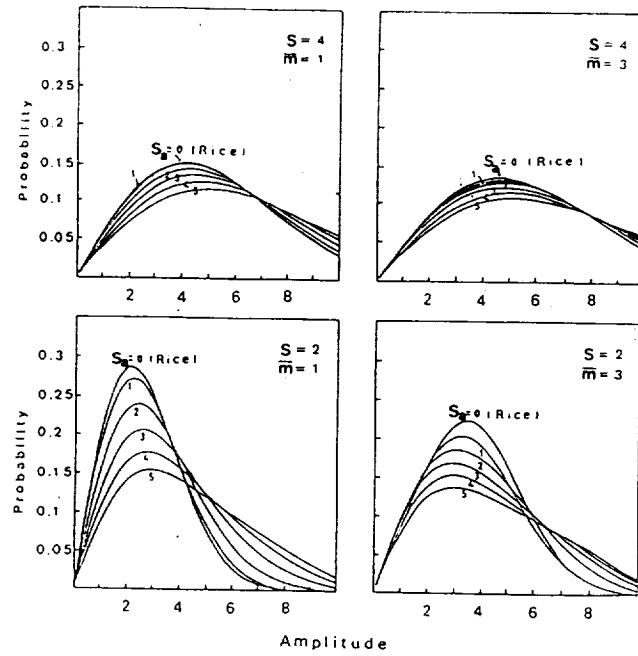
Figure 2. Same as Figure 1.

where

$$Q = (2 \cdot S^2 + S_a{}^2 + \bar{m}^2)^2 / ((\bar{m}^2 + S_a{}^2)^2 - 2 \cdot \bar{m}^4) \qquad (24)$$

Therefore, the value of the M parameter depends on the difference between $S_a{}^2$ and $(\sqrt{2}-1) \cdot \bar{m}^2$, that is, if $S_a{}^2 = (\sqrt{2}-1) \cdot \bar{m}^2$, $M = 1$; if $S_a{}^2 > (\sqrt{2}-1) \cdot \bar{m}^2$, $M < 1$; if $S_a{}^2 < (\sqrt{2}-1 \cdot \bar{m}^2$, $M > 1$. The relations between the M parameter, $S_a{}^2$ and $(\sqrt{2}-1) \cdot \bar{m}^2$ are plotted in Figure 3.

SUMMARY

From the previous discussion, it is apparent that the conventional pdf, such as Rayleigh, Rice, and Hoyte distribution, are just the special limits of the generalized pdf as shown in equations (4) to (7). Also, the quantitative relation between the Nakagami M parameter and the characteristics of the VHF radar target, such as S^2, $S_a{}^2$ and m, is derived and shown in (23) and (24). According to these results, it is clear that the value of the Nakagami M parameter cannot be used alone as the tool of VHF radar echo mechanism identification because it is impossible to distinguish the target characteristics from only one M value. Therefore, one has to be very careful when the Nakagami M parameter is used to identify the VHF radar echo mechanism.

REFERENCES

Booker, H. G., and W. E. Gordon, A theory of radio scattering in the troposphere, Proc.IRE, 39, 401-412, 1950.

Doviak, R. J., and D. S. Zrnic, Reflection and scatter formula for anisotropically turbulent air, Radio Sci., 19, 325-336, 1984.

Gage, K. S., and B. B. Balsley, On the scattering and reflection mechanism contributing to clear air radar echoes from the troposphere, stratosphere and mesosphere, Radio Sci., 15, 243-257, 1980.

Gage, K. S., B. B. Balsley, and J. L. Green, Fresnel scattering model for the specular echoes observed by VHF radar, Radio Sci., 16, 1447-1453, 1981.

Hocking, W. K., Reduction of the effects of non-stationarity in studies of amplitude statistics of radio wave backscatter, J. Atmos. Terr. Phys., 49, 1119-1131, 1987.

Kuo, F. S., C. C. Chen, S. I. Liu, J. Röttger, and C. H. Liu, Systematic behavior of signal statistics of MST radar echoes from clear air and their interpretation, Radio Sci., 22, 1043-1052, 1987.

Röttger, J., Reflection and scattering of VHF radar signals from atmospheric reflectivity structure, Radio Sci., 15, 259-276, 1980.

Röttger, J., and C. H. Liu, Partial reflection and scattering of VHF radar signals from clear atmosphere, Geophys. Res. Lett., 15, 357-360, 1978.

Sheen, D. R., C. H. Liu, and J. Röttger, A study of signal statistics of VHF radar echoes from clear air, J. Atmos. Terr. Phys., 47, 675-684, 1985.
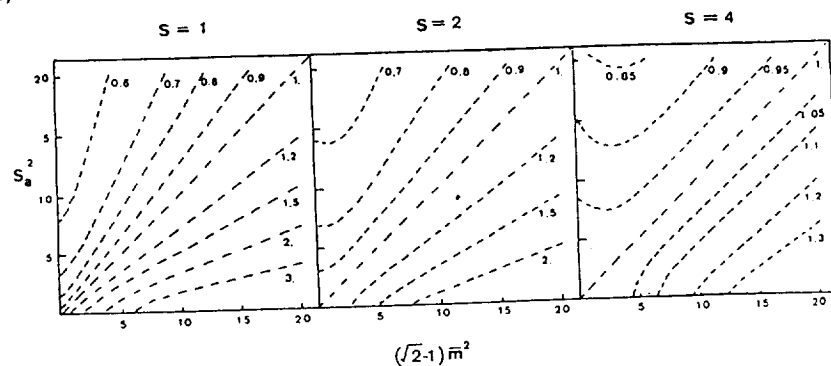
Figure 3. The quantitative relations between the values of Nakagami M parameters, $(\sqrt{2}-1)$ $\bar{m}^2$ and $S_a{}^2$.

A STATISTICAL REVIEW OF THE EISCAT PMSE 1988 DATA.

G.O.L. Jones,

University College of Wales, Aberystwyth, Dyfed, Wales, SY23 3BZ.

K.J. Winser,

R'therford Appleton Lab., Chilton, Didcot, Oxon, OX11 OQX, UK.

J. Rottger and C. La Hoz,

EISCAT Scientific Association, P.O. Box 812, S-98128 Kiruna, Sweden.

S. Franke,

University of Illinois, Urbana, Illinois, U.S.A.

In the summer of 1988 the EISCAT VHF radar made a series of measurements to study the very strong echoes which occur at heights near the summer mesopause. The behaviour of the observed "layers" is very dynamic; on occasions the layers are seen to ascend or descend with vertical velocities of up to 10 ms^{-1}, and the layer thickness can vary from a few hundred metres to a few kilometres. There are, however, some characteristics of the strong echoes which are consistently reproduced from day to day. We present results which show the typical strength and thickness of the layers, and the altitudes and times at which layers are most likely to form.

During the summer months, when the mesopause is at its coldest, very strong backscatter echoes have frequently been observed by radars operating at 50MHz (e.g. Ecklund and Balsley, 1981; Czechowsky and Ruster, 1985). In 1987 the EISCAT VHF radar observed similar strong echoes at 224MHz (Hoppe et al., 1988) which were not due to the usual incoherent backscatter since the inferred electron concentration would be unrealistically large. The spectral width of the scattered signal (0.5-15 Hz) was also much narrower than that expected from incoherent scatter (50-100 Hz) at these altitudes (Hall et al., 1987). The large echo power could not be explained by the traditional theory for turbulent backscatter from the neutral atmosphere (e.g. Hocking, 1986), since the half-wavelength of the VHF signal (0.67 m) is far in the viscous subrange. One explanation which has been proposed is that the echoes are due to small-scale electron density fluctuations due to the presence of heavy positive cluster ions in the cold summer mesosphere (Kelley and Ulwick, 1988; Rottger et al., 1988;) although details of the process are still under investigation.

A special campaign to study the polar mesosphere was carried out in the Summer of 1988 at Tromso in Norway involving the EISCAT and CUPRI radars. The specific aim was to investigate the very strong Polar Mesosphere Summer Echoes (PMSEs) using multi-frequency studies of the same scattering volume. Simultaneous echoes from the different radars have been studied by Rottger et al. (1989) but in this paper we simply outline the main characteristics of the PMSE layers as defined by the EISCAT VHF data.

The 1988 campaign was split into two parts covering the periods from June 25th to July 8th and from August 2nd to August 12th. The first part involved a number of different experiments with observations mainly during the daytime; the second part concentrated on measurements around midnight to coincide with

simultaneous noctilucent cloud observations. A total of over 100 hours of VHF
radar observations were made covering the altitude region between 80-90 km.
New complementary coding schemes were developed (La Hoz et al., 1989a) which
used coherent integration and decoding in the correlator to allow a complete
time series of complex raw data to be recorded for subsequent post-processing
and analysis. These programs achieved the very good height resolution (150 m)
necessary to study the fine structure of PMSEs. A preliminary analysis of the
whole dataset has been performed to give one-minute postintegrations of
scattered power and vertical velocity for each range gate for each experiment.
This data has then been used to produce a statistical evaluation of the PMSE
layers in terms of their height, time and strength.
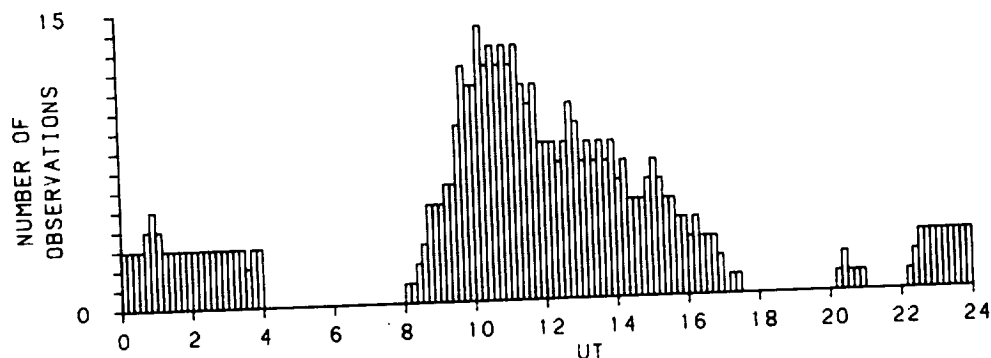
Figure 1. Times of mesospheric observations by the EISCAT
VHF radar during the 1988 PMSE campaign.

The times at which the VHF radar was operated during the PMSE campaign is
illustrated in Figure 1. It is clear that most observations were made around
midday with relatively fewer at night. There are times of the day when no data
were recorded so that a complete study of the diurnal variation of PMSE layers
cannot be undertaken. However, between 09-17 UT and 22-04 UT the data are
suitable for a statistical study of the layers so that both daytime and
"nighttime" layers can be investigated.

In order to illustrate the main features of a PMSE layer, a typical
example is shown in Figure 2. The data is for July 1st 1988 when the PMSE3C
program was run providing 41 range gates from 80-92.5 km, each with 300 m
height resolution. Figure 2(a) is a grey-scale contour plot showing the
strength of the returned power as a function of height and time. In this case
several PMSE layers are clearly seen at heights between 82 and 88 km where
extremely large echo powers are returned with the signal strength often more
than 20 dB above the background noise level.

In addition to the strength of the returned signal, the echoes are
characterised by their dynamic variability. This is consistent with the
hypothesis of Rottger et al. (1988) who suggest that fairly small and
localised refractive index structures exist within the scattering volume of
the radar. Such structures would not necessarily fill the scattering volume
homogeneously as they convect horizontally through the beam, and very narrow,
localised structures (<< 1 km in extent) would be produced. This feature is
shown not only by the narrow width of some layers, but also by the extensive,
fine structure within the thicker layers. Sudden temporal changes are often
seen with layers appearing or disappearing within a few minutes; occasionally,
as shown at 10:45 UT, a relatively thick layer splits to form distinct,

separate structures, which later merge together once again. Further examples of the dynamic features in PMSE layers are discussed by La Hoz et al. (1989b).

JULY 1 1988 PMSE3C
S/N POWER [dB]

ABOVE 20.0
15.0 - 20.0
10.0 - 15.0
6.0 - 10.0
3.0 - 6.0
BELOW 3.0

VELOCITY [m/s] (power above 2dB)

ABOVE 6.0
3.0 - 6.0
0.0 - 3.0
-3.0 - 0.0
-6.0 - -3.0
BELOW -6.0
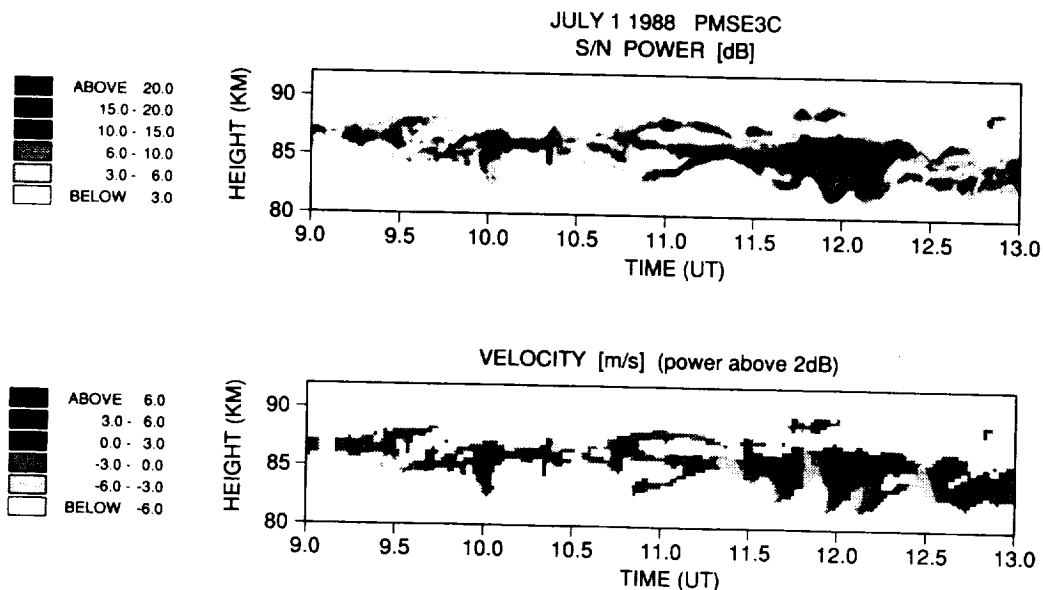
Figure 2. PMSE layers observed on July 1st 1988.
(a) Echo power, (b) Echo velocity.

Figure 2(b) shows the vertical velocity of the PMSE echoes on July 1st 1988, with positive velocities corresponding to upward flows. In order to eliminate the poor estimates of velocity outside the layers themselves, the velocity is only plotted at points where the signal power is at least 2 dB above the background noise level. Wavelike structures in the echo velocity are apparent in much of the data. Such quasi-periodic variations are a common feature in PMSE layers and are indicative of the influence of gravity waves (Williams et al., 1989). When such sinusoidal motion is apparent there is good agreement between rapid changes in the height of the layer (e.g. 11:40-12:20 UT at 82km) and the corresponding echo velocity. However, there are also occasions (e.g. at 10 UT) when changes in the width or height of the layer do not coincide with changes in velocity. It is also interesting to note that although the velocities vary with time, the velocity profile is relatively constant and rarely shows the same degree of vertical structure as the layers themselves.

One of the main aims of a statistical study of PMSE layers was to determine the heights and times at which the layers are most likely to occur. To illustrate the results, Figure 3 contains a series of plots which show the probability of occurrence of a layer as a percentage of the total number of observations (see Figure 1) at each particular time and height. It should be noted that the statistics are only really valid between 09-17 and 22-04 UT, the two periods when a suitable number of observations were made. Occurrence plots are shown for each of eight different heights between 81-88km with layers defined as those with echo strengths greater than 30 dB, i.e. those for which the echo power (signal+noise) is more than 30dB above the background noise level.

PERCENTAGE OCCURRENCE OF P.M.S.E. LAYERS > 30dB
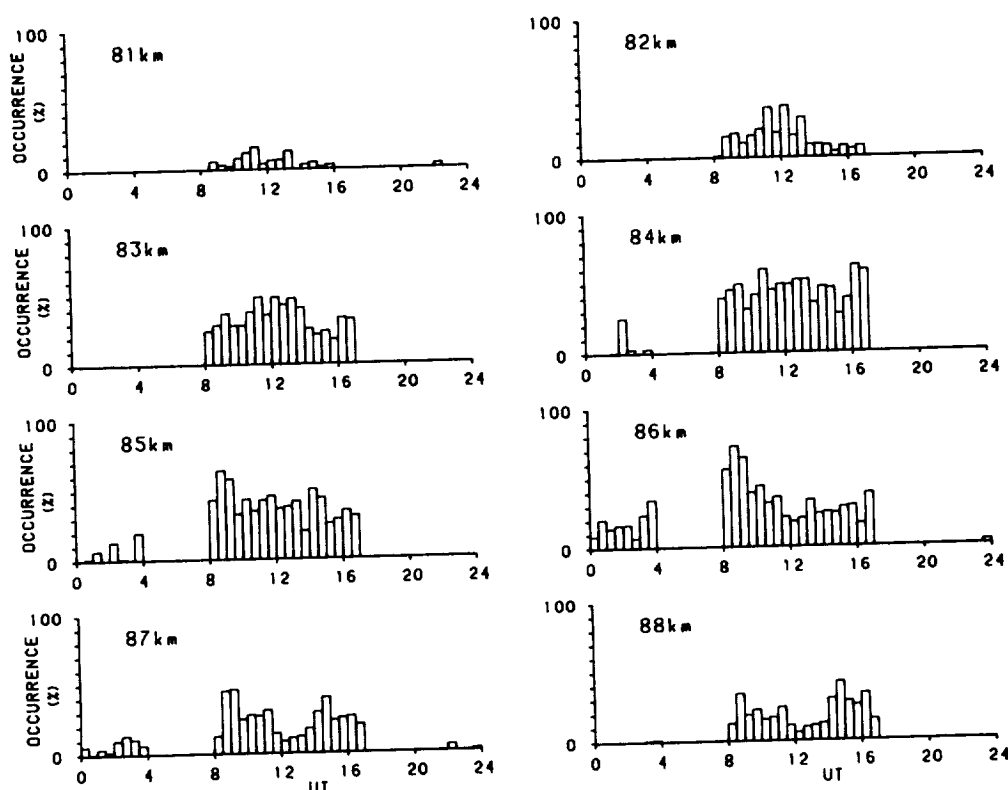
Figure 3. Plots showing the percentage occurrence of PMSE echoes
at heights between 81 and 88 km.

Looking first at the daytime observations, 09-17 UT, layers are most commonly seen at 84 km with over 50% probability, but occur with more than 40% probability at all heights between 83-85 km. This is in agreement with the idea that the layers are closely associated with the very cold summer mesopause which is also expected to occur at these heights (Philbrick et al., 1984). An interesting feature is shown by the tendency of the occurrence distribution to peak at about 12:30 UT for 82, 83 and 84 km, whereas the distribution shows a small trough at the same time for 86, 87 and 88 km. This reflects a slight change in the height at which layers tend to form around midday: i.e. layers tend to form at greater heights before and after midday than at midday itself. This effect is probably due to tidal variations in either neutral velocity or, more likely, temperature, (Fritts et al., 1988) but the observations are not complete enough to allow a full investigation of the diurnal variations of PMSEs.

Figure 3 shows that despite the 24 hour illumination of the mesosphere, 30 dB layers are much less likely to be seen during the "nighttime"; those that do occur are found at heights nearer 86 km. Layers of 15-20 dB are more frequent and occur with about 30% probability at 86 km. The observations also show a distinct asymmetry on either side of midnight; there are almost no 30 dB layers between 22-24 UT and very few 15 dB layers, but from 00-04 UT the occurrence distributions indicate a sharp increase. Once again lack of observations (04-09 and 17-22 UT) preclude a complete study, but layers are certainly more common post-midnight rather than pre-midnight.

The EISCAT PMSE campaign in the summer of 1988 has provided an extensive database for use in the study of strong, coherent echoes from the mesosphere. The data has shown that the strength of PMSE layers is extremely variable, with changes in height over a few hundred metres and changes in time over a few minutes. A statistical survey of the VHF data has shown that the layers occur near the mesopause with over 50% probability around midday and are most likely to occur at a height of 84 km. Layers show evidence of tidal activity in their tendency to form at slightly lower heights at 12:30 UT than at times on either side of this. The layers are weaker near midnight, and tend to occur slightly higher at about 86 km; an asymmetry is also observed with layers more likely to form in the early morning hours.

ACKNOWLEDGEMENTS

REFERENCES.

Czechowsky P. and R. Ruster, Power spectra of mesospheric velocities in polar regions, MAP Handbook, 18, 207-11, SCOSTEP Secretariat, Univ. of Illinois, 1985.

Ecklund W.L. and B.B. Balsley, Long-term observations of the arctic mesosphere with the MST radar at Poker Flat, Alaska,, J. Geophys. Res., 86, 7775-80, 1981.

Fritts D.C., S.A. Smith, B.B. Balsley, C.R. Philbrick, Evidence of gravity wave saturation and local turbulence production in the summer mesosphere and lower thermosphere during the STATE experiment, J. Geophys. Res., 93, 7015, 1988.

Hall C., U.-P. Hoppe, P.J.S. Williams, G.O.L. Jones, Mesospheric measurements using the EISCAT VHF system: first results and their interpretation, Geophys. Res. Lett., 14, 1187-90, 1987.

Hocking W.K., Observation and measurement of turbulence in the middle atmosphere with a VHF radar, J. atmos. terr. Phys., 48, 655-70, 1986.

Hoppe U.-P., C. Hall, J. Rottger, First observations of summer polar mesospheric backscatter with a 224 MHz radar, Geophys. Res. Lett.,15, 28-31, 1988.

Kelley M.C. and J.C. Ulwick, Large and small scale organization of electrons in the high latitude mesosphere: Implications of the STATE data, J. Geophys. Res., 93, 1988.

La Hoz, C., J. Rottger, M. Rietveld, G. Wannburg, S. Franke, The status and planned developments of EISCAT in mesosphere and D-region experiemnts, MAP Handbook, (this issue), 1989a.

La Hoz, C., J. Rottger and S. Franke, Dynamic spectra of PMSE measured by EISCAT at 224 MHz, MAP Handbook, (this issue), 1989b

Philbrick C.R., J. Barnett, R. Gerndt, D. Offermann, W.R. Pendleton Jr., P. Schlyter, J.F. Schmidlin, G. Witt, Temperature measurements during the CAMP program, Adv. Space Sci., 4, 153-6, 1984.

Rottger J., C. La Hoz, M.C. Kelley, U.-P. Hoppe, C. Hall. The structure and dynamics of polar mesosphere summer echoes observed with the EISCAT 224 MHz radar, Geophys. Res. Lett., 15, 1353-56, 1988.

Rottger J., M.T. Rietveld, C. La Hoz, T. Hall, M.C. Kelley, W. Swartz, Polar mesosphere summer echoes observed with the EISCAT 933 MHz radar and the CUPRI 46.9 MHz radar, MAP Handbook, (this issue), 1989.

Williams, P.J.S., A.P. van Eyken, C. Hall, J. Rottger, Atmospheric gravity waves and modulations in the polar mesospheric summer echoes as observed by EISCAT, Geophys. Res. Lett. (submitted, 1989).

PARAMETER ANALYSIS OF CHUNG-LI AND SOUSY RADAR ECHO SIGNALS

Hsiou-Yung Lue[1] and Fu-Shong Kuo[2]

[1]Department of Physics, Fu Jen University
Hsin Chuang, Taiwan, ROC
[2]Department of Physics, National Central University
Chung-Li, Taiwan, ROC

ABSTRACT

Echo parameters of MST radar signals, which are defined as the ratio between the layer reflection contribution and the volume scattering contribution to the echo signals, are calculated for SOUSY data between the heights of 1.8 km and 7.2 km at two different time periods under different dynamical conditions, and also for Chung-Li data from both vertical and oblique beams. Statistics of echo parameters and their correlation with echo power are analyzed. The results show that the radar echo signal returned in the oblique beam is predominantly from turbulence scattering contributions while there is a significant contribution from the layer's reflection in the vertical beam. From cross correlation analysis between the time series of echo power and echo parameter, we conclude that the variation of echo power is controlled by the variation of turbulence strength in the atmosphere.

1. INTRODUCTION

It has been demonstrated that sensitive MST radars can be used to study the dynamics of the atmosphere from tropospheric to mesospheric heights (WOODMAN and GUILLEN, 1974; RASTOGI and BOWHILL, 1976; VANZANDT et al., 1977; RÖTTGER and LIU, 1978; SHEEN et al., 1985). Parameterization of the echo signal's statistics can simplify our understanding of the physical process in the atmosphere. Conventionally, the Nakagami m coefficient computed from the signal's amplitude distribution has been one of the promising parameters. However, in our previous report (KUO and LIU, 1988) of the χ^2 test on the signal statistics it was concluded that, 1) the fitting of the echo signal's quadrature components by normal distribution is significantly better than the fitting of the signal's amplitudes by the Nakagami distribution. 2) The requirement of stationarity conditions, time interval of the dataset had better be shorter than 2 minutes. So, the echo parameter γ (KUO et al., 1987) calculated from the signal's quadrature components should be more reliable than the Nakagami m coefficient.

In this report, we will investigate the statistical property of the echo parameter obtained from SOUSY data and Chung-Li data. Its implication on dynamics will be discussed.

2. ECHO PARAMETER γ AND ECHO POWER P

Let the field E be the superposition of the volume scattering fields E_s and the layer's reflection field E_r, i.e.,

$$E = E_s + E_r = X + i\,Y$$

$$E_s = X_s + i\,Y_s$$

$$E_r = X_r + i\,Y_r \qquad (1)$$

$$X = X_r + X_s$$

$$Y = Y_r + Y_s$$

where Xs and Ys are the quadrature components of the field.

The volume scattered field is characterized by its stochasticity and isotropy with statistical properties described by the equations (KUO et al., 1987)

$$< X_s > = < Y_s > = < X_s\, Y_s > = 0$$

$$< X_s^2 > = < Y_s^2 > = \sigma_s^2$$

$$P_s = <|\, E_s|^2 > = 2\,\sigma_s^2 \tag{2}$$

where angle brackets denote the ensemble average and P_s denotes the echo power contributed from volume scattering. The layer's reflection is characterized by its coherency with statistical property described by

$$< X_r > = \mu_x^{(r)}$$

$$< Y_r > = \mu_y^{(r)}$$

$$< (X_r - \mu_x^{(r)})^2 > = < (Y_r - \mu_y^{(r)})^2 > \cong 0$$

$$< X_r^2 > \cong (\mu_x^{(r)})^2 \tag{3}$$

$$< Y_r^2 > \cong (\mu_y^{(r)})^2$$

$$P_r = <|\, E_r|^2 > = (\mu_x^{(r)})^2 + (\mu_y^{(r)})^2$$

where P_r represents the contribution of the layer's reflection to echo power. In addition, the scattering signal and reflection signal are uncorrelated

$$< X_r X_s > = < Y_r Y_s > = 0$$

so, from eqs (1) - (3) we obtain

$$\mu_x = < X > = < X_r > = \mu_x^{(r)}$$

$$\mu_y = < Y > = < Y_r > = \mu_y^{(r)}$$

$$\sigma_x^2 = < (X - \mu_x)^2 > \sigma_s^2 \tag{4}$$

$$\sigma_y^2 = < (Y - \mu_y)^2 > \sigma_s^2$$

Then, it is straightforward to see that

$$P = P_r + P_s \tag{5}$$

Since the echo parameter γ is defined by (KUO et al., 1987)

$$\gamma = \frac{\mu}{\sigma} = \frac{\sqrt{\mu_x^2 + \mu_y^2}}{\sqrt{\sigma_x^2 + \sigma_y^2}}$$

the square of γ is roughly equal to the ratio between the reflection power and the scattering power

$$\gamma^2 = \frac{P_r}{P_s} \tag{6}$$

3. DATA ANALYSIS

Examples of Chung-Li and SOUSY data were used for echo parameter analysis. The Chung-Li data were taken by the Chung-Li VHF radar between 0708 LT and 0922 LT October 14, 1986, with time resolution of 0.25 s and height resolution of 300 m between 2.7 and 10.8 km. The radar was operated at 30 MW peak power and 0.66 kW average at the frequency of 52 MHz with one beam pointed obliquely at an angle of 17° titled toward east and another beam pointed vertically. SOUSY data were taken with the Sounding System (SOUSY) VHF radar of the Max-Planck-Institut für Aeronomie in 1978 with time resolution of 1.03 s and height resolution of 0.15 km. The radar operated at 53.5 MHz, and it was pointed vertically with power beam width of 10°. Two separate sets of SOUSY data were selected for analysis on the basis of their difference in environmental conditions (Table 1).

Table 1. SOUSY Data.

Data Set	Start time (UT)			End Time (UT)			Time Lasted (hours)
	Month	Day	Time	Month	Day	Time	
T28	May	31	0407	May	31	1025	6.3
T35	June	2	1300	June	2	1925	6.4

Data set T28 was taken under clear sky conditions, while set T35 was taken during a time period when a thunderstorm was developing near the radar site.

Each 128 consecutive complex data from each height were used as a sample group, its echo parameter γ and echo power P were calculated for analysis. The time interval covered by each sample group is approximately 1.1 minute for the Chung-Li data and 2.2 minutes for SOUSY data.

Figure 1 plots the echo parameters of the Chung-Li data from the oblique and vertical beams at each height range. We can see that the echo parameters of the oblique beam are mostly smaller than 0.3 in each height range, an indication that the echo signals are mostly from turbulence scattering. On the other hand, the γ values of the vertical beam are significantly larger than that of the oblique beam. This fact confirms the general belief that the layer reflection contribution to the echo signal is much larger in the vertical beam than in the oblique beam. The contribution of the layer reflection to the vertical beam is reconfirmed by the average power profile as shown in Figure 2, which shows that the echo power in the vertical beam is significantly higher than that in the oblique beam at almost every height.

Figure 3 shows an example of the time variation (after smoothing) of $\sqrt{P}$ and γ from the height range between 3.45 km and 3.60 km of SOUSY data set T28 (Figure 3A) and T35 (Figure 3B). There exists strong evidence that the time series of $\sqrt{P}$ is negatively correlated with the time series of γ. Such negative correlation is found to exist in many height ranges as shown in Figure 4, which plots the cross correlation coefficients as a function of height. A simple physical meaning for negative correlation between echo power P and echo parameter γ can be easily reduced from equations (5) and (6). Namely, the time variation of echo power P is dominated by the contribution of volume scattering. In other words, the time variation of turbulence strength controls the variation of the echo power. When the correlation analysis between variable P and γ is coupled with their time averages as functions of height as shown in Figures 5 and 6, we gain further physical insight. As mentioned before, the data set T28 was taken under clear sky conditions, while T35 was taken when a thunderstorm was developing near the radar site. The thunderstorm will certainly increase the turbulence activity, hence will raise the echo power and
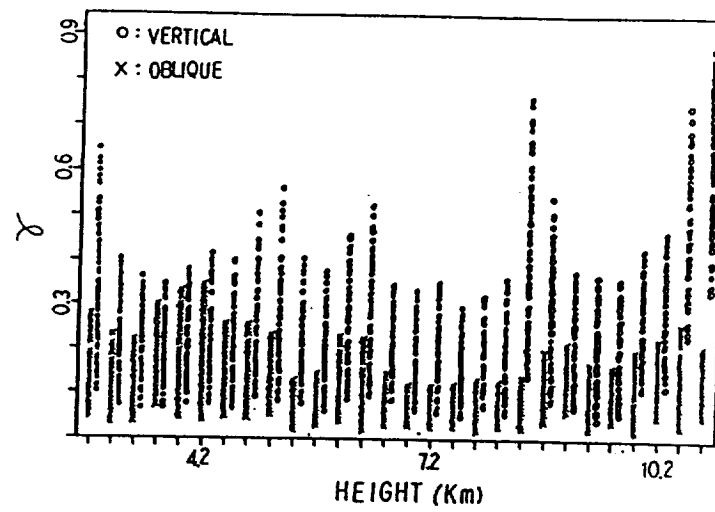
Figure 1. Plots of the echo parameters of Chung-Li data at each height range, the upper and lower 10% of the data are not included in this figure.
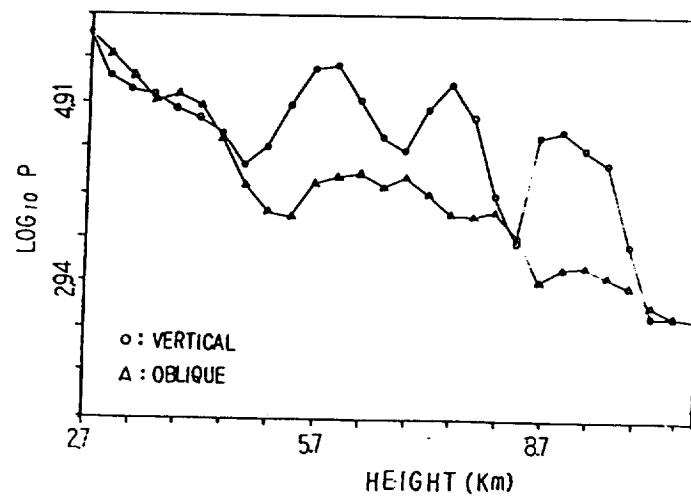
Figure 2. Average power profiles of Chung-Li data.
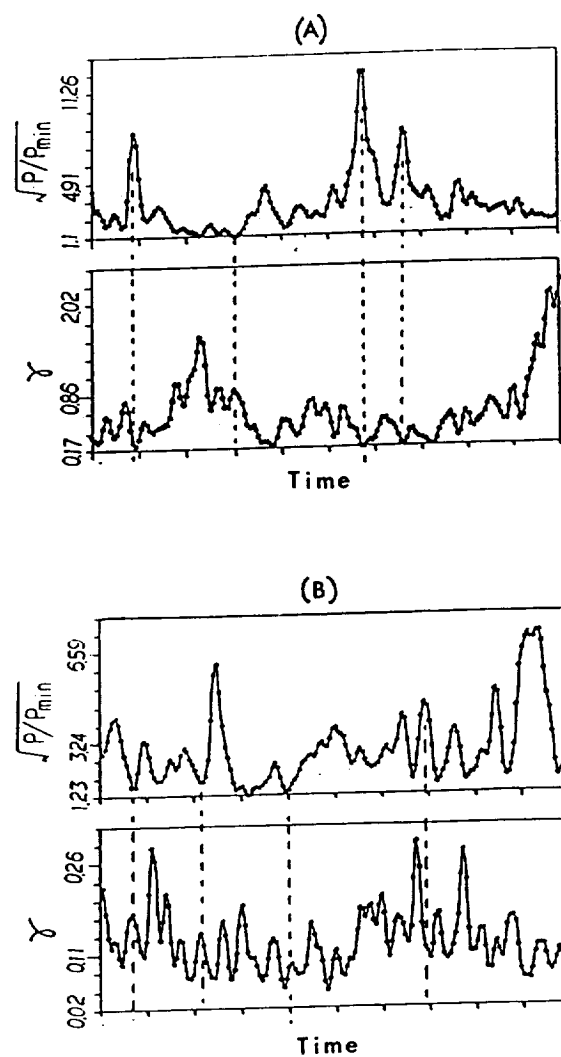
Figure 3. Time variations of the echo power and echo parameter of the height range between 3.45 km and 3.60 km of the SOUSY data sets (A) T28, (B) T35.
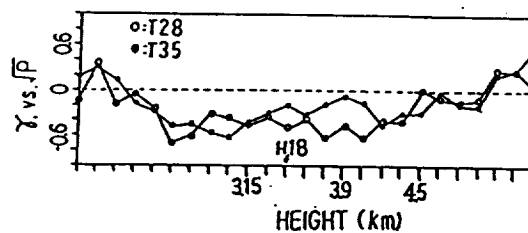
Figure 4. Cross correlation coefficients between the time series of the echo power P and the echo parameter γ at each height range.
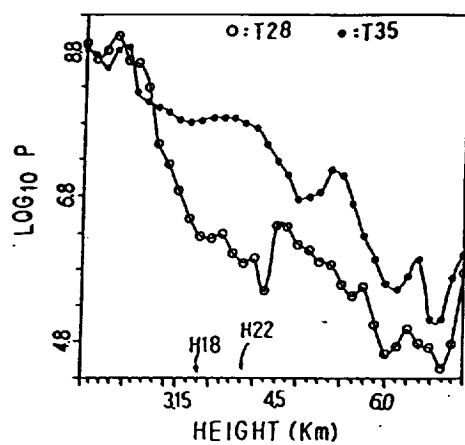
Figure 5. The averaged power profiles of SOUSY data sets T28 and T35.

Figure 6. Height dependence of the averaged echo parameters of SOUSY data sets T28 and T35.
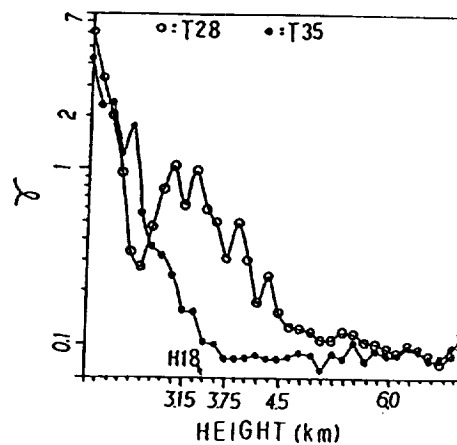
lower the echo parameter. Figure 5 reveals that in the height ranges between 3.15 km and 4.5 km, the mean echo power of T35 is at least 15 dB higher than T28, meanwhile, Figure 6 shows that the corresponding echo parameter of T35 is a factor of 5 lower than T28. This result is in agreement with the result of the correlation analysis. For height ranges higher than 5 km of both T28 and T35, the echo parameter γ is lower than 0.1 on the average (Figure 6), the echo power is low (Figure 5) and the correlation coefficients are negligibly small (Figure 4). So, the signal statistics is meaningful only when its echo power is significantly strong.

4. SUMMARIZATION

Our data analysis proves that the statistics of the echo parameter based on the signal's quadrature components is meaningful. Echo parameter analysis of the signals returned from the vertical and oblique beams confirms the general belief that signals returned from the oblique direction contains comparatively little contribution from the layer's reflection . Cross correlation analysis of echo power and echo parameter suggest that the variation of the echo power is predominantly controlled by the variation of the turbulence strength in the air. By combining these two reasonable results, it is fair to claim that the echo parameter γ has delicate physical meaning contained in its statistics.

REFERENCES

Kuo, F. S., and S. Y. Liu, Radar echo signal statistics, this volume.

Rastogi, P. K., and S. A. Bowhill, Gravity waves in the equatorial mesosphere, *J. Atmos. Terr. Phys., 38*, 51-60, 1969.

Röttger, J., and C. H. Liu, Partial reflection and scattering of VHF radar signals from the clear atmosphere, *Geophys. Res. Lett., 5*, 335-360, 1978.

Sheen, D. R., C. H. Liu, and J. Röttger, A study of signal statistics of VHF radar echoes from clear air, *J. Atmos. Terr. Phys., 47*, 675-684, 1985.

VanZandt, T. E., J. L. Green, K. S. Gage, and W. L. Clark, Reflectivity studies with the Sunset VHF pulsed Doppler radar, *Proc. URSI Comm. F. Open Symp. on Propagation in Non-Ionized Media*, 519-524, 1977.

Woodman, R. F., and A. Guillen, Radar observations of winds and turbulence in the stratosphere and mesosphere, *J. Atmos. Sci., 31*, 493-505, 1974.

138

RADAR ECHO SIGNAL STATISTICS

Fu-Shong Kuo[1] and Shu-Ing Liu[2]

[1]Department of Physics
[2]Institute of Statistics
National Central University
Chung-Li, Taiwan, ROC

ABSTRACT

A χ^2 test was made on VHF radar signal statistics by the presumed theoretical distribution function. The goodness of fitting improves as the time intervals of the data sets under test are shortened. Thus, the nonstationarity problem in signal statistics is reduced by shortening the data sets. Both simulation and data analysis indicate that it is better to fit the signal's quadrature components by normal distribution than to fit the signal's amplitudes by the Nakagami distribution. As far as parameterization of radar echo signals is concerned, we suggest that it is better to use the signal's quadrature components than to use the signal's amplitudes.

1. INTRODUCTION

Signal statistics provide important information about scatterers. One of the promising theories on signal statistics is the Nakagami theory from which the m coefficient of the amplitude distribution of the radar echoes can be computed. It is expected that the m coefficient will give a rough estimation of the ratio of contributions between turbulence scattering and the layer's reflection. But, in many cases, the amplitude distribution of radar echoes fails to follow the Nakagami distribution (SHEEN et al., 1985; KUO et al., 1987). Sheen et al. explained their findings as due to the focusing and defocusing effects of the signals returned from undulating moving layers; Kuo et al. summarized their results as due to stochastic effects on the signal generated in the variable process. These effects make the signal statistics nonstationary. Naturally, the stationary theory such as the Nakagami distribution is not suitable to explain the nonstationary data set.

In order to have accurate signal statistics, we may either derive a nonstationary theory to fit the data set, or make the data set as stationary as possible to meet the assumption of the stationary theory. Because the Nakagami distribution is so easy to apply, it is desirous to use the stationary data set for analysis. It is known that if the time interval of the data set is shorter, its data statistics will be more stationary. However, if the time interval is too short (hence the total number of counts of the data set is too small), its statistics will also become too poor to be meaningful. Requirements of stationarity put an upper limit, while requirements of meaningful statistics put a lower limit, on the length of the data set. Such an issue will be investigated in this report.

2. STATISTICAL MEANING OF THE χ^2 TEST ON SIGNAL DISTRIBUTION

The field $E = X + IY$ of the radar returned signal results from the superposition of a coherent component (i.e., reflected from layer) on a scattered component, which is a sum of the fields scattered from many different scattering targets. According to the Central Limit Theorem, the quadrature components X and Y of field E asymptotically approach a normal distribution (ISHIMARU, 1978; KUO et al., 1987), and the amplitude $A = \sqrt{X^2 + Y^2}$ should approximately follow the Nakagami distribution, i.e.,

$$p(A) = \frac{2m^2 A^{2m-1}}{\Gamma(m)<A^2>^m} \exp\left(-\frac{m}{<A^2>} A^2\right)$$

where Γ is the gamma function and m is the Nakagami coefficient given by

$$m = \frac{<A^2>^2}{<(A^2 - <A^2>)^2>}$$

The conventional method of judging how well the data set is fitting a theoretical distribution function is the so-called χ^2 test, or goodness-of-fit test; χ^2 is a measure of discrepancy between the histogram of the data set and the theoretical distribution function

$$\chi^2 = \sum_{i=1}^{k} \frac{(\text{observed-expected})^2}{\text{expected}}$$

The meaning of the values of χ^2 is rather statistical than deterministic. If the data set really comes from the presumed theoretical distribution function, then the occurrence probability of a χ^2 value should follow the χ^2 distribution

$$f(\chi^2) = \frac{1}{2^{v/2}\Gamma(v/2)} e^{-\chi^2/2} (\chi^2)^{\frac{v}{2}-1}$$

where $v = k - \gamma$ is the degree of freedom, γ is the number of restrictions imposed on the distribution function. For practical applications, another parameter, called the P value, is referenced as the probability that $\chi^2 \geq \chi_P^2$, i.e.,

$$P = \int_{\chi_P^2}^{\infty} f(\chi^2)\, d\chi^2 \tag{1}$$

$$0 \leq P \leq 1$$

The variable P is an alternative measure of the goodness-of-fit. Equation (1) implies

$$dP = -f(\chi_P^2)\, d\chi^2 \tag{2}$$

Again, the meaning of the P value is still statistical, not deterministic. If the data set truly comes from the presumed theoretical distribution, then its P value must follow a distribution function $g(P)$ such that

$$|g(P)\, dP| = |f(\chi_P^2)\, d\chi^2|$$

then

$$g(P) = |\ f(\chi_P^2)\ d\chi^2/dP\ | = 1 \tag{3}$$

So, the P value is uniformly distributed between 0 and 1. If there is only one data set, it will be meaningless to make a goodness-of-fit test because even if the data set truly comes from the presumed theoretical distribution, its P value has equal probability to be anywhere between 0 and 1. Only when we have many data sets from the same class, the goodness-of-fit test will become meaningful. Namely, if there exist many data sets with their P values uniformly distributed between 0 and 1, then we can assure that these data indeed come from the presumed theoretical distribution.

The above point of view on the χ^2 test can be better understood by the following simulations. We generate 200 data sets with each set consisting of N elements, $[(x_i, y_i), i = 1,2,3,...N]$, each element (x_i,y_i) are random variates of Gaussian distributions, i.e.,

$$x_i \in N(\mu_x,\sigma_x)$$

$$y_i \in N(\mu_y,\sigma_y)$$

the amplitude of each element is given by

$$A_i = \sqrt{x_i^2 + y_i^2}$$

These data sets simulate the time series of stationary VHF radar echo signals. The x and y distributions are χ^2 tested by normal distribution, and the A distributions are χ^2 tested by the Nakagami distribution with parameters μ_x, σ_x, μ_y, σ_y and m determined directly from each data set. Figure 1 presents the distributions of P values of each 200 data sets with prescribed parameters μ_x, σ_x, μ_y, σ_y and N. We can see that the P value of χ^2 test on the x and y distributions consistently satisfy uniform distribution between 0 and 1. But for the χ^2 test on A distributions, the percentage of small P values (representing bad fit to the Nakagami distribution) is slightly higher than expected as the ratio σ_x/σ_y between the variances of the quadrature components deviates away from 1, we see that the rate of bad fit to the Nakagami distribution increases significantly. The Nakagami theory on signal statistics is acceptable only when the variances of the two quadrature components are approximately equal.

3. χ^2 TEST OF VHF RADAR ECHOES

As an application of the χ^2 test, we have analyzed the radar echo signals taken by the SOUSY VHF radar between 2138 UT May 30 and 0359 UT May 31 of 1978. The data under analysis has a time resolution of 1.03 seconds and a height resolution of 0.15 km between 2.1 km and 7.2 km. For each height range the time series consists of 22215 elements. To do the χ^2 test, the time series of each height range is divided into many subsets with an equal number of consecutive elements. Table 1 presents the choice of the data divisions.

The procedure of analysis is exactly the same as in the previous simulation, namely, the histograms of the quadrature components are χ^2 tested by normal distribution while the amplitude distribution of the signals is χ^2 tested by the Nakagami distribution. Examples of the P values of each subset are shown in Figure 2. If we set our confidence level at 95%, then all the subsets with P values less than 0.05 are regarded as unacceptable by the presumed
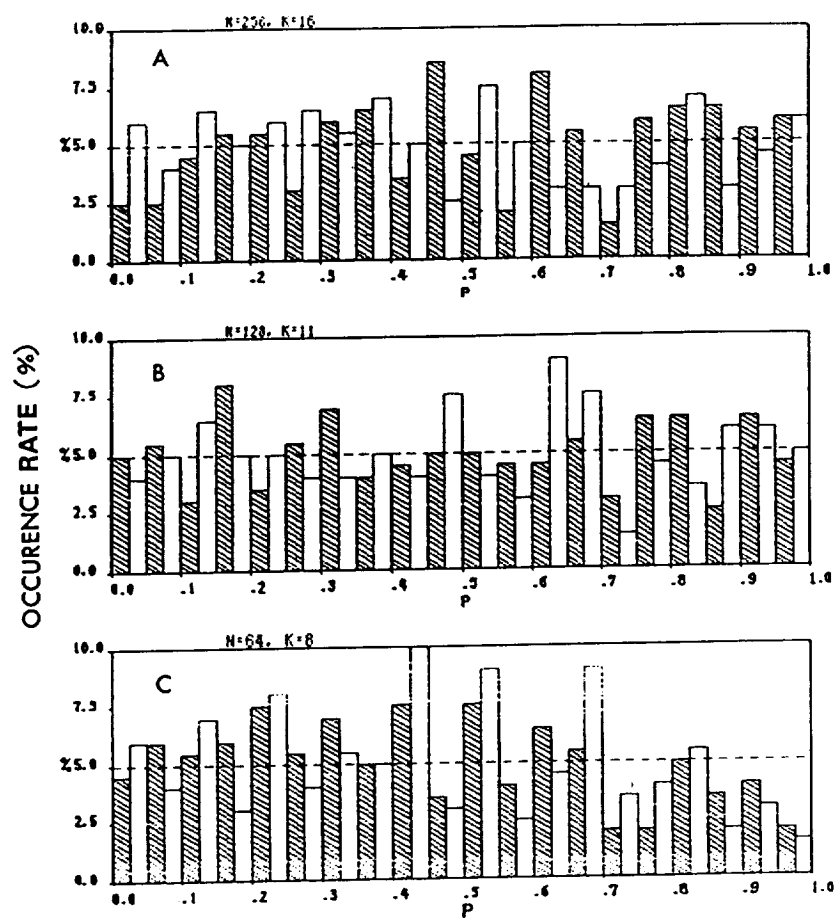
Figure 1(a). The distribution of the P values of the χ^2 test of the simulated Gaussian-variated by normal distribution function. (a) N = 256, K = 16; (B) N = 128, K = 11; (C) N = 64, K = 8.

N=128. K=11
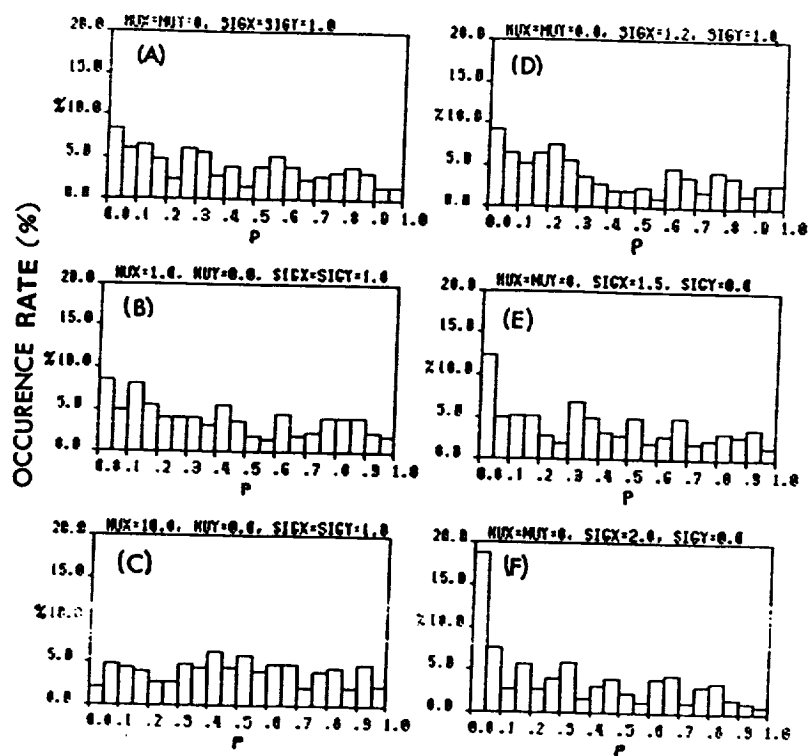
Figure 1(b). The distributions of the P values of the χ^2 test of the simulated amplitude distribution by the Nakagami distribution function.

(A) $\mu_x = \mu_y = 0$; $\sigma_x = \sigma_y = 1.0$

(B) $\mu_x = 1.0$; $\mu_y = 0$; $\sigma_x = \sigma_y = 1.0$

(C) $\mu_x = 10$; $\mu_y = 0$; $\sigma_x = \sigma_y = 1.0$

(D) $\mu_x = \mu_y = 0$; $\sigma_x = 1.2$; $\sigma_y = 1.0$

(E) $\mu_x = \mu_y = 0$; $\sigma_x = 1.5$; $\sigma_y = 1.0$

(F) $\mu_x = \mu_y = 0$; $\sigma_x = 2$; $\sigma_y = 1.0$
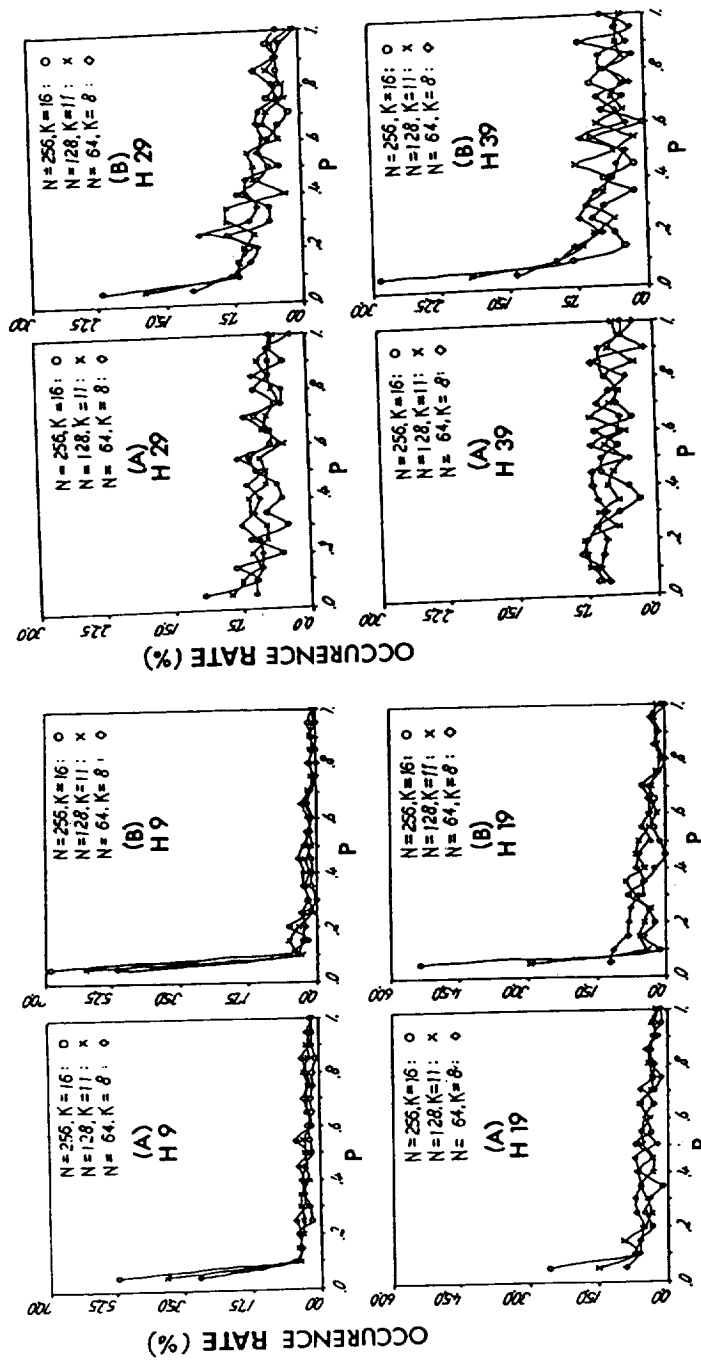
Figure 2. Distribution of the P values for (A) χ^2 test on the quadrature components by normal distribution, (B) χ^2 test on the amplitude by the Nakagami distribution of SOUSY data at 9th, 19th, 29th, and 39th height range (denoted by H9, H19, H29, and H39, respectively).

theory. Two important points can be summarized from Figure 2. First, as the time period of each subset decreases, the rejection rate decreases, and the P values tend more and more to uniform distribution; second, rejection rate of the amplitude distribution is always higher than that of the distribution of the quadrature components. The first point proves that the nonstationarity of the signal statistics improves by shortening the time interval of the data sets. The second point indicates that the fitting between the histogram of the signal's quadrature components and normal distribution is much better than the fitting between the signal's amplitude distribution and the Nakagami distribution.

Table 1

class	# of elements N for each subset	# of subsets	time period for each subset (min)
A	256	86	4.4
B	128	173	2.2
C	64	347	1.1

Figure 3 shows the rejection rates at different height ranges. It is natural to see that the effect of nonstationarity on the signal statistics is different at different heights, since our atmosphere is far from uniform.

4. CONCLUSION

VHF radar echo signals returned from the atmosphere are a stochastic process. The Central Limit Theorem insists that each quadrature component of the signal should be normally distributed, and the amplitude should approximately follow the Nakagami distribution. The goodness-of-fit by SOUSY data supports this theory, under the condition that the time periods of the data sets are short enough to be stationary. But analysis also indicates that the Nakagami distribution is not as well fitted by the signal's amplitude, as normal distribution is by the signal's quadrature components. Therefore, as far as parameterization of echo signal is concerned, statistics of signal's quadrature components is more reliable than the amplitude's statistics.

The nonstationarity problem of signal statistics can be reduced by shortening the time interval of data sets. In many cases of SOUSY data, stationarity condition indicates that the data sets should not be longer than 1 minute.

REFERENCES

Ishimaru, A., *Wave Propagation and Scattering in Random Media*, p. 89, Academic Press, Orlando, FL, 1978

Kuo, F. S., C. C. Chen, S. I. Liu, J. Röttger, and C. H.Liu, Systematic behavior of signal statistics of MST radar echoes from clear air and their interpretation, *Radio Sci., 22,* 1048-1052, 1987

Sheen, D. R., C. H. Liu, and J. Röttger, A study of signal statistics of VHF radar echoes from clear air, *J. Atmos. Terr. Phys., 47,* 675-684, 1985.
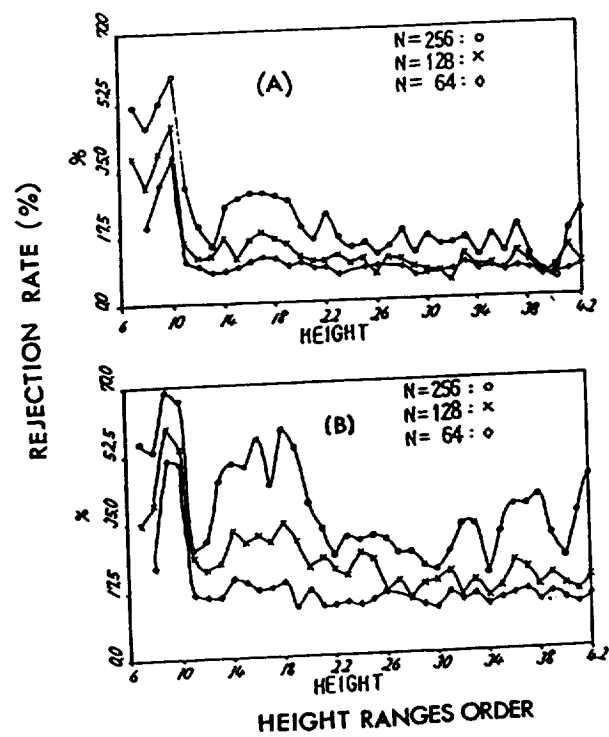
Figure 3. Rejection rate (percentage of data sets with P values less that 0.05) of (A) χ^2 test on the quadrature components by normal distribution, (B) χ^2 test on the amplitude by the Nakagami distribution at each height range of SOUSY data

DIRECT COMPARISON BETWEEN IN SITU AND RADAR MEASUREMENTS OF TEMPERATURE FLUCTUATION SPECTRA: A PUZZLING RESULT

F. Dalaudier[1], M. Crochet[2], and C. Sidi[1]

[1]Service d'Aeronomie du CNRS, B. P. 3
91371 Verrieres le Buisson Cedex, France
[2]L.S.E.E.T. Universite de Toulon (UA 705 CNRS)
83100 Toulon, France

Investigations of temperature fluctuation spectra of atmospheric turbulence were performed simultaneously by remote sensing and in situ measurements. A balloon-borne instrumented gondola measured temperature and velocity fluctuations up to an altitude of 18 km. Spectral analysis of these data led to one-dimensional spectra. Simultaneously, the nearby stratosphere troposphere radar "Provence" obtained vertical profiles of reflectivity for both vertical and oblique (15°) line of sight and for various range resolutions. According to the classical interpretation, the radar echoes result from the three-dimensional spectrum of refractive index fluctuations, and its aspect sensitivity reflects the spectrum anisotropy at the half radar wavelength. We thus separately reconstructed the reflectivity profiles for the two lines of sight. For the oblique one, the in situ observed spectral level of temperature fluctuations (assumed isotropic) was converted into radar reflectivity. For the vertical measurements, a theoretical "universal" level was used, along with an isotropic conversion formula. Comparison of the reconstructed reflectivity profiles with the observed one proves to be very puzzling. For oblique measurements, where the reconstruction process uses only the widely accepted hypothesis, the observed profiles are poorly reproduced. By contrast, for vertical measurements, the proposed model leads to a good reconstruction of the shape of the reflectivity profiles. In both cases, the predicted level is always strongly overestimated. The discussion concludes that the discrepancy is real and calls for further studies of this problem.

Since a paper with the same authors and title is accepted for publication in Radio Science, the interested reader is referred to DALAUDIER et al. (1989).

REFERENCE

Dalaudier, F., M. Crochet, and C. Sidi, Direct comparison between in situ and radar measurements of temperature fluctuation spectra: A puzzling result, *Radio Sci.* (in press), 1989.

MESOSPHERIC OBSERVATIONS USING THE CHUNG-LI VHF RADAR

Y. H. Chu and J. K. Chao

Department of Atmospheric Physics
National Central University
Chung-Li, Taiwan 32054, ROC

C. H. Liu
Department of Electrical and Computer Engineering
University of Illinois
Urbana, IL 61801, USA

ABSTRACT

In this paper, the echoes of meteor trails and returns of mesospheric intermittent irregularities observed by the Chung-Li radar are presented, and the characteristics of meteor trail echoes are analyzed. It is found that the lifetime of the observed meteor trails is less than one second and the altitude range where they occur is above 70 km and centered at about 88 km. During the periods of meteor showers Cygnus and Lyra, the occurrence rate of meteor trails was from 3.5 events/hour to 12.5 events/hour. Additionally, by using the SAD method, the mesospheric horizontal wind can be evaluated from the returns of mesospheric intermittent irregularities. The magnitude of the wind speed at 72 km on a special observation was 11.2 m/s. The scale size of the mesospheric intermittent structures (or patches) deduced from the horizontal wind speed and duration of these intermittent irregularities is about 300 to 400 meters. These features are similar to the results of other observations.

INTRODUCTION

Originally, the Chung-Li VHF radar was designed as an ST radar. The value of the power-aperture product of this radar is only about 10 WM orders of magnitude (the characteristics of the radar are listed in Table 1). Therefore it seemed impossible to make mesospheric observations; however, after carefully investigating the echo signals coming from mesospheric heights, we found that the Chung-Li VHF radar indeed has the ability to make mesospheric observations. In this paper, we shall present some mesospheric observation results made recently, including the statistical analysis of meteor trail echoes and an estimation of mesospheric winds from the returns of refractive index irregularities in terms of the spaced antenna drift (SAD) method.

RADAR PARAMETERS AND OPERATION MODE FOR MESOSPHERIC OBSERVATIONS

During the mesospheric experiment, the radar parameters were chosen especially; otherwise there would have been no returns from the mesosphere. In this study, the pulse width was 16 μs, and the interpulse period (IPP) was set as 1000 μs. The peak transmitted power for each module was about 40 kW (hence the total average power was only 2 kW). The coherent integration time was 0.25 s, and 40 range gates were taken starting at 3 km. The three antenna beams all pointed vertically to avoid receiving sidelobe signals.

There were seven special observations used for this study. The dates and duration of these observations are listed in Table 2, and, for convenience, each observation is marked with a capital letter. It must be noted that observation A was during the period of the Cygnus meteor shower and the observations from C to G were during the period of the Lyra meteor shower. Therefore, by using these data, it is reasonable to infer the mesospheric returns coming from the refractive index irregularities, and also the echoes of meteor trails can be studied since the Chung-Li VHF radar has the ability to receive these signals. In the following sections, the mesospheric returns observed either from meteor trails or from refractive index irregularities, will be presented and also some preliminary results of the mesospheric study will be shown.

Table 1. The Characteristics of the Chung-Li VHF Radar.

Location	Chung-Li, Taiwan (25°N, 121°E)
Frequency	52.2 MHz
Wavelength	5.77 m
Peak transmitter power (for each module)	60 kW
Pulse width	1 - 16 μs
Maximum duty cycle	2%
Antenna	
Type	3 square arrays of Yagi (8x8)
HPBW	7°
Steerability	Vertical and North, East, South, West with 17° zenith angle
Total geometrical area	3x1600 m^2

Table 2. The Dates and Durations of the Seven Spectral Observations Used for the Mesospheric Study With the Chung-Li VHF Radar.

	Date	Time	Remark
A	88/08/22	1132 ~ 1244	meteor shower
B	87/03/23	1240 ~ 1702	
C	88/04/19	1420 ~ 1620	
D	88/04/20	1607 ~ 1747	
E	88/04/21	1520 ~ 1637	meteor shower
F	88/04/22	1420 ~ 1624	
G	88/04/23	1000 ~ 1140	

OBSERVATIONS OF METEOR TRAILS

It is well known that when a meteor falls into the atmosphere ionization will occur because of the friction effect between the ambient atmosphere and the meteor itself. Therefore, the free electrons existing in the thermal and ionized meteor path (or trail) will change the properties of the atmospheric refractive index. According to electromagnetic wave propagation theory (TATARSKII, 1961; ISHIMARU, 1978), variations in the refractive index can be treated as radar targets and will scatter or reflect incident electromagnetic waves, depending on the structure of the refractive index variations. Figure 1 is one of the records of echo signals coming from meteor trails during the period of the Lyra meteor shower. It is obvious that in the three minutes three meteor events occurred at altitudes 69.3 km, 91 km, and 98 km, respectively. The lifetimes of meteor trail signals are always less than 1 s (note that the time resolution of the echo signals is 0.25 s); this can be further illustrated from Figure 2. Because meteor trail echoes appear not only as spikes in the records with relative low time resolution, they also occur in all three channels at the same altitude and time; therefore, it is easy to use statistical algorithms to pick up the meteor trail signals from the background noise. After collecting many correct meteor trail events, some statistical analyses may be made. Figure 3 is the occurrence rate of meteor events measured with the Chung-Li radar. It is clear from this plot that during the period of the Lyra meteor shower, the mean occurrence rate of meteor events is about 7 per hour; however, the daily variation in the occurrence rate is quite large, and during non-meteor shower periods the occurrence rate is relatively low (only 1.6 events/hour). Figure 4 is a histogram of the altitudes where meteor trails are produced. From this figure we can see that the lowest height where they may occur is 70 km, and the most likely altitude of occurrence is about 90 km. These results are quite agreeable with other observations (DAVIS, 1965; AVERY et al., 1983; WANG et al., 1988).

MESOSPEHRIC OBSERVATIONS

Although the power-aperture product of the Chung-Li VHF radar is very low (only about 10 WM), the echoes coming from some mesospheric refractive index irregularities can still be observed and analyzed. Figure 5 is the time series of amplitude variation of this kind of echo signals which occurred at 71.1 km. From this record it is apparent that there are five mesospheric refractive index irregularities passing through the radar volume, and the duration of these irregularities in the radar volume is about 30 to 40 seconds. The dynamic Doppler spectra of these mesospheric echo signals are represented in Figure 6. From the time variation of mean Doppler frequencies and the consistency of the Doppler spectral shapes, it is reasonable to infer that the structure of these refractive index irregularities will be "patch-like" or "blob-like" as suggested by RÖTTGER et al (1979). As for the horizontal scale sizes of these irregularities, they will be estimated later. In general, the mean echo power of these mesospheric returns are larger than the background noise level by 5 dB, 4 dB and 2 dB for antennas 1, 2, and 3, respectively. This is shown in Figure 7 for the signals of antenna 1. The right panels in Figure 7 are the averaged Doppler spectra corresponding to the different altitudes. Because the Chung-Li VHF radar has three square spaced antennas with a pyramidal arrangement as shown in Figure 8, it is possible to evaluate the mesospheric mean wind in terms of the so-called SAD method. Figure 9 is the cross correlation function of the echo signals which have been smoothed beforehand. From this plot it is easy to determine the time lags between each pair of signals. According to these time lags and the distances of the spaced antennas, the mean wind speed and the duration of irregularities, it can be estimated that the horizontal dimensions of the patch-like or blob-like irregularities are about 300 to 400 meters.

SUMMARY

From this report, it is confirmed that mesospheric observations can be made using the Chung-Li VHF radar. Some preliminary results have been presented.
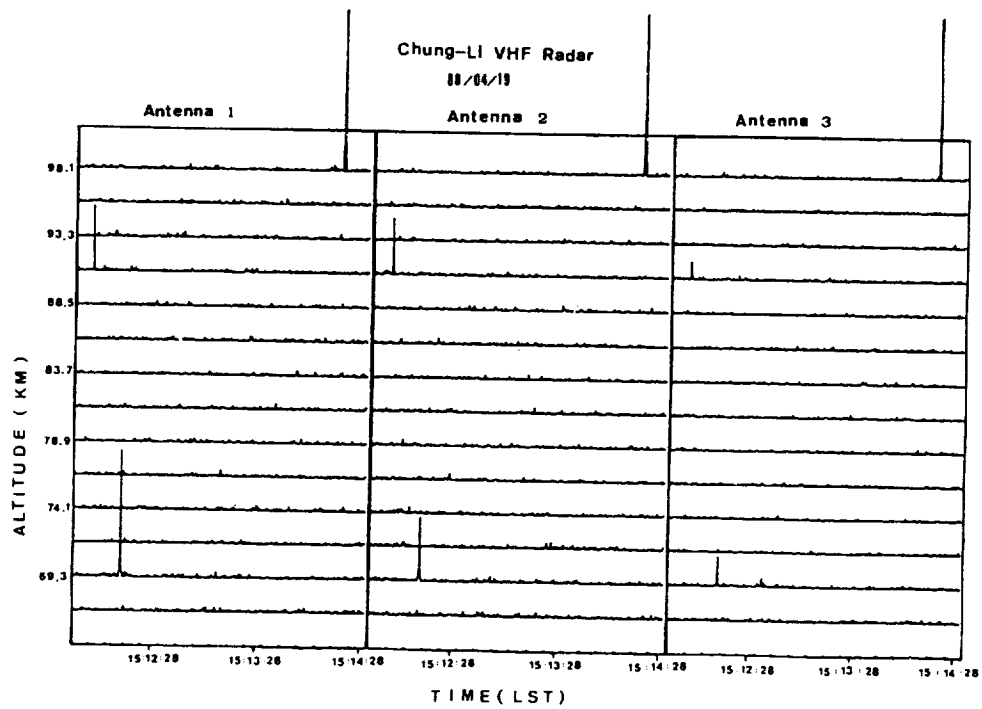
Figure 1. An example of the record of meteor trail returns.
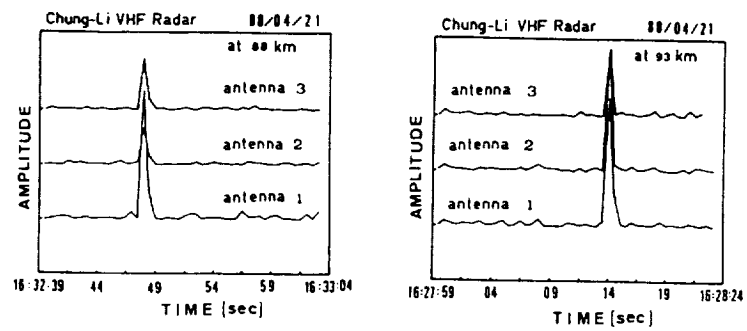
Figure 2. The detailed amplitude variations of meteor trail returns.
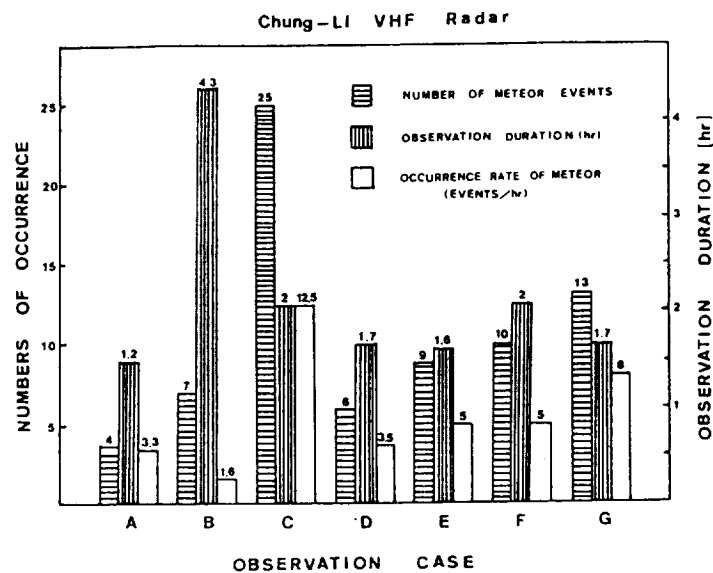
Figure 3. The occurrence rate of meteor trail events observed at the Chung-Li VHF radar. The date and period for each observation is listed in Table 2.
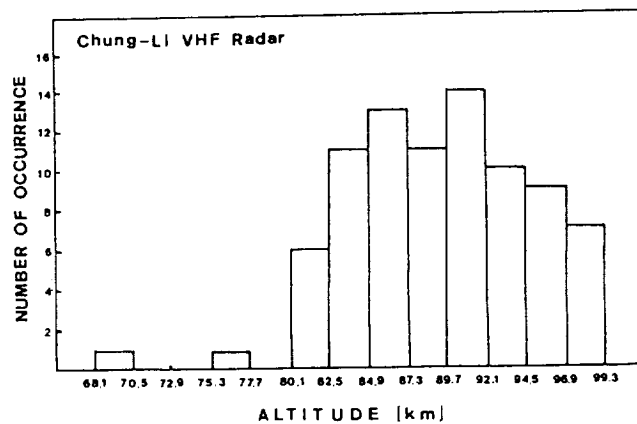
Figure 4. The histogram of the altitudes where meteor trail echoes have occurred.

152
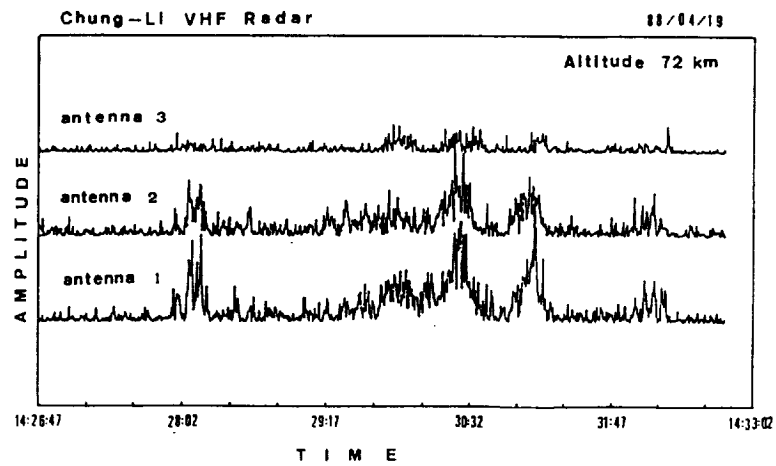
Figure 5. The records of the amplitude variations of the echoes coming from mesospheric refractive index irregularities.
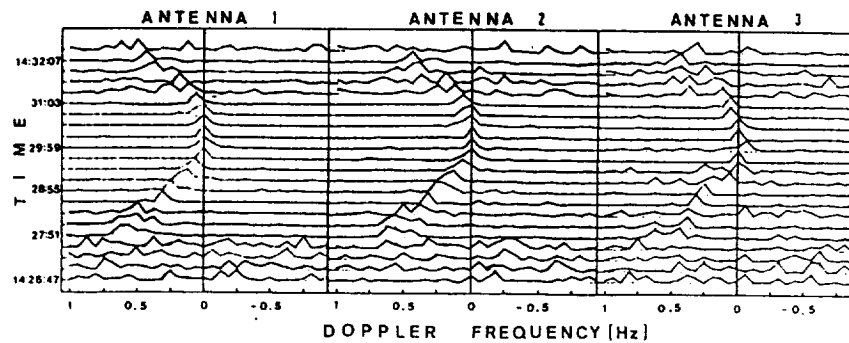
Figure 6. The temporal variation of the Doppler spectra corresponding to the data as shown in Figure 5.
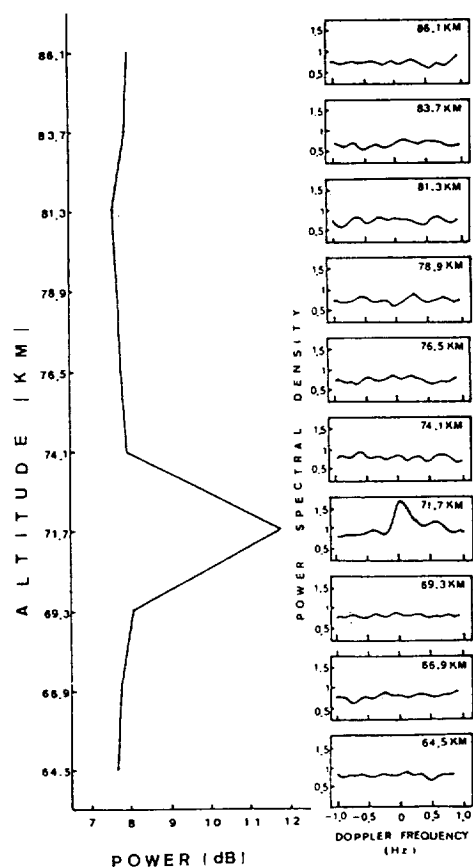
Figure 7. The echo power profile (left panel) and the corresponding averaged Doppler spectra with each altitude (right panel) for the data of antenna 1.
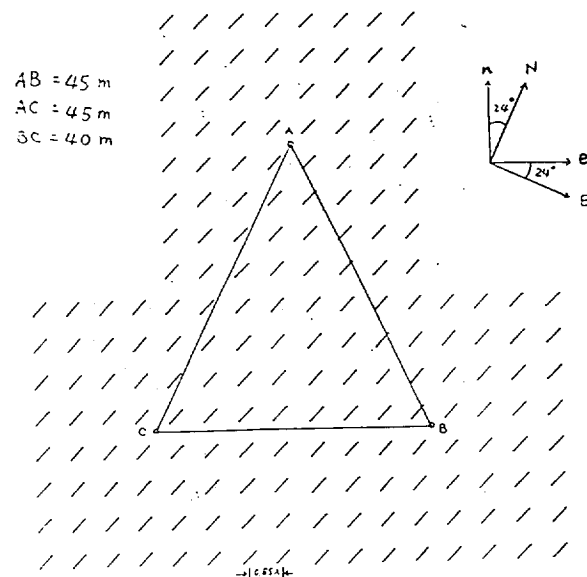
Figure 8. The configuration of the Chung-Li VHF radar antenna array. The short lines represent the polarization direction of the antenna element.
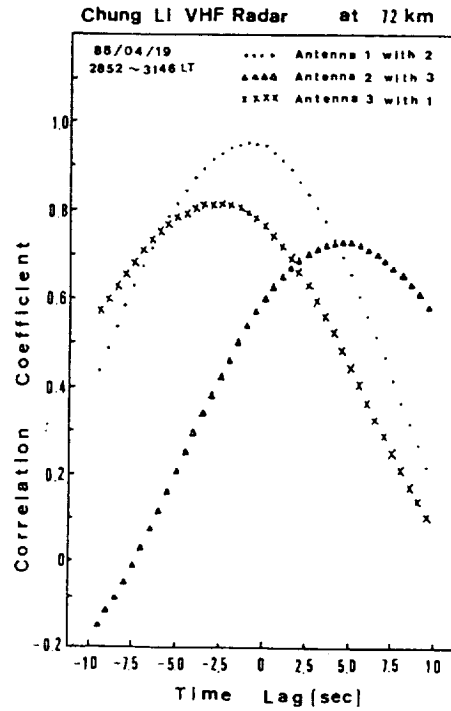
Figure 9.   The cross correlation functions between different echo signals which have been smoothed beforehand by using 13 points equal weight low pass filter.
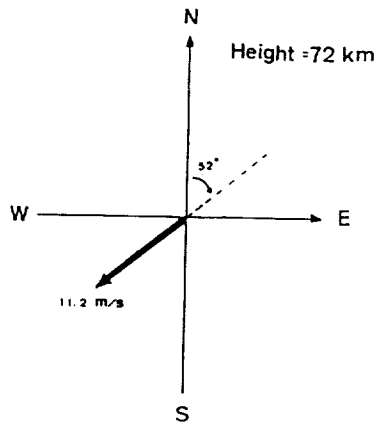
Figure 10. The wind speed and direction estimated from the data as shown in Figure 5 in terms of the SAD method.

REFERENCES

Avery, S. K., A. C. Riddle, and B. B. Balsley, The Poker Flat, Alaska, MST radar as a meteor radar, *Radio Sci., 18*, 1021-1027, 1983.

Davis, K., Ionospheric Radio Propagation, *NBS Monograph 80*, Washington, D. C., U. S. Government Printing Office, 1965.

Ishimaru, A., *Wave Propagation and Scattering in Random Media, Vol 1 and 2*, Academic Press, 1978.

Röttger, J., P. K. Rastogi, and R. F.Woodman, High-resolution VHF radar observations of turbulence structures in the mesosphere, *Geophys. Res. Lett., 6*, 617-620, 1979.

Tatarskii, V. I., *Wave Propagation in a Turbulent Medium*, McGraw-Hill, New York, 1961.

Wang, S. T., D. Tetenbaum, B. B.Balsley, R.L. Obert, S. K. Avery, and J. P. Avery, A meteor echo detection and collection system for use on VHF radar, *Radio Sci., 23*, 46-54, 1988.

VERTICALLY PROPAGATING FEATURES IN MF RADAR SIGNAL STRENGTH

C.E. Meek and A.H. Manson

Institute of Space and Atmospheric Studies
University of Saskatchewan, Saskatoon, Canada

Abstract: Aquisition of professionally designed coherent receivers at the Saskatoon (52°N, 107°W) MF radar (2.219 MHz, 20 µsec pulse: 3 Km resolution) allows reliable determination of signal strength height and time profiles. The height variation in time (5 min resolution) of local peaks in the signal-height profiles is compared with similar statistics for vertical Doppler velocity, horizonatal wind, wind shear etc. An apparent resolution of 1 Km is obtained from the 3 Km spaced data by parabolic fit.

INTRODUCTION

The data are from the new spaced antenna coherent wind system described elsewhere in these proceedings. Horizontal wind and pattern parameters (by "Full Correlation Analysis", FCA), "vertical" Doppler (from the mean auto-correlation phase slope at zero lag) and angle of arrival parameters (not used here) are available with 5 min resolution - depending on noise level and success or otherwise of the analyses.

DATA

For each 5 min record in a day, local peaks in height profiles of the various paramters are sought when data exist for 3 adjacent heights. A parabolic fit determines the height to 1 Km resolution. All peaks are used, regardless of their "strength". To avoid a painful re-write job, an existing printer display format was used: the 288 possible times are squeezed into 256 boxes. This produces a very compact format. Figure 1 shows 21 days of peak signal strength data. Vertical tics are spaced 12 Km (1 pixel/Km), and horizontal tics 3 hr apart (approximately 1 pixel per 5 min). Interesting features can be seen in the upper half of the plot, but except at night these have an additional virtual height component caused by changes in underlying ionization. The E-region echo is an obvious case. Thus the discussion in this paper will be restricted to the lower half of the height
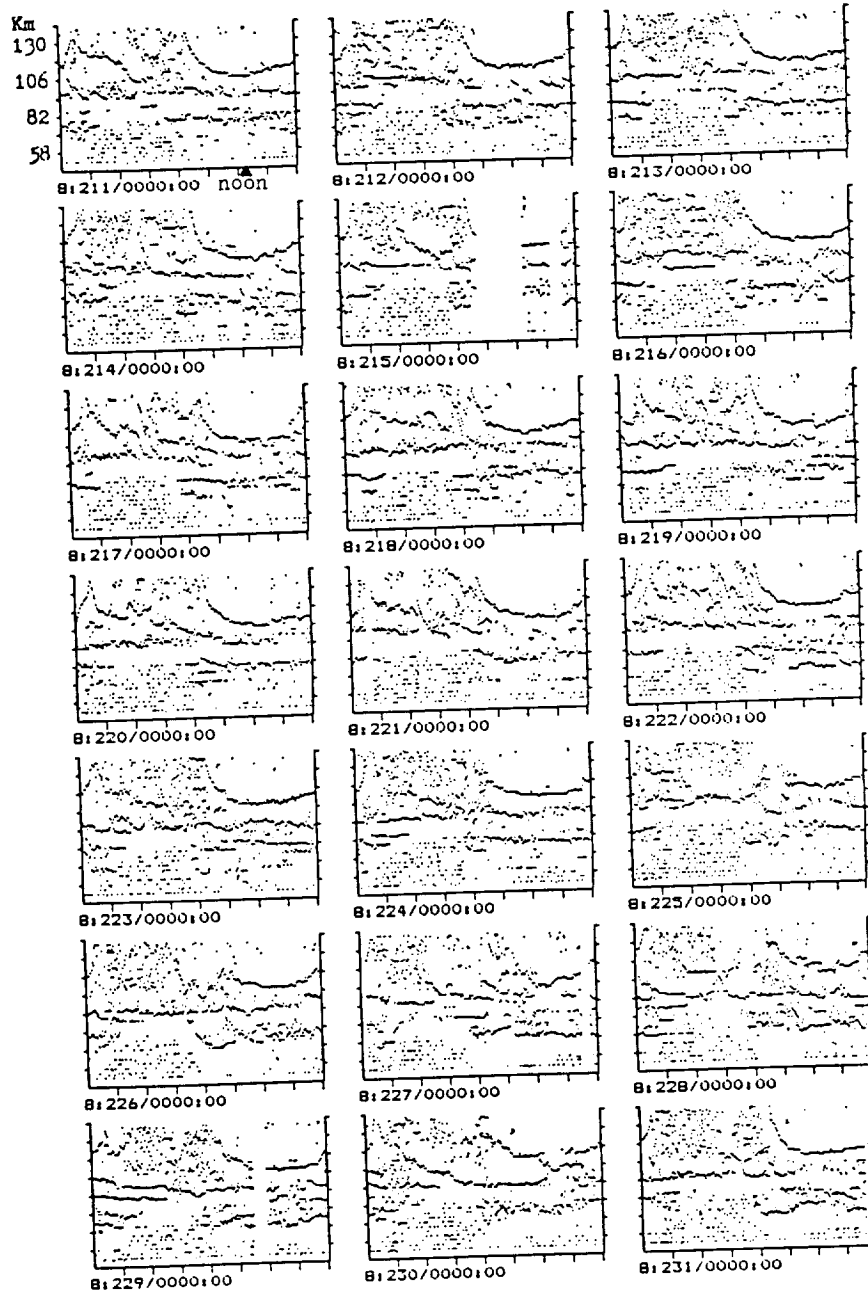
Figure 1. Heights of local peaks in signal (μV) vs. height profiles for 21 days: 1 frame per day (0000-2359 UT). Local noon and the height scale are marked on the top left frame.

range (below 94 Km).

In general when apparent motions are seen, they are downwards at speeds of the order of tidal phase propagation (1-2 Km/hr). There are some upward motions as well (e.g. day 226) but the continuity of data is not as good - and these may be due to layers forming at successively greater heights.

Non-tidal causes, such as changes in electron density (N(h)) gradients due to solar radiation or particle influx may combine with short period gravity waves or turbulence to produce slow height variations of the peak signals. For this reason, specific comparisons with features in the neutral wind are of necessity somewhat tentative, and purely based on similarity of height and vertical speed.

DETAIL FOR TWO SELECTED DAYS

Additional parameters are shown for days 225 (Figure 2) and 226 (Figure 3). The signal peaks are reproduced from Figure 1 along with the upward Doppler (VZ), total horizontal speed (VTR), vertical velocity shear (VSHR= magnitude of velocity vector difference), northward (VN), eastward (VE), southward(-VN), and westward (-VE) wind components, and fading speed in the moving diffraction pattern (-TC: that is, a peak represents local faster fading).

DISCUSSION

Day 225 signal (Figure 2) shows downward motion from ⌐85 to 79 Km over the last 5 hr in the plot (⌐ 1 Km/hr). This occurs approximately 3 Km below the height of a similar feature in VTR (the total wind speed) - although the slope is smaller, maybe 0.5 Km/hr. On other summer data (not shown) which have these slowly descending "layers", the peak signal occurs at the same height or just below the peak speed.

A harmonic analysis of 48 hrs of data (day 225-226 UT) is shown in Figure 4. The diurnal component is expected to be inaccurate, if not actually spurious, below ⌐85 Km because of the reduced data at night for these heights; but taking it at face value, the diurnal tide phase slope (16 Km vertical wavelength below 85 Km, 0.6 Km/hr) seems to be the closest to the VTR slope, while that of the semi-diurnal (36 Km wavelength, 1.5 Km/hr)
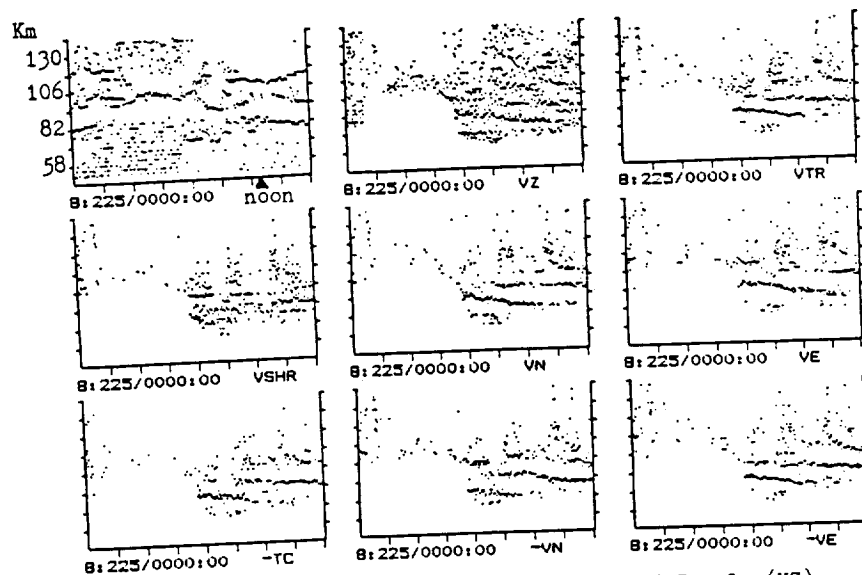
Figure 2. Heights of local peaks in signal, upward Doppler(VZ), horizontal speed(VTR), total vertical shear(VSHR), Northward(VN), Eastward(VE), Southward(-VN),Westward(-VE), and fading speed (-TC) for day 225 (Aug12),1988.
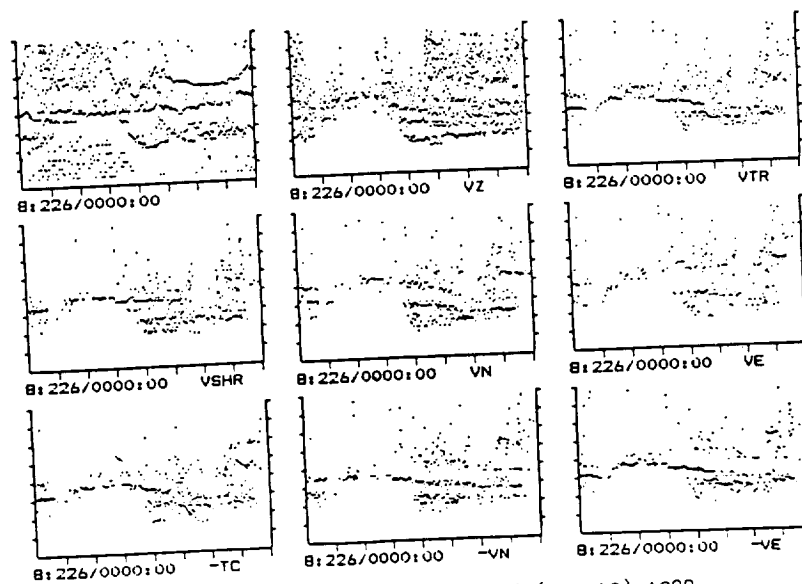
Figure 3. As in Figure 2, but for day 226 (Aug 13),1988
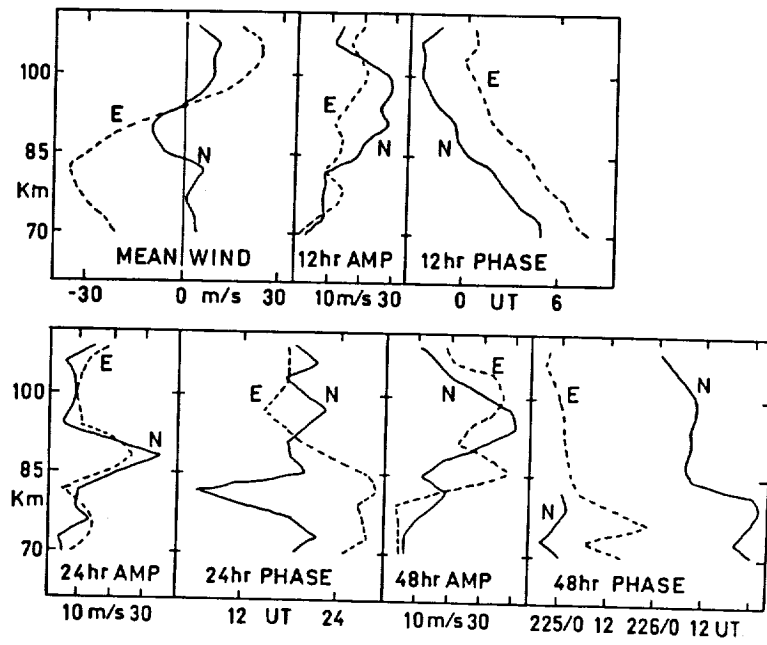
Figure 4. Tidal parameters for 1988:225-226 (Aug 12-13). Phases are plotted as hours of northward and eastward maxima.

is close to the signal slope.

The VZ parameter shows downward phase speeds of the same order, but a vertical wavelength of ∽12 Km. The height velocity shear, VSHR, shows no upward/downward propagation, and this is the normal finding for all the (summer) data examined. The fading speed (-TC) closely reproduces the features seen in VTR. (Over the long term these latter two paramters tend to be positively correlated in the FCA used on the spaced antenna data anyway - it is not known whether this is an analysis effect or a physical relation: but pattern scales - not shown- are similarly related to VTR in the coherent FCA.)

The horizontal wind components also show a ∽12 Km vertical wavelength, but the downward speeds vary between "propagating" features.

Day 226 shows an apparent upward motion from ∽70 to 82 Km over the last 9 hr, although it is difficult to be certain that the eye is not being led by different layers. It also exhibits some wavelike oscillations. The lowest VZ trace is the only other parameter with similar upward motion. Near the end of the day, the VZ traces are spaced by ∽ 6 Km.

CONCLUSIONS

Quantitative work needs to be done to explain these data. For example, non-linear interaction between the 12 and 24 hr components can produce an 8 hr component with a shorter wavelength than either, and a 24 hr component with upward phase propagation The monthly spectra (not shown) have hints of an 8 hr component at low heights with a clear peak at E-region. Another complication may be multiple tidal modes caused by interaction with the 48 hr components, which is the strongest of the three. The sudden height changes in the 24 hr amplitude and phase indicate the presence of several modes. However it is not clear why signal strength would react to a single tidal component of the wind, and not the total speed or shear.

The VZ, on the other hand, is liable to be greater for shorter wave motions, and these traces might be explained by the presence of an 8 hr, or less, wave, although their slope suggests much longer periods.

These connections are all very tentative because influence on the signal by N(h) gradients was not considered.

SEMI-DIURNAL VARIATIONS IN THE TIME SCALE OF TURBULENCE-LIKE IRREGULARITIES NEAR THE ANTARCTIC SUMMER MESOPAUSE

G.J. Fraser and Usman Khan

Physics Department,
University of Canterbury, Christchurch 1, New Zealand

ABSTRACT

Measurements from the MF SA-mode radar at Scott Base (78S, 167E) include an estimate of the autocorrelation time scale ($T_{0.5}$) of the scatterers, corrected for advection by the mean wind. Summer observations (December 1983) show a semi-diurnal variation of $T_{0.5}$. At heights of 87 to 95 km the minimum values of $T_{0.5}$ occur when the zonal component of the semi-diurnal tide is at its westward maximum. If it is assumed that decreasing values of $T_{0.5}$ are associated with increasing turbulence then these results are consistent with those of BALSLEY et al. (1983) who found that enhanced turbulence is generated in summer by low-frequency gravity waves and tidal components above the polar mesopause.

INTRODUCTION

Since HOUGHTON (1978) pointed out the importance of gravity waves in the overall transport of heat and momentum in the middle atmosphere there have been a number of theoretical and modelling studies of the way in which gravity waves influence the large-scale circulation. There have also been observational studies, some on quite small time and space scales, of gravity wave breaking. FRITTS et al. (1988) observed gravity wave breaking at one site (Poker Flat), with a time resolution of 15 minutes, on two days in summer. Their study supported previous work at the same site by BALSLEY et al. (1983) who concluded from 22 months' observations that their radar echoes from the Arctic summer mesosphere and lower thermosphere were mainly produced by unstable low (comparable with tidal) frequency gravity waves. The observations discussed below are also from the high-latitude summer mesosphere and lower thermosphere, but from the Antarctic and on a time scale of one month.

OBSERVATIONS

The full correlation analysis (e.g. BRIGGS, 1984) of observations from SA mode radars estimates a parameter, $T_{0.5}$, which is the time scale of random changes in the echoes after removing fluctuations due to advection of the scattering volume through the radar beam. There is a simple relationship between $T_{0.5}$ (measured with a coherent radar) and turbulence parameters such as the energy dissipation rate, if the scattering volume is filled with isotropic turbulence. However factors such as the anisotropic nature of atmospheric irregularities and the finite radar beam width necessitate caution (HOCKING, 1983) in using $T_{0.5}$ as a quantitative measure of atmospheric turbulence.

The Scott Base observations discussed here were made with incoherent radar receivers. Consequently the receiver output spectrum is not the linear superposition of the Doppler-shifted signals from individual scatterers but is the result of intermodulation between the individual Doppler signals. This results in a broadening of the power spectrum and a narrowing of its Fourier transform, the autocorrelation function.

Notwithstanding the above limitations it is reasonable to assume that an increase in atmospheric turbulence results in a decrease in the value of $T_{0.5}$ calculated from incoherent receiver data.

In a preliminary investigation KHAN (1988) found a semi-diurnal variation of $T_{0.5}$ in observations from the prototype MF SA-mode radar (on a wavelength of 100 m) at Scott Base (78S). Details of the radar and its successor have been given by FRASER (1988). Further analysis showed that this semi-diurnal variation is most apparent in summer and the observations for December 1983 presented below show that there is a close relationship between $T_{0.5}$ and the semi-diurnal tide.

Observations of the zonal and meridional wind components and of $T_{0.5}$ for the whole month were sorted into 24 one-hourly intervals. Planetary and gravity wave contributions thus appear as a random variation about the 24 one-hourly means. These monthly mean diurnal variations for an altitude of 95 km are shown in Figure 1. It can be seen that decreasing values of $T_{0.5}$ occur when the zonal wind component has its maximum westward excursion. The intensity of turbulence is thus a maximum with a maximum westward wind but a minimum with a maximum eastward wind of comparable speed.

MONTHLY MEAN DIURNAL VARIATION

SCOTT BASE   DECEMBER 1983   95.0 KM
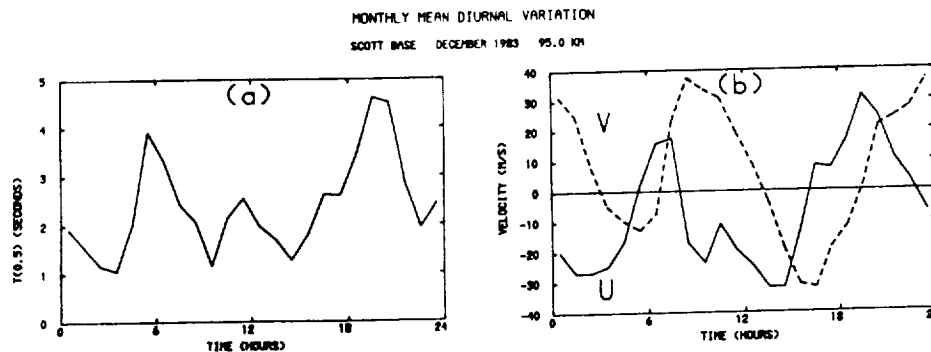
Figure 1(a). Mean diurnal variation in $T_{0.5}$ at Scott Base (78S) for December 1983. The standard deviation is 0.5s. (b) Mean diurnal variation in zonal (U) and meridional (V) wind components. The sample standard deviation of each point, due to non-tidal (planetary and gravity wave) components is 20 ms^{-1}. The mean winds are included ($U = -6.1$ ms^{-1}, $V = +7.6$ ms^{-1}).

DISCUSSION

In their observations of gravity wave saturation FRITTS *et al.* (1988) found that maximum turbulence occurred at heights where the temperature gradient was most negative and where the perturbation velocity was in the direction of wave propagation. The Scott Base results therefore suggest that the source of instability is a westward travelling gravity wave. The direction of propagation and the periodicity of ~12 hours imply that the source is the semi-diurnal tide.

Figure 2 shows the phase and amplitude of the zonal and meridional semi-diurnal tidal components together with the zonal and meridional mean winds. There were only data for 9 or less of the hourly intervals below 83 km so that the tidal components could not be calculated. There were 16 hours of data at 83 km and 23 or 24 hours of data at 85 km and above. The model results of FORBES and GILLETTE (1982) in Figure 3(a) show a similar amplitude structure, a similar vertical wavelength (25–30 km) above 90 km and also a phase discontinuity at 85–90 km. There is however a phase difference of about 3 hours in the zonal component between the model and the observations.
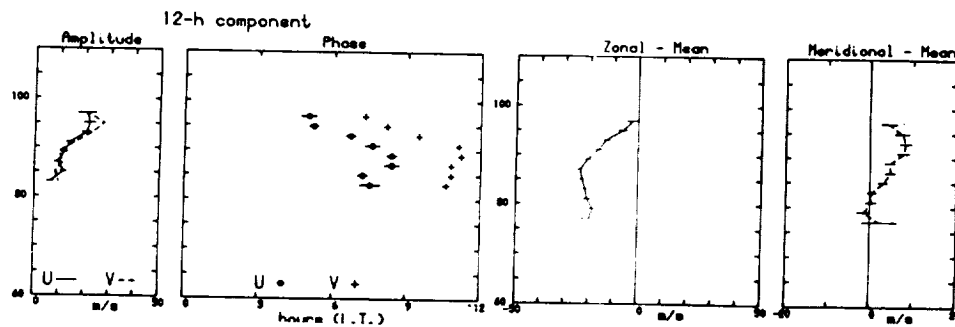
Figure 2.   Mean zonal and meridional winds, and semi-
diurnal tide at Scott Base for December 1983.
The phase slope between 89 and 97 km corresponds
to a vertical wavelength of 30 km.
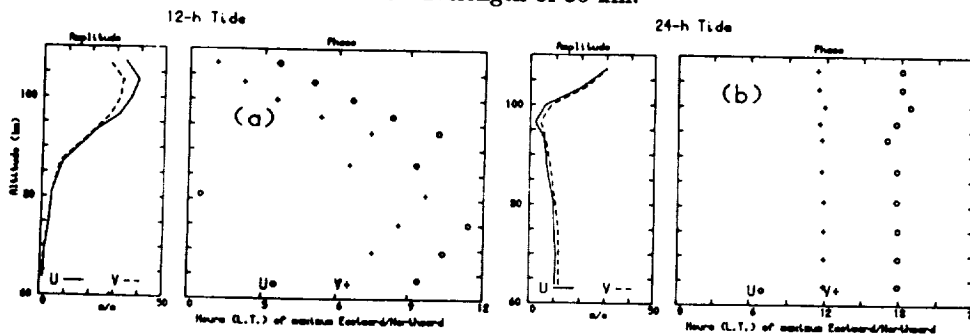
Figure 3.   Model results from FORBES and GILLETTE
(1982) for the semi-diurnal (a) and diurnal
(b) tides.

SCOTT BASE   1983 DEC 1 - 31

12-h component
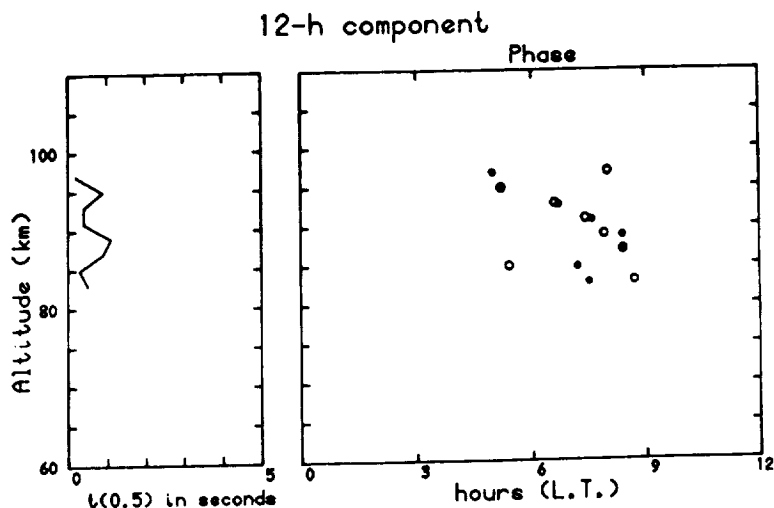
circles indicate the time of maximum $T_{0.5}$ and the
filled circles are the phases of the semi-diurnal zonal
tide from Figure 2.

Figure 4 shows a "tidal" plot for $T_{0.5}$. The phase of the zonal semi-diurnal tide
from Figure 2 is also included. The relationship between $T_{0.5}$ and the zonal wind
at 95 km, shown in Figure 1, is apparent at all heights between 87 and 95 km (it
should be noted that the effective transmitter pulse width is 6 km FWHP). The tidal
phases are times of maximum positive excursion so the closeness of the $T_{0.5}$ phase
and the zonal phase confirms that a maximum eastward zonal component is associ-
ated with a maximum in $T_{0.5}$ and a corresponding minimum in the amount of turbu-
lence. Assuming that the tidal phase discontinuity between 85 and 90 km indicates
the mesopause, the Scott Base observations are in good agreement with those from
Poker Flat (BALSLEY *et al.*, 1983; FRITTS *et al.*, 1988). Both Arctic and Antarc-
tic observations suggest that turbulence is induced by low-frequency gravity waves or
tides near and above the polar summer mesopause.

Figure 5 is a similar comparison for the diurnal component. There is not the sim-
ilarity between the variations of the zonal diurnal tide and $T_{0.5}$ as there is for the
semi-diurnal tide. The diurnal wind amplitude is comparable with the semi-diurnal
amplitude but both the observed and modelled (Figure 2b) diurnal phase gradients
show an evanescent mode. There is some structure in the $T_{0.5}$ "tide", although the
non-linearity of wave breaking and the indirect relationship between $T_{0.5}$ and turbu-
lence may lead to some interaction between the 12- and 24-hour components.
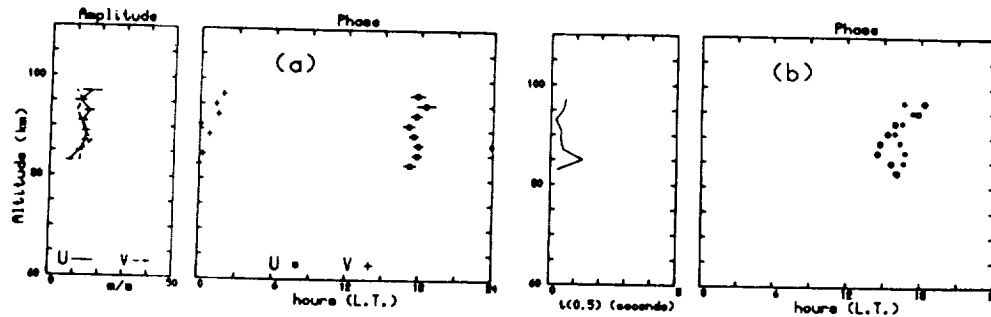
Figure 5. The diurnal tide (a) and 24-hour component in $T_{0.5}$ (b). The open circles in (b) are the time of maximum $T_{0.5}$ and the filled circles are the phases of the diurnal zonal tide from (a).

CONCLUSIONS

The observations from Scott Base in December 1983 show the existence of turbulence near and above the polar summer mesosphere similar to that observed at Poker Flat. Increased turbulence is frequency detected by the increased scattering of radar signals, as in the observations of BALSLEY et al., (1983). Further work is planned to compare the scattered signal power with the winds and $T_{0.5}$, and to study the transition to and from solstice conditions.

REFERENCES

Balsley, B.B., W.L. Ecklund and D.C. Fritts, VHF echoes from the high-latitude mesosphere and lower thermosphere: observations and interpretations, J. Atmos. Sci., 40, 2451-2466, 1983.

Briggs, B.H., The analysis of spaced sensor records by correlation techniques, Handbook for MAP, Vol. 13, 166-186, SCOSTEP Secretariat, Dept. Elec. Eng., Univ. Illinois, 61801, 1984.

Forbes, J.M. and D.F. Gillette, A compendium of theoretical atmospheric tidal structures, Part 1: Model description and explicit structures due to realistic thermal and gravitational excitation, Environmental Research Papers, No. 780(J), Air Force Geophysics Laboratory, Massachusetts, 01731, 1982.

Fraser, G.J., Monthly mean winds in the mesosphere at 44S and 78S, Pure Appl. Geophys., in press, 1988.

Fritts, D.C., S.A. Smith, B.B. Balsley and C.r. Philbrick, Evidence of gravity wave saturation and local turbulence production in the summer mesosphere and lower thermosphere during the STATE experiment, J. Geophys. Res., 93, 7015-7025, 1988.

Hocking, W.K., On the extraction of atmospheric turbulence parameters from radar backscatter Doppler spectra – I. Theory, J. Atmos. Terr. Phys., 45, 89–102, 1983.

Houghton, J.T., The stratosphere and mesosphere, Q. J. R. Meteorol. Soc., 104, 1, 1978.

Khan, U., Seasonal and height dependence of turbulence in the middle atmosphere, M.Sc. thesis, University of Canterbury, Christchurch, N.Z., 1988.

POLAR MESOSPHERE SUMMER ECHOES OBSERVED WITH THE
EISCAT 933-MHZ RADAR AND THE
CUPRI 46.9-MHZ RADAR

J. Röttger*, M.T. Rietveld, C. La Hoz
EISCAT Scientific Association
P.O. Box 812, S-981 28 Kiruna, Sweden
(*on leave from Max-Planck-Institut für Aeronomie)

T. Hall, M.C. Kelley and W.E. Swartz
Cornell University
Ithaca, NY 14853, USA

ABSTRACT

During a campaign to study polar mesosphere summer echoes (PMSE-88) the EISCAT UHF and VHF radars and the CUPRI VHF radar were operated in Tromsö in summer 1988. For the first time the EISCAT UHF radar detected coherent echoes from the mesosphere. Their relation to the echoes recorded simultaneously with the CUPRI radar is studied and some possible origins of the scattering process of the polar mesosphere summer echoes observed at 49.9 MHz and 933 MHz are outlined.

INTRODUCTION

A special campaign for studying polar mesosphere summer echoes (PMSE) was carried out in summer 1988 in Tromsö/Norway. The EISCAT UHF (933 MHz) and VHF (224 MHz) radars and the CUPRI (46.9 MHz) radar were operated at the same site to allow multi-frequency studies of the same atmospheric volume at the same time.

In addition to first direct comparisons of simultaneous VHF and UHF radar observations of the summer polar mesosphere we present here the first observations of polar mesosphere summer echoes (PMSE) at the UHF frequency 933 MHz, which cannot be due to conventional incoherent scatter. Polar mesosphere summer echoes are usually observed by VHF radars (Ecklund and Balsley, 1981, Czechowsky et al., 1985, Hoppe et al., 1988) and are due to backscatter or partial reflection from fluctuations or gradients of the radio refractive index in the mesosphere. The mechanism which generates the necessary variations of the refractive index is so far not established. These PMSE are usually orders of magnitude stronger and have a much longer coherence time than the incoherent scatter echoes from the D-region of the ionosphere. We will use here the term "coherent echoes" for echoes which have a much longer coherence time than the incoherent scatter echoes. The coherent echoes thus can only be suitably analyzed by means of data taking in the pulse-to-pulse radar operation mode (e.g., Röttger, 1989).

The observations of PMSE at 933 MHz are compared with simultaneous 46.9 MHz observations, where the incoherent scatter echo is negligibly weak. The coherent 933-MHz echoes occur around 85 km altitude and were more than an order of magnitude stronger than the concurrently existing incoherent scatter echoes. The spectra of PMSE are much narrower than those of the latter. The 933-MHz PMSE occurred in short bursts of maximum several minutes duration and were related to simultaneous increases of the 46.9-MHz echo strength. It is noted that these observations were during a magnetic storm when auroral particle precipitation enhanced the D-region electron density. It is also noted that wavelike vertical velocity variations with amplitudes above 10 m/s were observed around times when strong PMSE occurred at both 46.9 MHz and 933 MHz. It is likely that the strong

enhancements of PMSE, which usually are detected by VHF radars and now were seen also at UHF, are related to strong vertical updrafts, but additionally need large electron density and gradients to create the enhanced echo strength.

We recognize that the 933 MHz echoes, like the 46.9 MHz echoes, are not caused by incoherent scatter. We have to invoke other mechanisms, such as for instance turbulence-induced scatter by extension of the electron gas inertial subrange in the presence of cluster ions as suggested by Kelley et al. (1987). We argue that also strongly enhanced electron density gradients with unusually short scale lengths caused by small-scale patching of heavy cluster ions or some yet unknown instability mechanism can be responsible for the strong polar mesosphere summer echoes (PMSE).

EXPERIMENTS

The EISCAT UHF radar was operated for some periods during the campaign PMSE-88, which was carried out in Tromsö/Norway between 25 June and 8 August 1988 to study particular features of PMSE. This radar operates in the 933-MHz band with a pulse peak power of about 1.5 MW and a parabolic dish antenna with 48 dB gain, corresponding to a half-power beam width of 0.6 degree. The standard EISCAT D-region incoherent scatter program GEN-11 was applied (Turunen, 1986) and the UHF system was operated in the monostatic mode with the antenna direction fixed to the vertical direction. This program applies a special pulse-to-pulse modulation scheme with a 13-baud Barker code and 1.05 km range resolution. Autocorrelation functions with 22 lags and 2.222 ms lag spacing are computed on-line and after integration over 10 sec dumped to tape. The peak power-aperture product of the EISCAT UHF radar in the GEN-11 mode is estimated to be $9 \cdot 10^9$ $W \cdot m^2$. An introductory description of the EISCAT UHF radar system applied in MST radar investigations can be found in Röttger et al. (1983).

The Cornell University Portable Radar Interferometer CUPRI (Providakes et al., 1983) was brought to Tromsö for the PMSE-88 campaign and operated at 46.9 MHz. A 50m by 50m coaxial collinear (coco) antenna array was used for transmission and reception in the vertical beam mode. Additionally a N-S and a W-E baseline interferometer receiving antenna system consisting 2 sets of 4 Yagis were set up. The standard mode of CUPRI was to operate with the full coco antenna and a 10 µs pulse length, corresponding to 1.5 km altitude resolution. The peak power-aperture product of the CUPRI system in Tromsö is estimated to be $3.5 \cdot 10^7$ $W \cdot m^2$. The operation of the CUPRI system was frequently simultaneous with the EISCAT 224-MHz operation. These comparisons as well as the interferometer results will be published elsewhere. Here we will describe results from a simultaneous operation of CUPRI and the EISCAT UHF radar, since they show for the first time polar mesosphere summer echoes at 933 MHz, which occurred simultaneously with 46.9-MHz echoes recorded by CUPRI.

OBSERVATIONS

In Fig. 1 we show so-called RTgraph (real-time-graphics) plots of the EISCAT UHF radar operation, recorded close to local midnight on 1 July 1988. In these graphs the estimate of signal power is displayed as function of range. At 22:57 UT the power profile just shows the usual increase due to increase of the incoherent backscatter power in the D-region. We already had noticed earlier during that evening some hints of a notch in the profile and sometimes even a very small increase in echo power around 85 km altitude. At 22:58 UT suddenly a significant increase in signal power in the altitude gate 85.75 km occurred, and we were able to detect similar or even much stronger events of this kind in the following hours. The D-region ionization was fairly enhanced during the observing period due to strong particle precipitation which occurred during an ongoing

EISCAT UHF RADAR 1 JULY 1988
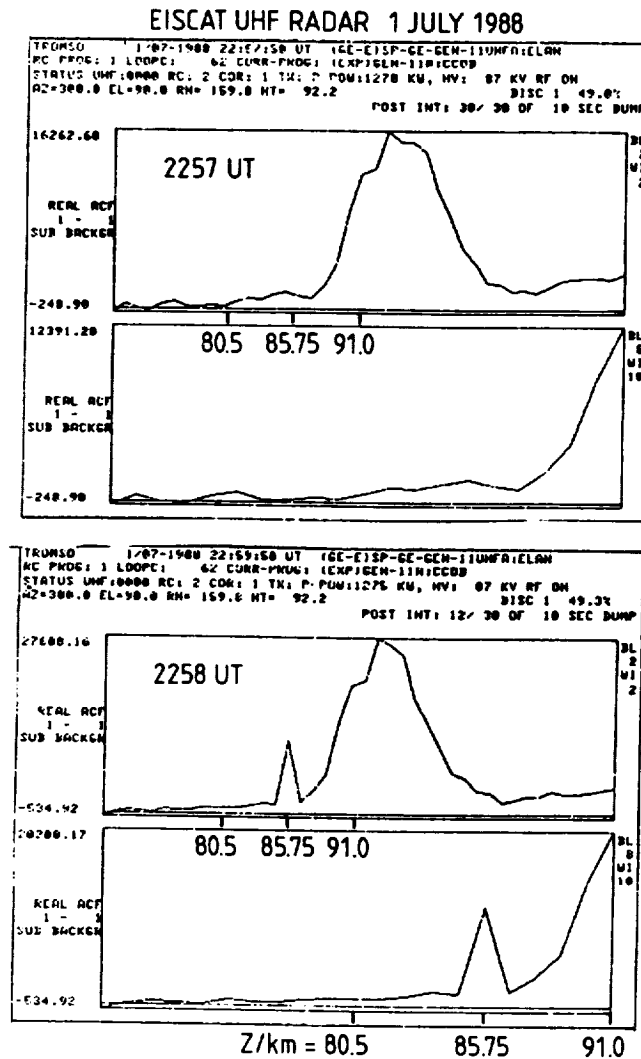
Figure 1. Real-time power profile displays of echoes from the D-region
and lower E-region, measured with the EISCAT UHF radar. The upper
panels show the usual profiles and the lower panels show profiles
with an enhanced echo from about 85 km altitude. These profiles
display an estimate of the signal power obtained from a lag of the
autocorrelation function which is very close to zero delay (some 80-
120 μs). This constitutes a proper power estimate for D-region but
no more for E-region altitudes. The part of the profile above 90 km
thus should be disregarded in this real-time display.

magnetic storm. This enhanced the signal-to-noise ratio of the incoherent back-
scatter echo and thus allows us to obtain relevant information on the D-region
electron density. However, the occasionally occurring coherent echoes would mask
the usual incoherent echoes and then the electron density could no longer be
deduced. During the simultaneous operation of the CUPRI radar similar features
of echo variation were already noted in real-time, but some form of the PMSE
were present most of the time for CUPRI.

Time series of signal power in certain altitude gates of the EISCAT UHF radar
(84.75 km) and the CUPRI radar (84.5 km) are displayed in Fig. 2. A somewhat
arbitrary dashed line is drawn to indicate above which signal level the EISCAT
echoes are assumed to be coherent echoes. The criterion used for this purpose is
that an echo enhancement did occur in only one or two altitude gates, since it
is unlikely to see an increase in incoherent scatter echo power only in such a
narrow altitude range. Signal levels below this dashed line, thus, can be regar-
ded as being predominantly due to incoherent scatter. A detailed study of the
spectra of these different echoes is necessary, however, and needs to be done
subsequently, to obtain a better estimate where the separation line between the
"coherent" and "incoherent" echoes should be drawn. A preliminary comparison of
the coherent echoes detected by CUPRI and by EISCAT thus should be confined only
to the times when the EISCAT echoes are in excess of this tentatively drawn
line. We notice some correlation of these "coherent" PMSE on both frequencies. A
more obvious correlation is evident when we compare the complete time series. We
note that this is due to the fact that the potential refractive index gradient,
which determines the scatter cross section of VHF radar echoes, in the meso-
sphere is very strongly dependent on the electron density and the electron
density gradient. This means that most of the time the echoes on 933 MHz and
those on 46.9 MHz result from different scattering processes, but are related to
each other because of their dependence on the electron density.
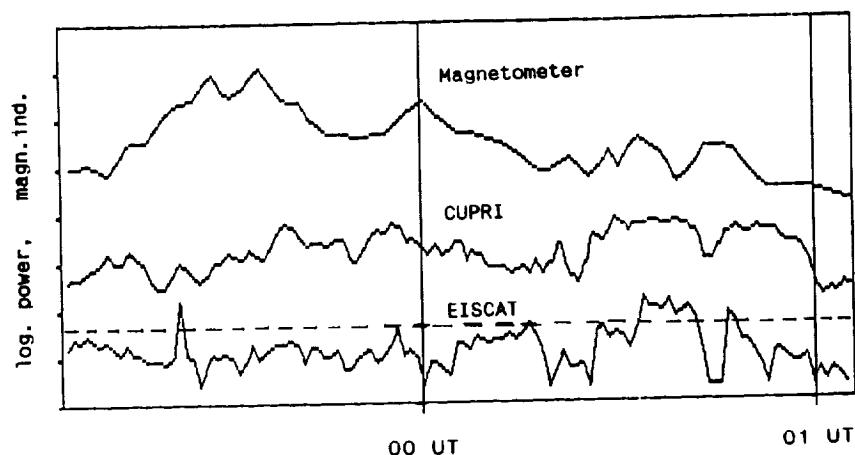
Figure 2. Time series of power received in the range gate closest to
85 km with the EISCAT UHF radar (933 MHz) and the CUPRI VHF radar
(46.9 MHz). The dashed line indicates the assumed limit of incohe-
rent scatter for the UHF radar. The upper curve shows the magne-
tometer record of the H-component of the Earth's magnetic field in
Tromsö (courtesy of Auroral Observatory, Tromsö). The difference of
tick marks on the left-hand ordinate corresponds to 100 nT for the
H-component, 15 dB for CUPRI and for EISCAT, respectively.

We also have included in Fig. 2 the records of the H-component of the Earth's magnetic field measured in Tromsö, since a possible relationship of magnetic field variations and PMSE strength was suggested by Rishbeth et al. (1988). In the time series shown in Fig. 2 we do not see any detailed correlation between the magnetometer and the radar records, and thus cannot immediately support this suggestion. We, however, have to note that the lack of a strict correlation could be due to the difference of the volumes over which the irregularities, causing the radar signals, and the electro-jet current variations, causing the magnetic field variations, have to be averaged.

In Fig. 3 we present several profiles of UHF radar echo power which in most cases (except when these strong PMSE and their code-sidelobes are present) are a good estimate of the electron density. The maximum of 15 dB corresponds to a signal-to-noise ratio of 100 %, and this is calibrated to correspond to an electron density $N_e \approx 3 \cdot 10^{10}$ m^{-3} and a volume reflectivity $\hat{n} \approx 6 \cdot 10^{-18}$ m^{-1}. The minimum value of 0 dB corresponds to a signal-to-noise ratio of 3 %, $N_e \approx 1.9 \cdot 10^{9}$ m^{-3} and $\hat{n} \approx 1 \cdot 10^{-9}$ m^{-1} respectively. These estimates are preliminary and are uncertain by about 20 %. The maximum volume reflectivity of the peak polar mesosphere summer echo observed on 933 MHz at about 15 dB relative scale is about a factor of 25 smaller than the maximum volume reflectivity observed in 1987 with the EISCAT VHF radar (Röttger et al., 1988). The system noise temperature of the EISCAT UHF radar is at about 100 K, this means that the peak effective temperature of a 933-MHz PMSE is about 100 K, too (SNR = 100 %). Defining an effective signal temperature as the ratio of the effective signal temperature and the power-aperture product allows us to compare measurements made at different radars. Taking the EISCAT UHF radar parameters, we obtain an effective signal temperature of $1 \cdot 10^{-8}$ K per W·m^2 on 933 MHz. The peak PMSE of CUPRI was about 30 dB, corresponding to $5 \cdot 10^{6}$ K, when assuming a system temperature estimate of 5000 K. With CUPRI's peak power-aperture product of $3.5 \cdot 10^{7}$ W·m^2 we obtain an effective signal temperature of 0.14 K per W·m^2 on 46.9 MHz. This means that the reflectivities on both frequencies are about seven orders of magnitude different.

There are some instances when the CUPRI echo shows peaks at altitudes of an increased electron density gradient. However, the relation is by far not conclusive. More detailed analysis is necessary to find out how the CUPRI signal strength depends on the gradient of electron density. We then have also to take into account in the further interpretations that the altitude resolution of both radars of some kilometer may not be sufficient and that the CUPRI beam is about ten times wider than the EISCAT beam. The echoes seen by CUPRI are thus an average over a much larger horizontal area than those of the EISCAT radar, which reduces the correlation of the echo variations and does not facilitate the analysis. It could be presumed that the interferometer analysis of the CUPRI data may ameliorate this horizontal averaging somewhat.

In Fig. 4 height-time-intensity plots are shown of the EISCAT 933-MHz radar signal power and the vertical velocity. We notice in the upper panel the distinct variability of the echo power demonstrating the enhancements of the electron density throughout all of the D-region (occasionally down to 72 km) due to particle precipitation. We also notice the further enhancements due to PMSE, which are confined to a narrow altitude region around 85 km. Very noticeable is also the depression of echo power, which occurred around the same altitudes before the PMSE did arise. This power byte-out may partially be explainable as a code-sidelobe effect, which is caused by the way the noise subtraction is done in the applied EISCAT radar program and which we will investigate further. Particularly the power depreciation, which was observed below the strong PMSE is likely resulting from such a sidelobe. It is to be noted in this context, how-

EISCAT UHF RADAR / CUPRI VHF RADAR 1-2 JULY 1988

UT
2308   2315

2340   2347

Z/km
93.1   0009
72.1

0011   0018

0042   0049

⊢ 15 dB ⊢   ⊢ 75 dB ⊢
EISCAT   CUPRI
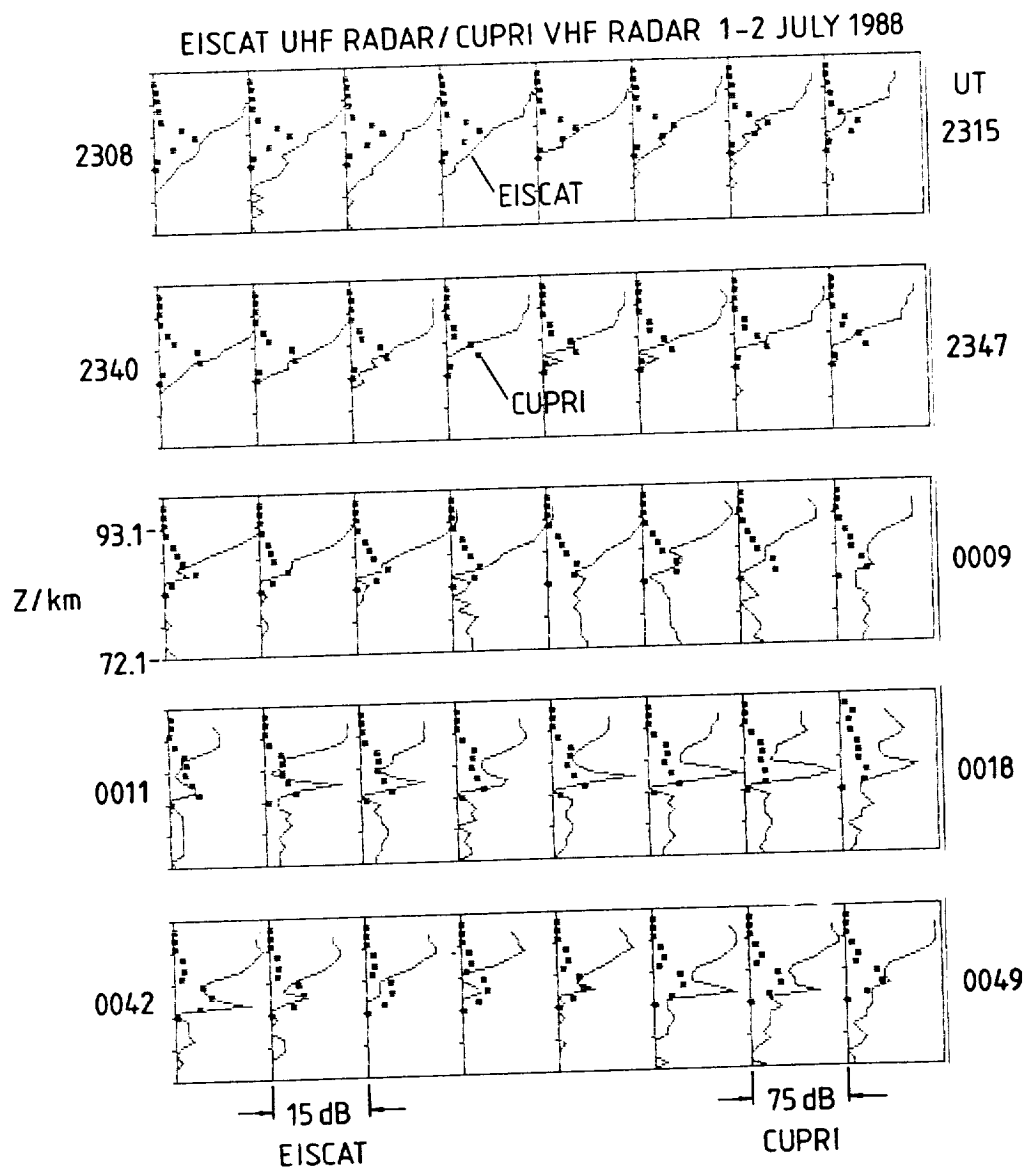
Figure 3. Series of height profiles of power measured with the EISCAT
UHF radar (solid lines) and the CUPRI VHF radar (squares). The
single profiles are averages over 1 minute. The relation of the
logarithmic power scales to estimates of electron density or volume
reflectivity are discussed in the text.

ever, that Ulwick et al. (1988) measured with rockets deep electron density
byte-outs and fluctuations in the polar summer mesosphere which compared well
with simultaneous measurements of PMSE with the Poker Flat MST VHF radar. Such
measurements were also carried out during the MAC/SINE campaign in summer 1987
by comparing the rocket electron density profiles with echo power profiles
measured with the SOUSY VHF radar and the EISCAT VHF radar. These comparisons
also showed a fair agreement (Kelley et al., 1989). We therefore have indica-
tions that the EISCAT UHF radar, in the times when there was no obvious PMSE on
933 MHz and the code-sidelobe effect was small, measured the same kind of elec-
tron density byte-outs as the rockets did.

EISCAT UHF RADAR   Tromsö, Norway

23:07 UT / 1 July 1988   2 July 1988 / 01:07 UT
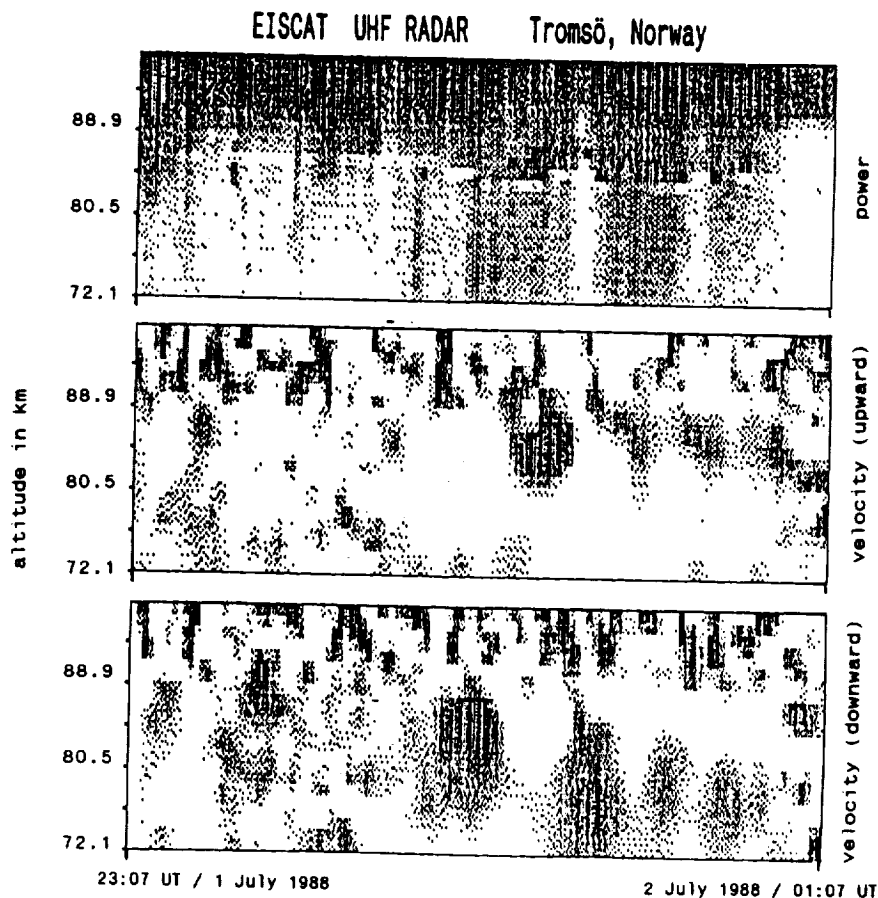
Figure 4. Height-time-intensity plots of echo power (upper panel),
upward velocity (centre panel) and downward velocity (lower panel).
The range of scale between white and black intensities is 15 dB,
+10 m/s and -10 m/s, respectively.

In the lower two panels of Fig. 4 the upward and downward velocity components measured with the EISCAT 933-MHz radar are shown. We see periodicities of 10 to 15 minutes in the vertical velocity. The velocity amplitude apparently peaks around 85-88 km, with a large amplitude of some 10 ms^{-1}. Above this altitude much shorter velocity periods are noted, which also appear more random than those lower down. It looks like that the PMSE occur preferably when the velocity is directed upward. Williams et al. (1989) and Röttger and La Hoz (1989) discuss and interpret these observations and their relation to atmospheric gravity waves in the mesopause region.

A sample set of Doppler spectra for these 933-MHz PMSE is shown in Fig. 5. These spectra are averaged over only 10 seconds, but separated in time by 2 minutes. We see the periodic variation of the Doppler shift and the narrowness of the spectra. The spectral width is partly caused by the varying Doppler shift during the integration period. In any case, it is very evident that these spectra are much narrower as well as stronger than the spectra of the incoherent scatter signal. The latter for instance can be clearly seen in the lowest altitude gate (82.6 km). We therefore find support that these 933-MHz strong and coherent echoes must result from a different mechanism than the conventional incoherent scatter mechanism. The spectra of the 933-MHz PMSE are so narrow that we cannot verify any enhancement of turbulence which would be necessary to explain these echoes to result from conventional turbulence scatter. We thus need another mechanism to explain the PMSE.
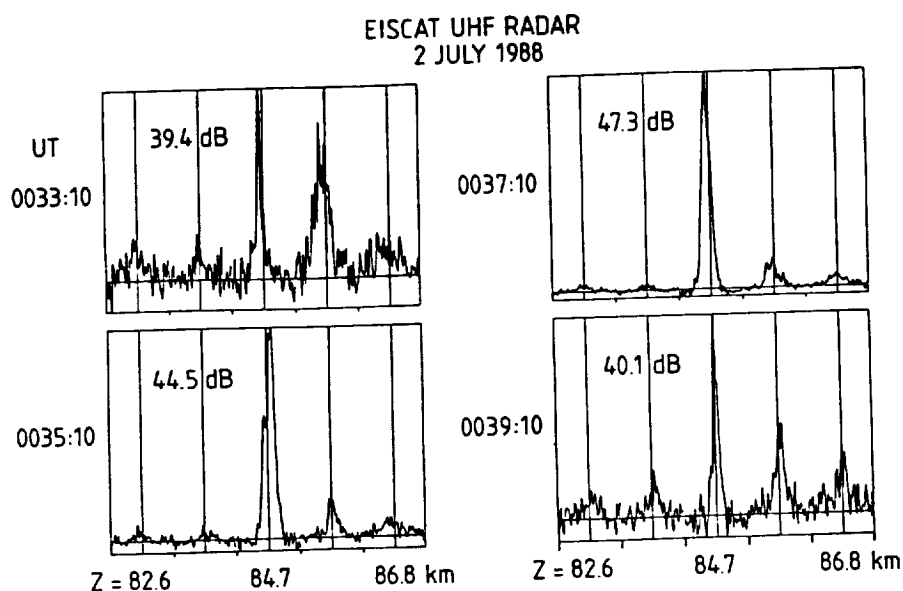
Figure 5. Spectra of UHF radar echoes, showing the strong coherent signal (narrow spectrum) and the weak and wide incoherent scatter signals in the other range gates. The dB-values denote the peak power of the spectra, which is used for single spectrum normalization. The spectra are averages over 10 seconds and display the frequency range between ±225 Hz.

176

INTERPRETATION

In a paper by Röttger and La Hoz (1989) some possibilities for the cause of these polar mesosphere summer echoes and the refractive index irregularities are discussed in some more detail. Here we will briefly summarize some of these possibilities.

Kelley et al. (1987) have noted that the presence of heavy ion clusters, which do occur in the cold polar mesopause, could result in a reduction of the diffusion coefficient although there is not yet a clear theoretical nor experimental basis for this. The reduction of the diffusion could yield electron density fluctuations at spatial scales which are much smaller than those of fluctuations in neutral air turbulence, and could thus explain the enhanced backscatter cross sections or reflection coefficients observed with the VHF and UHF radars. The deviations from the fluctuation spectrum of neutral turbulence can be expressed by the Schmidt number S, which is given by the ratio of the molecular diffusion coefficient v of the neutral air molecules and the molecular diffusion coefficient D of the electrons, which give rise to the scattering process. This means, if D is small in the presence of heavy ions, the Schmidt number is large and the backscatter cross section increases at smaller radar wavelengths. The formation of heavy ions is temperature dependent, i.e. the colder the environment the greater is the likelihood for formation of these heavy ions.

We have not yet analyzed the width of the 933-MHz spectra to search for the narrowing effect of the incoherent scatter spectrum reported by Collis et al. (1988) and Turunen et al. (1988) and interpreted by Kelley et al. to be an indicator for the presence of heavy positive ions and the suggested increase in Schmidt number. We on the other hand would like to add here a word of caution resulting from our observations of the coherent, i.e. non-incoherent scatter, polar mesosphere summer echoes detected on 224 MHz as well as on 933 MHz. It could not be excluded that the reported narrowing of the spectra is nothing else than the superposition of a (weak) coherent echo on top of the incoherent scatter echo. It is known that the mean temperatures in the polar mesopause in summer can be as low as 120 Kelvin and that therefore the chance for the formation of heavy cluster ions is large, but any conclusion on the enhancement of the Schmidt number must still be taken with great care.

It is also known that gravity waves with large velocity amplitudes are observed in the mesosphere. Williams et al. (1989) and have shown observed enhanced vertical velocities of 10 m/s and a relation to PMSE amplitudes was apparent. Although this is not a very common effect, those observations are very interesting, and would help us to understand one of the mechanisms behind the PMSE. We can also note this effect in the displays of Fig. 4.

The velocity magnitude increases gently with some periodicity up to about 85 km altitude and then reduces to almost zero velocity within a few kilometers or so. Above this altitude almost no clear periodic oscillations of the vertical velocity are noticeable. During the time of upward directed velocity coherent echoes are observed at the altitude where the velocity begins to cease. There are scarcely any coherent echoes during periods of downward velocity, rather, only the usual incoherent scatter echoes. This can be proven by evaluating the spectrum width (coherent echoes have an order of magnitude narrower spectrum than incoherent scatter echoes) as well as by trying to deduce electron densities from the echo power, which is far too large in case of the strong power returns from the coherent echoes. These observations are consistent with the idea published by Williams et al. (1989), that the adiabatic cooling during the uplift-phase of a gravity wave oscillation increases the chance for clustering of ions and thus increases the Schmidt number. The latter would result in PMSE

enhancements. It is very intriguing, however, that these PMSE are observed even at the short Bragg wavelength of 16 cm of the 933-MHz radar. Röttger and La Hoz (1989) have pointed out some other possibilities to explain the PMSE, such as localized recombination in the presence of heavy positive ions or charge separation due to electric fields.

CONCLUSION

We have shown that polar mesosphere summer echoes do occur even at 933 MHz and are correlated with the well established polar mesosphere summer echoes detected with concurrent 46.9-MHz radar observations. We have to exclude that turbulence can cause the coherent echoes on 933 MHz, since their extra-ordinary strength would need a huge and extremely unrealistic turbulence intensity, which we on the other hand cannot at all prove from our spectrum width measurements. Kelley et al. (1987) suggested a change in diffusion coefficient in the presence of heavy ions to be a possible cause of the PMSE. Röttger and La Hoz (1989) argue that small-scale gradients of electron density occur due to localized recombination of electrons in the presence of heavy positive ions, which may occur in patches of small scale length in the cold polar summer mesopause. They also propose a mechanism of charge separation in the presence of strong vertical updrafts and background electric fields, which could generate the necessary steep and short-scale electron density gradients. The arising gradients, if they can exist at these small scales (which may be the case in the electron gas but not in the neutral gas), can give rise to scattering and partial reflection of even 933-MHz radar waves. We therefore do not need enhanced turbulence to explain the PMSE on VHF (46.9 MHz) and UHF (933 MHz).

REFERENCES

Collis, P.N., T. Turunen and E. Turunen (1988), Evidence for heavy positive ions at the arctic mesopause from the EISCAT Incoherent Scatter Radar, Geophys. Res. Lett., 15, 148-151.

Czechowsky, P. and R. Rüster (1985), Power spectra of mesospheric velocities in polar regions, Handbook for MAP, 18, 207-211.

Ecklund, W.L. and B.B. Balsley (1981), Long-term observations of the arctic mesosphere with the MST radar at Poker Flat, Alaska, J. Geophys. Res., 86, 7775-7780.

Hoppe, U.-P., C. Hall and J. Rottger (1988), First observations of summer polar mesospheric backscatter with a 224 MHz radar, Geophys. Res. Lett., 15, 28-31.

Kelley, M.C., D.T. Farley and J. Röttger (1987), The effect of cluster ions on anomalous VHF backscatter from the summer polar mesosphere, Geophys. Res. Lett., 14, 1031-1034.

Hoppe, U.-P., C. Hall and J. Röttger (1988), First observations of summer polar mesospheric backscatter with a 224 MHz radar, Geophys. Res. Lett., 15, 28-31.

Kelley, M.C., D.T. Farley and J. Röttger (1987), The effect of cluster ions on anomalous VHF backscatter from the summer polar mesosphere, Geophys. Res. Lett., 14, 1031-1034.

Kelley, M.C., J.C. Ulwick, J. Röttger and B. Inhester (1989), PMSE observations during the EISCAT salvo of MAP/SINE (to be submitted to J. Atmos. Terr. Phys.).

Providakes, .P., W.E. Swartz, D.T. Farley and B.G. Fejer (1983), First VHF auroral interferometer observations, Geophys. Res. Lett., 10, 401-404.

Rishbeth, H., A.P. van Eyken, B.S. Lanchester, T. Turunen, J. Röttger, C. Hall and U.-P. Hoppe (1988), EISCAT VHF radar observations of periodic mesopause echoes, Planet. Space Sci., 36, 423-428.

Röttger, J. (1989), The instrumental principles of coherent and incoherent scatter radars and the configuration of radar system hardware, Handbook for MAP (in press).

Röttger, J. and C. La Hoz (1989), The fine-structure of Doppler spectra and signal power characteristics of polar mesosphere summer echoes (PMSE) observed with the EISCAT 224-MHz radar, (submitted to J. Atmos. Terr. Phys.).

Röttger, J., M. Baron and K. Folkestad (1983), Capabilities and limitations of EISCAT as an MST radar, Handbook for MAP, 9, 305-314.

Röttger, J., C. La Hoz, M.C. Kelley, U.-P. Hoppe and C. Hall (1988), The structure and dynamics of polar mesosphere summer echoes observed with the EISCAT 224 MHz radar, Geophys. Res. Lett., 15, 1353-1356.

Turunen, E., P.N. Collis and T. Turunen (1988), Incoherent scatter spectral measurements of the summertime high-latitude D-region with the EISCAT UHF radar, J. Atmos. Terr. Phys., 50, 289-299.

Turunen, T. (1986), GEN-system - a new experimental philosophy for EISCAT radars, J. Atmos. Terr. Phys., 48, 777-785.

Ulwick, J.C., K.D. Baker, M.C. Kelley, B.B. Balsley and W.L. Ecklund (1988), Comparison of simultaneous MST radar and electron density probe measurements during STATE, J. Geophys. Res., 93, 6989-7000.

Williams, P.J.S., A.P. van Eyken, C.M. Hall and J. Röttger (1989), Atmospheric gravity waves and modulations in the polar mesospheric summer echoes as observed with the EISCAT 224-MHz radar (submitted to Geophys. Res. Lett.).

MULTIFREQUENCY STRATOSPHERE AND TROPOSPHERE (ST) STUDIES AT MILLSTONE HILL: MOTIVATIONS AND PRELIMINARY RESULTS

Stephen A. Cohn

Haystack Observatory
Massachusetts Institute of Technology
Westford, MA 01886 USA

ABSTRACT

The capability to nearly simultaneously observe turbulent backscatter in the stratosphere and troposphere at three wavelengths is being developed using radars at Millstone Hill. In addition to the UHF (68cm) radar previously used for lower atmospheric turbulence studies, fully steerable dish antenna radars operating at L-band (23cm) and X-band (3cm) are being upgraded to allow ST measurements. Observing a common scattering volume with three widely separated wavelengths provides a unique opportunity to study the scale dependence of several properties of atmospheric turbulence. In particular the wavelength dependence of backscattered intensity can be measured and compared with that expected for a Kolmogorov-type spectrum of turbulence. Such an experiment, planned to make use of this unique capability, is discussed and some initial measurements are presented.

THEORY

The expression for the wavelength dependence of radar reflectivity, η, of a turbulent atmosphere is theoretically well established (e.g. OTTERSTEN, 1969)

$$\eta(\lambda) = 0.38 \, C_n^2 \, \lambda^{(-1/3)}$$

where C_n^2 is the refractive index structure constant (independent of wavelength), and λ is the radar wavelength.

This expression is derived by applying Tatarski theory for a wave propagating in a medium of random refractive index to a Kolmogorov spectrum of turbulence. Departure from this power law would indicate departure from the one dimensional power spectral density, $S(\lambda)$, expected for Kolmogorov-like turbulence, $S(\lambda) \propto k^{(-5/3)}$, where k is wavenumber. Measurements of η at three wavelengths could establish an observed power law to compare with this theoretical one. Also, such measurements could differentiate between the several possible scattering mechanism. If, for example, the returned power was due to reflection from insects, as Rayleigh scatterers the wavelength dependence would be $\eta \propto \lambda^{-4}$. The considerable difference between these dependencies on λ would be easily measurable.

MOTIVATIONS AND PREVIOUS WORK

In the 1960's three radars at Wallops Island, Virginia were available for experiments very similar to the ones planned at Millstone Hill. A number of studies were carried out using wavelengths of 71.5cm, 10.7cm, and 3.2cm (e.g. HARDY et al., 1966, HARDY and KATZ, 1969). The investigators found two types of returns, attributed to turbulence and insects. However, at the 3.2cm wavelength only insects were detected. It is possible that the X-band radar lacked the sensitivity needed to observe turbulence. Using data from the two longer wavelength radars, it was determined that the radar reflectivity of the turbulence had very little wavelength dependence, consistent with the $\lambda^{-1/3}$ power law predicted for a Kolmogorov-type spectrum.

Aside from the measurements at Wallops Island, no experiment similar to that planned at Millstone Hill has been attempted. However, the need for such an experiment has been emphasized in the intervening years. Discussion at the May, 1983 Workshop on Technical Aspects of MST Radar held in Urbana, Illinois recognized the importance of multiple frequency radar observations to the understanding of atmospheric turbulence and interpretation of MST radar data and recommended that such an experiment be carried out (LIU, 1983). More recently, discussion at the November, 1987 Battan Memorial Conference on Radar Meteorology suggested such an experiment and led to a feasibility test at Millstone Hill.

A number of features of the Millstone Hill site make it well suited to carry out a multifrequency experiment. First, of course, is the presence of the three high powered radars with appropriate wavelengths. Second is the steerability and narrow beam width of all three systems (see table 1). Finally, the large gain of the X-band radar (one of the most sensitive 3cm radars in the world) should permit probing of the turbulence close to its dissipation scale.

180

PRELIMINARY RESULTS

A test of the radar configuration in August, 1988 provided an opportunity to collect some data from each of the three systems. Although the power returned to each radar is at present uncalibrated, it is possible to compare the line of sight wind speeds measured by each system to confirm that each is indeed receiving and correctly processing the turbulence backscatter. Figure 1 shows a time series of wind speed measurements at each of five altitudes over a period when all radars collected data. The consistency of the wind speed from one measurement to the next with a single radar, and agreement between the three radars lend confidence that the measurements are valid. Signal power in arbitrary units is similarly displayed in figure 2. Since it is uncalibrated only self-comparison of measurements taken with a single radar is meaningful. Again the consistency gives no reason to doubt the measurement. For both velocity and power, however, values obtained with the X-band radar have larger variability from one measurement to the next than the other two systems.

Examination of the power spectra, from which velocity and signal power are derived, shows an unexpected feature. While the UHF and L-band spectra appear typical, the X-band spectra often consist of a number of spikes over a range of doppler frequencies rather than a continuous, Gaussian-like peak (figure 3). Further investigation will be needed to see if this is a technical problem or a result of geophysical significance. A few possible explanations that will be examined include 1) the spikes are returns from discrete targets (e.g. insects), 2) the 1.5cm Bragg scale is less than the turbulent dissipation scale at the observed altitudes so only some spots within the pulse volume provide backscatter, 3) an instrument problem could be corrupting the signal.

CONCLUSIONS AND FUTURE EMPHASIS

The feasibility test which produced the data presented here successfully demonstrated the following: 1) each of the three radars at Millstone Hill can be operated in an ST mode, 2) the UHF and L-band radars can receive turbulent backscatter, 3) the X-band radar receives backscattered power, possibly from both turbulence and hard targets, doppler shifted to the wind velocity, and 4) data collection can be cycled between the radars providing measurements at three wavelengths on time scales of less than 30 minutes.

The main emphasis in the near future will be on calibration of the radar power, on understanding the form of the X-band radar's spectra, and on collecting data to test the scale dependence of lower atmospheric turbulence.

Table 1
CHARACTERISTICS OF THE MILLSTONE HILL RADARS

		UHF Steerable	L-band	X-band
Wavelength	(m)	0.68	0.23	0.03
Diameter	(m)	46	26	37
Peak Power	(MW)	2.5	2.5	0.3
Gain	(dB)	46	47	67
System Temp	(K)	120	150	250
Beamwidth	(deg)	1.0	0.6	0.06

REFERENCES

Hardy. K.R., D. Atlas, and K.M. Glover, Multiwavelength backscatter from the clear atmosphere, *J. Geophys. Res.*, *71*, 1537, 1966.

Hardy, K.R., and I. Katz, Probing the clear atmosphere with high power, high resolution radars, *Proc. IEEE*, *57*, 468, 1969.

Liu, C.H., Interpretation of MST radar returns from clear air (Keynote paper), *MAP Handbook*, *9*, 49, 1983.

Ottersten, H., Atmospheric structure and radar backscattering in clear air, *Radio Sci.*, *4*, 1179, 1969.
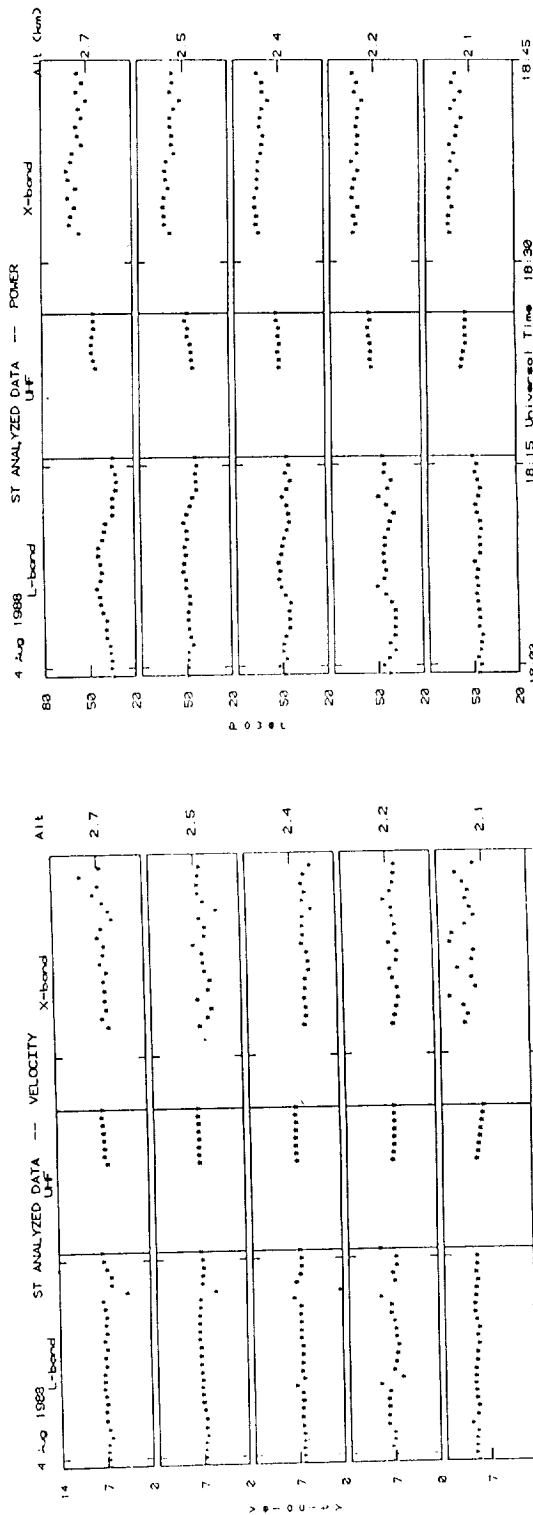
Figure 1. Wind speed as measured by the three radars

Figure 2. Intensity (uncalibrated) as measured by the three radars
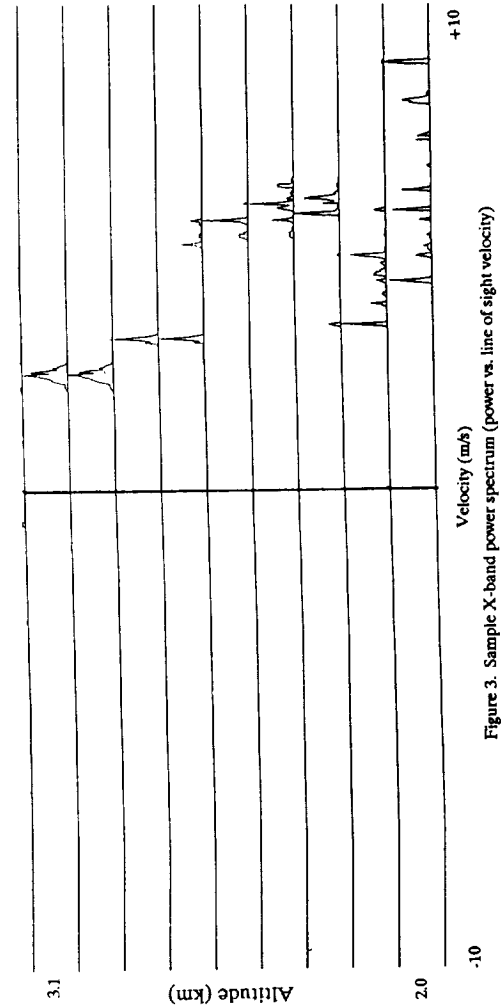
Figure 3. Sample X-band power spectrum (power vs. line of sight velocity)

USE OF TWO WIND PROFILERS FOR PRECIPITATION STUDIES

P. E. Currier

Aeronomy Laboratory
National Oceanic and Atmospheric Administration
Boulder, Co 80303

S. K. Avery

Cooperative Institute for Research in Environmental Sciences and
Department of Electrical and Computer Engineering
University of Colorado, Boulder, Co 80309

I. Introduction:

Two profilers were colocated at the Flatland Radar Site (near Champaign, Illinois) for coordinated observations during May and June of 1988. The following data was taken during the passage of a storm containing two rain bands. The operating parameters of these radars were

The 50 MHz profiler:

> 50 kw peak, 310 w average;
>
> 750 meter resolution;
>
> 128 point FFT;
>
> no spectral averaging.

The 915 MHz profiler:

> 300 w peak, 6 w average;
>
> 150 meter resolution;
>
> 64 point FFT;
>
> spectral averaging: 3 to 25 spectra;
>
> additional ground data included: surface rain rates, surface wind speed/direction, surface pressure, relative humidity, temperature.

II. The 915 MHz Profiler:

In clear air the UHF profiler's maximum range is approximately 2.5 km. While in the presence of precipitation it is closer to 9 km.

Assuming Raleigh scattering, the rain drop cross section is proportional to d^6/λ^4 (d: drop diameter; λ: radar wavelength). Thus the rain drop cross section is 52 dB higher at 915 MHz than at 50 MHz. This return completely overwhelms the clear air echos. With this sensitivity it is possible to study the evolution of precipitation from snowflakes/ice to rain, from 9 km in altitude down to 100 meters. To be able to determine a rain Drop Size Distribution (DSD), terminal fall speeds of the rain drop must be determined. Various methods have been used to infer vertical air motions from measured precipitation fall speeds. These methods require a priori assumptions about the DSD (SANGREN, 1984) or are empirical (JOSS, 1970) and not precisse enough (ATLAS, 1973).

III. The 50 MHz Profiler:

Because of the 915 MHz radar's inability to get clear air returns in the presence of precipitation, the 50 MHz capability to measure clear air is necessary. This data can then be used to correct the fall speeds mesured by the UHF profiler for updrafts and downdrafts.

At 50 MHz the simultaneous measurement of precipitation and clear air returns have been used to determine DSDs (FUKAO, 1985; WAGASUKI, 1987). However, at the melting later it is difficult to separate the two returns. Also, in the presence of clear air returns, ice particles do not have sufficient reflectivity to be detected at 50 MHz. Thus, DSDs determined from a 50 MHz radar are limited to certain meteorological conditions (rain rather than ice or melting snow).

IV. The Data:

This data was taken on May 23 1988 at 3:15:30 UT, during the passage of the second rain band. These spectra were chosen because of the presence, in the clear air, of both a downdraft (below 5 km) and an updraft at 7 km. The convention for vertical motions is reversed in figure 1.a (915 Mhz profiler: downward motions have positive velocities) from that of figure 1.b (50 MHz radar: downward motions have negative velocities). The velocity scales for the two spectra are essentially the same (15.13 m/s for the UHF versus 15.17 m/s for the VHF). The hydrometeors' fall velocities as seen in figure 1.a are the superposition of the drop's terminal fall velocity, vertical air motion and turbulence. In figure 1.b the maximum updraft/downdraft is approximately 1.5/1.0 m/s. Vertical air motions of this magnitude if not taken into account would severely bias the DSD obtained by the 915 MHz radar. It would be difficult to obtain a DSD from the 50 MHz profiler under these conditions (return from the rain is very weak compared to the clear air), and above 4 km there is no evidence of returns from the ice/snow.

V. Conclusion:

The 915 MHz profiler is well suited for the study of hydrometeors: high sensitivity to hydrometeors and excellent height coverage. This gives an unique opportunity to study the evolution of precipitation from snowflakes/ice to rain. Unfortunately the clear air information is absolutely necessary, and requires a 50 MHz profiler.

REFERENCES:

Atlas, D., R. C. Srivastava and R. S. Sekhon, Doppler radar characteriscs of precipitation at vertical incidence, Rev. Geophys. Space Phys.,11,1-35, 1973.

Fukao, S., K. Wakasugi, T. Sato, S. Morimoto, T. Tsuda, I. Hirota, I. Kimura, and S. Kato, Direct measurement of air and precipitation particle motion by very high frequency Doppler radar, Nature, vol. 316,712-714, 1985.

Joss, J. and A. Waldvogel, Raindrop size distributions and Doppler velocities, 14th Radar Meteor. Conf., Tuscon, Ariz., A. M. S., Boston,153-155, 1970.

Sangren, K. L., P. S. Ray and G. B. Walker, A comparison of techniques to estimate vertical air motions and raindrop size distributions, J. Atmos. Oceanic Technol.,1,152-165, 1984.

Wakasugi, K., A. Mizutani, M. Matsuro, S. Fukao and S. Kato, Further discussion on deriving drop size distribution and vertical air velocities directly from VHF Doppler radar spectra, J. Atmos. Oceanic Tech.,vol. 4,170-179, 1987.

184

Figure 1.b: spectrum from 50 MHz radar.
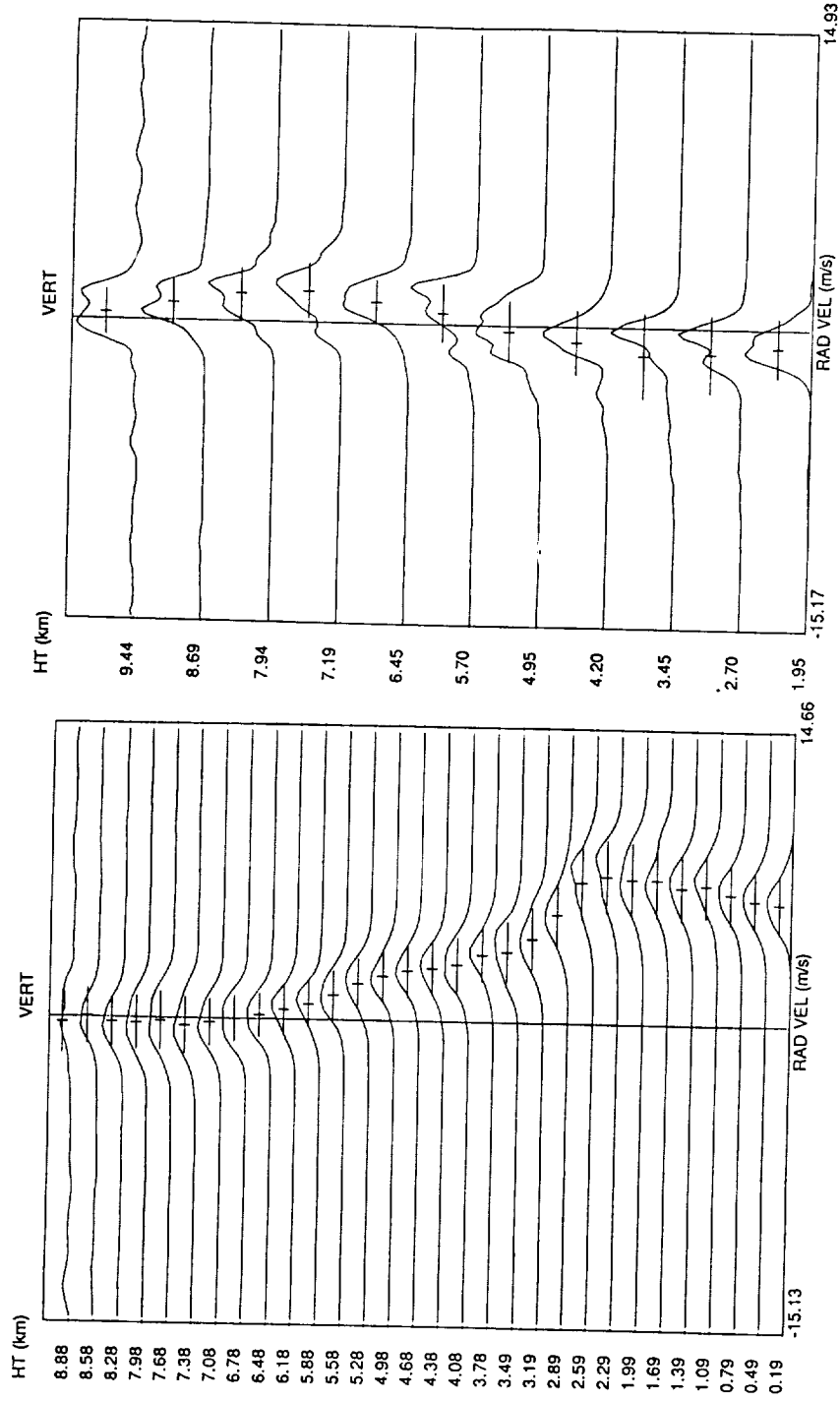
Figure 1.a: spectrum from 915 MHz radar.

SPATIAL INTERFEROMETRY MEASUREMENTS
WITH THE EISCAT VHF RADAR

C. La Hoz, J. Röttger[†]
EISCAT Scientific Association
P.O. Box 812, S-981 28 Kiruna, Sweden
([†] on leave from Max-Planck-Institut für Aeronomie)

S.J. Franke
University of Illinois
Urbana, 61801 Ilinois, USA

0. ABSTRACT

The EISCAT VHF radar system with its multiple beam antenna lends itself in a near optimum way for applications of spatial interferometry. At a wavelength of 1.339 metres and employing a configuration with two half antennas, the spatial displacement per degree of phase difference is 5.269 metres at 85 km altitude. Thus, for example, a transverse (to the antenna beams) velocity of 10 ms^{-1} would produce a change in the phase of the coherence function of 1.9 degrees per second. For typical integration times of the coherence function of 20 seconds, the phase smearing amounts to less than 40 degrees.

In a recent campaign carried out to investigate the Polar Mesosphere Summer Echoes—or PMSE (RÖTTGER et al., 1988)—we have made the first spatial interferometer measurements at EISCAT. The experiment was on July 5th 1988 11:30 to 15:15 UT and was characterised by mostly weak PMSE. Meaningful values of the coherence function amplitude (≥ 0.7) occurred only sporadically and were not sufficient to make estimates of the transverse velocity. The inference is that during this experiment the irregularities that cause the scattering were diffuse within the antenna beams for most of the time. However, the few cases when the coherence was close to one and the phase well organised within distinct frequency intervals demonstrates that discrete scatterers within the antenna beams do exist and that the radar spatial interferometer technique has a promising future at EISCAT.

1. INTRODUCTION

The radar interferometer technique that we implemented recently at EISCAT and is described here was developed at the Jicamarca Radar Observatory by FARLEY et al. (1981) and WOODMAN (1971). It has proven to be a powerful technique to study two-dimensional plasma turbulence in the ionosphere. The mentioned authors and their collaborators have used it extensively to investigate plasma turbulence in the equatorial and polar electrojets and in the equatorial F region.

The application of the radar interferometer technique to turbulence in the middle atmosphere is relatively new. FARLEY (1983) gives a complete and interesting account of previous attempts—most seem to have failed—to apply the interferometer technique to MST measurements. RÖTTGER and IERKIC (1985) seem to have been the first to employ this technique successfully in a study to compare their results with other traditional and less informative methods in applications to the stratosphere and mesosphere. A technique that is akin to the radar interferometer technique is the spaced antenna drift (SAD) technique that is described for example by HOCKING (1983), RÖTTGER (1983), BRIGGS (1984), and additional references therein. FARLEY (1983) has described the differences and similarities between the two techniques, as well as WOODMAN (1989) in this handbook. We may state succintly as a reference that the essential property of the radar interferometer technique is the measurement of the *relative phase* between the signals from the two intersecting antennas. In a more sophisticated version of the technique this phase measurement is done as a function of Doppler frequency through the use of the coherence function. In the simplest and so far most useful model of discrete scatterers that move at different radial velocities, the phase information can be readily

transformed successively into angle of arrival, transverse localisation, and transverse velocity, and the amplitude information into angular spread, transverse size, and transverse decay (or growth) rate.

Following FARLEY et al. (1981), the coherence function of the two received signals from antennas A and B separated by a distance d at their phase centers is:

$$S_{AB}(\omega) = \frac{\langle V_A(\omega) V_B^*(\omega) \rangle}{\langle |V_A(\omega)|^2 \rangle^{1/2} \langle |V_B(\omega)|^2 \rangle^{1/2}}$$

where V_A and V_B are the complex amplitude spectra (not power spectra) of the signals from antenna A and antenna B respectively, and the asterisk denotes complex conjugate.

For the simple model referred above of a discrete scatterer moving with a radial component of its velocity corresponding to an angular frequency ω, a transverse angular position $\bar{\theta}_\omega$, and an r.m.s. angular width of σ_ω, the coherence function is:

$$S_{AB}(\omega) = e^{ikd\bar{\theta}_\omega} exp(-\frac{1}{2}k^2 d^2 \sigma_\omega^2)$$

where k is the radar wave vector and i is the imaginary unit. The phase of the coherence function, $\delta\phi = kd\bar{\theta}_\omega$, at altitude h and angular frequency ω is related to the transverse position δx of the scatterer by:

$$\frac{\delta x}{\delta\phi} = \frac{h}{kd} = \frac{ch}{2\pi f d}$$

where f is the radar frequency and c the velocity of light. For the VHF radar at EISCAT, $f = 224$ MHz and $d = 60$ m (see Figure 1), and the above expression becomes:

$$\frac{\delta x}{\delta\phi} = 3.552 \times 10^{-3} h$$

As an example, the altitude of our mesospheric applications is typically around 85 km:

$$\frac{\delta x}{\delta\phi} = 5.269 \, m/degree$$

A transverse (horizontal) velocity of 10 m/s of a discrete scatterer will be measured as a change of phase at a rate of 1.9 degrees/s. The half power width of each antenna is about 1.2 degrees, or 1800 m at 85 km altitude, and the scatterer moving at 10 m/s will cross the beam in 180 seconds. The phase will fold by 2π in about 190 seconds. At EISCAT we have obtained individual samples of spectra and coherence functions at about every 2 sec giving a spectral resolution of 0.50 Hz which is equivalent to $0.33 ms^{-1}$ at 224 MHz (see below). Typical integration times are 5-10 spectral samples (10-20 sec) to give reasonable statistical stability. Thus, the "phase averaging" [1] amounts to ~20-40 degrees per integration period. Under these conditions we will still get 18-9 spectral samples per beam transit time, and 20-10 spectral samples before aliasing occurs. If the transversal velocity is substantially higher than $10 ms^{-1}$, the discouraging situation described by FARLEY (1983) will occur, and the technique, if it includes "frequency sorting", may fail. Depending on actual values, it may still be possible to obtain useful results by renouncing frequency decomposition of the phase difference and

[1] This "phase averaging" may become "phase broadning"—and thus be visible—if a narrow Doppler line "walks" in frequency (line broadning) due to the combined effect of an axial acceleration of the scattering center and a "long" integration time. This effect may explain the peculiar linear progression of the phase of the coherence seen by FARLEY et al. (1981) occasionally in the equatorial electrojet.
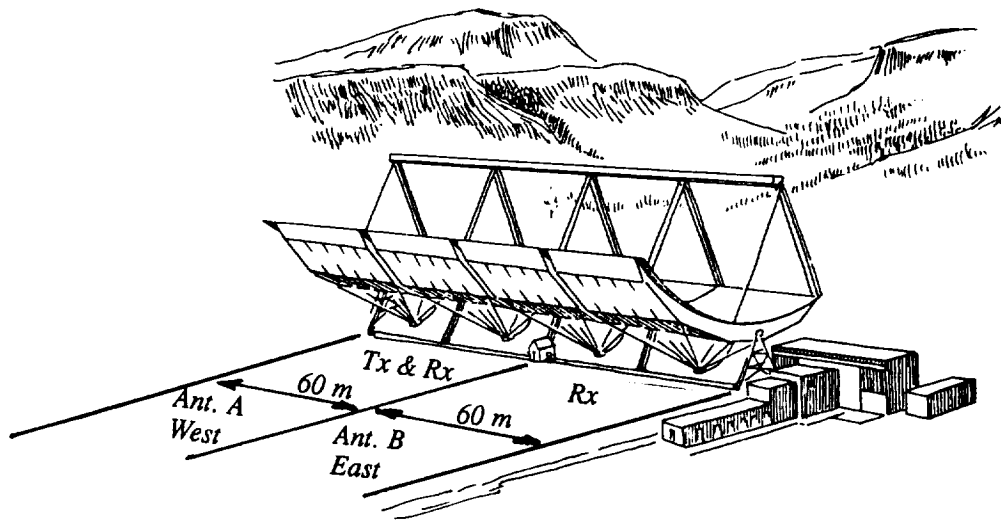
Fig. 1. The EISCAT VHF antenna: Interferometer configuration.

be happy with estimates of the phase difference in the time domain through the cross-correlation function at zero time delay as explained by FARLEY (1983).

2. THE EXPERIMENT

The EISCAT radars are described in this handbook in the paper by LA HOZ et al. (1989) and in additional references therein. The experiment was carried out during the EISCAT PMSE campaign in summer 1988. A frequency interferometer experiment was also carried out during this campaign (FRANKE et al., 1989). For the spatial interferometer experiment we employed the VHF radar in Mode II. See Figure 1. One transmitter was connected to one of the two half antennas, and phase coherent receivers were connected to both half antennas. The two antennas were pointed along the vertical direction throughout the experiment that took place on July 5th 1988 at 11:30 to 15:15 UT. Since the axes of the antennas are parallel and separeted by 60 m along the geomagnetic E-W direction (very close to the geographic E-W), they do not overlap completely. The E-W half power beam width of 1.2 degrees at 85 km translates into about 1800 m and the overlap length is then 1800-60=1740 m or about 97% in linear dimension.

The transmitter modulation employed was a pair of complementary codes of length 32 with a baud length of 2 μs giving a range resolution of 300 m. The first gate was taken at 80 km, the number of gates was 30, and the last gate was at 89 km. The real time processing consisted of decoding and coherently integrating the digitised signals. Coded pulses were transmitted every 4902 μs and the signals from 6 transmissions (including the complementary pair) were coherently integrated after decoding to give an effective sampling period of 29412 μs or a bandwidth of $\pm$17 Hz, or in units of Doppler velocity $\pm$11.4 m/s. The data were organised in records containing two seconds of data and subsequently stored in tape.

The calculation of the amplitude and power spectra and the coherence function of the two time series was done off line. The data were organised in time segments 1882 ms long containing 64 complex samples. A fast Fourier transform (FFT) routine was applied to these segments resulting in complex amplitude spectra with frequency resolution of 0.53 Hz, or in units of Doppler velocity 0.36 m/s. Power spectra and the coherence function were subsequently calculated and the results integrated for 20 seconds.

SP-EI-SDI1-V   05/JUL/88
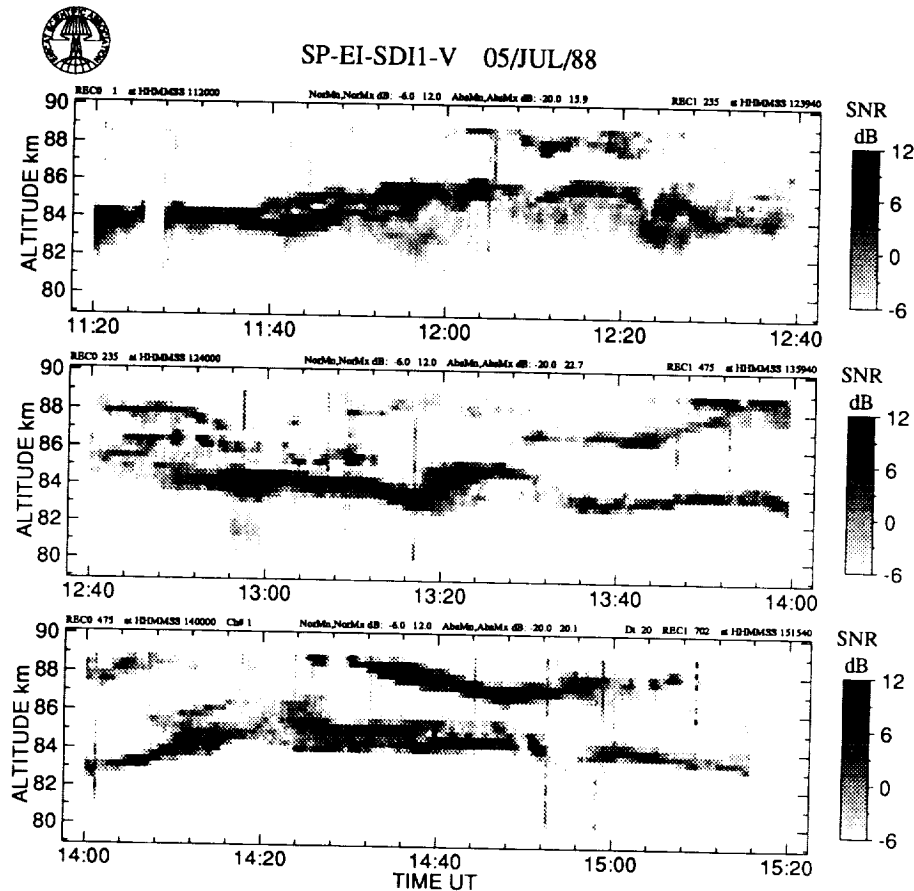
Fig. 2. Gray-scale power map measured with antenna A

3. RESULTS

Figure 2 shows the development of the PMSE as a grey scale plot of the total power as a function of altitude and Universal Time. In this figure, each time slice of 20 s has been self-normalised in order to enhance the contrast of the resulting image. These PMSE were rather weak and formed a thin layer of about 1 km or less in thickness and moved slowly between 83 and 85 km of altitude. During some periods there is a second layer at 87 km and higher up, and at about 12:45 UT even three layers can be seen.

Figure 3 shows the amplitude of the coherence in a format identical to that of Figure 2. Discrete scatterers were considered to be present when the amplitude of the coherence function was 0.7 or greater. Amplitudes less than 0.7 are plotted as a uniform light grey background. It can be seen that occurrence of discrete scatterers are very irregular and of very short duration. In most cases their life time was at most equal to the integration time of 20 s.

Figure 4 shows one example of the phase and amplitude of the coherence function and the power spectra of the two signals. This event lasted three integration periods, although we show here only the first two. Within a distinct interval of Doppler frequencies that coincides with sharp peaks in the power spectra, the amplitude of the coherence reaches a value of 0.9, and the phase is more or less constant, around 3 radians. It is clear from the figure that it is not possible to estimate the rate

C - 3
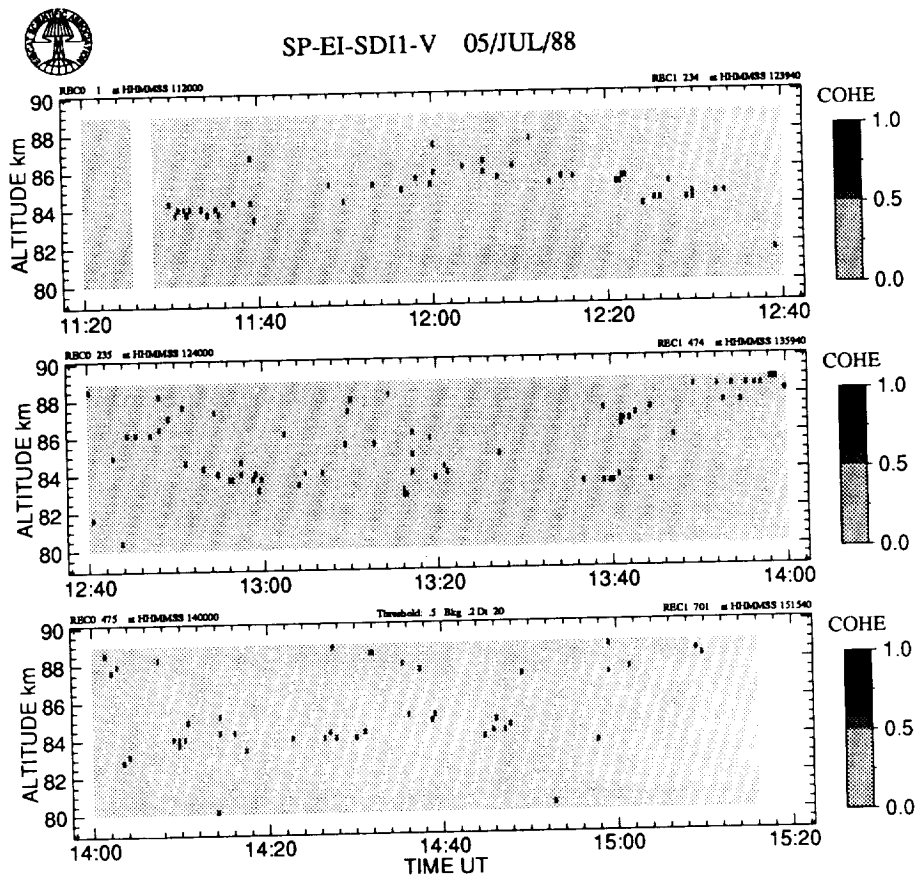
Fig. 3. Grey-scale coherence function as function of time and altitude

of change of the phase with reasonable reliability, and this holds also when taking into account the third period of the event. We surmise that the transverse velocity of the scatterer was small. Had the lifetime of the scatterer been longer, we may have been able to estimate the transverse velocity.

We also note that the signal to noise ratio in the two periods of Figure 4 is 3.62 and 3.86 dB. These values are representative of the values obtained during most of the duration of this particular run. The majority of the other experiments we carried out during this campaign had much higher intensities, sometimes up to 40 dB of SNR. Unfortunately, we ran the spatial interferometer experiment only on this occation. We hope to repeat it next year.

4. CONCLUSIONS

We have shown that the parameters of the EISCAT VHF radar, particularly the frequency and the antenna configuration, suit very well for spatial interferometer applications at mesospheric altitudes. A test experiment was carried out in the summer of 1988 during a campaign to investigate the Polar Mesospheric Summer Echoes. The results obtained have proven our contention. Further, during this experiment, the irregularities that produce the scattering were diffuse within the scattering volume during most of the time. Discrete scatterers were present only sporadically, and then their life time was probably less than the integration time of 20 seconds. In one event when a discrete scatterer was present for about 1 minute, the phase of the coherence function changed very little indicating
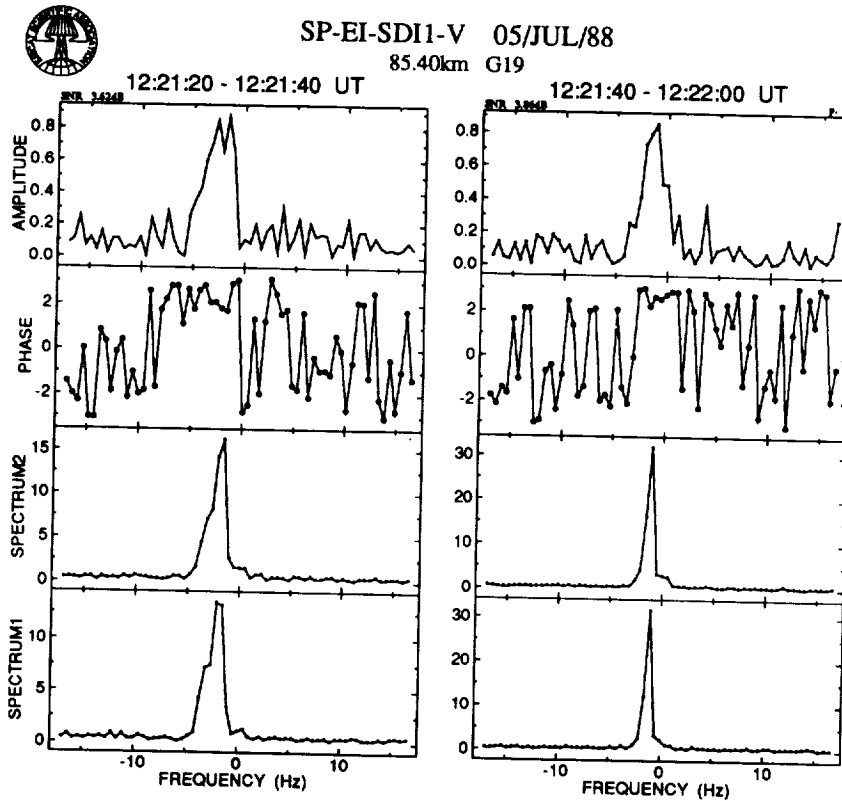
Fig. 4. Amplitude and phase of the coherence function for two consecutive time intervals.

a very small E-W velocity of the scatterer. The characteristics of this experiment were somewhat unsual when compared to experiments on other days during the same campaign in that the PMSE layer was rather thin, stable and weak. We plan to carry out more experiments to test whether the occurrence of discrete scatterers is correlated to the intesity of the scattering or whether the scattering irregularities at 66 cm (one half the wavelength of the EISCAT VHF radar) have the property of being homogeneous in the horizontal dimension.

5. ACKNOWLEDGMENTS

6.REFERENCES

Briggs, B.H. (1984), The analysis of spaced sensor records by correlation techniques, Handbook for MAP, Vol. 13, Ed. Bowhill and Edwards, 166-186.

Farley, D.T., H.M. Ierkic and B.J. Fejer (1981), Radar interferometry: A new technique for studying plasma turbulence in the ionosphere, *J. Geophys. Res.*, *86*, 1467-1472.

Farley, D.T. (1983), Radar interferometer measurements, *Handbook for MAP, Vol. 9*, Edit. Bowhill and Edwards, 237-240.

Franke, S.J., C. La Hoz, J. Röttger and C.H. Liu (1989), Frequency domain interferometry of PMSE, this issue.

Hocking, W.K. (1983), The spaced antenna drift method, *Handbook for MAP, Vol. 9*, Edit. Bowhill and Edwards, 171-186.

La Hoz, C., J. Röttger, M.C. Rietveld, G. Wannberg and S. Franke (1989), The status and planned developments of EISCAT in mesosphere and D-region experiments, this issue

Röttger, J., C. La Hoz, M.C. Kelley, U.-P. Hoppe and C.M. Hall (1988), The structure and dynamics of polar mesosphere summer echoes observed with the EISCAT 224 MHz radar, *Geophys. Res Lett.*, *15*, 1353-1356.

Röttger, J., and H.M. Ierkic (1985), Postset beam steering and interferometer applications of VHF radars to study winds, waves, and turbulence in the lower and middle atmosphere, *Radio Sci.*, *20*, 1461-1480.

Woodman, R.F. (1971), Inclination of the geomagnetic field measured by an incoherent scattering technique, *J. Geophys. Res.*, *76*, 178-184.

SPATIAL INTERFEROMETER MEASUREMENTS WITH THE CHUNG-LI VHF RADAR

J. Röttger*
EISCAT Scientific Association
S-981 28 Kiruna, Sweden
(*on leave from Max-Planck-Institut für Aeronomie)

C.H. Liu
Univ. of Illlinois
Urbana-Champaign, IL, USA

I-J. Fu and C.J. Pan
National Central University
Chung-Li, Taiwan/R.O.C.

ABSTRACT

The Chung-Li VHF radar consists of three separate transmitting-receiving antenna systems and thus allows an optimum application of interferometer and incidence angle measurements of radar echoes from the troposphere and the stratosphere. We describe here first measurements of cross spectra and the corresponding phases, which vary as function of frequency due to a mean wind. We also present first incidence angle measurements and show that the scattering-reflection structures in the troposphere can be inclined to the horizontal by about two degrees. We also notice a periodic change of the tilt as well as the vertical velocity as function of altitude which we attribute to lee waves.

INTRODUCTION

MST radars are usually operated in the Doppler mode, where several antenna beam directions are used to deduce the three-dimensional wind velocities from the Doppler spectrum. Occasionally also the so-called spaced antenna mode is applied to deduce the wind velocity from the cross correlation analysis of signals received at separate antennas (see for instance Röttger and Larsen (1989) for details). Both these methods of course allow the measurement of some additional parameters, such as the signal power, the coherence time, the angular dependence or the spatial coherence as well as the amplitude distribution functions. These are useful parameters to study the scattering/reflection mechanism. Neither the Doppler nor the spaced antenna method need the measurement of the spatial distribution of the signal phases on the ground. In this paper we will point out some advantages of amplitude and phase measurements with a spaced antenna set-up and prove the applicability of this radar interferometer method to deduce additional signal parameters, which the conventional Doppler and spaced antenna methods cannot supply.

In accordance to the term frequency domain interferometry, applied by Kudeki and Stitt (1987), we call the here applied method the spatial domain interferometry (see Röttger and Larsen, 1989) or simply spatial interferometry. It allows for instance to measure the angular spectrum (i.e., the aspect sensitivity, e.g. Vincent and Röttger, 1980), the incidence angle, the corrected vertical and horizontal velocity as well as to determine horizontal phase velocities of atmospheric gravity waves and to track turbulence blobs. The latter measurements were done by Röttger and Ierkic (1985) with the 53.5-MHz SOUSY-VHF-Radar, who applied the post-beam-steering and the cross spectra analysis to study waves and turbulence in the stratosphere and the mesosphere, respectively. The original

method of cross spectrum and coherence analysis was developed and applied by Farley et al. (1981) to study scattering from E-region irregularities with the 50-MHz Jicamarca VHF radar. This method recently was also applied by La Hoz et al. (1989) to investigate polar mesosphere summer echoes with the 224-MHz EISCAT VHF radar. In the present paper we present first interferometer measurements of the troposphere and lower stratosphere obtained with the 52-MHz Chung-Li VHF radar.

At the beginning of this paper we show first examples of amplitudes and phases of cross spectra of tropospheric and lower stratospheric VHF radar echoes, from which the incidence angle can be deduced as function of Doppler shift. The second part of this paper deals with the mean incidence angle measurements, from which the mean tilt or inclination angle of the scattering/reflecting medium or the inclination of barotropic surfaces can be deduced and the relevance of "vertical" velocity estimates can be inferred (e.g., Röttger, 1984a). We also will discuss results obtained from the coherent addition of signal amplitudes received at spaced antennas, which yields indications on the scattering-reflection mechanism as well as increases the signal-to-noise ratio. The angle of arrival statistics, which could be obtained from Doppler sorting of singular returns, will lead to more differentiated understanding of the scattering-reflection mechanism as discussed by Röttger (1984b). Detailed investigations of the latter procedures and the analysis of cross spectra will be described in a separate paper.

EXPERIMENTAL SET-UP

The data presented in this paper were taken with the Chung-Li VHF radar in Taiwan, which is operated on 52 MHz (see brief description by Brosnahan et al., 1983; Chao et al., 1986). This radar is a dual-mode radar, i.e. it allows the application of the Doppler mode with vertical and four off-vertical antenna beams at 16.7° zenith angle as well as the spaced antenna mode with three separate antenna modules. Each of these modules consist of 64 Yagi-antennas, which are fed by three phase-coherent transmitters. The beam width of a single module is 7 degrees and that of the combined 3x64 Yagi modules about 5 degrees. Three phase-coherent receiver channels allow the separate and simultaneous quadrature detection and digital acquisition of signals from the three antenna modules. The six quadrature components were analysed off-line in terms of cross spectra and mean phase differences between the antennas.

During the first test runs the radar was operated with one transmitting and two receiving antennas and 600 m altitude resolution. The following runs were done with the full capability of three phase-coherent transmitters and three complex receiving channels. In the latter run a single pulse of 2 µs duration was transmitted with a transmitter duty cycle of 1% and 40 kW peak power of each of the three transmitters. Range samples were taken in 1 µs increments, resulting in a slightly oversampled range resolution of 150 m. All three antenna modules were in the vertical beam mode. The complex data were as usual coherently integrated for 250 ms or 150 ms and dumped on tape for off-line analysis.

The applied new method of average phase analysis to deduce the mean incidence angle is very sensitive to phase-unbalance between the receiver channels as well as to remnant instrumental and groundclutter DC-components. During the digital preprocessing step therefore the DC-components were most suitably removed from the quadrature components. The existing phase off-set between the antenna modules was determined by minimizing the average phase differences over several longer data sets (each of more than one hour). The resulting significant phase off-sets of 40° and 50°, between antennas 1 and 2, and 1 and 3, respectively, were used to transform each coherently integrated complex signal sample to pro-

194

vide phase equality between the three receiver channels. Following this data preparation the cross spectra and cross correlation functions were computed. Note that the evaluation of these analyses needs the quadrature components of the cross spectra and cross correlation functions which is quite different from the usual Doppler and spaced antenna velocity deductions.

PRELIMINARY RESULTS

(A) Cross Spectra

Let us assume that diffuse reflection or anisotropic scattering from a particular refractive index structure takes place as indicated in the schematics of Fig.1. There may be certain sectors of the irregular structure which cause intensified echoes due to enhanced cross sections of scatterers or focussing from certain refractive index surfaces. If these sectors move with different radial velocity V_R', typical spikes will occur in the Doppler spectrum (e.g., Röttger, 1984b; Hocking, 1985). If the total structure moves with a horizontal velocity U_o due to a mean wind we will detect on the average echoes from these certain sections with negative as well as positive Doppler shift. The result on the data is well known as the "beam width broadening effect" of the Doppler spectrum, which could so far only indirectly be proved. If it would be possible to measure the incidence angle δ together with the Doppler shift one would obtain most direct information on this process and may be able to deduce the horizontal wind component U_o. The vertical wind component W_o conventinally is deducible from the mean Doppler shift.
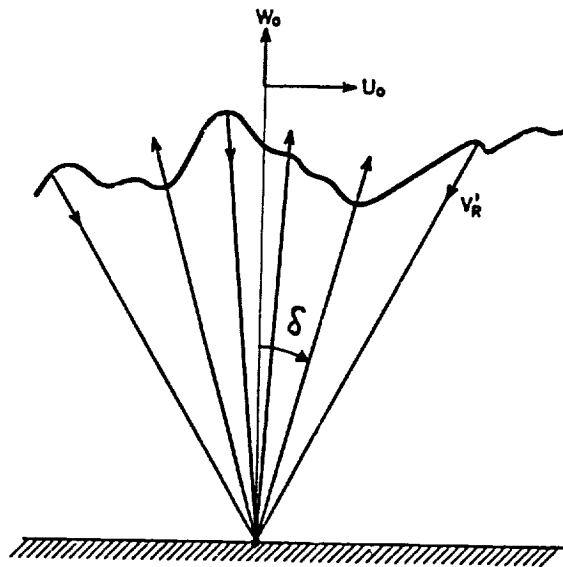
Figure 1. Schematic view of a rough surface of refractive index structure causing several radar echoes reflected back to the origin. Depending on the mean vertical (W_o) and horizontal (U_o) velocities as well as intrinsic fluctuating velocities different radial velocities occur for the different radar echoes from certain sections of the surface.

In Fig. 2 we show results of cross spectra analyses which yield the incidence angle δ as function of Doppler frequency f and more directly prove that the spectral widening is due to the stipulated off-vertical echoes. The average power densities P of the spectra are displayed by the large circles in the upper panels of Fig. 2a and 2b, whereas the phases $\emptyset$ of the cross spectra are displayed in the lower panels, respectively. Each single point represents a phase estimate in one Doppler bin for one data record of 6.4 s. The closed circles, which are connected by a line, indicate the mean phases deduced from the mean quadrature components of the cross spectra. The relative variances $\sigma_{r,i}$ of the normalised quadrature and in-phase spectral components are shown as dots in the upper panels, whereas the r.m.s. variance $\sigma = \sqrt{(\sigma_r^2 + \sigma_i^2)}$ of both these components is shown by the dots connected by the line in the upper panels. The notch at zero frequency of the variances results from a still remnant DC-component. It is noted that the variance is significantly smaller at Doppler frequencies below 0.1 Hz where the power of the spectrum maximises. The spectra of signals from near the tropopause (z = 16.2 km, Fig. 2a) indicate a clear dependency of the phase on the Doppler frequency. On the right-hand side of the phase diagrams the incidence or zenith angle δ corresponding to the phase angle $\emptyset$ between the antennas is given. The average zenith angles are obviously negative at negative Doppler shift and inverted at positive Doppler shift. This observation will be explained by off-zenith returns from a deterministic irregularity structure, which moves horizontally with the wind. The results from tropospheric returns (Fig. 2b) are not so evident but still the effect can principally be noticed.
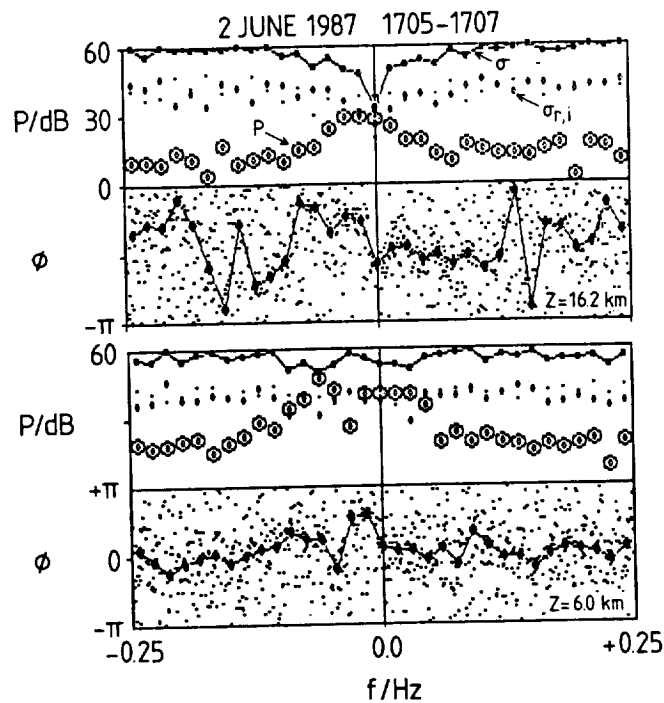
Figure 2. Cross power spectra P and the corresponding phases $\emptyset$ of VHF radar echoes from the altitudes z = 16.2 km (upper panels) and 6 km (lower panels). The terms σ denote the normalised variance of the quadrature components of the cross spectra and f denotes the Doppler frequency.

We take this observation as a proof that the widening of the spectra is mainly caused by off-zenith returns from a horizontally moving structure rather than by vertical velocity fluctuations. These measurements should also allow to estimate the mean wind velocity as well as should provide a test of the hypothesis of Briggs (1980) that the common spaced antenna method is in principle similar to the Doppler method. A simple computation yields the relation between the slope dØ/df of the phase in the cross spectrum and the mean horizontal wind speed Uo:

$$d\emptyset/df = -\pi \cdot d/U_0,$$ (1)

where d is the distance between the antennas in meters, U0 is measured in m/s, Ø in radian and f in Hz. This formula holds for the very simplified assumption of point-like antennas and a frozen-in refractive index structure moving in direction of the antenna baseline. A more detailed treatment of such observations, also done with the Chung-Li VHF radar, combined with theoretical derivations needs to be published elsewhere. The given formula using this primitive model already allows to explain the observed phase slope of the cross spectra to be caused by the horizontal wind. It, thus, also allows us to estimate the mean wind from the phase slope. Using d = 45 m between the centres of the antenna modules number 1 and 2 and the phase slope weighted by the power density of the spectra or by the inverse of the phase variance, we deduce the horizontal wind speed along the baseline direction (about N-S) of about 10 - 15 m/s at 6 km and at 6 km altitude, which is consistent with radiosonde data. It is to be noted that the phase slope is inversely proportional to the wind speed. This means that the slope is shallow for a strong wind, but steep for a weak wind speed. Although one may in principle be able to deduce wind profiles from such phase slope measurements with a set-up of three antennas, it may be more suitable to apply the spaced antenna drift analysis for this purpose. According to the relation Ø = 2π·d'·sinδ, we note that the phase difference of π corresponds to an incidence (or zenith) angle of 3.7 degrees for d' = d/Ω = 7.75. We thus find that the incidence angle of the echoes as function of Doppler shift are within about ±3 degrees, which is well within the antenna beam width. The clear behaviour of the phase slope, particularly at 16.2 km close to the tropopause, tells us on the other hand, that there is either a deterministic reflecting structure with some surface roughness or an ensemble of frozen-in scatterers moving through the beam. The frozen-in interpretation means that the intrinsic correlation time of the potential scatterers or of variations in the reflecting structure must be reasonably longer than the time a certain part of the scattering or refelecting layer needs to propagate through the beam. We also deduce from the significant slope of the phase that the radial fluctuating velocity (i.e., mainly the vertical component of the fluctuating velocity) has a very much smaller effect on the width of the Doppler spectrum than the component of the horizontal mean velocity in direction of certain incidence angles close to the zenith. This result comprises the presently most direct experimental proof of the widely accepted "beam-broadening effect" of VHF radar echoes from the troposphere and the stratosphere.

Under the described circumstances we can deduce the power density as function of the cross spectrum phase angle, i.e., the incidence angle. This allows us to determine the anisotropy of scatterers or the reflecting structure. This is best be possible if the phase slope is large, i.e. for small wind velocities. At 16.2 km altitude we for instance notice a fairly high aspect sensitivity of about 10 dB per 2 degrees. This large aspect sensitivity allows us to neglect the small decrease of power density with incidence angle caused by the antenna diagram. The value of 5 db per degree is a typical value of the aspect sensitivity for altitudes close to the tropopause. Apparently the anisotropy is smaller at 6 km altitude which is an expected observation for echoes from the troposphere as compared to those from the tropopause. We also find other spectra

which indicate a clear phase slope in the centre of the spectrum, which we can attribute to reflection from a rough surface structure. In the outer parts of the spectra at larger Doppler shifts the slope is almost constant (see indications of these observations in Fig. 2b). Since the power density is signifcantly above the noise level at these larger Doppler shifts, we could attribute this to spill-over of low frequency power to higher frequencies due to receiver non-linearity. On the other hand, this can also be an indication that the larger frequency power is due to isotropic scattering. This may appear as a reasonable explanation since the power density at larger Doppler frequencies is much lower than at smaller frequencies and the normalized variance is close to unity, which is an indication for a stochastic or scattering process.

It is to be noted that the characteristic phase slope can also be observed in case of isotropic scattering provided that the radial fluctuating velocity of the scatterers is smaller than the projection of the horizontal mean velocity and the intrinsic correlation time of the scatterers is larger than the time of transit of particular scatterers through the beam.

(B) Mean Incidence Angles

After we have briefly outlined some interpretations of cross spectra, which still need to be discussed in detail elsewhere, we will now present first measurements of the mean incidence angles and recapitulate the principle behind these measurements. Let us indicate the mean location of the scattering/reflecting structure by the line S in Fig. 3 (left-hand side). It is assumed that this
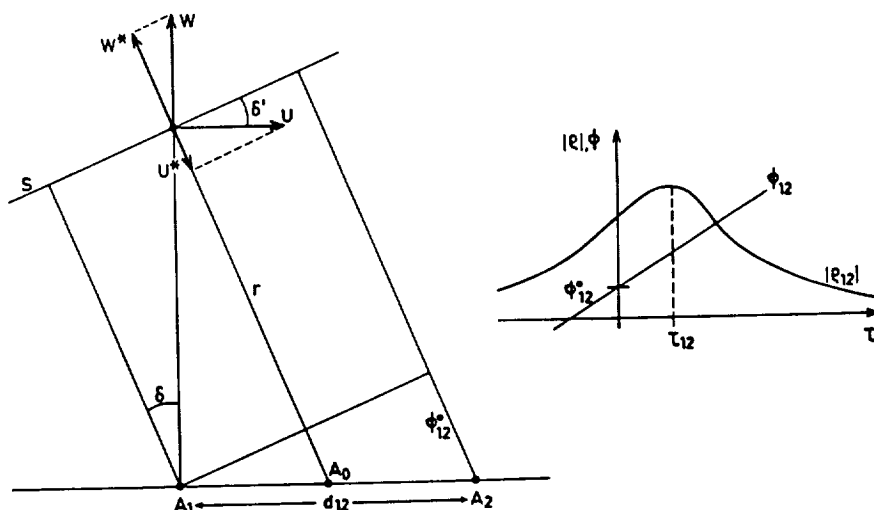
Figure 3. Left-hand side: Sketch of the geometry of phase measurements of a plane wave reflected from a straight surface S at a distance r from the centre Ao radar antennas A1 and A2, which are spaced at a distance d12. The surface is inclined with respect to the horizontal at an angle δ' which is equal to the incidence or zenith angle δ. The surface is moving horizontally with the velocity U and vertically with the velocity W, causing the velocity components U* and W* in direction of the reflected wave.
Right-hand side: Amplitude | ς | and phase ∅ of the complex cross correlation function as function of temporal lg τ.

structure is sufficiently far from the radar antenna, which consists of the two receiving antennas A_1 and A_2. It is also assumed that the structure is slightly tilted with respect to the horizontal by an angle δ'. The tilt angle δ', which is equal to the incidence or zenith angle δ, is

$$\delta' = \delta = \arcsin \left(\phi_{12} \cdot \Lambda / (2\pi \cdot d_{12}) \right), \qquad (2)$$

where d_{12} is the distance between the receiving antennas $A1$ and $A2$, Λ is the radar wavelength and ϕ_{12} is the phase difference of the radar signal received at the two separated antennas. The phase difference can be deduced from the complex cross correlation function ς_{12} of the radar signals received at A_1 and A_2. The amplitude $|\varsigma|$ and the phase ϕ of the correlation function as function of time lag τ is shown in the right-hand side of Fig. 3. The phase of the cross correlation function at zero lag gives the phase difference $\phi_{12}\,^{o}$. Since the distance between the antennas is known, the incidence angle can be determined by this method. It is to be noted that this procedure yields the mean incidence angle δ, which averages out any horizontal or vertical mean or fluctuating velocities. However, the incidence or tilt angle is a very meaningful and useful quantity, since it comprises an estimate of the inclination of the barotropic surfaces in which the refractive index structures are embedded. It also allows to determine the accuracy with which the real vertical and horizontal velocities can be measured. The latter argument is explained by the following simple example.

Assume that the structure S moves with a mean velocity consisting of a horizontal component U and a vertical component W. Since the structure is tilted the radar will see a mean incidence angle δ and measure the composite the radial velocity

$$V_R' = W^* + U^* = W \cdot \cos \delta + U \cdot \sin \delta. \qquad (3)$$

If the angle δ and the horizontal wind component U is not zero, the radial velocity V_R' measured by the radar may not be the real vertical velocity W as commonly assumed. To assess the relevance of this effect, the horizontal velocity as well as the incidence angle needs to be known. The former is usually measured with the Doppler or the spaced antenna method, but the latter, namely the angle δ, cannot usually be measured, if one would not apply the spatial interferometer technique.

In Fig. 3 we have also schematically drawn the amplitude and the phase of the cross correlation function as function of time lag to demonstrate two other parameters from which the velocities can be deduced. These are the delay τ_{12} which is needed together with delays from a group of three receiving antennas and other parameters to deduce the horizontal spaced antenna drift/wind velocity U with the full-correlation-analysis of the spaced antenna merthod (Briggs, 1980) as well as the slope of the phase ϕ' as function of temporal lag to deduce the radial velocity

$$V_R' = \Lambda / 4\pi \cdot \phi', \text{ with } \phi' = d\phi(\tau=0)/d\tau. \qquad (4)$$

Inserting V_R', deduced from equation (4), into equation (3) we could deduce the real vertical velocity W, if the described effect is relevant.

In Fig. 4 we show results from the analysis of mean incidence angle, radial velocity as well as power profile estimates. These displays show scatter plots, where each single sample is from a 30s-averaging period and the distributions of 30 of these samples are plotted in form of an intensity plot for each altitude gate. This display allows us to obtain an immediate view on the statistical distribution functions without becoming biased by the usual displays of mean

23 DEC 1988   1715-1730 LT
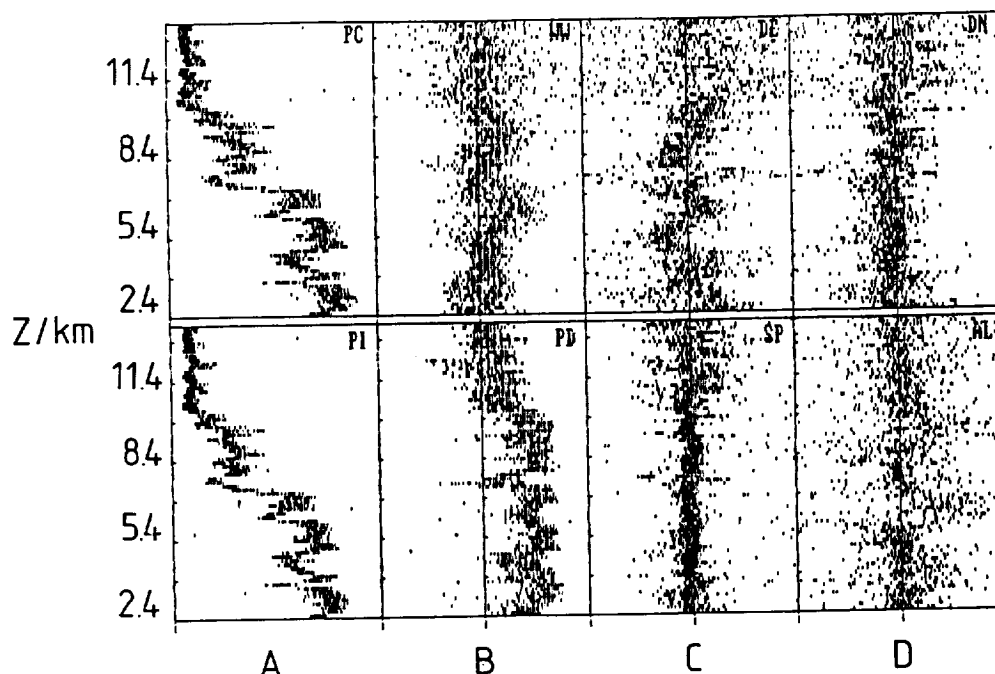
Figure 4. Distribution plots of:
(A) Power profiles resulting from the coherent addition of signal amplitudes (upper panel, PC) and from the incoherent addition of power (lower panel, PI) received in the three antenna channels. The limits are 60 dB.
(B) Radial velocity (WW) within ± 1 m/s limits (upper panel), and power difference (PD=PC-PI) within ± 6 dB (lower panel).
(C) Eastward component (DE) of the incidence angle δ (upper panel) within limits of ± 3 degrees, and sum (SP) of the phase differences (lower panel) between all three antennas within limits of ± π.
(D) Northward component (DN) of the incidence angle δ (upper panel) within limits of ± 3 degrees, and transformed velocity component AL (lower panel) within limits of 50 m/s.

values. We also have applied some test analyses in order to prove the proper functioning of the equipment and the data processing, which we will discuss first.

In the panels A of Fig. 4 power profiles are shown which indicate the well-known layered structure of VHF radar returns from the troposphere with vertical antenna beam. The upper profile results from the coherent addition of the signal amplitudes from the three receiving antennas. Following this coherent addition, the power P_C was computed. The lower profile of panel A results from the (incoherent) addition of the power values of the three antenna channels, yielding the power P_I. In order to emphasize the contrast between these profiles, we have plotted the difference P_D of powers P_C-P_I in the lower part of panel B. It is noted that this difference is significantly positive. In those altitudes where the signal-to-noise ratio is large enough, the difference is between 3dB and

4 dB. The coherent addition as compared to the incoherent addition of three coherent signals should result at most in a theoretical difference of 4.7 dB. We can draw the following conclusions from the fact that the experimental difference is close to the theoretical one:

(1) The phase-off-set compensation (mentioned in the chapter on the experimental set-up) between the antenna channels was performed correctly. This is a basic requirement to measure the incidence angle accurately.

(2) The observed signals from the troposphere have a spatial correlation distance which is equal to or larger than the mean spacing between the antenna centers, i.e. larger than some seven radar wavelengths. It is assumed that this large correlation distance is resulting from either partial reflection from stratified structures or from highly anisotropic scatterers.

Another test was done to prove that the phase computations were done accurately, namely that the phase differences between the three antennas should statistically add up to zero, i.e., $\Sigma\emptyset = \emptyset_{12} + \emptyset_{23} + \emptyset_{31} = 0$. The result is shown in the distribution plot S_P of the lower panel C in Fig. 4. We notice the following:

(1) The distributions as function of altitude are centered around zero, which is the expected result.

(2) There are a few significant outliers, which result either from receiver non-linearity at the lower gates or from remnant DC-components (fading ground clutter or instrumental bias off-set) at the gates with low signal-to-noise-ratio.

(3) Even in the upper altitudes above 10 km the data samples are not equally distributed between $+\pi$ and $-\pi$, which significantly indicates a signal in those gates. This is consistent with the observation of a positive power difference P_D in the lower panel B. However, it still needs to be carefully checked if this signal is not due to fading ground clutter.

In the upper panel B of Fig. 4 the distributions of the radial velocity V_R 'are plotted. We notice again a clustering around a mean value which is at a small positive velocity. Larger periodic excursions are superimposed. In the upper panel C of Fig. 4 the eastward component of the tilt angle δ_E, and in the upper panel D the northward tilt angle δ_N is shown. Except of a few cluster regions of larger δ at localised range gates, which likely are due to fading clutter, the tilt angle δ_E oscillates by about one degree amplitude around zero, whereas little periodic variation is noticed in δ_N.

These results can be interpreted as follows:

(1) The oscillation in δ is not due to a phase ringing effect in the receiver or the transmitter, since this should be manifest in all channels, i.e. in δ_E as well as in δ_N.

(2) There is a periodic variation of the eastward tilt with altitude, which correlates with the radial velocity. We imagine that this can be explained by a mountain lee wave structure. The radar is located about 40 km west of the high central mountain ridge of the island of Taiwan. The prevailing easterly winds should excite mountain waves in the troposphere, which have periodicities in the east-west but not in the north-south direction. Mountain waves are characterised by periodic tilts of the isotherms and the flow pattern. This could result in the observed east-west inclination of the refractivity structures causing the radar echoes. It could also result in a quasi-periodic variation of the power profile, which may be apparent in our observations (however, obviously diluted due to other effects of changing humidity, stability and turbulence). Lee waves also would exhibit themselves by periodic altitude variations of the radial ve-

locity, which we also observe (see upper panel B of Fig. 4). The fact that the tilt as well as the radial velocity is on the average fairly stationary during the observation period of 15 miutes, places some more confidence on our assumption that the observed features are caused by lee waves.

If we now would assume that the periodic variation of the radial velocity is due to a small component of the horizontal wind transformed into radial direction due to the tilt δ, we should see this effect by combining the measured V_R' with δ according to formula (3). Since the tilt angle is very small and the vertical velocity could be fairly large in the case of lee waves, this effect should be barely noticeable unless we would have an estimate of the horizontal wind. Since the latter is not yet available during the preparation of this note, we just have displayed in the lower panel D of Fig. 4 the ratio $V_R'/\sin\delta$ as a crude estimate of the horizontal velocity component. Except of two positive excursions around 6 km and 9 km we cannot see any evidence for the dilution of the vertical velocity by the horizontal velocity in these data. In any case, the measured incidence angle will allow us to correct the radial velocity as soon as we can include the measured horizontal wind and to obtain an estimate of a dilution. It anyhow can be concluded here that the radial velocities are the best estimate of the vertical velocity when the simultaneously measured incidence angle is zero or very small.

CONCLUSION

We have proved the applicabilty of phase measurements with three spaced antennas to obtain additional parameters for studying the scattering-reflection mechanism as well as to better understand some common features in the velocity and power profiles of ST radar measurements. Although these preliminary analyses cannot be finally conclusive and need much more refinement, we are convinced that the phase measuring capability is a very useful and necessary complement to MST radar investigations and wind profiler applications.

Acknowledgement:

REFERENCES

Briggs, B.H. (1980), Radar observations of atmospheric winds and turbulence: a comparison of techniques, J. Atmos. Terr. Phys., 42, 823-833.

Brosnahan, J.W., J.K. Chao and J. Röttger (1983), Chung-Li, Taiwan dual mode (Doppler and spaced antenna) VHF radar: preliminary specifications, Handbook for MAP, 9 (S.A. Bowhill and B. Edwards, eds.), 383-386 (publ. by SCOSTEP Secretariat, Dept. Elec. Engin., University of Illinois, Urbana, IL).

Chao, J.K., F.S. Kuo, Y.S. Chu, I.J. Fu, J. Röttger and C.H. Liu (1986), The first operation and results of the Chung-Li VHF radar, Handbook for MAP, 20 (S.A. Bowhill and B. Edwards, eds.), 359-363 (publ. by SCOSTEP Secretariat, Dept. Elec. Engin., University of Illinois, Urbana, IL).

Farley, D.T., H.M. Ierkic and B.G. Fejer (1981), Radar interferometry: a new technique for studying plasma turbulence in the ionosphere, J. Geophys. Res., 86, 1467-1472.

Hocking, W.K. (1985), Measurement of turbulent energy dissipation rates in the middle atmosphere by radar techniques: a review, Radio Sci., 20, 1403-1422.

Kudeki, E. and G.R. Stitt (1987), Frequency domain interferometry: a high resolution radar technique for studies of atmospheric turbulence, Geophys. Res. Lett., 14, 198-201.

La Hoz, C., J. Röttger and S.J. Franke (1989), Spatial interferometry measurements with the EISCAT VHF radar, Handbook for MAP (this issue).

Röttger, J. (1984a), Interferometer applications of VHF radars, Handbook for MAP, 14 (S.A. Bowhill and B. Edwards, eds.), 164-173 (publ. by SCOSTEP Secretariat, Dept. Elec. Engin., University of Illinois, Urbana, IL).

Röttger, J. (1984b), Signal statistics of the radar echoes - angle-of-arrival statistics, Handbook for MAP, 14 (S.A. Bowhill and B. Edwards, eds.), 84-87 (publ. by SCOSTEP Secretariat, Dept. Elec. Engin., University of Illinois, Urbana, IL).

Röttger, J. and H.M. Ierkic (1985), Postset beam steering and interferometer applications of VHF radars to study winds, waves, and turbulence in the lower and middle atmosphere, Radio Sci., 20, 1461-1480.

Röttger, J. and M.F. Larsen (1989), UHF/VHF radar techniques for atmospheric research and wind profiler applications, in: Radar in Meteorology (D. Atlas, ed.) (to be publ. by Amer. Meteor. Soc., Boston, MA).

Vincent, R.A. and J. Röttger (1980), Spaced antenna VHF radar observations of tropospheric velocities and irregularities, Radio Sci., 15, 319-335.

A POST-STATISTICS STEERING TECHNIQUE FOR MST RADAR APPLICATIONS

Erhan Kudeki[1] and Ronald F. Woodman[2]

I) INTRODUCTION

The use of multiple spaced antennas to receive return signals from common targets in the far field is becoming a common practice in atmospheric and ionospheric radar studies in recent years. The reason for the popularity of such "interferometric" radar configurations is the additional information contained in the phase relationships of the different receiver signals regarding the angular distribution of atmospheric targets within the classical radar resolution cell. This information can be exploited in a variety of ways in data processing stage. Some of the currently used processing techniques include the so called radar interferometry (RI), when the phase difference between independently sampled antenna signals and its temporal and Doppler frequency variations are inspected and interpreted directly [e.g., Woodman, 1971; Farley et al., 1981; Kudeki et al., 1981], imaging Doppler interferometry (IDI), when the angle-of-arrival information from phase differences at discrete Doppler frequencies are combined with the corresponding Doppler velocities to infer background wind velocities [e.g., Adams et al., 1986], and post beam steering (PBS), when received signals at individual antennas are combined, following suitable phase shift operations, to synthesize new beam directions [e.g., Rottger and Ierkic, 1985]. The choice of most suitable interferometric processing technique depends, to a large extent, on the spatial and temporal characteristics of the scattering targets under investigation, as well as what aspects of the investigated phenomena are desired to be emphasized.

The purpose of this note is to present a new interferometric data processing technique which will be referred to as "post-statistics steering" (PSS). In essence, PSS is a beam synthesis technique similar to PBS, but has distinct advantages over the latter in data storage and economy of computations, especially in beam scanning applications. Radar signals, being of statistical nature, invariably need to be interpreted in terms of suitable moments such as power, auto-correlation function and/or power spectrum. In PBS, moment calculations are postponed until beam synthesis is accomplished via some appropriate combination of individual antenna signals. In PSS, by contrast, beam synthesis is postponed until all the possible self- and cross-moment estimates are formed with the multiple receiver signals. Beam synthesis and scanning can then be performed with a simple arithmetic of the available self- and cross-moments. Since the computation of such moments (which can be performed in real time) results in vast data compression, data storage requirements for post-experiment PSS analysis are far more relaxed than raw data storage needed for post-experiment PBS analysis.

II) POST-STATISTICS STEERING (PSS)

Consider the interferometric radar configuration depicted in Figure 1, where identical antennas A and B, separated horizontally by some baseline D, are used to detect signals from far field targets illuminated by a single transmitting antenna T pointed in the vertical direction.

[1]Department of Electrical and Computer Engineering, University of Illinois, Urbana, IL 61801

[2]Jicamarca Radio Observatory, Apartado 3747, Lima, Peru

Let complex signals a and b received by antennas A and B, respectively, define a signal vector s:

$$s = \begin{bmatrix} a \\ b \end{bmatrix} \tag{1}$$

Assuming identical gains for the receiver channels connected to both antennas, return signals a and b should be identical for an idealized point target positioned directly overhead. Signals a and b should differ only by a phase factor for a similar target positioned off the zenith. Phase and amplitude differences in a and b may be expected for a more general and realistic configuration of randomly distributed multiple or diffuse targets within the common radar resolution cell.

The inner product of s with some transformation vector t defines a possible linear combination α of a and b:

$$\alpha = t \cdot s = t^T s = \begin{bmatrix} t_1 & t_2 \end{bmatrix} \begin{bmatrix} a \\ b \end{bmatrix} \tag{2}$$

When antennas A and B are regarded as the elements of a two element linear array, operation (2) amounts to beam synthesis selected by the transformation vector t. The operation may be performed in hardware, as is often done, by combining the array elements with desired phase shifts (cable lengths) and amplitudes (amplification factors), or in software as in PBS [e.g., Rottger and Ierkic, 1985]. When the operation is carried out in software, beam scanning is possible by varying t. Signals synthesized in a beam scanning operation may be organized in a new signal vector σ, which can be obtained from s by multiplication with a suitable transformation matrix T. To develop the idea of PSS it is useful to consider a linear transformation of the form

$$\sigma = \begin{bmatrix} \alpha \\ \beta \end{bmatrix} = T s = \begin{bmatrix} T_{11} & T_{12} \\ T_{21} & T_{22} \end{bmatrix} \begin{bmatrix} a \\ b \end{bmatrix} \tag{3}$$

where α and β correspond to signals at two new beam directions defined by the elements of T. If $|T|$ is non-singular, it is evident that σ carries the same information as s, since at any time s can be recovered via $s = T^{-1}\sigma$.

In atmospheric radar studies return signals are generally assumed to be of random nature. Therefore, data interpretation is typically attempted with suitably defined average statistical parameters derived from the radar signal, such as signal power, auto-correlation function, or power spectrum, etc. The essence of PSS is to avoid direct use of transformation (3) in beam synthesis, but to calculate the average statistical parameters associated with σ from those associated with s. To that end we define statistics matrices of s and σ as

$$S = <s\ s'^{*T}> = <\begin{bmatrix} a \\ b \end{bmatrix}\begin{bmatrix} a'^* & b'^* \end{bmatrix}> = \begin{bmatrix} <aa'^*> & <ab'^*> \\ <ba'^*> & <bb'^*> \end{bmatrix} = \begin{bmatrix} r_{aa} & r_{ab} \\ r_{ba} & r_{bb} \end{bmatrix} \qquad (4)$$

and

$$\Sigma = <\sigma\ \sigma'^{*T}> = <\begin{bmatrix} \alpha \\ \beta \end{bmatrix}\begin{bmatrix} \alpha'^* & \beta'^* \end{bmatrix}> = \begin{bmatrix} <\alpha\alpha'^*> & <\alpha\beta'^*> \\ <\beta\alpha'^*> & <\beta\beta'^*> \end{bmatrix} = \begin{bmatrix} r_{\alpha\alpha} & r_{\alpha\beta} \\ r_{\beta\alpha} & r_{\beta\beta} \end{bmatrix} \qquad (5)$$

respectively. In (4)-(5), * denotes complex conjugation, superscript T transposition, and angular brackets stand for ensemble or statistical averaging (or, time averaging in practical implementation). The primes denote possible time shifts between signal time series a and b, or α and β, in which case r_{aa}, r_{ab}, etc., may be taken to represent auto-correlation (ACF) and cross-correlation (CCF) functions, which, at zero time delay reduce to power and cross-power, respectively. Combining (3) and (5) Σ may be expressed as

$$\Sigma = <\sigma\sigma'^{*T}> = <(T\ s)((T\ s')^*)^T> = T\ <ss'^{*T}>\ T^{*T} = T\ S\ T^\dagger \qquad (6)$$

where $T^\dagger = T^{*T}$ is the Hermitian conjugate, or the adjoint of matrix T. Clearly the elements of the statistical matrix Σ of the synthesized beam signals σ are linear combinations of the elements of the statistical matrix S of the original signals s. In PSS this result is exploited to calculate the statistical parameters concerning synthesized beam signals using simple arithmetic operations involving only the elements of the statistical matrix S of the recorded vertical incidence signals.

Consider a particular transformation matrix

$$T = \begin{bmatrix} T_{11} & T_{12} \\ T_{21} & T_{22} \end{bmatrix} = \begin{bmatrix} e^{i\Delta/2} & e^{-i\Delta/2} \\ e^{-i\Delta/2} & e^{i\Delta/2} \end{bmatrix} \qquad (7)$$

which amounts to synthesizing two reception beams with array factor maxima at

$$\theta = \pm\sin^{-1}[\Delta/kD] \qquad (8)$$

off the zenith (α corresponds to +, and β to - signs), where k is the wavenumber corresponding to the radar carrier frequency. It can then be shown that the expansion of (6) leads to

$$r_{\alpha\alpha} = (r_{aa}+r_{bb}) + (r_{ab}e^{i\Delta}+r_{ba}e^{-i\Delta})$$

$$r_{\beta\beta} = (r_{aa}+r_{bb}) + (r_{ab}e^{-i\Delta}+r_{ba}e^{i\Delta})$$

$$r_{\alpha\beta} = (r_{ab}+r_{ba}) + (r_{aa}e^{i\Delta}+r_{bb}e^{-i\Delta})$$

$$r_{\beta\alpha} = (r_{ab}+r_{ba}) + (r_{aa}e^{-i\Delta}+r_{bb}e^{i\Delta})$$

(9)

Using relations (9), ACF and CCF of signals α and β, $r_{\alpha\alpha}$, $r_{\alpha\beta}$, etc., corresponding to new beam directions selected by Δ, can be computed once the ACF and CCF of signals a and b, that is r_{aa}, r_{bb}, r_{ab}, and r_{ba} are available. The results, and specifically $r_{\alpha\alpha}$ and $r_{\beta\beta}$, can be interpreted as the usual outputs of a beam swinging operation.

Finally, Fourier transforming relations (9), and remembering that r_{aa}, r_{ab}, etc., form Fourier transform pairs with the self- and cross-spectra $\Phi_{aa}(\omega)$, $\Phi_{ab}(\omega)$, etc., it is recognized that relations (9) can also be used to calculate the self- and cross-spectra $\Phi_{\alpha\alpha}(\omega)$, $\Phi_{\alpha\beta}(\omega)$, ... of synthesized beam signals α and β when r_{aa}, r_{ab}, ... are replaced by $\Phi_{aa}(\omega)$, $\Phi_{ab}(\omega)$, ... in (9). But, by definition, $\Phi_{ab}=\Phi_{ba}{}^*$, and Φ_{aa}, Φ_{bb} are purely real, so that (9) can be simplified and recast as

$$\Phi_{\alpha\alpha} = (\Phi_{aa}+\Phi_{bb}) + 2\mathrm{Re}\{\Phi_{ab}e^{i\Delta}\}$$

$$\Phi_{\beta\beta} = (\Phi_{aa}+\Phi_{bb}) + 2\mathrm{Re}\{\Phi_{ab}e^{-i\Delta}\}$$

$$\Phi_{\alpha\beta} = \Phi_{\beta\alpha}^* = 2\mathrm{Re}\{\Phi_{ab}\} + (\Phi_{aa}e^{i\Delta}+\Phi_{bb}e^{-i\Delta})$$

(10)

for purposes of spectral calculations. Note that Φ_{aa}, Φ_{bb}, and $\Phi_{ab}=\Phi_{ba}{}^*$ are also used in usual interferometric analysis [e.g., Kudeki, 1988], with the most useful interferometric information contained in the phase and the normalized amplitude of Φ_{ab}. Clearly, (10) indicates that both interferometric and beam swinging experiments can be obtained using the same antenna configuration and statistical processing.

In summary, then, PSS analysis first amounts to estimating the ACF and CCF, or the power- and cross-spectra of the vertical incidence signals a and b, and second, to repeated use of (9) or (10) with different Δ values for beam scanning. Clearly ACF or power-spectrum estimation in different beam pointing directions is reduced to simple arithmetic operations involving the self- and cross-moments of interferometric (see Figure 1) vertical incidence data.

III) PRACTICAL CONSIDERATIONS

In practice it is difficult to ensure identical receiver channel gains assumed above in interferometric experiments. Typically, unequal cable lengths, as well as differences in "front end" amplification factors contribute to gain differences between the receiver channels connected to different receiving antennas. This undesirable situation can be corrected for in the processing stage if and when the quantitative nature of the gain discrepancies is known as a result of calibration measurements. For example all gain discrepancies can be lumped into a single complex parameter g, defined as b/a when a single receiving antenna is connected to both reception channels used in the experiment (a typical calibration procedure). In PSS applications r_{bb}, r_{ab}, and r_{ba} and Φ_{bb}, Φ_{ab}, and Φ_{ba} need to be corrected via division by $|g|^2$, g
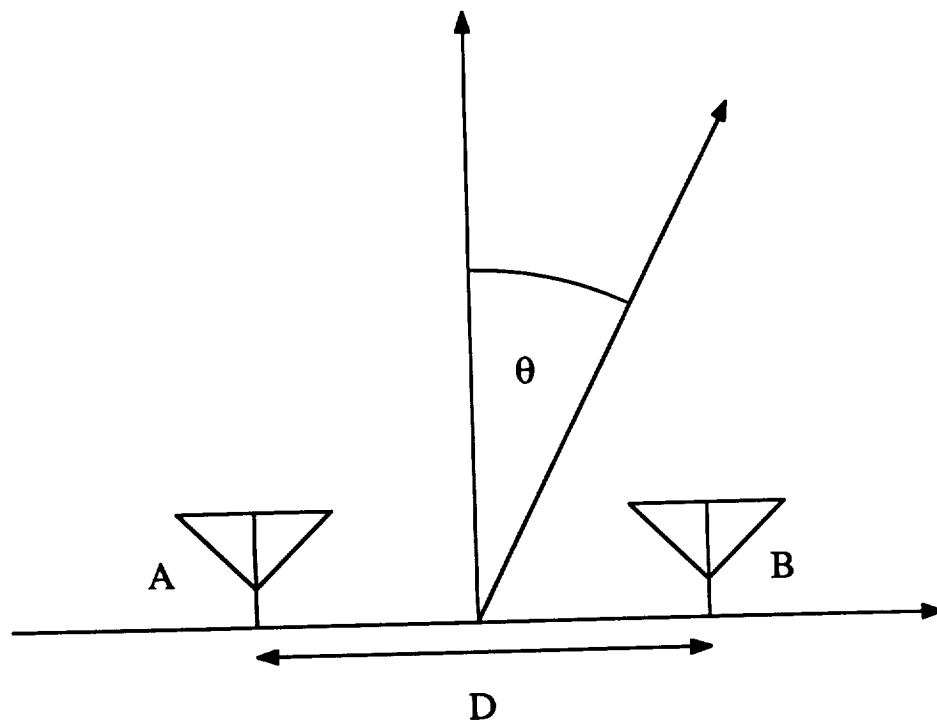
Figure 1. An interferometric radar configuration. Only reception antennas are shown.

and g^* respectively, prior to use in (9) and (10). The magnitude correction $|g|$ can also be obtained from the experiment itself, by simply comparing r_{aa} with r_{bb}, or, Φ_{aa} with Φ_{bb}.

The overall beam pointing direction is determined not only by Δ, but also by the transmission and reception element (antennas A and B in Figure 1) gain patterns, and the "aspect sensitivity distribution". The latter is related to the angular variation of target cross-section, determined by the nature of the scattering and/or reflecting irregularities in the medium. For an isotropic scatterer (no aspect sensitivity), only the two-way gain pattern, that is the product of transmission and reception gain patterns, need to be considered to estimate the effective pointing direction. Since the two-way gain pattern is usually well known, this is a relatively straightforward procedure. With aspect sensitive scatterers, however, the two-way gain pattern need to be multiplied with the aspect sensitivity distribution. Unless the latter is known *a priori* some amount of uncertainty will always accompany the calculation of effective beam directions and derived parameters.

Difficulties mentioned above are by no means unique to PSS technique. Gain discrepancies can bias all interferometric results and need to be corrected for, using similar procedures to that described above in connection with the PSS technique. Similarly, uncertainties related to unknown aspect sensitivity distribution contaminate all beam swinging techniques, including those accomplished in the hardware. In fact, even vertical wind measurements accomplished using a single vertically pointed radar beam are subject to aspect sensitivity related uncertainties, as pointed out by Rottger and Ierkic [1985]. Although rarely used in practice, one advantage of the interferometric technique is the possibility of eliminating such uncertainties by determining the aspect sensitivity variation within the radar beam through the use of software based beam scanning operations. As a result of its much simplified beam scanning procedures, PSS technique can be potentially important in this regard. Preliminary aspect sensitivity and wind velocity measurements obtained with a PSS analysis of mesospheric Jicamarca data will be presented in a separate publication, to illustrate this possibility.

IV) CONCLUSIONS

A new post-statistics beam synthesis and scanning technique (PSS) suitable for the analysis of interferometric radar data has been introduced. Beam synthesis and scanning is accomplished using the self- and cross-moments of multiple receiver signals as the ingredients of simple arithmetic operations. By contrast, the post beam steering (PBS) technique requires more costly raw data manipulations to obtain equivalent results. Data storage and computation requirements can be considerably relaxed in interferometric beam scanning applications through the use of PSS technique. The technique can be efficiently exploited in simultaneous aspect sensitivity and unbaised wind velocity measurements using vertically pointed interferometric radar systems.

Although only the two-receiver case has been explicitly treated in this note, the technique can be readily used to handle interferometric data collected with multiple-receiver radar configurations including orthogonal baselines. It is also suitable for range scanning applications with frequency-domain interferometry (FDI) [Kudeki and Stitt, 1987] data. The generalization of the technique for multiple-receiver, multiple-frequency applications will be treated in a future publication.

REFERENCES

Adams, G. W., J. W. Brosnahan, D. C. Walden, S. F. Nerney, Mesospheric observations using a 2.66-MHz radar as an imaging Doppler interferometer: Description and first results, *J. Geopys. Res.*, *91*, 1671, 1986.

Farley, D. T., H. M. Ierkic, and B. G. Fejer, Radar interferometry: A new technique for studying plasma turbulence in the ionosphere, *J. Geophys. Res.*, *86*, 1467, 1981.

Kudeki, E., B. G. Fejer, D. T. Farley, and H. M. Ierkic, Interferometer studies of equatorial F region irregularities and drifts, *Geophys. Res. Lett.*, *377*, 1981.

Kudeki, E., and G. R. Stitt, Frequency Domain Interferometry: A high resolution radar technique for studies of atmospheric turbulence, *Geophys. Res. Lett.*, *14*, 198, 1987.

Kudeki, E., Radar interferometer observations of mesospheric echoing layers at Jicamarca, *J. Geophys. Res.*, *93*, 5413, 1988.

Rottger, J., and H. M. Ierkic, Post beam steering and interferometer applications of VHF radars to study winds, waves and turbulence in the lower and middle atmosphere, *Radio Sci.*, *20*, 1461, 1985.

Woodman, R. F., Inclination of the geomagnetic field measured by an incoherent scatter technique, *J. Geophys. Res.*, *76*, 178, 1971.

Frequency Domain Interferometry of Polar Mesosphere Summer Echoes with the EISCAT VHF Radar

S. J. Franke[1], C. LaHoz[2], J. Rottger[2] and C.H. Liu[1]

[1]Wave Propagation Laboratory, University of Illinois
Urbana, 61801, Illinois, USA

[2]EISCAT Scientific Association
P.O. Box 812, S-981 28 Kiruna, Sweden

ABSTRACT

During the Polar Mesosphere Summer Echo (PMSE) campaign in 1988, the first multiple-frequency mesospheric measurements were carried out using the EISCAT 224 MHz radar. The radar was configured to perform essentially simultaneous measurements of coherent backscatter on two closely spaced frequencies. This type of data can be used to investigate the frequency coherence of the radar echoes and to perform frequency-domain-interferometry (FDI) analysis. When an isolated scattering layer is present the FDI technique can provide extremely high resolution information about the thickness and relative position of the layer. A case study of two-frequency data collected on July 3, 1988 is presented in this paper. For the frequency separation used in this experiment, statistically significant values of coherence greater than 0.5 imply layer thicknesses smaller than 200 m. Coherences as large as 0.83 were observed in the data indicating that scattering layers with thicknesses in the range 85-120 m are sometimes present in the polar summer mesosphere. In the example reported here, such a layer is shown to exist for a period of approximately 10 minutes and its position is tracked as it descends over more than 1km in altitude and transits from one range gate to the next. In addition, the FDI technique is used to study a case where a sudden frequency jump is observed in the Doppler spectrum. Spectral jumps appear to be a characteristic of the 224 MHz echoes (LaHOZ et al., 1989). We employ the FDI analysis with Doppler sorting and compute the coherence spectrum of the data before, during and after the jump. The phase of the coherence spectrum is shown to exhibit features that are consistent with scattering from relatively thin, tilted layers containing (nearly) isotropic turbulence. These preliminary results show that the multiple frequency measurement technique is a powerful tool for studying the mesospheric echoes and should be exploited in future mesospheric campaigns at EISCAT, perhaps in conjunction with spatial interferometry measurements.

INTRODUCTION

The Frequency Domain Interferometry (FDI) technique was first described and employed by KUDEKI and STITT (1987) as a means for obtaining high resolution information about the thickness and position of isolated scattering layers when they exist within the scattering volume defined by the radar pulse length (See also Kudeki and Stitt, this volume). These authors analyzed mesospheric echoes obtained on two closely spaced frequencies using statistical coherence analysis in a manner directly analogous to spatial domain interferometric analysis (FARLEY et al., 1981). They showed that when a single, thin scattering layer is present in the scattering volume defined by the radar pulse length it is possible to obtain an extremely accurate estimate of the thickness of the layer and to track the position of the layer within the vertical dimension of the scattering volume. The FDI technique employs measurements of the normalized complex correlation (coherence) between the backscattered returns from two closely spaced radar frequencies f_1 and $f_2=f_1+\Delta f$. Typically, alternate radar pulses are sent at the two carrier frequencies and the backscattered returns are coherently averaged separately for a time that is short compared to the correlation time of the scattering medium. Denoting the complex amplitude of the receiver output (after coherent integration) obtained at frequencies f_1 and f_2 by V_1 and V_2, then the coherence between the two time series, S_{12}, is defined by

$$S_{12} = \frac{<V_1 V_2^*>}{\sqrt{<|V_1|^2> <|V_2|^2>}} \tag{1}$$

where the * denotes complex conjugation and the angular brackets denote ensemble averaging. In practice the ensemble average is replaced by a time average over a length of time that is sufficiently long compared to the correlation time of the backscattered returns. Analytical models for the coherence have been given by KUDEKI and STITT (1989) and FRANKE (1989, this issue). The phase and magnitude of the coherence can be used to obtain estimates of the first and second central moments of the range distribution function of atmospheric targets inside scattering volume with vertical dimension defined by the pulse length. For example, FRANKE (1989) considered the case where the refractive index variations responsible for backscattered echoes from a vertically directed radar beam can be modeled by a random and statistically homogeneous refractive index field $\Delta n(\vec{r}, t)$ which is weighted by a gaussian function $e^{-(z-z_1)^2/2\sigma_1^2}$. This simple model represents a scattering layer with thickness σ_1 and centroid z_1 and can be used to obtain an explicit expression for the coherence. Under the assumption that the layer thickness is small compared to the radar pulse length and the antenna beamwidth is narrow so that wavefront curvature effects can be ignored (FRANKE, 1989) the coherence is found to be of the form

$$S_{12} = e^{j2\Delta k z_1} e^{-\Delta k^2 \sigma_1^2} \tag{2}$$

Thus, the magnitude of the coherence can be used to obtain an estimate of σ_1 and the phase is used to determine the relative position of the layer within the scattering volume, z_1. In some cases, it is useful to extend the coherence into the frequency domain, e.g. the coherence spectrum, $S_{12}(\omega)$, is computed:

$$S_{12}(\omega) = \frac{<V_1(\omega)V_2(\omega)^*>}{\sqrt{<|V_1(\omega)|^2> <|V_2(\omega)|^2>}} \tag{3}$$

where $V_1(\omega)$ and $V_2(\omega)$ are the Fourier transforms of the voltage time series. In order to avoid confusion we will use the term coherence *coefficient* when referring to data processed according to equation (1) and coherence *spectrum* when referring to equation (3). In the simplest situation where a thin layer is present in the scattering volume, the magnitude and phase of the coherence spectrum have the same interpretation as they do for the coherence coefficient discussed earlier. In certain cases this Doppler sorting can be used to separate multiple scattering layers with different line of sight velocities (KUDEKI and STITT, 1987) or, as will be discussed in this paper, to infer the characteristics of a thin, tilted scattering layer.

In this paper, we present a case study of two-frequency data collected within a 37 minute period on July 3, 1988. The data were collected during the "Polar Summer Mesosphere Echoes" (PMSE) campaign using the EISCAT VHF radar.

OBSERVATIONS

The EISCAT radars are described in this handbook in the paper by LaHOZ et al. (1989) and in additional references therein. For the two-frequency experiments reported here a double pulse scheme was employed whereby a 10 μs pulse at 223.8 MHz was transmitted and then followed 2 μs later by a 10 μs pulse at 224.0 MHz. Thus the altitude resolution of the data is approximately 1.5 km if conventional processing is employed. The interpulse period was 1.813 ms. Separate receiving channels were used to obtain 10 samples at altitudes corresponding to 80-93.5 km at each frequency. Coherent integration of 14 successive samples was employed to obtain time series with an effective sampling period of 25.4 ms. The coherently averaged samples were collected in memory until 192 samples (4.87 seconds) had been collected at each range gate and at

each frequency and were then dumped to tape. A new data collection cycle started every 5 seconds.

The coherence coefficient was calculated from a temporal average over 12 data records each consisting of 192 coherently integrated samples providing an estimate of the coherence coefficient every minute. Auto and cross-spectra were computed using the first 128 points of each 192 sample data record. The data were Fourier transformed using the FFT after removing the mean and applying a Hanning window. The resulting spectra were averaged for intervals ranging from 15-s to 1 minute and the resulting averaged spectral estimates were used to estimate the coherence spectrum.

Figure 1 shows how the magnitude of the theoretical coherence value depends on the thickness of the scattering layer for the 200 kHz frequency separation used in this experiment. Note that coherence values larger than 0.5 and 0.7 are associated with layer thicknesses smaller than 200 m and 150 m, respectively. When interpreting the coherence values computed from finite length time series it is necessary to take into account that fact that the (i) coherence estimates are biased, and (ii) spurious large values of coherence can be measured when the data segment length is not significantly larger than the correlation time of the backscattered radar signal (e.g. BLOOMFIELD, 1975). It is useful when interpreting the significance of measured values of coherence to determine the limiting (maximum) coherence at the 95% level under the hypothesis of zero population coherence. The limiting coherence is given by (BLOOMFIELD, 1975):

$$S_{0.95} = [1 - (0.05)^{1/(N-1)}]^{1/2} \qquad (4)$$

where N is the number of degrees of freedom in the sample used to obtain the coherence estimate. Observed values of $|S_{12}|$ less than $S_{0.95}$ should be regarded as not significantly different than 0. When the coherence is estimated as in (1) the approximate number of degrees of freedom can be obtained from $T/\tau^{1/2}$ where T is the length of the time series and $\tau^{1/2}$ is the time to 50% decorrelation. For estimation of the coherence spectrum, (4) still applies but in this case the number of degrees of freedom is equivalent to the number of independent spectra averaged to obtain the result. Note that in order for the limiting coherence to be smaller than 0.5 it is necessary to have N at least as large as 12.

In the absence of the noise, the expected value of the estimated coherence will be larger than the true coherence. An approximation for the bias in the coherence estimate that is valid when the coherence is not close to zero is (BLOOMFIELD, 1975):

$$B = \frac{1}{4(N-1)} \frac{(1-\gamma^2)^2}{\gamma} \qquad (5)$$

where γ is the true coherence value. Note that if the true coherence is larger than 0.5 and the number of degrees of freedom is at least 12, then the bias will smaller than 0.026 and can be neglected. An additional bias term is contributed when the signal to noise ratio is finite (e.g. KUDEKI and STITT, 1989 this issue). This term acts to decrease the measured coherence. This bias can be corrected for by multiplying the computed coherence values by $[(1+N_1/S_1)(1+N_2/S_2)]^{1/2}$ where S_1/N_1 and S_2/N_2 are the signal-to-noise power ratios obtained at f_1 and f_2, respectively.

RESULTS AND DISCUSSION

Figure 2 shows the signal-to-noise ratio during a 37-minute period beginning at 12:42:05 UT on July 3, 1988 at 6 range gates covering altitudes from 84.5 to 89.0 km. The signal-to-noise ratio ranges from 0 to 15 dB and corresponds to moderate PMSE echo strengths. Figure 3 shows high resolution (15-s integration time) spectrograms for the 4 middle range gates where significant signal power is observed. Velocities on the lower half of the spectrogram correspond to motions

Layer Thickness vs. Coherence for 200 kHz frequency separation
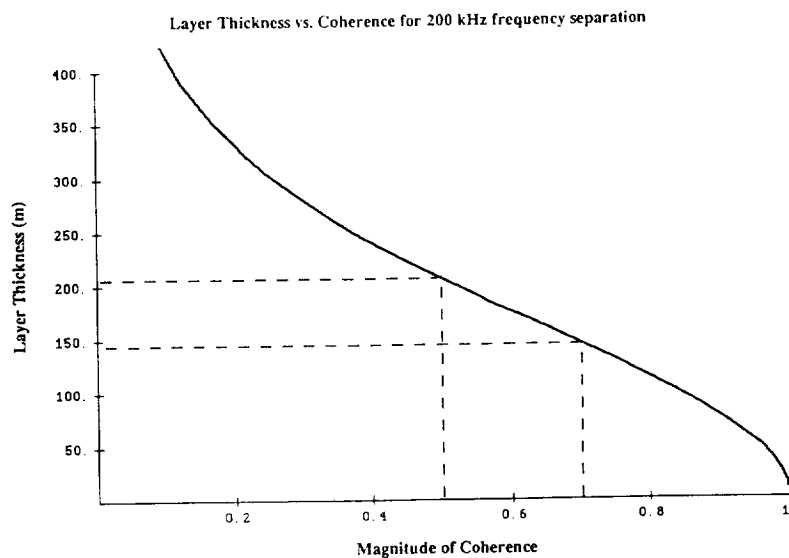
Figure 1. Theoretical relationship between the magnitude of the coherence coefficient and the thickness of the scattering layer for the 200 kHz frequency separation and 10 μs pulse length used in the experiment.

EISCAT July 3, 1989 12:42:05
Signal to noise ratio (dB) vs. Time
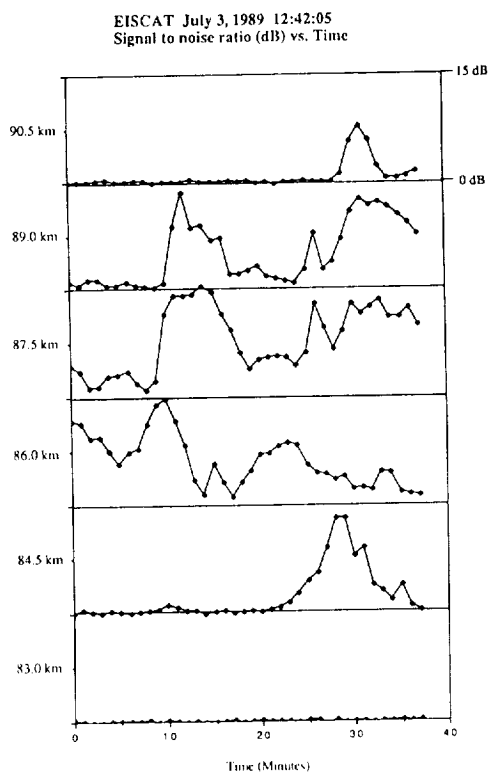
Figure 2. Signal-to-noise ratio averaged over one minute intervals plotted vs. time for a 37-minute interval beginning at 12:42:05 on July 3, 1988. The scale is 0-15 dB.

toward the radar (positive Doppler shifts). Several very interesting features are present in these data. First, we note that at the upper two range gates in Figure 3, that abrupt widening of the spectrum is associated with abrupt increases in the backscattered power level which can be seen by referring to Figure 2. The spectral width exceeds the ± 20Hz range of the spectral estimate and aliasing occurs at these times.

Turning to the lower two spectrograms, we note that a jump in the centroid of the spectrum occurs within the first 10 minutes at 86.0 km. During the transition period the spectrum widens considerably and the echo power is reduced. The transition occurs within one minute. This spectral feature appears to be a special characteristic of the 224 MHz PMSE data and several examples are discussed in more detail elsewhere (LaHOZ et al., 1989; ROTTGER et al., 1989; both in this issue). We will return to further analysis of this feature in a later section. Note also that the extremely wide spectra in the upper two range gates are associated with an extremely narrow spectrum at 86.0 km. Finally, we note the apparent transition of a layer from the 86.0 km gate to the 84.5 km gate which occurs at 25 minutes into the plot. It can also be seen in Figure 2 as a decrease in the power level in the 86.0 km gate and a corresponding increase in the 84.5 km gate. The overlap between the adjacent gates due to the smearing action of the receiver filters is apparent. The spectrograms show that the transition occurs during a the period where the velocity is downward (toward the radar) and accelerating. The abrupt transition indicates that the layer must be relatively thin compared to the range gate thickness and the coherence analysis discussed next bears this out.

Figure 4 shows the coherence coefficient computed using a 1 minute average (12 data records) for the same period shown in Figures 2 and 3. The closed symbols represent raw coherence values with no correction for the finite signal-to-noise ratio. The open symbols are obtained by multiplying the raw values by $[(1+N_1/S_1)(1+N_2/S_2)]^{1/2}$ which corrects for the bias due to noise contamination. This correction is only meaningful when the signal-to-noise ratio is sufficiently large on both channels. When the SNR is less than 1 on either channel, the corrected coherence coefficient is set to zero. When no signal is present, the theoretical coherence between the two frequencies is 0 and adjacent time samples are uncorrelated so the number of degrees of freedom in the coherence estimate is 12x192=2304. The corresponding limiting (maximum) coherence at the 95% level is 0.036. This level corresponds to the largest of the coherence values that are observed in the upper and lower range gates. Note that increases in the coherence coefficient above the no signal level are expected even when the mesospheric echoes are present even in the case when there is no significant correlation between the echoes at the two frequencies (i.e. when the scattering layer is more than 300-400 meters thick). This is simply a manifestation of the bias in the estimator and its dependence on the correlation time of the data. Thus, it is important to consider the computed coherence values together with the spectral width or, equivalently, the correlation time of the signal. Returning to Figure 4, we note the coherence levels seen in the 89.0 km and 87.5 km range gates near the end of the time period are generally less than 0.25 except at the beginning in the 87.5 km gate. In addition, the spectra are quite broad and even aliased at times indicating that the correlation time is short and on the order of or at most a few times larger than the sampling interval. Thus, the bias should be small which implies that the scattering layer thickness is at least several hundred meters thick (see Figure 1).

On the other hand, the coherence values seen in the 84.5 km and 86.0 km range gates are quite large (approximately 0.70 - 0.75) after the first 10 minutes. The sharp decrease in coherence observed at 86.0 km at 25 minutes and the corresponding increase at 84.5 km corresponds to the period where the layer moves from the upper to the lower range gate. The coherence at 84.5 km reaches a maximum value of 0.83 (corrected for SNR). In order to verify that these large values of coherence are not simply manifestations of the bias associated with the estimate due to extremely long correlation times or to some kind of spurious feature in the data we have plotted in Figure 5 the signal amplitude at the two frequencies for a representative 5-s period corresponding to the largest coherence value (0.83) observed in the 84.5 km range gate. This Figure shows the
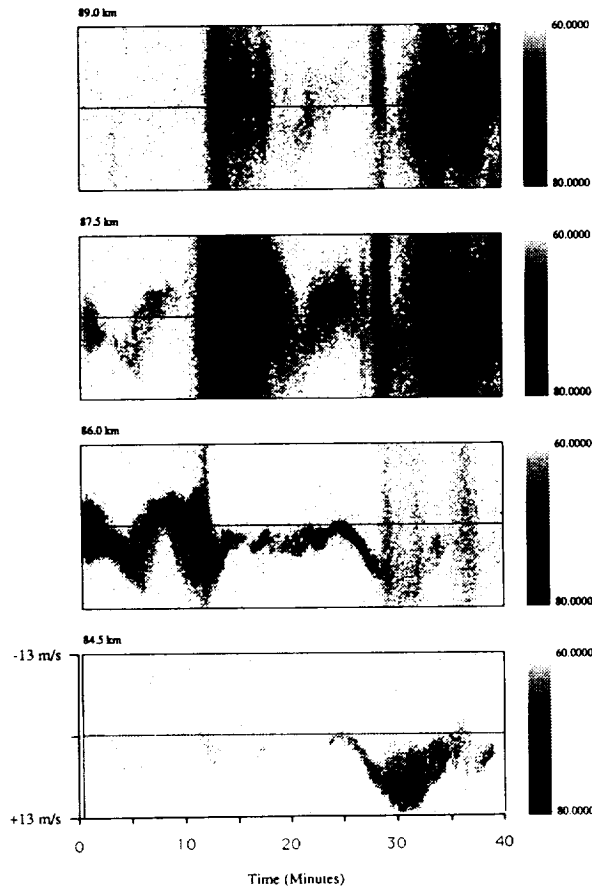
Figure 3. High resolution spectrograms averaged over 15-s intervals for time interval shown in Figure 1. The logarithm of the spectrum is plotted on a gray scale with dynamic range of 40 dB. Doppler shifts on the lower half of each plot are toward the radar. The range of Doppler shifts is ± 19.7 Hz which corresponds to ± 13.2 m/s.

EISCAT   July 3, 1989   12:42:05
Coherence vs. Time (60 s average)

Figure 4. Magnitude of the coherence coefficient averaged over one minute intervals for the time interval shown in Figure 1. Closed symbols represent raw coherence values and open symbols are coherences corrected for the finite signal-to-noise ratio. The scale ranges from 0 to 1.

216
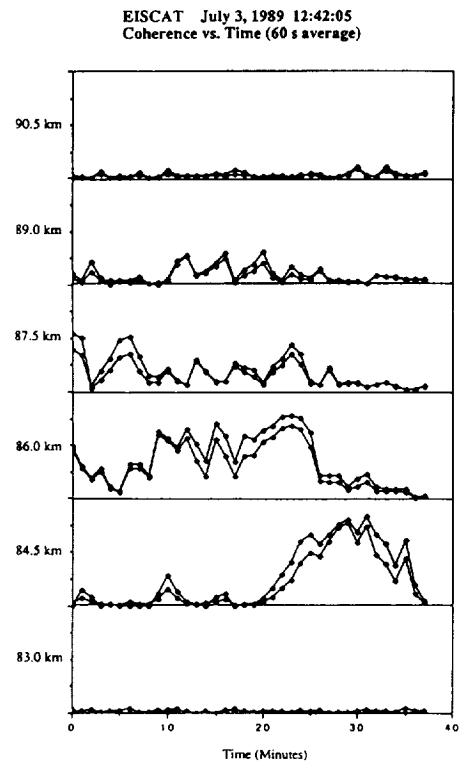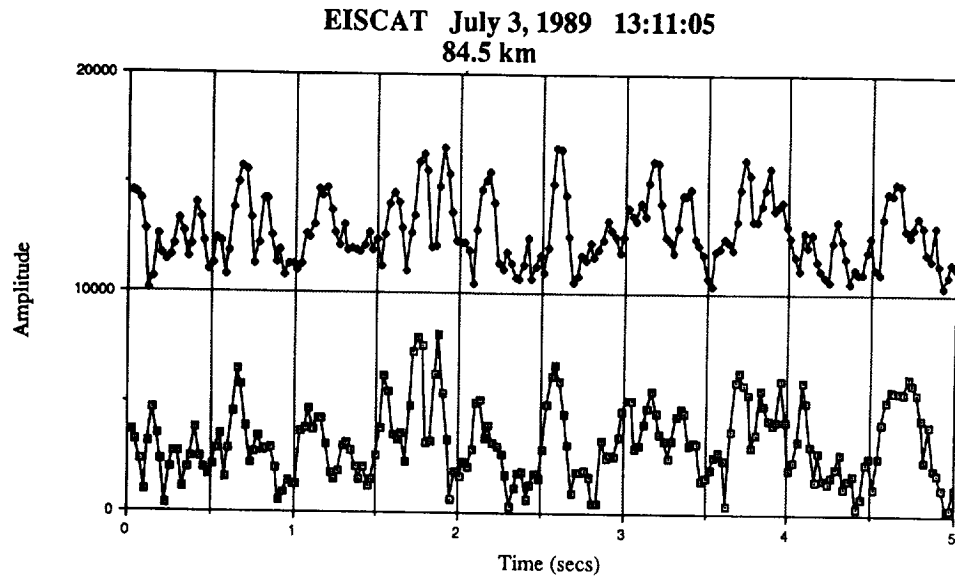
Figure 5. A 5-second segment of raw data corresponding to the interval exhibiting the largest coherence coefficient (corrected value=0.83) showing the correlation between the signal amplitude fluctuations at the two frequencies.

extremely high correlation between the amplitude fading on the two frequencies and also shows that the correlation time is significantly smaller than 1-s. In addition, inspection of the spectrogram for the 84.5.km gate shows relatively wide spectra during the interval when the coherence is largest. Thus the bias and variance of the coherence estimate will be very small and we can interpret the computed coherence values and the inferred layer thicknesses as accurate estimates.

The value of 0.83 for the coherence corresponds to an equivalent layer thickness of 104 m while the average value of 0.70 corresponds to a thickness of 145 m. An estimate of the 95% confidence interval for the estimated value of 0.83 was computed assuming a 0.5-second correlation time and is +0.04, -0.05 (BLOOMFIELD, 1975). The corresponding range of layer thicknesses is 86-120 meters. Referring back to Figures 3 and 2, it is interesting to note that the high coherence values observed at 84.5 km and earlier at 86.0 km are associated with rather large echo powers which are of the same magnitude as the echoes from the upper range gates where the coherence is small and large layer thicknesses are inferred. Thus, completely different signal characteristics are seen in adjacent range gates separated by only 1.5 km. We also note that preliminary analysis of 150 m vertical resolution data obtained using the EISCAT VHF radar and a 64 baud complementary phase code pair have shown on occasion that scattering layers are confined to one range gate - a result that is consistent with the FDI results presented here. Finally, we note that analysis of the phase of the coherence coefficient shows the rapid downward motion of the layer that carries it from the 86.0 km range gate to the 84.5 km gate. This is shown in Figure 6 where the 2π ambiguity of the phase estimate has been "unwrapped" and the values scaled to represent relative layer position. The results are computed using the phase estimate obtained from both range gates. The rapid downward motion of the layer between 20 and 29 minutes on the plot is clearly seen. The transition between range gates occurs near 25 minutes on this plot. Note that the layer moves down approximately 1200 meters within a period of 9 minutes. This corresponds to an average downward velocity of 2.2 m/s which is consistent with the spectrogram shown in Figure 3. Note also the downward acceleration of the motion that begins at 23 minutes on the plot. This coincides with the acceleration seen in the spectrogram during the transition.

We now turn to an analysis of the spectral jump that occurs in the 86.0 km range gate during the first 10-m of the plot. Inspection of the SNR and coherence plots show that the coherence coefficient is relatively low both before and after the jump and dips to an even lower value during the jump.

In order to obtain more information about the nature of the spectral jump, we have computed the coherence spectrum $S_{12}(\omega)$ for periods before, during and after the jump. Figure 7 shows the auto-spectra and magnitude and phase of the coherence spectrum averaged over 1 minute intervals. These spectra are shown for five 1-min. periods. The first and last two periods correspond to the periods immediately before and after the jump, and the middle period corresponds to the transition. The limiting coherence at the 95% level for this 1 minute average of 12 independent spectra is 0.49.

Note that the magnitude of the coherence spectrum attains large and statistically significant values both before and after the jump with values as large as 0.95 observed. This is in contrast to the relatively small values of the coherence coefficient during this interval. It should also be noted that the magnitude of the coherence spectrum is large over a frequency interval corresponding to only part of the auto-spectra. For example, at 12:46:05 and again at 12:48:05 and 12:49:05 the frequency interval containing large coherence is offset from the center of the auto-spectra. Note also that the portion of the spectrum that exhibits the highest coherence corresponds to the largest Doppler shifts both before and after the jump. Even more interesting is the phase spectrum which shows a distinct positive slope just before the jump and a negative slope just after the jump. A single example of a similar phase slope feature was reported by KUDEKI and STITT (1987) in their FDI analysis of the coherence spectrum of mesospheric echoes obtained at Urbana. Recalling that the phase of the coherence estimate is directly proportional to the distance of the scatterers from
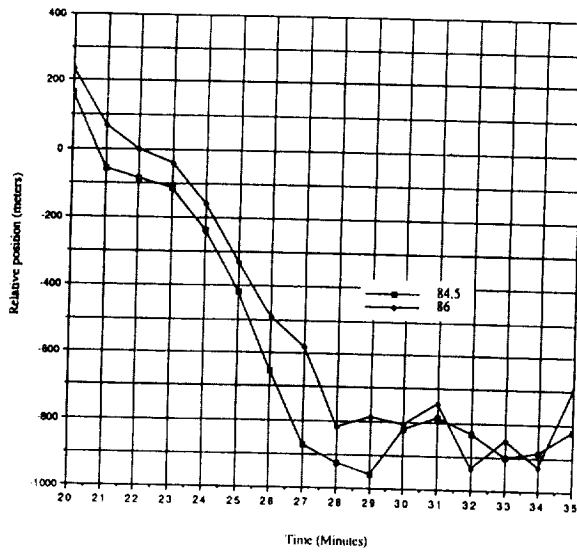
Figure 6. The relative position of the thin scattering layer as estimated from the phase of the coherence coefficient for the interval when the spectrogram indicates downward and accelerating motion.
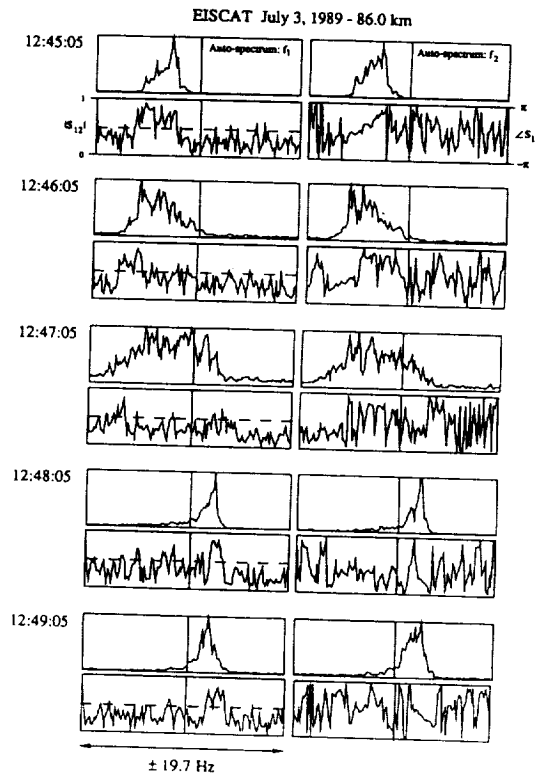
Figure 7. Auto spectra and coherence spectrum magnitude and phase for 5 one-minute intervals before, during, and after the jump in the Doppler frequency. Four curves are shown for each one-minute interval. Clockwise from the top left: auto-spectrum at f_1, auto-spectrum at f_2, phase of the coherence spectrum, and magnitude of the coherence spectrum. The limiting coherence at the 95% level is indicated by the dashed line for the magnitude of the coherence spectrum.

the radar, the range of phase angles covered by the tilted phase trace is therefore proportional to the extent of the scattering region along the line-of-sight. Referring to Figure 7 we note that the phase slope covers a range of angles corresponding to roughly π radians in the examples shown. This corresponds to an extent of the scattering region of approximately 375 m along the line-of-sight direction. This explains why the coherence *coefficient* was relatively small during this period.

The simplest explanation for the linear trend of the phase vs. Doppler frequency is a vertical gradient in the vertical component of the neutral velocity. The slope of the linear phase trend corresponds to an effective vertical gradient on the order of $16 m\text{-}s^{-1}\text{-}km^{-1}$. This is large and is difficult to justify on physical grounds. It is also difficult to imagine that such a large vertical gradient would suddenly change sign within less than one minute. Since any model that we choose to explain the phase tilts should also explain the jump in the spectrum we refer to ROTTGER et al. (1989) who suggested two scenarios that could explain the sudden frequency jumps. One possibility is that the echoes are partial reflections from sharp gradients in refractive index. If the reflecting surfaces are corrugated or rippled, then the echoes will come from one or more specular points on the surface. The specular points can rapidly disappear and new ones can re-appear causing discontinuities in the Doppler shift of the radar echoes. These authors have numerically simulated this possibility and have shown that jumps exactly like the one seen here can be reproduced. They also point out that partial reflection from a single layer is not necessary to produce this signature as rippled scattering layers containing highly anisotropic irregularities would provide the same signature. We have used the numerical simulation method to test whether this scenario could account for the observed cross-spectral phase signature. We find that linear phase variation with Doppler frequency can indeed be reproduced, however we were not able to reproduce such steep phase slopes with reasonable parameters. To illustrate the difficulty with this model we note that, in order for a specular point to exist within the beam, the tilt of the layer must be less than the half-width of the beam, or less than approximately 1.4° in this case. If we imagine a horizontally extended and tilted layer drifting horizontally, then in order for line-of-sight distance to the specular point to change by 375 m it is necessary that the tilted surface be translated horizontally over a distance of at least 375/tan(1.4°) = 15.3 km. Now in order for the distance to the specular point to change by 375 m within the one-minute averaging period the horizontal velocity of the layer would need to be on the order of 250 m/s. This velocity is a factor of 5-10 too high to be reasonable. Furthermore, when shorter integration periods are employed, the specular point model produces a narrower spectrum and a linear phase variation that covers a proportionally smaller range of angles because the specular point has less time to move. We have computed the phase spectrum from the experimental data using 15-s integration periods and find that the width of the spectra and the range of angles covered by the phase slope does not change significantly. Thus, the data are inconsistent with the specular point model.

A second possibility pointed out by Rottger et al. is that the frequency jumps could be the signature of "wave steepening or wave tilting" (e.g. WEINSTOCK, 1986) which occurs as gravity waves enter the amplitude regime where non-linear effects become important. A steepened wave can distort a thin reflecting layer or layer of turbulence in such a way as to cause jumps in the frequency spectrum. The idea here is similar to the reflecting surface idea mentioned previously, however, now we do not require specular reflections. Instead, a relatively thin tilted layer of isotropic, or nearly so, turbulence drifts through the beam. The geometry is more or less equivalent to a horizontal layer observed with a tilted radar beam. The effect is to add a component of the horizontal velocity to the line-of-sight velocity sensed by the radar. The spectrum will be broadened because the different parts of the beam sense different line-of-sight velocities. For narrow beams, both the line-of-sight velocity and the line of sight distance to the layer will change in an approximately linear manner from one side of the beam to the other. Thus, the linear variation of apparent distance (phase) and Doppler frequency can be reproduced. Furthermore, the linear variation of phase and the width of the spectrum due to beam broadening will not depend on the integration time used to produce the spectral estimate since the layer is always present in the beam. The sudden change in the Doppler frequency can be explained if the sign of the tilt changes

abruptly as in the picture presented by ROTTGER et al. (1989). This appears to be the most reasonable model and could explain the observations. For example, we noted earlier that the phase tilt corresponds to a range of line-of-sight distances on the order of 375 m. This distance is directly related to the tilt of the layer in the proposed model. The horizontal extent of the radar beam is approximately 2.0 km so the effective tilt of the layer is approximately $\tan^{-1}(0.35/2.0) = 10°$. The mean Doppler shift of the spectra both before and after the jump corresponds to a line-of-sight velocity on the order of ± 3 m/s. If this is caused by a tilted layer bringing the horizontal velocity into view then the relationship between horizontal and nominal line-of-sight velocity is $v_{los} = v_h \sin(10°) = 0.17 v_h$. Thus, the horizontal velocity would have to be on the order of $3/0.17 = 17.6$ m/s. Although independent estimates of the horizontal winds are not available, this is a reasonable number and shows that the observations can be explained by the proposed model.

CONCLUSIONS

We have presented a preliminary analysis of the first two-frequency "coherent scatter" measurements using the EISCAT 224 MHz radar. The FDI analysis technique was used to show that extremely thin scattering layers with thicknesses on the order of 100m are sometimes present in the polar summer mesosphere. We were able to infer the layer thickness with high accuracy even though the radar pulse length was 10 μs long, corresponding to a 1.5 km range gate thickness. The layer position was tracked for a period of 10 minutes until it appeared to dissipate. Furthermore, we have studied an example where the Doppler spectrum exhibits a frequency jump. Such frequency jumps have been found to be a characteristic of the PMSE observed at 224 MHz and several intriguing examples have been presented in LaHOZ et al. (1989) and ROTTGER et al. (1989). We found that the two-frequency coherence spectrum exhibited a sloped phase characteristic just before and after the discontinuity. This signature was found to be consistent with scattering from a tilted and relatively thin scattering layer. The frequency jump can be explained if the sign of the tilt changes abruptly which is expected if the layer is responding to a steepened gravity wave. These results are based on analysis of only a short data segment and cannot be taken to be representative of the overall characteristics of the polar summer mesosphere echoes. They serve to illustrate the potential of the FDI technique at EISCAT, however. Further analysis and interpretation of the excellent data set collected during the 1988 PMSE campaign is continuing and results will be reported in future publications. Finally, we hope that these preliminary results will encourage the further development of EISCAT as an MST radar. In particular, the possibility of running simultaneous spatial- and frequency-interferometry is exciting and should make it possible to obtain even more information about the structure and dynamics of the scattering irregularities.

References:

Bloomfield, Peter, *Fourier Analysis of Time Series: An Introduction*, John Wiley and Sons, 1975.

Farley, D. T., H. M. Ierkic, and B. G. Fejer, "Radar interferometry: a new technique for studying plasma turbulence in the ionosphere," *J. Geophys. Res., 86*, 1467, 1981.

Kudeki, Erhan and G. R. Stitt, "Frequency Domain Interferometery: A high resolution radar technique for studies of atmospheric turbulence," *Geophys. Res.Lett., 14*,198-201, 1987.

Kudeki, E. and G. Stitt, "Frequency domain interferometry studies of mesospheric echoing layers at Jicamarca," this volume.

LaHoz, C., J. Rottger, and S. J. Franke, "Dynamic spectra of PMSE measured by EISCAT at 224 MHz", this volume.

Rottger, J., C. LaHoz, S.J. Franke, and C.H. Liu, "Gravity wave steepening and tilting detected in high resolution Doppler spectra of polar summer mesosphere echoes (PMSE) observed with the EISCAT 224 MHz radar," this volume.

Weinstock, J., Finite amplitude gravity waves: harmonics, advective steepening and saturation, *J. Atmos. Sci., 43*, 688-704, 1986.

SIMULTANEOUS OBSERVATIONS OF ATMOSPHERIC TURBULENCE BY RADAR AND SCIDAR TECHNIQUES

M. CROCHET[1], J. VERNIN[2], O. GHEBREBRHAN[3] and M. AZOUIT[2]

(1) LSEET, Université de Toulon, UA 705 CNRS, 639 Bd des Armaris, 83100 TOULON, FRANCE

(2) Département d'Astrophysique, Université de Nice, Parc Valrose, 06034 NICE CEDEX, FRANCE

(3) Geophysical Observatory, Addis-Ababa University, ADDIS-ABABA P.O. BOX 1176, ETHIOPIA

ABSTRACT

Simultaneous data on the refractive index structure constant $C_n^2(z,t)$ have been obtained during a coordinated campaign conducted on the same site and involving a VHF ST radar and an optical SCIDAR (SCIntillation Detection And Ranging). Turbulent layers are detected at the same altitude by the two techniques with a turbulence of the same order of magnitude (discrepancy of the order of 4 due to calibration uncertainty) and the same variability in time above altitudes where humidity is contributing to radio refractive index and not to optical refractive index.

INTRODUCTION
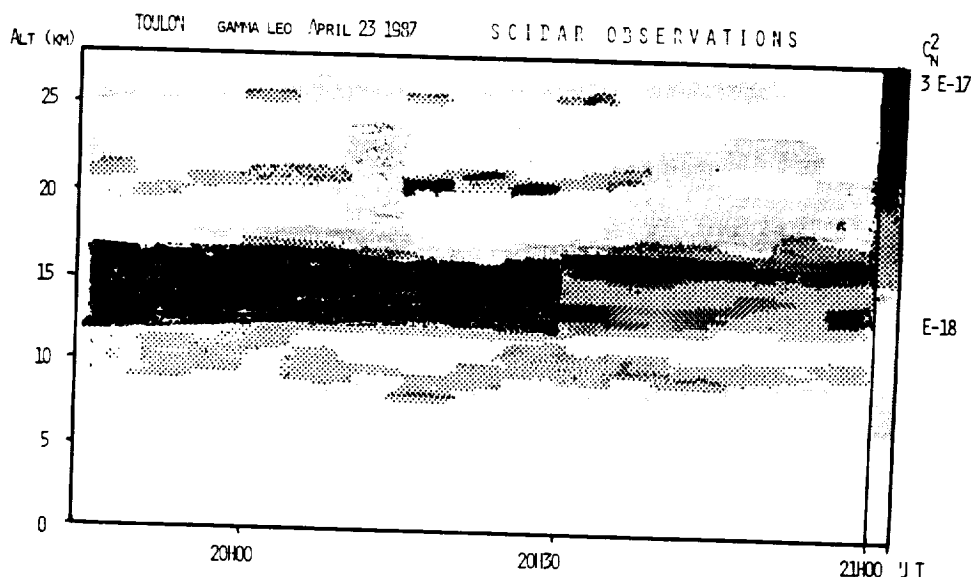
Fig. 1 - Time variation of C_n^2 measured by the scidar technique

Time variation of refractive index structure constant C_n^2 are presented between 1 and 27 km (Fig. 1). Strong signals can be identified as high as 21 or 26 kilometers like with a very powerful MST radar (Poker Flat, Jicamarca,

Arecibo, Mu or Sousy). But these signals have been observed in Toulon where the Provence Radar is not powerful enough to get oblique echoes higher than 20 kilometers. These results very similar to MST observations have been in fact obtained with a very different technique originally developped by the "Astrophysics Department" of Nice University using scintillations from double stars (gamma Virgo or gamma Leo). The SCIDAR experiment (SCIntillation Detection And Ranging) has been set up from late March to early May 1987 on the Toulon University campus at about 200 meters from the "Provence" ST radar.

Previously, a similar experiment has been performed near SUNSET radar in Colorado (GREEN and VERNIN, 1984) but due to meteorological and technical conditions only a few nights of comparison have been available and large discrepancies observed 2 nights amongst 4.

GENERAL DESCRIPTION OF THE EXPERIMENTS

i) The ST Radar

The "Provence" ST radar has been described elsewhere (CROCHET,1989 same issue) and the main parameters are the following :

- Transmitted peak power : 36 KW
- Antenna are: 3300 m^2
- Efficiency including loss in cable : 0.35
- Antenna efficiency : 0.51
- Radar frequency : 45 MHz

The 45 MHz ST radar is selecting a 3.14 meters wavelength in the turbulence spectrum and according to usual values for the internal and external lengths of turbulence this wavelength can be considered to be well inside the inertial subrange.

The turbulent structure constant is determined from measurements of the signal to noise ratio with the following hypothesis.

The noise is the cosmic noise obtained by interpolation from sky maps (DALAUDIER et al.,1989) and the mean value is of the order of 6000° K outside of the galaxy.

The value of the structure constant C_n^2 is then :

$$C_n^2 = 2 \ 10^{-17} (\frac{S}{B}) \ (\frac{r}{10.000})^2 \ (\frac{600}{\Delta r})^2 \ (\frac{512}{NCI})$$

with :   S : signal power
           B : noise power
           r : range in meters
           Δr : range resolution in meters
           NCI : number of coherent integrations

ii) The SCIDAR technique

The SCIDAR will select a range of horizontal wavelengths in the inertial subrange of the turbulente spectrum between approximately 5 to 20 centimeters (VERNIN and AZOUIT,1983).

The light from a star is perturbed by the optical index random fluctuations due only to temperature fluctuations and the scintillations observed on the ground are the results of a convolution of the random phase fluctuations and Fresnel diffraction filtering.

With the weak fluctuations approximation the spectral density can be related to the intensity of turbulence through the following equation :

$$W(\vec{K}_T) = [8 \pi k^2 |\vec{K}|^{\frac{-11}{3}}] \quad [0.033 \ c_n^2 \ (h) \ \delta h] \ \sin^2 \ (\frac{h \ K^2}{2k})$$

[Kolmogorov law] [turbulence intensity] [Fresnel term]

related to the space correlation function by Fourier transform

$$C(\vec{r}) = \quad W(\vec{K}_T) \quad e^{-i \ \vec{K}_T \cdot \vec{r}} d\vec{K}_T$$

with :
- k : optical wavenumber
- K : selected turbulent wavenumber
- h : altitude of the turbulent layer

The scintillation pattern through the 0.84 m plastic lens of a portable telescope is the superposition of the patterns of the double star. The angle between the two stars being known and the correlation distance being measured, it is then possible to determine the altitude of a single turbulent layer.

For multiple layers, an iterative inversion of the spatial correlation function is necessary.

With the double stars (gamma Virgo and gamma Leo) selected for the present experiment the height resolution of the scidar is about 1000 meters of the same order than the radar resolution (600/1200 m).

EXPERIMENTAL RESULTS

For about one month of experiments, 17 nights of simultaneous observations have been obtained.

During 3 nights, the radar has been seriously perturbed by industrial interferences due to sparks on an high voltage power line during mistral conditions and these nights have been eliminated from the comparisons as during another night when the moon was partially affecting the SCIDAR measurements.

Time evolution of the turbulent layers identified independantly by both techniques is similar and the mean turbulent level is of the same order of magnitude.

The data have been integrated in time during 1-2 hours periods corresponding to the time of observation of the same double star.
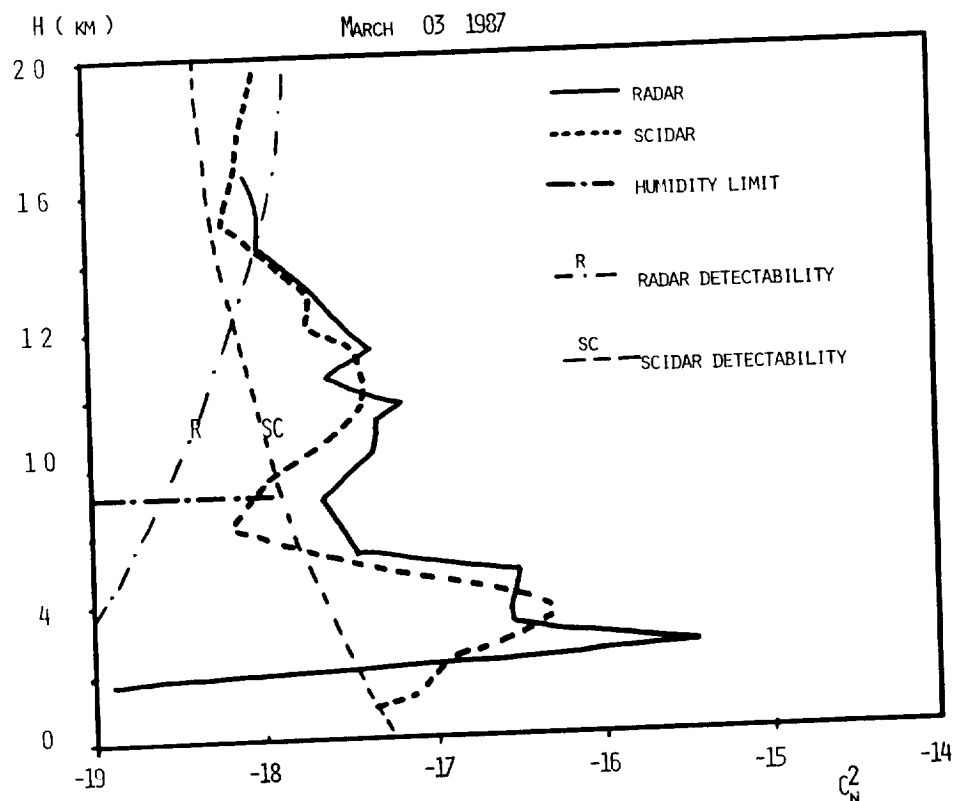
Fig. 2 - Comparison between radar and scidar measurements of the refractive index turbulent structure constant C_n^2

The results are presented (Fig. 2) with an adjustement factor of 4 (6db) corresponding to the mean difference between the absolute value of the structure constant determine independantly by the two techniques. At the present time, this permanent discrepancy with the scidar value larger than the radar one by 6 db cannot be explained and can be considered as due to the non perfect calibration of both instruments. Errors in the radar measurements are certainly due to inaccuracy in the antenna efficiency and variations in the cosmic noise used as a reference. Some errors in the scidar structure constant could be due at same altitudes to the complex iterative inversion process.

However, in spite of this adjustment factor of 6 db this two techniques very different by theirs principles are in fairly good agreement (Fig. 3) above 10 kilometers where humidity does not contribute.

The deep minimum which is sometimes indicated on Scidar data is not significant because it is below the sensitivity threshold of this instrument.

It has to be noted that the Scidar sensitivity increases with altitude (Fig. 2) at the opposite of the radar sensitivity. That explains the good results obtained by the scidar technique at 25 Km (Fig. 1) like a MST radar.
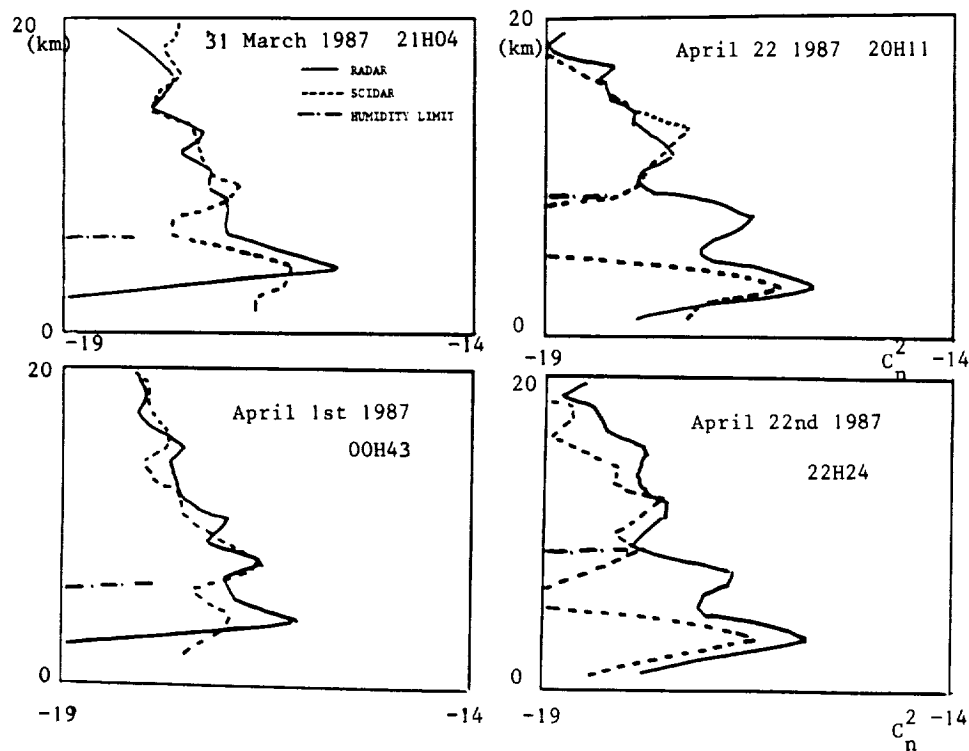
Fig. 3 - Some samples of radar and scidar measurements of C_n^2 during some of the 17 nights of observations

CONCLUSIONS AND PERSPECTIVES

The very different radar and scidar techniques identify in real time the same turbulent layers when they are sensitive enough and when humidity is not involve (above about 10 km).

There is a general agreement between the absolute measurement of the structure constants obtained independantly even if some progress have still to be made to explain a systematic discrepancy of about 6 db.

The scidar operating only during clear sky and new moon conditions is more sensitive at high altitudes and specially adapted to investigate stratospheric turbulent layers.

The ST radar which is an all-weather instrument is more sensitive at low altitudes due to the range dependance and to contribution of humidity fluctuations to the structure constant.

It would be very useful to compare scidar measurements of C_n^2 to measurements obtained by a powerful and well calibrated MST radar (MU, Arecibo, Jicamarca ?...) as a proof of the scidar exact calibration and then to use the calibrated transportable scidar as a standard to calibrate other ST radars.

REFERENCES

DALAUDIER F., M. CROCHET and C. SIDI (1989) - "Direct comparison between in-situ and radar measurements of temperature fluctuation spectra : A puzzling result" - Submitted to Radio Science.

GREEN J. and J. VERNIN (1984) - "Simultaneous remote sensing of atmospheric turbulence by radar optical means : a comparison" - Proc. IGARSS 84 Symp. ESA SP-215, p. 467-472.

VERNIN J., M. AZOUIT (1983) - "Traitement d'image adapté au speckle atmospherique :

I - Formation du speckle en atmosphère turbulente - Propriétés statistiques J. Optics (Paris), 14, n° 1, pp. 5-9

II - Analyse multidimensionnelle appliquée au diagnostic à distance en turbulence - J. Optics (Paris), 14, n° 3, p. 131-142"

RANGE DEPENDENCE OF VOLUME SCATTERING FROM A FRACTAL MEDIUM : SIMULATION RESULTS

Prabhat K. Rastogi
Electrical Engineering and Applied Physics Department
Case Western Reserve University, Cleveland, Ohio 44106

Karl F. Scheucher
Modtech Corporation
7136 Eagle Road, Willoughby, Ohio 44094

Summary

Variation of scattered signal power with range in atmospheric radar experiments is fully understood only for a point target and for volume scattering from a homogeneous random medium. In these cases the signal power decays, respectively, as inverse-fourth power and inverse-square of range. Intermediate cases of random media with partial space-filling characteristics are numerically examined in a fractal model. Planar targets are successively divided into cells of smaller size, eventually reduced to isotropic 'point' targets. At each stage of division, cells are activated with a probability p, which controls the degree to which the scattering region is filled - or its fractal dimension D. For each realization of the medium, the signal power is obtained by coherently adding the complex receiver voltage due to each point target. It is found that volume scattering is a good approximation even for targets that only fill-up a plane i.e. have fractal dimension D~2.

Introduction

In atmospheric radar experiments, the dependence of received signal power on range of the target is exactly known for only two ideal cases. The signal power due to a point target falls off as inverse-fourth power of range, but only as the inverse-square of range for a distributed homogeneous random medium.

The behavior of scattered signal power P_s in the two cases is best expressed through the radar equation [see e.g. Tatarskii, 1971; Doviak and Zrnic, 1984; Collin, 1985; or Sato, 1989]. We consider a monostatic radar experiment at a frequency f_o (or wavelength λ_o), using a circular antenna of diameter d with on-axis gain G. The gain is related to the effective antenna area A through

$G=4\pi A/(\lambda_o)^2$. The antenna radiates over a beam of width $\theta=\alpha\lambda_o/d$, where α is nearly one. The target is assumed to be in the far field of the antenna radiation pattern.

Consider first a point target of effective cross-section σ at range r. The target reradiates a small fraction of the incident flux towards the receiver antenna. The power in received signal is obtained as

$$P_s = \frac{(P_t G)}{4\pi r^2} \times \sigma \times \frac{(A)}{4\pi r^2} \times L = \frac{P_t A^2 L \sigma}{4\pi \lambda_o^2 r^4} \qquad [1]$$

where P_t is the transmitter power, and all the losses have been lumped together in L. We note that P_s falls with range r as r^{-4}.

Next we consider a homogeneous ensemble of many randomly distributed point targets. P_s is appropriately obtained through summing the contribution, on a voltage basis, of all the point targets. It is conventional to assume that the targets are statistically independent and their contributions are additive on a power basis. The effectiveness of this ensemble in scattering radio waves is specified through a cross section σ_v per unit volume. The region of medium that contributes to P_s is located at a range r and is delineated by the beam width θ and a resolution Δr in range. The nominal volume that contributes to P_s is then $V=r^2\,\delta\Omega\,\Delta r$, where $\delta\Omega=\theta^2/4$ is the solid angle subtended by the beam. Then the radar equation becomes

$$P_s = \frac{(P_t G)}{4\pi r^2} \times V\,\sigma_v \times \frac{(A)}{4\pi r^2} \times L = \frac{(P_t A)\alpha^2 L}{64\,r^2} \times \Delta r\,\sigma_v \qquad [2]$$

Since V increases with r^2 due to beam spreading, the final result that P_s varies as r^{-2} appears quite reasonable. We also note that P_s is independent of radar wavelength λ_o, except through σ_v. Other forms of the radar equation for specific antenna shapes and illumination patterns differ only in numerical constants from equation [2], which assumes a well defined scattering region limited by θ and Δr.

Whether atmospheric irregularities that contribute to scattering, conform to these extreme cases is dubitable, especially in view of empirical evidence for their temporally and spatially intermittent structure [Rastogi and Bowhill, 1975; Fritts and Rastogi, 1985]. The exact power-law dependence of P_s on range r is a function of the extent to which the target fills the medium. It

varies from r^{-4} for a point target to r^{-2} for a distributed random medium, which spatially fills up the scattering region V. Intermediate cases are not amenable to analysis but have some implications on suitable scaling laws for radar probing of realistic random media.

In this note we examine the range dependence of P_s for these intermediate cases. The extent to which the scattering region V is filled is controlled by the fractal dimension D of the ensemble of point targets. A brief review of fractals is included in the next section. The scattered signal power P_s is obtained by adding the contributions of point targets, at the receiver, on a voltage basis. Range dependence of P_s as a function of D is then examined.

Fractals as models for a random medium

Many natural objects which show structure at a hierarchy of scales cannot be described through smooth functions. Their structure can be convincingly represented through the use of fractals [see e.g. the authoritative essay and treatise by Mandelbrot, 1977 and 1983]. The following very brief remarks serve only to introduce the notation, specifically the definition of fractal dimension D and its relation to the Euclidean dimension E and topological dimension D_T.

The simplest fractal is any natural irregular curve (of topological dimension $D_T = 1$) drawn on a plane (in Euclidean dimension E=2). The length L along the curve can be measured by using yardsticks of length y, put end to end along the curve. L(y) generally depends on y, and in fact increases as y is made smaller unless the curve is a straight line. The slope or gradient of L(y) with y on a log-log plot indicates how irregular the curve is. For a straight line, the slope is indeed zero. The fractal dimension D of the curve is defined through

$$\frac{d \log L(y)}{d \log y} = 1\text{-}D \qquad [3]$$

and is indeed 1 for a straight line.

An artificial but instructive example of a fractal curve is the (triadic) Koch curve (Figure 1). We start with a line segment of unit length and divide it into three equal segments. The center segment is replaced by two sides of an equilateral triangle. The total length is now 4/3, measured with a yardstick y=1/3. If this operation is repeated on each segment, we obtain a total length

of $(4/3)^2$, now measured with a yardstick $(1/3)^2$. The operation can be iterated an arbitrary number of times. At each iteration the yardstick y reduces by a factor $(1/3)$, and L(y) increases by a factor $(4/3)$. The fractal dimension D of the Koch curve is obtained by equating the slope $\log(4/3)/\log(1/3)$ to 1-D as $D=\log(4)/\log(3)=1.262$. The value of D is greater than $D_T=1$ as the Koch curve is more irregular than a straight line. Yet D is considerably less than E=2, a value that is approached for a very irregular curve that tends to fill the entire plane. The Koch curve can be randomized, without changing D, by selecting the segment to be subdivided from the results of throwing a die. By putting Koch curves on the three sides of an equilateral triangle, one obtains a Koch island enclosed by a fractal coastline.
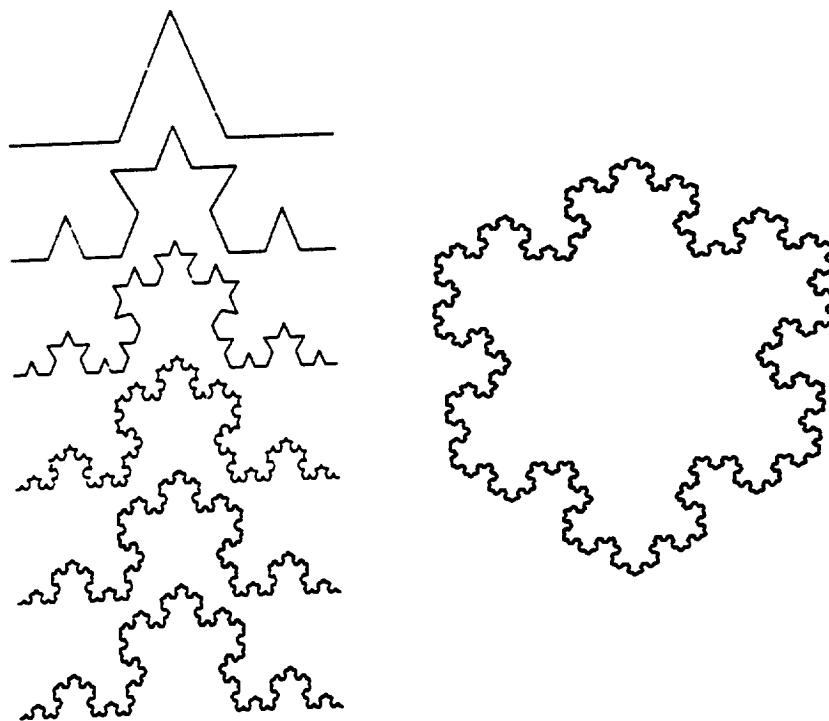
FIGURE 1. The fractal Koch curve in successive stages of construction, and the Koch island obtained by applying this construction to the sides of an equilateral triangle. These curves have a fractal dimension D=1.262 as discussed in the text.

A construction similar to above considers a distribution of points ($D_T=0$) on a straight line (i.e. in Euclidean dimension $E=1$). It begins with a unit line segment. The center one-third of the line segment is deleted. The same operation is applied iteratively to undeleted segments. This construction yields a distribution of points on a line, so called Cantor dust, with $D=\log(2)/\log(3)=0.631$. Once again we find that D lies between $D_T=0$ and $E=1$.

As our next example, we begin with a unit square (in $E=2$). The square is divided into n^2 equal subsquares of side n^{-1}, and this process can be iterated. The Euclidean dimension ($E=2$) for an area is recovered by noting that at each stage of division the yardstick length is reduced by a factor n, as n^2 new subsquares are created and $E=2=\log(n^2)/\log(n)$. Now suppose only a fraction $p \geq n^{-2}$ of subsquares is filled at a stage of division, and the process is applied iteratively only to those subsquares that have been filled. After several iterations, the unit square is filled with an apparent random pattern of 'points' or dots of finite size. The fractal dimension D of this pattern is at most E, but can be as small as 0. At each iteration, the number of subsquares covered by the pattern is $p\,n^2$ while their side is reduced by a factor n. D can now be defined in an analogous way as $\log(p\,n^2)/\log(n)$ or $2+\log(p)/\log(n)$. The additive factor is actually negative or zero, since $p \leq 1$.

The fraction p may also be regarded as a probability. Then the pattern is truly random, and statistically self similar under magnification. The extent to which the random pattern fills the unit square can be controlled by selecting p. When $p=n^{-2}$, D becomes 0. The extension to $E=3$ should be obvious with $D=\log(p\,n^3)/\log(n)$. Examples of realizations of random dots on a plane are shown in Figure 2. The dots may be regarded as random point targets in a radar scattering experiment. Such examples then serve as the basis for numerical experiments described next.

Formulation of scattering from a fractal medium

We have used a numerical simulation of radar scattering to study the variation of signal power with range, wavelength and aspect of the target. In this formulation, the response of a monostatic radar to an isotropic point target is evaluated as follows. A unit scattering cross section is assigned to the point target. A point target s_i at a point r_i is illuminated by a beam that is uniform over its width θ. The scattered electric field E_i at the receiver antenna under the far-field assumption varies with the distance r_i to the target

| p=0.30 | p=0.40 | p=0.50 | p=0.60 | p=0.70 |
| D=1.13 | D=1.34 | D=1.50 | D=1.63 | D=1.74 |
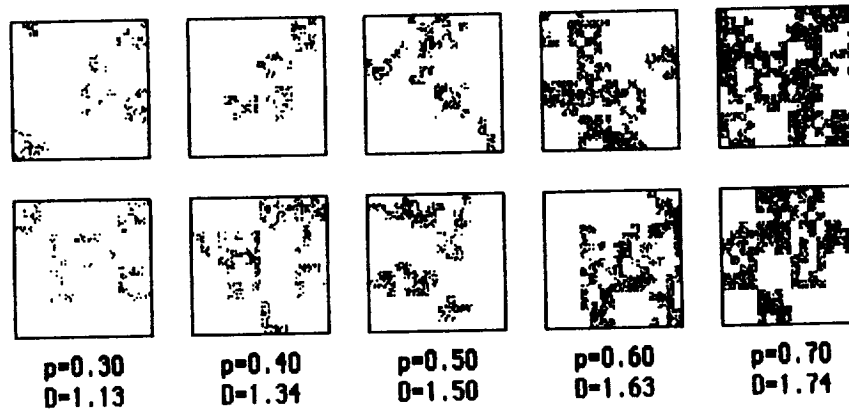
FIGURE 2. Random patterns of dots on a 64x64 grid. At each step of division a cell is divided into 4x4=16 subcells which are then selected with a probability p>4^{-2}. The steps are iterated three times due to finite pixel size. The parameters p and D increase from left to right. Two different realizations are shown for each case. Such patterns model realizations of point targets in a distributed random medium. The fractal dimension D, controlled by the parameter p, determines the extent to which the medium fills up the plane.

as $(r_i)^{-2}$, and its phase changes by $-4\pi r_i/\lambda_o$. The complex signal v_i at the receiver output is linearly related to E_i. The signal power due to an ensemble of point targets is obtained from the accumulated complex voltage $v=\Sigma_i v_i$, as $P_s=vv^*$. This assumes that the point targets are statistically independent and the Born approximation, that scattering of the scattered field is insignificant, holds.

In actual simulation, we have considered planar on-axis targets. This limits us to $D\leq2$ in a Euclidean dimension E=3. A fractal target with $D\leq2$ is generated by subdividing the scattering region of 4096x4096 points into 16=4x4 subcells at each of six successive steps. At each step, a subcell is switched on with a probability p. Typical realizations of random points on a plane are as shown in Figure 2. Full simulation of a volume target with ~64 billion points is clearly impractical for computational reasons.

In physical terms, a linear dimension of 0.1 m is associated with each point target. The linear size of the scattering region is then ~ 0.4 km. For

computational reasons, the beam width and range resolution are kept constant at $\theta=0.9°$ and $\Delta r=0.32$ km. Five values for each of the following parameters were used : target range r from 5 to 20 km, zenith angle ζ from 0° to 20°, wavelength λ_o from 3 m to 1 m. The probability parameter p that controls the fractal dimension D was varied from 0.3 to 0.7 in increments of 0.1. For each of the 625 distinct cases, P_s was averaged over 20 different realizations. The scaling law for dependence of P_s on any parameter e.g. the range, is then obtained through regression analysis. Only the range dependence is discussed in this paper.

The parameter values reflect typical middle-atmosphere radar experiments. At some radars that use large antennas, e.g. Jicamarca and Arecibo, near-field effects are significant. These are simple to include and will be of interest in our future work as the radar equations, [1] and [2], are valid for the far-field only.

Results for range dependence : Discussion and interpretation

We stipulate a power-law relation of the form $P_s \sim r^{-\beta}$ for range dependence of scattered signal power. The exponent β is 4.0 for a point target and 2.0 for a target that spatially fills up the beam, i.e. has D=3. The exponent β was obtained by linear regression of log (P_s) on log (r), in the numerical experiment described above, for five distinct values of D between 1.13 and 1.74 at wavelength $\lambda_o=2.5$ m and zenith angle $\zeta=10°$.

Figure 3 shows the variation of β with D for the five cases, and also the extreme cases D=0 and D=3. A linear-least square fit to the five points, and a cubic spline fit to all seven points are shown. The volume-filled case ($\beta=2.0$), is well-nigh attained for D as small as ~2 i.e.for targets that only tend to fill up a plane. For D>2.3, the approximation $\beta=2.0$ holds to within 5%.

The above result does not necessarily hold for for all target orientations. For a planar target oriented perpendicular to the beam, and for all targets near vertical incidence, signals from point targets within a Fresnel zone add coherently or on a voltage basis. Evidence for these coherent reflections [see e.g. Rastogi and Röttger, 1982] has been noticed in our numerical experiments and these cases are being examined further.

The simple fractal model of a random medium used above is still far from realistic as it does not include spatial inhomogeneity evident in thin, stratified

layers of turbulence routinely observed in the atmosphere. Improved fractal models e.g. those using an anisotropic cascade [Lovejoy and Schertzer, 1986] are successful in representing such layers and will be used in our future work.
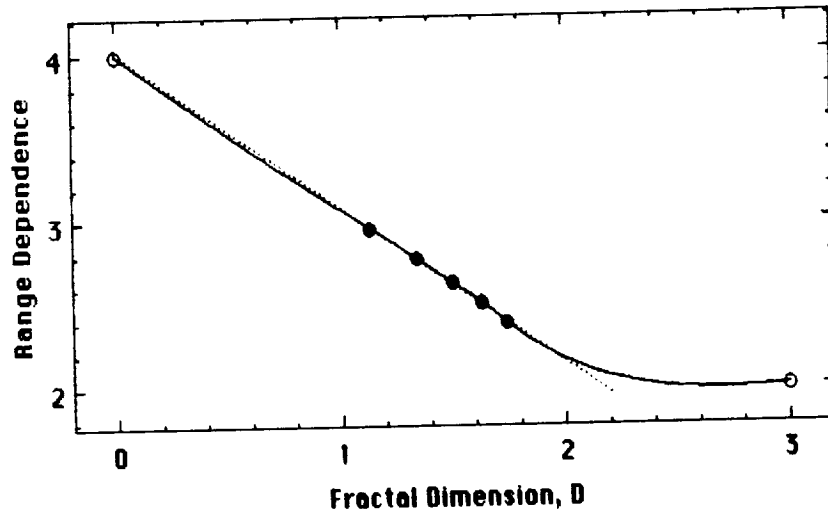
FIGURE 3. Variation of the parameter β, in a power-law range dependence of signal power, on fractal dimension D. Extreme cases of point target (D=0) and volume scattering from a homogeneous random medium (D=3) are shown by hollow circles. Solid circles are the averages over twenty realizations in a numerical experiment. Dotted line is the least square linear fit to these. Solid line is a cubic spline drawn through all the seven points. At first the parameter β falls linearly with D, but tapers off near D~2 to the volume-scattering case. [λ_0=2.5 m, ζ=10°].

References

Collin, R. E., *Antennas and radiowave propagation*, Mc-Graw Hill, New York, 508pp., 1985.

Fritts, D. C. and P. K. Rastogi, Convective and dynamical instabilities due to gravity wave motions in the lower and middle atmosphere : Theory and observations, *Radio Sci.*, **20**, 1247-1277, 1985.

Lovejoy, S. and D. Schertzer, Scale invariance, symmetries and stochastic simulation of atmospheric phenomena, *Bulletin. Am. Meteor. Soc.*, **67**, 21-32, 1986.

Mandelbrot, B. B., *Fractals : form, chance and dimension*, Freeman, San Francisco, 1977.

Mandelbrot, B. B., *The fractal geometry of nature*, Freeman, San Francisco, 468pp., 1983.

Rastogi, P. K. and S. A. Bowhill, Scattering of radio waves from the mesosphere 2. Evidence for intermittent mesospheric turbulence, *J. atmos. terres. phys.*, **38**, 449-462.

Rastogi, P. K. and J. Röttger, VHF radar observations of coherent reflections in the vicinity of the tropopause, *J. atmos. terres. phys.*, **44**, 461-469, 1982.

Sato, T., Radar Principles, Lecture given at *International School on Atmospheric radar*, Nov. 24-28, 1988 , Kyoto, Japan, to appear in *Handbook for MAP*, 1989.

Tatarskii, V. I.,*The effects of the turbulent atmosphere on wave propagation*, Translated from the Russian, U.S. Dep. Commerce, Springfield, Va., 472pp., 1971.

GRAVITY WAVES AND TURBULENCE IN THE MIDDLE ATMOSPHERE

R. A. Vincent

Department of Physics and Mathematical Physics
University of Adelaide
Box 498 GPO Adelaide
Australia 5001

Since the last MST radar workshop in 1985 there have been a number of studies, especially radar investigations, which have advanced our knowledge of waves and turbulence, including climatologies, spectral studies, flux measurements, and source effects.

The temporal variations in wave activity in the mesosphere and lower thermosphere have been addressed in detail at at least two stations. Observations at Saskatoon and Adelaide both show evidence for semi-annual variations in wave activity at heights below about 85-90 km, with the minima in activity coinciding with the reversals in zonal flow at the equinoxes (VINCENT and FRITTS, 1987; MANSON and MEEK, 1986; EBEL et al., 1987). An interesting feature is that the wave motions show pronounced anisotropies. At Saskatoon there is a distinct north-south alignment for waves with periods less than 1 hr (EBEL et al., 1987) while at Adelaide the motions tend to be aligned in the NW-SE quadrants in summer and almost NS in winter (VINCENT and FRITTS, 1987). An examination of rocket data by ECKERMANN and VINCENT (1989) shows that these anisotropies are also manifest in the stratosphere over central Australia. The found a very similar seasonal alignment of wave motions to those observed at Adelaide in the mesosphere. The anisotropies appear to be partly caused by the removal of waves by critical level interactions with the mean winds as they propagate up from below but also appear to indicate preferred sources of wave activity. Direct measurements of mesospheric momentum fluxes made with the dual-beam technique were reported by REID and VINCENT (1987) and FRITTS and VINCENT (1987). These studies supplied further evidence that the largest fluxes were associated with relatively short period waves. Accelerations of the order of several tens of $ms^{-1}day^{-1}$ were inferred. It is not yet certain what role gravity waves drag may play in the stratosphere, although it could be important. In this so-called "gap" region for radars, rocket measurements are still probably the main source of information. Indirect estimates of both zonal and meridional mean flow accelerations of $\sim 1\ ms^{-1}day^{-1}$ were made by ECKERMANN and VINCENT (1989).

To date, the only climatology of turbulence motions and dissipation rates in the 80-100 km region is the study reported by HOCKING (1988) made with the 2 MHz radar at Adelaide. Hocking finds a weak semi-annual variation in turbulence at heights near 80 km, which like the gravity wave activity at the same location, minimizes as the equinoxes, although there can be significant inter-annual variability.

Wavenumber and frequency spectra of atmospheric motions often exhibit a "universality" of slope and possibly of amplitude (to within a factor of two). To explain this universality, theories have been developed in terms of two-dimensional turbulence (GAGE, 1979) and in terms of the dispersive properties of internal gravity waves (VANZANDT, 1982). Recently, there has been considerable progress in describing the spectra in a manner consistent with the latter hypothesis. DEWAN and GOOD (1986) and SMITH et al. (1987) have suggested that the m^{-3} slope observed for the vertical wavenumber (m) spectra at high wavenumbers is due to amplitude limits imposed by saturation of the gravity wave motions. SMITH et al. (1987), for example, show that at

wavenumbers greater than some characteristic scale (m_*) the spectra asymptote to a value of $\sim N^2/(6m^3)$, where N is the Vaisala-Brunt frequency. At wavenumbers lower than m_* the slope tends to zero. A number of MST radar studies have made high height resolution investigations of wavenumber spectra in the lower atmosphere. FRITTS and CHOU (1987), using the Poker Flat MST, found excellent agreement with the saturation hypothesis and dominant vertical scales $(\sim 1/m_*)$ of about 2 km. Other studies show that the dominant scale increases monotonically with increasing height to reach approximate values $\sim 15-20$ km at the mesopause.

An important consequence of the gravity wave hypothesis of wavenumber and frequency spectra is that it has been possible to make predictions about the behaviour of the wave field as the properties of the background medium, such as stability and wind speed, change. VANZANDT and FRITTS (1989) have investigated how the distribution of wave energy changes as a function of m as the waves propagate into a region where N increases rapidly; they predict a rapid loss of energy which should be manifested as increased turbulence dissipation. It will be an important test to search for such effects in regions where significant height gradients of N often occur, such as at the tropopause and the high latitude mesopause. Doppler shifting effects become important when the background wind speed becomes comparable to, or greater than, the mean horizontal phase speed of the waves $(\sim N/m_*)$. How Doppler shifting affects both the spectra of horizontal and vertical fluctuations has been comprehensively investigated by FRITTS and VANZANDT (1987). Their work shows that great care is required when spectra measured in a ground based frame are compared with model spectra because energy can be redistributed to high (ground-based) frequencies. Hence frequency spectra can show significant departures from the $-5/3$ slope often invoked for the spectrum of horizontal motions; the spectrum of vertical motions can be even more severely affected.

There is an important need for a better understanding of the sources of gravity waves, for which task the excellent time and height resolution of MST radars is well suited. BOWHILL and GNANALINGAM (1986) found a good correlation between wave activity in the lower stratosphere and the height of cloud tops, which suggested that convection is an important wave source in topographically flat areas such as Illinois. They found that the levels of activity in both the stratosphere and mesosphere were also correlated, which is one of the few direct examples of gravity wave coupling between the lower and upper atmospheres. However, it is not always possible to determine the cause(s) of enhanced wave activity (e.g. FRITTS and CHOU, 1987). Certainly, in assembling a source climatology it is necessary to be aware of the full meteorological situation which pertains during the observations. For example, UCELLINI and KOCH (1987), in their analysis of strong wave events recorded by micro-barographs, found that they were confined to a region on the equatorward side of the exit regions of jet streaks and the probable wave source was shear or geostrophic adjustment associated with the jet. It is therefore possible that two radars located on opposite sides of a jet-stream axis might measure different levels of wave activity. An important source of mesoscale variability which radars have difficulty studying is topography. Aircraft measurements, made in the GASP campaign, show that topography contributes strongly, especially at horizontal scales in the 4 to 80 km range (NASTROM et al., 1987). Radars can help asses the importance of topography as a source of waves and turbulence in the middle atmosphere if observations made in flat reagions are compared with those made in topographical rich areas.

REFERENCES

Bowhill, S.A., and S. Gnanalingam, Gravity waves in severe weather, Handbook for MAP, 20, (ed Bowhill and Edwards), SCOSTEP secretariat, University of Illinois, 128-135, 1986.

Dewan, E.M. and R.E. Good, Saturation and the "universal" spectrum for vertical profiles of horizontal profiles of scalar winds in the atmosphere, J. Geophys. Res., 91, 2742-2748, 1986.

Ebel, A, A.H. Manson, and C.E. Meek, Short period fluctuations of the horizontal wind measured in the upper middle atmosphere and possible relationships to internal gravity waves, J. Atmos. Terr. Phys., 49, 385-401, 1987.

Eckermann, S.D., and R.A. Vincent, Falling sphere observations of anisotropic gravity wave motions in the upper stratosphere over Australia, Pageoph., (In Press), 1989.

Fritts, D.C., Gravity waves in the middle atmosphere: Recent progress and needed studies, Handbook for MAP, 20, (ed Bowhill and Edwards), SCOSTEP secretariat, University of Illinois, 90-95, 1986.

Fritts, D.C., and T.E. VanZandt, Effects of Doppler shifting on frequency spectra of atmospheric gravity waves, J. Geophys. Res., 92, 9723-9732, 1987.

Fritts, D.C., and H. Chou, An investigation of the vertical wavenumber and frequency spectra of gravity wave motions in the lower stratosphere, J. Atmos. Sci., 44, 3610-3624, 1987.

Fritts, D.C., and R.A. Vincent, Mesospheric momentum flux studies at Adelaide, Australia: Observations and a gravity wave/Tidal interaction model, J. Atmos. Sci., 44, 605-619, 1987.

Gage, K.S., Evidence for a $k^{-5/3}$ law inertial range in mesoscale two-dimensional turbulence, J. Atmos. Sci., 36, 1950-1954, 1979.

Hocking, W.K., Two years of continuous measurements of of turbulence parameters in the upper mesosphere and lower thermosphere made with a 2-MHz radar, J. Geophs. Res., 93D, 2475-2491, 1988.

Manson, A.H., and C.E. Meek, Dynamics of the middle atmosphere at Saskatoon (52°N, 107°W): A spectral study during 1981, 1982, J. Atmos. Terr. Phys., 48, 1039-1055, 1986.

Nastrom, G.D., D.C. Fritts, and K.S. Gage, An investigation of terrain effects on the mesoscale spectrum of atmospheric motions, J. Atmos. Sci., 44, 3087-3096, 1987.

Reid, I.M., and R.A. Vincent, Measurements of mesopause/mesospheric gravity wave momentum fluxes and mean-flow accelerations at Adelaide, Australia, J. Atmos. Terr. Phys., 49, 443-460, 1987.

Smith, S.A., D.C. Fritts, and T.E. VanZandt, Evidence of a saturated spectrum of atmospheric gravity waves, J. Atmos. Sci., 44, 1404-1410, 1987.

Uccellini, L.W., and S.E. Koch,, The synoptic setting and possible energy sources for mesoscale wave disturbances, Mon. Wea. Rev., 115, 721-729, 1987.

VanZandt, T.E., A universal spectrum of buoyancy waves in the atmosphere, Geophys. Res. Lett., 9, 575-578, 1982.

Vincent, R.A. and D.C. Fritts, A climatology of gravity wave motions in the mesopause region at Adelaide, Australia, J. Atmos. Sci., 44, 748-760, 1987.

SUMMARY AND RECOMMENDATIONS

A feature of gravity wave and turbulence observations presented at this workshop was the greater geographical diversity of the measurements. This was made possible by further radars coming into full-scale operation, such as the Flatland, and Chung-Li radars. Observations from these, and other stations, were particularly important in evaluating the significance of

tropospheric convection and fronts, as well as severe weather systems such as typhoons, as wave sources. Other relatively new radars including the the EISCAT VHF radar, the mobile SOUSY radar at Andennes, were able to make use of the strong scattering at VHF from the summer high-latitude mesopause to study a number of wave effects, including non-linearities and momentum fluxes.

The versatility and potential of the Kyoto MU radar was amply demonstrated by the number of papers devoted to a range of topics. Amongst these were studies which made use of the rapid beam steering capabilities to measure momentum fluxes in the troposphere and lower stratosphere. These measurements, which found significant temporal variability in the fluxes, were not inconsistent with theoretical expectations that gravity waves contribute a net drag in the lower stratosphere. Other multi-beam studies addressed the spatial variability of the wave structures, showing that the wave field often exhibited a complicated three-dimensional structure, presumably caused by a superposition of waves. This latter point illustrates a problem which has yet to be fully resolved in case studies of waves, viz. how often are quasi-monochromatic waves actually observed? In many situations it is probable that apparently quasi-monochromatic oscillations which persist for only a few cycles are actually the result of a random superposition of waves present in rather a wide spectrum.

Progress was apparent in spectral studies, with some previous uncertainties as to the cause of variations in spectral shape and magnitude in the frequency domain (especially for vertical motions), being resolved when the effects of Doppler shifting by the background flow are taken into account FRITTS and VANZANDT, 1987).

The observations presented at the meeting went some way to addressing some of the recommendations made by FRITTS (1986) and the needs that he identified at the last MST workshop and which bear repetition. (1) The need for a more diverse geographic coverage, which in turn will provide better measures of geographic variability of waves and turbulence. (2) What are the causes and effects of variability, including source effects and filtering? (3) How important are non-zonally propagating waves, and what is the importance? (4) What are the consequences of wave saturation? How does it affect the generation and evolution of turbulence, and what is the role of the turbulence in diffusion of heat and constituents.?

As a result of the present meeting, it is apparent that rather than making short term measurements of only a few hours in duration, a number of stations are now making more or less continuous observations of winds. This is a highly desirable situation, as it will help in the assessment of various source mechanisms. What is required is a 'source climatology' for each station. To achieve this goal will require the temporal variability to be quantified and the meteorological situations pertaining to be carefully assessed in order to relate the causes of variability to possible source mechanisms, such as shear, convection, geostrophic adjustment etc.

On a more pragmatic level, it is now apparent that care is required when frequency spectra from different sites are to be compared with each other and with model spectra. It is recommended that comparisons take place only after the spectra are 'binned' as a function of the background wind speed. It is also desirable that spectra should be accumulated over an appreciable time, several tens of hours at least, in order to achieve a significant degree of reliability.

In order to achieve a full understanding of the role of waves and turbulence in the middle atmosphere it is desirable that whenever possible radar measurements be made in conjunction with other techniques, such as Rayleigh scatter lidars. In this context, there is significant uncertainty about the conversion factors which relate Doppler velocity spectral widths to turbulence dissipation rates. To help overcome this deficiency, it is strongly recommended that simultaneous, common-volume intercomparisons between radar and in situ (e.g. balloon) measurements of turbulence intensities and dissipation rates should made wherever possible.

RADAR MEASUREMENTS OF ATMOSPHERIC TURBULENCE INTENSITIES BY BOTH C_n^2 AND SPECTRAL WIDTH METHODS

W.K. Hocking and K. Lawry

Department of Physics and Mathematical Physics
University of Adelaide

The VHF radar operated by the University of Adelaide in Australia has been used to measure turbulent energy dissipation rates in the troposphere and lower stratosphere. Two quite different techniques have been utilized; one utilizing the absolute back-scattered power of signals received (GAGE et al. 1980) and one utilizing the spectral widths of the scatterers (HOCKING, 1983a,b).

The first method requires that the radar be properly calibrated, and this has been achieved, by using a noise source. As an example, fig. 1 shows the noise temperature of the sky above the radar over one full 24 hour period. By comparing temperatures to those recorded by a small array of Yagi antennas, it has also been possible to place limits on the efficiency of the Co-Co antenna array used; it turns out to be about 30% - 40% efficient. The calibrations can then be used to convert the received signal strengths to estimates of C_n^2, as shown for example in fig. 2. A beam tilt of 11° from vertical was used. These values are comparable to those of the Platteville radar (NASTROM et al. 1986). Under certain assumptions, outlined by GAGE et al. (1980) these estimates of C_n^2 may be converted to estimates of turbulent energy dissipation rates, ϵ. A sample is shown in fig. 3.

An alternative method to determine ϵ is to use the experimentally determined spectral half-width. However this width is due to a combination of turbulence, and "instrumental" effects like beam-broadening and wind-shear broadening. A sample spectrum, with a Gaussian-fit, is shown in fig. 4. When the measured spectral half-widths are compared to the "instrumental" half-widths (fig. 5) it is clear that there is a contribution to the spectral widths over and above the "instrumental effect". This is in contrast to radars with wider beams, like the SOUSY radar (eg. HOCKING 1986) for which the major cause of the observed spectral widths is instrumental. (The Adelaide VHF radar has a two-way half-power-half-width of 1.1°).

Having removed the instrumental contribution, it is possible to use the residual spectral width to estimate the energy dissipation rates, provided that the Brunt-Vaisala N frequency is known. A sample height profile is shown in fig. 6 and a sample time series in fig. 7.

Radiosonde data have also been obtained for the period of late October, and sample profiles of humidity, temperature and Brunt-Vaisala frequency are shown in fig. 8. This profile was used in determining the energy dissipation rates of figs. 6 and 7, through the relation $\epsilon \approx 0.4 \ v^2.N$, v^2 being the mean square fluctuating velocity.

Each of the two methods of determining the turbulent energy dissipation rates have inherent problems and the next major step in these analyses is to make simultaneous measurements of ϵ by both techniques, in order to compare them for validity. These comparisons should be available in the near future.
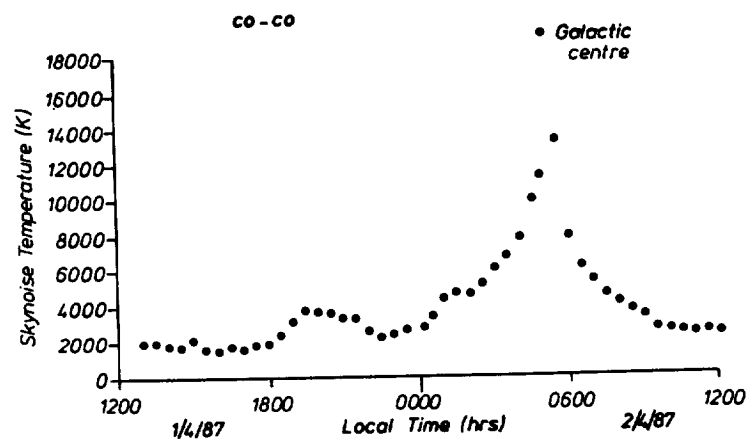
Fig. 1.   Sky-Noise temperature as a function of time of day.
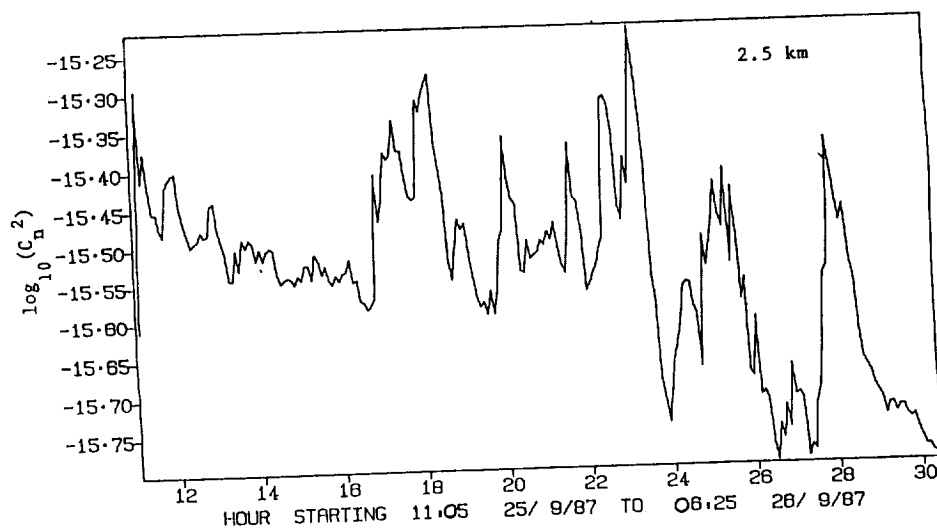
Fig. 2.   Typical C_n^2 values plotted over a 20 hour period in 1987.
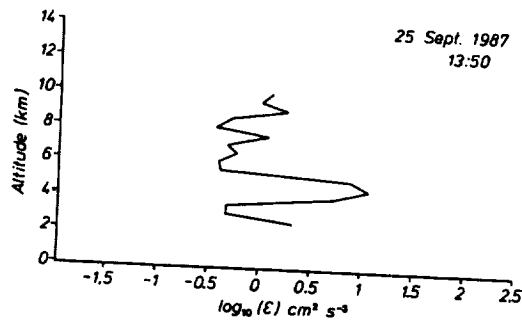
Fig. 3.   Typical height profile of energy dissipation rates determined by the
C_n^2 method.
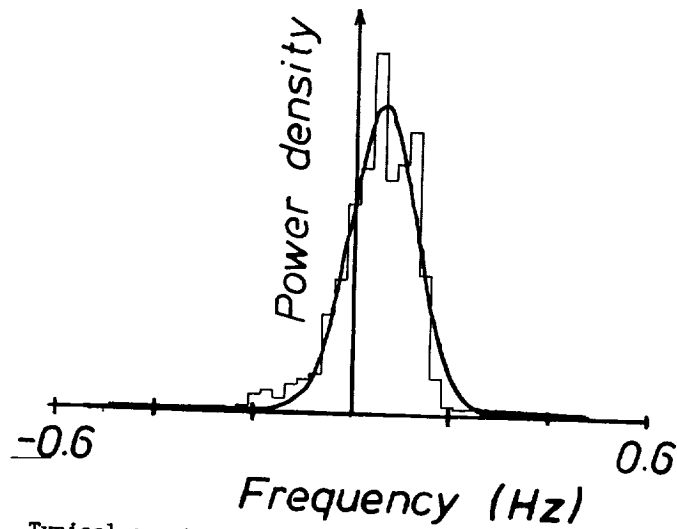
Fig. 4.   Typical spectrum recorded with the Adelaide VHF radar. The spectral
points have been averaged into frequency bins and then a Gaussian
function (plus constant offset) fitted to the spectrum.
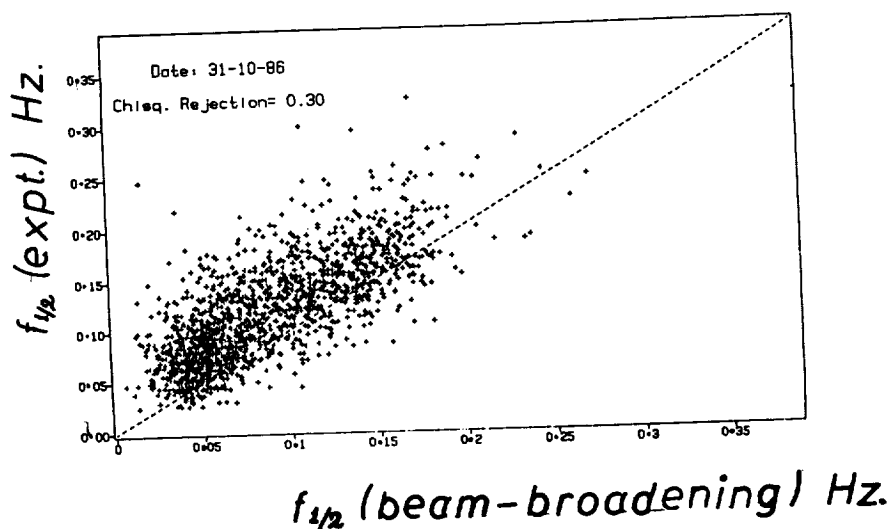
Fig. 5.   Scatter plot of experimental spectral half-power-half-widths vs. the
half-width expected due to beam- and wind-shear broadening
("instrumental"). If the only causes of the spectral widths were
instrumental, the points should be scattered symmetrically about the
broken line. Instead, they are predominantly above this line,
indicating an extra contribution due to turbulence. There are
points below the line, which arise due to statistical effects and
also possibly due to the effects of specular reflectors, although
attempts have been made to remove the latter contribution. By using
sufficient averaging, these statistical fluctuations are reduced.
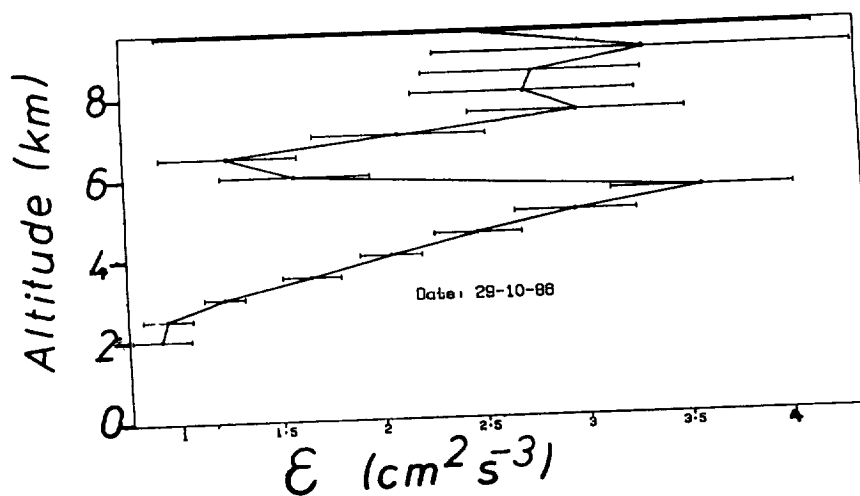
Fig. 6.   Typical height profile of mean energy dissipation rates, averaged
over a 24 hour period

ADELAIDE VHF RADAR, 1986
ALTITUDE 5 KM
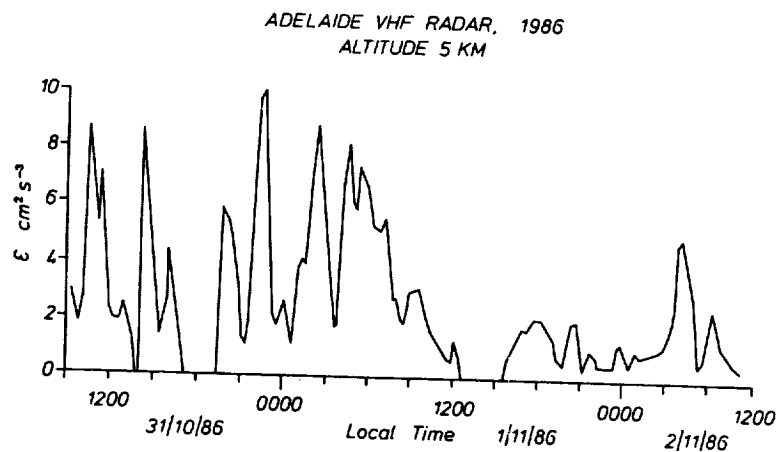
Fig. 7.   Time sequence of hourly mean turbulent energy dissipation rates for
an altitude of 5km in October and November 1986.
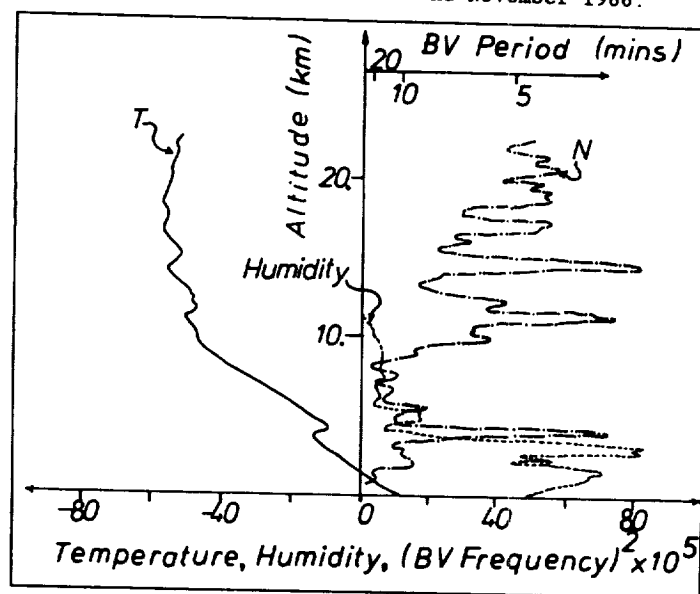
Fig. 8.   Height profiles of temperature, humidity and Brunt-Vaisala frequency
for Oct. 31. 1986 at 0730 local time (30 Oct 1986 at 2200 GMT). This
radiosonde release was made just prior to the data-run shown in fig.
7.

References

Gage, K.S., Green, J.L. and VanZandt, T.E. "Use of Doppler radar for the measurement of atmospheric turbulence parameters from the intensity of clear air echoes", Rad. Sci., 15, 407-416, (1980).

Hocking, W.K. "On the extraction of atmospheric turbulence parameters from radar backscatter Doppler spectra -I. Theory". J. Atmos. Terr. Phys., 45, 89-102, (1983a).

Hocking, W.K. "Mesospheric turbulence intensities measured with a HF radar at 35°S-II". J. Atmos. Terr. Phys., 45, 103-114, (1983b).

Hocking, W.K. "Observation and measurement of turbulence in the middle atmosphere with a VHF radar", J. Atmos. Terr. Phys., 48, 655-670, (1986).

Nastrom, G.D., Gage, K.S. and Ecklund, W.L. "Variability of turbulence, 4-20 km, in Colorado and Alaska from MST radar observations". J. Geophys. Res., 91, 6722-6734, (1986).

Dynamic spectra of PMSE measured by EISCAT at 224 MHz

C. La Hoz, J. Röttger[†]
EISCAT Scientific Association
P.O. Box 812, S-981 28 Kiruna, Sweden
([†] on leave from Max-Planck-Institut für Aeronomie)

S.J. Franke
University of Illinois
Urbana, 61801 Ilinois, USA

0. ABSTRACT

The spectral intensity of radar returns from scattering layers in the atmosphere is a powerful tool to investigate the origing and dynamics of the layers, the scattering mechanisms, and the relations of the layers to other geophysical and geomagnetic phenomena. The dynamic spectra of PMSE layers as a function of Doppler frequency, time and altitude of several experiments carried out during summer of 1988 show an impressive number of phenomena. Wave behaviour, evidenced by quasiperiodic variation of the Doppler frequency as a function of time, is present almost all the time. Doppler frequencies equivalent to vertical motions of $10\,ms^1$ and larger are not rare. Intriguing structures such as seeming discontinuities of the Doppler frequency and braid-like forms occur also quite frequently.

1.INTRODUCTION

The accompanying paper in this issue by LA HOZ et al. (1989a) contains a description of the experiments that we carried out during the EISCAT PMSE campaign in the summer of 1988. The data that we will show in this paper were collected during this campaign. As these results are preliminary, we will restrict our presentation mostly to a qualitative description of the data. More elaborated results and physical interpretations will be presented elsewhere.

The data base we have is relatively small and covers only the day time, mostly between 0900-1500 UT. However, the amount of new information contained in the data is substantial. Here we have selected four types of events and we will show illustrations of them in an equal number of sections. In Section 2 we describe a wave event; in Section 3 the occurrence of a seeming discontinuity in the vertical velocity of the scattering layers; Section 4 shows fine temporal structure of the vertical velocity; and in Section 5 we show an event characterised by a sudden broadning of the signal spectra.

2.LARGE AMPLITUDE WAVES

Figure 1 shows a grey-scale power map of the experiment code-named PMSE3C carried out on July 1st. 1988 between 0848 and 1402 UT. In this experiment we attained a range resolution of 300 metres and covered altitudes between 80 to 92 km. The data shown in the figure have been integrated for 30 seconds. In contrast to Figure 6 of LA HOZ et al. (1989a, this issue), the normalisation here is done in the conventional way so that relative changes of intensity in time are preserved by the grey code assignments.

Strong, multiple layers about 1 km in thickness are closely concentrated roughly between 82 and 88 km. The intensity in these layers reach up to 31 dB above the background noise on the high side, and down to -6 dB on the low side[1]. Often the weak signals reach outside the boundaries of these very visible layers, sometimes covering even the entire altitude window of the measurement—although they are not so obvious in this type of figure. Among other features, most of which we will not touch upon here, there are ondulations and oscillations sometimes with a striking sinusoidal

---

[1] The grey scale upper limit was chosen to cover 95% of the distribution of intensities. Since the lower side of the distribution contains also "pure" noise, the lower limit is set at a somewhat smaller value. As a consequence, the extreme values are outside the given limits of the code. Of course, they are coded at these limit values.
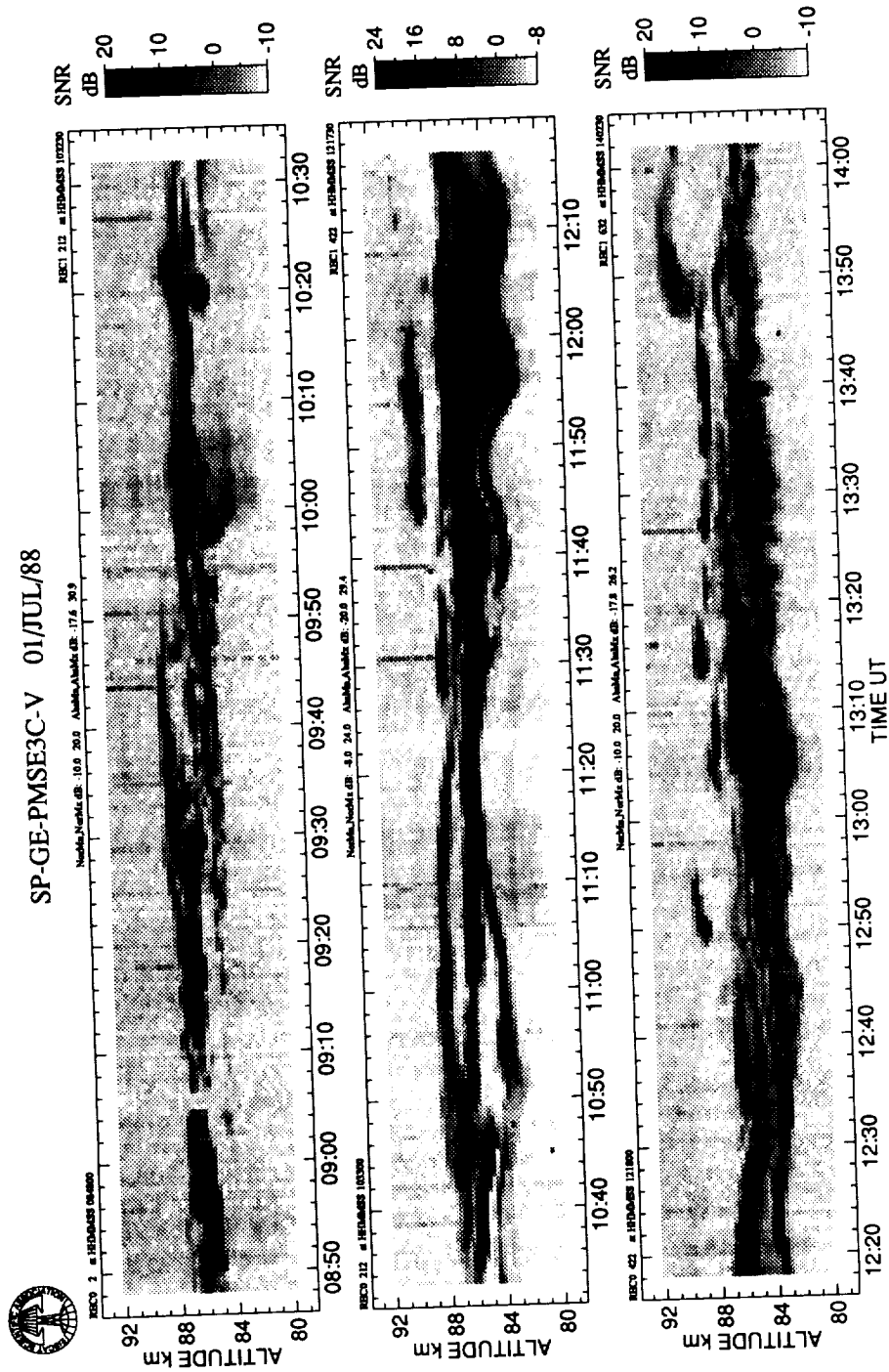
Fig. 1. Grey-coded power map of PMSE with illustrations of wave signatures

SP-GE-PMSE3C-V   01/JUL/88
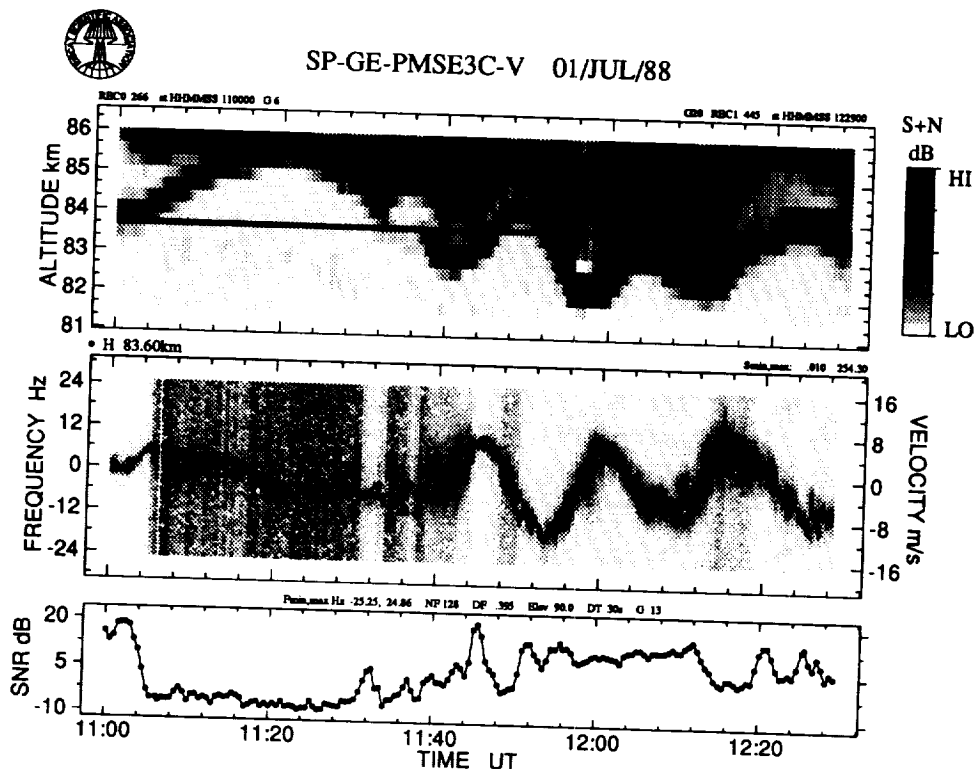
Fig. 2. A wave event. Top, signal intensity; middle, dynamic spectrum; bottom, signal to noise ratio

character. Such is the case of a thin layer on the bottom side between about 1140 and 1210 UT where a three cycle oscillation is clearly seen.

The top panel of Figure 2 contains an enlarged view of this oscillation. The middle panel contains the dynamic spectra at an altitude of 83.60 km that cuts approximately through the middle of the oscillating layer. This altitude is marked by a horizontal line through the top panel. The bottom panel contains a plot of the SNR in dB at this altitude. The oscillation has a period of 16 minutes with an altitude amplitude that varies between 1.5 and 3 km and a vertical velocity amplitude from -12 to +8 ms^{-1}. This oscillation is preceded by another oscillation that has a longer period of about 40 minutes that lasts at least one period.

The altitude and velocity oscillations are exactly coherent between each other, the velocity laging the altitude exactly by 90°. That is, the maxima and minima of the altitude are simultaneous with zero crossings of the velocity. What is more, the vertical displacement of the layer during any given period of time is completely accounted for by the integral of the velocity over that period. This observation—together with other evidence discussed elsewhere, e.g., a lack of correlation between spectral width and mean Doppler shift—suggests that the scattering entities are pasive tracers of the large scale dynamics of the mesosphere.

The shorter period altitude oscillation resembles a sinusoid with a changing amplitude. On the other hand, the corresponding velocity oscillation has the shape of a triangular oscillation. This mode of presentation is in a Eulerian coordinate system. That is, we sit at a fixed altitude and measure the

vertical velocity of the layer as it moves by. We have also constructed a Lagrangian coordinate system (not shown here) where we follow the vertical motion of the layer. In this coordinate system the velocity oscillation keeps the triangular shape, but the amplitude is from -16 to $+12$ ms^{-1}. These are rather large vertical velocities, to our knowledge, not seen before. At this stage of our study we can only speculate about the possibility of this event being a coherent gravity wave in a nonlinear regime that accounts for the triangular shape. But at the same time we wonder about the absence of signatures of "wave breaking", given the large amplitudes reached. So much for an illustration of waves evidenced by polar mesospheric summer echoes.

3.VELOCITY DISCONTINUITIES

On July 6th 1988 we carried out a unique experiment code-named PMSE3B. It was unique in that this was the only experiment that achieved an altitude resolution of 150 metres, and in that the physical conditions seem to have been remarkable. A grey-scale power map is contained in Figure 6 of LA HOZ et al. (1989a, this issue) which also contains more details on this experiment. Layers with highly varying structure persist during the whole experiment. The most visible layers maintain high signal intensities up to 37 dB above the background noise level. Often weak layers encompass the whole measurement window and possibly reach beyond it[2].

Figure 3 contains dynamic spectra of 5 gates at altitudes between 82.25 and 82.85 km, and between times 1100 and 1200 UT. The bottom panel contains plots of the SNR in dB of each of the five gates. They can be distinguished from each other by the different symbols used in the plots, and they can be identified with a corresponding dynamic spectrum by an equal symbol shown on the upper left corner of each spectral panel. The data have been post-integrated for 30 seconds. The normalisation of the grey code values is done in a way that each spectrum—or "time slice"—is normalised to its own maximum. The advantage of this normalisation technique is that it produces an image with a striking high contrast. The lost information regarding the relative variations of the spectral intensities can be recovered from the SNR plots. The spectral bandwidth of this measurement is ± 17 Hz and the spectral resolution is 0.52 Hz. These correspond to Doppler velocities of ± 11.4 ms^{-1} and 0.35 ms^{-1} respectively.

It is clear in the figure that a large, altitude dependent, velocity discontinuity develops at 1109 UT. The velocity in the top panel around this time varies still in a smooth manner. In the next panel down, the discontinuity has started to develop and the velocity difference between the two branches is about 2 ms^{-1}, that is, from 6 to 8 ms^{-1} downwards. There is a gradual growth of the discontinuity as the altitude decreases. The bottom panel shows that the second branch has migrated to the oposite side of the bandwidth due to harmonic aliasing, a trend that already started in the middle panel. In the bottom panel the amplitude of the discontinuity is about 5-6 ms^{-1}, that is, from 7 to 12-13 ms^{-1} downwards.

The proof that this event is authentic is contained in the very description of it as stated above. This is the smooth and systematic development of the discontinuity as a function of altitude[3]. We have convinced ourselves that this behaviour cannot be originated by a spurious effect. Events with similar properties occurred quite frequently during our campaign. Even in this one hour data set of Figure 3 it is possible to identify several other less dramatic events that share the same characteristics.

The question that arises is: How "discontinuous" can a dicontinuity in *Nature* be? The data we have presented has an integration time of 30 seconds. That is, we cannont distinguish temporal changes that occur within time intervals shorter than 30 seconds. It is plausible, and in fact most likely, that there is a smooth—albeit rather rapid—transition between the two velocity levels. Then

---

[2] These weak layers are not so obvious in the power maps, but they become clearly "visible" in dynamic spectrum plots shown elsewhere.

[3] That our data display gradual and systematic changes as a function of range-gate number is a demonstration that our experimental arrangements—specially the coding and decoding procedures—are functioning exceedingly well.

SP-GE-PMSE3B-V   06/JUL/88
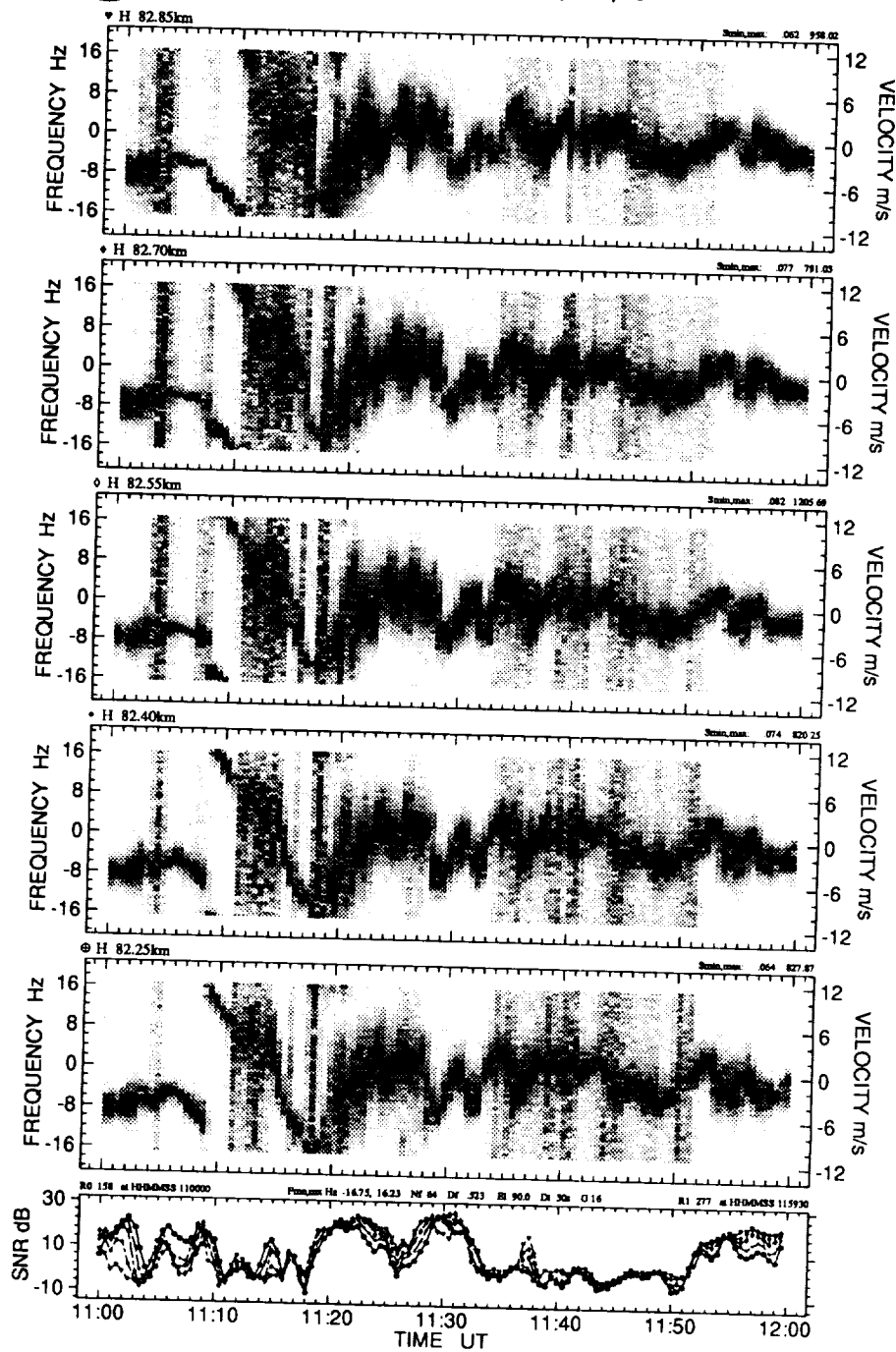
Fig. 3. Dynamic spectra illustrating a velocity discontinuity

the next question is: What physical processes exist, acting under this environment, that may have time scales that match these observations? Röttger et al. (1989, this issue, and references therein) have suggested that the observed discontinuities might be signatures of "wave breaking" events.

SP-GE-PMSE3B-V   06/JUL/88
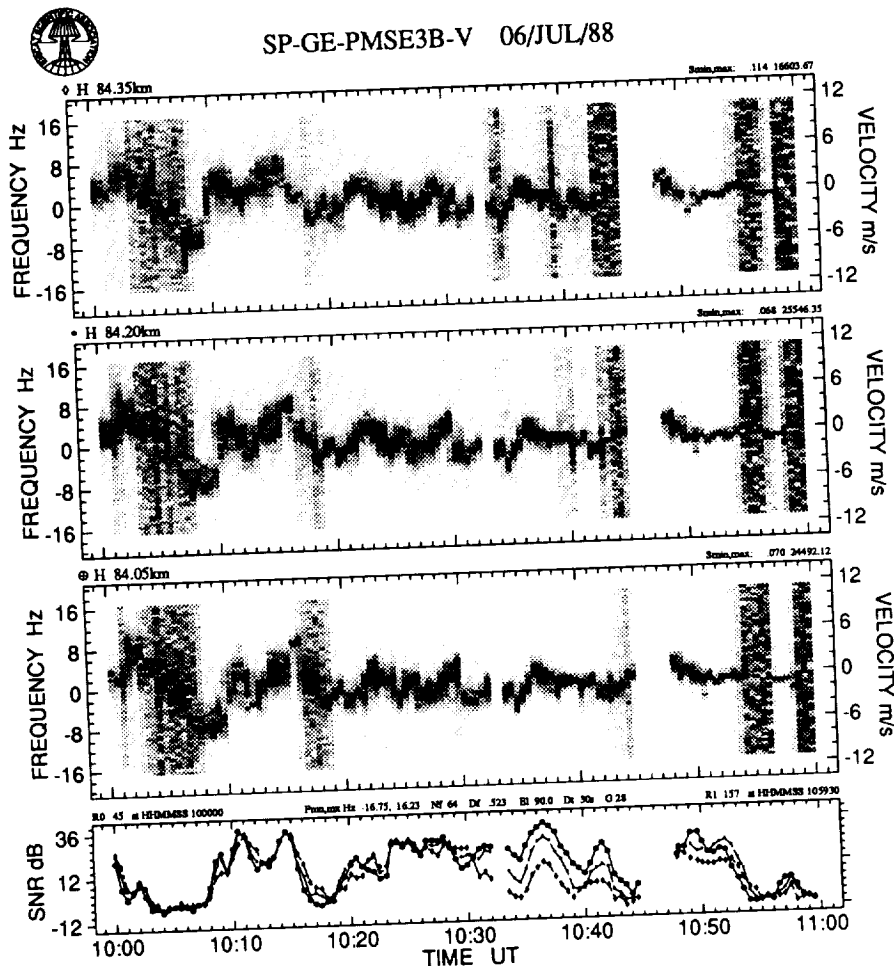
Fig. 4. Fine structure in the vertical velocity of PMSE

4.FINE STRUCTURE

Figure 4 shows dynamic spectra at three consecutive gates between 84.05 and 84.35 km and between 1000 and 1100 UT. This data were collected during the PMSE3B experiment described in the previous section. This figure illustrates a rather fine structure of the Doppler velocity in time, frequency and altitude. Small discontinuities and up-and-down alternations of the Doppler velocity occur from one integration period to the next. These features, in most cases, show a systematic variation with altitude similar to the one described in the previous section. One can also identify spectra with multi-modal characteristics. The latter is more clearly distinguished in Figure 5 that contains a close-up of the middle panel of Figure 4.

One could be tempted to atribute this fine structure to unavoidable—and undesired—statistical

SP-GE-PMSE3B-V 06/JUL/88
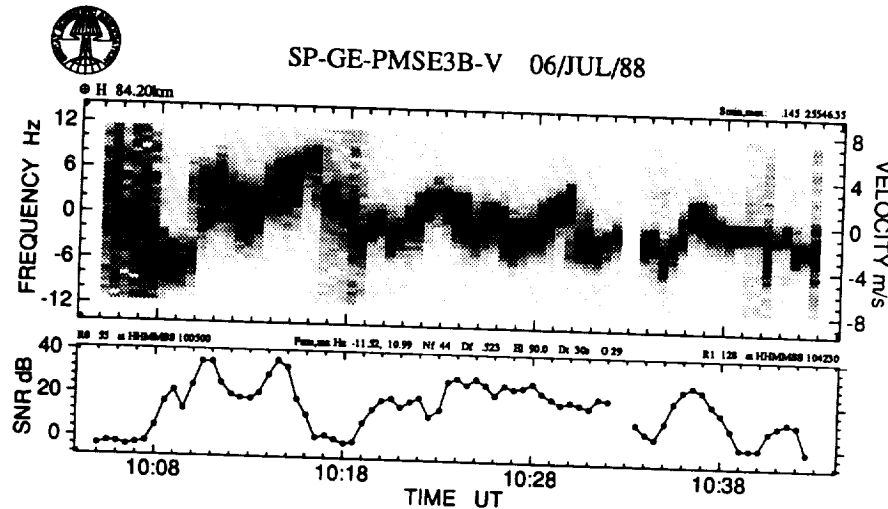
Fig. 5. A close-up of a part of Figure 4.

fluctuations. However, and again as in the previous section, the systematic behaviour of these structures, particularly as function of altitude, defeat the proposition that they are just due to statistical fluctuations. One can also argue that the similarity between consecutive range-gates is an indication of a correlation between range-gates introduced by the measuring technique. This speculation can also be discounted on the basis of the real changes that are seen to take place in Doppler velocity values as a function of altitude, as illustrated so clearly in the large discontinuity shown in Figure 3.

5.SPECTRAL WIDTH

Figure 6 contains again dynamic spectra at three altitudes, 84.20 to 84.80 km, between times 1230 and 1330 UT. This experiment was a test of the spatial interferometer technique carried out on July 5th 1988. A comprehensive report on this experiment and the results pertaining to this technique can be found in the paper by LA HOZ et al. (1989b, this issue).

At 1255 UT there is a sudden increase of the scattered power in the two lower altitudes accompanied by a simultaneous widening of the spectral widths. The power in the bottom panel, as measured by the SNR in dB, increases from about 4 dB to 24 dB within about one minute. A similar variation, although less intense, occurs also in the middle panel. The corresponding variations in the top panel do not seem to bear any appreciable correlation to the other two panels.

If the irregularities that cause the scattering are produced by turbulence—and even if they are not, but are passively imbeded in a turbulent environment—we expect them to be subject to the random motions produced by the turbulence. It is also clear that as the level of turbulence increases, the velocity fluctuations of the scattering irregularities will increase. Thus, the spectral width of the scattered signals will widen as the turbulence level increases. It is then conceivable that this event is a signature of a sudden increase of the turbulence level. We would expect to see also a well defined relationship between the spectral widths and the total scattered power. However, a counter-example is contained in Figure 7 in the paper by LA HOZ et al. (1989, this issue) which contains another event where the spectrum suddenly and dramatically widens without being accompanied by correlated variations in the scattered power. Within this—admittedly as yet—superficial account, the evidence of a clear correlation between scattered power and spectral width has been elusive.

6. IN LIEU OF A CONCLUSION

Perhaps it will later turn out, after resolutions to these puzzles are found, that the following verse due

SP-EI-SDI1-V   05/JUL/88
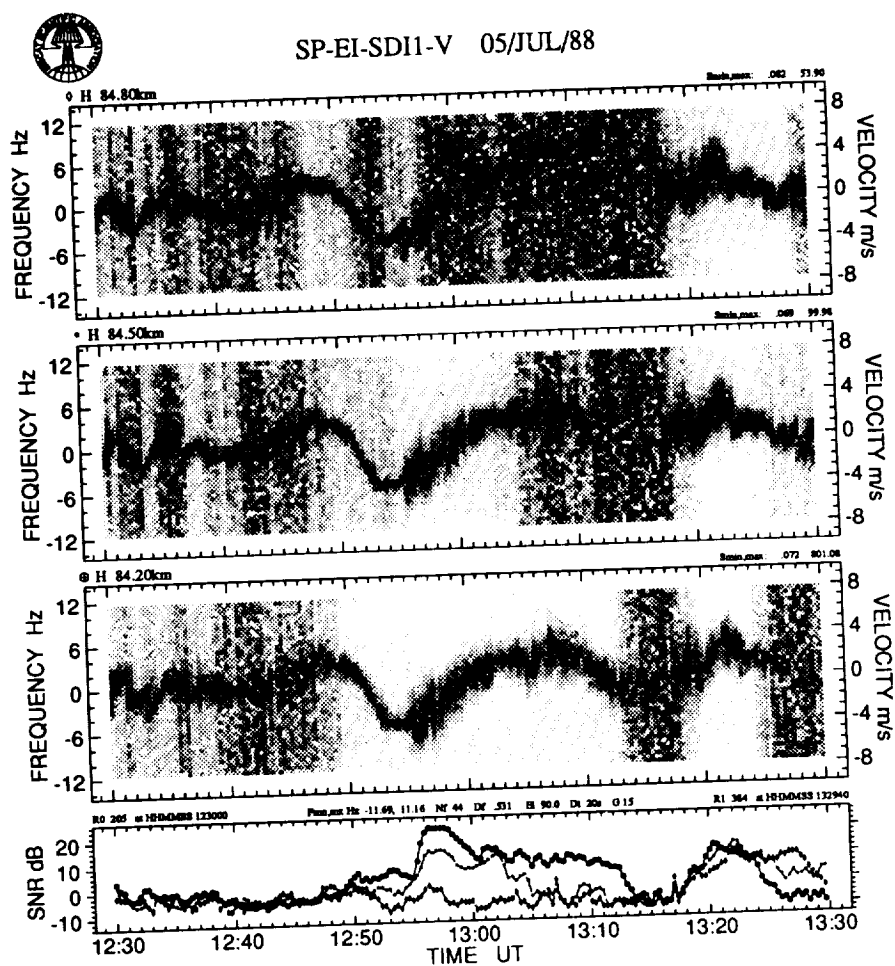
Fig. 6. A sudden widening of the spectrum.

to Lewis F. RICHARDSON (1922) is quite relevant to paraphrase in this context:

> *Big whaves have little whaves,*
> *Which feed on their velocity;*
> *And little whaves have lesser whaves,*
> *And so on to viscosity.*

(or "so on to turbulence" first?. . . or were they already "whorls"?. . . or. . .)

Acknowledgments

REFERENCES

La Hoz, C., J. Röttger and S. Franke (1989a), The status and planned developments of EISCAT in mesosphere and D-region experiments, this issue.

La Hoz, C., J. Röttger and S. Franke (1989b), Spatial interferometry measurements with the EISCAT VHF radar, this issue.

Richardson, L.F. (1922), Weather prediction by numerical processes, *Cambridge Univ. Press.*

Röttger, J., C. La Hoz, S.J. Franke and C.H. Liu (1989), Wave steepening and tilting detected in high resolution Doppler spectra of polar mesosphere summer echoes (PMSE) observed with the EISCAT 224 MHz radar, this issue.

Gravity Waves in the Mesosphere Observed with the MU Radar

T. Tsuda[1], S. Kato[1], T. Yokoi[1], T. Inoue[1],
M. Yamamoto[1], T. E. VanZandt[2], S. Fukao[1], and T. Sato[3]

1) *Radio Atmospheric Science Center, Kyoto University*
2) *Aeronomy Laboratory, NOAA, Department of Commerce*
3) *Department of Electrical Engineering, Kyoto University*

1 DESCRIPTION OF MU RADAR OBSERVATIONS

Gravity waves excited in the lower atmosphere dissipate in the mesosphere through dynamical or convective instabilities. As a result, they transport momentum flux and energy from the lower atmosphere to upper middle atmosphere, and accelerate/decelerate the general circulation [e.g., Lindzen, 1981]. Radar observations have been continued in order to clarify the behavior of gravity waves in the mesosphere. [e.g, *Meek et al.*, 1985; *Vincent and Fritts*, 1987; *Yamamoto et al.*, 1986, 1987]

This paper is concerned with presentations of 19-day observations of gravity waves in the mesosphere carried out during daylight hours (0800–1600 LT) on 13–31 October 1986 with the MU radar in Shigaraki (35°N, 136°E), Japan.

The antenna beam of the MU radar was steered every inter-pulse period into the vertical direction and four oblique beam directions aligned north, east, south and west at a zenith angle of 10°. The transmitted pulse was phase-modulated by a 16-bit complementary code with a sub-pulse width of 4 μs, which corresponds to the height resolution of 600 m. Data are collected at 60–90 km by oversampling every 300 m with a time resolution of 145 and 60 s for observations on 13–17 and 18–31 October, 1986, respectively. In this study, we have used wind velocity profiles determined at about 65–85 km where turbulent scattering is dominant.

2 QUASI-MONOCHROMATIC GRAVITY WAVES

Wind profiles are subsequently averaged for 2 hours by shifting the averaging period by one hour. The vertical profiles of meso-scale wind fluctuations in the mesosphere can be recognized as a superposition of many gravity waves with various vertical scales and frequencies. However, evident quasi-monochromatic gravity waves with a dominant

258
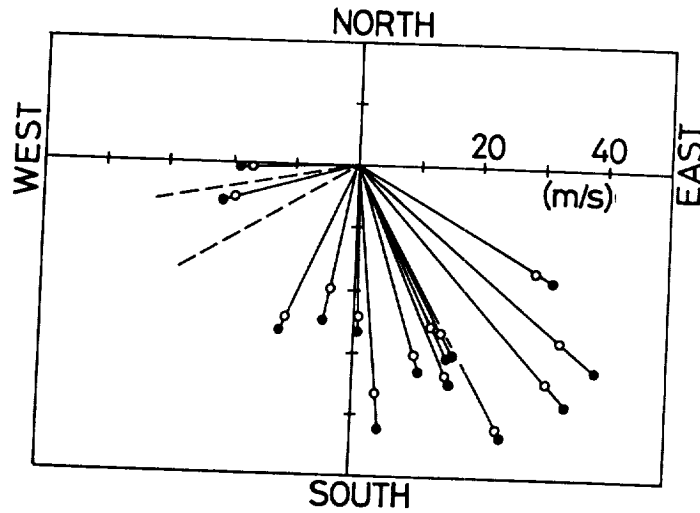
Figure 1: Distribution of horizontal propagation direction of gravity waves. A full and open circles correspond to phase and group velocities determined by using dispersion relation in no background mean wind condition. Only propagation direction is indicated by a dashed line for two cases, since vertical wavelength was not determined.

vertical scale ranging from 5 to 15 km were frequently detected. They mostly show downward phase progression, indicating an upward energy transportation. Amplitudes of the quasi-monochromatic gravity waves ranged up to 20–30 m/s, and were generally larger for the northward component than the eastward component. A dominant wave component in the profile can be extracted as a quasi-monochromatic wave by applying a band-pass filter with lower and higher cutoffs at 3–9 and 12–27 km, respectively, depending on the dominant vertical wavelengths. By assuming a linear dispersion relation with no background mean winds [Hirota and Niki, 1985], the horizontal propagation direction and intrinsic wave period of quasi-monochromatic gravity waves were determined for 16 cases out of 19 days of observations.

Fig. 1 shows distribution of horizontal phase and group velocities, where the group velocity is estimated by assuming a constant background temperature profile. Fig. 1 indicates that all of gravity wave propagated in the equatorward direction. For 7 cases quasi-monochromatic gravity waves propagated in a direction between south and 30° east from south.

On the average, it can be concluded that the preferential propagation direction of the gravity waves in this observation period is the south south-east direction. The amplitudes
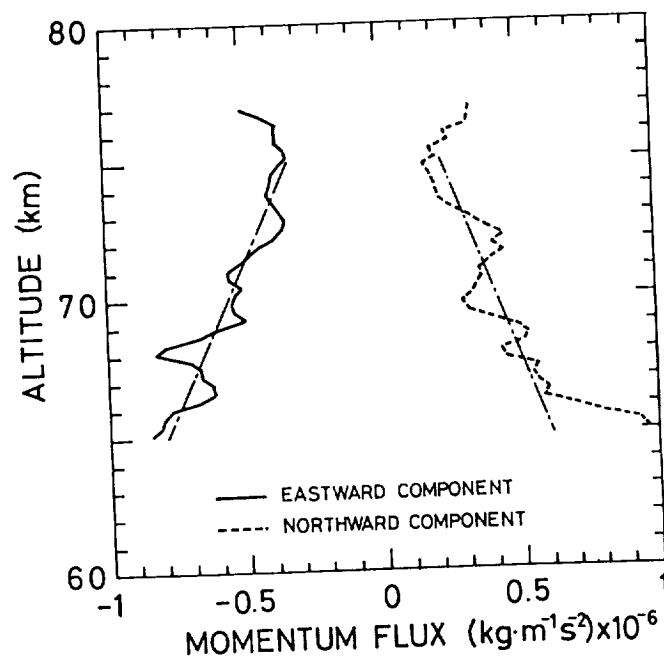
Figure 2: Vertical profiles of eastward and northward components of momentum flux for wave periods ranging from 10 min to 8 hours. Mean acceleration at 65–75 km is -5.1 and 4.0 m/s/day for eastward and northward components, respectively.

of the horizontal phase velocity tend to become larger, when the gravity waves propagated to the south-east direction, and smaller in the westward direction. The mean amplitude of the horizontal phase velocity averaged for 14 cases was 31.6 m/s.

The mean vertical phase velocity for these quasi-monochromatic gravity waves was -0.28 m/s, indicating upward energy propagation. Intrinsic wave periods mostly ranged from 8 to 11 hours with a mean value of 8.6 hours.

3 MOMENTUM FLUX

In this section we present a profile of wave-induced upward flux of horizontal momentum determined by using the beam-pair method [Vincent and Reid, 1983]. First, a linear trend is subtracted from a time series of radial wind velocities collected for 8 hours in

each range gate. The variance of radial wind fluctuations with periods ranging from 10 min to 8 hours is calculated independently at each height on each day, and are further averaged over 19 days of observations.

Both meridional and zonal variance increases with altitudes from 2.5 $(m/s)^2$ near 65 km to 4.0 $(m/s)^2$ at 75 km, although considerable height variations are recognized. When the kinetic energy is conserved, the variance must increase with a scale height of atmospheric density (about 9 km). However, the observed increase of variance was obviously smaller than the scale height, and therefore, the wave energy was dissipated in the course of upward energy propagation.

Azimuthal anisotropy of the variance was recognized such that the northward and westward components were generally larger for the meridional and zonal components, respectively.

Fig. 2 shows vertical profile of upward flux of the horizontal momentum flux determined from the MU radar observations, where atmospheric density is taken from CIRA 1972 model. Mean gradient of the eastward momentum flux, i.e. mean body force, is estimated as -5.1 m/s/day in the altitude range of 65–75 km by assuming the air density of 8.2×10^{-7} at 70 km. The northward acceleration is determined as 4.0 m/s/day.

References

Hirota, I., and T. Niki, A statistical study of inertia-gravity waves in the middle atmosphere, *J. Met. Soc. Japan*, *63*, 1055-1066, 1985.

Meek, C. E., I. M. Reid, and A. H. Manson, Observations of mesospheric wind velocities 1. Gravity wave horizontal scales and phase velocities determined from spaced wind observations, *Radio Sci.*, *20*, 1363-1382, 1985.

Vincent, R. A., and D. C. Fritts, A Climatology of Gravity Wave Motions in the Mesopause Region at Adelaide, Australia, *J. Atmos. Sci.*, *44*, 748-760, 1987.

Vincent, R. A., and I. M. Reid, HF Doppler Measurements of Mesospheric Gravity Wave Momentum Fluxes, *J. Atmos. Sci.*, *40*, 1321-1333, 1983.

Yamamoto, M., T. Tsuda, and S. Kato, Gravity waves observed by the Kyoto meteor radar in 1983-1985, *J. Atmos. Terr. Phys.*, *48*, 597-603, 1986.

Yamamoto, M., T. Tsuda, S. Kato, T. Sato and S. Fukao, A saturated inertia gravity wave in the mesosphere observed by the Middle and Upper Atmosphere Radar, *J. Geophys. Res*, *92*, 11993-11999, 1987.

SMALL-SCALE GRAVITY WAVES IN THE LOWER STRATOSPHERE REVEALED BY A MULTI-BEAM OBSERVATION WITH THE MU RADAR

Kaoru Sato and Isamu Hirota

Department of Geophysics, Faculty of Science, Kyoto University
Kyoto 606, Japan

1 Introduction

VHF Doppler radar is one of the most powerful tools to measure the small-scale phenomena, such as gravity waves, in the troposphere and lower stratosphere. For examining effects of the gravity waves on the large-scale circulation and/or their origins, it is important to estimate parameters characterizing the horizontal structure of gravity waves. In many cases, however, their horizontal structure has been inferred from vertical structure with the aid of theoretical consideration, e.g. the dispersion relation, because the number of beams directed for one measurement is limited by the usual radar system. The MU radar has a unique ability to measure radial velocities almost simultaneously with up to 16 beam directions, which is suitable for the detection of the horizontal structure. In the present study, therefore, an attempt was made to use the multi-beam technique for investigating the nature of wind fluctuations with small horizontal scales.

2 Observation

The wind measurements in the troposphere and lower stratosphere were carried out for 47.5 hours on 22–24 in January 1986. The antenna beam was pointed to 15 directions switched alternately from one pulse to another during the observation. Twelve beams out of 15 were directed in the sector area from 30° west of the zenith to 30° east so as to scan the wind field zonally. Zenith angles smaller than 10° were not chosen in order to avoid the effect of "aspect sensitivity" (Tsuda et al., 1986). Since the MU radar has the beam width of 3.6°, independent data are obtained for each beam position at the 4°'s interval of the zenith angle in each direction. Two beams were tilted to north and south by 14° from the zenith to measure the meridional wind, and the remaining beam was directed vertically to measure the vertical velocity directly. The height range for the observation is 2.4–24.6 km with a resolution of 300 m along the radar beam. The time resolution is about 7 minutes because of the integration of weak echoes. During the observation, a typical mid-winter pattern with a strong subtropical jet was situated synoptically over Japan. No convective clouds were observed above the MU radar site.

3 Data Analysis

The radial velocity $V_\theta(z,t)$ is expressed as

$$V_\theta(z,t) = u_\theta(z,t) \cdot \sin\theta + w_\theta(z,t) \cdot \cos\theta, \tag{1}$$

where θ is the zenith angle of the beam, z is the altitude, t is the time, u and w are the horizontal and vertical components of wind, respectively.
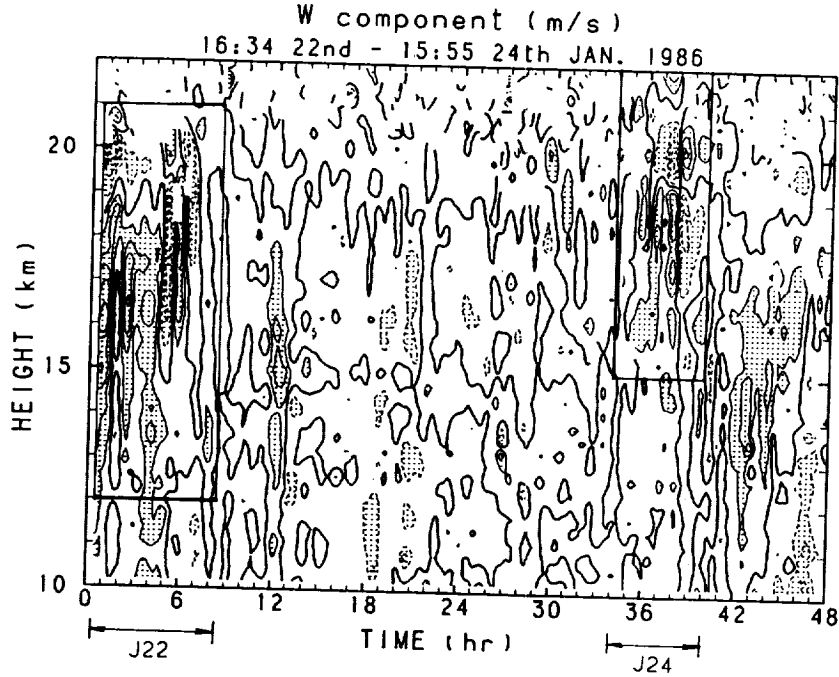
Figure 1: w-component of wind measured with the vertical beam during the whole observation period. Data were lowpass-filtered with a cutoff length of 1 hour. The contour interval is 0.5 m s^{-1}

Usually the horizontal and vertical components are obtained using two beams with equal and opposite angles $\pm\theta$ around the zenith, in such a way as,

$$[u(z,t)]_\theta = \frac{V_\theta(z,t) - V_{-\theta}(z,t)}{2\sin\theta}. \tag{2}$$

It is noted that we assume homogeneity of the wind field over the two symmetrical beam positions in (2).

On the other hand, with more relaxed assumption that wind field is uniform over each neighboring two beams with zenith angles of θ_1 and θ_2 out of the thirteen scanned zonally, we have

$$\left. \begin{array}{l} u(z,t\ ;\theta_{12}) = \frac{V_{\theta_1}(z,t)\cos\theta_2 - V_{\theta_2}(z,t)\cos\theta_1}{\sin(\theta_1-\theta_2)} \\ w(z,t\ ;\theta_{12}) = \frac{V_{\theta_1}(z,t)\sin\theta_2 - V_{\theta_2}(z,t)\sin\theta_1}{-\sin(\theta_1-\theta_2)} \end{array} \right\}, \tag{3}$$

where $\theta_{12} = (\theta_1 + \theta_2)/2$. This method provides the horizontal variation of u and w.

Figure 1 shows the w-component of wind measure by the vertical beam through the whole observation period. The regions of the velocity whose absolute value is more than 0.5 m s^{-1}, were hatched. Conspicuous strong oscillations with large vertical scale and with 1-2 hours period are found in the two rectangles of the figure. According to the spectral analysis, the oscillations appear mainly above the height of the subtropical jet ($\approx$ 12 km). This study analyzed the two distinct events which are referred to as J22 for the first appearing on the 22nd, and J24 for the second on the 24th, respectively. Analyzed data were the wind components having periods of 1-2.5 hours and vertical scales larger than 1.5 km.
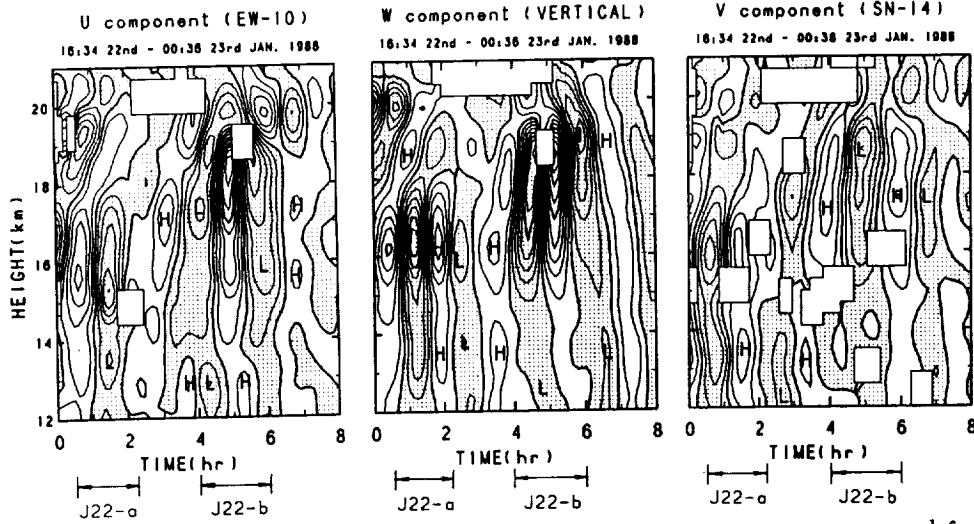
Figure 2: Vertical time-section of u, w, and v for J22. The contour intervals are $1 \, \mathrm{m\,s}^{-1}$ for u and v, and $0.2 \, \mathrm{m\,s}^{-1}$ for w.

4 Vertical time-section

Each component for J22 is represented in Fig. 2. The zonal and meridional components, u and v, were calculated from (2), as usually employed. For w-component we used the data obtained by the vertical beam. It is found that the amplitude of w is about $2 \, \mathrm{m\,s}^{-1}$ at the maximum, and the large amplitude continues only for several hours. Then the two events are further divided into the first and second halves, which are referred to as J22-a and J22-b for J22 as shown in Fig. 2, and J24-a and J24-b for J24. The period of the oscillation for each event is 1–1.5 hours.

The phase differences between wind components are important parameters to identify the oscillations. Judged from the short period, these oscillations are likely to be due to internal gravity waves. Internal gravity waves must have the phase difference of 0 or 180 degrees between horizontal and vertical components. In Fig. 2, however, the phase differences between u and w and between v and w appear almost 90 degrees. This might be caused by the impropriety of the assumption used in (2) that the wind field is uniform over height positions measured by symmetrical two beams, in the case of the waves having a small horizontal scale.

5 Horizontal time-section

In order to examine the zonal structure, we made horizontal time-section from 13 radial velocities in the zonal scanned region using (3) as shown in Fig. 3. Continuous monochromatic wavelike phases are found, migrating westward for J22-a and eastward for J22-b. However the magnitude of w is very large compared with that obtained by the vertical beam directly. Then we simulated the "observation" of u and w using (3) with the assumption that the wind field has a small monochromatic wavelike structure. As a result, it is found that the "observed" wave amplitude and phase are not represented correctly, but the zonal wavelength and period are well reproduced, as well as the sense of the phase difference between u and w. Therefore the zonal wavelength λ_x for each event can be estimated from the horizontal time-section as

U (Z - 15.9 km)

16:34 22nd - 00:38 23rd JAN. 1986

W (Z - 15.9 km)

16:34 22nd - 00:38 23rd JAN. 1986
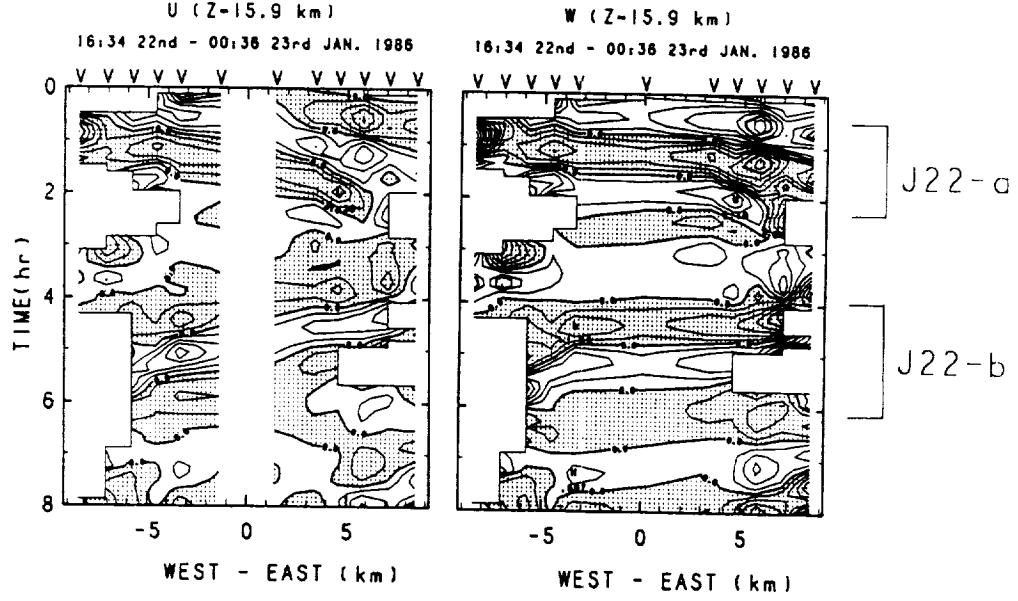
Figure 3: Horizontal time-section of u and w at a height of 15.9 km for J22. The contour intervals are 2 m s^{-1} for u and 0.5 m s^{-1} for w.

5–25 km.

6 Fitting analysis

In order to examine the phase difference between u and w, we fit the radial velocities assuming the wind field with a monochromatic wavelike structure by the least squares method, which can represent phases exactly. Thirteen radial velocities measured by the zonal scan of the beam at each time and height are used for fitting to the shape of

$$V_{\theta_i} = u_0 \sin(\frac{2\pi}{\lambda_x} x_i + \varphi_u) \cdot \sin \theta_i + w_0 \sin(\frac{2\pi}{\lambda_x} x_i + \varphi_w) \cdot \cos \theta_i, \tag{4}$$

where $x_i = z \cdot \tan \theta_i$. In order to decrease nonlinearity of the fitting function, unknown parameters are reduced to four: u_0, w_0, φ_u, and φ_w. Fitting is made by changing λ_x continuously near the values estimated from the horizontal time-sections, so as to find the λ_x having the minimum fitting residual. It is noted that this method of the fitting analyses is suitable for transient waves since the assumed structure (4) has no time parameters.

Figure 4 shows the time averaged standard deviation (S.D., the square root of the residual) as a function of the zonal wave length for the case of J22-a. The zonal wavelength λ_x^* corresponding to the minimum value of S.D. values is found for each profile. This is the same for the other cases, indicating that the oscillations are zonally sinusoidal. It is noteworthy that λ_x^* changes near a height of 16.8 km in Fig. 4. It follows that the oscillation is composed of at least 2 different waves in height. This is also the case with J24-b.

The histograms of the phase difference, $\Delta\Phi = \varphi_u - \varphi_w$, associated with almost the same zonal wavelength λ_x^* for each event are shown in Fig. 5. The distributions of $\Delta\Phi$ for all events have peaks near 0 or 180 degrees, except for J22-a at a height range of 16.8–17.4 km. This is consistent with the theoretical characteristics of gravity waves.
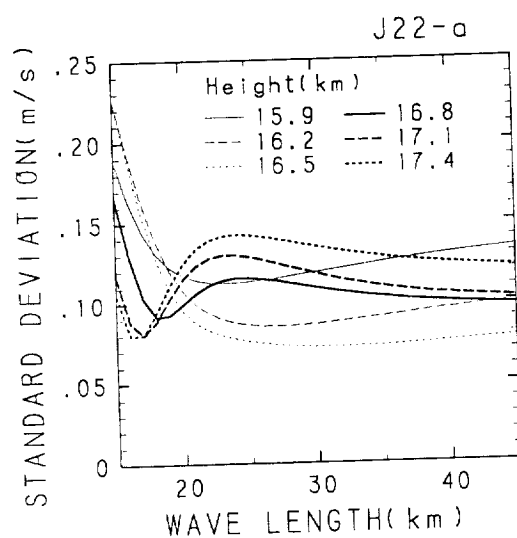
Figure 4: Time averaged standard deviation of the fitting as a function of λ_x for J22-a.
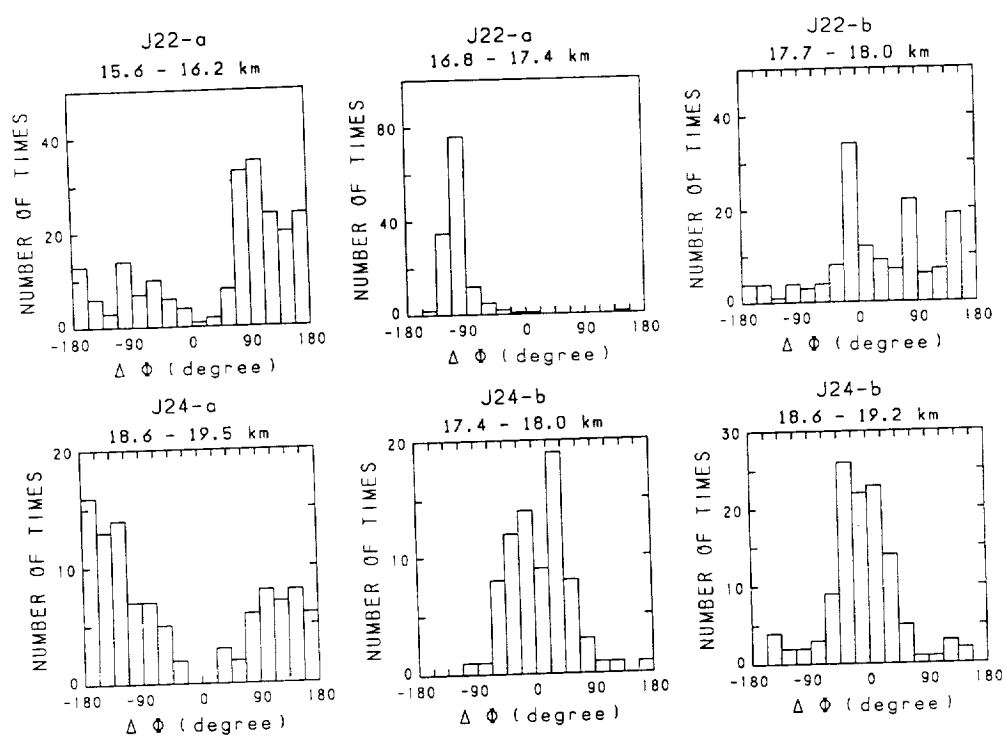
Figure 5: Histograms of phase difference between u and w.

In order to confirm that the oscillations are also sinusoidal in time, we made another fitting analysis which takes a time parameter, i.e., the period, into consideration but not the wave transiency. The obtained parameters were consistent with the previous analyses. Through the two types of the fitting analysis, we confirm that the oscillations are due to internal gravity waves.

7 Discussion

The zonal phase velocity estimated for each event from the zonal wavelength and period is 1–5 ms^{-1}, which is very small compared with the background wind ($\approx 50\ ms^{-1}$). This suggests that the waves are almost at rest relative to the ground as in the case of mountain waves. However, since no considerable high mountains exist near the radar site, and the oscillations appeared distinctly in the lower stratosphere, it is difficult to identify them as mountain waves.

The strong vertical disturbances have often appeared in the observations using VHF radars (e.g. Ecklund et al., 1981, 1982, 1985). Most of those are not regarded as simple oscillations having a single time-frequency as the case of this study, but as variations with over a wide range of frequency. The characteristics, the frequency of occurrence, the origin, the effect on the mean flow, and the seasonal variation are all the remaining and interesting subjects to be examined in detail about these disturbances. Improvement and continuation of the multi-beam observation promise to be of great importance.

The original paper of this study is published in the December issue of *J. Meteor. Sci. Japan*, 1988.

References

Ecklund, W. L., K. S. Gage and A. C. Riddle, 1981: Gravity wave activity in vertical winds observed by the Poker Flat MST radar. *Geophys. Res. Lett.*, **8**, 285–288.

Ecklund, W. L., K. S. Gage, B. B. Balsley, R. G. Strauch and J. L. Green,1982: Vertical wind variability observed by VHF radar in the lee of the Colorado Rockies. *Mon. Wea. Rev.*, **110**, 1451–1457.

Ecklund, W. L., B. B. Balsley, D. A. Carter, A. C. Riddle, M. Crochet and R. Garello, 1985: Observation of vertical motions in the troposphere and lower stratosphere using three closely spaces ST radars. *Radio Sci.*, **20**, 1196–1206.

Tsuda, T., T. Sato, K. Hirose, S. Kato, and S. Fukao, 1986: MU radar observations of the aspect sensitivity of the backscattered VHF echo power in the troposphere and lower stratosphere. *Radio Sci.*, **21**, 971–980.

GRAVITY WAVE STEEPENING AND TILTING DETECTED IN HIGH RESOLUTION DOPPLER SPECTRA OF POLAR MESOSPHERE SUMMER ECHOES (PMSE) OBSERVED WITH THE EISCAT 224 MHZ RADAR

J Röttger* and C. La Hoz
EISCAT Scientific Association
P.O. Box 812, S-981 28 Kiruna, Sweden
(*on leave from Max-Planck-Institut für Aeronomie)

S.J. Franke and C.H. Liu
University of Illinois
Urbana, IL, USA

ABSTRACT

Polar mesosphere summer echoes observed with the EISCAT 224-MHz radar frequently exhibit significant discontinuous offsets or jumps in the Doppler shift. We explain these jumps to be caused by a lifting of partially or anisotropically scattering layer. These can result from gravity waves, which also can be steepened or tilted. We notice frequently that these steepened wave structures do not obviously break up into turbulence.

INTRODUCTION

It is usually assumed that gravity waves can gain such large amplitudes in the mesosphere that they are saturated and break into turbulence (e.g., FRITTS, 1984; FRITTS and RASTOGI, 1985). MST radars are quite suitable tools to study these dynamic effects (e.g., RÖTTGER, 1987) and turbulence structures were observed with MST radar in the mesosphere (e.g., KLOSTERMEYER and RÜSTER, 1984; REID et al., 1987). MOBBS (1985) and WEINSTOCK (1986, 1987) computed the shape of gravity waves which had increased in amplitude close to the breaking level and found that the wave shape can be tilted or steepened during the saturation process. After the EISCAT VHF radar observed polar mesosphere summer echoes (HOPPE et al., 1988), the high spectral resolution program applied by RÖTTGER et al. (1988) allowed to study details of the Doppler spectra which showed characteristics of steepened waves.

BRIEF DESCRIPTION OF THE EXPERIMENT

The echoes detected by the EISCAT 224-MHz radar could not be explained by the common incoherent scatter mechanism, but were assumed to be related to those echoes which were earlier observed with the 50-MHz MST radars (e.g.,CZECHOWSKY and RÜSTER, 1985). Since it was noticed that these echoes detected on 224 MHz were very dynamic and non-stationary, a special radar program was developed to study details of their spectra with a much higher frequency resolution than was applicable with the original radar program. The program applied the pulse-to-pulse mode and Barker coding with 1.05 km altitude resolution. Autocorrelation functions were computed on-line allowing for a frequency resolution of 0.42 Hz, these were averaged over 5 sec and dumped on tape. The receiver gain was optimized to cope with the very strong signal variations. More details of this particular program and general results can be found in (RÖTTGER et al., 1988, and RÖTTGER and LA HOZ, 1989). Here we will concentrate on particular features of the spectra which we could not discuss in detail so far. We will also include more recent results which were obtained in summer 1988 after the complementary coding scheme had been introduced to the EISCAT VHF radar. During both summers the EISCAT VHF radar was operated in the 224 MHz band with about 1.5 MW peak

268

power and the 40m x 120 m cylindrical dish antenna for transmission. The corre-
sponding beam widths are 1.6° by 0.6° in the meridional and zonal direction,
respectively. During the experiments, which are reported here, the antenna beam
was pointed vertically.

RESULTS OF SPECTRAL MEASUREMENTS

Spectrograms or dynamic spectra of Polar Mesosphere Summer Echoes (PMSE) allow
to study in quite a detail the fine-structure of the radar returns and their
relation to refractivity structures, turbulence and gravity waves. Spectrograms
of PMSE observed on 224 MHz were published by RÖTTGER et al. (1988) and RÖTTGER
and LA HOZ (1989), which show the variability of the spectral width, the spec-
tral offset and occasionally a splitting. We notice in the examples shown in
Figures 2 and 3 of RÖTTGER et al. (1988) that periodic mean velocity oscillation
related to gravity waves are quite common. It was very evident also, that these
oscillations are quite frequently non-sinusoidal, but triangular-shaped or
sawtooth-like. It was even noticed sometimes that the complete spectrum is sud-
denly (within 10 sec or so) shifted by more than the width of the spectrum. This
particular feature was first observed in summer 1987 and again was evidently
detected in summer 1988 with completely different radar programs. We will here
discuss this feature in more detail.
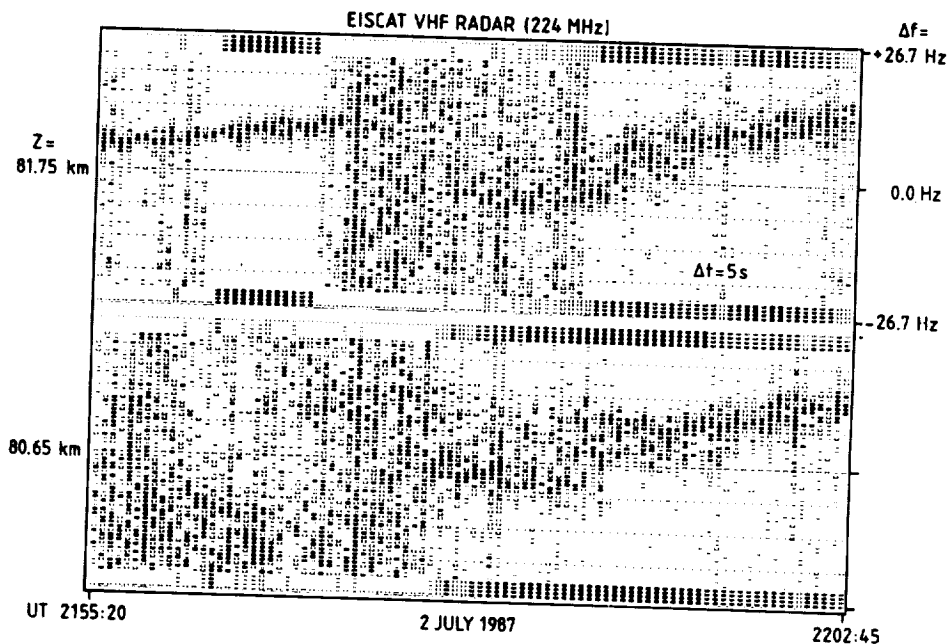
Fig. 1   High time resolution (5 sec) spectrograms of Polar Mesosphere
Summer Echoes (PMSE) deduced from data collected with the EISCAT
224-MHz radar in summer 1987. The altitude resolution is 1.05 km.

We show in Fig. 1 a spectrogram with the highest time resolution achievable during the summer 1987 operations. It is an enlargement of the spectrogram of Fig. 3 in RÖTTGER et al. (1988), highlighting the particular event which occurred at 81.7 km altitude around 21:58 UT on 2 July 1987. This was the first time when definitely a spectral jump was observed. In the displays of the dynamic spectra as shown in Fig. 1 the amplitude in each frequency bin is plotted in a grey scale. The amplitude is normalised to the maximum amplitude in the spectrum. Each vertical stripe thus displays one normalised spectrum for a certain time period. The sequence of many of these spectral stripes forms a dynamic spectrum for one range gate. Because the spectra are normalised, we also plotted the average amplitude in the spectral stripes in a logarithmic grey scale at the upper and lower margins of the stripes. Spectrograms of two adjacent range gates with 1.05 km resolution are displayed.

What is very interesting to notice in Fig. 1 is the fact, that the signal with the gentle increase in Doppler frequency at the altitude gate $z = 81.7$ km suddenly disappears after it had increased in amplitude. After about 1 minute a very weak signal recurred in the same altitude gate with small negative Doppler shift, and then increased in amplitude and Doppler frequency to again positive Doppler shift. Whereas during the last part of the display the spectra are fairly similar in both adjacent gates, this is not at all the case at the beginning, where we notice a very narrow and high-amplitude spectrum in the 81.7 km gate and a very weak and broad spectrum in the 80.65 km altitude gate. During the first two minutes of this display, thus, the scattering structure must have been very different over a vertical distance of 1 km. This was pointed out already in the preceding paper by RÖTTGER et al. (1988). Since the maximum positive frequency off-set in the first part of the display is only one third of the Nyquist frequency and the signal recurred at a negative Doppler shift, which is only about one fourth of the Nyquist frequency, we have to exclude aliasing causing this frequency change. Similar frequency changes did not occur in other range gates, and we therefore can exclude also a change of an oscillator frequency to cause this effect. We thus, suggest that this is a real shift in frequency, which we will call a "jump" or "bounce".
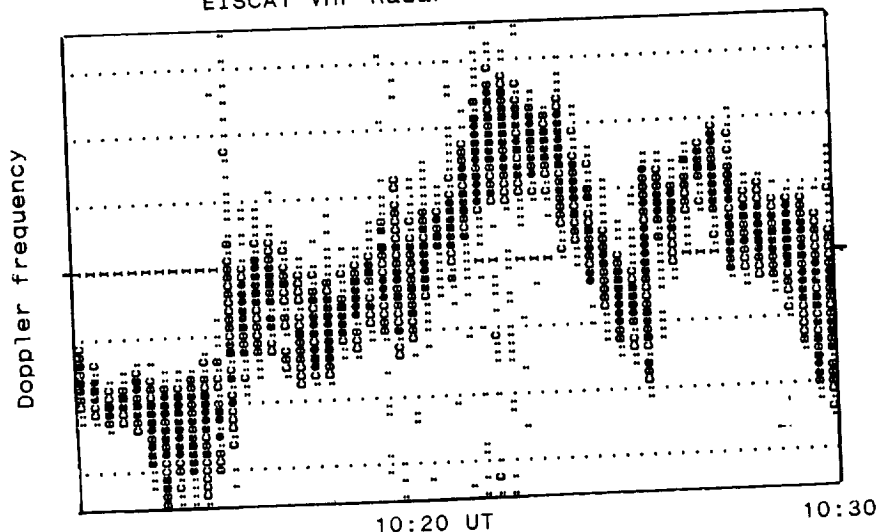
Fig. 2   Spectrogram of PMSE observed with the EISCAT 224-MHz radar in summer 1988 with altitude resolution of 300 m (see LA HOZ et al., 1989, for details).

Fig. 2 shows another example of a spectrogram or dynamic spectrum of PMSE, recorded in summer 1988 with 300 m altitude resolution. Frequency shifts or jumps are definitely occurring at 10:15:34 UT and 10:25:36 UT on 30 June 1988. Since the data for this spectrogram were recorded with a completely different data acquisition routine, we thus are even more confident that an instrumental or software effect is not misleading us in our interpretations. The latter is further proven by noticing the characteristic frequency jumps in the series of spectrograms by LA HOZ et al. (1989), which were obtained during another different observation period and were analyzed by a different software package. We have collected many more examples of these characteristic jumps and non-linear steepened oscillations, which we will publish elsewhere.
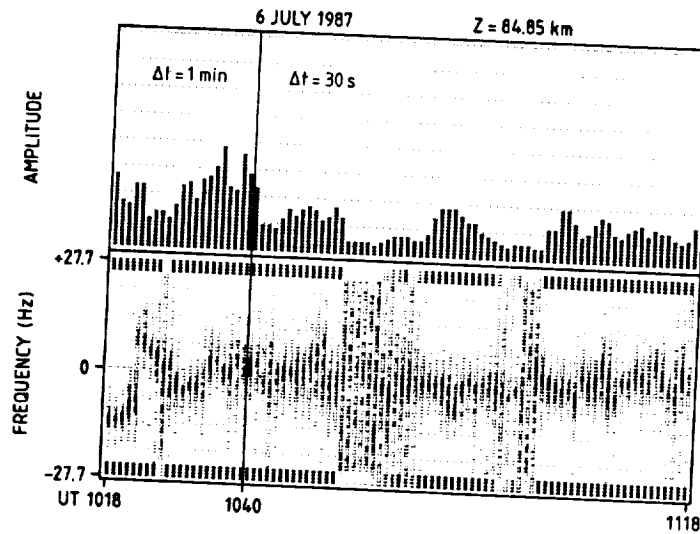
Fig. 3   Spectrogram and amplitude time series recorded on 6 July 1987.
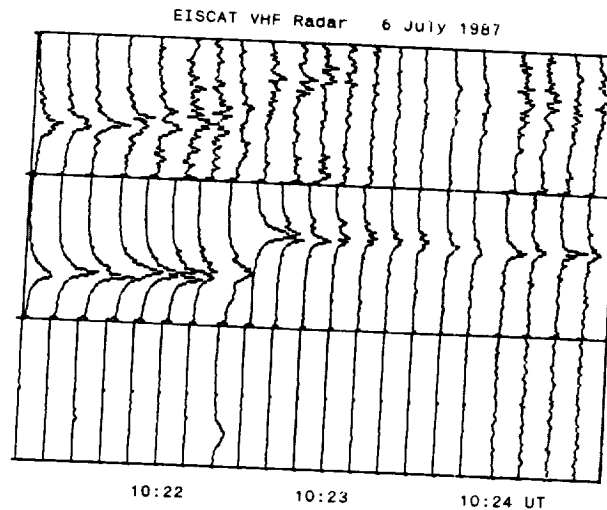
Fig. 4   Series of 10-sec averages of spectra (displayed in linear amplitude) observed on 6 July 1987 over a 2.5 min time period in the altitude ranges 83.80, 84.85 and 85.90 km.

An earlier example of a dynamic spectrum, recorded on 6 July 1987, is shown in
Fig. 3, together with the temporal development of the echo amplitude. A jump in
Doppler frequency is very apparent at 10:22 UT, - the spectral amplitude and the
spectrum width, however do not change. In Fig. 4 the temporal development of
10-sec averages of spectra is shown in the conventional display. It becomes evi-
dently clear from this display that the total spectrum in the altitude gate
84.85 km was shifted within 10 seconds without leaving a remnant behind. Checks
of spectra in the adjacent altitude gates 85.9 km and 83.8 km shows that there
is very little spill-over between the altitude gates and that there are com-
pletely different and isolated phenomena happening over vertical distances of
one kilometer. Another example of jump is presented in Fig. 5, which also shows
the event isolated in one altitude gate. This Figure also shows that the jump
occurs within the very short time scale of 5 seconds. We find that the jump or
the frequency off-set could be immediate (within seconds) or also overlapping,
as can be seen in Fig. 6. It is a very clear prove from this Figure that alias-
ing does not cause the frequency jumps. This Figure also shows the distinct
intermittency of the echo amplitude within the altitude range of 1 km.
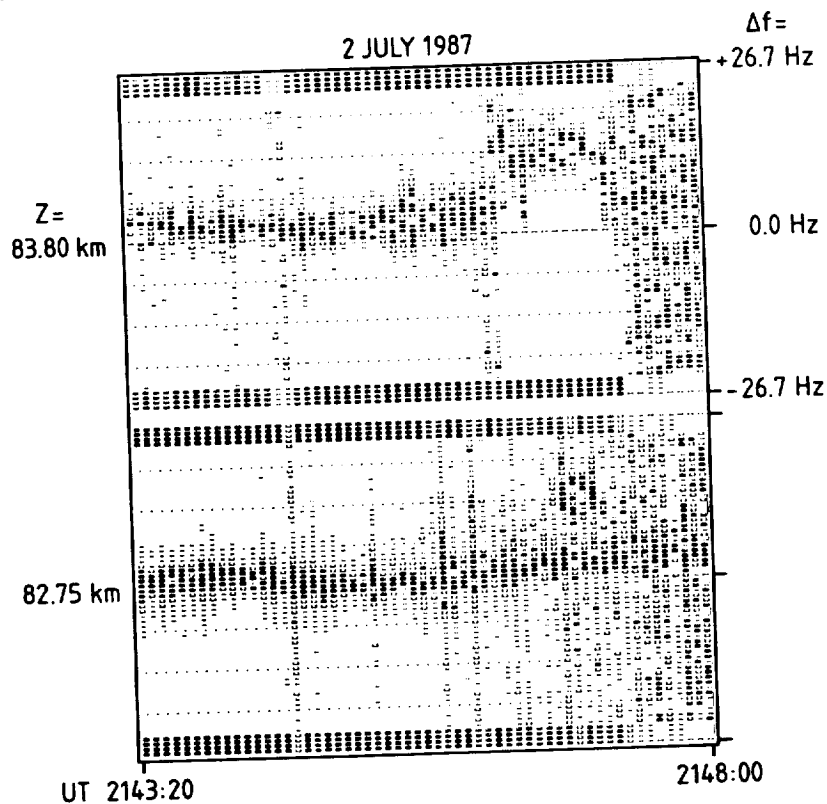
Fig. 5 Spectrograms of adjacent range gates showing a frequency jump
in only one altitude gate. There is a weak spill-over of the echo
from range gate 83.80 km to 82.75 km at about 21:47 UT, resulting in
a double structure in the lower range gate. The steady Doppler shift
in range gate 82.75 km in contrast to the jump in range gate 83.80 km
can be taken as a proof that frequency jumps are not of instrumental
origin.
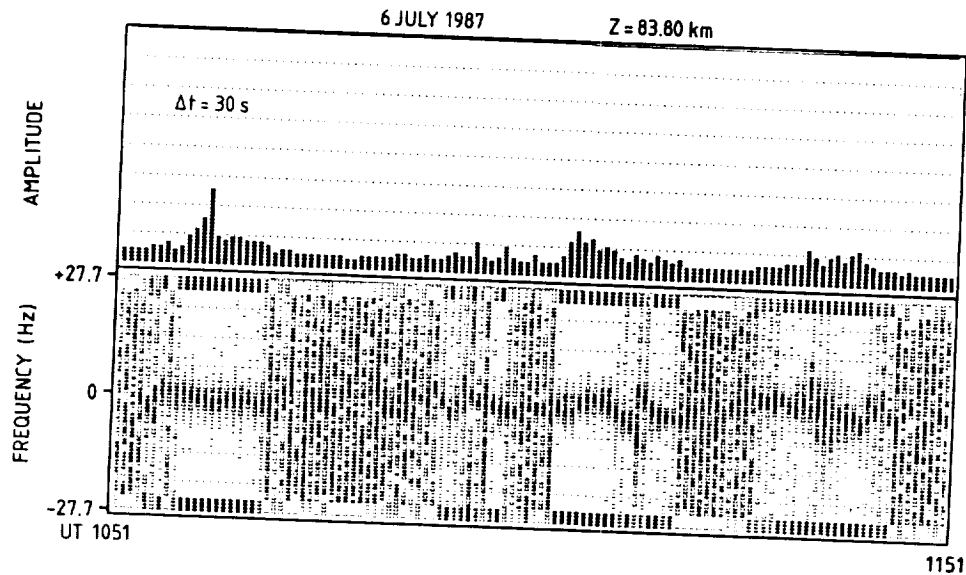
Fig.6 Spectrogram and amplitude time series showing the burst-like temporal variability and an overlapping frequency jump at 11:29 UT.

The consistency of these described observations done with independent radar programs and the convincing results, which we have presented so far, place a high confidence on the fact that these "jumps" are due to a real phenomenon and not instrumental. How can we explain these observations?

MODEL COMPUTATIONS

We could envisage a model as shown in the upper panel of Fig. 7, where a partially reflecting surface is undulated by a Gaussian shape bump. The layer or surface is assumed to move horizontally through the radar beam. Radar rays, which are reflected under perpendicular conditions from the surface reach the receiver and add up according to the different phase paths. The phase paths will change because the reflection point moves and there can be more than one reflection point at a time with different radial velocity, causing a superposition of different Doppler shifts. The corresponding amplitude and phase variation of the received signal is shown in the lower two panels of Fig. 7 as a function of time. These temporal variations are Fourier analyzed and yield the spectra of Fig. 8. The horizontal width and the vertical perturbation amplitude of the bump yielding these spectra is 2000 m and 300 m, respectively. The bump is assumed to be at 85 km altitude, and the antenna beam width is 1.50 for the upper panel and 3° for the lower panel spectrum of Fig. 8, respectively. The horizontal speed Uo of the bump yields a radial velocity of the reflection points which cause the varying Doppler shift seen in the model spectra. The total width of the spectra displays in Fig. 8 corresponds to a radial velocity of 0.15 Uo. We clearly notice that the spectral features, which we do observe, can be simulated by this model. Note that this model assumes partial reflection, characterised by a strong aspect sensitivity and the superposition of a few rays, but it would not work for isotropic scattering. However, a thin and highly anisotropic scattering layer, having the lifted bump shape and moving horizontally, could also cause these spectra.
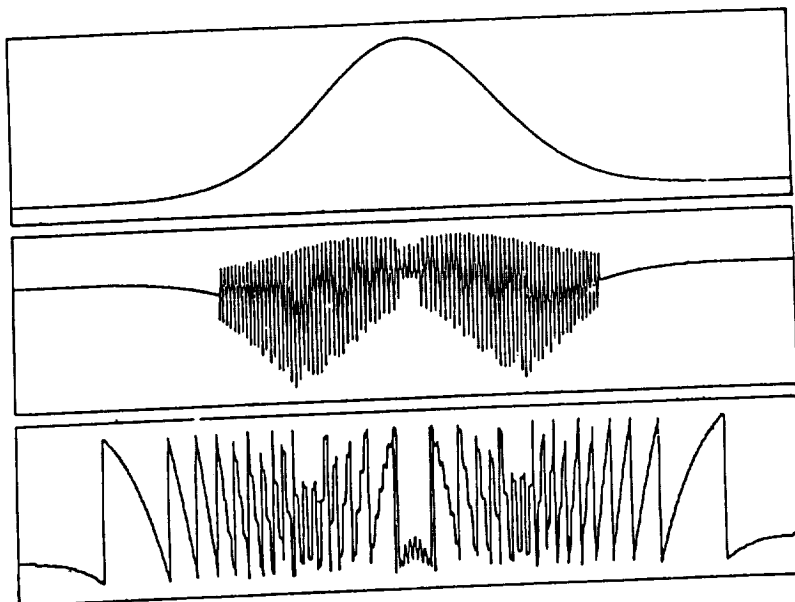
Fig.7   Model of a Gaussian shape bump of a thin layer (upper panel)
causing amplitude and phase variations as shown in the lower two
panels, when the layer moves horizontally.
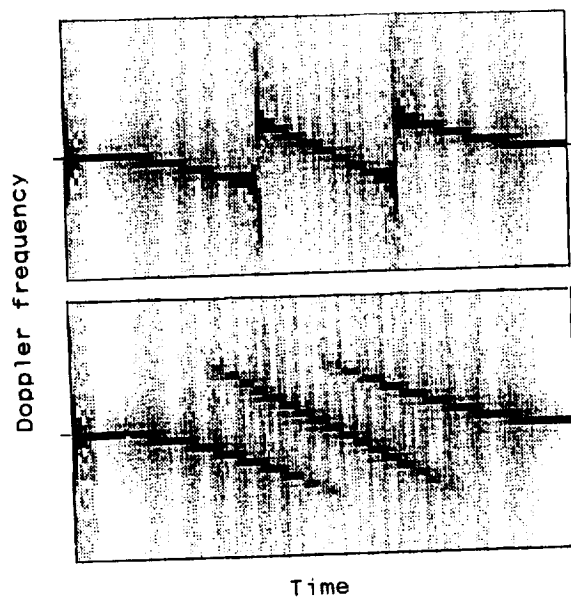
Fig.8 Doppler spectra computed from the model structure shown in
Fig. 7. The upper spectrum is for a 1.5° wide antenna beam and the
lower for a 3° wide beam.

274

One may not accept that partial reflection, as assumed in the latter model, would be possible because of the stringent criteria which are necessary for reflection, namely the stratification of the reflecting surface in the mesosphere. This model still would be applicable, however, for highly anisotropic turbulence, which we cannot yet prove to be observed on 224 MHz. We then have to enquire about another reflectivity structure which could cause these structures and how the physical mechanism could be behind these peculiar observations of frequency jumps. If we may not be convinced that a specular reflector or highly anisotropic thin scattering layer as used in the model is existent when we see these jumps, another model needs to be invoked. We now describe a model which works for scattering as well as reflection and offers a more generally acceptable explanation of these sudden frequency jumps. We can propose that the jumps and bounces could also be a signature of "Wave steepening or wave tilting" (e.g., Mobbs, 1985; Weinstock, 1986, 1987), which occurs when the amplitude of gravity waves increases but breaking into turbulence does not immediately take place. The latter apparently is not observed in our data, since it would mean that the spectrum has to widen substantially when jumps occur and the echo amplitude would have to increase when scatter from the enhanced turbulence would cause the echoes.
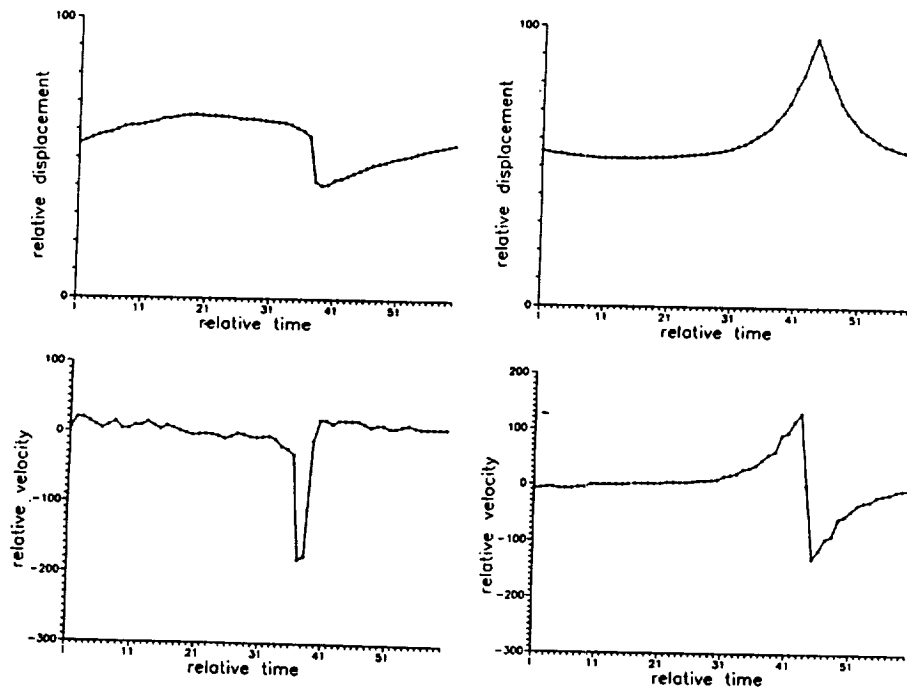
Fig.9 Model surfaces of a thin layer of turbulence or discontinuity in a Kelvin-Helmholtz-Instability (left panels) as well as in a steepened wave (right panels) and the corresponding relative velocities, i.e. Doppler shifts, shown in the lower panels.

When we consider that the mean Doppler shift usually is due to a vertical bulk motion of a thin layer of scatterers, the spectrum shift is directly given by the derivative of the spatial (radial = quasi-vertical) displacement of the scattering or reflecting layer. The spectral shift is deduced from our spectrograms and we thus can determine the radial displacement. For a purely sinusoidal wave, the displacement then would just be 90 degrees out of phase to the Doppler shift. However, for non-sinusoidal oscillations we obtain a quite different display as shown in the two models of Fig. 9. For the left-hand panels in Fig. 9 the model computations of Kelvin-Helmholtz-Instability of Fritts (1984) are reproduced (his Fig. 6) and converted into relative velocity (i.e. mean Doppler shift) as function of time. We have assumed in the following model that only a thin scattering layer or reflecting discontinuity exists in the KHI structure. Enhanced turbulence should be observed particularly around the relative time scale 30-40. We should then see an increase in spectrum width and echo amplitude, which is not so evident from our observations. We also would need to see a sudden and short drop of the Doppler frequency with quick return to about the same Doppler velocity. These evidences could only be very occasionally confirmed by our observations.

For the right-hand side panels the computations of MOBBS (1985) and WEINSTOCK (1986) are reproduced, which are for steepened waves. We again assume that only a thin reflecting or scattering layer exists in the wave structure. The reproduction of these computations then fits well with the observed frequency jumps, which take place within a very short time interval as compared to the wave period. According to Weinstock (personal communication), turbulence does not necessarily occur when the waves are steepened, which is consistent with our observations. We therefore assume that the frequency jumps observed during PMSE conditions with the EISCAT 224 MHz radar can also be an indication for steepening and tilting of gravity waves in the mesosphere. It is to be noted that the particular features of steepened wave structures should be obtainable also with the model computations corresponding to Figures 7 and 8. Then the Gaussian shape bump needs to be replaced by a steepened wave structure. Such simulations should be done in future.

One may argue why these jumps and other peculiarities in the spectra had not been reported to be seen so far with other radars. An explanation is that only the special kind of high-resolution spectrograms which we have chosen easily let detect such events. Another explanation could be that only a narrow beam, such as the about 1 degree wide beam of the EISCAT VHF radar, could resolve these structures. The rapid temporal changes, with time scales of seconds, let assume that there is a very distinct horizontal intermittency of the structures over less than a very few kilometers. A wide beam, say several degrees wide, would smear out these fine structures and therefore would seldom detect these features, which we regard as a typical characteristics of polar mesosphere summer echoes.

CONSEQUENCES

Let us now consider some data analysis consequences resulting from these jumps in the mean Doppler frequency, which are related to the steepening of gravity waves. When one deduces the estimates of the first three moments of the Doppler spectrum for averages over time intervals which are longer than the time step during which the spectrum jumps, one inevitably will smooth out the jump and not clearly see the steepened wave. More detrimental: the spectrum width which one would deduce will erroneously be widened and would more reflect the magnitude of the frequency jump than the real width of the spectrum. The steepening of waves preferentially occurs in certain phases of the waves, namely in the down-slope of the original non-steepened wave. When integrating too long one thus would

find the spectrum to widen in these certain phases. It is suspected that the maximum spectrum width will be seen close to the oscillation phase where rapid velocity changes occur. Only when the integration time is as short as the time it takes for the spectrum to jump, namely about ten seconds or less, one would deduce a more correct estimate of the spectrum width. We thus argue that longer integration times than some ten seconds could easily result in a conclusion that the spectrum widens in certain oscillation phases and one could erroneously suggest that the widening is due to enhanced turbulence. A similar result of erroneous spectrum width as well as Doppler shift could evolve if the Doppler frequency resolution is not sufficient to resolve the jumps. To avoid such possibilities of errors and misinterpretations we favour the application of high-spectral resolution data-taking procedures and to check the data by first displaying dynamic spectra with sufficient time and frequency resolution. This word of caution should be regarded also when one would intend to deduce the eddy diffusion coefficient from the width of the spectrum; even for very narrow beam antennas and narrow range gates (as were applied in the EISCAT observations of summer 1988) the eddy diffusion coefficients are likely overestimated because of the elucidated effect.

Acknowledgement:

REFERENCES:

Czechowsky, P. and R. Rüster (1985), Power spectra of mesospheric velocities in polar regions, Handbook for MAP, 18 (S. Kato. ed.), 207-211 (publ. by SCOSTEP Secretariat, Dept. Elec. Engin., Univ. of Illinois, Urbana, IL).

Fritts. D.C. (1984), Gravity wave saturation in the middle atmosphere: a review of theory and observations, Rev. Geophys. Space Phys., 22, 275-308.

Fritts, D.C. and P.K. Rastogi (1985), Convective and dynamical instabilities due to gravity wave motions in the lower and middle atmosphere: theory and observations, Radio Sci., 20, 1247-1277.

Hoppe, U.-P., C. Hall and J. Röttger (1988), First observations of summer polar mesospheric backscatter with a 224 MHz radar, Geophys. Res. Lett., 15, 28-31.

Klostermeyer, J. and R. Rüster (1984), VHF radar observation of wave instability and turbulence in the mesosphere, Adv. Space Res., 4, 79-82.

La Hoz, C., J. Röttger and S.J. Franke (1989), Dynamic spectra of polar mesosphere summer echoes. Handbook for MAP (this issue).

Mobbs, S.D. (1985), Propagation of nonlinear internal gravity waves at strato-spheric and mesospheric heights: part III: the wave shape, Ann. Geophysicae, 3, 599-608.

Reid, I.M., R. Rüster and G. Schmidt (1987), VHF radar observations of cat's-eye-like structures at mesospheric heights, Nature, 327, 43-45.

Röttger, J. (1987), VHF radar measurements of small-scale and meso-scale dynami-cal processes in the middle atmosphere, Phil. Trans. R. Soc. Lond. A, 323, 611-628.

Röttger, J. and C. La Hoz (1989), Fine-structure of Doppler spectra of polar mesosphere summer echoes (PMSE) observed with the EISCAT 224-MHz radar, Handbook for MAP, this issue.

Röttger, J., C. La Hoz, M.C. Kelley, U.-P. Hoppe and C. Hall (1988), The structure and dynamics of polar mesosphere summer echoes observed with the EISCAT 224 MHz radar, Geophys. Res. Lett., 15, 1353-1356.

Weinstock, J. (1986), Finite amplitude gravity waves: harmonics, advective steepening and saturation, J. Atmos. Sci., 43, 688-704.

Weinstock, J. (1987), The turbulence field generated by a linear gravity wave, J. Atmos. Sci., 44, 410-420.

OBSERVATION OF GRAVITY WAVES BY THE CHUNG-LI VHF RADAR

I. J. Fu[1], J. K. Chao[1], C. H. Liu[2], and J. Röttger[3]

[1]Center for Space and Remote Sensing Research, National Central University
Chung-Li, Taiwan, ROC
[2]Department of Electrical and Computer Engineering, University of Illinois
Urbana, IL 61801
[3]EISCAT Scientific Association, Box 705, S981 17 Kiruna, Sweden

The Chung-Li VHF radar has been in operation since 1986. During this period, the radar has been used to observe the dynamics of the troposphere and the lower stratosphere, especially the waves. In this paper some typical examples of the observed wave phenomena will be presented and discussed.

(i) Mountain Waves

As an example of mountain waves, Figure 1 shows a hodograph of the horizontal wind on June 7, 1986, observed by the Chung-Li VHF radar. The wind was obtained by averaging the whole data set which was approximately three hours. The wind increased in general from about 5 m/s at 2 km height to about 20 m/s at 10 km. The magnitude of the fluctuations was approximately 2.5 m/s and the vertical wavelength was about 3 km. We note the clockwise rotation of the wind vector. It turns out that such vertical variations of the wind are observed quite often at Chung-Li, for both westerlies and easterlies. To understand the phenomenon, we note that Chung-Li is located in the northern part of Taiwan. Approximately 30 km to the west of the radar is the ocean. The Central Mountain Range of the island is about 25 km to the east with a rather abrupt rise to peaks as high as 3000 to 3500 meters. Therefore, it is expected that lee waves will be generated when winds are blowing from the east. As for mountain waves observed at Chung-Li when the wind is from the west, we note that a recent paper by BACMEISTER and SCHOEBERL (1989) has shown that nonlinear processes may cause the orographically generated stationary waves to break and set up waves upstream. Since Chung-Li is quite close to the mountain, it is likely to observe such waves there if indeed they are generated. This might be the reason why mountain waves are observed in Chung-Li for both easterlies and westerlies.

(ii) Focusing by Layered Structures Modulated by Gravity Waves

Layered structures are also seen very often at Chung-Li. At times such layers are modulated by short-period gravity waves. When this happens the modulations of the layers may sometimes be sufficiently strong to effectively focus and defocus the radar beam causing periodic fluctuations in received echo power. The modulations are caused by the displacement of the layer as the wave propagates through. Therefore, if indeed this focusing mechanism is operative, one should also see simultaneous oscillations in the vertical velocity. As a matter of fact, since the displacement and the velocity are out of phase by 90 deg, one should expect to see maximum power occurring when vertical velocity goes through zero. GAGE et al. (1981) presented an example of this phenomenon for layers at tropopause height. At Chung-Li this phenomenon has been observed also on layers at lower tropospheric heights. Figure 2 shows such an example. The data were taken on June 9, 1986. The power and vertical velocity shown in Figure 2a are for a layer at 5 km height. The period of the wave was approximately 8 min. We note the time shift between the maxima of the power and the velocity. Figure 2b shows the correlation function of the two time series. The maximum correlation of 0.8 is found at the time lag of 2 min with vertical velocity leading the power. This is the 90 deg phase difference mentioned above.

(iii) Kelvin-Helmholtz Instability

It is well known that strong wind shears can generate Kelvin-Helmholtz instability (KHI) in the atmosphere which can be observed by VHF radar (KLOSTERMEYER and RÜSTER, 1980). The KHI occurs at a height where the local Richardson number is smaller than 0.25. One of the main features of the KHI-generated waves is the phase jump at the height where the

(Mean Wind Fluctuation)
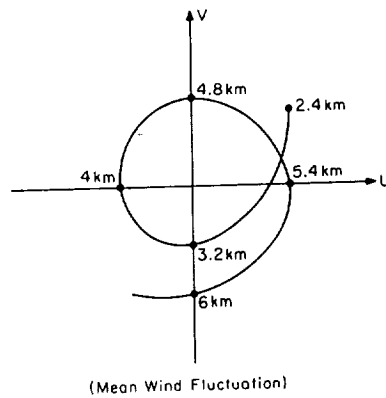
Figure 1. Hodograph of horizontal wind on June 7, 1986, observed by the Chung-Li radar.
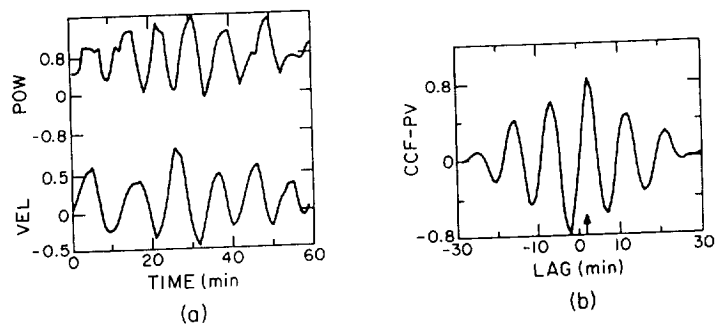
Figure 2. (a) Time series for echo power and vertical velocity at 5 km height observed by the Chung-Li radar on June 9, 1986. (b) Correlation function between vertical velocity and echo power.

instability is originated (KLOSTERMEYER and RÜSTER, 1980). In the following we discuss such a case observed in the troposphere at Chung-Li. Figure 3 shows the vertical velocity observed on June 9, 1986. The original sample period was 25.6 s. A 26-point running mean was applied to smooth the data. It is quite apparent that wave activities existed during the period. Spectral analysis identified a dominant component of 15.8 min. The phase of this wave was measured by correlating a cosine function with variable phase with the data at each height. Figure 4a shows the height profile of the computed phase. We note the jump of approximately 100 deg at about 7 km height. Figure 4b shows the Richardson number as a function of height calculated using the data from the radiosonde at Pan Chiao, which is approximately 25 km northeast of Chung-Li. We note that a minimum of Ri value of 0.4 was obtained at 7 km height. Although the computed Ri did not actually go below 0.25, due to the limitation of height resolution of the radiosonde data, it is quite clear that KHI occurred at about 7 km.

References

Bacmeister, J. T., and M. R. Schoeberl, Breakdown of vertically propagating two dimensional gravity waves forced by orography, to appear in *J. Atmos. Sci.*, 1989.

Gage, K. S., D. A. Carter, and W. L. Ecklund, The effect of gravity waves on specular echoes observed by the Poker Flat MST radar, *Geophys. Res. Lett., 8*, 599-602, 1981.

Klostermeyer, J., and Rüster, Radar observations and model computation of a jetstream-generated Kelvin-Helmholtz instability, *J. Geophys. Res., 85*, 2841-2846, 1980.
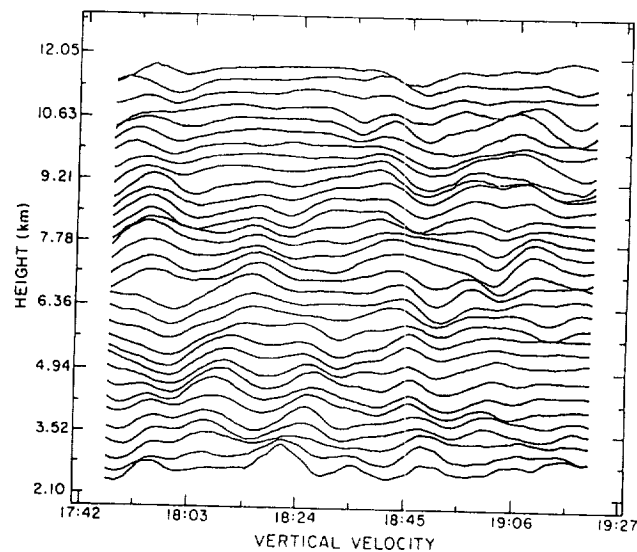
Figure 3. Vertical velocity observed by the Chung-Li radar on June 9, 1986, smoothed by 26 points running mean, sampling time was 25.6 s.
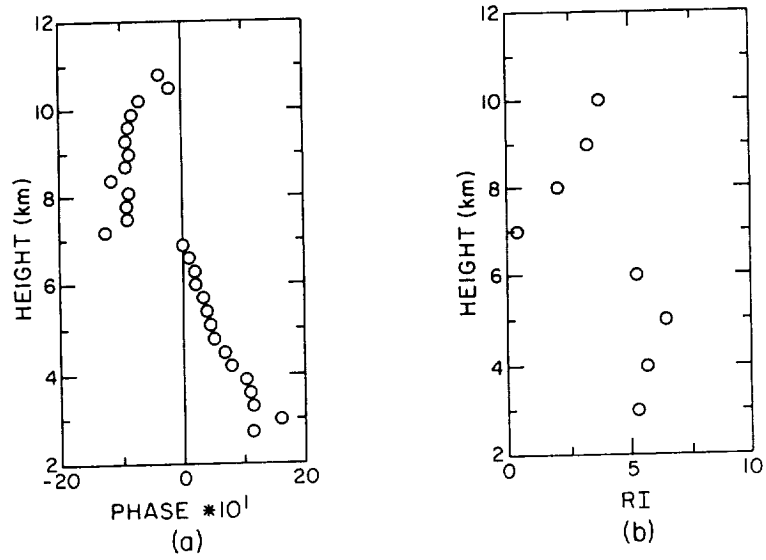
Figure 4. (a) Phase of the 15.8-min wave as a function of height deduced from data shown in Figure 3. (b) Richardson number as a function of height for the background atmosphere for the data set in Figure 3.

A Typhoon Observed with the MU Radar

Toru Sato[*], Naoki Ao, Mamoru Yamamoto,
Shoichiro Fukao, Toshitaka Tsuda, and Susumu Kato

Radio Atmospheric Science Center, Kyoto University
Uji 611, Kyoto, Japan

1 Introduction

The first observation of a typhoon with the MU radar (136.1°E, 34.9°N) was made on August 13-18, 1983 (Kato *et al.*, 1984). The MU radar was operational at that time with a partial system of about 1/8 of the current one both for the antenna area and the output power. Also, the antenna beam was not steerable during observations, so that the observation was made with one beam direction (10° to the east) only. Nevertheless, a clear vertical structure of the wind field associated with the typhoon was observed up to about 12 km height.

No close encounter of a typhoon to the MU radar had occurred since then until typhoon 8719 passed by at a distance of about 100 km from the radar on October 17, 1987. The MU radar was fully operational during the passage of the typhoon, and the observation was made continuously for about 60 hours around the closest encounter. Here we report the results of a preliminary analysis of this observation, concentrating on the wave activities associated with the typhoon.

2 Observational Techniques

The MU radar is a 46.5-MHz monostatic Doppler radar with an active-phased-array antenna of 103 m in diameter and with 1-MW peak output power. Readers are referred to Fukao *et al.* (1985a, b) for details of the system. The MU radar operated with two modes during the observation: the troposphere mode with 1-μs single pulse, which observes a height region of 1.5-10 km, and the stratosphere mode with 16-element complementary codes with 1-μs sub-pulse width, which covers 5.4-24 km. These two modes are switched alternately every 75 sec so that the entire height region of 1.5-24 km can be covered with 2.5-min time resolution. Five beam directions of the vertical, and the north, east, south and west directions with 10° zenith angle are observed with a height resolution of 150 m. The beam directions are switched every IPP of 400 μs in a cyclic manner.

The line-of-sight Doppler velocity and the echo power are determined on-line by fitting a Gaussian curve to the observed echo power spectrum at each range gate. The zonal wind velocity component is determined from the line-of-sight velocities of a pair of antenna beams pointing toward the east and west, and the meridional component from the north-south beam pair. The vertical component is directly determined using the vertically pointing antenna beam.

---

[*]Now at Department of Electrical Engineering II, Kyoto University, Kyoto 606, Japan
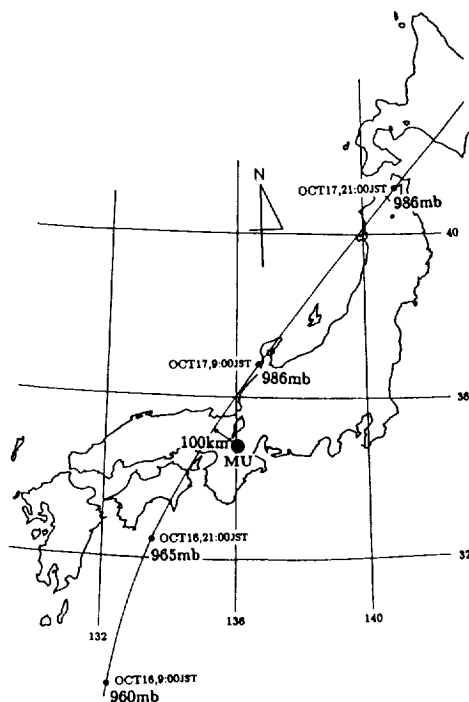
Fig. 1. Route of the center of typhoon 8719.

3 Mean Wind Associated with Typhoon 8719

Typhoon 8719 was upgraded from a tropical law on October 11, 1987 at east of Philippine. It evolved as proceeding toward northwest, reached to its most matured stage with a pressure of 975mb at the center and packed central winds of 40 m s^{-1} on October 15 at 80 km east of Minami-Daitojima island. It then steered its direction toward the north, and landed Shikoku-island at 0 JST, October 17, crossed the island, and landed Honshu-island (mainland Japan) at 4 JST. The pressure at its center at 3 JST was 975 mb, with central winds of 30 m s^{-1}. It speeded up and further proceeded toward north-northeast, and blew out into the Sea of Japan at 7 JST. Figure 1 shows the route of the typhoon. The typhoon is estimated to have passed by the northwest of the MU radar at around 5 JST, October 17 with the minimum distance of about 100 km. Observation with the MU radar started at 20 JST, October 15 and continued for 60 hours until 8 JST, October 18. Figure 2 shows a time-height variation of the mean horizontal wind velocity. Each arrow denotes the zonal and the meridional wind velocity component averaged over 1 hour in time and 600 m in height as a vector with a scale shown on the right of the figure. The thick arrow on the bottom of the figure indicates the passage of the center of the typhoon. Rotating wind field associated with the passage of the typhoon is clearly shown in the figure. Effect of the typhoon on the mean wind is observed up to about 18 km.

ZONAL-MERIDIONAL WIND
15-18 OCT 1987
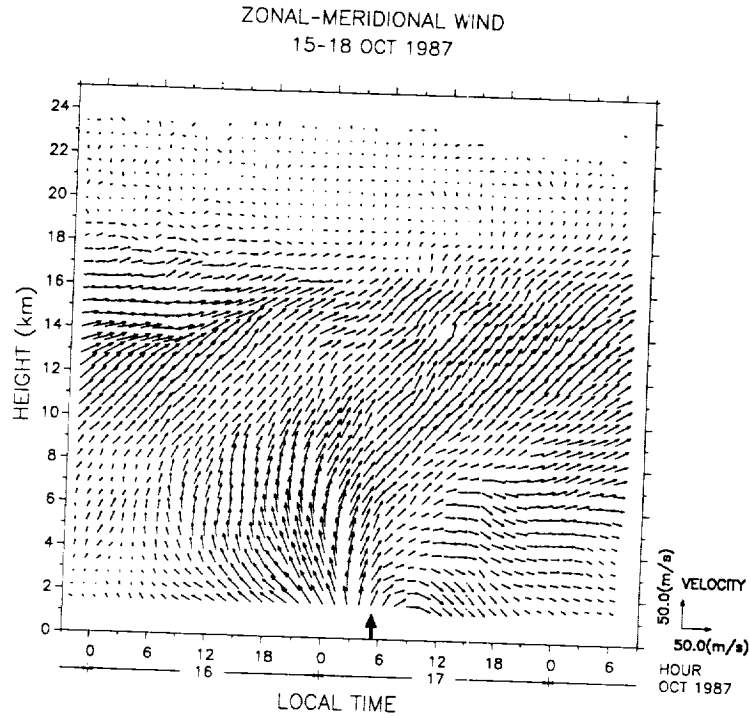
Fig. 2. Time-height variation of the mean horizontal wind.

4 Long Period Waves

Various wave-like fluctuations superimposed on the mean wind are found during this observation. One of the most pronounced among these is the fluctuations with fairly short (2-4 km) vertical wavelengths and with apparent periods of the order of 10 hours. Figure 3 shows the zonal wind component with vertical wavelengths of 2-4 km versus time and height. Contours are drawn every 2 m s^{-1}, and darker shade denotes eastward components. The average zonal wind profile is drawn on the right.

While no clear phase progression is observed before the passage of the typhoon, a remarkable tendency of upward and downward phase progression below and above about 14 km, respectively, appears after the passage. A similar result is obtained also for the meridional wind component. Although this apparent phase progression suggests the generation of inertia-gravity waves at that height, it can be affected by the Doppler shifting of the waves.

In order to avoid this problem, we checked the vertical propagation of these waves by a hodograph analysis introduced by Hirota and Niki (1985). which makes use of the rotation of the wind vector in the horizontal plane versus height to determine the vertical propagation characteristics of the wave. Considering the relatively short vertical wavelength and the large variability of the wave characteristics with height, we determined only whether the wave is propagating upward or downward at each height. It is judged by inspecting the trace of the horizontal wind velocity vector at three adjacent heights around the height of concern, and by determining whether the hodograph has a right-handed or a left-handed curvature with height.

Figure 4 indicates the portion of the waves propagating upward and downward by the

FLUCTUATING COMPONENT OF ZONAL WIND
15-18 OCT 1987

AVERAGE

(m/s)
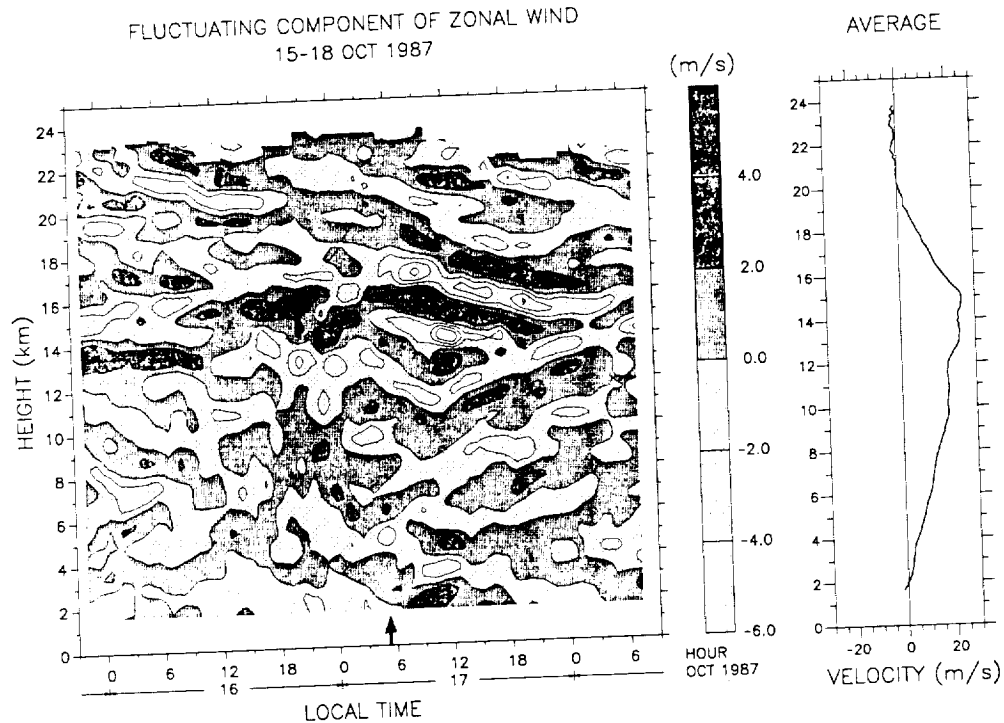
Fig. 3. Zonal wind component with vertical wavelengths of 2–4 km.

shading in the time-height section as Fig. 3. The dark and light shades denote downward and upward propagation, respectively. The predominance of upward propagation seems to indicate the general tendency of upward energy transport by gravity waves. An outstanding feature of this figure is a clear reversal of propagation direction starting from 7 JST on October 17 at about 9 km height. The boundary between downward and upward propagation ascends linearly with time, and reaches 12 km after about 19 hours. Existence of regions with clear downward and upward propagation below and above this boundary, respectively, suggests the generation of these waves there.

Coincidentally, a clear temperature inversion was observed by radiosondes launched from the MU observatory during this period at similar height, which also shows an ascending feature with time as the boundary shows. This temperature inversion agrees with the cloud top height estimated from the humidity profile observed by the radiosondes, and also observed by the radiosondes launched from neighboring weather stations with distances of a few hundred kilometers from the MU radar. The MU radar also observed an enhanced scattering layer at the same height. These observed features suggest that this inversion is caused by some atmospheric discontinuity such as a front. However, a small spatial gradient of this layer, as estimated from the radiosonde network data around Japan, indicates that this layer has no direct connection to a cold front observed on the ground after the typhoon had crossed the Honshu island. Nevertheless, the layer is most likely to be the source of the wave activity discussed here.
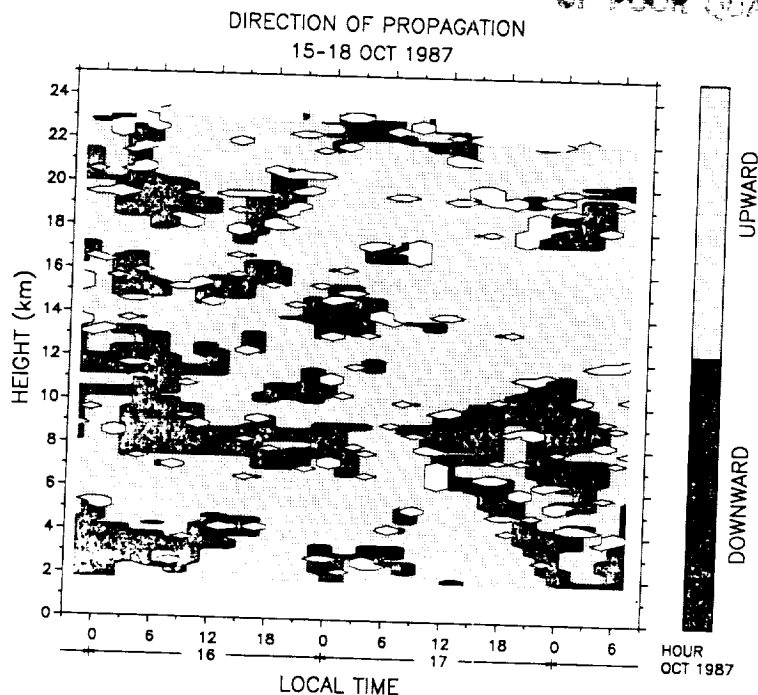
Fig. 4. Direction of vertical propagation of the waves shown in Fig. 3.

5 Short Period Waves and Oscillations

Besides such long period waves, a substantial amplitude was observed also for much shorter period components of the wind fluctuations. Figure 5 shows the variance of the vertical wind fluctuations with periods of less than 20 min versus height and time. These short period fluctuations are more directly related to the disturbances associated with the typhoon, including the convective motions.

Although the temporal growth and decay of the activity is readily explained by the convection inside the typhoon, it is surprising that the enhanced activity in the fluctuations reaches to the maximum observed height of 24 km, which is much higher than the top of the typhoon as indicated in Fig. 2. A vertical wavelength analysis revealed that most of the fluctuations which reached such high altitudes have very large, if not infinite, vertical wavelengths typical to the evanescent modes. These fluctuations are likely to be oscillations near the Brunt-Väisälä period excited by the convective motion within the typhoon. On the contrary, fluctuations at lower heights contain shorter vertical-wavelength components as well.

6 Summary

A few interesting examples were presented among various phenomena found while a series of observation of a typhoon made with the MU radar. Besides the importance of measuring the full vertical structure of a typhoon with the MST radar technique for the first time, the observation has shown the existence of various wave activities associated with the typhoon. Although the analyses are yet rather preliminary, they have shown a clear correspondence of

WIND VARIANCE (Az,Ze)=(0, 0)
15-18 OCT 1987
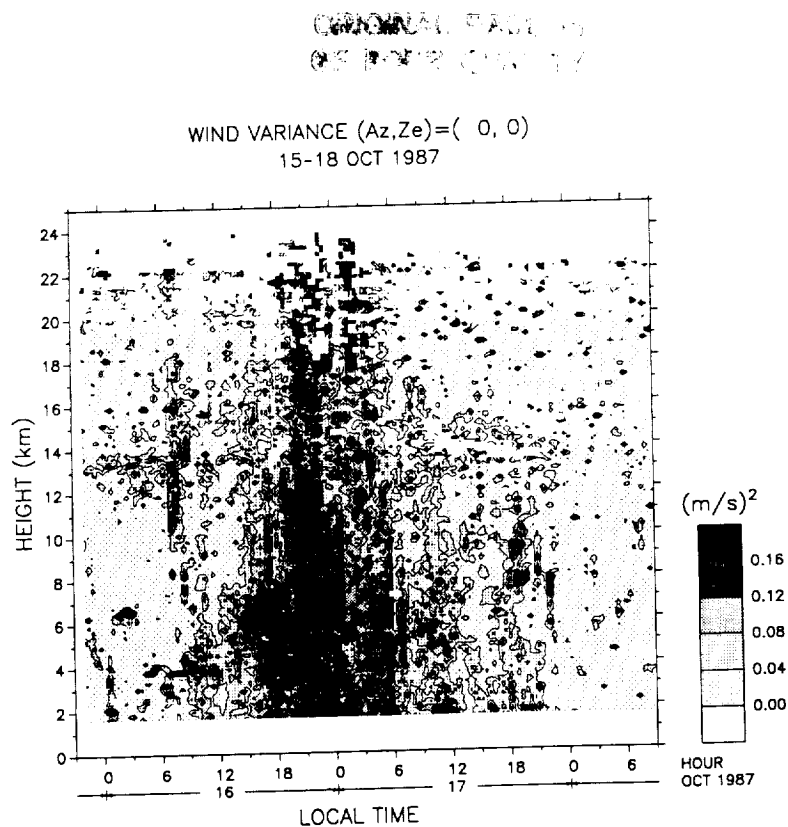
Fig. 5. Variance of the vertical wind fluctuations with periods of less than 20 min.

the waves with their sources, which is one of major advantages of studying isolated disturbances such as a typhoon.

References

Fukao, S., T. Sato, T. Tsuda, S. Kato, K. Wakasugi, and T. Makihira, The MU radar with an active phased array system: 1. Antenna and power amplifiers, *Radio Sci.*, **20**, 1155-1168, 1985a.

Fukao, S., T. Tsuda, T. Sato, S. Kato, K. Wakasugi, and T. Makihira, The MU radar with an active phased array system: 2. In-house equipment, *Radio Sci.*, **20**, 1169-1176, 1985b.

Hirota, I., and T. Niki, A statistical study of inertia-gravity waves in the middle atmosphere, *J. Meteor. Soc. Japan*, **63**, 1055-1066, 1985.

Kato, S., T. Ogawa, T. Tsuda, T. Sato, I. Kimura, and S. Fukao, The middle and upper atmosphere radar: First results using a partial system, *Radio Sci.*, **19**, 1475-1484, 1984.

CHAOTIC FEATURES OF THE MOTION OF THE UPPER TROPOSPHERE AND LOWER STRATOSPHERE REVEALED BY MU RADAR OBSERVATIONS -- CASE STUDY

Peicai Yang, Da-ren Lu, Wei Li, Beiying Wu

Institute of Atmospheric Physics, Academia Sinica
Beijing 100011, China

Susumu Kato, Toshitaka Tsuda, Shoichiro Fukao, Toru Sato, and Mamoru Yamamoto

Radio Atmospheric Science Center, Kyoto University
Uji, Kyoto 611, Japan

1. INTRODUCTION

In recent years, many researches have been devoted to the chaotic features of the atmosphere. There have been two routes of research in this field. The first route is the numerical modeling of certain models of the atmospheric dynamic system. The most famous model is the well-known Lorentz system and its strange attractors. These numerical simulations have made significant contributions to the understanding of chaotic characteristics of the atmosphere. But owing to the present limiting computation ability, those models have to be oversimplified which limits the application of modeling results directly to the real atmosphere. The second route is to deal with observation data of the real atmospheric motions. The key point of this route is to find a procedure of quantifying the chaotic features of the real atmospheric motions revealed by "incomplete" observation data, i.e., the data series of several parameters which are usually not enough to fully describe the system. In the last several years several techniques have been suggested for analyzing the real observation data, among them the technique of phase space reconstruction which plays an important role (NICOLIS and NICOLIS, 1984). All significant characteristics, for example, fractal dimensionality and Lyapunov exponent can be effectively estimated from real observation data with this technique. A few results have been published about the strange attractors in the weather and climate system verifying the existence of chaotic attractors in the atmosphere and indicating that the atmosphere is a system with low degrees of freedom (NICOLIS and NICOLIS, 1984; FRAEDRICH, 1986; ZHENG and LIU, 1988).

In the present paper we shall apply this technique to the investigation of chaotic features, in particular, the dimensionality and Lyapunov exponent, of the atmospheric motion near the tropopause with the MU radar observation data of the upper troposphere and lower stratosphere.

2. TECHNIQUE AND DATA

The technique of deducing dimensionality and Lyapunov exponent has been discussed by GRASSBERGER and PROCACCIA (1983) and WOLF et al. (1985), respectively. In the present paper we principally follow their procedures. First we reconstruct different reconstructed phase space. We start with a set of real data $X(t)$ consisting of a time series of L atmospheric variables (we call variable vector, such as wind components, temperature, etc.) as follows:

$$X(t) = \{x_1(t),...,x_L(t)\}; \quad t = t_0 + p\Delta t, \quad p = 0, 1,...,N \tag{1}$$

then define the reconstructed phase space with time lag τ, $Y(t)$, as

$$Y(t) = \{y_1^{(0)}(t),...,y_1^{(k-1)}(t);...;y_L^{(0)}(t),...,y_L^{(k-1)}(t)\}$$

$$t = t_0 + p\Delta t, \qquad p = 1,2,...,(N-(k-1)\tau)$$

$$y_i^{(j)}(t) = x_i(t+j\tau), \qquad j = 0,...,k-1; \qquad i = 1,...,L \tag{2}$$

Obviously in the present case τ should be some integer multiplying Δt. Based on $Y(t)$ with different lag τ, we can calculate the dimensionality and Lyapunov exponent. The procedures are simply described as follows:

(1) Algorithm of estimating correlation dimension (GRASSBERGER and PROCACCIA, 1983).

    A. Utilizing the vector time series (1), reconstruct a dynamic system such as (2).

    B. Calculate the correlation function

$$C(r) = \frac{1}{N^{2i}} \sum_{j=1}^{N} \theta (r - |Y(t_i) - Y(t_j)|) \tag{3}$$

where $|Y(t_i) - Y(t_j)|$ stands for the distance between the phase points $Y(t_i)$ and $Y(t_j)$. $\theta (x)$ is the Heaviside function, which is equal to zero or 1 if $x > 0$ or < 0, and N is the total number of phase points. In fact, $C(r)$ is a cumulative distribution function. It describes the probability of the event that the distance between any two points on the attractor is less than r.

    C. The relationship between $\ln C(r)$ and $\ln r$ should be linear in an adequate range of r. In other words, $C(r)$ should be a power function of r, i.e.,

$$C(r) \sim r^{d(m)} \tag{4}$$

Then the slope $d(m)$ of $\ln C(r)$ versus $\ln r$ is an estimation of the correlation dimension.

    D. Increase embedding dimension m and repeat the above procedure until $d(m)$ reaches a saturation limit. This saturation value d_∞ will be regarded as the dimensionality of the embedded attractor.

2. Algorithm of estimating the largest Lyapunov exponent (LLE) (WOLF et al., 1985)

    A. Same as above, the first step is to reconstruct an m-dimensional phase portrait such as (2) using given actual data (1).

    B. Setting the initial point $Y(t_0)$ as the fiducial point and its nearest neighbor (in the Euclidean sense) $Y(t_1)$ as the end point, construct an initial vector V_0 and calculate its length $L_0(t_0)$.

    C. As the initial vector travels along the trajectory, trace it until its length reaches a local maximum. The new vector is referred to as an evolved vector and written as $V_1(t_0 + T_0)$, where T_0 is the evolving time, then calculate the length of the evolved vector and denote it with $L_1(t_0 + T_0)$. Then the averaged rate of exponent growth of phase length L in the time period T_0 may be expressed as

$$\lambda_1 = \frac{1}{T_0} \log_z \frac{L_1}{L_n} \tag{5}$$

its unit is bit/second.

    D. Treat $Y(t_n + T_n)$ as the new fiducial point and look for a new end point that satisfies the following two conditions reasonably well: the length of the new constructed vector V_1 (referred to as the replacement vector), $L_1(t_1)$, is small, and the angular separation θ_1 between the evolved and the replacement vector is small, also.

    E. Use V_1 as the new initial vector and repeat steps B, C, and D. The calculated growth rate is denoted as λ_z. The above procedure goes on until the fiducial point reaches the end of the point set $\{Y(t_1)\}$. We take the average value of the growth rates λ_k as the estimation of the largest Lyapunov exponent, i.e.,

$$\lambda = \frac{1}{N_k} \sum \lambda_k = \frac{1}{N_k} \sum_{k=1}^{N_k} \frac{1}{T_{k-1}} \log_z \frac{L_k}{L_{k-1}} \tag{6}$$

where N_k stands for the total number of replacement steps.

In order to obtain a good estimation of the largest Lyapunov exponent, it is necessary that the given time series has enough length.

The data we used in the present case study is the MU radar observation on 18-20 August 1987, three days continuous observation. We selected three altitude ranges around the tropopause, i.e., 10 km, 14 km, and 18 km that represents the upper troposphere and lower stratosphere. We used wind components of u and v, the time interval of observation was about 2.5 min. The data consisted of two components and 1555 time points.

3. RESULTS AND DISCUSSIONS

Based on the MU radar observation data sets and the procedures for estimating correlation dimensions (D) and the largest Lyapunov exponent (LLE) described in the last section, D and LLE for three different altitudes (10, 14, and 18 km) were calculated separately. Table 1 lists the corresponding largest Lyapunov exponents. From Table 1 the following results can be obtained.

A. The atmospheric system as we studied in this paper is a system of low degrees of freedom.

B. In the upper troposphere the correlation dimension of the system is about 4 - 5, the corresponding saturated embedding dimension is about 10. It means that for a full description of this system, 5 independent parameters is the least and 10 is the most.

C. In the lower stratosphere, the correlation dimension and the saturated embedding dimension are about 6 - 7 and 14, respectively. That means the lower stratosphere contains more complicated motion scales than the upper troposphere.

D. The calculated Lyapunov exponents show that the time scale of predictability for the motion in these three altitude ranges are about 110 - 125, 125 - 150, and 135 - 160 minutes, respectively.

Table 1.

Altitude (km)	Correlation Dimension	Embedding Dimension	Lyapunov Exponent	Predictability (min)
10	4.14	10	0.156	110-125
14	4.45	10	0.137	125-150
18	6.84	13	0.124	135-165

4. SUMMARY

From the present case study we see once again that atmospheric motion is chaotic. Also, MST radar data, such as that from the MU radar, are very useful to research of the chaotic atmosphere, in particular in the free atmosphere where obtaining quasi-continuous data is very difficult. Since MST radars have the ability of obtaining more than six independent parameters, such as three components of wind vector and their gradients, echo power, etc., it will be a powerful tool to fully describe the performance of the atmospheric system. It is revealed that from

present results of values of the Lyapunov exponent, the observation with present time interval (about 3 minutes) will be useful for nowcasting in the corresponding altitude range.

REFERENCES

Fraedrich, K., *J. Atmos. Sci.*, *43*, 419-432, 1986.

Grassberger, P., and I. Procaccia, *Phys. Rev. Lett.*, *50*, 346-349, 1983.

Nicolis, C., and G. Nicolis, *Nature*, *311*, 529-532, 1984.

Wolf, A., et al., *160*, 285-317, 1985.

Zheng, Zuguang, and Shida Liu, *ACTA eteo SINICA* (in Chinese) *46*, 41-48, 1988.

A SIMPLE MODEL FOR THE ENHANCED FREQUENCY SPECTRUM OF VERTICAL VELOCITY BASED ON TILTING OF ATMOSPHERIC LAYERS BY LEE WAVES

K. S. Gage

Aeronomy Laboratory
National Oceanic and Atmospheric Administration
Boulder, CO   80303

G. D. Nastrom

Department of Earth Sciences
St. Cloud State University
St. Cloud, MN

1.   INTRODUCTION

Much has been learned in recent years concerning the nature of the observed spectrum of mesoscale variability in the free atmosphere. Major progress has been made, for example, through spectral analysis of time series of Doppler radar observations of horizontal and vertical velocities. The frequency spectra determined from radar observations have been compared with spectral models for internal waves and quasi-two-dimensional turbulence (VANZANDT, 1982, 1985; SCHEFFLER AND LIU, 1985; and GAGE AND NASTROM, 1985a,b).

While there is still considerable debate concerning the nature of the spectrum of horizontal velocities, there is general agreement that the vertical velocity spectra in undisturbed conditions are almost entirely due to internal waves. This view is supported by the climatological study of the frequency spectra of vertical motions reported by ECKLUND et al (1986) and the detailed analysis of vertical velocity observations from the Flatland radar (GREEN et al, 1988; VANZANDT et al, 1989).

Although the vertical velocity spectrum seems to result from internal waves, the horizontal velocity spectrum may be expected to have contributions from both internal waves and quasi-two-dimensional turbulence as discussed in GAGE AND NASTROM (1985a,b; 1986) and GAGE (1989). Recently, this subject has received increased attention from the oceanographic community in the recent work of MÜLLER et al (1988) who estimate the relative contributions of internal waves and vortical modes to the ocean current spectra observed during IWEX. The coexistence of waves and quasi-two-dimensional turbulence is anticipated in the analysis of stratified turbulence contained in RILEY et al (1981) and LILLY (1983). The subject of turbulence in stratified fluids has recently been reviewed by HOPFINGER (1987).

This paper is concerned with the explanation of the enhanced frequency spectra of vertical motions that are often observed near mountains under strong wind conditions. We hypothesize that these enhanced spectra of vertical motions are due to a contamination of the vertical motions by a component of the quasi-horizontal motions that occur on isentropic surfaces. According to this hypothesis, when isentropic surfaces are tilted as they are by lee waves, the vertical beam of the Doppler radar observes a component of the quasi-horizontal motions. This hypothesis is tested by employing a simple model that relates the observed vertical velocity spectrum to the observed horizontal velocity spectrum. Observations taken by the Platteville, Colorado radar are used for this purpose.

2. THE ENHANCED FREQUENCY SPECTRUM OF VERTICAL MOTIONS

A clear illustration of the enhanced frequency spectrum of vertical motions is shown in Figure 1. These spectra were reported by ECKLUND et al (1985) and were taken in southern France during the ALPEX experiment. The enhanced spectra contrast dramatically with the relatively flat spectra of vertical velocity observed under quiet conditions shown in Figures 1 and 2. Furthermore, the quiet-time spectra observed during ALPEX closely resemble vertical velocity spectra observed elsewhere under similar conditions (ECKLUND et al, 1986). They also resemble the Flatland vertical velocity spectra reported by VANZANDT et al (1989) observed under most conditions.
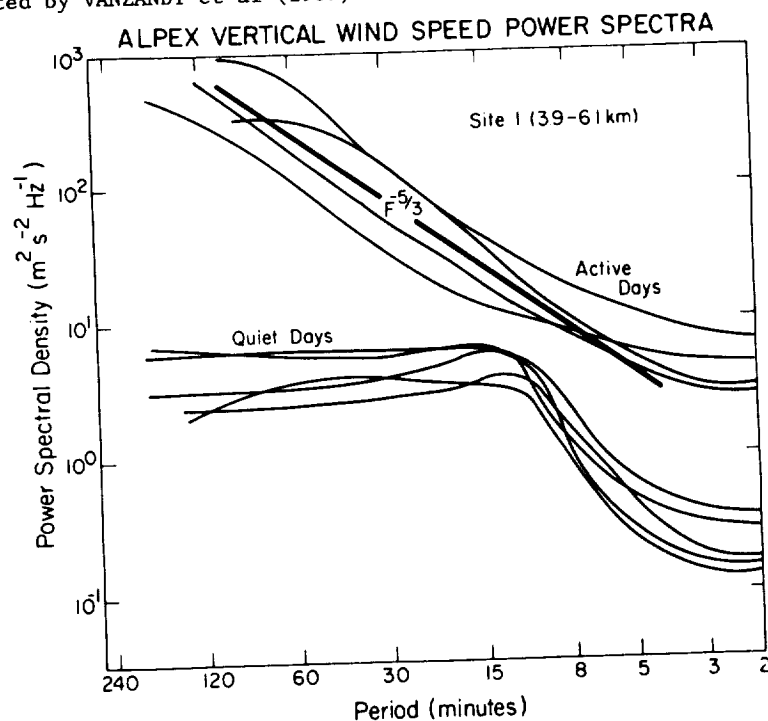
Figure 1. The frequency spectrum of vertical velocity observed in southern France during ALPEX for active and quiet days. (After ECKLUND et al, 1985).

The possibility that the enhanced frequency spectrum of vertical motions might be due to Doppler shifting of an internal wave spectrum by strong winds needs to be considered. Both SCHEFFLER AND LIU (1986) and FRITTS AND VANZANDT (1987) have analyzed the effect of mean winds on a spectrum of internal waves. Recently, VANZANDT et al (1989) have shown that the relatively small changes of vertical velocity spectra that are observed at Flatland can be explained by Doppler shifting.

The fact that enhanced vertical velocity spectra are not observed at Flatland is a strong argument that the enhanced vertical velocity spectra observed at other locations is due to the influence of terrain and not to Doppler shifting. In the remainder of this paper, we examine the enhanced vertical velocity spectra that are observed at Platteville, Colorado in the lee of the Rocky Mountains.
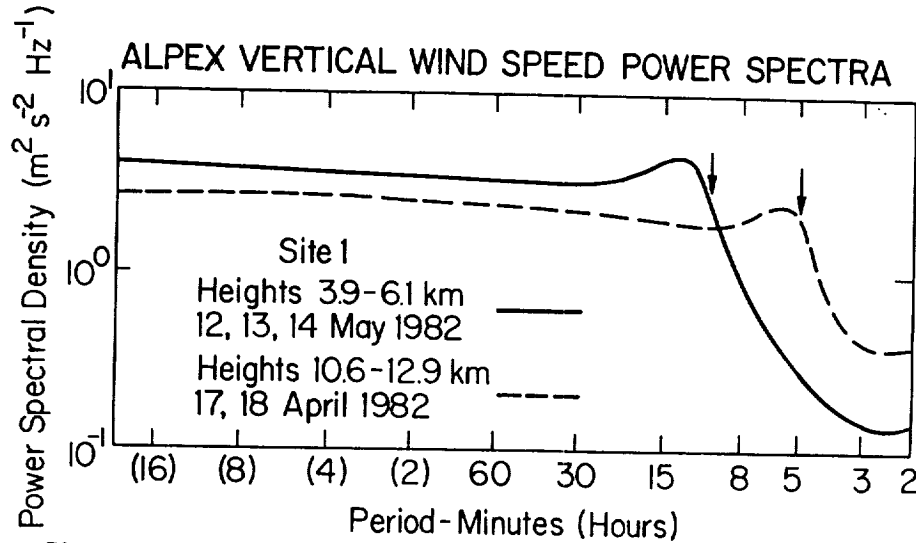
Figure 2. The frequency spectrum of vertical velocity observed in southern France during ALPEX for quiet days. (After ECKLUND et al, 1985).

3. FREQUENCY SPECTRA OF VERTICAL AND HORIZONTAL MOTIONS OBSERVED AT PLATTEVILLE, COLORADO

The Platteville radar has been in continuous operation since the early 1980's. It was originally constructed as a prototype for the Poker Flat MST radar (ECKLUND et al, 1979) and has been operated in recent years by NOAA's Wave Propagation Laboratory. The spectra presented in Figure 3 and Figure 4 are composite spectra averaged by season and stratified by the standard deviation of vertical velocity. At Platteville, there is a close relationship between the background wind speed and the vertical velocity variance as evident in Figure 3 and Figure 4.

Composite vertical velocity spectra for the winter season at Platteville, Colorado are shown in Figure 3. These spectra show clearly the enhancement in spectral magnitude and systematic variation of spectral slope that accompanies increasing winds at this location. The dashed curve indicates a spectral slope of -5/3. With increasing wind speed the observed vertical velocity spectra approach the -5/3 spectral slope. Only those time periods when both horizontal and vertical wind components were measured are used here, although the results are very similar when all available data are used.

Corresponding composite zonal wind spectra at 5.8 km for the winter season as stratified by vertical velocity variance are shown in Figure 4. These spectra also show a systematic but less pronounced variation with background wind speed. Note that the magnitude of the horizontal velocity spectra are in all cases considerably larger than the magnitude of the corresponding vertical velocity spectra. Again, the dashed line shows the -5/3 slope for comparison with the observed spectra.
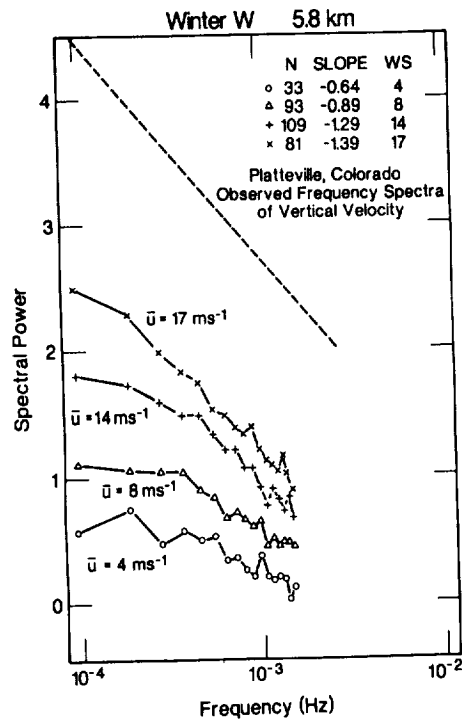
Figure 3. The frequency spectrum of vertical velocity observed at Platteville, CO during the winter season at 5.8 km. Spectra shown are composite spectra averaged over several years and stratified by vertical velocity variance.
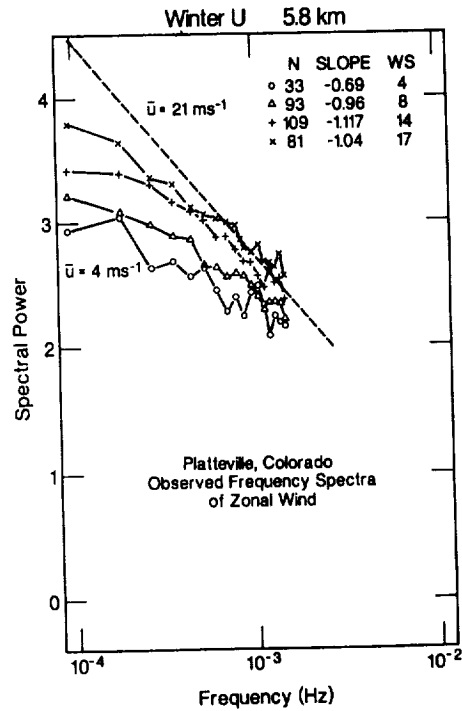
Figure 4. The frequency spectra of zonal wind speed observed at Platteville, CO during the winter season at 5.8 km. The spectra represent the same period of observation as the spectra in Fig. 3 and are stratified in a similar manner.

4. A SIMPLE MODEL FOR THE ENHANCED VERTICAL VELOCITY SPECTRUM

The simple model used here to explain the enhanced vertical velocity spectrum is based on the idea that in stably stratified flows the velocity field is comprised of both internal waves and potential vorticity modes (RILEY et al, 1981; LILLY, 1983; MÜLLER, 1984, HERRING AND METAIS, 1989). The potential vorticity modes are comprised of quasi-horizontal eddies that follow very closely isentropic surfaces in the stratified fluid. Accordingly, when the isentropic surfaces are horizontal and undisturbed, vertical motion will be due only to internal waves. The horizontal motion field, however, will be comprised of both internal waves and vortical modes. When isentropic surfaces are tilted, the vortical modes will also be tilted to conserve potential vorticity so that there will now be a vertical component to the vortical motion.

The consequences of the model on observations by a vertically directed radar are simple and straightforward. When isentropic surfaces are flat, the radar will observe only the internal gravity wave field and vortical motions will not be observed. However, when isentropic surfaces are tilted, as they may be by mountain lee waves, the radar will observe a component of the vortical motion.

The process can be quantified as follows. If the effective tilting angle is δ, the observed vertical velocity spectrum $\Phi_{ww}(\omega)$ is related to the horizontal velocity spectrum $\Phi_{uu}(\omega)$ by

$$\Phi_{ww}(\omega) = \sin^2 \delta \ \Phi_{uu}(\omega) + [\Phi_{ww}(\omega)]_{\text{internal waves}} \quad (1)$$

Thus if δ were known it would be possible to estimate the vertical velocity spectrum from the observed horizontal velocity spectrum since the internal wave spectrum is fairly well known. From the Platteville observations, we can deduce the effective tilting angle that satisfies Eq. (1).
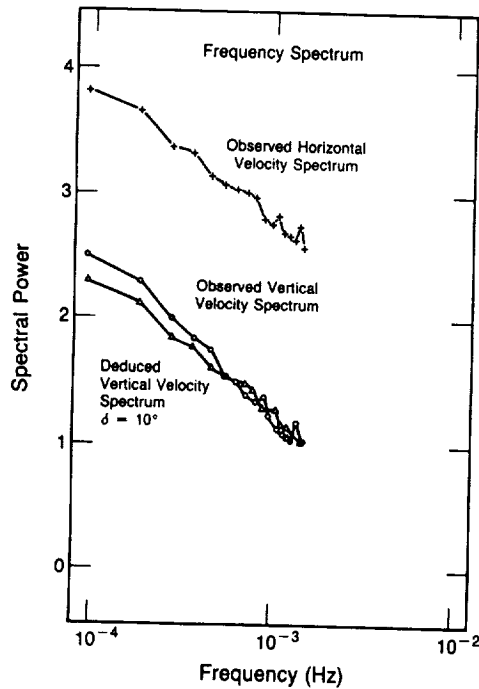
Figure 5. An illustration of the deduction of the vertical velocity spectrum from the observed horizontal velocity spectrum using Eq. 1. Also shown is the observed vertical velocity spectrum for $\bar{u} = 17 \text{ ms}^{-1}$ for comparison.
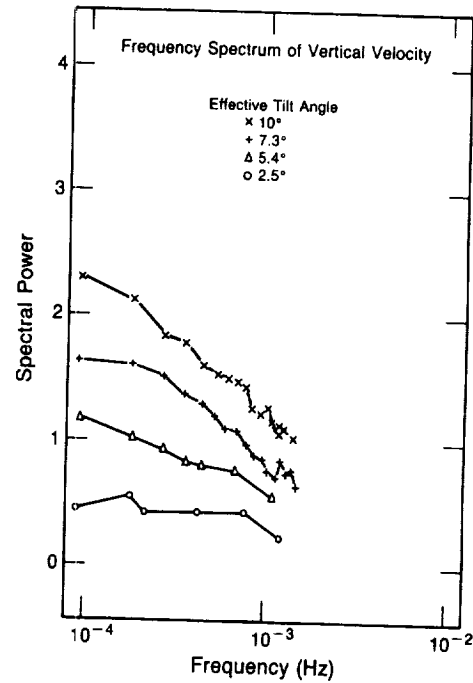
Figure 6. Frequency spectra of vertical velocity derived from the observed horizontal velocity according to Eq. 1. These spectra should be compared with the observed spectra in Fig. 3.

5. VERTICAL VELOCITY SPECTRA DEDUCED FROM THE SIMPLE MODEL

Vertical velocity spectra can be deduced from the observed horizontal velocity spectrum by first determining the effective tilting angle. The effective tilting angle is determined by the value of δ required to reduce the horizontal velocity spectrum to the observed magnitude of the vertical velocity

spectrum. For example, Figure 5 shows that $\delta = 10°$ brings the observed horizontal velocity spectrum for $U = 17$ ms^{-1} into near coincidence with the observed vertical velocity spectrum. Note that only when the effective tilt angle is less than about 5° does the internal wave spectrum become important in Eq. (1) for these observations.

Model vertical velocity spectra for the various background horizontal velocities in Figure 4 are shown in Figure 6. Comparison of the two sets of spectra shows excellent agreement. The effective tilt angles that are consistent with the model fall in the range of 2.5° - 10°. This magnitude of tilt is easily produced by lee waves that possess horizontal wavelengths of order ten kilometers and vertical displacements ranging from several hundred meters to greater than one kilometer (GAGE, 1986). Of course, in the absence of mountain lee waves tilting would not be sufficient to produce the enhanced vertical velocity spectrum. On the synoptic scale isentropic surfaces are generally tilted less than a few tenths of a degree. Propagating internal waves can cause tilting of perhaps a few degrees which could cause a slight enhancement in the observed magnitude of vertical velocity spectra at very low frequencies even over flat terrain.

6. CONCLUSIONS

A simple model has been used to simulate the enhanced frequency spectra of vertical motion observed at Platteville, Colorado under disturbed conditions. If it is hypothesized that the horizontal velocity spectrum is primarily due to quasi-horizontal motions associated with potential vorticity modes, the magnitude and shape of the observed vertical velocity spectrum can be explained by tilting of isentropic surfaces due to lee waves.

While the simple model proposed here is reasonably consistent with observations at Platteville, more stringent tests are required before too much confidence can be placed in the result. For example, independent estimates of the slope of isentropic surfaces associated with lee waves expected under various background wind conditions would strengthen the analysis. Alternatively, observations taken simultaneously at more than one oblique zenith angle would help with the evaluation of how much of the horizontal velocity spectra is associated with vortical modes and how much is due to internal waves.

7. REFERENCES

Ecklund, W. L., D. A. Carter, and B. B. Balsley, 1979: Continuous measurement of upper atmospheric winds and turbulence using a VHF Doppler radar: Preliminary results, J. Atmos. Terr. Phys., 41, 933-944.

Ecklund, W. L., B. B. Balsley, D. A. Carter, A. C. Riddle, M. Crochet, and R. Garello, 1985: Observations of vertical motions in the troposphere and lower stratosphere using three closely-spaced ST radars, Radio Sci., 20, 1196-1206.

Ecklund, W. L., K. S. Gage, G. D. Nastrom, and B. B. Balsley, 1986: A preliminary climatology of the spectrum of vertical velocity observed by clear-air Doppler radar, J. Clim. Appl. Meteor., 25, 885-892.

Fritts, D. C. and T. E. VanZandt, 1987: Effects of Doppler shifting on the frequency spectrum of atmospheric gravity waves, J. Geophys. Res., 92, 9723-9732.

Gage, K. S. and G. D. Nastrom, 1985a: On the spectrum of atmospheric velocity fluctuations seen by MST/ST radar and their interpretation, Radio Sci., 20, 1339-1347.

298

Gage, K. S. and G. D. Nastrom, 1985b: Evidence for coexisting spectra of stratified turbulence and internal waves in mesoscale atmospheric velocity fields, Preprint Vol., 7th Symp. on Turbulence and Diffusion, Nov 12-15, Boulder, CO, pp. 176-179.

Gage, K. S., 1986: Implications of tilting of stable layers on atmospheric measurements by clear-air Doppler radars, Preprint Vol., 23rd Conf. on Radar Meteorology, Sept 22-26, Snowmass, CO, pp. 33-37, Amer. Meteorol. Soc., Boston, MA.

Gage, K. S., 1989: "The structure and dynamics of the free atmosphere as observed by VHF/UHF radar" Chapter 28a in Radar in Meteorology, D. Atlas, ed., Amer. Meteorol. Soc., Boston, MA, in press.

Green, J. L., K. S. Gage, T. E. VanZandt, W. L. Clark, J. M. Warnock and G.D.Nastrom, 1988: Observations of vertical velocity over Illinois by the Flatland radar, Geophys. Res. Lett., 15, 269-272.

Herring, J. R. and O. Metais, 1989: Numerical experiments in forced stably stratified turbulence, J. Fluid Mech., in press.

Hopfinger, E. J., 1987: Turbulence in stratified fluids: A review, J. Geophys. Res., 92, 5287-5303.

Lilly, D. K., 1983: Stratified turbulence and the mesoscale variability of the atmosphere, J. Atmos. Sci., 40, 749-761.

Müller, P., 1984: Small-scale vortical motions, Proceedings of Hawaiian Winter workshop, edited by P. Müller and R. Pujalet, pp. 249-261, Institute of Geophysics, Honolulu, HI.

Müller, P., R.-C. Lien, and R. Williams, 1988: Estimates of potential vorticity at small scales in the ocean, J. Phys. Ocean., 18, 401-416.

Riley, J. J., R. W. Metcalfe, and M. A. Weissman, 1981: Direct numerical simulation of homogeneous turbulence in density-stratified fluids, Nonlinear Properties of Internal Waves, B. J. West, ed., Amer. Inst. of Physics, 76, 79-112.

Scheffler, A. O. and C. H. Liu, 1985: On observations of gravity wave spectra in the atmosphere by using MST radar, Radio Sci., 20, 1309-1322.

Scheffler, A. O. and C. H. Liu, 1986: The effects of Doppler shift on gravity wave spectra observed by MST radar, J. Atmos. Terr. Phys., 48, 1225-1231.

VanZandt, T. E., 1982: A universal spectrum of buoyancy waves in the atmosphere, Geophys. Res. Lett., 9, 575-578.

VanZandt, T. E., 1985: A model for gravity wave spectra observed by Doppler sounding systems, Radio Sci., 20, 1323-1330.

VanZandt, T. E., G. D. Nastrom, J. L. Green and K. S. Gage, 1989: The spectrum of vertical velocity from Flatland radar observations, Preprint Vol., 24th Conf. on Radar Meteorology, Tallahassee, FL, Amer. Meteorol. Soc., Boston, MA.

ON THE ROLE OF PARAMETRIC INSTABILITY IN RADAR OBSERVATIONS OF MESOSPHERIC GRAVITY WAVES

J. Klostermeyer

Max-Planck-Institut für Aeronomie, 3411 Katlenburg-Lindau, FRG

1. INTRODUCTION

Parametric instability of gravity waves has been investigated since many years both theoretically and in laboratory epxeriments (MCEWAN and ROBINSON, 1975; MIED, 1976; DRAZIN, 1977; KLOSTERMEYER, 1982, 1983). A monochromatic finite amplitude internal gravity wave is a simple example of a space and time dependent fluid flow that even at vanishingly small wave amplitude, is inherently unstable due to resonant wave-wave interaction (MIED, 1976). In the absence of molecular dissipation, there is no threshold for instability to occur as in the case of horizontally stratified time independent shear flows for which $Ri \geq 1/4$ (Ri: Richardson number) is a sufficient criterion for stability (MILES, 1961).

Only few authors have applied the theories of resonant interaction and parametric instability to atmospheric gravity waves (YEH and LIU, 1981, 1985; KLOSTER-MEYER, 1984; DUNKERTON, 1987; INHESTER, 1987; DONG and YEH, 1988). Whereas the application of weak resonant interaction theory to internal atmospheric gravity waves can be criticized because these waves are strong at least at mesospheric heights, the theory of parametric instability is not limited to small-amplitude primary waves and can be applied whenever there is a strongly dominant harmonic wave within a spectrum of otherwise weak waves. Such events may occasionally occur at mesospheric heights. Moreover, since the semidiurnal tide usually dominates the mesospheric wave spectrum (RÜSTER, 1984) it appears worth-while to extend the theory of parametric instability to waves in rotating stratified fluids and compare its predictions with mesospheric observations.

2. SUMMARY OF THEORY

The following short description of parametric instability theory is restricted to two-dimensional motions in an unbounded inviscid uniformly stratified Boussinesq fluid (cf. MIED, 1976; KLOSTERMEYER, 1982). In the atmosphere, the Boussinesq approximation is valid, if the gravity wave-associated fluid velocity is much smaller than the speed of sound and the wavenumber k is much larger than the reciprocal density scale height $H : k^2 >> (2H)^{-2}$. This relation is satisfied for wavelengths smaller than about 10 km. We introduce a stream function Ψ and buoyancy B by

$$\mathbf{U} = (\Psi_z, -\Psi_x), \quad B = -\frac{\rho - \rho_*}{\rho_*}\, g \tag{1}$$

with $\mathbf{U}$, ρ and g denoting, respectively, the fluid velocity, density and gravitational acceleration. ρ_* is some suitable constant reference density used in the Boussinesq approximation to replace ρ in the inertia term. x and z are horizontal and vertical coordinates, and the subscripts denote the corresponding partial derivatives. Then the fluid motion is described by the nonlinear vorticity and density equations

$$
\begin{aligned}
\nabla^2 \Psi_t + B_x &= \Psi_x \nabla^2 \Psi_z - \Psi_z \nabla^2 \Psi_x \\
B_t - N^2 \Psi_x &= \Psi_x B_z - \Psi_z B_x
\end{aligned}
\tag{2}
$$

with N the Väisälä–Brunt frequency.

The finite amplitude plane wave

$$\Psi = A \cos \Phi, \quad B = -N^2 l \omega^{-1} \cos \Phi \tag{3}$$

with $\Phi = lx + mz - \omega t$ is a solution of (2) if the dispersion relation

$$\omega^2 = N^2 \cos^2 \theta \tag{4}$$

with $\theta = \arctan(m/l)$ is satisfied. To investigate the stability of (3) we put

$$\Psi = A \cos \Phi + \psi, \quad B = -N^2 l \omega^{-1} A \cos \Phi + b \tag{5}$$

where ψ and b are perturbation quantities. We further define nondimensional variables by

$$(\tilde{x}, \tilde{z}) = k(x, z), \quad \tilde{t} = Nt, \quad \tilde{\Psi} = k^2 N^{-1} \Psi, \quad \tilde{B} = kN^{-2}B, \quad M = k^2 (2N)^{-1} A \tag{6}$$

with $k = (l^2 + m^2)^{1/2}$ and introduce a rotated coordinate system (ξ, η) such that the η axis coincides with the wavenumber vector $\mathbf{k}$ of the primary wave (3). Substituting (3) into (2) and neglecting all terms containing products of the perturbation quantities then yields

$$
\begin{aligned}
\nabla^2 \psi_t + \sin\theta\, b_\xi + \cos\theta\, b_\eta &= 2M \sin\Phi(\psi_\xi + \nabla^2 \psi_\xi) \\
b_t - \sin\theta\, \psi_\xi - \cos\theta\, \psi_\eta &= 2M \sin\Phi(\psi_\xi + b_\xi)
\end{aligned}
\tag{7}
$$

where the tilde of the nondimensional variables has been omitted and $\nabla^2 = \partial^2/\partial\xi^2 + \partial^2/\partial\eta^2$, $\Phi = \eta - \cos\theta\, t$.

Floquet theory requires solutions of the form

$$(\psi, b) = e^{i(-\alpha \sin\beta\xi + \alpha \cos\beta\eta) + \lambda t} \sum_{j=-\infty}^{\infty} (\psi_j, b_j) e^{ij\Phi}. \tag{8}$$

where the term with $j = 0$ is called a Floquet wave that has a wavenumber α and propagates at an angle β to the primary wavenumber vector $\mathbf{k}$. The complex quantities λ and (ψ_j, b_j) can be obtained from a linear eigenvalue problem. For $M \to 0$, the nondimensional perturbation wavenumbers and frequencies in $x - z$ coordinates are

$$\mathbf{k}_j = (\alpha \cos(\theta + \beta) + j \cos \theta, \alpha \sin(\theta + \beta) + j \sin \theta) \qquad (9)$$

$$\omega_j = j \cos \theta - \mathrm{Im}\lambda$$

so that for all j

$$\mathbf{k}_{j+1} - \mathbf{k}_j = \mathbf{k}, \quad \omega_{j+1} - \omega_j = \omega. \qquad (10)$$

Since $\omega_j = \cos \theta_j$ where θ_j is the angle between $\mathbf{k}_j$ and the horizontal, parametric instability reduces to nonlinear resonant interaction for $M \to 0$.

3. BRAGG SCATTER FROM FAST GROWING INSTABILITIES

The computed results in this and the next section were obtained for a fixed propagation angle $\theta = -72°$, i.e. for a primary wave with a period about three times larger than $2\pi/N$ while both the primary wave amplitude M and the Floquet vector have been varied systematically. The fastest growing instability modes for given M were generally found for Floquet wavenumber vectors pointing to the hatched areas along branches A and C of the interaction diagram in Figure 1.
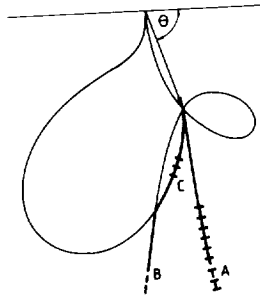
Figure 1. Resonant interaction diagram for a primary wave propagating at an angle $\theta = -72°$. Any point on a branch defines a resonant triad satisfying (10). Thick (thin) branches indicate unstable (stable) triads. The hatched parts of branches A and C are locations at which triads containing the primary and the Floquet waves give rise to fast growing parametric instabilities.

The maximum growth rates $\max_\beta (Re\lambda)$ near branches A and C as functions of α are shown in Figure 2. Note that the corresponding Floquet wavenumber vectors do not point exactly to the resonant interaction diagram because $M > 0$. Figure 2 indicates that near branch C, the fastest growing disturbance waves have wavenumbers comparable to the primary wavenumber k which is unity in nondimensional coordinates. These disturbances lead to a broadening of the wavenumber spectrum and dominate the small-scale disturbances along branch A at small primary wave

amplitudes ($M = 0.1$, $M = 0.2$). At larger M values (0.4 and 0.6), the small-scale disturbances along branch A grow faster than the disturbances along branch C. In the absence of molecular dissipation, the A curves extend to infinitely large α values whereas in the presence of dissipation there is a viscous cut-off (KLOSTER-MEYER, 1983). The relevance of parametric instability to atmospheric radar measurements is evident: *At sufficiently low molecular dissipation, a gravity wave of arbitrary amplitude gives rise to small-scale disturbances producing Bragg scatter*, i.e. it makes its own appearance without needing any external turbulence source like Kelvin-Helmholtz or static instability.
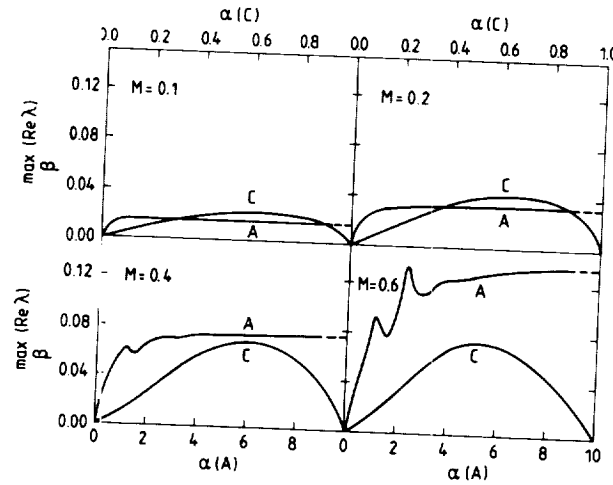
Figure 2. Nondimensional maximum growth rates $\max_{\beta} (Re\lambda)$ vs. Floquet wavenumber α near branches A and C of the resonant interaction diagram for several values of the primary wave amplitude M. Note the different scales for α along branches A and C.

4. LAYERED STRUCTURES AND TAYLOR'S HYPOTHESIS

Figure 3 shows the vertical structure of the Floquet solution (8) for x and t constant. The primary wave propagates at an angle $\theta = -72°$ and has an amplitude of $M = 0.1$, the Floquet wavenumber vector is given by $\alpha = 10$ and $\beta = -9.6°$. The solution is a high wavenumber oscillation due to the first factor on the right of (8) that is modulated by a Fourier series with a spatial periodicity determined by the vertical wavenumber m of the primary wave. The wave groups in Figure 3 thus move with a group velocity equal to the phase velocity of the primary wave. Closer examination further reveals that the wavenumber of the fast oscillations depends slightly on z. In general it turns out that at $\alpha \gg 1$, the Floquet solutions for ψ and b or any linear

combination of both quantities and their derivatives can be described by the WKB approximation

$$a(x, z, t)e^{i\varphi(x,z,t)} \tag{11}$$

where φ is a rapidly varying phase angle and a a slowly varying amplitude so that we can define a local wavenumber vector and a local angular frequency by

$$\mathbf{k}' = (\varphi_x, \varphi_z), \quad \omega' = -\varphi_t. \tag{12}$$

All instabilities arising from Floquet wavenumber vectors pointing to branch A of the interaction diagram thus form a continuous wavenumber spectrum.
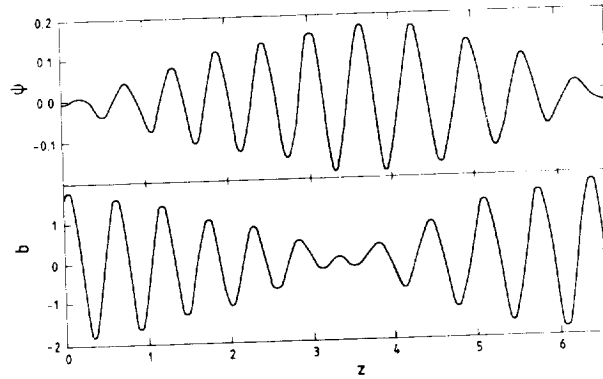
Figure 3. Stream function and buoyancy perturbations vs. height for constant x and t, produced by a primary gravity wave with $\theta = -72°$ and $M = 0.1$, and a Floquet wavenumber vector with $\alpha = 10$ pointing to branch A. All quantities are normalized according to (6).

Are the high-wavenumber disturbances frozen in the flow of the primary wave (Taylor's hypothesis)? We have to compare the time derivative ψ_t and the advective term $(\mathbf{U} \cdot \nabla)\psi$ calculated from (8) where the stream function perturbation ψ could also be replaced by the buoyancy perturbation b or some other perturbation quantity obtained from ψ and b. $\mathbf{U}$ is the space and time dependent fluid velocity of the primary wave (cf. (1)):

$$\mathbf{U} = A \sin \Phi(-m, l). \tag{13}$$

Since at $\alpha \gg 1$, all perturbation variables can be expressed by the WKB–ansatz (11) we have approximately

$$\frac{\partial}{\partial t} = -i\omega', \quad \mathbf{U} \cdot \nabla = i\mathbf{k}' \cdot \mathbf{U}. \tag{14}$$

Both ω' and $\mathbf{k}' \cdot \mathbf{U}$ have been computed at equidistant values of Φ in the interval $[0, 2\pi]$. The correlogram in Figure 4 shows that the majority of all values is in

fact strongly correlated. Only those values computed at small amplitudes a of the WKB–ansatz (11) show no or weak correlation. This does not necessarily mean that $\partial/\partial t - \mathbf{U} \cdot \nabla \neq 0$ because the relations (14) may be invalid at small a. Preliminary studies indicate that the range of Φ within $[0, 2\pi]$ yielding strong correlation between ω' and $\mathbf{k}' \cdot \mathbf{U}$ increases with increasing α. For a given Floquet wavenumber α, Taylor's hypothesis thus is valid at sufficiently large amplitudes a.
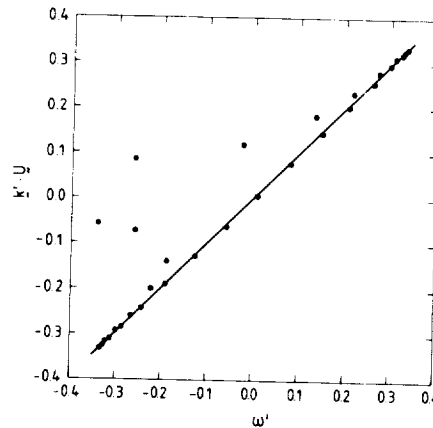
Figure 4. Correlogram: Disturbance wave frequency, ω', vs. advection by primary wave fluid velocity, $\mathbf{k}' \cdot \mathbf{U}$, for a primary wave with $\theta = -72°$ and $M = 0.1$ and a Floquet wavenumber $\alpha = 10$. The continuous line represents perfect correlation. The circles are obtained from pairs of values taken over one cycle of the primary wave. Deviations from strong correlation occur only at small disturbance wave amplitudes (cf. (11)).

If we asume for simplicity that the radar refractive index varies as the air density or, equivalently, as the buoyancy, the scattered radar signal power would show the same height dependence as the amplitude of b. *The radar signal power then has a layered structure moving at the phase velocity of the primary wave, and the signal Doppler shift yields the fluid velocity of the primary wave except perhaps at vanishingly small signal power.*

5. A CASE STUDY

In laboratory experiments, DAVIS and ACRIVOS (1967) demonstrated that an internal gravity wave propagating along the interface between fluids of different densities can be distorted by energy exchange within resonantly interacting triads. The power spectrum of a strong internal gravity wave in the lower thermosphere generated by the eruption of Mount St. Helens on 18 May 1980 was explained in terms of parametric instability by KLOSTERMEYER (1984). RÖTTGER (1987) has noted

that time series of mesospheric spectra intensity plots obtained from measurements with the mobile SOUSY VHF Radar at the Arecibo Observatory show high-frequency oscillations superposed on low-frequency gravity waves. He points out that the amplitude of the dominating low-frequency waves does not grow with increasing height even though wave breaking discernible from strong echo intensity bursts is absent. Therefore some other saturation process such as parametric instability must be considered.

Short-period gravity waves with frequencies close to the local Väisälä-Brunt frequency occur frequently in mesospheric MST radar observations of vertical or near vertical radial velocities [HARPER and WOODMAN, 1976; MILLER et al., 1978]. These waves do not show any vertical phase variation over height intervals of several kilometers indicating that they propagate horizontally and are generated in situ rather than in lower or higher atmospheric regions. Occasionally the local source mechanism is Kelvin-Helmholtz instability of a wind shear due to long-period inertial or tidal waves [KLOSTERMEYER and RÜSTER, 1984; YAMAMOTO et al., 1988]. But in general the simultaneously observed wind shear is too weak for Kelvin-Helmholtz instability to set in. An example of a measured high-frequency wave with a period near 10 min superposed on a low-frequency internal gravity wave with a period of 30 min and a downward propagating phase is shown in Figure 5.
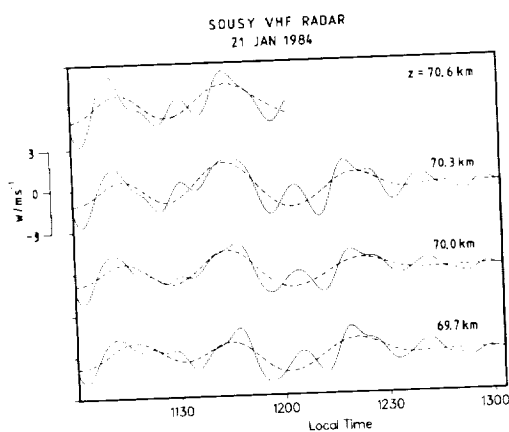
Figure 5. Vertical velocity component vs. time at four heights measured by the mobile SOUSY VHF Radar at Andenes (Norway) on 21 January 1984. Continous curves: time series after noise removal; dashed curves: time series after high-frequency wave removal. (The original time series without noise removal were published by RÜSTER (1984).)

To explain the measured results in Figure 5 in terms of parametric instability, we consider again the maximum growth rate along branch A in Figure 2. At $M \geq 0.4$,

the curves show one or two local maxima near $\alpha = 1$ and $\alpha = 2$. We will call the corresponding instabilities isolated because their Floquet wavenumber α is clearly separated from the continuous α range of the fast growing high-wavenumber instabilities. The exact nature of the isolated instabilities is still unknown but they might be due to resonant interactions of third or higher order because they occur only at the larger M values. Figure 6 shows a numerical simulation where the dashed curves represent the vertical velocity component of a primary wave with $\theta = -80°$ and $M = 0.5$, and the continuous curves the fastest growing isolated parametric instability. At finite amplitude, the growth of the instability is probably limited by nonlinear interaction with other waves including the primary wave. These effects have been parameterized in the computations by eddy viscosity and thermometric conductivity coefficients. Note that the height interval in Figure 6 is 75% of the basic vertical wavelength whereas in Figure 5, it is only about 10%. The observed and computed short-period oscillations show good qualitative agreement. Both reveal in particular considerable temporal amplitude modulation, and the dominating period is not an integer multiple of the basic period. There is in general also no vertical phase variation. But the computed short-period oscillations show sudden phase reversals, e.g. at $Nt = 20$ and $kz = 4.8$. The loci of sudden phase reversals lie on basic wave fronts. Whereas there is no clear evidence for phase reversals in Figure 5 (perhaps due to the small height interval) they become visible if velocity measurements can be obtained over larger height intervals (e.g. Figure 1 of MILLER et al. [1978]).
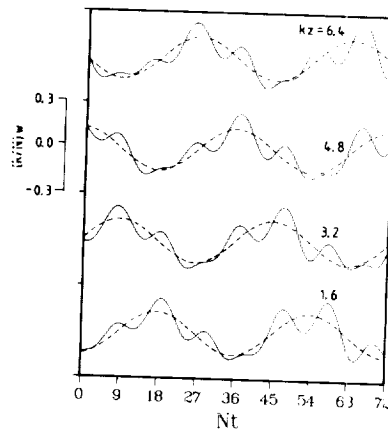
Figure 6. Numerical simulation of parametric instability. The dashed and continuous curves represent the primary wave and the sum of primary wave and fastest growing isolated parametric instability, respectively. Time, height and vertical velocity component are normalized according to (6).

References

Davis, R.E., and A. Acrivos, The stability of oscillatory internal waves, *J. Fluid Mech.*, **30**, 723-736, 1967.

Dong, B., and K.C. Yeh, Resonant and nonresonant wave–wave interactions in an isothermal atmosphere, *J. Geophys. Res.*, **93**, 3729-3744, 1988.

Drazin, P.G., On the instability of an internal gravity wave, *Proc. R. Soc. Lond.*, **A356**, 411-432, 1977.

Dunkerton, T.J., Effect of nonlinear instability on gravity-wave momentum transport, *J. Atmos. Sci.*, **44**, 3188-3209, 1987.

Harper, R.M., and R.F. Woodman, Preliminary multiheight radar observations of waves and winds in the mesosphere over Jicamarca, *J. Atmos. Terr. Phys.*, **39**, 959-961, 1977.

Inhester, B., The effect of inhomogeneities on the resonant parametric interaction of gravity waves in the atmosphere, *Annls. Geophys.*, **5A**, 209-218, 1987.

Klostermeyer, J., On parametric instabilities of finite-amplitude internal gravity waves, *J. Fluid Mech.*, **119**, 367-377, 1982.

Klostermeyer, J., Parametric instabilities of internal gravity waves in Boussinesq fluids with large Reynolds numbers, *Geophys. Astrophys. Fluid Dyn.*, **26**, 85-105, 1983.

Klostermeyer, J., Observations indicating parametric instabilities in internal gravity waves at thermospheric heights, *Geophys. Astrophys. Fluid Dyn.*, **29**, 117-138, 1984.

Klostermeyer, J., and R. Rüster, VHF radar observation of wave instability and turbulence in the mesosphere, *Adv. Space Res.*, **4**, 79-82, 1984.

McEwan, A.D., and R.M. Robinson, Parametric instability of internal gravity waves, *J. Fluid Mech.*, **67**, 667-687, 1975.

Mied, R.P., The occurrence of parametric instabilities in finite-amplitude internal gravity waves, *J. Fluid Mech.*, **78**, 763-784, 1976.

Miles, J.W., On the stability of heterogeneous shear flows, *J. Fluid Mech.*, **10**, 496-508, 1961.

Miller, K.L., S.A. Bowhill, K.P. Gibbs, and I.D. Countryman, First measurements of mesospheric vertical velocities by VHF radar at temperate latitudes, *Geophys. Res. Lett.*, **5**, 939-942, 1978.

Röttger, J., The relation of gravity waves and turbulence in the mesosphere, *Adv. Space Res.*, **7**, 10345-10348, 1987.

Rüster, R., Winds and waves in the middle atmosphere as observed by ground based radars, *Adv. Space Res.*, **4**, 3-18, 1984.

Yamamoto, M., T. Tsuda, S. Kato, T. Sato, and S. Fukao, Interpretation of the structure of mesospheric turbulence layers in terms of inertia gravity waves, *Physica Scripta*, **37**, 645-650, 1988.

Yeh, K.C., and C.H. Liu, The instability of atmospheric gravity waves through wave–wave interactions, *J. Geophys. Res.*, **86**, 9722-9728, 1981.

Yeh, K.C., and C.H. Liu, Evolution of atmospheric spectrum by processes of wave-wave interaction, *Radio Sci.*, **20**, 1279-1294, 1985.

SEASONAL VARIATION OF TURBULENCE INTENSITIES IN THE UPPER MESOSPHERE AND LOWER THERMOSPHERE MEASURED BY RADAR TECHNIQUES DURING THE 3-YEAR PERIOD 1985 - 1987.

W.K. Hocking,

University of Adelaide, Australia.

Since February 1985, the 2-MHz narrow beam radar operated by the University of Adelaide in Australia has been used to measure the short-term root-mean-square fluctuating velocities of radio-wave scatterers in the upper middle atmosphere (80-100km). To do this, the widths of the spectra of the signals recorded by the radar are utilized, as described for example by HOCKING, (1988). Briefly, the measured spectral widths of the received signal are due to a combination of beam broadening, wind-shear broadening ("instrumental effects") and natural fluctuation. The method involves determining the "instrumental contribution" and then removing its effect to leave the contribution due to natural effects. For the Adelaide radar the experimental spectral widths almost always exceed the widths expected due to "instrumental" effects by a small but significant amount (HOCKING 1988), and so it is possible to measure these fluctuating velocities.

The measured fluctuations are caused by a mixture of turbulence and gravity waves, and under certain reasonable assumptions the contribution due to turbulent fluctuations can be extracted. The results of the measurements made during 1985 and 1986 have been discussed in detail by HOCKING (1988), and this short article extends the data set to include 1987.

The results for 1985 and 1986 showed that the smallest values occur in the equinoxes (HOCKING, 1988). In 1986 there was some hint of a semi-annual oscillation in the median values, but it was not very strong. The extension of the data to include 1987 shows a semi-annual oscillation much more clearly. Fig. 1 shows the weekly means for 1987, with the 1986 variation super-imposed. It is interesting to reflect on the reasons for this significant inter-annual variability which clearly exists.

Of the three years during which measurements have taken place, the year 1985 stands out as being distinctly different to 1986 and 1987, chiefly because very large values of energy dissipation rate occurred at the equinoxes, in addition to very small values. These very large values may be related to the diurnal tide, which was extraordinarily large in 1985. It appears that the semiannual oscillation reflects a similar oscillation in gravity wave activity, and that it is energy deposition by such waves which is the primary source of turbulence in the middle atmosphere. However, other sources exist and can alter the normal semi-annual character; 1985 is an example, where the presence of the tides causes a significant departure from the normal trend. The tides may not themselves cause the extra turbulence, but may act as a trigger for enhanced gravity wave breaking by wave-tide interactions for example. The experiment is continuing in order to examine the interannual variability in more detail.

References   HOCKING, W.K. "Two years of continuous measurements of turbulence parameters in the upper mesosphere and lower thermosphere made with a 2-MHz radar". J. Geophys. Res., 93, 2475, 1988.

86 KM 1987

ADELAIDE, AUSTRALIA (35°S)
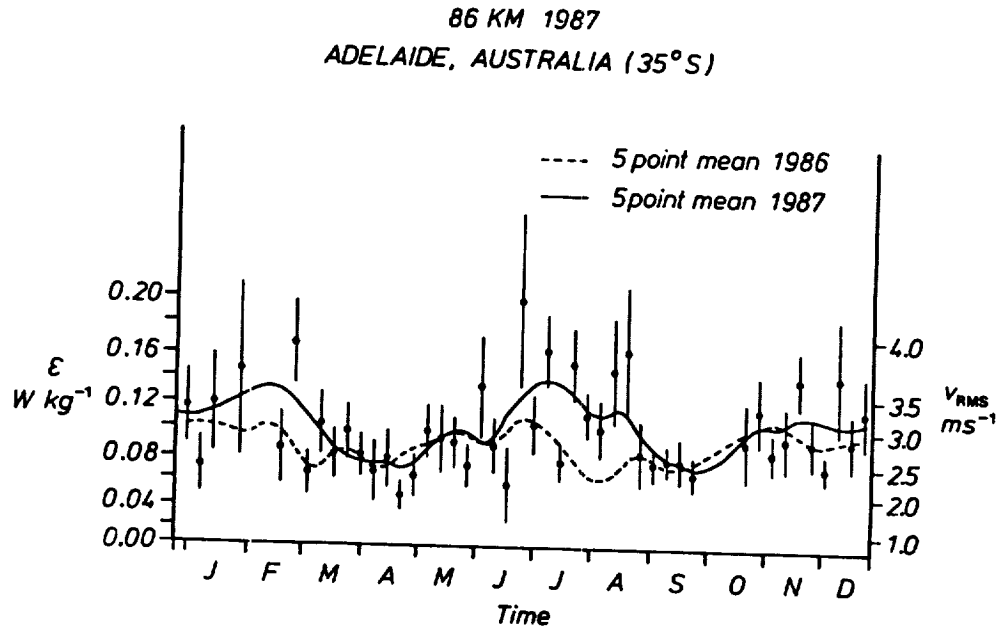
Fig. 1. Weekly means of the turbulent energy dissipation rates in the mesosphere at 86 km altitude. The data for both 1986 and 1987 are shown. The broken and continuous lines show five-point running means of the weekly means for 1986 and 1987.

OBSERVATIONS OF QUASI-INERTIAL PERIOD WAVES IN THE LOWER STRATOSPHERE OVER ARECIBO

M. F. LARSEN[1] and C. R. CORNISH[2]

[1]Department of Physics and Astronomy
Clemson University
Clemson, SC 29631

[2]School of Electrical Engineering
Cornell University
Ithaca, NY 14853

INTRODUCTION

A common feature of the wind profile observations carried out with the Arecibo Observatory 430-MHz radar has been the presence of a wavelike structure near the tropopause and in the lower stratosphere. Typical characteristics include a vertical wavelength of 1.5-3.0 km and a horizontal wind perturbation amplitude of 3-5 ms^{-1}. Obtaining observations over extended periods has been difficult at Arecibo due to the competition for time between astronomers, ionospheric physicists, and, to a lesser extent, meteorologists. However, the persistence of the structure, as well as the experiments carried out over periods of a day or two, indicate that the wave periods are of the order of a day or more.

The common interpretation of the observed wave structure has been that they are due to low-frequency quasi-inertial period waves, although the source of such waves has not been clear. Interpretations along these lines have been given by SATO AND WOODMAN (1982a), who first discovered the waves at Arecibo, by MAEKAWA et al. (1984), who reanalyzed the two-day data set first presented by SATO AND WOODMAN (1982a), and by CORNISH AND LARSEN (1984) and CORNISH (1987) based on a preliminary analysis of the more extended data set that we present in this article.

The presence of the wave structure at Arecibo and the associated dynamics are of interest in and of themselves, but there may be more universal interest in the phenomenon since observations of similar structure have been made at a variety of locations by a number of investigators over the past three decades. Common features of the observations have been the presence of low-frequency, large-amplitude oscillations in the lower stratosphere with periods in the earth-fixed reference frame of the same order as the inertial period, given by 12 hr/sin θ where θ is the latitude. The structures are characterized by horizontal perturbation velocity amplitudes of a few ms^{-1} up to 10 ms^{-1} and small

vertical wavelengths of 1-5 km. The waves may be present in the troposphere but are primarily observed near the tropopause and in the lower stratosphere. Some of the relevant studies that have shown the presence of the tropopausal and lower stratospheric waves include those by WEINSTEIN et al. (1966), MADDEN AND ZIPSER (1970), THOMPSON (1978), CADET AND TEITELBAUM (1979), BARAT (1983), PFISTER (1985), and SIDI AND BARAT (1986), as well as the radar studies mentioned above. The cited references have focused primarily on the wave structures.

Recently, HINES (1988) has proposed an alternative explanation for the wave structure observed at Arecibo, namely that the oscillations are essentially orographic waves produced by the flow over the Puerto Rican terrain. The fundamental difference between his interpretation and the previous ones is that the intrinsic period, i. e., the period in the frame moving with the mean wind, can be quite short, whereas the low-frequency gravity wave interpretation requires periods comparable to the inertial period. HINES' (1988) proposal is appealing in that it would explain the consistent presence of the waves in spite of changing meteorological conditions associated with changes in season and the passage of local disturbances. Also, the strong coherence of the vertical wavelength structure would be explained by the fact that the vertical wavelength for all orographic waves is the same, regardless of the intrinsic frequency, so that even a spectrum of waves will tend to add coherently and produce a structure similar to what we observe. While the interpretation appears to have considerable merit, the analysis carried out by HINES (1988) was based in large part on rough fits-by-eye to the characteristics of a single wind profile. Other parameters were also estimated coarsely from radiosonde profiles.

In this paper, we will present a more detailed analysis of a five-day data set obtained with the Arecibo Observatory 430-MHz radar in May of 1982. We will show that, although HINES' (1988) explanation of an orographic source for the waves appears to have merit, the waves also have low-frequency gravity-inertia wave characteristics.

EXPERIMENTAL SET-UP

In this paper we present data from two sets of wind measurements made in the subtropical upper troposphere and lower stratosphere with the Arecibo 430-MHz radar wind profiler.

The Arecibo Observatory is located at 18.3°N latitude, 66.7°W longitude, and the corresponding local inertial period is 38.1 hours. The observatory is situated in the subtropical zone characterized in the lower troposphere by the easterly flow of the trade winds, while the flow in the upper troposphere and the lower troposphere is westerly. The tropopause height is typically in the range from 14-16 km.

During April and May, the months when both data sets were taken one year apart, the prominent feature of the mean flow is a westerly subtropical jet maximizing near the tropopause. The general meterological conditions were mostly fair weather skies with some convective activity just before the onset of the summer rainy season. Intense convective activity typically begins late in May.

In the May 1982 experiment, the radar was operated in a variable azimuth display (VAD) mode by pointing the radar beam at a fixed zenith angle of 15° and rotating it sequentially to 16 different azimuths. The VAD technique can provide much information about the total wind field (WILSON AND MILLER, 1972), but our presentation here is limited to measurements of the vertical profiles of the horizontal winds derived from the line-of-sight velocities taken from the principal directions (north, east, south, west). Each VAD scan took 35 minutes to complete. At each compass point, the antenna-pointing system fixed the radar beam, and a profile of radial Doppler spectra was taken during an integration period of about 1 min. The transmitted signal was coded with a 32-baud quasi-complementary (QC) code with a baud length of 1 ms, which yielded a height resolution of 150 m, and was repeated at an interpule period (IPP) of 730 ms. Quasi-complementary codes have the advantage over complementary codes in that they reduce interference from fading clutter and transmitter ringing (SULZER AND WOODMAN, 1984). The number of coherent integrations was 48, which is equal to the length of the quasi-complementary code sequence. Subsequently, 32-point power spectra were computed on-line from a set of samples, and fifty spectra were averaged incoherently. The combined sampling and integration period was 56 s for each radial Doppler spectrum. The velocity, signal power, and spectral width were derived from the spectra off line with the nonlinear least-squares fitting procedure developed by SATO AND WOODMAN (1982b).

For the April 1983 experiment, the data-taking programs and experiment parameters were identical to the previous experiment. The primary difference was that the beam was pointed only in the vertical direction and toward north and east in the off-vertical direction. The zenith angle for the off-vertical positions was either 10° or 15°. The dwell time in each off-vertical position was 20 min and the time spent looking vertically was 90 min for each sequence. The analysis procedure used to derive the velocity and signal power parameters for the April 1983 data has been described in detail by CORNISH (1988).

For both data sets, horizontal wind velocities were calculated assuming that the contribution of the vertical velocity along the line-of-sight was negligible. The assumption will no doubt lead to errors, but LARSEN et al. (1986) have shown that the largest contribution of the vertical velocity component

at zenith angles of 15° is for periods less than 30 min to 1 hr. Therefore the errors will tend to average out when periods much longer than 1 hr are being considered.

WIND PROFILE MEASUREMENTS

May 1982 data

In May 1982, wind profile measurements were made on a nearly continuous basis over a seven-day period. Measurements commenced at 1449 AST (Atlantic Standard Time) on May 5 and the last profile was taken at 0715 AST on May 12. Due to intense competition for telescope time at Arecibo, continuous sampling over many days was not feasible. Our goal of sampling with gaps of 4 hr maximum duration was met 80% of the time; longer gaps occurred due to hardware breakdown and scheduling conflicts. In all, 2153 profiles were measured, though only 380 and 249 profiles from the meridional and zonal directions, respectively, are presented and analyzed here.

Profiles of the observed horizontal wind in the 6-24 km altitude range during the seven-day observation period in May 1982 are shown in Figures 1a and 1b for the meridional and zonal components, respectively. The profile of the mean wind during the entire observation period is plotted to the left of each figure. On the right, side-by-side profiles of the fluctuating wind component, i.e., the residuals after subtraction of the mean wind, are plotted sequentially with the same velocity scale as the mean profile. Linear interpolation was applied to the original time series of velocity profiles to produce hourly profiles for the entire period so that standard spectral analysis techniques could be applied to the data. Gaps of less than 10 hours duration have been interpolated; longer gaps remain blank. Since the periods of interest (20-54 hours) are much longer than the gaps ranging from 4 to 12 hours and the original sampling period of 35 minutes to 1 hour, the effects of smoothing and errors introduced by the resampling procedure should be minimal.

The profile of the mean wind is characterized by the strong westerly flow of the subtropical jet in the upper troposphere and lower stratosphere. The zonal component peaks at $\sim$20 m/s near 15 km and then reverses to easterly flow above 20 km altitude. The mean meridional component is relatively weak at all heights.

The most noticeable feature of the profiles is a wavelike structure between 14 km and 20 km. The structure oscillates in the vertical with a scale of 1-2 km and persists over most of the observation period. Below 14 km the fluctuating wind is more random and does not display coherent wavelike structure. Above 18-20 km the wave structure is not discernable. The wavelike structure generally
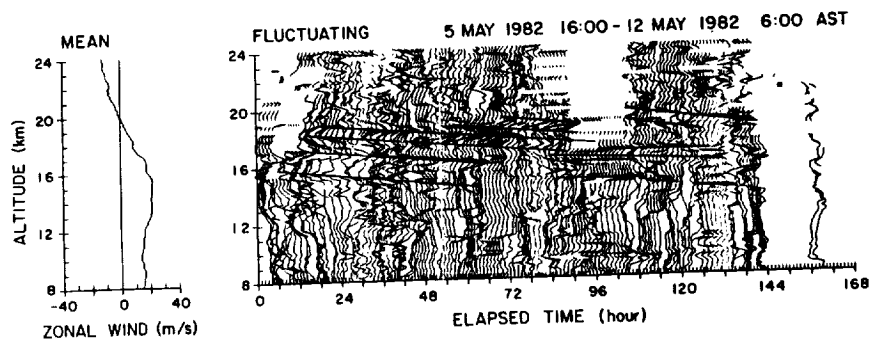
Figure 1a. Time versus height profile of the mean (left) fluctuating (right) components of meridional wind for a seven-day period May 1982. The velocity scale is shown on the horizontal axis of the mean component. Note the structure between 14 and 20 km that oscillates in height with a vertical wavelength of 1-2 km.
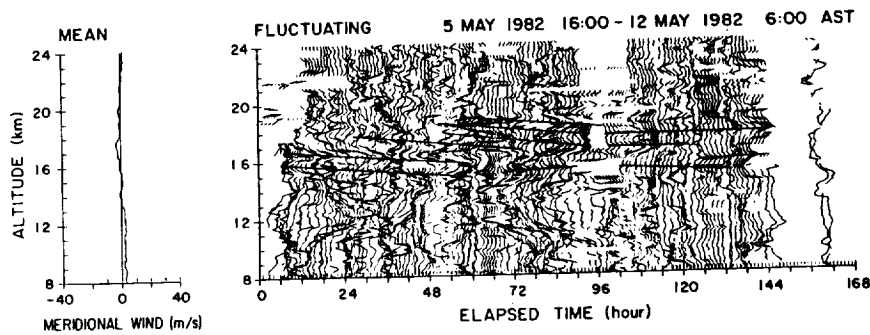
Figure 1b. Time versus height profile of the mean (left) and fluctuating (right) components of zonal wind for a seven-day period in May 1982. Like the meridional component, a wavelike structure is observed in the lower stratosphere at and above the tropopause.

descends slowly in altitude with time with estimated vertical phase velocities of a few cm s^{-1}.

The tropopause height was measured by the twice-daily radiosonde ascents at 0000 and 1200 GMT (700 and 1500 AST) from soundings taken at the San Juan airport, located 90 km east-northeast of the Arecibo Observatory. For the 15 soundings between 5 May 1982 and 13 May 1982 the mean tropopause height was 15.8 km and ranged from 14.1 to 17.7 km. The tropopause height was generally within 1 km of the lowest height where the wave structure could be discerned. Also the mean wind profile from the balloon measurements was in excellent agreement with the mean wind profile from the radar measurements. The two curves are not shown here because they are effectively indistinguishable.

April 1983 data

In April 1983, horizontal wind measurements were made over a 12-hr period beginning at 1019 AST and ending at 2149 AST on 23 April 1983. In all, 5 sets of 20 one-minute wind profiles were taken for both the meridional and the zonal directions during the 12-hour period. The antenna was pointed vertically during the gaps for observations of vertical velocities. The data set is too short for adequate time series analysis of the wind velocities, but it does provide additional information about the wave structure in the lower stratosphere.

Wind profiles for the meridional and zonal components are shown in Figures 2a and 2b, respectively, for the observations on 23 April 1983. The gaps between adjacent sets of profiles is 150 min. The first profile of each of the last three observation sets for the zonal component (Figure 2b) is of the wrong sign due to aliasing of the Doppler frequency. A short vertical wavelength ($\sim$1.5 km) structure, similar to that observed in the May 1982 data set, persists during the entire observation period of about 12 hours. The structure is first evident at 16 km altitude and continues up through the maximum plotted height (22 km).

The mean wind during the 12 hour observation period was westerly at 10-15 ms^{-1} and, below 16 km, had a northerly component of $\sim$10 ms^{-1}. The subtropical jet was considerably weaker in April 1983 than in May 1982. The zonal flow was fairly uniform between 6 and 20-km altitude and did not peak near the tropopause. The tropopause level, as determined by San Juan radiosonde temperature measurements, was between 16 and 17 km, close to the lower level of the fluctuating wind structure.

A comparison between the first and last set of profiles for each component in Figures 2a and 2b reveals a slow variation in time and gradual downward phase progression of the wind structure.

ORIGINAL PAGE IS
OF POOR QUALITY
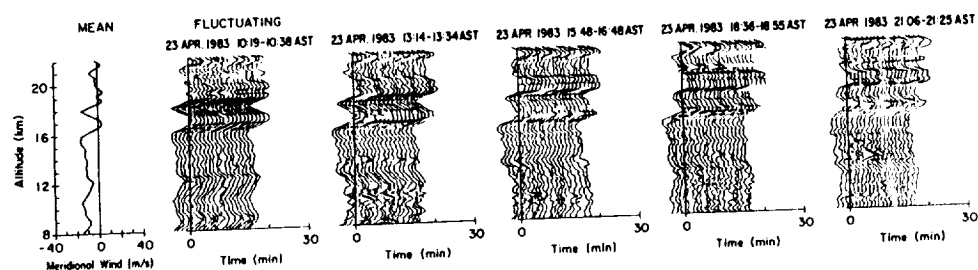
Figure 2a. Profiles of meridional wind for five observation intervals during a 12-hour period on 23 April 1983. Each interval consists of 20 one-minute profiles, and time of observation for each interval is indicated. Gaps of approximately 2-1/2 hour duration occur between intervals when the antenna beam was swung at other azimuth and zenith positions. Spacings between intervals are not proportional at the time periods of gaps. The velocity scale is indicated at the left on the mean wind profile of the first observation period.
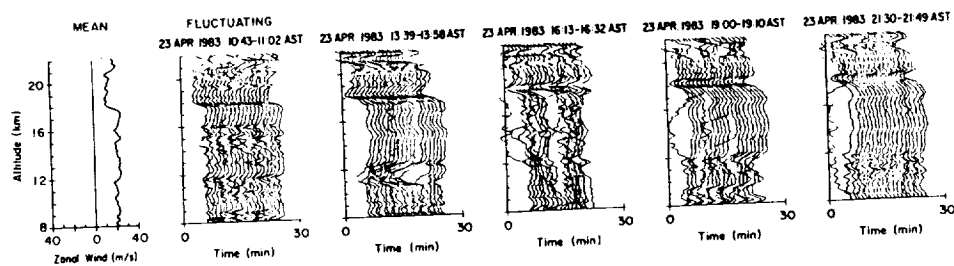
Figure 2b. Profiles of zonal wind for five observation intervals during a 12-hour period on 23 April 1983. The plot is in a format similar to that of Figure 2a. The first profile of the last three observation sets is of the wrong sign due to aliasing and wrapping of the Doppler spectra.

Unfortunately, the observation period of 12 hours is too short for meaningful time series analysis, but the period is clearly longer than the observation interval.

ROTATION OF THE WIND FIELD

A common characteristic of the oscillations near the tropopause and in the lower stratosphere is the rotation of the perturbation horizontal wind vector with both time and height, such that the tip of the wind vector traces out an ellipse. Time hodographs for the May 1982 data are shown in Figure 3 for heights between 14.78 and 19.13 km. The resampled time series has been used, which results in a spacing of 1 hour between points. The first two heights at 14.78 and 15.65 km do not display any particular pattern. The hodographs for heights between 16.52 and 18.26 trace an approximately circular arc with the sense of rotation in the clockwise direction marked by the arrow. At 19.13 km, the polarization appears to be nearly linear. Height hodographs in a similar format are shown in Figure 4 for two of the hourly profiles obtained in May 1982. The spacing between consecutive points is 150 m. Both hodographs trace out an elliptical pattern with a clockwise sense of rotation with increasing height, as indicated by the arrows. Height hodographs for the April 1983 data are not presented but show a similar pattern. The rotation of the wind vector with height and time evident in the Arecibo data shown here and in the earlier study by MAEKAWA et al. (1984) was also a common characteristic of the wind data obtained by THOMPSON (1978), CADET AND TEITELBAUM (1979), and SIDI AND BARAT (1986), although THOMPSON's (1978) data which was obtained in the southern hemisphere showed a predominantly counterclockwise rotation while the sense of rotation was reversed in the northern hemisphere observations.

The dispersion and polarization relations derived from the linearized equations describing low-frequency inertio-gravity waves (see, e.g., THOMPSON, 1978) show that the perturbed wind field becomes more horizontal as the time scale of the perturbation approaches the inertial period. Furthermore, the wave polarization changes from linear polarization when the intrinsic period is close to the Brunt-Vaisala period to circular polarization when the intrinsic wave period approaches the inertial period. The horizontal wind vector is elliptically polarized for intermediate intrinsic periods. A consequence of these relationships is that the direction of rotation of the wind vectors will be anticyclonic when the waves are upward propagating, i. e., clockwise in the northern hemisphere and counterclockwise in the southern hemisphere. The opposite sense of rotation is expected if the waves are downward propagating. The wind field rotation in the studies by THOMPSON (1978), CADET AND TEITELBAUM (1979), SATO AND WOODMAN (1982a), MAEKAWA et al. (1984), COT AND BARAT (1986), and ours have revealed an anticyclonic rotation of the horizontal wind vector which

TIME HODOGRAPH

6 MAY 1982 12:00 - 8 MAY 1982 03:00 AST
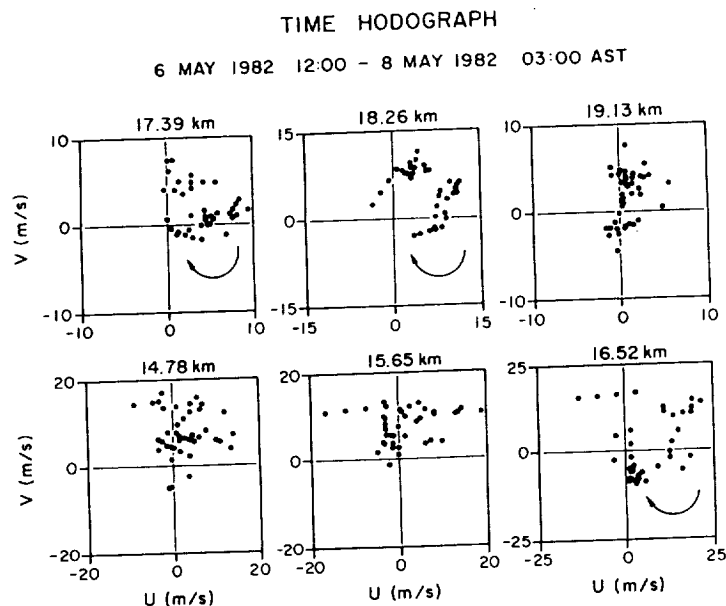
Figure 3. Time hodographs of horizontal wind vector at selected heights between 15 and 19 km for 38 consecutive hourly samples between 1200 on 6 May 1982 and 0300 on 8 May 1982. A clockwise rotation pattern of the horizontal wind vector is observed at 16.52, 17.39, and 18.26 km.

HEIGHT HODOGRAPH

15.938 - 18.980 km
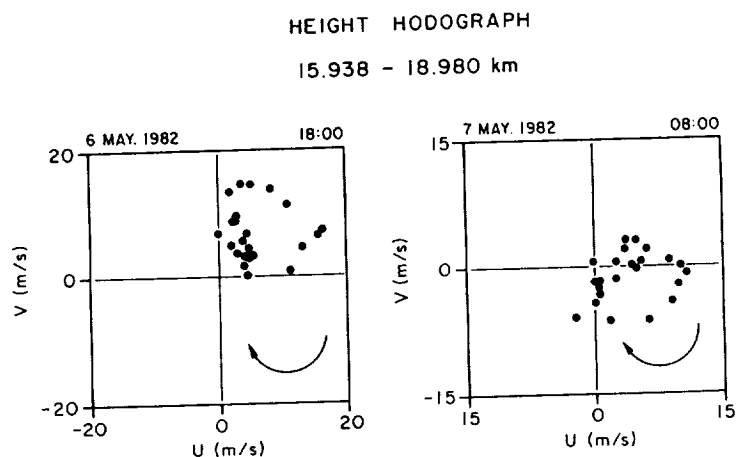
Figure 4. Height hodographs of horizontal wind between 15.9 and 18.9 and 18.9 km at 1800 on 6 May 1982 (left) and 0800 on 7 May 1982 (right). The height resolution was 150 meters. The horizontal wind vector shows clockwise rotation with increasing height.

has been interpreted to be consistent with the expectations for low-frequency, upward-propagating inertio-gravity waves.

Although the rotation of the wind vector is a characteristic generally attributed only to waves with low intrinsic frequencies, HINES (1988) has suggested that waves with high intrinsic frequencies can produce a rotation of the horizontal perturbation winds if there is a vertical shear in the mean wind component perpendicular to the direction of propagation of the wave. For higher frequencies, the velocity components parallel to the propagation direction and in the vertical are essentially in phase, but the vertical displacement is 90° out of phase with the horizontal winds. Therefore, the maximum pertubation in the wind component perpendicular to the propagation direction will be 90° out of phase with the perturbation wind component parallel to the propagation direction, giving an effect that is similar to the rotation in the wind component produced by the Coriolis force for waves with low intrinsic periods. We will analyze the relevance of such an effect to the May 1982 data set in more detail in a later section.

WAVE CHARACTERISTICS

Observed Wave Period

One advantage of the May 1982 data set is that the time series of velocities is long enough so that time series analysis can reasonably be applied to determine the period in the earth-fixed reference frame. The data set analyzed by MAEKAWA et al. (1984) only covered a two-day period and was marginally short for a study of waves with periods close to the inertial period. The May 1982 data set was used as input for a power spectrum calculation using standard FFT routines. An example of the results is shown in Figure 5 for the zonal wind component at 16.95 km.

We can estimate the errors in the amplitude determination for the frequency spectrum by the following arguments. The variance σ^2 of a real time series $v(t)$ with mean subtracted is related to its power spectral density, $P(f)$, by

$$\sigma^2 = \int_{-\infty}^{\infty} P(f)\, df \tag{1}$$

(BLACKMAN AND TUKEY, 1958, p. 9). For the velocity time series under consideration, contributions to the variance include: (1) instrumental noise due to measurement and processing errors; and (2) meteorological noise. If we assume a white noise spectrum for both, the power spectral density $P(f)$ has a constant value P_1 at all frequencies across the width of the spectrum. A real time

series of N points has a power spectral density of N/2 positive frequencies. For a discrete Fourier transform, i.e., FFT, with equally spaced frequency bins each of width Δf, Equation 1 becomes

$$\sigma^2 = 2 \frac{N}{2} P_1 \Delta f \qquad (2)$$

The product $P_1 \cdot \Delta f = S_0$ is the spectral power at each frequency and is constant for a white noise spectrum. Since $\sigma^2 = <v^2> - <v>^2$ which can be computed directly from the velocity time series, we can estimate $S_0 = \sigma^2/N$, and the spectral variance at each frequency bin can be estimated. $\sqrt{S_0}$ is an upper bound estimate of the error in the Fourier amplitudes due to noise from meteorological and instrumental sources; spectral amplitudes above the threshold are significant. The average values of $\sqrt{S_0}$ calculated from the velocity time series for heights between 15.0 and 17.0 km are 0.4 and 0.7 m/s for the zonal and meridional components, respectively. The noise level is indicated by the horizontal dashed line in the plot of spectral amplitudes in Figure 5. The spectrum displays two prominent peaks at 26 hr and 53 hr with amplitudes of 3.75 m/s and 6.0 m/s, respectively, which are both several standard deviations above the noise level. Another factor that has to be considered in evaluating the significance of the peaks is the background spectrum of the velocity fluctuations. LARSEN et al. (1986) have analyzed the frequency spectrum of horizontal velocities at Arecibo for an extensive data set and have shown that the spectra follow power laws with exponents between $-5/3$ and -2. The amplitudes corresponding to the two power laws are shown by the thin solid and dashed curves superimposed on the spectral amplitudes. While the peak near the 26-hr period appears to be significant, even in comparison to the background spectrum, the significance of the the 53-hr wave is less clear. Therefore we will focus our attention on the shorter period wave in the remainder of the article.

Spectral amplitudes of velocities for periods between 14 and 53 hours are plotted versus height in a three-dimensional format in Figures 6a and 6b for the zonal and meridional winds, respectively. The zonal component shows a prominent ridge centered at the 26-hr frequency bin that rises out of background levels at about 14 km, peaks at 17 km with an amplitude of 4-5 m/s, and disappears above 18 or 19 km. The fact that the spectral peak occurs at approximately the same period over a range of heights lends credence to the idea that the observed wave structures are part of a coherent oscillation since theory dictates that the frequency in the earth-fixed reference frame should be constant with height despite shears in the background winds or variations in the background mean temperatures. There is only a hint of a similar ridge in the spectra for the meridional winds.
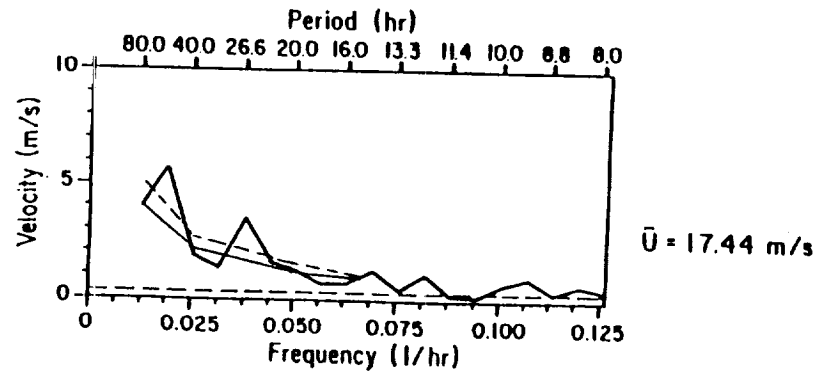
Figure 5. Computed spect:al amplitudes for the zonal wind component at 16.95 km for the May 1982 data. Spectral peaks are prominent at 26 and 53 hours. The horizontal dashed line on the spectral plot indicates the estimated noise level. The thin solid line and dashed line superimposed on the spectral curve show the background values expected for spectral power laws with exponents of −5/3 and −2, respectively. The mean zonal wind during the observation period was 17.4 m/s.
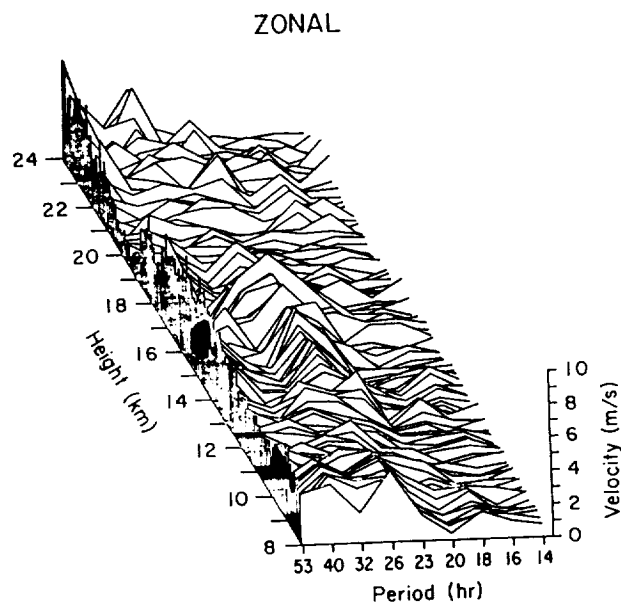
ZONAL

Figure 6a. Pseudo-3D plot of spectral amplitudes of the zonal wind component for May 1982 data. The wave period is displayed on x-axis, and the velocity amplitude is displayed on the y-axis. Successive spectra are plotted for heights between 8 and 24 km along the z-axis.
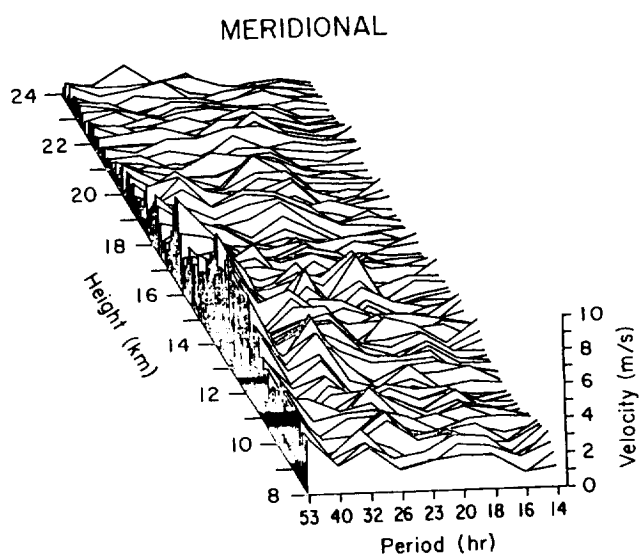
MERIDIONAL

Figure 6b. Pseudo-3D plot of spectral amplitudes for the meridional wind component of May 1982 data in a format similar to Figure 7a.

The frequency resolution of the spectral analysis is determined by the length of the sampling period of 160 hr and yields an uncertainty of $+.00312$ hr^{-1} in the determination of wave frequencies. Therefore, the 26-hr bin includes contributions from oscillations between $\sim$24 and 29 hr.

Velocity Amplitudes and Phases

We have isolated the phase and amplitude information for the 26-hr components in the zonal and meridional spectra. The amplitudes of the zonal (dashed line) and meridional (solid line) perturbation wind components of the 26-hr wave are show in Figure 7. Just above the mean tropopause height of 15.8 km, the velocity amplitude of the 26-hr component is 3.5-5.0 m/s for the zonal component and 2-3 m/s for the meridional component. For both components, the velocity amplitudes drop off to $\sim$1 ms^{-1} above 18 km, close to the estimated uncertainty level of 0.4-0.7 ms^{-1} for the spectral analysis.

The values plotted in Figure 8 show the ratio of the zonal and meridional perturbation wind amplitudes on the left and the phase difference between the two velocity components on the right. Circular polarization, as an example, would require a u/v amplitude ratio of one and a phase difference of 90°. The criteria are satisfied approximately just below 19 km, but the polarization will generally be elliptical at other heights. Also, the combination of amplitude ratio and phase difference parameters will determine the orientation of the ellipses which are not necessarily aligned in the zonal direction.

Intrinsic Wave Periods

The degree of ellipticity of the hodograph of the horizontal wind vector is indicative of the intrinsic wave period and horizontal propagation direction if the oscillations have low intrinsic frequencies, as is usually assumed. The hodograph is circularly polarized for wave periods close to the inertial period and becomes increasingly elliptical, and finally linear, as the wave period deviates from the inertial period and becomes shorter. The intrinsic wave period can be calculated from the ratio of the major to the minor axis of the ellipse which is the same as the ratio of the intrinsic wave frequency ω' to the Coriolis parameter f. The orientation of the major axis of the elliptical hodograph is aligned with the wave propagation direction (KUNDU, 1976).

The values obtained from the spectral analysis and shown in Figure 8 were used to calculate the parameters of the ellipses as a function of height. The results are shown in Figure 9. The middle and right-hand panel parameters were derived first. The curve on the right shows the orientation of the ellipses in terms of degrees north of east. The values range from $\sim$15° near 16 km to $\sim$60° near 19 km. The middle curve shows the ratio of the major to minor axes of the ellipses as a function of height
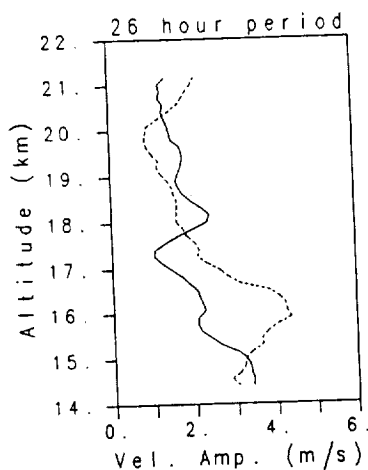
Figure 7. Height profile of velocity amplitudes for the 26-hour period determined from Fourier analysis. Zonal and meridional components are indicated by dashed and solid lines, respectively.
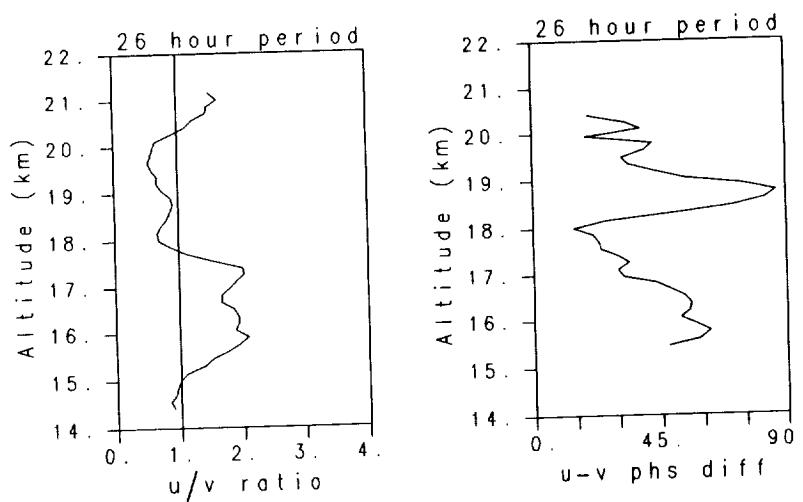
Figure 8. Ratio of zonal (u) to meridional (v) perturbation velocity amplitude for the 26-hr component on the left and the phase difference between the zonal and meridional velocities for the same frequency component on the right.

which should be the same as the ratio of the intrinsic frequency to the Coriolis parameter, if the intrinsic frequencies are low. The range of frequencies in the frame of the mean wind varies from approximately one to six times the Coriolis parameter. The curves on the left represent the mean wind components in a coordinate system shifted 30° north of east. The rotation angle was chosen somewhat arbitrarily based on the propagation direction shown in the lower part of the right-hand panel. More justification for the choice will be given in the next section.

HINES (1988), using a fit-by-eye of an ellipse to the SATO AND WOODMAN (1982a) data, found a propagation direction toward northeast, similar to our findings. COT AND BARAT (1986) also determined propagation directions that were rotated 40° or more from the zonal wind direction, consistent with the observation by PFISTER (1985) that lower stratosphere inertio-gravity waves have a cross-wind propagation component.

Horizontal Wavelength

The difference between the observed periods and the intrinsic periods deduced in the last section is due to Doppler shifting by the mean wind. For a horizontal mean flow U_0, the earth-fixed and intrinsic frequencies are related by:

$$\omega' = \omega - k_h U_0 \tag{3}$$

where k_h is the horizontal wavenumber. The value of ω is fixed in this case to $\omega = 2\pi/26$ hr, but ω' varies considerably with height, as shown in Figure 9. We have chosen the value of $\omega' = 2.5 \cdot f$ which corresponds to the height range below 17 km. In this range, the shear in the meridional wind is essentially zero which should eliminate the effects due to vertical advection of the cross-propagation shear which HINES (1988) has discussed. Also, the propagation direction is fairly constant with height. The mean wind component parallel to the propagation direction is 20 ms^{-1} at 16 km.

Although the magnitude of ω' is known, the sign can still be either positive or negative corresponding to waves propagating faster or slower than the mean wind. A choice of positive ω' leads to a horizontal wavelength of 3065 km. The wavelength is rather long, raising questions about whether coherent oscillations of the type that we observe can exist over such extensive regions. The parameters lead to values of $\omega' = 2 \cdot f$ near 18 km where the mean wind is 10 ms^{-1} and $\omega' = 1.8 \cdot f$ near 19 km where the mean wind is 5 ms^{-1}. The implied intrinsic frequency values at higher altitudes do not agree with the values shown in Figure 9.
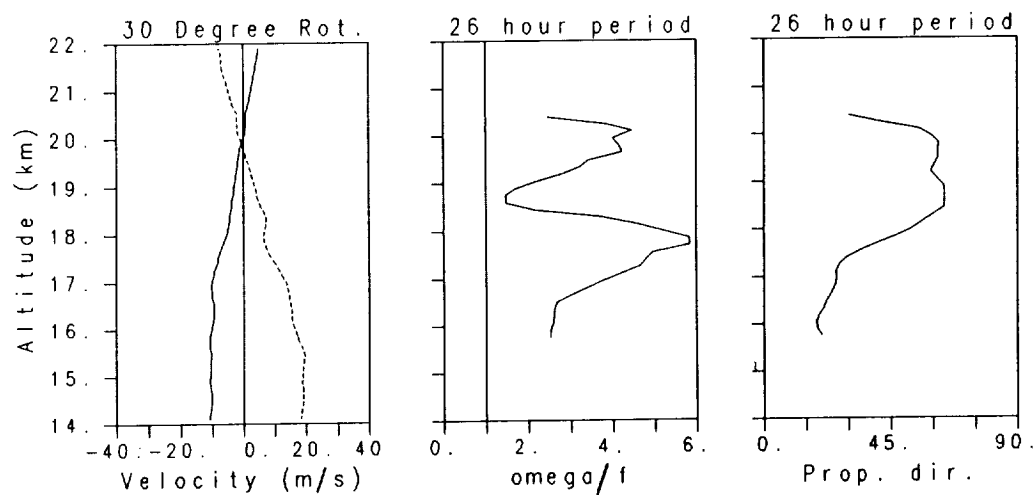
Figure 9. Ratio of major to minor axes of wind hodograph ellipses calculated from parameters in Figure 8 are shown in the center panel. The right-hand panel shows the orientation of the ellipses in degrees north of east. The left-hand panel shows the mean winds for the observation period in a coordinate system rotated 30° north of east. The eastward component is indicated by the dashed line and the southward component by the solid line.

The alternative choice of negative ω' leads to a horizontal wavelength of 700 km, and an implied critical level would occur at a height where $U_0=7.7$ ms^{-1}. A level where $\omega'=f$ would occur when $U_0=12.6$ ms^{-1}. The latter condition is satisfied between 16.5 and 17 km which corresponds to the height where the rapid change with height of the ellipse orientation and ω'/f ratio first occurs. The former condition, i. e., the critical level, corresponds to the height around 18 km, which is also the cut-off height above which the wave amplitudes diminish rapidly to the uncertainty level. The arguments in favor of the choice of negative ω' are still circumstantial at best, but the derived parameters seem to explain more features of the observations than the alternative choice. The values of ω' inferred from the calculations between 16 and 18 km would lead us to expect a linear decrease with height in the ratio of ω'/f such that the value should be ~ 1 near 17 km and close to zero near 18 km. The uncertainty in the spectral calculation makes it unlikely that ratios less than one can be achieved since both velocity components will fluctuate around the uncertainty level. Below 18 km where the amplitudes are above the uncertainty level, the amplitude ratio curve still shows behavior different from the expected behavior, but that is perhaps not unexpected since the waves must be highly nonlinear in the height range where the intrinsic frequency has values between f and zero.

In earlier work, CADET AND TEITELBAUM (1979), MAEKAWA et al. (1984), and PFISTER (1985) have also interpreted the disappearance of subtropical inertia-gravity waves near 18-20 km as being due to critical level absorption. However, BARAT (1983) and COT AND BARAT (1986) have observed inertial wave structure up to 29 km at mid-latitudes.

Vertical Wavelength

Visual inspection of the wind profiles in Figures 1 and 2 reveals that wavy structures for both May 1982 and April 1983 have vertical scales on the order of 1-3 km. Spatial power spectra of the radial wavenumber have been computed for the 1983 data for the height ranges 7.5-15 km, 15-24 km, and 7.5-24 km, and are plotted in Figure 10. The near-vertical wavenumber spectra of the zonal and meridional velocity components are denoted by solid and dashed lines, respectively. The most noticeable feature is the presence, in the 15.0-24.0 km height range, of a strong peak at 2.2 km. The peak is absent in the 7.5-15.0 km range.

The absence of the vertical wavelength structure below 15 km may be an indication that the oscillations are generated near the tropopause, perhaps by instability or ageostrophy in the subtropical jet, but the waves generated by such a mechanism would be expected to have a broad range of spectral components rather than the extremely coherent structure seen in the observations. In this respect,

23 APRIL 1983

7.5-15.0 km

Power Spectrum (m² s⁻² km⁻¹)

500
400
300
200
100
0

—— Zonal
········ Meridional

15.0-24.0 km

2.2 km

1.0 km

7.5-24.0 km

2.8 km

1.7 km

1.0 km

$K_z/2\pi$ (km⁻¹)
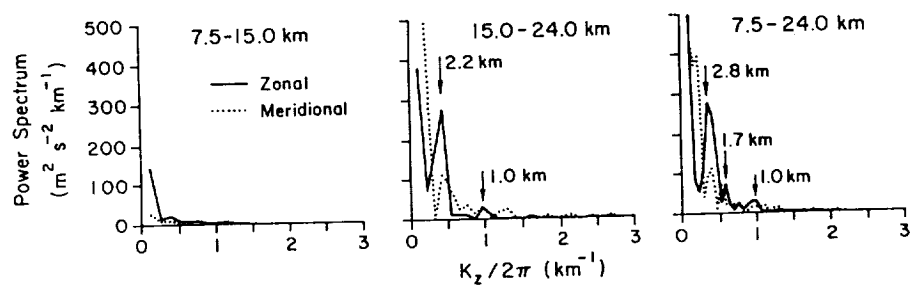
Figure 10. Vertical wavenumber spectra for height ranges (left) 7.5-15.0, (center) 15.0-24.0, and (right) 7.5-24.0 km calculated from the zonal (solid) and meridional (dashed) components of horizontal wind profiles of the April 1983 data.

HINES' (1988) suggestion of an orographic source is very appealing since all orographic waves will have the same vertical wave number. Thus, even a spectrum of mountain waves with a range of horizontal wavelengths will show coherence in the vertical direction. As HINES (1988) has pointed out, the absence of the waves below the tropopause can be explained by the variation in the Brunt-Vaisala frequency with height. The San Juan radiosonde data corresponding to the observations in May 1982 show an increase in the Brunt-Vaisala frequency by a factor of $\sim$3 between the troposphere and lower stratosphere. The vertical wavelength of waves propagating upward through the troposphere is expected to decrease by the same factor, and the effect would explain the characteristics of the vertical wave number spectrum shown in Figure 10. Our vertical wavelength estimates are in good agreement with the values found in the earlier studies that we have already cited several times.

A vertical wavelength of $\sim$2 km and a wave period of $\sim$24 hr gives a vertical phase velocity of 2.3 cm s^{-1}, in rough agreement with the values estimated by inspection of Figure 1.

DISCUSSION

There are a great many similarities between the characteristics of the waves observed during the seven days in May 1982 and the waves that were present in the data sets analyzed by HINES (1988) and earlier by SATO AND WOODMAN (1982a) and MAEKAWA et al. (1984). The vertical wavelengths are comparable, the height range over which the waves are observed is the same, and even the propagation direction is similar, being 30-45° north of east. HINES' (1988) suggestion that the source of the waves is orographic is consistent with the similarity in the features observed not only in the two data sets discussed here but in hundreds of hours of other observations at Arecibo. The winds above Puerto Rico change less than would be expected at a midlatitude site, but, nonetheless, the strength of the flow and the direction change as a function of season and as disturbances propagate through the area. Waves generated by instabilities in the subtropical jet are unlikely to have characteristics as consistent as those that are observed. Also, the orographic source explains the coherence in the vertical wavelength structure.

Generally, the analysis of lee waves assumes a steady wind that produces waves that are stationary with respect to the ground and have zero frequency in the earth-fixed reference frame. Our observations show that the earth-fixed frequency for the waves corresponds to a period around 26 hr. The uncertainty in the spectral analysis does not exclude a period of 24 hr which can be explained by the strong diurnal variation in the surface winds on the island of Puerto Rico. We are not aware of any theory for lee waves produced by diurnally varying flows, but we surmise that such a flow would

produce oscillations with earth-fixed frequencies corresponding to the frequency of the forcing. HINES (1988) attributed the vertical phase progression to random fluctuations in the mean surface winds, although he did not discuss the possibility of a strong periodicity in the surface winds. MAEKAWA et al. (1984) also found evidence of a wave component with a period in the earth-fixed reference frame close to 24 hr, although their observations only covered a period of approximately 2 days which is generally too short for a meaningful analysis of 24-hr oscillations.

One feature of HINES' (1988) analysis not borne out by our data is his suggestion that the rotation in the wind vector with height or time is due to the vertical advection of the cross-propagation shear component. The intrinsic frequency which varies between zero and 2.5·f is sufficiently small to explain the wind vector rotation without the need for the vertical advection effect. Also, we have found that the perturbation winds show an elliptical pattern even at heights where the shear in the cross-propagation wind component is essentially zero. The observations of THOMPSON (1978) would also argue against the importance of the vertical shear advection effect, to the extent that the source of the waves he observed is the same as we are postulating for the Arecibo data. Since his observations in the southern hemisphere showed a predominant rotation in the winds that was in the opposite sense to the northern hemisphere observations, the importance of the Coriolis force is implied.

The inferred horizontal wavelength of ∼700 km is somewhat long when compared to the dimensions of the island of Puerto Rico, but a half wavelength is comparable to its length. For the orographic forcing mechanism to explain the observations, the entire island must be involved in producing the oscillations rather than a few of the prominent peaks which have much shorter horizontal scales.

We have emphasized the similarity in wave parameters over long periods and the coherence of the oscillations at Arecibo where the day-to-day changes in the mean flow are small. However, variations in the flow are expected to produce changes in the wave characteristics if the source is the orography. CADET AND TEITELBAUM (1979) found evidence in their balloon data of a change in the vertical scale as the mean wind varied which is consistent with the predictions of lee-wave theory. PFISTER (1985) and MAEKAWA et al. (1984), albeit with a short two-day data set, also found evidence of modulation of the wave amplitudes with time.

CONCLUSION

The quasi-inertial period structure in the lower stratosphere shown in our observations at Arecibo, Puerto Rico, appear to be typical of the results of a number of other studies. We have summarized a

number of diverse studies that describe observations of such structures with a variety of high-resolution measurement techniques. The indications are that quasi-inertial period waves are a ubiquitous feature in the lower stratosphere, similar to what is observed in the oceans. The waves do not propagate rapidly, but the associated velocity amplitudes of 3-10 m/s imply that a significant amount of energy is associated with the low-frequency modes.

The indications are that the waves are generated by the flow over the island topography, as suggested by HINES (1988), but with a strong diurnal periodicity in the earth-fixed reference frame probably associated with the diurnal fluctuations in the surface winds. The low frequency in both the earth-fixed and intrinsic reference frames lead to waves with characteristics generally associated with inertio-gravity waves.

REFERENCES

Barat, J., 1983: The fine structure of the stratospheric flow revealed by differential sounding. *J. Geophys. Res.*, *88*, 5219-5228.

Blackman, R. B. and J. W. Tukey, 1958: *The Measurement of Power Spectra.* Dover, New York, 190 pp.

Cadet, D. and H. Teitelbaum, 1979: Observational evidence of internal inertia-gravity waves in the tropical stratosphere. *J. Atmos. Sci.*, *36*, 892-907.

Cornish, C. R., 1987: *Observations of Inertial Period Waves and Vertical Velocities in the Tropical Middle Atmosphere using the MST Radar Technique,* Ph. D. Thesis, Cornell University, Ithaca, New York, 216 pp.

Cornish, C. R., 1988: Observations of vertical velocities in the upper troposphere and lower stratosphere using the Arecibo UHF radar, *J. Geophys. Res.*, in press, 1988.

Cornish, C. R., and M. F. Larsen, 1984: Use of the VAD technique and measurements of momentum flux in the stratosphere at Arecibo, *Handbook for Map, 14*, 208-210, SCOSTEP Secretariat, University of Illinois, Urbana.

Cot, C. and J. Barat, 1986: Wave-turbulence interaction in the stratosphere: a case study. *J. Geophys. Res., 91*, 2749-2756.

Hines, C. O., 1988: Tropopausal mountain waves over Arecibo: A case study, *J. Atmos. Sci.*, in press.

Kundu, P. K. 1976: An analysis of inertial oscillations observed near Oregon coast. *J. Phys. Oceanogr., 6*, 879-893.

Larsen, M. F., R. F. Woodman, T. Sato, and M. K. Davis, 1986: Power spectra of oblique velocities in the troposphere and lower stratosphere observed at Arecibo, Puerto Rico, *J. Atmos. Sci., 43*, 2230-2240.

Madden, R. A., and E. J., Zipser, 1970: Multi-layered structure of the wind over the equatorial Pacific during the Line Islands experiments. *J. Atmos. Sci., 27*, 336-343.

Maekawa, Y., S. Fukao, T. Sato, S. Kato, and R. F. Woodman, 1984: Internal inertia-gravity waves in the tropical lower stratosphere observed by the Arecibo radar. *J. Atmos. Sci., 41*, 2359-2367.

Pfister, L., 1985: Aircraft ozone and temperature observations in a turbulent zone in the tropical lower stratosphere. *Second AMS Conference on Mesoscale Processes*, University Park, PA, June 3-7, 1985, Paper 5.3.3.

Sato, T. S., and R. F. Woodman, 1982a: Fine altitude resolution radar observations of upper-tropospheric and lower-stratospheric winds and waves. *J. Atmos. Sci., 39*, 2539-2545.

Sato, T. S. and R. F. Woodman, 1982b: Spectral parameter estimation CAT radar echoes in the presence of fading clutter. *Radio Sci., 17*, 817-826.

Sidi, C., and J. Barat, 1986: Observational evidence of an inertial wind structure in the stratosphere. *J. Geophys. Res., 91*, 1209-1217.

Sulzer, M. P. and R. F. Woodman, 1984: Quasi-complementary codes: a new technique for MST radar sounding. *J. Atmos. Sci., 19*, 337-344.

Thompson, R. O. R. Y., 1978: Observation of inertial waves in the stratosphere. *Quart. J. R. Met. Soc., 104*, 691-698.

Weinstein, A. I., E. R. Reiter, and J. R. Scoggins, 1966: Mesoscale structure of 11-20 km winds. *J. Appl. Meteorol., 5*, 49-57.

Wilson, D. A. and L. J. Miller, 1972: Atmospheric motion by Doppler radar. *Remote Sensing of the Troposphere*. V. E. Derr, Ed., NOAA and University of Colorado, pp. 13.1-13.20.

MOMENTUM FLUXES OBSERVED BY THE MU RADAR UNDER A STRONG VERTICAL-WIND CONDITION IN THE TROPOSPHERE AND LOWER STRATOSPHERE

Kaoru Sato

Department of Geophysics, Faculty of Science, Kyoto University
Kyoto 606, Japan

1 Introduction

Using the MST radars, large variations of the vertical wind have been observed in the troposphere and lower stratosphere at some locations around the world. Previous studies of the phenomena examined, mainly, the differences in the frequency power spectra of the vertical wind between active and quiet conditions, and the correlation with the background wind. According to these studies, the strong vertical-wind variations are due to gravity waves caused by topographic effects.

This study investigated the vertical momentum fluxes in a strong vertical wind condition. The profiles of vertical momentum fluxes provide a lot of useful information for the examination of the wave interaction with the mean wind and/or wave characteristics, such as, the direction of wavenumber vectors.

2 Calculation method of momentum fluxes

The momentum fluxes are examined as a function of frequency. The method of calculation is an expansion of Vincent and Reid's (1983). Vincent and Reid suggested that the momentum fluxes are calculated from the difference between mean squares of radial velocities measured by two beams with equal and opposite angles $\pm\theta$ around the zenith. The present method makes use of two frequency power spectra of radial velocities of the symmetrical beam pair instead of the mean squares. The two frequency power spectra of the radial velocities, $P_{V_{\pm\theta}}(\omega)$, are expressed as,

$$P_{V_{\pm\theta}}(\omega) = P_u(\omega) \cdot \sin^2\theta + P_w(\omega) \cdot \cos^2\theta \pm \overline{u(\omega)w(\omega)} \cdot \sin 2\theta, \qquad (1)$$

where ω is frequency, $P_u(\omega)$ and $P_w(\omega)$ are frequency power spectra of zonal and vertical velocity components, respectively. The term $\overline{u(\omega)w(\omega)}$ in (1) shows the zonal component of the vertical momentum flux due to oscillations having each frequency, which is calculated immediately from (1),

$$\overline{u(\omega)w(\omega)} = \frac{P_{V_{+\theta}}(\omega) - P_{V_{-\theta}}(\omega)}{2\sin 2\theta}. \qquad (2)$$

Thus the total vertical momentum flux is obtained in such a way as,

$$\overline{u'w'} = \sum_\omega \overline{u(\omega)w(\omega)}. \qquad (3)$$

Similarly, we can obtain not only the spectra of zonal and meridional components of the momentum fluxes but also the power spectra of three wind components, from the power spectra of 5 radial velocities measured using 5 beams tilted to east, west, north, south, and vertical.
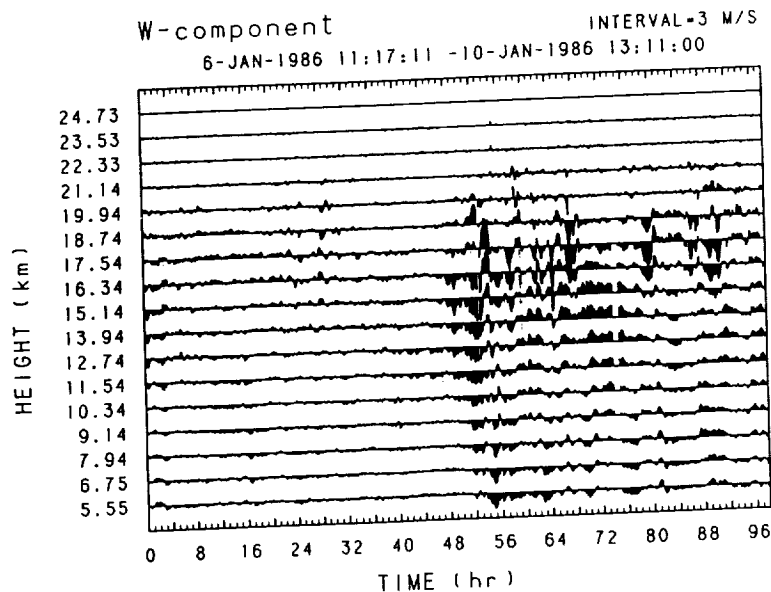
Figure 1: The profile of w-component at each height measured with the vertical beam during the whole observation period. The components having periods of less than 1 hour were removed by a lowpass-filter. The interval of horizontal lines show a velocity of 3 m s^{-1}.

3 Data description

The wind data measured by the MU radar in January 1986 were analyzed. Figure 1 shows the w-component profile at each height during the whole observation period. Apparently the wind feature is divided into the first and second halves, which are referred to as quiet and active periods, respectively. In the active period, we observe large velocities of more than 3 m s^{-1}. Since the observation period is about 48 hours for each period, we can examine statistically the components with periods of less than 10 hours. In view of a large vertical scale of the disturbance, the wind components with vertical scales of larger than 1.5 km were analyzed.

On the other hand, in the mean horizontal wind profile, large differences between in the active and quiet periods were not seen. An almost-westerly subtropical jet having a maximum speed of about 70 m s^{-1} was observed at around a height of 11 km. Decreasing in height above 13 km, the horizontal wind was only several m s^{-1} at 20 km.

4 Profiles of vertical momentum fluxes

The contour maps represented in Fig. 2 are vertical profiles of the frequency spectra of the momentum fluxes in the active and quiet periods. In the quiet period, there are no large fluxes at the whole period and height ranges. On the other hand, for the active period, in both zonal and meridional components, large momentum fluxes are distinctly seen in the height ranges between the height just above the jet of 13 km and 19-20 km, at almost all frequencies. Broken and solid contour lines show negative and positive values of the momentum fluxes, respectively. Whereas the meridional components are distributed evenly between positive and negative values of momentum fluxes, the zonal components are biased toward negative at all

336
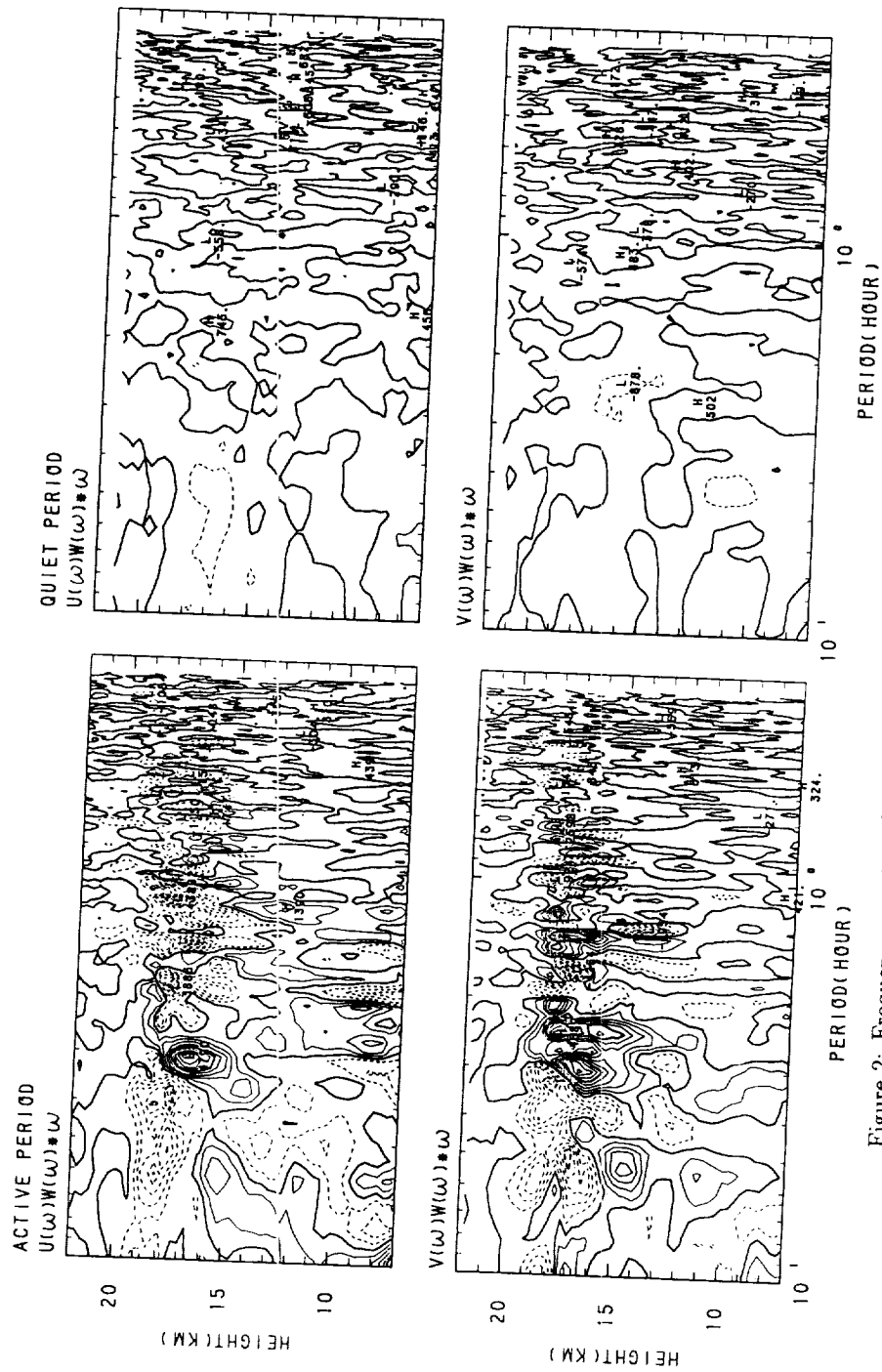
Figure 2: Frequency spectra of vertical momentum fluxes for active and quiet periods in the "flux content" form. Top and bottom figures show the zonal and meridional components of the momentum fluxes, respectively. The contour interval is the same for every profile.
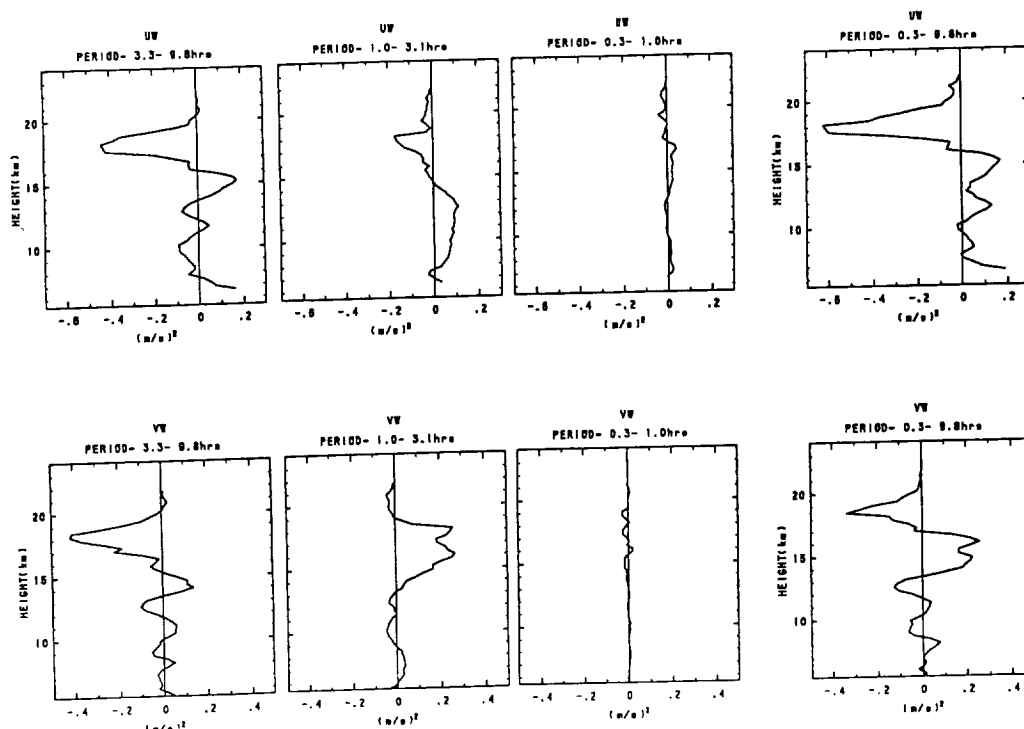
Figure 3: Vertical profiles of the momentum fluxes for each frequency range for the active period. Top and bottom figures show the zonal and meridional components of the momentum fluxes, respectively.

frequencies. This indicates that most of the gravity waves, which contribute to the momentum fluxes appearing in Fig. 2, have wavenumber vectors directing westward.

Another important feature of Fig. 2 is that the momentum fluxes at almost all frequencies vanish at around 20 km. If such a profile shows the absorption of each gravity wave due to the existence of the critical layer, the waves must have the same horizontal phase velocities which equals the mean horizontal wind speed at 20 km of several $m s^{-1}$. The phase velocity is very small as those of topographic waves.

Next, in order to examine differences for the frequency and the detailed vertical profiles in the active period, the momentum fluxes are examined for three frequency ranges, i.e., 3–10, 1–3, and 0.3–1 hours, having the same length in the log scale. The vertical profiles for each and the total frequency ranges are shown in Fig. 3. From the figure, it is found that in this case, larger fluxes were observed in the lower frequency ranges.

It is also interesting that a peak value is observed at about 18 km in the profiles of both zonal and meridional components for the frequency range of 3–10 hours. This suggests the negative acceleration of the mean horizontal wind above the height of the peak, and the positive below it, which tend to strengthen the vertical shear of the mean wind. The magnitude of the accelerations calculated from the vertical profile of the momentum fluxes is about 15 $m s^{-1} day^{-1}$ at the maximum, which is very large for lower stratospheric values. Moreover, it is
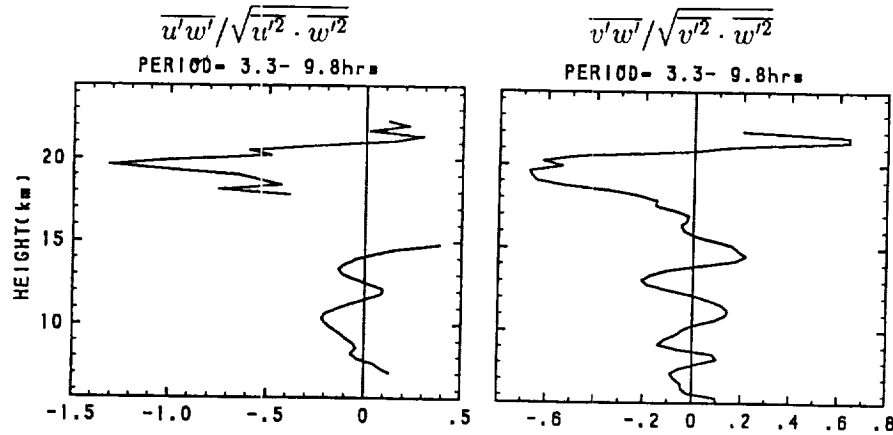
Figure 4: Vertical profiles of the normalized correlation between wind components for a frequency range of 3-10 hours in the active period. Left and right figures show the correlations of vertical component with zonal and meridional components, respectively.

noteworthy that such profiles cannot be explained unless the selective transmission of gravity waves propagating upward happened.

5 Correlation between horizontal and vertical components

Using the power spectra of horizontal and vertical components and the momentum fluxes, we can estimate the normalized correlation between horizontal and vertical component at each frequency. Figure 4 is a result for the frequency range of 3-10 hours. The values for a height range of 15-17.4 km in the left figure could not be estimated because of the small power of the zonal component u. Large correlations are observed above 18 km which is the height of the peak in the momentum flux profiles shown in Fig. 3. This is also consistent with the concept of the selective transmission of gravity waves.

6 Summery and discussion

An analysis was made of momentum fluxes in an active period of the vertical wind component. As results, several interesting features of the gravity waves were revealed, such as, large momentum fluxes, the selecivity of directions of wavenumber vectors, small horizontal phase velocities over the whole ranges of the frequency analyzed, a large acceleration of the mean wind, and the selective vertical transmission. Some of the results are well explained if the fluctuations are due to topographic waves: The slight variation of the mean wind cannot cause the frequency modulation, but probably cause the phase modulation. And the MU radar observed the phase modulation as fluctuations in time.

However, some features like large momentum fluxes observed only in the lower stratosphere is a remained issue to be explained. Furthermore, it is necessary to investigate the interactions

between gravity waves the mean flow in more detail. If the momentum fluxes observed in this study are due to topographic waves, there is a possibility that only a few parts of the spatial phases of the waves might be appeared in the data. The momentum fluxes must be averaged not only temporally but also spatially.

Some results about the momentum fluxes obtained here are different from those by other studies, e.g. the vertical profiles obtained by Fritts et al. (1989) through a similar analysis using the lower-stratospheric wind data measured in March by the MU radar, and the distribution for the frequency in the mesosphere examined by Reid and Vincent (1987). Probably, these differences are due to the differences of the seasons, heights and synoptical situations. Statistical analyses and accumulation of case studies will be important.

References

Ecklund, W. L., K. S. Gage and A. C. Riddle, 1981: Gravity wave activity in vertical winds observed by the Poker Flat MST radar. *Geophys. Res. Lett.*, **8**, 285-288.

Ecklund, W. L., K. S. Gage, B. B. Balsley, R. G. Strauch and J. L. Green, 1982: Vertical wind variability observed by VHF radar in the lee of the Colorado Rockies. *Mon. Wea. Rev.*, **110**, 1451-1457.

Ecklund, W. L., B. B. Balsley, D. A. Carter, A. C. Riddle, M. Crochet and R. Garello, 1985: Observation of vertical motions in the troposphere and lower stratosphere using three closely spaces ST radars. *Radio Sci.*, **20**, 1196-1206.

Fritts, D. C., T. Tsuda, T. E. VanZandt, S. A. Smith, T. Sato, S. Fukao and S. Kato, 1989: An investigation of the momentum flux due to gravity wave motions in the troposphere and lower stratosphere using the MU radar. *J. Atoms. Sci.*, (to be published).

Reid, I. M. and R. A. Vincent, 1987: Measurements of mesospheric gravity wave momentum fluxes and mean flow accelerations at Adelaide, Australia. *J. Atmos. Terr. Phys.*, **49**, 443-460.

Vincent R. A. and I. M. Reid, 1983: HF Doppler measurements of mesospheric momentum fluxes. *J. Atoms. Sci.*, **40**, 1321-1333.

MOMENTUM FLUX MEASUREMENTS AT 69°N AT VHF

Iain M. Reid and Rüdiger Rüster

Max-Planck-Institut für Aeronomie, Katlenburg-Lindau, FRG

The mobile SOUSY VHF (53.5 MHz) Radar, located near Andenes (69°N, 16°E) on the Norwegian Island of Andøya, has been used to measure the component of the upward flux of horizontal momentum per unit mass in the SW–NE plane. This is $\overline{u'w'}sin\phi + \overline{v'w'}cos\phi$, where ϕ is 45°. The individual covariance terms cannot be separated using the present beam configuration (shown in Figure 1), but clearly, the arithmetic sum of the $\overline{u'w'}$ and $\overline{v'w'}$ terms may also be obtained. This is useful, because on some occasions the signs of the individual flux terms may also be inferred. The horizontal anisotropy $(\overline{v'^2} - \overline{u'^2})$ may be derived directly from the mean square radial velocities.

The application of multibeam Doppler radar techniques in the mesosphere at VHF is greatly facilitated at high latitudes in summer by the presence of the so-called "Polar Summer Mesopause Echo" or PMSE. As shown in Figure 2, signal-to-noise ratios associated with the PMSE are very high, and the echoes exhibit excellent continuity in height and time. Consequently, data acceptance rates are high in all six beams.

Note that spectral widths measured in the vertical beam of the radar are narrowest near the region of highest power, possibly suggesting a partial reflection type backscatter mechanism (see REID and CZECHOWSKY, this volume). Mesospheric velocities measured over Andenes are sometimes large enough to produce aliasing in off-vertical beams (Figure 3), but they are also found to be aliased in the vertical beam, on occasion. This requires a radial velocity exceeding 13.1 m s^{-1}. The large fluctuations in velocity are also accompanied by relatively large covariance terms.

Values of the density normalized flux in the SW–NE plane in the 83-90 km height interval obtained in two periods during the MAC/SINE campaign in summer 1987 are shown in Figure 4. When averaged over a period of about 3 h, during which radar returns from the PMSE were the strongest observed during the whole campaign, values reached 47 m^2 s^{-2} near 86 km. Over a two day period earlier in the campaign, maximum values were found to be about 16 m^2 s^{-2}, and this probably represents a more typical mean result. It is also shown in Figure 4. In both cases, values are generally positive and tend to increase with increasing height. Frequency decomposition of the results for the longer interval, after the tidal components are removed, indicates that the largest contribution comes from motions with observed periods in the 10 min – 12 h range. The major contribution to this comes, in turn, from motions in the 10 min – 6 h period range. The mean flow acceleration in the SW–NE plane due to motions in the 10 min – 12 h period range is negative and takes a mean value of about 116 m s^{-1} day^{-1}. The corresponding value for the three hour period is 273 m s^{-1} day^{-1}. A more complete description of these results is given in REID et al. (1988) and RÜSTER and REID (1988).
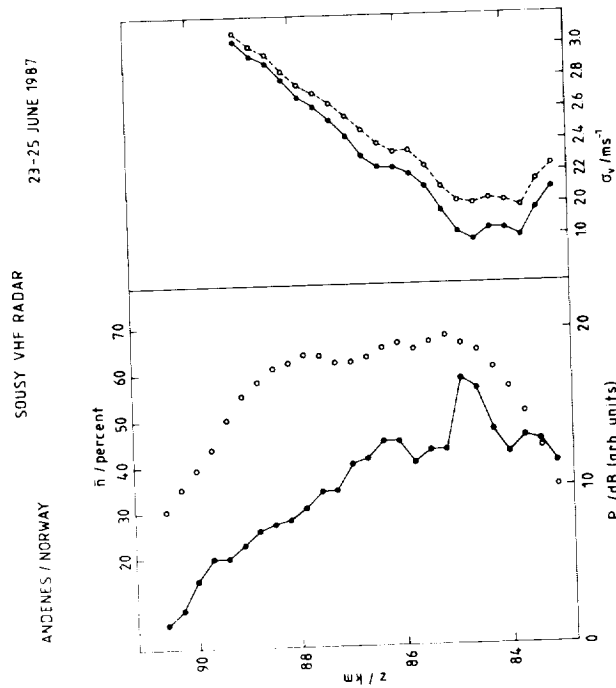
Fig. 2 Height profiles of the mean signal-to-noise ratio P_V and spectral widths σ_V measured in the vertical beam, and the percentage acceptance rate of spectra $\bar{n}$ with P_V exceeding 3 dB. Spectral widths are shown uncorrected (solid line) and corrected (broken line) for beam broadening.
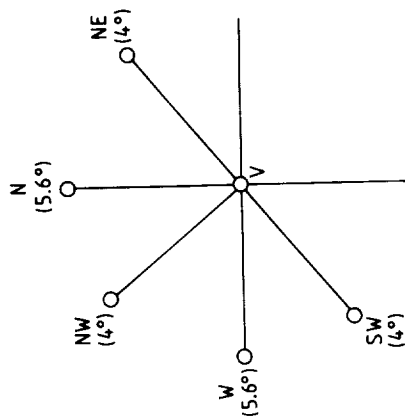
Fig. 1 Antenna configuration of the mobile SOUSY VHF Radar. The beams are directed vertically, at 4° off-zenith towards the north-east, north-west and south-west, and at 5.6° off-zenith towards the north and west.

Fig. 4 left: Height profiles of the SW–NE component of the upward flux of horizontal momentum for 23 – 25 June 1987 (300 m resolution) and for 1312 – 1555 LT, 16 July 1987 (600 m resolution). The straight lines indicate the results of a linear least squares fit.
right: calculated mean flow acceleration corresponding to the straight lines shown on the left. The mean value for all heights is 116 and 273 m s⁻¹ day⁻¹, respectively.

Fig. 3 Radial velocities measured in the north-east beam on 16 July 1987 in three adjacent range gates. The midpoint of each vertical bar corresponds to the mean Doppler shift at that time, and their length to the spectral width. The maximum unambigious frequency is 4.67 Hz, which corresponds to a velocity of 13.1 m s⁻¹. Frequencies or radial velocities larger than this are aliased, as is evident before 1323 LT. In this time interval, radial velocities vary by more than 20 m s⁻¹.

REFERENCES

Reid, I. M., R. Rüster, P. Czechowsky, G. Schmidt, VHF Radar Measurements of Momentum Flux in the Summer Polar Mesosphere Over Andenes (69°N, 16°E), Norway, *Geophys. Res. Lett.*, in press, 1988.

Rüster, R., and I. M. Reid, VHF Radar Observations of the Dynamics of the Summer Polar Mesopause Region, submitted to *J. Geophys. Res.*, 1988.

Vertical Wavenumber Spectra of Meso-Scale Wind and Temperature Fluctuations in the Middle Atmosphere

T. Tsuda[1], D. C. Fritts[2], T. E. VanZandt[3],
S. Kato[1], S. Fukao[1] and T. Sato[4]

1) *Radio Atmospheric Science Center, Kyoto University*
2) *Geophysical Institute, University of Alaska*
3) *Aeronomy Laboratory, NOAA, Department of Commerce*
4) *Department of Electrical Engineering, Kyoto University*

1   INTRODUCTION

Meso-scale wind and temperature fluctuations in the middle atmosphere are sometimes better described by using frequency and wavenumber spectra, since they are observed as a superposition of many waves with various frequencies and wavenumbers. *Dewan and Good* [1986] and *Smith et al.* [1987] proposed a vertical wavenumber spectrum of gravity waves that are saturated due to convective or Kelvin-Helmholtz instabilities. *Smith et al.* predicted the saturated vertical wavenumber spectrum $F_u(m)$ for the horizontal wind velocity u as follows:

$$F_u(m) = \frac{N^2}{6m^3} \tag{1}$$

where m and N are the vertical wavenumber and Brunt-Väisälä frequency, respectively.

From (1) the spectra $F_{T'/T_0}(m)$ and $F_{N^2}(m)$ for the normalized temperature T'/T_0 and N^2 fluctuations, respectively, are further deduced as

$$F_{T'/T_0}(m) = \frac{N^4}{10g^2m^3} \tag{2}$$

$$F_{N^2}(m) = \frac{N^4}{10m} \tag{3}$$

where T', T_0 and g are the perturbed temperature, background temperature and the acceleration of gravity, respectively.

Fritts et al. [1988] have shown quantitative agreement between the model and the observed $F_u(m)$ and $F_{T'/T_0}(m)$ in the troposphere and lower stratosphere. This paper is concerned with simultaneous observations of $F_u(m)$ in the troposphere, lower stratosphere and mesosphere conducted in October 1986 with the MU radar in Shigaraki (35°N,

136°E), Japan, and observations of $F_{T'/T_0}(m)$ and $F_{N^2}(m)$ with radiosondes launched from the MU radar site.

2 WIND VELOCITY SPECTRA

The zonal and meridional wind velocities were determined at 5–21 km on 17–24/25 October 1986 from MU radar observations with a range resolution of 150 m. Because (1) includes the dependence of $F_u(m)$ on the background N^2, we need to separate the entire observation range into height regions with constant N^2. We have chosen 5–9 km and 12–19 km altitudes for a spectral analysis as tropospheric and stratospheric regions, respectively, where N^2 averaged over each height ranges was 1.1×10^{-4} and 4.1×10^{-4} (rad/s)^2.

Mesospheric wind motions were likewise monitored during daylight hours (0800–1600 LT) on 13–31 October 1986. Wind velocity profiles were determined at about 65–85 km with a height resolution of 600 m. Since a simultaneous observation of a temperature profile near mesopause was not available, we assumed $N^2 = 4.3 \times 10^{-4}$ (rad/s)^2 based on the *CIRA 1972* model at the altitudes of the radar observation.

An autocorrelation function is calculated from the fluctuating wind component after applying a pre-whitening, and removing a linear trend. Further, it is multiplied by a Hanning window in order to suppress end effects due to finite data series, then it is Fourier-transformed into a wavenumber spectrum $F_u(m)$.

Fig. 1 shows the observed $F_u(m)$ in the mesosphere (M), lower stratosphere (S) and troposphere (T), together with the model values of $F_u(m)$ calculated from (1) by using a value of N^2 in each height region.

In the mesosphere the zonal spectrum has a slope near -3 between $m=2$ and 4×10^{-4} (c/m) showing a good agreement with the model, while the meridional spectrum has a slightly steeper slope in the same wavenumber range. It is also suggested that the dominant vertical scale of gravity waves in the mesosphere is longer than about 10 km.

In the lower stratosphere, the meridional spectrum agrees fairly well with the model, showing a slope of -3 or somewhat steeper for $m > 6 \times 10^{-4}$ (c/m). The zonal spectrum exhibits a similar shape between $m = 1.4 \times 10^{-4}$ and 8×10^{-4} (c/m), although the spectral density is smaller by about 25 %. The dominant vertical scale can be estimated as 2–3 km. The zonal spectrum in the lower stratosphere, however, is largely enhanced at $m > 1 \times 10^{-3}$ (c/m) compared to the meridional spectrum and the model, which can be explained by the finite range volume effect [*Fukao et al.*, 1988]. Therefore, the increase of the zonal spectral density at large wavenumbers is artificial, and the meridional spectrum appears to be a better measure of the spectral amplitude of the gravity wave field.

The spectral density of the zonal and meridional components in the mesosphere and lower stratosphere are similar at large wavenumbers, while the meridional spectrum has larger energy density at small wavenumbers where the spectrum is not saturated.
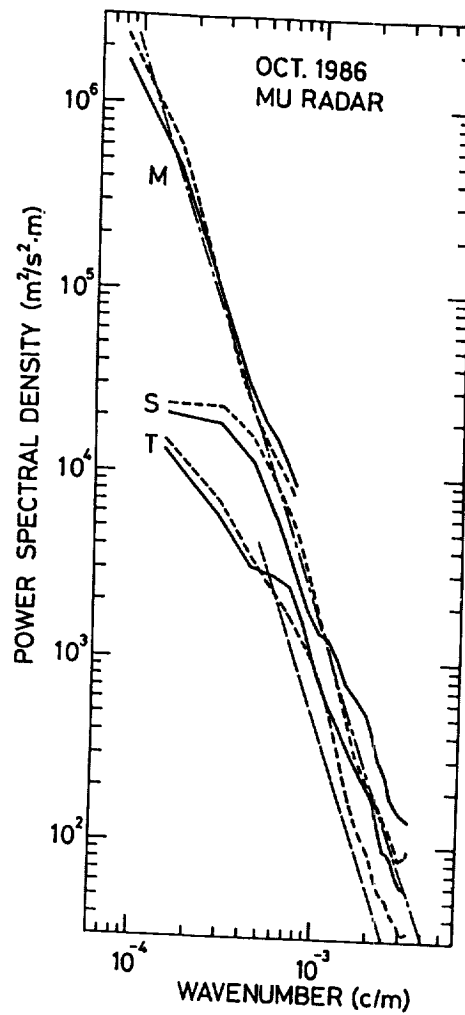
Figure 1: Vertical wavenumber spectra determined from the MU radar observations in October 1986. Thick solid and broken lines show zonal and meridional components, respectively. Thin chained and broken lines correspond to the model spectrum predicted by equation (1) in the lower stratosphere and mesosphere, and in the troposphere, respectively.

Spectra in the troposphere are enhanced relative to the model by a factor of up to 2 excluding the spurious enhancement of the zonal spectrum at large wavenumbers. This suggests that the meso-scale wind fluctuations in the troposphere are not entirely caused by gravity waves, but include considerable contributions from other activities such as convective motions.
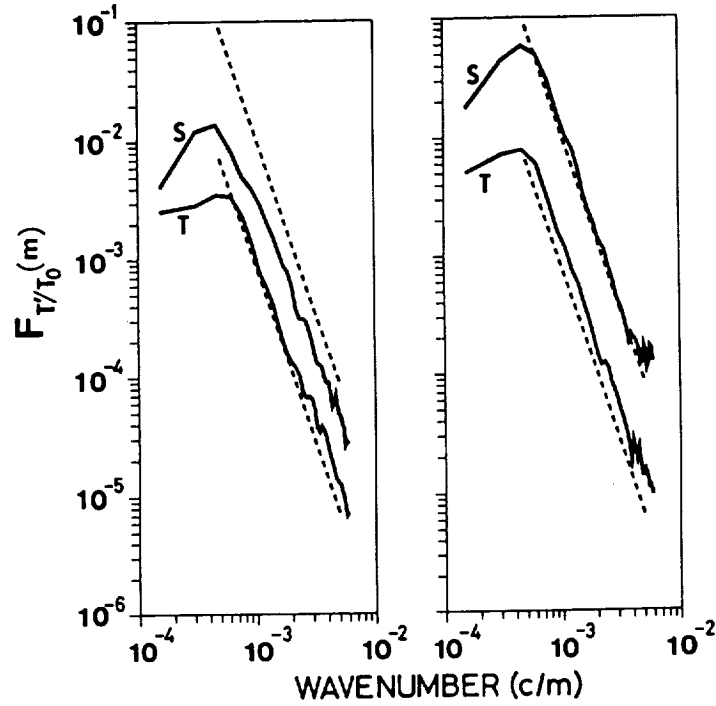
Figure 2: The mean $F_{T'/T_0}(m)$ observed in summer (left panel) and winter (right panel). The spectra with larger amplitudes are from 18.5–24.5 km altitude (stratosphere), while the others are from 2.0–8.5 km (troposphere). The dashed curves correspond to the model spectrum, where the mean N^2 in the troposphere and stratosphere are assumed as 1.84×10^{-4} and 6.49×10^{-4} $(\text{rad/s})^2$ in summer, and 1.75×10^{-4} and 6.36×10^{-4} $(\text{rad/s})^2$ in winter, respectively.
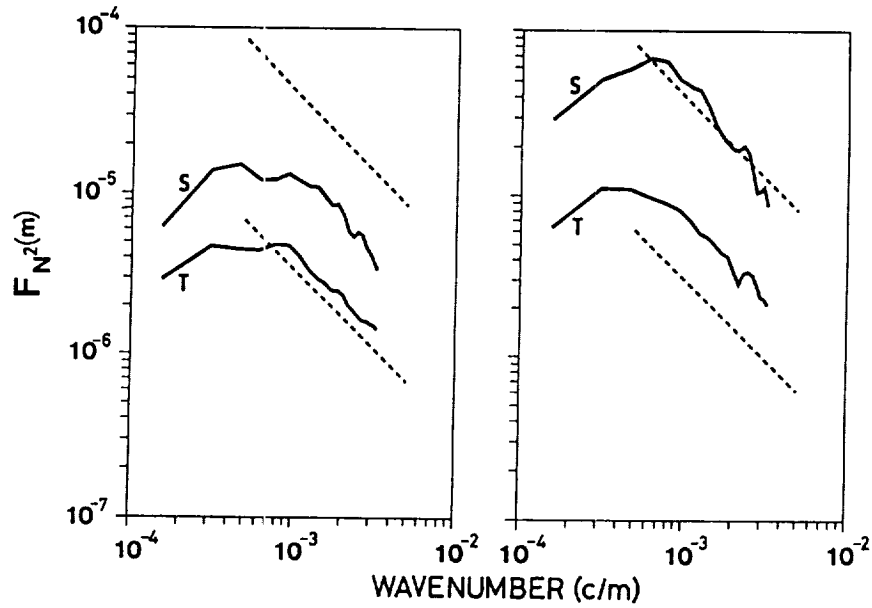
Figure 3: The same as Fig. 9 except for N^2 spectra.

3 NORMALIZED TEMPERATURE AND N^2 SPECTRA

By using a high-resolution radiosonde sounding system we have observed temperature profiles over the MU observatory for 34 times during five campaigns in summer from 30 June to 4 September 1987, and for 31 times in winter from 22 December 1986 to 25 February 1987.

Figs. 2 and 3 show $F_{T'/T_0}(m)$ and $F_{N^2}(m)$ determined in the 2.0–8.5 km (troposphere) and 18.5–25.0 km (lower stratosphere) altitude ranges, where a vertical spacing to calculate T'/T_0 and N^2 was 150 m.

Except for the spectrum detected in summer stratosphere the slope of the mean spectra is very near -3 and -1 for $F_{T'/T_0}(m)$ and $F_{N^2}(m)$, respectively, for $6 \times 10^{-4} \geq m \geq 3 \times 10^{-3}$ (c/m), which suggests an agreement with the model described by (2) and (3). On the other hand, the amplitudes of the observed spectra in the summer stratosphere were as small as 0.4 of the model value, implying that the gravity waves were not fully saturated.

To summarize, vertical wavenumber spectra of meso-scale fluctuations of the wind velocity, normalized temperature and N^2 in the middle atmosphere are fairly well ex-

plained by a saturated gravity wave spectrum. However, we have also found that the gravity waves in the summer stratosphere significantly above the tropopause are not necessarily fully saturated.

References

Dewan, E. M., and R. E. Good, Saturation and the "Universal" Spectrum for Vertical Profiles of Horizontal Scalar Winds in the Atmosphere, *J. Geophys. Res.*, *91*, 2742-2748, 1986.

Fritts, D. C., T. Tsuda, T. Sato, S. Fukao, and S. Kato, Observational evidence of a saturated gravity wave spectrum in the troposphere and lower stratosphere, *J. Atmos. Sci.*, *45*, 1741-1759, 1988.

Fukao, S., T. Sato, P. T. May, T. Tsuda, S. Kato, M. Inaba, and I. Kimura, A systematic error in MST/ST radar wind measurement induced by a finite range volume effect, 1, Observational results, *Radio Sci.*, *23*, 59-73, 1988.

Smith, S. A., D. C. Fritts, and T. E. VanZandt, Evidence of a saturation spectrum of atmospheric gravity waves, *J. Atmos. Sci.*, *44*, 1404-1410, 1987.

ANISOTROPY OF THE VELOCITY FLUCTUATION FIELD IN THE LOWER STRATOSPHERE

T.E. VanZandt[1], S.A. Smith[2], T. Tsuda[3], D.C. Fritts[4], T.Sato[3], S. Fukao[3], and S. Kato[3]

[1]Aeronomy Laboratory
National Oceanic and Atmospheric Administration
Boulder, Colorado, U.S.A.

[2]NASA/Marshall Space Flight Center
Huntsville, Alabama, U.S.A.

[3]Radio Atmospheric Science Center
Kyoto University
Uji, Kyoto 611, Japan

[4]Geophysical Institute
University of Alaska
Fairbanks, Alaska, U.S.A.

In March 1986 the MU radar (FUKAO et al., 1985) measured the radial velocity in the upper troposphere and lower stratosphere at 20° zenith angle at every 30° of azimuth during four days and at every 45° of azimuth during two days. The pulse length was 300m and the range gates were spaced 282km apart in altitude. A jet stream was present during the entire period, with overhead peak winds usually between about 12 and 13km ranging from 35 to 58m/s. The altitude of the tropopause increased from about 10.5km on the first two days to about 12km on the last day.

The mean radial velocity variance averaged over range gates centered from 10.43 to 19.17km was calculated every four minutes and then averaged over 20 minutes. Some examples of the variance versus azimuth are shown in Figure 1. The points are the measured variances and the curves are least-square fits of a function consisting of the mean plus the first two azimuthal harmonics. The mean is proportional to the total kinetic energy per unit mass of the fluctuation field and the first harmonic is proportional to the vertical flux of horizontal momentum per unit mass. In the panel labeled No. 640 the azimuthal variation is dominated by the first harmonic. In No. 645, only 20min later, there is in addition a large second harmonic. In Nos. 660 and 700 the second harmonic is much larger than the first harmonic, but in No. 700 the second harmonic is much smaller than in No. 660. These examples show that the variance varies strongly versus both azimuth and time.

Figure 2 shows each successive fitted curve centered on records from 29.0h to 80.3h from the beginning of the experiment, with the zero for each successive curve shifted to the right by 1(m/s)^2. The four examples in Figure 1 are indicated by the arrows between 40 and 50h in the margin of the upper panel. The predominance of the second harmonic, particularly during the amplitude peaks at 42, 57, and 70h is clearly visible. Note also the phase changes during the 42 and 70h peaks.

The amplitudes a_0, a_1, and a_2 and the phases ϕ_1 and ϕ_2 of the harmonic terms are plotted versus time in Figure 3. These quantities are averages over 1h plotted every 4min. It is evident that a_2 is rather well correlated with a_0, but that a_1 is only slightly correlated. There does not appear to be any overall correlation or relation between ϕ_1 and ϕ_2.

By using a model of the azimuthal variation of variance due to gravity waves (VANZANDT, 1985), we show that probably all of the observed azimuthal variations can be explained with a frequency spectrum similar to observed spectra but with a restricted azimuthal distribution of propagation vectors.

REFERENCES

Fukao, S., T. Sato, T. Tsuda, S. Kato, K. Wakasugi, and T. Makihira (1985), The MU radar with an active phased array system: 1. Antenna and power amplifiers, 2. In-house equipment, Radio Sci., 20, 1155-1176.

VanZandt, T.E. (1985), A model for gravity wave spectra observed by Doppler sounding systems, Radio Sci., 20, 1323-1330.
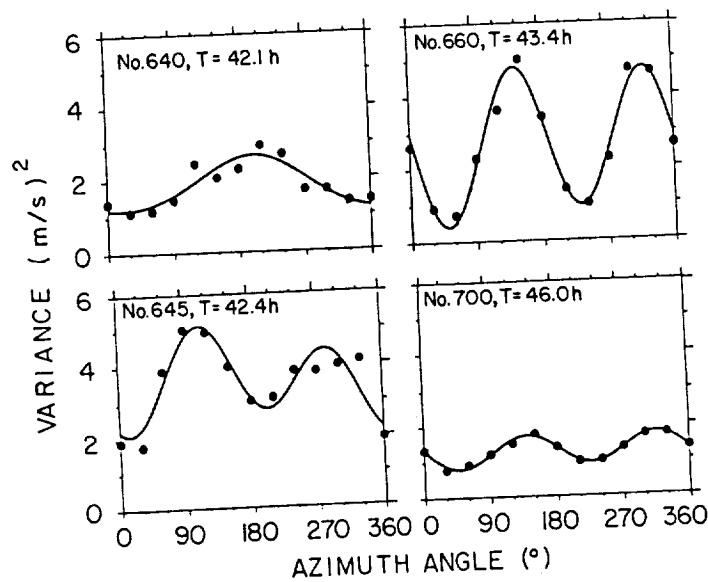
Figure 1. Examples of the variance versus azimuth. The data points are averaged over 20min. The curve is the sum of the mean and first and second harmonics fitted to the data points by least squares. Note that the panels labeled No. 640 and No. 645 are only 20 minutes apart.
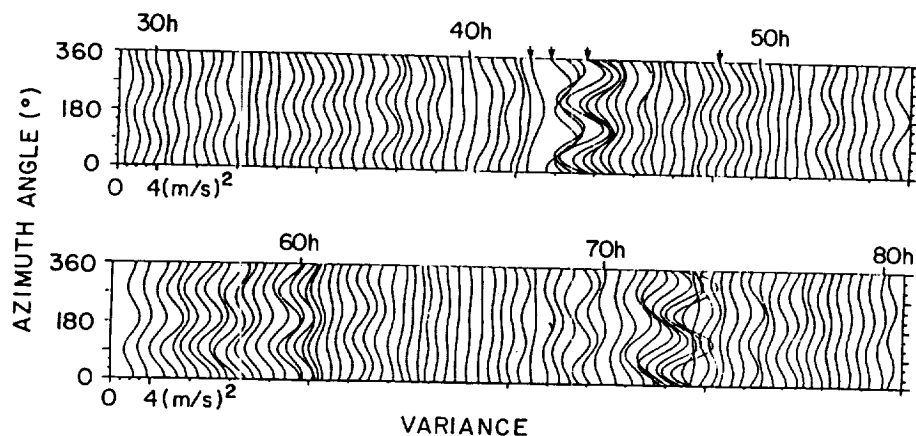
Figure 2. Successive fitted curves centered 20 min apart from 29.0 to 80.3h, with the zero for each successive curve shifted to the right by $1(m/s)^2$. The four examples shown in Figure 1 are indicated by the arrows in the margin of the upper panel.
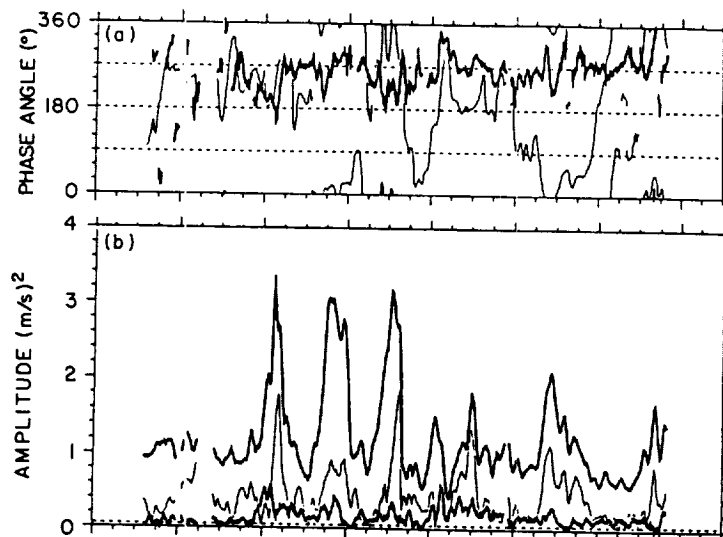
Figure 3. (a) The phases ϕ_1(bold) and ϕ_2 (thin) of the maxima of the first and second harmonics. ϕ_1 is not plotted when $a_1 \leq 0.2$. (b) The amplitudes a_0 (bold), a_1 (bold), and a_2 (thin) of the harmonic components.

MOMENTUM FLUX IN THE TROPOSPHERE AND LOWER STRATOSPHERE USING THE MU RADAR

D.C. Fritts[1], T. Tsuda[2], T.E. VanZandt[3], S.A. Smith[4],
T. Sato[2], S. Fukao[2], and S. Kato[2]

[1]Geophysical Institute
University of Alaska
Fairbanks, Alaska, U.S.A.

[2]Radio Atmospheric Science Center
Kyoto University
Uji, Kyoto 611, Japan

[3]Aeronomy Laboratory
National Oceanic and Atmospheric Administration
Boulder, Colorado, U.S.A.

[4]NASA/Marshall Space Flight Center
Huntsville, Alabama, U.S.A.

We calculated the momentum flux from the variances in each opposite pair of azimuths averaged from 10.43 to 19.17km presented in paper 4.6.5, using the method of VINCENT AND REID (1983). The mean momentum flux over the days when each pair was separated by 30° and over the days when each pair was separated by 45° are shown in Figure 1. The curves are the least-squares fits of a sinusoid to the points. The mean momentum flux over the entire six-day period was about 0.20(m/s)^2 towards 270°.

The density-weighted momentum flux versus altitude and the resulting acceleration of the mean flow averaged over the entire period are shown in the upper and lower panels of Figure 2. The total zonal acceleration varied smoothly from ∝ +2(m/s)/day at 8-10km to ∝ -1.5(m/s)/day above 15km.

The inferred drag above the peak of the jet stream is in reasonable agreement with that inferred by PALMER et al. (1986) from the needs of large-scale circulation models. The change in sign of the acceleration across the peak of the jet stream is thought to be due to filtering by the jet stream of zonally propagating gravity waves.

REFERENCES

Palmer, T.N., G.J. Shutts, and R. Swinbank (1986), Alleviation of a systematic westerly bias in general circulation and numerical weather prediction models through an orographic gravity wave drag parameterization, Quart. J. Roy. Met. Soc., 112, 1001-1040.

Vincent, R.A., and I.M. Reid (1983), HF Doppler measurements of mesospheric momentum fluxes, J. Atmos. Sci., 40, 1321-1333.
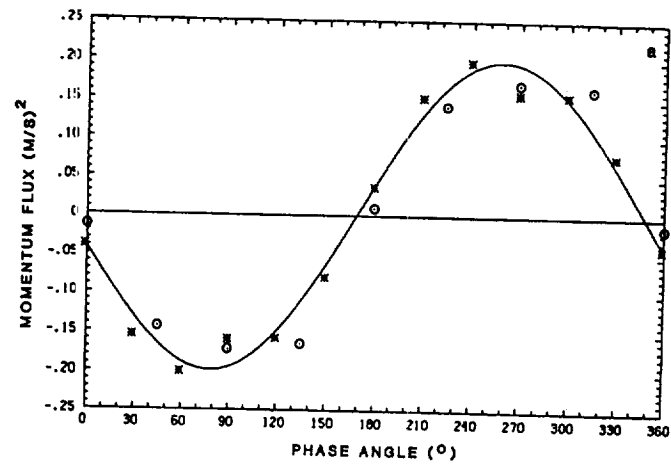
Figure 1. Azimuthal variations of the vertically averaged momentum flux for the four- and two-day periods. The sinusoid is fitted by least squares to the * points.
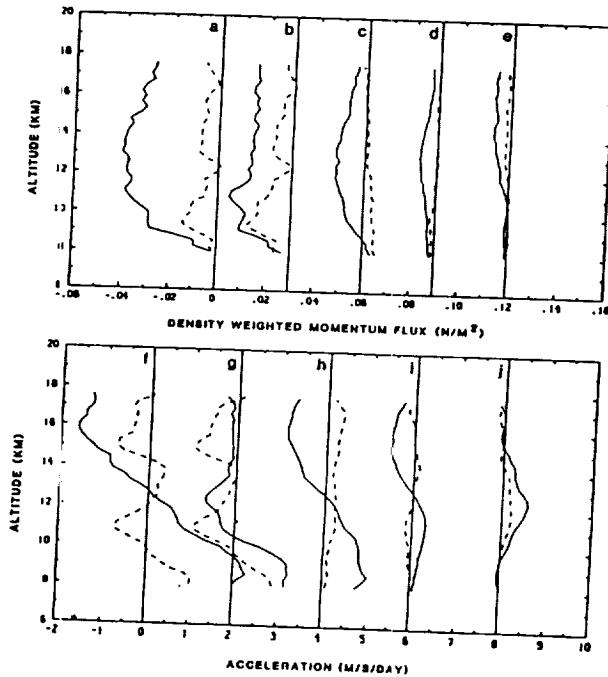
Figure 2. Upper panels: Profiles of the zonal (solid) and meridional (dashed) density-weighted momentum fluxes for a) all periods, b) 7-24h, c) 2-7h, d) 30min-2h, and e) 8-30min. Lower panels: Profiles of the zonal and meridional mean flow accelerations, with f) through j), corresponding to a) through e).

FRACTAL ANALYSIS OF GRAVITY-WAVE SPECTRA IN THE MIDDLE ATMOSPHERE

Richard L. Collins
Department of Electrical and Computer Engineering
University of Illinois, Urbana, Illinois 61801

Prabhat K. Rastogi
Electrical Engineering and Applied Physics Department
Case Western Reserve University, Cleveland, Ohio 44106

Summary

Velocity fluctuations in the middle atmosphere show a continuum of scales without dominant features and their power spectra often decay with frequency f as $f^{-\beta}$. Plots of noise processes with such power-law spectra also show varying fractal plane-filling properties, characterized by a fractal dimension (D), for different values of spectral index β. A relation between β and D has been numerically found and its validity is verified for limiting cases. Fractal dimension D is obtained for middle atmospheric velocity data from the Poker Flat radar. Variations of D follow those in β from an earlier analysis but show an offset of 0.1-0.2 even after corrections for outliers, gaps, and additive noise. We surmise that a fractal representation of the atmospheric velocity field may be possible.

Introduction

Our interest in colored noise and its fractal behavior relates specifically to time series of wind fluctuations in the middle atmosphere, monitored with sensitive high-power radars (see e.g. Röttger, 1987). The power spectrum density (PSD) S(f) of these series often follows a power-law variation with frequency (f)

$$S(f) = \alpha\, f^{\beta} \quad \text{for } a < f < b; \quad \alpha, \beta, a \text{ and } b \text{ constants} \tag{1}$$

with spectral index β in the range of 1-3 at temporal scales of 0.1-100 hr and spatial scales of 1-1000 km (Balsley and Carter, 1982). The PSD is usually obtained through classical spectral estimation techniques (Marple, 1987), and the spectral index β is found by a least-square fit.

Colored noise phenomena with PSD given by equation (1) shows trends and fluctuations at many scales, but conspicuously lack any dominant ones. Their only interesting parameter is the spectral index β. The frequency f may correspond to variations in time or space. The important f^{-1} or $\beta=1$ case is widely encountered in electronics and astronomy [see e.g. D'Amico and Mazzetti, 1986]. Velocity fluctuations in fluid turbulence have energy spectra with $\beta=5/3$ in the inertial range, and as high as $\beta=7$ in the viscous range [see e.g. Tennekes and Lumley, 1972].

Figure 1 shows an interesting aspect of colored noise, viz. the varying extent to which it fills-up the plot region for different spectral indices β. It is apparent that white noise ($\beta=0$) tends to fill up a strip of the plane, but noise for larger β lacks this property. Plane-filling characteristics of irregular curves can be described through fractals - objects and constructs with fractional dimension [see e.g. the treatises by Mandelbrot 1977, 1983]. We examine whether this aspect of colored noise processes can be used for analysis of atmospheric velocity data with power-law spectra. The idea originated from a similar analysis of f^{-1} noise in galactic X-ray emissions using the concept of scale invariance and fractals by McHardy and Czerny (1987), hereafter MC.

In this paper, we first briefly outline the relevant definitions of fractal dimension D. An empirical relationship between the index β and dimension D for colored noise is then numerically obtained, and its validity is confirmed for limiting cases. The relationship is used for analysis of middle-atmospheric velocity data from the Poker Flat radar with known spectral-index profiles. Profiles of D and β are shown to be remarkably similar. We conclude that fractal analysis is a qualitative method for finding spectral index of colored noise processes. Implications of our results are briefly discussed in the context of atmospheric dynamics models.

Relationship between Fractal Dimension D and Spectral Index β

The concept of fractal dimension of irregular objects, that show structure over a very broad range of scales, is originally due to Mandelbrot [1977, 1983]. Briefly, we note that a unique length cannot be attributed to an irregular curve. If the length L is measured with yardsticks of length μ, put end-to-end along the curve, then $L(\mu)$ increases as μ is made successively smaller. For a straight line, L does not depend on μ. But extremely irregular
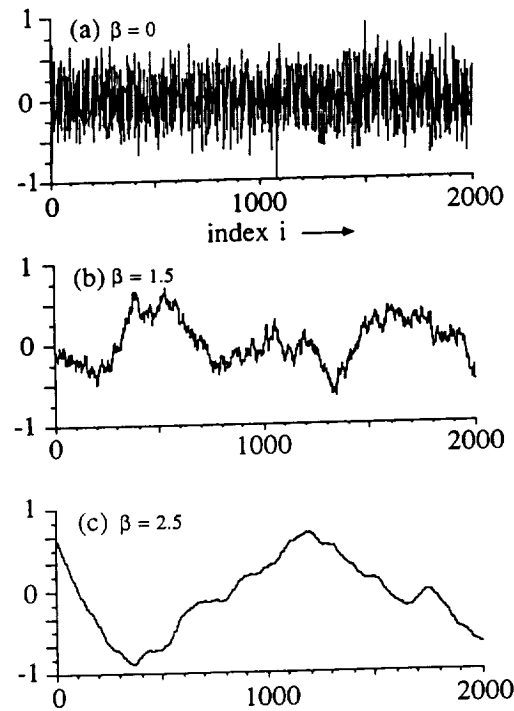
FIGURE 1. Plane-filling characteristics of plots of simulated time series with different values of spectral index β for i=1 to 2000 samples. White Gaussian noise, (a) β=0, almost entirely fills a strip about zero amplitude. Noise with (b) β=1.5 and (c) β=2.5 has successively weaker plane-filling characteristics.

curves tend to fill up the plane. The fractal dimension D' is defined by Mandelbrot, through a linear dependence between log L(μ) and log(μ), as

$$\frac{d \log L(\mu)}{d \log \mu} = 1\text{-}D' = \text{-}D \qquad (2)$$

A straight line has a fractal dimension D'=1. An extremely irregular curve that tends to fill up the plane has D'~2. Many examples e.g. the triadic Koch curve with D'=1.262, have been discussed in detail by Mandelbrot(1983). Fractal curves on a plane are self similar under magnification.

For a noise time series F(t) of duration T, MC defined a length metric L(μ)

$$L(\mu) = \frac{1}{\mu} \int_0^T |\ F(t+\mu) - F(t)\ |\ dt \qquad (3)$$

which is in same units as F, and used $D = D'-1$ as the fractal dimension for the time series. This circumvents the need for two different scaling factors or magnifications, in amplitude and time, necessary for defining the fractal dimension of a physical time series or random process. Such processes are self-affine and calculation of a meaningful value of fractal dimension for them is not straightforward [see e.g. Voss, 1988]. We follow MC's usage below.

A noise process with a power-law spectrum defined in equation (1) entails a hierarchy of scales, similar to that encountered for fractals, with a suitable assignment of power to each scale. Intuitively, we expect β and D to be related as suggested by figure 1. We are, however, unaware of specific results relating these two quantities except for a conjecture due to D. Raine

$$\beta = 2(1-D); \quad \text{for } 0 \le \beta \le 2 \qquad (4)$$

mentioned in MC. Raine's result is an approximation valid only for β< 2, as it implies negative D for β>2. The ~f^{-1} time series analyzed by MC have D=0.6, sufficiently close to the value D=0.5, given by equation (4) .

White noise with β=0 almost entirely fills up a strip in the plot region as shown in figure 1. On this basis, D' approaches the topological dimension 2 of an area, while D approaches 1. On the other hand, the PSD for a process with very large β can be approximated with an impulse at the low-frequency end. Realizations of F(t) become sinusoids at this frequency. D' for a sinusoid approaches 1 (same as for a straight line), and D vanishes. These limiting results are verified analytically in the Appendix. It can also be shown analytically that D=0.5 for f^{-1} noise.

An empirical relationship between D and β has been found by computing dimensions D for time series of colored noise with known indices β. Generating series with β=0 and β=∞ is simple. Algorithms also exist for generating series with specific β, e.g. a $t^{-1/2}$ weighting of white noise gives β=1, and integrated white noise has β=2. For arbitrary β, the time series can

be generated as the sum of n weighted sinusoids (Bemra, Rastogi and Balsley, 1985, hereafter BRB) of random frequencies f_i and in arbitrary phases ϕ_i,

$$F(t) = \alpha' \sum_{i=1}^{n} \frac{1}{(f_i^{\beta/2})} \sin(2\pi f_i t + \phi_i); \quad \alpha' \text{ constant} \tag{5}$$

Frequencies f_i should be chosen from a uniform distribution on $\log(f)$ to reduce computation time. Hereafter a unit sample interval for t is assumed.

Time series with 40960 points were generated using equation (5) for $\beta=0.0$ to 2.5 at steps of 0.5. For a sequence $F(i)$; $i=1,..N$, $L(m)$ was computed over three decades of m in 1 octave steps. The following modification of equation (2) with end corrections, that converges to it for $N \gg m$, was used

$$L(m) = \frac{1}{m} \frac{N}{N-m} \sum_{i=1}^{N-m} |F(i+m) - F(i)| \tag{6}$$

The metric $L(m)$ was averaged over several independent sequences of 4096 points. D was then obtained by linear least-square regression of $L(m)$ versus step size m on a log-log plot.

The results for average D versus β are shown in figure 2. The uncertainty in regression analysis has been shown at three standard deviation level, on either side, following Brownlee(1965). Raine's linear equation (4) is exact for $\beta=0$ and $\beta=1$, but is only approximately valid for $1 < \beta < 2$.

Fractal Analysis of Middle Atmosphere Velocity Data

The data used in this study are time series of 30-min averages of zonal and meridional winds (sampled every 15-min) in the troposphere and stratosphere, derived from 3-min radial velocity observations with the Poker Flat radar in Alaska. Averaging makes it possible to resolve the radial observations along three beams into three orthogonal wind components at each height, assuming statistical homogeneity at horizontal scales < 10 km. Data is available from 3.8 km to 36.4 km heights at increments of 2.2 km, but is deemed unreliable below 6.0 km due to ground-clutter, and above 21.4 km due to weak echoes. Two 20-day periods cover winter (1-20 Jan 1984) and summer (12 Jun-1 Jul, 1984). This data has been analyzed by BRB to show the variability of spectral index β for zonal and meridional winds with
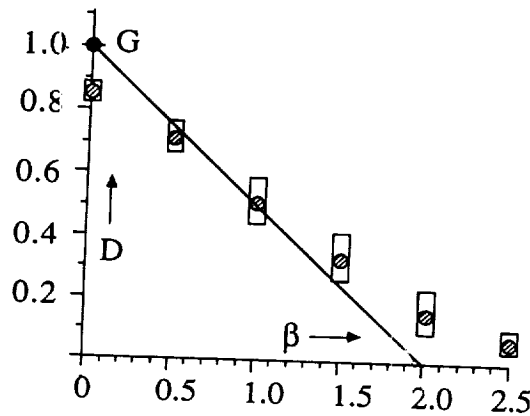
FIGURE 2. Plot of fractal dimension D versus spectral index β for simulated time series obtained as sums of scaled random-frequency sinusoids in random phase (shaded circles), and Gaussian white noise (solid circle, G). Bars indicate the uncertainty in estimating D, at three standard deviation level on either side. Diagonal line shows Raine's result. The difference in the two cases for β=0 is significant as discussed later in the text.

altitude and season. Figures 3(a) and 3(c) show typical summer and winter time series of zonal and meridional winds.

The time series are contaminated with sporadic but sparse spikes, termed outliers, and have several gaps. Outliers and measurement errors contribute to a white-noise component that influences the results of fractal analysis. Following scheme has been used to find outliers : (i) Trend is identified as the running median at a long time scale. (ii) Running mean and standard deviation of the detrended series is obtained at a local time scale. (iii) If a data point in the detrended series is not within three standard deviations of the local mean, it is classified as an outlier and the corresponding point in the original series is flagged as a gap. Finally, (iv) a local running median filter is applied to eliminate low amplitude spikes. Effect of this scheme on the time series of figure 3(a) is shown in figure 3(b). The scheme detects outliers with a high probability (>99%) but, as in communication in a noisy environment, it occasionally accepts an outlier or rejects a good data point.

Fractal dimension D of the time series with detected ouliers and data gaps is obtained in two steps. First the length metric L(m) is found for several scales m, and then D is obtained by least-square regression of log[L(m)] versus
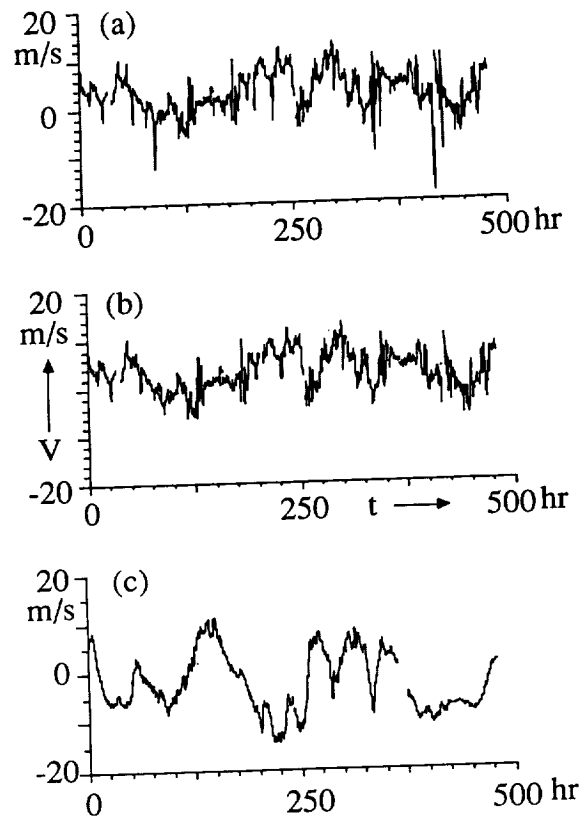
FIGURE 3. Examples of horizontal velocity time-series at 10.33 km altitude from Poker Flat radar and effect of outlier detection. (a) unedited meridional velocity during summer, (b) same as above with outliers suppressed and local median filtering, (c) unedited zonal velocity during winter. Summer observations are noisier.

log(m). Contribution to the metric L(m) from outliers and points in the gaps is excluded. To account for the number M of excluded points, the second factor in equation (6) for L(m) is replaced by N/(N-m-M). This is found to be satisfactory if the number of outliers and gaps is small and their total duration M << N.

BRB used classical spectral analysis and linear least-square regression of PSD estimates on a log-log plot to find the index β. Their results show distinct altitude and seasonal variations in β, with minima near tropopause. In

classical spectral analysis, data must be equispaced and so gaps must be interpolated. BRB used cubic splines with zero end-point derivatives to interpolate across some long gaps. Still, interpolation across gaps may introduce discontinuities with spurious spectral trends that decay as f^{-2}. Data windows with spectral sidelobes decaying at rates steeper than the index β of the time series suppress the effect of discontinuities. BRB used a triangular data window with f^{-4} sidelobes. Overall uncertainty in their β estimates, at the one standard deviation level, is ± 0.1.

For comparing D profiles obtained by fractal analysis with β profiles of BRB, the latter have been scaled to a corresponding dimension D_β using the empirical β-D relation of figure 2. Comparison for summer data is shown in figures 4(a) and 4(d), and for winter, in 4(b) and 4(e). Uncertainty in the D_β profiles is not explicitly shown but is of the order of ± 0.15 at the three standard deviation level. Altitude and seasonal variations in D mimic those of D_β. Profiles of D are, however, systematically offset to values higher than D_β. The offset is larger for the noisier summer data.

Initially this offset is attributed to residual white noise due to measurement errors. Suppose observations $r(t)$ are obtained by adding white Gaussian noise $g(t)$ to a signal $s(t)$. Then for high signal-to-noise ratio, the length metrics for r, s and g at scale μ are related quadratically through

$$L_r^2(\mu) = L_s^2(\mu) + L_g^2(\mu) \tag{7}$$

MC used this to correct for additive white noise of known variance. Corrected profiles of D for the Poker Flat data have been obtained for several plausible values of measurement error (0.1 to 0.6 m/s) assumed constant at each altitude. Correction causes a shifting of the fractal dimension D to values closer to D_β, but as the measurement error depends on altitude, it may also distort the D profiles. This distortion is more severe for the very noisy summer data. For the winter data, correction preserves the shape of D profiles. Figures 4(c) and (f) show the corrected winter D profiles for a measurement error of 0.6 m/s at all heights. Agreement with D_β profiles is very reasonable in the stratosphere, above 10 km. The disparity of the two profiles in the troposphere may be due to small-scale gravity waves that weaken the assumption of homogeneity mentioned before.

We find that fractal analysis gives values of D that are in reasonable agreement with D_β values inferred from BRB, though systematically higher by about 0.1-0.2. MC also found an offset of 0.1 in their analysis of '1/f noise'.
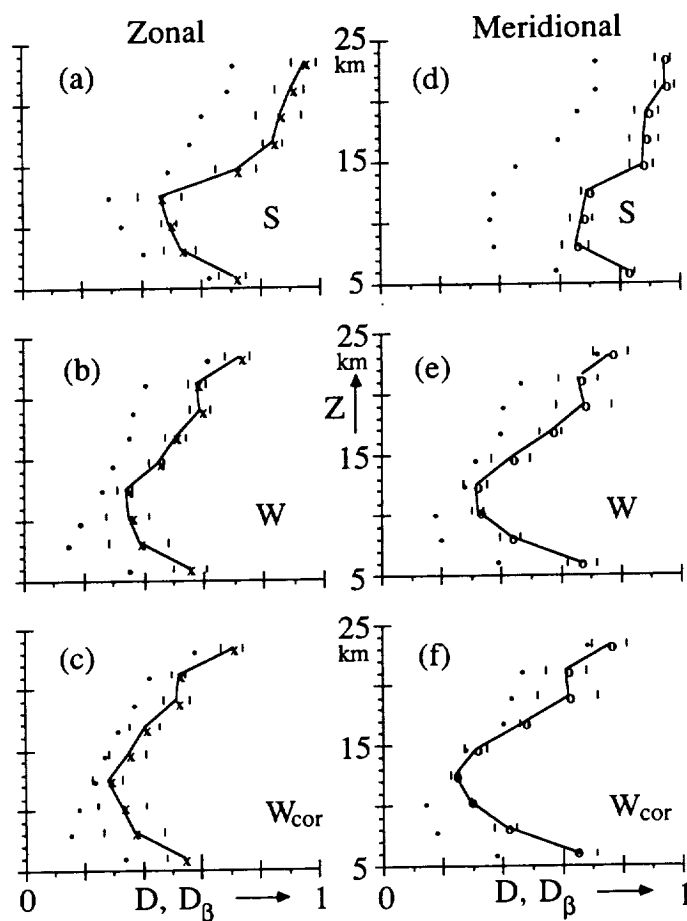
FIGURE 4. Comparison of fractal dimension D (line) with D_β (solid circles) obtained from β-profiles of BRB using figure 2. Panels show profiles for (a) summer zonal (b) winter zonal (c) winter zonal with 0.6 m/s measurement error (d) summer meridional (e) winter meridional (f) winter meridional with 0.6 m/s measurement error. Uncertainty in D at the three standard deviation level is shown by vertical bars and is about ±0.15 in D_β.

Discussion

Fractal analysis provides an alternative method for examining processes with a power-law PSD. It is simpler and more efficient than Fourier methods, which need $\sim N \log_2 N$ multiplications and additions, and evaluation of trigonometric functions, for N data points. For scales m selected one octave apart, fractal analysis uses only $\sim N \log_2 N$ additions and positive-difference operations. In typical applications, computational effort for fractal analysis may be two orders of magnitude smaller. Fourier methods restrict the number of data points to powers of 2, and these must be equispaced (requiring interpolation through gaps and nonuniform points). These restrictions are entirely relaxed in fractal analysis. Finally, processes with power-law PSD's exhibit strong trends which may produce spurious f^{-2} components in the PSD estimates, if not removed by detrending (which requires extrapolation) or suppressed by windowing. In fractal analysis trends are automatically removed at each scale.

Fractal analysis results do not afford a proper discrimination between processes with $\beta > 2$ as D becomes small, or between processes differing only slightly in β. It systematically gives D higher than D_β by 0.1-0.2. We surmise that two processes with the same index β but with different distributions may have different fractal dimensions. An example of this is shown in the β-D diagram of figure 2 for white-noise. Gaussian white noise has D=1, but an arbitrary sum-of-sinusoids distribution gives D≈0.9.

Qualitatively, however, all the major characteristics of data are preserved in fractal analysis. We do not expect it to replace the more accurate and more involved spectral analysis methods. Our results and discussion suggest that it may be an efficient exploratory data analysis tool for screening large amounts of data as an aid to refined spectral analysis.

Observed PSD of horizontal velocity components show features that cannot always be uniquely and unequivocally associated with a field of two-dimensional turbulence (Gage,1979), a universal spectrum of buoyancy waves (VanZandt, 1982), or with refined wave and turbulence models (see e.g. Liu and Kato, 1985). We find that time evolution of the velocity field is reasonably consistent with a fractal description. Power-law behavior of spatial spectra of atmospheric velocity field and its intermittent nature suggest that a fractal description may hold for its evolution in space and time. We surmise that generalized scale-invariance fractal model of Lovejoy and Schertzer (1986) may e.g. provide an alternative phenomenological basis for describing the atmospheric velocity field.

Appendix : Fractal Dimension D for limiting cases

We first show that D=1 for a white Gaussian random process $g(t)$. Without loss of generality, let $g(t)$ be zero mean with variance s^2. Then $z(t)=g(t+\mu)-g(t)$ is also zero-mean Gaussian with variance $2s^2$ and the expected value of $|z(t)|$ is $2s/\pi^{1/2}$ (see e.g. Papoulis, 1984). For $T>>\mu$, by ergodicity

$$L(\mu) = \frac{1}{\mu}\int_0^{T-\mu} |\, g(t+\mu) - g(t)\, |\, dt \approx \frac{2sT}{\mu\sqrt{\pi}} \qquad (A.1)$$

Since $L(\mu) \propto \mu^{-1}$, from equation (2) it follows that D=1.

We next consider a process $y(t)$ with $\beta >> 1$, and show that D vanishes asymptotically. With a power-law PSD for $y(t)$ given by equation (1) over the frequency range (a,b) and a large index β, $y(t)$ may be replaced by a single sinusoid of the form $c\sin(2\pi at)$. In this case

$$L(\mu) = \frac{c}{\mu}\int_0^T |\, \sin\{2\pi a(t+\mu)\} - \sin(2\pi at)\, |\, dt \qquad (A.2)$$

Writing the integrand about $t+\mu/2$, and integrating over many half cycles of the sinusoid i.e. for $T>>(2a)^{-1}$, the integral reduces to $L(\mu)=(4acT)\sin(a\mu)$. For $\mu<<1/a$, $L(\mu)$ tends to a constant (4acT), and D vanishes asymptotically.

References

Balsley, B. B. and D. A. Carter, The spectrum of atmospheric velocity fluctuations at 8 km and 86 km, *Geophys. Res. Lett.,* 9, 465-468, 1982.

Bemra, R. S., P. K. Rastogi and B. B. Balsley, A study of gravity-wave spectra in the troposphere and stratosphere at 5-min to 5-day periods with the Poker Flat MST radar, *Handbook for MAP,* 20, SCOSTEP Secretariat, Urbana, Ill.,Eds. S. A. Bowhill and B. Edwards, 216-224,

Brownlee, K. A., *Statistical theory and methodology in science and engineering,* 2nd edition, J. Wiley, New York, 590pp., 1965.

D'Amico, A. and P. Mazzetti (editors), *Noise in physical systems and 1/f noise - 1985*, North-Holland, New York, 531pp., 1986.

Gage, K. S., Evidence for a $k^{-5/3}$ law inertial range in mesoscale two-dimensional turbulence, *J. Atmos. Sci.*, **36**, 1950-1954, 1979.

Liu, C. H. and S. Kato, Eds., Technical and scientific aspects of MST radars, *Radio Sci.*, **20(6)**, 1129-1517, 1988

Lovejoy, S. and D. Schertzer, Scale invariance, symmetries, fractals, and stochastic simulations of atmospheric phenomena, *Bull. Am. Meteor. Soc.*, **67**, 21-32, 1986.

Mandelbrot, B. B., *Fractals : form, chance and dimension*, W. H. Freeman, San Francisco, 365pp, 1977.

Mandelbrot, B. B., *Fractal geometry of nature*, W. H. Freeman, San Francisco, 468pp, 1983.

Marple, S. L., *Digital spectral analysis with applications*, Prentice Hall, Englewood Cliffs, N.J., 492pp., 1987.

McHardy, I. and B. Czerny, Fractal X-ray time variability and spectral invariance of the Seyfert galaxy NGC5506, *Nature*, **325**, 696-698, 1987.

Papoulis, A., *Probability, Random Variables and Stochastic Processes*, 2nd Edition, McGraw-Hill, New York, 576pp., 1984.

Röttger, J, VHF radar measurements of small-scale and meso-scale dynamical processes in the middle atmosphere, *Phil. Trans. Royal Soc. Lond.*, A **323**, 611-628, 1987.

Voss, R. F., Fractals in nature : From characterization to simulation, in *The science of fractal images*, Eds. H. Peitgen and D. Saupe, Springer, New York, p. 21-70, 1988.

Tennekes, H. and J. L. Lumley, *A first course on turbulence*, MIT Press, Cambridge, MA, 300 pp., 1972.

VanZandt, T. E., A universal spectrum of buoyancy waves in the atmosphere, *Geophys. Res. Lett.*, **9**, 575-578, 1982.

MEASUREMENT OF LARGE-SCALE VERTICAL VELOCITY USING CLEAR-AIR DOPPLER RADAR

G.D. Nastrom
Department of Earth Sciences, St. Cloud State University
St. Cloud, MN 56301

J.L. Green, T.E. VanZandt, K. S. Gage, W.L. Clark
NOAA Aeronomy Laboratory, R/E/AL3
325 Broadway, Boulder, CO 80303

1. Introduction

Attempts to observe the vertical motion field at synoptic and larger scales with MST radars have been frustrated by the presence of geophysical "noise" in the data, consisting of contributions from small scales, which usually overwhelms any large-scale signal in the data. Two recent such studies are Nastrom, et al. (1985), and Larsen, et al. (1988), where more detailed discussion of the background and references to other work may be found. Briefly, all past studies were performed in regions where the noise produced by orographic effects could not usually be ignored, and the possibility existed that a station well-removed from such effects might be able to observe the large scale components in the wind field under more general conditions. Ongoing studies at the Flatland radar in central Illinois, USA, are testing this hypothesis, and an emerging result is that the vertical motion field is still dominated by scales smaller than synoptic even though orographic effects are evidently not present. This effect is clearly reflected in the power spectrum of observed vertical motions (Figure 1) as there is much more energy at periods less than an hour or so than at the longer periods commonly associated with synoptic-scale activity. While the high frequency variations in vertical velocity are apparently due to a field of propagating gravity waves which are Doppler shifted by the ambient horizontal wind field (VanZandt, et al., 1989), we expect that much of the energy at longer periods represents contributions from large-scale motion systems such as baroclinic storms. However, it is not obvious that temporal noise at a single station can in general be filtered to provide mean values consistent with a large spatial average (i.e., application of the Taylor hypothesis). Consequently, the observation of synoptic scale vertical motions, believed to be of the order of a few cm s^{-1}, may not be straightforward even at Flatland. The removal of orographic effects from the signal has simplified the problem to the extent that the nature of the other noise sources may now be more clearly identified. In this study we explore some preliminary aspects of these problems: first, we show that periods of enhanced variance of the vertical velocity during the interval studied are associated with the passage of
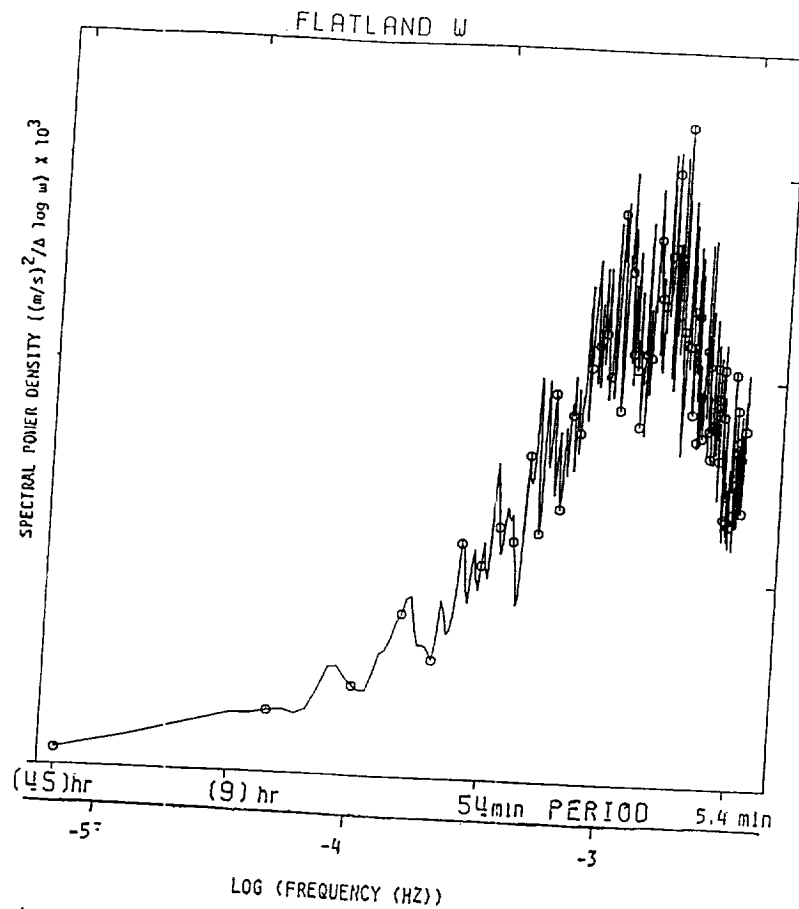
Figure 1. Average of 34 spectra of vertical velocity over 48-hour data periods at Flatland during March through September, 1987, in area preserving coordinates.

fronts at the surface, and identify a frontal signature that is sometimes present in the lower troposphere. Second, we illustrate the difficulties in verification of the Taylor hypothesis by comparing radar observed vertical motions with those deduced from the horizontal wind field derived from the twice daily NWS rawinsonde network, and discuss the problems associated with such a comparison.

2. Analysis

Time series of vertical velocity over Flatland during March 1987 are shown in Figure 2. As at other locations (e.g., Ecklund, et al., 1982), the presence of quiet and active periods is clearly visible , though the variance in all cases is less at Flatland than that at mountain sites (Green, et al., 1988). Along the bottom of Figure 2 letters have been entered to indicate when cold (c), warm (w), occluded (o), or quasi-stationary (qs) fronts passed or were in the vicinity of Flatland. Note that every active period is coupled with a front. While this coupling suggests the interesting notion that fronts are a source of gravity waves, it hinders the prospects for retrieving large-scale vertical motions from the Flatland data because the geophysical "noise" apparently increases just at those times when we hope to find a large-scale signal.

Next we will examine two cases in detail to illustrate two points: first, there is a frontal passage "signature" which is found in the vertical velocity time series in some cases; second, matching the signal at one station with a system which may be moving at an unsteady rate (as fronts and storms often move) and which may be decaying or developing at a rate which is only poorly defined by the 12-hourly radiosonde observation schedule is an extremely complex problem. Weather systems are fully three-dimensional phenomena which move and change with time. The Flatland radar provides a continuous record of the vertical motions over a single place. The morphology of the low-frequency signal in vertical velocity varies from case to case, depending upon the rate and consistency of the movement of the weather system and upon its rate of development or stage of maturity. In some cases the vertical velocity pattern seen by the radar is relatively clear and the synoptic feature easily discerned, while in other cases it is less well defined. We illustrate each of these points with specific examples.

First, we consider a relatively clear frontal passage signature. On 5 March a weak low was over western Illinois at 06 UTC with a warm front moving northward across the Flatland area. The front passed near 05 UTC based on surface observations at Champaign airport, although the National Weather Service analysis indicated it was weak and nearly dissipated by 12 UTC (Figure 3). The time series of vertical velocities display upward motion ahead of the surface frontal passage and downward motions behind it below 5 km, as seen in Figure 2 and as shown more clearly by the analysis of hourly mean velocities in Figure 4. This pattern was noticed by Larsen and Rottger (1982) in connection with the passage of a warm front, and we have seen it in other cases of
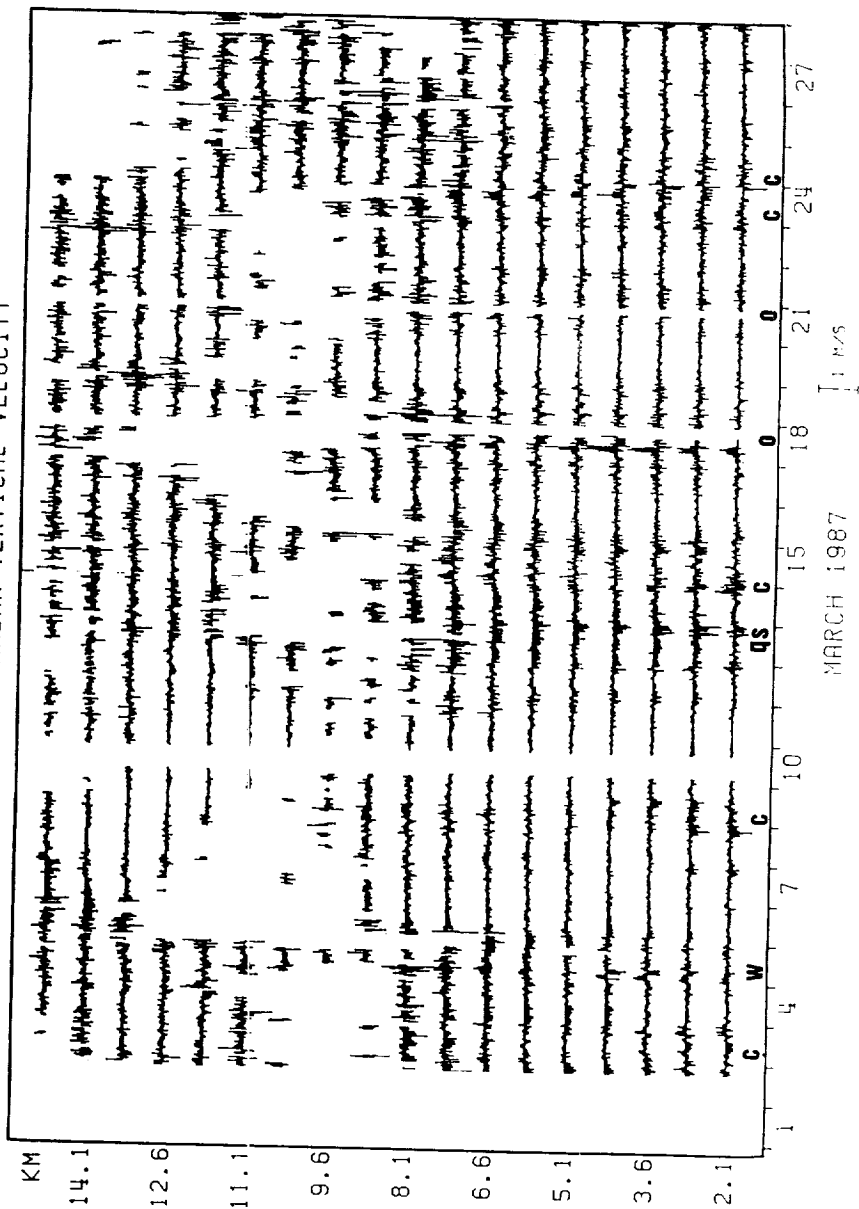
Figure 2. Time series of 15-minute average vertical motion over Flatland during March 1987. The letters along the bottom indicate times when fronts passed or were near Flatland.

1200 UT, MARCH 5, 1987
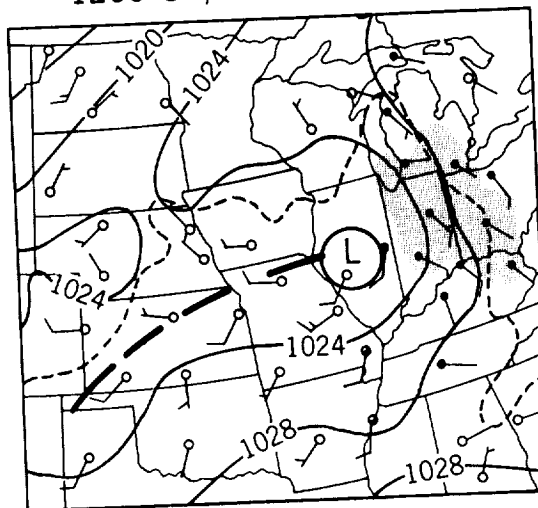
Figure 3. Synoptic weather map for 5 March 1987, 12 UTC.

FLATLAND VERTICAL VELOCITY (CM/S)
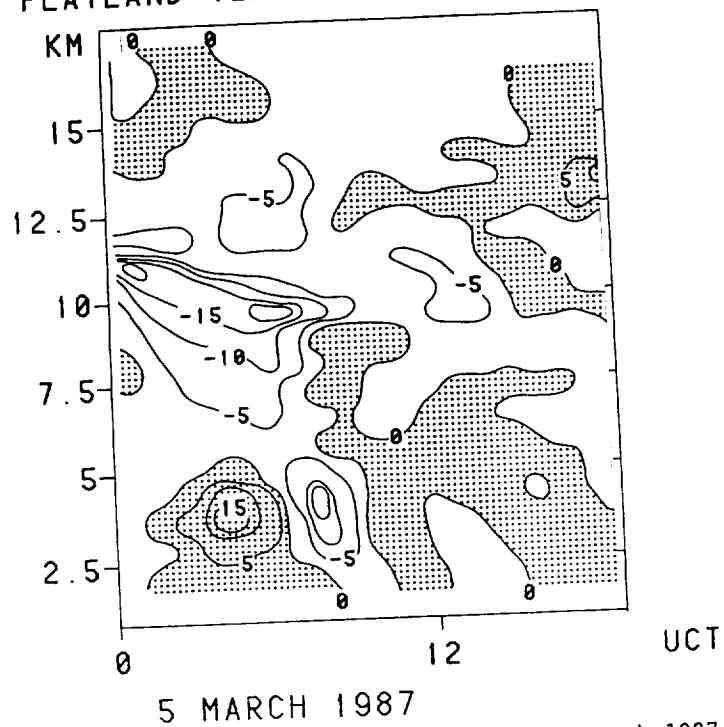
5 MARCH 1987

Figure 4. Vertical motions over Flatland on 5 March 1987. Upward is positive.

moving fronts. While it seems unlikely that the regions of
upward and downward motion, located only about 4 hours (150 km if
the front moved at 10 m s^{-1}) apart, are due to the front itself
as envisioned in the Norwegian frontal model, we suggest it is a
typical frontal signature. Perhaps it is due to a gravity wave
launched by the front and propagating along with it, similar to
the events discussed by Gall, et al.(1988).

A front is in many respects a mesoscale feature, yet in
order to compute vertical motions aloft from conventional data we
must rely on the radiosonde network which reflects only larger
scales. For example, around Flatland the triangle of radiosonde
stations at Peoria, Salem and Dayton has an average leg-length of
379 km; which defines the smallest horizontal scale observable
with this network over Flatland. The vertical motions computed
using the continuity equation applied to the rawinsonde data over
this triangle for 5/00 and 6/00 UTC; using Ekman pumping as a
lower boundary condition following Nastrom, et al.(1985), are
compared with radar time-averages in Figure 5. The radar data
represent 6-hour averages and the error bars are the standard
error of the mean. At 5/00 UTC the agreement appears
satisfactory and at 6/00 UTC it appears excellent. However, the
period centered at 6/00 UTC is depicted by plus-signs, and that
centered at 6/03 UTC by triangles. The point of this case is
that the rawinsonde based values are mean values over a very
large area (of course, the radiosonde data contain errors and
noise which we have ignored here), and the radar time mean is for
only one position inside the triangle, and that even though the
radar is near the center of the triangle the time-mean and the
space-mean do not necessarily match. This lack of agreement does
not imply any error in either the radar data or the radiosonde
data, but rather points to the frequent mismatch of the scales of
motion they represent. In the next case we will use NMC data to
further illustrate this notion of "shooting at a moving target".

On March 18th an occluded front approached Flatland from the
southwest, as illustrated in Figure 6. The mean vertical motions
during this period were upward as seen in Figure 2 and also in
Figure 7. Green, et al.(1988), used proxy indicators of vertical
motions, such as clouds and precipitation from surface reports
and widespread echoes from storm surveillance radars, to
corroborate the upward motions observed by the radar. Also, they
noted that the 12-hour forecasts from the NMC model showed that a
region of large vertical motion apparently passing Flatland
during this period. Computation of diagnostic vertical motions
specific to the Flatland location suitable for comparison with
time-mean radar observations was outside the scope of their
study.

We have computed vertical motions over Flatland based on the
NMC gridded analyses using the kinematic method, the adiabatic
method, and the adiabatic quasi-geostrophic omega-equation
method. Details follow Nastrom, et al.(1985). The results for
18/12 UTC are compared with 9-hour averages from the radar in
Figure 8. There is general agreement among all curves that the
motion is upward at several cm s^{-1}, although at any height the
comparison is not exact. We have included radar curves for two
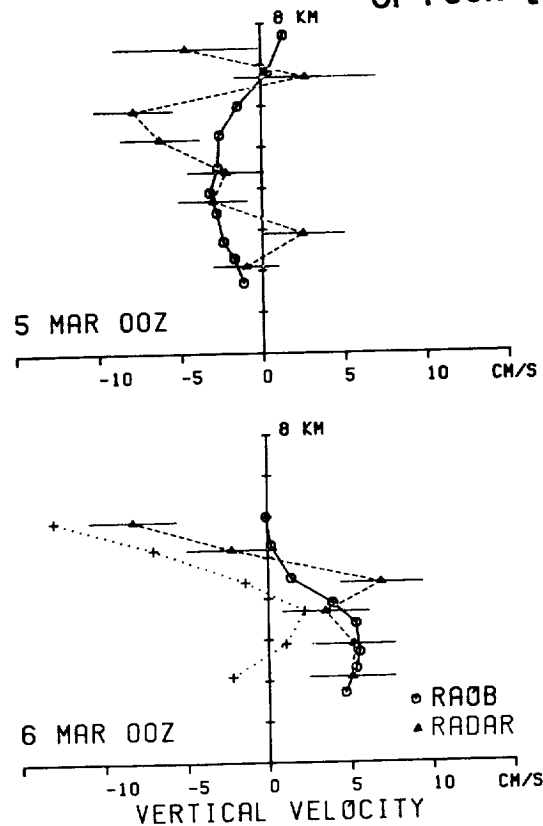
Figure 5. Vertical motions computed using the continuity
equation and horizontal winds from the radiosonde station
triangle around Flatland compared with 6-hourly mean radar
motions. See text.
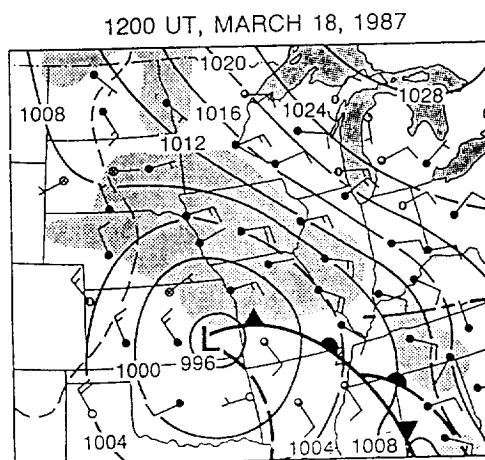
Figure 6. Synoptic weather map for 18 March 1987, 12 UTC.
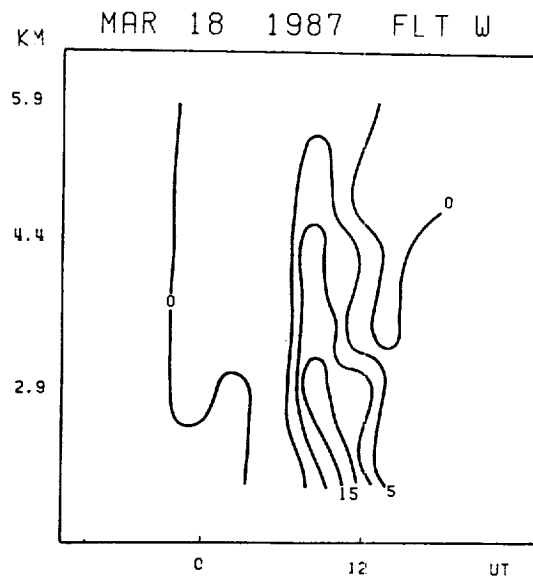
Figure 7. Vertical motions over Flatland on 18 March 1987.
Upward is positive.
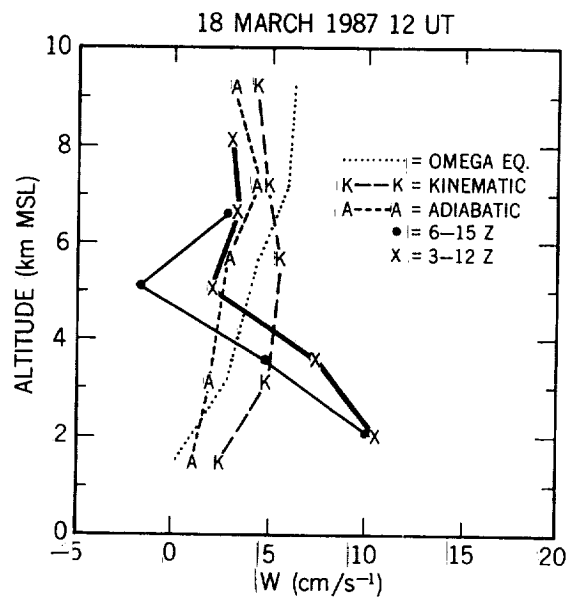
Figure 8. Vertical motions computed from NMC gridded analyses
compared with 9-hourly mean radar motions. See text.

overlapping time periods as the radar is representative of only a portion of one NMC grid square and the storm is moving in this square throughout the averaging period. The large difference between the radar means and the indirect values at lowest heights may reflect a difference in the scales each data type represents, or it may be due to limitations of the indirect methods, such as the neglect of latent heat release and the use of linear interpolation.

3. Conclusion

The Flatland radar experiment has provided copious data on the vertical motions over flat, mid-continental temperate latitude terrain, free from the effects of mountains. Preliminary studies of this data set have begun to shed light on the nature of the motion field in the absence of nearby sources of orographic effects. In particular, qualitative comparison of the time series of vertical motions with those times when surface fronts passed or were near Flatland indicates an association with active periods throughout the troposphere and sometimes into the stratosphere of large lateral extent. Further, the passage of fronts is often accompanied in the lower troposphere with a region of upward motion ahead of and downward motion behind the front, creating a signature of frontal passage.

Although these effects related to synoptic-scale features are easily observable, the observation of the large-scale vertical motion itself in the midst of larger amplitude signals due to small-scale motions is difficult. The absence of orographic noise in the signal has greatly facilitated the understanding of other aspects of the signal, such as the effect of doppler-shifted gravity waves, and this understanding may contribute to the eventual understanding of the large scale signal as well.

Verification of the Taylor hypothesis through comparison of temporal and spatial averages is also difficult. In particular, it has become clear that the velocity and rate of decay or development of a given system will determine the horizontal scale to which a temporal average at the radar site can be properly compared. Only in certain cases will this scale match that of the radiosonde network.

Each of these questions has important implications for the future application of MST radars. It appears that a very promising avenue for future progress is using multiple radars to assess spatial correlation features.

4. References

Ecklund, W. L., K. S. Gage, B. B. Balsley, R. G. Strauch, and J. L. Green, 1982: Vertical wind variability observed by VHF radar in the lee of the Colorado Rockies. Mon. Wea. Rev., 110, 1451-1457.

Gall, R. L., R. T. Williams, T. L. Clark, 1988: Gravity waves generated during frontogenesis. J. Atmos. Sci., 45, 2204-2219.

Green, J. L., K. S. Gage, T. E. VanZandt, W. L. Clark, J. M. Warnock, and G. D. Nastrom, 1988: Observations of vertical velocity over Illinois by the Flatland radar. Geophys. Res. Lett., 15, 269-272.

Larsen, M. F., and J. Rottger, 1982: VHF and UHF Doppler radars as tools for synoptic research. Bull. Amer. Meteor. Soc., 63,996-1008.

Larsen, M. F., J. Rottger, and T. S. Dennis, 1988: A comparison of operational analysis and VHF wind profiler vertical velocities. Mon. Wea. Rev., 48-59.

Nastrom, G. D., W. L. Ecklund, and K. S. Gage, 1985: On the direct measurement of large-scale vertical velocities using clear-air Doppler radars. Mon. Wea. Rev., 113, 708-718.

VanZandt, T. E., G. D. Nastrom, J. L. Green, and K. S. Gage, 1989: The spectrum of vertical velocity from Flatland radar observations, Preprint Vol., 24th Conf. on Radar Meteorology, Tallahassee, Amer. Meteor. Soc., Boston.

THE SPECTRUM OF VERTICAL VELOCITY FROM FLATLAND RADAR OBSERVATIONS

T. E. VanZandt[1] G. D. Nastrom[2] J. L. Green[1] and K. S. Gage[1]

[1]Aeronomy Laboratory
National Oceanic and Atmospheric Administration
Boulder, Colorado 8030

[2]Department of Earth Sciences
St. Cloud State University
St. Cloud, Minnesota 56301

1. INTRODUCTION

The clear-air Doppler radar technique (also called the wind-profiling or MST radar technique) has been applied to a wide range of meteorological problems since its development by WOODMAN and GUILLEN (1974) and GREEN et al. (1975). Nevertheless, research on some important problems has been frustrated by the location near mountains of most such radars. The resulting geophysical noise is especially serious for studies of the vertical velocity w.

When the background wind was light RÖTTGER (1981) and ECKLUND et al. (1986) found that frequency spectra of w were flat at frequencies less than the buoyancy frequency and broke to a steep negative slope at higher frequencies. Very similar w spectra are observed in the ocean, which GARRETT and MUNK (1972, 1975) modelled as a spectrum of internal gravity waves. Thus, we can be confident that the light-wind spectra are due to gravity waves.

But when the background wind speed was large at stations near mountains, ECKLUND et al. found that the spectral amplitude increased and the shape changed so as to become quite inconsistent with the light-wind spectra, as shown in Figure 1. They suggested that these changes might be due to mountain waves. Also, NASTROM et al. (1985) found that large-scale vertical velocities due to synoptic-scale motions could be extracted from the data when the wind blew toward the mountains from the plains, but not when the wind blew over the nearby Rocky Mountains in Colorado.

It appeared, therefore, that a clear-air Doppler radar located in flat terrain might be used to study vertical gravity wave motions and large-scale vertical motions. For this reason we have constructed the Flatland radar near Champaign-Urbana, Illinois. In this paper we show that the behavior of w over flat terrain is indeed quite different from that near mountains.

2. DATA AND METHODS

The Flatland radar is located about 8km west of Champaign-Urbana, Illinois, at 40.05°N, 88.38°W, 212m above sea level. It operates at a frequency of 49.8MHz. The antenna is a 60mx60m array of coaxial-collinear dipoles, with a two-way, half-power to half-power beamwidth of 3.2°. The data analyzed here were taken using 750m pulse lengths and range gates centered from 1.4 to 19.4km, but useful data were usually obtained only from 2.2 to 16.4km, with often a region of missing echoes just below the tropopause. The Doppler spectra have 128 points with a velocity resolution of 5cm/s and an unaliased velocity range of ±3.2m/s. Further details, including examples of the data, are given in GREEN et al. (1988).
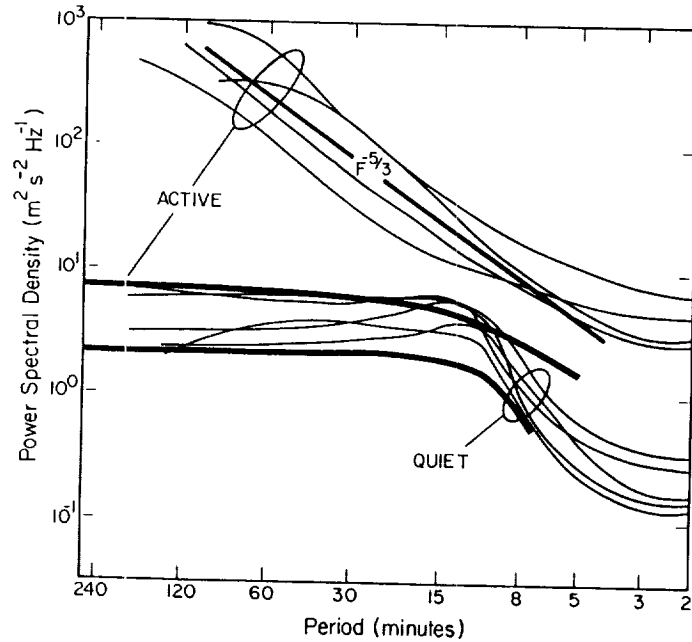
Fig. 1. Frequency spectra of w in the troposphere. The thin curves are from southern France (ECKLUND et al., 1986) and the two thick curves are from Flatland. The spectra labeled QUIET and ACTIVE were obtained when the wind speed was ≤ 5 and ≥ 20m/s, respectively.

The vertical velocity was measured about every 2 1/2min from 2 March 1987 until April 1988, with brief interruptions due to power failures, etc. and a break of about six weeks in the summer of 1987. Power spectra were derived from time series of two different lengths, 6h and 45h. If more than three successive observations were missing or eliminated by the quality control procedures described in GREEN et al. (1988), that is, if there was a gap greater than 10min, then the time series was rejected. The data in the accepted time series at each altitude were then linearly interpolated to uniform 153s intervals. The mean and a linear trend were removed and power spectra were derived by Fourier transform of the residuals.

Horizontal wind and temperature profiles were obtained from routine National Weather Service radiosonde ascents from Peoria, Illinois, about 130km northwest of the Flatland radar. The data were obtained from the National Climatic Data Center.

3. RESULTS: 6h SPECTRA

We computed 6h spectra from March through May centered on the nominal times of the routine radiosonde balloons, 0000 and 1200Z (1800 and 0600 90°W time). Because the number of individual 6h spectra is large, we are able to to study the dependence of the spectra on altitude, wind speed, buoyancy frequency, etc.

In Figure 2 the spectra are stratified by altitude from 2.2 to 15.6km.
For each mean spectrum the number N of individual spectra that enter the
average and the variance VAR in (cm/s)² are given in the table in the upper
righthand corner. (Note that the 15.6km spectrum is unreliable because N is
only 4.) During this period the average tropopause altitude was about 12km.
There is no discernible altitude variation within the troposphere and the
stratosphere, but at long periods the spectral energy density in the tropo-
sphere is about a factor of two larger than in the stratosphere.
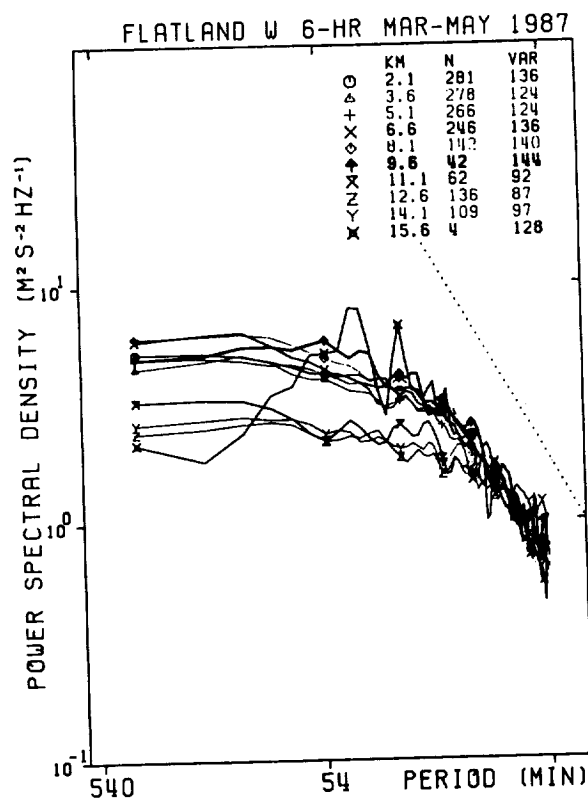
Fig. 2. Frequency spectra stratified by altitude. The mean
spectrum at 15.6km is noisy because it includes only 4 spectra.

These spectra closely resemble the QUIET spectra at ALPEX in Figure 1,
even though the mean horizontal wind for the present spectra was about 15m/s,
and they are quite different from mean spectra at sites near mountains (see
BEMRA et al., 1985; KUO et al., 1985; ECKLUND et al., 1986; and LARSEN et al.,
1988).

We have also sorted the spectra at 3.7 and 5.2km according to the buoyancy
frequency N_B over the layer from 700hPa to 500hPa (about 3.0 to 5.5km) at
Peoria. There was not any detectable difference between the mean spectra
corresponding to the upper and lower quartiles, with N_B = 13.1 and
9.6×10^{-3} rad/s, respectively, a ratio of 1.4. This is surprising, since in Fig.
2 the ratio of 1.8 between the stratosphere and the troposphere causes very
noticable differences.

In Figure 1 the mean of the Flatland spectra for quiet and active condi-
tions is superimposed on the ALPEX spectra. Under all wind speeds the Flatland
spectra resemble the QUIET ALPEX spectra.

This behavior is considered in more detail in Figure 3, where the spectra
at 3.7km are plotted in five bins as a function of the horizontal wind speed WS
at the same altitude from Peoria, with boundaries at 0, 3.5, 5.5, 11, and
22m/s. These boundaries were selected so that each bin contains at least ≈10
spectra and so that the boundaries lie near minima in the histograms of wind
speeds. The spectra have been multiplied by WS^2 to separate them visually and
divided by VAR to facilitate comparison with model Doppler-shifted spectra in
the next section.
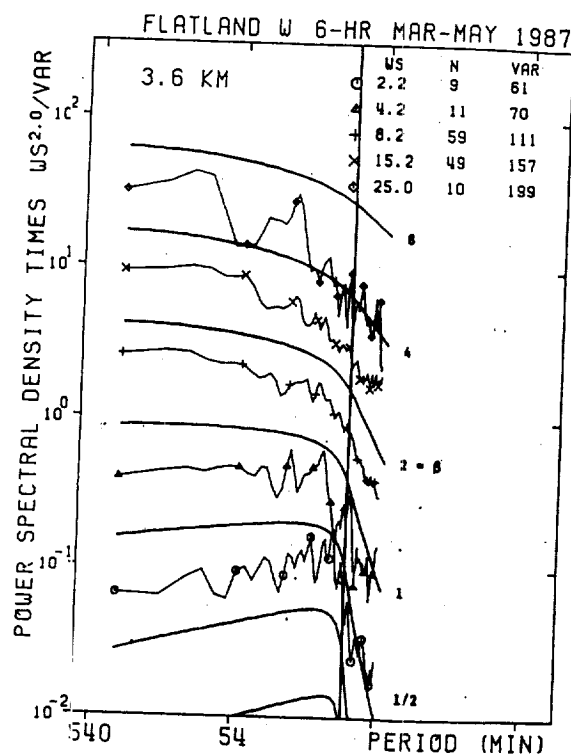
Fig. 3. Observed spectra and model Doppler-shifted spectra
stratified by wind speed. The observed and model spectra
have been multiplied by WS^2 and β^2, respectively, and divided
by the variance.

It is evident that the shape of the spectra changes systematically with
increasing WS. As WS increases, the slope becomes more negative at periods
longer than the buoyancy period $1/N_B$ and less negative at shorter periods, so
that the spectra become flatter. The spectra at other altitudes behave in much
the same way. It will be shown in the next section that this behavior is
consistent with Doppler-shifted spectra of gravity waves.

Figure 4 shows that VAR increases as a power of WS. This behavior will be discussed more quantitatively in the next section.
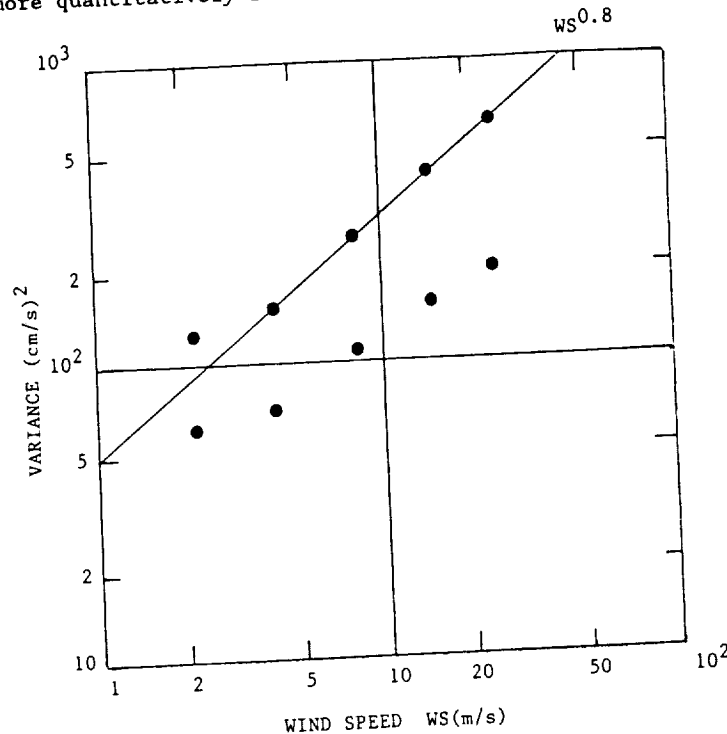
Fig. 4. Variance $(cm/s)^2$ versus wind speed WS (m/s). The lower set of points are the observed variances VAR. The upper set fitted by the straight line are the total variances estimated using the Doppler-shifting model.

4. COMPARISON WITH MODEL DOPPLER-SHIFTED GRAVITY WAVE SPECTRA

Models for Doppler-shifted atmospheric gravity wave spectra have been presented by SCHEFFLER and LIU (1986) and by FRITTS and VANZANDT (1987). In this paper we have chosen to use the approach of FRITTS and VANZANDT, because we are more familiar with it. Their model has been programmed numerically in order to be able to investigate the effect of their approximations to the physics of gravity waves and to the assumed intrinsic spectrum. We found that the physical approximations had little effect on the results. On the other hand, some of the approximations to the intrinsic spectrum are important.

FRITTS and VANZANDT used $p = 2$ in order to obtain solutions in closed form. We find that in order for the calculated spectra to agree with the observed spectra, p must be nearer 5/3, as is commonly observed.

We also considered two different extreme azimuthal distributions. First, we used the approximation of FRITTS and VANZANDT, with a fraction a_+ of the wave energy propagating in the azimuth of the background wind vector and a fraction $1 - a_+$, in the opposite direction. Alternatively, we assumed that a fraction a_+ was uniformly distributed in the semicircle containing the wind vector and a fraction $1 - a_+$, in the opposite semicircle. We found that if a_+

$\approx 1/2$, then either distribution can fit the observed spectra, but that if a_+ is not near $1/2$, then the model spectra cannot fit the observed spectra.

The model Doppler-shifted spectra depend on the wind speed through the scaled background wind speed $\beta = WS/c_*$, where c_* is the characteristic horizontal phase speed, estimated to be ≈ 5.5m/s in the troposphere (FRITTS and CHOU, 1987).

In Figure 3 the model Doppler-shifted spectra are shown by the curves labeled with β. In order to scale them in the same way as the observed spectra they have been multiplied by β^2 and divided by the variance over the same frequency range as the observed spectra. It is evident that the shape of the model spectra changes in the same way as the observed spectra. The results at other heights are similar. From this we conclude that the observed spectra are Doppler-shifted gravity wave spectra.

The Doppler-shifting model assumes that the shape of the intrinsic spectrum is invariant, independent of altitude, wind speed, wind shear, etc. However, agreement with the observed spectra could be achieved even if the intrinsic shape did vary somewhat at large wind speeds, since at large β the intrinsic spectrum is strongly smeared in frequency.

VAR for the observed spectra was plotted versus WS in Figure 4. However, VAR is only a fraction of the total variance in the gravity wave field, since part of the wave energy has been Doppler-shifted outside the observed frequency range, especially toward higher frequencies. The total variances estimated using the model are also plotted in Figure 4.

For WS ≥ 3.5m/s the total variance varies almost linearly with WS, approximately as $WS^{0.8}$, or, to compare variance with variance, as $(WS^2)^{0.4}$. This increase must be taken into account when comparing spectra taken at different wind speeds.

It is important to note that if the intrinsic wave spectrum were generated at an altitude very different from 3.6km or in a location very much farther away than Peoria, then the Doppler-shifted spectra and the total variance could hardly depend so strongly on the local wind speed. The implication that the gravity wave field is locally generated is at variance with usual ideas concerning the sources of the gravity wave field, and it may have important consequences for the physics of the field.

5. CONCLUSIONS

We find that the high-frequency vertical velocity spectra are essentially invariant in the troposphere and in the stratosphere, but that the spectral density is about a factor of two larger in the troposphere. The spectra stratified by wind speed are quite consistent with Doppler-shifted gravity-wave spectra. This implies that the shape of the intrinsic spectrum is only weakly dependent on the wind speed. The variance of the spectra increases about as 0.8 power of the wind speed at the same altitude at Peoria, 130km away. The invariance of the shape of the intrinsic spectrum and the strong dependence of the variance on the local wind speed indicates that the gravity wave field is generated at about the same altitude and not very much farther away than Peoria.

6. ACKNOWLEDGMENTS

7. REFERENCES

Bemra, R. S., P. K. Rastogi, and B. B. Balsley (1986), A study of gravity-wave spectra in the troposphere and stratosphere at 5-min to 5-day periods with the Poker Flat MST radar, Handbook for MAP, 20, 216-224.

Ecklund, W. L., K. S. Gage, G. D. Nastrom, and B. B. Balsley (1986), A preliminary climatology of the spectrum of vertical velocity observed by clear-air Doppler radar, J. Clim. Appl. Meteorol., 25, No. 7, 885-892.

Fritts, D. C., and H.-G. Chou (1987), An investigation of the vertical wavenumber and frequency spectra of gravity wave motions in the lower stratosphere, J. Atmos. Sci., 44, 3610-3624.

Fritts, D. C., and T. E. VanZandt (1987), Effects of Doppler shifting on the frequency spectra of atmospheric gravity waves, J. Geophys. Res., 92, 9723-9732.

Garrett, C., and W. Munk (1972), Oceanic mixing by breaking internal waves, Deep-Sea Res., 19, 823-832.

Garrett, C., and W. Munk (1975), Space-time scales of internal waves: a progress report, J. Geophys. Res., 80, 291-297.

Green, J. L., J. M. Warnock, R. H. Winkler, and T. E. VanZandt (1975), Studies of winds in the upper troposphere with a sensitive VHF radar, Geophys. Res. Lett., 2, 19-21.

Green, J. L., K. S. Gage, T. E. VanZandt, W. L. Clark, J. M. Warnock, and G. D. Nastrom (1988), Observations of vertical velocity over Illinois by the Flatland radar, Geophys. Res. Lett., 15, 269-272.

Kuo, F.-S., H.-W. Shen, I-J. Fu, J.-K. Chao, J. Röttger, and C.-H. Liu (1985), Altitude dependence of vertical velocity spectra observed by VHF radar, Radio Sci. 20, No. 6, 1349-1354.

Larsen, M. F., J. Röttger, and D. N. Holden (1987), Direct measurements of vertical velocity power spectra with the SOUSY-VHF-radar wind profiler system, J. Atmos. Sci., 44, 3442-3448.

Nastrom, G. D., W. L. Ecklund, and K. S. Gage (1985), Direct measurement of large-scale vertical velocities using clear-air Doppler radars, Monthly Weather Rev., 113, 708-718.

Röttger, J. (1981), Preprint volume, 20th Conference on Radar Meteorology, Boston, MA, Wind Variability in the stratosphere deduced from spaced antenna VHF radar measurements, American Meteorological Soc., Boston, MA, 22-37.

Scheffler, A. O., and C.-H. Liu (1988), The effects of Doppler shift on the gravity wave spectra observed by MST radar, J. Atmos. Terr. Phys., 48, 1225-1231.

Woodman, R. F., and A. Guillen (1974), Radar observations of winds and turbulence in the stratosphere and mesosphere, J. Atmos. Sci., 31, 493-505.

A FIRST LOOK AT CONVECTION WAVES OBSERVED BY AN ST RADAR

Kenneth S. Gage, Warner L. Ecklund and David A. Carter

Aeronomy Laboratory
National Oceanic and Atmospheric Administration
Boulder, Colorado 80303

1. INTRODUCTION

KUETTNER et al (1987) have recently drawn attention to the occurrence of internal gravity waves in the free troposphere above the convectively active planetary boundary layer. These waves, commonly referred to as "convection waves", appear to have their origin in the free troposphere when the planetary boundary layer is disturbed by either two-dimensional convective rolls or three-dimensional convection. In some respects the convection waves resemble lee waves that are forced by the flow over rough terrain. Convection waves could be an effective agent for momentum transfer in the free atmosphere even in regions of relatively flat terrain. If they are as ubiquitous as some early studies seem to indicate, they may play an important role in the momentum budget of the free atmosphere.

Aircraft observations of convection waves have been conducted for several years and the results are summarized in KUETTNER et al. (1987). Related numerical experiments have been reported by CLARK et al. (1986). Typical results indicate that convection waves occur in synoptic regimes that favor active convection in the planetary boundary layer and considerable vertical shear in the horizontal wind through the low to mid-troposphere. Under these circumstances lower tropospheric convection provides an undulating lower boundary surface to the flow in the free troposphere above. Waves forced in the free troposphere by vertical displacements above the convectively active planetary boundary layer can propagate to tropopause altitudes within an hour. Under favorable conditions these convection waves become trapped in the troposphere and may resonantly develop into preferred modes that are highly tuned to their environment.

Much of what we know of convection waves has been learned from a series of case studies performed by NCAR scientists from flight data of individual events. Typical characteristics for convection waves (KUETTNER et al. 1987) are wavelengths of 5-15 km, and vertical motion amplitude of 1-3 ms^{-1}. The waves often are observed to altitudes greater than 9 km and they tend to occur when vertical wind shear exceeds $3 \times 10^{-3} s^{-1}$.

The NCAR studies used aircraft to fly to regions where synoptic conditions favored the formation of convection waves. When present, convection waves should also be observable by wind-profiling Doppler radar. For this study we examined the vertical velocity data observed by the VHF radar that was located near Liberal, Kansas during the Pre-Storm experiment (AUGUSTINE AND ZIPSER, 1987). Vertical velocity observations from this radar were made throughout most of May and June 1985. During this period several episodes of possible convective wave activity could be identified in the observations. However, the clearest example was found at the end of the experiment on 29 June 1985.

2. THE VHF RADAR LOCATED NEAR LIBERAL, KANSAS

The Aeronomy Laboratory participated in the Pre-Storm experiment by providing a 50-Mhz wind-profiling Doppler radar. The radar provided by the Aeronomy Laboratory had been constructed for operation on Christmas Island. The Pre-Storm Experiment in the spring of 1985 provided a convenient test for the

ORIGINAL PAGE
BLACK AND WHITE PHOTOGRAPH

VHF radar before it was shipped to Christmas Island. The site that was selected for the VHF radar is located on the Kansas-Oklahoma border near the town of Liberal, Kansas. The 50-Mhz antenna shown in Figure 1 is a phased array (100 m x 100 m) similar to that used in the Platteville radar described by ECKLUND et al (1979). The VHF radar was comprised of three fixed beams. One beam was directed vertically and the remaining two beams were directed 15° off-Zenith in the north-south and east-west planes. Peak transmitted power was 40 kW and average power was 200 Watts. The pulse width was 4 microseconds which corresponds to a range resolution of 600 m.

Figure 1. The VHF radar located near Liberal, Kansas.

During the Pre-Storm Experiment the radar was operated in the full 3-beam mode giving continuous measurements of horizontal and vertical velocities. At the end of the experiment the radar was operated for several days in a vertical-only mode. It was operating in the vertical-only mode on 29 June 1985 for the observations presented here.

3. OBSERVATIONS OF CONVECTION WAVES ON 29 JUNE 1985

Atmospheric gravity waves are commonly observed in multi-height time series of vertical velocities measured by wind-profiling Doppler radars. Examples can be found in ECKLUND et al (1981, 1982, 1986) and GAGE et al (1981). Most of these observations were made by radars located in or near regions of mountainous terrain and were influenced by lee waves. Observations over flat terrain have recently been reported by GREEN et al (1988) using the Flatland Radar located in central Illinois. The terrain near Liberal, Kansas is also very flat so that the observations presented here should not have been influenced by orographically-generated lee waves.

Multi-height time series of vertical velocities observed by the VHF radar are shown in Figure 2 and Figure 3. The observations contained in Figure 2 show the vertical velocities measured above the radar for the entire day. While there is some evidence of activity before noon, the major activity commences about 1300 CST. This activity appears to start at the lowest heights

386

just prior to 1300 and by 1500 extends throughout the troposphere. The tropopause is located near 12 km and there is little evidence of the activity extending into the lower stratosphere. A clear pattern of quasi-monochromatic waves can be seen in Figure 2 between 1800 and 2000. These waves are shown in greater detail in Figure 3. The waves achieve their maximum amplitude of about 2 ms^{-1} just after 1900 CST. While the waves show some amplitude variation with altitude there does not appear to be much phase change with altitude. The waves have a period of close to 20 minutes and achieve their maximum amplitude near 8km.

LIBERAL ST RADAR
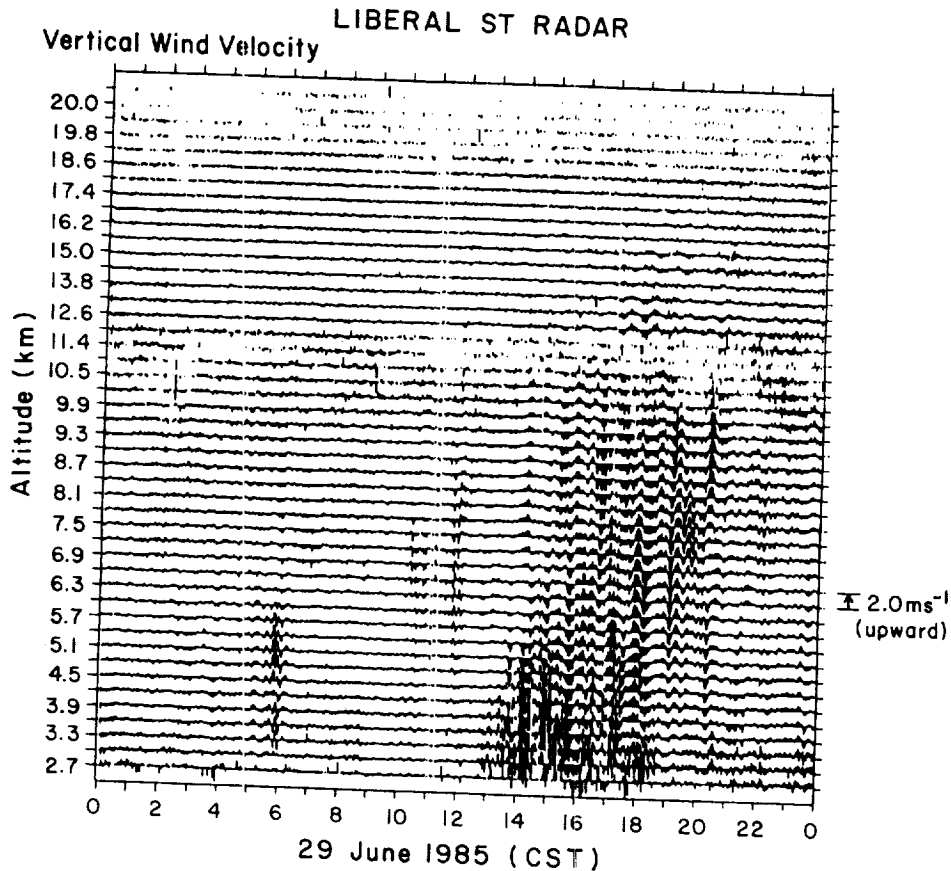
Figure 2. Multi-height time series of vertical velocities observed near Liberal, Kansas on 29 June 1985.

4. SYNOPTIC SETTING

The waves observed on 29 June 1985 occurred on a hot, dry day. At 0950 CST surface observations at Liberal, Kansas indicated a temperature of 84°F and dew point temperature of 48°F. At 1545 the surface temperature had risen to 99°F and the dew point temperature was 54°F. Broken clouds were reported at 10,000 and 20,000 feet.

LIBERAL ST RADAR

Vertical Wind Velocity
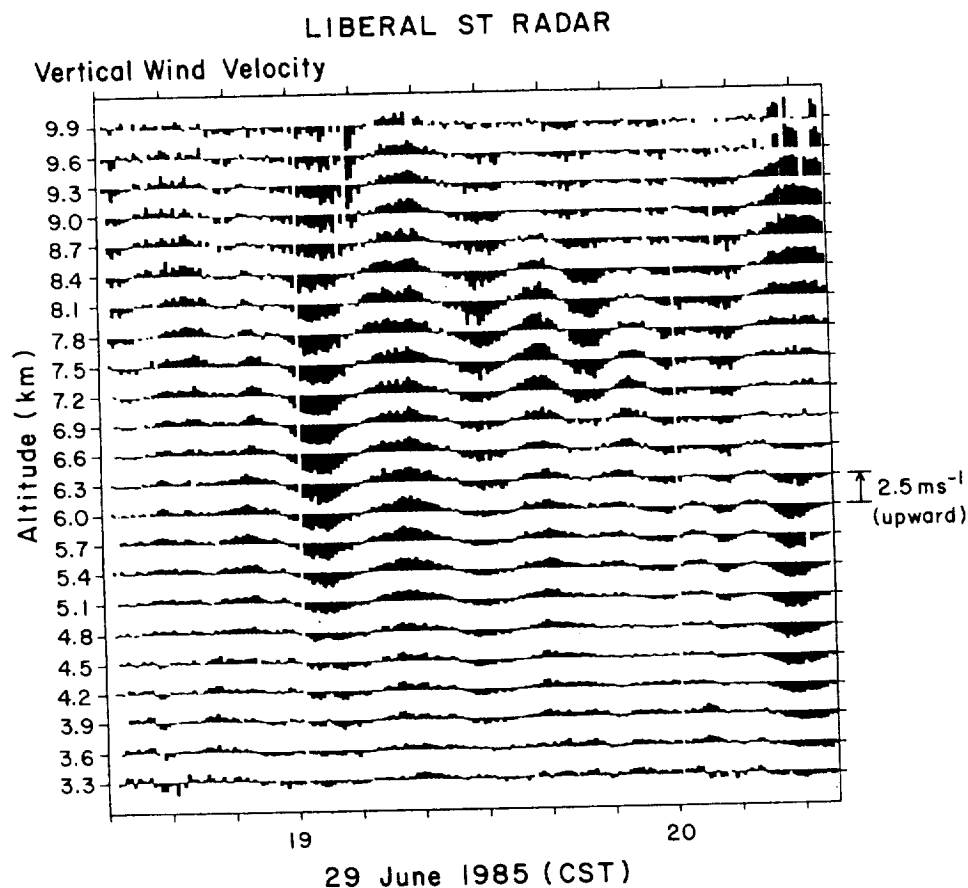
29 June 1985 (CST)

Figure 3. Convection waves seen in multi-height time series of vertical velocities near Liberal, Kansas during the afternoon of 29 June 1985.

Synoptic maps for 850 mb and 500 mb are shown in Figure 4 and Figure 5, respectively. A thermal low circulation is evident at 850 mb over the southwestern U.S. Southerly flow prevails east of the low center in the Texas-Oklahoma Panhandle region. At 500 mb a weak ridge is located over the Rocky Mountain states and the winds over the Texas-Oklahoma Panhandle are from the northwest. The wind reversal evident between these two levels can be seen clearly in the 30 June, 00 UT (29 June, 1800 CST) wind sounding for Dodge City, Kansas, reproduced in Figure 6.

A satellite photograph of visible clouds at 2330 UT is shown in Figure 7. A few isolated convective cloud masses are evident over eastern New Mexico, northern Texas, western Kansas and western Nebraska. The central U.S. is relatively free of clouds.
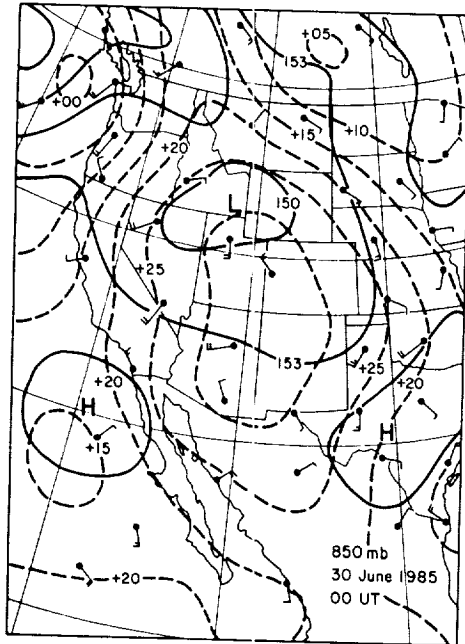
Figure 4.   Synoptic analysis for
850 mb at 00 UT on 30 June 1985.
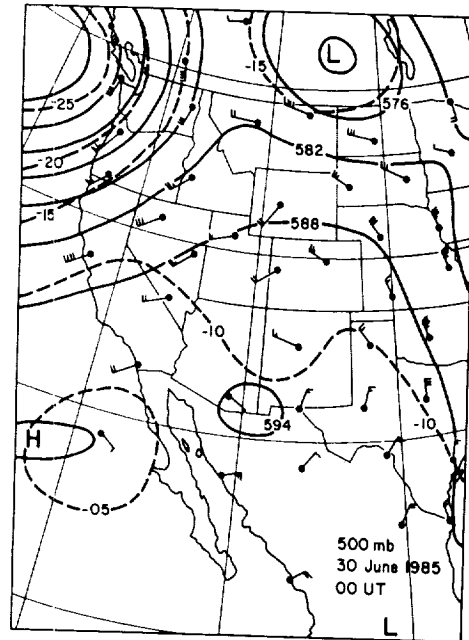
Figure 5.   Synoptic analysis for
500 mb at 00 UT on 30 June 1985.
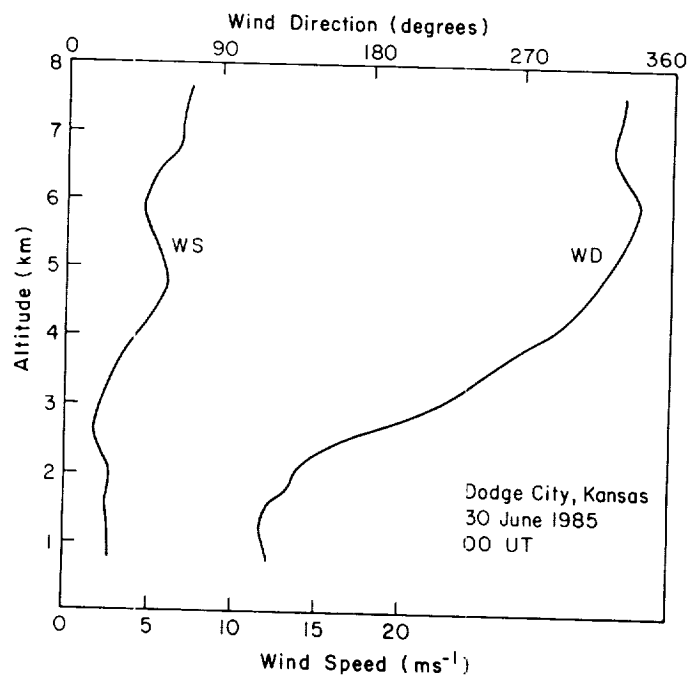
Figure 6.   Vertical profile of wind speed and direction
obtained at 00 UT at Dodge City, Kansas.
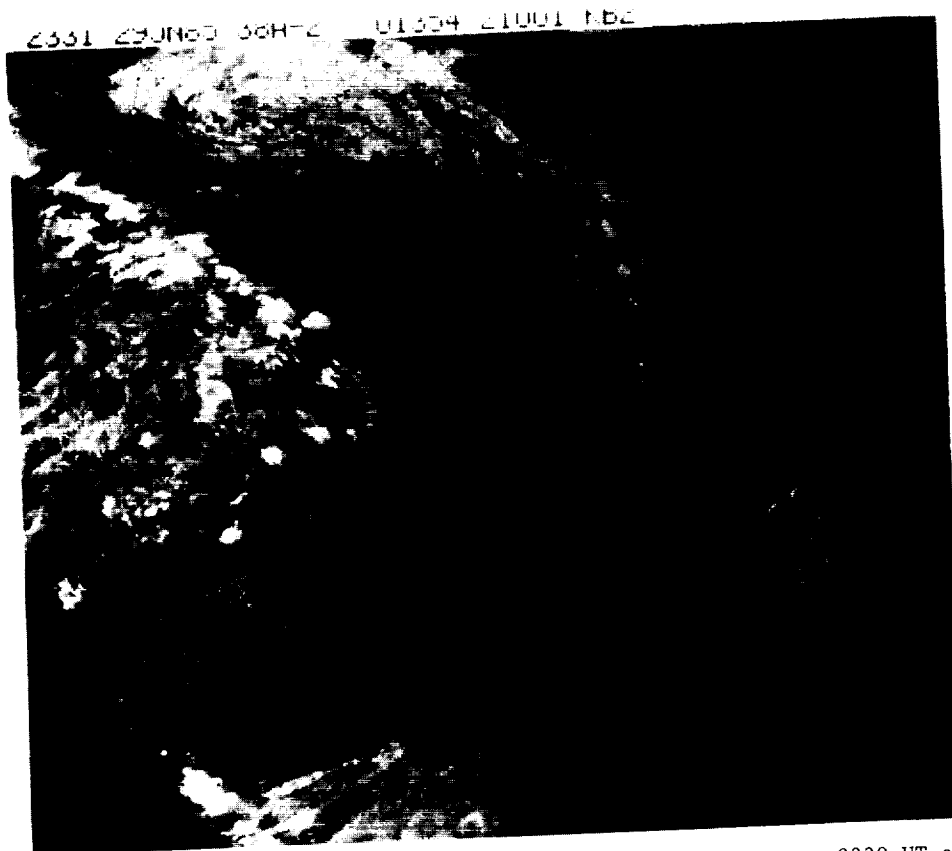
Figure 7. Visible satellite imagery for the Central U.S. at 2330 UT on
29 June 1985.

5. INTERPRETATION

The synoptic conditions on 29 June 1985 favored the development of convec-
tion waves over western Kansas and Oklahoma. A well developed southerly flow
over this region was overlain by a northwesterly flow at mid tropospheric
altitudes. Warm surface temperatures and the relative lack of clouds as-
sociated with the dry atmosphere led to intense convection in the planetary
boundary layer.

Radar observations of convection waves presented here complement the
aircraft observations reported by KUETTNER et al (1987). The aircraft samples
only one altitude but gives an excellent spatial picture of the waves. The
radar gives excellent temporal resolution of the wave motion simultaneously at
many altitudes, but only at one location. If it is assumed that the aircraft
and radar are looking at the same general phenomenon, it is possible to draw
some tentative conclusions concerning the nature of the waves that are being
observed by the radar.

Since the background wind changes with altitude, vertically-propagating
waves will be Doppler shifted as discussed, for example, by BRETHERTON (1969)
and GAGE (1989). In the frame of reference of a ground-based observer, waves
generated by the convection below should retain their wavelength, period and
phase velocity as they propagate upwards through the region of wind shear.

However, within the framework of the WKB approximation, the intrinsic frequency in the frame of reference moving with the wind is Doppler shifted by an amount $\vec{U}\cdot\vec{K}$ where $\vec{U}$ is the mean wind velocity and $\vec{K}$ is the wavenumber. The intrinsic frequency is related to the observed frequency ω_0 by

$$\omega = \omega_0 - \vec{U}\cdot\vec{K} \qquad (1)$$

If $\vec{U}$ changes with height in such a way that the upper-level wind has an appreciable component opposing $\vec{K}$, $\vec{U}\cdot\vec{K}$ will become negative and the intrinsic frequency will increase with height. If the intrinsic frequency approaches the Brunt-Väisälä frequency, the vertical wavelength will become very large and the waves will become trapped. It would take a network of profilers such as was used during the ALPEX Experiment in Southern France to measure the horizontal wavelength and phase velocity of the waves to demonstrate conclusively that the interpretation given here is correct.

If we assume the waves are similar to the convection waves observed by KUETTNER et al (1987), we can estimate the intrinsic frequency from Eq (1). Using a typical wavelength of 9 km and a wind velocity of 6 ms $^{-1}$, we find $\Delta\omega = 2\pi U/\lambda = .0041s^{-1}$. The observed frequency is $2\pi/\tau$, or $.0052s^{-1}$ for a 20-minute period wave. Thus, from Eq. (1) the intrinsic frequency is $.0093s^{-1}$, consistent with an intrinsic period of about 11 minutes. From the Dodge City sounding at 00 UT on 30 June 1985 the Brunt-Väisälä frequency calculated between the 500 mb and 250 mb levels is $.0096s^{-1}$. Evidently, conditions on this day were favorable for trapping of convection waves. Trapping is also supported by the fact that the vertical wavelength of the observed waves is very large and that there is little wave activity extending into the stratosphere.

6. CONCLUDING REMARKS

Observations of vertical velocities by a VHF wind-profiling Doppler radar located near Liberal, Kansas on 29 June 1985 reveal a pattern of wave activity in the free troposphere that closely resembles convection waves reported from aircraft measurements by KUETTNER et al. (1987). Synoptic conditions near Liberal, Kansas on 29 June 1985 favored the formation of convection waves as a result of strong surface heating and considerable vertical wind shear above the planetary boundary layer. An analysis of the wave event of 29 June 1985 also supports the idea that the waves observed on this occasion were trapped in the troposphere owing to the influence of the background wind shear.

The radar observations reported here clearly show the presence of convection waves and complement the earlier aircraft observations in several respects. While we have made no attempt here to examine the frequency of occurrence of convection waves, vertical velocity measurements from wind-profiling Doppler radars should be well suited for assessing occurrence statistics of convection waves at any given location. Furthermore, networks of three or more radars could be used to determine the wavelength and phase velocity of the waves by techniques discussed in CARTER et al (1989). Future studies should determine the influence of convection waves on the momentum budget of the lower atmosphere.

7. ACKNOWLEDGEMENTS

8. REFERENCES

Augustine, J. A. and E. J. Zipser (1987), The use of wind profilers in a mesos-
cale environment. Bull. Amer. Met. Soc., 68, 4-17.

Bretherton, F. P. (1969), Waves and turbulence in stably stratified fluids.
Radio Sci., 4, 1279-1287.

Carter, D. A., B. B. Balsley, W. L. Ecklund, M. Crochet, A. C. Riddle,
R. Garello, and K. S. Gage (1989), Investigations of internal gravity waves
using three vertically-directed, closely-spaced wind profilers. Submitted
to J.G.R.-Atmospheres.

Clark, T.L., T. Hau, and J.P. Kuettner (1986), Convectively forced internal
gravity waves: results from two-dimensional numerical experiments. Q. J.
Roy. Meteorol. Soc., 112, 899-925.

Ecklund, W. L., D. A. Carter, and B. B. Balsley (1979), Continuous measurement
of upper atmospheric winds and turbulence using a VHF Doppler radar. J.
Atmos. Terr. Phys., 41, 933-944.

Ecklund, W. L., K. S. Gage, and A. C. Riddle (1981), Gravity wave activity in
vertical winds observed by the Poker Flat MST radar. Geophys. Res. Lett.,
8, 285-288.

Ecklund, W. L., K. S. Gage, B. B. Balsley, R.G. Strauch, and J. L. Green
(1982), Vertical wind variability observed by VHF radar in the lee of the
Colorado Rockies. Monthly Weather Rev., 110, 1451-1457.

Ecklund, W.L., K.S. Gage, G.D. Nastrom, and B.B. Balsley (1986), A preliminary
climatology of the spectrum of vertical velocity by observed clear-air
Doppler radar. J. Clim. Appl. Met., 25, 885-892.

Gage, K.S., D.A. Carter, and W. L. Ecklund (1981), The effect of gravity waves
on specular echoes observed by the Poker Flat MST radar. Geophys. Res.
Lett., 8, 599-602.

Gage, K. S. (1989), "The Structure and Dynamics of the Free Atmosphere as
Observed by VHF/UHF Radar", chapter 28a in Radar in Meteorology, D. Atlas,
ed. A.M.S., Boston, in press.

Green, J. L., G. D. Nastrom, K. S. Gage, T. E. VanZandt, W. L. Clark and J. M.
Warnock (1988), Observations of vertical velocity over Illinois by the
Flatland radar. Geophys. Res. Lett., 15, 269-272.

Kuettner, J. P., P. A. Hildebrand and T. L. Clark (1987), Convection waves:
Observations of gravity wave systems over convectively active boundary
layers. Quart. J. Royal Meteorol. Soc., 113, 445-467.

INTERCOMPARISON AND CALIBRATION OF WIND AND WAVE MEASUREMENTS AT VARIOUS FREQUENCIES

Marvin A. Geller

Laboratory for Atmospheres
NASA/Goddard Space Flight Center
Greenbelt, Maryland, 20771 U.S.A.

It has now been about 15 years since the first MST measurements were reported by Woodman and Guillen using the Jicamarca radar. During the intervening years, the great value of MST measurements of wind velocities and turbulence parameters has become obvious to the atmospheric community. The passage of time has brought about a transformation in the MST community from its early years when its mission was to demonstrate the value of the technique to the present time when its activities have changed toward asking difficult questions about errors in the technique, how MST measurements compare with measurements made by other techniques, and how best to utilize MST measurements for scientific studies.

The topics covered in session 5 concern several of these present issues being dealt with by the MST community. The session is comprised of papers on very diverse topics ranging from triangle size effects in spaced antenna drift measurements to how the MST community can best interact with the satellite measurements of horizontal winds that will become available with the launch of the Upper Atmosphere Research Satellite in 1991.

TRIANGLE SIZE EFFECT IN SPACED ANTENNA WIND MEASUREMENTS

C.E. Meek

Institute of Space and Atmospheric Studies
University of Saskatchewan, Saskatoon, Canada

Abstract: A formula for the "triangle size effect" (the finding of lower velocities from smaller antenna spacings) is derived for a one-dimensional pattern on the assumption that noise level is the critical factor. Experimental data from two arrays, each with two available spacings, is shown to support this assumption.

INTRODUCTION

The spaced antenna method involves cross and auto correlations of echo amplitude sequences measured on antennas separated by distances of the order of one radio wavelength. Usually these are assumed to be Gaussian for theoretical development of analyses to find the mean velocity of the ground diffraction pattern. The FCA model (BRIGGS, 1968) accounts for a two dimensional spatial diffraction pattern and pattern decay with time. The theory assumes that the only reason for a drop in correlation is a time delay or spatial separation between measurements. Not accounted for are multiple motions in the same pattern or random noise - atmospheric or measurement (e.g. digitization). This paper is concerned with the latter.

GOLLEY and ROSSITER (1970) presented a comparison between wind values measured with various antenna arrays, finding that the FCA velocity tended to increase with array size, approaching a limiting value which agreed with the spatial pattern shift in time found on their large array. They suggested random noise as a possible cause for this variation - that is noise has a greater reducing effect on calculated velocity when correlations are high (as with small spacings). Some numerical simulations (1-D spatial pattern assumption) were later done by CHANDRA (1978) with the same conclusions.

The present paper derives an equation for the noise-dependent reduction in FCA velocity for the 1-D case, and tests it experimentally.

1-DIMENSIONAL THEORY

Figure 1 illustrates correlation functions which would be measured
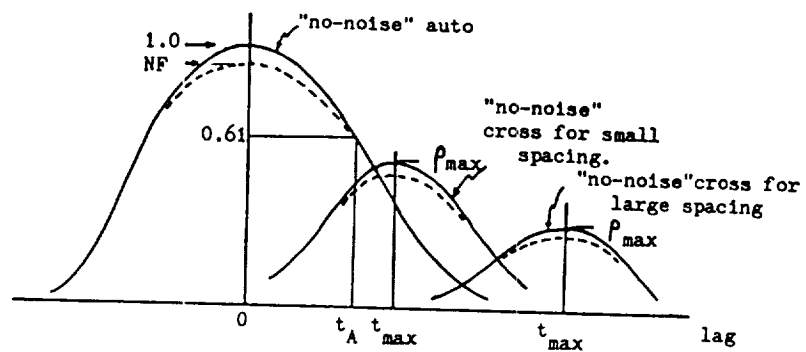
Figure 1. Illustration of the effect of noise on the auto and cross correlations for different antenna spacings. The dashed lines show the "noisy" case.

at two receiver spacings for no-noise and noisy data when a moving, decaying pattern is present. The fractional reduction in peak correlation due to noise is termed the "noise factor", NF. The signal-to-noise, S/N(power) is given by NF/(1-NF).

In the no-noise case, the correlation function is assumed to be Gaussian:

$$\rho(D,t) = e^{-\frac{1}{2}\left(\frac{(D-Vt)^2}{A^2} + \frac{t^2}{C^2} \right)} \tag{1}$$

where D is the receiver spacing, V is the "true" velocity of the ground pattern (i.e. it is the result of correcting the apparent velocity, $V_a = D/t_{max}$, for effects of pattern decay which shift the measured lag for peak correlation closer to zero-lag), A is the pattern scale, and C is the characteristic time (or decay time) in the pattern - both evaluated at $\rho = 0.61$. The width of the auto-correlation (i.e. from (1) with D=0) is

$$t_a^2 = \frac{1}{\frac{V^2}{A^2} + \frac{1}{C^2}} . \tag{2}$$

The lag for peak cross correlation is

$$t_{max} = \frac{DV}{V^2 + \frac{A^2}{C^2}} , \tag{3}$$

and the peak value of cross correlation is given by

$$-2 \ln(\rho_{max}) = \frac{D^2}{C^2 \left(V^2 + \frac{A^2}{C^2} \right)} . \tag{4}$$

In analysis, t_a, t_{max}, and ρ_{max} are the measured parameters (note that t_a is the same for any receiver spacing). The pattern parameters are solved from these by the following set of equations.

$$A_o^2 = \frac{D^2}{-2 \ln(\rho_{max}) + \frac{t_{max}^2}{t_a^2}} \tag{5}$$

$$V_o = \frac{D}{t_{max}\left(-2 \ln\rho_{max} \cdot \frac{t_a^2}{t_{max}^2} + 1 \right)} \tag{6}$$

$$c_o^2 = \frac{-2 \ln \rho_{max} \cdot t_a^2 + t_{max}^2}{-2 \ln \rho_{max}} \tag{7}$$

Now suppose the record is noisy, with noise factor $e^{-\Delta}$, and assume that t_a is not affected. (In practice it is, but when comparing large and small spacings, both will have the same t_a.) Then the pattern parameters can be found from equations (5) to (7) when $\ln \rho_{max}$ is replaced by $\ln \rho_{max} - \Delta$, and after some pages of manipulation, the ratio of non-noise to noisy parameters can be found:

$$\frac{V_o}{V} = 1 + \frac{2 \Delta A_o^2}{D^2} \tag{8}$$

$$\frac{A_o^2}{A^2} = 1 + \frac{2 \Delta A_o^2}{D^2} \tag{9}$$

$$\frac{c_o^2}{c^2} = 1 + \frac{2 \Delta c_o^2 V_o^2}{2 \Delta A_o^2 + D^2} \tag{10}$$

All ratios are seen to be greater than 1. Thus the pattern scale, "true" speed, and characteristic time are always less for the noisy case, and also the effect is greater for smaller receiver spacings.

QUALITATIVE EXPERIMENTAL TEST

Two arrays have been used. Each consists of an equilateral array of antennas with a fourth placed in the centre of the triangle, so that large (outer antennas) and small (centre compared with each outer) spacings are available in each array. For the "loop" array these are 116.7 m and 67.5 m (0.5λ), and for the "main array" they are 270 m (2λ) and 156 m. (In the case of the main array, the centre is a single dipole while the outer antennas are pairs of parallel dipoles spaced at $\frac{1}{2}\lambda$ and connected in parallel - so the noise level could be different in large and small spacings if interference is a problem - as opposed to digitization noise for example.)

Approximately 2 hr of data have been recorded on each array. Each record was 3.6 min length. In the analysis, correlations were calculated to the same maximum lag. In order that the noise level not change with

different antenna separation, no data averaging was done, but the data spacing was varied to give greater maximum lag times for the larger spacing (the same number of lags was used for all analyses). Every amplitude point was used for the smallest spacing (810 points), every second point for the two medium spacings (410 points) and every third for the large (270 points). The analysis was according to MEEK (1980). Data were discarded if either the large or small spacing analysis failed. All heights (60-110 Km) are lumped together in the results. Histograms for each spacing and for large and small spacings (when the analysis was successful for both in the same record) are shown in Figure 2. Since the analysis assumes a 2-D pattern, the "1-D" pattern scale is estimated by $\sqrt{AB}$, where A and B are the major and minor axes. This is not entirely accurate, but will have to do for now since efforts to re-analyse the data as a 1-D pattern led to at least 50% failure in analysis. The figure shows the effects expected from theory - viz. smaller spacings show smaller V, A, and C.

To see whether the determining factor is the pattern scale, data were sorted according to the median pattern scale, and medians of the resulting patterns are shown in Table 1. (Note that none of these pattern scales is the desired A_o. They should be closely related in size, but quantitative conclusions cannot be drawn.)

TABLE 1. Medians of pattern paramter ratios after separation based on pattern scale

		loop array medians				main array medians		
	#	$\dfrac{V_S}{V_L}$	$\dfrac{\sqrt{AB}_S}{\sqrt{AB}_L}$	$\dfrac{C_S}{C_L}$	#	$\dfrac{V_S}{V_L}$	$\dfrac{\sqrt{AB}_S}{\sqrt{AB}_L}$	$\dfrac{C_S}{C_L}$
$\sqrt{AB}_S$ < med.	51	0.69	0.85	0.83	51	0.97	0.92	0.70
$\sqrt{AB}_S$ > med.	47	0.69	0.74	0.89	54	0.79	0.81	0.83
$\sqrt{AB}_L$ < med.	49	0.69	0.83	0.85	55	0.95	0.89	0.71
$\sqrt{AB}_L$ > med.	49	0.69	0.76	0.87	50	0.81	0.85	0.81

From the table it can be seen that large versus small spacing effects are greater for larger pattern scales- except for the velocity in the loop

2(a)   2(b)
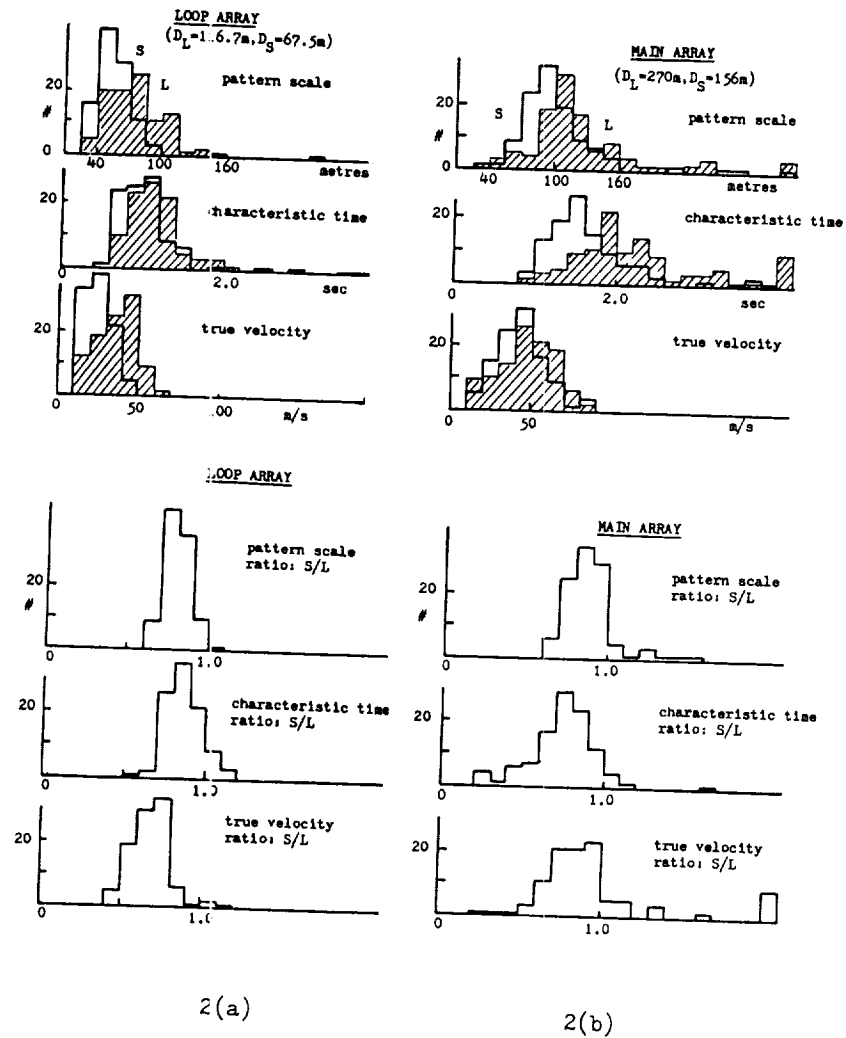
Figure 2. Histograms of pattern parameters for the large and small spacings of loop (2a) and main (2b) arrays; and ratios, small-to-large spacing, of FCA paramters.

array. The latter finding is puzzling.

QUANTITATIVE TEST

A test is required which doesn't use V_o, A_o, or C_o. The first obvious choise is to use the large (L) and small (S) pattern scales to solve for Δ and A_o. This is done by taking the difference of equation (9) for large and small spacings:

$$\frac{1}{A_L^2} - \frac{1}{A_S^2} = 2\Delta \left(\frac{1}{D_L^2} - \frac{1}{D_S^2} \right) . \tag{11}$$

Since D_S and D_L are known, and A_S and A_L come from the FCA, the noise parameter Δ can be found. Again note that this noise parameter is only good for the present large versus small spacing test - it is not the real noise because noise effects on t_a have not been considered (and these will depend on the type of numerical analysis done to find t_a). Then A_o can be found from (9), again with the above caveat, and then V_S/V_L from equation (8):

$$\frac{V_S}{V_L} = \frac{1 + 2\Delta A_o^2 / D_L^2}{1 + 2\Delta A_o^2 / D_S^2} . \tag{12}$$

(In some cases, possibly due to statistical scatter or the fact that $\sqrt{AB}$ is not an accurate estimate of the 1-D pattern scale, A_S is greater than A_L - i.e. noise factor > 1. This is theoretically impossible, however these data are retained for the plot.)

This predicted value of speed ratio is compared with the measured ratio in Figure 3. The loop data agree well with the theory, but the main array data are skewed - the predicted speed ratio is somewhat less than the measured. A possible reason for this is that the centre antenna in the main array - which is not used for the large spacing, is a single dipole and thus more susceptible to noise. This means in terms of the predicted ratio that the pattern scale A_S will be smaller than expected from spacing considerations alone, and look as though it were measured with an even smaller D_S. Thus the predicted ratio, found from (12) will be smaller than expected - and this is shown by the scatter plot.

CONCLUSIONS

The triangle size effect seen at Saskatoon can be explained as a
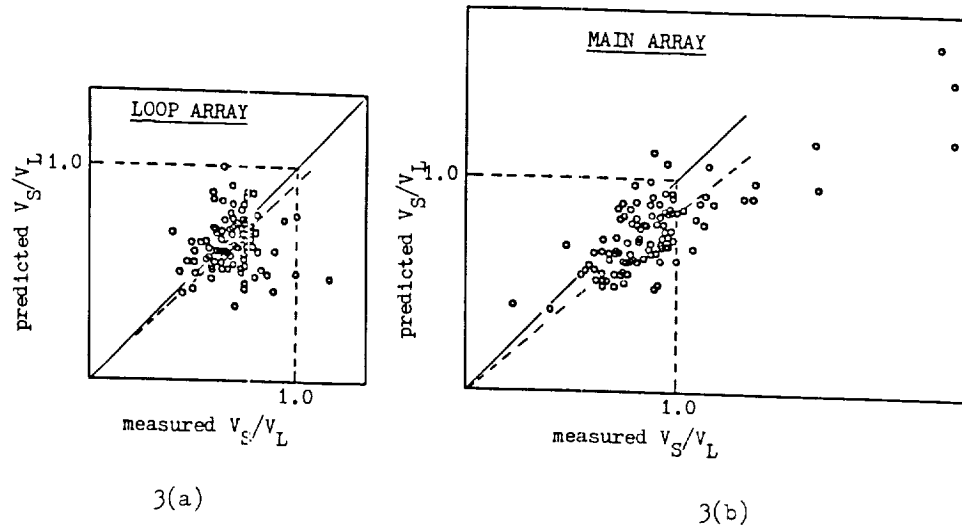
Figure 3. Scatter plots of predicted (based on antenna spacing and measured pattern scale) FCA velocity ratio, small/large spacing, for loop (3a) and main (3b) arrays against measured velocity ratio. The medians are shown by diagonal dashed lines.

result of random noise in the data. In theory it is simple to correct the data for noise - simply divide all the correlations by the noise factor, NF, before analysis, or re-work the FCA parameters backwards and forwards putting in the noise correction if it is known; but in practice an accurate value of NF is sometimes difficult to determine (particularly in cases where the auto-correlation is narrow); and when the peak cross correlations are high to begin with, correction often leads to spurious or impossible FCA results.

REFERENCES

Briggs, B.H. (1968) "On the analysis of moving patterns in geophysics I: Correlation analysis" J.Atmos.Terr.Phys,30, 1777-1788

Chandra, H. (1978) "On triangle size effect in spaced receiver drift experiments" Indian Journal of Radio and Space Physics, 7, Feb 1978, 13-15

Golley, M.G. and D.E. Rossiter (1970) "Some tests of methods of analysis of ionospheric drift records using an array of 89 aerials" J.Atmos.Terr.Phys, 32, 1215-1233

Meek, C.E. (1980) "An efficient method of analysing ionospheric drift data" J.Atmos.Terr.Phys, 42, 835-839

GRAVITY WAVE OSCILLATIONS AS A CAUSE OF SPECTRAL BROADENING

W.K. Hocking

Department of Physics and Mathematical Physics,
University of Adelaide, Adelaide, SA 5001 Australia

Signal fading of echoes received in radar studies of the clear atmosphere occurs due to variety of reasons. For VHF, HF and MF studies the main cause is generally the horizontal mean motion of the scatterers through the beam, which broadens the spectrum of the signal and so causes fading (beam-broadening). Other lesser contributions occur due to due to wind-shears, and also due to the fluctuating velocities of the scatterers. By calculating and separating out the beam- and wind-shear-broadened contributions it is possible to make an estimate of the Root-mean-square fluctuating velocity v_{RMS} of the scatterers, and this is often ascribed to turbulence. However, there are other effects which contribute to v_{RMS}, and in any determination of turbulence intensities it is necessary to consider and remove these effects. One important cause of this broadening is gravity wave oscillations. Although a gravity wave may only go through a fraction of a cycle during the data collection period, this will still contribute to v_{RMS} if the wave amplitude is more than a few ms^{-1}.

Such oscillations will produce not only a broadening which increases as a function of data length, but can also lead to non-Gaussian spectra. These two features may be used to help determine the relative contributions of gravity wave oscillations and turbulence in experimental spectra. Below, the types of deformation of the spectra which occur due to gravity waves are illustrated, and the variation of the spectral width as a function of data length is derived analytically.

If a wave of period T is sampled for a length of time τ, then the velocity variance which results is dependent on τ. If τ is less than T, then the variance is less than the variance which would result if a full period of the wave had been used. If a radar observes a gravity wave for such a period τ, then the spectrum recorded will be broadened by an amount depending on the measured variance of the radial velocity. Of course the value of the variance will depend in part on which phase of the wave is sampled. However, for statistical purposes it is more important to know the average variance averaged over all phases.

Consider the radial velocity fluctuation being observed by the radar to be of the form $v = v_0 \sin(\omega t + \phi)$, where $\omega = 2\pi/T$ and suppose that the radar observes for a time interval τ. The parameter v_0 is the peak radial velocity observable with the radar. Then the variance of velocities observed by the radar is

$$\sigma^2_{v\tau} = \int P(v) \cdot v^2 dv - [\int P(v) \cdot v \, dv]^2 \qquad (1)$$

where $P(v)dv$ is the frequency of occurrence (normalized to 1) of velocities in the range v to $v + dv$, and the integral is over all v which occur in the time interval between 0 and τ.

The form of the probability distribution function $P(v)$ of the velocity fluctuations is given by

$$P(v) - n/\tau \quad dt/dv$$

$$= \frac{n}{\tau} \quad \frac{1}{\omega v_0 \, \cos(\omega t + \phi)}$$

where v may only take on the values covered during the time interval τ. Here, n is the number of occasions when the wave has a radial velocity of v in the time interval between 0 and τ. For example, if $\tau - T$, then n=2, as there are 2 occasions when a velocity v occurs in each wave cycle. In this case,

$$P(v) = \frac{1}{\pi} \cdot \frac{1}{v_0 \sqrt{(1 - v^2/v_0^2)}} \quad ,$$

An example is shown in Fig. 1. Note the bimodal nature of the distribution, which arises because the wave spends a relatively large fraction of the time around the maximum and minimum velocities, and passes through the point where v = 0 rather quickly. Experimental spectra of this type should be rejected if the spectra are being used to determine turbulent energy dissipation rates, since they are likely to be due to high frequency gravity waves. It should also be noted that if both turbulence and such wave activity co-exist, the turbulent spectrum will be convolved with that due to the gravity wave, and this will therefore partly or even completely mask the bimodal character.

The variance of the velocity fluctuations is most easily calculated as

$$\sigma^2_{v\tau} = \int_{t=0}^{\tau} v^2 dt/\tau - [\int_{t=0}^{\tau} v \, dt/\tau]^2 \tag{2}$$

or

$$\sigma^2_{v\tau} = 1/\tau \cdot \int_{t=0}^{\tau} v^2_0 \cdot \sin^2 (\omega t + \phi) \cdot dt$$

$$- [1/\tau \cdot \int_{t=0}^{\tau} v_0 \sin (\omega t + \phi) \, dt]^2 \tag{3}$$

Note that we do not have to concern ourselves with the factor n seen in our expression for P(v), since we now do the integral over time and so each interval dt is unique. Thus we need not be concerned that the same velocity occurs several times, since by integrating over t we cover all velocities. The above expression may readily be integrated to give an expression for $\sigma^2_{v\tau}$ in terms of v^2_0, τ, ω, and ϕ.

A more important parameter than $\sigma^2_{v\tau}$ is the mean variance $<\sigma^2_{v\tau}>$ averaged over all phases ϕ. Then

$$<\sigma^2_{v\tau}> = \int_{\phi=0}^{2\pi} \sigma^2_{v\tau} \cdot \frac{d\phi}{2\pi} \tag{4}$$

Evaluating (3) and substituting into (4) shows that

$$<\sigma^2_{v\tau}> - F. \, v^2_0/2 \tag{5}$$

where $v^2_0/2$ is of course the variance of the wave had it been sampled for an integral number of periods, and

$$F = 1 - \frac{1}{2\pi^2} \cdot (\frac{T^2}{\tau}) \cdot \{1 - \cos (\frac{2\pi\tau}{T})\}$$

(6)

Naturally F = 1 when T is an integral number of wave periods, and F tends to 0 as τ tends to 0. The functional form of F is plotted in Figure 2.

As an example, if the wave period is 5 min, and a sampling length of 100s is used, then F = 0.33, while if τ = 200s then F = 0.845. The ratio of these two is 0.38. By recording spectra using two different data lengths (e.g. 100s and 200s) and measuring the ratio of spectral widths recorded using each different data length (after removal of beam and shear broadening), it is possible to use such theoretical calculations of F to estimate the relative turbulence and gravity wave contributions to the measured spectral widths. Examples of the application of this theory in removing gravity wave contamination have been illustrated by HOCKING, 1988; more sophisticated applications can and should be developed.

References

Hocking, W.K. "Two years of continuous measurements of turbulence parameters in the upper mesosphere and lower thermosphere made with a 2-MHz radar", J. Geophys. Res., 93, 2475-2491, 1988.
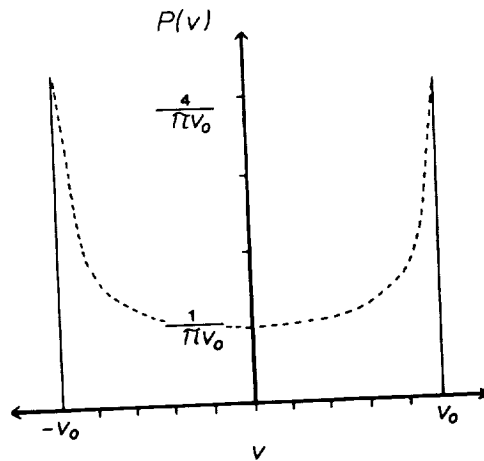
Fig. 1. Probability density function for the radial velocities observed by a radar if the radar observes over one full cycle of a wave. This shape is also representative of the spectrum which would be recorded by the radar. Even if the radar observes for less than a full cycle, similar bimodal shapes can result.

Fig. 2. Mean squared fluctuating velocity measured when sampling the velocity fluctuations of a gravity wave of period T for a sampling time τ, relative to the actual mean squared fluctuating velocity of the wave (and averaged over all possible phases).
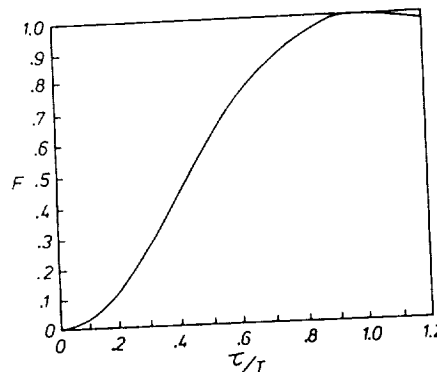
MF RADAR INTERFEROMETER MEASUREMENTS OF METEOR TRAIL MOTIONS

C.E. Meek and A.H. Manson

Institute of Space and Atmospheric Studies
University of Saskatchewan, Saskatoon, Canada

Abstract: Angle of arrival and Doppler velocity of meteor trails are measured with a medium frequency radar (2.219 MHz) and compared with spaced antenna, correlation analysis, winds.

INTRODUCTION

Recent statistical work on MF meteor trail echoes has been done by OLLSON-STEEL and ELFORD (1987). Their interest was in meteors, ours is wind measurements. Previous comparisons of interferometer and ground diffraction pattern motions on ionospheric echoes have been done by MEEK and MANSON (1987a,b). The general result was that the full correlation type analysis (FCA, e.g. BRIGGS, 1968) gave a smaller velocity estimate than the interferometer. The main drawback with the interferometer is that it is uncertain whether the selected "scatterers" were isolated physical scattering centres carried along by the background wind, or perhaps just moving glints on a reflecting layer. By definition, a meteor trail is a physical entity, and should produce a good wind estimate. The best time to observe meteor trails is at night, when the "ionospheric clutter" is small- of course this is the worst time to do FCA measurements, but over long periods, and assuming that tidal motions predominate, a reasonable comparison should be possible between "mean daily variations" from the two systems.

During operation of the meteor trail system, an improved real time wind (COHRTW) system was installed which employs coherent integration and complex correlation in the FCA. With the resulting increased S/N, direct comparisons with single trails are feasible.

METEOR TRAIL EQUIPMENT

The MF transmitting system is the same for both experiments: 50 KW power, 20 μsec pulse width(3 Km resolution), 60Hz PRF, a vertically

pointing 4x4 array of folded half-wave dipoles with half-power at ∿22° zenith, operating at 2.219 MHz.

In the spaced receiver FCA, echoes are normally assumed to come from near the zenith - and the chosen spacing of the antennas is based on expected motions of the ground pattern. Meteor trails, on the other hand, can be seen at almost any zenith angle - especially at night when the ionosphere is weak and despite the relatively narrow transmitter antenna beam. Angle of arrival (AOA) measurements require closely spaced antennas to avoid phase ambiguities. This spacing in the normal folded dipole receiver arrays would exhibit unacceptable coupling. Thus a loop (shielded, 1.5 m diam.) array was used (Figure 1): the outer loops are ½ wavelength (67m)

from the centre loop, and form an equilateral triangle - so AOA can be measured down to the horizon without ambiguity. The advantage of the "Y" arrangement is that 3 independent phase differences are available for a plane-phase-front (i.e. single scatterer) test. The measured loop-pair isolation is better than 90 dB. However the loops exhibit a measured sacrifice of 40 dB in gain and 25 dB in signal-to-noise (S/N).
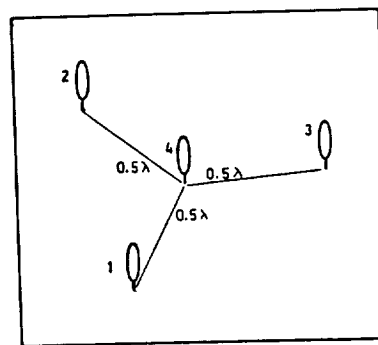
Figure 1. Loop array

The night-time ionospheric MF noise level is also at least 20 dB higher, so the loss of S/N in the equipment is not as serious as it first appears. A 40 dB pre-amp is located at each loop. Calibrations must be done frequently to monitor possible unequal temperature induced shifts in phase between pre-amps.

OPERATION

A single coherent receiver is cycled around the four loops, pausing at each for coherent integration: 8, 4, and 6 pulse integration were used at various times. 16 heights (ranges) are monitored (85-130 Km). The average amplitudes are stored continually according to a rotating memory pointer (128 point sequences). The Apple II which runs the system picks out meteor trails strictly on dead time/rise time at each range gate - that is

there must be a period (∿8 sec) with the signal below a threshold T1
followed by a jump to a level above T2 (∿8 dB) within one antenna cycle
time (∿0.4 sec), and it must stay above T1 for more than∿4 sec. (The
exact times vary a little depending on the amount of integration used.)
The trails are monitored until they fill the available storage, or end, at
which time the (integrated) amplitude sequences are dumped to tape. Re-
ceiver gain is constant for each transmitted pulse, and controlled in the
long term so that most range gates have signals below T1. This trail
selection method is very similar to that of Ollson-Steel and Elford. Two
sample trails are shown in Figure 2.
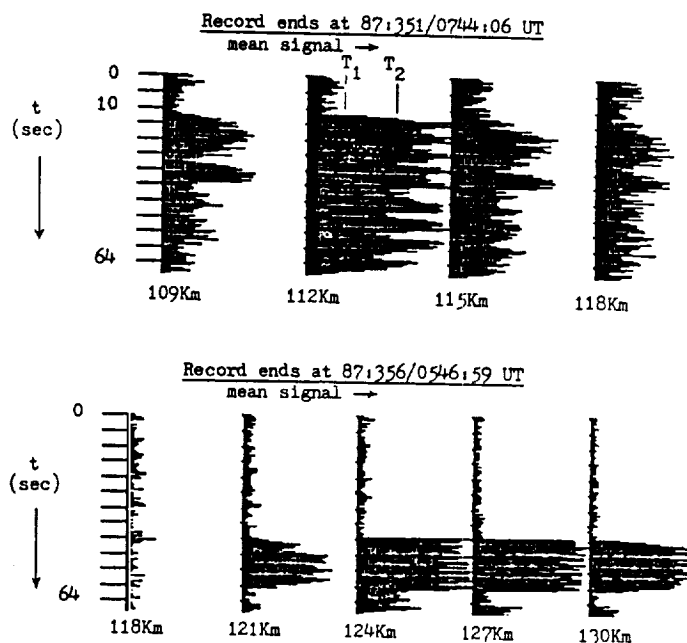
Figure 2. Two sample trails (8 pulse coherent integration); a selected
subset of range gates is plotted. Only those heights showing
the required dead/rise time are analysed further.

PHASE CALIBRATION

Phase calibration is the critical part of the experiment. Initial
attempts to find trails on all-sky film failed, so the method presently in
use is to run the system on ionospheric echoes in the daytime. In the long
term, most echoes should come from the zenith. Histograms were plotted for
phase differences found from pairs of antenna cycles weighted in such a way

as to eliminate Doppler shifts (These would not be a problem if there were one receiver per antenna.). Unfortunately the histograms (not shown) are not sharply peaked, and there is some variation in calibration on different days. 5-10° in peak location (~3° in zenith) is the best accuracy that can be expected from this method. Other methods included feeding the centre loop and measuring the phase at the outer loops; holding a transmitting test loop near each antenna loop; and comparing the AOA from shower meteors (Quadrantids) with the predicted locus of lines-of-sight perpendicular to the known radiant. The first two showed large phase differences from the ionospheric method, possibly due to ground reflections, while the last, although good agreement was obtained using the ionospheric calibration, was too insensitive to "fine tune" the phase corrections.

Another method being tried is airplane tracking, although their line-of-sight velocities are usually near the system limit (integrated amplitude rate) for Doppler phase wrap-around, and they can disappear in ground clutter.

ANALYSIS

The trails are divided into ~6 sec segments. Two types of analysis were tried. In method "A" a parabolic function is fitted to the mean complex auto-correlation phase over the first two lags to get an accurate phase slope at zero lag for calculating Doppler velocity. If the phase slope changes by more than 20% between the first and second lags, the data are rejected (Phase curvature is caused by multiple scatterers with different Dopplers.). If the phase at the first lag is greater than 90°, the second lag phase is "unwrapped" to a value beyond $\pm180°$ with the same sign as the first lag, and then the above criterion is applied.

The "zero lag" cross correlation phases are then found and corrected from the calibration data. Since there are cycling delays between antennas, a Doppler correction must also be made. Then the normalized phase discrepancy (NPD) is calculated. This is the sum of the three phase differences divided by the sum of their absolute values taken as a positive number. A low value indicates a plane phase front - i.e. only one AOA present in the signal. If NPD $\gtrsim$ 0.3, the data are rejected (~70% significance criterion). Otherwise a fit of an AOA to the data is done which minimizes the squared error in phase differences (As an aside: although the array can measure AOA

down to the horizon, there can be can be cases in which the AOA cannot be calculated from 3 phase differences - even if NPD=0. An extreme case, for example, is 0°, -180°, $+180^\circ$, in which the scatterer must be simultaneously on the horizon in two antenna pair directions. There were two such cases in the long term data. These could have been caused by calibration error, or by statistical fluctuations in the phase differences.).

The long term data presented later had the following processing statistics: 630 trails (average of 19 per night) giving 1356 original trail segments, of which there were 291 rejected on phase curvature, 207 on zenith $< 10^\circ$ (see below), and 230 on NPD > 0.3, leaving 628 for wind analysis.

Method "B" is the same as "A" except that only the first lag auto phase is used to define Doppler and correct the cross phases. There is no rejection on curvature, but data are rejected if the first lag auto phase is greater than 90°. The latter criterion effectively eliminates high Doppler speeds but the main reason is to avoid possibly large errors in AOA during Doppler correction of the cross phases.

Usually the results from different segments of the same trail agree very well.

At least 2 trails at different azimuths are needed to calculate a horizontal velocity vector (the vertical velocity is assumed to be zero over the long term - but it can be found if desired). Because of doubts about the phase calibration, zenith angles less than 10° are rejected. For the purpose of the present comparison the trail data are separated into GMT hour bins and 9 Km height bins (the height is found from the AOA and range and includes the curvature of the earth). Then a fit of a horizontal velocity vector, which minimizes the squared error in Doppler velocity, is done.

It is assumed implicitly that there is no ionosphere at night, i.e. the ray paths are straight.

VELOCITY COMPARISON

Figure 3 compares the meteor and RTW (real time wind system, GREGORY et al.,1979; MEEK,1980) velocities. The meteor values are a single fit to the selected trail data over the month Dec 7'87 to Jan 11'88. The minimum/maximum number of accepted trail segments in an hour was 9/38 (some of which may be from the same trail). The RTW values are found by averaging

all the values in each GMT
hour - typically 150-250
values per GMT hour in the
month for the height layer
100-109 Km. RTW daytime values
at T+12h are also plotted to
identify any noise bias (lower
velocities) at night. A noise
bias is not evident - the dif-
ference exhibited is probably
due to the 24 hr tide.

The meteor "A" analysis
seems to produce a better be-
haved value than the "B" (the
number of trail segments used in
each are similar), but shows an
unusually strong background com-
ponent of approximately 20 m/s
southward and westward, where-
as the "B" value is closer to
zero. The "B" analysis agrees
quite well with the RTW in tidal
amplitude (taking maximum to
minimum wind spread), but is noisy.
The mean background wind of ∿10

Figure 3. Long term comparison of
meteor and spaced ant-
enna (FCA) winds. Local
midnight is near 07 GMT

m/s is reasonable (GROVES,1972; MANSON et al.,1987). It is possible that
the "B" magnitude is smaller than "A" because of the rejection of high
Doppler velocities (phase wrap-around) in "B", but in theory, if the
meteor trail data were accurate, there should be no difference.

The 20 m/s offset in meteor background wind would be hard to explain
by phase calibration errors if the trails were uniformly distributed in
azimuth - that is low Doppler shifts on one side of the zenith (due to
errors in identifying the zenith) would "cancel" the effect of high shifts
in the other side - but the trails are not uniformly distributed.

Figure 4. shows the distribution (all heights combined) of AOA's for
the first accepted segment in each trail. Thus it appears that phase cal-

ibration errors could have a strong effect on the calculated winds
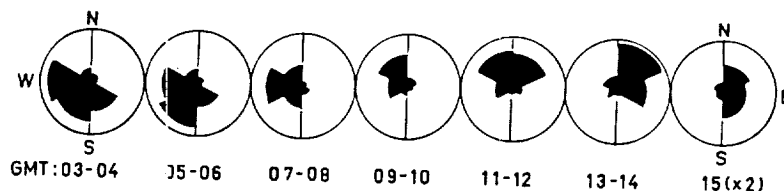
Figure 4. Distribution of trails in azimuth for Dec 7'87 to
Jan 11'87 by analysis "A". Trails at all heights are
included. The outer circle represents 30 different
trails. The number at 15 GMT (1 hour) has been doubled
before plotting. Zenith angles < 10° are not included.

DIRECT COMPARISON OF METHODS

The coherent real time wind system (COHRTW) was put into operation
in June 1988. As with the RTW system, this does 5 min analyses for winds,
but has one receiver per antenna and does 32 point integration at night
(60 Hz transmitter PRF). At this rate there is a possibility of seeing
multiple hop echoes, but since the separate pulses are not phase locked,
these signals should cancel to a large extent. The increase in data is
considerable (see separate paper in these proceedings) which allows some
direct comparisons. However examination of daytime data shows that COHRTW
velocities are some 20-30% smaller than RTW values on the average (for as
yet unknown reasons).

Figure 5 shows one direct meteor-COHRTW comparison. These data are for
2 hr on May 29'88 for a layer 100-106 Km. The location of trails are plotted
as the origin of a vector representing the calculated horizontal velocity
component (assuming zero vertical velocity). Also plotted are the results
of a 2-D (no vertical velocity) and a 3-D fit to these 8 trail segments (2
of which are from the same trail). The large difference in speeds is due
to the fact that all trails are on one side of the zenith. The end points
of the 5-min COHRTW vectors are shown by X (1025-1120 GMT) and O (1125-
1215 GMT). There is fair agreement between the two: a 30° difference in
direction, which could be due to the "bunching" of the trails on one side
of the zenith, and 30% in speed, possibly due to the mentioned speed bias
in COHRTW data.
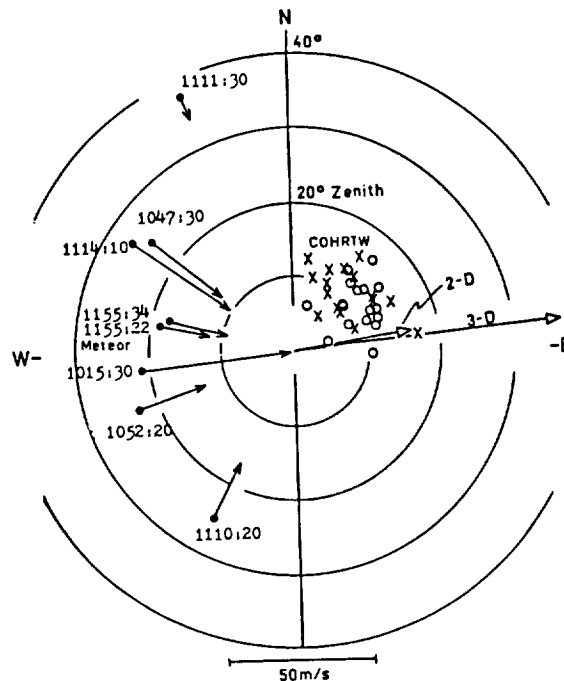
Figure 5. Direct comparison between spaced antenna wind analysis (FCA-COHRTW) and meteor trails over a 2 hr period on May 29'88.

CONCLUSIONS

The long term meteor data shows a tidal oscillation, which means that the system is measuring winds. A major drawback is that there are few trails, and those which are measured are not uniformly distributed in azimuth. Nothing can be done about the latter problem- the ecliptic is not going to move, but 6 dB more sensitivity could be attained with a separate receiver for each loop. An increase in transmitter PRF is not practical at this time. Other improvements would include better gain control (a separate gain for each range gate) and well engineered loops and pre-amps to reduce the system noise level.

REFERENCES

Briggs, B.H. (1968) "On the analysis of moving patterns in Geophysics I: Correlation analysis", J.A.T.P. 30, 1777-1788

Groves, G.V. (1972) in COSPAR International Reference Atmosphere 1972, Part 2. Akademie-Verlag, Berlin

Gregory, J.B., C.E.Meek, A.H.Manson, and D.G.Stephenson (1979) "Developments in the radiowave drifts technique for measurement of high-altitude winds", Jour. Appl. Met., 18, 682-691

Manson, A.H., C.E.Meek, M.Massebeuf, J.L.Fellous, W.G. Elford, R.A. Vincent, R.L.Craig, R.G.Roper, S.Avery, B.B.Balsley, G.J.Fraser, M.J.Smith, R.R.Clark, S.Kato, and T.Tsuda (1987) "Mean winds of the upper middle atmosphere (70-110 Km) from the global radar network: Comparisons with CIRA72, and new rocket and satellite data", Adv. Space Res. 7,(10)143-(10)153

Meek, C.E. (1980)"An efficient method for analysing ionospheric drift data", J.A.T.P. 42, 835-839

Meek, C.E. and A.H.Manson (1987a) "Mesospheric motions observed by simultaneous medium-frequency interferometer and spaced antenna experiments" J.G.R. 92D, 5627-5639

Meek, C.E. and A.H.Manson (1987b) "Medium frequency interferometry at Saskatoon, Canada", Physica Scripta 35, 917-921

Ollson-Steel, D. and W.G. Elford (1987) "The height distribution of radio meteors: observations at 2 MHz", J.A.T.P. 49, 243-258

A COMPARISON OF WIND PROFILERS OPERATING AT 915, 405 AND 50 MHZ

W. Ecklund, K. Moran[*], P. Currier, B. Weber[*], D. Carter, and D. Wuertz[*]

Aeronomy Laboratory
[*]Wave Propagation Laboratory
National Oceanic and Atmospheric Administration
Boulder, Colorado 80303

In November, 1987 two new small portable radars operating at 405 and 915 MHz were located near the existing 50 MHz radar at NOAA's Platteville field site. The purpose of the experiment was to compare radial velocities and reflectivities measured by the different radars as a function of height and time. The comparisons were made on beams pointing toward the East at 15 degrees from the zenith with 1-minute averaging and matched range resolutions. The one-way half-power beamwidths of the antennas ranged from 6 to 7.5 degrees. Profiles of radial velocities measured under clear-sky conditions with 150 meter resolution at 915 and 405 MHz and averaged for a 1-hour period are plotted in Fig. 1. The r.m.s. differences in radial velocities for these data sets are .26 m/s for 1-minute averages, and .17 m/s for 5-minute averages. Fig. 2 shows profiles of radial velocity and S/N observed by the 405 and 915 MHz radars. The S/N at 405 MHz is about 15 dB higher than the S/N at 915 MHz as expected for the relative power-aperture products of the two radars.

Fig. 3 shows profiles of radial velocity and S/N observed in rain. The S/N for the two radars should be about equal under these conditions (particle scattering), but note that the actual difference varies considerably with height. Finally, Fig. 4 shows 1-minute profiles of radial velocity and S/N observed by the 50 and 915 MHz radars. The enhanced S/N above 3 km at 915 MHz is probably due to small cloud particles with low fall speeds since the radial velocities observed by the two radars in this height range are in reasonable agreement. In summary, a preliminary comparison of radial velocities observed by 405, 915 and 50 MHz wind profilers shows good agreement over the heights covered.
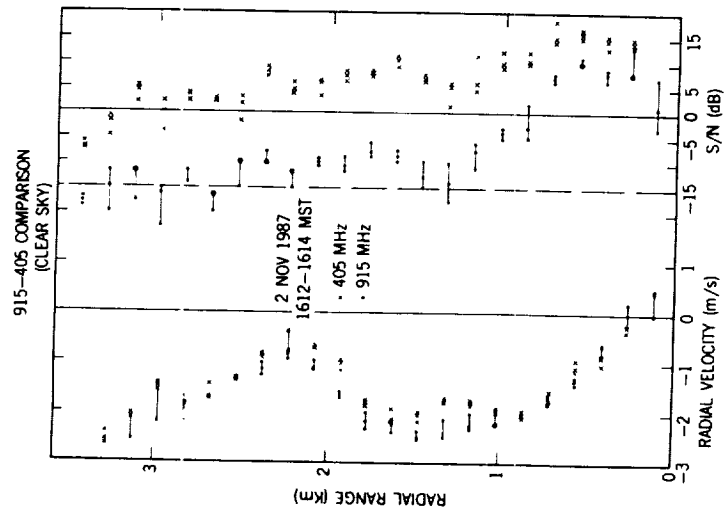
Fig. 2. One-minute average profiles (clear sky).
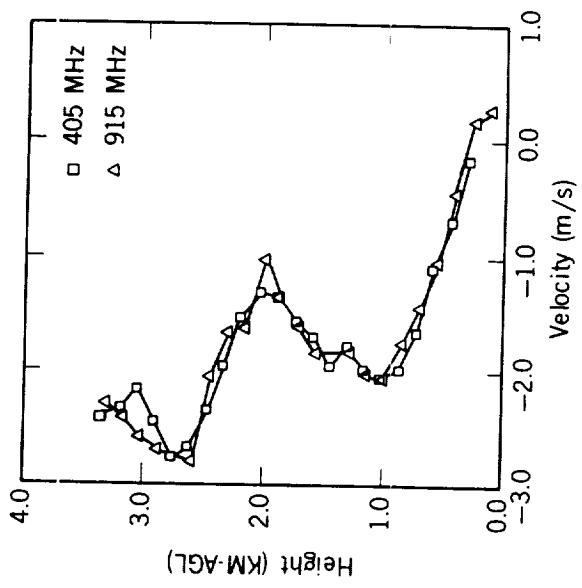
Fig. 1. Profiles of radial velocity observed at 405 MHz (boxes) and at 915 MHz (triangles).

Fig. 4. One-minute average profiles at 50 and 915 MHz.

Fig. 3. One-minute average profiles (rain).

SAD AND INTERFEROMETRY ANALYSIS WITH THE MU RADAR SIMULATIONS AND PRELIMINARY RESULTS

J.S. Van Baelen[1,2], A.D. Richmond[1], S.K. Avery[2,3],
T. Tsuda[4], S. Kato[4], and S. Fukao[4]

1. HAO/NCAR, P.O. Box 3000, Boulder, CO 80307. USA.
2. Dept. of Electr. & Computer Eng., Univ. of Colorado, Boulder, CO 80309, USA.
3. CIRES, Campus Box 439, Univ. of Colorado, Boulder, CO 80309, USA.
4. RASC, Kyoto University, Uji, Kyoto 611, JAPAN.

1/ INTRODUCTION

Since Woodman's discovery and interpretation of mesospheric echoes (WOODMAN and GUILLEN, 1974), there has been a strong interest in the middle atmosphere dynamics as revealed by ground based radars. Atmospheric radar techniques such as Doppler MST radars and spaced antenna radars have undergone extensive development and are now joined by new applications such as interferometry to study the atmosphere from the troposphere to the mesosphere and beyond. State-of-the-art radars of both kinds have shown generally good agreement between their measurements and those obtained by other means including baloons and rockets. However, it is also important to perform direct comparisons of the different atmospheric radar analysis techniques in order to better understand the nature of their differences.

In that prospect, the MU radar appears to be a well suited tool considering its outstanding flexibility of use. Therefore, we designed an experiment to compare the horizontal winds, and possibly other characteristics of the atmosphere dynamics, obtained by different analysis techniques. This report presents a brief description of the experimental setup , of the analysis procedures implemented, and of a simulation program. A test run on the MU radar provided some preliminary results on actual atmospheric data.

2/ EXPERIMENTAL SETUP

The MU radar is a monostatic radar operating at VHF (46.5 MHz). Its antenna is a circular array of 475 crossed three-subelement yagi which can be divided into 25 groups of 19 elements each. Nineteen of those groups are identical hexagonal subarrays. For further details, see (FUKAO et al., 1985a,b). There are four receiving channels available which can be connected to any combination of groups of elements.

The primary goal of the experiment we developed is to compare horizontal wind velocities obtained by the Doppler method to those obtained by spaced antenna drift (SAD) analysis and interferometry. Therefore, we alternate periods of 5 beam Doppler beam swinging (DBS) (one of the MU radar regular modes of operation), with the entire radar array used as transmitter and receiver, and periods of data (i.e. time series of complex signal) taken with only 4 hexagonal groups as individual receivers while the whole array is used for transmission. The later receiving setup is shown in figure 1a. This combination of receivers allows us to perform both the SAD and the interferometry analysis on the same set of data. Two possible baselines can be used: the outside triangle (receivers 1-2-3, figure 1b) or the inside "star" pattern (receiver pairs 1-4, 2-4, 3-4, figure 1b). These correspond to receiver spacings of 68 meters and 39 meters, respectively.
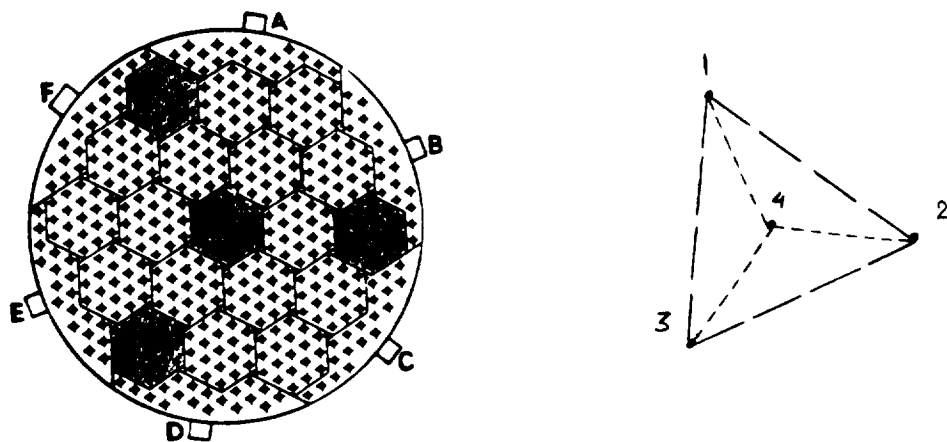
Figure 1. a. Top view of the MU radar array. The shaded areas correspond to the four hexagonal groups used as individual receivers. b. Schematic of the receiving setup. Long dash: outside triangle, short dash: star pattern.

3/ ANALYSIS TECHNIQUES

A program was written to implement both the SAD and the interferometry analyses. Fully developed software already exists at the Radio Atmospheric Science Center (RASC, Kyoto University) to analyse the data taken under the DBS mode of operation.

The SAD analysis method implemented so far follows the one described in MEEK (1978) and MEEK (1980) with the addition that the auto and cross correlations can be computed from the full complex signal rather than the amplitude alone. Some data rejection criteria have also been relaxed, but compensated by extensive information along with the results in order to allow post-processing consideration of their efficiency and eventual rejection of the results. It has been suggested (VINCENT, private communication, 1988) that using the full correlation analysis (FCA) (BRIGGS, 1984) as well as removing time series DC offsets in the real and quadrature components of the signal, suppressing the zero-lag peaks in the autocorrelation by a Gaussian fit, and normalizing the cross-correlations accordingly, might prove valuable. This will be addressed in the near future.

The interferometry technique implemented corresponds to the work done at Jicamarca by FARLEY et al. (1981) and KUDEKI (1988), using an equilateral triangle in our case.

For both techniques, many of the analysis parameters are user-defined: number of points in the time series, number of averages, maximum lag for the correlations (SAD), number of points for the FFT (interferometry), etc.

4/ SIMULATED SCATTERING BACKGROUNDS

In order to verify the analysis routines and to help define the optimum radar configuration to be used during the actual experiment, it was decided to provide different ways to generate a simulated scattering background. The atmospheric volume created corresponds to a radar cell defined by its altitude, width (half-power beam-width at that altitude) and thickness (range gating). The horizontal mean wind is also specified by the user through its meridional and zonal components.

To approximate a turbulent scattering mechanism, the volume is filled with randomly distributed point scatterers (this is a 3-dimensional equivalent to the screen of scatterers described in WRIGHT and PITTEWAY, 1978). An echoing amplitude is randomly given to all scatterers and their complex signal with respect to each individual receiver is summed to provide the resulting signal amplitude and phase (real and quadrature components). This process defines the first point of the time series necessary for the analysis procedure to take place. The successive points are determined by displacing the scatterers in the radar volume as advected by the mean wind. When a scatterer moves out of the volume a new one is injected on the opposite side of the radar cell. The user can request that the amplitude of each scatterer remain constant or vary randomly while it drifts through the radar volume. A 3-dimensional random displacement (turbulence) can also be specified.

A variation on the point scatterer background allows the addition of a high density patch (ellipse) of scatterers to drift across the radar volume.

To account for specular reflection, a reflecting background is defined as a tilted plane on which a long-wavelength and a short-wavelength structure are superimposed. The whole pattern is advected by the mean wind but, in addition, an independent phase velocity can be specified for the long-wavelength structure. The amplitude of the echo at every reflecting point of the corrugated surface is a function of the curvature at that point.

To exemplify the interest of these simulations in preparation for the experiment, figure 2 shows the effect of spacing between the receivers for the SAD analysis. In a perfect case, the
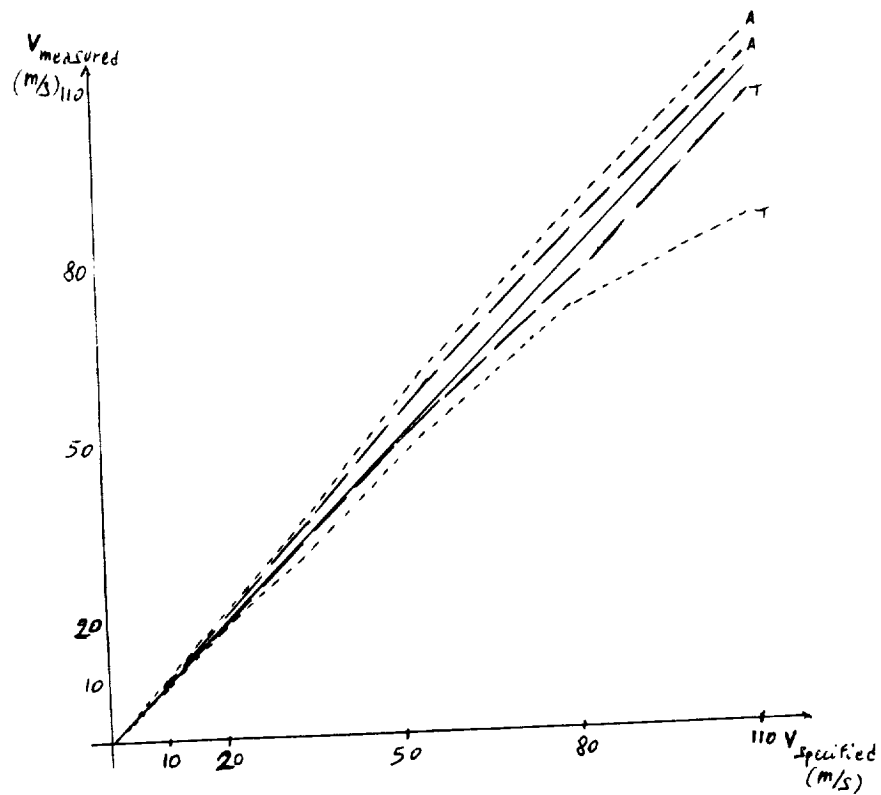
Figure 2. Measured velocities vs specified velocities. Ideal case: plain line at 45 degrees. Long (68 meters) baseline: long dash. Short (39 meters) baseline: short dash. Letters A and T denote the "apparent" and the "true" wind measured, respectively.

measured wind velocities are equal to those specified by the user. Simulations show that the "apparent" velocity results are higher than the input while the "true" velocity results are under-estimates of the specified wind. Also, "true" wind measurements appears to saturate (yield an almost constant output value) when the input wind velocity gets higher than some critical value. Moreover, it can be seen that for smaller spacing of the receivers the "true" wind measurements saturate at lower wind velocities. A similar reduction of the maximum wind velocity obtainable before saturation is observed, is produced when random variations of the echo power of the scatterers are included in the atmospheric motion.

The complex auto and cross correlations are also a benefit for the analysis. Cross correlograms present enhanced peaks (as shown in figure 3) which can yield a better rate of valid results. Indeed, a low value of the cross correlation peak is one of the usual rejection criteria.

The significance of many other parameters of the experiment and analysis procedures could also be checked through simulations by varying the number of points in the analysis, the time step between successive points of the time series, etc.

The simulations can also prove valuable to asses the feasibility of new experiments and serve as a didactic tool for envisioning the effect of different parameters on the analysis.

5/ PRELIMINARY RESULTS

A test observation was performed on the MU radar in October 1988. A preliminary analysis of one 4 minute segment of data, both with the SAD and the interferometry techniques, is presented here. The SAD analysis used the outside triangle while the interferometric method made use of the star pattern. The range gate spacing is 300 meters.

The results of the SAD analysis are presented in figure 4. It shows the meridional and zonal components of the "true" wind. For each 300 meter range gate (from 12 kilometers to 21.3 kilometers of altitude), a star represent the value given by the analysis routine. No star means that the data was rejected during the analysis procedure. The solid curves correspond to a fitted 10 minute average DBS profile obtained with the MU radar 40 minutes later than the SAD profile shown. It can be said that a reasonably good agreement appears, even though some SAD points, especially in the North/South component, exhibit a clear departure from the averaged DBS curve.

Figure 5 shows the interferometry results obtained for two successive range-gates (altitudes of 15 and 15.3 kilometers, respectively). In the first one, a strong echo appears, corresponding to values of normalized cross spectra close to one as well as a well structured phase diagram. KUDEKI (1988) has discussed how the slope of the phase with respect to frequency is related to the horizontal wind velocity. In contrast, the next range gate does not show echoes (only random noise) and the cross spectra amplitudes and phases are randomly distributed. This could indicate that a sharp reflective layer was detected in a single 300 meter range gate and that its dynamics can be derived.

REFERENCES

Briggs, B.H., The analysis of spaced sensor records by correlation techniques, *MAP Handbook* 13, 1984.

Farley, D.T., H.M. Ierkic, and B.G. Fejer, Radar interferometry: a new technique for studying plasma turbulence in the ionosphere, *J. Geophys. Res., 86*, 1467-1472, 1981.
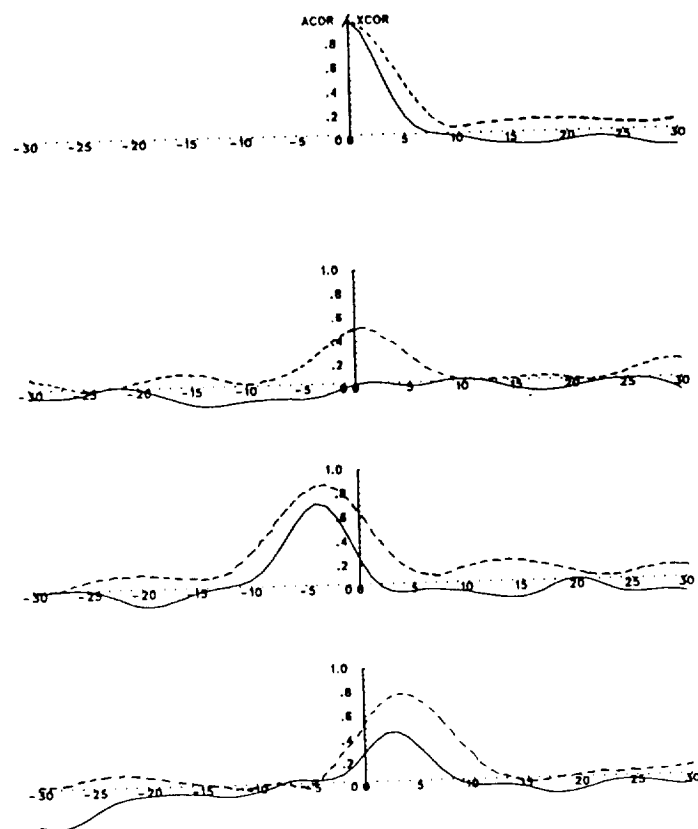
Figure 3. One example of the averaged autocorrelogram and the three cross correlograms corresponding to the three possible pairs of receivers calculated using the amplitude of the signal only (plain curves) or the full complex signal (dotted curves).
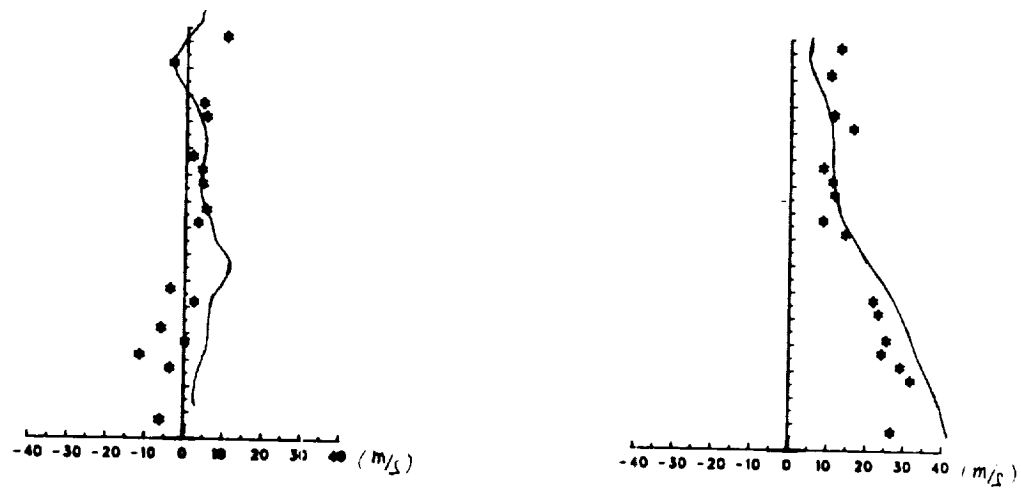
Figure 4. Meridional (left) and zonal (right) components of the wind velocity profiles as derived by SAD and DBS methods.
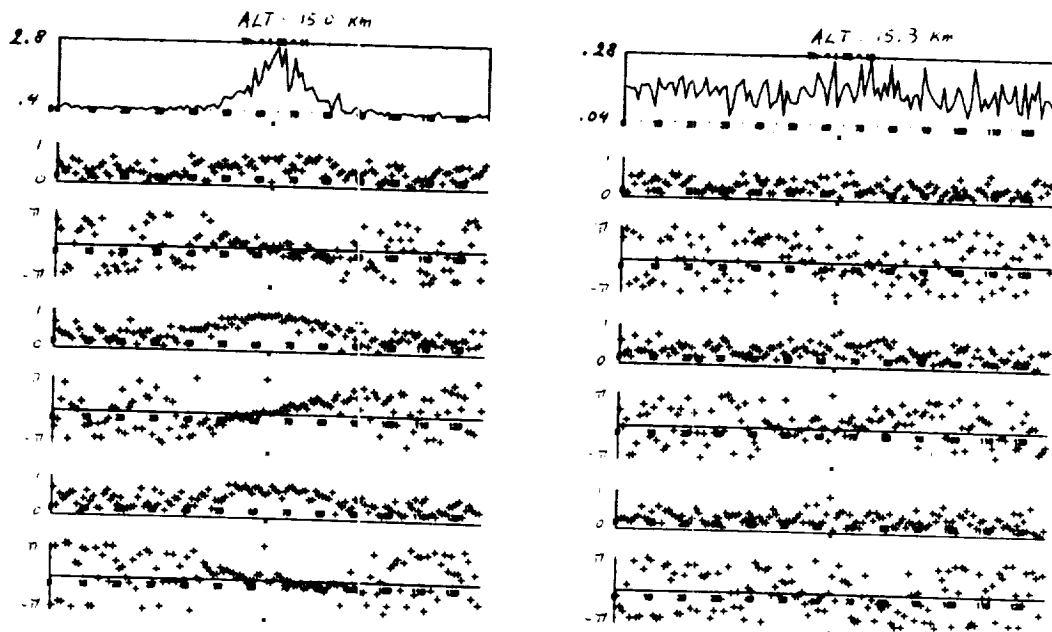
Figure 5. Averaged power spectrum and the three cross spectra (normalized amplitude between 0 and 1, and phase between + π and − π) for two successive range gates at 15 and 15.3 kilometers.

Fukao, S., T. Sato, T. Tsuda, S. Kato, K. Wakasugi, and T. Makihira, The MU radar with an active phased array system: 1. Antenna and power amplifiers, *Radio Sci., 20*, 1155-1168, 1985.

Fukao, S., T. Tsuda, T. Sato, S. Kato, K. Wakasugi, and T. Makihira, The MU radar with an active phased array system: 2. In-house equipment, *Radio Sci., 20*, 1169-1176, 1985.

Kudeki, E., Radar interferometer observations of mesospheric echoing layers at Jicamarca, *J. Geophys. Res., 93*, 5413-5421, 1988.

Meek, C.E., The analysis of ionospheric drift measurements, *ISAS report*, U. of Saskatchewan, Saskatoon, February 1978.

Meek, E., An efficient method for analysing ionospheric drift data, *J. Atmos. Terr. Phys., 42*, 835-839, 1980.

Woodman, R.F., and A. Guillen, Radar observations of winds and turbulence in the stratosphere and mesosphere, *J. Atmos. Sci., 31*, 493-505, 1974.

Wright, J.W., and M.L.V. Pitteway, Computer simulation of ionospheric radio drift measurements and their analysis by correlation methods, *Radio Sci., 13*, 189-210, 1978.

SPACED ANTENNA OBSERVATION BY THE CHUNG-LI VHF RADAR: PRELIMINARY RESULTS*

Chien-Ching Chiu and Yean-Woei Kiang
Department of Electrical Engineering, National Taiwan University
Taipei, Taiwan, ROC

Abstract

The spaced antenna drift (SAD) technique is a simple means to remotely sense atmospheric wind velocities by using radars. In this study the so-called "full correlation analysis (FCA)" method is applied to processing the echo signals received by three spaced antennas of the Chung-Li VHF radar. Detailed analysis provides useful physical quantities, such as horizontal wind velocity, random velocity of the irregularities, pattern size and axial ratio of the characteristic correlation ellipse, etc. Although only the preliminary data of the radar are analyzed, the numerical results we computed are in good agreement with the radiosonde measurements by the Central Weather Bureau, ROC.

1. Introduction

Scientific attention has recently been paid to the middle atmosphere which plays a significant role in the coupling between the solar-dominated ionosphere and the meteorologically important lower atmosphere. A variety of techniques have been proposed to probe the middle atmosphere to investigate the structure and the dynamics of this region. Among them, the MST (mesosphere-stratosphere-troposphere) radar is the most powerful one which usually operates in the range of VHF (very high frequency, 30-300 MHz) or UHF (ultrahigh frequency, 300-3000 MHz) (GAGE and BALSLEY, 1980; BALSLEY, 1981; RÜSTER et al.,1986). The pioneering work of WOODMAN and GUILLEN (1974) caused people to focus attention on using the VHF radar to probe the middle atmosphere via echoing from turbulence, layer structure or free electrons. With the advent of the MST radar technique, the atmosphere ranging from 1 km to 100 km can be observed and investigated.

One of the major advantages of the MST radar is its capability of continuously monitoring the variations of the atmosphere with large spatial coverage and with high temporal and spatial resolution. The radar echoes are caused by small variations of refractive index which are due to fluctuations in temperature, humidity, and pressure. By properly analyzing the echo signals, details about the structure and the dynamics, such as winds, waves, turbulence, atmospheric stability, etc., in the atmosphere can be determined (BALSLEY, 1981; RÜSTER et al., 1986).

The most direct and important measurement that the radar provides is the wind field as a function of height and time. In general, there are two methods for measuring wind velocity. One is Doppler beam swinging (DBS) and the other is spaced antenna drift (SAD) (RÖTTGER, 1983). For the DBS, a narrow radar beam is used and it is capable of being directed into different directions. The Doppler shift in the frequency of the echo gives the radial component of the drift velocity of the scatterers. By steering the radar beam in three directions, the three-dimensional wind velocity can be obtained. For SAD, the transmitting radar beam is directed vertically and several (usually three) spaced antennas are used to record the echoes. In the presence of a horizontal wind, the returned signals received by the spaced antennas show relative time displacements. These time displacements are determined from the cross correlation functions of the records taken in antenna pairs and from the time displacements the horizontal wind velocity can be computed (HOCKING, 1983; ROYRVIK, 1983a). Although these two techniques are experimentally different, they are closely related in the fundamental sense (BRIGGS, 1980).

The SAD method was earlier applied to the measurement of electron drift in the ionospheric E and F regions and later to the measurement of neutral wind in the ionospheric D region. Recently

this technique has been implemented for a VHF radar to probe the stratosphere-troposphere region (RÖTTGER and VINCENT, 1978; VINCENT and RÖTTGER, 1980). Moreover, the works of RÖTTGER (1981) and ROYRVIK (1983b) indicate that the SAD method is also applicable to VHF returns from the mesosphere.

In this study, the preliminary spaced antenna observations of the Chung-Li VHF radar are analyzed by using the "full correlation analysis (FCA)" (BRIGGS, 1968, 1984) which is the most useful and important numerical method of the SAD technique. Through signal processing, some physical quantities, such as horizontal wind velocity, random velocity of the irregularities, pattern size and axial ratio of the characteristic correlation ellipse, etc., are investigated in detail. These results may be useful in understanding the physics of the middle atmosphere. The measurements from the radar are compared with those obtained from the radiosonde by the Central Weather Bureau, ROC, and fairly good agreement is found.

The experimental operation is briefly described in Section 2, and the principle of full correlation analysis illustrated in Section 3. Included in Section 4 are the data analysis and numerical results. The experimental raw data of the Chung-Li radar are processed and the numerical results discussed. Finally, some conclusions from investigations are given in Section 5.

2. Experimental Operation

The reported experiments were made with the Chung-Li VHF radar located at Chung-Li, Taiwan, ROC (25°N, 121°E). As shown in Figure 1, the antenna of the radar system consists of three independent identical arrays of 8x8=64 Yagis which can be steered in a zenith and four off-zenith directions with total effective aperture equal to 2500 m^2. Three separate arrays are required for the SAD mode operation besides DBS mode.

The radar operates at a frequency of 52 MHz. The experimental data reported here were recorded on January 5, 1987, with a height resolution of 300 m from altitudes 1.5 km to 13.2 km and with a time resolution of 0.25 s. In other words, the pulse duration of the radar wave is 2 μs and the pulse repetition frequency 2 kHz. Only one antenna array (antenna 2, transmitted signals vertically with peak power 40.3 kW and the three receiving antenna arrays were beamed vertically to receive the scattered echoes. The returned signals were preintegrated (or coherently averaged) over 500 pulses for each of 40 height ranges and the resultant data were stored on magnetic tapes for analysis. Radar operating parameters are summarized in Table 1.

Table 1. Radar Operating Parameters

Parameter	Value
Frequency, MHz	52
Peak power, kW	40.3
Pulse duration, μs	2
Range resolution, m	300
Pulse repetition frequency, kHz	2
Coherent averaging, pulses	500

3. Full Correlation Analysis (FCA)

To obtain the horizontal wind velocity and related physical quantities from the received echoes of three spaced antennas, the "full correlation analysis (FCA)" (BRIGGS, 1984) is employed. Sometimes some records and results have to be rejected, either because of inadequacy of the data themselves (e.g., weak signals), or because the data do not satisfy the assumptions of the analysis. Therefore the application of the FCA method requires proper rejection criteria which of course depend on the nature of the data. Based on the criteria suggested by BRIGGS (1984),
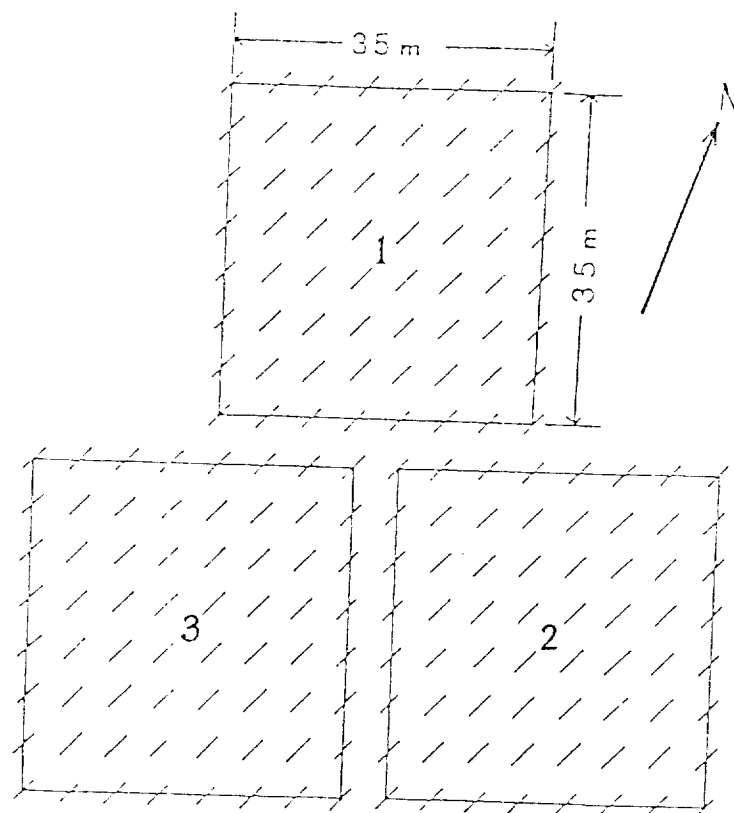
Figure 1. Arrangement of three antenna arrays of the Chung-Li radar.

and with some modifications, we implemented appropriate rejection criteria on the computer program and the numerical results show that they are satisfactory for the purpose.

4. Numerical Results

The recorded data are time series of preintegrated complex signals. Before further processing, the flash noise, which suddenly rises with the amplitude much larger than the normal values of signals, and the ground clutter should be eliminated.

Flash noise is eliminated by the following iterative process. First, from the sampled data s_j we calculate the mean $<s>$ and the standard deviation σ of either real or imaginary part. Secondly, if $| s_j - <s>| > 3.5 \, \sigma$, for some j, s_j is replaced by the average of s_{j-1} and s_{j+1}. Then, the new mean $<s>$ and standard deviation σ are calculated again from resultant data. Again, if $| s_k - <s> |$ 3.5 σ, for some k, s_k is still replaced by the average of s_{k-1} and s_{k+1}. Such process is repeated until no more data separate from the mean by 3.5 σ are left.

Ground clutter is further eliminated by subtracting out the average value from the signals. Note that the averaging time period should be much larger than the characteristic time scale of the echo signals. Here an averaging time period of about 30 min is chosen in our analysis process. Besides, to compare the power levels of signals from different heights at a time, we renormalize the signal by multiplying its amplitude by height range z.

The echo signals were recorded from 0901 to 0932 LST on January 5, 1987, with a time resolution of 0.25 s. The autocorrelation and cross correlation functions are calculated for each antenna and for each antenna pair. Signals are divided into segments and each segment is of length 128 points (i.e., of time duration 0.25 x 128 = 32 s). Over each segment the auto- and cross correlation functions are computed and processed to obtain the horizontal wind velocity and related quantities. Inspecting the autocorrelation function, we can easily determine the signal-to-noise ratio (SNR) from the spike at zero time lag, under the assumption of white noise. The autocorrelation function is then reshaped by removing that spike and modifying the value of zero time lag by its adjacent values through interpolation.

Figure 2 shows the profiles of echo power for time periods (0901 to 0916 LST) and (0916 to 0931 LST), normalized to the power from heights above 10 km. The SNR is about 10 - 20 dB from height 5.4. km to height 6.9 km. For higher ranges, the SNR is too low to give good results for wind velocity analysis. However, few reliable results are obtained at altitudes below 5.4 km even though the SNR there is in the range of 20 - 30 dB. This may possibly be caused by the partial saturation of the receiver and an incomplete removal of ground clutter (VINCENT and RÖTTGER, 1980). Therefore only the echoes from heights 5.4 km to 6.9 km are analyzed in detail and are discussed here. Numerical results show that in this region about 80% of the records result in reasonably good values of drift velocity, random velocity, pattern size, axial ratio, etc.

The height time plot of the magnitude of the horizontal wind velocity is illustrated in Figure 3a. The direction (measured clockwise from the north) from which the wind blows is given in Figure 3b, with zero degree giving the direction of north. Note that the mean speed is about 40 m/s and the wind direction is about 250°, a fairly acceptable result. It is found that from height 5.7 km to 6.6 km approximately 90% of data pass our criteria of FCA. Since the variations of CTD (corrected time delay (ROYRVIK, 1983b)) are computed to be as small as 5% or so, we may conclude that the estimates of velocities are quite reliable and the variations of the velocity with time are mostly due to the meteorological effect itself. Plotted in Figure 4 is the profile of the horizontal wind velocity averaged from 0901 to 0931 LST. The radiosonde measurements by the Central Weather Bureau at Pan Chiao (30 km away from Chung-Li) recorded at 0830 LST on the same day are also presented (by dots) for comparison. Evidently, the agreement between the radar and radiosonde measurements is quite good.

As mentioned in the previous section, the random changes of the irregularities in the atmosphere can be characterized by the random velocity v_c. Thus the ratio of the random to true
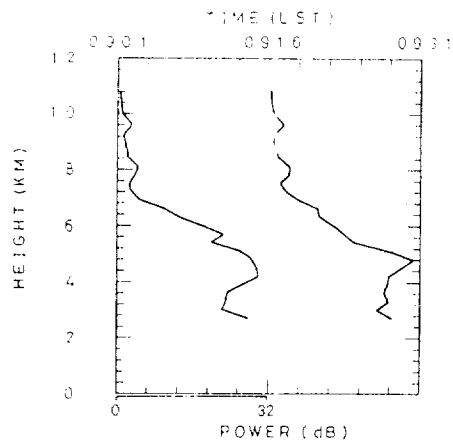
Figure 2. Profiles of echo power for time periods 0901 to 0916 LST and 0916 to 0931 LST.
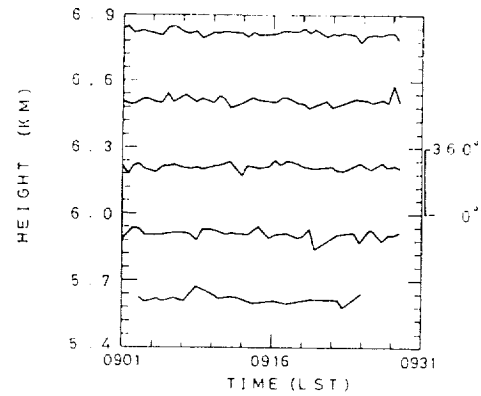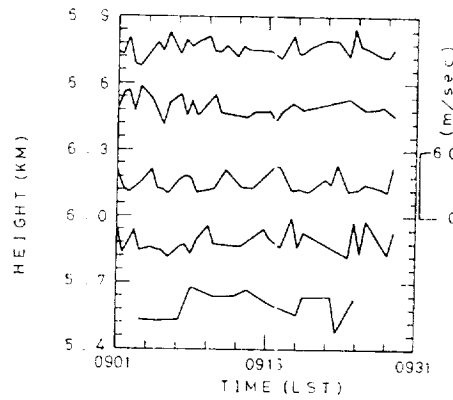
Figure 3. Horizontal wind velocity versus time at heights of 5.4 km to 6.9 km. (a) Magnitude of horizontal wind velocity. (b) Angle of direction (measured clockwise from north) from which the wind blows.
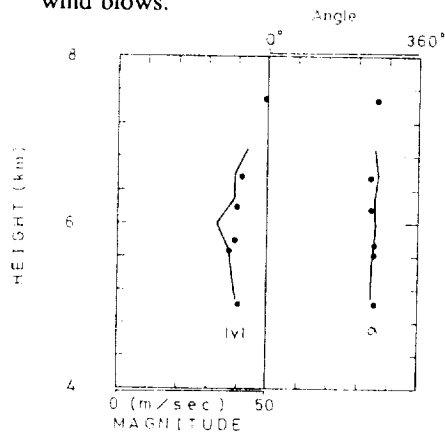
Figure 4. Profile of horizontal wind velocity for time period from 0901 to 0931 LST (|v|), magnitude; α, direction). The dots denote values of radiosonde measurements recorded at Pan Chiao.

velocity gives a measure of the relative importance of the random changes compared with the movement in producing time variation at a fixed receiver. The random velocity versus time at various heights is shown in Figure 5, and the random/true velocity ratio is plotted in Figure 6. Note that the mean random/true velocity ratio is about 1.4, indicating that the random changes of the pattern are large during the period of investigation.

To characterize the spatial correlation property of the field pattern, the histograms of minor axes (or pattern sizes) and axial ratios of the characteristic ellipses are plotted in Figures 7 and 8, respectively. Here data for all heights from 5.4 km to 6.9 km are shown together since there is no significant variation for characteristic ellipses over this range. The mean of the pattern sizes is about 40 m, which is compatible with the antenna spacing ($\simeq$ 40 m) of the radar system. Generally speaking, when the pattern size and antenna space are close to each other, the FCA method will give good results. This can also explain why the data below 5.4 km and above 6.9 km do not provide reliable results since the pattern size increases with the increasing height (VINCENT and RÖTTGER, 1980). It is found from Figure 8 that the axial ratios are generally less than 2 with a most probable value of 1.1. Therefore the anisometric property of the irregularity pattern in our case is not important. The distribution plot of the direction of the major axis (not shown here) also indicates that there is no preferential direction for the major axis of the characteristic ellipse.

5. Conclusions

In this study we have successfully obtained some physical quantities of the lower atmosphere by processing the echoes from the Chung-Li VHF radar using the full correlation analysis (FCA) technique. Although this is only a preliminary spaced antenna observation by the Chung-Li radar, the analyzed results are quite satisfactory. It has been found that both the magnitude and the direction of the horizontal wind velocity obtained from the radar are quite consistent with the radiosonde measurements by the Central Weather Bureau, ROC. Moreover, the pattern sizes of the characteristic correlation ellipses are found to be close to the antenna spacing for those echo data returned from the heights ranging from 5.4 km to 6.9 km, where good analyzed results are obtained by the FCA method. Also the anisometric property of the irregularities is insignificant in this region owing to the small values of axial ratios (around 1.1) obtained.

References

Balsley, B. B., The MST technique--A brief review, *J. Atmos. Terr. Phys.*, *43*, 495-509, 1981.

Briggs, B. H., An the analysis of moving patterns in geophysics -- 1. Correlation analysis, *J. Atmos. Terr. Phys*, *30*, 1777-1788, 1968.

Briggs, B. H., Radar observations of atmospheric winds and turbulences: A comparison of techniques, *J. Atmos. Terr. Phys.*, *42*, 823-833, 1980.

Briggs, B. H., The analysis of spaced sensor records by correlation techniques, *Handbook for MAP*, *13*, 166-186, 1984.

Gage, K. S., and B. B. Balsley, On the scattering and reflection mechanisms contributing to clear air radar echoes from the troposphere, stratosphere, and mesosphere, *Radio Sci.*, *15*, 243-257, 1980.

Hocking, W. K., The spaced antenna drift method, *Handbook for MAP*, *9*, 171-186, 1983.

Röttger, J., Investigations of lower and middle atmosphere dynamics with spaced antenna drifts radars, *J. Atmos. Terr. Phys.*, *43*, 277-292, 1981.

Röttger, J., Techniques for measurements of horizontal and vertical velocities, *Handbook for MAP*, *9*, 150-163, 1983.
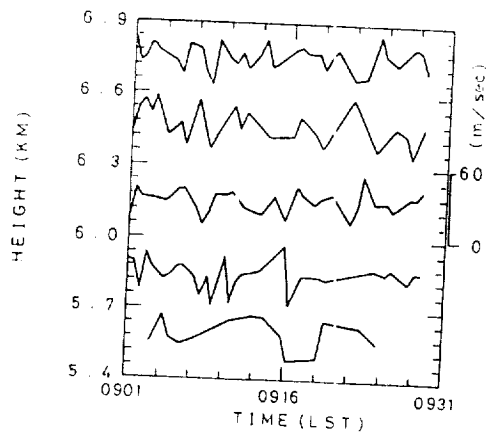
Figure 5. Random velocity versus time at heights of 5.4 km to 6.9 km.
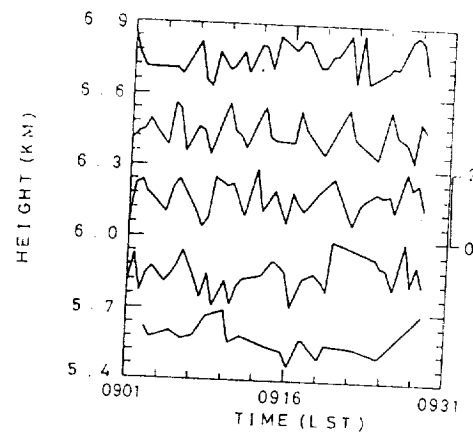
Figure 6. Random/true velocity ratio versus time at heights of 5.4 km to 6.9 km.
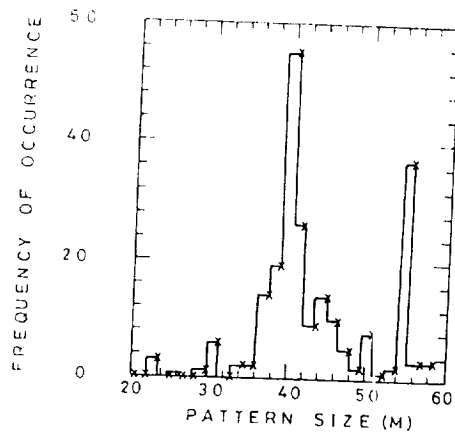
Figure 7. Histogram of pattern sizes of characteristic correlation ellipses from heights of 5.4 km to 6.9 km.
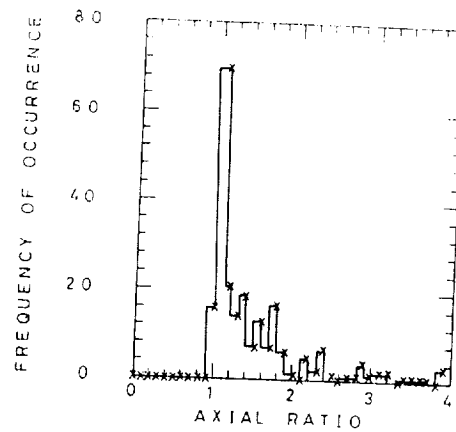
Figure 8. Histogram of axial ratios of characteristic correlation ellipses from heights of 5.4 km to 6.9 km.

Röttger, J., and R. A. Vincent, VHF radar studies of tropospheric velocities and irregularities using spaced antenna techniques, *Geophys. Res. Lett., 5,* 917-920, 1978.

Royrvik, O., Spaced antenna drift, *Handbook for MAP, 9,* 187-191, 1983a.

Royrvik, O., Spaced antenna drift at Jicamarca, mesospheric measurements, *Radio Sci., 18,* 461-476, 1983b.

Rüster, R., J. Klostermeyer, and J. Röttger, SOUSY VHF radar measurements in the lower and middle atmosphere, *IEEE Trans. Geosci., Remote Sensing, GE-24,* 966-974, 1986.

Vincent, R. A., and J. Röttger, Spaced antenna VHF radar observations of tropospheric velocities and irregularities, *Radio Sci., 15,* 319-335, 1980.

Woodman, R. F., and A. Guillen, Radar observations of winds and turbulence in the stratosphere and mesosphere, *J. Atmos. Sci., 31,* 493-505, 1974.

COMPARISON AMONG CLEAR-AIR RADAR, THERMOSONDE AND OPTICAL MEASUREMENTS AND MODEL ESTIMATES OF C_n^2 MADE IN VERY FLAT TERRAIN OVER ILLINOIS

J.M. Warnock[1], R.R. Beland[2], J.H. Brown[2], W.L. Clark[1], F.D. Eaton[3],
L.D. Favier[3], K.S. Gage[1], J.L. Green[1], W.H. Hatch[3], J.R. Hines[3],
E.A. Murphy[2], G.D. Nastrom[4], W.A. Peterson[3], and T.E. VanZandt[1]

[1]Aeronomy Laboratory
National Oceanic and Atmospheric Administration/ERL
Boulder, CO 80303

[2]Air Force Geophysics Laboratory
Hanscom Air Force Base
Bedford, MA 01731

[3]Atmospheric Science Laboratory
White Sands Missile Range, NM 88002

[4]Department of Earth Sciences
St. Cloud State University
St. Cloud, MN 56301

INTRODUCTION

An experimental campaign was conducted in June 1988 at the Flatland VHF clear-air Doppler Radar site, which is located in very flat terrain far removed from mountains near Champaign-Urbana, Illinois, to measure height profiles of the refractivity turbulence structure parameter C_n^2 and related turbulent parameters. Three different techniques were used to measure profiles of C_n^2: the Flatland radar (GREEN et al., 1988), a stellar scintillometer (OCHS et al., 1977), and thermosonde balloon flights (BROWN et al., 1982). Both the radar and scintillometer measured C_n^2 remotely by sensing the effect of the fluctuations of refractive index on the propagation of electromagnetic waves. At radio wavelengths the humidity and its gradient as well as the temperature gradients contribute significantly to the refractive index, whereas at optical wavelengths only the temperature fluctuations are important. In contrast to the remote sensors, the thermosonde measures the temperature fluctuations directly by measuring the RMS temperature difference between two very fast temperature sensors separated by a meter. The balloon instrument also made measurements of the height profile of the standard thermodynamic parameters (pressure, temperature, and humidity), plus wind speed and direction. Model estimates of C_n^2 were calculated from the thermodynamic and wind measurements using the numerical methods described by WARNOCK AND VANZANDT (1985). In addition, optical measurements were made of the transverse coherence length (EATON et al., 1988), and of the isoplanatic angle (EATON et al., 1985). Both these parameters depend on a weighted integrated value of C_n^2 through the atmosphere.

Comparisons among these measurements taken simultaneously in simple topography provide a unique opportunity to compare these different measurement techniques and to contrast these measurements with previous comparisons made in rough terrain (e.g., GOOD et al., 1982; GREEN et al., 1984; EATON et al., 1988). In this paper we present some preliminary results, which emphasize the radar measurements.

EXPERIMENTAL SET UP

Thermosonde System

The thermosonde system consisted of two parts, which were mounted below an ascending balloon (BROWN et al., 1982). One part was a standard VIZ digital microsonde, the other was a micro-thermo bridge thermosonde linked to the microsonde. The thermosonde measured the RMS temperature fluctuations between two unheated fine wire tungsten probes separated horizontally by one meter. The noise level of the instrument is about 0.002° C, and the data were recorded every four seconds giving about a 20-meter height resolution. The microsonde makes excellent height-resolution measurements of the standard thermodynamic parameters (pressure, temperature, and relative humidity), and wind speed and direction. The thermodynamic data were recorded every four seconds, which gave about a 20 m height resolution. The wind speed and direction were determined by using the Loran-C navigator system, and the data were recorded every ten seconds, which gave about a 50 m height resolution. A 1200-gram meteorological balloon was used to lift the instrument package with an ascent rate of about 5 m/s. The package was suspended from 90 to 180 meters below the balloon to ensure that the turbulent wake from the two meter balloon did not affect the measurements.

Flatland Radar

The Flatland radar (GREEN et al., 1988) is located about 8 km west of the Champaign-Urbana Airport [40.05° N, 88.38° E, 212 m above mean sea level (MSL)]. This clear-air Doppler radar (also called wind profiler or ST radar) operates at a frequency of 49.8 MHz (6.02 m wavelength), with peak and average power of about 10 kw and 150 watts, respectively. The pulse length and the range resolution are selectable from 150 to 2400 m. All the data reported in this paper were taken with a pulse length of 1.5 km and over-sampled with a range resolution of 750 m. In this experiment, the antenna beam was tilted twenty degrees off the vertical toward the east or south directions. With this tilt angle, echoes due to specular scattering were essentially eliminated, so that unambiguous C_n^2 measurements were obtained.

Optical Systems

Three optical systems were used in this study: a stellar scintillometer, an isoplanometer (EATON et al., 1985), and a transverse coherence length system (EATON et al., 1988). The isoplanometer measures the isoplanatic angle θ_0, which is the maximum angular extent of an extended object that can be viewed through turbulence, and the transverse coherence system measures the transverse coherence length r_0, which is related to the spread of a star image due to turbulence. The scintillometer, described below, measures a height profile of C_n^2, whereas both the isoplanometer and transverse coherence systems measure an optical quantity which is related to the weighted integrated value of C_n^2 through the atmosphere, i.e., θ_0 (radians) and r_0 (meters) are

$$\theta_0 = 0.528 \left[k^2 \int_0^\infty C_n^2(z) \, z^{5/3} \, dz \right]^{-3/5}$$

$$r_0 = 2.1 \left[1.46 \, k^2 \int_0^\infty C_n^2(z) \, dz \right]^{-3/5}$$

where k is the wavenumber of the light and z is the height above ground.

Stellar Scintillometer Model II

The stellar scintillometer Model II was developed by the Wave Propagation Laboratory of NOAA (OCHS et al., 1977). To operate the system, a star of second magnitude or brighter and within 45° of the zenith is selected. The system is sensitive to spatial wavelengths ranging from 5 to 15 cm, and measures seven different height regions of optical turbulence ranging from 2.2 to 18.5 km above ground level (AGL). The height weighting functions for these seven heights are broad, and are broadest at the highest altitudes.

Surface Measurements

An instrumented tower was installed near the telescope domes. In addition to the standard meteorological measurements, the temperature structure parameters C_T^2 and the solar radiation were measured. The temperature, dew point temperature, wind speed and direction, and C_T^2 measurements were made at both one and four meters above the surface, and the pressure and solar radiation were each measured at one height, one and four meters, respectively.

Model Estimates of C_n^2

Model calculations of C_n^2 were made from the microsonde upper air data; i.e., pressure, temperature, humidity, and wind speed and direction. The basic model concepts are given by VANZANDT et al. (1981). Since then, the model has been extended and revised considerably. We used the latest version described by WARNOCK et al. (1985), and used the numerical techniques described by WARNOCK AND VANZANDT (1985), to evaluate the model estimates. To compare the model estimates with results from previous comparisons with the Sunset and Stapleton radars, which are located in and near the mountains, respectively (WARNOCK et al. 1986; 1988), we used identical values of all the model parameters and constants except one: the constant in the equation giving the distribution of wind shear. This parameter quantifies the shear environment in the range of scales important in the onset of turbulence flow; therefore, the evaluation of this parameter allows the shear environment at these scales above the Flatland radar to be contrasted with its value above rough terrain.

Description of Campaign

This experimental campaign was conducted at the Flatland radar site from 6 to 15 June 1988. The scintillometer and isoplanometer systems shared a single telescope; the scintillometer operated at night and the isoplanometer operated during the day and in twilight. Thermosonde balloon launches were usually made after noontime and before midnight local time. A typical schedule was to launch a few packages in the afternoon and a few after dark. The radar operated during clear and cloudy conditions, whereas the optical systems operated during clear sky conditions. The optical telescopes were located about forty meters northeast of the center of the radar antenna, and the thermosonde launch site was about sixty meters east of the antenna center.

PRELIMINARY RESULTS

Measurements made by both the radar and scintillometer remote sensors are average values over both time and space. Five-minute data averages were used in this paper by both systems, and the height profiles measured by both systems are relatively smooth. In contrast, each thermosonde in situ measurement is an average over four seconds, which gives about a 20-meter height resolution. The four-second thermosonde data displays many very thin layers with large peaks in C_n^2. Frequently, the measured C_n^2 values fall to the observing noise level. Thus, to compare the thermosonde profile with the others we smoothed the thermosonde data. We used a Gaussian filter with $\sigma = 0.5$ km and truncated the filter at $\pm 2.5\,\sigma$.

Figures 1 through 3 show height profiles of the C_n^2 measurements from the radar, thermosonde, and scintillometer together with two model estimate profiles. All the radar data used in this preliminary study were taken with the antenna pointed 20° towards the east. The thermosonde and model profiles have been smoothed with the same Gaussian filter. One model profile gives the total C_n^2 including the humidity terms; this model, called model (radar), is compared to the radar data. The other model, called model (dry), omits the humidity terms; it is compared to the scintillometer and thermosonde profiles. Note that the dry and radar model profiles merge together at about ten km and are identical at higher altitudes.

Figure 1 shows the first example in this data set that has data from all three instruments. Recall that the thermosonde, scintillometer, and dry model profiles form one set of profiles, and that these three profiles are to be compared with each other; whereas the radar and radar model are a separate set of profiles. The agreement among the profile in each set is very good to excellent. The radar data are on the model (radar) curve except for the lowest point at 4.85 km; at that height the model (radar) is smaller than radar measurement. The next example, shown in Figure 2, is a daytime example, so there are no scintillometer data. Figure 3 shows the next nighttime example. In both cases the model (radar) is smaller than the radar data for the lowest two to three range gates. The data from the other range gates fit the model (radar) well.
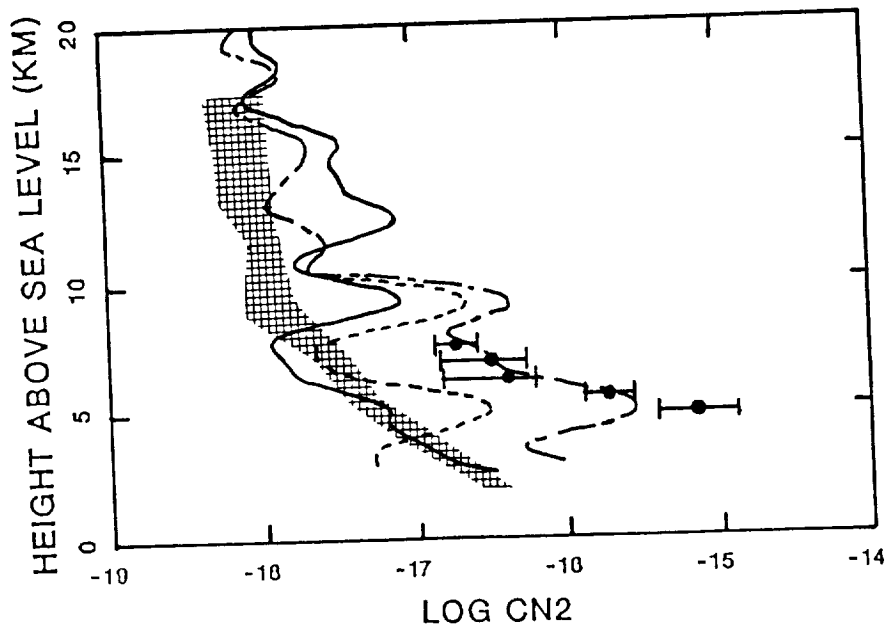
Figure 1. Height profile of Log C_n^2 for 02-03 hours, 8 June 1988 UT. The large solid dot is the median of the radar data for the hour, and the horizontal bars give the extreme values of the radar measurements for the hour. The solid line is the thermosonde profile; the balloon was launched at 02:04 UT. The hatched area gives the range of scintillometer measurements over the hour. The long-short dashed line is the model (radar) profile, and the dashed line is model (dry), which is to be compared with the thermosonde and scintillometer profiles.
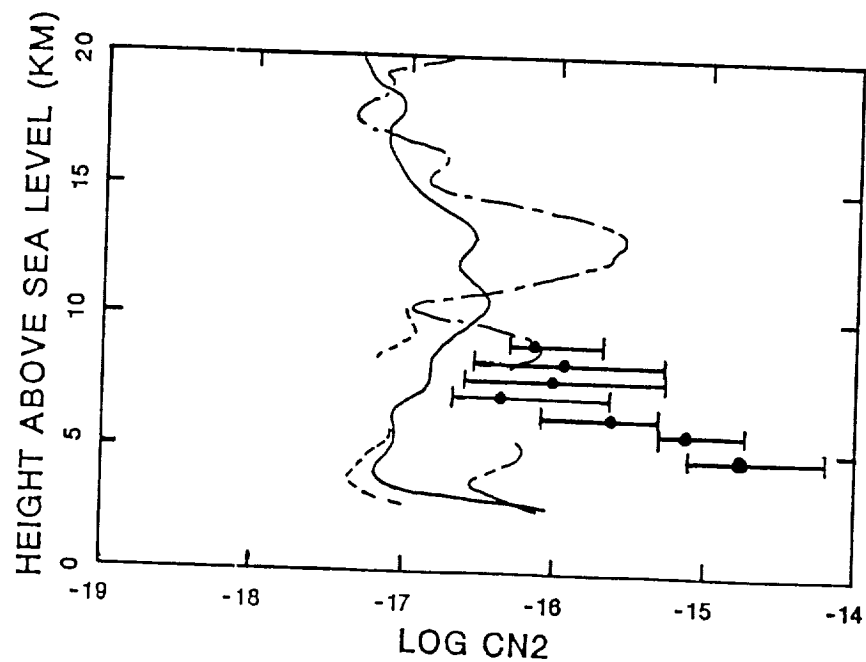
Figure 2. Same as for Figure 1 except for 18-19 hours, 10 June 1988 UT; the thermosonde balloon was launched at 17:12 UT. Because this was a daytime flight, there are no scintillometer data.
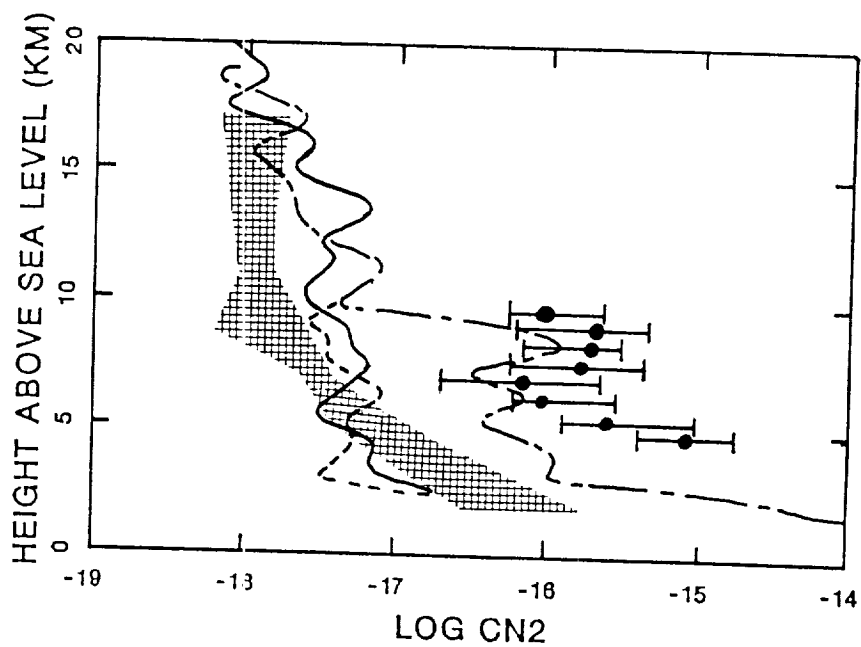
Figure 3. Same as for Figure 1 except for 00-01 hours, 11 June 1988 UT; the balloon was launched at 00:44 UT.

Figure 2 is not a typical example of the thermosonde measurements made during the day. For flights later in the afternoon, the thermosonde data were much larger than the nighttime measurements. This day/night effect is not yet understood.

All observational methods used in this study make several fundamental assumptions to derive a C_n^2 value from the raw data. The most important assumption is that the mixing is due to turbulent flows, and, further, that the turbulent flows are homogeneous and isotropic and that the observing scales are in the inertial subrange. Since the measurements and model estimates used in this preliminary study are generally consistent, these simplifying assumptions and analysis in terms of the C_n^2 structure parameter are generally useful. The relative importance of convective mixing, viscous damping at scales smaller than the innerscale, and anisotropic turbulent fluctuations will require further research.

SUMMARY AND CONCLUSIONS

An experimental campaign was conducted at the Flatland clear-air VHF radar site located near Champaign-Urbana, Illinois, in June 1988 to measure height profiles of the refractivity turbulence structure parameter C_n^2 and related turbulent parameters. This Flatland site was chosen because it is located in very flat terrain far removed from mountains, so that orographic effects are minimized. Three different techniques were used to measure the height profiles of C_n^2. The 50 MHz clear-air Doppler Flatland radar and a stellar scintillometer measured the profile remotely, and high resolution in situ measurements of C_n^2 were obtained from over 20 thermosonde balloon flight. The balloon instruments also measured the standard thermodynamic and wind data with excellent height resolution.

Model estimates were calculated from the standard balloon data and compared with the measurements. Because the radar measurements are sensitive to humidity and its gradient, whereas the thermosonde and scintillometer are not, two model profiles were calculated. One model profile included the humidity terms, called model (radar), and the other, called model (dry), did not.

During the nighttime, all the measurements and model profiles are generally consistent. There are two exceptions that occur systematically through the data set. One difference is that the model (radar) values of C_n^2 near five kilometers are consistently lower than the values measured by the radar. Another difference is that the scintillometer measurements at about 14 km are always smaller than the thermosonde and model estimates, and are near the instrumental noise level.

In all the nighttime cases, identical values of all the model parameters and constants were used in the model calculations. Furthermore, these values were identical to those used in previous studies using the Sunset and Stapleton radars except for one very important parameter. This parameter is the constant in the distribution function of wind shears. Its value at Sunset and Stapleton was 50% greater than its value at Flatland. This suggests that the wind shears at scales of the fine structure are smaller over Flatland than over mountainous terrain.

ACKNOWLEDGMENTS

REFERENCES

Brown, J.H., R.E. Good, P.M. Bench, and G.E. Faucher (1982), Sonde experiments for comparative measurements of optical turbulence, AFGL-TR-82-0079, AD-A118740, Air Force Geophysics Laboratory, Hanscom Air Force Base, MA.

Eaton, F.D., W.A. Peterson, J.R. Hines, and G. Fernandez (1985), Isoplanatic angle direct measurements and associated atmospheric conditions, Appl. Opt., 24, 3264-3273.

Eaton, F.D., W.A. Peterson, J.R. Hines, K.R. Peterman, R.E. Good, R.R. Beland, and J.H. Brown (1988), Comparisons of VHF radar, optical and temperature fluctuation measurement of C_n^2, r_o, and θ_o, Theor. Appl. Climatol., 39, 17-29.

Good, R.E., B.J. Watkins, A.F. Quesada, J.H. Brown, and G.B. Loriot (1982), Radar and optical measurements of C_n^2, Appl. Opt., 21, 3373-3376.

Green, J.L., J. Vernin, T.E. VanZandt, W.L. Clark, and J.M. Warnock (1984), A comparison of optical and radar measurements of C_n^2 height profiles, Preprint volume, 22nd Conf. on Radar Meteorol., Sept. 10-13, Zurich, Switzerland, 470-475.

Green, J.L., K.S. Gage, T.E. VanZandt, W.L. Clark, J.M. Warnock, and G.D. Nastrom (1988), Observations of vertical velocity over Illinois by the Flatland radar, Geophys. Res. Lett., 15, 269-272.

Ochs, G.R., T.-I. Wang, and T. Merrem (1977), Stellar scintillometer Model II for measurement of refractive-turbulence profiles, NOAA Tech. Memo ERL WPL-25.

VanZandt, T.E., K.S. Gage, and J.M. Warnock (1981), An improved model for the calculation of profiles of C_n^2 and ϵ in the free atmosphere from background profiles of wind, temperature, and humidity. Preprint volume, 20th Conf. on Radar Meteorol., Nov. 30-Dec. 3, Boston, MA, 129-135.

Warnock, J.M., and T.E. VanZandt (1985), A statistical model to estimate the refractivity turbulence structure constant C_n^2 in the free atmosphere, NOAA Tech. Memo ERL AL-10.

Warnock, J.M., T.E. VanZandt, and J.L. Green (1985), A statistical model to estimate mean values of parameters of turbulence in the free atmosphere. Preprint volume, 7th Symp. on Turbulence and Diffusion, Nov. 12-15, Boulder, CO, 156-159.

Warnock, J.M., J.L. Green, and W.L. Clark (1986), Studies of C_n^2 and its variability measured by the Sunset clear-air radar. Preprint volume, 23rd Conf. on Radar Meteorol., Sept. 22-26, Snowmass, CO, 34-37.

Warnock, J.M., N. Sengupta, and R.G. Strauch (1988), Comparison between height profiles of C_n^2 measured by the Stapleton UHF clear-air Doppler radar and model calculations. Preprint volume, 8th Symp. on Turbulence and Diffusion, Apr. 26-29, San Diego, CA, 267-270.

Simultaneous observations of the troposphere and lower stratosphere by the Flatland and Urbana ST radars: initial results

G. D. Dester, C. H. Liu, and S. J. Franke, G. R. Stitt

Department of Electrical and Computer Engineering, University of Illinois, Urbana, Illinois

J. L. Green

Aeronomy Laboratory, National Oceanic and Atmospheric Administration, Boulder Colorado

ABSTRACT

Simultaneous VHF radar observations of the troposphere and lower stratosphere were carried out on August 17-19, 1988 near Urbana, Illinois using the Flatland radar and the Urbana ST radar, which are operated by the Aeronomy Laboratory of the National Oceanic and Atmospheric Administration and the University of Illinois Department of Electrical and Computer Engineering, respectively. The two radar sites are located on the vast plain area of Central Illinois, separated by approximately 25 kilometers. The geographical and observational configuration is considered most suitable for investigating mesoscale structures in the troposphere-stratosphere region. One horizontally stratified layer at about 15.5 km related to the tropopause, and another in the troposphere at about 8 km were observed at both radar sites for a long period of time. Velocity fluctuations with periods of 100 minutes < T < 200 minutes were observed to be well correlated during a period of quiet horizontal wind. A convective thunderstorm on the evening of August 18 coincided with the dissipation of the tropospheric layer and a decrease in the amount of correlation observed at 8 km for both echo power and velocity. We present here a qualitative comparison of lowpass filtered echo power and radial velocities, and a comparison of vertical power profiles from the two radars.

The Doppler radar technique has been used in the past two decades or so to measure a variety of atmospheric parameters and phenomena. Doppler radars have proved to be quite valuable instruments in the study of atmospheric gravity waves, vertical velocity fluctuations, backscattered power, and other atmospheric properties. Different radar systems have been employed to study the atmospheric characteristics in a wide variety of climates and terrains, including those arranged in special network configurations, such as the Colorado profiler network [Strauch, et al., 1984] and the Penn State Doppler Network [Williams and Peters, 1986] for compilation of simultaneous data at several related sites. In the near future the planned wind profiler demonstration system will utilize 30 radar stations on a grid with spacings of ~400 km in an attempt to assess the impact of such a profiling system on meteorological forecasting [Chadwick, 1988]. However, each of these networks mentioned, and most other clear-air Doppler radars, or wind profilers, currently in use are separated by spacings on the order of 100 km or more. It would therefore be advantageous to have some radars separated by distances of less than 100 km to aid in the understanding of certain atmospheric parameters and phenomena on scales less than 100 km.

Ecklund, et al. [1985] and later, Carter, et al. [1989] have made simultaneous comparisons of stratospheric-tropospheric vertical velocities in the ALPEX campaign in France, which utilized three closely spaced (~4-6 km) 50 MHz radars. Carter, et al. [1989]

were able to observe several specific internal gravity wave events and determined detailed information on their wave parameters. Now with the recent completion of the Flatland radar [Green, et al., 1988] by the Aeronomy Laboratory of the National Oceanic and Atmospheric Administration (NOAA), and with the recent modifications for stratospheric-tropospheric (ST) observations made to the Urbana VHF radar, operated by the Department of Electrical and Computer Engineering at the University of Illinois at Urbana- Champaign, it has now become possible to study some of the atmospheric characteristics on an ~25 km scale in the vast plain area of Central Illinois.

When originally proposed, it was hoped that measurements made by the Flatland radar could be compared with those made by the Urbana radar in a joint scientific experiment [Green, et al., 1986]. It is of particular interest to carry out such a study in the plain area where the orographic effects are at a minimum [Green, et al., 1988]. Hence, a study of this type might help in providing answers for questions such as: without the dominant common source of an orographic nature, how are the velocity fluctuations observed at distances of 25 km apart related to each other? Under what conditions and in what frequency bands are these velocity fluctuations correlated? Can such a combination of radars aid in the study of the wavelength and speed of gravity waves? It is also well known that horizontally layered structures in the atmosphere contribute to the enhanced echo power of vertically pointing VHF radars [Gage and Green, 1978; Röttger and Liu, 1978]. With a 25 km spacing between radars it might also be possible to determine if certain layers observed in the troposphere and stratosphere exist on such a scale.

Thus, the study of the spatial and temporal structures of those horizontal layers using the echo powers and measurements of vertical velocities observed in the troposphere and stratosphere at the Flatland and Urbana sites will provide us with important information in the effort to understand mesoscale structures and vertical velocity activity in the absence of orographic influences. In this paper we report the initial results from the analysis of the data recorded by the Flatland and Urbana ST radars during a 47 hour period on August 17-19, 1988. In particular, echo power and velocity fluctuations were examined for correlation between sites in the bands with periods T < 100 minutes, 100 minutes < T < 200 minutes, and T > 200 minutes.

To the best knowledge of the authors, our results are the first attempt to study the stratosphere and troposphere using VHF radar data from two sites separated by about 25 km. In our observations, two horizontally stratified layers which extended for a long period of time at both radar sites were observed at approximately 15.5 km and 8 km, indicating that these layers are of a scale size greater than 25 km (Figure 1). The upper layer is most likely related to the tropopause, and we observed that longer period echo power fluctuations were better correlated than those observed at a band of higher frequencies (with periods 100 minutes < T < 200 minutes) at this layer. Correlation of power fluctuations with periods T < 100 minutes was not apparent. The lower layer existed throughout most of the data set, but disappeared 5 or 6 hours before the approach of a convective thunderstorm, which approached the area at approximately 2300 LT. Echo power comparisons at this height (8.5 km) indicate that good correlation can be observed in the lower frequency band (T > 200 minutes), but that it may also be possible to see good correlation in other frequency bands as well. It is difficult to say that one frequency band of echo power is more correlated than another at 8 km, as a whole, since the data set observed was for a short period of time and correlation of varying degrees was observed in each band.

Perhaps the item of most interest was the extremely good correlation observed in the vertical velocity fluctuations during the first 600 minutes of data on August 18, a period of low horizontal winds at 6.5 km. Figure 2 shows the radial velocities at both sites at the tropospheric heights for the entire campaign. Figure 3 displays the bandpass filtered radial velocities at 6.5 km for August 18. We note the excellent correlation. Here, we observed that in the frequency band 100 minutes < T < 200 minutes, the correlation was clearly much better than that observed at periods of T > 200 minutes, although this was not

(a)

Flatland
0830 08/17/88 - 0730 08/19/88
Power averaged over 40 minutes

(b)

Urbana
0830 08/17/88 - 0730 08/19/88
Power averaged over 40 minutes
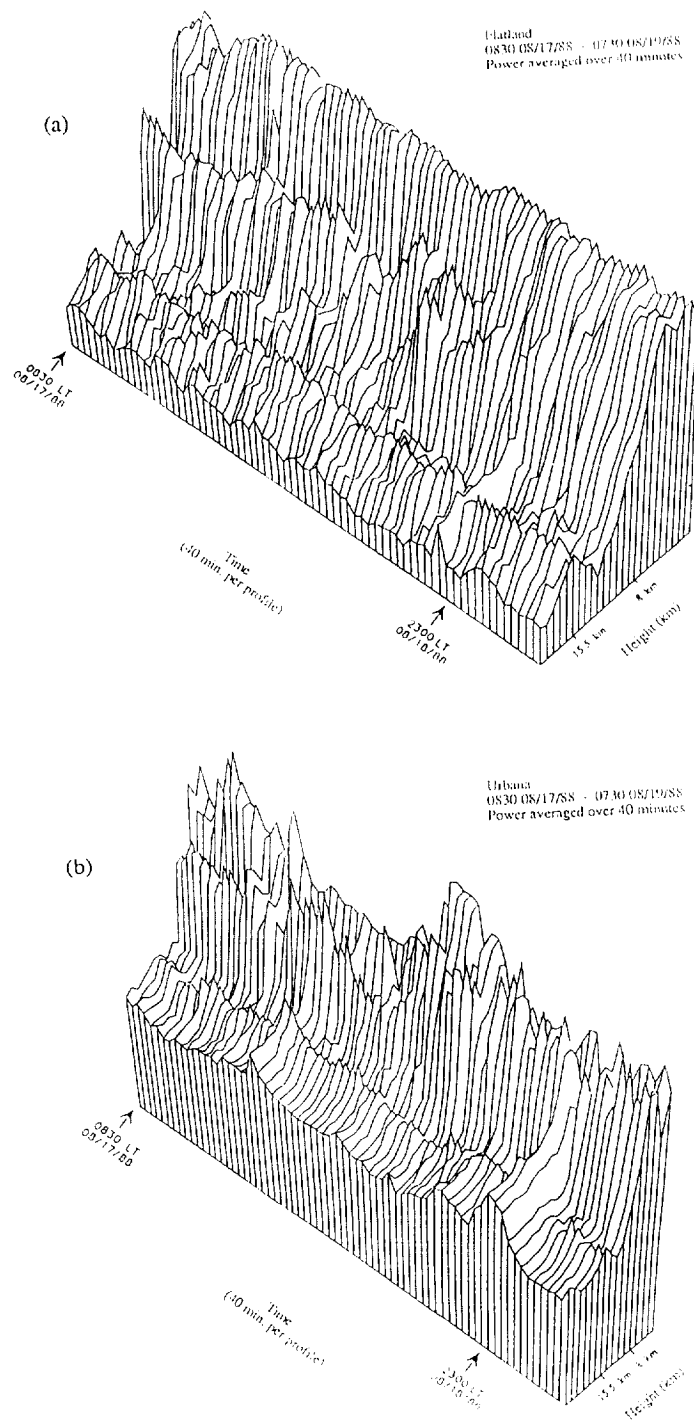
Figure 1. Echo power profiles as a function of time and height for (a) the Flatland radar and (b) the Urbana radar, averaged over 40 minutes on August 17-19, 1988.
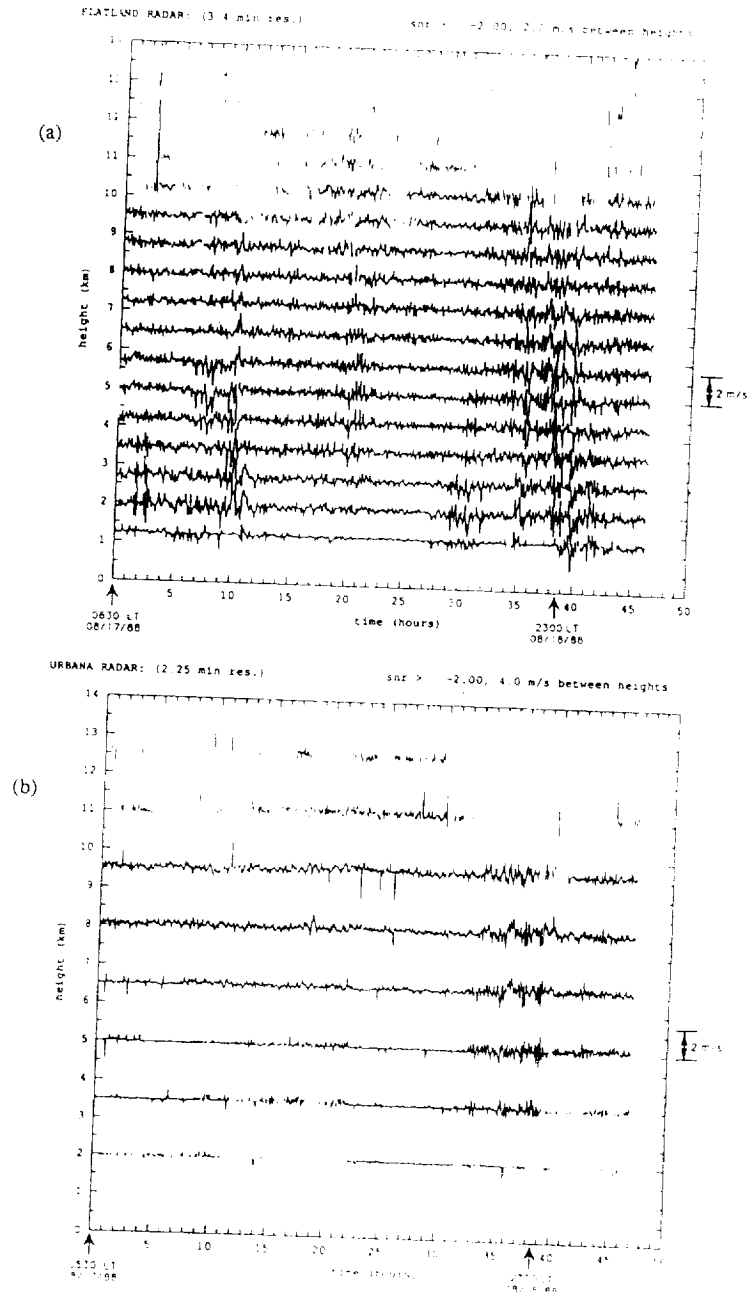
Figure 2. Radial velocity time series for August 17-19, 1988. (a) Flatland velocities are separated by 2.0 m/s between range gates (.75 km = 2.0 m/s). (b) Urbana velocities are separated by 4.0 m/s between range gates (1.5 km = 4.0 m/s). Only velocity estimates with a corresponding signal-to-noise ratio > 2.0 are shown.
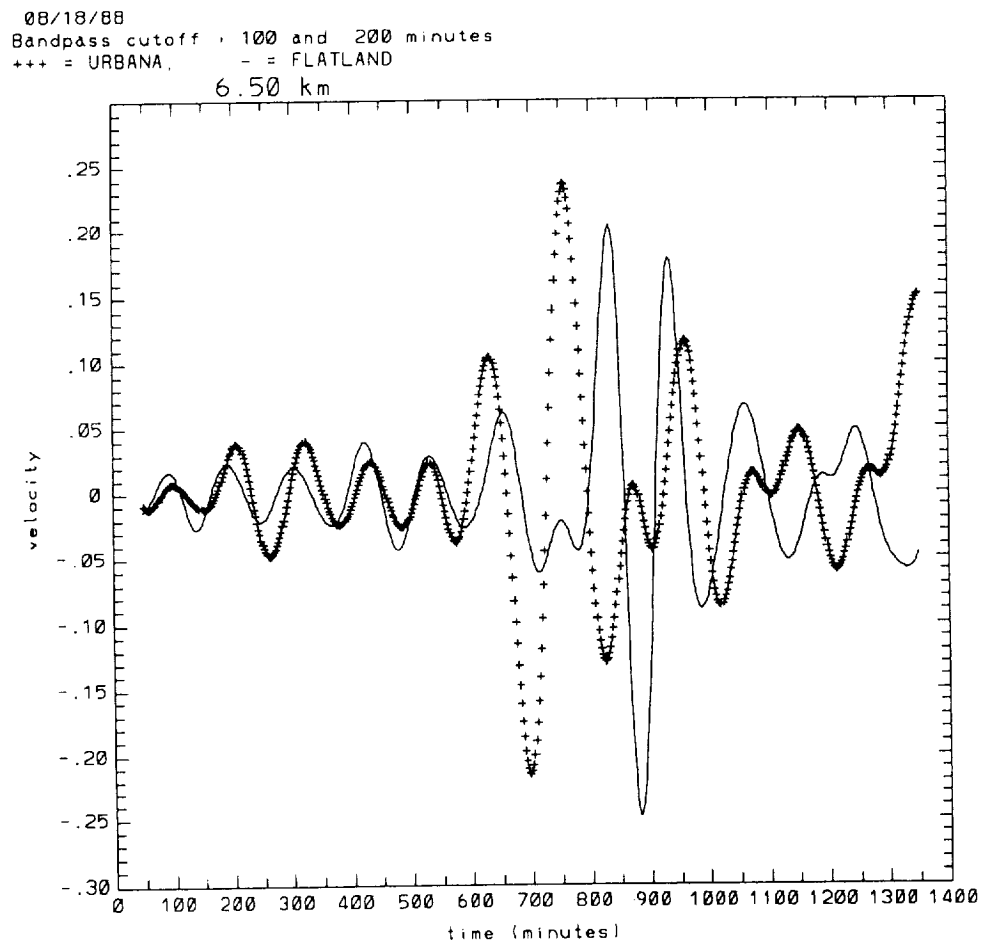
Figure 3. Simultaneous filtered radial velocity plots at 6.5 km for the Urbana and Flatland radars. A bandpass filter with cutoff periods of 100 minutes and 200 minutes was applied to the August 18 data. Solid lines and crosses indicate the filtered Flatland and Urbana data, respectively. We note the excellent correlation during the first 600 minutes.

necessarily the case at other times or heights. During periods of higher winds, the correlation in most bands was not quite as good as this specific instance during low winds. Carter, *et al.* [1989] observed that over a six week period the vertical velocity fluctuations at stations spaced ~4-6 km apart tended to exhibit increased correlation with decreasing frequency. However, on several days they isolated some specific wave events during periods of quiet winds which had periods of ~30-90 minutes. We were able to observe correlated vertical velocity fluctuations here with periods slightly longer than that, but it is reasonable to expect that stations spaced farther apart might be able to observe waves with longer periods. It was hoped that greater correlation would be seen during periods of higher winds due to the absence of orographic effects; this was not necessarily the case, however. One reason for this lack of significant velocity correlation could be due to the fact that the Urbana beam points ~3° off-vertical receiving contamination from the horizontal wind during more active periods. But this study does show that correlated velocity fluctuations do occur over a 25 km separation during a period of quiet horizontal wind.

As previously mentioned, *Carter, et al.* [1989] have recently published a more detailed analysis of internal gravity waves observed during the ALPEX campaign using three wind profilers with a spacing of ~ 4-6 km. They have shown that wind profiling Doppler radars can be quite useful for studying gravity waves in the lower atmosphere. Although it is beyond the scope of this paper, future experiments could be designed and conducted at the Flatland and Urbana radars to supply more detailed information on wave observations on the 25 km scale. The wind profiler demonstration network currently planned for deployment in the central United States will provide stations with a separation of ~400 km [*Chadwick*, 1988]. Additional information from Flatland-Urbana comparisons, coupled with comparisons of other radar stations could give a more complete description of wave parameters over a wide variety of scale sizes.

The particular method of analysis used here has been helpful in identifying the general frequency bands in which fluctuations in vertical velocity and echo power are correlated over a spacing of 25 km. However, this method does have problems in determining the specific frequency or frequencies of waves present in the data set. In the future, if a data set of longer length is available, additional methods such as the coherence method used by *Ecklund, et al.* [1985] and *Carter, et al.* [1989] would be helpful in detecting some of the weaker, underlying waves which are not visible with the present technique. This analysis would be especially helpful in determining the amount of correlation present for fluctuations with $T < 100$ minutes, which our present study was not able to do. Of additional interest to this experiment, another ST system is presently under construction at the University of Illinois Aeronomy Laboratory Field Station. This system will be steerable and will have improved range resolution, enhancing the observational capabilities for future comparisons with the Flatland radar.

REFERENCES

Carter, D. A., B. B. Balsley, W. L. Ecklund, K. S. Gage, A. C. Riddle, R. Garello, and M. Crochet, Investigations of internal gravity waves using three vertically directed closely spaced wind profilers, *J. Geophys. Res.*, 94, 8633-8642, 1989

Chadwick, R. B., The wind profiler demonstration network, in *Extended Abstracts, Symposium on Lower Tropospheric Profiling: Needs and Technologies*, pp. 109-110, American Meteorological Society, Boulder, Colo., 1988

Ecklund, W. L, B. B. Balsley, D. A.Carter, A. C. Riddle, M. Crochet, and R. Garello, Observations of vertical motions in the troposphere and lower stratosphere using three closely spaced ST radars, *Radio Science*, 20, 1196-1206, 1985.

Green, J. L., K. S. Gage, T. E. VanZandt, and G. D. Nastrom, The proposed Flatland radar, *Handbook for MAP*, 20, SCOSTEP Secretariat, Dept. of Electr. and Computer Eng., Univ. of Ill., Urbana, IL, 326-330, 1986.

Green, J. L., K. S. Gage, T. E. VanZandt, W. L. Clark, J. M. Warnock, and G. D. Nastrom, Observations of vertical velocity over Illinois by the Flatland Radar, *Geophys. Res. Lett.*, 15, 269-272, 1988.

Röttger, J., and C. H. Liu, Partial reflection and scattering of VHF signals from the clear atmosphere, *Geophys. Res. Lett.*, 5, 357-360, 1978.

Strauch, R. G., D. A. Merritt, K. P. Moran, K. B. Earnshaw, and D. D. van de Kamp, The Colorado wind profiling network, *J. Atmos. Oceanic Tech.*, 1, 37-49, 1984.

Williams, S. R., and R. Peters, The Penn State Doppler Network Progress Report, *Handbook for MAP*, 20, SCOSTEP Secretariat, Dept. of Electr. and Computer Eng., Univ. of Ill., Urbana IL, 339-341

INTERACTION OF MST WIND MEASUREMENTS WITH THOSE FROM THE UARS MISSION

Marvin A. Geller

Laboratory for Atmospheres
NASA/Goddard Space Flight Center
Greenbelt, Maryland, U.S.A.

Abstract

NASA's UARS (Upper Atmosphere Research Satellite) will be launched in late 1991 to increase our understanding of the radiative, chemical, and dynamical processes in the upper atmosphere. Cooperating MST measurements during this period will be very important in not only validating the UARS wind measurements but also in contributing to joint scientific studies.

1. INTRODUCTION

UARS, the Upper Atmosphere Research Satellite, is a major NASA mission that is planned to be launched in late 1991. The goals of UARS are as follows:

(1) to understand the mechanisms that control upper atmosphere structure and variability;

(2) to understand the response of the upper atmosphere to natural and anthropogenic perturbation; and

(3) to define the role of the upper atmosphere in climate and climate variability.

The UARS instruments will measure energy input into the upper atmosphere, upper atmosphere species concentrations, upper atmospheric temperature, and upper atmosphere winds. Thus, during the period of UARS, near global measurements of winds will be obtained from an altitude of about 10 km up to about 120 km. MST wind measurements will be important in complementing the UARS wind measurements in at least two ways. One is to help in the validation of the UARS measurements and the other is to use the continuous wind measurements at MST sites to complement the synoptic satellite wind measurements from UARS.

2. UARS WIND MEASUREMENTS

UARS will include the first satellite direct remote sensing measurements of the horizontal vector wind field in the upper atmosphere. Previous to this, winds have either been derived by applying balance relationships (e.g., geostrophic balance) to the satellite measured temperature fields, or wind fields have been generated by models that are constrained by satellite data. The directly measured winds on UARS will give heretofore unavailable information on ageostrophic winds in the tropics and at high altitudes where geostrophic balance breaks down. It will also allow direct determination of mean meridional motions rather than the indirect determinations that are being used now.

The UARS wind measuring instruments are HRDI and WINDII.

HRDI

The HRDI (High Resolution Doppler Imager) is a triple etalon Fabry-Perot interferometer that views the Earth's atmosphere through a two-axis gimbal telescope and measures atmospheric emission and scattering. The HRDI will measure horizontal vector winds over the altitude range of 10-110 km with an accuracy of 5 meters per second. The HRDI will also give measurements of atmospheric temperature. Since the HRDI utilizes scattered sunlight to make its stratospheric wind measurements, these are daytime only measurements.

The Principal Investigator for HRDI is Dr. P. B. Hays of the University of Michigan.

WINDII

The WINDII (WIND Imaging Interferometer) utilizes a Michelson interferometer to sense atmospheric emission and scattering to determine the vector horizontal wind as well as temperatures over the altitude range of 70 to 310 km.

The WINDII Principal Investigator is Dr. G. G. Shephard of York University in Canada.

3. SOME JOINT UARS/MST INVESTIGATIONS

The combination of MST and UARS measurements will enable research to be accomplished that would be impossible with either data set taken by itself. To illustrate this, we will first briefly discuss some of the ways in which MST measurements can contribute to UARS studies.

The first of these is to help in validating UARS wind measurements. There are many radar wind measurement stations around the globe. At several locations. wind profiles that cover a portion of the UARS wind measurement altitudes can be obtained. Radar wind measurements at the time of UARS overpass will be of great help in validating the UARS wind data. At some altitudes in the mesosphere and above, tides will become sufficiently strong so that it would be meaningless to construct synoptic maps of UARS winds at these altitudes. Radar winds will be most useful in determining where this is the case. In this connection, it will be most useful to validate UARS wind mapping procedures by comparing radar measured winds with UARS mapped wind products.

Radar measurement of gravity waves will be useful in establishing subgrid scale momentum flux effects that are needed to fulfill the momentum budget of the large scale equations of motion. Also, radar measurements of wave amplitudes might be able to be used to detect signatures in the UARS data that occur in the presence of large amplitude gravity wave events.

Radar measurements of turbulence will be useful in defining the morphology of turbulent diffusion for use in constituent studies. For example, the vertical gradients of constituent mixing ratios should be less in the presence of large turbulent intensities.

UARS data will be very valuable to MST radar investigations. The most obvious of these is that the UARS data will provide a global context in which single station MST data may be viewed. Also, UARS data and station MST data can be used together to view the interactions between small-scale and large-scale motions as well as the effects of small-scale motions on the UARS measured constituent structure.

4. SOME GUIDELINES FOR COOPERATION

A guiding principal since the inception of the UARS program is that all UARS data will be made available to all of the UARS Principal Investigators. Accompanying this principal, it was also decided that the UARS data will be under the control of the Science Team for a period of two years after which it shall be made available to the overall community. This is to allow the Science Team to validate the data before release.

Thus, it is recommended that a UARS Investigator be identified as the interaction point between UARS and the ground-based radar community.

The Separated Polar Winter Stratopause:
A Gravity Wave Driven Climatological Feature

Matthew H. Hitchman[1], John C. Gille[2], Clive D. Rogers[3], and Guy Brasseur
National Center for Atmospheric Research[4],
Boulder, Colorado 80307, U.S.A.

Abstract

An examination of temperatures derived from the Nimbus 6 PMR and Nimbus 7 LIMS instruments reveals that the winter polar stratopause is usually elevated and warmer than the adjacent midlatitude stratopause. This "separated stratopause" occurs in both hemispheres, but is more pronounced and persistent in the southern winter. It descends with time toward spring, and exibits week-to-week variability. Observational diagnostics and results from a 2-D model suggest that gravity wave driving can account for this separated polar stratopause by driving a meridional circulation, with downwelling over the winter pole. In the model, the solar heating pattern induces stronger winter westerlies than summer easterlies, which leads to a stronger gravity wave driven circulation in the winter hemisphere. Spherical geometry and the high latitude location of the winter westerly jet combine to yield a concentrated region of downwelling. Model results suggest that descent of the temperature maximum with time is probably caused by wave-mean flow interaction.

[1] Permanent affiliation: Meteorology Department, University of Wisconsin-Madison
[2] Presently Visiting Professor, Radio Atmospheric Science Center, Kyoto University
[3] Permanent affiliation: Department of Atmospheric Physics, Oxford University
[4] The National Center for Atmospheric Research is sponsored by the National Science Foundation.

PROGRESS IN EXISTING AND PLANNED MST AND ST RADARS

T. E. VanZandt

Aeronomy Laboratory
National Oceanic and Atmospheric Administration
Boulder, Colorado 80303, U.S.A.

Since the Third Workshop on Technical and Scientific Aspects of MST Radar in October 1985 two radars have gone out of operation: Sunset and Poker Flat. These radars played important roles in the development of the MST radar technique and the use of the technique for atmospheric research and operational meteorology. The Sunset radar, inspired by the research of Woodman and Guillen at the Jicamarca radar, was the first VHF radar developed specifically to use the MST radar technique. It demonstrated the feasibility of studying wind and turbulence using small, relatively inexpensive radars. The Poker Flat radar was the first MST radar to use distributed transmitters. Some of these transmitters, as well as parts of the antenna, have been used in the development of other radars discussed later in this session.

Since the last Workshop, several radars have been modified or upgraded, several more have been brought into operation, and the planning and development of others has progressed.

At least three themes may be noted in the recent developments. First, the importance of networks of radars for studying atmospheric dynamics has been increasingly recognized. In particular, the installation in the central United States of the 31 radars in the Wind Profiler Demonstration Network starting in January 1989 will have important impacts on the use of the MST radar technique for both research and operational meteorology. Unfortunately, there was not any report on this system at the present Workshop. Second, the global importance of tropical meteorology has stimulated the location of several radars in the tropics. Finally, several of the recent and planned radars are located in very flat terrain, to obviate the geophysical noise from orographical effects.

New developments at the Jicamarca radio observatory

Ronald F. Woodman, Miguel Leiva C. and Otto Castillo G.
Jicamarca Radio Observatory
Instituto Geofísico del Perú.
Aptdo. 3747, Lima, Perú.

An important step has been completed at the Jicamarca Observatory. The new data acquisition system, including a coherent integration preprocessor, has been placed in operation. It matches the improved bandwidth obtained with the new transmitter final stage. The system can process 256 range gates in parallel, from 4 receiver channels, at a resolution of 250 meters. Two receivers, 128 altitudes can be processed with 125 meter resolution. User friendly subroutines have been developed which facilitate the writing of data taking programs using the new system. A fairly general program for MST radar type observations has been written and tested. The program has been written as a module of EXCO, the general Jicamarca data taken supervisor programs. The system has been used already for two fifteen day campaigns of mesospheric observations designed to study gravity wave momentum deposition (Fritz et al,1988) the implementation of a frequency domain interferometer(Kudeki and Stitt, 1987) and new high altitude–resolution mesospheric and stratospheric observations. A sample of high resolution measurements will be presented.

A new set of steering cables has been cut. They allow antenna pointing into four different symmetrical directions, approximately 2.5° from zenith in the N, S, E, and W directions, and therefore momentum deposition experiments using Vincent and Reed's technique.

A new Harris H–800 computer is being installed. The system has two 300 Megabytes disk units and a fast 6250 b.p.i tape drive. The CPU should allow three times as fast processing as compared with the present system. Two 286 Zenith PC's with EGA graphics (one color) have been added as terminals and a Apple Laserwritter as a printer–plotter.

The second transmitter final module is 90% complete. We hope to have it in operation in a few months. A new solid state power supply at 20,000 Volt, 20 Amp, for the final stages has been put in operation.

The new data acquisition system, including the special software, and the solid state power supply have been designed and build at the observatory.

With 2.5 megawatts (5 MW upon completetion of the transmitter upgrade) of power, 9 hectare antenna and the new resolution, the Jicamarca radar should recover a leading position as the most sensitive radar in the MST field.

40 kms

80

70

± ⅛ →

60

10:00   **11:00**   **12:00**   L.T.
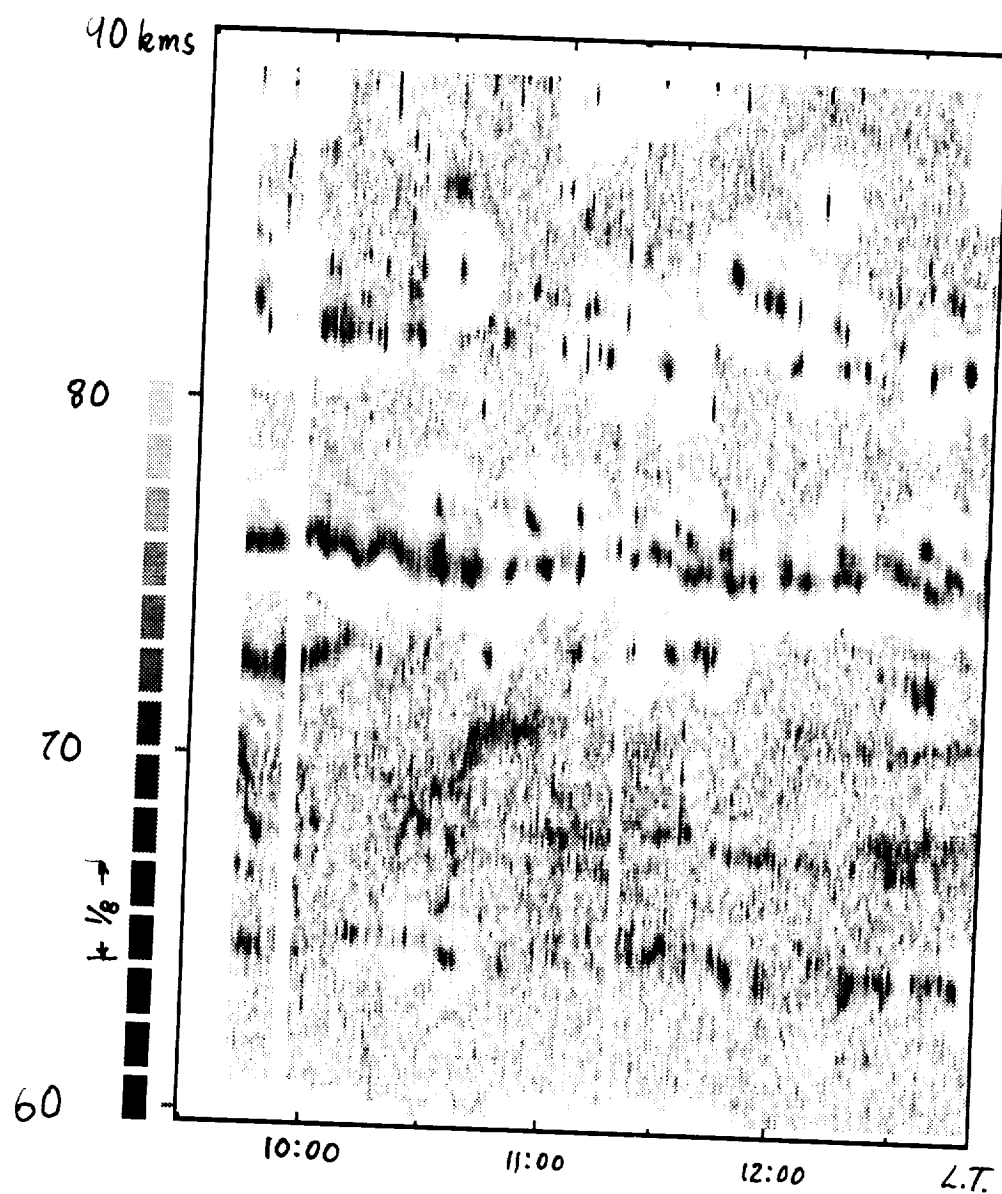
Figure 1. Range-time-intensity plot of mesospheric echoes taken with the new system at 150 meter resolution. The power shades represent a linear scale to enhance the narrowness of the layers and its intermittence. Powers are normalized with respect to a maximum in the neighborhood of (± 1 km, ± 10 min). Note that all layers have about 300 meters in width.
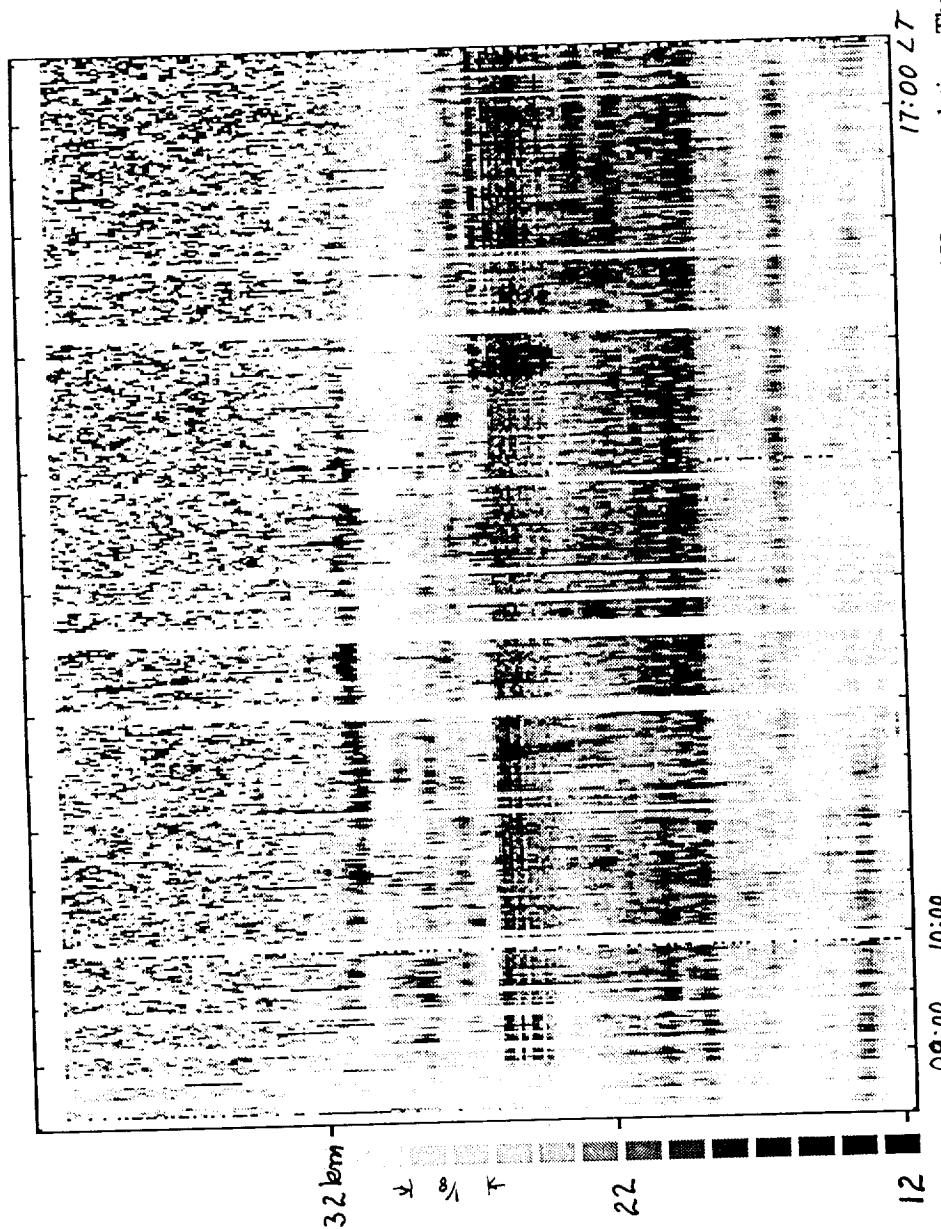
Figure 2. Range-time-intensity plot of stratospheric echoes taken with the new system at 150 meter resolution. The power shades represent a linear scale. Powers have been normalized with respect to the maximum power at 16 km. The normalization is varied exponentially with altitude to keep the powers within the dynamic range of the gray scales. Please ignore the digital noise around 25 km.

PRESENT AND PLANNED NEW CAPABILITIES OF THE
ARECIBO RADAR SYSTEMS

H. Mario Ierkic V.

Arecibo Observatory, P.O. Box 995, Arecibo P.R. 00613.

I.   Notes of interest

At Arecibo there are 3 radars (also) used for MST work. Significant improvements have been made both in the software and hardware parts of the systems and will be described next. The HF facility near Arecibo has been used for mesospheric work before but is not mentioned here (interested users are kindly asked to contact the author).

VHF radar

- System operational with very good performance. It has been used primarily for ST and Ionospheric Modification work and in conjunction with the UHF radar.
- We are working on a severe interference problem that prevents the use of the automatic pointing capabilities.
- Radio interference at nearby frequencies is often severe.
- Echoes have been observed also from the mesosphere.
- Circular polarization capability is being installed.

UHF radar

- Improvement of system's recovery time that should allow us to cover a region closer to the boundary layer.
- We have operated the 430 Mhz system in a monostatic and a bistatic fashion to observe a common scattering volume from two angles widely separated (more than 10 degrees).
- We have received 16 additional (used) klystrons.
- A new digitizing system will make it possible to recuperate 150m resolution and also allow us to carry on dual frequency experiments with improved efficiency. The system will be installed during 1989.
- New data acquisition software has been written.

S-band radar

- New software package to carry on experiments leading to the estimation of spectral characteristics of echoes from the lower stratosphere with unprecedented (15m) height resolution. This last development was made possible by using our new 2048 channel, 40 Mhz correlator. Figure 1 shows a gray scale plot of intensities in the tropopause with coherent wave activity (height resolution is about 20m).

II. Acknowledgements

I want to thank P. Perillat for the superb software development work and B. Sisk and D. Albino for the improvements of the 46.8 and 430 Mhz radar systems.

A O S-Band System
Intensity
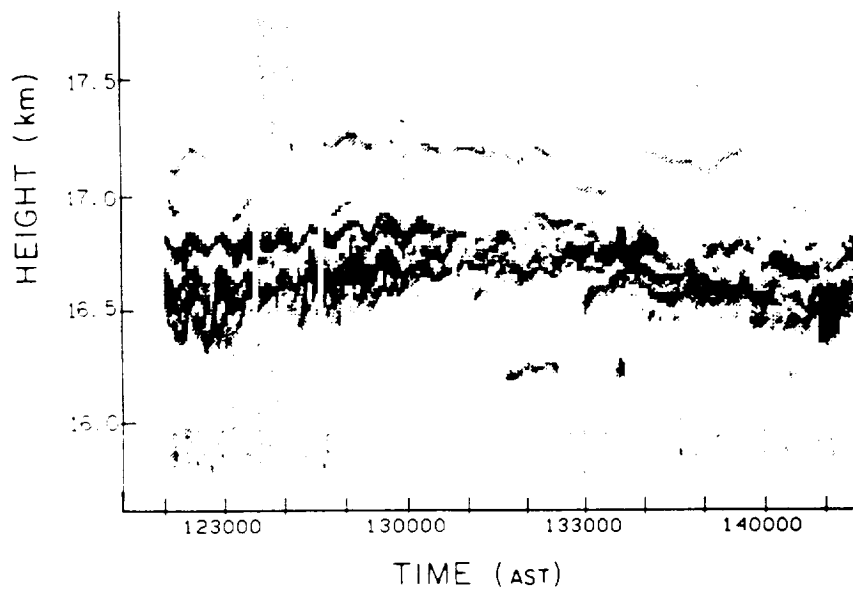
FIGURE I

STRATOSPHERE AND TROPOSPHERE STUDIES WITH THE MILLSTONE HILL UHF RADAR: RECENT IMPROVEMENTS AND FUTURE PLANS

Stephen A. Cohn

Haystack Observatory
Massachusetts Institute of Technology
Westford, MA 01886 USA

ABSTRACT

After several years of dormancy the S-T mode of operation at the Millstone Hill UHF radar is again active. During these years a number of hardware improvements were made to the radar system in conjunction with the continuing incoherent scatter research program. These improvements and other significant changes expected in the near future are discussed in the context of improved S-T observations. In addition, expansion of a limited S-T capability to the L-band and X-band radars also located at Millstone Hill is outlined.

IMPROVEMENTS IN THE PAST FIVE YEARS

A review of the status of the S-T program at Millstone Hill in 1983, as well as a description of the Millstone Hill UHF radar system is given in RASTOGI, 1983. Between 1983 and 1988 the program was inactive but a number of improvements were made to the hardware which have enhanced our ability to collect turbulence backscatter:

1. The original X626 UHF transmitter was retrofitted with L-3403 Litton klystrons with 2.5 MW peak / 75 kW average output.
2. A second UHF transmitter was also built with 2.5 MW peak output and brought on line in September 1986.
3. Both UHF transmitters are operational with a combined peak power output of 5.0 MW.
4. Both UHF modulators were redesigned incorporating fiber optic links for timing control. The modulator switch tubes were upgraded from Machlett 7248's to Thompson CSF TH-5188's. With the new modulators high repetition rate operation is now a reality. The present modulator capability is from $1\mu s$ to 2ms with full peak power output. Typical modulator pulse rise time is $11\mu s$ and fall time $10\mu s$.
5. The improved modulator fall time allows sampling at a shorter range. It is now possible to sample down to an altitude of 1.0 km when using a low elevation angle.
6. The receiver system was upgraded using low noise G-As FET's, and receiver TR circuitry was moved up onto the back of the 150 foot UHF antenna. Typical system noise temperatures are now 120 K.

The circuit modifications to the receiver room, transmitters, and RF system have given the Millstone UHF radar a perfect record of meeting project commitments for the past two and one-half years.

CURRENT IMPROVEMENT: EXPANSION TO A MULTIFREQUENCY FACILITY

An effort is currently underway to use two other radars at Millstone Hill for lower atmospheric turbulence studies. The main scientific motivations for this and some preliminary results are presented in COHN, 1989. In addition to allowing multiwavelength experiments, the other radars (the Millstone L-band and Haystack X-band radars) could, when available, be used independently for S-T experiments. Updated UHF parameters and parameters of the L-band and X-band systems are presented in table 1. Also, typical parameters used during a lower atmospheric experiment are included in table 2.

To minimize the modifications to these systems the following is planned for radar control and signal processing. Pointing and transmitter control is handled by each radar individually. The received signal is mixed to an intermediate frequency (IF) and sent through intersite cables to the UHF receiver room. Also, a timing pulse is sent from the remote system to synchronize the UHF timing to that of the other system. The UHF system mixes the remote IF to 2 MHz, samples it, and does the same processing as would be done to a local UHF measurement. Although this arrangement does not allow simultaneous use of the three systems, control can be switched between them in just a few minutes. In the future, multiple copies of the proposed MIDAS will allow truly simultaneous operations.

FUTURE IMPROVEMENT: A NEW DATA ACQUISITION SYSTEM

The Millstone Ionospheric Data Acquisition System (MIDAS) is being developed for ionospheric experiments at Millstone Hill. MIDAS is portable and, together with an interface specific to each radar, will control antenna motion, transmitter waveforms, and signal sampling and processing. Many of the new and enhanced capabilities of the system will be beneficial for collecting S-T as well as ionospheric data; however, to take advantage of these some development specific to the S-T program will be necessary.

The added capabilities include:

1. The MIDAS system will have a larger processing capability, allowing more samples to be collected per pulse. This could eliminate the tradeoff now made between higher spatial resolution and greater height coverage.
2. The MIDAS system will be capable of supporting coded pulse experiments at higher resolution than the existing system.
3. When several of the receiver chains have been built, simultaneous observations with the site's three radars will be possible.
4. The configuration of the computers controlling the MIDAS will allow much more real-time processing than is now possible.

In addition to its use at Millstone Hill, it is possible to use the MIDAS system with other radars which have adequate transmitters but cannot at present do S-T measurements because they lack the processing software.

Table 1
CHARACTERISTICS OF THE MILLSTONE HILL RADARS

		UHF Steerable	L-band	X-band
Wavelength	(m)	0.68	0.23	0.03
Diameter	(m)	46	26	37
Peak Power	(MW)	2.5	2.5	0.3
Gain	(dB)	46	47	67
System Temp	(K)	120	150	250
Beamwidth	(deg)	1.0	0.6	0.06

Table 2
TYPICAL PARAMETERS DURING AN ST EXPERIMENT

Points in spectrum		256		
Pulse Length	(μs)	10		
Range Resolution	(km)	1.5		
Receiver Bandwidth	(KHz)	100		
Minimum altitude	(km)	1.		
Interpulse period	(μs)	1036		
		UHF Steerable	L-band	X-band
Coherent Integrations		8	3	1
Frequency Window	(Hz)	±60	±161	±483
Frequency Resolution	(Hz)	0.47	1.26	3.77
Max Radial Velocity	(m/s)	±21	±19	±7.2
Velocity Resolution	(m/s)	0.16	0.14	0.06

458

REFERENCES

Cohn, S.A., Multifrequency stratospheric and tropospheric (ST) studies at Millstone Hill: Motivations and preliminary results, *MAP Handbook*, this volume, 1989.

Rastogi, P.K., Stratospheric and tropospheric (S-T) studies at Millstone Hill: Recent results, capabilities and limitations, *MAP Handbook, 9*, 357, 1983.

RECENT PROGRESS WITH THE SOUSY VHF RADARS

Peter Czechowsky, Bernd Inhester, Jürgen Klostermeyer,
Iain M. Reid, Rüdiger Rüster and Gerhard Schmidt
Max–Planck–Institut für Aeronomie, Katlenburg–Lindau, FRG

The antenna system of the mobile SOUSY VHF Radar on the island of Andøya (69°N, 16°E) in Northern Norway has recently been upgraded from four to six beam directions. Beams are now directed towards the SW, W, NW, N, and NE. Apart from this, the systems have not been improved. However, more of their capabilities have been utilized. In August 1986, the mobile radar was operated with a 44 Yagi antenna and 17 kW peak power in Lindau, 30 km from the Harz radar (52°N, 10°E). Both radars operated in a 5 beam (EWNSV) configuration (see Figure 1), and seven days of simultaneous observations were obtained. These allowed the upward fluxes of horizontal momentum to be calculated, and an example from the radar located at Lindau is shown in Figure 2. These observations are also being used to the vertical energy flux and its power spectral density (Figure 3). During the MAC/SINE campaign in Northern Norway in summer 1987, the very thin strong layers near 86 km typical at this time of year were detected in the grating lobes of the antenna at apparent ranges of about 104 km (see REID and CZECHOWSKY, this volume). These additional beam directions have been used to investigate the anisotropy of the scattering irregularities. Measurements of the component of the upward flux of horizontal momentum per unit mass in the SW-NE direction, and the anisotropy of the horizontal velocity field were obtained from measurements made in the main lobes of the antenna (see REID and RÜSTER, this volume). High resolution measurements were obtained within periods characterized by strong vertical motions. The time and range resolutions were 3.5 s and 75 m respectively. Results are shown in Figure 4, 5 and 6. The Harz radar was operated on a campaign basis during summer 1988 using a 13 beam configuration (EWNS at 3.5, 7 and 10°, and vertical) that permits redundant estimates of the Reynolds stress tensor and of the two dimensional aspect sensitivity of the scattering irregularities to be obtained. These observations demonstated for the first time that the very strong radar returns from the summer polar mesopause region are also obtained, on occasion, from the mesopause in summer at 52°N. An example is shown in Figure 7. The development of a UV (351 nm) Lidar has proceeded in parallel, and it is now capable of measuring density and temperature up to 90 km.
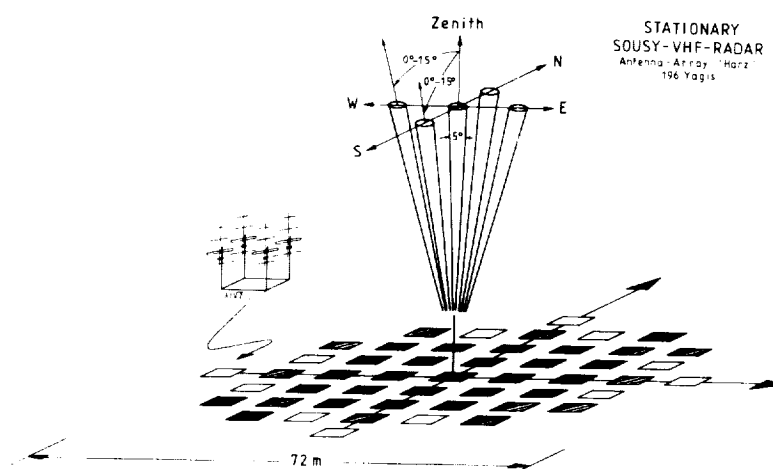
Fig. 1 Configuration of the antenna array of the stationary SOUSY VHF Radar, located in the Harz mountains (FRG). Each square represents a subsystem consisting of four 4-element Yagi antennas. The grey scale indicates the electrical tapering: darker symbols are fed with higher power. The main beam is steerable by means of electronic phase shifters in any requested azimuth up to an off-zenith angle of 15°. This kind of configuration is now used routinely with this radar.
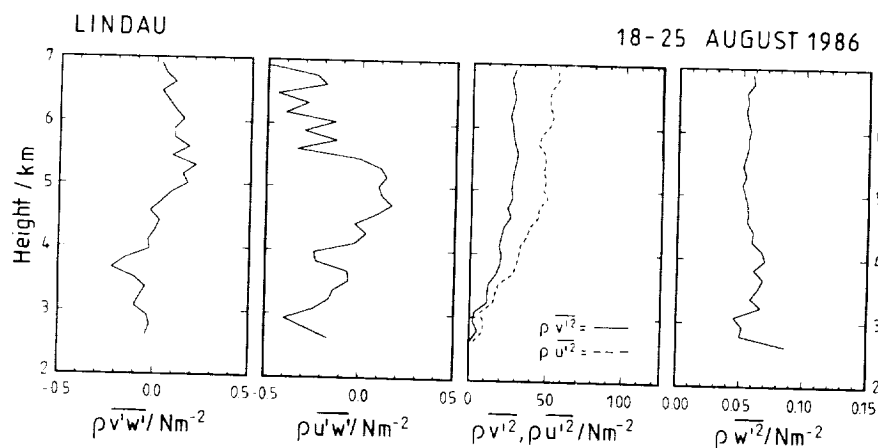
Fig. 2 Tropospheric values of the upward flux of zonal $(\overline{\rho u'w'})$ and meridional momentum $(\overline{\rho v'w'})$ for a seven day period and the density weighted zonal, meridional and vertical square velocities.
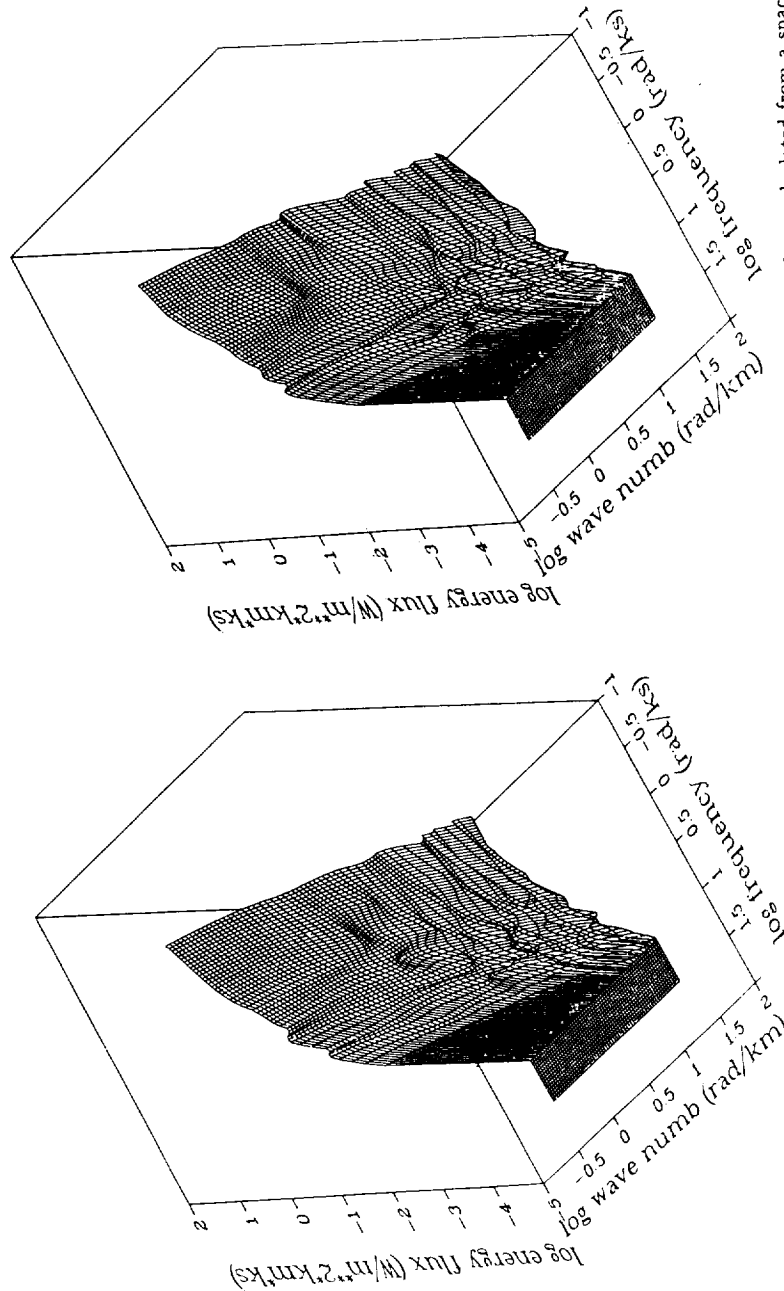
Fig. 3 Power spectral density of the vertical energy flux in the troposphere. The vertical energy flux has been calculated from a space–time Fourier transform of the vertical velocity fluctuations in the height range between 3 and 11.8 km observed between 9 and 18 hours (LT) by the stationary SOUSY VHF Radar. The calculation is based on the assumption that the energy flux is due to linearily superposed gravity waves and the Brunt–Väisälä period is 160 s. The spectra show the downward (left) and upward (right) directed fluxes. In the spectral range that we can observe, the total downward flux is 0.081 W/m² which is slightly less than the associated upward flux of 0.095 W/m². Note, however, the maximum contribution to the energy flux stems from small vertical wave numbers for which the vertical group velocity is very large.

ORIGINAL PAGE IS
OF POOR QUALITY
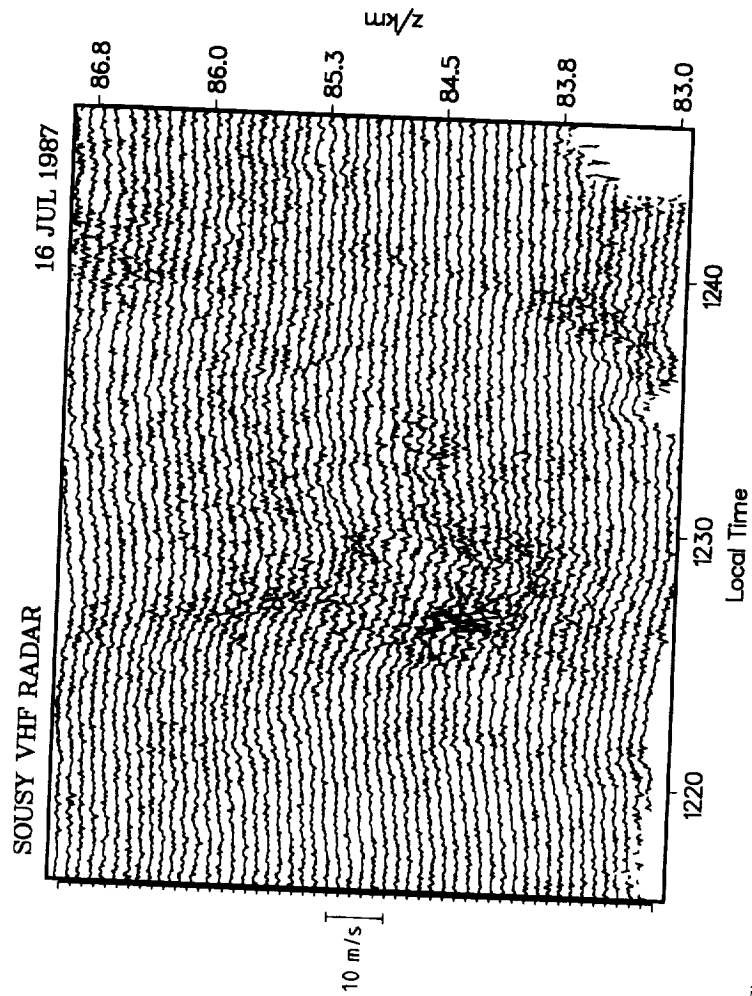
Fig. 4 Time series of the vertical velocities at 52 heights with a range resolution of 75 m and a time resolution of 3.5 s (missing data correspond to a signal–to–noise ratio less than 3 dB).

Fig. 6 Three minute average of the height profile of the vertical velocity. The periodic structure has a vertical wavelength of 2 km.

Fig. 5 Temporal variation of the vertical velocity at 12 heights with a range resolution of 75 m and a time resolution of 3.5 s. The time series, which have been low pass filtered, clearly show an oscillation with a period of about 10 min and an amplitude of about 5 m s^{-1}.
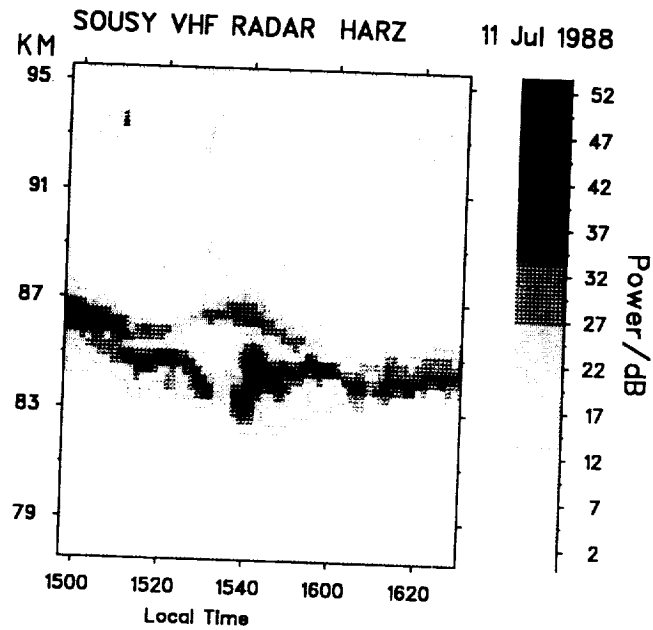
Fig. 7 Height-time intensity plot of the signal-to-noise ratio (P_V) measured in the vertical beam of the stationary SOUSY VHF Radar located in the Harz mountains of Germany in summer 1988. Values are very high, and the echoes occur above 80 km. This is in contrast to radar returns obtained at other times of the year using the same facility, but very similar to the characteristics of echoes returned from near the polar mesopause in summer (the so-called Polar Mesopause Summer Echoes or PMSE). We have termed this echo the "Mesopause Summer Echo" or MSE (see REID et al., 1988).

RECENT SOUSY PUBLICATIONS

Czechowsky, P., G. Schmidt and R. Rüster, The Mobile SOUSY-Doppler Radar – Technical Design and First Results, *Handbook for MAP*, 9, 433 – 446, 1983.

Czechowsky, P., G. Schmidt and H. Kopka, Medium Frequency Radar Observations in the Middle Atmosphere, *J. Atmos. Terr. Phys.*, 45, 729 –732, 1983.

Czechowsky, P., G. Schmidt and R. Rüster, The mobile SOUSY Doppler Radar: Technical design and first results, *Radio Science*, Vol. 19, No. 1, 441-450, 1984.

Czechowsky, P., R. Rüster and G. Schmidt, First results of VHF-radar measurements during the MAP/WINE Campaign, *Adv. Space Res.*, Vol. 4, No. 4, 47-50, 1984.

Czechowsky, P., I. M. Reid, R. Rüster and G. Schmidt, VHF Radar Echoes Observed in the summer and Winter Polar Mesosphere over Andoya, Norway, *J. Geophys. Res.*, accepted for publication, 1988.

Czechowsky, P., I. M. Reid and R. Rüster, VHF Radar Measurements of the Aspect Sensitivity of the Summer Polar Mesopause Echoes over Andenes (69°N, 16°E), Norway, *Geophys. Res. Lett.*, 15, 1258 – 1262, 1988.

Franke, J., C. H. Liu, J. Fu, R. Rüster, P. Czechowsky and G. Schmidt, Multi–Beam Radar Observations of Winds in the Mesosphere, *J. Geophys. Res.*, in press, 1988.

Hocking, W. K., R. Rüster and P. Czechowsky, Absolute reflectivities and aspect sensitivities of VHF radio wave scatters measured with the SOUSY radar, *J. Atmos. Terr. Phys.*, 48, 131-144, 1986.

Klostermeyer, J., Parametric Instabilities of Internal Gravity Waves in Boussinesq Fluids with Large Reynolds Numbers, *Geophys. Astrophys. Fluid Dyn.* 26, 85 – 105, 1983.

Klostermeyer, J., Observations Indicating Parametric Instabilities in Internal Gravity Waves at Thermospheric Heights, *Geophys. Astrophys. Fluid Dyn.*, 29, 117 – 138, 1984.

Klostermeyer, J. and R. Rüster, VHF radar observation of wave instability and turbulence in the mesosphere, *Adv. Space Res.*, Vol. 4, No. 4, 79-82, 1984.

Klostermeyer, J., Experiments with maximum entropy and maximum likelihood spectra of VHF radar signals, *Radio Sci.*, 21, 731 – 736, 1986.

Klostermeyer, J., P. Czechowsky, R. Rüster and G. Schmidt, Die SOUSY-VHF-Radars, *Meteorol. Rdsch.*, 41. Jg. Heft 1, 12 – 22, 1988.

Maekawa, Y., T. Aso, R. Röttger, P. Czechowsky, R. Rüster, G. Schmidt, I. Hirota, R. F. Woodman and S. Kato, A cooperative synchronous observation of winds and tides in the tropical lower stratosphere and mesosphere using VHF radars at Jicamarca and Arecibo, *J. Geomag. Geoelectr.*, 38., 81-97, 1986.

Meyer, W., Philbrick, Röttger, Rüster, Widdel and Schmidlin, Mean winds in the winter middle atmosphere above northern Scandinavia, *J. Atmos. Terr. Phys.*, 49, 675 – 687, 1987.

Reid, I. M., R. Rüster and G. Schmidt, VHF Radar Observations of Cat's-eye-like Structures at Mesospheric Heights, *Nature*, 327, 43-45, 1987.

Reid, I. M., R. Rüster, P. Czechowsky and G. Schmidt, VHF Radar Measurements of Momentum Flux in the Summer Polar Mesosphere Over Andenes (69°N, 16°E), Norway, *Geophys. Res. Lett.*, 15, 1263 – 1266, 1988.

Reid, I. M., P. Czechowsky, R. Rüster and G. Schmidt, First VHF Radar Measurements of Mesopause Summer Echoes at Mid-Latitudes, *Geophys. Res. Lett.*, in press, 1988.

Reid, I. M., Observation of stratified layers in the mesosphere and lower thermosphere (50 – 100 km) using radar techniques, *Adv. Space Res.*, in press, 1988.

Röttger, J., P. Czechowsky, R. Rüster and G. Schmidt, VHF Radar Observations of Wind velocities at the Arecibo Observatory, *J. Geophys.*, 52, 34-39, 1983.

Rüster, R., P. Czechowsky, G. Schmidt and K. Labitzke, VHF radar observations in the stratosphere and mesosphere during a stratospheric warming *J. Atmos. Terr. Phys.*, Vol. 45, 161-169, 1983.

Rüster, R. and J. Klostermeyer, VHF Radar Observations of a Kelvin-Helmholtz Instability in a Subtropical Jet Stream, *Geophys. Astrophys. Fluid Dynamics*, Vol. 26, 107-116, 1983.

Rüster, R., Winds and waves in the middle atmosphere as observed by ground-based radars, *Adv. Space Res.*, Vol. 4, No. 4, 3-18, 1984.

Rüster, R., J. Klostermeyer and J. Röttger, SOUSY VHF radar measurements in the lower and middle atmosphere, *IEEE Trans. Geosc.*, GE-24, 966-974, 1986.

Rüster, R. and J. Klostermeyer, Propagation of turbulence structures detected by VHF radar, *J. Atmos. Terr. Phys.*, 49, 743 – 750, 1987.

Rüster, R., P. Czechowsky and G. Schmidt, Planetary waves and tides in the summer mesosphere at polar latitudes, *J. Atmos. Terr. Phys.*, in press, 1988.

Rüster, R., J. Klostermeyer, P. Czechowsky and G. Schmidt, VHF-Radarmessungen in der Atmosphäre, *PROMET*, to be submitted, 1988.

Rüster, R. and I. M. Reid, VHF Radar Observations of the Dynamics of the Summer Polar Mesopause Region, *J. Geophys. Res.*, submitted, 1988.

Schmidt, G., R. Rüster and P. Czechowsky Complementary Code and Digital Filtering for Detection of Weak VHF Radar Signals from the Mesosphere, *Handbook for MAP*, 9, 338 – 343, 1983.

Schmidt, G. and P. Czechowsky, Technical Design and Application of the SOUSY Doppler Radars, *Kleinheubacher Ber.*, 43 – 51, 1987.

Thomas, L., R. J. Winder and R. Rüster, The characteristics of VHF radar echoes from the tropopause region near a jet stream, *J. Atmos. Terr. Phys.*, 48, 261-265, 1986.

Thrane, E. V., T. A. Blix, C. Hall, T. L. Hansen, U. von Zahn, W. Meyer, P. Czechowsky, G. Schmidt, H.-U. Widdel and A. Neumann, Small Scale Structure and Turbulence in the Mesosphere and Lower Thermosphere at High Latitudes in Winter, *J. Atmos. Terr. Phys.*, 49, 751 – 762, 1987.

Waterman, A. T. and P. Czechowsky, Upper tropospheric structures with VHF radar at Arecibo, *Proc. Ursi Commission F 1983 Symposium*, Louvain, Belgium, June 1983 (ESA SP-194), 89 – 94, 1983.

Waterman, A. T., T-Z Hu, P. Czechowsky and J. Röttger, Measurement of Anisotropic Permittivity Structure of Upper Troposphere with Clear Air Radar, *Radio Sci.*, 20, 1580 –1592, 1985.

Waterman, A. T., T-Z Hu, P. Czechowsky and J. Röttger, Variability in Doppler Slant-Beam Measurement of Horizontal wind, A Case Study, *Radio Sci.*, 10, 1214 – 1222, 1985.

PROGRESS IN MF RADAR MEASUREMENTS AT SASKATOON

C.E. Meek, A.H. Manson, and N.D. Lloyd

Institute of Space and Atmospheric Studies
University of Saskatchewan, Saskatoon, Canada

Abstract: A coherent real time wind (COHRTW) system has been installed at the MF radar site. With the aquisition of professionally designed receivers it is now possible to set optimum gain for each height gate (3 Km resolution), increase the signal-to-noise ratio with coherent integration, and obtain reliable signal strength estimates. The system is described, and some long term angle of arrival statistics discussed.

The institute Fabry-Perot interferometer has been running for more than a year now on green line (557.7 nm). A comparison of airglow winds with the radar data is shown.

COHERENT REAL TIME WIND SYSTEM

The coherent receivers were designed and built by Rob Strother-Stewart to have 80 dB gain control (eight 10 dB steps) with gain switching faster than 20 μsec (3 Km), minimum detectable signal of 0.25 μV across 50Ω, and 0/180° phase flip control. Four of the receivers are dedicated to the coherent wind system, which operates on our normal 4-antenna "Y" array. The phase flip is not used to eliminate receiver offsets at the moment. Instead a long term running mean is maintained.

The receiver interface, built by R.T. Miller, has 8 A/D channels, and is run by an Apple II micro-computer which controls receiver gain, reads the A/D data at 32 height gates (49-142 Km), does coherent integration, maintains running mean receiver offset tables and RMS values (for use in setting gains), and converts the integrated amplitudes to bit-amplitudes using the running offset values. When each block of bit-amplitudes (4 sec) is completed, it is sent to a second Apple II, which does running complex cross and mean auto correlations by counting bit-matches between sequences.

This second Apple is in charge of the system, and sends a gain-height pattern, integration, and record length parameters to the first to start a record. It also sends the completed correlations to a third computer, a

C128, which does the full correlation analysis (FCA) and sends the results back to the Apple which writes them on 9-track tape. Records are 5 min in length (512 point bit-amplitude sequences).

There are several advantages to a coherent system. One is that external interfering signals reflected from the ionosphere which have a ground fading pattern similar to the wanted signal are automatically rejected because they are non-coherent. The system also reduces the problem of multiple hop echoes (which can appear at any height in the receiving interval of a subsequent transmitted pulse) because the transmitter synch timing is independent of the 2 MHz signal phase. Thus the pulse/integration rate can be as high as the hardware will allow.

In addition to the normal FCA parameters (wind magnitude and direction, mean pattern shape and tilt, and internal decay rate), the signal strength, mean vertical Doppler (from auto-correlation phase versus lag), and the mean phase difference between antennas (for angle of arrival, AOA, calculations) are also available.

A comparison between this system and the RTW system - non-coherent, which has been running for more than 10 years now, and probably will be kept running as long as possible - shows a bias in wind speed (COHRTW smaller than RTW) of 20-30%. The reason for this is not known as yet. Until it is, we confine our use of the data to dimensionless quantities such as wind direction and phase parameters (Doppler, AOA).

The data rate is much improved with coherent integration: Figure 1 compares the RTW and COHRTW number of wind values per hour. The minima in the RTW plot at 85, 91, ... Km are due to the poor gain switching characteristics of the non-coherent receiver.

ANGLE OF ARRIVAL

The zero lag cross correlation phases can be used to calculate AOA, if it exists. Figure 2 shows histograms of these phases for the three pairs of antennas in the array. The position of the peak at the lowest heights is taken to represent the zenith, and is used to calibrate the other phase differences. The sense of tilt of the AOA is indicated on either side of the histogram. The change in phase with height is interesting - almost as if the ray normal rather than the phase normal were being measured.

To see how often the AOA can be calculated, distributions of the norm-
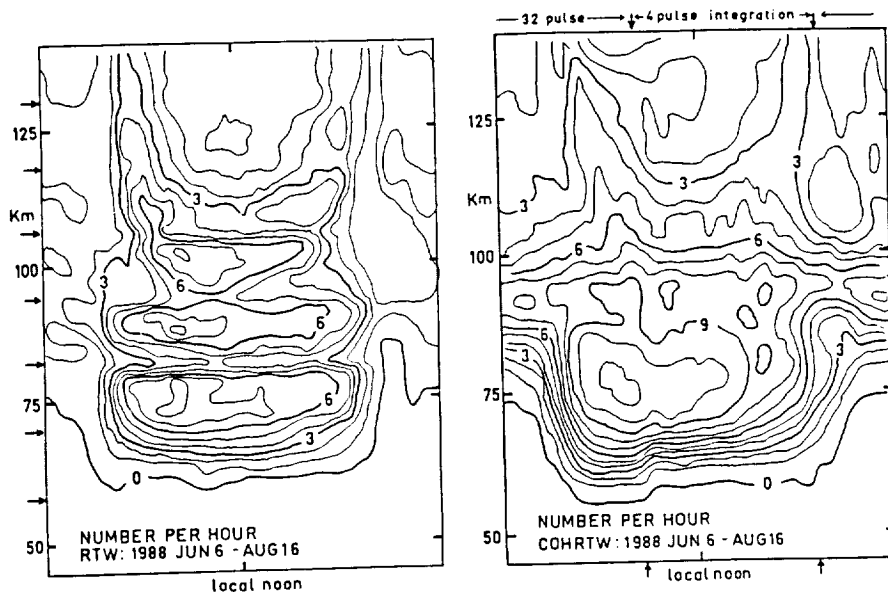
Figure 1. Comparison between RTW (no integration) and COHRTW (4/32 pulse integration day/night) for number of wind values produced per height per hour. Maximum possible number is 12.
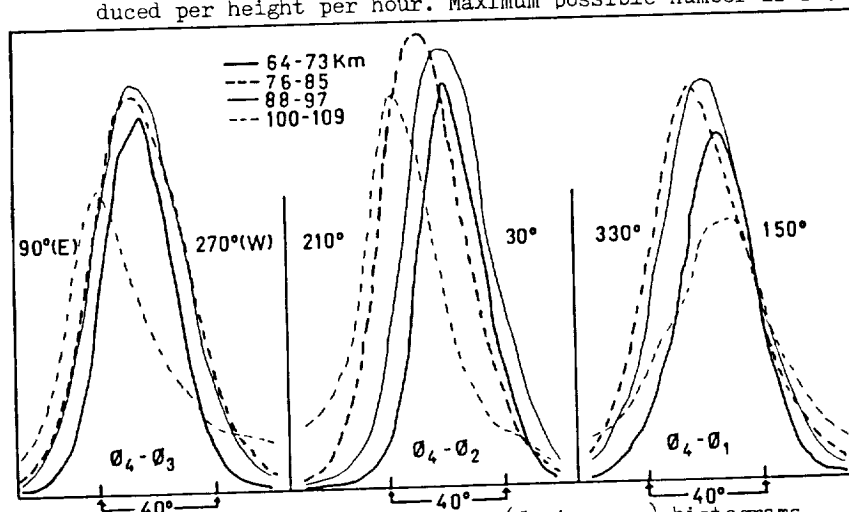
Figure 2. Antenna pair phase difference (5 min mean) histograms, daytime data, 1988 May 31 - July 19. A phase difference of 40° represents ∿5 in pointing direction (antenna pair spacing is 1.15 λ). "Zero phase" is taken from the peak of the 64-73 Km histogram. Geographic tilt directions are noted on either side of centre. Data gave been rejected if any of the three zero-lag correlations in a height/record is less than 0.2 .

alized phase discrepancy (NØD: the absolute value of the sum of the three phase differences divided by the sum of their absolute values) have been plotted in Figure 3. This parameter should be zero for a plane phase front (i.e. a defined AOA). The expected distribution for random phases is also plotted. It appears from this data that the AOA cannot be found for the lowest heights on the average, and is best (though still near random) at E-region heights. Plans to routinely correct the vertical Doppler for possible oblique propagation on an individual basis are now of doubtful value. However large scale waves might produce some good segments of AOA data.
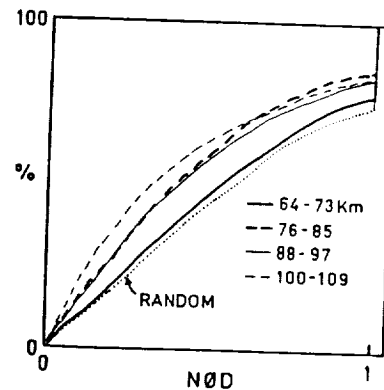
Figure 3. NØD distributions for the data presented in Fig. 2.

FABRY-PEROT INTERFEROMETER (FPI)

Figure 4 shows a sample comparison between airglow (15 min resolution) and radar (RTW, hourly means) data : Sept. 19-21, 1987. Because of the reduced number of RTW winds at night, a mean day has also been formed for the month. If tidal oscillations are dominant, this will be a reasonable representation of night-time data. This mean day appears at the top of the figure, repeated for each day compared. The middle of the figure shows the available hourly means for the specific date/time, and the bottom gives the FPI data. The agreement is generally good - except maybe in the early morning of Sept. 20.

The three month period from which these FPI data were selected had only 9 good airglow nights - uncontaminated by moon, clouds, or aurora.
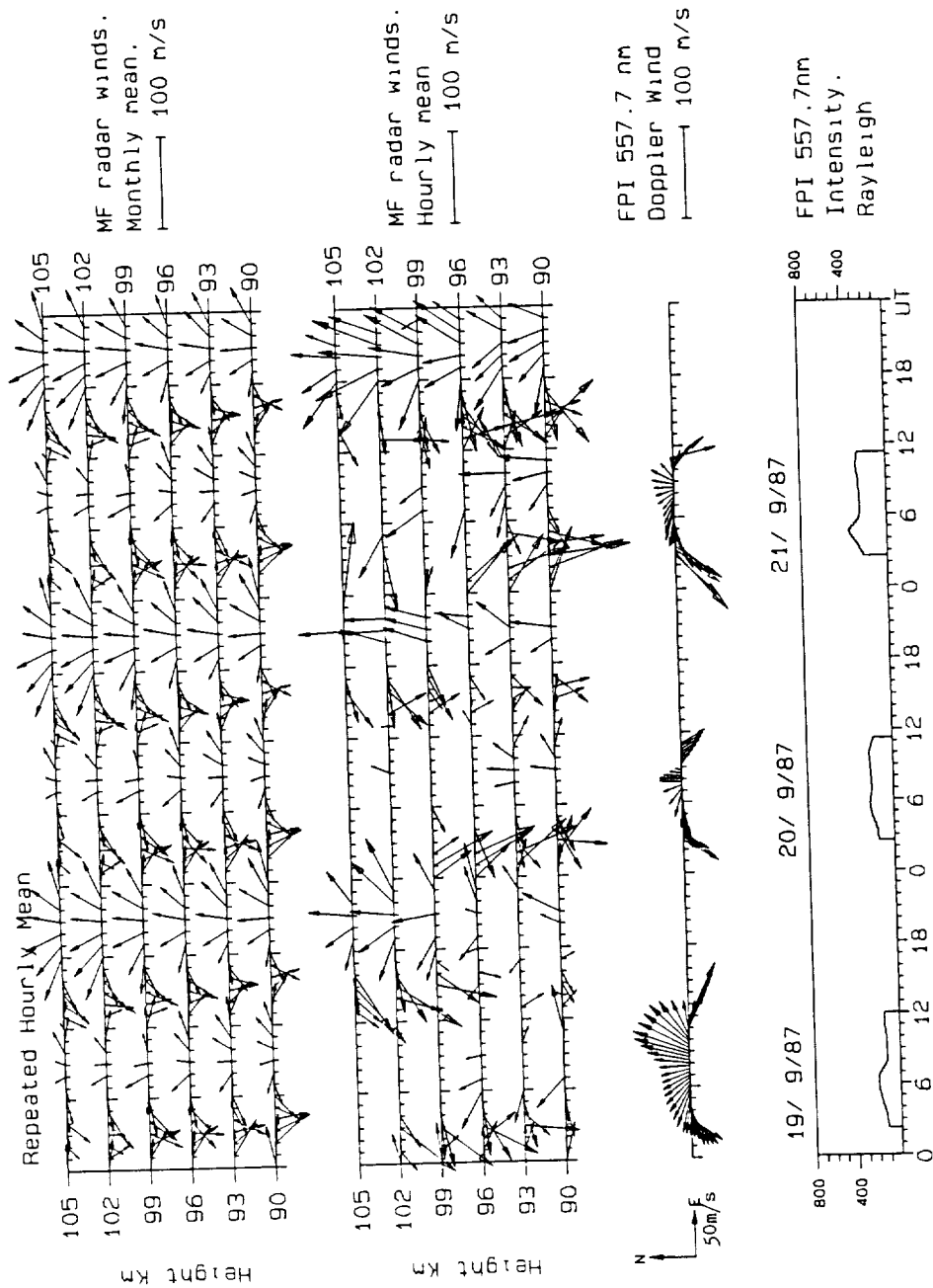
Figure 4. Fabry-Perot airglow winds compared to MF radar spaced antenna (FCA) winds

REAL TIME WIND SYSTEM AT TROMSØ

T.L. Hansen and T. Trondsen

Institute of Mathematical and Physical Sciences
University of Tromso, Tromso, Norway

and

C.E. Meek

Institute of Space and Atmospheric Studies
University of Saskatchewan, Saskatoon, Canada

Abstract: A real time wind measuring system (spaced antenna) has been placed at the Tromsø MF radar site to run continuously in conjunction with the partial reflection experiment and especially during the MAC-SINE and MAC-EPSILON campaigns. Since Tromsø is north of the arctic circle, it is interesting to see how well such a system operates here summer and winter. Data on signal strength and quantity of wind results are presented.

EXPERIMENTAL SYSTEM

A loop array (figure 1) of 2 metre diameter shielded loops and a real time wind (RTW) analysis system, similar to that at Saskatoon, was set up at the Ramfjordmoen MF radar site (69.6°N, 19.2°E) near Tromsø in June '87 to run during the MAC-SINE (June-July'87) and MAC-EPSILON (Oct,Nov'87) campaigns. It operates on O-mode transmission in parallel with the partial reflection experiment (PRE) or alone when the PRE is not in use. Transmitted power is 50 KW with a 20 μsec pulse (3 Km resolution) at 2.78 MHz. Sampling is at 3 Km intervals from 49 to 142 Km (range). Up to the end of August '87, the system ran at a rate of 1 pulse per antenna per 0.36 sec (the antennas are cycled through one receiver), and despiking was employed - viz. in each antenna amplitude sequence, if a signal is greater than the sum of the two adjacent signals, it was replaced with the average. Later

in the summer the system program was modified to do non-coherent averaging over 3 or 6 pulses depending on whether the PRE, which needs X-mode, was operating. Given a normal random noise background, this increases the effective signal-to-noise (S/N) ratio for correlation analysis by 5 or 8 dB respectively; however despiking is no longer possible, which is a draw-back if spike interference (e.g. from co-located experiments) is common.

Comparisons between loops and the normally used half-wave folded dipoles are not yet possible at Tromsø, but experiments at Saskatoon on admittedly inferior loops suggest a loss of ∿25 dB in S/N with respect to dipoles at a quiet site. On the positive side, shielded loops seem to be relatively unaffected by sur-rounding structures, and mutual coupling for close spacings is not a concern.

Figure 1. Loop array
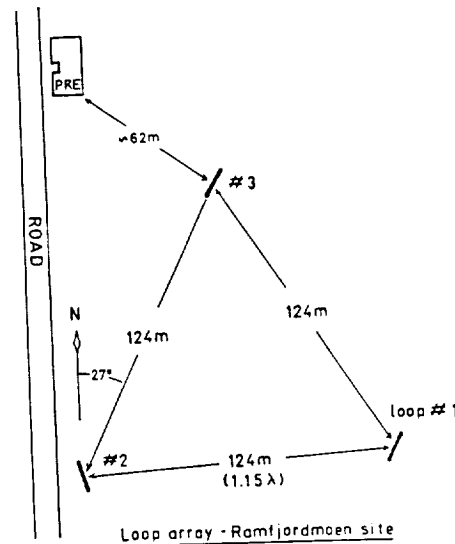
SIGNAL STRENGTH

Figure 2 shows smoothed signal/ noise contours (very unrefined cal-ibration) for summer and winter data. The noise level is the signal at the
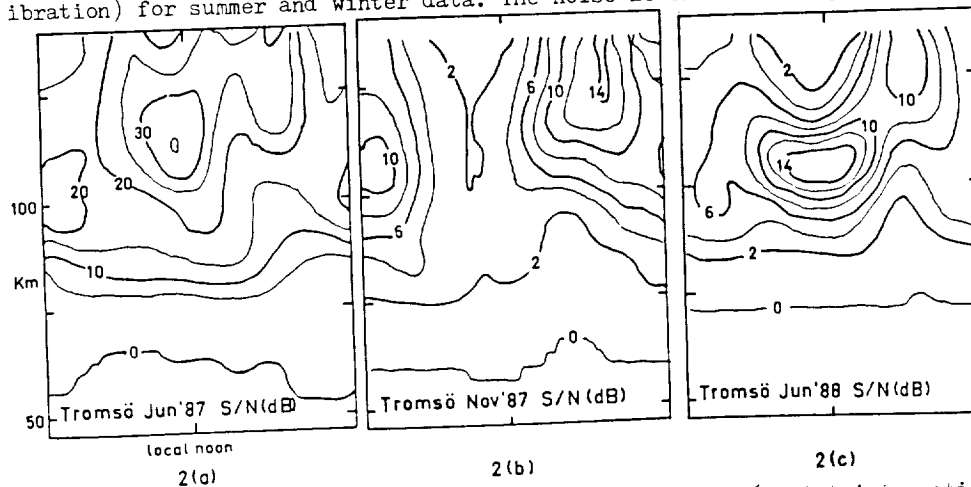
Figure 2. Signal/Noise contours. Nov'87 and Jun'88 used 6 point integration.

lowest height gate. Note that all heights in this paper are "virtual" (i.e. based on echo delay only). There is a marked change, with summer maxima near local noon and winter maxima near local midnight. The Jun'88 profile indicates a solar controlled E-region. The puzzling difference between Jun '87 and Jun '88 contours is still under investigation. The change to summer scatter occurs just after the end of March, and may be connected with the change to summer circulation. The reason for the drop in S/N between Jun '87 and Jun '88 is undetermined. It is likely that the transmitter, which broke down in July, was deteriorating at this time.

NUMBER OF WIND VALUES

Figure 3 shows the average number of wind values per height per hour (maximum of 12) for summer and winter 1987. Attempts have been made to
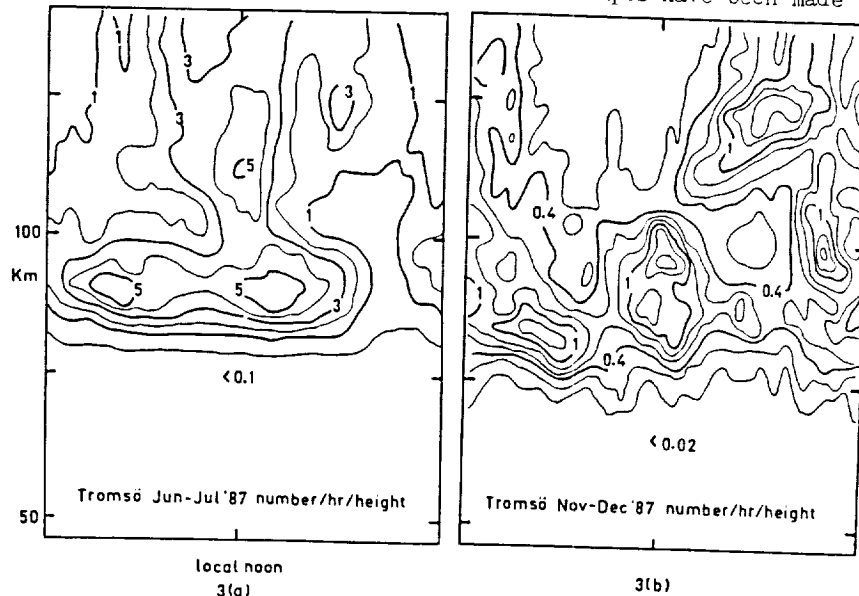
Figure 3. Number of wind values per height gate per hour.

eliminate spurious values caused by external interfering signals, usually by requiring that the signal be at least 3 dB above the "noise". The major loss in winter data is probably due to lower echo strength (i.e. not just a reduction in S/N).

COMMENTS

Finally, Figure 4 shows a histogram of the angle of pattern elongation produced by the full correlation analysis. Although not shown in Figure 1, there is a ∿70m lattice tower supporting a log-periodic ionosonde antenna between loop #1 and #2. It was expected that this tower would distort the pattern, but the data show no consistent distortion at different heights.

Figure 4. Histograms of pattern tilt angles.
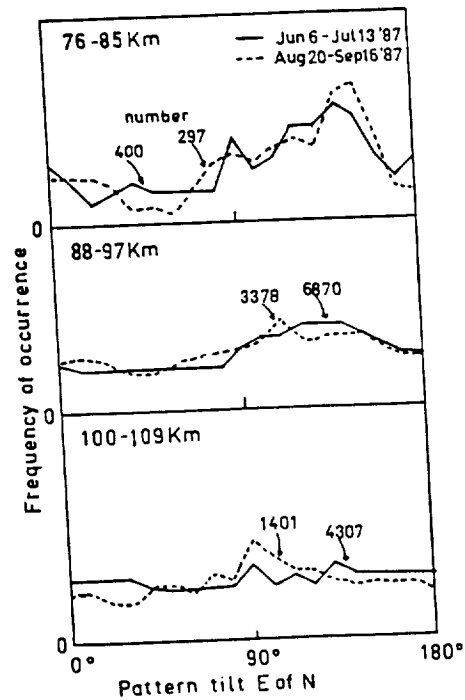
THE STATUS AND PLANNED DEVELOPMENTS OF EISCAT IN MESOSPHERE AND D-REGION EXPERIMENTS

C. La Hoz, J. Röttger[†], M. Rietveld, G. Wannberg
EISCAT Scientific Association
P.O. Box 812, S-981 28 Kiruna, Sweden
([†] on leave from Max-Planck-Institut für Aeronomie)

S.J. Franke
University of Illinois
Urbana, 61801 Ilinois, USA

0. ABSTRACT

The EISCAT VHF radar system at 224 MHz is a very powerful instrument for the study of the mesosphere and the D-region of the ionosphere. Recently, important new measurements have been carried out in these regions of the polar atmosphere employing advanced techniques. The focus of the research effort in two campaigns in the summer of 1987 and 1988 has been the Polar Mesospheric Summer Echoes or PMSE. These radar returns originate from very thin scattering layers that seem to occur only during summer in the cold polar mesopause between 80 and 90 kilometres of altitude. The seemingly extreme fine structure in time and in space of these echoes constitutes a challenge to the experimentalist and the theoretician alike.

We have made extensive use of the advanced capabilities of the EISCAT system to study the PMSE, particularly in the 1988 campaign. To resolve the sub-kilometer structure present in these layers we have implemented long Barker codes, complementary codes and space and frequency interferometer schemes. The spatial resolution attained with the pulse codes in the longitudinal direction (that is, along the antenna beam) has been 150 and 300 metres. Depending on the level of longitudinal structuring, it might be possible to improve this resolution to tens of metres with the use of frequency interferometry. Spatial interferometry allows to resolve transverse structuring, and most important, it provides measurements of the transverse velocity when such structuring exists.

The relatively small data base so far obtained has considarable potential to help understand the dynamics of the polar mesosphere and the mutual influences with other geophysical and geomagnetic phenomena. Witness the many papers presented in this conference based on these EISCAT measurements. The capabilities of the EISCAT radar system will play an important role in the resolution of intriguing questions posed by the observation of mesospheric turbulence with characteristics unaccounted for by conventional theories of turbulence.

There is ample room for further improvements and optimisation of the experiments. In particular, real-time and off-line data processing and analysis require considerable work. Development of new processing schemes and special processors are an important part of our plans for the future. A challenging problem is the design of an experiment to measure simultaneously, although perhaps not at the same altitudes, the strong coherent scattering produced by PMSE layers, and the very weak scattering produced by the tenuous plasma of the D-region.

1. INTRODUCTION

The EISCAT radar system has been described for the first time in a MAP Handbook in Volume 9 (RÖTTGER et al., 1983) and subsequent developments in middle and lower atmosphere applications in Volume 14 (RÖTTGER, 1984). The present report describes the further developments that have occurred in the interim period until autumn 1988.

Improvements in the UHF radar have taken place in the area of system reliability, the basic system and its specifications remaining fairly stable. Therefore, the description of the UHF system contained in the two references above are still actual. In contrast, the VHF system has undergone

repeated changes and modifications with consequent off and on periods. Despite the fact that the situation has not been—and is not yet—stable, a good number of important technical and scientific results in middle atmospheric research have been achieved. In section 2 we will briefly describe the specifications of the VHF system making parenthetical remarks on temporary limitations that exist at the time of writing.

An important experiment code-named GEN-11 was designed in 1986 (TURUNEN, 1986a,b) and used regularly for aeronomical and dynamical studies of the D-region, mostly with the UHF radar. In Section 3 we will first briefly describe GEN-11 and follow up with a summary of selected scientific results that have been obtained using this program.

The so-called Polar Mesospheric Summer Echoes were observed for the first time at EISCAT in 1987 with the GEN-11 program running the VHF radar (HOPPE et al., 1988a; RÖTTGER et al., 1988). Further technical developments have been stimulated by the PMSE, as GEN-11 is very suitable for incoherent scattering studies of the D-region but does not match well the space and time scales of the PMSE. Section 4 describes these developments, namely the first application of complementary codes and coherent integration at EISCAT embodied in a series of programs that were employed for the first time in a campaign in summer of 1988. A brief highlight of scientific results obtained during this campaign is also included in this section. Other papers in this volume give more detailed reports on several scientific results obtained in the 1987 and 1988 campaigns. The long term plans to improve the MST capabilities of the EISCAT radars is discussed in detail by WANNBERG et al. (1989) in this issue.

2. THE EISCAT VHF SYSTEM

The VHF radar operating at 224 MHz should be in general better suited for middle atmosphere studies than the UHF radar. When the scattering mechanism is turbulent scattering, the half-wavelength of the VHF radar is within the inertial sub-range of atmospheric turbulence up to about 40 km, whereas the one of the UHF radar up to about 20 km (RÖTTGER, 1982). When the scattering mechanism is incoherent scattering, the sensitivity of the radar is larger at the longer wavelength due to the fact that the electrons—which cause the scattering—have stronger coupling to the ions at the larger scale sizes[1]. Another important "scattering" mechanism is specular reflection, and in this case the reflections are also stronger at the longer wavelength.

Within the conventional picture described above of the known scattering mechanisms, it is not surprising to conclude that the VHF radar is a better tool for middle atmosphere studies than the UHF radar. Experiments demonstrate that this conclusion is correct. However, the experiments also point to fundamental gaps in our understanding of scattering mechanisms in the middle atmosphere, as strong scattering is observed under conditions where no scattering would be expected, vis-á-vis, the PMSE.

Table I summarises the more important characteristics and parameters of the EISCAT VHF radar. At the time of writting (March 1989), the VHF system was only in partial operation. The parameters that apply at present temporarily until full operation is achieved are as follows: There is only one klystron with 1.5 MW of peak power at 4.5 % duty cycle and operating frequencies at $n = 5, 6, 7, 8$.

The range of allowed pointing directions has also been constrained temporarily to directions near vertical and at low elevations towards the north due to interference problems. It is expected that the transmitter shortcomings will be resolved in the course of the present year. The restrictions on the pointing directions may take longer, even as when gradual extensions of the allowed limits are

---

[1] We recall that the ion line in incoherent scattering exists at all due to the collective Coulomb coupling between electrons and ions and that it is the electrons alone that produce the scattering. At some scales that are related to the Debye length, the collective interactions cease.

Table I. EISCAT VHF Radar Condensed Specifications

Transmitters (Tx)	: Two Klystron based Tx's (A and B)
Peak power	: 2.5 MW per Tx
Maximum duty cycle	: 12.5%
Operating frequencies	: $222.4 + 0.2\,n$ MHz, $n = 1, 2, \ldots 16$
Pulse width	: 1–$1000\ \mu$sec
Pulse Rise time	: $\leq 0.1\ \mu$sec
Maximum Pulse Rep. Freq.	: 1000 Hz
Modulations	: Pulsed, phase flip, Freq. step
Antenna	: Four Parabolic cylinders (Panels 1,2,3,4)
Location	: 69°35′11.9408″ N
	: 19°13′13.2300″ E, 85.3m alt.
Frequency band	: 224 ± 1.25 MHz Tx, ± 11.25 MHz Rx
Panel Dimensions	: 30m (E-W) × 40m (N-S)
Feed system	: 128 crossed dipoles (32 per panel)
Drives and Controllers	: One per panel, Master-Slave modes
Slew rate	: 5° per minute. See below.
Mechanical Steerability	: In magnetic meridian plane (0.5° W of N)
	: Between 30°S and 60°N of zenith
Electronic Steerability	: By manual recabling of the feed
	: Off-axis ±21.3°, Step=1.25°
On-axis Beam-width	: 1.7° N-S, 0.6° E-W
Gain	: 46 dBi
On-axis Effective Aperture	: $3250\ m^2$
Normal Operating Modes	: Mode I and Mode II
Mode I	: One antenna with all 4 panels aligned
	: Klystron A feeding V dipoles
	: Klystron B feeding H dipoles
	: Linear and R or L circular polarization
	: Pol. flipping from pulse to pulse
Mode II	: Two independent antennas Tx/Rx
	: with panels 1 + 2 and 3 + 4
	: Only circular polarization
Receivers (Rx)	: 8 tunable channels at 2nd IF level
Front end Amplifiers	: 4 Solid state, > 50 dB gain
System temperature	: 250-350°K, depends on pointing
IF bandwidths	: 1.2, 8.8, 18.0 MHz
Detector type	: Phase coherent demodulator
Post-detection filters	: Butterworth and Linear, variety of BW's

taking place. Persons that are interested in more detailed information or in updated characteristics are advised to contact the EISCAT Headquarters in Kiruna, Sweden.

In addition to the general advantages of the VHF radar mentioned above, the properties of the antenna make it a very promising tool for applications of space interferometry. The paper by LA HOZ et al. (1989b) in this issue on the first interferometry measurements at EISCAT contains additional information on the VHF system relevant to this application. This paper contains also a schematic

diagram of the VHF antenna. The multifrequency transmitter makes it easy to implement frequency interferometry. See Franke et al. (1989a) in this issue.

3. THE GEN-11 EXPERIMENTS

The GEN-11 program belongs to the GEN family of programs designed by T. TURUNEN (1986a). and is optimised for D-region incoherent scattering measurements (GEN stands for GENeralised). The UHF version of this program measures 22 lags of the autocorrelation function at 42 gates. The lag separation is 2.222 msec and the maximum lag is at 46.662 msec. The first gate is at 70 km. With a range increment equal to the range resolution of 1.05 km, the last gate is at 113.05 km.

Figure 1 shows a schematic diagram of the transmit/receive signals. We will give a somewhat simplified explanation of this diagram. For more details the interested reader may consult TURUNEN (1986a). Pairs of Barker coded pulses are transmitted. The code has 13 bauds with a baud length of is 7 μsec that gives a range resolution of 1.05 km. The separation between two consecutive pairs of pulses is 2.222 msec. The separation between the two pulses that constitute a pair is itself variable and has a cycle of 5. This pair separation (between trailing and leading edges of the pulses) is equal to one baud length, or 7 μsec, for the first pair, 14 μsec for the second pair, and so on, up to 35 μsec for the separation between the last (fifth) pair of the cycle. The second pulse of each pair is the negative of the first, i.e., it has a 180° phase flip.
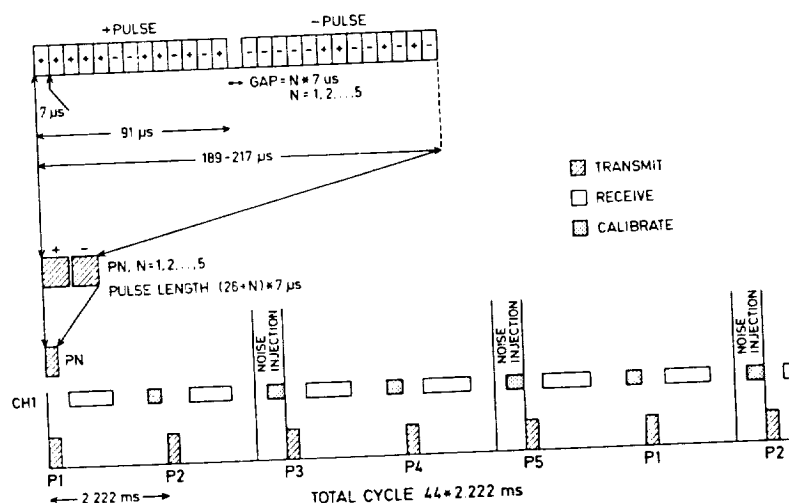
Fig. 1. Transmit/Receive modulation of GEN-11

The autocorrelation function is estimated in real time by averaging products of samples corresponding to the four possible delays between any two pairs of double pulses up to a maximum delay equal to 21 × 2.222 = 46.662 msec. These 4 products are not all at exactly the same delay, but differ by at most 2 × 5 × 7 = 70 μsec, which happens for the 5th lag, all the other lags having smaller "lag averaging". The calculation is done taking proper care of sorting out the effects of the phase flip of the second pulse of each pair by proper change of signs and by using separate storage arrays.

The zero lag of the ACF, that is, the total scattered power, is obtained in an approximated way: it is in fact an average of the ACF at the different lags determined by the 5 pulse pairs. Since the first pair is separated by 91 + 7 = 98 μsec and the last pair by 91 + 5 × 7 = 126 μsec, the middle point of these lags occurs at 112 μsec. This approximated zero lag is termed the "quasi-zero lag" or

the "pseudo-zero lag". For the intended altitude ranges that GEN-11 is used this approximation is usually very good, since then the correlation times are much greater than $112\,\mu$sec. The accuracy of the zero lag can be easily improved during off line analysis by extrapolation techniques.

GEN-11 includes also the calculation of estimates of the background noise power as well as the power of a known calibration signal.

The benefits paid by this relatively complicated design are in terms of a drastic reduction of contaminating contributions due to several types of clutter and to DC offsets that are specially deleterious in these experiments since they can be much larger than the wanted signals.

The analysis of data obtained with GEN-11 typically involves first the sorting out of the complicated structure of the output of the real time program in order to obtain conventional gated ACF's. This step is usually preceded by post-integration, as the real time integration is only 10 sec. Correction algorithms are applied such as noise and additional DC/clutter substraction and elimination of Barker code sidelobes (HUUSKONEN et al., 1988). Estimates of the Doppler velocity and spectral widths can be done readily. Other parameters such as electron density, collision frequency, temperature, and positive/negative ion concentration are more difficult to obtain due to the fact that— with the exception of the electron density—all are directly related to the spectral width according to the generally accepted model of incoherent scattering from a partially ionised collisional plasma that gives a Lorentzian spectral function with width:

Fig. 2. Measured (dots) and fitted spectra (lines).

$$\Delta f = \frac{aT(1 + \lambda)}{m_i \nu} \tag{1}$$

where Δf is the spectral width, a is a constant, T is the temperature, λ is the negative-ion to electron number density ratio, m_i is the ionic mass and ν is the ion-neutral collision frequency (DOUGHERTY and FARLEY, 1963; FUKUYAMA and KOFMAN, 1980). The simple dependence of Δf on T, λ, m_i and ν constitutes a difficult problem when interpreting measured data. More often than not there are no independent measurements of the parameters on the right hand side of (1). The interpretation of the data then depends on assumptions made and on atmospheric models.
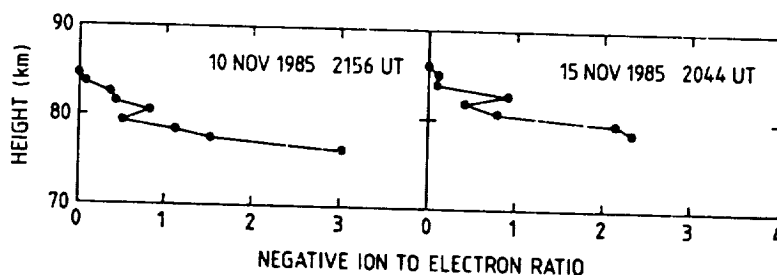
Fig. 3. Profiles of negative ion to electron density number.

Figure 2 shows a set of measured spectra (dotted curves) at consecutive altitudes alongside fitted Lorentzians (solid curves) obtained by HALL et al. (1987). This type of analysis, with the help of

neutral atmosphere models, has been at the heart of arguments leading to estimates of λ and m_i. Figure 3 shows profiles of λ reported by HALL et al. (1988), and Figure 4 shows time series of m_i at several altitudes reported by COLLIS et al. (1988).

In further developments, equation (1) has also served to make estimates of the Schmidt number, $S_c = \nu/D$ (HALL and BREKKE, 1988). An increase of the Schmidt number is associated with a reduction of the electron diffusion coefficient, D, which has been interpreted by KELLEY et al. (1987) as a causative explanation of the observation of strong coherent scattering—the PMSE—at scale lengths otherwise not consistent with turbulent scattering. The estimates obtained by HALL and BREKKE (1988) indicate an increase of the Schmidt number at altitudes where PMSE layers are normally observed.

HOPPE and HANSEN (1988) and HALL et al. (1987) have analysed also the Doppler shift of the radar returns to infer vertical velocities at mesospheric heights. They have found variations of the velocity that indicate the presence of gravity waves with periods mostly around 20 minutes. In one interesting measurement (HALL et al., 1987), the likely source of a gravity wave with period 38 min was identified to be the subsonic solar terminator.

Fig. 4. Time series of the mass of positive heavy ions in the D region.

4. THE PMSE EXPERIMENTS

With the experience gained in a campaign in summer 1987 it was clear that the spectral signatures of the PMSE were very variable. The observations indicated that the bandwidths ranged at least between a fraction of a Hz and several tens of Hz. The structuring of the layers in altitude was also of sub-kilometer dimension. These considerations implied that the use of GEN-11 was not adequate, as the frequency resolution, frequency bandwidth and altitude resolution of GEN-11 are 10.72 Hz, ±225 Hz and 1.05 km respectively. A predecessor to the more sophisticated experiments described below was improvised during the 1987 campaign (RÖTTGER et al., 1988). This experiment name-coded MESO used a simple configuration with one transmitted pulse and a pulse-to-pulse correlation technique (KOFMAN, et al., 1984).

Table II. PMSE Programs June-July 1988

	Code	Baud μs	IPP μs	Coh. Int.	Pts	Dump Time sec	Heights km
PMSE2B	28 b Barker	7	5270	5	128	5	68.0–99.5
PMSE3A	32 b Compl.	2	2350	10	128	5	80.0–89.0
PMSE3B	64 b Compl	1	2985	10	64	2	80.0–89.15
PMSE3C	32 b Compl.	2	2475	8	96	2	80.0–92.3
FDI1	Uncoded	10	1813	28	192	5	80.0–95.0
FDI2	32 b Compl.	2	4902	6	64	2	80.0–89.0
SDI1	32 b Compl.	2	4902	6	64	2	80.0–89.0

For the 1988 campaign we embarked in the development of experiments that employed complementary codes for the transmitted pulses and performed coherent integration of the received signals. This task turned out to be non-trivial due to the internal architecture of the EISCAT correlator. The

heart of the problem is that the output memory of the correlator is an only-write memory—all operations to the data must be done "on the fly" through a one way route.

We should state, however, that this configuration of the EISCAT system in the area of real time signal processing is exceptionally powerful for applications to incoherent scattering, specially at E-region altitudes and beyond where the radar signals are overspread—that is, the signal spectral widths are larger than the radar repetition frequency—and the physical processes are often stationary within minutes or more. A large library of experiment programs exists that usually matches most observational needs at these altitudes. This is not the case for middle and low atmosphere investigations where the radar signals are usually underspread which permits the use of complementary codes as well as coherent integration. This type of signal processing is imperative for mesospheric applications since they are produced by sub-kilometer structures and often are non-stationary within time scales of seconds and perhaps less. This implies that for the PMSE the integration time is more related to the stationarity of the signals rather than to the SNR as is normally the case for incoherent scattering. However, under auroral conditions, incoherent scattering faces the same problems created by non-stationarity.

A project is well under way to construct a special digital processor that will fill this gap (Postila, 1988). In the meantime, stimulated by the exciting prospects of having the oportunity to study a physical phenomenom so little understood as the polar mesospheric summer echoes, we found unorthodox solutions to our difficulties to decode and simultaneously perform the coherent integration of the sampled signals using the EISCAT correlator. Table II is a summary of the programs that were developed for the summer campaign of 1988.
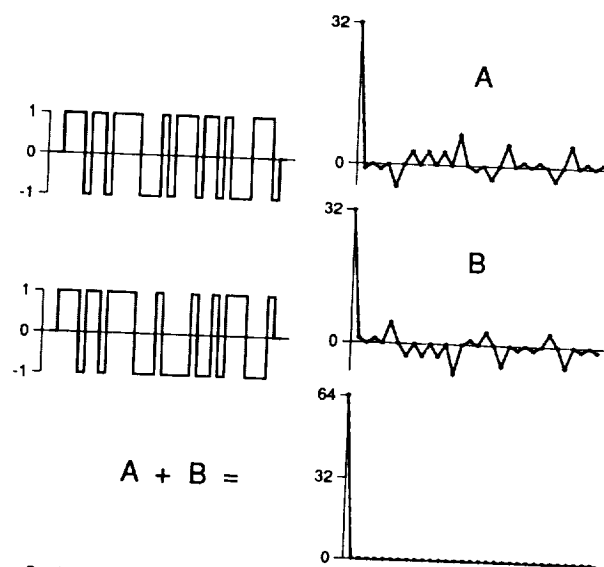
Fig. 5. A 32-baud complementary set and ambiguity functions

The program that was used most was PMSE3C. Figure 5 shows the complementary coded pulses and their range ambiguity functions that were employed in this program. Plotted on the left hand side are the two complementary coded pulses. The ± 1 on the ordinate axis denotes the two phases of the

modulation—zero and 180°. The baud length of 2 μs is equivalent to 300 metres range resolution. The number of bauds is 32. Plotted on the right hand side of Figure 5 are the range ambiguity functions of the two complementary codes denoted A and B. On the lower right corner is the resulting ambiguity function after combining A and B. Note that the effective ambiguity function has no sidelobes.

PMSE3B is an interesting and useful program because with it we achieved a range resolution of 150 m with a complementary pair of length 64 and baud length of 1 μs. The bandwidth required by such code is near the limits of the present configuration of the VHF radar. We had only one successful run of about 6 hours on July 6th 1988. Below we show some of the results obtained with PMSE3B and PMSE3C.

The FDI and SDI programs were developed to carry out frequency and space interferometric measurements respectively. Some of these experiments are described in this issue (FRANKE et al., 1989; LA HOZ et al., 1989b).

There were also other programs not shown in Table II that had a more exploratory character. STRAT, ST90P4 AND SOUND are modified versions of PMSE3C. STRAT, ST90P4 were employed to make test measurements in the stratosphere, and SOUND was used to search for signatures of acoustic sound waves. CC4D5 is a program similar to the PMSE set but it solves the problem of using the correlator as a decoder/integrator in a different manner and was developed independently (STURK et al., 1989). GEN-11 was also used during some periods, in particular during an event of strong solar and geomagnetic activity that seemed to have a dramatic effect on the PMSE (RÖTTGER et al., 1989). SSLA is a program used to suport lidar observations of sodium layers over the norwegian island of Andøya. More details and results from these experiments will be reported elsewhere.

In all these programs, the only operations executed in real time are the decoding and coherent integration of the digital signals. Normally, the real time integration time is set to 2 seconds, upon which the data are saved to magnetic tape. This meagre processing—originally forced upon us by the limitations of the correlator—turned out to be of great value as we later discovered that the echoes were highly non-stationary with time scales down to seconds or perhaps even less.

In addition to the standard on-line monitoring facilities—called RTGRAPH in EISCAT—that allowed us to display the result memory of the correlator, we developed a package to display also on-line the spectral functions and power profiles with or without post-integration.

The analysis of the data to investigate various scientific aspects is under way with the participation of several groups. As an illustration we show here in Figure 6 a grey-coded power map of the experiment carried out on July 6th 1988 using the program PMSE3B. As mentioned before this is the only experiment that had an altitude resolution of 150 metres. The data here have been post-integrated for 30 seconds. The normalisation is done in a way that each altitude profile—or "time slice"—is normalised to its own maximum value. The advantage is that the resulting image has a striking high contrast—although at the expense of loosing the relative variations of the signals along the time axis. This figure shows the remarkable variety of time and space structures present in these echoes. A closer examination of the data shows that during most of the time during this experiment, weak but unambiguous signal structures exist over the entire altitude window of the measurement. The SNR spans more than 4 decades, from about -8 dB—probably determined by the sensitivity of the radar—up to 37 dB in this experiment. Special care was taken throughout the campaign to cover the large dynamic range of the signals and at the same time avoid saturation of the receivers and
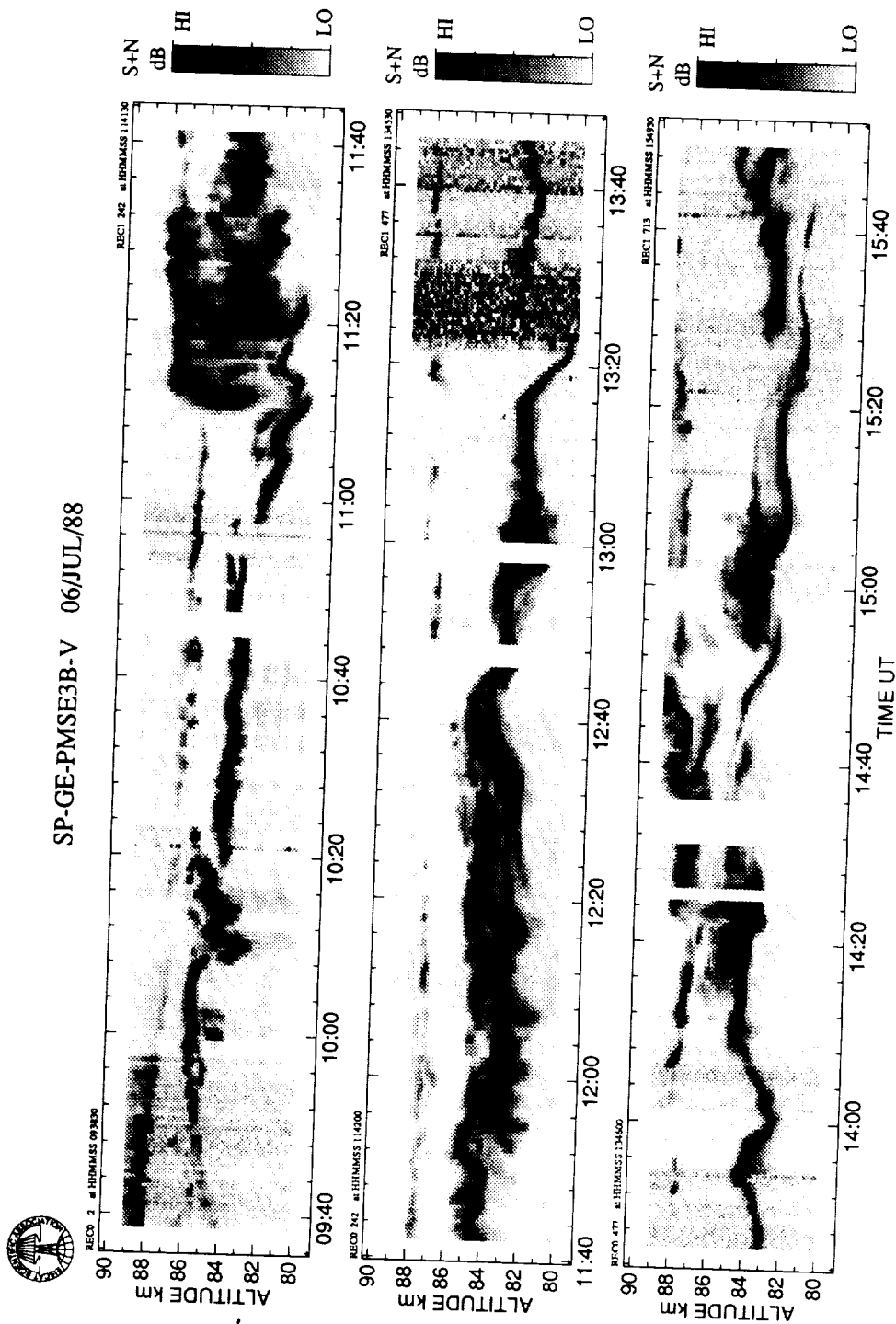
Fig. 6. A grey-scale power map of polar mesospheric summer echoes

digital to analog converters. Nevertheless, there might be short periods during the experiments when saturation has occurred.
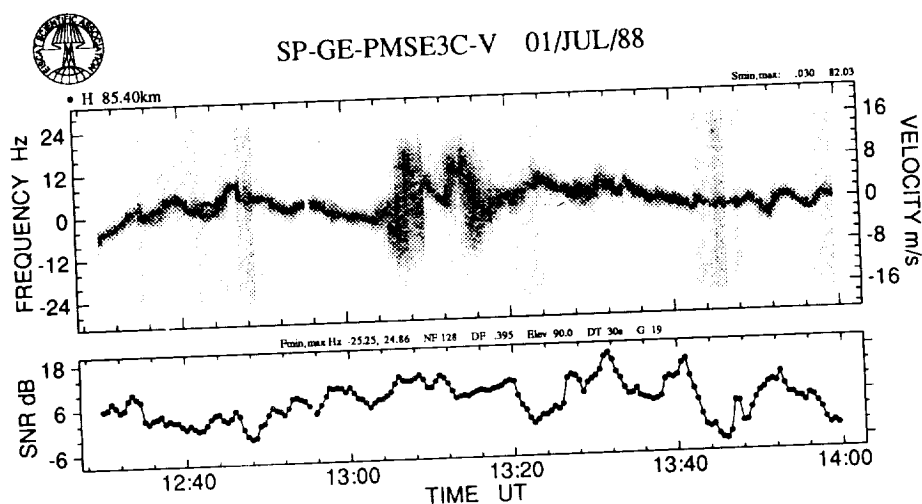
Fig. 7. Spectrogram of PMSE at 85.4 km

Figure 7 is a partial illustration of the variety of spectral forms that exist in the PMSE. Here again the normalisation is of the same type as described above for the power map. The bottom panel, however, shows the intensity of the signals in terms of the SNR. Of note here is the coexistence of very narrow spectral forms, with widths of the order of the frequency resolution of the measurement of 0.5 Hz., together with wide, multi-modal spectra that appear as two bursts between 13:04 and 13:20 UT. The latter spectra are as wide as ± 16 Hz, or equivalently $\pm 11\,ms^{-1}$. The accompanying paper in this issue by LA HOZ et al. (1989a) contains more illustrations of the dynamics of the PMSE.

Acknowledgments

Publications related to EISCAT MST science

(The following list of publications contains also the References made in this paper)

Collis, P.N., S. Kirkwood and C.M. Hall (1986), D-region signatures of substorm growth phase and onset observed by EISCAT, *J. Atmos. Terr. Phys.*, *48*, 807-816.

Collis, P.N., T. Turunen and E. Turunen (1988), Evidence of heavy posistive ions at the summer arctic mesopause from EISCAT UHF incoherent scatter radar, *Geophys. Res. Lett.*, *15*, 148.

Dougherty, J.P. and D.T. Farley (1963), A theory of incoherent scattering of radio waves by a plasma, 3. Scattering in a partially ionised gas *J. Geophys. Res.*, *68*, 5473-5486.

Devlin, T, J.K. Hargreaves and P.N. Collis (1986), EISCAT observations of the ionospheric D-region during auroral radio absorption events, *J. Atmos. Terr. Phys.*, *48*, 795-805.

Franke, S.J., C. La Hoz, J. Röttger and C.H. Liu (1989), Frequency domain interferometry of PMSE, this issue.

Fukuyama, K., and W. Kofman (1980), Incoherent scattering of an electromagnetic wave in the mesosphere: a theoretical consideration, *J. Geomag. Geoelectr.*, *32*, 67-81.

Hall, C.M., U.-P. Hoppe, P.J.S. Williams and G.O.L. Jones (1987), Mesospheric measurements using the EISCAT VHF system: first results and their interpretation, *Geophys. Res. Lett.*, *14*, 1187-1190.

Hall, C.M. and A. Brekke (1988), High Schmidt numbers in the mesopause region from 224 MHz incoherent backscatter, *Geophys. Res. Lett.*, *15*, 561-564.

Hall, C.M., T. Devlin, A. Brekke and J.K. Hargreaves (1988), Negative ion to electron number density ratios from EISCAT mesospheric spectra, *Physica Scripta*, *37*, 413-418.

Hargreaves, J.K., H. Ranta, A. Ranta, E. Turunen and T. Turunen (1987), Observations of the polar cap absorption event of February 1984 by the EISCAT incoherent scatter radar, *Planet. Space Sci.*, *35*, 947-958.

Hoppe, U.P., C.M. Hall and J. Röttger (1988a), First observations of summer polar mesospheric backscatter echoes with a 224 MHz radar, *Geophys. Res. Lett.*, *15*, 28-31.

Hoppe, U.-P., and T.L. Hansen (1988b), Studies of vertical motions in the upper mesosphere using the EISCAT UHF radar, *Ann. Geophys.*, *6*, 181-186.

Huuskonen, A., P. Pollari, T. Nygrén and M.S. Lehtinen (1988), Range ambiguity effects in Barker-coded multipulse experiments with incoherent scatter radars, *J. Atmos. Terr. Phys.*, *50*, 265-276.

Jones, G.O.L., K.J. Winser, J. Röttger, C. La Hoz and S.J. Franke (1989), Characteristics of the polar mesosphere summer echoes at 224 MHz: A statistical review of the EISCAT PMSE 1988 data, this issue.

Kelley, M.C., D.T. Farley and J. Röttger (1987), The effect of cluster ions on anomalous VHF backscatter from the summer polar mesosphere, *Geophys. Res. Lett.*, *14*, 1031-1034.

Kofman, W., F. Bertin, J. Röttger, A. Cremieux and P.J.S. Williams (1984), The EISCAT mesospheric measurements during the CAMP campaign, *J. Atmos. Terr. Phys.*, *46*, 565-575.

La Hoz, C., J. Röttger and S. Franke (1989a), Dynamic Spectra of PMSE measured by EISCAT at 224 MHz, this issue.

La Hoz, C., J. Röttger and S. Franke (1989b), Spatial interferometry measurements with the EISCAT VHF radar, this issue.

Meyer, W., C.R. Philbrick, J. Röttger, R. Rüster, H.-U. Widdel and F.J. Schimidlin (1987), Mean winds in the winter middle atmosphere above northern Scandinavia, *J. Atmos. Terr. Phys.*, *49*, 675-687.

Postila, M. (1988), Status of the EISCAT MUFFIN, *Proc. EISCAT Ann. Rev. Meeting*, Riksgränsen, Sweden, 1988, Ed. C. La Hoz, 154-155.

Ranta, A., H. Ranta, T. Turunen, J. Silén and P. Stauning (1985), High resolution Observations of D-region by EISCAT and their comparison to riometer measurements, *Planet. Space Sci.*, *33*, 583-589.

Rishbeth, H., A.P. van Eyken, B.S. Lanchester, T. Turunen, J. Röttger, C.M. Hall and U.-P. Hoppe (1988), EISCAT VHF radar observations of periodic mesopause echoes, *Planet. Space Sci.*, *36*, 423-428.

Röttger, J. (1982), Mesosphere-Stratosphere-Troposphere Radar, Proc. EISCAT Ann. Rev. Meeting, Riksgränsen, Sweden, 1982, Ed. K. Folksetad, 155-169.

Röttger, J., M. Baron and K. Folkestad (1983), Capabilities and limitations of EISCAT as an MST radar, *Handbook for MAP*, *Vol. 9*, 305-314.

Röttger, J. (1984), Further developments of ESICAT as an MST radar, *Handbook for MAP*, *Vol. 14*, 309-318.

Röttger, J. (1987a), The relation of gravity waves and turbulence in the mesosphere, *Adv. Space Res.*, *7*, (10)345-(10)348.

Röttger, J. (1987b), Contributions of radar observations of winds, waves, turbulence and composition to study transport processes in the middle atmosphere, in *Transport Processes in the Middel Atmosphere, D. Reidel Publ. Co. Dordrecht, The Netherlands*, Eds. G Visconti and R. Garcia, 439-457.

Röttger, J. (1987c), VHF radar measurements of small-scale and meso-scale dynamical processes in the middle atmosphere *Phil. Trans. R. Soc. Lond., A, 232*, 611-628.

Röttger, J., and W. Meyer (1987), Tidal wind observations with incoherent scatter radar and meteorological rockets during MAP/WINE, *J. Atmos. Terr. Phys., 49*, 689-703.

Röttger, J., C. La Hoz, M.C. Kelley, U.-P. Hoppe and C.M. Hall (1988), The structure and dynamics of polar mesosphere summer echoes observed with the EISCAT 224 MHz radar, *Geophys. Res Lett., 15*, 1353-1356.

Röttger, J., C. La Hoz, S.J. Franke and C.H. Liu (1989a), Some considerations on the fine-structure in Doppler spectra of polar mesosphere summer echoes (PMSE) observed with the EISCAT 224 MHz radar, this issue.

Röttger, J., C. La Hoz, S.J. Franke and C.H. Liu (1989b), Wave steepening and tilting detected in high resolution Doppler spectra of polar mesosphere summer echoes (PMSE) observed with the EISCAT 224 MHz radar, this issue.

Röttger, J., M.T. Rietveld, C. La Hoz, T. Hall, M.C. Kelley and W. Shwartz (1989d), Polar mesosphere summer echoes observed with the EISCAT 933 MHz radar and the CUPRI 46.9 MHz radar, this issue.

Schlegel, K., and J. Röttger (1987), Thermodynamics and electrodynamics of the auroral E-region during the D salvo of the MAP/WINE campaign, *J. Atmos. Terr. Phys., 49*, 819-826.

Sturk, T., A. Westman, G. Wannberg and J. Röttger (1989), A first look at EISCAT meosospheric data measured using a complementary code technique, this issue.

Thrane, E.V., T.A. Blix, C. Hall, L. Hansen, U. von Zahn, W. Meyer, P. Czechowsky, G. Schmidt, H.-U. Widdel and A. Neumann (1987), Small scale structure and turbulence in the mesosphere and and lower thermosphere at high latitudes in winter, *J. Atmos. Terr. Phys., 49*, 751-762.

Turunen, T (1986a), GEN-SYSTEM—A new experimental philosophy for EISCAT radars, *J. Atmos. Terr. Phys., 48*, 777-785.

Turunen, T. (1986b), Correlator programs for the GEN-System, *EISCAT Technical Note 86/46.*

Turunen, E., P.N. Collis and T. Turunen (1988), Incoherent scatter spectral measurements of the summertime high-latitude D-region with the EISCAT UHF radar, *J. Atmos. Terr. Phys., 50*, 289-299.

Wannberg, G., J. Röttger, C. La Hoz and P.J.S. Williams (1989), Long range planning for the development of full MST capabilities at EISCAT, this issue.

Williams, P.J.S., A.P. van Eyken, C Hall and J. Röttger (1989), Atmospheric gravity waves and modulations in the polar mesospheric summer echoes as observed by EISCAT, to be submitted to Geophys. Res. Lett.

CURRENT STATUS AND RECENT DEVELOPMENTS OF THE UNIVERSITY OF ADELAIDE RADARS

R. A. Vincent and W. K. Hocking

Department of Physics and Mathematical Physics
University of Adelaide
GPO Box 498
Adelaide
Australia 5001

1. The Adelaide MF Radar

The 2 MHz partial-reflection radar located at Buckland Park, 40 km north of Adelaide (35°S, 138°E) has continued to operate on a continuous basis through the period November 1983 to the end of 1988; the only down-time being due to infrequent transmitter and computer failures. A spaced antenna system has been operated with a real-time wind analysis to provide climatologies of mean winds, tides and gravity waves (VINCENT et al., 1988, VINCENT and FRITTS, 1987). Since the beginning of 1985, these measurements have been combined with Doppler measurements of spectral widths to produce a climatology of turbulence dissipation rates (HOCKING, 1988).

The radar also operates at the third-harmonic of 6 MHz, for which purpose it has been used for D-region scattering investigations and for meteor studies (ELFORD and OLSSON-STEEL, 1988). The 6 MHz transmitting array and transmitter are currently being upgraded to provide a better angular discrimination and remove ambiguities caused by the grating lobes of the receiving array. The higher system gain will be valuable in extending the studies of the dynamics of the lower thermosphere and enable better multi-frequency comparisons at 2 and 6 MHz of D-region scattering processes.

2. The 54.1 MHz ST Radar.

This radar, also located at the Buckland Park field site, is being used for a number of studies into the dynamics of the troposphere and lower stratosphere (VINCENT et al., 1987). Current studies under way are spaced antenna wind measurements with on-line data analysis of cold-fronts (in association with the local Australian Bureau of Meteorology), and gravity waves. Continuous observations spanning several weeks have been made and the accumulated data is being used to provide a climatology of wave sources as well as is being compared with wave activity in the mesosphere, obtained with the 2 MHz system, in a search for possible wave coupling between the lower and upper atmosphere. Doppler measurements of turbulence are also in progress, and it is planned to make simultaneous comparisons between radar and balloon measurements of turbulence.

3. The Mawson Radar

A 2 MHz partial-reflection radar has been in operation continuously since June 1984 at Mawson Base in the Antarctic (67°S, 63°E) to study winds in the 70-110 km altitude region. Continuing studies have been made of the mean circulation, planetary waves, tides, and gravity waves (PHILLIPS and VINCENT, 1989). Some emphasis has also been given to studies of the interaction between the dynamics of the neutral atmosphere and the ionized atmosphere in the 100-150 km region during geomagnetically active periods (PRICE, 1988).

REFERENCES

Elford, W.G., and D. Olsson-Steel, The height distribution of radio meteors:
Observations at 6MHz, J. Atmos. Terr. Phys., 50, 811-818, 1988.

Hocking, W.K., Two years of continuous measurements of of turbulence
parameters in the upper mesosphere and lower thermosphere made with a 2-
MHz radar, J. Geophs. Res., 93D, 2475-2491, 1988.

Phillips, A. and R.A. Vincent, Radar observations of prevailing winds and
waves in the southern hemisphere mesosphere and lower thermosphere,
PAGEOPH. (In Press) 1989.

Price, G.D., Upper atmosphere dynamics in the auroral zone, Ph. D. Thesis,
University of Adelaide, 1988.

Vincent, R.A., P.T. May, W.K. Hocking, W.G. Elford, B.H. Candy and B.H.
Briggs, First results with the Adelaide VHF radar: spaced antenna studies
of tropospheric winds, J. Atmos. Terr. Phys. 49, 353-366, 1987.

Vincent R.A., and D.C. Fritts, A climatology of gravity wave motions in the
mesopause region at Adelaide, Australia, J. Atmos. Sci. 44, 748-760,
1987.

Vincent, R.A., T. Tsuda and S. Kato, A comparative study of mesospheric solar
tides observed at Adelaide and Kyoto, J. Geophys. Res., 93, 699-708, 1988.

CHARACTERISTICS OF PROVENCE RADAR

M. CROCHET

LSEET, Université de Toulon, UA 705 CNRS
639, Bd des Armaris, 83100 TOULON, FRANCE

ACCOMPLISHMENTS

The Provence Radar is a VHF, pulsed Doppler transportable radar usually located near the city of Toulon. It has been integrated to cooperative meteorological campaigns and/or ST radar networks :

- ALPEX 1982 in the Rhône Delta (South of France)
  (BALSLEY et al.,1983, ECKLUND et al.,1985, CARTER et al.,1985,1989)

- FRONTS 1984 and MESOGERS 1984 in Armagnac (South-west of France)

- FRONTS 1987 in Brittany (West of France)
  (CROCHET et al.,1989)

Comparisons have been (or will be) performed with other instruments :

- Balloons in-situ measurements in Armagnac 1984
  (DALAUDIER et al.,1985,1989)

- Stellar scintillometer (SCIDAR - TOULON 1987)
  (CROCHET et al., the same issue)

- Balloons and SCIDAR (Aire-sur-Adour, 1989).

The Provence Radar has also been used for preliminary investigations in VHF Radar Oceanography at the sea level by surface wave and from a cliff by sky-wave in order to investigate different oceanographic parameters : sea state, surface wind, surface currents, salinity and fronts (BROCHE et al., 1987).

BRIEF DESCRIPTION

The Provence Radar has been operated successively at 48.85, 47.8, 45 MHz due to frequency allocation problems with $\simeq$ 50 Kw peak power and a 60x60 m^2 antenna.

The capabilities have been recently upgraded.

- A new preprocessor is driven by an INI computer with pulse generation of 1, 2, 4, 8, 16 μs pulse widths and related IPP for 2% duty cycle and selection of the receiver adapted filter.

- A maximum of 48 gates can be sampled; with 8 bits conversion and a maximum of 4095 coherent integrations.

- Coding is available but not usually necessary due to the low duty cycle of the present tube transmitter.

- Low altitude investigations have been performed at low power with a totally passive duplexer and encouraging preliminary results have been obtained down to 500 m (CROCHET and BOURDIER, same issue).

PULBICATIONS RELATING TO PROVENCE RADAR

BALSLEY B.B., M. CROCHET, W.L. ECKLUND, D.A. CARTER, A.C. RIDDLE and R. GARELLO (1983) - "Observations of vertical motions in the troposphere and lower stratosphere using three closely-spaced ST radars" - 21st Conference on Radar Meteorology, pp. 148-152.

BROCHE P., P. FORGET, J.C. de MAISTRE, J.L. DEVENON and M. CROCHET (1987) "VHF radar for ocean surface current and sea state remote sensing" - Radio Science 22, n° 1, pp. 69-75.

BRUN E., M. CROCHET, W. ECKLUND (1986) - "Simultaneous multibeam sounding of wind and turbulence" - MAP HANDBOOK, 20, pp. 402-408.

CARTER D.A., B.B. BALSLEY, W.L. ECKLUND, M. CROCHET, A.C. RIDDLE and R. GARELLO (1985) - "Tropospheric gravity wave observed by three closely-spaced ST radars" - MAP HANDBOOK, 18, pp. 260-263.

CARTER D.A., B. BALSLEY, W.L. ECKLUND, A.C. RIDDLE, R. GARELLO, K.S. GAGE and M. CROCHET (1989) - "Investigation of Internal gravity waves using three vertically-directed closely-spaced wind profilers" - Submitted to JGR.

CROCHET M., F. CUQ, F.M. RALPH and S.V. VENTKATESWARAN (1989) - "Clear air radar observations of the great october storm of 1987" - Submitted to Dynamics of Oceans and Atmospheres.

DALAUDIER F., J. BARAT, F. BERTIN, E. BRUN, M. CROCHET, F. CUQ (1985) - "Comparison between ST radar and in-situ balloon measurements" - MAP/WINE, Lohen Norway.

DALAUDIER F., M. CROCHET and C. SIDI (1989) - "Direct comparison between in-situ and radar measurements of temperature fluctuation spectra : A puzzling result" - Submitted to Radio Science.

STATUS AND PLANS FOR THE POHNPEI, F.S.M. (7°N, 157°E) ST RADAR

W.L. Ecklund, K.S. Gage, D.A. Carter, and B.B. Balsley

Aeronomy Laboratory
National Oceanic and Atmospheric Administration
Boulder, Colorado 80303

The Pohnpei ST radar has been operated in a vertical only mode since 1984. The radar operates at 50 MHz and has a 100m × 100m phased array. At the present time the radar hardware and data processing systems are located in the communications building about 2 km from the town of Kolonia. The antenna is located in a field 450 meters from the communications building. The long run of cable has led to two problems. The radar signals are attenuated and the cable itself is vulnerable. The antenna was cut during the past year during plowing operations. The radar was restored to operating condition during a site visit in early October 1988.

Since commencing operation in 1984 much valuable data has been collected on vertical motions during convective storms. Upward vertical motions in excess of 10 ms⁻¹ have been observed during the passage of convective "hot towers" over the Pohnpei site. Average vertical motions have been studied extensively at Pohnpei by using rainfall and cloud cover observations from the Pohnpei weather station in Kolonia. Results of this analysis have been published (BALSLEY et al. 1988). They confirm that convective storms are largely responsible for the upward vertical motions observed in the tropics and that under relatively clear conditions subsidence prevails. Another study is underway linking the magnitude of vertical velocity variability to the occurrence of lee waves and the detailed profile of tropospheric horizontal winds (BALSLEY AND CARTER, 1989).

In the near future we plan to modify the Pohnpei radar so that horizontal winds can be measured. First, a small building will be constructed next to the existing antenna and the radar hardware and data processing systems will be moved to this location. Then a second polarization will be added to the antenna and a five-beam system will be used. The five-beam system will provide redundant wind information and permit us to evaluate the degree to which winds observed at Pohnpei are compromised by mountain lee waves. Because of the winds available from the balloon soundings at Pohnpei we will be able to evaluate whether wind profiler data is affected more or less than balloon data by the presence of lee waves.

REFERENCES

Balsley, B.B., W.L. Ecklund, D.A. Carter, A.C. Riddle, and K.S. Gage (1988), Average vertical motions in the tropical atmosphere observed by a radar wind profiler on Pohnpei (7°N latitude, 157°E longitude), J. Atmos. Sci., 45, 396-405.

Balsley, B.B., and D.A. Carter (1989), Mountain waves in the tropical Pacific atmosphere: a comparison of vertical wind fluctuations over Pohnpei and Christmas Island using VHF wind profilers, submitted to J. Atmos. Sci.

PROGRESS REPORT OF THE CHUNG-LI RADAR FACILITY

A. J. Chen and S.-Y. Su

Center for Space and Remote Sensing Research
National Central University
Chung-Li, Taiwan, ROC

Since the first report on the Chung-Li VHF radar specifications (BROSNAHAN et al., 1983) and the first operation and results reported at the workshop held in Aquadilla, Puerto Rico, October 21-25, 1985 (CHAO et al., 1986), several significant advances have been made on the radar facility and observational techniques. An updated summary of the Chung-Li radar characteristics is listed in Table 1.

A major system overhaul was carried out in the winter of 1987-1988. The improvements on the radar facility are listed in the following: First of all, the fastest data sampling rate for 40 range gate data is 1 data point per channel every 0.064 sec, an advance from 1 data point per channel every 0.2 sec. This is adequate for observing fast moving events and helpful in studying the echo mechanism. Secondly, a 16-bit complementary code system has been implemented. This will increase the observation height yet retain the maximum height resolution of 150 m. A first test run result of using the coded data is shown in Figure 1, adopted from a paper by CHU and HUANG (1988). Although the general agreement of wind velocity and direction is good among the coded, uncoded and rawinsonde data, more tests are still needed to perfect the decoding technique. Thirdly, the optional dc removal is also implemented in the system. This will improve the accuracy of the wind field measurements and echo power determination. Furthermore, it enables us to apply the observational techniques such as SAD and interferometry methods correctly.

As was known, the Chung-Li radar was designed to operate in dual mode, DBS and SAD modes. A simultaneous observation using the DBS and SAD methods has been analyzed by FU (1988). We show in Figure 2 one of his results. Notice that in the figure the results from the DBS, SAD and rawinsonde data are quite in agreement in wind velocity and direction. However, it should be noted that the wind velocity from the SAD method is the "apparent velocity" obtained from auto- and cross-correlation analyses. This is not the "true velocity" from the full correlation analysis (BRIGGS, 1984), in which the random changes of the scattering pattern have been removed. Apparently, other effects such as the broad radar beam (7.4°) and the vertical wind correction (under certain weather conditions) need to be further investigated for SAD observations with the Chung-Li radar in order to understand the discrepancy.

Finally, the Chung-Li radar has observed quite a few wave events because of its proximity to the Taiwan central mountain range and frequent severe weather changes such as the approach of typhoons and cold fronts. Figure 3 shows a wave event that seems to be related to the so-called "cat eye" phenomenon developed from K-H instability of wind shear observed at the same height. The out-of-phase of the vertical wind oscillations between layers with Z > 7 km and layers with Z < 7 km around 17:52 of June 9, 1986, in the figure can be related to the wind shear observed at Z = 7 km shown in Figure 4. Detailed analysis of this event has been presented by FU (1988).

In conclusion, the Chung-Li radar facility offers a unique opportunity to observe wave phenomena related to mountain waves, typhoons, and cold fronts. More extended observations can certainly be made in order to understand the wave phenomena in subtropical regions. Furthermore, some additional hardware acquisitions such as MEDAC, RASS, and lidar are planned in the near future for the Chung-Li radar facility to increase its capability in studying the middle atmospheric phenomena.

Table 1. Characteristics of the Chung-Li VHF Radar.

Location	24°58'N, 121°11'E
Frequency	52 MHz
Antenna Array	
configuration	3 modules
elements	(8 x 8) 4-element Yagi/module
area	1600 m^2/module
gain	28 dB (one module)
	33 dB (3 modules)
beam directions	vertical; 17° off zenith toward east, west, north, and south
	5 discrete directions every module
HPBW	7.4° (one module)
	4° - 5° (3 modules)
Transmitter	3 coherent transmitters, max power 60 kW/transmitter
Pulse Width	1 - 16 μs
Duty Cycle	≦ 2%
Pulse Coding	16-bit complementary codes; 2, 4, 8, or 16 bits
Receiver	Monostatic
Bessel filter	Bandwidth 1 MHz, 0.5 MHz, 0.25 MHz, or 0.125 MHz
Computer	CODATA computer
Data Resolution	$\Delta H \geq 150$ m
	$\Delta t \geq 0.064$ s
Max Height	24 km (normal operation)
Operating Mode	Dual mode (DBS and SAD)

REFERENCES

Briggs, B. H., The analysis of spaced sensor records by correlation techniques, *Handbook for MAP, 13*, 166, 1984.

Brosnahan, J., J. Chao, and J. Röttger, Chung-Li, Taiwan dual mode (Doppler and spaced antenna) VHF radar: Preliminary specifications, *Handbook for MAP, 9*, 383, 1983.

Chao, J., S. S. Chu, Y. H. Chu, I. J. Fu, J. Röttger, and C. H. Liu, the first operation and results of Chung-Li VHF radar, *Handbook for MAP, 20*, 359, 1986.

Chu, Y. H., and J. H. Huang, The application of phase coding technique in Chung-Li radar, Proc. 1988 Telecommun. Symp., Dec 9-10, 1988.

Fu, I. J., Observations of gravity waves by Chung-Li VHF radar, Ph.D. Thesis, National Central University, 1988.

CHUNG-LI-VHF-RADAR

DATE: 88/7/12
TIME 14:40 -- 15:30
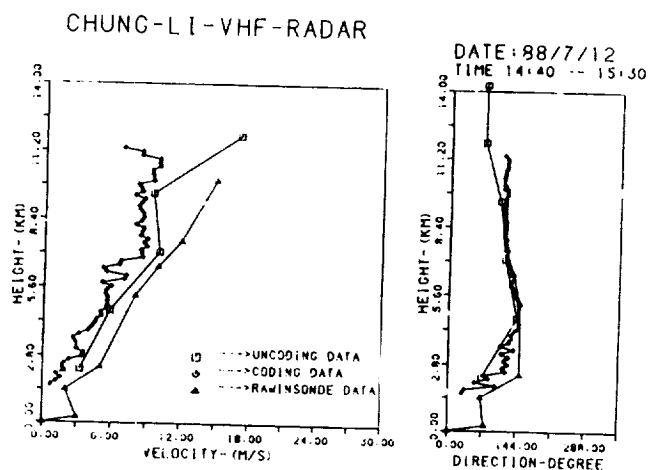
Figure 1. First results of Chung-Li radar coded data in comparison with the uncoded data taken consecutively and with the rawinsonde data taken at 25 km off the radar site and at an earlier time (8:00 am).
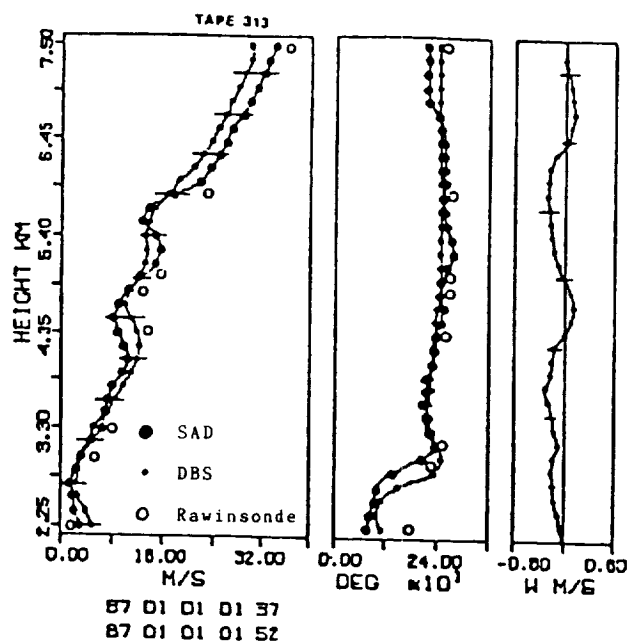
Figure 2. Comparison of the average wind velocity in magnitude and direction by the Chung-Li radar with SAD and DBS operation modes.

ORIGINAL PAGE IS
OF POOR QUALITY
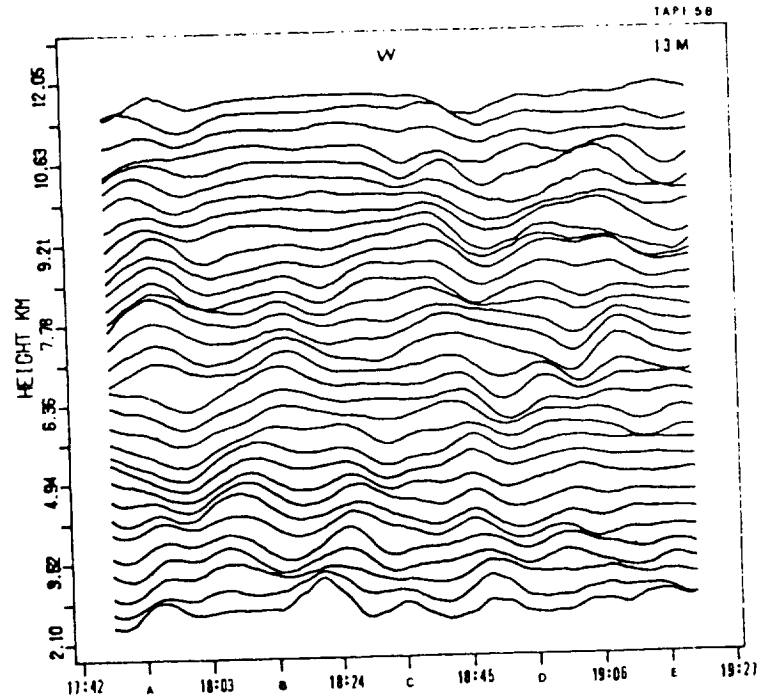
Figure 3. Observation of a possible "cat eye" phenomenon by the Chung-Li radar at 17:52 of June 19, 1986, displayed by the out-of-phase oscillation of the vertical wind component.
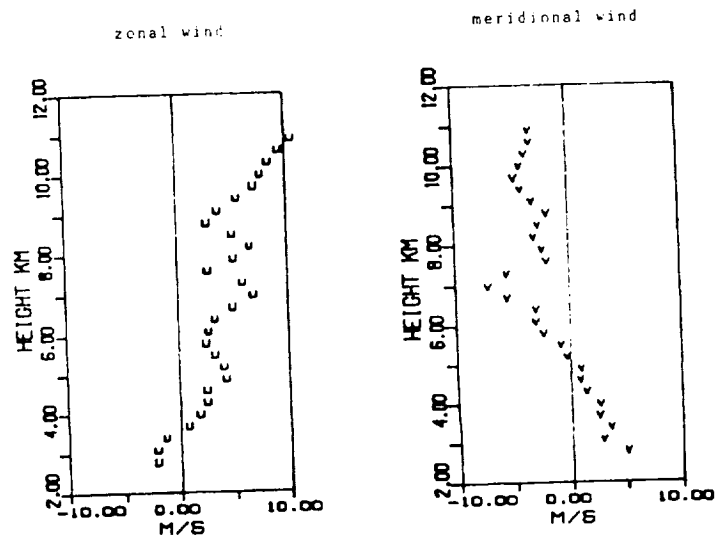
Figure 4. The corresponding zonal and meridional wind components of the "cat eye" event between 17:42 and 18:03 of June 9, 1986.

THE CHRISTMAS ISLAND ST RADAR (2°N, 157°W)

K.S. Gage, B.B. Balsley, D.A. Carter, W.L. Ecklund, and J.R. McAfee

Aeronomy Laboratory
National Oceanic and Atmospheric Administration
Boulder, Colorado 80303

S.K. Avery

Cooperative Institute for Research in the Environmental Sciences
University of Colorado
Boulder, Colorado 80309

The wind-profiling Doppler radar at Christmas Island has been in routine operation since April 1988. The profiler is a 50 MHz VHF Doppler radar with a 100m × 100m phased array antenna. The construction phase was completed in 1985 but the early observations were compromised by the presence of sea clutter. The sea clutter was mostly eliminated by modifications to the antenna which were completed in early 1986. A detailed analysis of the sea echoes can be found in BALSLEY et al. (1987), and the antenna modifications are described in BALSLEY et al. (1988).

The Christmas Island wind profiler is supported by NOAA's TOGA Program Office as part of its concerted effort to improve upper-air wind observations over the tropical Pacific. The TOGA program is striving to understand the dynamics of low frequency climate variability associated with the El Niño and Southern Oscillation. The Christmas Island radar is located in a data-sparse region in the central Pacific. Compared to the western Pacific, Christmas Island weather is generally fair except during ENSO events when convection moves eastward across the equatorial Pacific.

Wind observations from Christmas Island have routinely been transmitted via GOES Satellite and incorporated into the Global Telecommunication System (GTS) since early 1987. This is the first wind profiler data to be disseminated globally in near real-time and to be used in operational analysis and forecast products by the National Meteorological Center (NMC) and the European Center for Medium Range Weather Forecasts (ECMWF). We have made extensive comparisons between the NMC and ECMWF analyses interpolated to Christmas Island (GAGE et al. 1988).

During the past summer a meteor echo detection and collection system (MEDAC) (WANG et al. 1988) was added to the Christmas Island radar. The addition of meteor echo observations via MEDAC will enable mesospheric and lower thermospheric observations to be made at Christmas Island simultaneously with lower atmospheric observations. In the future we plan to incorporate a UHF boundary layer radar (ECKLUND et al. 1988) into the Christmas Island system and to cooperate with R.A. Vincent of the University of Adelaide, Australia, to establish an HF SAD radar at Christmas Island.

REFERENCES

Balsley, B.B., W.L. Ecklund, D.A. Carter, and A.C. Riddle (1988), A note on reducing the horizontal sidelobes of near-vertically directed COCO arrays, IEEE Trans. Antennas Propag., 36, 139-141.

Balsley, B.B., A.C. Riddle, W.L. Ecklund, and D.A. Carter (1987), Sea surface currents in the equatorial Pacific from VHF radar backscatter observations, J. Tech., 4, 530-535.

Ecklund, W.L., D.A. Carter, and B.B. Balsley (1988), A UHF wind profiler for the boundary layer: brief description and initial results, J. Tech., 5, 432-441.

Gage, K.S., J.R. McAfee, W.G. Collins, D. Söderman, H Böttger, A. Radford, and B.B. Balsley (1988), A comparison of winds observed at Christmas Island using a wind-profiling Doppler radar with NMC and ECMWF analyses, Bull. Amer. Meteorol. Soc., 69, 1041-1046.

Wang, S.T., D. Tetenbaum, B.B. Balsley, R.L. Obert, S.K. Avery, and J.P. Avery (1988), A meteor echo detection and collection system for use on VHF radars, Radio Sci., 23, 46-54.

THE STATUS OF THE FLATLAND RADAR AND RECENT STUDIES

J.L. Green, T.E. VanZandt, K.S. Gage, J.M. Warnock, W.L. Clark

Aeronomy Laboratory
National Oceanic and Atmospheric Administration
Boulder, CO 80303 U.S.A.

G.D. Nastrom

Department of Earth Sciences
St. Cloud State University
St. Cloud, MN U.S.A.

The Flatland radar, a VHF (49.8 MHz) ST radar located about 8 km west of the Champaign-Urbana, Illinois airport, at 40.05° N, 88.4° W, 212 m MSL, was constructed and is operated by the Aeronomy Laboratory of the National Oceanic and Atmospheric Administration (GREEN et al., 1988). It is sited in a large region of very flat terrain to avoid orographic influences. The antenna is a 60m × 60m coaxial-collinear array that is steerable in 2° steps in the N-S and E-W vertical planes. The vertical beam is carefully adjusted to be < 0.02° from the vertical in order to minimize contamination of vertical velocity measurements by horizontal winds.

From March, 1987 through April, 1988, the radar measured the vertical wind velocity every 2-1/2 min. These data have been used to study frequency spectra of vertical velocity (VANZANDT et al., 1988) and the vertical velocity and reflectivity structure during tropopause folding events (NASTROM et al., 1988). During May-July, 1988, comparisons were made with a collocated boundary layer radar (ECKLUND et al., 1988) and with the Chill Radar (MUELLER AND SILHA, 1978). During June, 1988, C_n^2 was studied by comparing simultaneous data from the Flatland radar, the boundary layer radar, thermosonde, an isoplanometer, a r_0 device, and the Aeronomy Laboratory model for C_n^2 (WARNOCK et al., 1988). During August, 1988, simultaneous observations were made with the Urbana radar and Flatland radar (DESTER et al., 1988).

At present the Flatland radar is being operated in a five antenna beam configuration in order to study the vertical flux of horizontal momentum by means of gravity waves. This data will also be used in a study of winter storms.

REFERENCES

Dester, G.D., J.L. Green, G.R. Stitt, S.J. Franke, and C.H. Liu (1988), Simultaneous observations of the troposphere and lower stratosphere by the Flatland and Urbana radars - initial results, Paper 5.5.1, Handbook for MAP, (in press).

Ecklund, W.L., J.L. Green, D.A. Carter, W.L. Clark, P.E. Currier, J.M. Warnock, and K.S. Gage (1989), Summertime observations in Illinois using two wind profilers, Preprint volume, 24th Conf. on Radar Meteorol., Mar. 27-31, Tallahassee, FL.

Green, J.L., G.D. Nastrom, K.S. Gage, T.E. VanZandt, W.L. Clark, and
J.M. Warnock (1988), Observations of vertical velocity over Illinois by
the Flatland radar, Geophys. Res. Lett., 15, 269-272.

Mueller, E. A., and E.J. Silha (1978), Unique features of the CHILL radar
system, Preprint vol., 18th Conf. on Radar Meteorol.,
Mar. 28-31, Atlanta, GA, 381-382.

Nastrom, G.D., J.L. Green, T.E. VanZandt, K.S. Gage, and W.L. Clark (1988),
Measurement of large-scale vertical velocity using clear-air Doppler
radar, Paper 4.7.4, Handbook for MAP, (in press).

VanZandt, T.E., G.D. Nastrom, and J.L. Green (1988), Comparison of observed
frequency spectra of vertical velocity with model Doppler-shifted gravity
wave spectra, Paper 4.7.5, Handbook for MAP, (in press).

Warnock, J.M., R.R. Beland, J.H. Brown, W.L. Clark, F.D. Eaton, L.D. Favier,
K.S. Gage, J.L. Green, W.H. Hatch, J.R. Hines, E.A. Murphy, G.D. Nastrom,
W.A. Peterson, and T.E. VanZandt (1988), Comparison among clear-air radar,
thermosonde and optical measurements and model estimates of C_n^2 made in
very flat terrain over Illinois, Paper 5.4.1, Handbook for MAP, (in
press).

OTHER PUBLICATIONS

Clark, W.L., and J.L. Green (1988), Flatland data analysis system, Paper 9.1.1,
Handbook for MAP, (in press).

Clark, W.L., J.L. Green, and J.M. Warnock (1988), Monitoring VHF system perfor-
mance using cosmic noise, Paper 8.1.1, Handbook for MAP, (in press).

Clark, W.L., G.D. Nastrom, K.S. Gage, J.L. Green, R.G. Strauch, and
J.M. Warnock (1988), Utilization of a vertical beam clear-air Doppler
radar beam to measure vertical divergence, Symp. on Lower Tropospheric
Profiling: Needs and Technologies, May 31-June 3, Boulder, CO.

Green, J.L., R.R. Beland, J.H. Brown, W.L. Clark, F.D. Eaton, L.D. Favier,
K.S. Gage, W.H. Hatch, J.R. Hines, E.A. Murphy, G.D. Nastrom,
W.A. Peterson, T.E. VanZandt, and J.M. Warnock (1989), Comparisons of
refractivity turbulence from the Flatland VHF radar with other measurement
techniques, Preprint vol., 24th Conf. on Radar Meteorol., Mar. 27-31,
Tallahassee, FL.

Green, J.L., and W.L. Clark (1988a), The Flatland radar antenna steering im-
plementation, Paper 7.1.1, Handbook for MAP, (in press).

Green, J.L., and W.L. Clark (1988b), Flatland online signal processing and
radar control system, Paper 8.5.1, Handbook for MAP, (in press).

Nastrom, G.D., J.L. Green, K.S. Gage, M.R. Peterson, and T.E. VanZandt (1989),
Sources of variability of vertical velocity as seen by the Flatland VHF
radar, Preprint vol., 24th Conf. on Radar Meteorol., Mar. 27-31,
Tallahassee, FL.

Nastrom, G.D., J.L. Green, M.R. Peterson, and K.S. Gage (1988), Tropopause
folding and the variability of the tropopause height as seen by the
Flatland VHF radar, submitted to J. Appl. Meteorol.

VanZandt, T.E., J.L. Green, G.D. Nastrom, K.S. Gage, W.L. Clark, and
J.M. Warnock (1988), Measurement of vertical velocity using clear-air
Doppler radars, Symp. on Lower Tropospheric Profiling: Needs and
Technologies, May 31-June 3, Boulder, CO.

VanZandt, T.E., J.L. Green, G.D. Nastrom, K.S. Gage, W.L. Clark, and
J.M. Warnock (1988), Measurement of vertical velocity using clear-air
Doppler radars, Symp. on the Middle Atmosphere after MAP, COSPAR 1988,
Helsinki, Finland, Handbook for MAP, (in press).

VanZandt, T.E., G.D. Nastrom, and J.L. Green (1988), Comparison of observed
frequency spectra of vertical velocity with model Doppler-shifted gravity
wave spectra, Paper 4.7.5, Handbook for MAP, (in press).

VanZandt, T.E., G.D. Nastrom, J.L. Green, and K.S. Gage (1989), The spectrum of
vertical velocity from Flatland radar observations, Preprint vol., 24th
Conf. on Radar Meteorol., Mar. 27-31, Tallahassee, FL.

Warnock, J.M., K.S. Gage, and J.L. Green (1988), Flatland radar measurements of
tropopause heights and comparison of specular echo strength with model
estimates, Paper 1.5.3, Handbook for MAP (in press).

Warnock, J.M., K.S. Gage, and J.L. Green (1989), Studies of the radar reflec-
tivity of vertical echoes measured by the Flatland VHF clear-air Doppler
radar, Preprint vol., 24th Conf. on Radar Meteorol., Mar. 27-31,
Tallahassee, FL.

ST RADAR: FIRST STEP TO INDIAN MST RADAR

B. K. Sarkar and A. Agarwal

Society for Applied Microwave Electronics Engineering and Research
IIT Campus, Hillside, Powai
Bombay 400 076, India

INTRODUCTION

ST (stratospheric/tropospheric) radar works over heights extending up to the lower stratosphere. A typical height covered by ST radar is somewhere between 20 - 25 km.

ST radars are most useful for studying jetstream dynamics, tropopause heights, etc. They can be used to measure wind velocity, all three vectors of wind velocity, variation of clear air turbulence near and above thunderstorms, etc.

ST mode operation is an important milestone in the development of MST radar. ST radar is smaller in size and hence it is easier to construct to prove the concept of MST radar. ST radar should be an integral part (wholly or partially) of the final MST radar so that minimum changes will be needed to construct an MST radar from the ST radar configuration.

ST mode configuration of the Indian MST radar is proposed here, keeping in mind minimum changes from the final MST radar configuration, thus reducing the extra costs and time.

CONFIGURATION FOR ST MODE OPERATION

The Indian MST radar is a phased array radar consisting of plannar array of 32 x 32 (= 1024) dual Yagi antennas. There are 32 transmitters. Each transmitter feeds a row of 32 Yagi antennas with the help of directional couplers. Transmitter power and directional coupler outputs are tapered to get a Taylor distribution, resulting in 20 dB sidelobe for the plannar array. The beam is tilted by the low power phase shifters associated with the exciters of the transmitters.

It is proposed not to rearrange or disturb the feeding structure of the MST radar. For ST mode operation, 16 x 16 dual Yagi antennas (instead of 32 x 32 antennas as in the MST radar) will be excited feeding power from 16 transmitters (instead of 32 transmitters as in MST radar) as shown in Figures 1 and 2. Each transmitter feeds 16 antennas. Since 16 x 16 antennas are excited instead of 32 x 32 antennas, the power left out after feeding 16 antennas in each row is absorbed in matched terminations. The 16 x 16 array of the ST mode will radiate 70% of the total transmitter power. The remaining 30% is absorbed in matched terminations. The sidelobe level of the 16 x 16 array ST radar will be 13.1 dB and 3 dB beam width will be 6°.

Each transmitter of the MST radar will consist of the exciter, solid-state amplifier, 2 stages of triode driver amplifiers and finally high power amplifier. In ST mode operation, transmitters consisting of exciters, low power solid-state amplifiers and triode driver amplifiers will be used. It is proposed to use 12 nos. of 6 kW (peak) and 4 nos. of 4.5 kW (peak) transmitters resulting peak power aperture product of 2.244×10^8 Wm^2.

Table 1 gives transmitter power levels, beam widths, sidelobe levels and peak power aperture products for arrays of different sizes.
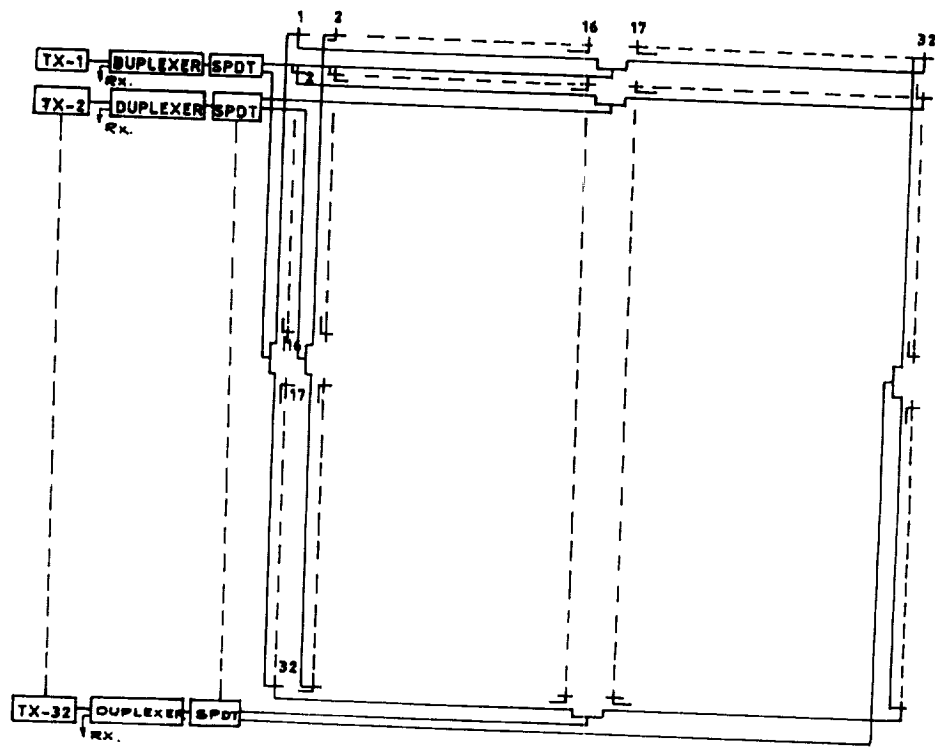
Figure 1. MST radar feed network configuration.

Tx. HUTS

POWER DIVIDER

DIRECTIONAL COUPLER

YAGI ANTENNA

INTER CONNECTION BETWEEN COUPLERS.
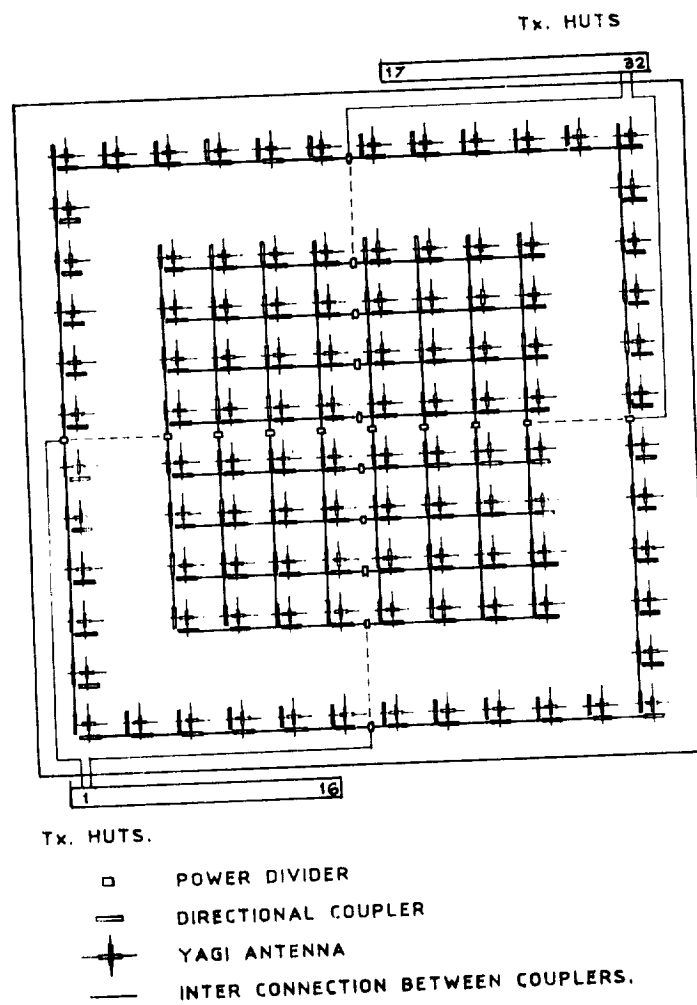
Figure 2. ST radar configuration.

ADVANTAGE OF THE PROPOSED ST RADAR

There exists flexibility of adding transmitters one by one and increasing the elements symmetrically so that beam widths are equal. By adding four more transmitters, it will give beam widths of 4.8° x 4.8°. Data can be collected with increasing antenna aperture and increasing transmitted power. Testing of smaller arrays of ST radar with all capabilities will give confidence to scientists and engineers. Since the radar will be built by adding elements stage by stage from the ST configuration, any problem in the radar during the developmental period can also be rectified easily. In the proposed configuration of ST radar, once antennas, feeder network, transmitters, etc. are installed in the antenna field, they remain unperturbed for MST mode operation. The only additional work involved is to make 64 matched terminations.

Table II compares the parameters of the proposed Indian ST radar with the existing ST radars of USA and Australia.

Table 1

Parameters of Indian ST Radar With
Increasing Elements and Transmitted Power

No. of elements	Sidelobe level dB	3 dB beam-width deg	Tx power level kW	No	Peak power aperture product (Wm^2)
16 x 16	13.1	6	6	12	2.244×10^8
			4.5	4	
20 x 20	14.75	4.8	6	12	4.85×10^8
			4.5	4	
			3.5	4	
24 x 24	16.0	4	6	12	8.66×10^8
			4.5	4	
			3.5	4	
32 x 32	19.6	3	6	12	19.19×10^8
			4.5	4	
			3.5	4	
			2.7	4	
			1.8	4	
			1.1	4	

Table II

Comparison of Existing ST Radars
With The Proposed Indian ST Radar

SUBSYSTEMS	EXISTING ST RADARS				Planned ST Radar
	Platteville USA	Sterling USA	Sunset USA	Buckland Park AUSTRALIA	Tirupati INDIA
I. TRANSMITTER					
Frequency (MHz)	49.92	49.80	40.475	54.1	53.0
Total peak power (kW)	15	30	50	40	90
Peak power aperture product(Wm^2)	1.5×10^8	0.75×10^8	1.1×10^8	3.2×10^8	2.24×10^8
Duty cycle (%)	1.7	2.0	2.5	0.7	2.5
Average power	133 W	400 W	1 kW	200 W	2.25 kW
Pulse width min.(μs)	4	4	1	7	1
Average power aperture product (Wm^2)	2.66×10^5	10.0×10^5	22.0×10^5	15.0×10^5	79.47×10^5
II. ANTENNA					
Type	Coax. dipoles	Co-Co	Co-Co	Co-Co	Yagi
Total no. of dipoles	-	-	-	-	16 x 16
Physical aperature (m^2)	2000	2500	2200	7500	3532
Beam width	5°	5°	4.8°	3.2°	6°
Beam direction from Zenith	15°(2)	15°(2)	60°	15°(1)	±20°
Mode	PAD	PAC	PAC	PAC,PAY	PAY

PAD - Phased Array Dipoles
PAC - Phased Array Co-axial Collinear
PAY - Phased Array Yagis

PROGRESS IN THE DESIGN AND DEVELOPMENT OF THE INDIAN MST RADAR

G. Viswanathan

MST Radar Project
Indian Space Research Organization
Bangalore 560 058, India

The system level specifications of the Indian MST radar were brought out in MAP Handbook Vol. 20, dated June 1986. The present status of progress in the design and development of the Indian MST radar is summarized below:

A contract was awarded in January 1987 to the Society for Applied Microwave Electronics Engineering and Research (SAMEER), Bombay, an autonomous Society under the Department of Electronics, Government of India for the design and development of the Indian MST radar.

A Preliminary Design Review was organized to decide on the design approach to the system as well as the individual subsystems of the radar. The following major decisions emerged during the PDR.

- It was decided to use crossed three element Yagi for the antenna array instead of the coaxial collinear system originally contemplated. The antenna will now consist of 1024 such Yagi elements.

- Antenna illumination using a modified Taylor series was decided to provide better control over sidelobe levels.

- While the peak power of 2.5 MW and the average power of 60 kW for the system was retained, the configuration of the transmitter was changed to use 32 transmitter units varying in power output from 120 kW peak to approximately 20 kW peak to enable the Taylor series illumination.

- The concept of using a semiactive array instead of a totally passive array was finalized, resulting in a moderate level of flexibility.

- The configuration of the data acquisition and real-time processing system was modified to have a dedicated data acquisition and preprocessing unit followed by a general purpose Super Microcomputer (MASS COMP 5600) based on 68030 processor, coupled with a vector accelerator and standard peripherals.

A site was chosen for the installation of the Indian MST radar facility at Gadanki village (Lat 13°27'34"N, Long 79°10'34"E, MSL 190 mtrs.) near Tirupati, in the state of Andhra Pradesh. A noise survey was conducted to characterize the possible radio noise interference. Exhaustive measurements are planned for characterizing cosmic noise levels at the site. The necessary coordination with the other user agencies for the frequency allocation and site clearance is completed under the aegis of the Wireless Planning Committee, Ministry of Communication of the Government of India. Frequency allocation is made at the carrier frequency of 53 MHz with operating bandwidth of 2 MHz.

Engineering design for the buildings and infrastructure for establishing the facility was completed and tendering of the civil and electrical works is in progress. The design and development effort for the various subsystems of the MST radar consisted of:

- Validation of the design by the development of a laboratory prototype.

- Development of an engineering prototype to meet the performance requirements as well as the environmental specifications.

- Subcontracting the production of units required in large numbers to industries after detailed vendor evaluation.

- Inhouse development of critical subsystems as well as software packages.

The present status of the development has crossed the state of validating the design approach by way of laboratory prototypes and vendor evaluation in the case of the antenna units.

The first phase of the commissioning of the system is expected to be over by the middle of 1990. At this time the facility will be operated in the ST mode while continuing to augment the system to reach the full-fledged MST level in terms of power aperture product. Scientists from the different National Laboratories plan to extract meaningful science output during the ST mode operation.

LEGEND

1. Antenna Array
2. Main Building
3. Terminal Building
4. Transmitter Huts
5. Site Office
6. GLR and Pump House

Layout Plan

of

Indian

M S T Radar

ISRO / DOS

At Gadanki.
79°11' E & 13°28'N
190 mts above MSL
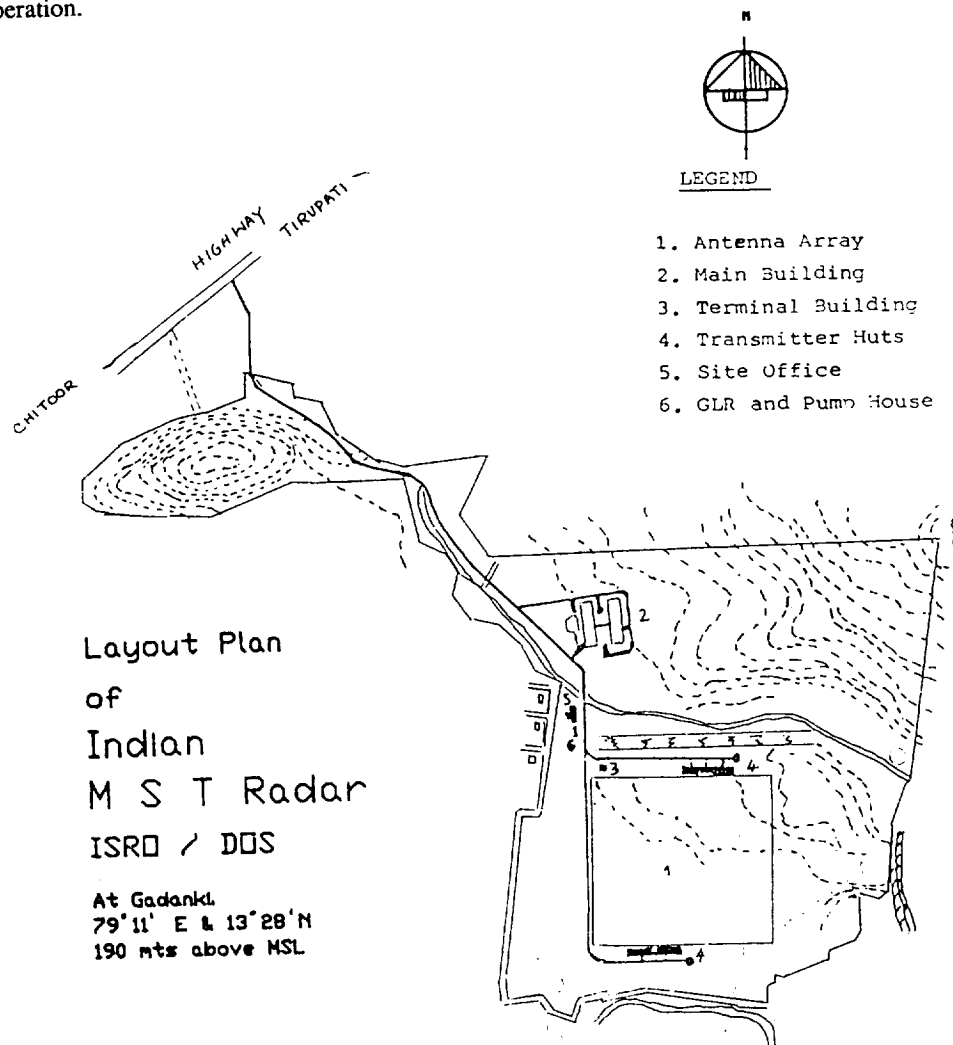
THE ST RADAR UNDER CONSTRUCTION AT PIURA, PERU (5°S, 81°W)

B.B. Balsley, W.L. Ecklund, D.A. Carter, and K.S. Gage

Aeronomy Laboratory
National Oceanic and Atmospheric Administration
Boulder, Colorado 80303

R. Mugica, A. Mabres, and R. Rodriguez

Universite de Piura
Piura, Peru

S.K. Avery and E.J. Violette

Cooperative Institute for Research in the Environmental Sciences
University of Colorado
Boulder, Colorado 80309

R.F. Woodman

Instituto Geofisico del Peru
Lima, 100 Peru 00612

The Piura ST radar currently under construction at the Universite de Piura in Piura, Peru will be a 50 MHz VHF system. This radar will form the easternmost facility in the proposed trans-Pacific network of ST radars that will eventually span the equatorial Pacific. Support for the construction of the Piura radar is being furnished by the U.S. National Science Foundation. The ST radar at Piura is part of a cooperative research program involving NOAA's Aeronomy Laboratory and the University of Colorado in the United States, and the Universite de Piura and the Instituto Geofisica del Peru in Peru. The radar is being constructed on the campus of the Universite de Piura.

A container filled with antenna cables and radar hardware was shipped from Alaska during the past few months. Site preparations are now underway and the antenna construction will begin about the first of the year. A building will be constructed next to the antenna site to house the radar equipment. A diesel generator has been purchased to provide a continuous source of power to the radar. The first phase of construction will be completed by mid-1989 and the radar will be operated for the first year in a vertical-only mode. During 1990 the radar will be modified so that horizontal as well as vertical velocities can be measured.

THE INSU / METEO BIFREQUENCY S.T. RADAR

M. Petitdidier[1], V. Klaus[2], F. Baudin[1], C. Bourdier[3], M. Crochet[3], A. Desautez[4],
C. Guérin[1], R. Ney[1], G. Penazzi[4], P. Quinty[2]

(1) C.R.P.E., Saint Maur, France
(2) C.N.R.M./E.E.R.M., Toulouse, France
(3) L.S.E.E.T., Toulon, France
(4) I.N.S.U., Saint Maur, France

In 1984, two networks of ST radars were proposed, one devoted to research (INSU network), the other to meteorological operations (DMN Network). In order to go deeper into these two projects, the different institutions involved have coordinated their scientific, technical and financial resources for a better efficiency. The first stage began in 1985 and was the realization of a prototype fulfilling the requirements of both atmospheric research and operational meteorology. Consequently, a bifrequency UHF/VHF radar has been built : the UHF radar covers the lowest altitudes from several hundred meters up to 7 km and the VHF radar the highest ones from 1.5 km up to 20km. As a matter of fact, we build two VHF radars working at 72.5 MHz and 45 MHz respectively and a radar at 961 MHz. Any of the two VHF radars can be included into the bifrequency radar.

The second stage was a long run in a multi-instrument environment from October 1987 to January 1988 during the FRONTS 87 experiment (Clough, 1987). A network of three S.T. radars, 100 km apart, was set in order to study small and meso scales circulations. Two of them, the bifrequency (961/45MHz) and the 72.5 MHz radars, came from this prototype and were continuously operating for the first time. The third one was the "PROVENCE" radar from the LSEET.

Characteristics of the radars

Figure 1 is a schema of the bifrequency radar system. The UHF and VHF radars are driven by the same computer and work independently and simultaneously according to their own measurement sequences. Tables 1 and 2 give the characteristics of the different radars .
Both of them use solid state amplifiers, developped for this purpose. During the transmission and reception, the system direct component is eliminated by a 180° flip from pulse-to-pulse and subsequent coherent integration. The VHF transmitted pulse may be coded using a 10-baud complementary code and decoded after coherent integrations in the numerical device. The 256 point power spectra are computed on-line using a TMS320, incoherently added and recorded on a magnetic tape with a time rate as fast as 20s. Spectrum plots are available in real time.
Different running modes of the radar are memorized and can be activated using the computer function keys. A mode is constituted by the working parameters of the radars under operation. For each radar, the sequence is defined by the alternance of the directions of observation, and of coded or non coded pulse in case of VHF radar. Any alternance is possible. The number of coherent integrations is a characteristic of each term of the sequence and the number of incoherent integration of each radar.

Preliminary FRONTS 87 results

The UHF/VHF(45 MHz) and the VHF(72.5 MHz) radars worked continuously during the 4 month FRONTS 87 experiment in a satisfactory way and thus pointed out their reliability.
Afterwards, some optimization have been carried out.
The VHF radar had worked continuously with a duty cycle of 16% without any problems during and after the experience.
In order to take advantage of this large set of S.T. radar data, a database has been implemented. So far, it contains the informations relative to all the experiments carried out by the INSU/METEO prototype; it will be a major help to make case and statistical studies.
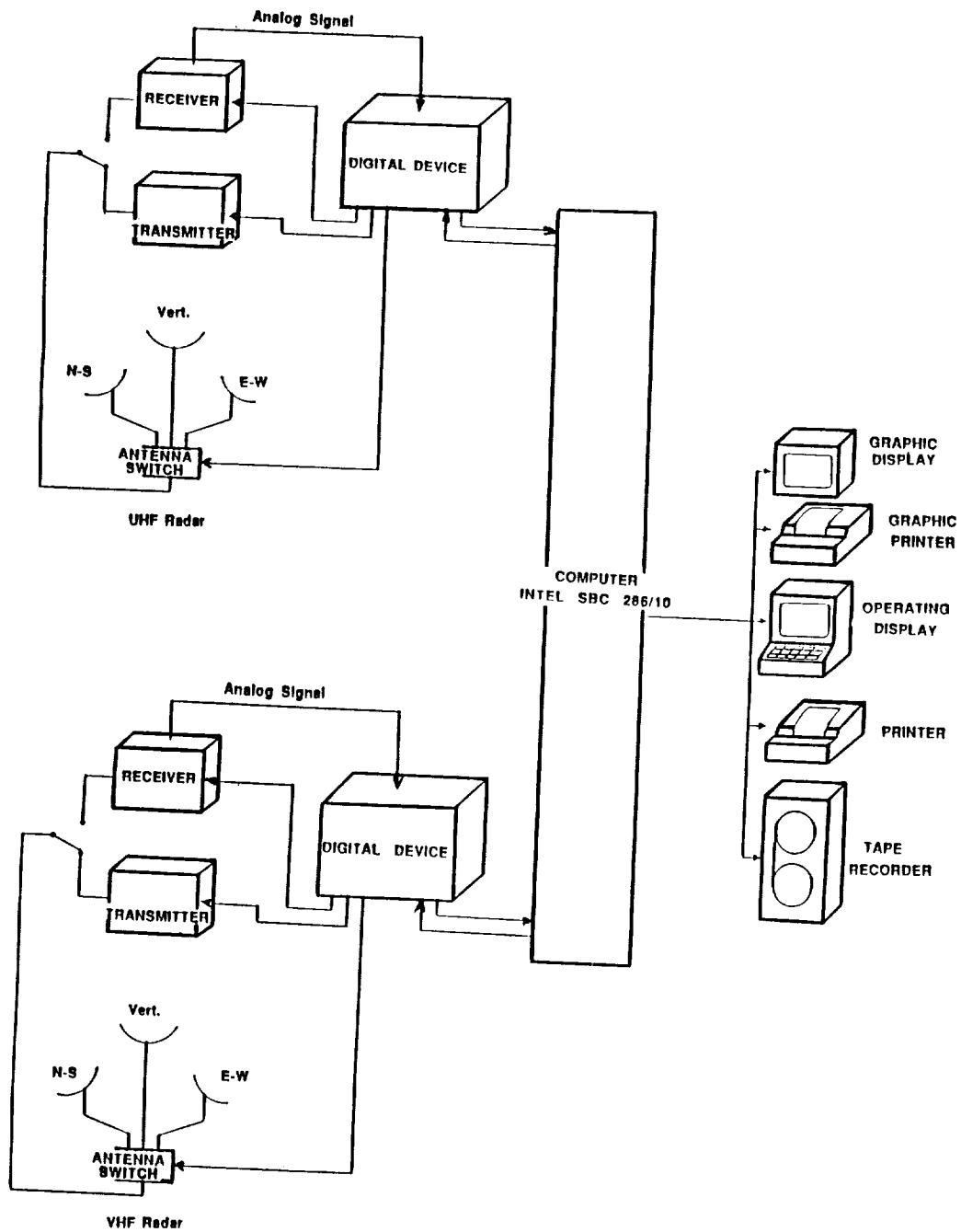
Figure 1. Schema of the bifrequency INSU/METEO S.T. Radar

TABLE 1. UHF - Radar Characteristics and Operating Parameters

Radar Characteristics

Frequency (MHz)	961
Bandwidth (MHz)	1
Peak Power (kW)	4
Average Power (W)	80
Pulse Width (μs)	1
Pulse Repetition Period (μs)	50
Duty cycle (%)	2
Antenna, Parabola diameter (m)	4.60
Beamwidth	4°
Antenna Pointing	Zenith, 15° off-Zenith to North and East

Typical Operating Parameters during FRONTS 87

Time Domain Average	64	256
Spectral Resolution (ms^{-1})	0.19	0.048
Maximum Radial Velocity (ms^{-1})	± 24.4	± 6.1
Height Resolution (m)	150	
First Height (m)	260	
Number of Gates	47	
Time Resolution (s)	0.82	3.28
Spectral Average	50	100

TABLE 2. VHF - Radar Characteristics and Operating Parameters

Radar Characteristics

Frequency (MHz)	72,5 (λ = 4.13 m)	and	45 (λ = 6.7 m)
Antenna Type	array of COlinear COaxial dipoles		
Antenna Area	40 x 40 m^2		70 x 70 m^2
Beamwidth	5.6°		
Peak Power (kW)	5		
Pulse Repetition Period (μs)	156.25 (6400 Hz)		
Pulse Width (μs)	25 (coded)	2.5 (non coded)	15 (non coded)
Average Power (W)	800	8 0	480
Duty Cycle (%)	16	1.6	9.6
Height Resolution (m)	375	375	2250
Code Type	10 baud Complementary Codes		

Typical Operating Parameters during FRONTS 87

Time Domain Average	256	1024
45 MHz Maximum Radial Velocity (m/s)	± 41.7	± 10.4
45 MHz Spectral Resolution (m/s)	0.2	0.05
Time Resolution (s)	10.24	41.96
Spectral Average	2	6

The comparisons between ST radar and radiosonde data show a global good agreement but it must be examine in details especially during front passage.For one of the major events, the 12th of January 1988, preliminary radar results point out the fine structure of the frontal surface with a low level jet ahead the front and at upper altitude tropopause foldings.

Future Developpement

The INSU/METEO radar was built as a prototype of the Research Network ST radars. This goal has been reached as this network was accepted by the French scientific Community in september 1987. Two other bifrequency radars will be built as a copy of the prototype in the next three years. As these radars are transportable, they could be set into a network during multi-instrument campaigns as ALPEX, FRONTS 84 and 87 or in fixed locations, close by the laboratories, for routine experiments .

REFERENCES

Clough S.A.,Meteor. Mag., 116, 32-42, 1987.

Addresses:
CNRM/EERM, 42 Avenue Gustave Coriolis, 31057 Toulouse Cedex, France
CRPE, 4 Avenue de Neptune, 94107 Saint Maur des Fossés Cedex, France
INSU , 4 Avenue de Neptune, 94107 Saint Maur des Fossés Cedex, France
LSEET, 639 Boulevard des Armaris, 83100 Toulon, France

VHF AND UHF RADARS BEING DEVELOPED IN THE BEIJING AREA, CHINA

Da-ren Lu

Institute of Atmospheric Physics
Academia Sinica
Beijing 100011, China

There is one VHF radar and one UHF radar being developed in the Beijing area. The VHF Doppler radar will be devoted to both middle atmosphere and mesoscale nowcasting research. The UHF radar is mainly devoted to mesoscale meteorology and, in particular, nowcasting operation. The Institute of Atmospheric Physics, Chinese Academy of Sciences is responsible for the development and operation of the VHF radar and the Academy of Meteorological Science, State Meteorological Administration of China for the UHF radar. These two radars will be located in the Beijing area. The distance between them is about 60 km. The main parameters of these two radars are as follows:

	Beijing VHF (CAS/IAP)	Beijing UHF (SMA/AMS)
Location	~40°N, 117°E Xianghe county, Hebei Province	40°N, 116°E Daxing county, Beijing
Antenna	108 x 108 m^2 36 x 36 Yagi elements 2 polarizations 5 bit phase-shifter	108 Yagi elements 3 beams
Frequency	78 MHz	365 MHz
Transmitter	Distributed 36 sets Total P_t 640 kW-900 kW Total P_{max} 28 kW (depend on pulse length and pulse repetition rate)	1 set P_t ~ 30 kW
Pulse length PRR	2-10 μs, variable 2,500 Hz	1-9 μs, variable ~5-20 kHz
Data acquisition and processing	1 MHz A/D converter 8 bit PC-386 (to be determined) FFT Hardware	1 MHz A/D converter 8 bit PC-AT FFT Hardware
Height range	64-128	
Expected operating time	End of 1990	Middle of 1989

A PROPOSED ST RADAR FOR BIAK, INDONESIA (1°S, 136°E)

K.S. Gage, W.L. Ecklund, and B.B. Balsley

Aeronomy Laboratory
National Oceanic and Atmospheric Administration
Boulder, Colorado 80303

J. Soegijo, M. Pardede, and S.M. Notosuyidno

LAPAN
Aerospace Research Center
Bandung, Indonesia

The island of Biak is located just south of the equator at the eastern end of the "maritime continent" of Indonesia. The town of Biak is at the southern end of the island, which is located north of the mainland of Irian Jaya. Biak is served by a modern airport. Air Garuda maintains regularly scheduled flights connecting Biak with Los Angeles, Honolulu, Denpasar, Jakarta, and Hong Kong.

The proposed Biak radar will be constructed as part of a joint Indonesian and U.S. cooperative research program, and the Biak radar will form an integral part of the network of equatorial radars being built by the Aeronomy Laboratory with the support of the U.S. National Science Foundation. The radar will be constructed at a field station maintained and operated by the Indonesian National Institute of Aeronautics and Space (LAPAN). The radar site is located a short distance from the town of Biak and the civilian airport with good access to a reliable power source. The LAPAN field station is about 1 km inland on a plateau about 100 m above sea level. The LAPAN station maintains a satellite ground station and an ionosonde facility.

The proposed radar will be very similar to the Christmas Island radar. It will operate at 50 MHz and will have a 100m × 100m coaxial-collinear antenna. A detailed description of the Christmas Island radar antenna is given by ECKLUND, et al. (1985). It is currently anticipated that construction will begin in the middle of 1989 and be completed in 1990.

REFERENCES

Ecklund, W.L., D.A. Carter, and B.B. Balsley (1985). The NOAA TOGA antenna array, Handbook for MAP, Vol. 20, 379-380.

DEVELOPMENT OF THE UK RADAR SYSTEM

Lance Thomas

Department of Physics
University College of Wales
Aberystwyth, Dyfed, UK

A radar system operating at 46.5 MHz is being developed jointly by the Rutherford Appleton Laboratory of the Science and Engineering Research Council (SERC) and the University College of Wales at Aberystwyth. Its background as a national facility funded by the SERC, together with the main design features, have been described by A. J. Hall in a previous report, HANDBOOK FOR MAP, VOL. 9, 1983, p. 387.

The radar site is located near Aberystwyth, covers an area of about 120 m x 120 m, and has been excavated to provide a surface flat to about 10 cm. To date, an antenna array comprised of 64 4-element Yagis, covering an area of about 2000 m^2, has been set up and two Tycho transmitter modules and a receiver, a Hewlett Packard computer system and associated electronics are housed in a trailer at the site. This configuration has been used to test radio interference levels and operation procedures, the mean power aperture of 5.10^6 Wm^2 providing wind measurements up to heights near the tropopause and vertical incidence signal strength measurements for heights up to 20 km. In preparation for the extension of the system, a 50 ft x 22 ft technical block has been constructed to which the pre-integrator unit currently under test and the PDP 11/73 computer to be used for radar control and real-time data analysis will be transferred early in 1989. The extension of the antenna array to a total of 400 Yagis occupying an area of 12,000 m^2 is in hand and it is hoped to increase the number of transmitter modules to five by the autumn of 1989. The enlarged mean power aperture of 7.5 x 10^7 Wm^2 will be suitable for MST operation.

HARDWARE DESIGN FOR MST, ST AND LOWER TROPOSPHERE/BOUNDARY LAYER RADARS

W. L. Ecklund

Aeronomy Laboratory
National Oceanic and Atmospheric Administration
Boulder, Colorado 80303

OVERVIEW

All of the present day atmospheric profiling radars have their roots in early high-powered ionospheric and meteorological radar designs. Short-term studies of the atmosphere using these radars demonstrated the great potential of atmospheric profiling. These early radars operated over a wide range of frequencies from 50 MHz up to 3000 MHz, but from a hardware point of view all used tube transmitters and parabolic reflector (dish) antennas with the exception of Jicamarca which used a coaxial-collinear antenna array.

The dedicated atmospheric profilers that have been developed over the last 15 years span a large size range in terms of their power-aperture product. Table 1 gives an approximate range of power-aperture product and operating frequency for different sized radars classified according to the atmospheric levels which they can observe. MST stands for mesosphere, stratosphere, troposphere; LT indicates lower troposphere and BL denotes the boundary layer. We note from this table that all MST radars operate in the lower VHF range but that ST radars operate up to 404 MHz and that the lower troposphere/boundary layer radars operate up to 3000 MHz. We also note that the sensitivity of the present-day atmospheric profilers expressed in terms of power-aperture product ranges over 8 orders of magnitude.

Table 2 is a partial list of present day MST, ST, T and LT radars. Although the table may have some errors or omissions, its purpose is to show the range of hardware designs (types of antennas and transmitters) used with current atmospheric profilers. Starting with the MST category, we see that all of the MST radars use Yagi antennas with the exception of Poker Flat. This can be explained primarily by the requirement for most MST radars to have flexible antenna beam steering. The coaxial-collinear (co-co) antenna limits beam steering to the plane perpendicular to the antenna elements, but has the advantage that a number of elements are driven from a single feed point, reducing the cost and complexity of feed networks. The MST transmitters range from a single large tube (greater than 100 kW peak power) at SOUSY to transmitters distributed throughout the antenna array using medium power (50 kW peak power) tubes at Poker Flat to distributed solid-state transmitters at the MU radar.

The list for ST radars shows that the coaxial-collinear antenna is most commonly used for this class of radar. This is probably due to the fact that a number of these radars operate as routine wind profilers with only 3 fixed beams. For this simplified operation, the co-co antennas are adequate and have the advantage of simplified feed networks mentioned above. It is interesting to note that the new commercial ST radars operating at 404 MHz also use co-co antennas. Although most of the ST radars use nominal 50 kW tube-type transmitters, there is a trend toward using solid-state transmitters in the latest designs. The smaller radars designed to cover the troposphere (T) and lower troposphere (LT) typically operate at 404 MHz and above and use a variety of antennas. In addition, the smaller transmitters used with these radars are almost all solid-state.

Table 1.   Classification of Atmospheric Profilers.

CLASS	P x A $(W-m^2)$	FREQUENCY (MHz)
MST (ST)	$\sim 10^7$ to 10^{9+}	41 to 55
ST (T)	$\sim 10^5$ to 10^7	41 to 404
T (LT)	$\sim 10^2$ to 10^5	404 to 961
LT (BL)	~ 10 to 10^2	915 to 3000

Table 2. Partial List of Atmospheric Radars.

MST (ST)

RADAR	(MHz)	ANTENNA	TRANSMITTER
SOUSY	53	YAGI	LARGE TUBE
URBANA	41	DIPOLE	LARGE TUBE
POKER FLAT	50	CO-CO	DIST. MED. TUBES
MU	47	YAGI	DIST. SOLID-STATE
INDIA	53	YAGI	COMB. MED. TUBES
EQ. OBS.	47	YAGI	DIST. SOLID-STATE
UK	47	YAGI	COMB. MED. TUBES

ST (T)

SUNSET	41	CO-CO	LARGE TUBE
PLATTEVILLE	50	CO-CO	MED. TUBE
COLORADO NET	50	CO-CO	MED. TUBE
FRANCE (LSEET)	45	CO-CO	MED. TUBE
PENN STATE NET	50	CO-CO	MED. TUBE
CHUNG-LI	52	YAGI	MED. TUBE
ADELAIDE	54	CO-CO/YAGI	COMB. SOLID-STATE
TROPICAL NET	50	CO-CO	MED. TUBE
PLATTEVILLE	404	YAGI	SOLID-STATE/TUBE
FLATLAND	50	CO-CO	MED. TUBE
COMMERCIAL	404	CO-CO	MED. TUBE/SOLID-STATE
ALASKA	222	DISH	TUBE
CAPE CANAVERAL	50	CO-CO	LARGE TUBES
CHINA	365	YAGI	TUBE
WHITE SANDS	50	CO-CO	LARGE TUBES

T (LT)

DENVER	915	DISH	SOLID-STATE
PENN STATE	404	CO-CO	TUBE
WPL PORTABLE	404	STEERED YAGI	SOLID-STATE
FRANCE	961	DISH	SOLID-STATE

LT (BL)

NEL (RICHTER)	3000	DISH	TUBE
WPL (FM-CW)	3000	DISH	TUBE
NOAA (AL)	915	MICROSTRIP	SOLID-STATE

Continuing improvements in signal processing hardware make the use of coded transmitter pulses increasingly attractive. This development tends to favor the use of solid-state transmitters since in general they are better suited to operation at the higher duty cycles possible with coded pulses. Safety considerations also favor solid-state transmitters since they use low voltages that are not dangerous to personnel. In addition, new developments in small (LT) radars suggest that they will be capable of unattended operation in remote locations. Finally, using atmospheric profilers with acoustic sources to obtain temperature profiles with the RASS (Radio Acoustic Sounding System) technique holds great promise. To date the technique has been demonstrated with 47, 50, 404 and 915 MHz radars. Height coverage is best at lower VHF, particularly if the radar beam can be steered, and is limited to about 1 km above the surface at 915 MHz due primarily to acoustic attenuation. The use of atmospheric profilers in the RASS mode to obtain temperature profiles is currently under active investigation and RASS equipment may well be a standard addition to operational wind profilers in the future.

SUMMARY OF HARDWARE DESIGN SESSION

Papers presented in this session covered a number of hardware design subjects. Antenna topics ranged from the design of new antenna elements to steering, feeding and calibrating array antennas. Antenna element designs for a new Yagi antenna for the planned Equatorial Observatory were presented as were designs for a novel hexagonal grid antenna and a microstrip antenna for use with lower troposphere profilers. Other antenna papers discussed steering for the Flatland radar, feed systems for the Indian radar and calibration of the Chung-Li antenna. Results from LSEET (France) suggest that the height coverage of lower VHF ST radars can be extended down to 500 meters above the surface by the use of a low-power solid-state transmitter. Another paper described proposed modifications to the EISCAT radar to allow it to operate as an MST radar. The largest and smallest atmospheric profiling radars were discussed in papers describing the design of the very large Equatorial Observatory radar and a new small UHF radar for the boundary layer. Finally, results from temperature profiling using the RASS technique with both the MU radar and a small UHF boundary layer radar were also presented.

It was pointed out in the discussion that the most difficult problem for operational atmospheric profiling is obtaining a clear frequency assignment. This has important implications for the new commercial profilers since it would be most efficient in terms of hardware development and manufacturing if one frequency could be used in all countries. We also discussed the important role that atmospheric radars can play in education, since their design and use spans the disciplines of electrical engineering, computer science and atmospheric science.

THE FLATLAND RADAR ANTENNA STEERING IMPLEMENTATION

J.L. Green and W.L. Clark
Aeronomy Laboratory
National Oceanic and Atmospheric Administration
Boulder, CO 80303

Rapid antenna beam steering has been added to the Flatland Radar system (GREEN, et al., 1988) to provide for additional atmospheric studies. Such studies include the measurement of the angular properties of scattering from the troposphere and stratosphere and the estimation of the vertical transport of horizontal momentum. The use of rapid switching between multiple beams also facilitates the automatic editing of radar data and allows more reliable operation in the presence of convective storms where the returns from only one beam are affected.

The Flatland Radar antenna is comprised of two orthogonal collocated arrays of lines of coaxial-colinear dipoles. The orientation of these lines of dipoles are arranged so that one array can be steered in the east-west vertical plane and the other in the north-south. Each of these arrays is treated by the Flatland control and data processing system as being a part of an independent radar (GREEN AND CLARK, 1988). Individual radio frequency phase shifter units are provided for each line of dipoles so that it is possible to steer the beams from these arrays independently by adjusting the phase shift between the lines of dipoles. Each of these arrays can be steered from horizon to horizon with an angular resolution of 1.7° near the zenith.

The radio frequency shifters are of the binary type, that is, summable phase increments of 1/2, 1/4, 1/8, 1/16, 1/32, and/or 1/64 wavelength can be switched in or out of the circuit under the control of the online computer. The switching elements are encapsulated reed relays that can withstand 10,000 volts and have an expected lifetime of $> 1.5 \times 10^7$ operations, if switched in the absence of radio frequency power.

REFERENCES

Green, J.L., G.D. Nastrom, K.S. Gage, T.E. VanZandt, W.L. Clark, and J.M. Warnock (1988), Observations of vertical velocity over Illinois by the Flatland Radar, Geophys. Res. Lett., 15, 269-272.

Green, J.L. and W.L. Clark (1988), Flatland online signal processing and radar control system, Handbook for MAP, (in press).

FEEDER NETWORK FOR THE INDIAN MST RADAR

B. K. Sarkar, P. B. Tole, and A. Agarwal

Society for Applied Microwave Electronics Engineering and Research
IIT Campus, Hill Side, Powai
Bombay 400 076, India

INTRODUCTION

The Indian MST radar work started in March 1987. The radar is to be made operational by September 1991. The Indian MST radar is a phased array radar consisting of 32 transmitters feeding 32 x 32 (= 1024) crossed dual Yagi antennas (Figure 1). The operating frequency is 53 MHz. The peak rf power is 2.5 MW and the average power is 60 kW. Pulse width varies from 1 µs to 32 µs. The array aperture power distribution follows a modified Taylor distribution for 20 dB sidelobe level. There will be six beam positions, viz., zenith, ±20° north-south, ±20° east-west and 12° due north from zenith. The aperture power distributions of the planar array of 32 x 32 Yagi antennas are achieved in one direction by tapering the power outputs of each of the transmitters and in the other direction by tapering the power by the feeding network. The beam tilt angles are changed by 32 low power phase shifters associated with the exciters for 32 transmitters and by polarization switches. The feeding network is to connect each transmitter to a row of 32 Yagi antennas and taper the power input to each of the Yagis to get a modified Taylor distribution of aperture power.

FEEDING NETWORK CONFIGURATION

Each transmitter can be connected to 32 dual Yagis by parallel feed consisting of unequal binary power dividers or by series feed consisting of directional couplers. Though parallel feed has better bandwidth performance, in the case of the Indian MST radar where a row of 32 Yagis occupies 123 meters and the separation between two consecutive rows or columns of Yagi antennas is 0.7λ (= 3.96 meters), it will be difficult to lay physically all the binary power dividers between two consecutive rows or columns besides the difficulties of achieving better isolation and unequal power division. Therefore, series feeding network consisting of directional couplers is chosen for the Indian MST radar. The coupling of the directional couplers are chosen such that the coupled outputs form a modified Taylor distribution. Due to bandwidth consideration, the array is center-fed instead of end-fed. For two polarizations (north-south or east-west), two similar sets of feeder lines and power divider/combiners with 32 nos. of high power polarization switches (SPDT) will be used (Figure 2). Power from each of the 32 transmitters is fed to a duplexer. The output of the duplexer is connected to a high power SPDT switch. Each output of the polarization switch (SPDT) is connected to a high power divider (1:2) (situated in the antenna field) by rigid coaxial cable (LCF-CU2Y), 1 5/8" and 7/8"). Each output of the power divider is connected to 15 directional couplers in series. The outputs of the divider is connected to 15 directional couplers in series. The outputs of the coupled ports (which make the modified Taylor distribution) are connected to Yagi antennas by RG-8 cables. The maximum and minimum powers delivered by transmitters are 118 kW and 22 kW, respectively. Distributed couplers (rectangular coaxial line) will be used for power level above 25 kW, whereas lumped coupler (using capacitances and inductances) will be used for power level below 25 kW. The total number of distributed and lumped couplers are 608 and 1312, respectively. Experimental results for distributed and lumped couplers are shown in Figure 3. The transmitters are located in huts outside the antenna field as shown in Figure 2. The location of the huts are optimized to get minimum possible cable length required to connect the transmitters to the input of the power divider. The electrical length of the cable from each transmitter to input of the power divider is kept equal. The one-way loss due to feeder network is about 2.8 dB (including duplexer and SPDT switch losses). The calculated bandwidth for the center-fed feeding network is about 3 MHz. Table 1 gives the various components of the feeding network.

Figure 1. MST radar block diagram.
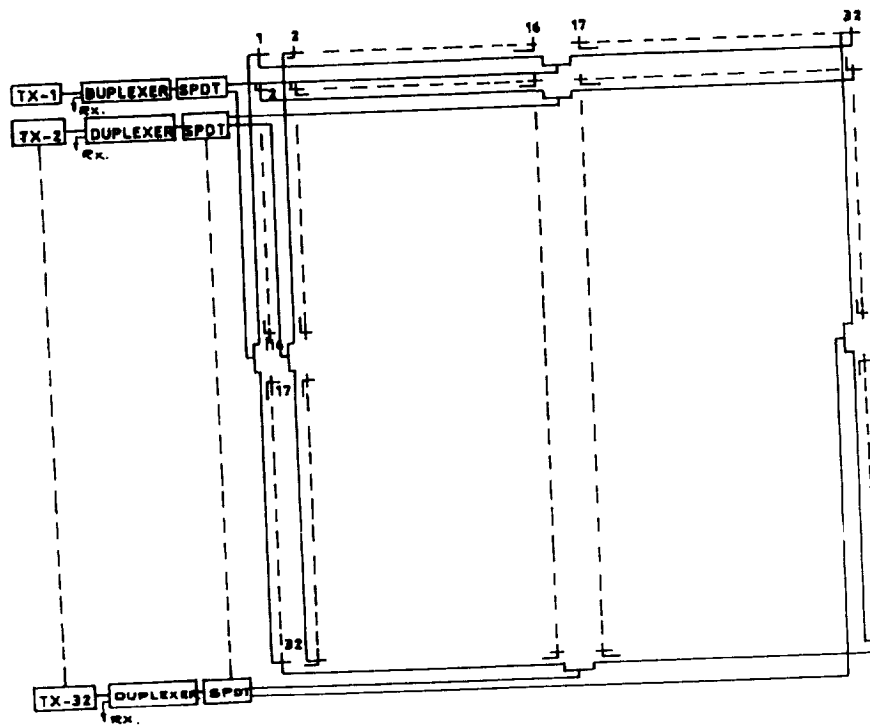
Figure 2. MST radar feed network configuration.
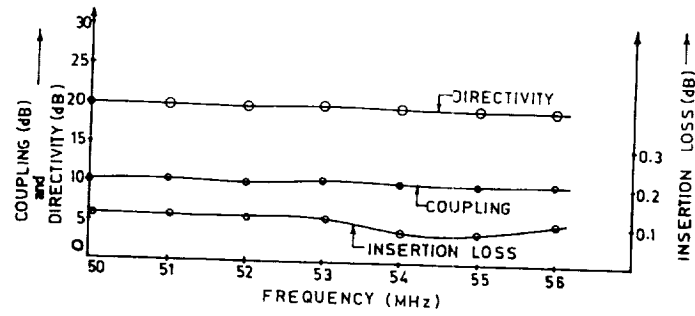
Fig 3(a) RESPONSE OF 10.0 dB DISTRIBUTED DIRECTIONAL COUPLER
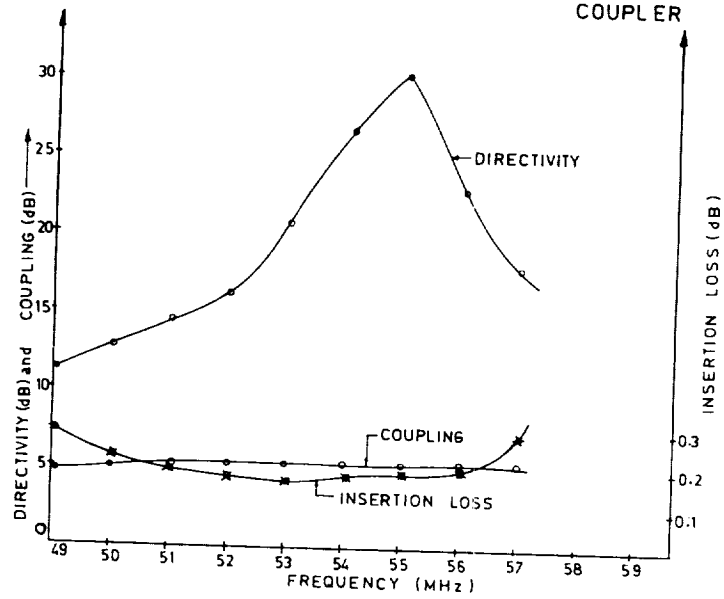
Fig 3(b) RESPONSE OF 5.0 dB LUMPED COUPLER

Figure 3. (a) Response of 10.0 dB distributed direction coupler. (b) response of 5.0 dB lumped coupler.

Table 1. Components for the Feeding Network.

COMPONENTS	REQUIREMENTS
In-phase power divider including power monitor for phase calibrator	64 Nos.
High power SPDT switch	32 Nos.
Couplers: a. Distributed type b. Lumped type	608 Nos. 1312 Nos.
LCF-CU2Y 1 5/8" coaxial cable	5.2 K.M.
LCF-CU2Y 7/8" coaxial cable	8.2 K.M.
50 ohms rigid line 1 5/8"	500 Nos. (2.3 meters length each)

TEMPERATURE PROFILING WITH AN ACOUSTIC SOURCE AND A UHF WIND PROFILER

P. E. Currier, W. L. Ecklund, D. A. Carter, J. M. Warnock, and B. B. Balsley

Aeronomy Laboratory
National Oceanic and Atmospheric Administration
Boulder, Colorado 80303

MATUURA et al. (1986) were the first group to use a wind-profiling radar (the 47 MHz MU radar) in the radio acoustic sounding system (RASS) mode to measure temperature profiles. Following their example, in October, 1987 a small 915 MHz wind-profiling radar (ECKLUND et al., 1988) was also operated with an acoustic source to obtain temperature profiles using the RASS technique (CURRIER et al., 1988). In our adaptation of this technique a continuous acoustic source is stepped or swept across those frequencies that have a wavelength in the atmosphere of 1/2 the radar wavelength. The temperature at a given height is determined (with corrections for relative humidity and the wind component along the radar beam) by noting the acoustic frequency that gives the maximum radar return at that height (Bragg matching). Preliminary comparisons of temperature profiles measured with the 915 MHz RASS and by a nearby balloon showed good agreement.

Since wind-profilers measure the wind component along the radar beam, the temperatures measured in the RASS mode can be corrected for wind speed to give temperature measurements with relatively high time resolution. This should allow measurement of heat flux as described by PETERS et al. (1985). The RASS returns at 915 MHz are very strong at the lowest altitudes so that we may be able to obtain temperature profiles with resolution to 30 meters in the lowest few hundred meters. The only obvious problems with operating the 915 MHz radar in the RASS mode are the noise pollution from the continuous acoustic source and the limited height coverage (up to about 1 km above the surface) due primarily to acoustic attenuation.

REFERENCES

Currier, P.E., W.L. Ecklund, D.A. Carter, J.M. Warnock and B.B. Balsley (1988), Temperature profiling using a UHF wind profiler and an acoustic source, Symposium on Lower Tropospheric Profiling: Needs and Technologies, 31 May-3 June, Boulder, CO.

Ecklund, W.L., D.A. Carter and B.B. Balsley (1988), A UHF wind profiler for the boundary layer: Brief description and initial results, J. Atmos. and Oceanic Tech., 5, 432-441.

Matuura, N., Y. Masuda, H. Inuki, S. Kato, S. Fukao, T. Sato and T. Tsuda (1986), Radio acoustic measurement of temperature profile in the troposphere and stratosphere, Nature, 323, 426-428.

Peters, G., H. Hinzpeter and G. Baumann (1985), Measurements of heat flux in the atmospheric boundary layer by sodar and RASS: A first attempt, Radio Sci., 20, 1555-1564.

A MICROSTRIP ANTENNA ARRAY FOR UHF WIND PROFILING

W. L. Ecklund

Aeronomy Laboratory
National Oceanic and Atmospheric Administration
Boulder, Colorado

A small boundary layer radar operating at 915 MHz has been developed at NOAA's Aeronomy Laboratory (ECKLUND et al., 1988). The radar uses a microstrip antenna panel which combines radiating elements and transmission lines on a single printed-circuit board. The .9 by .9 meter circuit board (based on a design by ASHKENAZY et al., 1983) is mounted above a lightweight, rigid metal honeycomb panel that is both a support structure for the antenna and also the antenna ground plane. The RF connection to the board is at a single point near the center, and the connector is located on the back of the panel. All of the 16 patches are driven in phase for broadside radiation. A single antenna module has a measured half-power, one-way beamwidth of 18 degrees, and modules can be connected together to achieve the desired antenna area and beamwidth.

The microstrip antenna panel described above is lightweight, rugged and lends itself to mounting low to the ground to reduce unwanted ground clutter. To date we have operated the microstrip antenna panels either fixed in azimuth and elevation or fixed in elevation (15 degrees from zenith) and rotated in azimuth. Although the inverted circuit board serves as a tough, weatherproof cover, we have found that water on the panel reduces antenna efficiency. However, if the water is separated from the circuit board by several centimeters, the reduction in efficiency is negligible. This suggests that either the board will have to be covered by a layer of low-loss spacer material, or that the panel will have to be mounted under a waterproof radome for operation in rain.

REFERENCES

Ashkenazy, J., P. Perlmutter and D. Treves (1983), A modular approach for the design of microstrip array antennas, IEEE Trans. Antennas and Propag., AP-31, 190-193.

Ecklund, W.L., D.A. Carter and B.B. Balsley (1988), A UHF wind profiler for the boundary layer: Brief description and initial results, J. Atmos. and Oceanic Tech., 5, 432-441.

HEXAGONAL GRID PHASED ARRAY FOR WIND PROFILING

R.J. Jost, J.J. Wilcox, and K.S. Kelleher

System Planning Corporation
Arlington, Virginia

I. INTRODUCTION

This paper examines the effects of random phase errors on the performance of a phased array antenna system designed for wind profiling. System performance is measured by principal gain, main-lobe to side-lobe ratio, and the half-power beamwidth. An array created by placing individual antenna elements one wavelength apart in equilateral triangles on a hexagonal grid is shown to be reasonably insensitive to random errors in phase shift.

This design, while maximizing the antenna aperature with a minimum number of elements, may not be generally optimal in terms of the field pattern generated. In fact, the apparent separation between elements exceeds one-half wavelength at several azimuthal aspects and results in the formation of grating lobes at the horizon. This can result in significant return from the plane horizontal to the array (ground clutter) depending on the individual element pattern. By carefully controlling the element factor, the amount of energy radiated in the ground plane may be reduced to -40 dB from the main beam.

The analysis relates the distribution of random phase errors to the degredation of the performance indices. In this way, a determination can be made as to which of the performance indices are sensitive to phase error. Also, it can be determined how much phase error can be tolerated and still have the system meet a given set of specifications.

II. SYSTEM DESIGN

The wind profiler phased array antenna system under consideration is composed of 61 elements arranged in equilateral triangles on a hexagonal grid. Adjacent elements are separated by a distance of one wavelength (Figures 1, 2). The individual elements are dipole antennas located in a
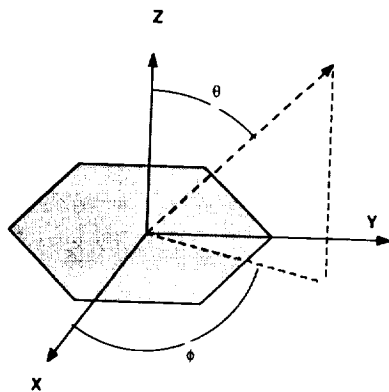
Figure 1: 3 Dimensional Coordinate System
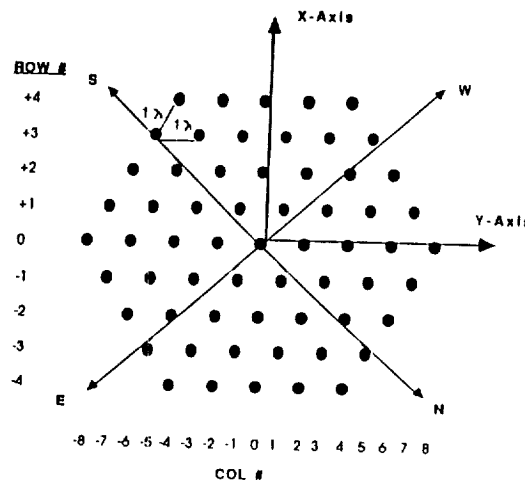
Figure 2: Top View of 61 Element Wind Profiler System

reflective trough designed to reduce the amount of energy radiated horizontal to the plane of the array. Using the center element as the reference and labeling scheme of Figure 1, the distance from the center element to the k,jth element is given by 0.866kλ in the x direction and 0.5j λ in the y direction.

The electric far field pattern for the array can be calculated by combining the element factor (the power pattern of a single array element) with the array factor. The element pattern for the antenna used in this system was obtained by direct measurement and is a function of elevation only (independent of azimuth.) The array factor is calculated by summing the contributions of each element according to

$$E(\theta,\phi) = 20\log \left| \sum_{k=-4}^{4} \sum_{j=[k]-8}^{[[k]-8],step\ 2} A_{k,j}\exp\{i\beta(dxU+dyV)+i\alpha_{k,j}\} \right| - 10\log\left(\sum_{k=-4}^{4} \sum_{j=[k]-8}^{[[k]-8],step\ 2} A_{k,j}^2 \right) \quad (1)$$

where: $A_{k,j}$ = voltage driving the k,jth element

$\beta = \dfrac{2\pi}{\lambda},$ $U = \sin\theta\cos\phi,$ $V = \sin\theta\sin\phi,$ $i = \sqrt{-1}$

$\alpha_{k,j}$ = phase shift of the k,jth element relative to the center element

The second term in (1) normalizes the power gain so that it can be expressed in dBi (dB relative to an isotropic source).

From (1), the direction of maximum field intensity occurs when $\alpha_{k,j} = -\beta(dxU+dyV)$. By altering the relative phase shifts, the main beam can by 'steered' in any direction within the envelope of the individual element pattern. The system is currently configured to take data at 4 oblique beam positions in addition to directly above the array (vertical beam position). These beam positions are each 15 degrees off of vertical in the north, east, south and west directions respectively (Figure 1).

PERFORMANCE CRITERIA

System performance is measured in terms of the following performance indices:

- Main Lobe Gain -- Gain at the main lobe in dB relative to an isotropic source (dBi)
- Main Lobe to Side Lobe Ratio
- 3 dB Beamwidth -- width of the main lobe from the maximum to the half-power point.

In Figure 1 the far field pattern for the vertical beam position is plotted. The azimuthal cut is taken along the N-S axis ($\phi = \pi/4$). In Figure 2 the elevation is fixed at $\pi/2$ and all 360 degrees of azimuth are swept through, thereby yielding the energy radiated in the ground (horizontal) plane. The goal of this analysis is to determine how each of these 3 performances indices are affected by random phase error.

III. PHASE ERROR ANALYSIS

The goal of the phase error analysis is to quantify the effects of phase error on system performance. System performance will be measured by the three performance indices defined above.

PHASE ERROR ASSUMPTIONS

Regardless of the type of phase shifter employed in the phased-array architecture, there will be some error introduced into the system during phase shifting. The error contributed by a given

phase shifter is a random variable drawn from some distribution. The nature of the error distribution depends on the phase-shifter used, however, the following assumptions can be made about $\Delta\alpha_j$, the error term contributed by the jth phase shifter.

1. The error term contributed by any phase shifter $\Delta\alpha_j$ is independent of the error term associated with any other phase shifter $\Delta\alpha_k$ $(k{\neq}j)$

2. The errors $\Delta\alpha_j$ and $\Delta\alpha_k$ are drawn from the same, Gaussian distribution with standard deviation σ_α.

Phase error, therefore, is defined in terms of the standard deviation of its distribution. As the standard deviaion of the error increases, the probability that the actual phase shifter will lie near the expected value of the phase shift decreases.

PROCEDURE

First, a system is defined by drawing 61 random phase errors (one error term for each phase shifter is evaluated) from the same Gaussian distribution with a given standard deviation. Next, the performance of the system under these conditions is evaluated. Having evaluated the system, a new set of phase errors is drawn from the same distribution and system performance for this new architecture is evaluated. This process is repeated until enough samples of performance have been obtained to define the distribution for the performance index.

This would complete the analysis of array performance assuming a given set of error terms with a given standard deviation. The next step in the analysis would be to increase the standard deviation of the error terms and examine how that error distribution would affect system performance.

INTERPRETATION

The results of the phase error analysis are interpreted as follows. Consider the following example for an error distribution with a standard deviation of 10 degrees. If the mean beamwidth were found to be 7 degrees and the standard deviation of the beamwidth were found to be 0.1 degree, under these conditions, the probability that the actual beamwidth lies between 6.8 and 7.2 degrees is greater than 95%. This is the approach that would allow a system to be designed with any desired level of confidence in a given performance index.

CALCULATIONS

Using the method outlined above, the effects of random phase error on beamshape can be quantified. The 'amount' of error present is represented by the standard deviation of the phase errors. This value has been measured at approximately 9 degrees. The expected value of each performance index is presented along with its standard deviation as a function of error. A given phase error standard deviation can yield significantly different beamshapes depending on the exact values of the phase error. That is, simply knowing the standard deviation of the error terms only allows the expected values for the performance indices to be presented. Only when given the exact values for phase shift can exact parameters be extracted from the beamshape.

Main Lobe Gain

From (1) and the element pattern the ideal gain at the main lobe is found to be 28.9 dBi. When random phase errors are introduced into the system, there is some loss in gain at the main lobe. In Table 1 this degredation is quantified.

Table 1. Effects of Error on Main Lobe Gain

standard deviation of error	mean gain	standard deviation	mean power loss
1 degree	46.68	2.27E-04	0.00 dB (0.0%)
3 degrees	46.67	2.04E-03	0.01 dB (0.0%)
5 degrees	46.65	5.68E-03	0.03 dB (0.1%)
15 degrees	46.38	5.13E-02	0.30 dB (6.7%)
30 degrees	45.49	2.08E-01	1.19 dB (24%)

3dB Beamwidth

Using the procedure outlined in section 2.2 the degradation in the 3dB beamwidth can be quantified. The results appear in Table 2.

Table 2. Effects of Error on 3 dB Beamwidth

standard deviation of error	mean BW	standard deviation
1 degree	6.5 degrees	0.0170 degrees
3 degrees	6.5 degrees	0.0511 degrees
5 degrees	6.5 degrees	0.0853 degrees
15 degrees	6.5 degrees	0.2578 degrees
30 degrees	6.5 degrees	0.5246 degrees

These results can be interpreted as follows: Errors in phase shift can either increase or decrease the 3 dB beamwidth and are equally likely to do either. As the error increases, the deviations from 6.5 degrees increase in magnitude.

Main Lobe to Side Lobe Ratio

In Table 3 we present the effects of random phase error on the main lobe to side lobe ratio. Recall that Side lobes are evaluated along a N-S azimuthal cut.

Table 3. Effects of Error on Sidelobe Level

standard deviation of error	mean ratio	standard deviation
1 degree	18.51 dB	0.0843 dB
3 degrees	18.51 dB	0.2518 dB
5 degrees	18.51 dB	0.4229 dB
15 degrees	18.81 dB	3.220 dB
30 degrees	20.94 dB	9.350 dB

IV. CONCLUSIONS

It has been shown that a 61-element phased array system, configured as in Figure 2, is relatively insensitive to errors in phase shift. Also, system performance will not be significantly affected by errors in element location as this is also a form of phase error.

Actual errors in phase shift for this system have been measured and in Figure 5 a far field pattern based on these measurements is presented. For comparison, the error-free field pattern is also presented and the difference is highlited. The standard deviation of these error terms is approximately 9 degrees.

534

Fig 3: Field Pattern Along N-S Azimuth
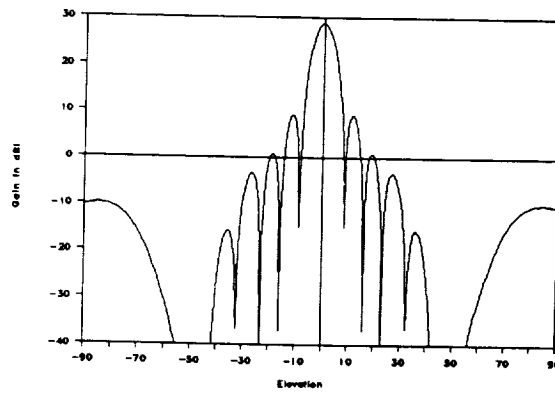
Fig 4: Energy Radiated in Ground Plane
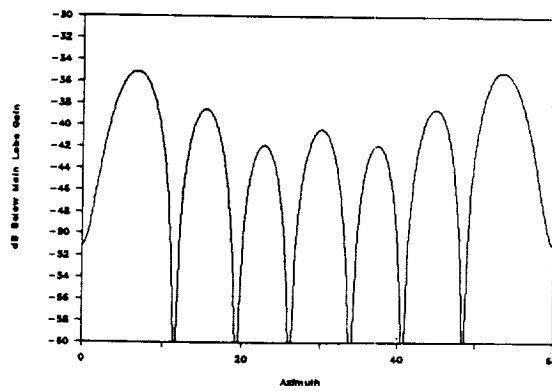
Fig 5: Measured vs Calculated Fields
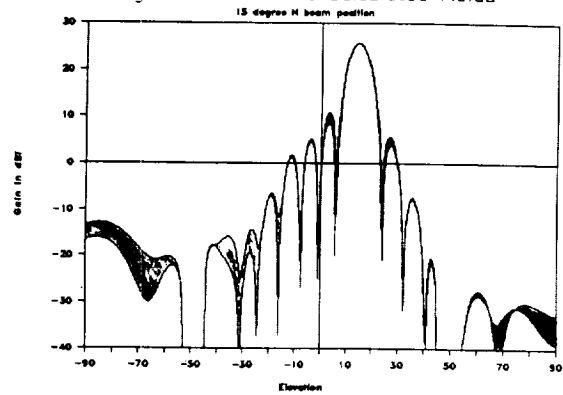
Antenna Design for an Equatorial Radar

Toru Sato*, Shin-ichi Taniguchi, Shoichiro Fukao,
Toshitaka Tsuda, Mamoru Yamamoto and Susumu Kato

Radio Atmospheric Science Center, Kyoto University
Uji 611, Kyoto, Japan

1 Introduction

A large 47-MHz Doppler radar, which is to be constructed on the equator in Indonesia, is under design at the Radio Atmospheric Science Center (RASC), Kyoto University. The importance of studying the equatorial region in understanding the global climatology has been pointed out in many occasions, so it is not repeated here.

The radar system will be an enlarged version of the MU radar at Shigaraki, Japan, which is designed to cover both the middle and the upper atmosphere, and characterized by its unique active-phased-array antenna design (Fukao *et al.*, 1985). Basic requirement for the capability of this new radar is that it should be able to observe the entire atmospheric region, starting from the lower troposphere up to the upper ionosphere of around 1000 km in height, with a good height and time resolution so that the dynamical coupling between different regions can be studied. Here we report the current status of the antenna design for this equatorial radar.

2 Technical Specifications

Based on the experiences of the MU radar and other atmospheric radars, it is requested that the new radar should have about ten times more sensitivity, or namely, the power-aperture product, than that of the MU radar. Taking the advantage of availability of wide area in Indonesia, it has been decided to realize this enlargement in terms of the antenna aperture rather than the transmitter output power, which means that the antenna should have a diameter of about 300 m.

As for the steerability is concerned, it is requested that we can point the antenna beam perpendicular to the magnetic field at ionospheric heights, which condition takes place when the beam is tilted 20° from the zenith to the north. From meteorological viewpoint, it is desirable to have a steerability as flexible as possible. The current agreement is that the antenna beam can be pointed to any direction within the zenith angle of 20°.

Other practical requirements are that the entire array should have periodic or at least quasi periodic arrangement from constructional considerations, and that the all antenna elements should be identical from economical reasons.

*Now at Department of Electrical Engineering II, Kyoto University, Kyoto 606, Japan
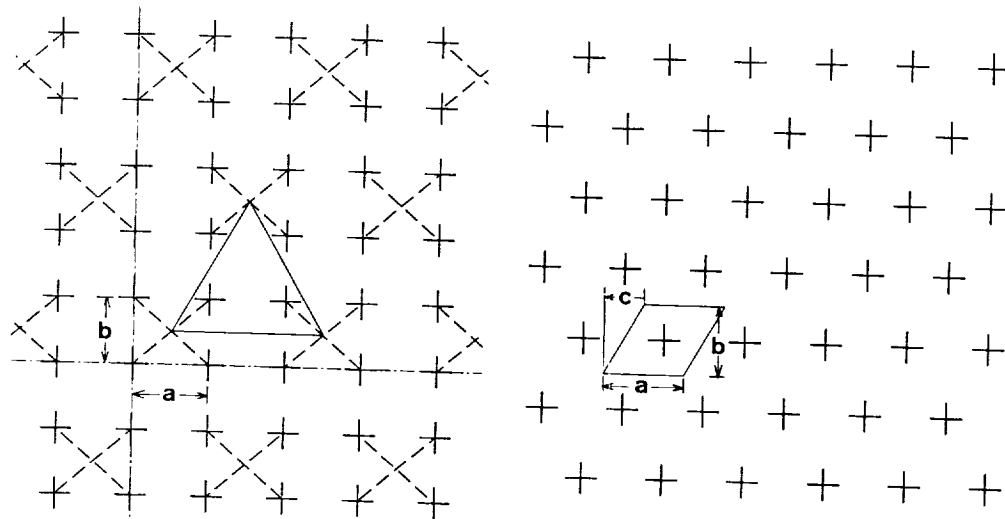
Fig. 1. Arrangement of antenna elements in an array. The left panel shows the sub-array configuration, and the right panel is for ordinary triangular array.

3 Considerations on a Sub-array Design

Under the constraints stated above, we first tried to minimize the number of transmitter-receiver (TR) modules, which has functions of phase shifting, power amplification, and TR switching, and naturally is the most costly component in the entire radar system.

The idea was to feed a group of 4 antenna elements by a single TR module, and arrange the groups, which are called sub-arrays, on a equilateral triangular grid. Figure 1 schematically draws the arrangement of the array for this sub-array design on the left, and ordinary equilateral triangular arrangement, as used for the MU radar, on the right. Each + sign in the figure denotes an array element.

It is known that a equilateral triangular grid provides the largest steerability of the antenna beam for a given spacing between elements. By choosing $b = \sqrt{3}a/2$ in the left panel, the elements of sub-arrays constitute a rectangular grid, while sub-arrays are arranged on triangular grid. In the right panel, $b = \sqrt{3}a/2$ and $c = a/2$ for the equilateral triangular grid.

If we choose that $a = \lambda$, where $\lambda = 6.38$ m is the radar wavelength, we can obtain an aperture size of about ten times larger than that of the MU radar with the same number of TR modules. The largest advantage of this design is that we can apply entire MU radar design to the new radar without any modifications except for the antenna. This conservative way reduces the chances of troubles in constructing a large system at a very distant location from the RASC.

However, this sub-array design obviously have a problem of grating lobes, since the spacing between the sub-arrays is as large as 2λ. With a periodic array configuration, several grating lobes with comparable magnitude to that of the main lobe appear even with a small beam steering angle from the zenith. This problem can be reduced to some extent by relaxing the constraint on the periodicity of the array. However, a large deviation from the periodic array, such as a random array configuration, should be avoided for two reasons: Firstly, the mutual coupling between elements becomes variable from element to element, resulting in phase and amplitude errors of the elements, which are hard to evaluate nor to compensate. Secondly, the construction and maintenance becomes more complicated and difficult than a periodic array
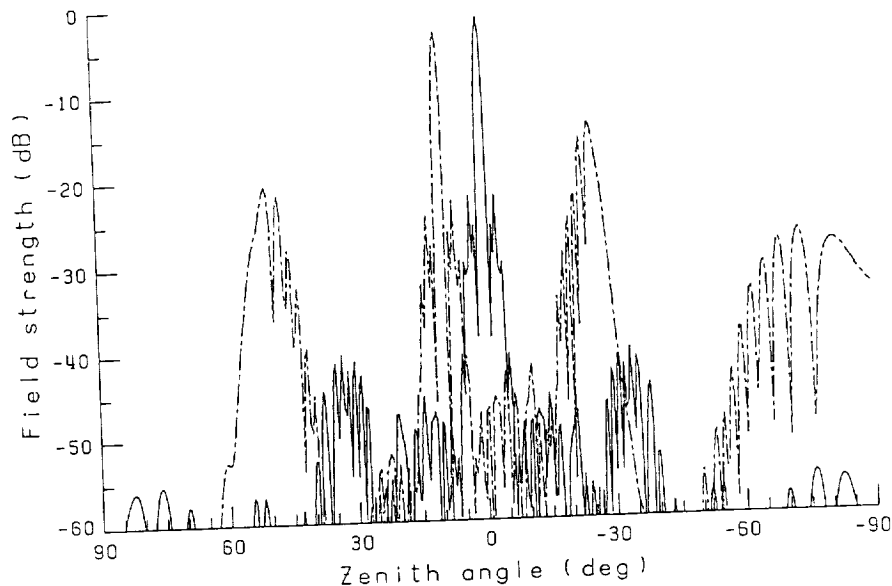
Fig. 2. Antenna pattern for a quasi-circular array having a diameter of about 300 m with a sub-array configuration and a uniform space tapering. The solid line is a pattern for the vertically pointing beam, and the dotted line is for a beam with 10° zenith angle.

as the irregularity of the arrangement increases.

We thereby considered a uniform space tapering as a possible solution, with which the spacings between the rows and columns of elements are linearly increased from the center of the array toward the outer edge. Figure 2 shows an example of the total antenna pattern for a quasi-circular array having a diameter of about 300 m with a sub-array configuration and a uniform space tapering. Spacing between elements is changed from $a = 0.9\lambda$ at the center of the array to $a = 1.1\lambda$ at the outer edge. The element pattern used in this figure is an empirical one for a single Yagi antenna. The solid line is a pattern for the vertically pointing beam, and the dotted line is for a beam with 10° zenith angle. As shown in this pattern, the space tapering is effective in scattering the grating lobes at low elevation angles, but has little effect on grating lobes near the main lobe. This tendency is the same with a larger tapering of as large as 30%. Further more, the peak level of a grating lobe becomes higher than the desired beam if the zenith angle of the beam is increased to 20°. These results convinced us to employ a more conservative design of exciting all array elements with independent TR modules.

4 Design of the Array

Abandoning the sub-array design means an increase of the TR modules by a factor of four. Accordingly, we decided to reduce the output power of each TR module to 1/4 of that of the MU radar by reducing the number of power transistors.

The upper limit of the element spacing a for a equilateral triangular array as shown in the right panel of Fig. 1 for which no grating lobe appears when the beam is steered by 20° from the zenith is 0.83λ, or 5.3 m at 47 MHz. Figure 3 shows the current plan for the arrangement of the antenna array. The entire array consists of 43 groups, each of which contains 61 array elements and identical number of TR modules. The group is a minimum unit which can be

538
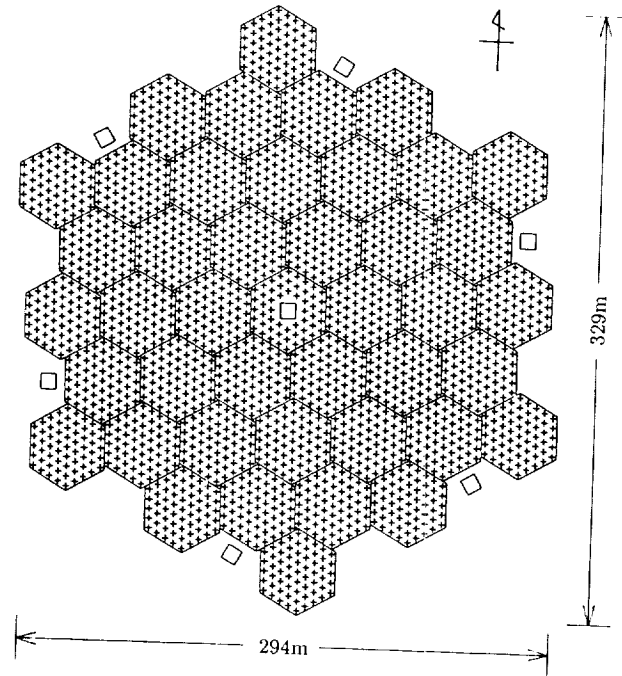
Fig. 3. Planned arrangement of the array. Each + sign denotes an array element, and squares are the booth which contain TR modules. The physical area of the array is 63,600 m².

used as a separate radar system, and controlled by a micro-processor. Plus signs in the figure denote array elements, and seven squares are the booths which contain TR modules. The total number of array elements is 2,616 covering an area of 63,600 m².

Figure 4 shows the antenna pattern of the array as shown in Fig. 3. The element pattern is the same empirical one as used in Fig. 2. The solid and dashed lines show the patterns when the antenna beam is pointed to the vertical and 20° off-vertical directions, respectively. The one-way half-power beamwidth is 1.2°. The first sidelobe level is 20 dB lower than the main lobe level, and low elevation sidelobes are suppressed to less than -40 dB.

5 Design of the Element

We have chosen crossed Yagi-Uda antenna as the array element because of its simple structure, relatively high gain, and capability in synthesizing various polarizations. A numerical optimization procedure as used for designing the MU radar is employed. It maximizes the element gain by adjusting the length and spacings of subelements in the absence of the reflecting ground so that backward radiations can be minimized. The mutual coupling between the elements are taken into consideration by assuming an infinite array for which all elements have identical current. The assumption of the infinite array is a good approximation for arrays with more than a few hundred elements (Fukao et al., 1986).

Since the spacing between array elements is slightly larger than that of the MU radar, we examined both three-subelement Yagi's and four-subelement Yagi's in the design, and applied the numerical optimization procedure for both of them. Although the optimized three-subelement
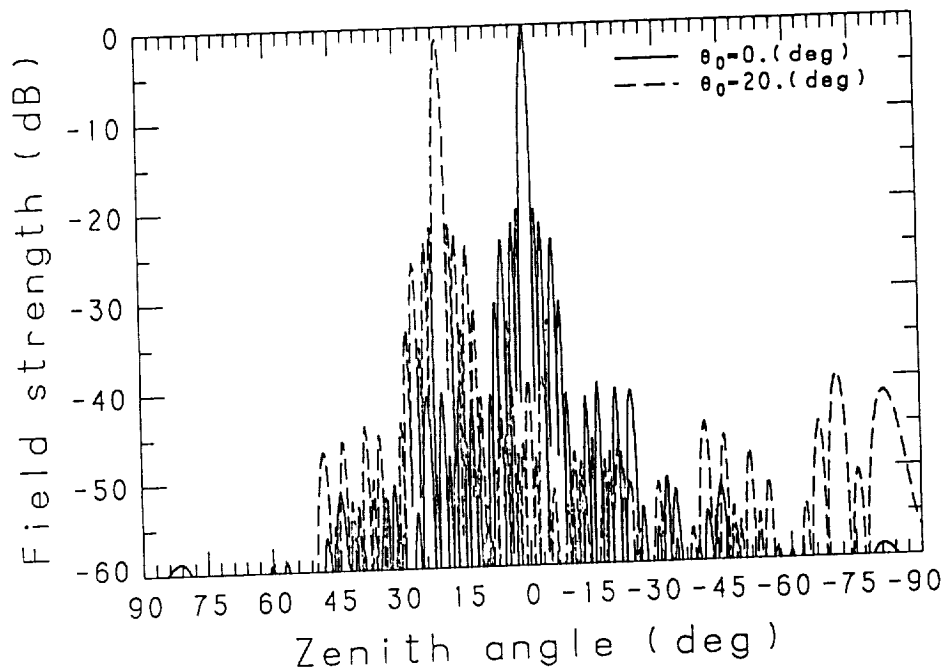
Fig. 4. The one-way total pattern of the planned array shown in Fig. 3 for the vertical (solid line) and 20° off-vertical (dashed line) beam directions. The half-power beam width is 1.2°.

Yagi has an element gain very close to the theoretical upper limit determined by the physical area which an element occupies, it showed a large variability in its characteristics when the height of the antenna above ground is changed. While the optimized four-subelement Yagi showed no better performance than the three-subelement one in the absence of the reflecting ground, it suffers a much less effect from the ground. Figure 5 shows the dimension of the optimized four-subelement Yagi and its characteristics. The four panels show the resistance and the reactance components of the active impedance, the voltage standing wave ratio (VSWR), and the element gain versus frequency. The solid and dotted curves denote characteristics in the presence and absence of the reflecting ground, respectively. The dashed line in the figure of gain shows the theoretical upper limit of the element gain.

6 Summary

Current status of the antenna design for the new equatorial radar has been reported. After the technical specifications for the antenna were summarized, the current design for the array and the array element were reviewed. The attempt to increase the antenna aperture without increasing the number of TR modules from that of the MU radar did not satisfy the requirements. Characteristics of the current design consisting of 2,616 four-subelement Yagi's were presented.
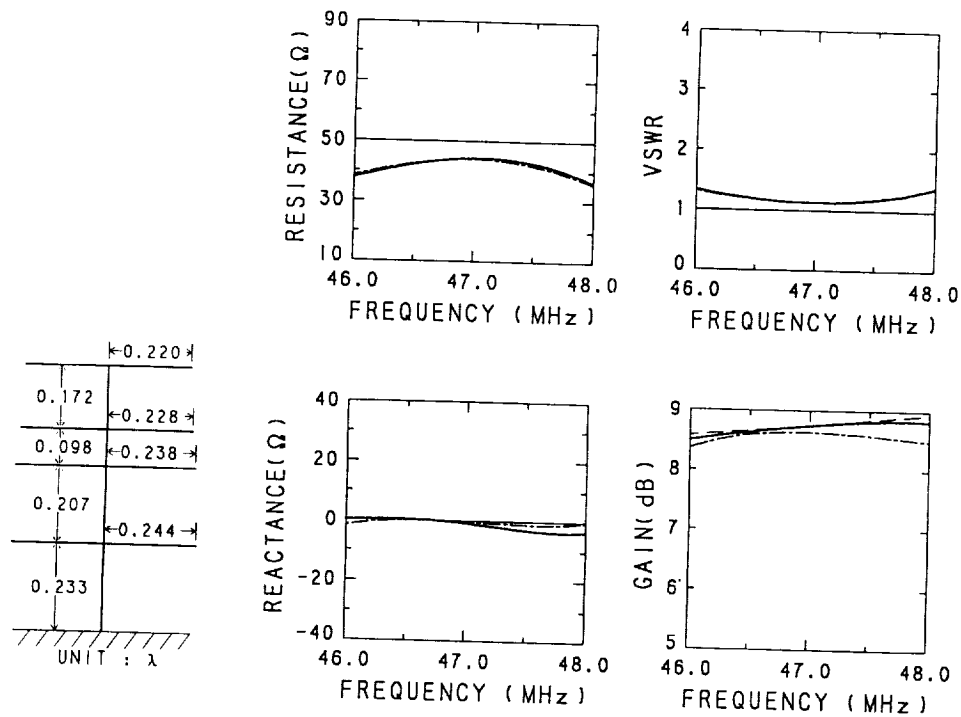
Fig. 5. Dimension and frequency characteristics of the optimized four-subelement Yagi. The solid and dotted curves denote characteristics in the presence and absence of the reflecting ground, respectively.

References

Fukao, S., T. Sato, T. Tsuda, S. Kato, K. Wakasugi, and T. Makihira, The MU radar with an active phased array system: 1. Antenna and power amplifiers, *Radio Sci.*, **20**, 1155-1168, 1985.

Fukao, S., T. Sato, H. Hojo, I. Kimura, and S. Kato, A numerical consideration on edge effect of planar dipole phased arrays, *Radio Sci.*, **21**, 1-12, 1986.

STATUS OF THE KENNEDY SPACE CENTER ASCENT WIND PROFILER

Paul Johnston

Tycho Technology
Boulder, Colorado

A new wind profiler has started operation at the Kennedy Space Center (KSC). This radar started operation in November 1, 1988. Located near the Shuttle runway, this radar is designed to give NASA increased information about winds aloft. This information is to be used primarily for assessing the variability of wind fields, so that increased confidence in the validity of jimsphere measurements made prior to shuttle launch can be established.

The system currently operating at KSC is a limited capability subset of the final system. It is operating in a temporary building, using only the solid-state predriver amplifier for a transmitter. Table 1 shows the current capabilities, and the final system capabilities.

Table I.

Nasa Kennedy Space Center Ascent Wind Profiler System

	PRESENT CONFIGURATION	FINAL CONFIGURATION
Antenna		
Elevation Angle	90°, 75°	90°, 75°
Azimuth	45°, 135°	45°, 135°
E Plane Beamwidth	2.9°	2.9°
H Plane Beamwidth	2.7°	2.7°
Sidelobe levels		
Elevations $> 40^\circ$	$< -20dB$	$< -20dB$
$5^\circ <$ elevation $< 45^\circ$	$< -25dB$	$< -25dB$
Elevations $\leq 5^\circ$	$< -40dB$	$< -40dB$
Transmitter		
Peak Power	4 kW	250 kW
Average Power	400 W	12.5 kW
System Noise Temperature	< 500 K	< 500 K
Time Resolution (full wind vector)	6 min.	3 min.
Spatial Resolution	150m and 600m	150m
Number of Range Gates	56	112
Pulse Coding	8 Bit Complimentary	8 bit Complimentary

The current system operates in two modes. One mode uses 150 meter resolution to get winds in the troposphere. The other mode uses 600 meter resolution to get data into the lower stratosphere. Figures 1 and 2 show wind data from each mode. These figures show hour winds obtained at the radar. A consensus average is used to omit noise points.

The installation of the final building and the high power equipment will take place in the spring of 1989.

542
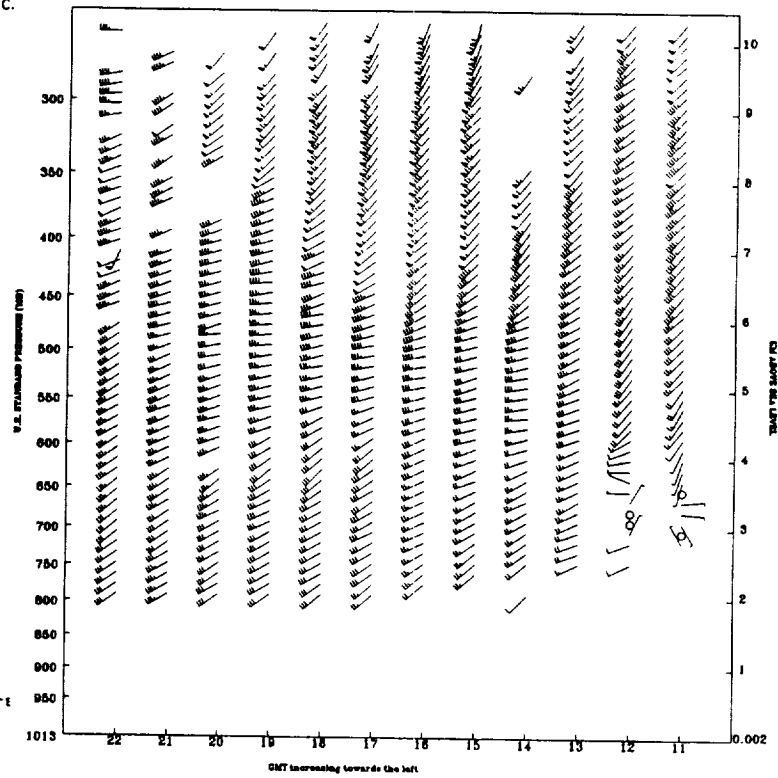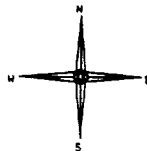
Fig. 1 Wind field measured with 150m resolution by the KSO 50 MHz Radar.
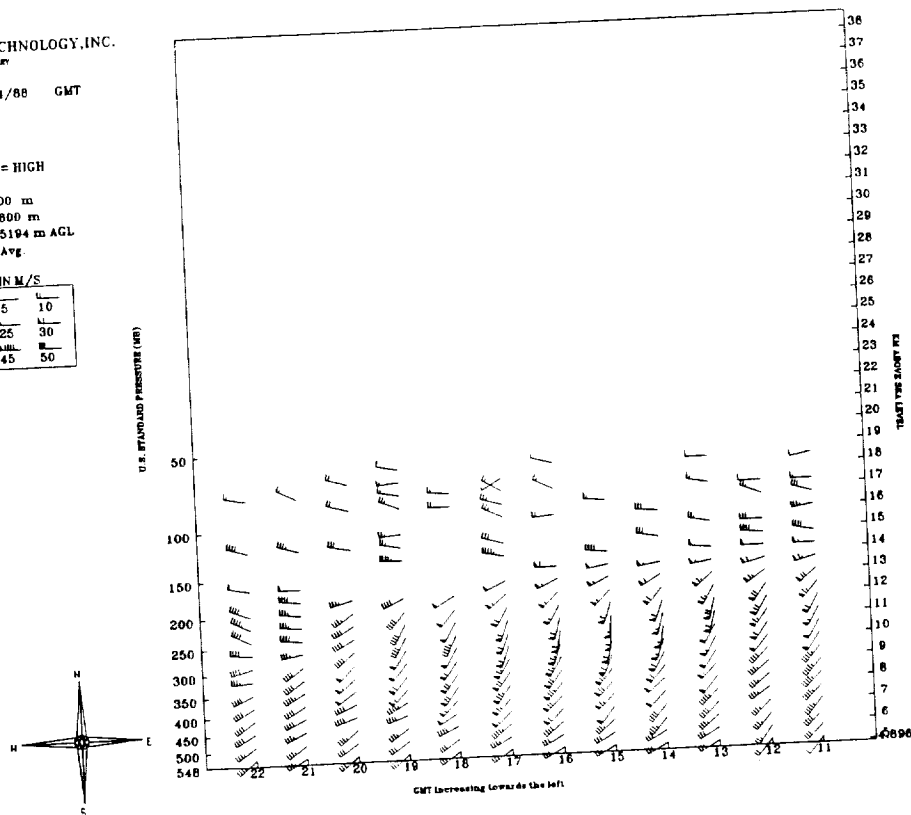
Fig. 2 Wind field measured with 600m resolution by the KSO 50MHz Radar.

LONG RANGE PLANNING FOR DEVELOPMENT OF FULL MST CAPABILITIES AT EISCAT

Gudmund Wannberg, Jürgen Röttger and Cesar LaHoz
EISCAT, Box 812, S-981 28 Kiruna, Sweden

P.J.S. Williams
University College of Wales
Aberystwyth Dyfed SY23 2AX, UK

Introduction: The EISCAT radar first went into regular operation in 1981, using the 933 MHz tristatic UHF system for incoherent scatter observations of the altitude region from just below 90 km up to above 500 km. The performance of the radar over this range has gradually improved over the years and is now generally recognized to be excellent. The relatively short wavelength of this system, $\lambda = 0.32$ m, has been a limiting factor in applying it to middle atmosphere research, and the commissioning of the EISCAT VHF system ($\lambda = 1.34$ m) has therefore been eagerly awaited by the MST community.

The EISCAT radars were originally planned only for ionospheric work (BARON, 1984, 1986). As a consequence, many subsystems were designed to process only incoherently scattered signals. This made for economy at the time but will now make it very hard to achieve acceptable ST performance without major redesign. Some of the more important system parameters are listed in Table 1.

Present status:

Although the VHF system is still only partially operational, practical experience with it, accumulated over the last two summer seasons, has shown that its sensitivity is more than good enough for observation of some types of scattering mechanisms in the mesosphere, even though conventional wisdom would have it that the 1.34 m wavelength should be well within the viscous subrange (RÖTTGER et al., 1988). This experience, supported by a continually growing interest from middle atmosphere scientists in the EISCAT member countries, has prompted the Scientific Advisory Committee of EISCAT to appoint a working group, with the task of looking into how the VHF system could be enhanced into a fully capable MST radar. The working group is supported in its task by EISCAT excecutive staff. The ideas for upgrading presented below have been largely worked out at EISCAT Headquarters over the last year, and do not represent the final views of the working group. Even so, the design targets listed in Table 2 are probably very close to what may ultimately be achieved.

Meanwhile, a set of complementary coded experiments have been developed, which can run in the existing hardware/software environment without any changes to the system being necessary. They allow the use of the VHF system as a mesosphere radar with altitude resolution down to 300 m and spectral resolution approaching 0.5 Hz. These programs will become part of the program library available to all visitors in the immediate future.

TABLE 1: System parameters of the EISCAT radars

	UHF	VHF
Transmitter type		- multicavity klystron -
Transmitter bandwidth (MHz)	3.0	> 8.0
Associated altitude res. (m)	50	< 19
T/R switching time (us)	?	> 100
Radar controller time resolution (us)	1	1
ADC resolution (bits)	8 + 8	8 + 8
Max. sampling frequency (MHz)	10	10
Associated buffer memory (words)	4K complex	4K complex
Buffer memory available when sampling at 500 kHz (words)	16K complex	16K complex
Preprocessor	- not available -	
Correlator max. multiply-add rate (MHz, complex products)	5	5
Correlator input word length (bits)	8 + 8	8 + 8
Correlator result memory (words)	4K	4K
Raw data disc storage	450Mbyte total	

TABLE 2: Design targets for the MST upgrading of EISCAT

Range resolution	15 m (dedicated transmitter)
	45 m (existing VHF transmitter)
Associated modulation bandwidth	10 MHz (dedicated transmitter)
	3 MHz (existing VHF transmitter)
T/R switching time	>50 us (existing VHF transmitter)
Radar controller time resolution	100 ns
ADC sampling frequency	10 MHz
ADC resolution	>10 bits
Buffer memory capacity	>4 K complex words
Preprocessor throughput rate	>4 M complex samples/s

Discussion:

It is obvious from an inspection of Table 1, that the VHF system is not at all well suited for tropospheric work in its present form. The bandwidth of the klystron transmitter cannot be increased by any known means; furthermore, the present frequency allocation for the VHF system borders on the European TV Channel 11 on the low side, so a significant increase in transmitted bandwidth can only be achieved after securing additional frequency allocations upward of the present one. Whether we can get these at all is unclear at present.

The T/R switching time of the VHF system is tabulated as unknown, because the VHF radar is capable of being operated with its front end configured in at least four different ways, each of which may show different recovery time. In the most commonly used configuration, the actual switching takes some 50 us. To this one must add the recovery time of the receiver, which is at least of the same order. Altogether, this makes the system marginally acceptable for stratospheric work as it is. A group at the Swedish Institute of Space Physics, Kiruna, Sweden, has plans to do a series of tests at stratospheric ranges during 1989, which should lead to more conclusive knowledge about the actual performance. The altitude resolution will still be limited to > 150 m at this time.

The present radar controller is in many ways the most limiting piece of equipment in EISCAT - it has too coarse time resolution for MST applications and no provisions for looping, conditional branching or subroutines. It will be replaced by a new design, based on integrated microprogram controllers and address generators, in about two years. Thereafter, 100 ns timing and control resolution will be available. The new unit will permit advanced

coding strategies to be realized by compact control codes. We have not yet investigated how the binary phase modulator of the VHF exciter behaves at baud rates greater than 1 MHz, but it is likely that it can be made to perform well at least at 3 MHz. Any further improvement would require the installation of a dedicated wideband transmitter, possibly of relatively low power, which could then be operated much more regularly for MST work than the case would be with the existing transmitter - it could for instance be kept in operation even while the EISCAT UHF system is running other experiments, which is impossible today.

In the mesosphere experiments performed so far, the existing correlator has been used as a coherent preprocessor, with all FFT or ACF processing of the time series being done off line. As can be seen from Table 1, the correlator speed is sufficient in practice to handle a few tens of range gates. It is, however, seriously limited both with respect to the small amount of result memory available as well as to the short word length (8 + 8 bits).

Using the correlator as a preprocessor amounts to using its result memory as an intermediate buffer, where the decoded data samples are coherently integrated before being dumped to the next processing stage. When partitioned into 64 timing bins, the 4K*32 bit memory can only accommodate some 60 range gates. Even more awkward is the lack of double buffering at the output to the host computer; this results in a gap of at least 65 ms in the sample series whenever data are dumped, i.e. almost equivalent to two preintegration intervals at 224 MHZ High frequency resolution studies using long, uninterrupted time series are therefore not practical at present.

The (8+8) bit word length of the correlator is almost an overdesign for incoherent scatter purposes. It provides an instantaneous dynamic range of about 45 dB, of which perhaps 10 - 15 dB are actually used in IS work. It would also be sufficient for normal mesosphere work, if the gain of the analog part of the receiver were reduced. However, processes like the PMSE occasionally provide signals in excess of this dynamic range. At stratospheric and tropospheric altitudes, the amount of ground clutter at Tromso, using the existing antenna, is also so large that this alone will exhaust the resolution. These limitations have been recognized by EISCAT, and work is already in progress to provide enhanced features. This proceeds along two main directions:

i) EISCAT is presently developing a generalized device, the MUFFIN (MUlti-channel FIR Filter and INtegrator)(POSTILA, 1987), which will meet or surpass all requirements for MST processing tabulated above. It will also include double buffering and flexible scaling of output data. The MUFFIN is not likely to become available for operational use until the beginning of 1990, possibly even later, and to become fully useable, it must be complemented by fast high resolution ADCs. In the interim,

ii) EISCAT is working together with scientists from the Swedish Institute of Space Physics at Kiruna, Sweden, to tie a stand-alone MST signal processor, now under construction at the Institute, into the existing EISCAT process computer system. This device is built to the VME bus standard and resides together with a host computer and 140 Mbyte of hard disk storage in a standard VME crate. At present, it contains one complex ADC channel operating with 12 bits of resolution at an uninterrupted 5 MHz sampling rate. Data transfer into the EISCAT system will be over a IEEE 488 (GPIB) link. The EISCAT process control computer will merge the data stream from the preprocessor with the block of auxiliary parameters normally recorded by the system and then write the composite data dumps to high density tape in the standard EISCAT format. We have selected this approach because it avoids any intermediate storage of data and produces tapes in a format which is immediately

readable by a large community.

This system will become operational during the second half of 1989, and will give us an opportunity to test the performance of other parts of the radar under realistic conditions. In particular, the strong signal handling capability of the receiver RF and IF parts may need to be improved in order to obtain an overall dynamic range matching that of the signal processor.

REFERENCES:

Röttger, J., C. La Hoz, M.C. Kelley, U.-P. Hoppe and Chris Hall, The structure and dynamics of polar mesosphere summer echoes observed with the EISCAT 224 MHZ radar, Geophys.Res.Lett., 15, 1353-1356, 1988.

Baron, M., The EISCAT facility, J.Atm.Terr.Phys., 46, 469-472, 1984.

Baron, M., EISCAT progress 1983-1985, J.Atm.Terr.Phys., 48, 767-772, 1986.

Postila, M., Integrator-decoder specifications, in Proc.of the EISCAT Annual Review Meeting 1987, 114-115.

GAIN AND PHASE CALIBRATION OF THE EISCAT RECEIVERS IN MST APPLICATIONS

Gudmund Wannberg and Jürgen Röttger
EISCAT Scientific Association
Box 812, S-981 28 Kiruna, Sweden

Tommy Sturk
Swedish Institute of Space Physics
Box 812, S-981 28 Kiruna, Sweden

Introduction:

As a step towards achieving full MS capabilities at the EISCAT radar, we have developed a program system which performs coherent integration and decoding of arbitrary codes in the existing EISCAT correlators. Additionally, a gain, phase and absolute power calibration, which is free of ionospheric clutter from ambiguous ranges, is performed in every receive cycle. This calibration feature may become extremely valuable when studying highly dynamic processes with large cross sections, such as the PMSE (Polar Mesospheric Summer Echo) phenomenon (Hoppe et al., 1988, Röttger et al., 1988).

Our program system was tested during the July 1988 PMSE campaign. Typical PMSE type signals were observed for part of the time. There are also several quiet periods in the four hour data set. In the following we discuss the radar receiver performance as a function of signal strength, using the calibration data as a reference.

Technical details:

The architecture of the EISCAT correlator does not permit the recirculation of data from the output (result) memory to the input of the multiplier/ALU unit. Consequently, the decoding must be performed before the coherent integration. Normally, this does not pose a problem, as the correlator is fast enough to do the operations in this order for a practical number of range gates. The decoding algorithm simply performs a cross-correlation of the sampled data points with a stored replica of the transmitted code sequence. The decoded results are then integrated by direct summation into the correlator result memory. Fig. 1 presents a schematic picture of the organization of the resulting data vector.

Our implementation differs from some other approaches, in that it uses a feature of the correlator input buffer memory, which permits the downloading of arbitrary integer numbers from the host computer to any area of the memory. Replicas of the complementary codes used to modulate the transmitter are generated by a FORTRAN program and stored in a disk file. When the experiment is started, a device handler in the EISCAT real time operating system retrieves this file and downloads its contents to an area of the buffer address space, into which the ADC never writes when sampling.

Once stored, the code sequences remain in memory for the duration of the experiment and can be randomly accessed by the correlator microprogram. In our test, a sequence of four 64 baud codes was used. These were grouped as two complementary pairs of opposite initial
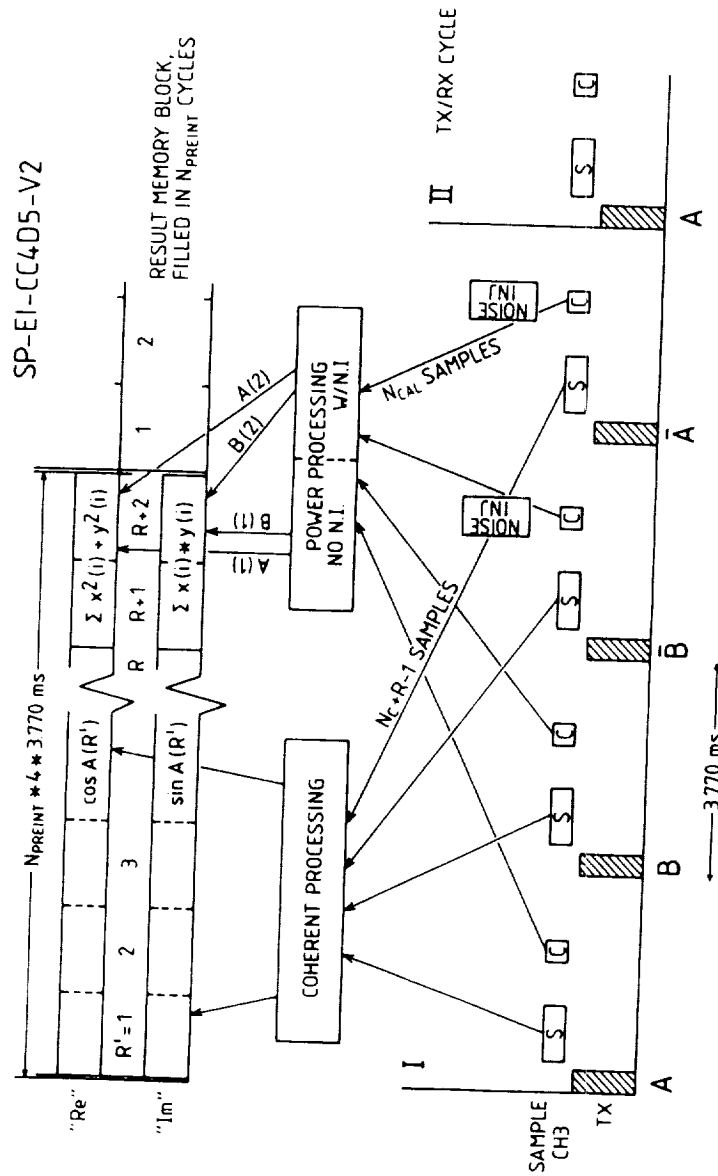
Figure 1: Block diagram of the transformation of data from the sample domain to the decoded amplitude/power representation used in SP-EI-CC4D5-V2. In the bottom row, transmission is denoted by crosshatched blocks and reception of signal or calibration data by open blocks, labelled with S or C respectively.
In the top row, the layout of the data vector is represented by one block - the experiment generated 64 such blocks every 2 seconds. R is equal to the number of range cells, which was 61 in this experiment.

signs, so that after decoding and summing over the complete sequence, system generated offset voltages were cancelled.

The program has a built-in "self test" mode. In addition to the replica of the transmitted modulation, a second data vector containing time shifted copies of the same modulation patterns is loaded into a different area of the buffer. The operator can change the start address of the area from which the correlator reads input data by an interactive command. When the test data area is selected, a sidelobe free and properly compressed response will appear in a single range gate if everything works properly. Any bit error or address shift either in the master code or the test codes will manifest itself as incomplete compression and the appearance of sidelobes.

Receiver gain and phase calibration:

The EISCAT receivers transpose incoming signals down to baseband. The final frequency translation is combined with the Hilbert transformation of the signal in a quadrature detector, and the two mutually orthogonal components of this signal are sampled synchronously, using parallelled ADC's. Every signal processing system using this technique will produce spectral estimates which are biased by deviations from gain equality or phase quadrature in the quadrature detector or in the signal path to the ADC's. In the most general case, the biases must be assumed to be non-linear functions of the instantaneous signal level and cannot be corrected for by using a constant error model. However, provided that the receiver has a suitable signal coming through it most of the time, the offsets can be determined from simple relations between some statistical averages of the signals from the two quadrature channels (RUSTER and WOODMAN, 1978).

The correction procedure used by Ruster and Woodman does not define the time extent of the averaging over amplitudes. This may not be too critical anyway in their application, as they are dealing with an ST radar system, whose receiver output is dominated by ground clutter under most circumstances. In that case, the level dependent gain and phase offsets will be much stronger functions of the clutter level than of the actual signal level, and the averaging period can be chosen to obtain reasonable statistics. When the EISCAT system is used at mesospheric ranges, we are faced with a quite different situation, because:

i) the ground clutter is almost nonexistent in the 80-90 km range, so the echo signals define the instantaneous signal amplitude (and hence the offsets),

ii) we do not see a signal all the time in any gate, so a straightforward averaging over time would lead to an underestimate of the effective signal level during the (sometimes transient) PMSE events,

iii) the signals which we do see in such events are highly structured and exhibit an extremely dynamical behaviour, with instantaneous S/N ratios sometimes exceeding 30 dB, which we now know is strong enough to drive the quadrature detector into non-linearity.

Considering the above points, it is clear that a calibration routine is almost mandatory in future EISCAT mesosphere experiments using the existing receiver, but it is also evident that the calibration must be based on something else than the actual signals. We have implemented a scheme which uses injection of white noise into the receiver front end to obtain a stochastic signal, on which the calibration is performed. The procedure used is as follows:
In every receive cycle, a programmable number of calibration samples are taken at a far

range, from which only incoherent scatter returns are to be expected (about 200 km). In our test, N(cal.samples)=32. We denote the cosine and sine components of sample number i by

x(i)   and   y(i) ,

The correlator program contains a subroutine which produces the two sums

$$A = \sum_{i=1,N} x(i)^2 + y(i)^2 \qquad \text{and } B = \sum_{i=1,N} x(i) \, y(i)$$

The first quantity, A, is of course proportional to total power, whereas B should have an expectation value of zero for all input combinations, if the receiver is working properly. A nonzero value indicates a deviation from sample quadrature and can be used to implement first order corrections to the spectral estimates in the analysis phase. A full correction requires the independent computation of Σx_i^2 and Σy_i^2. As this was not done here, we assume in the following that $\Sigma x(i)^2 = \Sigma y(i)^2$

The "total power" quantity A must be assumed to contain some contribution from the incoherent scattering (IS) of the previous transmit pulse by the ionospheric plasma at the first ambiguous range (about 600 km), and so it cannot be immediately used as a true representation of system gain. In our code, the incoherent scatter contribution is cancelled in an average sense by the following technique:

The basic transmit/receive pattern is a group of four subcycles. In the first two, the calibration samples are taken with the calibration noise source turned off, so that those samples contain only background noise and IS contributions. In the next two, the calibration noise source is turned on while the sampling is active. The correlator computes independent A and B estimates for the "noise off" and "noise on" cases and stores them in separate locations at the end of each range gated time bin in the result memory. If we denote these by A(1), B(1), A(2) and B(2) and assume the average clutter level to be constant within a preintegration interval, then

receiver gain G∞ A(2) - A(1)

receiver quadrature angle θ(i) = arccos (2 B(i)/A(i)), i=1,2

on the average. This gives us a number of possibilities to monitor the system performance and to correct for imperfections.

As an illustration, we use a sequence of data covering about 10 minutes on July 2, 1988 at 10.25.30 UT. (See Fig.2). The calibration values from all 64 time bins in each dump have been summed and the sums postintegrated over 30 seconds, i.e. 15 dumps. There are thus 4·32·64·15 = 1.23·10^5 estimates in each plotted value. If these were truly statistically independent, the normalized variance should be $1\sqrt{(1.23 \cdot 10^5)} = 2.85 \cdot 10^{-3}$. The actually observed variance is about $1.97 \cdot 10^{-3}$ both for the background series as well as for the (background+calibration) one. This discrepancy is almost totally due to the correlation between adjacent samples induced by the non-instantaneous impulse response of the receiver.

The behaviour of the phase quadrature term is more alarming. The value obtained as long as the signal level is low is very close to 90 degrees. During noise injection, however, the
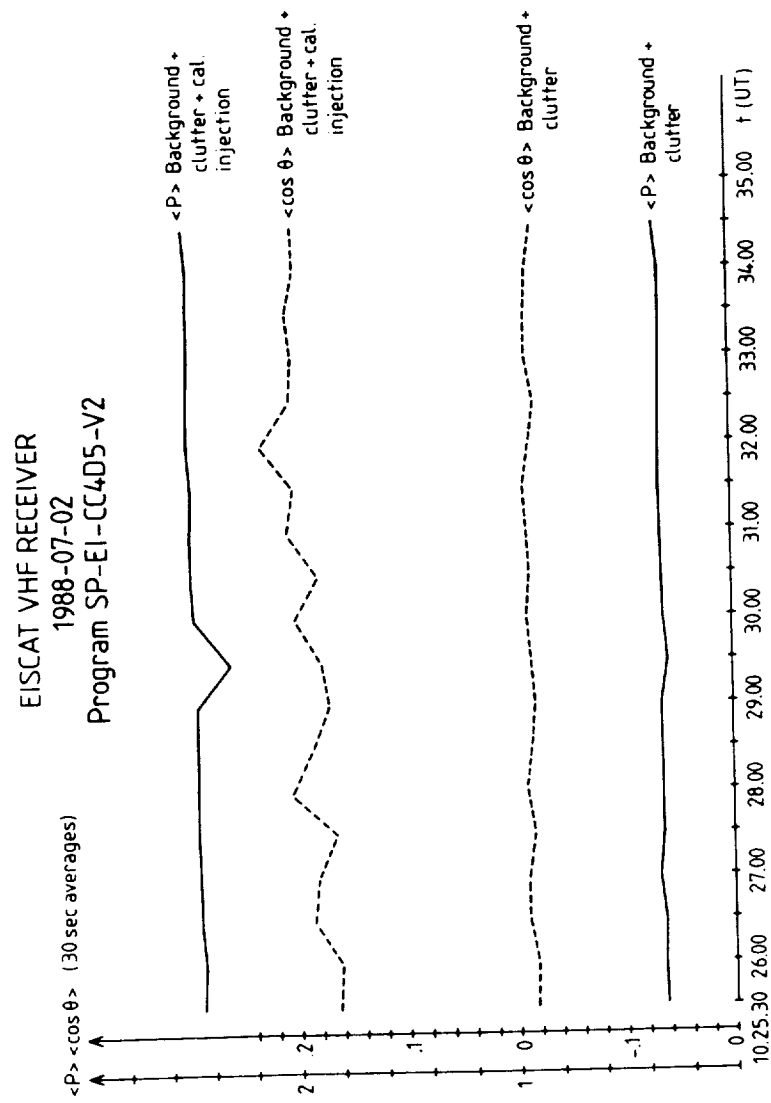
Figure 2: Gain and phase calibration data from SP-EI-CC4D5-V2, showing the strong influence of mean signal level on the phase quadrature behaviour of the receiver.

phase offset becomes very large, of the order of 10 degrees! The receiver phase quadrature is obviously strongly dependent on signal strength. It should be pointed out, that the calibration noise level was much higher than normal during this experiment, due to a mistake when configuring the receiver front end, approaching the equivalent of 1500 Kelvin antenna temperature or about + 7 dB relative to the receiver noise floor. Normally, this would have been disastrous, but since the PMSE echoes were occasionally several tens of decibels above the noise floor, it was rather an advantage.

The present result suggests that the phase quadrature offset is even worse at the signal levels produced by the PMSE than at the calibration level. This will affect all velocity estimates to some extent. Unfortunately, the experiments used for the actual data taking during the PMSE campaign did not contain the calibration feature, so it will be very hard to obtain proper correction factors for those data sets. Assuming that the attenuator settings used in the two different experiments were approximately the same, i.e. that the actual signal levels seen at the quadrature detector were comparable for equal echo strength, we can at least obtain an order-of-magnitude estimate of the velocity error as follows:

In the lag domain, the signal amplitude phase angle at time τ is

$\phi\ (\tau) = \arctan\ (\mathrm{Im}\ R(\tau)/\mathrm{Re}\ R(\tau)),$

where $R(\tau)$ is the complex autocorrelation coefficient at time τ. Following (RUSTER and WOODMAN) we can compute an equivalent estimate based on the actual sampled (uncorrected) data:

$\phi(\tau) = \arctan\ (\cos\delta \bullet \mathrm{Im}\ R'(\tau)/\mathrm{Re}\ R'(\tau))$

where δ is the correction for imperfect quadrature, i.e.

$\delta = -\ (\pi/2 - \theta)$

For small phase angles, i.e. for the condition expected at the first few lags of the ACF,

$\phi\ = \tan\phi \approx\ (1-\sin\ \delta/2)(\mathrm{Im}\ R'(\tau)/\mathrm{Re}\ R'(\tau))$

The phase error at a given lag is thus multiplicative and of the order of $\sin\ \delta/2$. For our case with $\delta = 10°$, the effect is one of expanding the velocity scale by some 9 %. For larger phase offsets the effect increases more slowly; it is about 17 % at $\delta = 20°$. We do not know at present how the offset behaves for really strong signals, so it is hard to estimate how large the maximum error is in the PMSE data set. As the S/N ratio was quite frequently greater than + 30 dB (LaHOZ et al., 1989), we must suspect velocity errors of maybe 20% or so.

One thing to be learned from our brief test is that the EISCAT receivers are in need of a major revision before they can be considered to be fit for handling the kind of signal dynamics encountered in the mesosphere. In the meantime, our calibration procedure will be extended to several power levels (we are thinking of + 7, + 17 and + 27 dB S/N) and the

gain calibration will be performed independently on the sine and cosine channels, thereby enabling us to do a full correction to the measured data.

Acknowledgement

References:

Hoppe, U.-P., C. Hall and J. Röttger (1988), First observations of summer polar mesospheric backscatter with a 224 MHz radar, Geophys.Res.Lett., 15, 28-31.

La Hoz, C., J. Röttger, M. Rietveld and G. Wannberg, The status and planned developments of EISCAT in mesosphere and D-region experiments, Handbook for MAP, this issue.

Röttger, J., C. La Hoz, M.C. Kelley, U.-P. Hoppe and C. Hall (1988), The structure and dynamics of polar mesosphere summer echoes observed with the EISCAT 224 MHz radar, Geophys.Res.Lett., 15, 1353-1356.

Rüster, R. and R.F. Woodman, Digital Filtering, Calibration and Correlation Analysis of Radar-Echoes from the Tropo- and Stratosphere, Kleinheubacher Berichte 21, 239-246, (1978).

A 915 MHZ BOUNDARY LAYER WIND PROFILER

W. L. Ecklund, D. A. Carter, B. B. Balsley, and P. E. Currier

Aeronomy Laboratory
National Oceanic and Atmospheric Administration
Boulder, Colorado 80303

INTRODUCTION

The Tropical Dynamics and Climate group of NOAA's Aeronomy Laboratory operates several large 50 MHz wind profilers in the tropical Pacific (GAGE et al., 1988). In order to fill in the lower few km not covered by the large radars, a small 915 MHz UHF radar has been developed to operate in a hybrid mode with the 50 MHz profilers (ECKLUND et al., 1988a). Initial testing of the 915 MHz radar has demonstrated that this small radar will not only fill in the lower heights in the tropics but will also be valuable as a relatively inexpensive stand-alone wind profiler for the lower troposphere. The 915 MHz radar has good height resolution and allows coverage down to about 100 meters above the ground. It can be used (either singly or in networks) in experimental studies of: low level transport of water vapor (for example by the trade winds), boundary layer convergence, frontal passages, low-altitude turbulence and vertical profiles of precipitation. Operational uses include air pollution prediction, wind shear monitoring and temperature profiling in the RASS mode.

SYSTEM DESCRIPTION

A block diagram of the prototype UHF wind profiler system is shown in Fig. 1. The equipment to the left of the vertical dashed line is used with our standard 50 MHz radar systems. Although all of the data presented in this report were obtained with our standard radar controller and processor, we have developed a new controller/processor for use with the 915 MHz radar that is described later in this section. The equipment to the right of the dashed line in Fig. 1 is located in the field (up to about 20 meters from the equipment shelter). The transmit/receive module is located under the panel antenna and low-level VHF signals are sent between the module and the shelter via inexpensive coaxial cable. The antenna is a microstrip design that allows the antenna to be made of thin (2 cm thick), rugged 91 by 91 cm panel-like modules that are easy to transport and that can be mounted low to the ground to reduce ground clutter. Additional details of the prototype small UHF radar system are given in ECKLUND et al. (1988a).

We have developed a new PC(AT)-based controller/processor for the UHF radar (CARTER et al., 1988) since this radar requires sub-microsecond pulses and sampling (our 50 MHz system was limited to 1 microsecond) as well as a more powerful FFT processor. Using PC technology substantially reduces the cost of the controller and processor so that the complete UHF radar is relatively inexpensive. Operating parameters are entered from the keyboard into set-up screens displayed on the monitor. The system is very flexible and easy to operate.

RESULTS

The prototype UHF radar was initially operated in Colorado for brief periods in the summer and fall of 1986. This unit had a power-aperture product of only 2 W-m^2 but was usually able to obtain useful returns (at 150 meter resolution) up

Boundary Layer Wind Profiler
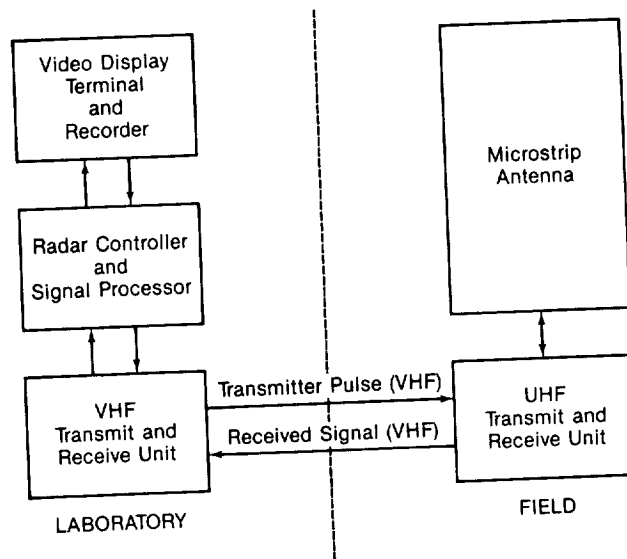
Fig. 1. Block diagram of the small UHF wind profiler.

to 1 to 1.5 km under clear-sky conditions. The prototype UHF radar was also operated for several days at our site on Christmas Island to test its operation in a tropical environment. For this test the power-aperture product was 1 W-m^2. Fair weather height coverage was essentially continuous up to 1.8 km and extended to 2.4 km for several one hour periods. Comparison with the 50 MHz radar indicated that increasing the power-aperture product of the UHF radar to 10 or 100 W-m^2 would increase the height coverage at Christmas Island to about 3 or 5 km (80% of the time) when using 150 meter height resolution. The UHF radar was also tested in Illinois from May to July in 1988. This version of the radar had a power-aperture product of about 20 W-m^2. Figure 2 shows the distribution of maximum altitude coverage at the Flatland site (no precipitation) for both 150 and 300 meter height resolution. The height coverage depended on air mass and wind conditions and also on time of day. Highest coverage was obtained in mid-afternoon, and the lowest coverage was observed in the early morning. The UHF radar is very sensitive to hydrometeors so that height coverage greatly increases when heavy clouds or precipitation are present. Observations of precipitation with the UHF radar are presented later in this report.

The first wind measurements with the small UHF radar were made in Colorado with an antenna panel tilted 15 degrees from vertical and rotated in azimuth. The initial paper by ECKLUND et al. (1988a) shows results obtained in clear air, light rain and thundershower using the rotating antenna. A preliminary test of the small radar in the tropics showed that wind profiles measured by the 915 and 50 MHz radars agreed fairly well in the limited region of overlapping coverage, and that operation of the two radars in a hybrid mode would provide wind profiles from near the surface upward into the stratosphere.

Fig. 3. Low-level jet observed by the 915 MHz radar.
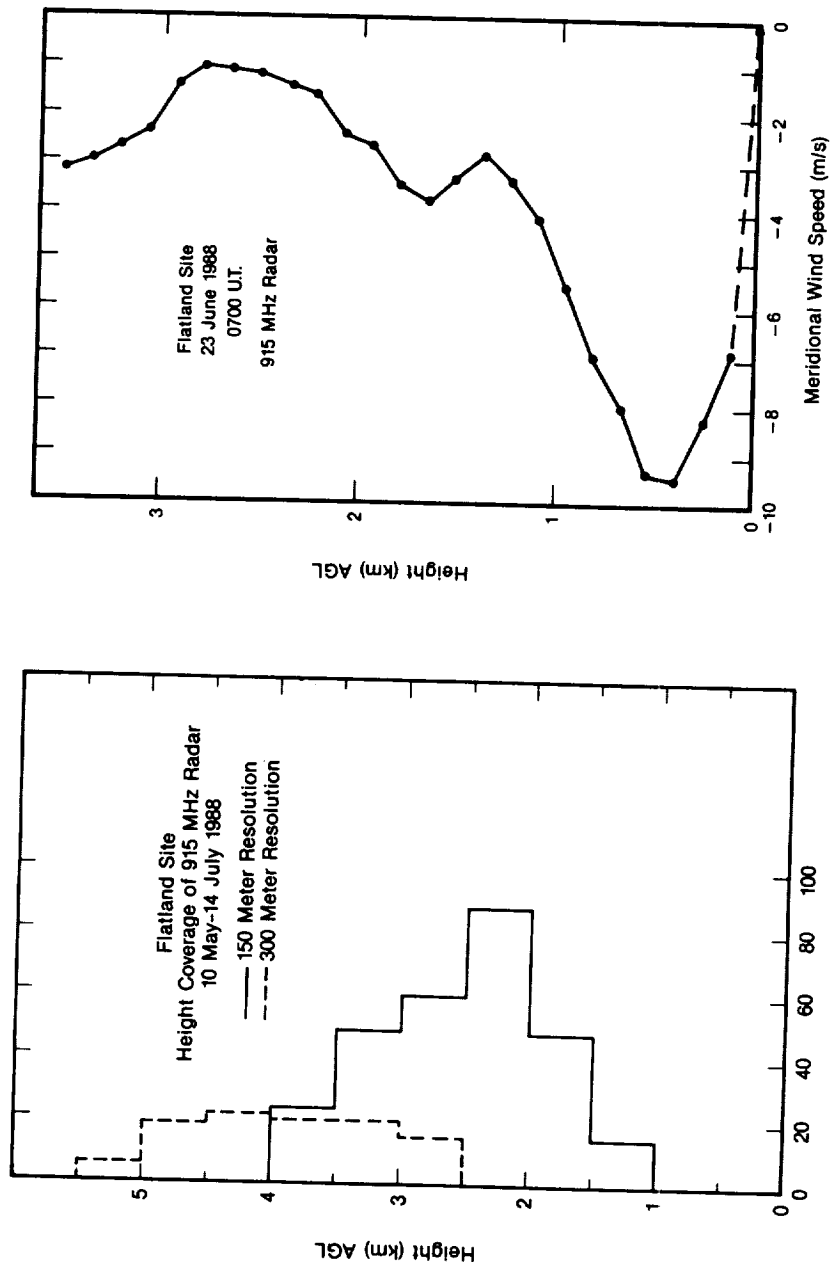
Fig. 2. Distribution of maximum height coverage by the UHF radar at 3-hour intervals during the 2-month experiment (no precipitation).

In November, 1987 the 915 MHz radar was installed at Platteville, Colorado near a portable 405 radar built by Strauch and colleagues of NOAA's Wave Propagation Laboratory. Preliminary comparisons between the 915 and 405 MHz radars gave r.m.s. differences in radial velocities of .26 m/s for 1-minute averages, and .17 m/s for 5-minute averages. More details of this comparison are given in ECKLUND et al. (1988b).

Because the small UHF radar is capable of observing winds down to about 100 meters above the ground it is well suited to studies of low-level jets which are important in transporting water vapor and pollutants over long distances. The 915 MHz radar was operated in very flat terrain in central Illinois during May and June 1988. Figure 3 shows an example of a low-level jet in the meridional wind component observed during the nighttime hours. The surface wind speed was less than 1 m/s, but the radar showed a southward wind component of nearly 10 m/s at a height of 500 meters above the ground.

When precipitation or heavy clouds are present, the UHF radar coverage increases dramatically. For example, during summer thundershowers in Colorado coverage extended to over 8 km above the ground. Under these conditions the returns from hydrometeors overwhelm the clear-air returns so that the determination of vertical air motion is not possible. However, it is still possible to obtain profiles of the horizontal wind since the hydrometeors are advected horizontally by the mean winds (WUERTZ et al., 1988). An example of the 915 MHz radar response to heavy clouds and rain is shown in Figure 4. For these observations the antenna was pointed vertically, and the range resolution
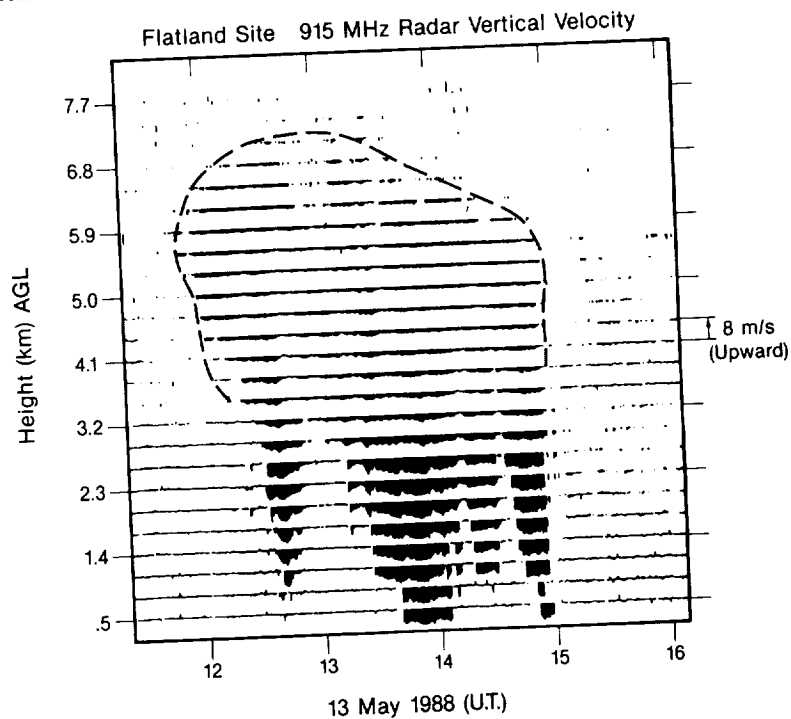
Fig. 4. Vertical velocity observed at 915 MHz versus height and time. The cloud-enhanced echoing region is indicated by the dashed line.

was 300 meters. Before 1200 U.T. the radar was observing continuous echoes up to a height of 3.2 km, and as heavy clouds moved into the antenna beam the height coverage increased to over 7 km. The downward velocity in this upper region is on the order of 1 to 2 m/s, and is consistent with the fall speed of snow and ice crystals. Below 3 km the fall speed increases to about 5 m/s as the particles melt. The first rain shaft observed at about 1240 U.T. dissipated before reaching below 1 km. The more extensive rain echoes from 1330 to 1500 U.T. resulted in less than .25 mm of rainfall as measured by an on-site rain bucket. This example shows how strongly the 915 MHz radar response is dominated by heavy clouds and rain.

The small UHF radar has also been used to obtain temperature profiles by using it in conjunction with an acoustic source (Currier et al., 1988). Preliminary comparisons with balloon-derived temperature profiles show good agreement, and the only obvious shortcomings to the technique are noise pollution from the acoustic source and the limited height coverage (up to about 1 km above the surface) due primarily to acoustic attenuation. Since the RASS returns at the lowest altitudes are very strong, we may also be able to use the enhanced resolution of the new PC-based controller/processor with the small UHF radar to obtain temperature profiles with height resolution of 30 meters in the lowest few hundred meters.

GROUND CLUTTER AND BIRD ECHOES

Although the preceeding sections have shown that the small UHF profiler can obtain high-resolution wind profiles in the lower troposphere and can also obtain vertical profiles of precipitation and temperature, there are several aspects of lower tropospheric profiling that present special problems. First, nearby objects which are visible in antenna sidelobes present problems if they move back and forth in the wind so that a strong, near-zero Doppler signal is generated at the lowest heights (CURRIER and ECKLUND, 1988). Under these conditions the algorithm that determines the first moment of the Doppler spectrum may select the strong clutter peak near zero and not the weaker (but wanted) peak due to atmospheric scattering. This type of ground clutter is very site specific and it may be necessary to use a clutter "fence" or structure to reduce low elevation sidelobe response at sites with nearby power lines, trees, etc. However, at one flat prairie site (Platteville, Colorado) ground clutter was not a problem when using an unshielded antenna.

A second problem that is unique to lower troposphere profiling with a UHF radar is interference from migrating small birds. We observed a large increase in spurious echoes from migrating birds on a number of nights in early May in Illinois. After midnight the number of bird echoes decreased and were at low levels by sunrise. On the nights with the highest number of bird echoes it was difficult, at times, to derive the wanted clear-air motions at the lower heights from the 30-second average spectra. Bird echoes decreased substantially during the 2-month observing period and no longer posed a problem for wind profiling by the middle of June. We conclude from this experience that at some sites during peak bird migration periods it will be necessary to do special signal processing in order to obtain wind profiles at the lowest heights.

SUMMARY

In this report we have presented a small, portable, relatively inexpensive UHF wind profiler. Although the height coverage of the 915 MHz radar is limited due to its relatively small power-aperture product, we have shown that it can obtain high resolution wind profiles from near the ground upward to 2 to 3 km depending on antenna size and transmitter power. Preliminary tests show that the small radar performs well in the tropics and will be able to monitor the trade winds on a continuous basis from our tropical sites. The demonstrated low-altitude coverage (down to about 100 meters above the surface)

shows that the small radar will also be valuable for monitoring the transport of pollutants and water vapor by low-level winds. We have also shown that the UHF radar is very sensitive to heavy clouds and rain with the result that the small radar can be used to determine the height of the melting layer and can also be used to monitor the vertical distribution of hydrometeors. Finally, preliminary tests of the small radar operated in the RASS mode show that it is possible to obtain temperature profiles up to a height of about 1 km with good time and height resolution.

REFERENCES

Carter, D.A., P.E. Currier and W.L. Ecklund (1988), A PC-based radar controller/signal processor, Fourth MST Workshop, 29 Nov.-2 Dec., Kyoto, Japan.

Currier, P.E. and W.L. Ecklund (1988), Ground clutter suppression at UHF by the use of surface wind measurements, Fourth MST Workshop, 29 Nov.-2 Dec., Kyoto, Japan.

Currier, P.E., W.L. Ecklund, D.A. Carter, J.M. Warnock and B.B. Balsley (1988), Temperature profiling using a UHF wind profiler, Symposium on Lower Tropospheric Profiling, 31 May-3 June, Boulder, Colorado.

Ecklund, W.L., D.A. Carter and B.B. Balsley (1988a), A UHF wind profiler for the boundary layer: brief description and initial results, J. Atmos. and Oceanic Tech., 5, 432-441.

Ecklund, W.L., K.P. Moran, P.E. Currier, B.L. Weber, D.A. Carter and D.B. Wuertz (1988b), A comparison of wind profilers operating at 915, 405 and 50 MHz, Fourth MST Workshop, 29 Nov.-2 Dec., Kyoto, Japan.

Gage, K.S., B.B. Balsley, W.L. Ecklund, R.F. Woodman and S.K. Avery (1988), A trans-Pacific network of wind-profiling doppler radars for tropical atmospheric research, Fourth MST Workshop, 29 Nov.-2 Dec., Kyoto, Japan.

Wuertz, D.B., B.L. Weber, R.G. Strauch, A.S. Frisch, C.G. Little, D.A. Merritt, K.P. Moran and D.C. Welsh (1988), Effects of precipitation on UHF wind profiler measurements, J. Atmos. and Oceanic Tech., 5, 450-465.

ECHO INTENSITY OF A RADIO ACOUSTIC SOUNDING SYSTEM (RASS)

Y. Masuda

Communications Research Laboratory
Ministry of Posts and Telecommunication

T. Tsuda, T. Takami, T. Sato, S. Fukao and S. Kato

Radio Atmospheric Science Center, Kyoto University
Kyoto, Japan

We have studied the intensity of a radio acoustic sounding system (RASS) when the acoustic and the wind velocities are a function of altitude. Measuring temperature profiles of the troposphere and stratosphere by using a RASS it is possible to estimate the effective backscattering region that the acoustic wavefront and radar beam are perpendicular to each other. The profiles of the wind and the temperature, to use the calculation, are measured by using a Doppler radar and a radiosonde before the RASS measurement.

When the radar beam width is much larger than the angle subtended by the arc of the acoustic wavefront of the effective backscattering region, it is shown that the intensity of the RASS echo falls off, not only as a function of the inverse square of the range, but also as a function of the subtended angle. The estimation of the intensity of the RASS echo from the subtended angle agrees well with the observed results using the MU radar/RASS.

The RASS, consisting of an acoustic source and a Doppler radar, is a promising technique to remotely measure vertical profiles of the atmospheric temperature (MARSHALL et al., 1972: MATUURA et al., 1987). The RASS uses radar to receive echoes (RASS echoes) backscattered from periodic perturbations in the atmospheric refractive index produced by an incident acoustic pulse and to measure the atmospheric temperature from the local speed of sound which is derived from the Doppler frequency shift of the RASS echo signal.

Naturally, the underlying assumption needed for the implementation of RASS observation is the existence of the regions from which the radar wave is effectively backscattered. For monostatic radar configurations, there are two necessary conditions to receive RASS echoes. First is the condition that the radar beam must be incident normal to the acoustic wavefront, and now an acoustic wavelength must be equal to half the radar wavelength in order to satisfy the Bragg condition.

The effective backscattering region is defined as those portions of acoustic wavefronts over which the radar beam is incident perpendicularly (MASUDA, 1988). It is of practical importance for RASS observation to know how the effective backscattering region is modified by the atmospheric wind and temperature profiles. We studied the effects of wind and temperature on the height limit of RASS measurements.

First, this presentation shows the results of numerical calculations on the effective backscattering regions. The numerical analyses show that the positions and dimensions of the effective backscattering regions are strongly affected by wind and temperature gradients, antenna aperture, and distance between acoustic and radar antennas.

Next, it shows that the numerical estimations of the height range for effective reception of RASS echoes agree quite well with actual RASS observations carried out by using the MU radar (KATO et al., 1984).

Finally, when the radar beam width is much larger than the angle subtended by the arc of the acoustic wavefront of the effective backscattering region, it is shown that the intensity of the RASS echo falls off with distance and subtended angle: the intensity is proportional to the

inverse square of the distance and to the fourth power of the subtended angle. Observed results using the MU radar/RASS agree well with the numerical estimations.

REFERENCES

Kato, S., T. Ogawa, T. Tsuda, T. Sato, I. Kimura, and S. Fukao, The middle and upper atmosphere radar: First results using a partial system, *Radio Sci., 19*, 1475-1485, 1984.

Marshall, A. M., A. M. Peterson, and A. A. Barnes, Jr., Combined radar-acoustic sounding system, *Appl. Opt., 11*, 108-112, 1972.

Masuda, Y., Influence of wind and temperature on the height limit of a radio acoustic sounding system, *Radio Sci., 23*, 647-654, 1988.

Matuura, N., Y. Masuda, H. Inuki, S. Kato, S. Fukao, T. Sato, and T. Tsuda, Radio acoustic measurement of temperature profile in the troposphere and stratosphere, *Nature, 323*, 426-428, 1986.

LOW ALTITUDES INVESTIGATIONS AT VHF

M. CROCHET and C. BOURDIER

LSEET, Université de Toulon, UA 705 CNRS
639, Bd des Armaris, 83100 TOULON, FRANCE

INTRODUCTION

One of the main **advantages** of the ST radar is its capability to obtain an extended coverage in altitude both for operational and research purposes. High altitude measurements are necessary to investigate the upper level jet, the tropopause and the lower stratosphere while low altitude measurements are required for low level jet and boundary layer studies and to obtain the continuity with measurements from other techniques (sodar, ground network ...). High altitude coverage is obtained at VHF by increasing the mean power-antenna area product and using coding to improve the signal to noise ratio. Low altitude measurements are usually much more easy at UHF (ECKLUND, 1986) than VHF. The combination of the advantages of VHF radars (high altitude measurements, tropopause detection) and UHF radars (low altitude measurements, high resolution) has been taken in consideration to develop hybrid UHF/VHF radars (French INSU-METEO radar at 45/961 MHz, NOAA radar at 50 MHz/1 GHz, this issue). The 403 MHz operational profiler is supposed to cover a large altitude range but will probably not detect the tropopause and will be sensitive to precipitations. So, an hybrid solution seems to be the more relevant at least for research purposes :

- for a VHF/UHF system, progress towards low altitude at VHF will be useful in order to extend the altitude range of simultaneous measurements at the 2 frequencies or to use a mini UHF radar,

- for a lower cost system a possible solution is to use an hybrid bipower VHF system.

VHF OBSERVATIONS AT LOW ALTITUDES

Since VHF ST radars are operating, it has been very difficult to obtain measurements both at very low and very high altitudes. The usual minimum altitude was around 2 km with some variations of this minimum according to the system and the site (ECKLUND,1986).

The main problems at low altitude are related to :

- the switching time of the TR system,

- the receiver recovery time,

- the internal reflections in cables, switches and antennas,

- the clutter from the ground, building, power lines, sea, trees, mobiles.

Most of these effects are proportional (or related) to the high power necessary to get high altitudes measurements and it seems reasonable to use a low power system to improve the measurements at low altitude as already shown with the french ST radar in 1984-1985 during atmospheric or oceanographic investigations (ECKLUND,1986).

Two solutions have been successively explored with the low altitude system of the Provence radar :

i) a fast pin diode TR adapted to the low peak power of 3 KW (ECKLUND,1986) or 400 watts with a minimum system range of about 500 meters when transmitting in a dummy load,

ii) a system using a classical hybrid junction (instead of the active pin diode TR) with a transistorized amplifier of 400 watts (Fig. 1).
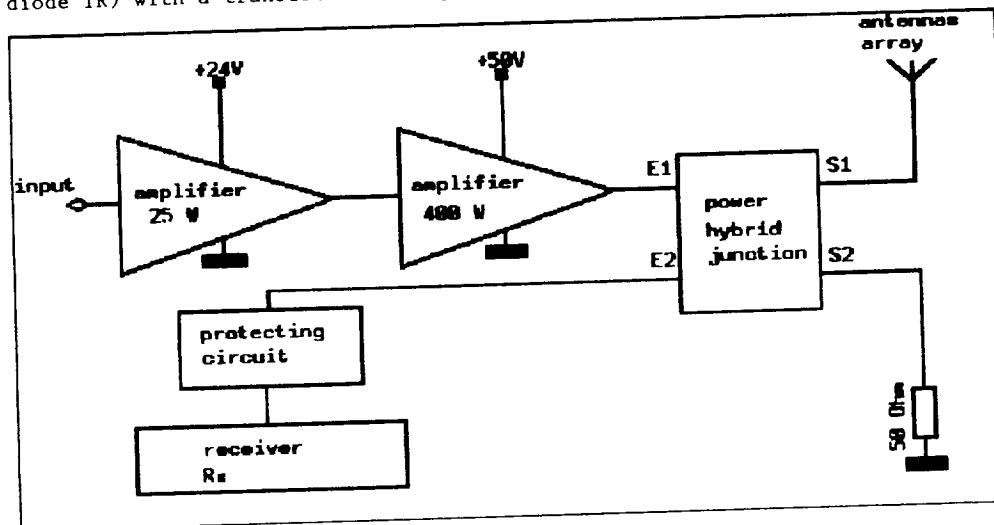
Fig. 1 - Schematic of the low power system using an hybrid junction with a 50 Ω dummy load instead of a pin diode TR

EXPERIMENTAL RESULTS

The second system with the hybrid junction has been set up very recently (october-november 1988) at the new LSEET radar station of Tourris near Toulon. Due to the hilly environment of the station, this location is probably not the most favourable for low altitudes soundings and future improvments can be expected in flatland conditions has observed previously in the Rhône Delta.

The 400 watts peak power amplifier is very compact $(10x10$ cm$^2)$ and reliable with possible duty cycles from 1 to 20%; it has been used in two configurations :

i) Low altitude observations

With a pulsewidth of 1 microsecond and a 3% duty cycle (6 watts transmitted to the antenna and 6 watts to the dummy load), it is possible to measure winds down to 600 meters (Fig. 2) without ambiguity and until 450 meters by Doppler continuity even if saturation effects are generating symmetrical echoes.

It has to be noted that these results are obtained with an antenna beam pointing 15° off the zenith with h = 0.96 r . As the minimum altitude is range dependant, it would be possible to measure winds around an altitude of 250-300 meters at the same ranges and an antenna beam pointing 60° off the zenith.
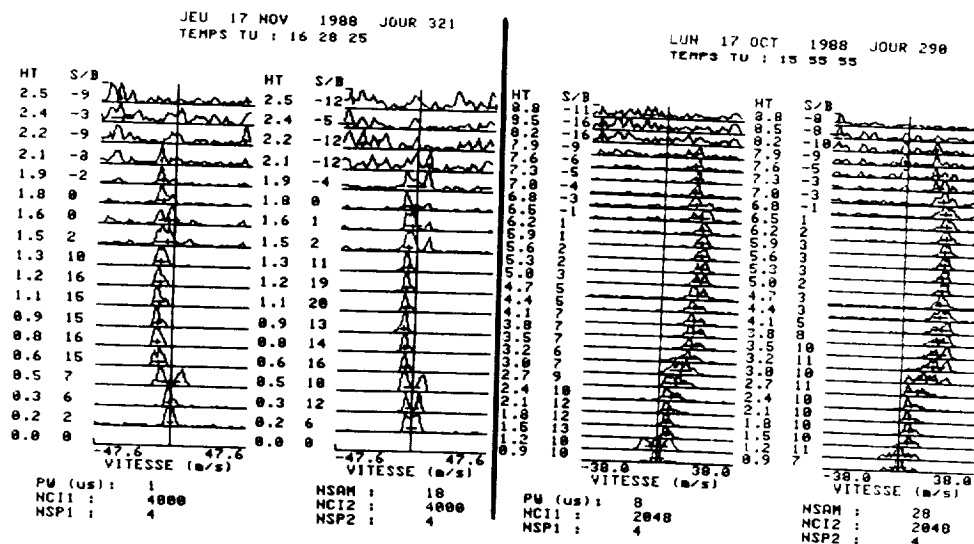
Fig. 2 - Low altitude observations with 150 range resolution, 3% duty cycle (6 watts transmitted power) and Doppler observations down to 600 or 300 meters

Fig. 3 - Highest altitudes observed with 20 watts transmitted power (1200 m range resolution, 10% duty cycle) and Doppler observations up to 8000 meters.

ii) Higher altitude with the small radar system

For small budgets or for easy transportable radars it would be interesting to know the maximum altitude using the same system with other pulse widths and duty cycles. Some preliminary conclusions can already be deduced from the results (Fig. 3) obtained at 8 microseconds and a 10% duty cycle; in these conditions, observations can be performed until about 8000 meters.

DISCUSSION AND CONCLUSIONS

Near zone effects of the antenna have to be taken into account in velocity and C_n^2 measurements accuracies at low altitudes. These effects will decrease if the beam is pointed 60° off instead of 15° off the zenith.

Further investigations in different conditions (orography, antenna size, antenna type, beam direction, level of peak power, type of duplexer, pulse width...) are still necessary in order to clearly identify the extreme limits of the system and the best configuration.

An operational system can be considered for low budget organizations with a time sharing by the 2 high and low power systems of the two perpendicular arrays (for coco antennas). Simultaneous soundings in perpendicular directions seem possible without decreasing of the time resolution.

Simultaneous investigations at low altitude by low power VHF radar and UHF radar have to be made simultaneously in order to study the effect of precipitations on wind measurements and to investigate precipitations at 2 different frequencies using complementary advantages of both systems.

REFERENCE

ECKLUND W. (1986) - "Low altitude coverage of ST radars" - MAP HANDBOOK, Vol.20, p. 398.

Signal Processing and Data Analysis in Middle Atmosphere Radar

Prabhat K. Rastogi

Electrical Engineering and Applied Physics Department

Case Western Reserve University, Cleveland, Ohio 44106

Abstract

Use of signal-processing and data-analysis methods in radar studies of middle-atmospheric motions is examined. Detection of weak Doppler-shifted signals from thin atmospheric regions in a noise background requires an optimum receiver. It is shown that the basic radar signal-processing operations implement an optimum receiver in successive stages using matched-filter, correlator, and filter-bank structures. Effectiveness of coherent integration in reducing high data rates, and as an efficient but crude low-pass filter, is discussed. Use of noise-like binary phase codes and decoding in improving range resolution is outlined. It is emphasized that decoding and coherent integration operations can be interchanged only for a nearly stationary medium. Spectral analysis of radar signals using time-averaged periodogram implements an optimum filter bank for detecting weak Doppler-shifted returns. Methods of reducing undesirable artifacts in spectral analysis of nonstationary signal components, using windows and trend removal, are discussed. Estimation of signal parameters through spectral moments and least-square estimation is reviewed. Finally, simple data-editing methods are outlined for suppressing outliers and interference.

1. INTRODUCTION AND SCOPE

The use of high-power VHF and UHF radars is an established method for monitoring the dynamical processes in the middle atmosphere. These radars detect weak, turbulence-induced, refractive-index fluctuations over parts of the mesosphere, stratosphere and troposphere, and monitor their bulk motion by measuring the very small Doppler shift of the received signal. In view of their altitude coverage, these radars are also collectively referred to as MST radars [Balsley, 1981; Röttger, 1984]. The received signals are often weaker than a picowatt, and their Doppler frequency shifts are as small as $\sim 10^{-9}$ of the radar frequency. Physical parameters of interest viz. strength of refractive-index fluctuations (C_n^2) and the energy-dissipation rate (ϵ) due to turbulence, bulk velocity (v) of the medium along the radar axis, and spread

of this velocity (σ_v) can be derived from the low-order moments of power spectra of received signals. Turbulence parameters (C_n^2 and ϵ) can only be inferred within the framework of a suitable scattering model [see e.g. Ottersten, 1969a,b; Hocking 1985; Rastogi et al. 1988]. Time-series analysis of the derived parameters provides information on atmospheric wind and turbulence fields, wave continuum, and instabilities [Röttger, 1987; Fritts and Rastogi, 1985].

Dynamical processes of interest have time scales of at least a few minutes to a few days. Data rates in middle-atmospheric radar experiments, however, are typically 0.5 Mbyte/sec. It is, therefore, desirable to carry out as much signal processing as possible in real time to reduce the data rates. The aim of basic real-time signal processing operations is to obtain acceptable time-averaged estimates of power-spectrum density (psd) or autocorrelation function (acf) of atmospheric echoes in presence of noise, ground clutter, and interference. These estimates are often required with a 0.1-1 km range resolution, at 0.5-5 min time intervals, and at ~100 or more ranges for one or more radar beam directions. Subsequent off-line data analysis includes spectral parameter estimation, and time-series analysis of these parameters. Off-line analysis of stored data may use non-causal or physically nonrealizable algorithms.

The first middle-atmosphere radar experiments at Jicamarca [Woodman and Guillén, 1974], while limited in on-line computations, used the slow fading of atmospheric signals and innovative computational shortcuts to estimate the low-order spectral moments at some ranges. Parallel array processors or specialized computational hardware attached to a host computer can now obtain time-averaged signal spectra at a few hundred ranges with nearly a thousand-fold reduction in data rate. These enhanced capabilities inevitably produce larger volumes of data, that can be organized as a data base.

In this paper, the routine signal processing and data analysis methods in use with MST radars are examined. This review supplements those at earlier workshops [Farley, 1984; Rastogi, 1983a, 1986]. Only the salient methods viz. optimum-receiver implementation, signal integration, coding and decoding, spectral analysis, spectral moment and parameter estimation, automated data editing, and analysis of power-law spectra are discussed at length. Signal processing algorithms depend on radar frequency, antenna size and pointing direction, transmitter power, altitude, terrain, meteorological conditions and interference sources, and are limited by on-line computing resources. Data analysis methods depend on analysis objectives, models, the amount and quality of data, and available computational resources. They often entail considerable exploratory and

graphical analysis [Tukey, 1977; Chambers, 1977; Cleveland, 1985; Press et al., 1986].

First, the optimum receiver implementation in successive stages of radar signal processing is discussed in Section 2, and the nature of radar signals is outlined. Coherent integration of sampled receiver output efficiently implements a crude low-pass filter as shown in Section 3. Its effectiveness in reducing data rates is emphasized. The use of noise-like binary phase codes and decoding for improving range resolution is described in Section 4. Problems in combining coherent integration with decoding are stressed, and reasons for pulse-by-pulse decoding are delineated. Classical periodogram analysis and spectral-moment estimation to derive the key parameters in radar experiments are discussed in Section 5. The effect of a non-stationary component with application to ground clutter suppression and analysis of velocity data with power-law spectra is also considered here. Alternative spectral estimation methods using autoregressive and maximum entropy models are briefly mentioned. Automated data editing methods based on sorting are outlined in Section 6. Their use in removing outliers and for suppressing interference components in signal spectra is discussed. Finally, the impact of enhanced and affordable computational resources on signal processing and data analysis techniques is examined in the concluding remarks in Section 7.

2. RADAR SIGNAL PROCESSING AND MATCHED FILTERING

The signal processing operations in a basic middle-atmospheric radar experiment can be summarized with reference to the block diagram of Figure 1. The radar transmitter is excited by a periodic impulse train. The transmitter response to an impulse is a narrow pulse with envelope $p(t)$ modulated by a carrier signal at the radar frequency f_o. This pulse is radiated by the antenna along the radar beam as an electromagnetic wave-packet. Monostatic radars share the same antenna between the transmitter and the receiver. A duplexer is used to disconnect the antenna from the transmitter after the pulse $p(t)$ has subsided, and to connect it to the receiver. The electromagnetic wave packet, as it sweeps along the radar beam, is scattered by atmospheric refractive-index irregularities. A small part of the electromagnetic energy also leaks through the antenna sidelobes and is reflected by ground targets. Atmospheric and ground returns from a distance r are received at a range delay $\sim 2r/c$, where c is the free space speed of light. The received signal also comprises a noise component and unwanted radio interference. The scattered signal is Doppler shifted by a frequency $2v/c$ for irregularities moving along the radar axis with a speed v towards the radar.

The receiver input is therefore complex, with components that are in phase and in phase quadrature with the carrier signal.

The received signal is mixed with the output of a phase-stable local oscillator to obtain an intermediate-frequency signal that is first amplified, and then coherently demodulated to recover the complex envelope of the received signal at the receiver output. The receiver output is uniformly sampled in range delay, and these samples are digitized. As successive impulses are applied to the transmitter, new sets of digitized range samples become available. The fading time of atmospheric signals is usually very much larger than the interpulse period between successive impulses. It is therefore desirable to coherently integrate the complex digitized range samples over several transmitted pulses. Blocks of coherently integrated samples are used to form time-averaged estimates of *psd* at each range delay. Suitable break-points for off-line analysis are indicated in Figure 1. It usually entails estimation of spectral-moment parameter and data analysis of their time series. It is desirable, however, to display at least crude estimates of low-order spectral moments in real time.
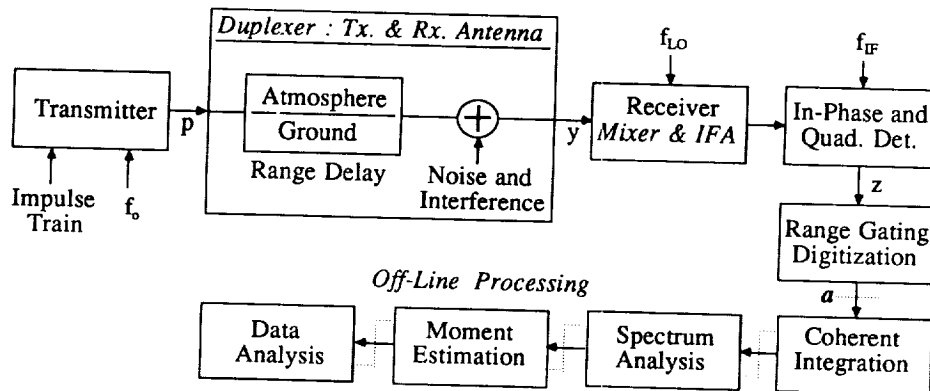
FIGURE 1. Block diagram of signal processing operations in middle-atmosphere radar experiments. These operations implement an optimum matched-filter receiver for detection of weak Doppler-shifted atmospheric returns in presence of noise, as discussed in the text. Modifications for high-resolution experiments are shown in Figure 2. Off-line analysis can be relegated to any suitable stage after a.

If the pulse envelope $p(t)$ has a duration T_p, with a peak at delay t_p, then the radiated wave packet has a spatial extent cT_p, where c is the free-space speed of light. The modulated transmitter output is of the form $p(t) \exp(\iota 2\pi f_o t)$, where $\iota = \sqrt{-1}$. For a point target $\delta(r-r')$ at range r', the range delay is $t' = 2r'/c$, and the antenna output is of the form $\alpha(r') \sigma p(t-t') \exp(\iota 2\pi f_o[t-t'])$, where the term $\alpha(r')$ includes the effects of attenuation due to two-way trip to and from the target, and σ is its radar cross-section. With additive white Gaussian noise $n(t)$ of constant power spectral density N_n, the net signal $y(t)$ at the antenna output or the receiver input is

$$y(t) = s(t) + n(t) = \sigma \alpha(r') \, p(t-t') \exp(\iota 2\pi f_o[t-t']) + n(t) \qquad (1)$$

For maximum signal-to-noise ratio (*snr*) at the output, the optimum receiver can be implemented either as a correlation receiver, as a matched-filter receiver, or as a bank of narrow-band filters [Wozencraft and Jacobs, 1965; Davenport and Root, 1958]. Ideally, the matched-filter receiver should have an impulse response $h_m(t) = \beta s^*(t''-t)$, where β is a constant, t'' is a delay parameter, and $*$ denotes the complex conjugate. The receiver output is then the convolution of $y(t)$ with $h_m(t)$. In equation (1), the term $\alpha(r')$ varies quite slowly, but the target range r' is arbitrary. The impulse response $h_m(t)$ can only be matched to the known part $p(t) \exp(\iota 2\pi f_o t)$ of $s(t)$ with

$$h_m(t) = \beta p^*(t''-t) \exp(-\iota 2\pi f_o[t''-t]) \qquad (2)$$

It is readily seen that the the signal component $z_s(t)$ in the receiver output $z(t) = z_s(t) + z_n(t)$ is

$$z_s(t) = s(t) \otimes h_m(t) = \sigma\beta \, \alpha(r') R_{pp}(t''-t+t') \exp(-\iota 2\pi f_o[t''-t+t']) \qquad (3)$$

where $\otimes$ denotes the convolution, and $R_{pp}(t) = E[p(t')p^*(t+t')]$ is the autocorrelation function of the pulse envelope $p(t)$ defined here as an expectation. Since $p(t)$ is deterministic, $R_{pp}(t)$ is evaluated as a time integral. The output reaches a peak magnitude at $t = t'' + t'$. The term t'' is usually applied as a correction to offset the delays in the transmitter and the receiver. Therefore replacing t by $t-t''$, equation (3) is modified to

$$z_s(t) = \sigma\beta \, \alpha(r') R_{pp}(t'-t) \exp(-\iota 2\pi f_o[t'-t]) \qquad (4)$$

and the output reaches a peak at $t = t'$, the range delay corresponding to the target. It should be noted that errors in delay correction t'' can produce

uncertainties in both the range r' and in the estimated target cross-section σ. The noise component $z_n(t)$ has a *psd* $N_o = \beta^2 N_n |H_m(f)|^2$ over the receiver bandwidth B. Since the receiver impulse response is matched to p(t), the receiver bandwidth has a nominal value $B \sim (1/T_p)$.

For a point target at an initial range r_i moving with a finite speed or range rate $v_i = dr_i'/dt$, the range r_i' and range delay t_i' increase linearly with time as $r_i' = r_i + v_i t$ and $t_i' = 2(r_i + v_i t)/c = t_i + (2v_i/c)t$. If the target speed v_i is small, then the term $\alpha(r_i')$ can be replaced by $\alpha(r_i)$ and $R_{pp}(t_i'-t)$ by $R_{pp}(t_i-t)$. The phase term is modified, however, and equation (4) becomes

$$z_s(t) = \sigma\beta \, \alpha(r_i) \, R_{pp}(t_i-t) \, \exp(-\imath 2\pi f_o[t_i-t]) \, \exp(-\imath 2\pi f_o[2v_i/c]t) \qquad (5)$$

where $f_o(2v_i/c) = F_i$ is the Doppler shift due to the point target. Since the target speed v_i is not known in advance, it is not possible to design a single matched filter to estimate the Doppler shift F_i. The transmitter is excited, however, by a periodic impulse train of the form $\Sigma_k \delta(t-kT_I)$ of period T_I. It is possible, therefore, to apply successive samples $z_s[k] = z_s(t-kT_I)$ to a bank of narrow-band filters, in lieu of a matched filter, for optimal detection of the Doppler shifted signal. This is readily accomplished by subjecting blocks of these samples to spectral analysis, which yields the time-averaged *psd* in terms of Fourier transform $Z_s(f)$ of $z_s(t)$

$$P_s[m] = \langle Z_s[m] \, Z_s^*[m]\rangle \qquad (6)$$

as a function of the frequency index m as discussed further in section 5. The angular brackets <> denote time averaging.

The atmospheric medium contains a continuum of irregularities. A full analysis of radio-wave scattering from such media may be found e.g. in Booker (1956), Tatarski (1971), and Monin and Yaglom (1975) and is required for estimation of turbulence parameters. For illustrating the signal-processing aspects, however, it suffices to regard the medium as a collection of many point targets. The received signal at a range delay $t_o = 2r_o/c$ is then

$$z_s(t_o) = \sum_i \{\sigma\beta \, \alpha(r_i) \, R_{pp}(t_i-t_o)\} \, \exp(-\imath 2\pi f_o[t_i-t_o]) \, \exp(-\imath 2\pi f_o[2v_i/c]t_o) \qquad (7)$$

Only the point targets near range r_o, with range delay within the correlation time of the pulse envelope p(t), weighted by R_{pp} and the slowly changing function α, contribute to the signal $z_s(t_o)$. Each term in equation (7) may be represented in an Argand diagram at frequency f_o, as a phasor with distinctly

identifiable amplitude, phase, and rotation frequency (the Doppler shift F_i). For targets that are spaced $\lambda_o/2$ apart in range, the phasors are in phase and their contributions to $z_s(t_o)$ add constructively. The radar thus acts as a spatial filter on refractive-index fluctuations in the medium, and is sensitive primarily to fluctuations at the Bragg scale [$\lambda_o/2$] along the radar axis. Contributions from targets on thin sheets transverse to the radar axis also add constructively within a Fresnel zone of the antenna radiation pattern. These target configurations produce coherent, aspect sensitive signals frequently observed at near vertical incidence [Röttger and Liu, 1978; Rastogi and Röttger, 1982; Woodman and Chu, 1989].

For arbitrary configurations of a large number of point targets, the sum $z_s(t_o)$ of phasors in equation (7) approaches Gaussian statistics due to central limit theorem [see e.g. Papoulis, 1984]. If the target velocities v_i have a mean value v_o and a standard deviation σ_v, then once again by the central limit theorem, the *psd* of $z_s(t_o)$ defined in equation (6) tends to a Gaussian shape with parameters related to v_o and σ_v.

The net receiver output $z(t_o)$ at a range delay $t_o=2r_o/c$ may then be expressed as the sum of an atmospheric component z_s, noise z_n, ground clutter z_g, and interference z_i as

$$z(t_o) = \{\xi_s(t_o) + \iota\,\eta_s(t_o)\}\,\exp(-\iota 2\pi f_o[2v_o/c]t) + z_n(t_o) + z_g(t_o) + z_i(t_o) \quad (8)$$

The complex low-pass random process $\zeta_s(t_o)= \xi_s(t_o)+\iota\eta_s(t_o)$ is related to the characteristics of turbulence at range r_o through physical models, and to radar parameters. The noise component is due to an effective system noise temperature θ_s. In VHF radars the average θ_s is ~290 λ_o^2 K (with λ_o in meters) due primarily to cosmic noise, but at UHF it is of the order of ~200 K or less. The total noise power is of the order of $\beta^2 k_B \theta_s B$ where k_B is the Boltzmann's constant. The ground clutter is due to a slowly varying phase component from refraction along multiple paths to terrain through the antenna sidelobes. The fading rate of ground clutter is negligible at VHF, but significantly (~10 times) larger at UHF. Detection of Doppler shifted signal components in the presence of strong, fading ground clutter poses some difficulties as discussed in Section 5. Interference from inadvertent transmitters in the receiver passband B about the radar frequency f_o is usually unavoidable. Methods for removing interference in postprocessing of *psd* estimates are discussed in Section 6.

The range resolution is obviously limited by the correlation width of the pulse envelope $p(t)$ and is of the order of $cT_p/2$. The requirements on signal

detectability and range resolution are contradictory. To detect the weak atmospheric component $z_s(t_o)$ in the presence of unwanted components in equation (8), the transmitted signal duration T_p should be as large as possible within the peak and average power limitations of the transmitter. This is possible only by increasing T_p, but thereby impairing the range resolution. The range resolution can be improved by imposing a noise-like phase modulation on the transmitted pulse, derived in practice from low autocorrelation binary sequences or codes. If the pulse envelope is phase modulated at subintervals T_b then the receiver bandwidth B should be augmented to $1/T_b$. The structure of the optimum receiver is now modified at the point a in Figure 1, and is illustrated in Figure 2. To permit flexibility in the use of phase-coded pulses, the optimum receiver is implemented as a correlation receiver, in which the range gated receiver output is cross-correlated with delayed replicas of the transmitted code. It is possible, even advantageous, to use different codes A,B,C... etc. and to accumulate the decoded signal for these. The use of phase codes and decoding in middle atmosphere radar experiments followed their use in incoherent-scatter studies [Ioannidis and Farley, 1972; Schmidt et al. 1979; Woodman, 1980]. Signal coding and decoding methods are discussed further in Section 4.

In summary, we note that the signal processing methods used with middle atmospheric radars attempt to optimize the detection of weak Doppler shifted signals from thin sections of the atmosphere, with additive white Gaussian noise. The optimization is attained in successive stages making use of matched-filter, correlation-receiver, and filter-bank structures.
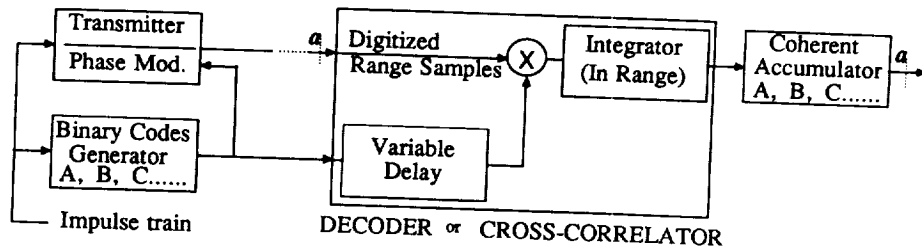
FIGURE 2. Block diagram of a high-resolution radar experiment using phase modulation with low-autocorrelation binary sequences. The optimum receiver for phase modulated signals is implemented as a correlator which precedes the coherent integration block at point a in Figure 1. With complementary code pairs, it is often possible to switch the order of coherent accumulation and decoding.

3. SAMPLING AND COHERENT INTEGRATION

The receiver output $z(t)$ in pulsed Doppler radar experiments is a complex random process, sampled at several disparate time scales. In simple radar experiments, the smallest time scale is the pulse width T_p. The range sampling interval T_r is comparable to T_p. The modulated pulses are transmitted at a pulse-repetition interval T_I. In high-resolution experiments with phase coding and decoding, the pulse is also phase modulated at regular subintervals T_b, called the baudlength. A suitable value for T_r is then T_b. These time scales and their typical values are shown in Table 1.

TABLE 1 : Typical Time Scales in Middle Atmosphere Radar Experiments

Time scale	Simple Experiment	Coded Pulse Experiment
Baud Length		1 us
Pulse length	10 us	32 us*
Range Sampling Int.	10 us	1 us
Inter Pulse Period	1 ms	1 ms

*for 32-bit codes. 1 ms = 0.001 second. 1 us = 0.001 ms.

The sampled signal $z[j,i]$ depends on the range index j, and the pulse index i. The sample time for these indices is given by $t=(i-1)T_I + t_{min}+(j-1)T_r$, where t_{min} is the minimum range delay. In simple radar experiments, samples $z_j[i]$ for a given range index j are available at interpulse period T_I. The corresponding Nyquist frequency interval of $\pm(2T_I)^{-1}$ is usually many times larger than the maximum expected Doppler shift of atmospheric signal component $z_s(t)$.

Coherent integration provides a computationally effective means of shortening the Nyquist frequency interval so that it is better matched to the expected Doppler shifts, and for reducing the data rate. It comprises two steps. First, a moving sum of $z_j[i]$ is obtained by accumulating or integrating it over I samples. Next, the moving sum $u_j[i]$ is re-sampled every I^{th} point to obtain the coherently-integrated samples $u_j[k]$ with time spacing $T=IT_I$. The moving sum

$$u_j[i] = T_I \{z_j[i] + z_j[i-1] + z_j[i-2] + \ldots + z_j[i-I+1] \} \tag{9}$$

is efficiently computed through the recursion $u_j[i] = u_j[i-1] + z_j[i]$, with the initial condition $u_j[0]=0$, executed I times. The final result is optionally scaled by T_I. The moving-sum operation is equivalent to applying a filter with the frequency response

$$H(f) = \frac{U_j(f)}{Z_j(f)} = T_I \{1 + e^{-\iota 2\pi f T_I} + e^{-\iota 2\pi f 2 T_I} + \ldots + e^{-\iota 2\pi f [I-1] T_I} \} \tag{10}$$

to the samples $z_j[i]$. Summation of the series in equation (7) gives

$$H(f) = e^{-\iota 2\pi f [I-1] T_I} \cdot T_I \frac{\sin(\pi f I T_I)}{\sin(\pi f T_I)} \tag{11}$$

and involves the Dirichlet kernel. The re-sampling operation implies a new Nyquist frequency interval of $\pm(2T)^{-1}$ which is I times narrower. The response $|H(f)|^2$, which shapes the *psd*, approximates a crude low-pass filter. It falls off by ~4 dB near the edges of the Nyquist interval [Rastogi, 1983b]. The signal power for echoes with large Doppler-shifts should be corrected for this fall off. Frequency components outside the Nyquist interval $\pm(2T)^{-1}$ are weighted in power by $|H(f)|^2$ and aliased or folded back into it. Since $|H(f)|^2$ is periodic, signal components with an unexpectedly large Doppler shift, e.g. from an aircraft, are not always completely rejected in coherent-integration.

It is instructive to examine the effect of coherent integration on noise. For convenience the multiplier T_I in equation (9) is taken as unity. The received signal $z(t)$ is merely the sum of $z_s(t)$ and noise $z_n(t)$ in the absence of other components. The noise $z_n(t)$ is originally bandlimited by the receiver bandwidth B, matched to $(T_p)^{-1}$ or $(T_b)^{-1}$, whichever is larger. On sampling at the pulse repetition interval T_I, $z_n(t)$ is aliased many times over into the Nyquist interval $\pm(2T_I)^{-1}$, but the total noise power is unaltered. After coherent integration over I samples and resampling, the noise power increases I-fold, and the Nyquist interval becomes $\pm(2T)^{-1}$. A consequence of this two-fold aliasing is to whiten the noise *psd*, even if it is originally nonwhite. Alternatively, if we regard the well-correlated signal $z_s(t)$ as a constant s, and $z_n(t)$ as a zero mean process with variance σ^2, then the pre-integration *snr* in samples of $z(t)$ is s^2/σ^2. When I samples of $z(t)$ are integrated, the noise variance becomes $I\sigma^2$ and signal power is $(Is)^2$. Hence the post-integration *snr*, Is^2/σ^2, is improved by a factor I. It should be stressed that this does not imply improved detectability of spectral peaks,

barely above the noise level, in the Nyquist window $\pm(2T)^{-1}$. This is because the *psd* of *both* the noise and signal components is amplified by the same factor $|H(f)|^2$.

The simplest modification to coherent-integration is the use of a constant $\mu<1$ in the recursion $u_j[i] = u_j[i-1]+\mu z_j[i]$. Then

$$u_j[i] = T_I \{z_j[i] + \mu z_j[i-1] + \mu^2 z_j[i-2] + \ldots + \mu^{I-1} z_j[i-I+1] \} \qquad (12)$$

The frequency response H(f) can be readily shown to be

$$H(f) = e^{-\pi(I-1)\nu T_I} \cdot e^{-\iota \pi f(I-1)f T_I} \cdot T_I \cdot \frac{\sinh(\pi I T_I[\nu+jf])}{\sinh(\pi T_I[\nu+jf])} \qquad (13)$$

where $\nu = -\ln(\mu)/2\pi$ has been introduced for simplicity. The modified filter obtains sum over past samples with exponentially decaying weights. By selecting a large I, and a suitable value of μ, a sufficiently narrow filter response is obtained which may be useful in estimating the ground-clutter component. Otherwise, the response is slightly modified from the $\mu=1$ case.

Any further improvement in the frequency response $|H(f)|^2$ would require filtering of past samples stored in a pipeline or buffer. This adds considerably to on-line computing requirements. An interesting alternative is provided through a bank of identical analog low-pass filters, which do not suffer from aliasing [Clark and Green, 1988].

For a radar pointed at 15° from zenith, and maximum horizontal wind of 70 m/s, the maximum Doppler shift is ~6.7 Hz at VHF and ~57.3 Hz at UHF. Only a fraction of the available Nyquist frequency interval of ± 500 Hz for $T_I=1$ ms contains useful information about atmospheric motions. Suitable values of I are then 75 for VHF, and 8 for UHF.

4. SIGNAL CODING AND DECODING

The detectability of point targets is optimized when the receiver impulse response is matched to the transmitted pulse shape p(t) at the radar frequency f_o. The signal at receiver output is the same as the *acf* $R_{pp}(\tau)$ of p(t), except for a scaling factor. For simple pulse shapes, the range resolution Δr in often set by the pulse width T_p as $\Delta r \sim cT_p/2$. To map the structure of an extended target, it is desirable to keep T_p small. Yet, detectability of weak targets is

improved by keeping T_p as large as possible within the peak and average power limitations of the radar transmitter. These requirements for outlining the structure of weak extended targets are contradictory.

The point-target case suggests, however, that the range resolution can be improved by using a noise-like pulse envelope p(t) so that $R_{pp}(\tau)$ approaches an impulse. The problems to be circumvented in this approach are twofold. First, the transmitter power, hence the amplitude of p(t), should be kept nearly constant over its duration T_p. This necessitates the use of phase modulation. Second, the phase modulating signal is limited in duration by T_p, and to avoid complexity in the receiver only a few phase levels should be allowed. These considerations have led to the use of short binary sequences or codes with an impulse-like autocorrelation function [Turyn, 1968] for phase modulation of the transmitted pulse. The improved resolution in range is obtained only with the use of a matched filter, i.e. after the receiver output is cross-correlated or decoded with the modulating sequence. Phase coded binary sequences were first introduced in atmospheric radar applications for D-region electron density measurements at Arecibo [Ioanniddis and Farley, 1974]. More sophisticated codes were later used with MST radars [Schmidt et al. 1979; Woodman, 1980, Sulzer and Woodman, 1984].

A single amplitude and phase modulated pulse at the radar frequency f_o in response to an impulse $\delta(t)$ may be expressed as $p(t) \exp\{\imath \phi(t)\} \exp\{\imath 2\pi f_o t\}$ where the modulating terms p(t) and $\phi(t)$ are of duration T_p. The interval T_p is subdivided into K smaller subintervals or bauds of duration T_b. The phase term $\phi(t)$ is derived from a K-bit binary sequence $\{b_k\}$. Over each baud, the transmitter phase is shifted by 0°/180° or by ±90° depending e.g. on whether b_k and b_{k-1} are same or different. The receiver bandwidth B must now be at least as wide as $1/T_b$. The receiver output is sampled in time at intervals T_b, and is cross correlated or decoded with the sequence $\{b_k\}$. The cross-correlator output closely resembles the acf of the sequence $\{b_k\}$. For suitable binary sequences, the autocorrelation function $R_b[k']$ should approximate an impulse in that $R_b[0]=K$ and $|R_b[k']|\sim 0$ for $k'\neq 0$. Such sequences are called low autocorrelation binary sequences. The effective resolution in range is then $\sim cT_b/2$. This entire set of operations is repeated at the pulse repetition interval T_I. It is often advantageous to use different binary sequences for encoding successive pulses as elaborated later. The effect of finite receiver bandwidth is to introduce a small delay and loss in the decoder, which must be corrected for after decoding. Table 2 shows some of the simpler codes that have been used with middle-atmosphere radars.

TABLE 2 : Low Autocorrelation Binary Code Sequences For Radar Applications

Barker	2	++	or	+-
	3	++-		
	4	++-+	or	+++-
	5	+++-+		
	7	+++--+-		
	11	+++---+--+-		
	13	+++++--++-+-+		

Complementary	2	++	
		+-	
	4	+++-	
		++-+	
	8	+++-++-+	
		+++---+-	
	16	+++-++-+++----+-	
		+++-++-+---+++-+	
	32	+++-++-++++---+-+++-++-+---+++-+	(32A)
		+++-++-++++---+----+---+-+++----+-	(32B)

acf(32A):32-1 0-1 0-5 0+3 0+3 0+3 0+7 0-1 0-3 0+5 0+1 0+1 0-3 0+5 0+1 0+1
acf(32B):32+1 0+1 0+5 0-3 0-3 0-3 0-7 0+1 0+3 0-5 0-1 0-1 0+3 0-5 0-1 0-1

A familiar example of low-autocorrelation binary sequences is the set of Barker codes with the property that $|R_b[k']| \leq 1$ for $k' \neq 0$. Barker sequences are known only for lengths $K=2,3,4,5,7,11$ and 13 [see e.g. Cooke and Bernfeld, 1967]. There are strong reasons to believe that Barker sequences do not exist for $K>13$ [Turyn, 1968]. The highest correlation sidelobes ($k' \neq 0$) for the length-13 Barker code are 22.2 dB below $R_b(0)$. This sidelobe level can be reduced to -43.8 dB with a 3-term inverse digital filter [Rihaczek and Golden, 1970].

Pairs of binary sequences $A=\{a_k\}$ and $B=\{b_k\}$ are known with the complementary property that

$$R_a[0] + R_b[0]=2K, \text{ and } R_a[k'] + R_b[k']=0 \text{ for } k' \neq 0,$$

i.e. the sum of their autocorrelations exactly cancels out for non-zero lags [Golay, 1961]. The complementary property can be extended also to sets of binary sequences [Tseng and Liu,1972]. While complementary code pairs and sets attain the ideal autocorrelation properties of white noise with short binary sequences, it should be noted that the net zero correlation for $k' \neq 0$ is

obtained by cancellation of two or more usually large values. This can be seen for the 32-bit complementary pair in Table 2. For realistic radars with weak system nonlinearities and for a moving medium, the cancellation is far from perfect.

If the atmospheric medium does not change significantly within an interpulse period T_I, then complementary code pairs can provide near ideal high-resolution performance. Indeed, the fading time of middle-atmosphere radar signals is usually very much larger than T_I. In situations where radar signals are coherently integrated over a duration IT_I, it is possible to interchange the order in which decoding and coherent integration are performed with a very substantial reduction in the amount of on-line computations [Woodman, 1980]. Thus instead of transmitting I pulses coded according to the sequence ABAB.. with pulse by pulse decoding and integration of the receiver output, pulses coded with the sequence AAA...BBB.. may be used. The receiver output is coherently integrated over the subsequences AAA..., and BBB..., and then decoded. This results in an ~I/2 fold saving in computations for decoding, but it is necessary to assume that the medium is stationary for the entire duration IT_I. Otherwise, cancellation of autocorrelation values for $k' \neq 0$ is not perfect. For acceptable performance it is desirable to keep the phase shift $2\pi[2v_o/\lambda_o] IT_I < 1$ radian due to an atmospheric velocity v_o. This condition is clearly violated for $v_o \sim 2$-3 m/s or larger. Effectively, then only a part of the sequence AAA...BBB.. contributes to the cancellation of net $\Sigma R(k')$ for $k' \neq 0$. For moving media, the performance of coding and decoding schemes should be examined through the fine structure of the range-Doppler ambiguity function at small Doppler shifts [Rihaczek, 1969].

Sets of low-autocorrelation binary sequences selected at random, offer the possibility that in their net *acf* $\Sigma R(k')$, accumulated across the set, the sidelobes for $k' \neq 0$ will tend to cancel out. These quasicomplementary code sets (*qccs*) were introduced by Sulzer and Woodman (1984), who found that 32-bit *qccs* obtained by an extensive partial computer search perform better than complementary pairs, especially for non-linear transmitters. An exhaustive search has been made for 32-bit *qccs* with near optimum correlation properties [Rastogi and Sobolewski, 1988]. The fine structure of range-Doppler ambiguity function for these and several other codes has also been examined.

Pulse-by-pulse decoding is mandatory for *qccs*, and is also desirable for complementary code pairs. In a typical experiment with 256 range cells, and 32-bit codes, nearly 16,384 multiply-add operations are required per ms for pulse-by-pulse decoding. Multiplications between digitized multibit samples

and the binary code sequence (±1) can be reduced to additions and subtractions only. This requires an addition cycle time in the processor of ~61 ns, possibly less. For this reason, pulse-by-pulse decoding is currently available only at some installations.

5. SPECTRUM ANALYSIS AND PARAMETER ESTIMATION

In the final stage of signal analysis in middle-atmosphere radar experiments, coherently-integrated and decoded samples of the receiver output $z(t)$ are passed through a bank of narrow-band filters to detect the Doppler-shifted signal component and to estimate its parameters. The filter bank is usually implemented through spectral analysis. Signal parameters are estimated as the low-order spectral moments of $z(t)$, which yield the signal power, radial velocity (v) and its spread (σ_v). Spectral analysis of inferred velocity (v) time series is also useful in studies of gravity-wave phenomena. Often the *psd* of velocity time-series follows a power-law shape with $S_v(f) \sim f^{-\gamma}$. Then the spectral index γ is the parameter of interest.

The random signal or process $z(t)$ is assumed zero-mean, statistically stationary, and ergodic [see e.g. Papoulis, 1984] with a signal power or variance $p_z = R_z(0)$ and *acf*

$$R_z(\tau) = E[z(t) \, z^*(t+\tau)] \tag{14}$$

where E denotes the expectation operation. The *psd* of $z(t)$ is obtained from the Wiener-Khinchin theorem as

$$S_z(f) = \Im\{R_z(\tau)\} \tag{15}$$

where $\Im$ is the Fourier transform (*FT*). The *psd* denotes the distribution of signal power with frequency f. The *FT* $Z_D(f)$ of a truncated realization of $z_D(t)$ that vanishes outside $\pm D/2$ is similarly defined. The *psd* $S_z(f)$ can be related to the *FT* $Z_D(f)$ through

$$S_z(f) = E\left\{ \lim_{D \to \infty} \frac{1}{D} |Z_D(f)|^2 \right\} \tag{16}$$

The quantity $P(f) = |Z_D(f)|^2/D$ is called the periodogram. The expectation in equation (16) may be evaluated, by ergodicity, as a time average. Thus the *psd* may also be obtained as the time averaged periodogram [Marple, 1987], provided that D is large compared to time scales of fluctuations in $z(t)$.

Only discrete-time samples z[k]=z(kT) of the process z(t) are available with a sampling interval T. This limits the maximum frequency to the Nyquist value $f_N=(1/2T)$. For sampled signals, the *FT* is replaced by its discrete version (*DFT*). The *DFT* Z[m] of a block of N samples of z[k] is evaluated at N equispaced frequency points in the Nyquist interval $\pm f_N$, or $[0,2f_N)$. The *DFT* pair is defined as [see e.g. Brigham, 1988; Marple, 1987]

$$Z[m] = DFT\{z[k]\} = \sum_{k=0}^{N-1} z[k]\, e^{-\iota\, 2\pi km/N} \text{ for } m=0,1..(N-1) \qquad (17)$$

$$z[k] = IDFT\{Z[m]\} = \frac{1}{N}\sum_{k=0}^{N-1} Z[m]]\, e^{+\iota\, 2\pi km/N} \text{ for } k=0,1..(N-1) \qquad (18)$$

These definitions show that both z[k] and Z[m] have a period N. The discrete time analog of the periodogram is then

$$P_z[m] = \frac{1}{N}\{\, |Z[m]|^2\} \qquad (19)$$

and the *psd* $S_z(f)$ is evaluated by time averaging of the N-point periodograms over M blocks. This is usually the preferred method of psd estimation as the *DFT* can be quite efficiently evaluated with the fast Fourier transform (*FFT*) algorithms. Some caution is warranted, however, in the use of this method as elaborated below.

The statistical uncertainty or standard deviation σ_P, and the average value μ_P, of the periodogram $P_z[m]$ are usually comparable. Moreover, the effect of finite block length is to smear the periodogram values with the squared Dirichlet kernel $\sin^2(\pi fTN)/\sin^2(\pi fT)$. The contribution of a sampled-frequency component at other sampled frequency points is thus nearly zero if z(t) is a noise-like process. Then adjacent value of $P_z[m]$ are nearly uncorrelated. This gives a very jagged appearance to the periodogram [see e.g. Marple, 1987]. For a Gaussian noise process of total power $p_z=\sigma^2$, the periodogram values $P_z[m]$ have a χ_2^2 statistics with $\mu_P=\sigma_P\sim\sigma^2/T$. It follows that after averaging over M periodograms, the periodogram is smoother and its standard deviation is reduced by a factor $\sqrt{M}$. Even for values of M as small as 6, the averaged periodogram approaches a Gaussian statistics with mean σ^2/T and standard deviation $\sigma^2/T\sqrt{M}$. The chance of observing a periodogram value exceeding $\alpha\sigma^2/T$ may then be obtained as

$$Prob\ [P_z[m] > \frac{\alpha\sigma^2}{T}] < erfc([\alpha-1]\sqrt{M}) \qquad (20)$$

For example, the probability that a periodogram value at least 1.5 times larger than the average will be observed after averaging over 16 realizations is less than 0.5-erf(2)=0.023. This inequality is very useful for specifying a threshold criterion for detectability of Doppler-shifted signal peaks over a noise background in *psd* estimates.

The consequence of smoothing by the squared Dirichlet kernel is conspicuous for a frequency component f' not exactly at the sampled DFT frequencies m/NT. The contribution at a frequency f'' is weighted by

$$sin^2(\pi[f''-f']TN)/sin^2(\pi[f''-f']T)$$

and falls-off as $\sim[f''-f']^{-2}$ at frequencies far removed from f'. This effect is most serious for signals with a strong unresolved low-frequency component, with f'<1/NT. Examples include signals z(t) containing a strong slowly-fading ground clutter component, or velocity time series v(t) with a power-law *psd* of the form $\sim f^{-\gamma}$. In both cases, the assumption of a stationary random process is invalid. This conclusion is justified below from two other viewpoints.

An *acf* estimate $R_\Delta[k]$ can be obtained directly from a block of N samples of z[k]. $R_\Delta[k]$ has triangular weights at the [2N-1] lags between $\pm(N-1)T$. The N-point *IDFT* $R_P[k]$ of the periodogram $P_z[m]$ is not usually a valid *acf* estimate. It is possible, however, to obtain $R_P[k]$ as an N-point aliased version of $R_\Delta[k]$. Only when $R_\Delta[k]$ is uncorrelated beyond $\sim N/2$ points, is it possible to recover it from the N-point periodogram. Otherwise, to obtain $R_\Delta[k]$ unambiguously, it becomes necessary to augment the block size to 2N points, by adding N zeros to z[k], and then taking a 2N-point periodogram. Thus, in presence of components of period exceeding the block length N, the standard N-point periodogram does not yield an acceptable *psd* estimate.

An unresolved low-frequency component produces a large disparity between z[0] and z[N-1]. In view of the N-point periodicity of z[k], this disparity is equivalent to a step-like discontinuity in the time series. The frequency response of this discontinuity in the *psd* estimate is $\sim f^{-2}$. This explains the Lorenzian *psd* shape of the ground-clutter component, and at least some velocity 'observations' with a spectral index $\gamma\sim2$.

The simplest method for reducing the effect of a nonstationary component is to use the largest possible value of the block-size N and to multiply the samples z(k) with a data window w[k] which smoothly decays to zero at the end points. The effect of applying the data window is to reduce the step-like discontinuity at the two end points, i.e. to render the data nearly stationary. The frequency response $|W[m]|^2$ of the data window should decay much more steeply than $\sim f^{-2}$. Since the data window weights the central part of a block more heavily, successive blocks may be allowed to overlap. The most useful data windows in this context are the triangular or Bartlett window, von-Hann window, windows with power-law response derived from the modified Blackman window, or the near-optimal windows such as the Dolph-Chebychev and Kaiser-Bessel windows [Blackman and Tukey, 1958; Harris, 1978, Marple, 1987]. Selection of a good data window, and its use, is an important and necessary step in spectral analysis of signals with ground clutter, and of velocity data with power-law *psd*. There is a small overhead in computational effort, but it obviates round-about corrective measures in later stages of data analysis. Alternatively, the nonstationary trends must be estimated and removed from the time series before spectral analysis. A simple method of estimating trends is by the running median over blocks of N points [see Section 7]. This method is useful for long time series of prestored data. Care must also be exercised in treating end effects. Other algorithms for trend identification and removal may be found, e.g., in Gottman(1981).

We now briefly mention alternatives to classical spectral analysis that are based on a model representation of the time series [see e.g. Marple, 1987]. The coefficients h[k] of a feedback filter excited by white noise n[k] of variance σ^2 are sought such that the filter output is the random process z[k]. In the autoregressive moving average (*ARMA*) model, z[k] is obtained as a linear sum of the current input, q past inputs weighted by coefficients b_j for j=1,2..q, and p past outputs weighted by coefficients a_i for i=1,2..p. For this *ARMA*(p,q) model, the *psd* $S_z(f)$ may be represented as

$$S_z(f) = \sigma^2 T \frac{|B(f)|^2}{|A(f)|^2} \tag{21}$$

where the polynomials A and B have p and q zeros. These polynomials are simply related to the coefficients a_i and b_i. The *ARMA*(p,q) model thus represents the *psd* $S_z(f)$ using q zeros and p poles. The *AR* model is suitable for representing a *psd* with sharp peaks, and *MA* model for representing a *psd* with flat peaks. It is possible to overdefine an *ARMA*(p,q) process and represent it in an AR(p') or MA(q') model with p'>>p and q'>>q. Whereas

we expect the ground clutter component $z_g(t)$ to have an *AR* representation with q'=1 or 2, and the Doppler shifted signal component $z_g(t)$ to have a *MA* representation, it is also possible to model the total signal z(t) as an *AR*(p) process with several poles. The coefficients a_i, (p+1) *acf* values of the process z[k], and the noise variance σ^2, are related through the linear Yule-Walker equations. These equations can be solved for the coefficients a_i using a recursive algorithm due to Levinson [see e.g. Marple, 1987; Press et al. 1986]. Thus the *psd* $S_z(f)$ of an *AR*(p) process is completely defined from (p+1) *acf* values. The use of discrete form of the Wiener-Khinchin theorem, through equation (15), would have required *acf* values at <u>all</u> lags. The order p for the *AR*(p) model must be found by separate analysis.

When observations of a process z(t) are limited to an interval (0,T), classical spectral analysis methods unrealistically assume it to be zero or periodic outside the observation interval. Natural extensions of z(t) outside the interval (0,T) may be sought consistent with maximizing its entropy rate. With the process z(t) thus extended, it is possible to obtain high-resolution *psd* estimates from short data sequences. The details of this method due to Burg may be found in appendices in Haykin (1986) and Robinson and Treitel (1980), and algorithms in Marple (1987). The maximum entropy method (*MEM*) is closely related to the *AR* model for a Gaussian process.

The *MEM* and *AR* model have, so far, found limited application in the analysis of middle atmosphere radar signals and data. One basic problem is that the order p of the *AR* model must be found empirically for time-series of interest. Klostermeyer (1986,1989) has used *MEM* *psd* estimates of coherently-inetgrated ST data from the Sousy VHF radar to find the Doppler shift and spread at low to moderate *snr*. It is found that these quantities are estimated with better accuracies using *MEM*.

The normalized *psd* $s_z(f)=S_z(f)/p_z$ satisfies all the properties of a probability density function (*pdf*). The mean μ_{z1} and variance μ_{z2} of this *pdf* are the first and second spectral moments of z(t). The zeroth-order spectral moment μ_{z0} of z(t) is then simply the area under $S_z(f)$, or the signal power p_z. If z(t) contains only the atmospheric component, then the first and second spectral moments are related to the radial velocity v and its spread σ_v through

$$\mu_{z1} = \frac{1}{p_z} \int_{-\infty}^{+\infty} f\, S_z(f)\, df = \frac{v}{[\lambda_o/2]} \tag{22}$$

$$\mu_{z2} = \frac{1}{P_z} \int_{-\infty}^{+\infty} [f - \mu_{z1}]^2 \, S_z(f) \, df = \frac{\sigma_v^2}{[\lambda_o/2]^2} \tag{23}$$

The *psd* $S_z(f)$ is fully characterized by the spectral moments $\mu_{zo}, \mu_{z1}, \mu_{z2}$ if it has a single Gaussian peak. The effect of additive white noise $z_n(t)$ is to add a platform to $S_z(f)$. The fading ground clutter $z_c(t)$ produces a smeared Lorenzian peak at $f \sim 0$, as discussed earlier. Corrections should be applied either to the *psd* estimate or to the spectral moments to remove the effect of these undesired components.

Just as the moments of a random variable are related to the derivatives of its characteristic function at the origin [Papoulis, 1984], the spectral moments can be obtained directly and efficiently from *acf* estimates at just one or two lags. This method was used in the first middle-atmosphere radar experiments at Jicamarca [Woodman and Guillén, 1974]. Statistical errors in the *acf* method of spectral moment estimation have been given by Miller and Rochwarger (1972) and Woodman (1985).

In as much as each spectral component in the N-point *psd* estimate $S_z[m]$ can be characterized by a few parameters related to its spectral moments, the entire *psd* can be described by a model or transformation M with a J-point parameter vector p. For each value p of the J-point parameter vector, the model output $M(p)$ is an N-point *psd* vector S. The problem of *psd* parameter estimation may be rephrased as : Given an observed N-point *psd* vector S_o, find a J-point parameter vector p_o such that the N-point vector $M(p_o)$ is as close as possible to S_o. The parameter vector p_o should be such that the mean square value of the N-point error vector $\varepsilon(p_o) = S_o - M(p_o)$, or $e^2(p_o) = \varepsilon(p_o).\varepsilon(p_o)$, is minimum. Ideally, a global minimum in the error surface $e^2(p_o)$ is sought. An exhaustive search is hopeless for two reasons. First, we note that even for only ten parameters and ten possible values for each parameter, the parameter space has 10^{10} points. Second, the error surface $e^2(p)$ is a nonlinear function of p. The problem is solvable, however, if a reasonably good initial guess p' of p_o is available, the error surface is smooth, and a local minimum in the vicinity of p' is acceptable. It is possible then to vary p' in small steps towards the local minimum, e.g. along the path of steepest local gradient. Only a local approximation to the error surface is needed at each step. Note that the model M can be as sophisticated as desired. Details of adaptive methods available for solving this problem may be found e.g. in Widrow and Stearns (1985), Alexander (1986), and Stearns (1988). Algorithms and subprograms are available in Press et al. (1986), and Stearns and David (1988).

Sato and Woodman (1982) have used a matrix form of the least mean-square (*lms*) error method to estimate the parameter vector **p** from the observed *psd* vector **S**. The parameter vector **p** specifies the shape of the Lorenzian ground clutter, one or two Gaussian Doppler-shifted signal peaks, and a flat noise platform. The model **M(p)** gives the *acf* estimate, including aliasing artifacts with the use of periodogram. The *DFT* of **S** is then compared with the model **M(p)** to find the squared error $e^2(p)$. Linearization of the model output **M(p)** about an initial estimate of **p** can be used to solve *exactly* for the increment δp required to minimize $e^2(p)$. This step is iterated with the new parameter value $p+\delta p$, until either $e^2(p)$ stabilizes or is sufficiently small. Additional comments on the *lms* method may be found in Woodman (1975). It has been extensively used for parametrizing UHF radar data at Arecibo. The *lms* method is extremely computation intensive. The only caveat in its use is that, unlike incoherent-scattering from the ionosphere, the model **M(p)** lacks a sound theoretical basis.

6. DATA EDITING AND INTERFERENCE SUPPRESSION

Sampled time series $z[k]$ of experimental data are often contaminated with outliers or bad data points that do not belong with the rest. A similar problem arises in *psd* estimation of radar signals in the presence of radio interference localized in time and/or frequency. There is usually insufficient information on outlier statistics and their occurrence. The only justifiable criteria for detecting relatively sparse outliers are, (i) outliers deviate substantially from the local statistics, and (ii) their value(s) violate some underlying physical model. All outlier detection schemes erroneously reject some good data points and accept some bad ones. The probability of these errors should be small for a good scheme. The situation is quite similar to communication in a noisy environment [Wozencraft and Jacobs, 1965]. Statistically rigorous methods for treatment of outliers may be found in David(1970), Tukey (1977), and Barnett and Lewis (1978). A simple algorithm based on order statistics is outlined below.

To decide whether a data point $z[k]$ is an outlier, N samples in the vicinity of the index k are examined. These samples are first sorted by their value in an ascending or a descending order. Nx values at the top and Nx values at the bottom of this list are excluded, for some x<<1. The sample mean m_z and sample variance s_z^2 are found from the remaining $N(1-2x)$ points in between. Now a quantity y is selected such that the probability that a sample value lies outside $(m_z \pm y s_z)$ is less than $(1/N)$. The point $z[k]$ is classified as an outlier if it falls outside $(m_z \pm y s_z)$. The choice of y is best illustrated with an example.

Suppose N=16, and x=0.125. Then m_z and s_z are found from 12 samples, by excluding the two highest and the two lowest values. The distribution of z[k] is unknown. Use of distribution-independent Tchebycheff inequality [see e.g. Papoulis, 1984] gives y as $\sqrt{N}=4$ or more. This is a stringent criterion for detecting outliers. On the other hand, for a Gaussian distribution of z[k] tables of error function indicate that y should be ~1.9 or more. A value of y near 2.5 may be quite suitable, but its validity should be checked with a visual inspection of the time series and detected outliers. Exploratory data analysis with several values of parameters N, x and y, using real and simulated data, is often required. This method has been successfully used for automated editing of long sequences of velocity data from the Poker Flat radar [Bemra et al., 1986].

The effect of outliers on time averages and other statistical quantities can be quite significant. The sample mean m_z and sample variance s_z^2 used above, by excluding few lowest and highest values, are relatively unaffected by outliers. Accordingly, median is a more robust indicator of average behavior than the sample mean. Running median evaluated at different time scales, i.e. for different N, is a reasonable indicator of trends in data.

Editing method discussed above can also be applied to *psd* estimates for removal of sporadic interference localized in frequency and time. A very simple method of *psd* averaging with interference removal is based on two *psd* estimates $S_1[i]$ and $S_2[i]$ that are sufficiently close in time to have nearly the same atmospheric and noise components. Some values of frequency index in either $S_1[i]$ or $S_2[i]$ may be contaminated with interference. The average *psd* estimate formed as

$$S_0[i] = \frac{1}{2}\{ (S_1[i] + S_2[i]) - |S_1[i] - S_2[i]| \} \qquad (24)$$

is independent of interference. In this method, the noise variance of $S_0[i]$ is larger than that for either S_1 or S_2. Alternatively, $S_0[i]$ may be obtained as the point-by-point median of several *psd* estimates at closely spaced times. These methods have been found useful in analysis of *psd* estimates at Millstone Hill.

Finally, we note that in data analysis of stored time-series, samples on either side of a data point are available. This is in contrast with real-time signal analysis where 'future' samples are unavailable. Access to 'future' values in stored data makes it possible to use non-causal or physically unrealizable signal processing algorithms. In applications such as data smoothing, e.g., it is possible to obtain a zero phase-shift filter by applying any filter once in the forward and then in the backward direction.

7. CONCLUSION AND DISCUSSION

In this paper we have reviewed statistical signal processing and data analysis methods used in middle-atmosphere radar experiments. Steps in radar signal processing use optimum receiver structures in several successive stages. Coherent integrations is used primarily to reduce the data rates and the signal bandwidth, by implementing a crude low-pass filter. Use of sophisticated codes and fast pulse-by-pulse decoding circumvents some of the problems in earlier high-resolution experiments. Effect of ground clutter in *psd* estimates obtained with time-averaged periodogram can be reduced, especially at UHF, with longer data blocks, zero-padding, and windowing. This step should also simplify *psd* parameter estimation with adaptive least-square error methods. The *psd* parameter estimates can also be improved with the use of *MEM* and related spectral analysis methods.

These methods have evolved with rapid changes in computer technology. Currently available desktop personal computers and workstations provide ample memory (4-8 Mbyte), disc storage (~150-300 Mbyte), fast floating-point coprocessors, and advanced graphics capabilities necessary for analyzing large volumes of geophysical data. Particularly noteworthy is the availability of several texts with well-documented software subprograms for numerical and signal processing applications [Press et al., 1986; Marple, 1987; Stearns and David, 1988]. Real-time signal processing applications also benefit from these developments, and from the availability of faster digital-signal processing chips. Some aspects of real-time radar signal processing that need further efforts are (i) fast pulse-by-pulse decoders in high-resolution experiments, (ii) multi-channel spectral analysis with ground clutter suppression, (iii) spectrum analysis using *MEM* and *AR* methods, and (iv) spectral-moment parameter estimation in real time.

References

Alexander, S. T., *Adaptive signal processing : Theory and applications*, Springer-Verlag, New York, 1986.

Balsley, B. B., The MST technique - a brief review, *J. atmos. terres. phys.*, 43, 495-509, 1981.

Barnett, V. and T. Lewis, *Outliers in statistical data*, J. Wiley, Chichester and New York, 1978.

Bemra, R. S., P. K. Rastogi, and B. B. Balsley, A study of gravity wave spectra in the troposphere and stratosphere at 5-min to 5-day periods with the Poker Flat MST radar, *Handbook for MAP*, **20**, Ed. S. A. Bowhill and B. Edwards, 216-224, 1986.

Blackman, R. B. and J. W. Tukey, *The measurement of power spectra from the point of view of communications engineering*, Dover, New York, 1958.

Booker, H. G., A theory of scattering by nonisotropic irregularities with application to radar reflections from the aurora, *J. atmos. terres. phys.*, **8**, 204-221, 1956.

Brigham, E. O., *The fast Fourier transform and its applications*, Prentice-Hall, Englewood-Cliffs, N.J., 1988.

Chambers, J. M., *Computational methods for data analysis*, Wiley, New York, 1977.

Clark, W, L. and J. L. Green, Flatland radar online signal processing and radar control system, paper 8.5.1, presented at the *Fourth MST Radar Workshop*, Kyoto, Nov. 29 - Dec. 2, 1988.

Cleveland, W. S., *The elements of graphing data*, Wadsworth, Monterey, Calif., 1985.

Davenport, W. B. Jr, and W. L. Root, *An introduction to random signals and noise*, McGraw-Hill, New York, 1958.

David, H. A., *Order statistics*, J. Wiley, New York, 1970.

Farley, D. T., Overview of on-line data processing for MST radars, *Handbook for MAP*, **14**, Ed. S. A. Bowhill and B. Edwards, 262-267, 1984.

Fritts, D. C. and P. K. Rastogi, Convective and dynamical instabilities due to gravity wave motions in the lower and middle atmosphere : Theory and observations, *Radio Sci.*, **20**, 1247-1277, 1985.

Golay, M. J., Complementary series, *IEEE Trans. Inf. Th.*, IT-7,82-87, 1961.

Gottman, J. M., *Time-series analysis : A comprehensive introduction for social scientists*, Cambridge, New York, 1981.

Harris, F. J., On the use of windows for harmonic analysis with the discrete Fourier transform, *Proc. IEEE*, **66**, 51-83, 1978.

Haykin, S., *Adaptive filter theory*, Prentice-Hall, Englewood Cliffs, New Jersey, 1986.

Hocking, W. K., Measurement of turbulent energy dissipation rates in the middle atmosphere by radar techniques : a review, *Radio Sci.*, **20**, 1403-1422, 1985.

Ioannidis, G. and D. T. Farley, Incoherent scatter observations at Arecibo using compressed pulses, *Radio Sci.*, **7**, 763-766, 1972.

Klostermeyer, J., Experiments with maximum entropy and maximum likelihood spectra of VHF radar signals, *Radio Sci*, **21**, 731-736, 1986.

Klostermeyer, J., Maximum entropy estimation of Doppler shift and spectral width of VHF radar signals, *Radio Sci*, **24**, 47-63, 1989.

Marple, S., *Digital spectral analysis with applications*, Prentice-Hall, Englewood-Cliffs, N.J., 1987.

Miller, K. S. and M. M. Rochwarger, A covariance approach to spectral moment estimation, *IEEE Trans. Information Th.*, **IT-18**, 588-596, 1972.

Monin, A. S. and A. M. Yaglom, *Statistical Fluid Mechanics*, **v.2**, English translation, Ed. J. L. Lumley, MIT press, Cambridge, Mass, 1975.

Ottersten, H., Atmospheric structure and radar backscattering in clear air, *Radio Sci.*, **4**, 1179-1193, 1969a.

Ottersten, H., Mean vertical gradient of potential refractive index in turbulent mixing and radar detection of CAT, *Radio Sci.*, **4**, 1247-1249, 1969b.

Papoulis, A., *Probability, random variables and stochastic processes*, second edition, McGraw-Hill, New York, 1984.

Press, W. H., B. P. Flannery, S. A. Teukolsky, and W. T. Vetterling, *Numerical recipes - the art of scientific computing*, Cambridge, New York, 1986.

Rastogi, P. K., Data processing techniques used with MST radars:A review, *Handbook for MAP*, **9**, Ed. S. A. Bowhill and B. Edwards, 477-488, 1983a.

Rastogi, P. K., A note on the use of coherent integration in periodogram analysis of MST radar signals, *Handbook for MAP*, **9**, Ed. S. A. Bowhill and B. Edwards, 509-512, 1983b.

Rastogi, P. K., An overview of data acquisition, signal coding and data analysis techniques for MST radars, *Handbook for MAP*, **20**, Ed. S. A. Bowhill and B. Edwards, 431-440, 1986.

Rastogi, P. K. and J. Röttger, VHF radar observations of coherent reflections in the vicinity of the tropopause, *J. atmos. terres. phys.*, **44**, 461-469, 1982.

Rastogi. P. K. and G. Sobolewski, New quasi-complementary code sets for atmospheric radar applications, paper 8.9, presented at the *Fourth MST Radar Workshop*, Kyoto, Nov. 29 - Dec. 2, 1988.

Rastogi, P. K., J. D. Mathews, W-P Ying and J. Röttger, Simultaneous VHF and UHF radar observations of the mesosphere at Arecibo during a solar flare : a check on the gradient-mixing hypothesis, *Radio Sci.*, **23**, 97-105, 1988.

Rihaczek, A. W., *Principles of high-resolution radar*, McGraw-Hill, New York, 1969.

Rihaczek, A. W. and R. M. Golden, Range sidelobe suppression for Barker codes, *IEEE Trans. Aero. Elec. Sys.*, **AES-7**, 1087-1092.

Robinson, E. A. and S. Treitel, *Geophysical signal analysis*, Prentice-Hall, Englewood-Cliffs, New Jersey, 1980.

592

Röttger, J, The MST radar technique, *Handbook for MAP*, **13**, Ed. R. A. Vincent, 187-232, 1984.

Röttger, J., and C. H. Liu, Partial reflection and scattering of VHF radar signals from the clear atmosphere, *Geophys. Res. Lett.*, **5**, 357-360, 1978.

Röttger, J., VHF radar measurements of small-scale and meso-scale dynamical processes in the middle atmosphere, *Phil. trans. Royal Soc. London*, **A323**, 611-628, 1987.

Sato, T. and R. F. Woodman, Spectral parameter estimation of CAT radar echoes in the presence of fading clutter, *Radio Sci.*, **17**, 817-826, 1982.

Schmidt, G, R. Rüster and P. Czechowsky, Complementary codes and digital filtering for detection of weak VHF radar signals from the mesosphere, *IEEE Trans. Geosci. Electr.*, **GE-17**, 154-161, 1979.

Stearns, S. D., *Fundamentals of adaptive signal processing*, in *'Advanced topics in signal processing'*, Ed. J. S. Lim and A. V. Oppenheim, pp. 246-288, Prentice-Hall, Englewood-Cliffs, N.J., 1988.

Stearns, S. D. and R. A. David, *Signal processing algorithms*, Prentice-Hall, Englewood-Cliffs, N.J., 1988.

Sulzer, M. P. and R. F. Woodman, Quasi-complementary codes : A new technique for radar sounding, *Radio Sci.*, **19**, 337-344, 1984.

Tatarski, V. I., *The effect of the turbulent atmosphere on wave propagation*, English translation, National Technical Information Service, Va., 1971.

Tseng, C. C. and C. L. Liu, Complementary sets of sequences, *IEEE Trans. Inf. Th.*, **IT-18**, 644-652, 1972.

Tukey, J. W., *Exploratory data analysis*, Addison-Wesley, Reading, Mass., 1977.

Turyn, R., Sequences with small correlation, in *Error Correcting Codes*, Ed. H. B. Mann, Wiley, New York, p. 194-228, 1968.

Widrow, B. and S. D. Stearns, *Adaptive signal processing*, Prentice-Hall, Englewood-Cliffs, N.J., 1985.

Woodman, R. F., High-altitude resolution stratospheric measurements with the Arecibo 430 MHz radar, *Radio Sci.*, **15**, 417-422, 1980.

Woodman, R. F., Spectral moment estimation in MST radars, *Radio Sci.*, **20**, 1185-1195, 1985.

Woodman, R. F. and Y-H Chu, Aspect sensitivity measurements of VHF backscatter made with the Chung-Li radar : Plausible mechanisms, *Radio Sci.*, **24**, 113-125.

Woodman, R. F. and A. Guillén, Radar observations of winds and turbulence in the stratosphere and mesosphere, *J. Atmos. Sci.*, **31**, 493-505, 1974.

Wozencraft, J. M. and I. M. Jacobs, *Principles of communication engineering*, J. Wiley, New York, 1965.

MONITORING VHF RADAR SYSTEM PERFORMANCE USING COSMIC NOISE

W. L. Clark, J. L. Green, and J. M. Warnock

Aeronomy Laboratory
National Oceanic and Atmospheric Administration
Boulder Colorado 80303, USA

1. INTRODUCTION

Here we describe the use of cosmic noise at the Flatland radar (GREEN et al., 1988) in preliminary calibration and the monitoring of system performance.

2. RADAR CALIBRATION

A typical Doppler spectrum is shown in Figure 1. Riding below the echo is a randomly fluctuating but uniform signal which, at VHF frequencies, is due primarily to cosmic noise, which limits VHF radar receiver performance (SKOLNIK, 1962). Over usual receiver bandwidths, the cosmic noise appears in Doppler spectra as essentially white noise of power

$$P_N = \frac{1}{n} \cdot B_r \cdot k \cdot T_N \quad [watts]$$

where n is the number of coherent integrations performed on the signal, B_r is the bandwidth of the receiver, k is Boltzman's constant, and T_N is the noise temperature. If T_N is known at the receiver input, the total system gain G_s may be found using

$$T_o = \frac{n \cdot P_{No}}{k \cdot B_r \cdot G_s} = T_N = \frac{n \cdot P_N}{k \cdot B_r} \quad [K]$$

where T_o is the observed noise temperature which must be equal to the source noise temperature, and P_{No} is the observed noise power in digitizer units. Thus,

$$G_s = \frac{P_{No}}{P_N} \quad [watts/(digitizer\ power\ unit)].$$

Using the current Flatland system, the receiver noise temperature T_r is about 600K and the antenna loss factor α is approximately 0.5. Consequently,

$$T_N = T_r + \alpha \cdot T_c \approx 600 + 0.5 \cdot T_c \quad [K]$$

where T_c is the cosmic noise temperature.

3. CASE STUDY

The apparent cosmic, or sky temperature, Tc, in the VHF frequency range, varies in a known way across the celestial sphere, being the strongest in the direction of our galactic center, and the weakest in directions approximately orthogonal to this. In Figure 2 we show the noise temperatures observed directly overhead at the Flatland radar for a 24 hour period. The plotted circles represent the noise temperatures extrapolated from sky survey maps for 200 MHz and a 10° beam-width (MENZEL, Harvard College Observatory Sky Survey). The relation

$$T50 = T200 \cdot (200/50)^{(2.7 \pm 0.1)} \quad [K]$$

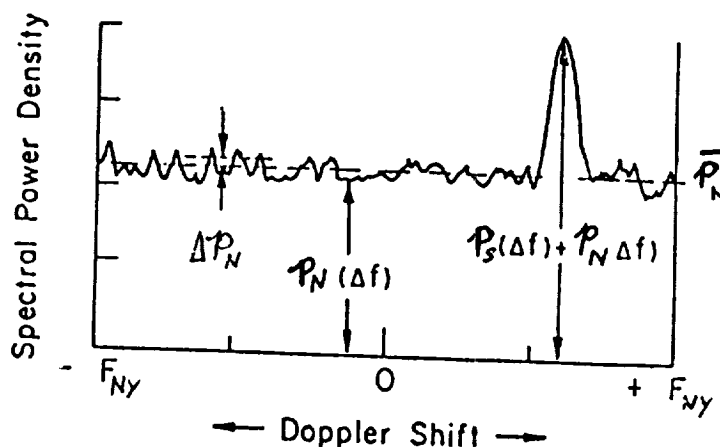Figure 1. Schematic of a typical Doppler spectrum taken from BALSLEY (1978). Here, F_{NY} represents the Nyquist frequency, Δf represents the frequency resolution, while $p_S(\Delta f)$ and $p_N(\Delta f)$ represent the echo power and noise power per spectral bin, respectively. $\overline{p}_N$ represents the mean of p_N across the spectrum, while Δp_N represents the mean fluctuation about $\overline{p}_N$. The total noise power in the spectra is then $P_N = 2 \cdot \overline{p}_N \cdot F_{NY}$, and is mostly due to cosmic noise in an optimized VHF radar system.

was used in the extrapolation, where T50 represents the noise temperature at 50 MHz and T200 the temperature at 200 MHz. The gain factor G_s was adjusted by eye to make the data and the sky map values roughly agree. This was sufficiently accurate for our purposes here, though it could easily have been done by least squares. More accurate results would require a more accurate determination of the power in the sky noise, a task which includes consideration of other sky surveys and the current effects of ionospheric absorption, which are variable in time. Use of some other calibration source, such as a reference noise diode, would be a better approach to such precision work (e.g., GREEN et al., 1983).

4. MONITORING SYSTEM PERFORMANCE

It should be noted that the particular value of G_s found here is only valid as long as no adjustments are made to the radar system. For example, the digitizing threshold at Flatland is resettable by turning a screw. Monitoring the sky noise power observed is a useful way to detect such changes. It is also a good way to detect and study changes in system performance, whether due to intentional modification (e.g., installation of new antenna feed lines), or natural causes (e.g., failure of a system component).

Examination of the noise power is also a good way to study the observing limits of a specific radar system. For example, radars have a close in range below which they will have difficulty observing echoes without distortion. Two important reasons for this are ground clutter contamination and receiver recovery problems. As an example, Figure 3 shows the apparent reduction of noise power at ranges below about 5 kilometers observed with the current Flatland system. For studies requiring interpretation of the echo power, such information is invaluable to ensure that observed effects are not instrumental.

x 10⁴

(From median of all but first 5 range gates)
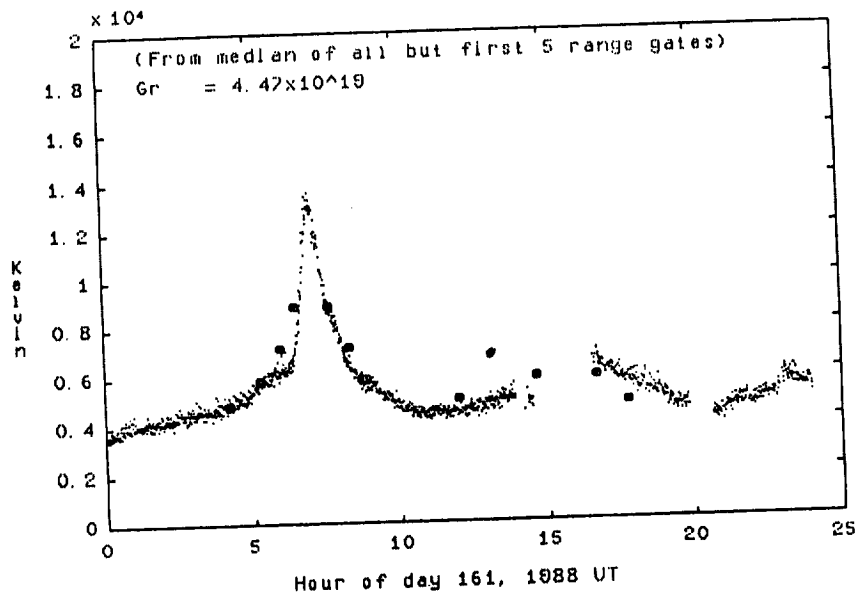
Gr   = 4.47x10^19

Hour of day 161, 1988 UT

Figure 2.   The small dots represent the median over height of the observed noise temperature plotted versus UT for day June 9, 1981. The circles represent noise temperatures extrapolated from the Harvard College Observatory sky noise maps.   The gain was adjusted by eye to bring the data into rough agreement with the map extrapolations.

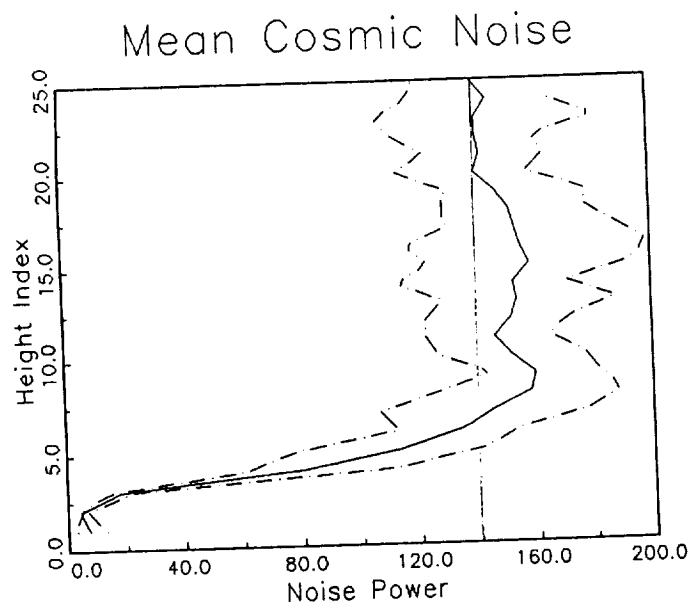# Mean Cosmic Noise

Noise Power

Figure 3. A typical hourly mean height profile of noise power as observed sometime in June of 1988 at the Flatland radar.   The noise power along the horizontal axis is in digitizer units. The height axis is in terms of height index, and is related to actual height above see level by h(i) = 1.49 + 0.75·(i-1) [km].

5. SUMMARY

The cosmic noise signal, while limiting the performance of the VHF radar receiver, has been used at Flatland as a system test signal. Rough calibration of the system has been made using this signal, and its use in monitoring system performance is anticipated.

REFERENCES

Balsley, B.B. (1978), Design considerations for coherent radar systems for probing the troposphere, stratosphere, and mesosphere, Preprint Vol., 18th Conf. on Radar Meteorology, Mar. 28-31, Atlanta, GA.

Green, J.L., W.L. Clark, J.M. Warnock, and K.J. Ruth (1983), Absolute calibration of MST/ST radars, Preprint Vol., 21st Conf. on Radar Meteorology, Sept. 19-23, Edmonton, Alta., Canada; American Meteorological Society, Boston, MA, 144-147.

Green, J.L., K.S. Gage, T.E. VanZandt, W.L.Clark, J.M. Warnock, and G.D. Nastrom (1988), Observations of vertical velocity over Illinois by the Flatland radar, Geophys. Res. Lett., 5, 269-272.

Menzel, D.H. (about 1949), Cosmic noise survey sky maps for 200 MHz and 600 MHz, Harvard College Observatory.

Skolnik, M.I. (1962), Introduction to Radar Systems, McGraw-Hill Book Company, 366-368.

ON THE OPTIMAL SPECTRAL SMOOTHING OF MST RADAR SIGNALS

P. K. Pasricha, A. R. Jain, and B.M. Reddy

Radio Science Division
National Physical Laboratory
New Delhi 110 012,India

ABSTRACT

An estimate of the spectral smoothing on a Doppler spectrum may be obtained by representing the signal (component) characteristics with a suitable statistical model. Autocorrelation analysis of the MST signal data may be performed to estimate the characteristic time (T_0) between "independent estimates" in the data. The characteristic time T_0 may be taken to represent the correlation period of the scattering medium. Both the correlation period and the total sample period (T) may be optimally determined by representing the autocorrelation function by a statistical model. Then the optimal number of signal spectra, which may be incoherently averaged, is given by $I = (T/T_0)^{1/2}$. The effective spectral resolution bandwidth is $\Delta f = 1/T$. Thus the number of frequencies over which a measured Doppler spectrum may be optimally smoothed is given by $I_s = I = (T/T_0)^{1/2}$. The effective spectral resolution bandwidth is $\Delta f = I_s/T$, T being the observation period. The optimal value of the spectral smoothing parameter is shown to be 6. The optimal value of the observation period is shown to be ~ 24 seconds, with the spectral resolution bandwidth of ~ 0.25 Hz.

INTRODUCTION

The processing of the backscattered echoes with a receiver such as an MST radar is usually carried out in different phases. First, coherent integration, through maximal matching of the receiver filter with signal spectrum is done to retrieve weak signals in the form of a time series. Next, an incoherent integration of this time series is performed to improve upon the detectability of the weak signals. Incoherent integration is usually performed on the Doppler spectra by cumulatively averaging a number (I) of Doppler spectra. Spectral smoothing over a (I_s) number of frequencies on a Doppler spectrum may also be done to further improve the detectability of the weak signals (WOODMAN, 1985).

In the present study, some samples of Doppler spectra obtained with the Poker Flat radar are analyzed. It is shown that a Yule model may be used to represent the autocorrelation function of the signal-plus-noise samples, with signal-to-noise (S/N) ≤ -6 dB. A Gaussian (or a Markovian) model may be used to represent the autocorrelation function of the signal (alone) samples, with S/N > -6 dB. Some samples with larger S/N values, showing the presence of the "oscillatory" nature of the signal component, may also be represented by a Yule model. The Doppler spectra represented by a Yule model are termed as "weak Doppler", and those represented by a Gaussian model as "strong Doppler" samples. For the strong Doppler samples the noise spike (at zero lag) may be easily interpolated through and the autocorrelation functions renormalized to the signal component alone. For the weak Doppler samples signal-plus-noise must be treated, since it is a difficult task to separate out the signal and the noise components in an autocorrelation analysis. T_0, T and $I = (T/T_0)^{,1/2}$ are computed for the weak Doppler samples. A statistical test on the detection of "real" signals is made.

THEORY

(A) An expression for the signal detectability

A statistical test on the detection of real signals may be made by examining the mean (input) signal level (μ) with respect to the rms noise figure $(\sigma$, both receiver and cosmic). The input signals (at an interval of $\Delta\tau$, interpulse period) may be coherently integrated to obtain a (time)

series, $\phi(\tau)$, of single sample energies (with mean μ). This a predetection detectability factor, apart from common radar parameters, may be given as (BALSLEY, 1978)

$$D = \frac{\mu^2}{\sigma^2} \qquad (1)$$

The variance of the time averaged sequence $\bar{\phi}(\tau)$, (incoherently averaged over a period T) is given by BARTLES (1935) and JONES (1975)

$$\sigma_T^2 = \sigma^2 \frac{T_0}{T} \qquad (2)$$

where σ^2 is the noise variance of the original random sequence, and T_0 and T are the correlation and the total sample periods, respectively. A number $I = (T/T_0)^{1/2}$ of signal spectra may be incoherently averaged over a sample period T. Equivalently, a measured Doppler spectrum may be smoothed over a number of $I_s = I = (T/T_0)^{1/2}$ of frequencies; T is the observation period.

The mean input level μ may be obscured within $\pm \frac{1}{2}\sigma_T$ (half power points) error bars, associated with finite time average estimates of the mean μ. For the detection of "real" input signals; $\mu/\sigma_T \geq 1$ (LEITH, 1973). Accordingly, the post detection expression of the S/N ratio may be modified (from expression 1) as

$$D \approx \frac{\mu}{\sigma} \frac{\mu}{\sigma_T} = \frac{\mu^2}{\sigma^2} (\frac{T}{T_0})^{1/2} = \frac{\mu^2}{\sigma^2} I \qquad (3)$$

(B) Estimation of the correlation and the total sample periods through various statistical processes

The autocorrelation function of an unaveraged time series for a Markov model is given by

$$\rho_k = \rho_1^k \qquad (4)$$

or, equivalently, $\rho(\tau) = \exp(-\nu\tau)$

$$\qquad (5)$$

where k is an integer, ρ_1 the lag -1 autocorrelation value and ν a measure of the equivalent decorrelation width of the autocorrelation function. The correlation period T_0 for a Markov model, used by meteorologists, is given as

$$T_0 = 1 + 2(1 - \frac{1}{T})\rho_1 + 2(1 - \frac{2}{T})\rho_1^2 + \ldots + (\frac{2}{T})\rho_1^{T-1} \qquad (6)$$

If T is the averaging time in seconds then ρ_1 is the lag -1 (seconds) autocorrelation value. A set of plots of T_0 vs T for different values of ρ_1 (after MADDEN, 1979) are given in Figure 1a. Here T_0 is defined for a very large value of T. The autocorrelation function for a Yule model is given as (KRANDALL and STUART, 1966)

$$\rho_k = p^k \sin(k\theta + \psi) / \sin\psi \qquad (7)$$

where

$$\alpha_1 = -\rho_1(1 - \rho_2)/(1 - \rho_1^2)$$

$$\alpha_2 = |-(\rho_2 - \rho_1^2)/(1 - \rho_1^2)|$$

$$p = \sqrt{\alpha_2}, \cos\theta = -\alpha_1|(2\sqrt{\alpha_2})|$$

$$\tan\psi = (1 + p^2)/(1 - p^2) \cdot \tan\theta$$

The correlation period T_0 for the Yule model is a generalized form of expression (6) (JONES, 1975)

$$T_0 = 1 + 2(1 - \frac{1}{T})\rho_1 + 2(1 - \frac{2}{T})\rho_2 + \ldots + (\frac{2}{T})\rho_{T-1} \qquad (8)$$
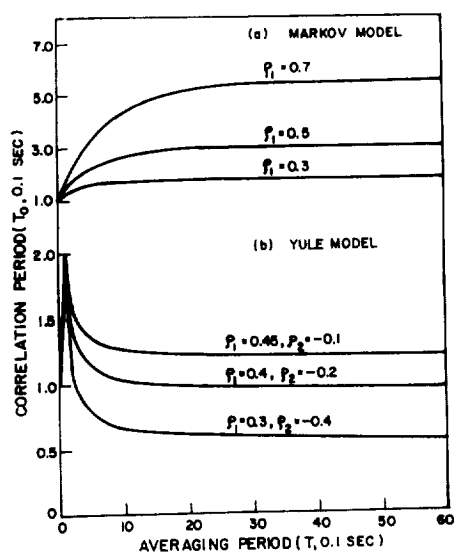
Figure 1. A set of curves between the correlation period (T_o) and the total sample period (T) for different values of the autocorrelation functions (i.e., ρ_1 and ρ_2. (a) the Markov model is in terms of ρ_1 value and (b) the Yule model in terms of ρ_1 and ρ_2.
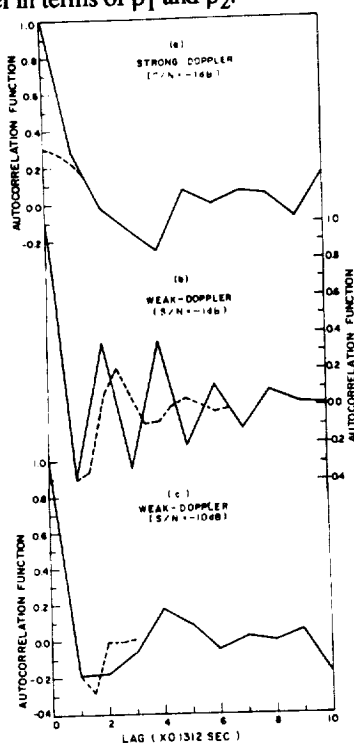

Figure 2. Representative autocorrelation functions for the (a) strong Doppler, and (b) and (c) for the weak Doppler samples. The dotted curve in (a) represents only a schematic interpolation to allow for the noise "spike" to be removed. In (b) and (c) the dotted curves are the Yule model curves fitted to the measured data. The dotted curves in (b) and (c) are sampled at 0.1312/2 sec.

A set of curves of T_o vs T for different combinations of the values of ρ_1 and ρ_2 are given in Figure 1b. The value of T_o again corresponds to a sufficiently large value of T. Expression (8) is used to estimate the correlation period and the incoherent averaging parameter for the weakly Doppler shifted MST echoes. The criterion for the detectability of "real" input signals (expression 3) is tested for the weak Doppler samples.

DATA ANALYSIS

A limited amount of data on Doppler spectra (obtained at Alaska) with the Poker Flat MST radar operating at 50 MHz have been used in the present analysis. Estimates of Doppler shift (Ω) and signal spectral width (W), from moment analysis of "raw" data, were also made available. Spectral estimates were obtained by averaging four contiguous spectra. Smoothed Doppler spectra, at 32 frequency points, and at 44 levels in the atmosphere, were provided (with a spectral resolution bandwidth of $\Delta f = 0.2382$ Hz). The observation period was ≈ 16 seconds. 'Real" autocorrelation functions were computed through an inverse FFT algorithm. Finally, ten seconds of autocorrelation functions were selected at various S/N ratios for the analysis of weak Doppler samples (corresponding to Yule type autocorrelation functions). Representative autocorrelation functions for the strongly (S/N > – 6 dB) and weakly (S/N ≤ – 6 dB) Doppler shifted samples are presented in Figure 2.

RESULTS

For the weak Doppler samples, the correlation periods lie in the range of 0.01 to 0.1 second (Figure 3). The total sample period (T) is ≈ 4 seconds. A plot of the incoherent averaging parameter I vs S/N, for the weak Doppler samples, is given in Figure 4. It is evident that to detect weakly Doppler shifted signals, I be ≈ 6. Thus a six-point frequency smoothing ($I_s = I = 6$) of a measured Doppler spectrum may be affected for optimum processing of the MST radar signals. The observation period in the data analyzed is ≈ 16 seconds and the spectral smoothing used in the data is over $I_s = 4$ number of frequencies. A six-point spectral smoothing would require that the observation period be about 24 seconds. The effective spectral resolution bandwidth is ≈ 0.25 Hz.

CONCLUSIONS

The detectability of weak signals with an MST radar technique requires that an appropriate spectral smoothing of the received backscattered echoes be performed. An estimate of the magnitude of the spectral smoothing may be obtained by representing the signal characteristics with a suitable statistical model. Then the correlation period (T_o), the total sample period T, and the incoherent averaging parameter $I = (T/T_o)^{1/2}$ are optimally determined. The signal detectability is improved by a factor of $I = (T/T_o)^{1/2}$ in the incoherent averaging of I number of signal spectra. Equivalently, a spectral smoothing over I_s (=I) number of frequencies in a measured Doppler spectrum may be performed. Then T is the observation period. In the case of weakly Doppler shifted MST echoes, the autocorrelation of signal-plus-noise may be represented by a Yule auto-regressive model; T_o is in the range of 0.01 to 0.1 second. The optimal value of the incoherent averaging parameter is I = 6. The total sample period is ≈ 4 seconds, with the spectral resolution bandwidth $\Delta f \approx 0.25$ Hz. Thus the optimum spectral smoothing parameter I_s would be $I_s = I = 6$. The optimum observation period would be ≈ 24 seconds, $\Delta f \approx 0.25$ Hz. A reduction in Δf, to say, 0.06 Hz, would require that unaveraged Doppler spectrum of about 16 seconds of duration may be processed.
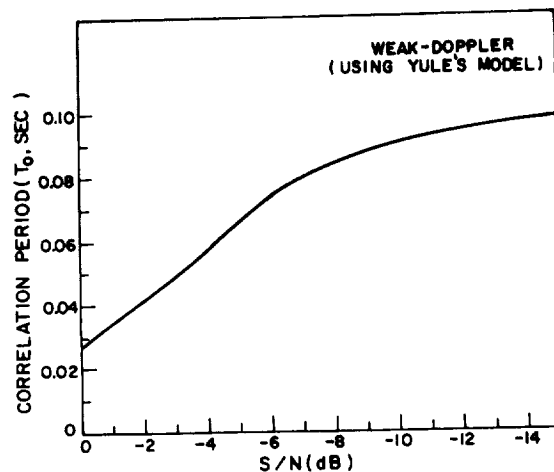
ACKNOWLEDGMENTS

Figure 3. Estimates of the correlation period (T_0) for the weak Doppler samples for different values of the measured S/N ratios. These estimates have been made through the use of the Yule statistical model.
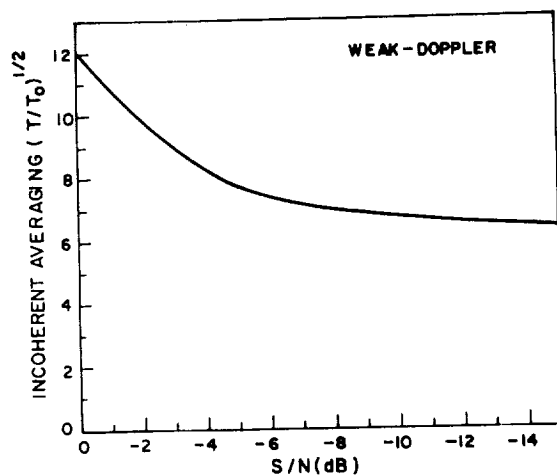

Figure 4. Computed values of the mean incoherent averaging parameter (I) for the weak Doppler samples for different values of the measured S/N ratios.

REFERENCES

Balsley, B. B., Design considerations for coherent radar systems for probing the troposphere, stratosphere and mesosphere, 18 Conf. on Radar Meteorology, Atlanta, GA, March 1978.

Bartels, J., Random fluctuations, persistence and quasi-persistence in geophysical and cosmical periodicities, *Terr. Magn. Atmos. Electr.* (Presently, J. Geophys. Res.), *40*, 1-60, 1935.

Jones, R. H., Estimating the variance of time averages, *J. Appl. Meteorol.*, *14*, 159-163, 1975.

Kendall, M. G., and A. Stuart, *The Advanced Theory of Statistics, Vol. 3*, 418-419, Charles Griffin, London, 1966.

Leith, C. E., The standard error of time-averaged estimates of climatic means, *J. Appl. Meteorol.*, *12*, 1066-1069, 1973.

Madden, R. A., A simple approximation for the variance of meteorological time averages, *J. Appl. Meteorol.*, *18*, 703-706, 1979.

Woodman, R. F., Spectral moment estimation in MST radar, *Radio Sci.*, *20*, 1185-1195, 1985.

SPECTRAL ANALYSIS OF ATMOSPHERIC SIGNALS WITH A POWER-LAW SPECTRUM

Prabhat K. Rastogi
Electrical Engineering and Applied Physics Department
Case Western Reserve University, Cleveland, Ohio 44106

Abstract

The assumption of wide-sense stationarity in the classical framework of spectral analysis is readily violated by atmospheric radar signals with a fading ground clutter component, and by velocity data with a power-law power spectrum density (PSD). Consequences of nonstationarity or trends on time-averaged periodograms using the discrete Fourier transform (DFT) methods are examined. Non-stationary trends have a very low frequency, but manifest as leakage at all DFT frequencies. The autocorrelation function (ACF) has a non-decaying component due to trends, which is aliased due to the periodicity imposed by the DFT. Hence, ACF cannot simply be recovered as the inverse DFT of the time-averaged periodogram. These artifacts of nonstationarity can be minimized by removing trends from the data. Alternatively, a window with 'good' frequency sidelobes should be applied to the data or to its ACF estimated through time-averaged lagged products. Several useful windows with low sidelobe levels are reviewed. A family of windows with frequency side-lobes decaying as an odd power of frequency is obtained by a modification of the approximate Blackman window. Trade-offs between the required duration of a data segment, frequency resolution, and statistical uncertainty of PSD estimates are briefly examined.

FLATLAND RADAR ONLINE SIGNAL PROCESSING AND RADAR CONTROL SYSTEM

J. L. Green and W. L. Clark

Aeronomy Laboratory, R/E/AL3
National Oceanic and Atmospheric Administration
325 Broadway, Boulder CO 80303, USA

1.0 INTRODUCTION

The new Flatland radar controller and signal processor will have a number of novel features. It is based on an in-house developed control interface with a special purpose, addressed data bus, a readily available personal computer system, an inexpensive signal processing interface card, and data archiving to optical disk. The controller has several innovative features, including a standard IEEE-488 General Purpose Interface Bus (GPIB) interface to the computer (thus eliminating dependence on any particular type of computer), a special purpose addressed data control bus which allows modularization of the control functions (e.g., each range gate is an addressed device), individual analog anti-aliasing filters for each range gate, and special modules to phase steer the antennas. As a consequence of these special features, the controller can handle more than one radar system at once, as well as simultaneously monitor the output of some other types of instruments as well (e.g., data from an associated boundary layer radar, or perhaps surface pressure, temperature, humidity, etc.).

2.0 THE RADAR CONTROLLER

The radar controller has a number of separate functions. For example, it

coordinates the actions of the transmitter and receiver;

controls the transmitted pulse length;

selects range gate filters;

enables each range gate at the appropriate time;

performs anti-aliasing filtering on each received signal;

digitizes the anti-aliased output of each range gate;

sends the digitized received data to the signal processor (i.e., system computer).

Physically, the controller consists of a chassis with a custom backplane accepting control modules. Each module is an interface card, which may perform one or more of the above functions or even more general functions, such as monitoring the transmitter power or atmospheric surface pressure. Electronically, the controller is composed of a parallel address/data bus driven by a 10 MHz clock pulse. Each device module is individually addressable via the address lines on the bus. Thus, some addresses may be thought of as commands to start a process (such as

starting the transmitter), others as commands to set registers controlling a process (such as initializing a count down register with the number of clock cycles to count down before turning on a range gate), while others interrogate registers holding data (such as the anti-aliased output available from a range-gate module).

2.1 Device Modules

The functions necessary to run the radar are implemented as modules, each having its own independent interface card and address on the bus. This greatly increases the flexibility of the system and eases the burdens of both software and hardware development, since each function is addressable and controllable through a standard interface. Furthermore, it is easy to introduce devices unrelated to the ST radar into the data stream. For example, some modules could represent output from a co-located boundary layer radar, or perhaps surface meteorological measurements. The computer software would be able to input and control information from this variety of sources through a uniform interface.

2.1.0 Radar-Pulse Module

This specific module, designed for the Flatland radar, is an interface card which can simultaneously control two partially independent radar systems, which we denote NS and EW, representing the vertical planes in which their associated antennas are able to steer. This capability allows atmospheric profiling in two cardinal compass directions at once. Currently, to simplify the data-throughput, the two radars have synchronized TX and TR pulses. Other parameter settings are independent. The TX pulse is an integral number of 10 MHz clock pulses in duration. Thus, digitally speaking, transmitter pulses as short as 15m could be used, which is shorter than any pulse-length likely to be practical utilizing a 50MHz radar. The TR and TX pulse are, of course, gated to ensure that the receiver is off during transmissions.

2.1.1 Range-Gate Modules

The range gates in this system are addressed and controlled as any other device on the controller bus. Consequently, the range gates for the radars NS and EW are differentiated only by their bus addresses. The range gates are implemented in 4-gate modules, each module consisting of a standard interface card with all the logic to handle the gating, anti-aliasing, and sampling for eight (i.e., 4 real and 4 quadrature) signals from the coherent detector. Each range gate is individually addressable on the bus, and range settings, which are independent of each other, are adjustable to within the 15m increment based on the 10 MHz bus clock. Each signal is detected through an analog anti-aliasing filter, which has selectable bandwidths corresponding to a selected number of desired radial-velocity spectral widths. At pre-set intervals, this filtered signal is digitized using a 12-bit ADC, and read by the system computer.

The use of anti-aliasing filters for each channel is different from the coherent integration used in many other radars, though it is similar to the method used with the Sunset radar (GREEN et al., 1979). This method sacrifices the automatic adaptation of the filter function inherent in the coherent integration anti-aliasing but obtains improved signal-to-noise

ratios for radial velocities observed near the spectral velocity limits, and greatly reduces the amount of data that the signal processing computer must handle. This reduction of data facilitates the ability of the signal processor to handle more than one radar system.

2.1.2 Antenna Steering Modules

The current Flatland antenna has 32 separately fed elements, with 16 assigned to the north-south steering directions and 16 to the east-west. Steering is accomplished in a similar fashion to that used at the Sunset radar (GREEN et al., 1980), wherein a phase shift box is assigned to each transmission line. The phase steering interface cards each handle 8 phase shift boxes. The computer control program is thus able to steer the radar through setting the phase-delay in each of the 32 phase-shift boxes.

2.2 Controller I/O Bus

The radar controller is itself controlled by a system computer over a separate I/O bus. On the controller side, the address/data bus described above is used. On the computer side, the standard computer bus is used. The link between the two is accomplished through conversion of the controller bus to IEEE-488 with a commercial parallel to 488 bus converter box. A readily available IEEE-488 computer interface card is used to accomplish the same task in the computer. This arrangement conveniently ensures complete independence of the interface from any specific type of system computer. This versatility is made possible because of the low data-throughput provided by sending only anti-aliased data to the system computer for signal processing.

3.0 THE SYSTEM COMPUTER

Primary control of the radar operation is implemented using the C programming language on a COMPAQ Deskpro 386 Model 40 personal computer. This computer is IBM-PC AT compatible, though having extended capabilities based on its 32-bit data paths and use of the Intel 80386 cpu and 80387 numerical coprocessor IC's. The computer keyboard is used for operator input, and a color EGA interface and monitor provide on-line graphics and control menus. The software consists of an integrated mix of in house programming in Microsoft C 5.1 and commercial peripheral drivers. communication with the radar controller and the peripherals is through interface cards using the standard PC-bus.

4.0 THE SIGNAL PROCESSOR

The Doppler power-spectra are calculated using the DSP32-PC signal processing board supplied by Communications Automation & Control. This board is based on the AT&T WE-DSP32 Digital Signal Processor chip. Its 1024 point complex floating-point FFT benchmark time is 14 msec, so that we perform all calculations in floating point. This chip is also capable of performing logic at high speed, allowing its use to find the Doppler spectrum moments as well as the Doppler spectrum itself. It is described in more detail in another paper in this volume (CARTER et al., 1989).

5.0 DATA ARCHIVING

The Doppler spectra and online moment calculations will be saved to 5 1/4" optical disks, utilizing a Storage Dimensions LS-800 Optical Subsystem with their proprietary software. This software is installed on the PC as a DOS driver, so that the optical disk might be thought of and is used in the same manner as a 400MByte floppy disk, with the exception that data once written may not be erased. The use of optical disks for this purpose has two great advantages:

The capacity is larger than for the more traditional 9-track magnetic tape systems;

The random access nature of the optical disk technology is allows much more efficient access to data embedded in such large data sets.

On the minus side, however, we note that this technology is rapidly evolving, and their is no common disk format. Thus, brand is important for compatibility, so that there is no second source. Furthermore, there are no guarantees that a manufacturer will not drop a particular format when such standards become available. Nonetheless, the advantages cited allow modes of operation at the radar that otherwise would not be obtainable.

6.0 SUMMARY

The Flatland radar control and signal processing system incorporates a mix of inexpensive, off-the shelf computer and signal processing equipment where possible and custom devices where necessary. It is designed in such a way that any part, including the computer, can be changed without impacting the rest of the system. The system is very flexible, and incorporates some novel abilities. Perhaps the most important is its ability to handle more than one radar simultaneously. This will immediately allow a doubling of the data rate and opens the door to easy incorporation of boundary layer radar data into the data set should such a radar be installed. Along these same lines, it can incorporate complementary observations , such as surface meteorological observations, into its data flow easily. Furthermore, implementation of phase steering is easily handled by assigning each phase box an address on the bus.

The availability of the new signal processing integrated circuits has greatly facilitated the processing of this type of data. Indeed, since these new chips include logic for flow control, even such tasks as reducing the Doppler spectra to edited moments can be handled in floating point at online speeds.

REFERENCES

Carter, D.A., P.E. Currier, and W.L. Ecklund (1989), A PC-based radar controller/signal processor, _MAP Handbook_, Proceedings of the Fourth MST Radar Workshop, Nov. 29-Dec. 2, 1988, Kyoto, Japan, paper 8.5.2.

Green, J.L., K.S. Gage, and T.E. VanZandt (1979), Atmospheric measurements by VHF pulsed Doppler radar, _IEEE Trans. Geosci. Elect._, _GE-17_, 262-280.

Green, J.L., J.M. Warnock, W.L. Clark, and F.J. Eggert (1980), Modifications to the Sunset radar to provide beam steering, Proceedings of the 19th Conf. on Radar Meteor., April 15-18, 1980, Miami Beach, FL, 575-576.

A PC-BASED RADAR CONTROLLER/SIGNAL PROCESSOR

D. A. Carter, P. E. Currier, and W. L. Ecklund

Aeronomy Laboratory
National Oceanic and Atmospheric Administration
Boulder, Colorado 80303

A new 915 MHz boundary layer radar has been developed at NOAA's Aeronomy Laboratory. For optimum performance this radar requires a faster, more powerful controller/processor than is used with our existing 50 MHz radars. To meet this need we have developed a personal-computer-based system that performs all the functions necessary for controlling the radar, acquiring the data samples, and carrying out the spectral analysis. This PC system not only outperforms our previous mini-computer-based system but is also considerably less expensive.

The radar controller/processor system consists of a PC-AT compatible computer with internal pulse generator, coherent integrator, and signal processing cards plus an external ADC module. The computer uses EGA graphics for display and a dot-matrix printer for hardcopy output. Mass storage of Doppler spectra is currently on 9-track tape, although higher density optical disks or helical-scan digital tapes may be used in the future.

The pulse generator card, built in-house, is a flexible programmable device that can generate transmitter/receiver pulses and range gates as short as 150 nsec. The coherent integrator card adds the 8-bit data samples (sent from the flash converters in the external ADC module) into 16-bit sums and can handle up to 512 range gates.

The coherently integrated data is sent via a 1 Mbyte/sec serial port to the signal processor card, which is a commercial board that uses the AT&T DSP-32 floating point processor. This board is low-cost (about $800 US) and relatively easy to program (a C compiler is available). All instructions execute in 250 nsec including a floating point multiply, accumulate, and store instruction. A complex 128-point FFT can be done in 2 msec. The operations performed by the DSP card in our system include pulse decoding (if required), dc filtering, windowing, and calculating the FFT's, power spectra, and spectral moments, all in essentially real-time.

The program running on the PC-AT is written in Microsoft C. An easy-to-use interface allows the user to set up the radar parameters and pulse sequences. Once the radar is started, the PC does little but handle some communication between the cards, which do the bulk of the processing, and then plot and store the resulting spectra.

There are several areas where the system performance can be improved in the future. With small changes in the timing circuitry in the external ADC module, the system should be capable of sampling and processing range gates only 100 nsec apart. The coherent integrator can be expanded from 16-bit sums to up to 27-bit sums by plugging additional FIFO's into sockets on the card and writing a DSP program to convert the long integers to floating point. The current amount of memory on the DSP card limits the system to 50 range gates with 128-point spectra. A new version of the DSP chip is now available which can access more external memory (16 Mbytes vs. 56 kbytes) and which is also much faster (100 nsec vs. 250 nsec instruction time).

610

The PC-based radar controller/processor described here is a significant improvement over the mini-computer-based system that we have used for many years. The PC with disk drive, display, printer, and DSP card costs about one-third as much as the previous system. The DSP card can perform floating point FFT's about 20 times faster than the mini-computer can calculate integer FFT's. The PC program is much easier to develop and modify compared to the previous assembly-language program. Because of the large selection of PC compatible computers, peripherals, and accessories available on the market, the radar controller/processor system should be easy and relatively inexpensive to maintain and upgrade in the future.

PERFORMANCE OF THE S-BAND STRATOSPHERIC DECODING SYSTEM AT THE ARECIBO OBSERVATORY

H.M. Ierkic V. (1) and R.F. Woodman (2)

(1) Arecibo Observatory, P.O. Box 995, Arecibo P.R. 00613.
(2) Instituto Geofisico del Peru, Apartado 3747, Lima 100, Peru.

I. Abstract

The objective of our work is to propose and analyze a decoding procedure useful to achieve unprecedented spatial and temporal resolution in CW S-band radar measurements at the AO. We find that using hard limiting transformations of the detected echoes (to achieve computational speed) does not distort significantly the process of spectral estimation. Moreover our procedure is efficient in the sense that statistical accuracy of individual estimates is kept with small increase in (coherent) integration time specially if the time series is oversampled. These characteristics make our estimation method very convenient.

II. Introduction

There is a real need for a detailed spatial and temporal description of the atmosphere. This need has been defended by several workers of the different regions of the atmosphere but in particular, for the stratosphere, by WOODMAN R.F. (1980). A problem that we are interested is the description of the morphology of turbulence in the lower stratosphere and its contribution to the diffusion characteristics in the region. To accomplish our goals we require continuous observations of the medium using tools that are capable of achieving spatial and temporal resolutions of, say 15 meters and 10 seconds respectively. At the Arecibo observatory the S-band radar system (2380 Mhz), used in a bistatic fashion (because it lacks a T/R switch), has the potential to be used for our scientific goals.

In this paper we propose and evaluate a procedure that is being successfully used in the lower atmosphere . Some preliminary results have already been presented by IERKIC H.M. (1987), and more will be shown, in another work, at this workshop. The next section is dedicated to the presentation of the theory and later we close pointing the important results of our study as well as the orientation that our effort is taking. We want to state here that the linear characteristic of the calculated transfer function has been verified under laboratory conditions.

III. Theory and discussion

Consider, for the purposes of this work that a CW coded signal is being scattered in the stratosphere and that it is being received and demodulated to base band. Furthermore, assume that the specific code used is a pseudo-noise one (MacWILLIAMS and SLOANE, 1976) and that the scattering medium has large correlation times relative to the duration of the code. The detected signal contaminated by diverse sources of noise is first digitized and then decoded using a correlator. We will present results for the cases when the echoes are

digitized using 1 bit, 1.6 bits (3 levels) and many bits; the discussion will concentrate in the 3 levels case for the algebraic development that follows.

Assuming that there is only a single scattering target, the action of the decoder is described by the following formula,

$$e(k) = \sum_i \{g(V_s*c(i)+V_n(i))*c(i+k-1)\}, \quad i=1,2,\ldots,q*N. \tag{1}$$

Here, N is the number of bauds of the code, q the number of times the code is recycled before the coherent integration time is reached, V_s represents the intensity of the echo, $V_n(i)$ is the i-th noise sample, $c(i)$ is the i-th value of the code (either -1 or +1), g describes the transfer function characteristic of the digitizer and $e(k)$ is the decoded signal corresponding to lag k with the idealized scatterer located at k=1. The noise samples have an underlying Gaussian distribution with probability density function f and distribution function P. The expected value of the output given by the correlator is,

$$\mu(k) = E[e(k)] \tag{2}$$

Equation (2) can be readily evaluated to give,

$$\mu(1) = p0+2*p1-1 \tag{3a}$$

$$\mu(k) = -\mu(1)/N \tag{3b}$$

where,

$$p0 = P(V_c-V_s/V_n)+P(V_c+V_s/V_n)-1 \tag{4a}$$

$$p1 = 1.-P(V_c-V_s/V_n) \tag{4b}$$

with V_n denoting the standard deviation of the noise and V_c the threshold level of the digitizer. Equation (3) shows that in order to keep range contamination low the length of the pseudo noise (PN) sequence should be as long as possible.

Figure 1 illustrates the behavior of $\mu(1)$ versus V_s keeping V_c as a parameter and the several curves can be understood intuitively. In order to evaluate the performance of the proposed decoding procedure we find convenient to calculate the variance of the statistical estimator $e(k)$ in the usual way,

$$Var(k) = E[e(k)**2]-\mu(k)**2 \tag{5}$$

To actually compute the variance we assume that the noise samples are uncorrelated and use the property of the PN sequences that out of the N bauds of the code, (N+1)/2 are minus one and the rest plus one. Explicit computation reduces (5) to

$$Var(k) = (1-p0 -(1-p0-2*p1)**2)/(q*N) \tag{6}$$

The measure of performance that we use can now be formulated by requiring to find for each V_s/V_n the value of V_c/V_n that minimizes the modified variance defined as MVar(k) below,
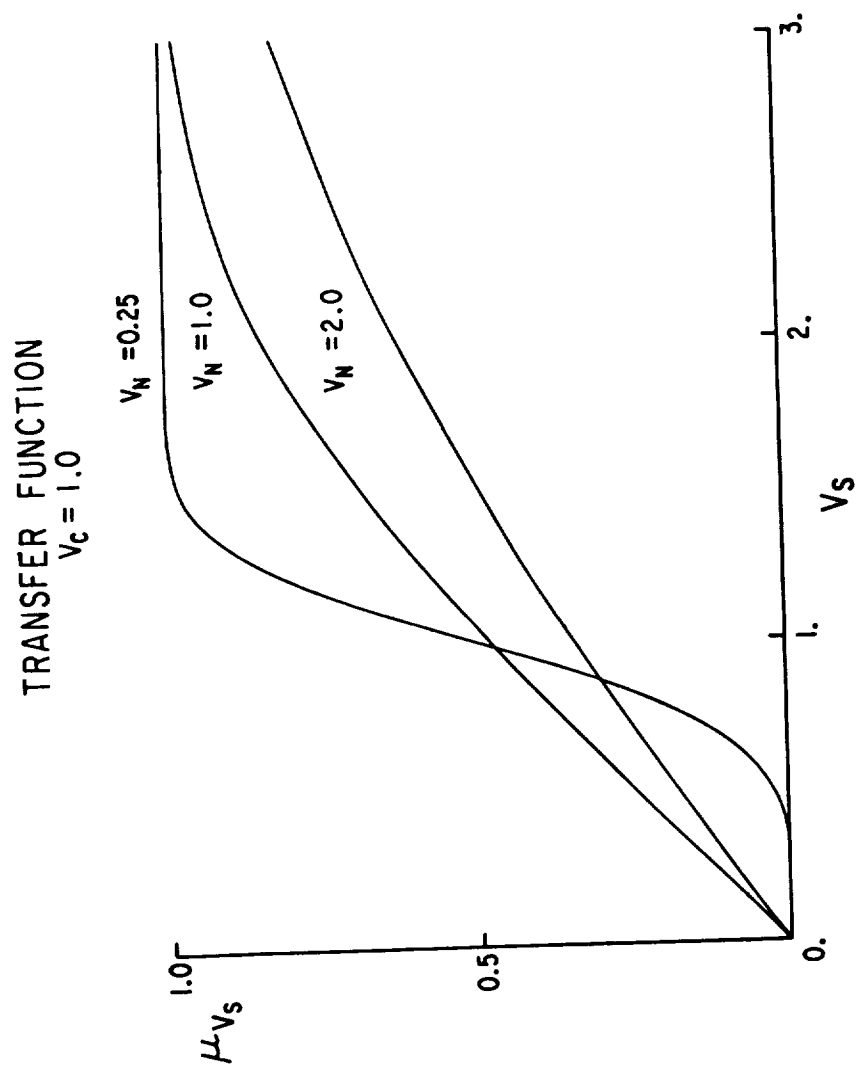
TRANSFER FUNCTION
$V_c = 1.0$

$V_N = 0.25$

$V_N = 1.0$

$V_N = 2.0$

μ_{V_S}

FIGURE 1

$$MVar(k)=(Var(k)/\mu(k)**2)*(V_s/V_n)**2 \tag{7}$$

the result of the optimization procedure is presented in figure 2 and can be summarized by saying that for small values of V_s/V_n (the actual situation in our experiments) the optimum value of V_c/V_n is about 0.60. Moreover by comparing the performance of the three level scheme with the multibit case (when, $\mu(1)=V_s$, $\mu(k)=-\mu(1)/N$ and $Var(k)=\mu(k)**2/q*N$) we can see from figure 2 that the relative efficiency turns out to be about 0.81. This last result implies that with about 25% longer coherent integration time we achieve the same accuracy as in the many bit case.

Another very encouraging property of the scheme we are considering is that the decoded signal does not show appreciable distortion over a wide range of values of V_s/V_n, including those found under practical circumstances. To see this linearity property we use a Taylor expansion of $\mu(1)$ to get,

$$\mu(1)= 2.*f(V_c/V_n)*(V_s/V_n)*(1+0.167*((V_c*V_s)/(V_n**2))**2) \tag{8}$$

with V_s/V_n small and the quadratic term contribution minor. The similar expansion for the variance is,

Var(k)=

$$\{2.*(1.-P(V_c/V_n))+f(V_c/V_n)*(V_s/V_n)**2*(V_c/V_n-4.*f(V_c/V_n))\}/q*N \tag{9}$$

The description of the 1 bit case (2 level digitizer) can be obtained by simply setting $V_c=0$ in the equations above, so that in particular we are ready to get the result that this decoding scheme has a performance such that it requires about 1.6 times longer to get the same accuracy as in the multibit case. Another interesting property to be evaluated is the improvement that oversampling (i.e. the noise samples become correlated) will bring about. The analysis now is again simple but cumbersome and we will just state some results; before, we assume that the noise has flat spectral characteristics a fact that can be altered with no major consequences. It can the be shown that for the multibit case the variance is given by

Var(k)=

$$2.*V_n**2/(M**2*q*N)*(M/2.*r(0)+(M-1)*r(1)+ \ldots +r(M-1)) \tag{10}$$

with M representing the degree of oversampling (e.g. M=2 is twice the Nyquist rate) and $r(k)=E[V_n(i)*V_n(i+k)]$. Evaluating (10) for M=2 and M=1 we find that there is an improvement in the variance of about 0.82. For M large this improvement asimptotically reaches a value of about 0.77 which normally does not justify going beyond M=2. The variance for the 1.6 bit case with oversampling can be shown to be,

Var(1)=

$$1/(M*q*N)**2*[2*q*N*(M/2*Re(0)+(M-1)*Re(1)+ \ldots +Re(M-1))+$$
$$(q*(N-1)/2)*((M-1)*Re(M-1)+ \ldots +Re(1))+(q*(N+1)/2-1)*((M-1)*$$
$$Ru(M-1)+ \ldots +Ru(1))-(q*N*M**2+(q*N-1)*M*(M-1))*\mu(1)**2] \tag{11}$$

where,

$$Re(k)=E[g(V_s+V_n(i))*g(V_s+V_n(i+k))] \tag{12a}$$
$$Ru(k)=E[g(V_s+vn(i))*g(V_s-V_n(i+k))] \tag{12b}$$

DIGITIZER'S THRESHOLD
AND
CORRELATOR'S PERFORMANCE
$V_N = 1.0$

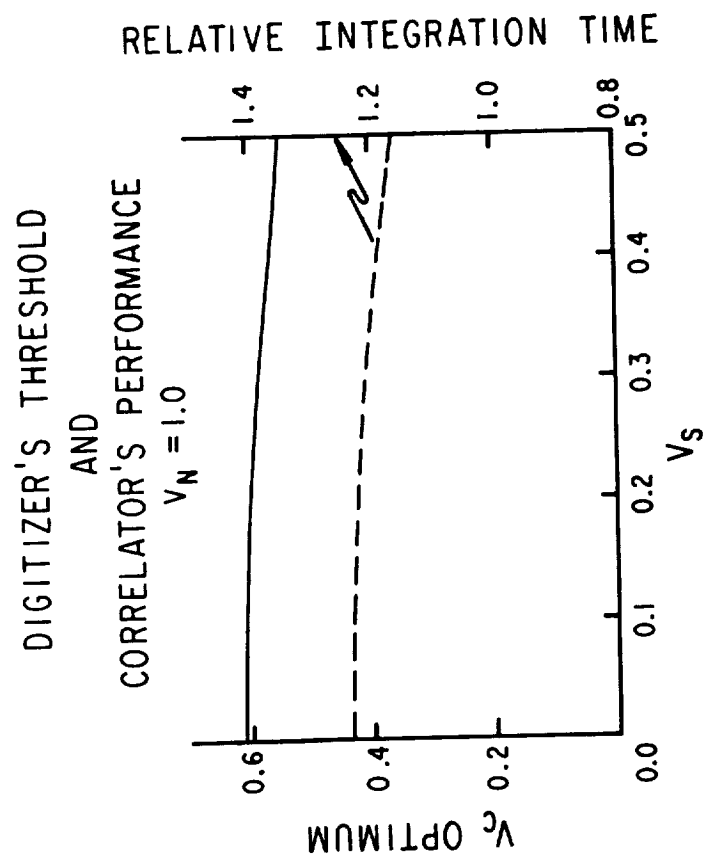RELATIVE INTEGRATION TIME

V_C OPTIMUM

FIGURE 2

and specific properties of the PN codes were used to get (11). Equation (11) is cumbersome to work with analitically, however if we consider V_s-0, then we can use the results obtained by HAGEN and FARLEY (1973). In particular, using their figure 7 (curve 11) to find Re(k) (note Ru(k)--Re(k) when V_s-0), we can readily conclude that with oversampling the performance of the three level scheme is at least as good as the many bit case with no oversampling. A final point is that the correlator at the AO is peculiar in that, first it does not reset the 6 least significant bits of its accumulators and second it drops those bits at the end of the operation. We have verified that this fact will cause an error of plus or minus one in the final count and turns out to be unimportant within the range of values used in the experiments.

IV.   Conclusions

We have shown that within a wide margin of values of V_s the estimator (1) is linear, consequently we can say that our statistical procedure introduces no distortion in the measurements. We have also shown that the method in consideration (1 bit, 1.6 bits) is fairly efficient when compared with the multibit case specially if the random series is oversampled (in the sense that the points are correlated). It is also worth mentioning that crude sampling makes it possible to achieve fast computational speeds which in turn imply that we can do our atmospheric studies with unprecedented height resolution. A simple extension of the theory presented shows that in the presence of a continuum of scattering (a scenario closer to the actual physical situation) the measured quantity will be,

$$\mu(k)- 2.*f(V_c/V_n)*(V_s(k)/V_n)-2.*f(V_c/V_n)*\{\Sigma_j(V_s(j)/V_n)\}/N \tag{13}$$

for the three level case, with the index j s.t. q-< j -< N and j different than k. In the multibit case the expression reads,

$$\mu(k)-V_s(k)-\Sigma_j(V_s(j)/V_n)/N \tag{14a}$$

$$Var(k)-V_c**2/q*N \tag{14b}$$

We are proceeding forward with the analysis to consider more realistic conditions (instrumental and scattering models). We also want to carry on, the analysis considering the codes as random variables (here we regarded them in a strictly deterministic way) and would like to find further common grounds with the work of HAGEN J.B. and D.T. FARLEY (1973). Finally, we are exploring the application of the technique to measurements in the presence of strong reflections or clutter.

V. Acknowledgements

VI.   <u>References</u>

Hagen, J.B. and D.T. Farley, Digital-correlation techniques in radio science, Radio Sci., 8(8,9), 775-784, (1973).

Ierkic, H.M., R.F. Woodman and P. Perillat, Spectral measurements of stratospheric echoes with the Arecibo 2380 Mhz radar, Eos, 68(44),1223, (1987), Abstract.

MacWilliams, F.J. and N.J.A. Sloane, Pseudo-random sequences and arrays, Proc. IEEE, vol. 64(12), 1715-1730, (1976).

Woodman, R.F., High-altitude-resolution stratospheric measurements with the Arecibo 2380-Mhz radar, Radio Sci., 15(2),423-430, (1980).

SIGNAL PROCESSING SYSTEM FOR THE INDIAN MST RADAR

Y. G. K. Patro, Anjali Bhatia, N. N. S. S. R. K. Prasad, P. Balamuralidhar,
A.Kulkarni, and V. K. Jain

SAMEER, I.I.T. Campus
Powai, Bombay 400 076, India

INTRODUCTION

The signal processing system of the Indian MST radar is designed to have on-line spectral processing capability in 256 range bins with provision to easily upgrade to 512 range bins. The range bins may be selected to be in two windows, each with selectable start point and width. This scheme has the advantage that the user has an option to position the range windows to cover the altitudes of interest in the stratosphere, troposphere, or in the mesosphere. The design also caters to on-line decoding of the received signal with a biphase-shift keyed coded pulse transmission where the code is up to 32 bits long and is changeable from pulse to pulse. Sixteen or 32-bit complementary code pairs are selectable as standard. Coherent integration prior to spectral processing is done to achieve data reduction to the extent possible such that the maximum expected radial velocity of the atmospheric turbulence can be estimated ambiguously. The received signal in each range bin can be processed to 512 point spectral resolution in order to yield a velocity resolution in the range 0.09 to 2.8 m/s. In order to have a processing dynamic range of 70 dB, the video signals in the I and Q channels of the receiver are digitized to 12-bit resolution. The A to D converter in each channel has 1 MHz word rate. Uncoded pulse transmission is treated as a code of a series of 1s and thereby the decoder is used as a digital matched filter. In order to correct for instrumental bias error, the phase of transmission is reversed for every alternative pair of transmitted pulses.

The signal and data processing system, shown in Figure 1, mainly consists of a preprocessor, a timing signal generator, a radar controller and a data processing system. The preprocessor and timing signal generator are designed inhouse to meet the special requirements of the radar. The radar controller is an IBM PC-AT compatible in the role of an instrumentation controller. The data processing system is based on a 32-bit super minicomputer MC 5600 system from M/s. Masscomp. USA.

TIMING SIGNAL GENERATOR (TSG):

The timing signal generator is a programmable multichannel pulse generator and supplies the pulse signals required by various subsystems of the radar, including the preprocessor. It supplies the sampling pulses to the A to D converter of the preprocessor from the start of the first range window to the end of the second range window. In case of coded transmission, the sample window is extended by one transmit pulse period. The TSG is designed around the microprocessor 8085A and a programmable interval timer 8254 (INTEL). It gets its control inputs from the radar controller through IEEE 488 interface. Details of the subsystem can be found elsewhere (PATRO and PRASAD, 1988). This design differs from other designs like TSG of the SOUSY radar, where two memories are involved. The program memory contains the various commands and rate memory has respective time intervals for which the commands have to be carried out.

PREPROCESSOR

The bipolar video signals in the in-phase (I) and quadrature phase (Q) channels of the radar receiver are sampled, digitized, decoded and integrated as shown in Figure 2. The interface circuit multiplexes the I and Q channel integrated outputs and feeds to the computer through a parallel interface a complex integer formatted data corresponding to the range bins of the user-selected range windows. The Control Communication and Test (CCT) subsystem of the preprocessor communicates with the radar controller through IEEE 488 interface for passing parameters such as

code, number of range bins, their locations, etc. It is also designed to perform diagnostic self-test procedures for testing the decoder and integrator. The decoding operation essentially involves correlating the incoming data stream from the ADC with the transmit code (FUAKO et al., 1985). As the maximum code length is 32 and maximum data rate 1 MHz, the decoder needs to be able to perform 32 additions and 32 multiplications within 1 microsecond if it is to decode the received signal in real-time. The implementation of the decoder was highly simplified by the availability of a 16-bit 32-tap correlator/transversal filter IMS A100 chip from INMOS Inc. (USA). The INTEL 8086 microprocessor is used to configure the A100 mode of operation, and to load the current and update coefficient register banks of the A100. At the end of each interpulse period, the 32-bit code of the next transmit pulse is swapped into the active coefficient register bank. The 12-bit data from the ADC are clocked into the 16-bit wide data-in port of the correlator and the output is clocked out through the 24-bit wide data-out port into the integrator. The use of the A100 reduces the amount of hardware required to implement the decoder by a very large factor, when compared to other approaches such as the shift-registers-serial addition implementation of the MU radar, or one involving the use of one-bit correlators (TDC 1023) in parallel.

Integration is done in a double buffer mode for a user-specified number of interpulse periods. Two RAM memory banks, each 2 K long and 32-bit wide are used for the buffers. At any given time one memory bank acts as the storage buffer for the data of the range bins under observation, while the returns of the successive transmit pulses are integrated on to them in real-time in a read-add-write cycle. The other memory bank, containing the integrated data from the previous integration time period is accessible by the interface circuit to be put on the data bus of the 10-bit parallel interface.

ADC, decoder and integrator blocks have been implemented and tested in real-time with simulated data and their performance was found to be satisfactory. The design and implementation details of the preprocessor may be found elsewhere (PATRO et al., 1988).

DATA PROCESSING SYSTEM

The data processing system is responsible for high speed data acquisition from the preprocessor at a maximum rate of 0.5 Mb/s for 256 range bins), high speed processing at a maximum estimated speed of 5 MFLOPS and data storage on to tape or disk media. The MASSCOMP MC5600 computer system configuration includes a data acquisition control processor (DACP), a tightly coupled vector accelerator and an independent graphics processor. It operates in a Real Time Unix Operation System environment. This is different from the earlier data processing systems in which a loosely coupled vector accelerator is used.

The DACP acquires data from the preprocessor and transfers to the host memory using DMA in a double buffer mode. When data in one FFT frame is acquired the full buffer is released for FFT processing with acquisition still continuing in the second buffer. At the end of FFT processing of the first buffer it is released for further data acquisition. The processed data are transferred to the shared memory buffer where a specified number of incoherent spectral integrations are carried out. At the end of the last averaging, the data are formatted and stored in magnetic tape media. This process repeats until the specified number of observations are completed or until a 'stop' command is received from the radar controller. On user request, the processed data may be displayed on the graphic console of the host computer.

RADAR CONTROLLER

The radar controller is responsible for the proper coordination, control and monitoring of the various subsystems of the radar including the data processor. The communication with inhouse equipment such as TSG, preprocessor, radar receiver, and modulator is through IEEE 488 interface. Communication with four satellite processors which are in four remote transmitter buildings, each monitoring and controlling eight transmitters is through a serial RS422 interface. Communication with the host processor is through RS232 interface.

SOFTWARE STRUCTURE

The software is divided into the following subprocesses on a functional basis. (1) The first level control process (P$_1$) establishes communication with the radar controller and controls the system operation by communicating with other subprocesses. (2) The data acquisition and processing (P$_2$) in the double buffer mode of operation is a child process of P1. (3) Another child process of P1 is data formatting and storage process P3. (4) The data presentation process (P$_4$) which can be invoked independently by a user on the graphics console provides graphical presentation of the processed data either in on-line or off-line modes. For the synchronization of each process with the total system operation, interprocess communication mechanisms like shared memory, Asynchronous System Traps and Signals are used. The software is in an advanced state of development. The detailed design of the data processing software may be found elsewhere (PATRO et al., 1988).

ACKNOWLEDGMENTS

REFERENCES

Fukao, S., T. Tsuda, T. Sato, K. Wakasugi, and T. Maklhira, The MU radar with an active phased array system 2, Inhouse equipment, *Radio Sci., 20,* 1169-1176, 1985.

Patro, Y. G. K., K. C. Anand, and P. Balamuralidhar, Design of data processing software for MST radar, *Tech. Rep. SMR/MST/S/880203.*

Patro, Y. G. K., Anjali Bhatia, N. N. S. S. R. K Prasad, Preprocessor for MST radar, *Tech. Rep. SMR/MST/SP/881011.*

Patro, Y. G. K., and N. N. S. S. R. K. Prasad, Timing signal generator for MST radar, *Tech. Rep. SMR/MST/RC/880201.*

Schmidt, G., R. Ruster, and P. Czechowsky, Complementary code and digital fitting for detection of weak VHF radar signal from the mesosphere, *IEEE Trans. Geosci. Electron. GE-17*
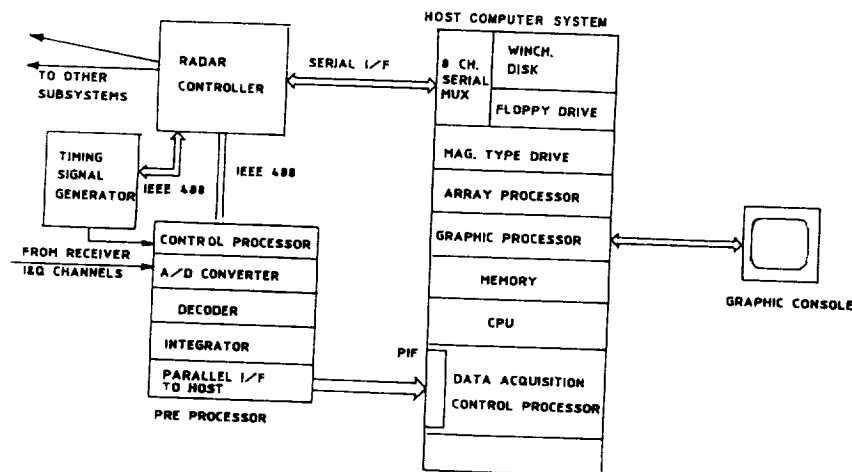
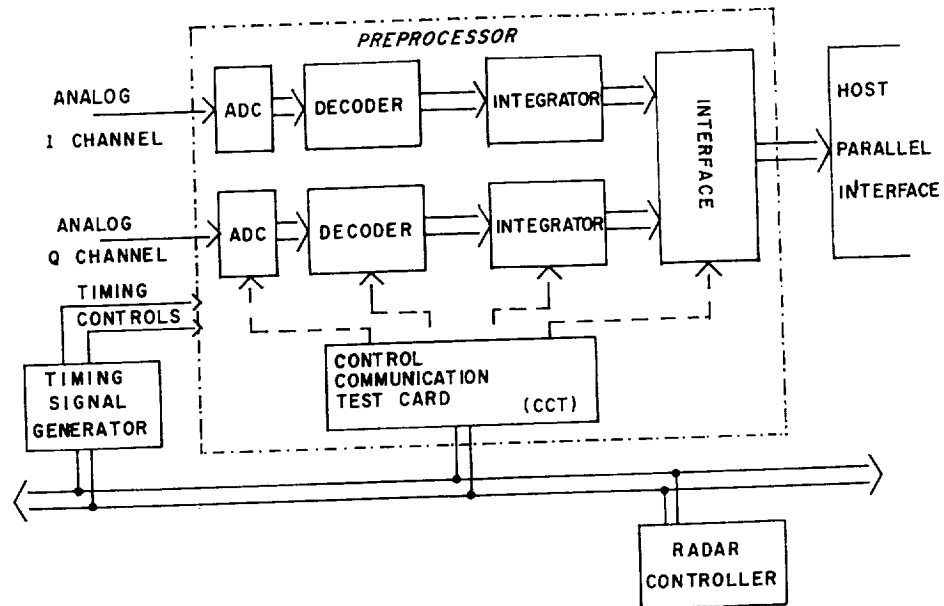Figure 1. Block schematic of signal and data processing system.

Figure 2. Block schematic of preprocessor.

MAXIMUM ENTROPY ESTIMATION OF DOPPLER SHIFT AND SPECTRAL WIDTH OF VHF RADAR SIGNALS

J. Klostermeyer

Max-Planck-Institut für Aeronomie, D-3411 Katlenburg-Lindau,
Federal Republic of Germany

ABSTRACT

Empirical investigations show that at low and moderate signal-to-noise ratios, maximum entropy (ME) Doppler shift and spectral width estimates of VHF radar signals have significantly higher accuracies than conventional periodogram estimates with noise thresholding. The variances of the ME estimates decrease with decreasing spectral width and clearly indicate a limiting signal-to-noise ratio below which the Doppler shift estimates are dominated by cosmic and instrumental noise rather than fluctuating radar signals. Two criteria are derived empirically that yield estimates of the optimum ME prediction-error filter lengths for computing the Doppler shift and spectral width of individual radar signals. At small signal-to-noise ratios, the Doppler shift criterion produces variances that are close to the minimum variance bounds of spectral methods. Fast ME algorithms for computing signal power, Doppler shift and spectral width are described. At large signal-to-noise ratios, the ME Doppler shift estimator is faster than the corresponding periodogram estimator based on a fast Fourier transform whereas at low signal-to-noise ratios, it is slower. For computing a typical height profile of the mean radial velocity in the troposphere and lower stratosphere, the ME estimator is as fast as the periodogram estimator whereas for a height profile of the mean spectral width, it needs approximately the three-fold computation time of the periodogram estimator.

OPTIMIZATION OF SIGNAL PROCESSOR PARAMETERS AND A SUGGESTED SCHEME FOR THE PARAMETERIZATION OF SPECTRA FOR THE INDIAN MST RADAR FACILITY

A. R. Jain

Radio Science Division
National Physical Laboratory
New Delhi 110 012, India

INTRODUCTION

MST radars are ground-based coherent Doppler radar systems, operating usually in the VHF band, which are now extensively used in middle atmospheric research. One such facility is under development in India for the study of atmospheric dynamics, turbulence characteristics and stable layers of the atmosphere, etc. The range of the velocity measurement, velocity, time and height resolutions would depend on the parameters of the signal processor. However, once the spectrum is obtained, a procedure is required for scaling and parameterization of the spectra. Various schemes have been implemented at different MST radar facilities.

In this note some of the design features of the signal processor of the planned Indian facility are brought out. A suitable scheme for the parameterization of the spectra, that can be adopted at the Indian facility is suggested.

SIGNAL PROCESSOR CHARACTERISTICS

Some of the specifications of the radar signal processor as per user's requirements are as follows:

1. Pulse repetition frequency (PRF)	62.5 Hz to 8 kHz (binary steps)
2. Pulse width (PW)	Uncoded, 1-32 μs (binary steps)
	Coded: 16, 32 μs (complementary coding, band length = 1 μs)
3. Maximum duty factor	0.025
4. Signal processing	Real time (FFT based)
5. Number of points for FFT	64, 128, 256, 512 (selectable)
6. Maximum velocity	11, 22, 44 ms^{-1} (selectable) (Special provision of 200 ms with velocity resolution of 2 ms^{-1})
7. Velocity resolution	0.1 ms^{-1} or 0.2 ms^{-1} (selectable)

Using basic principles, the number of samples that can be coherently integrated and number of spectra that can be incoherently averaged to improve the signal-to-noise ratio (SNR) and to match the above requirements are worked out.

PRE-FFT ANALYSIS (ON-LINE PROCESSING)

The following scheme is to be adopted in the case of the new facility.

Decoding the signal
Coherent integration of the predetermined number of sweeps
An appropriate weight function is applied to minimize the truncation effects
FFT using desired number of points
Detection of the spurious spectra before incoherently adding number of spectra
Incoherent addition of desired number of spectra

The SNR can be improved by summing the complex video samples from a number of consecutive received pulses. For VHF radar at 50 MHz, the correlation time is ~ 1 s. If I is the number of samples averaged, the SNR would improve by a factor of I. However, this time domain averaging filters the input signal components, so that the maximum velocity that can be deduced can be written as:

$$V_{max} = \lambda / (4IT) \text{ or } I = \lambda / (4TV_{max})$$

(1)

where λ is the radar wavelength and T is the interpulse period (i.e., T = 1/PRF). Once the coherent integration has been carried out, the next obvious question is to decide the number of points to be taken for FFT. If N, the number of coherently averaged points, is too small the velocity resolution would be poor. If N is too large, although the velocity resolution would improve, the time resolution would be poorer. STRAUCH (1983) has shown that for dwell time T_D (= INT) longer than $\lambda/2W$ (W = spectral width = 1 ms^{-1}) there would be improvement in velocity resolution but little improvement in SNR. The velocity resolution (ΔV) is given by

$$\Delta V = \lambda/(2 T_D) = \lambda/(2 \text{ INT}) \text{ or } N = \lambda/(2IT \cdot \Delta V)$$

(2)

Table 1 gives the V_{max} and ΔV for various integration periods and sample lengths for different pulse repetition frequencies (PRF) and pulse widths (PW). This table would be helpful in planning the experiments. From Table 1 the following can be noticed:

i)   IPP after coherent averaging is 31 to 125 ms.

ii) For $\Delta V \sim 0.2$ ms^{-1} and $V_{max} = 48$ ms^{-1}, the number of points to be used for FFT is 512.

iii) For $\Delta V \sim 0.1$ ms^{-1} and 0.2 ms^{-1}, the dwell time is 32 and 16 s, respectively.

Incoherently averaging a number of spectra before taking the moments further improves the SNR. The factors which determine how many spectra can be averaged are the time resolution requirement of the experiment from scientific consideration and gain in SNR. Of course, the first gets priority over the second. For average velocity $V \sim 10$ ms^{-1}, the time over which the spectra can be fruitfully integrated is ~ 1 min (JAIN, 1986). The net gain due to coherent and incoherent integration is ~ 20 dB.

PARAMETERIZATION OR POST FFT ANALYSIS

The method of averaged spectra is now routinely used at most MST radar facilities. The periodogram P(f) of an equispaced sequence is the magnitude squared of the discrete Fourier transform (DFT). The P(f) is a weighted and aliased estimate of the spectrum. A small number of parameters such as noise power (P_n), signal power (P_s), the Doppler shift (f_s) and spectrum width (W_s) give complete information on the spectra.

The suggested scheme for parameterization is shown in Figure 1. This part of the analysis can be done ON-line or OFF-line, but recommended (JAIN, 1987) to be carried out ON-line.

(i) Determination of noise power. Several methods are available for determining the noise. However, the method used at Poker Flat, based on the statistics of Gaussian random variables given by HILDERBRANDT and SEKHON (1974), appears to be most appropriate.

(ii) Removal of clutter and noise base. For VHF radars, clutter is expected to have zero Doppler and small width. Therefore, to start with, it is proposed to reject zero frequency point and substitute the same with the average of two neighboring frequency points. However, difficulty may arise in the case when the signal also has small Doppler.

Table 1.

PW (µs)	PRF (kHz)	Duty factor	COHERENT INTEGRATION No. of Samples Integrated	After Integration PRF Hz	After Integration IPP m sec	ϑ_{max} ms⁻¹	FFT Analysis N = 512 T_D Sec	N = 512 $\Delta\vartheta$ ms⁻¹	N = 256 T_D Sec	N = 256 $\Delta\vartheta$ ms⁻¹	N = 128 T_D Sec	N = 128 $\Delta\vartheta$ ms⁻¹
1,2	8	8x10⁻³	256	32	31.25	48	16	0.188	8	0.376	4	0.752
		1.6x10⁻²	512	16	62.50	24	32	0.094	16	0.188	8	0.376
4	4	1.6x10⁻²	128	32	31.25	48	16	0.188	8	0.376	4	0.752
			256	16	62.50	24	32	0.094	16	0.188	8	0.376
			512	8	125.00	12	64	0.047	32	0.094	16	0.188
8	2	1.6x10⁻²	64	32	31.25	48	16	0.188	8	0.376	4	0.752
			128	16	62.50	24	32	0.094	16	0.188	8	0.376
			256	8	125.00	12	64	0.047	32	0.094	16	0.188
16	1	1.6x10⁻²	32	32	31.25	48	16	0.188	8	0.376	4	0.752
			64	16	62.50	24	32	0.094	16	0.188	8	0.376
			128	8	125.00	12	64	0.047	32	0.094	16	0.188
32	0.5	1.6x10⁻²	16	32	31.25	48	16	0.188	8	0.376	4	0.752
			32	16	62.50	24	32	0.094	16	0.188	8	0.376
			64	8	125.00	12	64	0.047	32	0.094	16	0.188

T_D = Dwell time; N = No. of points used for FFT and $\Delta\vartheta$ = Velocity resolution

626
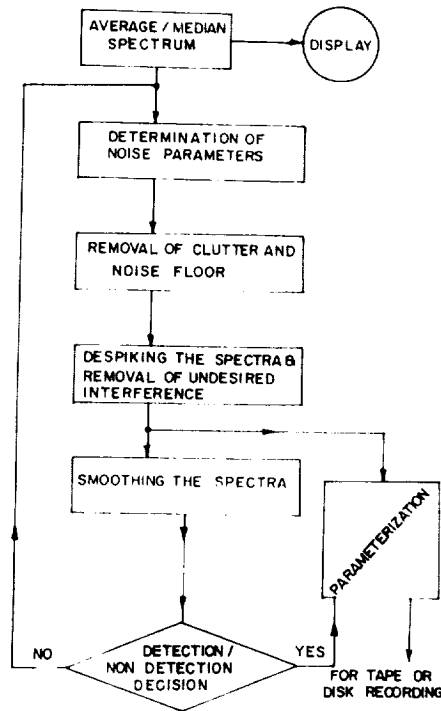
Fig. 1. Flow chart of scheme (post FFT) for parameterization of spectra.

Once the noise power is determined as discussed above, the same can be easily subtracted.

(iii) Detection of the signal. The unwanted spikes are removed by applying a median filter which examines a few points either side of a data point. The data point is replaced by the median value if it was found to deviate too much from the median. Some fixed spikes are more conveniently removed by applying a notch filter. After despiking the spectra, to enhance the detectability, a certain amount of smoothing of P(f) is necessary. This could be 3 point running mean over P(f) or some similar function which has to be chosen carefully.

After smoothing, smoothed spectra can be used to extract the initial Doppler profile. A threshold level has to be carefully chosen for identifying the signal from the noise. The atmospheric returns show a temporal and spatial continuity. This would further help in identifying the signal from spurious echoes.

(iv) Parameterization. Once the initial Doppler profile has been obtained the signal parameters are obtained by computing the zeroth, first and second moments of P(f). To reduce the effect of smoothing, the moments are taken of the spectra before smoothing. There are many approaches for determining the moments of the spectra. In one approach the Doppler width is chosen from the previously determined value and the first window width is varied. In the second step the window width is kept fixed and Doppler shift is then varied. The iteration can be repeated if necessary. Full Gaussian fitting is also used at the Arecibo and MU facilities.

DISCUSSION

1. Analysis of the on-line processing shows that it should be possible to achieve $\Delta V \sim$ 0.1/0.2 ms and $V_{max} \sim$ 12/24/48 ms^{-1}. It is, however, to be remembered that there would be a range ambiguity for PW < 8 µs and PRF > 2 kHz. A special feature of the on-line processing to be used is that decoding is done prior to coherent integration. This would enable the radar to be used for incoherent applications as well.

2. A simple scheme for scaling and parameterization of the spectrum is suggested. However, the following points need to be considered:

a) Coherent integration, finite beam width and wind shear introduce spectral broadening. Therefore, to obtain the true signal spectral width, proper deconvolution function should be used (HOCKING, 1983).

b) The selection of smoothing function is important. Undersmoothing would not improve detectability, whereas oversmoothing would tend to flatten the signal peak itself.

c) Threshold signal level is used for identifying signal from noise (after smoothing), i.e., for detection/nondetection decision. Therefore threshold level should be chosen carefully.

ACKNOWLEDGMENTS

REFERENCES

Hilderbrandt, P. H., and R. S. Sekhon, Objective determination of the noise level in Doppler spectra, *J. Appl. Meteorol.*, *30*, 808-811. 1974.

Hocking, W. K., Mesospheric turbulence intensities measured with a HF radar at 35° S-II, *J. Atmos. Terr. Phys.*, *45*, 103-113, 1983.

Jain, A. R., Some design considerations for the signal processing system of the proposed Indian MST radar, *NPL Res. Rep., No. NPL-86-C.1-0166*, 1986.

Jain, A. R., On the scaling and parameterization scheme for the spectra from proposed Indian MST radar facility, *NPL Res. Rep. No. NPL-87-C.3-0034*, 1987.

Strauch, R. G., *Handbook for MAP, Vol. 9*, 523-534, 1983.

ESTIMATION ERROR OF SPECTRAL PARAMETERS OF MST RADAR OBTAINED BY LEAST SQUARES FITTING METHOD

Mamoru Yamamoto, Toru Sato, Peter T. May[1]
Toshitaka Tsuda, Shoichiro Fukao and Susumu Kato

Radio Atmospheric Science Center, Kyoto University, Uji, Kyoto 611, JAPAN
1) Present affiliation: Wave Propagation Laboratory, National Oceanic and Atmospheric Administration, Boulder, CO 80303, U.S.A.

1 Introduction

In MST (Mesosphere-Stratosphere-Troposphere) radar observations there are several techniques to estimate parameters such as echo power, radial wind velocity and spectral width. For the return signal of MST radars we can assume that a power spectrum of the radar returns shows a Gaussian distribution which is described as follows (e.g., WOODMAN, 1985),

$$S(f) = \frac{P}{\sqrt{2\pi}\sigma} \exp\left[-\frac{(f - f_d)^2}{2\sigma^2}\right], \tag{1}$$

where f is frequency and P, f_d and σ are echo power, mean Doppler shift and spectral width, respectively.

One of the techniques to determine these parameters is a moment method. The zeroth, first and second moments of the spectral density correspond to the echo power, mean Doppler shift and spectral width, respectively. Another technique is a least squares fitting method. A Gaussian spectrum is fitted to the observed one so as to minimize the squared sum of the residual by changing the parameters. The spectral parameters may also be estimated from the autocorrelation function of the time series of the radar returns. The radial velocity is estimated from the phase angle of the autocorrelation function at the first lag (e.g., WOODMAN and GUILLÉN, 1974).

The performance of many estimators were compared by ZRNIĆ (1979) and WOODMAN (1985), and the performance of the pulse-pair method was shown to be better than that of the moment method at low signal-to-noise ratio (SNR) although they are the same at infinite SNR. ZRNIĆ (1979) also showed the theoretical minimum estimation error (Cramer-Rao bound) of spectral parameters which is obtained by maximum-likelihood (ML) estimators. However, there are no theoretical calculations for the performance of the fitting method, which may be expected to show better results compared with other techniques especially in the region with low SNR.

In this paper, we discuss the performance of the fitting method by using the computer simulation technique, and compare it with the moment method. We also investigate problems which may occur with the fitting method when it is applied to the power spectrum of a random process, and show a possibility to improve the performance of the fitting method and to approach the Cramer-Rao bound.

2 Model spectrum and computer simulation technique

In our calculation, we have calculated a power spectral density of $S(f_i) + P_N$ at 128 discrete frequencies f_i, where P_N is noise level density. For convenience, the Doppler shift f_d is assumed to be zero. The SNR is defined as the power ratio between the signal and the noise as follows,

$$S_N = P/(M P_N),\qquad(2)$$

where $M = 128$ is the number of discrete frequencies. In the following sections, we use normalized frequency and spectral width

$$F = f/\Delta f,\qquad(3)$$

$$W = \sigma/\Delta f,\qquad(4)$$

where Δf is a frequency interval between the discrete spectral components.

The output of the receiver, which is a time series of data, is a random process with a Gaussian distribution. Because the Fourier transform is a linear transformation and power spectral density is a squared sum of both real and imaginary parts of the spectral component, the power spectral density has a statistical fluctuation with a χ^2-distribution (e.g., BENDAT and PIERSOL, 1971). The statistical fluctuation of the spectrum is simulated by generating random numbers with χ^2-distribution, and the model power spectrum is calculated as a product of the Gaussian spectrum and the statistical fluctuation. The amplitude of the statistical fluctuation can be reduced by averaging successive power spectra, which is called incoherent integration. The standard deviation of the model spectrum is proportional to the spectral density itself and is equal to $S(f_i)/\sqrt{n}$, where n is number of the incoherent integration.

Spectral parameters are estimated for each spectrum by using both the moment and the least squares fitting method. First, the generated spectrum is smoothed by using a numerical low pass filter with a -3dB cutoff period of $20\Delta f$. We find the frequency point with the largest spectral density in the smoothed spectrum, which is used as the first guess of the Doppler shift. After subtracting the real P_N from the original spectrum, we have applied both techniques to 64 spectral points around the first guess.

In order to obtain the estimation errors of parameters, we have calculated 500 model spectra and obtained the bias b_F and variance σ_F^2 of the estimates. We define the estimation error of the Doppler shift, E_F, as follows:

$$E_F = \sqrt{\sigma_F^2 + b_F^2}.\qquad(5)$$

This is called the "rms (root mean square) error" (BENDAT and PIERSOL, 1971).

3 Estimation error at finite signal-to-noise ratio

Figure 1 shows E_F for both the fitting and moment methods versus S_N when $n = 5$. When $W = 2$ for the fitting method, E_F is 0.44 in the region with large S_N. The fitting is successful at $S_N > 10^{-1}$, but we recognize a rapid increase of E_F below this level. The wider spectrum causes a larger estimation error of the Doppler shift; e.g., $E_F = 0.91$ for $W = 10$ at $S_N = 10^4$. However, E_F starts increasing at a similar S_N to that for $W = 2$. It is noted that estimation errors are almost constant with S_N above this level. Comparing the results with that of the moment method, at high S_N, the estimation error of the moment method becomes less than that of the fitting method; at $S_N = 10^4$, $E_F = 0.25$ and 0.52 for $W = 2$ and 10, respectively.
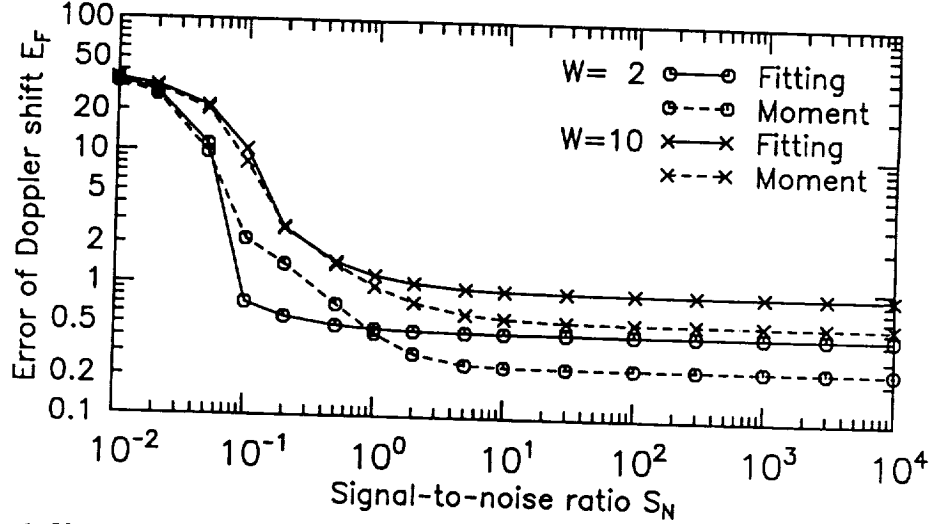
Figure 1: Variation of the estimation error of the Doppler shift versus signal-to-noise ratio for $n = 5$. Circle and X symbols show results for $W = 2$ and $W = 10$, respectively. Solid and dotted lines correspond to the errors obtained by the fitting and moment methods, respectively.

The estimation error of the moment method is approximately 60% of the fitting method in this region. As S_N decreases, the estimation error of the moment method gradually increases. The errors of moment method at $10^{-1} < S_N < 1$ are almost the same as that of the fitting method for $W = 10$, and worse for $W = 2$. There is no significant bias shown in the low S_N region. Below $S_N = 10^{-1}$, both methods show a rapid increase of the estimation error. The large error is obtained because the numerical filter captures the highest peak randomly distributed in the fluctuating noise level, and accepts it as the first guess of the Doppler shift. When we assume a constant distribution of E_F within the spectral window of $F = \pm 64$, the standard deviation is approximately 37, which is consistent with E_F at $S_N = 10^{-2}$.

4 Estimation error at infinite signal-to-noise ratio

Figure 2 shows the estimation error of the Doppler velocity versus number of incoherent integrations of the spectra. The estimation error of the Doppler shift is almost proportional to $\sqrt{W}$, and inversely proportional to $\sqrt{n}$. At infinite S_N, the estimation error E_F of F_d can be described as

$$E_F = k\sqrt{W/n}, \tag{6}$$

where k is a constant. From the data shown in Fig. 2, $k = 0.63$ and $k = 0.38$ for the fitting and the moment methods, respectively.

In order to determine the estimation error of the radial wind velocity, we put physical dimensions to the normalized estimation error E_F. The estimation error ε_v (ms^{-1}) of radial wind is

$$\varepsilon_v = K\sqrt{\sigma_v/T_0}, \tag{7}$$

where $K = k\sqrt{\lambda/2}$ is a constant, $T_0 = nT$ is the total observation period to obtain a set of spectral parameters, T (s), λ (m), and σ_v (ms^{-1}) are the length of the time series of the data, the wavelength of the radar, and the spectral width, respectively. Eq. (7) shows that, if S_N
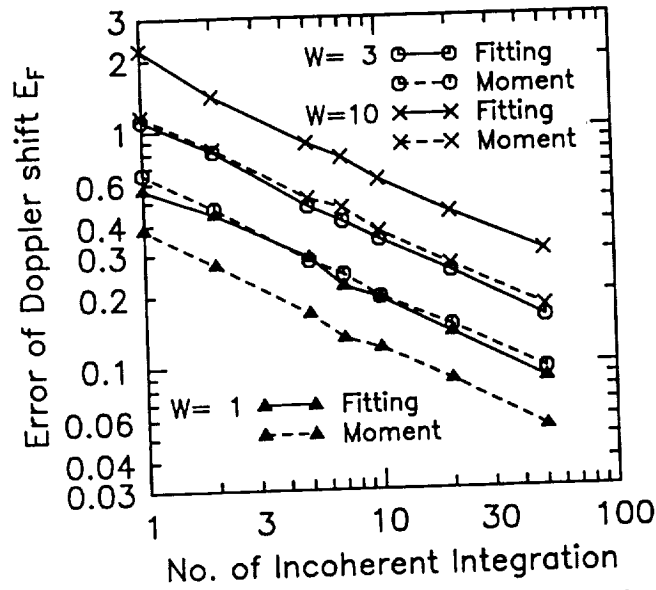
Figure 2: Estimation error of the Doppler shift versus number of incoherent integration of the spectra at infinite S_N. Triangle, circle and X symbols show that $W = 1$, $W = 3$ and $W = 10$, respectively. Solid and dotted lines correspond to the errors for the fitting and moment methods, respectively.

is infinite, the observation period is the only factor that we can choose when we observe the radial velocity by using the radar.

The coefficients K for the estimation errors expected in the MU radar observations ($\lambda = 6.45$ m) are $K = 1.1$ and $K = 0.67$ for the fitting and the moment methods, respectively. When we observe the radial wind velocity every one minute by using the fitting method, $\varepsilon_v = 0.12$ ms^{-1} for $\sigma_v = 0.7$ ms^{-1} which is typical spectral width in the stratosphere, and $\varepsilon_v = 0.20$ ms^{-1} for $\sigma_v = 2.0$ ms^{-1} which is typical in the mesosphere.

We infer that the larger errors with the fitting method occur because of the nature of the statistical fluctuations of spectral coefficients. Because the amplitude of the statistical fluctuations are proportional to the spectral density, components around the spectral peak have larger fluctuations than the spectral components with low spectral density. Thus, the sum of the squared residual is almost solely determined by the spectral components around the peak, which implies that we actually use only a portion of the spectrum when we estimate the parameters by the fitting method.

5 Lower bound of the spectral parameter estimation

The least squares fitting method gives maximum-likelihood (ML) estimates when the statistical fluctuations of the samples at different frequency points are uncorrelated, and the samples at each frequency point have Gaussian distribution with known variance (e.g., BRANDT, 1970). The second condition is not satisfied in the least squares fitting applied to the power spectrum. We use an uniform weight for all spectral components although the variance of the spectral components is proportional to the spectral density itself. Also, the statistical fluctuation shows the χ^2-distribution. The χ^2-distribution is not symmetrical with respect to mean of the
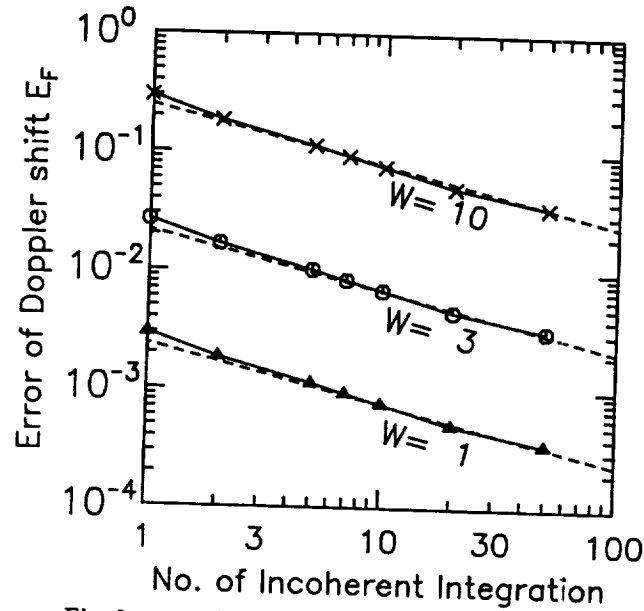
Figure 3: The same as Fig. 2 except for the estimation error of the Doppler shift obtained by the parabolic fitting in the logarithmic domain. Dotted lines show the Cramer-Rao bound of the ML estimator shown by ZRNIĆ (1979).

spectral coefficient, and tends to have larger spikes on the higher side in its distribution. The spikes of the statistical fluctuations which appear around the peak of the Gaussian spectrum cause a large bias to the sum of the squared residual, and set the fitted spectrum higher at the center and narrower than the true width. The estimation of the Doppler shift is also affected by the positions of the spikes.

Since the amplitude of the statistical fluctuation is proportional to the spectral density itself, we can equalize the amplitude of the statistical fluctuation by taking the logarithm of the spectral density. The variance of the samples at different frequency points become constant, although its statistical distribution is not Gaussian. When $S_N \to \infty$, we can estimate the spectral parameters by fitting a parabolic curve to $\log[S(F)]$ with an uniform weight. We have simulated the estimation error of the Doppler shift for this method. The result of this parabolic fitting is shown in Fig. 3. The estimation error obtained by this method is, for example, approximately 20 times less than that by the moment method when $W = 3$. The dashed line is the theoretical lower bound (Cramer-Rao bound) obtained for the error expected to the ML estimator (ZRNIĆ, 1979). The estimation error of the normalized Doppler shift agrees very well with the Cramer-Rao bound. The estimation error is inversely proportional to $\sqrt{n}$. Also, we recognize that it is almost proportional to W^2. This is different from the $\sqrt{W}$ dependence shown in Eq. (6), but agrees well with the theoretical formula given by ZRNIĆ (1979). The improvement of the estimation error obtained by this fitting in the logarithmic domain is larger for spectra with narrow width than spectra with larger width.

In theoretical evaluations of the accuracy of the pulse-pair or moment method (DOVIAK and ZRNIĆ, 1984; WOODMAN, 1985), the accuracy was shown to be comparable to the Cramer-Rao bound. It is because they replaced the sampling interval by the signal correlation time when they calculate the Cramer-Rao bound. They have mentioned that a sampling faster than the correlation time is redundant, and only introduces higher frequency compo-

nents with small spectral density. However, for a Gaussian spectrum with infinite S_N, every spectral component should have significant information no matter how far the component is from the spectral peak. This implies that we can arbitrarily increase the number of independent points in the spectrum, and improve the performance of estimators as much as we wish. The performance of the moment and the fitting methods in the linear domain is restricted because the equivalent number of effective spectral components is limited around the spectral peak according to the spectral width. The result clearly shows that at infinite S_N, even very high frequency components of the signal spectrum with very small amplitude have substantial importance, and can be used to derive its spectral parameters. In the linear domain, contribution from these components are masked by the much larger fluctuations of the frequency components around the peak. Our simulation shows that the parabolic fitting in the logarithmic domain is one technique to realize the lower bound of the ML estimator by making use of such high frequency components.

This method is not realistic for real data with finite S_N. As cited by ZRNIĆ *et al.* (1977), the logarithmic fit is better if spectra are free of artifacts. However, the spectra are contaminated and distorted by truncation distortion, aliasing effects, quantization error and so on. The estimation error of the noise level will also affect the result. However, if we produce a fitting routine for $\log[S(F)]$ which contains these contaminations, it should show much better performance than the existing methods.

Acknowledgements

References

Bendat, J. S. and A. G. Piersol, *Random data: Analysis and measurement procedures*, pp. 189–193, Wiley-Interscience, New York, 1971.

Brandt, S., *Statistical and computational methods in data analysis*, pp. 170–173, North-Holland, Amsterdam, 1970.

Doviak, R. J. and D. S. Zrnić, *Doppler radar and weather observations*, pp. 113–115, Academic Press, Orlando, 1984.

Woodman, R. F., Spectral moment estimation in MST radars, *Radio Sci.*, *20*(6), 1185–1195, 1985.

Woodman, R. F. and A. Guillén, Radar observations of winds and turbulence in the stratosphere and mesosphere, *J. Atmos. Sci.*, *31*(2), 493–505, 1974.

Zrnić, D. S., Estimation of spectral moments for weather echoes, *IEEE Trans. Geosci. Electron.*, *GE-17*(4), 113–128, 1979.

Zrnić, D. S., R. J. Doviak and D. W. Burgess, Probing tornadoes with a pulse Doppler radar, *Quart. J. R. Met. Soc.*, *103*(438), 707–720, 1977.

INVESTIGATION OF MEM SPECTRAL ESTIMATION TO MU RADAR OBSERVATION

Da-ren Lu, Wei Li

Institute of Atmospheric Physics, Academia Sinica
Beijing 100011, China

Susumu Kato, Toshitaka Tsuda, Shoichiro Fukao, Toru Sato, and Mamoru Yamamoto

Radio Atmospheric Science Center, Kyoto University
Uji, Kyoto 611, Japan

1. INTRODUCTION

In recent years there has been considerable interest in a technique of spectrum analysis called the Marimum-Entropy Method (MEM), developed about 1966 by J. P. Burg. This method appears to offer results which have higher resolution, higher accuracy and smoother spectra than traditional methods. It is important to have a reliable method of spectrum analysis in real-time processing of mesosphere-stratosphere-troposphere (MST) radar signals. In a conventional case the traditional periodogram method is used in MST radar data processing. A question that arises is whether MEM is an appropriate spectral estimator for MST radar signals. How about the degree of improvement obtained in the spectral resolution and the signal detectability? KLOSTERMEYER (1986) reported first results of applying MEM and MLM (maximum likelihood method) to estimate signals of VHF radars, and to compare the accuracy of those methods with the conventional periodogram method. He found that at large signal-to-noise ratios (S/N > 100), differences between the Doppler shift estimate are one order of magnitude smaller than the frequency resolution of the periodogram. At moderate signal-to-noise ratios (0.3 < S/N < 10), MEM and MLM estimates have significantly higher accuracies than the periodogram estimates, with the largest differences in accuracy occurring just above S/N = 0.3. In contrast to the periodogram method, MEM and MLM clearly indicate a limiting signal-to-noise ratio (S/N = 0.3) below which the Doppler shift estimates are dominated by noise rather than radar signals.

It is the purpose of this paper to primarily investigate MEM spectral estimates to MU radar observations. We will compare the conventional periodogram method and MEM with the same MU data sets, and discuss improvement of the spectral resolution and signal detectability in the MEM.

2. DATA AND METHOD

The MU radar, located at Shigaraki, Japan, is an MST radar with the operating frequency of 46.5 MHz. The troposphere-stratosphere data used here were taken at 1241-1242 JST on 18 December 1987 (JST: Japan Standard Time). The antenna beam was steered every interpulse period (IPP) to two directions, i.e., 10° off zenith toward the east and vertical. IPP was 400 μs. In each direction 64 heights in the range 5.4 - 24.5 km were sampled at 300-m intervals. In order to improve the signal-to-noise ratio, the number of coherent integrations was up to 80. The time series of each signal sample consists of 512 complex points at each height and beam direction.

Using this data set we performed the results of the conventional periodogram method and maximum entropy method. In the conventional periodogram method power spectra were calculated with an FFT algorithm, then spectral parameters (echo power, radial wind velocity and spectral width) were derived by a nonlinear least squares Gaussian fitting method. The spectral resolution of the FFT method is determined by the length of the data sample. However, a power spectrum obtained by MEM is a continuous function of frequency which

may be evaluated over an arbitrary grid of any density. The maximum entropy method produces a smoother spectrum with higher resolution than the FFT method.

3. RESULTS

Figure 1 shows the results of the FFT method and MEM for a sample obtained in the 10° off zenith toward the east at an altitude of 8.4 km. Figures 1(a) and (b) show the power spectra of the FFT method and MEM separately. In Figure 1(a) the dashed curve indicates nonlinear fitting curve of Gaussian spectra of the FFT method. It can be seen that the FFT method and MEM give almost the same Doppler shift estimate. The power peak near zero-Doppler-shift indicates ground clutter echo. The other power peak with double-peak structure indicates atmospheric signal. We can see clearly the double-peak structure of atmospheric signals in both methods. Due to the frequency resolution limitation of the FFT method, the double-peak structure cannot be distinguished by a nonlinear fitting curve. The double-peak structure of the atmospheric signal is an interesting phenomenon, about which detailed discussion is given below.

As in most cases, the vertical velocity of atmospheric motion is very small, the atmospheric echo and ground clutter echo often overlapped in the zenith observation, as seen in Figure 2(a). So there is a difficulty in estimating very weak vertical velocity with the FFT method. For the MEM with higher frequency resolution, there will be some improvements in the atmospheric vertical velocity detectability, as seen in Figure 2(b).

We will think of the double-peak structure below. From Figure 1 we can see clearly that the two-peak structure obtained from the MEM can be roughly identified with the result of the FFT method. But from only the FFT method we cannot find the clear double-peak structure due to its lower frequency resolution. It has proved that the double-peak structure is a real characteristic of the atmospheric signal rather than the spontaneous line splitting in maximum entropy power spectrum. To understand fully the physical significance, we investigated the variations of the double-peak structure obtained from the MEM with height and time. Figure 3 shows the variations of the double-peak structure at altitudes 8.4 - 9.9 km and shows the emerging, disappearing and transferring of the dominant peak of the double-peak structure. Figure 4 shows the power spectrum of the four time sections which the time series of 512 complex points divided into, a time section consists of 128 complex points. From Figure 4 we find the transferring of the dominant peak of the double-peak structure with time. The variations of the double-peak structure reveals the detailed structure of the atmospheric motion, such as the thin layered structure, the small-scale turbulence and so on. Whereas the FFT method applied to the same data sets produces power spectra with large statistical fluctuations which may obscure the true spectral variations, as seen in Figure 1(a). The MEM would be a useful method for investigating the detailed structure of atmospheric motion.

4. CONCLUSIONS

In the previous section we described the spectral analysis of the MU radar observations with both the MEM and the FFT method. All the results we have obtained lead us to conclude:

a. There is excellent agreement between the radial velocity estimations calculated by the MEM and the FFT methods. Therefore the MEM is suitable for MST radar.

b. It is found that the MEM is useful to get the detailed structure of the spectra which may be useful to understand the atmospheric structure.

c. Because of the higher resolution of MEM, we have the possibility to study the way of eliminating ground clutter and improving the detectability of weak vertical velocity.

In the present case study, the ratio of the computer CPU time for FFT and MEM is about 1. The prediction error filter length of MEM is determined by the final prediction error
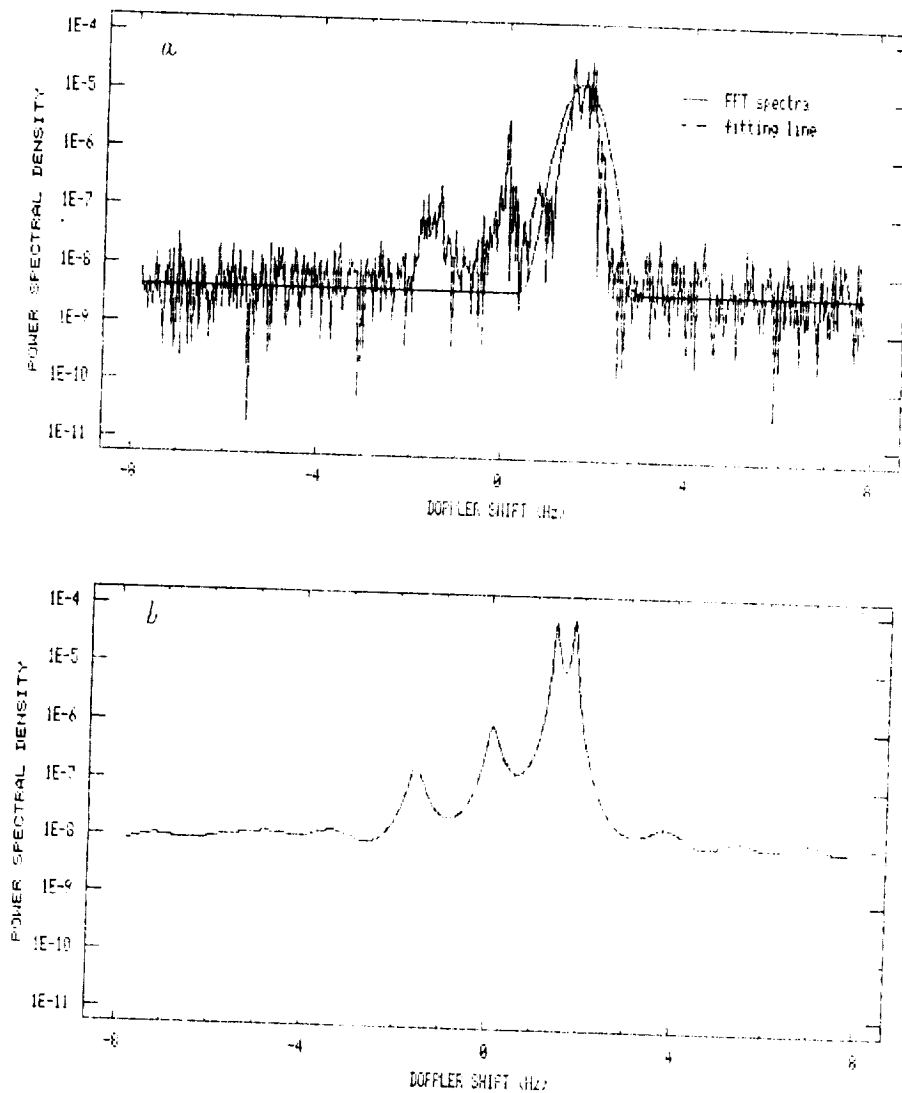
Figure 1. The power spectrum at 8.4 km, in the 10° off zenith toward the east. (a) For the FFT plus Gaussian fitting method, (b) for MEM.
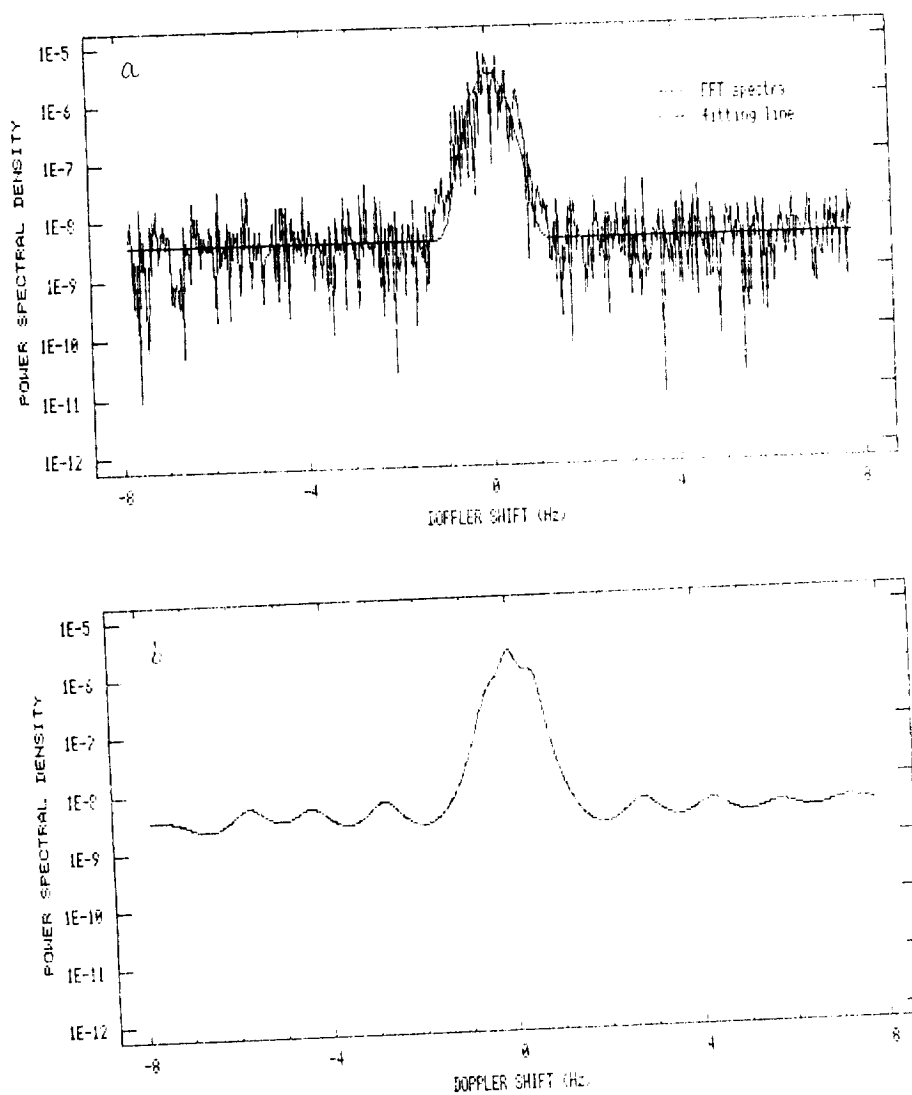
Figure 2. The power spectrum at 14.1 km, in the vertical direction. (a) For the FFT plus Gaussian fitting method, (b) for MEM.
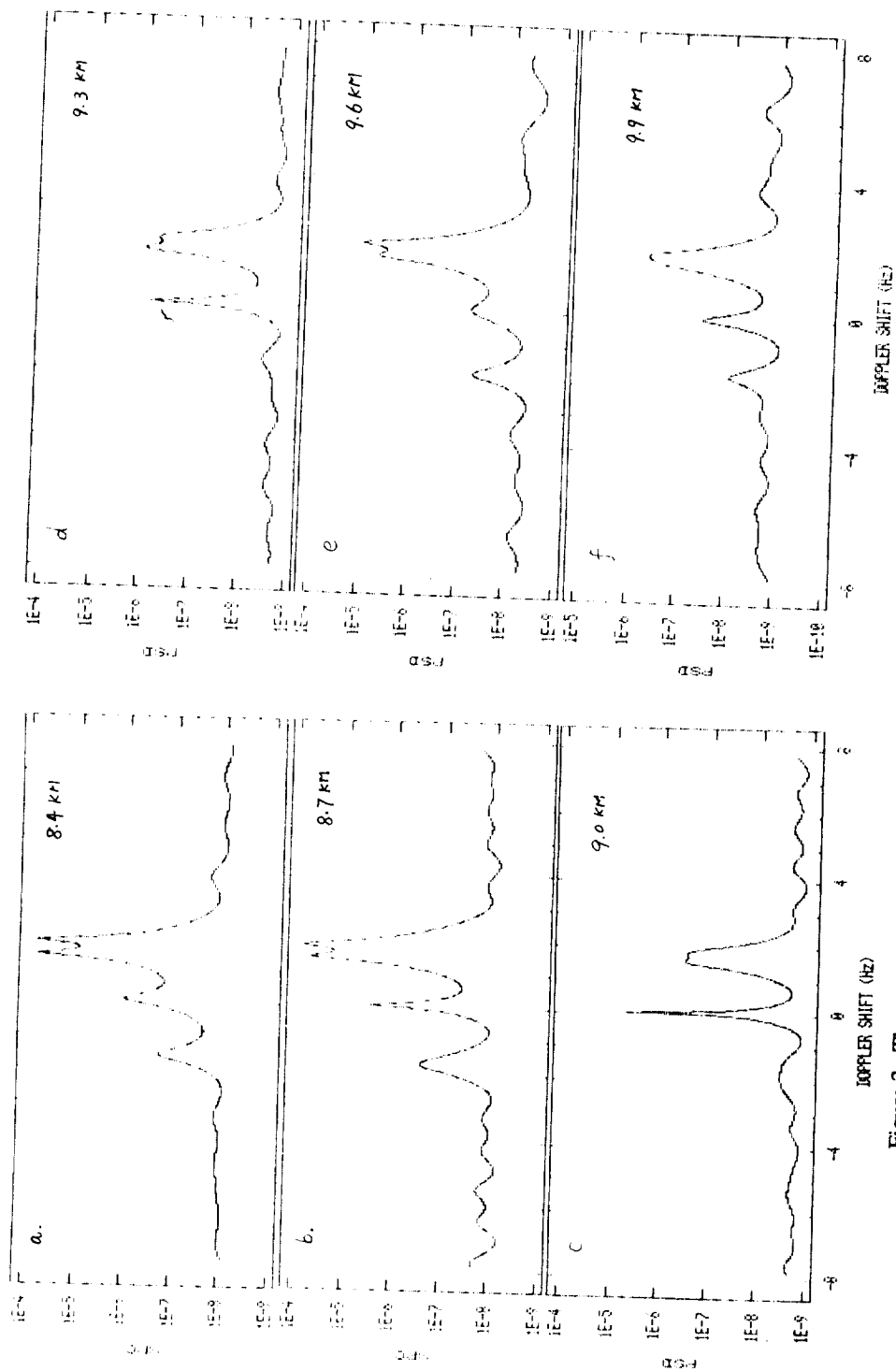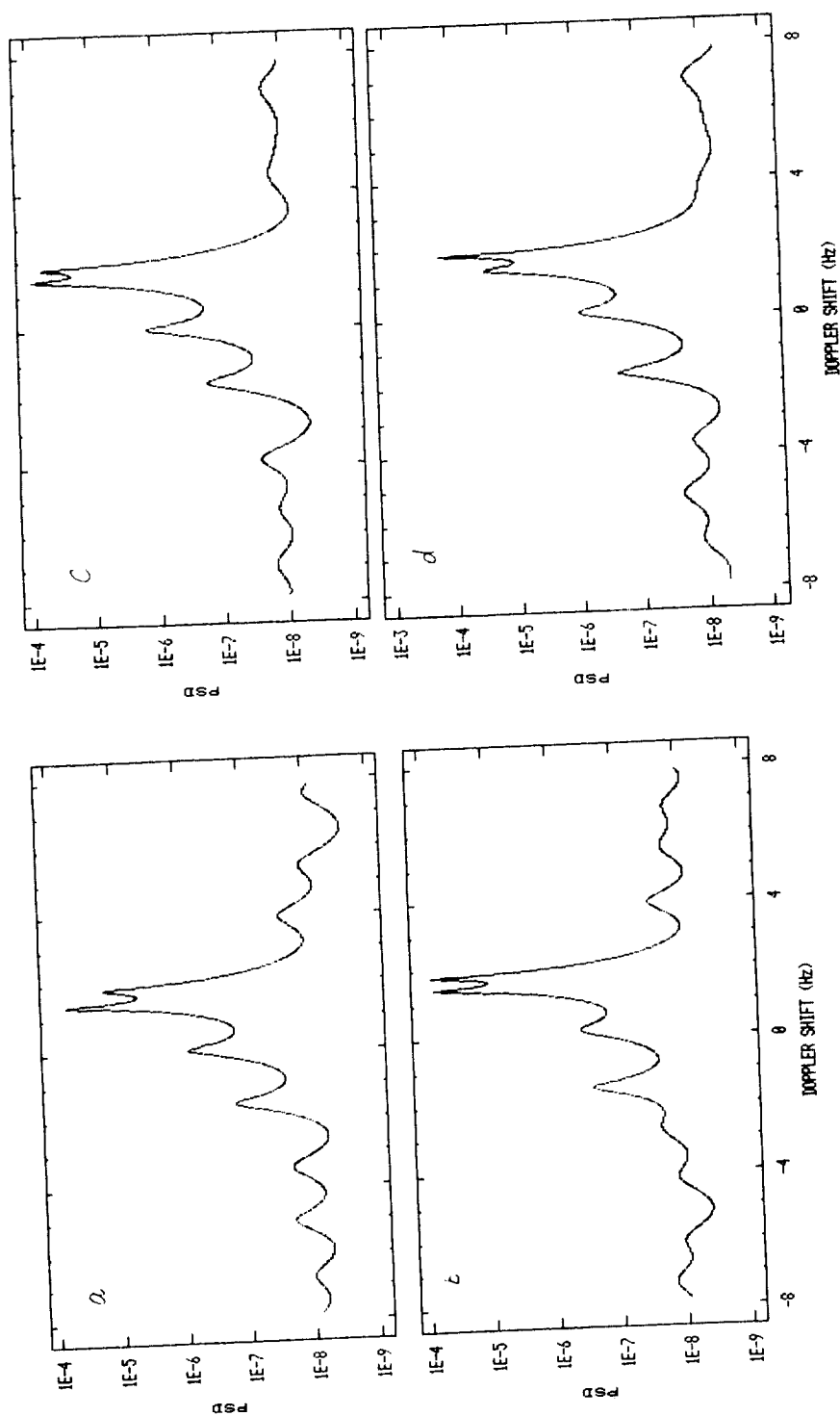
638

Figure 3. The power spectrum for MEM in the 10 off zenith toward the east at each height.

Figure 4. The power spectrum of the four time sections which the time series of 512 complex points divided into, in the 10° off zenith toward the east, at 8.4 km, for MEM. (a), (b), (c), and (d) show the first, second, third, and fourth time section, separately.

(FPE) criterion, about 15. Since MEM has the advantage of using shorter time series, it has the potential for operational application.

REFERENCES

Klostermeyer, J., Experiments with maximum entropy and maximum likelihood spectra of VHF radar signals, *Radio Sci., 21*, 731-736, 1986.

Robinson, E. A., A historical perspective of spectrum estimation, *Proc. IEEE, 70*, 885, 1982.

Kay, S. W., and S. L. Marple, Spectrum analysis -- A modern perspective, *Proc. IEEE, 69*, 1380-1419, 1981.

GROUND CLUTTER SUPPRESSION AT UHF BY THE USE OF SURFACE WIND MEASUREMENTS

P. E. Currier and W. L. Ecklund

Aeronomy Laboratory
National Oceanic and Atmospheric Administration
Boulder, Colorado 80303

UHF wind profilers can observe, in principle, down to very low altitudes (on the order of 100 meters above the surface). However, ground clutter from nearby stationary objects such as trees and power lines can be a serious problem when these objects are moved back and forth with respect to the radar by surface winds. This movement causes the ground clutter Doppler spectrum to spread around zero frequency so that the clutter signal may overwhelm or distort the wanted spectrum of atmospheric returns in the lowest altitudes.

From May to July 1988 a small 915 MHz boundary layer radar was operated at the Flatland field site in Illinois. This site is surrounded at a range of about 150 meters by vertical wires suspended from 20 meter tall poles that are part of an old antenna which is no longer in use. Some of the vertical wires are loose and move freely in the wind providing a controlled "worst-case" close-range ground clutter as observed by the 915 MHz radar. We noted that the intensity and spread of the Doppler spectrum of the clutter from the moving wires increased in a predictable way as the surface wind speed measured at the site increased. This allowed us to develop a template of the Doppler spectrum of the unwanted clutter as a function of surface wind speed. Observed Doppler spectra were then "cleaned" after the fact by noting the recorded wind speed and subtracting the corresponding template values from the spectra.

This technique is demonstrated in Figs. 1 and 2. A Doppler spectrum with ground clutter obtained at a surface wind speed of 5 m/s is shown in Fig. 1. The contours show S/N in 4 dB intervals above the background noise level. The clutter due to the moving wires is centered around zero radial velocity and overwhelms the wanted clear-air return (on the left side of the spectrum) at the lowest altitudes. The first moment of the Doppler spectrum at each height is shown by a vertical tick mark on the horizontal bar. Note that the first moment is progressively biased toward zero radial velocity as height decreases below 1 km. Fig. 2 shows the same spectrum after the template values for ground clutter at this wind speed are subtracted and the first moments recalculated. In this case the first moments track the clear-air returns and are not biased by ground clutter.

The technique of clutter subtraction described above worked well in the well-defined clutter environment at the Flatland field site, but it remains to be determined if the method will be satisfactory in more general clutter environments. Although this technique can be used to "clean" spectra obtained from sites with bad low-level ground clutter, the best approach is to locate the radar away from nearby clutter-producing structures. If this is not possible, the low-elevation antenna response to clutter producing objects may be reduced by shielding or screening the antenna.
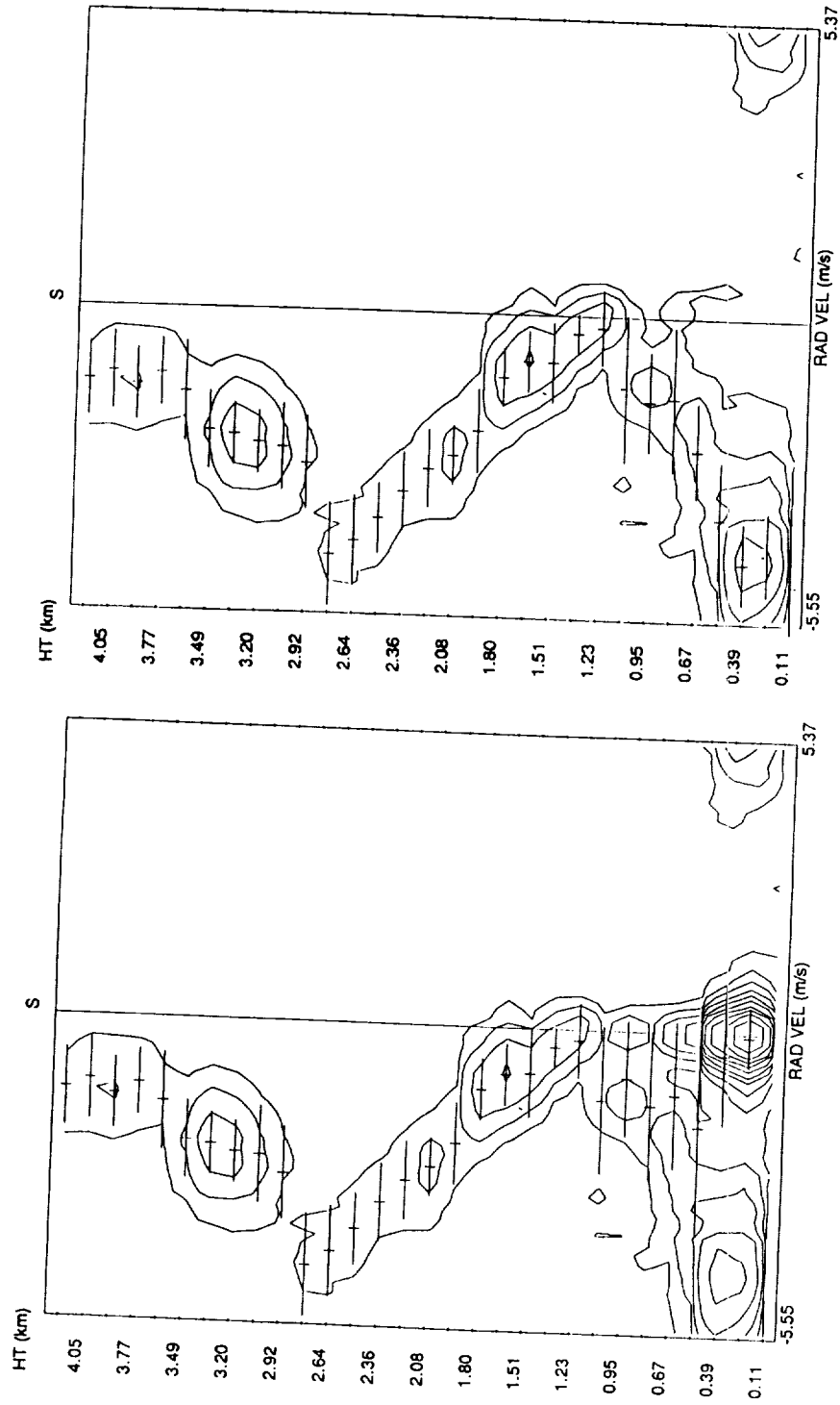
Fig. 1. Doppler spectrum with ground clutter.

Fig. 2. Same as Fig. 1 with ground clutter removed.

RANGE SIDELOBE PERFORMANCE IN A SIMULATED PULSE COMPRESSION RADAR SYSTEM USING COMPLEMENTARY BIPHASE CODED SIGNALS

Y. G. K. Patro, and K. R. Suresh Nair

SAMEER, IIT Campus
Hill Side, Powai, Bombay 400 076, India

INTRODUCTION

The complementary biphase coded signal is known to result in zero range sidelobes for a stationary point target in an ideal situation. But the system parameters like receiver bandwidth, delay distortion, amplitude and phase droop within the pulse can degrade the range sidelobe performance in a practical radar system.

The Indian MST radar which is using a complementary biphase coded signal is modeled to analyze the effects of various factors like transmitter bandwidth, signal-to-noise ratio, initial delay, delay distortion, amplitude droop and the intrapulse phase distortion, on the range resolution characteristics of the radar when coded pulse transmission is used. The real-time waveforms at different stages and the ambiguity diagrams are plotted. The simulation is performed for an eight-bit complementary code sequence for convenience, though a 16- or 32-bit code is planned to be used in the radar.

DESCRIPTION OF THE MODEL

The radar system is modeled as shown in Figure 1. The reference oscillator generates 5-MHz signals and is phase modulated in the modulator which receives the code from the code generator. The code generator generates 8-bit complementary code sequences, A, B, $\bar{A}$, $\bar{B}$, namely (11101101, 11100010, 00010010, 00011101), with '1' signifying 0 deg phase shift and '0' signifying 180 deg phase shift (LORIOT, 1983). The signal waveform is considered to have a pulse width of 8 microseconds and a code subpulse width of 1 microsecond. The code clock (1 MHz) is considered to be in phase with the reference at 5 MHz. The spectrum of the transmitted signal is calculated over a period of 32 microseconds, by padding '0's for 12 microseconds on either side of the transmitted pulse and subjecting the time domain data to a 2048 point FFT. This spectrum is then multiplied with the transfer function of the bandpass filter. The filter is assumed to have in the passband a rectangular amplitude characteristic and a linearly sloping group delay characteristic as shown in Figure 2. The time domain response of the filter at its output is then obtained by subjecting this to a 2048 point inverse FFT. The linear operations of up converting to a higher frequency of 53 MHz before transmission and subsequent down converting to 5 MHz after reception were considered to have no effect on the signal characteristics.

It is assumed that the received pulse from a stationary point target would be exactly identical to the transmitted waveform obtained above, except that it is added with random noise. Random noise is generated by first generating a sequence of 2048 random numbers representing noise samples at every 1/64th microsecond over the signal period of 32 microseconds. The noise samples are then scaled to suit the peak signal-to-noise ratio specified, with peak signal amplitude as unity and then added with the 2048 signal time samples. The random noise that is so simulated may be considered to have a bandwidth of ± 32 MHz.

The video outputs are obtained by modeling the mixer as a true multiplier and the video low pass filter as having a rectangular amplitude and a linearly sloping delay characteristic. The I and Q channel outputs are thus obtained by multiplying the modeled received signal with in-phase and quadrature-phase-shifted 5 MHz reference signals, respectively.

The video outputs are then sampled with a 1 microsecond sample clock over the 32 microsecond period in 8 channels. The sampling period in each of the above 8 channels is considered to be staggered by 1/8th microsecond such that the signal may be reconstituted after it
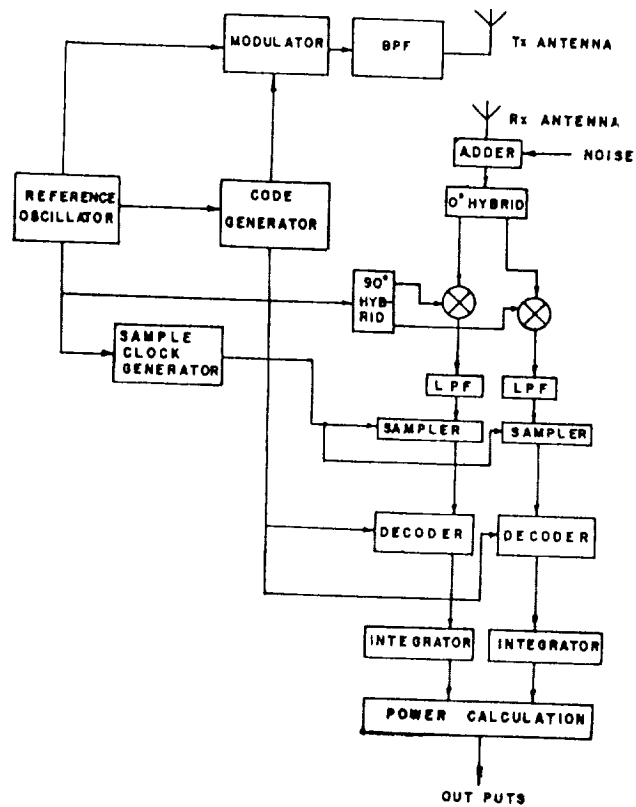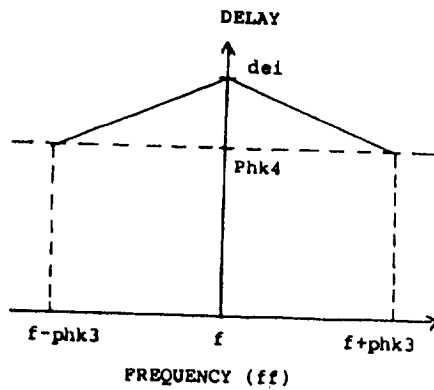
Figure 1. Simulated model of the signal processing scheme of MST radar.

Figure 2. Assumed group delay characteristics of the filter.

f - Center frequency

f-phk3 to f+phk3 pass band

dei- initial delay

Phk4 - delay at the frequency
offset of phk3

passes through the various signal processing operations by virtue of the 8 samples per microsecond interval. Decoding operation is done in each of these 8 channels for the sequences A, B, Ā, and B̄, respectively (SULZER and WOODMAN, 1983) and the outputs in each of the 32 range bins is integrated over four interpulse periods. The output in the 8 channels is thus used to get the range ambiguity diagram by placing the respective range bin outputs at 1/8th bin intervals.

The above model has been used to analyze the effects of various factors like transmit/receive bandwidth under high and low signal-to-noise ratios, and delay distortions in filters. Transmitter irregularities such as amplitude and phase droops within the transmit pulse period are modeled by multiplying the above amplitude and phase versus time characteristics with the instantaneous amplitude and phase of each time sample in the transmitted signal waveform. Thus the effects of these irregularities have also been studied.

The details of the algorithm and the flow chart can be found elsewhere (PATRO and SURESH NAIR, 1988).

RESULTS

Figure 3 shows the time domain waveforms of the transmit signal, I and Q video channels signal for a high SNR situation and a transmit bandwidth of 1.7 MHz and video bandwidth of 0.85 MHz.

Figures 4(a) and (b) summarize the effect of transmit bandwidth on range sidelobes under situations of a high SNR and a low SNR (of −10 dB), respectively. The following inferences may be drawn from these figures.

(a) The (nearly) unrestricted bandwidth case is ideal in the sense that there are no range sidelobes, but it also allows significant noise to enter into the decoded output and final SNR is poor.

(b) A low transmit bandwidth of 1 MHz and video bandwidth of 0.5 MHz may be ideal from the point of view of minimum interference with adjacent channel and noise suppression but it gives rise to an unacceptable 16 dB sidelobe level and poorer range resolution.

(c) A transmit bandwidth of 1.7 MHz and video bandwidth of 0.85 MHz may be considered to be a suitable compromise.

Figure 5 shows that a differential delay of 100 nanoseconds in the transmit path and the same in the receive path make the range sidelobe on one side rise to a level of 20 dB below the main peak.

Figure 6(a) shows that amplitude droop, considered alone may not contribute to significant performance degradation, except that the far off sidelobes get prominent. Figure 6(c) shows that a phase droop of 30 deg within the pulse would increase the range sidelobe to about 20 dB below the peak.

CONCLUSION

The above simulation studies indicate the performance of the system under actual non-ideal conditions encountered in a physical radar system. They help in drawing the subsystem specifications to meet a desired system goal.

ACKNOWLEDGMENTS

Thanks are due to Prof. R. V. S. Sitaram, Shri P. B. Tole and Shri S. H. Damle for their suggestions.
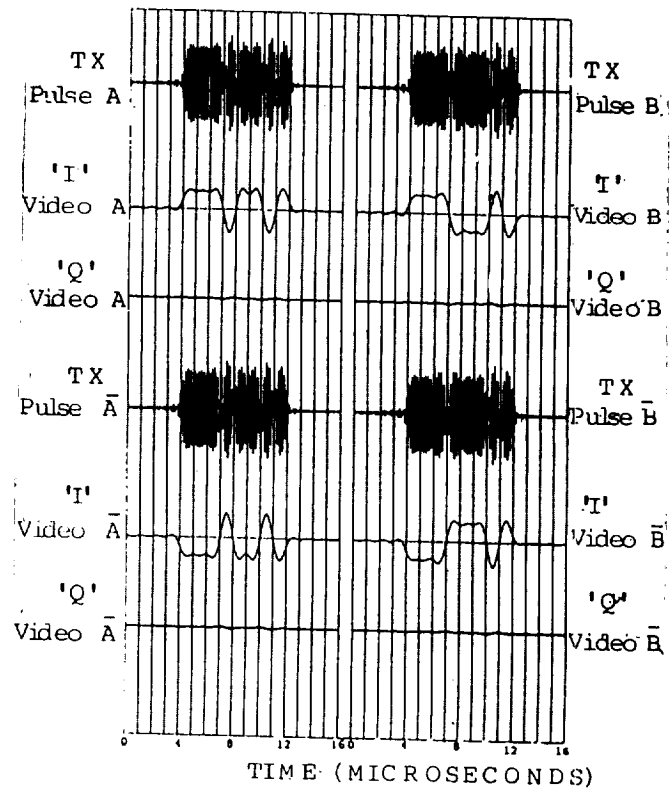
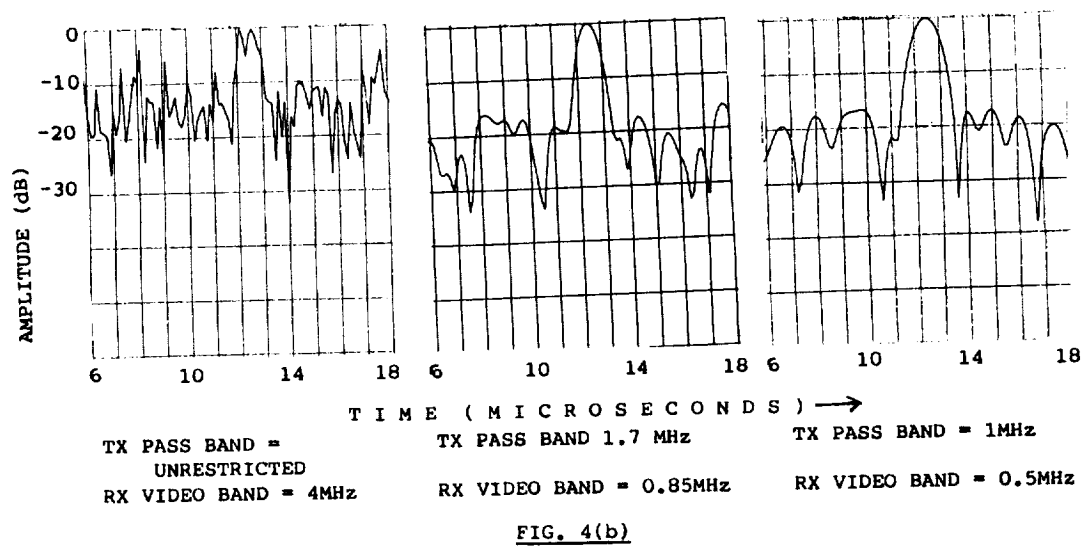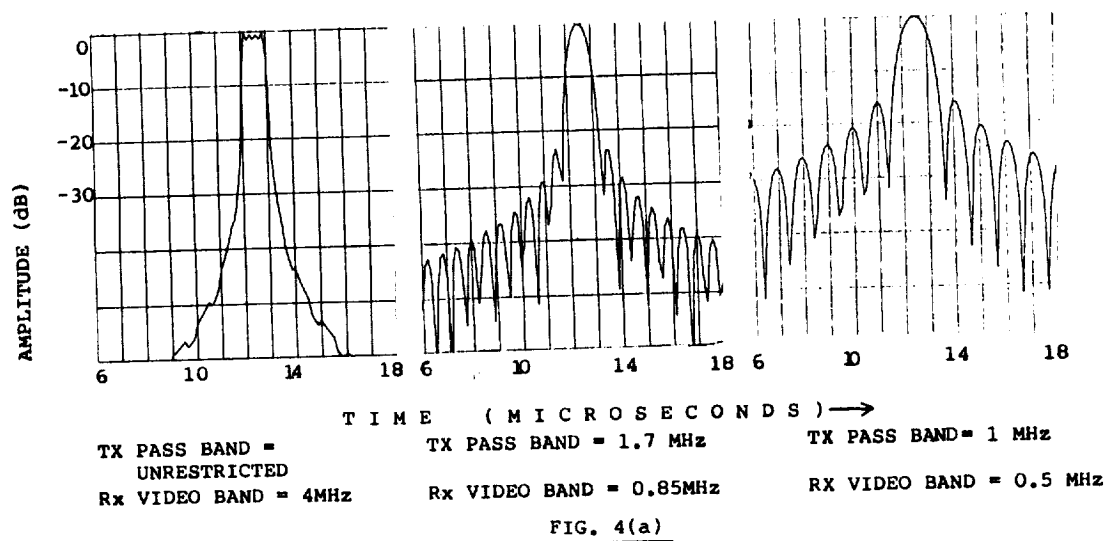Figure 3. Time domain waveforms for 1.7 MHz bandwidth.

FIG. 4(a)

FIG. 4(b)

Figure 4. Effect of transmit bandwidth on range sidelobes. (a) under high SNR, (B) under low SNR (−10 dB).
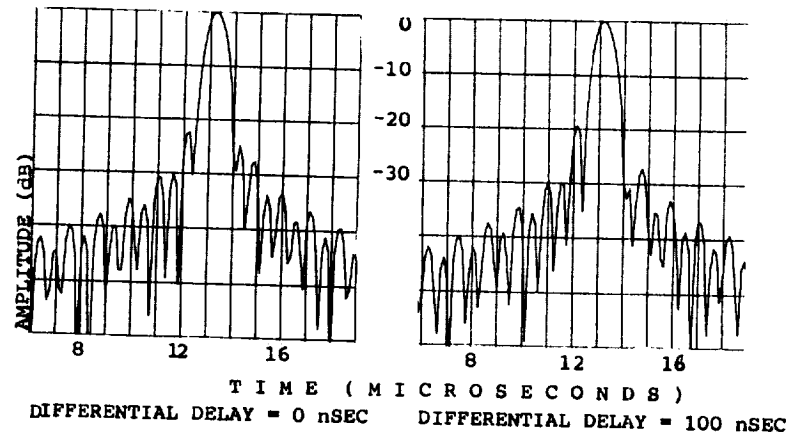
Figure 5. Effect of delay distortion on range sidelobes. Initial delay in BPF = 350 nsec, TX pass band = 1.7 MHz; initial delay in video LPF = 350 nsec; RX video band = 0.85 MHz. SNR = 100 dB.
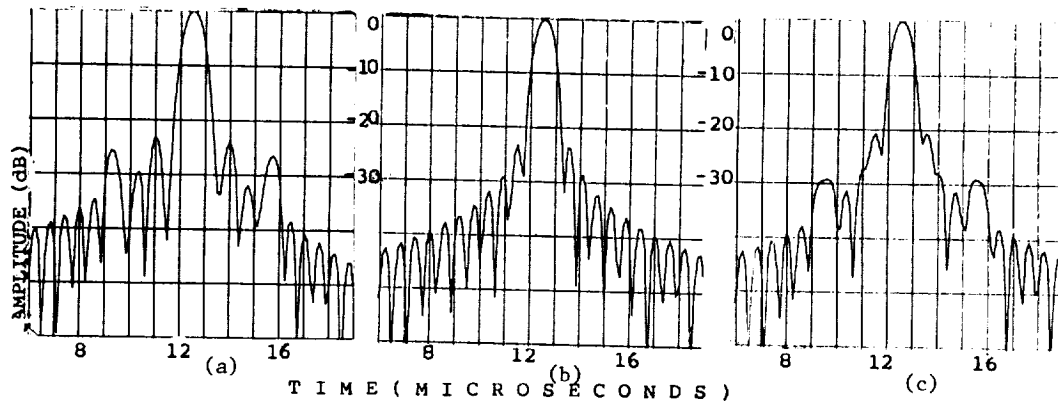

Figure 6(a) Effect of amplitude droop, amplitude droop = 50%; (b) amplitude droop = 0%, phase droop = 0 deg; (c) effect of phase droop, phase droop = 30 deg TX pass band = 1.7 MHz, RX video band = 0.85 MHz, initial delay = 0 nsec, delay distortion = 0 nsec, SNR = 100 dB.

REFERENCES

Loriot, G. B., Decoding: Software implementations, *Handbook for MAP VOL 9*, 496, SCOSTEP Secretariat, Univ. Ill., Urbana-Champaign, 1983.

Patro, Y. G. K., and K. R. Suresh Nair, Range sidelobe performance in a simulated pulse compression radar system using complementary bi-phase coded signal, *Tech. Rep. No. SMR/MST/SY/880902*, 1988.

Sulzer, M. P., and R. F. Woodman, Decoding: Codes and hardware implementations, *Handbook for Map, VOL 9*, 498, SCOSTEP Secretariat, Univ.Ill, Urbana-Champaign, 1983.

Accuracy of Precipitation Measurements with the MU Radar

Toru Sato, Hiroshi Doji and Iwane Kimura

Department of Electrical Engineering II, Faculty of Engineering, Kyoto University
Kyoto 606, Japan

Shoichiro Fukao, Toshitaka Tsuda, and Susumu Kato

Radio Atmospheric Science Center, Kyoto University
Uji, Kyoto 611, Japan

1 Introduction

It has been found that a sensitive VHF Doppler radar can detect precipitation echoes simultaneously with echo from the ambient atmosphere (Fukao et al., 1985). Wakasugi et al. (1986, 1987) investigated a computer algorithm to derive parameters of drop-size distribution as well as the mean vertical velocity and fluctuations due to turbulence from the radar spectra. Namely assuming an exponential form which was suggested by Marshall and Palmer (1948) for the drop-size distribution and a Gaussian distribution for the atmospheric turbulence spectra, they have applied least-square fitting to the observed spectra.

This method gives rise to reasonable parameters, in case good initial values are used for the parameters to be estimated. Their algorithm needed, however. human intelligence in determining these initial values except when the rain echo component is clearly separated from the atmospheric echo component in the observed power spectra. We have extended their method to find appropriate initial parameters purely by computer in order to enable us to deduce the drop-size distribution and vertical atmospheric velocity automatically from original data by using computer.

We have also quantitatively investigated the capability of the MU radar in measuring various parameters associated with precipitation, such as the number density of rain drops, the drop-size distribution, and the maximum fall velocity by means of numerical simulations.

We present the accuracy of individual parameters in terms of the number of incoherent integration, and then compare the resultant rainfall rate with that measured on the ground.

2 Derivation of Rain Parameters from Echo Power Spectra

The Doppler spectrum $S(v)$ of rain echo in the absence of turbulence echo and atmospheric motion is represented by

$$S(v) = C \cdot N(D)D^6 |\frac{d(v(D))}{dD}|, \tag{1}$$

where C is a constant which represents all factors in the radar equation, $v(D)$ is the fall velocity (positive upward) of rain drops with diameter D, and $N(D)$ is the number density distribution of the drops, which can be approximated by the Marshall-Palmer distribution:

$$N(D) = \begin{cases} N_0 exp(-\Lambda D) & \text{for } v_{max} \leq v \leq 0 \\ 0 & \text{for } v < v_{max}, \ 0 < v \end{cases} \tag{2}$$

where N_o is a constant proportional to the number density of rain drops, Λ is the spectral index of the drop size distribution, and v_{max} is the maximum drop fall velocity. For the case of VHF radars, another spectrum due to turbulence scattering with comparable or larger amplitude is superimposed on the spectra of (1). The spectral shape of this component is usually approximated by a Gaussian, whose width represents turbulence motion inside the scattering volume and other broadening factors such as the beam broadening. If we assume that the rain drops closely follow the atmospheric motion, the spectra of (1) is convolved with this Gaussian in the presence of turbulent motion. Further, the observed spectra is distorted due to truncation of the time series in applying the periodogram method as used by the MU radar real-time data processing.

Taking all these effects into consideration, we can derive parameters in (2) from an observed spectrum by comparing the observed and theoretical spectra in a least squares manner. The actual parameters to be determined are the three parameters in (2), three parameters which describe the Gaussian turbulence spectrum, and the background noise level. Since the theoretical spectrum is nonlinear with respect to those parameters, a nonlinear least squares fitting algorithm (e.g., Bard, 1974) is used. The algorithm expands the theoretical function into a Taylor series around some suitable set of initial values of the parameters, applies the linear least squares fitting procedure recursively revising the initial values.

The initial values for the three parameters of the atmospheric turbulence component can be obtained fairly easily by taking three spectral moments around its peak. On the other hand, the three parameters for the rain component are more difficult to choose since this component is usually weaker than the turbulence component, and not well separated in frequency either. The fitting procedure is repeated for all combinations of three different values of the three parameters, and the one which gives the minimum variance between the observed and the theoretical spectra is used.

Figure 1 is an example of observed echo power spectrum (irregular curve) and the best-fit theoretical one (smooth curve). The observed spectra were averaged over 1 min. The height resolution is 150 m. The larger peak around zero-Doppler is the atmospheric turbulence component, and the smaller peak with negative (downward) Doppler velocity is the rain echo component. A small bump at around $+8$ m s^{-1} is an image of the rain component due to nonlinearity of the A/D converter in the presence of strong ground clutter, which is subtracted in this figure. The noise level is slightly overestimated probably because of this bump.

3 Intrinsic Accuracy of the Estimation

As shown in Fig 1, the observed spectra always contain random fluctuations based on the statistical nature of the scattering process even in the absence of the background noise. The magnitude of the fluctuation is proportional to the spectral density, and can be reduced only by averaging a larger number of independent observations. This fluctuation is the most important source of the intrinsic error in estimating the rain parameters. Since the fitting procedure is highly nonlinear, the error in the derived parameters cannot be estimated directly from the residual of the fitting, as can be done for the linear least squares fitting.

We have evaluated the accuracy of the estimated parameter by means of numerical simulations. We generated theoretical spectra according to (1) and (2), convolved with and added the turbulence component, added statistical fluctuations expected for real data, and smeared to simulate the effect of finite data length in the periodogram method. We gave the spectra to the fitting program, retrieved the spectral parameters, then compared the estimated parameters with those used to generate theoretical spectra. We repeated simulations 50 times for
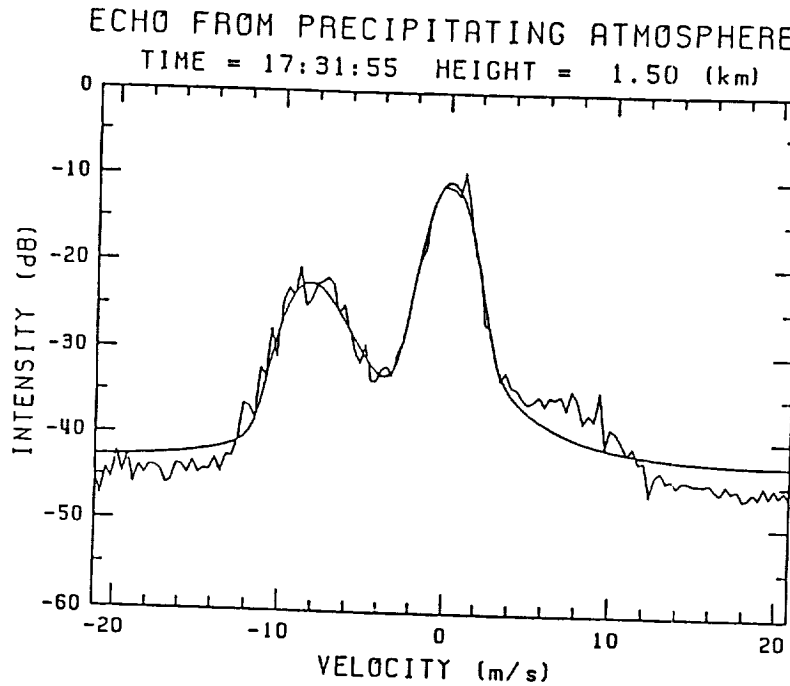
Fig. 1. Example of observed echo power spectrum (irregular curve) and the theoretical one (smooth curve) determined by the nonlinear least squares fitting procedure.

each set of parameters with different random numbers in order to examine the mean value of the errors.

Figure 2 shows an example of the result of this simulation versus the number of incoherent integration N_{icoh} (averages of independent power spectra). The model values given are $N_o = 6 \times 10^3$, $\Lambda = 25\ \mathrm{cm}^{-1}$, and $v_{max} = -7\ \mathrm{m\,s^{-1}}$, which are typical values for a relatively strong rain condition. The left panels are the estimated mean values of N_o, Λ, and v_{max}, respectively from top to bottom, and the right panels show the standard deviation of the estimated values of corresponding parameters from the given values. The dotted line in the right panels indicate a slope proportional to $N_{icoh}^{-1/2}$, which is the rate of improvement expected for averages of independent random numbers.

The left panels indicate that the estimated values converge to the model values when the number of averages increases, while the right panels show that error is quite large, especially for the estimation of N_o. For example, error amounts to about 100% for N_o when $N_{icoh} = 6$, which corresponds to a time resolution of 1 min if the average is made in time. Apparently, a larger number of averages is required in order to obtain reliable estimates. This proportionality suggests that a reasonably good accuracy of 10% can be achieved by averaging over 10 min of time and 1.5 km of height ranges.

4 Comparison with Ground Measurements

Although the evaluation made above considers all of important statistical and numerical factors which affect the estimates, it assumes that the strength of rain and the drop size distribution, as
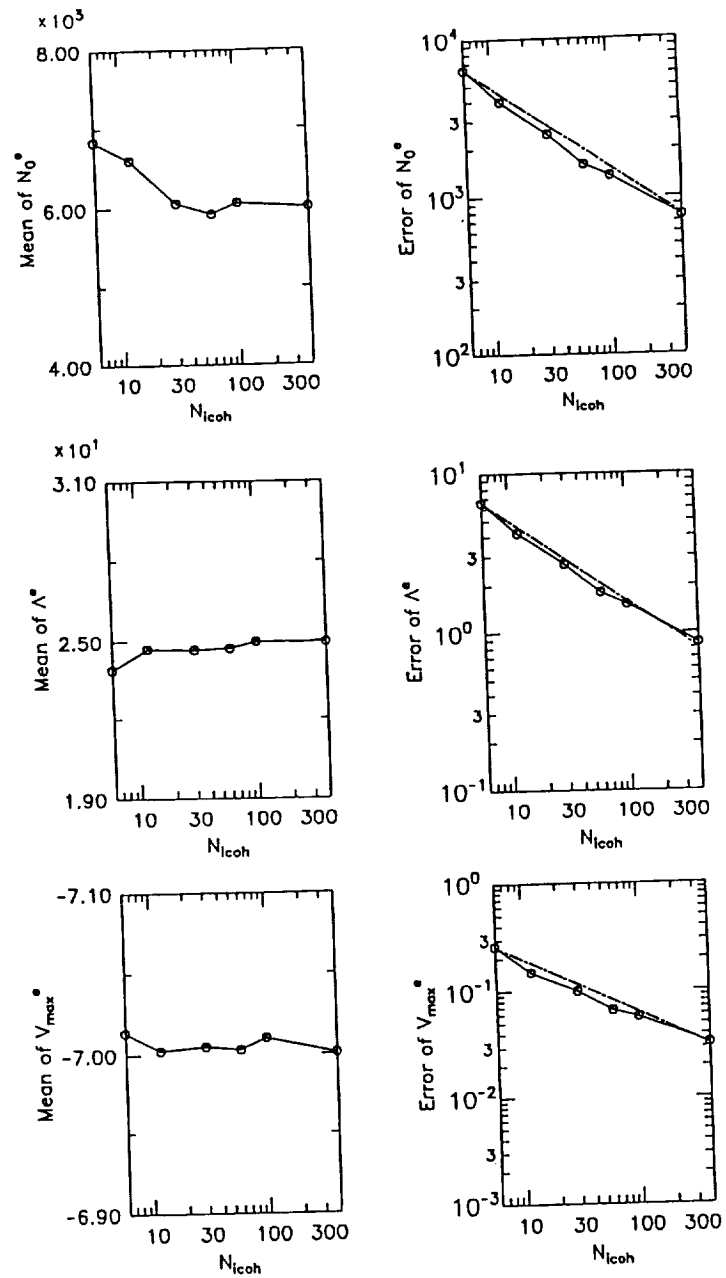
Fig. 2. Statistical error of the fitting algorithm evaluated by numerical simulations. The left panels are the estimated mean values of N_o, Λ, and v_{max}, respectively from top to bottom, and the right panels show the standard deviation of the estimated values of corresponding parameters from the given values.

well as the background atmospheric conditions, do not change during the incoherent averaging. Fluctuations in the wind velocity, for example, broaden the observed spectra and makes the estimation of the rain parameters harder.

We have made direct comparisons of the rain intensity deduced from the MU radar data with that measured on the ground by a high-resolution rain gauge located at the MU radar site. The top panel of Figure 3 indicates the detection of rain echoes by the MU radar for a series of observation made during a rainy condition. Large dots denote that the spectral component due to rain echo was identified by the fitting program, and small dots denote that only the atmospheric turbulence component was found. Blank area means that the no echo was detected. The middle and lower panels compare the rain intensity measured by the rain gauge and by the MU radar, respectively. Both values are 10-min mean intensity expressed in the unit of mm/hour. The rain intensity calculated from the parameters we derived from the MU radar echo-power spectra by our algorithm are also averaged over 1.5–3.5 km height region. Since the echo power of the MU radar does not have an absolute calibration, the vertical scale of the bottom panel is adjusted to match that of the middle panel.

The ground and radar measurements agree within a factor of 2 for most of the period, and the correlation coefficient between the two is 0.87. It should be noted that some of the discrepancies are attributed to the advection of the rain cells between the height measured by the radar and the ground. comparison between the top and the middle panels indicates that the minimum rain intensity detected by the MU radar is about 1 mm/hour.

5 Summary

Accuracy of a fully automated estimation procedure of rain parameters from the MU radar data was evaluated by numerical simulations, and the estimated rain intensity was compared with that measured on the ground. The intrinsic accuracy of the estimation procedure is expected to be about 10% for the rain intensity when the data is averaged over 10 min in time and 1.5 km in height. Correlation between the radar and the ground measurements of rain intensity was 0.87 for a 12-hour observation.

References

Bard, Y., *Nonlinear parameter estimation*, Academic Press, New York, 1974.

Fukao, S., K. Wakasugi, T. Sato, S. Morimoto, T. Tsuda, I. Hirota, I. Kimura and S. Kato, Direct measurement of air and precipitation particle motion by VHF Doppler radar, *Nature*, **316**, 712-714, 1985.

Marshal, J. S., and W. M. Palmer, The distribution of raindrops with size, *J. Meteor.*, **5**, 165-166, 1948.

Wakasugi, K., A. Mizutani, M. Matsuo, S. Fukao and S. Kato, A direct method for deriving drop-size distribution and vertical air velocities from VHF Doppler radar spectra, *J. Atmos. Oceanic. Technol.*, **3**, 623-629, 1986.

Wakasugi, K., A. Mizutani, M. Matsuo, S. Fukao and S. Kato, Further discussion on deriving drop-size distribution and vertical air velocities from VHF Doppler radar spectra, *J. Atmos. Oceanic. Technol.*, **4**, 170-179, 1987.
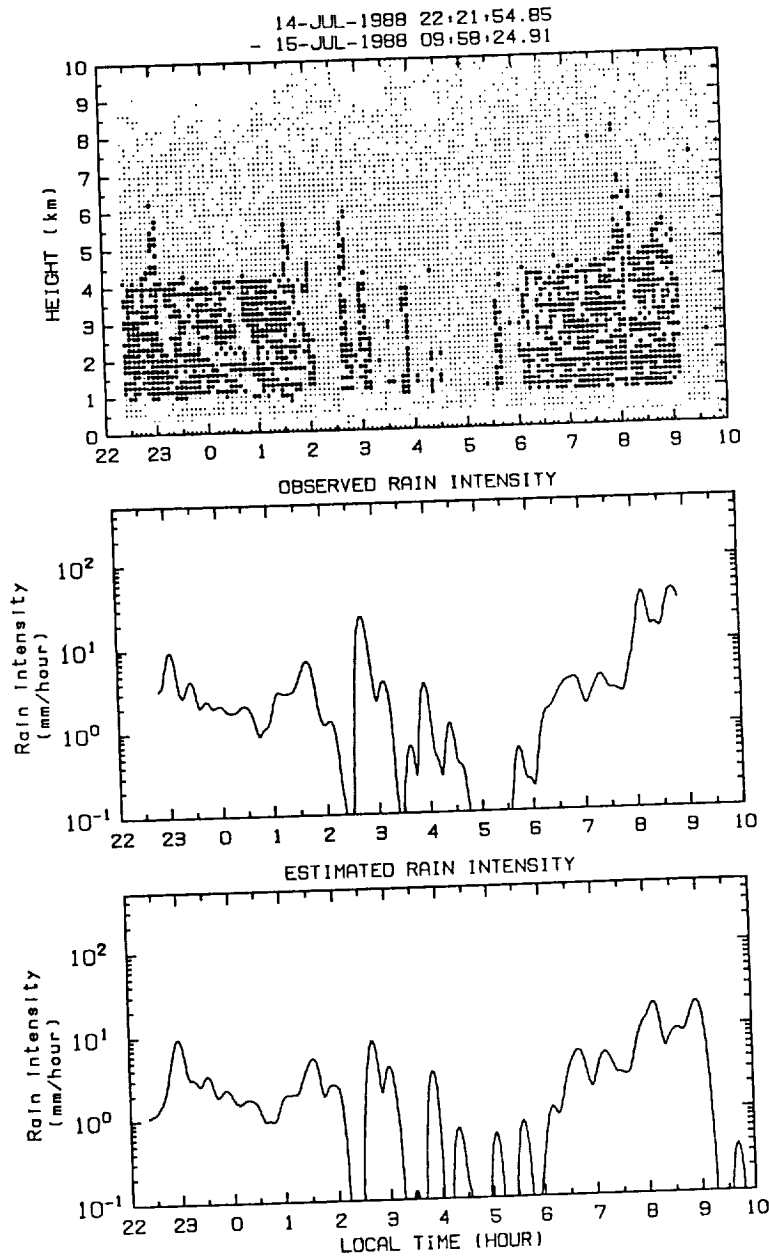
Fig. 3. Comparison of radar and ground measurements of the rain intensity. The top panel indicates the detection of rain echoes by the MU radar. Large dots denote that the spectral component due to rain echo was identified, and small dots denote that only the atmospheric turbulence component was found. The middle and lower panels compare the rain intensity measured by the rain gauge and by the MU radar, respectively. Both values are 10-min mean intensity expressed in the unit of mm/hour.

NEW QUASI-COMPLEMENTARY CODE SETS FOR ATMOSPHERIC RADAR APPLICATIONS

Prabhat K. Rastogi and Gregory Sobolewski
Electrical Engineering and Applied Physics Department
Case Western Reserve University, Cleveland, Ohio 44106

Summary

An exact cancellation of correlation sidelobes in high-resolution atmospheric radar experiments with complementary code pairs is not attained due to nonlinearities in radar transmitter, and due to poor coherence of atmospheric targets. Quasi-complementary code sets (QCCS) are sets of binary sequences with low correlation sidelobes. These sidelobes nearly cancel out in the correlation function accumulated over a QCCS. Sulzer and Woodman (1984) used an intensive, but partial, computer search at Arecibo to find 32-bit QCCS of size 48 at a maximum residual correlation sidelobe level of 4. We have conducted an exhaustive computer search through all 32-bit sequences for a base set of 844 sequences (and their binary complements) with a maximum correlation sidelobe level of 3. Codes in the base set are then combined to generate QCCS of specified size, and a maximum residual correlation sidelobe level of 2. The base set is sufficiently large to allow more stringent selection criteria using, e.g., lower r.m.s. correlation sidelobes and better Doppler ambiguity characteristics.

Introduction

The objective of pulsed-Doppler radar experiments for probing the middle atmosphere is to detect thin regions of weak turbulence and to measure their bulk velocity. The measurement accuracies for turbulence intensity and radial velocity depend on the received signal-to-noise ratio (SNR). To maximize the SNR, widest possible radar pulses should be used within the peak and average power limitations of the transmitter. Yet for improved range resolution, which is inversely related to the pulse width, pulses should be as narrow as possible within the allowed transmitter bandwidth .

These contradictory requirements on range resolution and SNR can be attained with the use of pseudo-random binary phase codes in transmission, and an inverse operation, or decoding, on the received signal. Effectively, a long pulse at a constant carrier power level is transmitted. At subintervals or bauds within the pulse, the phase of the carrier is encoded or modulated by +90° or -90° in accordance with a pseudo-noise binary sequence. In the

inverse operation of decoding, the received signal is cross-correlated with the binary sequence. As different subintervals within the transmitted signal are nearly uncorrelated, the cross correlation attains is maximum at the expected target range delay, but it remains relatively small at all other delays. The range resolution after decoding corresponds to the baud length, but the SNR depends on the pulse length.

First use of binary phase codes in atmospheric radars is due to Ioannidis and Farley (1972) in early incoherent-scatter measurements of the D-region at Arecibo. They used Barker sequences which have the property that their correlation sidelobes are within ±1 (Barker, 1953). These sequences are known only for some code lengths ≤13 (Turyn, 1968). Figure 1 shows the 13-baud Barker code and its autocorrelation function. The cross-correlation function of the signal received from a point target with the code is also shown, for an assumed band-pass frequency response of the receiver. The finite receiver passband causes a loss in signal power and introduces a finite group delay. Corrections for these must be applied after decoding.
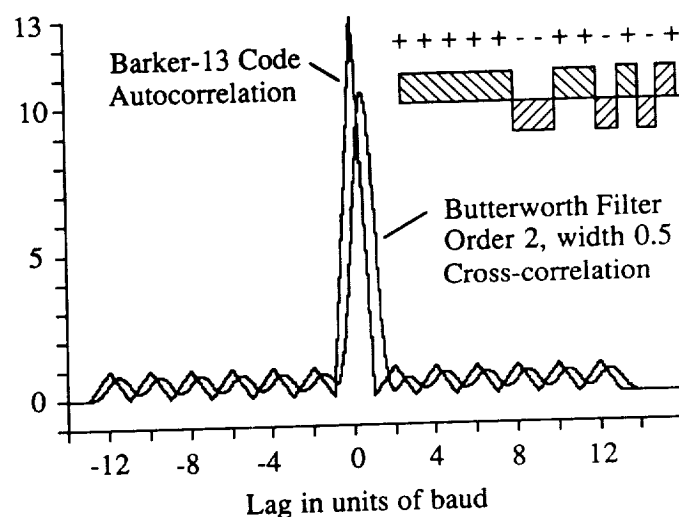
FIGURE 1. The 13-baud Barker sequence (inset) and its autocorrelation function. Cross correlation of the code with the receiver output due to a point target is shown centered at the nominal range delay for the target. The receiver frequency response is that due to a second-order bandpass Butterworth filter. The total 3-dB bandwidth of this filter, about the carrier frequency, is half of the inverse baud length.

658

In many other radar experiments, the received signal fades slowly compared to the inter-pulse period (~1 ms) i.e. the atmospheric medium behaves as a relatively coherent target over many transmitted pulses. It is then possible to modulate successive pulses with different phase codes. Particularly useful are code pairs with complementary property, that the sum of their correlation sidelobes vanishes exactly [Golay, 1961]. Such code pairs were initially used in middle atmosphere experiments with the SOUSY and Arecibo radars [Schmidt et al. 1979, Woodman, 1980]. Since only two different codes are used, often with coherent averaging of received signal over many transmitted pulses [Rastogi, 1983], an efficient implementation of the cross-correlation or decoding scheme is obtained by relegating it after coherent averaging. Figure 2 shows a 32-bit complementary code pair, and the autocorrelation function for one of the two codes. Codes in the pair have poor pseudo-noise properties as evidenced by their high correlation sidelobes at level ±7 or ~22% of the zero-lag value. These large correlation sidelobes do not exactly cancel in practice due to transmitter nonlinearities, and due to rapid changes in the atmospheric medium. This often results in ghost echoes from thin strong layers of turbulence.
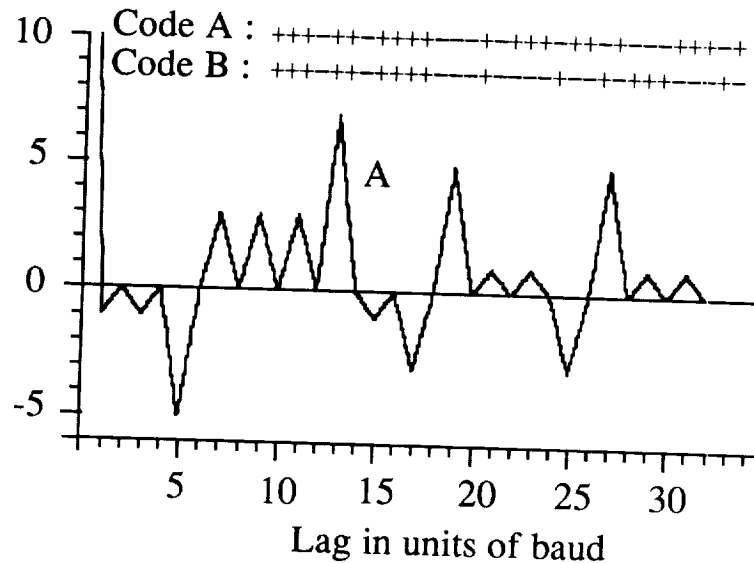
FIGURE 2. A 32-baud complementary code pair and the autocorrelation function for one (A) of these. The zero lag value of 32 is out of scale. Correlation sidelobes of codes A and B are inverted replicas of each other. The sum of their autocorrelation functions is 64 at zero lag, but zero elsewhere. Large sidelobes of magnitudes 3, 5 and 7 do not perfectly cancel in practice and produce ghost echoes after decoding.

When the on-line computing resources permit pulse-by-pulse decoding, it is possible to use complementary code sets (CCS) of binary sequences with the complementary property, that the correlation sidelobes cancel exactly upon addition across the set [Tseng and Liu, 1972]. Generation of CCS as feedback shift register sequences is discussed by Sarwate (1984). The number of sequences in a CCS depends on the sequence length, e.g. a CCS of 2^n codes of length $2^n - 1$ can be readily generated, but the limitation on number of codes is often too restrictive for atmospheric radar applications. Individual codes in a CCS usually have large correlation sidelobes. An exact cancellation of these sidelobes would be difficult as with complementary code pairs, and ghost echoes may arise. An alternative method (Sulzer and Woodman, 1984) is to first select binary sequences with good correlation sidelobes, and then to combine an arbitrary number of these in a quasi-complementary code set (QCCS). Theoretical methods for finding QCCS are apparently unavailable.

Quasi-Complementary Code Sets (QCCS)

The first use of QCCS in atmospheric radar experiments is due to Sulzer and Woodman (1984). They used an intensive, but partial, computer search for 32-bit QCCS. As indicated above, the search comprises two parts (i) finding a base set of codes with 'good' correlation sidelobes, and (ii) a method of combining an arbitrary number of these to form a QCCS with acceptably low residual sidelobes in the correlation function accumulated over the set.

In discussing QCCS, we first remark that the decoder output is a voltage signal. If the autocorrelation function of a binary code sequence is r(k) at a shift k (in units of a baud), then the signal due to a point target will leak at other range delays as ~r(k) on a voltage basis, and as ~r^2(k) on a power basis. Codes in the base set should, therefore, have a uniformly low correlation sidelobe level to reduce ghost echoes. The effect of a uniformly distributed background of random point targets on signal power at any given range is minimized by requiring that the integrated power $\Sigma_{k \neq 0} r^2(k)$ in the correlation sidelobes of a code sequence should be minimum.

Sulzer and Woodman (1984) specified the criterion that the total power in the correlation sidelobes should be 20% or less than that of the main lobe, i.e.

$$\{\Sigma_{k \neq 0} r^2(k)\} \leq 0.2 \; r^2(0).$$

With this criterion, they found a base set of ~300 codes in a partial search through ~0.7 billion codes. They formed QCCS by selectively combining codes from this set in groups of four. In an actual experiment, the residual correlation sidelobe level of a 32-bit QCCS of size 48 was found to be better than for complementary codes. We have therefore undertaken an exhaustive search for a base set of 32-bit codes and have devised a simple algorithm for forming near optimum QCCS of arbitrary size.

New QCCS : Search Criteria and Code Properties

An exhaustive search for a base set of codes with minimum correlation sidelobe level is a computation intensive task. There are 2^{32} or over 4-billion 32-bit codes. Since sequences $\{a_j\}$ and $\{-a_j\}$ have the same autocorrelation function, even with the sign bit omitted, the search must still be carried through 2^{31} codes. Turyn (1968) gives the lower bounds on $\max_k |r(k)|$ for several codes of length up to 34. The lowest value of $\max_k |r(k)|$ is 3 for 32-bit codes. Lindner (1975) has conducted an exhaustive search for binary codes with minimum correlation sidelobe level, for code lengths up to 40 .

The speed of currently available workstations has enabled us to conduct an exhaustive sequential search for a base set of 32-bit codes in about 400 hr on a Sun 3/52. A code is excluded as soon as a correlation sidelobe magnitude $|r(k)|$ above 3 is encountered. A total of 1688 codes with correlation sidelobes within ± 3 have been found. After excluding the binary complements, only half of these or 844 codes have been retained in the base set. The size of the base set agrees with that reported by Lindner (1975).

Codes in the base set of 300 codes found by Sulzer and Woodman (1984) have an r.m.s. correlation sidelobe level below 1.82, but their maximum sidelobe level may be as high as 6. Codes in the base set of 844 codes reported above have a maximum correlation sidelobe level of 3, and a minimum r.m.s level of 1.52. It includes 104 codes with an r.m.s. sidelobe level below 1.82. Codes in this subset have optimum correlation sidelobes in both the absolute and r.m.s. sense. The envelope of correlation sidelobes in our base set is shown in Figure 3. For comparison the correlation sidelobes of codes in the sample QCCS given by Sulzer and Woodman (1984) are also shown.

The task of forming optimum QCCS of a given size from the base set is, in principle, quite formidable. Selecting a QCCS of m codes from a base set of size n requires a search through $^nC_m = n!/ m!(n-m)!$ possibilities. In our case the number of possibilities is too large to exhaust e.g. for m=10 and n=844 it is ~4.8 x 10^{22}, and even with n=104 it still is ~2.6 x 10^{13}. It suffices therefore

to search for QCCS with acceptable properties in terms of a threshold for sidelobes of accumulated correlation function.

We have sought QCCS with a threshold level of 2 (or 3 for some odd m). A two-step algorithm is used in which a code is included in the QCCS if it does not increase the residual correlation sidelobe level, and a finite number of codes is tried at the last stage while testing for the threshold level. It routinely yields a QCCS for $m \leq 64$ in less than 5 min. For a set with $m=48$, the correlation at zero lag is 32x48=1536. The correlation sidelobes are 57.7 dB below the zero-lag value. The theoretical performance of this QCCS is about 6 dB better than the one reported by Sulzer and Woodman (1985), as shown below in Figure 4. The performance can be improved even further by using the subset of 104 codes in the base set with optimum correlation sidelobe levels. An example of a QCCS of 32 codes is appended as Table A-1. Despite its smaller size, its residual sidelobes at ±2 or -54.2 dB are slightly lower than the QCCS of 48 codes given by Sulzer and Woodman. QCCS of small size are desirable as they permit a larger Doppler bandwidth.
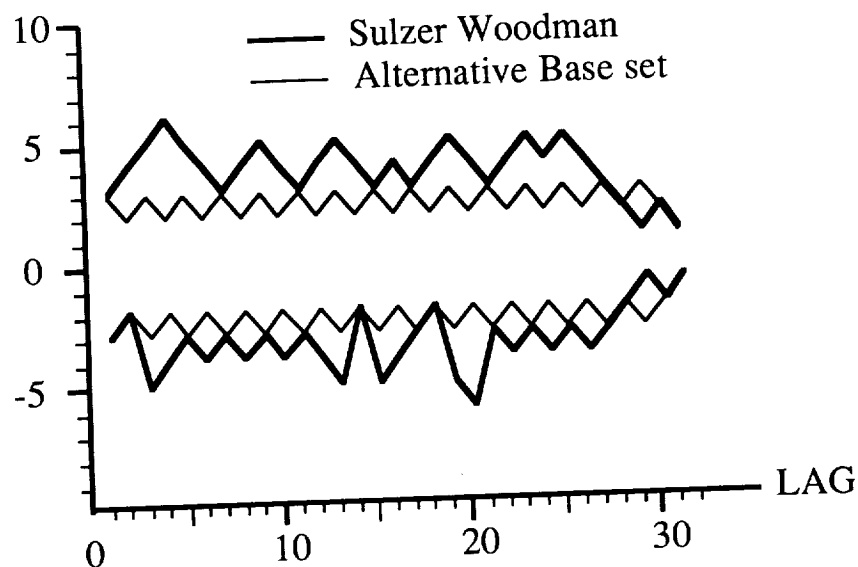
FIGURE 3. Envelope of correlation sidelobes for a 32-bit QCCS of 48 codes given by Sulzer and Woodman(1984), and for the alternative base set of 844 codes described in this paper.
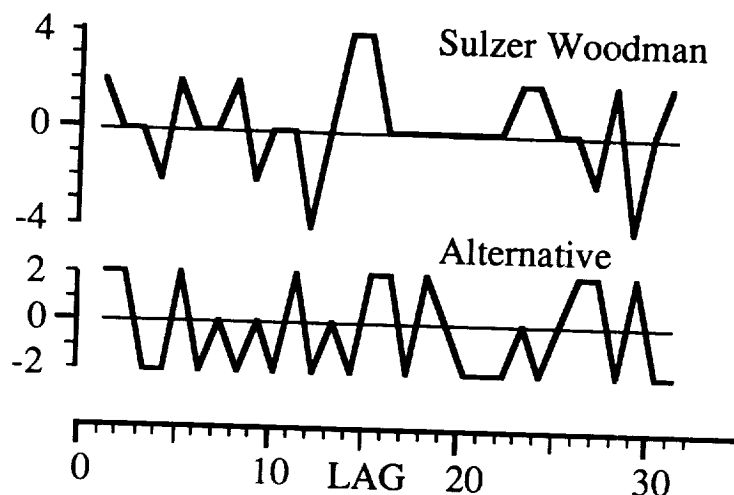
FIGURE 4. Residual sidelobes in the sum of autocorrelation functions for a 32-bit QCCS of size 48 given by Sulzer and Woodman (1984), and an for alternative set . The zero-lag value of 1536 is out of scale.

Discussion and Future Directions

In summary, we have found a base set of 32-bit codes with minimum absolute correlation sidelobes, and have identified a subset with low r.m.s correlation sidelobes. This base set has been used for obtaining many QCCS with better residual correlation sidelobe levels than reported earlier. These QCCS should be useful in middle-atmosphere experiments at any radar installation with pulse-by-pulse decoding capability.

QCCS of longer length, up to 64, may be useful for mapping the structure of weak Kelvin-Helmholtz instabilities in the mesosphere, and the transition region from turbulent scattering to incoherent scattering (at VHF). We have found a partial base set for 64-bit codes.

A selection criterion may further be imposed on these QCCS in terms of their ambiguity-function behavior. In UHF (430 MHz) radar experiments, a constant radial wind of 2.5 m/s produces a harmonic component of ~140 ms period. The phase change introduced by the medium in 35 ms is $\pm 90°$, comparable to the phase modulation imposed on the carrier. In probing a moving medium, the code performance is impaired even for small Doppler shifts. We are examining the ambiguity functions for QCCS to select the ones with better performance for Doppler measurements.

References

Barker, R. H., Group synchronizing of binary digital systems, in *Communication theory*, Ed. W. Jackson, Butterworth, London, 1953.

Golay, M. J. E, Complementary series, *IRE trans. Inf. Th.*, **IT-7**, 82-87, 1961.

Ioannidis, G. and D. T. Farley, Incoherent scatter observations at Arecibo using compressed pulses, *Radio Sci.*, **7**, 763-766, 1972.

Lindner, J., Binary sequences up to length 40 with best possible autocorrelation function, *Electronics Lett.*, **11**, 507, 1975.

Rastogi, P. K., A note on the use of coherent integration in periodogram analysis of MST radar signals, *Handbook for MAP*, **9**, Eds. S. A. Bowhill and B. Edwards, SCOSTEP Secretariat, Urbana, Ill., 509-512, 1983.

Sarwate, D. V., Construction of complementary code sequence sets, *Handbook for MAP*, **14**, Eds. S. A. Bowhill and B. Edwards, SCOSTEP Secretariat, Urbana, Ill., 266-267, 1984.

Schmidt, G., R. Rüster and P. Czechowsky, Complementary code and digital filtering for detection of weak VHF radar signals from the mesosphere, *IEEE trans. Geosci. Elect.*, **GE-17**, 154-161, 1979.

Sulzer, M. P. and R. F. Woodman, Quasi-complementary codes : A new technique for MST radar sounding, *Radio Sci.*, **19**, 337-344, 1984.

Tseng, C.-C. and C. L. Liu, Complementary sets of sequences, IEEE trans. Inf. Th., IT-18, 644-652, 1972.

Turyn, R., Sequences with small correlation, in *Error Correcting Codes*, Ed. H. B. Mann, Wiley, New York, 194-228, 1968.

Woodman, R. F., High-altitude resolution stratospheric measurements with the Arecibo 430-MHz radar, *Radio Sci.*, **15**, 417-422, 1980.

Appendix

The following table gives a sample QCCS. The residual correlation sidelobes are given in the figure.

TABLE A-1 : An Alternative 32-bit QCCS of 32-bit Codes

CODE	LVL	AUTOCORRELATION FUNCTION AT LAGS 1 TO 31
ce4b06a8	3	-3-2-3-2-1 2-1 0 3 2-1 2-1 2-1 0 1-2-3 2 1 2 1 0-3-2 1 2-1-2-1
a0bce244	3	1 0-1 2 1 0-3 0-3-2-1 0-3 0-3 2 3 0-1 0 1 2 3 0 3 0 3-2 1 0-1
af812462	3	1 2 3 2-1-2 1 2-1 2 3-2 1-2 1-2-1 2 3-2 1-2-3-2-1 2-3 2-3 2-1
87aa3124	3	-3 0-3 0-1 2 3 0-1-2 3 2 1 2-1-2-3 2 3-2 1-2 1 0-3 2 1 0 3 0-1
e6165cbf	3	3-2 1-2-1 2 3 0-1-2-1-2 3 0 3-2-3 0 1-2-3-2-3 0 1 2 1 2 3 2 1
dadceba0	3	-3 2 1 2 3 0-3 2 1 0-1 2-1 2-1 0 1-2-3 2-3 0 3-2-1 0-3-2-1-2-1
c3fd666b	3	3-2 1 2 1-2-3-2 3 2 1-2 3-2 3 0 1 2 1 2 3 2-3 2 3-2-1-2-1 2 1
9cf8156d	3	-1 2-1-2-1-2-1-2-3-2-3-2-3 0-1 2 1 0-1 2 3-2 3-2 1 2-3 2 1-2 1
8c3e9bb5	3	-1-2-1-2-3 0 3 0 1 2-1 2 1-2 3 0-3-2 3-2-3 2-1 0-3 0 3-2 1-2 1
ccb507df	3	3 2 3 0-1 0 1-2-3 2-3-2-3' 2-3-2 3-2-1 2-1-2 3 2-1 0 1 0 1 2 1
b42ebe73	3	-1 0-3-2 3 2-1 2 1-2 1-2 1 0-3 2 3 0-1 2-1 2-1-2 1-2 1 2-1 0 1
b4b9dfa2	3	-3 2 3 0 3-2 1-2 1-2 1 0-1 2-1-2-3 2 1 0 3 2-1 2-1-2 1 0-3 2-1
935387fd	3	3 2 3-2-1 0 3 2-1-2-1 0-1-2 3 2 1 2-3 0-3 2-3-2 1 0-3 2 1-2 1
84e126ae	3	-3-2-1 0-1 2-3 2-1 2 1 0 3 0-1 0-3 0 1 0 3-2-3 2-1-2-3 0 1 2-1
d1b473fb	3	3-2 1 0 1 2 3 2 1 2-1 0-3 0 1 0 3 0-1 0-3-2 3 2 1-2 3 0-1 2-1
8c2a0f64	3	1 0-3 0-3 0-3 0 1 2 1 2-1-2 3 2 1-2-3-2 3 2-1 0 3 0-1 0 3 0-1
8c5afe9b	3	-1 0 3 0 3 0 3 0-1 2-1 2 1-2-3 2-1-2 3-2-3 2 1 0-3 0 1 0-3 0 1
e16e6510	3	1-2-1 2 3-2-3-2 3 0 3-2-1 2-3 0-1-2-3 2 1 0 1-2 3 2 1-2-3-2-1
a9b6073d	3	-1-2 1-2-3 2-3-2-3-2-3-2 1 2 3-2-3 2 3-2 3-2-1 2-1-2 3-2 3-2 1
d5621270	3	-3 2-3 2 3-2 3 0 3 0 3-2-1 2 3-2-1 2 1 2 1-2-3 2-3 0 1 2 1-2-1-2-1
dac511f0	3	1 2-3-2-3-2-3-2 1 2 1 0-3-2 1-2-1 2 1 2 3 0-1-2 3 2-1 2-1-2-1-2-1
ddbbca0f	3	3 2 3 2-1 0 3 0-3-2-1 2-1 2 1 0 3-2 1-2 1-2-1 0 1 0 1 2 1 2 1
9655881c	3	-3 0-3 0 1 2 3-2 1-2 1 0 3 0-1 2 1 0-3 0-1 2 3 2-3-2-1 0 3 0-1
84e049ab	3	-1 0 3 0-1-2 1 2 1 2 3 0-1 2 3-2-3 2-3 0 1-2 3-2-1 2-3 0-3 0 1
c622e04b	3	3-2-3 2 1-2-3 0-1-2 3 2 1 2 1 2 3 2-1 2-3-2-3 0 3-2-1-2-1 2 1
cb2f5fc4	3	1 2 3-2-1 2 1 0 1 2-3-2 1-2 1-2-1-2 3-2-1 2 3 0 3-2-3 2 1-2-1
ea6c873f	3	3-2 1 2-3 2-1-2-1 2-3 0-3-2-3-2 3-2-1 0 3 2-3-2 1 2 3 2 3 2 1-2-1
b5a28330	3	-3 0 1-2 3 2 1 2 1-2 3 2 1 0-3 2-1 0 3 2-3-2-1 2-1-2 1-2-1 0-1
aed9cfc2	3	1-2-1 2-1 0-1 0 3-2-1 2 3-2 3 2 1 2 1-2 1-2-3 0 1 0-3 2-3 2-1
91282f38	3	1 0-1-2 3 0-1 0-3 2 1-2-1 0 3 2-3 0 3 2-1-2 3 0 1 0 1 2 1 0-1
ad88be7d	3	-1 2 1 2-3 0 1 2-1 0-3-2 1 2-3-2-1-2-1 2 3 0 1 2-1 0 3-2 3-2 1
8fb6c46a	3	-3-2 1 2-1-2 1-2 3-2 1-2-3-2-3-2 3-2-1 2 3 2-3-2-1 2-3 2-1 2-1

32   54.2 dB
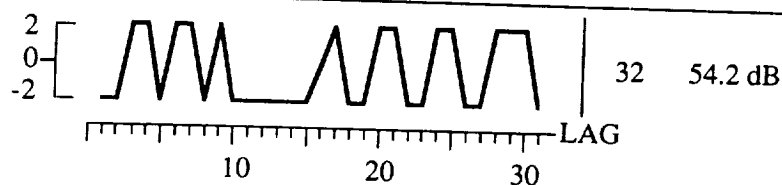
FLATLAND DATA ANALYSIS SYSTEM

W. L. Clark and J. L. Green

Aeronomy Laboratory
National Oceanic and Atmospheric Administration
Boulder, Colorado 80303

1. INTRODUCTION

A major effort of the Flatland radar project is to disseminate understanding and use of clear-air radar data to a broader academic and research community. Thus, it is important that the original and processed radar data be easily conveyed to a number of different users at a number of different facilities. This process of data communication can be greatly facilitated by providing not only numbers, but also a readily available platform (i.e., software and hardware) for displaying and analyzing them, thus eliminating redundant effort re-developing display and analysis systems.

To meet this need, we are developing an off-the-shelf "plug and play" workstation. Here, we describe the workstation as presently implemented for joint use of the Flatland data base between co-investigators in Colorado, Minnesota, and Illinois. We also discuss some problems associated with the rapidly changing computer technology.

2. FLATLAND DATA ANALYSIS SYSTEM

Implementation of the analysis system began in 1985. At that time, it was necessary to select a computer and the criterion in Table 1 were used. From the large selection of computer systems then available, the MacIntosh II^{tm} (^{tm} indicates a trademark, detailed in Table 3) and the Compaq Deskpro 386^{tm} computers seemed best suited. Others were either too expensive, not powerful enough, or not well enough supported with respect to needed peripherals. Although both the MacIntosh II and the Compaq 386 were new machines, the 386 was IBM-PC compatible, and so had a large software base, strong support, demonstrated user acceptance, and a clear indication of multiple manufacturers in the near future. The MacIntosh II, on the other hand, was supplied by only one manufacturer and had a different bus than the previous MacIntosh line. This made it uncertain that all the needed peripherals and software could be obtained. Consequently, the Compaq 386 was selected. At the present time, there are a number of manufacturers of these IBM PC-compatible 386 machines, most of which should be suitable for implementing a Flatland workstation. This computer choice still seems adquate in 1988.

Once the computer system was determined, a study was made to determine which high-level language was most suited to implementing a system on a PC-compatible. The decision was made by examining the available driver software for the peripherals needed, both for this workstation and to actually run and control the Flatland radar. The only language in common to all the devices needed was Microsoft C, which we selected. This led directly to the choice of GraphiC^{tm} as the plotting library package of choice.

TABLE 1
CRITERIA FOR COMPUTER SELECTION

* Computing Power
   - Speed: 10 MHz or faster clock
   - Memory available to user program 640 K or more
   - Open Architecture
       • Well Documented Bus
       • Available Expansion Slots
* Stability
   - Upgradability
       • Software Upward Compatible
       • Peripheral Interfaces Upward Compatible
   - Third Party Support
   - Good Track Record
* Cost
   - Computer
   - Software
   - Peripherals
* Availability
   - Computer
   - Software
       • High Level Languages
       • Well-documented and Debugged Operating System
       • Applications Libraries
       • Peripheral Drivers
   - Peripherals
       • 1600 cpi 9-track Tape Interface, Industry Compatible
       • Readily Available with Multiple Sources
   - Appropriate Commercial Packages
* General Acceptance in User Community

Much of the software for routine data analysis for such a workstation is experiment-dependent, and will be done in-house, utilizing Microsoft C. However, many scientific uses of the data are one-time uses, and although the inherent constraints of such packages in the past often hindered, rather than aided, the analysis, the savings inherent in avoiding development of I/O, command processing, and quality graphics products motivate us to at least evaluate the state-of-the-art commercial packages. We have had a chance to test GAUSS^{tm} and MATLAB^{tm}. Both seem to have the needed power and flexibility. Our preliminary choice is GAUSS because it is less expensive.

The exact make and model for the printer is not important, but parts of the system software may not work if Epson^{tm} FX compatibility is not available. Similarly, a plotter is most likely to be supported if it is HPGL^{tm} (HP Graphics Language) compatible.

The choice of a particular WORM optical disk drive system was somewhat arbitary. We chose a system that provides good performance per dollar spent and that seems to be gaining in popularity. However, which current system, if any, will become "industry standard" is uncertain. The Storage Dimensions LaserStor^{tm} optical subsystem uses 5.25" double-sided optical disks. Each side of the optical disk has an unformatted capacity of about 400 MBytes. Only one side is available at a time, since the disk must be turned over to gain access to the other side.

The 9-track tape drive interface has not yet been selected. Any 1600 cpi drive will work, but custom software may have to be written to support the interface card.

More specific identification of the components of the system are detailled in Table 2.

TABLE 2
FLATLAND DATA WORKSTATION COMPONENTS

I. Hardware
    A. Compaq 386 or compatible microcomputer
        1. 80386 CPU
        2. EGA color graphics card (VGA would be better)
        3. 40 MByte hard disk
        4. 1.2 MByte 5.25" floppy disk drive
        5. 3 MByte RAM
        6. 80387 numeric co-processor chip
    B. Storage Dimensions' LaserStor^{tm} LS800 Optical Disk Drive
    C. Epson FX-86e dot matrix printer (other Epson FX-compatibles would do)
    D. HP 7475A 6-pen plotter
II. Software
    A. MS-DOS operating system
    B. Microsoft program editor (other editors would also work)
    C. Microsoft C 5.1 compiler
    D. Scientific Endeavors' GraphiC^{tm} C plotting library
    E. Aptech Systems' GAUSS^{tm} 2.0 matrix handling system

3. SUMMARY

Today's personal computers have sufficient power to handle the data analysis requirements of the Flatland radar experiment. Because of the low cost so implied, and the easy availability of such systems, it is feasible to broaden the meaning of a data base to include the hardware and software on which it is manipulated. This should facilitate exchange of data among a broad set of co-investigators. We are partially through the process of implementing such a system, sharing data between stations in several states. The basic hardware and software platforms are detailed in Table 2. Although all of the components in this system are vulnerable to becoming obsolete through the advancement of technology, we feel the choices of an IBM-PC Compatible, 80386-based microcomputer, and the C programming language, are likely to continue as good choices for the next few years. The choices for data archiving and the commercial data processing package have a more uncertain future.

TABLE 3
TRADE MARKS

COMPAQ Deskpro	COMPAQ Computer Corporation
EPSON FX	Epson America, Inc. 2780 Lomita Boulevard Torrance, CA 90505
GAUSS	Aptech Systems, Inc. 26250 - 196th Place S. E. Kent, WA 98042 (206) 631-6679
GraphiC	Scientific Endeavors Corporation Route 4, Box 79 Kingston, TN 37763 (615) 376-4146
HP 7475A	Hewlett Packard San Diego Division 16399 West Bernardo Drive San Diego, CA 92127-9989
IBM-PC	International Busines Machines Corp. 1-800-447-4700
LaserStor	Storage Dimensions 2145 Hamilton Avenue San Jose, CA 95125-9870 (408) 979-0300
MacIntosh II	Apple Computer 10260 Bandley Drive Cupertino, CA 95014
MATLAB	The Math Works, Inc. 21 Eliot Street South Natick, MA 01760 (508) 653-1415
Microsoft C MS-DOS	Microsoft 10700 Northrup Way Bellevue, WA 98004

PREPARATION OF AN ARCHIVAL DATA BASE FOR THE POKER FLAT, ALASKA, MST RADAR

A. C. Riddle

Cooperative Institute for Research in the Environmental Sciences
University of Colorado
Boulder, Colorado 80305

K. S. Gage and B. B. Balsley

Aeronomy Laboratory
National Oceanic and Atmospheric Administration
Boulder, Colorado 80303

1. THE DATA

Data from the Poker Flat, Alaska, MST radar operated by the NOAA Aeronomy Laboratory have been recorded from March 1979 through June 1985. The raw data base included Doppler spectral information, but most analysis to date has been done using a "compacted" data base consisting only of quantities derived from the Doppler spectra. The derived quantities are the velocity, width and signal power of the greatest peak on the spectrum at each height (CARTER et al., 1983; CLARK AND CARTER, 1983). For many records the largest peak corresponds to a return signal from the atmosphere and the derived parameters are of great interest in studies of the atmosphere. These records we will call "genuine" signals. Where there is no return echo, the Doppler spectrum consists solely of random noise and the derived parameters contain no useful information regarding the atmosphere. These signals we shall call "noise". There also exist records for which the largest peak corresponds to power reflected from an aircraft, some interfering radio signal or other known or unknown causes. These signals we shall call "spurious". Most persons using the compacted data set would like to select and concentrate only on the genuine signal records and ignore the spurious and noise records.

2. SIMPLE SELECTION

The simplest selection technique commonly used to separate "genuine" signals from noise is based on the fact that the likelihood of a noise signal exceeding some threshold value is a decreasing function of the threshold level. By setting a threshold above which few noise signals are expected to exist, most noise signals can be eliminated. However, the higher and safer the threshold, the more genuine signals are eliminated from further analysis.

3. MORE COMPLICATED SELECTION

Use of other characteristic differences between noise and genuine signals allows more sophisticated selection processes to be developed. One such characteristic is the maximum expected velocity. However, for good technical reasons, the radar parameters are often set so that the maximum measurable velocity and maximum expected velocity are quite close. When this is the case, not much is gained by rejecting velocities greater than the maximum expected velocity.

Continuity of velocity is a characteristic which provides a similar but much more effective selection mechanism. When the timescale for significant variation of velocity is greater than the time between measurements, a very effective filter for removing noise can be made. The filter uses a velocity acceptance window whose center is an estimate of the current mean velocity and whose size is based on an estimate of the likely variation. Much of the Poker

Flat data analysis has been performed on data subjected to such a filter. For computational efficiency the window was centered at the running mean of the velocity and the size was based on a running mean of the absolute difference between the mean and the current value. The window size was constrained to be larger than a minimum value to accommodate the changing character of the wind field with time. This type of filter is very effective in removing what are commonly called "outliers". However, in common with other "consensus"-type filters, it is possible for the window to lock onto spurious data values when these values become both very frequent and reasonably consistent.

One characteristic of spurious signals that often distinguishes them from genuine signals is their rapid onset, often in many range gates simultaneously. A primitive selection process often used on Poker Flat data kept track of the total number of significant signals at each time and rejected records when the total number increased more rapidly than normal or exceeded some limit.

4.   THE CLEANING SELECTION PROCESS

For future analysis of the Poker Flat data it was decided that, rather than continue to subject the original data set again and again to a variety of selection algorithms, it would be better to subject the data set to an optimal cleaning process and save the resulting "cleaned" data set. In addition to providing users with a better data set containing a minimum of spurious or noise data, this approach minimizes the volume of data by not including any of the rejected data.

Encouraged by the success of the earlier algorithms we decided that the cleaning process should be an elaboration of those algorithms.

For a given receiver and time the apparent signal at each range is ranked according to signal strength. The rank takes the values 4 (if above threshold) through 3 (if in the range 3 dB below threshold), 2 (if in the range 3 dB below rank 3) and 1 (if even lower). The ranges with rank 1 echoes are used only to determine a background noise level as they almost certainly contain no genuine signals. At the same time, a record quality indicator is formed by examining the character of signals of ranks 3 and 4. As noted before, spurious signals often appear over many range gates and so a sudden increase in the number of signals of high rank may indicate spurious signals. Also, the presence of strong signals in the range 35 to 45 km, where there are normally no genuine signals, is a potential trouble indicator. The quality indicator ranges from 0 (spurious signals likely) to 3 (spurious signals unlikely). The quality in- dicator is also lowered for one set when adjacent sets have low values.

An additional indicator is now formed at each range by adding the signal ranks at that range for the ten data sets on each side of the one under con- sideration. This indicator essentially measures the likelihood of a significant echo at each range.

Now the signals of ranks 2 and 3 are examined in the light of the three indicators above. The rank is raised to 4 if the likelihood of significant echoes is high at this range or the two adjacent ranges on either side. It is lowered to 1 if the same likelihood measures are low. The criteria for raising or lowering are more or less stringent according to both the original rank and the quality indicator for that record. This process tends to select as genuine those signals occurring in close proximity to other genuine signals, while at the same time rejecting spurious signals that occur at many heights or occur randomly   The process is without directional bias in that time or range order could be reversed without changing the results. The drawback is that it tends to reject meteor echoes which, because of their random occurrence characteris- tic, look more like noise than genuine signals. However, as many meteor echoes

span several range gates, or are very strong, the criteria still do pass many meteor echoes.

Having made an initial selection, attention is turned to the velocity and width parameters. The window filter described earlier is applied separately to each parameter. In order to keep the amount of computation within reasonable bounds the running mean and absolute deviation technique of the simpler selection process are used. However, in an attempt to reduce the directional sensitivity of that process, a contribution is added at each step from a data set in advance of the one under consideration. An added refinement is that the contributions are weighted according to the quality indicator, more weight being given to the data of higher quality. Only when both velocity and width parameter values are within the appropriate window is the signal accepted as genuine. After each height has been examined, the window mean and size values are subjected to a smoothing filter (as a function of range). At all ranges a simple triangular weighted boxcar is applied. This smoothing takes advantage of the continuity of the data in range and is useful to help prevent the windows locking on to persistent spurious data values. Such bad values are quite common in the two lower range gates where receiver saturation often generates false peaks in the spectra. At ranges for which there is no genuine signal, an additional component of the filter ensures that the window mean tends towards zero and the window size to the lower limit. This ensures that after a significant data gap the filter is not biased towards data values that existed previously. The window lower limits are different below and above 40 km and also different for vertical and oblique data to accommodate the different character of the data in these ranges. Because the timescale for parameter variation in the vertical data is closer to the typical sampling period (1 min.), the window filters are slightly less effective on the vertical data than on the oblique data.

Operation at Poker Flat was such that aliasing, although not common, was occasionally present in the records. While examining the velocity in the step above, the data are examined for potential aliasing, which is corrected if found.

Start up for the process filters is accomplished by letting the program see a mirror image copy (i.e., time reversed) of the first ten data sets. At the end of a contiguous set of data a similar mirror ensures that the process can operate up to the final set of data records. A break in the data is assumed to occur whenever a time gap larger than 30 minutes existed, or whenever the instrument parameters changed significantly.

After the computer program has made its decisions, the data are displayed in two panels. In the first the velocity for all signals originally of rank 3 or 4 is presented. This data is more than normally would be accepted by the simpler selection processes and contains a higher percentage of spurious or noise signals than is usually considered reasonable. However, it allows the operator to get a good picture of the character of the data at that time. On the second panel is displayed the data selected by the computer using the algorithms above. The operator can remove any of the data on that display which still seems to be spurious. When the operator has finished examining the data the remaining acceptable data are written to tape and are used as the basis for the "cleaned" data set.

The program currently takes about one hour on a Sun workstation to process the data originally collected in one day. Although onerous, this is an acceptable level of effort.

5. ACKNOWLEDGEMENT

6. REFERENCES

Carter, D.A., B.B. Balsley, and W.L. Ecklund (1980), The Poker Flat MST Radar: Signal analysis and data processing technique with examples, Preprint volume, AMS 19th Conference on Radar Meteorology, April 15-18, Miami Beach, FL, 563-567.

Clark, W.L., and D.A. Carter (1980), Real time scaling of atmospheric parameters from radars using the MST technique, Preprint volume, AMS 19th Conference on Radar Meteorology, April 15-18, Miami Beach, FL, 599-604.

AUTHOR INDEX

CUMULATIVE LISTING FOR THE MAP HANDBOOK

Volume	Contents	Publication Date
1	National Plans, PMP-1 , PMP-2, PMP-3 Reports, Approved MAP Projects	June 1981
2	Symposium on Middle Atmosphere Dynamics and Transport	June 1981
3	PMP-5, MSG-1, MSG-2, MSG-3 Reports, Antarctic Middle Atmosphere Project (AMA), EXOS-C Scientific Observations, WMO Report No. 5., Updated Chapter 2 of MAP Planning Document, Condensed Minutes of MAPSC Meetings	November 1981
4	Proceedings of MAP Assembly, Edinburgh, August 1981 Condensed Minutes of MAPSC Meetings, Edinburgh, Proceedings of MAP Open Meeting, Hamburg, August 1981,	April 1982
5	A Catalogue of Dynamic Parameters Describing the Variability of the Middle Stratosphere during the Northern Winters	May 1982
6	MAP Directory	November 1982
7	Acronyms, Condensed Minutes of MAPSC Meetings, Ottawa, May 1982, MAP Projects, National Reports, Committee, PMP, MSG, Workshop Reports, Announcements, Corrigendum	December 1982
8	MAP Project Reports: DYNAMICS, GLOBUS, and SSIM, MSG-7 Report, National Reports: Czechoslovakia, USA	July 1983
9	URSI/SCOSTEP Workshop on Technical Aspects of MST Radar, Urbana, May 1983	December 1983
10	International Symposium on Ground-Based Studies of the Middle Atmosphere, Schwerin, May 1983	May 1984
11	Condensed Minutes of MAPSC Meetings, Hamburg, 1983, Research Recommendations for Increased US Participation in the Middle Atmosphere Program, GRATMAP and MSG-7 Reports	June 1984
12	Coordinated Study of the Behavior of the Middle Atmosphere in Winter (PMP-1) Workshops	July 1984
13	Ground-Based Techniques	November 1984
14	URSI/SCOSTEP Workshop on Technical Aspects of MST Radar, Urbana, May 1984	December 1984
15	Balloon Techniques	June 1985
16	Atmospheric Structure and its Variation in the Region 20 to 120 km: Draft of a New Reference Middle Atmosphere	July 1985
17	Condensed Minutes of MAPSC Meeting, Condensed Minutes of MAP Assembly, MAP Project, MSG, and National Reports	August 1985
18	MAP Symposium, Kyoto, November 1984	December 1985
19	Rocket Techniques	March 1986
20	URSI/SCOSTEP Workshop on Technical and Scientific Aspects of MST Radar, Aguadilla, October 1985	June 1986
21	MAPSC Minutes, ATMAP Workshop, Atmospheric Tides Workshop, MAP/WINE Experimenters Meetings, National Reports: Coordinated Study of the Behavior of the Middle Atmosphere in Winter	July 1986 July 1986
22	Middle Atmosphere Composition Revealed by Satellite Observations	September 1986
23	Condensed Minutes of MAPSC Meetings, Toulouse, June/July 1986	December 1986
24	MAP Directory	May 1987
25	First GLOBMET Symposium, Dushanbe, August 1985	August 1987
26	MAPSC Minutes, Abstracts and Report of Workshop on Noctilucent Clouds, Boulder,	June 1988 October 1985
27	COSPAR Symposium 6, The Middle Atmosphere After MAP,Espoo, July 1988, MAPSC Minutes, Espoo, July 1988; Workshop on Noctilucent Clouds, Tallinn, July 1988	April 1989
28	URSI/SCOSTEP Workshop on Technical and Scientific Aspects of MST Radar, Kyoto, November/December 1988	August 1989